

Hanlong Liu
An Deng
Jian Chu
Editors

Geotechnical Engineering for Disaster Mitigation and Rehabilitation

Proceedings of the 2nd International
Conference GEDMAR08, Nanjing, China

 Science Press
Beijing

 Springer

Geotechnical Engineering for Disaster Mitigation and Rehabilitation

**Proceedings of the 2nd International
Conference GEDMAR08, Nanjing, China
30 May – 2 June, 2008**


Geotechnical Engineering for Disaster Mitigation and Rehabilitation

**Proceedings of the 2nd International
Conference GEDMAR08, Nanjing, China
30 May – 2 June, 2008**

Editors:

**Hanlong Liu
An Deng
Jian Chu**

**Sponsored by National Natural Science Foundation of China
Books Series of National Key Subject in Geotechnical Engineering**

 **Science Press
Beijing**

 **Springer**

EDITORS:

Hanlong Liu

Hohai University
College of Civil Engineering
Nanjing, Jiangsu 210098, China

An Deng

Hohai University
College of Civil Engineering
Nanjing, Jiangsu 210098, China

Jian Chu

Nanyang Technological University
School of Civil and Environmental Engineering Block
N1, 50 Nanyang Ave, Singapore 639798

ISBN 978-7-03-021634-2 Science Press Beijing
ISBN 978-3-540-79845-3 Springer Berlin Heidelberg New York
e ISBN 978-3-540-79846-0 Springer Berlin Heidelberg New York

Library of Congress Control Number: 2008926088

This work is subject to copyright. All rights are reserved, whether the whole or part of the material is concerned, specifically the rights of translation, reprinting, reuse of illustrations, recitation, broadcasting, reproduction on microfilm or in any other way, and storage in data banks. Duplication of this publication or parts thereof is permitted only under the provisions of the German Copyright Law of September 9, 1965, in its current version, and permission for use must always be obtained from Springer-Verlag. Violations are liable to prosecution under the German Copyright Law.

© 2008 Science Press Beijing and Springer-Verlag GmbH Berlin Heidelberg

Co-published by Science Press Beijing and Springer-Verlag GmbH Berlin Heidelberg

Springer is a part of Springer Science+Business Media

springer.com

The use of general descriptive names, registered names, trademarks, etc. in this publication does not imply, even in the absence of a specific statement, that such names are exempt from the relevant protective laws and regulations and therefore free for general use.

Cover design: Frido Steinen-Broo, EStudio Calamar, Spain

Printed on acid-free paper

PREFACE

This 2nd International Conference on Geotechnical Engineering for Disaster Mitigation and Rehabilitation (GEDMAR08), held at the Hohai University, Nanjing, China from 30 May to 2 June, 2008, is one of the activities of International Society for Soil Mechanics and Geotechnical Engineering (ISSMGE) Technical Committee TC39: Geotechnical Engineering for Coastal Disaster Mitigation and Rehabilitation. It is organized jointly by Hohai University, Chinese Institution of Soil Mechanics and Geotechnical Engineering (CCES), and Chinese Society of Environmental Geotechnics (CSRME) under the support of TC39, TC4 on Earthquake Geotechnical Engineering and Associated Problems, and the Joint Working Group on Geotechnical Engineering for Disaster Mitigation and Rehabilitation (JWG-DMR). This conference is the second in the series. The first conference was held at the Furama Riverfront Hotel in Singapore from 12-13 December 2005.

One hundred and forty-four papers from 20 countries and regions are included in this Proceedings. The papers were selected from more than 200 abstract submissions after a rigorous review process. This Proceedings contains 7 keynote and special invited plenary lectures written by international renowned experts and 18 special session and invited papers that reflect the special topics discussed in this conference. Not all the keynote or invited papers are included in this Proceedings due to various constraints. The other 119 papers cover a range of topics including disasters related to earthquake, landslide, soil dynamics, risk assessment and management, slopes, disaster mitigation and rehabilitation and others.

It is hoped that this Proceedings will be a useful source of reference to geotechnical engineers and professionals in other disaster related fields.

Editors

H.L. Liu, A. Deng and J. Chu

ACKNOWLEDGEMENTS

The Editors gratefully acknowledge the significant contributions from the following people and organizations:

- Staff of GeoHohai and Hohai University for their support in organizing this conference;
- Chinese Institution of Soil Mechanics and Geotechnical Engineering (CCES) and Chinese Society of Environmental Geotechnics (CSRME) for co-hosting the conference;
- Members of Conference Steering Committee, members of ISSMGE TC39: Geotechnical Engineering for Coastal Disaster Mitigation and Rehabilitation, members of ISSMGE TC4: Earthquake Geotechnical Engineering and Associated Problems, in particular, Professor Takaji Kokusho, Chair of TC4, and members of the Joint Working Group on Geotechnical Engineering for Disaster Mitigation and Rehabilitation (JWG-DMR) for their support to the organization of this conference;
- Members of the International Advisory Committee, in particular, Professor P. S. Sêco e Pinto, President of ISSMGE, Professor M. R. Madhav, Vice-President for Asia, ISSMGE for their support and advice, and Prof. Jie Han, The University of Kansas, USA, for his advice and help on conference organization;
- Keynote lecturers and invited special plenary lecturers;
- Special session organizers, special session speakers, invited speakers and panelists;
- Sponsors, National Natural Science Foundation of China and Hohai University, for their generous sponsorship;
- Supporting staff and students to the conference, in particular, Mr Liang Chen.

CONFERENCE ORGANIZERS

Hohai University, China
Chinese Institution of Soil Mechanics and Geotechnical Engineering, CCES
Chinese Society of Environmental Geotechnics, CSRME

SUPPORTING ORGANIZATIONS

TC-39 on Geotechnical Engineering for Coastal Disaster Mitigation and Rehabilitation
TC-4 on Earthquake Geotechnical Engineering and Associated Problems, and
The Joint Working Group on Geotechnical Engineering for Disaster Mitigation and
Rehabilitation (JWG-DMR)

ORGANIZING COMMITTEE

Chair: H.L. Liu (HHU)
Co-Chairs: J.M. Zhang (TSU), M.T. Luan (DLUT)

Y.Q. Cai (WZU)	A.B. Huang (NCTU)	S.Y. Liu (SEU)	X.M. Yuan (IEM)
Z.Y. Cai (NHRI)	H.W. Huang (TONGJI)	C.W.W. Ng (HKUST)	Z.Q. Yue (HKU)
G.X. Chen (NJUT)	M.S. Huang (TONGJI)	C.A. Tang (DLUT)	L.M. Zhang (HKUST)
L.Z. Chen (SJU)	R.Q. Huang (CDUT)	M.Y. Wang (UST)	Y.X. Zhang (CQU)
Y.M. Chen (ZJU)	L.W. Kong (WHRSM)	L.M. Wang (GSSB)	M.H. Zhao (HNU)
X.L. Du (BUT)	N. Li (XUT)	X.G. Wang (IWHHR)	G. Zheng (TJU)
X.T. Feng (WHRSM)	S.C. Li (SDU)	J. Xu (CNMEG)	C.B. Zhou (WHU)
Y.F. Gao (HHU)	W.H. Li (NSFC)	Y.P. Yao (BUAA)	
M.C. He (CMU)	H.D. Liu (NCWU)	J.H. Yin (HKPU)	

Secretaries: A. Deng (HHU), T. Zhang (HHU)

CONFERENCE STEERING COMMITTEE

J. Chu (Chair, TC39, Singapore)	T. Kokusho (Chair, TC4, Japan)	D. Bergado (Thailand)
K.K. Phoon (Secretary, TC39, Singapore)	A. Ansal (Co-Chair, TC4, Turkey)	C.T. Chin (Taiwan, China)
D. De Groot (USA)	R. Boulanger (USA)	M.M. Kim (Korea)
M. De Puy (Panama)	A. Pecker (France)	S.R. Kim (Korea)
B. Indraratna (Australia)	K. Pitilakis (Greece)	M.R. Madhav (India)
H.L. Liu (China)	M. Romo (Mexico)	H.G.P.A. Ratnaweera (Sri Lanka)
S.C.R. Lo (Australia)	I. Towhata (Japan)	N. Seneviratne (Sri Lanka)
F. Nadim (Norway)	R. Verdugo (Chile)	Y.C. Tan (Malaysia)
H. Ohta (Japan)	S. Yasuda (Japan)	S. Wardani (Indonesia)
W. Sengara (Indonesia)		J.M. Zhang (China)

INTERNATIONAL ADVISORY COMMITTEE

P. S. Sêco e Pinto (President, ISSMGE)	T.A. Ooi (Malaysia)
M.R. Madhav (Vice-President for Asia, ISSMGE)	J. Otani (Japan)
G. Auvinet (Mexico)	J. Pappin (China)
A.S. Balasubramaniam (Australia)	Q.H. Qian (China)
Z.Y. Chen (China)	R.B. Seed (USA)
G. Filz (USA)	K.H. Stokoe (USA)
V.T. Frits (The Netherland)	F. Tatusoka (Japan)
S.R. Ghandi (India)	T.M. Thu (Vietnam)
J. Han (USA)	W.H. Ting (Malaysia)
B.M. Hutapea (Indonesia)	D.G. Toll (UK)
S. Iai (Japan)	S. Varaksin (France)
K. Ishihara (Japan)	S.J. Wang (China)
F. Kulhawy (USA)	K.Y. Yong (Singapore)
S. Lacasse (Norway)	H.S. Yu (UK)
M.L. Lin (China)	Z.M. Zhang (China)
Z.C. Moh (China)	A. Zhusupbekov (Kazakhstan)

CONTENTS

Preface

Acknowledgements

Qian Jiahuan Lecture

Flow Slides of Underwater Sand Deposits in Jamuna River Bed3
Kenji Ishihara

Keynote and Special Invited Plenary Lectures

Interaction Between Eurocode 7 - Geotechnical Design
and Eurocode 8 – Design for Earthquake Resistance of Foundations.....37
P.S. Sêco e Pinto

Liquefaction Mitigation Of Sand Deposits by Granular Piles- An Overview 66
M. R. Madhav, A. Murali Krishna

Estimation of Liquefaction-Induced Settlement of River
Dikes and Their Effect in Lowland Area During Earthquakes..... 80
Susumu Yasuda

Mitigation of Seismic Damage of River Dikes..... 96
Yasushi Sasaki

Some Aspects of the Mitigations and Rehabilitations
of Natural Disasters in Malaysia 116
T.A.Ooi

Seismic Performance Evaluation of Geotechnical Structures 134
Susumu Iai, Tetsuo Tobita

Invited or Special Session Lectures

Debris-Budget-Based Debris-Flow Susceptibility Analysis 145
Jia-Jyun Dong, Chyi-Tyi Lee, Kuang-Ping Lin and Yu-Hsiang Tung

Geosynthetic Reinforcement for Riverside Slope Stability
of Levees due to Rapid Drawdown 153
Jie Han, Jianfeng Chen and Zhenshun Hong

Study on Earthquake and Typhoon Induced Regional Debris Flows in Ta-Chia River, Taiwan	159
<i>Ming-Chin Ho, Chien-Jung Chen, Yei-Sain Lee, Cheng-Yu Ku and Sue-Yung Chi</i>	
Instrumented Full Scale Test and Numerical Analysis to Investigate Performance of Bamboo Pile-Mattress System as Soil Reinforcement For Coastal Embankment on Soft Clay	165
<i>Masyhur Irsyam, Sugeng Krisnanto and S. P. R. Wardhani</i>	
Progressive Damage Simulation of Foundation Pile of The Showa Bridge Caused by Lateral Spreading During the 1964 Niigata Earthquake	171
<i>Motoki Kazama, Noriaki Sento, Ryosuke Uzuoka and Makoto Ishimaru</i>	
Earthquake-Induced Submarine Landslides in View of Void Redistribution	177
<i>Takaji Kokusho, Tetsuya Takahashi</i>	
Landslide Hazard Mapping Using Monte Carlo Simulation- A Case Study in Taiwan.....	189
<i>Chia-Nan Liu</i>	
Statistical Evaluation for Strength of Pile by Deep Mixing Method	195
<i>Yong Liu, Junjie Zheng and Jia Guo</i>	
Limited Flow Behaviour of Sand with Fines under Monotonic and Cyclic Loading.....	201
<i>S. R.Lo, M.D. Mizanur Rahman and D. Bobei</i>	
Travel Distance of Debris Flows Triggered by Slope Failures	210
<i>Hideki Ohta, Hirohiko Kusaka, Yutaka Miura, Katsumi Ohkubo, Masaru Takemoto and Kiyoyuki Amano</i>	
Some Numerical Considerations in Unsaturated Slope Stability Analysis due to Rainfall Infiltration	216
<i>Kok Kwang Phoon, Yonggang Cheng</i>	
Probabilistic Seismic and Tsunami Hazard Analysis for Design Criteria and Disaster Mitigation in Rehabilitation and Reconstruction of a Coastal Area in City of Banda Aceh	224
<i>I. Wayan Sengara, Hamzah Latief and Syahril B.Kusuma</i>	
Some Case Studies on Debris Flow in Peninsular Malaysia	231
<i>B.K. Tan, W.H. Ting</i>	

Gps/Gis Integration Used to Establish a Disaster Risk Mapping System for Nantou County in Central Taiwan	236
<i>Kuang-Jung Tsai, Kun-Ting Chen and Chin-Chuan Lin</i>	
Types of Flowslide Failures and Possible Failure Mechanisms	244
<i>Dariusz Wanatowski, Jian Chu and Robert S.C. Lo</i>	
Disaster Management in Central Java Province, Indonesia.....	254
<i>S.P.R. Wardani, R.J. Kodoatie</i>	
On the Relationship between Reliability Indices for Ultimate and Serviceability Limit States of Building Foundations	260
<i>Yu Wang, Fred H. Kulhawy</i>	
Planning Slope Stabilization Actions	268
<i>Limin Zhang, Dianqing Li</i>	
Earthquakes and Soil Dynamics	
Modeling of Stress-Strain Behavior of Soft Clay under Cyclic Loading	277
<i>Yuanqiang Cai, Jun Wang</i>	
Analysis and Evaluation of Ground Vibration Response Induced by Rapid Rail Transit	284
<i>Bin Chen, Guoxing Chen and Xiaomei Su</i>	
Dynamic Shear Modulus and Damping Ratio of Recently Deposited Soils in the Coastal Region of Jiangsu Province	294
<i>Guoxing Chen, Binghui Wang and Jianda Liu</i>	
Experiment on Earthquake-Induced Permanent Deformation of Nanjing Recently Deposited Muddy Soil	301
<i>Guoxing Chen, Dinghua Zhu, Junjian Shi and Xuezhu Liu</i>	
Probabilistic Evaluation of Earthquake-Induced Liquefaction Potential for Large Region Site Based on Two-Dimensional Gis Technique.....	309
<i>Guoxing Chen, Hao Tang</i>	
Evaluation of Liquefaction Potential of Pond Ash.....	315
<i>Ashim Kanti Dey, S. R. Gandhi</i>	
Analysis on Dynamic Response of Cast-in-Place Concrete Thin-Wall Pipe Pile Composite Foundation under Lateral Seismic Excitation	321
<i>Xuanming Ding, Hanlong Liu</i>	

The Analysis of Composite Foundation with CFG and Gravel Piles to Resist Soil Liquefaction	327
<i>Yuqin Feng, Yinghao Wang and Chunmei Zhang</i>	
Computation of Passive Earth Pressure of Cohesive Backfill on Retaining Wall Considering Earthquake Force	333
<i>Zhen Feng, Na Wang and Lianjun Wang</i>	
Applicability of Newly-Developed Instrument for Microtremor Measurements to Estimate the Loosened Zone in Shallow Ground	339
<i>Taiji Hanakawa, Seiji Kano, Toshikazu Sawamatsu and Koji Ichii</i>	
Experimental Study on the Relationship between Degree of Saturation and P-Wave Velocity in Sandy Soils	346
<i>Munenori Hatanaka, Takemi Masuda</i>	
Effects of Anisotropic Consolidation and Initial Shear Load on Liquefaction Resistance of Sand in Simple Shear Condition	352
<i>Yasuyo Hosono, Mitsutoshi Yoshimine</i>	
The Research on Dynamic Rheological Mechanical Response and Rheological Dynamic Model of Geological Disaster of Soft Rock-Soil	359
<i>Hua Hu, Hengxing Gu and Dengrong Yu</i>	
Seismic Responses of Bridge Pier Considering the Effect of Hydrodynamic Pressure	367
<i>Furong Li, Guoxing Chen and Zhihua Wang</i>	
Numerical Study on Sandpile Formation of Granular Materials with Different Grain Size Distributions	374
<i>Jun Liu, Jing Zhou</i>	
Analysis of Seismic Disaster of Masonry Pagodas	381
<i>Junlong Lu, Yin Zhang and Qianfeng Yao</i>	
Liquefaction of Sand under Bi-Directional Cyclic Loading	387
<i>Maotian Luan, Dan Jin, Zhendong Zhang and Qiyi Zhang</i>	
Earthquake Shocks and Liquefaction Threat to Dha and Clifton Areas, Karachi Pakistan. a Case Study	398
<i>Syed Amir Mahmud, Shamim Ahmed Sheikh</i>	

Study on Dynamic Properties of Saturated Clay and Undisturbed Silty Clay.....	406
<i>Ying Nie, Maotian Luan, Qi Shao, Shujie Liu and Meng Wang</i>	
Numerical Simulation of Dynamic Compaction Using Ls-Dyna.....	412
<i>Xiayong Qin, Maotian Luan, Qing Yang, Xiaojie Li and Zheng Zhao</i>	
Axial Vibration of Floating Pile Groups with Flexible Caps.....	421
<i>Q. Ren, M.S. Huang</i>	
Estimation of Ground Motion Parameters for Muzaffarabad Earthquake, Pakistan on 8th OCTOBER 2005	427
<i>D. Neelima Satyam, K.S. Rao and M.R. Madhav</i>	
Effective Stress Analysis for the Effects of Liquefaction Condition on Ground Motions	433
<i>J. Z. Sun, G. L. Shi</i>	
Influence of Cushion on Dynamic Response of Cast-in-Place Concrete Thin-Wall Pipe Pile Composite Foundation under Lateral Seismic Excitation	439
<i>Huiming Tan, Hanlong Liu</i>	
Numerical Modelling of Seismic Performances of Passive Pile Groups Adjacent to Soil Slope	446
<i>Mingwu Wang, Li Li</i>	
Dynamic Behaviour of Rigidly-Capped Pile Groups of Vertical and Rocking Oscillations.....	452
<i>Bin Yan, Lihua Liu, Xiaotong Peng and Mingdong Wang</i>	
Effects of Single Joint with Different Nonlinear Normal Deformational behaviors on P-Wave Propagation	458
<i>J. Yu</i>	
Geotechnical and Seismic Hazard Study for a Marine Site Development in Southern California.....	466
<i>Endi Zhai, Liping Yan</i>	
Numerical Analyses of Dynamic Response of Saturated Porous Seabed-Pipeline Interaction under Seismic Loading.....	472
<i>Xiaoling Zhang, Maotian Luan</i>	

Landslides and Slopes

Deformation and Stability Analyses of a Pile Supported T-Wall with Deep Mixed Shear Panels in Plaquemines Parish, Louisiana.....	481
<i>Tiffany E. Adams, George M. Filz, Peter R. Cali and Mark L. Woodward</i>	
Analysis of Typical Expansive Soil Slope Project.....	487
<i>Liang Chen, Pei Zhang and Sheng Lu</i>	
Study on Parameters Sensibility Analysis Model of Landslide Stability Considering Correlation	492
<i>Shengguo Cheng, Xianqi Luo</i>	
Evaluation of Bianloo Landslide Using Cellular Automata	497
<i>A. Fahimifar, M. A. Bahri</i>	
The Limit Analysis of Reinforced Slopes	502
<i>Xiaojing Feng, Qing Yang</i>	
Study on Rainwater Infiltration in Subsoil of Sandy Slopes during Rainfall by Field Monitoring	508
<i>Thi Ha, Yasushi Sasaki, Takashi Tsuchida and Seiji Kano</i>	
Acid Mine Drainage Erosion and Earthquake Coupling Action to Slope in Rich Sulfide Open Pit	516
<i>Lichun Jiang, Jilong Zhang</i>	
Danger of the Landslide Activity of Slopes on the Railway Line China – Kyrgyzstan – Uzbekistan on Site Karasu-Torugart	526
<i>K.Ch. Kojogulov, O.V. Nikolskay</i>	
Study on Uplift Test of Pressure-Dispersive Prestressed Cable in Slope Reinforcement Project.....	533
<i>Wei Li, Haigui Kang</i>	
Application of in Situ Stress Regression Method in Rock Slope Stability Analysis	540
<i>Yao Liang, Depei Zhou, Tao Yang and Gang Zhao</i>	
Displacement Characteristic of Soil Slope in Shear Strength Reduction Method Based on Mohr-Coulomb Model.....	546
<i>Hang Lin, Ping Cao, Jiangteng Li and Xueliang Jiang</i>	

An Interface Model to Predict the Stability of Landslide with Weak Intercalated Layer	552
<i>Yulong Luo, Hua Peng</i>	
Catastrophe Evaluation of Landslide Instability	559
<i>Qiang Ren, Weiya Xu</i>	
Nonlinear Finite Element Reliability Analysis of Slope Stability	565
<i>Xiaohui Tan, Jianguo Wang</i>	
Finite Element Analysis of Strain Localization Problems for Slope Based on Cosserat Continuum Model	572
<i>Hongxiang Tang, Daguo Wang</i>	
Evaluation of In-Situ Shear Strength of Natural Slopes Vulnerable to Heavy Rainfall by Lightweight Dynamic Cone Penetrometer	578
<i>Takashi Tsuchida, A.M.R.G. Athapaththu, Seiji Kano and Kazuaki Suga</i>	
The Visualization Study of a Green Slope System	585
<i>Baocheng Wei, Zhende Zhu and Qing Wang</i>	
Application of Nonlinear Time Series Analysis in Slope Deformation Analysis and Forecast	591
<i>Jia Xu, Fenghai Ma</i>	
The 3-D Stochastic Analysis of Progressive Failure of Rock Slopes	597
<i>Lingqiang Yang, Jing Ma and Zuping Chen</i>	
Numerical Simulation Analysis on Stability of a Surrounding Rock of Underground Cavities	603
<i>Yisi Zhuge, Xiutong Chen</i>	
Mitigation and Rehabilitation	
Recovery of Anisotropic Slope after The Landslide	611
<i>Rysbek Baimakhan, Nargozy Danaev, Aigerim Baimakhan, Gulnaz Salgaraeva, Gulaym Ylyasova, Nurgul Kurmanbekkizy, Ainagul Kozhebayeva, Zhumazhan Kulmaganbetova, Beket Zhakashbayev and Sarandulam Dashdorj</i>	
Mining Environment Regeneration and Induced Caving Technology in Mine Engineering	616
<i>Feng Gao, Keping Zhou and Qingfa Chen</i>	

Vibration Isolation Behavior of EPS Reinforced Highway Embankments.....	622
<i>Hongmei Gao, An Deng and Hanlong Liu</i>	
A Repairing Method for the Clay Landslide in Shaoguan of Guangdong Province	630
<i>Jian Gao, Jiaoli Zhu and Jian Pan</i>	
Improving Soft Soil Using Concrete-Cored Sand-Gravel Pile Composition Foundation	637
<i>Yunfei Guan, Jin Yu</i>	
Study on Relationship between Wheel Load and Rut Depth of Geogrid-Reinforced Unpaved Road.....	642
<i>Youchang Hu</i>	
Research on The Characteristics of the Subsidence of Soft Soil Foundation in Yangtze River Delta Area Based on Original Position Monitor.....	648
<i>Chenguang Jiang, Yong He</i>	
Breakage Mitigation Method for Culverts under High Embankments Using EPS Geof foam.....	654
<i>Fenglin Jiang, Anquan Gu</i>	
Rehabilitation of the Tower of Pisa, My Methods	660
<i>Wuyi Jiao</i>	
The Analysis of Geological Calamity and Countermeasures for Nanping City Fujian Province	669
<i>Baoming Jin</i>	
Coastal Barrier Island Creation/Augmentation as a Mitigation Means of Mainland Disaster Protection Against Water and Wind Forces	675
<i>Randy A. Knott</i>	
Evaluation of Disaster Assistance Projects Involving the Engineering Community in Reconstruction and Prevention.....	683
<i>Bastiaan De Laat, Claudine Voyadzis and Baris Trak</i>	
Case Study of Movement and Damage to a Residential Building Founded on Expansive Clays.....	689
<i>Jie Li</i>	

Study on Electrical Resistivity Related Parameters of Contaminated Soils	695
<i>Songyu Liu, Lei Chen and Lihua Han</i>	
Monitoring and Feedback for Ground Freezing and Pile-support Deep Foundation Pit.....	702
<i>Jianhong Lu, Yanrong Zhao and Baoyuan Yuan</i>	
Soil Improvement for Damage Mitigation along Izmit Bay during the 1999 Kocaeli Earthquake.....	709
<i>James R. Martin II, C. Guney Olgun</i>	
Mitigation System of Coal Bumping in Mining Extremely Thick Coal Seam.....	717
<i>Hua Nan, Ying Zhou</i>	
A New Kind of Three-Dimensional Steel Bar Shotcrete Liningand its Application in Soft Rock Tunnels	724
<i>Jianyong Pang</i>	
Temperature Crack Control Analysis for Pedestal in Jinping-1 High Arch Dam Engineering.....	735
<i>Sheng Qiang, Yueming Zhu, Ting Hu and Zhantao Shao</i>	
Geotextile Reef as a Coastal Protection Against Tsunami	742
<i>Agnieszka Strusińska, Hocine Oumeraci</i>	
Study on Reinforcement Wall of Geogrid through Model Test on Slope	748
<i>Chengzhi Wang, Guangchun He and Ying Nie</i>	
Application of Splitting Grouting on the Dam Reinforcement.....	755
<i>Ke Wu, Yongnian Bai and Shucai Li</i>	
Geological Disasters and Mitigation Measures Along the Coastal Cities of China.....	762
<i>Yeshuang Xu, Shuilong Shen and Longzhu Chen</i>	
Effectiveness of Jet-Grout Columns for Mitigation of Liquefaction during Earthquakes	768
<i>C. Guney Olgun, James R. Martin II</i>	
Supporting Method of Jinchuan Deep Roadway 1178 Sublevel	774
<i>Chunli Yang, Yongcai Wang</i>	

Soil Erosion Caused by Highway Construction In Expansive Soils Districts and Its Prevention Measures.....	781
<i>Heping Yang, Liping Lin and Yingxi He</i>	
Construction and Quality Analysis of Curtain Grouting in Foundation of Dam for Yangtze Three Gorges Project.....	790
<i>Xuexiang Yang, Yan Li</i>	
Mechanism and Prevention of Highway Distress in Seasonal Frost Area.....	797
<i>Yongtang Yu, An Deng</i>	
Integrated Reinforcing Methods for Excavated Slopes of Tanxiwan Villa Area on Considering Reforest Afforestation, China.....	803
<i>Faming Zhang, Tao Li, Yajie An, Xia Wang and Zhiyao Kuai</i>	
Fly-Ash-Stabilized Gypsiferous Soil as an Embankment Material.....	809
<i>Jie Zhang, Ruben Solis</i>	
Reduction of Earth Pressure and Displacement of Abutment with Reinforcement Filling.....	815
<i>Wenhui Zhang, Bangmin Qin, Baotian Wang and Jiandong Ye</i>	
Analysis and Treatment of Ground Ruptures in Xi'An.....	821
<i>Yin Zhang, Qianfeng Yao and Junlong Lu</i>	
Research on Technology of Coupling Support in Soft Roadway and Its Application in Mine Disaster Mitigation.....	827
<i>Bin Zhu, Jinchuan Hu, Fenglin Jiang and Peili Su</i>	
Risk Assessment and Management	
Forecasting of Rockfall in K2403+500 of G320.....	835
<i>Helin Fu, Xianfeng He, Qiang Luo, Yong Zhou and Wanxue Long</i>	
Research on Space-Time Prediction Model and Criteria for High Altitude Slope in the First Stage Jinping Hydropower Station.....	841
<i>Haiyuan Jin, Weiya Xu</i>	
Characterization of Deterioration on the Shotcrete Lining Immersed in Various Sulfate Solutions.....	847
<i>Ho-Seop Jung, Dong-Gyou Kim, Hyu-Soung Shin and Seong-Soo Kim</i>	

Long-Term Characteristics of Shotcrete Lining in Test Tunnel	853
<i>Dong-Gyou Kim, Ho-Seop Jung, Kwang-Pil Park and Seong-Soo Kim</i>	
Occurrence of Thaumassite In Lining Concrete of Old-Tunnel Structure	860
<i>Seung-Tae Lee, Da-Hyun Lee, Dong-Kyou Kim, Ho-Seop Jung, Kwang-Pil Park, Seong-Soo Kim and Chang-Soo Lee</i>	
Stability Assessment and Protection Design for the Rock Filling of Dumping Site in Ravine.....	866
<i>Honggang Li, E'Chuan Yan, Dongli Li and Jiangtao Cheng</i>	
Pseudospectral Method for Seepage behind Earth Retaining Wall.....	874
<i>Nansheng Li, Lihui Xie</i>	
Multiparameter Technology on Dam Leakage.....	880
<i>Tong Lin, Jiansheng Chen and Liang Chen</i>	
Risk Analysis of Soil-Nail Supporting Slope under the Earthquake Effect	887
<i>G. C. Lou, Z.L. Ye</i>	
Study on Strength Criterion of Intact Soft Clay after Monotonic Principal Stress Rotation.....	892
<i>Yang Shen, Jian Zhou, Xiaonan Gong and Hanlong Liu</i>	
Study and Application of Reliability Analysis Method in Open-Pit Rock Slope Project	899
<i>Bing Sun, Sheng Zeng and Dexin Ding</i>	
The Application of Fuzzy Evaluation on Determination of a Slope in a Dam Region.....	907
<i>Dongfang Tian, Yisi Zhuge</i>	
Study on Damage Style of Over-erection Wharf in Inland River.....	913
<i>Duoyin Wang, Chengzhi Wang and Ying Nie</i>	
Investigation on the Nanjing Gypsum Mine Flooding.....	920
<i>Guangya Wang, Guanlin You and Yulin Xu</i>	
Modeling of Periodic Elastic Strain Energy Change and Failure Process of Rock Specimen with Random Imperfections in Biaxial Compression	931
<i>X.B. Wang</i>	

Study on Isotope Model of Dyke Leakage	937
<i>Yongsen Wang, Jiansheng Chen</i>	
Ground Settlement Model for Excavation of A Non-Partial Pressure and Shallow Buried Double-Arch Tunnel	942
<i>Jihong Wei, Shaorui Sun</i>	
Evaluate the Risk of Land-Sliding Based on Geophysical Data.....	949
<i>Jianhua Xiao</i>	
The Security Alarm and Application of the Horizontal Displacement Monitoring of the Retaining Structure	955
<i>Zhibiao Xiong, Qiyun Wang</i>	
Evaluation of Seismic Induced Relative Displacement for Container Cranes on Caisson Walls	961
<i>Yutaka Yamamoto, Koji Ichii</i>	
Pile Horizontal Displacement Monitor Information Calibration and Prediction for Ground Freezing and Pile-support Foundation Pit	968
<i>Baoyuan Yuan, Xianggang Liu and Xufeng Zhu</i>	
A New Predicting Method of Landslide by Fractal Theory	975
<i>Mingxin Zheng</i>	
Application of Infrared Photography and Image Processing in NATM Tunnel.....	981
<i>Chunlin Zhou, Hehua Zhu and Xiaojun Li</i>	
Model Tests on Subgrade in Seasonal Frozen Region under Freezing-Thawing Circulation.....	989
<i>Ming Zhu, Ronggui Deng and Feng Li</i>	
Numerical Simulation for the Drainage Holes in Seepage Field with Disaster Status	994
<i>Yueming Zhu, Haodong Cui</i>	
Others	
Two-Dimensional Finite Element Analysis of Laboratory Embankment Model.....	1003
<i>A. Ahmed, A.M.K. El-Tohami and N.A. Marei</i>	
Some Studies on Recycled Aggregate Concrete with and without Polymer.....	1019
<i>G. D. Awchat and N. M. Kanhe</i>	

Research on the Dry Compactness Technology in Subgrade Filled with Wind-Blown Sand in Sand Damage Area.....	1026
<i>Faming Chen, Ruonan Liu</i>	
Experimental Study on the Interfacial Friction Behavior of Geogrids in Silt Mixing Rubble	1034
<i>Rong Chen, Maotian Luan and Wei Zhao</i>	
Three-Dimensional Fem Analysis on Mechanical Characteristics of Deping Metro Station Foundation Pit during Project Excavation.....	1042
<i>Youliang Chen, Lebin Yang, Jingxue Liu and Rafiq Azzam</i>	
The Underwater Detection of Scour and Analysis of Stability of Bridge Piers	1049
<i>Ligang Fang, Jiatao Kang and Guangxiu Qu</i>	
Rigorous Numerical Analysis of Cylindrical Cavity Expansion in Sands Based on Smp Criterion	1055
<i>Dongxue Hao, Maotian Luan and Rong Chen</i>	
Study on Determination of Rock Mass Quality Parameter m, s Value and Impact of It to Rock Mass Strength	1061
<i>Hailang Hu, Qiufeng Huang and Jianlin Li</i>	
A Comparative Study on Monotonic Shear Behaviors of Granular Soils under Different Drainage Conditions	1068
<i>Maotian Luan, Yi Leng</i>	
Study on the Interaction Law between Squeezed Branch Pile – Structure and Soil.....	1079
<i>Dongpo Wang</i>	
Elastic-Plastic Analysis for Surrounding Rock of Pressure Tunnel with Liner Based on Material Nonlinear Softening.....	1085
<i>Liming Zhang, Zaiquan Wang, Huafeng Li and Hengbo Zhao</i>	
Study on Ultimate Bearing Capacity of Two-layered Subsoil under Horizontal and Vertical Loading.....	1093
<i>Qiyi Zhang, Maotian Luan</i>	

Author Index

Qian Jiahuan Lecture

FLOW SLIDES OF UNDERWATER SAND DEPOSITS IN JAMUNA RIVER BED

Kenji Ishihara

*Research and Development Initiative, Chuo University
1-13-27 kasuga, Bunkyo-ku, Tokyo 112-8551, Japan*

When excavation was under progress by dredging through the sandbar deposit in Jamuna River in Bangladesh, a number of slips occurred underwater. Features of the slips are first described herein together with the results of in-situ investigations on the ground conditions. In the fluvial deposit in the Jamuna riverbed the sand is known to contain several percent of mica mineral composed of plate-shaped grains. The inclusion of mica has been known to make the sand behave more strain-softening leading to increased vulnerability to flow type deformation. This was conceived to have been the seminal cause of the underwater slides. To confirm this aspect, the sand was recovered from the river site and triaxial tests were performed in the laboratory extensively. The outcome of the tests was compiled and arranged in a manner where the residual strength could be evaluated in a general framework of interpretation on sand behaviour. The results of the tests showed that the mica-containing sand from Jamuna River site exhibited contractive or strain-softening behaviour over a wide range of void ratio. The residual strength at the steady-state deformation obtained in the present test scheme was used to provide an explanation for the flow-type instability of the slopes in the light of what actually happened during the underwater excavation in Jamuna River.

INTRODUCTION

The vast expanse of the flood plain in Jamuna River in Bangladesh has experienced volatile shifts of river course during the flood period. In a large project to construct a long bridge, it was considered necessary to protect the abutment of the bridge from scouring and erosion in which the level of the riverbed is purported to change by more than 10m overnight. In order to provide a countermeasure, excavation of underwater channels was executed by dredging the sand deposit by ships through the sandbar area. The aim was to reinforce the underwater slope with stones and geotextiles on the side of abutment. During the excavation, a number of slides took place underwater thereby inhibiting the operation of construction. In-situ investigations were carried out extensively by Dutch company and consultants and original design modified.

To clarify the cause of the slides, various kinds of investigations were carried out both in the field and in the laboratory. Although the causes were variously speculated, one of the

points unanimously recognized was the fact that the fluvial sand deposit in Jamuna River contains several percents of mica mineral exhibiting peculiar behaviour of deformation. In recognition of this, the extensive studies were performed in the laboratory by Hight et al. (1999) and various factors such as anisotropic mode of deposition were addressed as possible seminal cause leading to highly collapsible nature of the mica-containing sand. At the Tokyo University of Science, the scheme of laboratory studies had been underway to clarify the steady-state deformation characteristics of sandy soils. Some of the results of tests were reported by Ishihara et al. (2003).

With an aim to examine behaviour of Jamuna River sand in terms of the framework established as above, a large amount of Jamuna River sand was shipped to Japan and multiple series of triaxial tests were performed to clarify the deformation characteristics of the sand. The results of the undrained triaxial compression and extension tests will be introduced in this paper within the framework of data arrangements and interpretation established thus far.

As a result of the study, it was pointed out that the use of the major principal stress would be most appropriate to take into account effects of confinement on the residual strength of sand, and if based on this, there is no need to consider the effect of various K_c -conditions at the initial stage of anisotropic consolidation. The outcome of these laboratory tests was incorporated into a simple analysis to examine the instability of the slopes observed in Jamuna River. The analysis targeted for the post-failure conditions was performed based on the residual strength. The consequence of these studies will be described in the following pages. This paper is a modified version of the paper with the same content which was published previously by Ishihara and Tsukamoto in 2007.

PROJECT

In the middle reaches of the Jamuna River in Bangladesh about 110km northwest of Dhaka, a 4.8km-long bridge called Bangabandhu Bridge connecting the towns of Sirajganj and Bhuapur was planned and constructed in 1995-1999. Its location is shown in Figure 1. The Jamuna is a shifting braided river, consisting of numerous channels which change their width and course significantly with reasons. Thus, training the river to ensure that it would continue to flow under the bridge corridor was the most difficult technical challenge of the project.

As shown in the more detailed map in Figure 2, the width of the river channel was about 11km. This area is the vast expanse of flood plain and had suffered severe destruction over the years due to intense flooding over the river channel and its surroundings. Devastation was particularly conspicuous at the time of the flooding in 1987 and 1988. In some areas, river channels are purported to have shifted their courses overnight through several hundred meters. The tendency of the drift is reported to have been westwards whereby involving a huge amount of sandy soils removed by scouring in the riverbed in the west side of the Jamuna River.

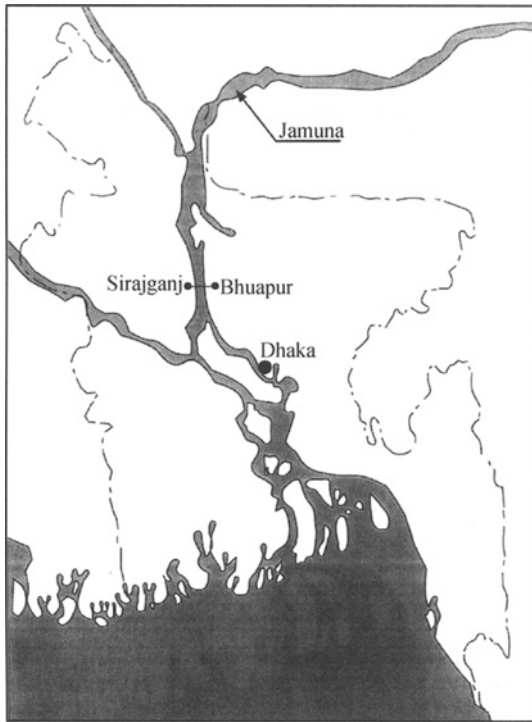


Figure 1. General location map

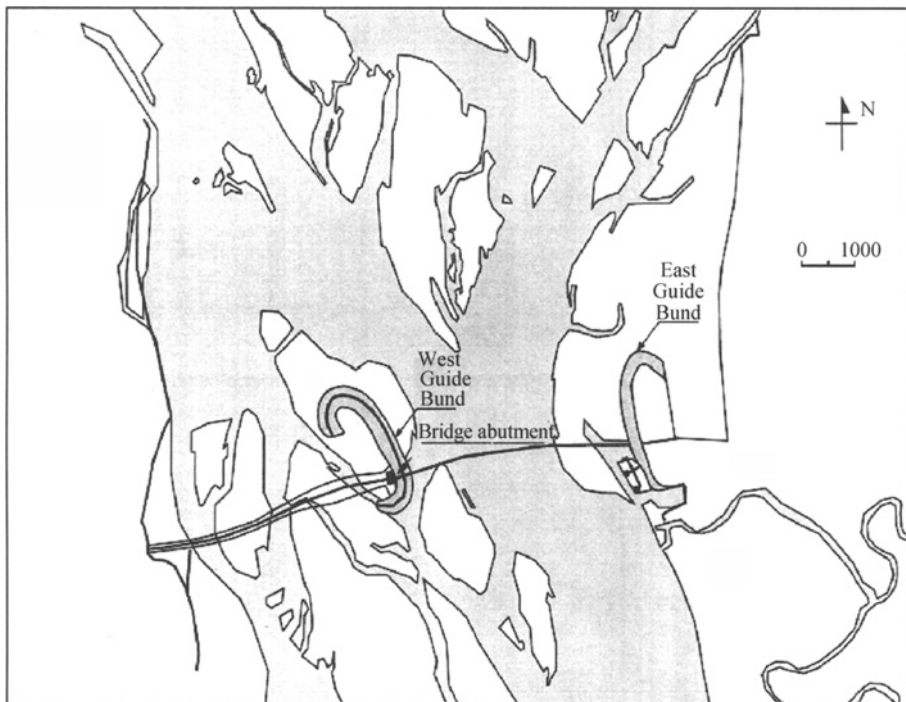


Figure 2. Locations of the Guide Bunds in Jamuna bridge site

In the design of the abutment of the Bangabandhu Bridge, it was considered mandatory to implement some countermeasures against the deleterious effects due to such scouring and to duly control the river channel. With this aim, construction of guide bunds was planned on both sides of the river as shown in Figure 2. Of particular importance was the construction of the West Guide Band, as it was intended to protect the bridge abutment behind the river from scouring or erosion of the riverbed. The construction consisted of excavating the riverbed by dredging the sand by ships and placing erosion-protecting armors such as geotextiles and stones over the underwater slopes on the west side. A typical cross section with an armored slope is shown in Figure 3. The location and horseshoe-shaped plan view of the Guide Bunds are displayed in Figure 4. The trench varying from 22 to 30m in depth was dug below water by means of cutter-suction dredgers which were operated from ships at the site of each guide bund.

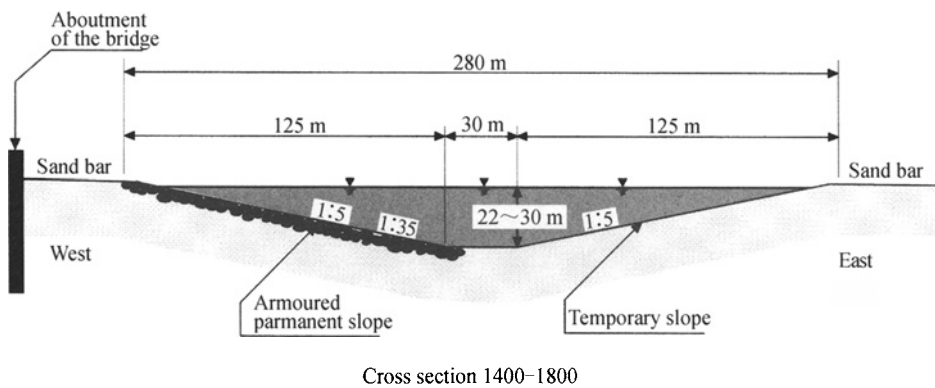


Figure 3. Cross section for the dredging of West Guide Band for the bridge at Jamuna River site

UNDERWATER SLIPS ON EXCAVATED SLOPES

The West Guide Bund was constructed at the site of a recently formed sand island as seen in Figure 2. The materials forming the dredged slopes were composed of young, rapidly deposited sediments. The detailed plan view of the excavation is shown in Figure 4 and a typical section (E-W section) across the dredged channel is displayed in Figure 5.

The slope on the west side was to be protected by the geotextiles-stone armor against the scouring, because the bridge abutment was to be installed due west of the West Guide Bund. Thus the underwater slope on the west side designated as “permanent slope” was designed so as to have a gentle slope of 1:5.0 in the middle portion. On the contrary, the slope on the east side of the dredged channel was to be left unprotected. Even though slides occur and the sand bar disappears in future due to scouring or erosion, it was considered it did not matter. Thus, the eastern slope was designed to form a steeper slope with an angle of 1:3.0 and designated as “temporary slope” in Figure 5.

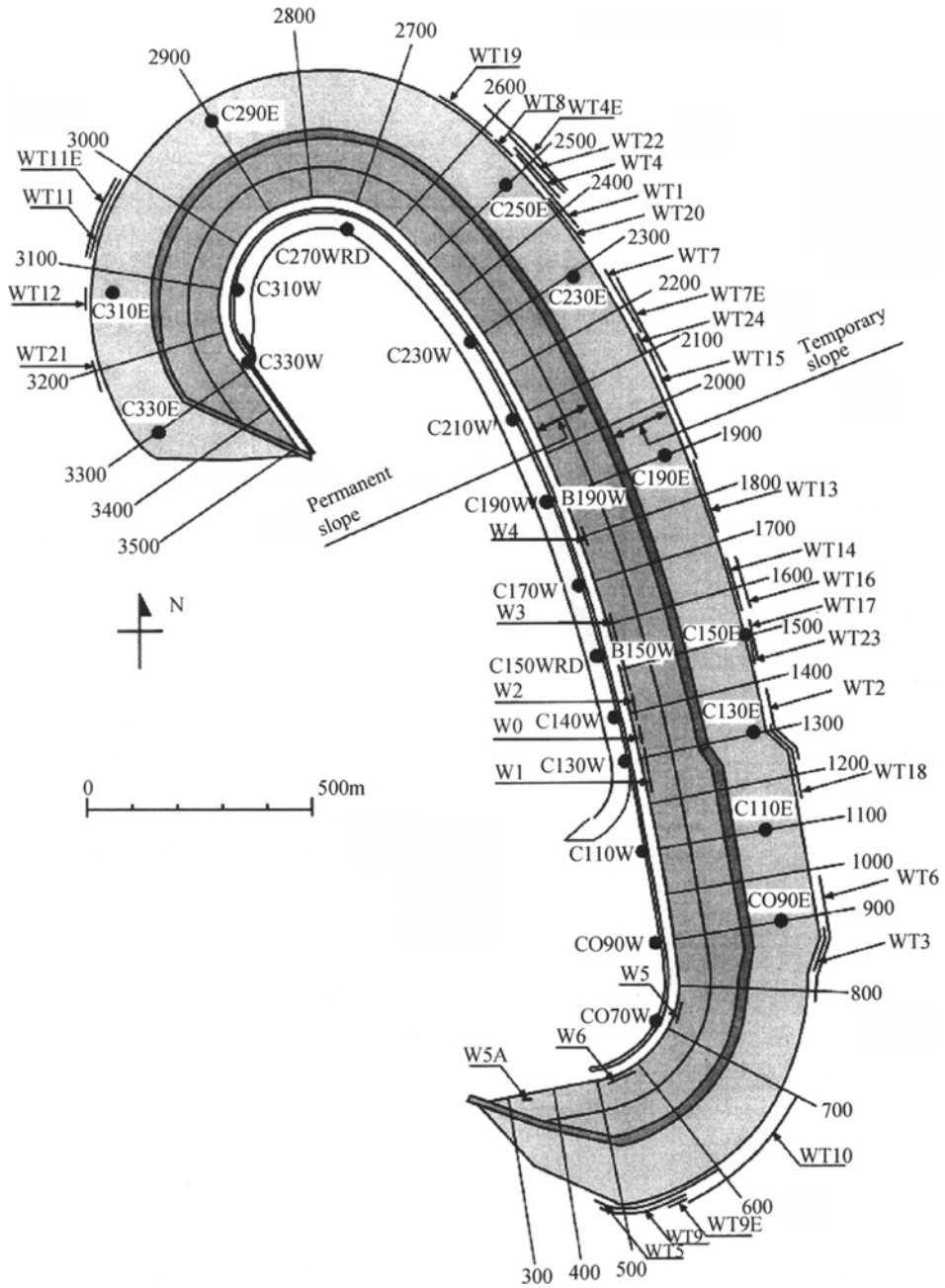


Figure 4. Locations of slides in the West Guide Bund

The dredging work began northwards in October 1995 from the southern rim of the sand bar. As the dredging proceeded, slope failures occurred on the permanent slope on November 19th in 1995 in the cross section 1270 and another on November 22nd in the cross section

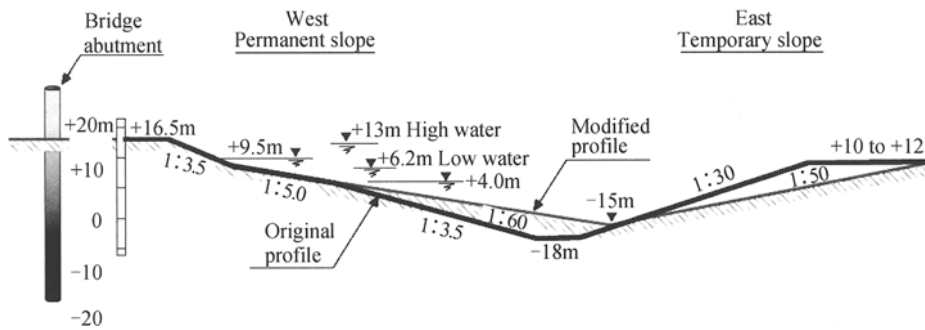


Figure 5. East-west section through West Guide Bund Channel (from Hight et al., 1999)

1410. They are respectively called W1 and W 2 slide as shown in Figure 4. On December 3, 1995, the largest-in-scale slide denoted by W3 took place on the permanent slope at a location of Chainage 1550. This slide covered an area of about 150m wide and 150m long over the permanent slope. Afterwards many failures were found to have occurred on the temporary slope during the period of rising water level in 1996. Eleven of them were larger in scale than W3, and these are indicated by the symbol WT 6, 7, 9, 9E, 13, 15, 16, 17, 18, 22, 24 in Figure 4. Many of these slides delayed the progress of construction works, but of most serious concern were the failures on the permanent slope, because they had to be repaired to construct an erosion-free slope. In recognition of the instability with an angle of 1:3.5, the design cross section on the permanent slope was changed so as to have a slope of 1:6.0 near the bottom and for the temporary slope, the angle was changed from 1:3.0 to 1:5.0 as illustrated in Figure 5. Then, the dredging work to full depth was resumed to finish excavation of the trench. As the dredging went on, a number of slope failures began to occur again but only on the temporary slope. The failures occurred mostly during the period of March to June in 1996. The exact locations of all of these slope failures including those prior to and after the design change as well are indicated together in Figure 4.

CAUSES OF SLOPE FAILURES

There are two aspects to be distinguished in elucidating mechanisms of slope failures in sand deposits. These are the seminal cause and the consequence of failures.

Causative incidents

It was difficult to precisely identify generic causes of the slides, which occurred apace in underwater environments. It was envisioned that the over cutting, overstepping or rapid cutting associated with the dredging operation had been responsible for triggering the slips. There were slow falls in the water level of the river after storms of the order of 0.1m per day over a period of five days. There might have been other seminal causes leading to the slips. The factors such as wave actions and thunderstorms were also suspected to have triggered the slips. No matter what causes might have been, it is certain that the sand deposits had been in a precarious state narrowly keeping the stability when the excavation was made.

Consequences of failure

After the initial failure is triggered involving a small or medium deformation, the soil may or may not develop large displacement later on. One kind of sand deposits might induce only limited deformation which is tolerable, but in another type a fairly large amount of displacement will continue further on. In the latter case, the level of devastation incurred will be intolerably large. Thus, identification of the damage level in terms of continuation or discontinuation of deformation after triggering of the failure will pose an important aspect in recognizing the feature of the problem particularly in saturated sand deposits under water.

The identification of the consequence of failure as above can be made generally by examining the state of an existing deposit as to whether it will exhibit contractive or dilative behaviour after it has undergone triggering. In the case of the sand deposit in the Jamuna riverbed, the deposit seems to have had characteristics showing the contractive or strain-softening type of behaviour in which the residual strength at a largely deformed state is reduced significantly leading to an intolerable level of deformation after the slips were triggered. In the above context, soil characteristics were investigated in details in the field as well as in the laboratory as described below.

INVESTIGATION OF SOIL CONDITIONS

Following the occurrence of the slides as well as at the time the design was made, multiple series of tests were conducted both in the field and in the laboratory to elucidate nature and properties of soils which are deemed to be a cause of the flow type slides.

In-situ tests

Deep borings were performed at three locations, viz., B1 on the west bank, and B2 and B3 on the east bank, as shown in Figure 6. The standard penetration test (SPT) was also conducted at these boring sites. At the site B3, the measured N-value was, for example, 15 at a depth of 9.25m. Considering the use of a free falling hammer in the SPT practice at the Jamuna River sites, the energy level is deemed as about 80% of the theoretical energy in hammer dropping. This energy level actually consumed for penetration is considered about the same as the level normally achieved in the Japanese practice. The SPT N-value at a shallow depth of 6.25m was found to be 7 at B3, 10 at B2 and 19 at the site B1. These values are relatively small indicating the presence of loose sand layer which might be responsible for triggering the slope failure.

Dutch one-penetration tests (CPT) were also performed at the stage of feasibility study and design at 15 locations as indicated by C1 to C13 shown in Figure 6. The results of CPT showed q_c -values of 4–5MPa at depths from 6–8m at the location CDI which is close to the site B3. This value indicated as well the presence of a loose sand layer at this depth. After the failures, an additional set of CPT was carried out at the shoulders of the excavation as shown in Figure 7. The results of the CPT are reported by Yoshimine et al. (2001) as displayed in Figure 8 in terms of the q_c -value and sleeve friction ratio F . It may be seen that the q_c -value at the depth of 10m takes values ranging between 5–12MPa, indicating that the sand is in loose states of deposition. By comparing the SPT N-value and the CPT q_c -value obtained each in their vicinity, an empirical correlation was established by Delft Geotechnics as follows,

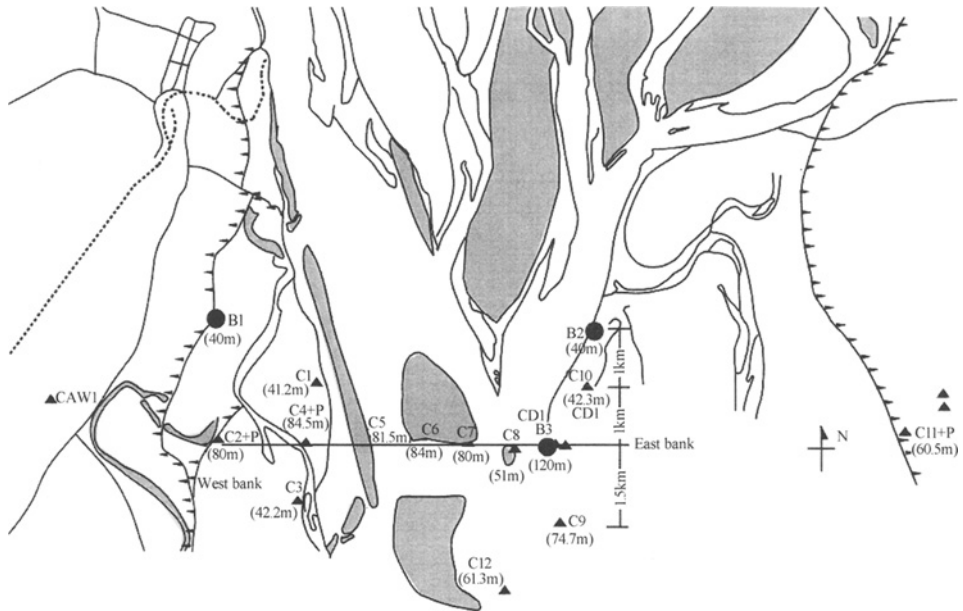


Figure 6. Location of soil investigations at Jamuna multipurpose bridge construction

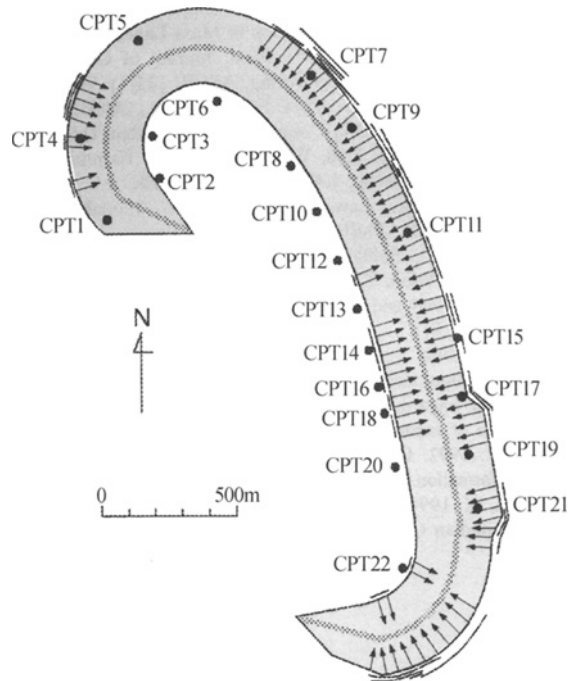


Figure 7. Location of the slips by arrows and cone penetration tests (CPT)
(from Yoshimine et al., 2001)

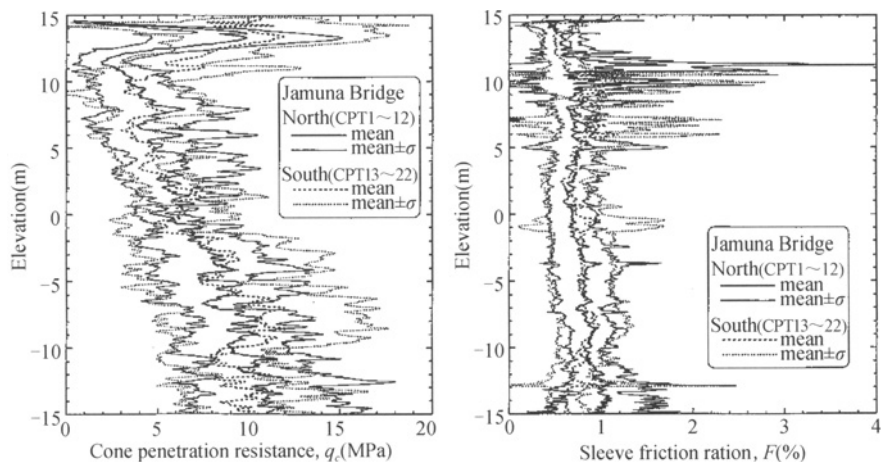


Figure 8. Results of CPT along the shoulder of the dredging in the West Guide Band (After Yoshimine et al., 2001)

$$q_c = 0.31 \cdot N_{60} \quad (1)$$

where N_{60} indicates the SPT N-value corresponding to 60% of the theoretical energy. In view of the 80% of the energy achieved in the Jamuna River investigation, the above relation would be rendered to,

$$q_c = 0.37 \cdot N_{80} \quad (2)$$

where N_{80} indicates SPT N-value obtained by the free fall hammer which is considered to exert 80% of the theoretical energy in the SPT operation. The relative density at the site was estimated based on the data of SPT and CPT. One of the typical data by Hight et al. (1999) is shown in Figure 9, where it may be seen that the relative density takes values around 50%, but the majority of data indicate values less than 65%.

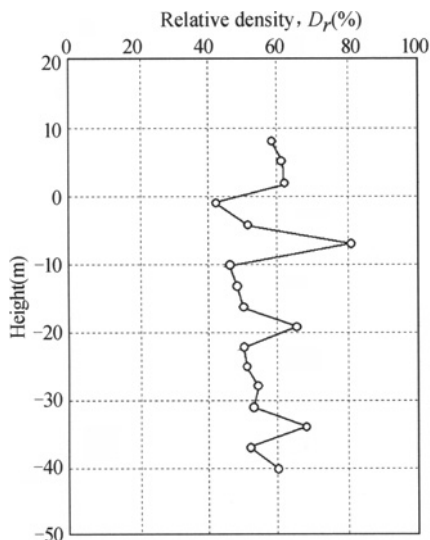


Figure 9. A typical profile of relative density at a site in Jamuna River

Laboratory tests

Sand samples were obtained in-situ by means of the tube sampling technique. However, the degree of disturbance appears to be somewhat high in loose deposits of sand and therefore the outcome of the laboratory triaxial tests on such samples is considered not truly representative of the conditions of sand deposits prevailing in the field.

Apart from the laboratory tests on intact sand samples, it was discovered that the sand in the Jamuna River contains several percent of mica and its presence was suspected to have created conditions of the deposits which were highly vulnerable to triggering failure and consequent flowage of the sand. The distribution of mica content versus depth is shown in Figure 10. Thus, attention has been drawn to the peculiar behaviour of mica-containing sand by several investigators. One of the results of simple shear tests reported by Hight et al. (1999) is reproduced in Figure 11, in which the behaviour of clean silica sand is compared with that of the same sand but containing 1% mica.

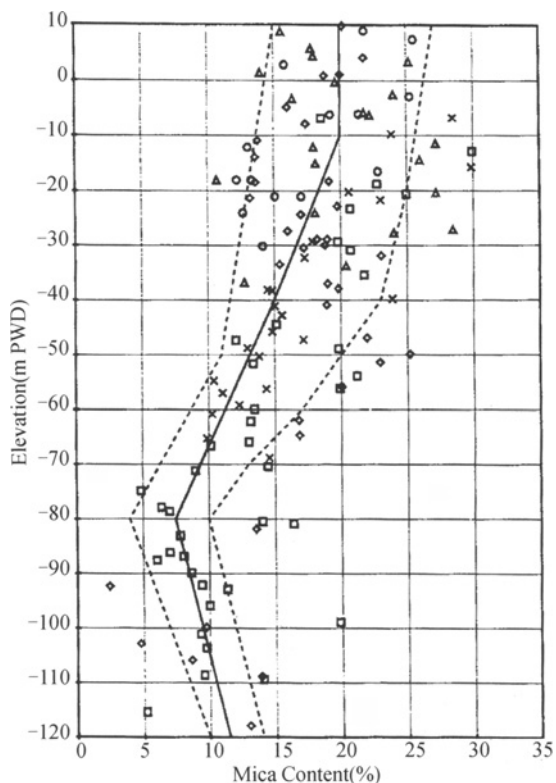


Figure 10. Distribution of mica content at sites of the Jamuna River

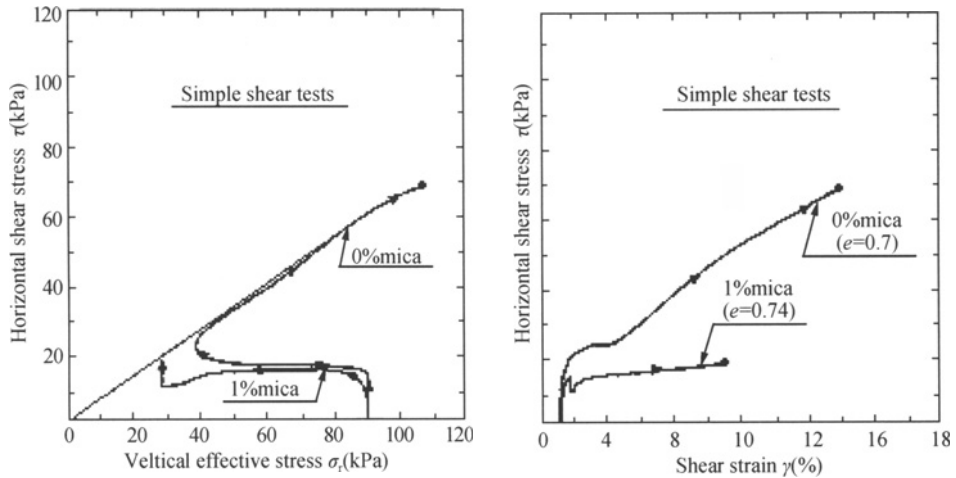


Figure 11. Effect of 1% mica on the undrained behaviour of sand in simple shear (Hight et al., 1999)

It can be seen that the loose sand with a void ratio of $e=0.70$ exhibits ductile behaviour with a tendency to dilate at largely strained states, bringing up the effective stress path along the failure line. In stark contrast, the sand with $e=0.74$ containing 1% mica is shown to be brittle and have a potential to collapse at medium strains resulting in a small residual strength at a largely strained state. Hight et al. (1999) argued that, because of the aspect ratio of the mica plate as high as approximately 50:1 compared to the rotund sand particles, the presence of even 1% mica by weights is approximately equivalent to that of 25% of mica by number of grains.

In an effort to investigate more thoroughly the behaviour of mica-containing sand, multiple series of triaxial tests have been conducted at the Tokyo University of Science on reconstituted samples of the sand recovered from the Bangabandhu Bridge site in Bangladesh. The details of the tests procedures and the manner in which data are arranged are described in more detail in the paper by Tsukamoto et al. (2007). The conduct of the tests on the Jamuna River sand and its outcome will be described somewhat in details in the following pages.

CONDUCT OF TRIAXIAL TESTS ON BANGLADESH SAND

Material properties

The sand with 4.5% to 5% percents mica recovered from the bridge site has a typical grain size distribution curve shown in Figure 12. It is a sand with $D_{50} = 0.2$ mm and contains 10% non-plastic fines. Its specific gravity is $G_s = 2.745$ and the maximum and minimum void ratios as measured by the Standard of the Japanese Geotechnical Society were $e_{\max} = 1.202$ and $e_{\min} = 0.602$, respectively.

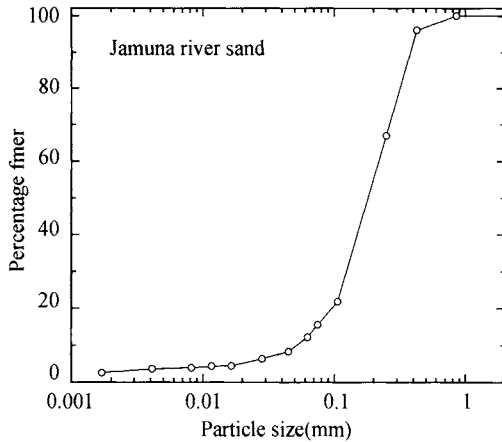


Figure 12. Grain size distribution of the Jamuna River sand tested

Test procedures

In the triaxial tests, the samples with 6cm in diameter and 12cm in length were prepared by the method of wet tamping, in which moist sand was placed in the mould with varying energy of compaction. By this method, it was possible to prepare reconstituted samples with a widely varying range in void ratio. After preparing the samples, de-aired water was circulated to achieve a state of full saturation with a B-value greater than 0.95. Then, the samples were consolidated anisotropically under different K_c -conditions. The axial load was then increased under undrained condition, when the mode of the test was triaxial compression. The triaxial extension tests were also performed by decreasing the cell pressure under undrained conditions.

Results of tests

The results of the undrained compression test on samples with void ratios ranging between 0.804 and 0.871 are displayed in Figure 13, where the deviator stress $q = \sigma_1 - \sigma_3$ is plotted versus the effective mean confining stress defined as $p' = (\sigma_1 + 2'\sigma_3)/3$. The saturated samples were consolidated with a vertical stress of $\sigma'_{1c} = 98\text{kPa}$ and a lateral stress of $\sigma'_{3c} = 49\text{kPa}$ producing an initial state of $K_c = 0.5$. It may be seen in Figure 13 that the dilatant behaviour is exhibited when the sample is prepared with a void ratio less than about 0.83, but otherwise the sample is contractive. It is to be noticed that the sample with $e=0.871$ has reached a steady-state with a deviator stress of $q = 15\text{kPa}$, which is smaller than the initially applied deviator stress of $q = 49\text{kPa}$. It is seen in Figure 13(b) that a large deformation began to occur at an early stage of load application and continues further on until an axial strain of 20% developed.

The smallness of the deviator stress at the steady state as compared to the deviator stress at the outset would be regarded as a criterion to indicate an unstable condition where flow-type deformation could be triggered if the peak shear stress is passed over by application of a slight agitation at the beginning. Another series of tests with the same initial lateral stress of

$\sigma'_{3c} = 49\text{kPa}$ but with an increased K_c -value of 0.7 is demonstrated in Figure 14 for samples with various void ratios where the general tendency is seen to be the same as those shown in Figure 13. It may be seen in Figure 14 that the sample consolidated with a deviator stress $q_c = \sigma'_{1c} - \sigma'_{3c} = 20\text{kPa}$ with a void ratio of 0.827 has reached a steady-state with the deviator stress $q = 95\text{kPa}$ which is much greater than the initially applied deviator stress of 20kPa. In such a condition, the flow type deformation will not be induced because of the gain in shear strength as compared to the initially applied shear stress. The last series of the tests with $K_c = 1.0$ are demonstrated in Figure 15 where it is apparently noted that the specimen with $e=0.767$ exhibited highly dilative behaviour. The characteristic feature of deformation as deduced from the above test results may be summed up as follows.

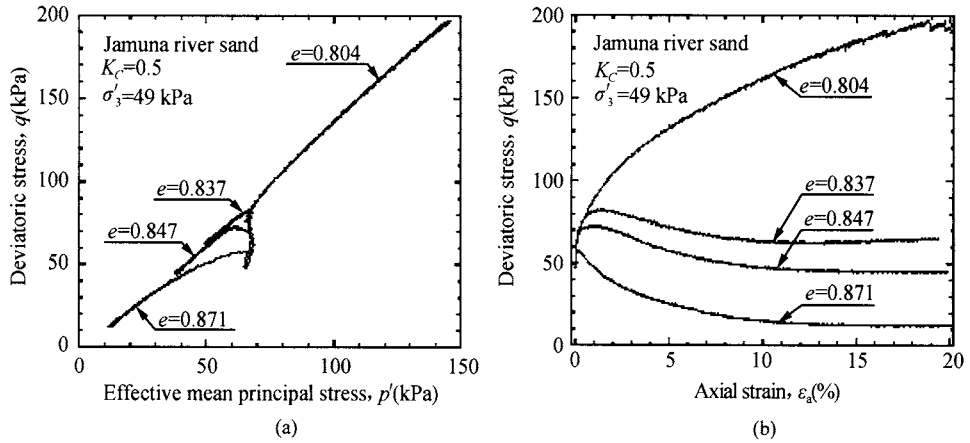


Figure 13. Results of undrained triaxial compression tests

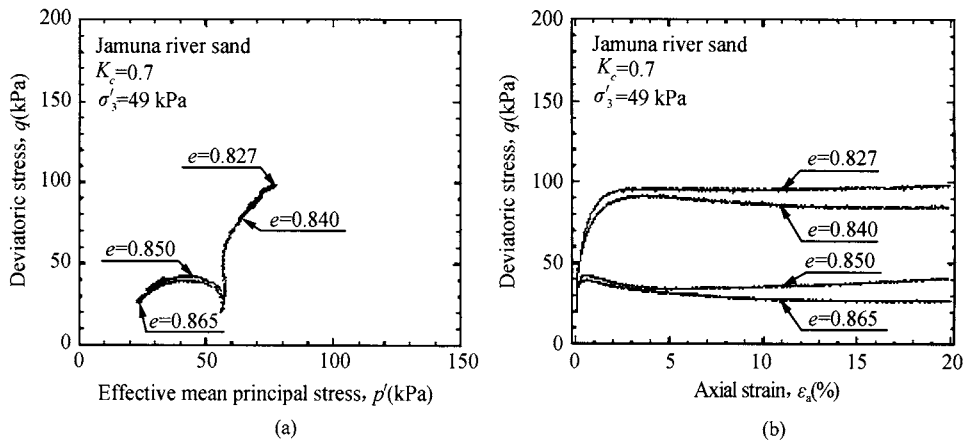


Figure 14. Results of undrained triaxial compression tests

1. It is apparent that the deformation characteristics become more dilative with decreasing void ratio and vice versa. The void ratio for the threshold can be read off as approximately $e=0.83$ from Figures 13 to 15.
2. Although not clearly displayed in the test results shown in Figures 13 and 14, a number of tests on Jamuna River sand with greater confining stresses or tests on other sands have

coherently shown that the deformation characteristics become more contractive with increased K_c -value at the stage of anisotropic consolidation. This is consistent with the main conclusion derived by Chern (1995), Vaid and Chern (1985), Kato et al. (1999) and Tsukamoto et al. (2007).

3. Similar undrained triaxial tests have been performed on several other sands in Japan which do not contain mica. The outcome of the tests on such non-mica sand showed that the sand behaviour becomes more starkly dilative or strain hardening with decrease in void ratio. In contrast, the mica-containing sand from Jamuna River tends to become contractive or to remain at an intermediate state between contractive and dilative whereby developing large deformation at constant shear stress q_s and effective confining stress p_s' . This implies that the mica-containing sand would easily be put into a steady-state over a wide range of void ratio. This is consistent with the results of the tests reported by Hight et al. (1999).

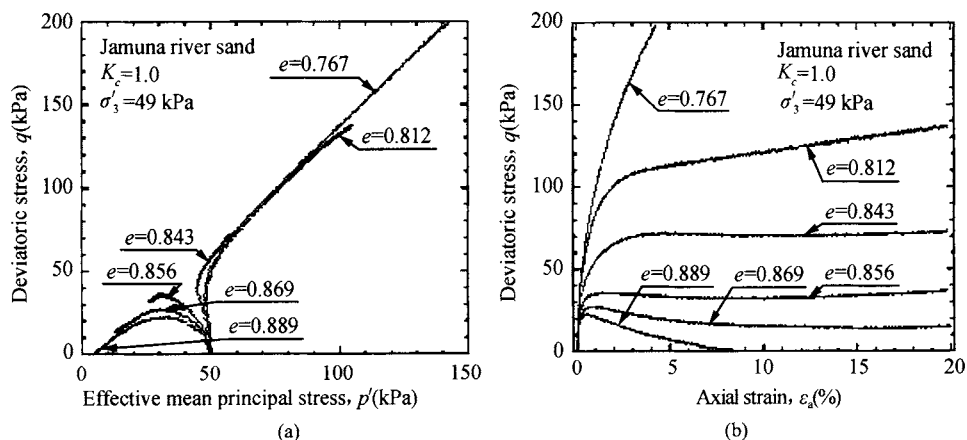


Figure 15. Results of undrained triaxial compression tests

FLOW CHARACTERISTICS OF JAMUNA RIVER SAND

From a number of other tests including those shown in Figure 13 through 15, the void ratio, e , deviator stress q_s and effective mean confining stress p_s' at the steady state were read off and plotted in Figure 16 in terms of e versus p_s' . In this plot, those data from the tests with $K_c = 1.0$ are displayed with white circles and those from anisotropically consolidated samples with K_c -values less than 1.0 are shown with black circles. It can be seen in Figure 16 that the steady state line is established uniquely irrespective of the K_c -conditions.

In the whole program of the tests executed at the Tokyo University of Science, it was shown, however, that the most appropriate parameter indicative of the effects of confinement at the steady state is not necessarily the mean principal stress $p_s' = (\sigma'_{1s} + 2\sigma'_{3s})/3$, but instead the major principal stress σ'_{1s} alone. In accordance with this concept, the plot is made of the same data set as alternatively displayed in Figure 17 in terms of the void ratio

versus the effective major principal stress σ'_{1s} at the steady state. It can be seen that the steady-state line is established equally well again irrespective of K_c -conditions.

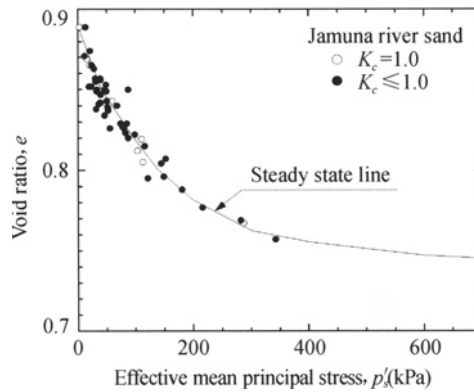


Figure 16. Steady-state line for Jamuna River sand as a plot of void ratio and effective mean principal stress

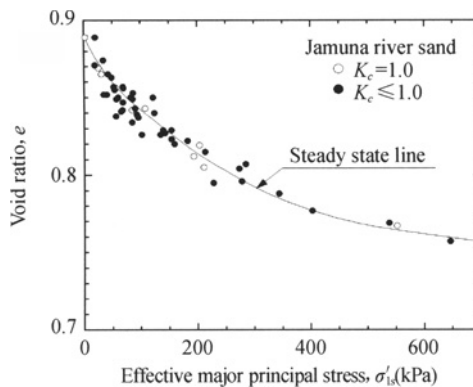


Figure 17. Steady-state line for Jamuna River sand as plots of void ratio and effective major principal stress

It is to be recalled that the steady-state lines established in Figures 16 and 17 all do pertain, not to the initial un-deformed state of the sand, but to the state where the sample is largely deformed to a strain level greater than about 5%. One might argue that the specification of a state of soil at the time it is already deformed may not be appropriate. Thus, it is claimed to be a parameter at the initial state prior to load application that is more convenient and hence desirable in view of its practical application when soil behaviour is to be estimated for subsequent application of shear stress. Looking back over the development of soil mechanics, one can realize that, in the majority of problems, such as consolidation and undrained shear strength, it was the initial state of the confining stress that was taken up as a parameter to specify the soil behaviour in the subsequent loading. In the context as above, the initial state of void ratio and the major principal stress σ'_{1c} before the application of shear stress were

picked up from the whole file of test data on Jamuna River sand and they are plotted in the diagram of Figure 18. In this diagram, a line is drawn which differentiates the sample behaviour between contractive and dilative. Such a line was called the Initial Dividing Line (Ishihara, 1996). It may be seen in Figure 18 that the Initial Dividing Line (IDL) can be obtained consistently irrespective of the K_c -state of samples at the time of anisotropic consolidation. It is to be noticed here that the steady-state line, quasi-steady state line and initial dividing line are almost coincident particularly in the range of a small confining stresses less than about $\sigma'_{1c} = 100\text{kPa}$. The angle of internal friction at the steady state derived from the same data is shown in Figure 19. Although the values are slightly different between the triaxial compression test (TC-test) and triaxial extension test (TE-test), the average value would be taken as $\phi_s = 30^\circ$.

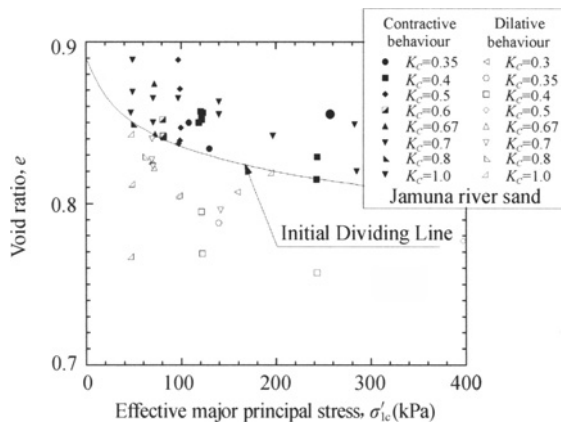


Figure 18. Initial dividing line for Jamuna River sand as plots of void ratio and initial major principal stress

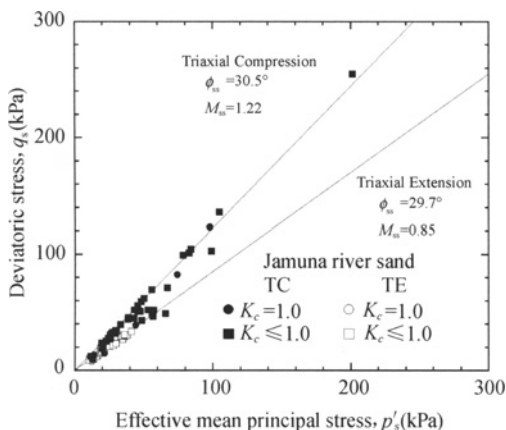


Figure 19. Angle of internal friction for the steady state

RESIDUAL STRENGTH OF JAMUNA RIVER SAND

It has been customary to define the residual strength, S_{us} , by referring to the minimum shear stress at the quasi-steady state (QSS) which is mobilized at the state of phase transformation for sands exhibiting contractive behaviour. In the mica-containing Jamuna River sand, the test data in Figures 13 to 15 show that the quasi-steady state (QSS) is almost coincident with the steady state (SS). Thus, these two states could be regarded practically identical for the mica-containing Jamuna River sand being considered. By denoting the deviator stress at this state as $q_s = \sigma'_{1s} - \sigma'_{3s}$, the residual strength is expressed as (Ishihara, 1996).

$$S_{us} = \frac{q_s}{2} \cos \phi_s = \frac{M}{2} \cos \phi_s \cdot p_s', \quad M = \frac{6 \sin \phi_s}{3 - \sin \phi_s} \quad (3)$$

where p_s' is the mean effective confining stress at the QSS or SS as defined by $p_s' = (\sigma'_{1s} + 2\sigma'_{3s})/3$, M is a parameter related to the angle of phase transformation in the p' - q plot, and ϕ_s is the angle of internal friction at QSS or SS. When normalizing the residual strength S_{us} to the initial mean principal stress, it is written as

$$\frac{S_{us}}{p_c'} = \frac{M}{2} \cos \phi_s \cdot \frac{1}{r_c}, \quad \text{where } r_c = \frac{p_c'}{p_s'} = \frac{\sigma'_{1c} + 2\sigma'_{3c}}{\sigma'_{1c} + 2\sigma'_{3s}} \quad (4)$$

If the residual strength is normalized to the initial major principal stress σ'_{1c} , it is written as

$$\frac{S_{us}}{\sigma'_{1c}} = \frac{M}{2} \cdot \frac{3 - \sin \phi_s}{3(1 + \sin \phi_s)} \cdot \cos \phi_s \cdot \frac{1}{r_c'}, \quad r_c' = \frac{\sigma'_{1c}}{\sigma'_{1s}} \quad (5)$$

From the majority of data on undrained triaxial compression tests "TC-test", the residual stress at largely deformed state of the Jamuna River sand was read off and normalized to p_c' and σ'_{1c} . Similar undrained triaxial tests were also performed in the extension mode of deformation which is referred to as "TE-test". The residual strength from the TE-test was also normalized to p_c' and σ'_{1c} . The outcome of such a data compilation is demonstrated in Figure 20, in terms of the plot of the normalized residual strength versus the K_c -values employed in each of the tests. Among the cluster of data points, the initial states of the samples exhibiting the contractive behaviour in subsequent undrained loading are indicated by black symbols and those showing dilative response by white symbols.

It is to be noted that those data with smaller values of S_{us}/p_c' correspond to loosely prepared samples and with increasing values of S_{us}/p_c' , the samples become denser. A line dividing the two types of behaviour is drawn for each of the TC-tests and TE-tests. The two lines thus determined each from TC and TE tests are indicated in Figure 20, together with the empirical equations suggested for each of these threshold conditions. The same data sets are plotted in Figure 21 now choosing the residual strength normalized to the initial major principal stress σ'_{1c} . From the two kinds of plot shown in Figures 20 and 21, the following observation can be made.

1. In the case when the residual strength is normalized to the initial mean confining stress, the value of S_{us}/p_c' tends to increase with decreasing K_c -value, and also it depends upon the mode of deformation as to whether the loading is triaxial compression or triaxial extension.

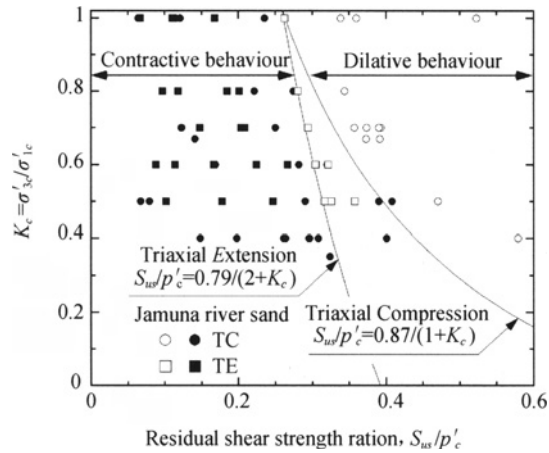


Figure 20. K_c -value versus residual strength normalized to the initial mean principal stress – comparison between triaxial compression and extension tests

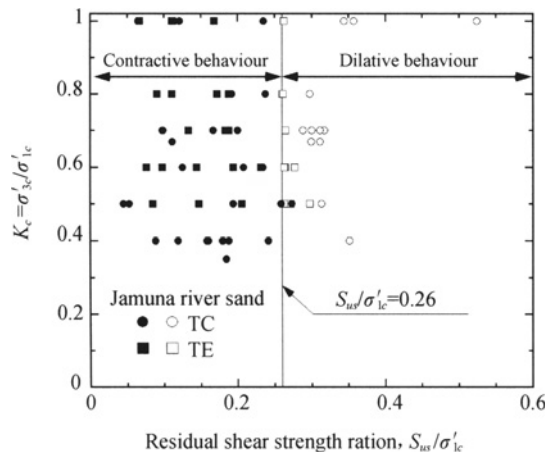


Figure 21. K_c -value versus residual strength normalized to the initial major principal stress – comparison between triaxial compression and extension tests

2. If the residual strength is normalized to the initial major principal stress, the value of S_{us}/σ'_{1c} is determined uniquely irrespective of the K_c -value in the anisotropic consolidation, and also independently of whether the mode of deformation is triaxial compression or triaxial extension. For the mica-containing sand from the Jamuna River site, the threshold value of the normalized residual strength separating conditions of contractive and dilative behaviour is found to be $S_{us}/\sigma'_{1c} = 0.26$ as accordingly indicated in Figure 21.
3. Each data in Figure 21 belongs to the samples having different void ratios but a close examination of the data has shown, although not shown explicitly in the figure, that for the state with a given void ratio, the normalized residual strength S_{us}/σ'_{1c} takes a constant value irrespective of the K_c -condition at the time of consolidation. Thus, the limiting value of $S_{us}/\sigma'_{1c} = 0.26$ can be taken as the upper bound of S_{us}/σ'_{1c} -values within the range of the void ratio in which the sand exhibits contractive behaviour.

In the type of plots shown in Figures 20 and 21, the looseness or denseness of the samples is not indicated explicitly in the figures. In order to visualize this effect, the same test data are now shown in Figure 22 in terms of the S_{us} / σ'_{1c} plotted versus the void ratio, e . It may be seen in the figure that effects of the minor principal stress, that is, σ'_{3c} -value in the TC-test and σ'_{1c} -value in the TE-test, are not so important but the influence of the mode of deformation as to whether it is TC-test or TE-test would be somewhat significant with the mode of the TE-test giving smaller normalized residual strength S_{us} / σ'_{1c} as compared to that from the TC-tests. It is to be noticed that no matter whether the mode is TC-test or TE-test, the upper limit of S_{us} / σ'_{1c} takes the identical value of 0.26. The density of each samples tested is also shown by way of the relative density, Dr , with the scale indicated on the right hand side of Figure 22. If the average is taken, it can be conclusively mentioned that, for the Jamuna River sand deposited with a relative density smaller than $Dr \cong 65\%$, it will exhibit contractive behaviour. Therefore the in-situ deposits under such condition will have a potential to develop flow type deformation irrespective of the K_c -condition, if it is subjected to an external agency for triggering the slide.

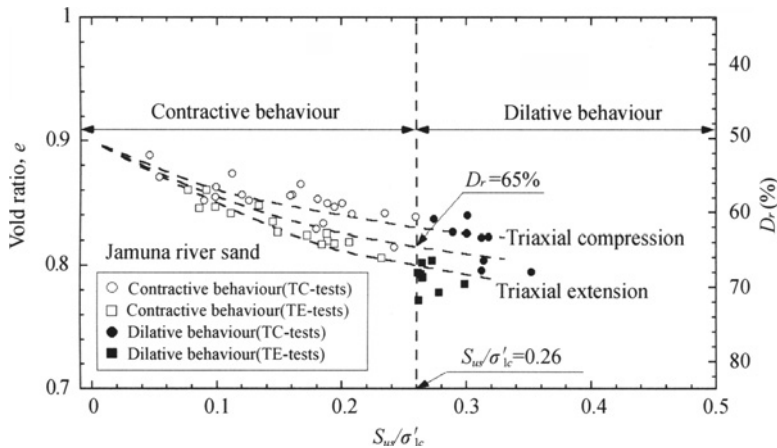


Figure 22. Residual strength ratio S_{us} / σ'_{1c} versus void ratio-comparison between triaxial compression and extension tests

SIMPLE METHOD OF ANALYSIS OF THE SLIDE AT JAMUNA RIVER

Basic concept

For the sake of simplicity, let a potential sliding plane be located in parallel to the surface of the submerged slope as illustrated in Figure 23. Then, from the equilibrium of forces amongst the submerged weight of a soil mass and normal and tangential forces N and S acting on the potential sliding plane, the stresses σ_α and τ_α are obtained as

$$\sigma_\alpha = \frac{N}{l} = \gamma' H \cos^2 \alpha, \quad \tau_\alpha = \frac{S}{l} = \gamma' H \sin \alpha \cdot \cos \alpha \quad (6)$$

where γ' is the submerged unit weight of the soil, α is the angle of the potential sliding plane, and H is the height of the soil mass being considered. Then, given the values of stress components, σ_α and τ_α , as above, it is possible to locate a point B in the Mohr diagram as illustrated in Figure 24. The direction of the line OB indicates the angle of obliquity of stress application, α , or the angle of stress mobilization. By drawing a half circle through the point B so that it is tangential to the line OB , it becomes possible to identify the points of the major and minor principal stresses σ_1 and σ_3 on the Mohr diagram. Then, from geometrical considerations, the following relations are obtained.

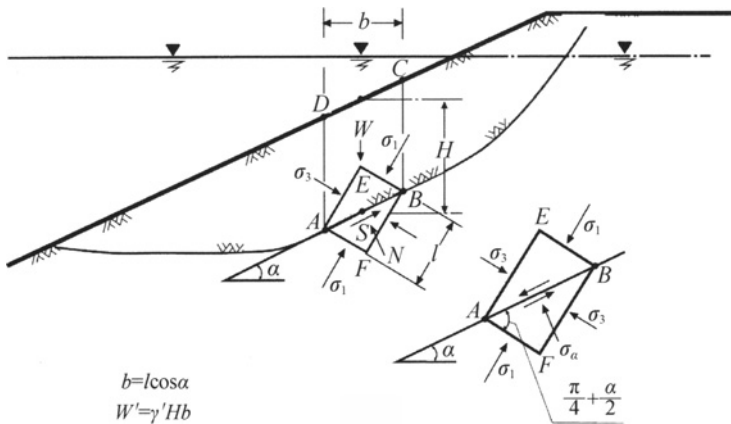


Figure 23. Forces acting on a soil element above a sliding plane in a submerged slope

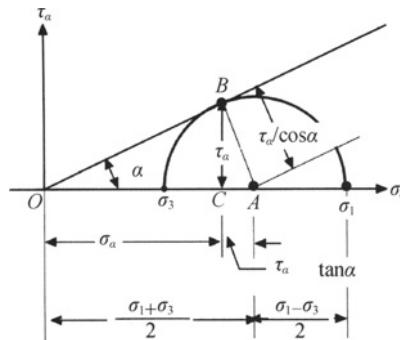


Figure 24. Mohr circle to determine σ_1 and σ_3 from σ_α and τ_α

$$\sigma_1 = \sigma_\alpha + \left(\tan \alpha + \frac{1}{\cos \alpha}\right) \tau_\alpha, \quad \sigma_3 = \sigma_\alpha + \left(\tan \alpha - \frac{1}{\cos \alpha}\right) \tau_\alpha \quad (7)$$

Introducing Eq. (6) into Eq. (7), one obtains

$$\sigma_1 = \gamma' H (1 + \sin \alpha), \quad \sigma_3 = \gamma' H (1 - \sin \alpha) \quad (8)$$

Thus, the ratio between the minor and major principal stresses is obtained as

$$K_c = \sigma_3 / \sigma_1 = \frac{1 - \sin \alpha}{1 + \sin \alpha} \quad (9)$$

The relation of Eq. (9) is displayed in Figure 25. It is known that the majority of natural slopes consisting of relatively soft soils have an angle ranging approximately between

$\alpha = 0$ and $\alpha = 30^\circ$. Thus, the ratio, K_c , between the two principal stresses has a value between 0.3 and 1.0.

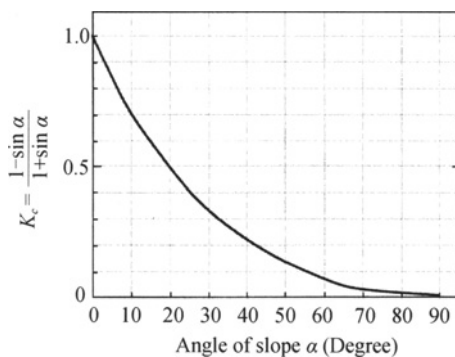


Figure 25. Relation between K_c -value and angle of slope

Typical pattern of deformation

The typical pattern of undrained deformation of anisotropically consolidated specimens is schematically illustrated in Figure 26 in terms of stress path and stress-strain curve. In Figure 26(a), the abscissa indicates the mean principal effective stress defined by $p' = (\sigma'_1 + 2\sigma'_3) / 3$ and the ordinate represents the shear stress defined by $q = \sigma'_1 - \sigma'_3$. In Figure 26, point A indicates an initial state of K_c -consolidation whereupon undrained shear stress application starts. When the specimen is loose, it shows an increase in deviator stress, q , to a point B at peak strength and then a decrease down to a point C corresponding to the state of phase transformation or the quasi-steady state. The bent-over in the stress path takes place at point C and the shear stress increases to a point D where large deformation starts to occur without any change in the effective mean stress p' and shear stress q . This state is called the steady state. Specimen is loose, the minimum deviator stress is encountered, concomitant with fairly large deformation, at point C where the phase transformation takes place from contractive to dilative behaviour.

Thus, the residual strength is defined by the shear stress q_{QS} which is mobilized at point C. The residual strength thus defined is called the strength at quasi-steady state. When the sand is very loose, the gain in the deviator stress from point C to D is not achieved. The sample continues to deform with a constant deviator stress. In other words, the quasi-steady state (QSS) becomes coincident with the steady state (SS). In the case of the Jamuna River sand, the samples are seen deforming at a constant deviator stress as apparent from the test data shown in Figures 13 through 15. This may be due to the presence of mica. Thus, in the present study, the quasi-steady states will be taken as being identical to the steady state.

As touched upon in the foregoing section, the residual strength ratio can be established by normalizing the residual strength, S_{us} , to the major principal stress σ'_{1c} at consolidation, and the ratio S_{us} / σ'_{1c} thus determined was found to be independent of the K_c -condition at the time of consolidation. In unison with this fact, it might be of use if the major principal stress σ'_1 is taken, instead of p' , as a variable to represent the state of confinement. The $q - \sigma'_1$ and $q - \varepsilon_1$ curves in this context can be established as

illustrated in Figure 27 in the fashion similar to those shown in Figure 26. It is to be noted that there is no essential difference between these two methods of representing the undrained behaviour of sand. Thus, from now on, the method of using σ'_1 as shown in Figure 27 will be adopted in the subsequent pages of this paper.

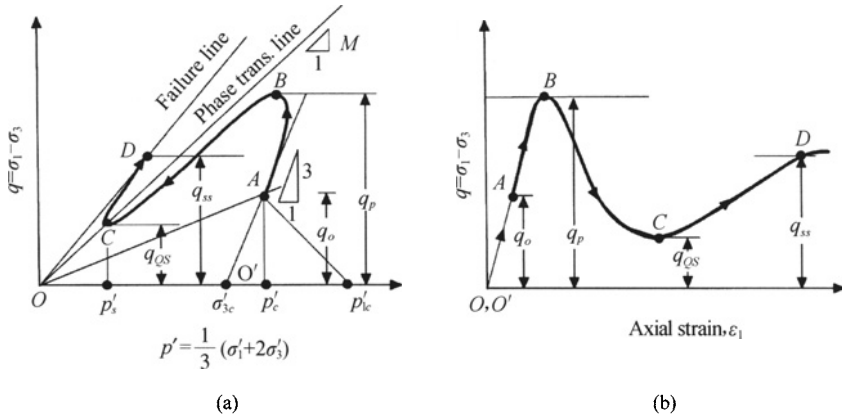


Figure 26. Typical stress-path and stress-strain relation for loose sand

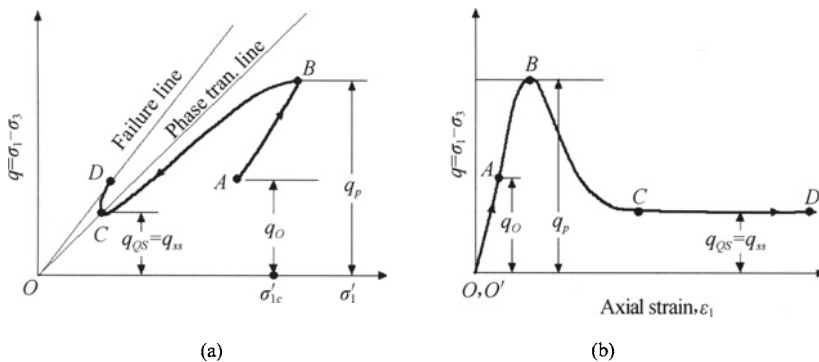


Figure 27. Stress-path and stress-strain diagrams in terms of σ'_1

Consideration for failure of underwater slopes in Jamuna River Bridge site

Sequence of scenarios to flow failure

The series of event leading to the flow-type failure under water would be envisioned to consist of a sequence of events as illustrated in Figure 28.

- (1) The deposit under the level ground was excavated by dredgers to form a slope with an angle α , as illustrated in Figure 28(b). At this stage, a soil element under water was brought to a state of anisotropic consolidation with a $K_c = \sigma'_{3c} / \sigma'_{1c}$ which is evaluated by Eq. (9) through the slope angle α .
- (2) A small magnitude of external agency must have been applied to the soil element to trigger the slip. Although it is not possible to identify a single generic cause as mentioned above, the slip was in fact induced by an additional force $\Delta\sigma_1$ which is deemed to have been applied under an undrained condition. This scenario is illustrated in Figure 28(c).

- (3) After the slip had been triggered, the sand mass continued to deform largely, if the sand was deposited sufficiently loose. The feature of soil deformation at this stage is illustrated in Figure 28(d).

Following the slope failures, configuration of underwater slope surface was detected by means of echo sounding. The outcome of these bathymetric surveys is shown in Figures 29 through 34, where the surface of underwater slopes before and after the failure are indicated for typical cross sections in the permanent and temporary slopes. Looking over the configuration of the post-failure slopes, one may envision that the failure was triggered initially at the toe of the slope and followed by flow-type movement of the soil behind it. The profiles of slopes shown in Figures 29 through 34 disclose that the soils have slid down the slope through a considerable distance resulting in thick deposits of debris at the bottom of the dredged channel. Thus, the post-failure surface in the upper part of the submerged slope can be considered to have been the plane where the soil mass had actually slid down. This surface may therefore be considered as the sliding surface on which flow of liquefied sand had taken place. It is apparent that the sliding surface thus determined is inclined with an angle smaller than the original slope angle of 1:3.0 and 1:5.0. However, to simplify calculation, it may be assumed that the moving surface of the slope during flow with large deformation was in parallel with the sliding plane, as schematically illustrated in Figure 23.

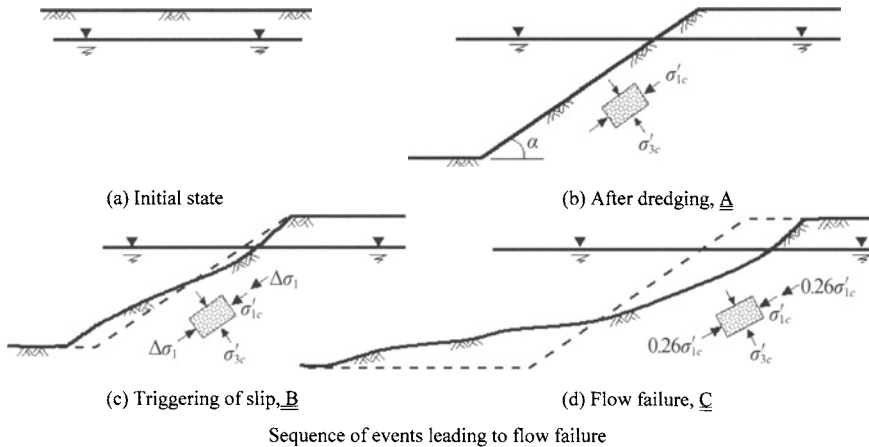


Figure 28. Sequence of events leading to flow failure

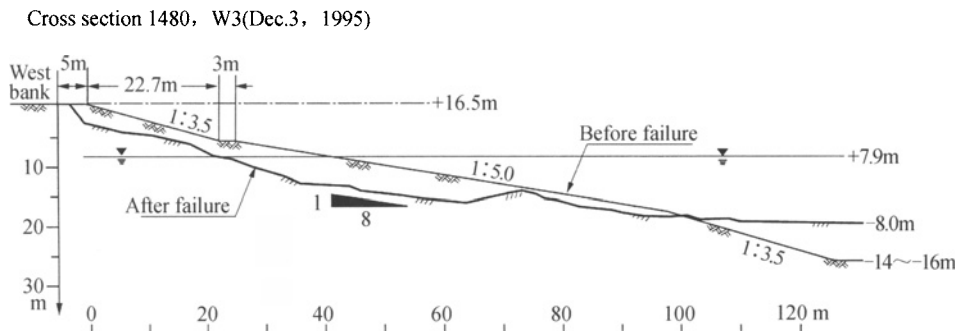


Figure 29. Slide on Dec. 3, 1995 in the permanent slope

Cross section 1500, W3(Dec.3, 1995)

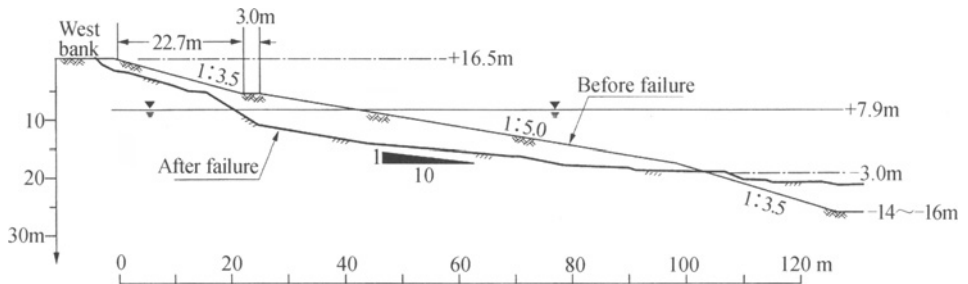


Figure 30. Slide on Dec. 3, 1995 in the permanent slope

Cross section 1550, W3(Dec.3, 1995)

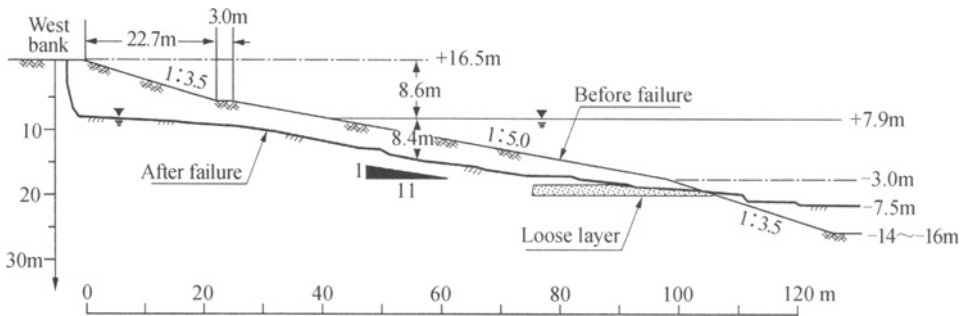


Figure 31. Slide on Dec. 3, 1995 in the permanent slope

Cross section 1800, W4(Dec.15, 1995)

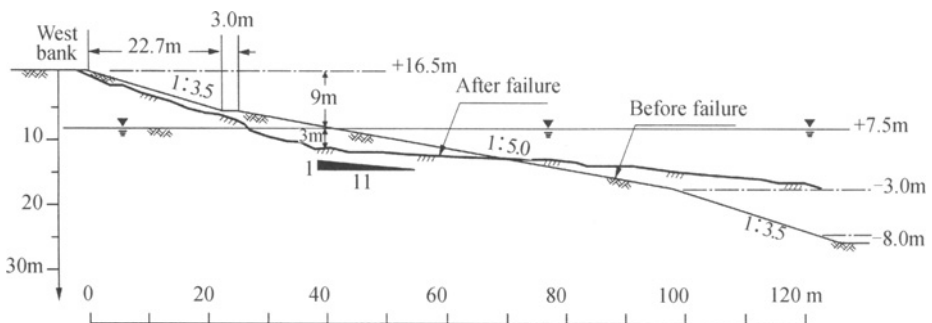


Figure 32. Slide on Dec. 3, 1995 in the permanent slope

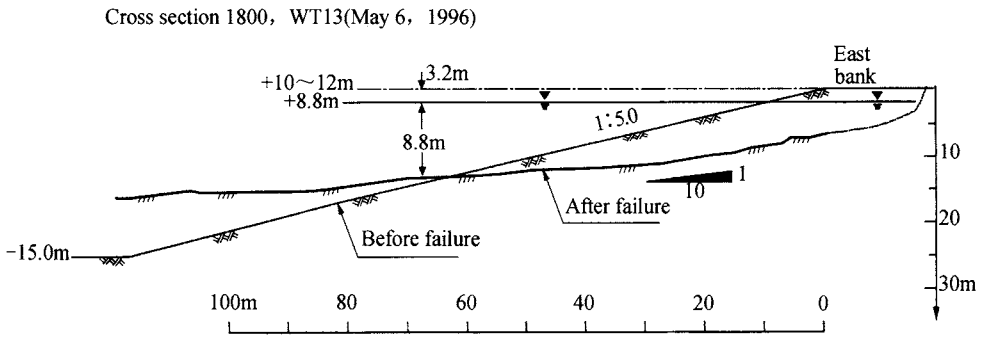


Figure 33. Slide on May 6, 1996 in the temporary slope

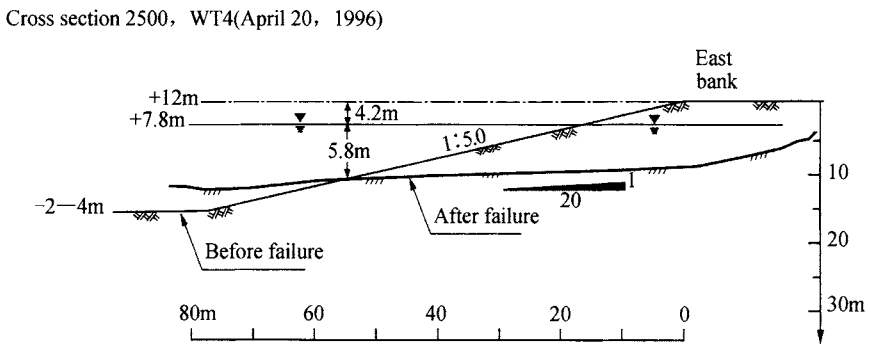


Figure 34. Slide on April 20, 1996 in the temporary slope

Triggering mechanism

There are several cases of submarine landslides documented in the literature. One of the large submarine landslides ever reported in details would be the slide which occurred at the rim of the recent fill towards the sea at the Port of Nice in France on October 16, 1979. The fill, much of which was deposited through or in water, was constructed on a deltaic deposit of stratified clayey silt and silty sand. Features and some analysis results are reported by H.B. Seed et al. (1988). Regarding the triggering mechanism, multiple events were cited to have been possible causes for initiating the slide. These are (1) the tidal wave first inducing about 3m lowering of the sea level due presumably to an off-shore landslide, and (2) the increase in an artesian pressure due to rainfalls in the preceding days which occurred at depths of about 40m in the pervious sand layer which is connected with water levels on land. Thus, it was difficult to narrow down the conceivable causes into a single event.

The clarification of the triggering cause for the slides in the Jamuna River channel is also a difficult task but the reasons variously conceived may be summarized as follows.

- (1) During the process of underwater excavation, the cutting by a dredger might have been carried out so fast that the rapid change in the state of stress did occur creating a highly

undrained condition with the result that a local failure was triggered first and retrogressed into a large slide.

- (2) In the course of the excavation conducted stepwise, one step of cutting might have been so large in block that the steep slope locally created did collapse enlarging the zone of slips into the entire slide.
- (3) There were natural phenomena frequently occurring in the region of Jamuna River. These include torrential downpour, wave actions and falling water levels. None of these phenomena could be pinpointed as a single seminal cause, but the effects of falling water level are most likely to be one of the reasons triggering the slips.
- (4) Besides the externally imposed agencies as cited above, there would be an internal reason. That is the nature of the sand itself containing the mica mineral as mentioned above. The sand in the Jamuna River environment must be deposited in a precarious state narrowly keeping its stability and thus easily susceptible to triggering a failure. This aspect was addressed by Kramer and Seed (1988), who asserted that the sand deposited with a large initial shear stress, that is, the one anisotropically consolidated with a smaller K_c -value, the margin of stability is narrow against additional external agency. This fact holds true for many of sand deposits, as exemplified by the test data demonstrated in Figures 13 to 15. It may be seen for example that the sand consolidated with $K_c=0.5$ with the void ratio of 0.875 could collapse if a small deviator stress of $q=10\text{kPa}$ is applied additionally.

Among several reasons as cited above, there are not strong reasons in support of the above hypotheses 1 and 2, that is, the rapid cutting and overstepping. Once these operations turned out to be undesirable, it is likely that the operators must have changed the way the cutting was performed. Therefore the sliding must have been limited to a certain area throughout the length of the channel. However, the slips did actually occur along the long-stretched zone in the channel. This fact appears to indicate that the hypotheses 1 and 2 are not likely to be the scenario triggering the slips.

It is the author's view that (1) the lowering of water levels and (2) the potentially susceptible nature of the mica-containing sand in the K_c -condition are most likely the two major reasons creating conditions about to trigger the failure. Although the scenario is envisaged as above, it was not possible to come up with a single parameter such as a factor of safety to define the triggering mechanism in a quantitative manner. Thus, the discussion on this aspect is out of consideration in the present study.

Analysis of flow slides in Jamuna River

In this section, consideration is given to whether or not the flow type deformation could be induced in the sand deposit in Jamuna River. Thus, the following discussion is related to the flow mode of slide as illustrated in Figure 28(d).

Factor of safety against flow slide

The flow-type failure will be induced in loose sandy deposits, if the magnitude of the residual strength is equal to or smaller than that of the shear stress induced by the gravity force. It is to be mentioned here that, in the flow mode of slide, the gravity-induced stress

would be the main force driving the soil mass to move further downhill. If the soil deposit is in a loose state exhibiting the contractive behaviour with a residual strength which is smaller than the gravity-induced shear stress, then the soil mass would continue to move downwards leading to the follow-type slide. The deviator stress, q_o , applied initially to a soil element at a depth of H under the submerged slope is evaluated, as follows, with reference to Eq. (8).

$$q_o = \sigma'_{1c} - \sigma'_{3c} = 2\gamma' H \sin \alpha \quad (10)$$

The residual strength, S_{us} , in the soil after it has been deformed largely is known to depend on the void ratio, but if the largest possible normalized residual strength, $S_{us} / \sigma'_{1c} = 0.26$, within the range of contractive behaviour, is taken up for consideration, the residual strength would be estimated with reference to Eqs. (5) and (8) as

$$S_{us} = \frac{q_{Q_s}}{2} \cdot \cos \phi_s = 0.26 \sigma'_{1c} = 0.26 \gamma' H (1 + \sin \alpha) \quad (11)$$

The factor of safety against the flow deformation may be defined as the ratio between the deviator stress q_{Q_s} at the quasi-steady state and the initial deviator stress q_o as illustrated in Figure 27. With reference to the definition given by Eq. (3), the deviator stress $q_{Q_s} = q_s$ is expressed as $q_s = 2S_{us} / \cos \phi_s$ and the initial deviator stress is given by $q_o = \sigma'_{1c} - \sigma'_{3c} = 2\gamma' H \sin \alpha$ from Eq. (8). Thus, the factor of safety against flow is expressed as

$$F_s = \frac{q_{Q_s}}{q_o} = \frac{S_{us}}{\gamma' H \sin \alpha} \cdot \frac{1}{\cos \phi_s} \quad (12)$$

Introducing Eq. (11) into Eq. (12), one obtains,

$$F_s = 0.26 \frac{1 + \sin \alpha}{\sin \alpha} \cdot \frac{1}{\cos \phi_s} \quad (13)$$

The factor of safety thus defined is shown plotted in Figure 35 (a) versus the angle of slope α and also versus the K_c -value as evaluated by Eq. (9). The individual values of F_s obtained from the data of the TC-tests with a relative density of about 65% and 60% are indicated in Figure 35(a) by circles and those from the TE-tests are indicated by rectangles. The plot of Figure 21 showing the relation between K_c -value and S_{us} / σ'_{1c} is reproduced in Figure 36 where the value of void ratio is now indicated for each value of $S_{us} / \sigma'_v = 0.04, 0.09, 0.15$ and 0.26 .

It is known from the plot of Figure 36 that if the relative density in-situ is assumed to have been $D_r \cong 60\%$ corresponding to $e \cong 0.84$, the residual strength ratio would have been $S_{us} / \sigma'_{1c} \cong 0.15$.

For this value, the factor of safety is obtained simply by changing the coefficient in Eq. (13) from 0.26 to 0.15. The relation between F_s and K_c for such a case is also shown in Figure 35 (a). The zone enclosed by these two curves is indicated by shaded colour. In the same fashion, the zone corresponding to the residual strength ratio between 0.15 ($D_r \cong 60\%$) and 0.09 ($D_r \cong 58\%$) is displayed in Figure 35(b).

The factor of safety corresponding to smaller values of $S_{us} / \sigma'_{1c} \cong 0.04$ to 0.09 is shown plotted against K_c -value in Figure 35(c).

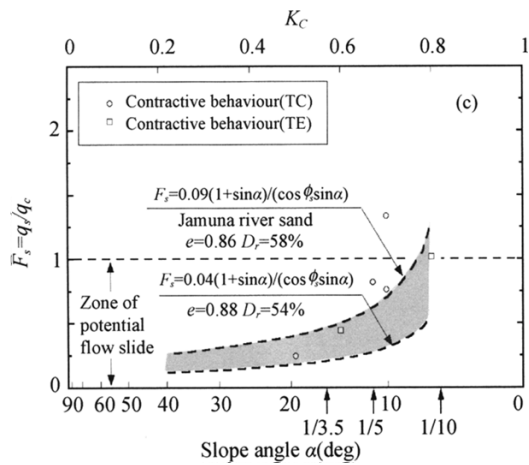
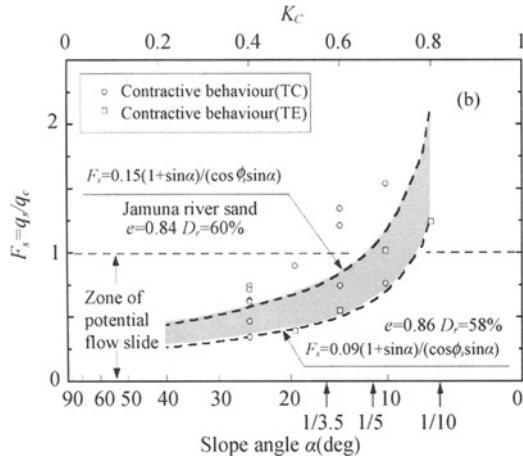
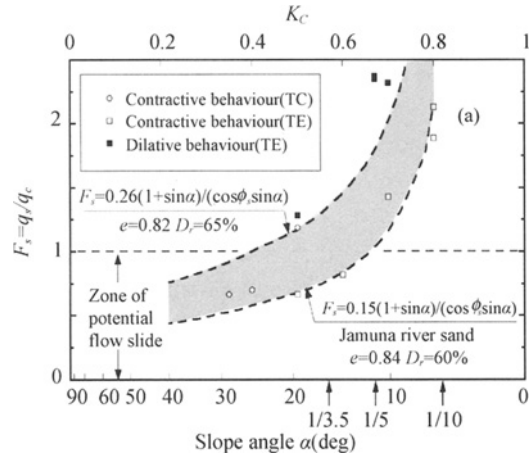


Figure 35. Factor of safety versus K_c -value or angle of slope for the Jamuna River sand

Considerations for flow slides in underwater slopes at Jamuna River bridge site

As mentioned in the foregoing section (see Figure 5, the angle of underwater slope in the Jamuna River excavation was 1:3.5 in the upper and lower parts on the permanent slope and 1:5.0 in the middle portion. The slide took place on Dec. 3, 1995 at the cross sections of 1480, 1500, 1550 within the zone of W3 (see Figure 4) and cross section 1800 in W4 on Dec. 15, 1945. These are shown in Figure 29 to 32. The slide on the temporary slope occurred in April and May in 1996. The cross sections for these slides are shown in Figures 33 and 34.

There are no reliable test data available to assess the relative density of the field deposit in the Jamuna River bed, but judging from the nature of fluvial sediments and from the SPT and CPT data, it is envisaged as shown in Figure 9 that the relative density may be around $D_r = 50\%$ and more likely less than $D_r = 65\%$. With this assumption in mind, the residual strength of the sand in Jamuna River may be estimated roughly from the diagram of Figure 36 in which the normalized residual strength is indicated in terms of void ratio or relative density.

It might be difficult to assess the normalized residual strength only by way of relative density but if attention is paid to the range in the normalized residual strength assumed in the chart of Figure 35, that is, $S_{us} / \sigma'_{1c} = 0.04$ to 0.26, this value seems to be in an appropriate range which is acceptable in the light of many data on other sands ever obtained. Under the consideration as above, it may conclusively mentioned that, (1) for the slope with 1:3.5, the factor of safety against flow slide could easily be less than 1.0 for the Jamuna River bed sand with the normalized residual strength less than about which could be most likely the case, and (2) for the slope with 1:5.0 slope, the value of with $F_s = 1.0$ could be read off from Figure 35(a) as being about 0.15 which could be the case if there exist loose zones in in-situ deposits.

The outcome of the evaluation as described above is summed up in the diagram of Figure 37 where the lines giving a factor of safety $F_s = 0.9, 1.0$ and 1.7 are indicated in terms of slope angle α and relative density. For reference sake, SPT N-value converted by the empirical relation

$$N_1 = 25 \left(\frac{D_r}{100} \right)^2 \quad (14)$$

is demonstrated in the ordinate of Figure 37 with the scale indicated on the right-hand side. Eq. (14) is quoted from the study by Cubrinovski and Ishihara (1999) by assuming that $e_{\max} - e_{\min} = 0.60$. The N_1 -value in Eq. (14) indicates the SPT N-value corresponding to an overburden pressure of 1 kg/cm^2 and also about 80% of the theoretical energy in hammer hitting.

Drawing attention to the line $F_s = 1.0$ in Figure 37, one may recognize that for the slope angle between 1:5.0 and 1:3.0, the factor of safety estimated lies in the zone of flow-type instability with $F_s < 1.0$ assuming the relative density smaller than about 65%.

In view of the actual conditions in the field at Jamuna River as described in the foregoing sections, the results of the simple analysis summarized in Figure 37 would appear to provide evidences with a reasonable level of credibility for the occurrence of the underwater flow-type slides on the excavated slopes in Jamuna River.

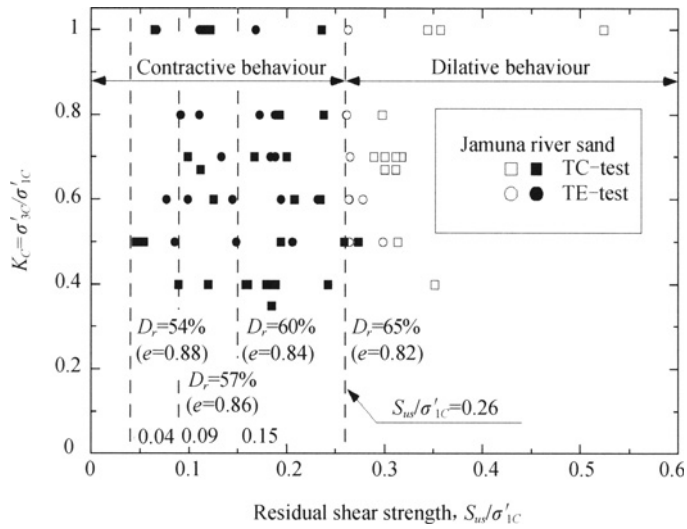


Figure 36. Void ratio versus the normalized residual strength

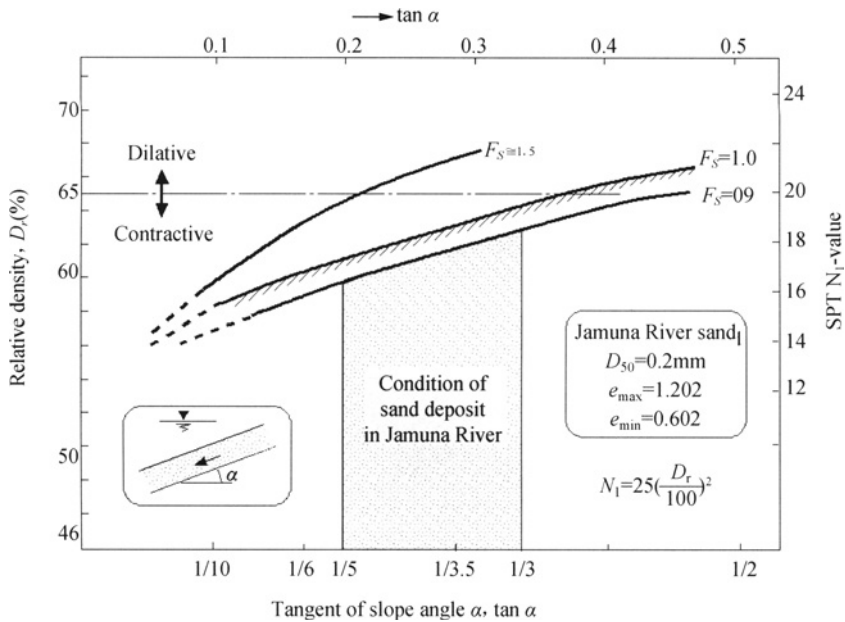


Figure 37. Relation between density, SPT N-value and slope angle for given factor of safety

CONCLUSIVE REMARKS

The failure of the underwater slopes during the dredging excavation in the sand bar deposit in Jamuna River in Bangladesh was introduced first and then some speculative reasons for such slips to have occurred were pointed out. To provide a sound basis for interpretation of

failure mechanism, the results of multiple series of triaxial tests in the laboratory were introduced with the framework of the concept in line with the test results on other sands in Japan. The main points derived from the tests are summarized as follows.

1. It is known that the sand initially consolidated with higher degrees of anisotropy, that is, with a smaller K_c -value, tends to exhibit more contractive (or collapsible) behaviour when it is deformed largely into a steady-state. To take into account of this effect, it was found more appropriate to select the major initial principal stress, σ'_{1c} , not the mean initial principal stress, $p'_c = (\sigma'_{1c} + 2\sigma'_{2c})/3$, as an index parameter to express the effects of confinement. Thus, when the residual strength S_{us} at the steady state is normalized to the major principle stress, σ'_{1c} , it was found that the value of S_{us} / σ'_{1c} takes a constant value irrespective of K_c -conditions.
2. The normalized residual strength S_{us} / σ'_{1c} was found to be expressed uniquely as a function of relative density or void ratio. Within the range of relative density in which the behaviour is contractive, the upper limit of the normalized residual strength for the Jamuna River sand was found to be $S_{us} / \sigma'_{1c} = 0.26$ and this value is encountered when the sand is deposited at a relative density of approximately $D_r = 65\%$. On the basis of the SPT and CPT data, the in-situ relative density at the site of Jamuna River was found to be somewhere around $D_r = 50\%$ which is less than 65%. This fact implies that the in-situ deposit is within the range of density where the sand exhibits contractive behaviour indicating high potentiality to flow type deformation once the slip is triggered by some other external forces.
3. On the other hand, the slope angle of dredged channel in Jamuna River at the time of sliding is known to have been 1:3.5 ($\cong 16$ degree) and 1:5.0 ($\cong 11.31$ degree). By assuming the flow slides to have occurred on the straight-line sliding plane which is parallel to the surface of the slope, it was possible to assess the magnitude of shear stress and the major principal stress σ'_{1c} which was mobilized by gravity force in the sand deposits in the slopes excavated with the angle of 1:3.5 and 1:5.0.
4. By comparing the magnitude of gravity-induced shear stress assessed as above with the value of residual strength evaluated from the results of the laboratory tests, it was found that the gravity-driven shear stress must have become greater than the residual strength available at the riverbed deposit, if the in-situ sand were deposited with a relative density in the range less than 65%. Thus, the flow-type failure might have occurred.
5. It is to be noticed here that for many other sands in Japan, the upper limit of density showing contractive behaviour is, by and large, smaller than $D_r = 40\%$. This implies that only loosely deposited sand with a relative density less than about 40% could develop flow type deformation and therefore such a sand is identified potentially more stable in the state of in-situ deposition. In contrast, with a higher value of upper-limit density such as the mica-containing Bangladesh sand, the likelihood is high for in-situ deposits to exist with a relative density less than the upper limit density. Thus, such a sand is to be identified as potentially unstable. In the sense as above, the identification of the upper limit density or threshold density differentiating between conditions of contractive and dilative behaviour of a given sand will pose a important challenge in future development in this area of soil mechanics.

ACKNOWLEDGEMENTS

The study described in this paper was initiated by the author who paid a visit of inspection to the Jamuna River site upon recommendation by Professor W. Van Impe, Past president of ISSMGE. The engineers of HAM-van Oord kindly showed the author around the site. The triaxial tests in the laboratory were carried out under the supervision of Professor Y. Tsukamoto by Mr. Y. Nakayama and T. Shibayama, who were graduate students at the Tokyo University of Science. Professor M. Yoshimine of Tokyo Metropolitan University kindly provided data on the cone penetration tests in Jamuna River site. The author wishes to express his sincere gratitude to the persons cited above.

REFERENCES

- Chern J.C. (1985). *Undrained response of saturated sands with emphasis on liquefaction and cyclic mobility*. Ph. D. Theses, University of British Columbia, Vancouver.
- Cubrinovski M. and Ishihara K. (1999). Empirical correlation between SPT N-value and relative density for sandy soils. *Soils and Foundations*, 39 (5): 61-71.
- Hight D. W., Georgiannou V.N., Matin P.L. and Mundegar A.K. (1999). Flow slides in micaceous sands. *Proc. International Symposium on Problematic Soils*, Sendai, Japan, 2: 945-958.
- Ishihara K. (1996). *Soil behaviour in earthquake geotechnics*. Oxford Clarendon Press, 259-260.
- Ishihara K., Tsukamoto Y. and Shibayama T. (2003). *Evaluation of slope stability against flow in saturated sand*., Reports on Geotechnical Engineering, Soil Mechanics and Rock Mechanics, 5, Jubilee Vol. of 75th Anniversary of K. Terzaghi's Erdbaumechanik, 41-54.
- Ishihara K., Tsukamoto Y. (2007). Underwater slides of sand deposits during dredging excavation. *Proc. of International Geotechnical Symposium on Geotechnical Engineering for Disaster Prevention and Reduction*, Yuzhno-Sakhalinsk, Russia, 3-21.
- Kato S., Ishihara K. and Towhata I. (2001). Undrained shear characteristics of saturated sand under anisotropic consolidation. *Soils and Foundations*, 41 (1): 1-11.
- Kramer S.L. and Seed H.B. (1988). Initiation of soil liquefaction under static loading conditions. *Journal of Geotechnical Engineering Division, ASCE*, 114 (4): 412-430.
- Seed. H. B., Seed R.B., Schlosser F., Blondeau F. and Juran I. (1988). The landslide at the port of Nice on October 16, 1979. Report No. UCB/EERC-88/10, University of California, Berkeley.
- Tsukamoto T., Ishihara K. and Kamata T. (2007). *Residual strength of soils under flow deformation in triaxial tests*. submitted to a journal.
- Vaid Y.P., Chern J.C. (1985). Cyclic and monotonic undrained response of saturated sands. Advances in the Art of Testing Soils under Cyclic Condition. *Proc. of ASCE Convention in Detroit, Michigan*, 120-147.
- Yoshimine M., Robertson P.K. and Wride C.E. (1999). Undrained shear strength of clean sands to trigger flow liquefaction. *Canadian Geotechnical Journal*, 36: 891-906.
- Yoshimine M., Robertson P.K. and Wride C.E. (2001). Reply to discussion. *Canadian Geotechnical Journal*, 38: 654-657.

**Keynote and Special Invited
Plenary Lectures**

INTERACTION BETWEEN EUROCODE 7 – GEOTECHNICAL DESIGN AND EUROCODE 8 – DESIGN FOR EARTHQUAKE RESISTANCE OF FOUNDATIONS

P.S. Sêco e Pinto

*Professor of Geotechnical Engineering Faculty of Engineering, University of Coimbra
National Laboratory of Civil Engineering (LNEC), Lisbon, Portugal
President of International Society for Soil Mechanics and Geotechnical Engineering*

This keynote lecture summarises the main topics covered by Eurocode 7 and the interplay with Eurocode 8 and also identify some topics that need further implementation.

INTRODUCTION

The Commission of the European Communities (CEC) initiated a work in 1975 of establishing a set of harmonised technical rules for the structural and geotechnical design of buildings and civil engineers works based on article 95 of the Treaty. In a first stage would serve as alternative to the national rules applied in the various Member States and in a final stage will replace them.

From 1975 to 1989 the Commission with the help of a Steering Committee with the Representatives of Member States developed the Eurocodes programme.

The Commission, the Member states of the EU and EFTA decided in 1989 based on an agreement between the Commission and CEN to transfer the preparation and the publication of the Eurocodes to CEN.

The Structural Eurocode programme comprises the following standards:

EN 1990 Eurocode – Basis of design

EN 1991 Eurocode 1 – Actions on structures

EN 1992 Eurocode 2 – Design of concrete structures

EN 1993 Eurocode 3 – Design of steel structures

EN 1994 Eurocode 4 – Design of composite steel and concrete structures

EN 1995 Eurocode 5 – Design of timber structures

EN 1996 Eurocode 6 – Design of masonry structures

EN 1997 Eurocode 7 – Geotechnical design

EN 1998 Eurocode 8 – Design of structures for earthquake resistance

EN 1999 Eurocode 9 – Design of aluminium alloy structures

The work performed by the Commission of the European Communities (CEC) in preparing the “Structural Eurocodes” in order to establish a set of harmonised technical rules is impressive. Nevertheless, due the preparation of these documents by several experts, some provisions of EC8 with the special requirements for seismic geotechnical design that deserve

more consideration will be presented in order to clarify several questions that still remain without answer.

The actual tendency is to prepare unified codes for different regions but keeping the freedom for each country to choose the safety level defined in each National Document of Application. The global safety of factor was substituted by the partial safety factors applied to actions and to the strength of materials.

This keynote lecture summarises the main topics covered by Eurocode 7 and the interplay with Eurocode 8 and also identify some topics that need further implementation.

In dealing with these topics we should never forget the memorable lines of Lao- Tsze, Maxin 64 (550 B.C.): “The journey of a thousand miles begins with one step”.

EUROCODE 7 – GEOTECHNICAL DESIGN

Introduction

The Eurocode 7 (EC7) “Geotechnical Design” gives a general basis for the geotechnical aspects of the design of buildings and civil engineering works. The link between the design requirements in Part 1 and the results of laboratory tests and field investigations run according to standards, codes and other accepted documents is covered by Part 2.

EN 1997 is concerned with the requirements for strength, stability, serviceability and durability of structures. Other requirements, e.g. concerning thermal or sound insulation, are not considered.

Eurocode 7 - geotechnical design–part 1

The following subjects are dealt with in EN 1997-1 - Geotechnical design:

Section 1: General

Section 2: Basis of Geotechnical Design

Section 3: Geotechnical Data

Section 4: Supervision of Construction, Monitoring and Maintenance

Section 5: Fill, Dewatering, Ground Improvement and Reinforcement

Section 6: Spread Foundations

Section 7: Pile Foundations

Section 8: Anchorages

Section 9: Retaining Structures

Section 10: Hydraulic failure

Section 11: Overall stability

Section 12: Embankments

Design requirements

The following factors shall be considered when determining the geotechnical design requirements:

site conditions with respect to overall stability and ground movements;

nature and size of the structure and its elements, including any special requirements such as the design life;

conditions with regard to its surroundings (neighbouring structures, traffic, utilities, vegetation, hazardous chemicals, etc.);
ground conditions;
groundwater conditions;
regional seismicity;
influence of the environment (hydrology, surface water, subsidence, seasonal changes of temperature and moisture).

Each geotechnical design situation shall be verified that no relevant limit state is exceeded.

Limit states can occur either in the ground or in the structure or by combined failure in the structure and the ground.

Limit states should be verified by one or a combination of the following methods: design by calculation, design by prescriptive measures, design by loads tests and experimental models and observational method.

To establish geotechnical design requirements, three Geotechnical Categories, 1, 2 and 3 are introduced

Geotechnical Category 1 includes small and relatively simple structures.

Geotechnical Category 2 includes conventional types of structure and foundation with no exceptional risk or difficult soil or loading conditions.

Geotechnical Category 3 includes: (i) very large or unusual structures; (ii) structures involving abnormal risks, or unusual or exceptionally difficult ground or loading conditions; and (iii) structures in highly seismic areas.

Geotechnical design by calculation

Design by calculation involves:

- actions, which may be either imposed loads or imposed displacements, for example from ground movements;
- properties of soils, rocks and other materials;
- geometrical data;
- limiting values of deformations, crack widths, vibrations etc.
- calculation models.

The calculation model may consist of: (i) an analytical model; (ii) a semi-empirical model; (iii) or a numerical model.

Where relevant, it shall be verified that the following limit states are not exceeded: loss of equilibrium of the structure or the ground, considered as a rigid body, in which the strengths of structural materials and the ground are insignificant in providing resistance (EQU);

internal failure or excessive deformation of the structure or structural elements, including footings, piles, basement walls, etc., in which the strength of structural materials is significant in providing resistance (STR);

failure or excessive deformation of the ground, in which the strength of soil or rock is significant in providing resistance (GEO);

loss of equilibrium of the structure or the ground due to uplift by water pressure (buoyancy) or other vertical actions (UPL);

hydraulic heave, internal erosion and piping in the ground caused by hydraulic gradients (HYD).

The selection of characteristic values for geotechnical parameters shall be based on derived values resulting from laboratory and field tests, complemented by well-established experience.

The characteristic value of a geotechnical parameter shall be selected as a cautious estimate of the value affecting the occurrence of the limit state.

For limit state types STR and GEO in persistent and transient situations, three Design Approaches are outlined. They differ in the way they distribute partial factors between actions, the effects of actions, material properties and resistances. In part, this is due to differing approaches to the way in which allowance is made for uncertainties in modeling the effects of actions and resistances.

In Design Approach 1 partial factors are applied to actions, rather than to the effects of actions and ground parameters,

In Design Approach 2 this approach, partial factors are applied to actions or to the effects of actions and to ground resistances.

In Design Approach 3 partial factors are applied to actions or the effects of actions from the structure and to ground strength parameters.

It shall be verified that a limit state of rupture or excessive deformation will not occur.

It shall be verified serviceability limit states in the ground or in a structural section, element or connection.

Design by prescriptive measures

In design situations where calculation models are not available or not necessary, the exceedance of limit states may be avoided by the use of prescriptive measures. These involve conventional and generally conservative rules in the design, and attention to specification and control of materials, workmanship, protection and maintenance procedures.

Design by load tests and experimental models

When the results of load tests or tests on large or small scale models are used to justify a design, the following features shall be considered and allowed for:

- differences in the ground conditions between the test and the actual construction;
- time effects, especially if the duration of the test is much less than the duration of loading of the actual construction;
- scale effects, especially if small models are used. The effect of stress levels shall be considered, together with the effects of particle size.

Tests may be carried out on a sample of the actual construction or on full scale or smaller scale models.

Observational method

When prediction of geotechnical behaviour is difficult, it can be appropriate to apply the approach known as "the observational method", in which the design is reviewed during construction.

The following requirements shall be met before construction is started:

- the limits of behaviour which are acceptable shall be established;

- the range of possible behaviour shall be assessed and it shall be shown that there is an acceptable probability that the actual behaviour will be within the acceptable limits;
- a plan of monitoring shall be devised which will reveal whether the actual behaviour lies within the acceptable limits. The monitoring shall make this clear at a sufficiently early stage and with sufficiently short intervals to allow contingency actions to be undertaken successfully;
- the response time of the instruments and the procedures for analysing the results shall be sufficiently rapid in relation to the possible evolution of the system;
- a plan of contingency actions shall be devised which may be adopted if the monitoring reveals behaviour outside acceptable limits.

Eurocode 7 -part 2

EN 1997-2 is intended to be used in conjunction with EN 1997-1 and provides rules supplementary to EN 1997-1 related to the:

- planning and reporting of ground investigations;
- general requirements for a number of commonly used laboratory and field tests;
- interpretation and evaluation of test results;
- derivation of values of geotechnical parameters and coefficients.

The field investigation programme shall contain:

- a plan with the locations of the investigation points including the types of investigations,
- the depth of the investigations;
- the type of samples (category, etc) to be taken including specifications on the number and depth at which they are to be taken;
- specifications on the ground water measurement;
- the types of equipment to be used;
- the standards that are to be applied.

The laboratory test programme depends in part on whether comparable experience exists.

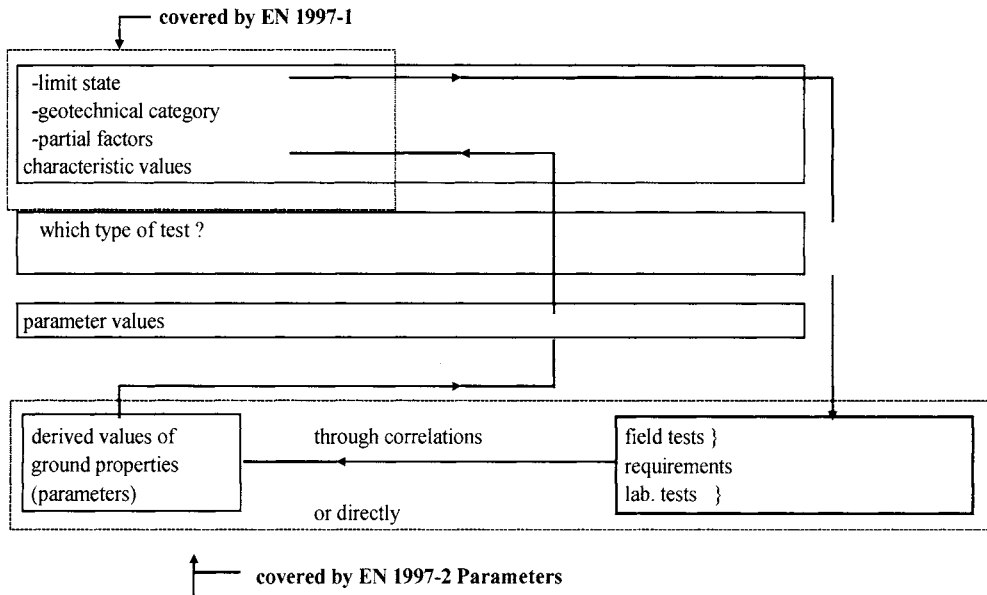
The extent and quality of comparable experience for the specific soil or rock should be established.

The results of field observations on neighbouring structures, when available, should also be used.

The tests shall be run on specimens representative of the relevant strata. Classification tests shall be used to check whether the samples and test specimens are representative.

This can be checked in an iterative way. In a first step classification tests and strength index tests are performed on as many samples as possible to determine the variability of the index properties of a stratum. In a second step the representativeness of strength and compressibility tests can be checked by comparing the results of the classification and strength index tests of the tested sample with entire results of the classification and strength index tests of the stratum.

The flow chart shown below demonstrates the link between design and field and laboratory tests. The design part is covered by EN 1997-1; the parameter values part is covered by EN 1997-2.



EUROCODE 8 – DESIGN OF STRUCTURES FOR EARTHQUAKE RESISTANCE

Introduction

The Eurocode 8 (EC8) “Design of Structures for Earthquake Resistant” deals with the design and construction of buildings and civil engineering works in seismic regions is divided in six Parts.

The Part 1 is divided in 10 sections:

Section 1 - contains general information;

Section 2 - contains the basis requirements and compliance criteria applicable to buildings and civil engineering works in seismic regions;

Section 3 - gives the rules for the representation of seismic actions and their combination with other actions;

Section 4 - contains general design rules relevant specifically to buildings;

Section 5 - presents specific rules for concrete buildings;

Section 6 - gives specific rules for steel buildings;

Section 7 - contains specific rules for steel-concrete composite buildings;

Section 8 - presents specific rules for timber buildings;

Section 9 - gives specific rules for masonry buildings;

Section 10 - contains fundamental requirements and other relevant aspects for the design and safety related to base isolation.

Further Parts include the following:

Part 2 contains relevant provisions to bridges.

Part 3 presents provisions for the seismic strengthening and repair of existing buildings.

Part 4 gives specific provisions relevant to tanks, silos and pipelines.

Part 5 contains specific provisions relevant to foundations, retaining structures and geotechnical aspects.

Part 6 presents specific provisions relevant to towers, masts and chimneys.

In particular the Part 5 of EC8 establishes the requirements, criteria, and rules for siting and foundation soil and complements the rules of Eurocode 7, which do not cover the special requirements of seismic design

The topics covered by Part 1- Section 1 namely: seismic action, ground conditions and soil investigations, importance categories, importance factors and geotechnical categories and also the topics treated in Part 5 slope stability, potentially liquefiable soils, earth retaining structures, foundation system, topographic aspects are discussed.

Seismic action

The definition of the actions (with the exception of seismic actions) and their combinations is treated in Eurocode 1 “Action on Structures”.

Nevertheless the definition of some terms in EN 1998-1 further clarification of seismic hazard analysis as stressed by Abrahamson (2000) is needed.

In general the national territories are divided by the National Authorities into seismic zones, depending on the local hazard.

In EC 8, in general, the hazard is described in terms of a single parameter, i.e. the value a_g of the effective peak ground acceleration in rock or firm soil called “design ground acceleration”(Figure 1) expressed in terms of: a) the reference seismic action associated with a probability of exceeding (P_{NCR}) of 10 % in 50 years; or b) a reference return period (T_{NCR})= 475.

These recommended values may be changed by the National Annex of each country (e.g. in UBC (1997) the annual probability of exceedance is 2% in 50 years, or an annual probability of 1/2475).

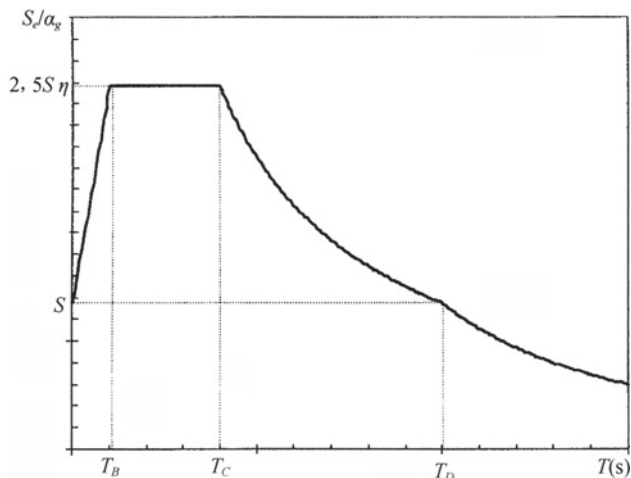


Figure 1. Elastic response spectrum (after EC8)

where:

$S_e(T)$ elastic response spectrum;

T vibration period of a linear single-degree-of-freedom system;

α_g design ground acceleration;

T_B, T_C limits of the constant spectral acceleration branch;

T_D value defining the beginning of the constant displacement response range of the spectrum;

S soil parameter with reference value 1.0 for subsoil class A;

η damping correction factor with reference value 1.0 for 5 % viscous damping.

The earthquake motion in EC 8 is represented by the elastic response spectrum defined by 3 components.

It is recommended the use of two types of spectra: type 1 if the earthquake has a surface wave magnitude M_s greater than 5.5 and type 2 in other cases.

The seismic motion may also be represented by ground acceleration time-histories and related quantities (velocity and displacement). Artificial accelerograms shall match the elastic response spectrum. The number of the accelerograms to be used shall give a stable statistical measure (mean and variance) and a minimum of 3 accelerograms should be used and also some others requirements should be satisfied.

For the computation of permanent ground deformations the use of accelerograms recorded on soil sites in real earthquakes or simulated accelerograms is allowed provided that the samples used are adequately qualified with regard to the seismogenic features of the sources.

For structures with special characteristics spatial models of the seismic action shall be used based on the principles of the elastic response spectra.

Ground conditions and soil investigations

For the ground conditions five subsoil classes A, B, C, D and E are considered:

Subsoil class A – rock or other geological formation, including at most 5 m of weaker material at the surface characterised by a shear wave velocity V_s of at least 800 m/s.

Subsoil class B – deposits of very dense sand, gravel or very stiff clay, at least several tens of m in thickness, characterised by a gradual increase of mechanics properties with depth shear wave velocity between 360-800 m/s, $N_{SPT} > 50$ blows and $c_u > 250$ kPa.

Subsoil class C – deep deposits of dense or medium dense sand, gravel or stiff clays with thickness from several tens to many hundreds of meters characterised by a shear wave velocity from 160 m/s to 360 m/s, N_{SPT} from 15-50 blows and c_u from 70 to 250 kPa.

Subsoil class D – deposits to loose to medium cohesionless soil (with or without some soft cohesive layers), or of predominantly soft to firm cohesive soil characterised by a shear wave velocity less than 180 m/s, N_{SPT} less than 15 and c_u less than 70 kPa.

Subsoil class E – a soil profile consisting of a surface alluvium layer with $V_{s,30}$ values of type C or D and thickness varying between about 5m and 20m, underlain by stiffer material with $V_{s,30} > 800$ m/s.

Subsoil S_1 – deposits consisting - or containing a layer at least 10 m thick - of soft clays/silts with high plasticity index ($PI > 40$) and high water content characterised by a shear wave velocity less than 100 m/s and c_u between 10-20 kPa.

Subsoil S_2 – deposits of liquefiable soils, of sensitive clays, or any other soil profile not included in types A-E or S_1 .

For the five ground types the recommended values for the parameters S , T_B , T_C , T_D , for Type 1 and Type 2 are given in Tables 1 and 2.

Table 1. Values of the parameters describing the type 1 elastic response spectrum

Ground type	S	$T_B(s)$	$T_C(s)$	$T_D(s)$
A	1.0	0.15	0.4	2.0
B	1.2	0.15	0.5	2.0
C	1.15	0.20	0.6	2.0
D	1.35	0.20	0.8	2.0
E	1.4	0.15	0.5	2.0

The recommended Type 1 and Type 2 elastic response spectra for ground types A to E are shown in Figures 2 and 3.

Table 2. Values of the parameters describing the Type 2 elastic response spectrum

Ground type	S	$T_B(s)$	$T_C(s)$	$T_D(s)$
A	1.0	0.05	0.25	1.2
B	1.35	0.05	0.25	1.2
C	1.5	0.10	0.25	1.2
D	1.8	0.10	0.30	1.2
E	1.6	0.05	0.25	1.2

The recommended values of the parameters for the five ground types A, B, C, D and E for the vertical spectra are shown in Table 3. These values are not applied for ground types S_1 and S_2 .

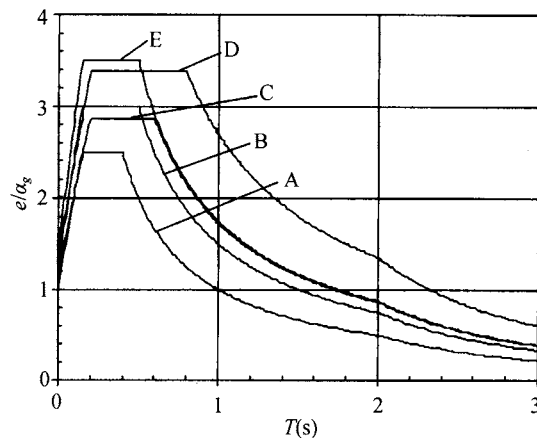


Figure 2. Recommended type 1 elastic response spectrum (after EC8)

Table 3. Recommended values of the parameters for the five ground types A, B, C, D and E

Spectrum	α_{vg}/α_g	$T_B(s)$	$T_C(s)$	$T_D(s)$
Type 1	0.9	0.05	0.15	1.0
Type 2	0.45	0.05	0.15	1.0

The influence of local conditions on site amplification proposed by Seed and Idriss (1982) is shown in Figure 4. The initial response spectra proposed in the pre-standard EC8 based in Seed and Idriss proposal was underestimating the design levels of soft soil sites in contradiction with the observations of the last recorded earthquakes.

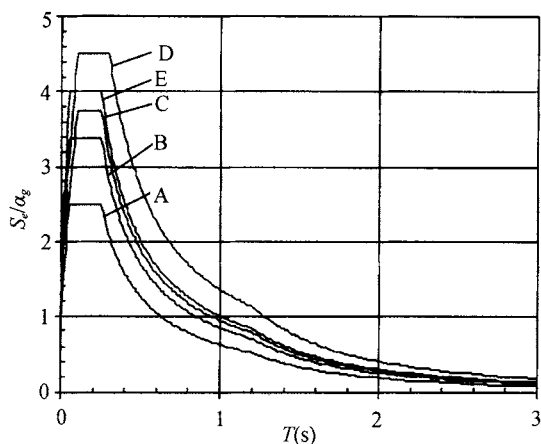


Figure 3. Recommended type 2 elastic response spectrum (after EC8)

Based on records of earthquakes Idriss (1990) has shown that peak accelerations on soft soils have been observed to be larger than on rock sites (Figure 5). The high quality records from very recent earthquakes Northridge (1994), Hyogo-ken-Nambu (1995), Kocaeli (1999), Chi-Chi (1999) and Tottoriken (2000) have confirmed the Idriss (1990) proposal.

Based in strong motions records obtained during Hyogoken-Nambu earthquake in four vertical arrays sites and using and inverse analysis Kokusho and Matsumoto (1997) have plotted in Figure 6 the maximum horizontal acceleration ratio against maximum base acceleration and proposed the regression equation:

$$\text{Accsurface}/\text{Accbase}=2.0 \exp(-1.7 \text{ Acc}/980) \quad (1)$$

This trend with a base in a Pleistocene soil is similar to the Idriss (1990) proposal where the base was in rock.

The downhole arrays are useful:(i) to understand the seismic ground response; and (ii) to calibrate our experimental and mathematical models.

Following the comments proposed by Southern Member States the actual recommended elastic response spectrum of EC8 incorporates the lessons learnt by recent earthquakes.

The soil investigations shall follow the same criteria adopted in non-seismic areas, as defined in EC 7 (Parts 1, 2 and 3).

The soil classification proposed in the pre-standard of EC8, based only on the 3 ground materials and classified by the wave velocities was simpler. The actual ground classification of EC8 follows a classification based on shear wave velocity, on SPT values and on undrained shear strength, similar to UBC (1997) that is shown in Table 4.

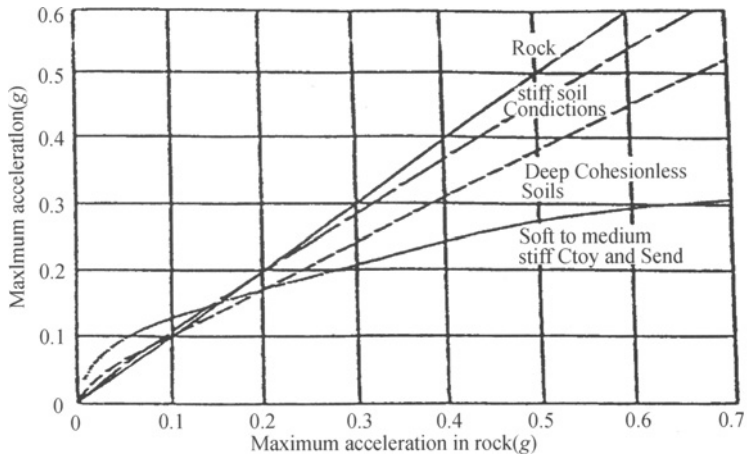


Figure 4. Influence of local soil conditions on site response (after Seed and Idriss, 1982)

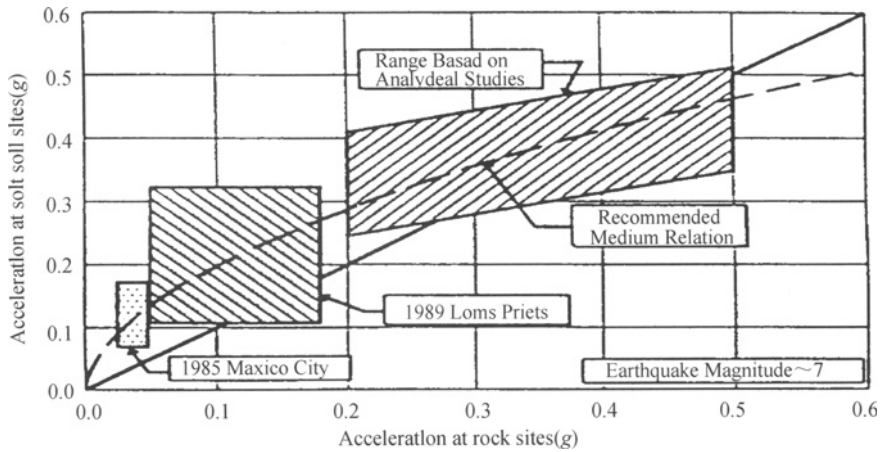


Figure 5. Influence of local soil conditions on site response (after Idriss, 1990)

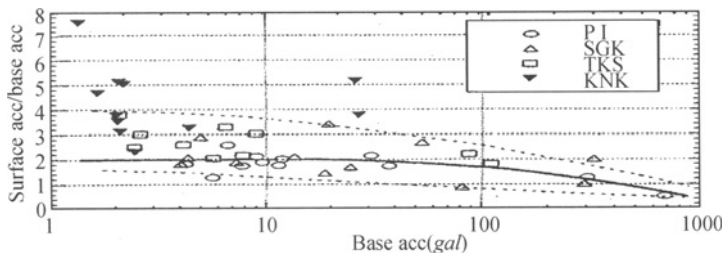


Figure 6. Maximum horizontal acceleration ratio plotted against maximum base acceleration (after Kokusho and Matsumoto, 1997)

Based on the available strong-motion database on equivalent linear and fully nonlinear analyses of response to varying levels and characteristics of excitation Seed et al. (1997) have

proposed for site depending seismic response the Figures 7 and 8, where A_0 , A and AB are hard to soft rocks, B are deep or medium depth cohesionless or cohesive soils, C, D soft soils and E soft soils, high plasticity soils.

Table 4. Ground profile types (after UBC, 1997)

Ground profile type	Ground description	Shear wave velocity $V_s(m/s)$	SPT test	Undrained shear strength (kPa)
S_A	Hard rock	1500	—	—
S_B	Rock	760-1500	—	—
S_C	Very dense soil and soft rock	360-760	>50	>100
S_D	Stiff soil	180-360	15~50	50~100
S_E	Soft soil	<180	<15	<50
S_F	Special soils			

Comments: The following comments are pointed: (i) as seismic cone tests have shown good potentialities they should also be recommended; (ii) the EC 8 (Part 5) stress the need for the definition of the variation of shear modulus and damping with strain level, but doesn't refer to the use of laboratory tests such as cyclic simple shear test, cyclic triaxial test and cyclic torsional test. It is important to stress that a detailed description of laboratory tests for the static characterisation of soils is given in EC 7 Part 2 and the same criteria is not adopted in EC 8 – Part 5.

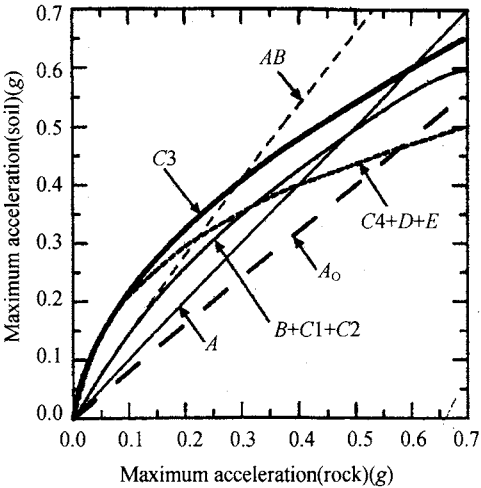


Figure 7. Proposed site-dependent relationship (after Seed et al., 1997)

Importance categories, importance factors and geotechnical categories

The structures following EC 8 (Part 1.2) are classified in 4 importance categories related with its size, value and importance for the public safety and on the possibility of human losses in case of a collapse.

To each importance category an important factor γ_I is assigned. The important factor $\gamma_I = 1,0$ is associated with a design seismic event having a reference return period of [475] years.

The importance categories varying I to IV (with the decreasing of the importance and complexity of the structures) are related with the importance factor γ_I assuming the values [1,4], [1,2], [1,0] and [0,8], respectively.

To establish geotechnical design requirements three Geotechnical Categories 1, 2 and 3 were introduced in EC 7 with the highest category related with unusual structures involving abnormal risks, or unusual or exceptionally difficult ground or loading conditions and structures in highly seismic areas.

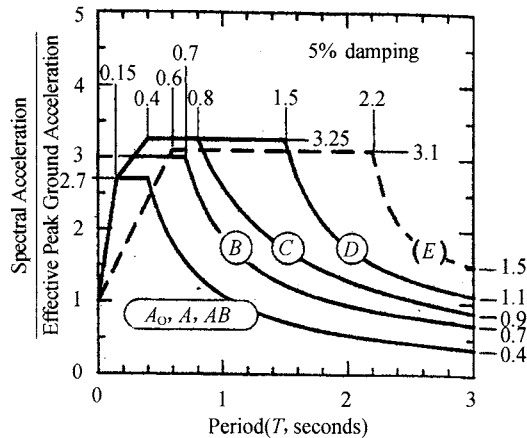


Figure 8. Proposed site-dependent response spectra, with 5% damping (after Seed et al.,1997)

Also it is important to refer that buildings of importance categories [I, II, III] shall generally not be erected in the immediate vicinity of tectonic faults recognised as seismically active in official documents issued by competent national authorities.

Absence of movement in late Quaternary should be used to identify non active faults for most structures.

It seems that this restriction is not only very difficult to follow for structures such as bridges, tunnels and embankments but conservative due the difficult to identify with reability the surface outbreak of a fault.

Anastapoulos and Gazetas (2006) have proposed a methodology to design structures against major fault ruptures validated through successful Class A predictions of centrifuge model tests and have recommended some changes to EC8 - Part 5.

Comments: The following comments are presented: (i) no reference is made for the influence of strong motion data with the near fault factor (confined to distances of less than 10 km from the fault rupture surface) with the increases of the seismic design requirements to be included in building codes; (ii) also no reference is established between the ground motion and the type of the fault such as reverse faulting, strike slip faulting and normal faulting; (iii) EC8 refers to the spatial variation of ground motion but does not present any guidance; (iv) basin edge and other 2D and 3D effects were not incorporated in EC8. The importance of shapes of the boundaries of sedimentary valleys as well as of deeper geologic structures in determining site response was shown from the analysis of records in Northridge and Kobe earthquakes.

SLOPE STABILITY

For the natural or artificial slopes a verification of ground stability to ensure safety or serviceability under the design earthquake should be performed.

The following methods of analysis: (i) dynamic analysis, using finite elements; (ii) rigid block models; and (iii) simplified pseudo – static methods can be used.

For the pseudo–static analyses the following design seismic inertia forces can be taken:

$$F_H = 0,5 \alpha_{gr} \gamma S W / g \text{ for the horizontal direction} \quad (2)$$

$$F_V = \pm 0,5 F_H \text{ when the ratio } \alpha_{vg} / \alpha_{gr} \text{ is greater than } 0.6 \quad (3)$$

$$F_V = \pm 0,33 F_H \text{ otherwise} \quad (4)$$

where α_{vg} is the applicable design ground acceleration in the vertical direction, α_{gr} is the reference peak ground acceleration for class A ground ratio, γ is the importance factor of the structure, S is the soil parameter and W is the weight of the sliding mass.

Pseudo-static method shall not be used for soils that develop high pore water pressure or significant degradation of stiffness under cyclic loading.

The serviceability limit state condition may be checked using simplified analyses with a rigid block sliding for the computation of the permanent displacement.

A modified Newmark model to compute displacements of natural slopes that includes pore pressure generation, time interval, computation of cycles involved in the cycle degradation and the computed degradation path of the slope critical acceleration was proposed by Biondi and Maugeri.

For a saturated soil in zones where $\alpha_{gr} \gamma S > 0.15$ it is important to incorporate the strength degradation and pore pressure increase due to cyclic loading.

Dense sands with strong dilatant effects do not exhibit reduction of shear strength.

Kramer and Paulsen (2004) have proposed a model to assess the deformations of reinforced slopes that incorporates the yielding of reinforced zone, the failure and tension of the reinforcements. The model was calibrated by shaking table and centrifuge tests.

ISSMGE TC4 Manual (1999) presents methods for rock slopes stability based on the hardness of rock and characteristics of faults proposed by Kanagawa Prefectural Government (Japan) and Mora and Vahrson.

Comments: The following items deserve more consideration: i) some guidelines to assess the residual strength of the soil; ii) some guidelines to assess the rock slopes stability.

Two mitigation methods namely anchors and soft layers were applied to study the case of Aegion slope. The following conclusions were obtained (Stamatopoulos, 2005): (i) With the use of anchors the whole body connected with anchors will move with less total and differential acceleration. There is a need to optimise the anchors inclination and length. (ii) The use of soft barrier will allow a decrease of acceleration and consequently a reduction of displacement.

POTENTIALLY LIQUEFIABLE SOILS

Following 4.1.3. (2)-Part5-EC8 “An evaluation of the liquefaction susceptibility shall be made when the foundations soils include extended layers or thick lenses of loose sand, with or without silt/clay fines, beneath the water level, and when such level is close to the ground surface”.

Soil investigations should include SPT or CPT tests and grain size distribution (Idriss and Boulanger, 2004). Normalisation of the overburden effects can be performed by multiplying SPT or CPT value by the factor $(100/\sigma'_{vo})^{1/2}$ where σ'_{vo} (kPa) is the effective overburden pressure. This normalisation factor should be taken not smaller than 0.5 and not greater than 2.

The seismic shear stress τ_e can be estimated from the simplified expression:

$$\tau_e = 0,65 \alpha_{gr} \gamma_i S \sigma_{vo} \quad (5)$$

where α_{gr} is the design ground acceleration ratio, γ_i is the importance factor, S is the soil parameter and σ_{vo} is the total overburden pressure. This expression should not be applied for depths larger than 20 m. The shear level should be multiplied by a safety factor of [1.25].

The magnitude correction factors in EC8 follow the proposal of Ambraseys (1988) and are different from the NCEER (1997) factors. A comparison between the different proposals is shown in Table 5.

Table 5. Magnitude scaling factors

Magnitude M	Seed & Idriss (1982)	Idriss NCEER (1997)	Ambraseys (1988)
5.5	1.43	2.20	2.86
6.0	1.32	1.76	2.20
6.5	1.19	1.44	1.69
7.0	1.08	1.19	1.30
7.5	1.00	1.00	1.00
8.0	0.94	0.84	0.67
8.5	0.89	0.72	0.44

A new proposal with a summary of different authors presented by Seed et al. (2001) is shown in Figure 9.

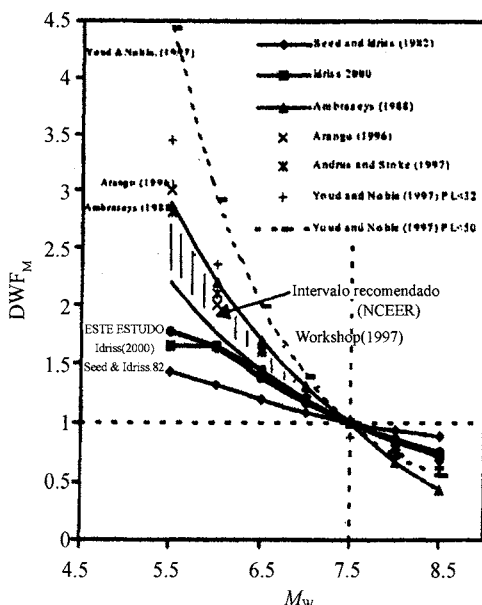


Figure 9. Recommendations for correlations with magnitude (after Seed et al., 2001)

Empirical liquefaction charts are given with seismic shear wave velocities versus SPT values to assess liquefaction. A comparison between NCEER (1997) and EC8 proposal for pre-standard is shown in Figure 10. It is important to refer that the proposal for EC8 is based on the results of Roberston et al.(1992) and the proposal of NCEER(1997) incorporates very recent results.

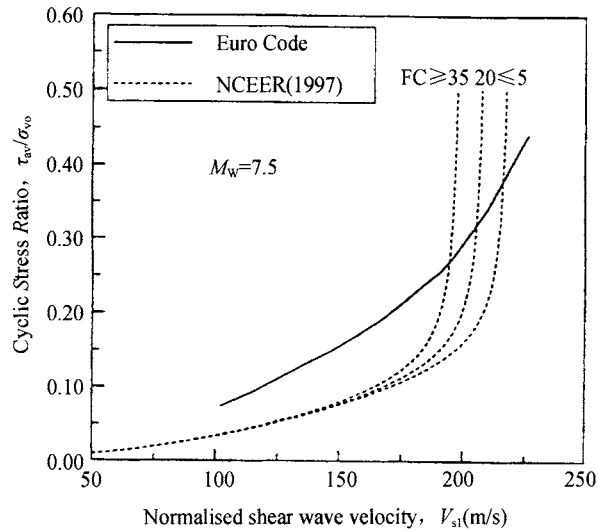


Figure 10. Liquefaction potential assessment by NCEER (1997) and EC8 (pre-standard)

However the EC8 standard version considers that these correlations are still under development and need the assistance of a specialist.

The importance of this topic has increased and the assessment of liquefaction resistance from shear wave crosshole tomography was proposed by Furuta and Yamamoto (2000).

A new proposal presented by Cetin et al. (2001) is shown in Figure 11 considered advanced in relation with the previous ones, as integrates: (i) data of recent earthquakes; (ii) corrections due the existence of fines; (iii) experience related a better interpretation of SPT test; (iv) local effects; (v) cases histories related more than 200 earthquakes; (v) Baysiana theory.

Bray et al. (2004) have shown that the chinese criteria proposed by Seed and Idriss (1982) was not reliable for the analysis of silty sands liquefaction and have proposed the plasticity index.

The topic related with the assessment of post liquefaction strength is not treated in EC8, but it seems that the following variables are important: fabric or type of compaction, direction of loading, void ratio and initial effective confining stress (Byrne and Beaty, 1999).

A relationship between SPT N value and residual strength was proposed by Seed and Harder (1990) from direct testing and field experience (Figure 12).

Ishihara et al.(1990) have proposed a relation of normalized residual strength and SPT tests, based on laboratory tests compared with data from back-analysis of actual failure cases (Figure 13). Also Ishihara et al. (1990) by assembling records of earthquake caused failures

in embankments, tailings dams, and river dykes have proposed the relation of Figure 14, in terms of the normalized residual strength plotted versus CPT value.

Alba (2004) has proposed Bingham model, based in triaxial tests of large samples, to simulate residual strength of liquefied sands.

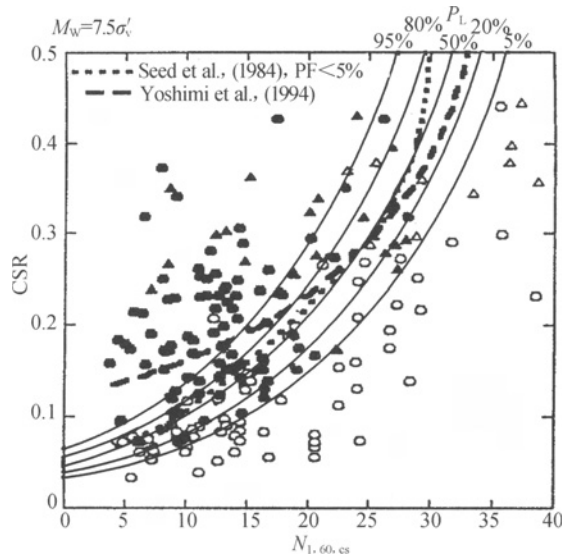


Figure 11. Probabilistic approach for liquefaction analysis (after Cetin et al., 2001)

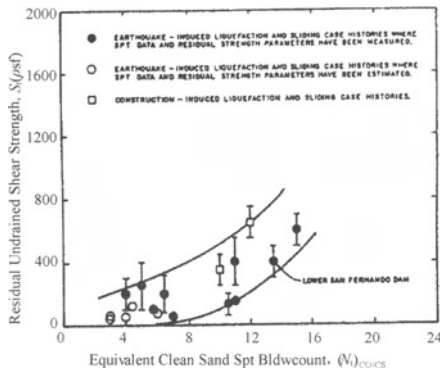


Figure 12. Relationship between $(N_1)_{60}$ and undrained residual strength (after Seed and Harder, 1990)

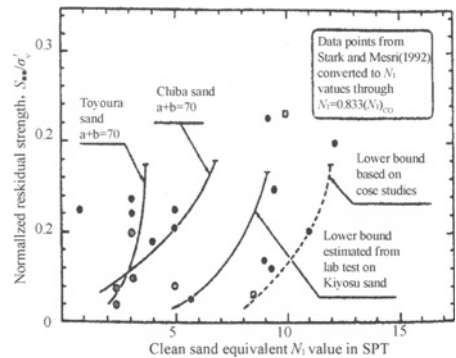


Figure 13. Relation of normalized residual strength and SPT tests (after Ishihara et al., 1990)

The susceptibility of foundations soils to densification and to excessive settlements is referred in EC8, but the assessment of expected liquefaction - induced deformation deserves more consideration.

By combination of cyclic shear stress ratio and normalized SPT N-values Tokimatsu and Seed (1987) have proposed relationships with shear strain (Figure 15).

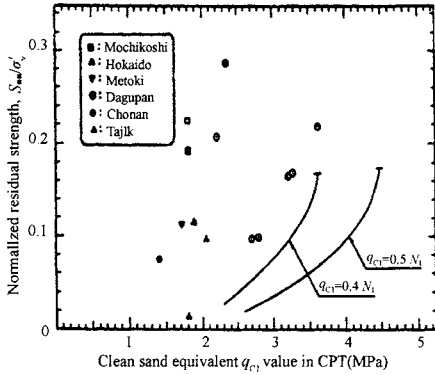


Figure 14. Normalized residual strength plotted versus CPT values (after Ishihara et al., 1990)

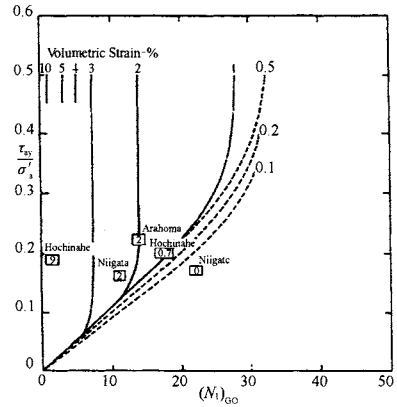


Figure 15. Correlation between volumetric strain and SPT (after Tokimatsu and Seed, 1987)

To assess the settlement of the ground due to the liquefaction of sand deposits based on the knowledge of the safety factor against liquefaction and the relative density converted to the value of N_1 a chart (Figure 16) was proposed by Ishihara (1993).

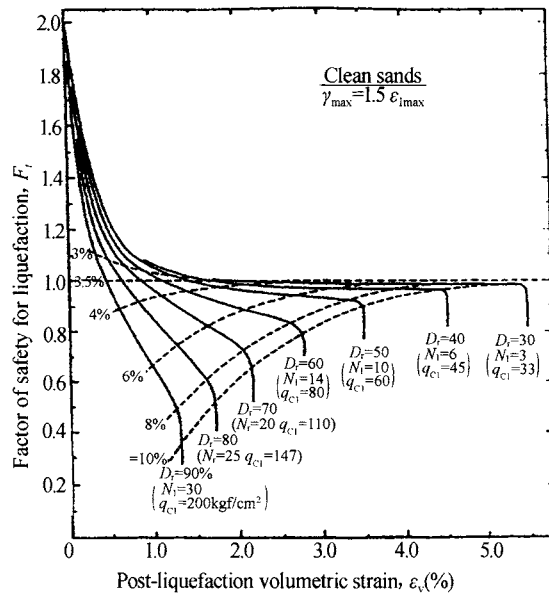


Figure 16. Post cyclic liquefaction volumetric strain curves using CPT and SPT results (after Ishihara, 1993)

Following EC8 ground improvement against liquefaction should compact the soil or use drainage to reduce the pore water pressure. The use of pile foundations should be considered with caution due the large forces induced in the piles by the liquefiable layers and the difficulties to determine the location and thickness of these layers.

Two categories of remedial measures against liquefaction were proposed: (i) Solutions aiming at withstanding liquefaction - Confinement wall: stiff walls anchored in a non liquefied layer (or a bedrock) to avoid lateral spreading in case of liquefaction; Soil reinforcement - transfer of loads to a non-liquefiable layer. (ii) Solutions to avoid liquefaction: - Soil densification: compaction grouting to minimise the liquefaction potential; - Dewatering: to lower the water table in order to minimise the risk of liquefaction; - Drainage to facilitate the dissipation of pore pressure; - Fine grouting: to increase the soil cohesion.

The liquefaction prediction/determination methods are covered by the following main Japanese standards: (i) Design standards for Port and Harbour Structures, (ii) Design Standards of Building Foundations, (iii) Design Standards for Railway Structures; (iv) Design Specifications for Roads.

Following EC8 ground improvement against liquefaction should compact the soil or use drainage to reduce the pore water pressure. The use of pile foundations should be considered with caution due to the large forces induced in the piles by the liquefiable layers and the difficulties to determine the location and thickness of these layers. The remedial measures against liquefaction can be classified in two categories (TC4 ISSMGE, 2001; INA, 2001): (i) the prevention of liquefaction; and (ii) the reduction of damage to facilities due to liquefaction.

The measures to prevent occurrence of liquefaction include the improvement of soil properties or improvement of conditions for stress, deformation and pore water pressure. In practice a combination of these two methods is adopted.

The measures to reduce liquefaction induced damage to facilities include (1) to maintain stability by reinforcing structure: reinforcement of pile foundation and reinforcement of soil deformation with sheet pile and underground wall; (2) to relieve external force by softening or modifying structure: adjusting of bulk unit weight, anchorage of buried structures, flatter embankments.

In NEMISREF Project the following criteria for selection was used (Evers, 2005): (i) Potential efficiency; (ii) Technical feasibility; (iii) Impact on structure and environmental; (iv) Cost-effectiveness; (v) Innovation.

Two methods were selected: (i) Soil grouting using calcifying bacteria; (ii) confinement wall.

Related with calcifying bacteria the objective of soil consolidation is to create a cementation between the grains of soil skeleton increasing the cohesion.

With confinement wall even if partial liquefaction could occur the final deformations will be controlled.

The improvement of soil properties, to prevent soil liquefaction, by soil cementation and solidification is performed by deep mix method (Port Harbour Research Institute, 1997), so within this framework the use of bacteria technique is innovative.

The structural strengthening is performed by pile foundation and sheet pile (INA, 2001) and so the confining wall can be considered innovative.

The proposed methods of remediation have an additional advantage minimizing the effects on existing structures during soil improvement.

Comments: From the analyses of this section it seems that the following items deserve more clarification (Sêco e Pinto, 1999):

- i) It is important to quantify the values of extended layers or thick lenses of loose sand;
- ii) What is the meaning of “.....when such level is close to the ground surface”? What depth? What is the maximum depth liquefaction can occur?
- iii) No recommendation is presented to compute seismic shear stress τ_e for depths larger than 20 m;
- iv) The use of Becker hammer and geophysical tests to assess the liquefaction of gravely materials should be stressed;
- v) The recommended multiplied factor CM for earthquake magnitudes different from 7.5 deserves more explanation. It is important to refer that the well known correlation proposed by Seed et al (1984) for cyclic stress ratio versus N_1 (60) to assess liquefaction and adopted in Annex B of EC8 – Part 5 use different correction factor for earthquake magnitudes different from 7.5;
- vi) No reference is given for the residual strength of soil.

FOUNDATION SYSTEM

In general for the Soil-Structure Interaction (SSI) the design engineers ignore the kinematic component, considering a fixed base analysis of the structure, due the following reasons: (i) in some cases the kinematic interaction may be neglected;(ii) aseismic building codes, with a few exceptions e.g. Eurocode 8 do not refer it; (iii) kinematic interaction effects are more difficult to assess than inertial forces (Sêco e Pinto, 2003).

There is strong evidence that slender tall structures, structures founded in very soft soils and structures with deep foundations the SSI plays an important role.

The Eurocode 8 states:” Bending moments developing due to kinematic interaction shall be computed only when two or more of the following conditions occur simultaneously: (i) the subsoil profile is of class D , S_1 or S_2 , and contains consecutive layers with sharply differing stiffness;(ii) the zone is of moderate or high seismicity, $\alpha > 0.10$;(iii) the supported structure is of important category I or II.

The stability of footings for the ultimate state limit design criteria shall be analysed against failure by sliding and against bearing capacity failure.

For shallow foundations under seismic loads failure can not be defined for situations when safety factor becomes less than 1, but is related with permanent irrecoverable displacements.

The seismic codes recommend to check the following inequality:

$$S_d < R_d, \quad (6)$$

where S_d is the seismic design action and R_d the system design resistance.

In the inequality (3) partial safety factors shall be included following the recommendations of Eurocode 8.

Theoretical and experimental studies to provide bearing capacity solutions to include the effect of soil inertia forces led to the inequality (Pecker, 1997):

$$\phi(N, V, M, F) < 0 \quad (7)$$

where $\phi = 0$ defines the equation of the bounding surface (Figure 17).

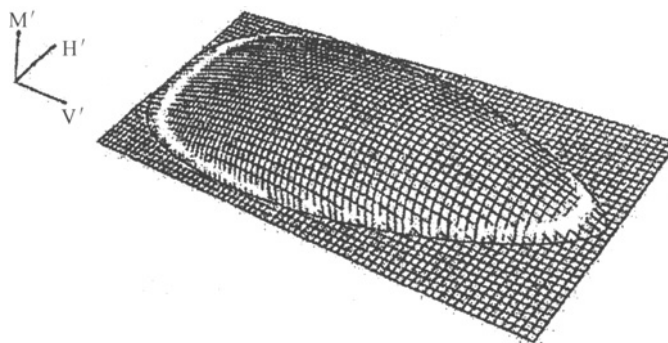


Figure 17. Bounding surface for cohesive soils (after Pecker, 1997)

The combination of the loading lying the outside the surface corresponds to an unstable situation and the combination lying inside the bounding surface corresponds to a potentially stable situation.

Piles and piers shall be designed to resist the following action effects: (i) inertia forces from the superstructure; and (ii) kinematic forces resulting from the deformation of the surrounding soil due the propagation of seismic waves.

The complete solution is a 3D analysis very time demanding and it is not adequate for design purposes. The decomposition of the problem in steps is shown in Figure 18 and implies (Gazetas and Mylonakis, 1998): (i) the kinematic interaction involving the response of the base acceleration of the system considering the mass of superstructure equal to zero; (ii) the inertial interaction that involves the computation of the dynamic impedances at the foundation level and the dynamic response of the superstructure.

For the computation of internal forces along the pile, as well as the deflection and rotation at the pile head, both discrete (based in Winkler Spring model) or continuum models can be used (Finn and Fujita, 2004).

The lateral resistance of soil layers susceptible to liquefaction shall be neglected.

In general the linear behaviour is assumed for the soil.

The nonlinear systems are more general and the term non linearities include the geometric and material nonlinearities (Pecker and Pender, 2000).

The engineering approach considers two sub-domains (Figure 19):

- i) a far field domain where the non linearities are negligible;
- ii) a near field domain in the neighbouring of the foundation where the effects of the geometrical and material linearities are concentrated.

The following effects shall be included: (i) flexural stiffness of the pile; (ii) soil reactions along the pile; (iii) pile–group effects; and (iv) the connection between pile and structure.

The use of inclined piles is not recommended to absorb the lateral loads of the soils. If inclined piles are used they must be designed to support axial as well bending loads.

Piles shall be designed to remain elastic, if this is not possible potential plastic hinging shall be considered for: (i) a region of depth $2d$ (d -diameter of the pile) from the pile cap; (ii) a region of $\pm 2d$ from any interface between two layers with different shear stiffness (ratio of shear moduli > 6).

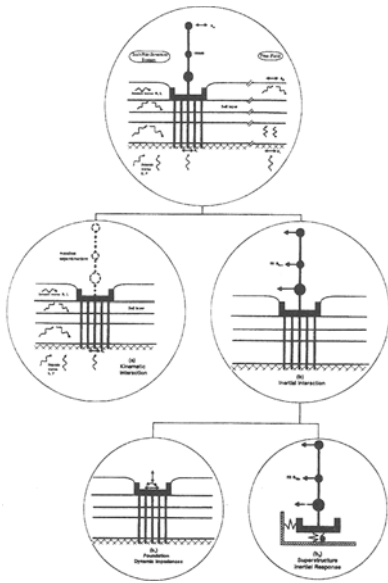


Figure 18. Soil-structure interaction problem (after Gazetas and Mylonakis, 1998)

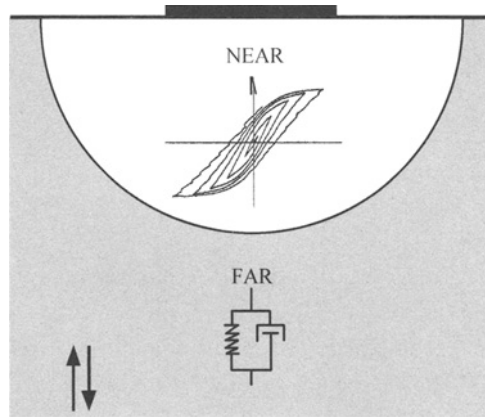


Figure 19. Conceptual subdomains for dynamic soil structure analyses (after Pecker and Pender, 2000)

Evidence has shown that soil confinement increases pile ductility capacity and increases pile plastic hinge length. Piles have shown the capability to retain much of their axial and lateral capacity even after cracking and experienced ductility levels up to 2.5 (Gerolymos and Gazetas, 2006).

The investigation methods for pile foundation damage are: direct visual inspection, the use of borehole camera inspection and pile integrity test. The ground deformation can be investigated by visual survey and GPS survey (Matsui et al. 1997).

Comments: The following topics deserve more consideration:

- i) The influence of pile cap;
- ii) The moment rotation capacity of pile footing;
- iii) The incorporation of the non linear behaviour of the materials in the methods of analysis;
- iv) The instrumentation of the piles for design purposes;
- v) Some guidelines about group effects, as there are significant different opinions on the influence of group effects related with the number of piles, spacing, direction of loads, soil types and construction methods of piles.

For the evaluation of mitigation methods a preliminary analysis of the following solutions was performed (Evers, 2005): (i) Stiffening solutions - hard layer, reinforced concrete walls, soil stiffening at foundation level and inclined piles; (ii) Soft material barriers - soft layer, expanded polystyrene (EPS) walls, air-water balloons and soft caisson; (iii) oscillators.

For the criteria of selection the following factors were used: Potential efficiency, technical feasibility, impact on structure and environment, cost-effectiveness and innovation.

From this analysis the following two mitigation methods: i) soil stiffening (inclined micro-piles) and ii) deformable soft barriers (soft caisson) were selected.

EARTH RETAINING STRUCTURES

The methods of analyses of an earth-retaining structure shall incorporate: (i) the non-linear behaviour of the soil; (ii) the inertia effects associated with the masses of the soil; (iii) the hydrodynamic effects generated with by the presence; (iv) the compatibility between deformations of the soil, wall and the tiebacks.

For the pseudo-static analysis of rotating structures the seismic coefficients can be taken as:

$$k_h = \alpha_{gr} \gamma_f S / g \cdot r \quad (8)$$

$$k_v = \pm 0,5 k_h \text{ when the ratio } \alpha_{vg} / \alpha_{gr} \text{ is greater than } 0.6 \quad (9)$$

$$k_v = \pm 0,33 k_h \text{ otherwise} \quad (10)$$

where α_{gr} is the reference peak ground acceleration for class A ground, S is the soil parameter, γ_f is the importance factor of the structure and the factor r takes the values listed in Table 6.

Table 6. Factor affecting the horizontal seismic coefficient

Type of retaining structure	r
Free gravity walls that can accept a displacement $dr \leq 300 \alpha S(\text{mm})$	2
As above with $dr \leq 200 \alpha S(\text{mm})$	1.5
Flexural r.c. walls, anchored or braced walls, r.c. walls founded on vertical piles, restrained basement walls and bridge abutments	1.0

For saturated cohesionless soils susceptible to develop high pore pressure the r factor should not be taken larger than 1.0, and the safety factor against liquefaction should not be less than 2.

The point of application of the force due to dynamic earth pressure shall be assumed to lie at midheight of the wall and for walls which are free to rotate about their toe it is appropriate to consider the dynamic force acting at the same point as the static force.

For a soil permeability coefficient less than 5×10^{-4} m/s the pore pressure is not free to move and the soil will behave as an undrained situation, during the occurrence of seismic action.

The earth pressure coefficient can be computed from the Mononobe and Okabe formula.

The point of application of the force due to the hydrodynamic water pressure lies at a depth below the top of the saturated layer equal to 60% of the height of such layer.

The pressure distributions on the wall due to the static and the dynamic action shall be assumed to act with an inclination with respect to the normal to the wall not greater than $(2/3) \phi'$ for the active state and equal to zero for the passive state.

The stability of soil foundation shall be assessed for the following conditions: (i) overall stability; and (ii) local soil failure.

The anchoring system (tiebacks and anchors) provided behind walls and bulkheads shall have enough strength to assure equilibrium of the critical soil wedge under seismic conditions, as well as a sufficient capacity to adapt to the seismic deformations of the soil.

The EC8 does not refer to the behaviour of reinforced walls. The behaviour of these structures during recent earthquakes suggests that these types of structures are well suited for seismically active regions (Sitar et al., 1997).

The EC8 only refers the condition of walls to slide, but it is important to stress the rocking of large concrete gravity walls under earthquake loading (Sêco e Pinto, 1995).

For an embedded retaining structure characterised by a ductile behaviour, it can be anticipated that the equivalent value of the acceleration to use in a pseudo-static calculation, as if it were constant in time, should be significant smaller than the expected peak acceleration (Anastassopoulos, 2004).

Comments: From the analyses of this section it seems that the following items deserve additional consideration:

(i) Design methods for the computation of permanent displacements that allow the couple computation of rotation and translation movements should be referred;

(ii) For retaining walls of medium heights (greater than 6 m) the computed displacements are larger than the values listed by EC 8 (Wu and Prakash, 2001);

(iii) The permanent displacements should be related with the height of the wall;

(iv) The good behaviour of geogrid – reinforced soil retaining walls in comparison with reinforced concrete cantilever retaining walls, during the occurrence of earthquakes, should be stressed.

TOPOGRAPHIC AMPLIFICATION FACTORS

For the stability verification of ground slopes EC8 recommends simplified amplification factors for the seismic action to incorporate the topographic effects. Such factors should be applied for slopes with height greater than 30 m.

The following recommendations are given:

(i) for slopes angles less than 15° the topography effects can be neglected;

(ii) for isolated cliffs and slopes a value of $S \geq [1,2]$ should be used;

(iii) for slopes angles $> 30^\circ$ a value of $S \geq [1,4]$ should be used and $S \geq 1,2$ for smaller slope angles;

(iv) in the presence of a looser surface layer more than [5] m thick, the smallest value given in (ii) and (iii) shall be used increased by at least [20%].

No reference is made for 2 D models or 3 D models and for the frequency range amplifications observed in 2 D and 3 D models.

However Paolucci (2005) have pointed that amplification factors for 2D analyses are of the same range of EC8, but for 3D analyses the values are 25% higher.

To assess the topographic amplification is important to separate from the site amplification. Also topographic amplification varies with the frequency content of the earthquake (Pitilakis et al., 2005).

One recent example is related with the topographic amplification occurred in the coastal bluffs of the Pacific Palisades during the January 17, 1994 Northridge earthquake. The slopes with 40 to 60 m height and steep between 45 to 60 degrees failure.

Parametric studies conducted by Idriss (1968) on 27 and 45 degrees clay slopes using finite element method have shown that the magnitude of peak surface acceleration was greater at

the crest surface of the slope than at points lower on the slope, but comparing the peak ground acceleration at the crest to that at some distance behind the crest in some cases the acceleration at the crest was much greater, in other case cases there was little difference. The natural period of the soil column behind the crest of a slope was responsible for much more amplification of the input motion than the slope geometry.

Ashford et al (1997) concluded that topographic effects can be normalized as a function of the ratio of the slope height and wave length of the motion and the trend is shown in Figure 20.

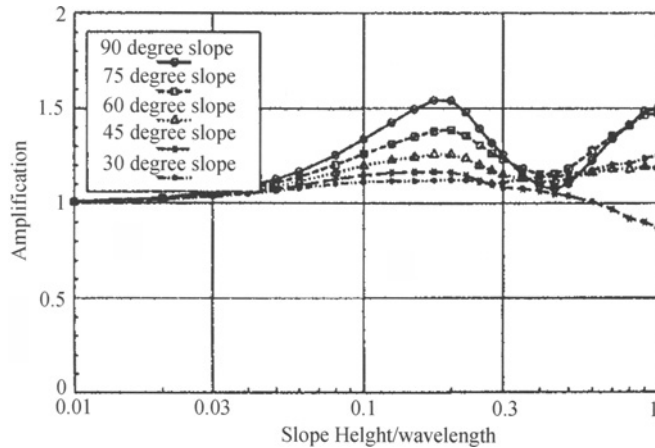


Figure 20. Amplification effects of steep slopes

INTERACTION WITH OTHER SEISMIC CODES

The continuous process of elaborating codes and standards that incorporates the lessons learned by earthquakes has a significant effect for the design and construction in seismic areas. As an example due the consequences of Kobe earthquakes new improvements have been implemented for the assessment of liquefaction in Japanese codes (Yasuda, 1999).

The actual tendency in almost every region of the world is to elaborate unified codes. This was the main purpose of Eurocodes.

In United States, nevertheless the long tradition of existing different codes in the states, due the different geographic regions of the U. S., where the western region in comparison with eastern region faces the largest levels of probabilistic seismic risk, efforts to elaborate an uniform code incorporating the UBC (Uniform Building Code) with NEHRP (National Seismic Hazard Reduction Program) in IBC (International Building Code), not an international code, but a unified national code, are undertaken (Seed and Moss, 1999).

In general all geotechnical codes use factored parameters for loads, resistance and strength to harmonize with structural practice. But the way of doing is different, for instance the Eurocode uses partial safety factors for loads and strength (Cuellar, 1999) and in the New Zealand code the LRFD (load and resistance factored design) is used (Pender, 1999).

It is important to stress that Eurocodes represent a significant step forward and allows various Nationally Determined Parameters (NDP) which should be confirmed or modified in the National Annexes.

FINAL REMARKS

The work performed by the Commission of the European Communities (CEC) in preparing the “Structural Eurocodes” in order to establish a set of harmonised technical rules is impressive. However we feel that some topics deserve more consideration.

Earthquakes are very complex and dangerous natural phenomena, which occurs primary in known seismic zones, although severe earthquakes have also occurred outside these zones in areas considered being geologically stable. As a result, regulatory agencies became more stringent in their requirements for demonstration of adequate seismic stability and design engineers responded by developing new and more convincing design approaches than had previously used. Thus the past years have seen a major change in interest and attitude towards this aspect of design.

The lessons learned from recent earthquakes such as: Northridge (1994), Kobe (1995), Umbria-Marche (1997), Kocaeli (1999), Athens (1999), Chi-Chi (1999) and Bhuj (2001) have provided important observational data related with the seismic behavior of geotechnical structures.

The need of cost effective methods to upgrade buildings by developing new specific foundations techniques is a major problem. So the objective of reducing the earthquake motion transferred to the structure through the foundation by developing innovative constructive techniques for soil improvement and soil reinforcement is getting increase attention.

One very important question to be discussed is: (i) how detailed a seismic code must be; (ii) what is the time consuming to establish a set of harmonised technical rules for the design and construction works? (iii) How to improve the relations between the users: relevant authorities, clients and designers? and (iv) how to implement in practice that codes may not cover in detail every possible design situation and it may require specialised engineering judgement and experience? It is hoped that the contributions to be presented by CEN members, in the next years, will help to clarify several questions that still remain without answer.

In dealing with this subject we should always have in mind:

All for Love

“Errors, like straws, upon the surface
flow;

He who would search for pearls must
dive below”.

(John Dryden)

REFERENCES

Abrahamson N.A. (2000). State of the practice of seismic hazard evaluation. 1: 659-685. GEOENG 2000, Melbourne.

- Alba P. (2004). Residual strength after liquefaction: a rheological approach. *Proc. of 3rd International Conference on Earthquake Geotechnical Engineering*, Berkeley, Editors Doolin D., Kammerer A., Nogami T., R.B. Seed e I.Towhata, 1: 740-746.
- Ambraseys N. N. (1998). Engineering seismology. *Earthquake Engineering and Structural Dynamics*, 17: 1-105.
- Anastassopoulos I., Gazetas G. (2006). Design of foundations and structures against fault displacement. *ETC 12- Workshop*, Athens.
- Bray J., Sancio R.B., Riemer M. and Durgunoglu H.T. (2004). Liquefaction susceptibility of fine grained soils. *Proc. of 3rd International Conference on Earthquake Geotechnical Engineering, Berkeley*, Editors D.Doolin, A. Kammerer, T. Nogami, R.B. Seed and I.Towhata, 1: 665-662.
- Byrne P.M. and Beaty M.H. (1999). Assessment residual strength for embankments. *Proc. of the Second International Conference on Earthquake Geotechnical Engineering*. Edited by Pedro S.Sêco e Pinto. Published by Balkema. 3: 1069-1075.
- Cetin K.O e Seed R.B., Kiureghian. (2001). Reliability based assessment of seismic soil liquefaction initiation. *XV ICSMGE TC4 Satellite Conference on Lessons Learned from Recent Strong Earthquakes*, Edited by Atila Ansal, 327-332.
- Cuellar V. (1999). Codes and standard for Europe. *Proc. of the Second International Conference on Earthquake geotechnical Engineering*. Edited by Pedro S.Sêco e Pinto. Published by Balkema. 3: 1129-1133.
- EN 1990 Eurocode 0 – “Basis of structural design”.
- EN 1991 Eurocode 1 – “Actions on structures”.
- EN 1997 Eurocode 7 – “Geotechnical design”.
- EN 1998 Eurocode 8 – “Design of structures for earthquake resistance”.
- Evers G. (2005). Horizontal shaking mitigation implementation. NEMISREF Seminar, CD-Rom, Athenes.
- Evers G. (2005). Liquefaction mitigation implementation. NEMISREF Seminar, CD-Rom, Athenes.
- Finn W. D., Fujita N.(2004). Behavior of piles in liquefiable soils during earthquakes: Analysis and design issues. *Proc. of the Fifth Case Histories in Geotechnical Engineering Conference*, New York, NY, SOAP, 16.
- Furuta, Yamamoto. (2000). Liquefaction assessment by shear wave crosshole tomography tests. Paper n° 831. 12 th WCEE, Auckland, New Zealand.
- Gazetas G., Mylonakis G. (1998). Seismic soil structure interaction: new evidence and emerging issues. *Geotechnical Earthquake Engineering and Soil Dynamics*, ASCE II, 1119-1174.
- Gerolymos G., Gazetas G. (2006). Capacity design of pile foundations: Evidence in support of allowing pile yielding. *ETC 12- Workshop*, Athens.
- Idriss I.M. (1968). Finite element analysis for seismic response of earth banks. *J. Soil Mechanics and Foundations Division*, ASCE, 94(SM3): 617-636.
- Idriss I. M. (1990). Response of soft soil during soil earthquakes. *Proc. H. Bolton Seed Memorial Symposium*, 273-290.
- Idriss I.M., Boulanger R.W. (2004). Semi-empirical procedures for evaluation liquefaction potential during earthquakes. *Proc. of the Fifth Case Histories in Geotechnical Engineering Conference*, New York, Ny, SOAP, 16.
- International Navigation Association (2001). *Seismic design guidelines for port structures*. A.A. Balkema Publishers.
- Ishihara K. 1985. Stability of natural deposits during earthquake”. *Proc. 11 th ICSMGE*, S. Francisco, 2: 321-376.

- Ishihara K., Yasudfa S. and Yoshida Y. (1990). Liquefaction induced flow failure of embankments and residual strength of silty sands. *SF*, Vol. 30, n° 3, 69-80.
- Ishihara K.(1993). Liquefaction and flow failure during earthquakes. 33rd Rankine Lecture. *Geotechnique* 43(3): 351-415.
- Kokusho T., Matsumoto M. (1997). Nonlinear site response during the Hyogoken-Nanbu earthquake recorded by vertical arrays in view of seismic zonation methodology. *Proc of the Discussion Special Technical Session on Earthquake Geotechnical Engineering during 14th ICSMFE*, Hamburg, Edited by Pedro S.Sêco e Pinto. Published by Balkema., 61-69.
- Kramer S., Paulsen S.B. (2004). The prediction of reinforced slope performance during earthquakes. *Proc. of 3rd International Conference on Earthquake Geotechnical Engineering, Berkeley* , Editors D.Doolin, A. Kammerer, T. Nogami, R.B. Seed and I.Towhata, 2: 275-282.
- Matsui Y., Kitazawa M., Nanjo A. and Yasuda F. (1977). Investigation of damaged foundations in the Great Hanshin earthquake. *Proc of the Discussion Special Technical Session on Earthquake Geotechnical Engineering during 14th ICSMFE*, Hamburg, Edited by Pedro S.Sêco e Pinto. Published by Balkema., 235-242.
- NCEER. (1997) *Proc. NCCER workshop on evaluation of liquefaction resistance of soils, summary report*, Edited by T. Leslie Youd and I.M. Idriss, National Center for Earthquake Engineering Research, University of Buffalo, Technical Report NCEER-97-0022.
- Paolucci R. (2006). Numerical investigation of 3D seismic amplification by real steep topographic profiles and check of the EC8 topographic amplification coefficients. *ETC 12- Workshop*, Athens.
- Pecker A., Pender M.J. (2000). Earthquake resistant design of foundation. *New construction*. 1: 313-332. *GEOENG 2000*, Melbourne.
- Pecker A. (1997). Analytical formulae for the seismic bearing capacity of shallow strip foundations. *Proc of the Discussion Special Technical Session on Earthquake Geotechnical Engineering during 14th ICSMFE*, Hamburg, Edited by Pedro S.Sêco e Pinto. Published by Balkema., 262.268.
- Pender M.J. (1999). Geotechnical earthquake engineering design practice in New Zealand. *Proc. of the Second International Conference on Earthquake geotechnical Engineering*. Edited by Pedro S.Sêco e Pinto. Published by Balkema. 3: 1129-1133.
- Pitilakis K. Ktenidou O.-J. Apostolidis P. Raptakis D., Manakou M., Makropoulos K. and Diagourtas, D. (2005). Experimental and theoretical studies of topographic effects. *Proc. 16 th ICSMGE*, Osaka, Japan, 175-182.
- Roberston P.K., Woeller D.J. and Finn W.D.L. (1992). Seismic cone penetration test for evaluating liquefaction under cyclic loading. *Canadian Geotechnical Journal*, 29: 686-695.
- Sêco e Pinto P. S. (1999). The relation between Eurocode 8 and Eurocode 7. *Proceedings of the twelfth european conference on soil mechanics and geotechnical engineering*. 3: 2223-2228, Amsterdam, Edited by F.B.J. Barends, J. Lindenberg, H.J. Luger, L. de Quelerit and A. Verruit. Publisher A. A. Balkema.
- Sêco e Pinto P. (2003). Seismic behaviour of geotechnical structures. Inaugural lecture. *Proc. 13 th Regional African Conference of Soil Mechanics and Geotechnical Engineering* 3- 24., Marrakech, Edited by M.Sahli, L.Bahi & R.Khalid.
- Seed H. B. and I. M. Idriss. (1982). Ground motions and soil liquefaction during earthquakes. *Earthquake Engineering Research Institute*, Oakland, California.
- Seed H. B., Tokimatsu K., Harder L. and Chung R. (1984). The influence of SPT procedures in soil liquefaction resistance evaluations. *Earthquake Engineering Research Centre Report n°84/15 U.C.*
- Seed R.B., Cetin K.O. and Moss R.E.S. (2001). Recent advances in soil liquefaction hazard assessment. *XV ICSMGE TC4 Satellite Conference on Lessons Learned from Recent Strong Earthquakes*, Istanbul, 319-326. Edited by Atilla Ansal .

- Seed R.B., Chang S. W., Dickenson S.E. and Bray J. B. (1997). Site dependent seismic response including recent strong motion data. *Proc of the Discussion Special Technical Session on Earthquake Geotechnical Engineering during 14th ICSMFE*, Hamburg, Edited by Pedro S.Sêco e Pinto. Published by Balkema., 125-134.
- Seed H.B., Harder L.F. (1990). SPT-based analysis of cyclic pore pressure generation and undrained residual strength. *Proc. of Memorial Symposium of H. B. Seed*, 2: 351-376.
- Seed R.B. and Moss R.E.S. (1999). Recent advances in U.S. codes and policy with regard to seismic geotechnics. *Proc. of the Second International Conference on Earthquake geotechnical Engineering*. Edited by Pedro S.Sêco e Pinto. Published by Balkema. 3: 1111-1116.
- Sittar N., Roessig L.N., Ashford S. and Stewart J. (1997). Seismic response of steep natural slopes, structural fills and reinforced soil slopes and walls. *Proc. of the Discussion Special Technical Session on Earthquake Geotechnical Engineering during 14th ICSMFE*, Hamburg, Edited by Pedro S.Sêco e Pinto. Published by Balkema., 341-350.
- Stamatopoulos A. (2005). Slope effect-problem definition and mitigation. *NEMISREF Seminar*, CD-Rom, Athens.
- TC4 (ISSMGE). (1999). *Manual for zonation on seismic geotechnical hazards*. (Revised Version).
- TC4 (ISSMGE). (2001). *Case histories of post-liquefaction remediation*. Committee on Earthquake Geotechnical Engineering.
- Tokimatsu K. and Seed H. B. (1987). Evaluation of settlements in sands due to earthquake shaking. *JGE*, ASCE, 113, 861-878.
- UBC. (1997). *Uniform buiding code, international conference of building officials*. Whittier, California, Vol. II.
- Yasuda S. (1999). Seismic design codes for liquefaction in Asia. *Proc. of the Second International Conference on Earthquake geotechnical Engineering*. Edited by Pedro S.Sêco e Pinto. Published by Balkema. 3: 1117-1122.
- Wu Y. and Prakash S. (2001). Seismic displacements of rigid retaining walls. Proceedings of the 4th International Conference on Recent Advances in Geotechnical Earthquake Engineering and Soil Dynamics, San Diego, USA.

LIQUEFACTION MITIGATION OF SAND DEPOSITS BY GRANULAR PILES- AN OVERVIEW

M. R. Madhav

*Professor Emeritus, Jawaharlal Nehru Technological University
Hyderabad 500072, India*

A. Murali Krishna

*Research Scholar, Indian Institute of Science
Bangalore 560012, India*

Soil liquefaction and associated ground failures have been a major source of damage during the past earthquakes. The risk of liquefaction and associated ground deformation can be reduced by various ground-improvement methods including the stone column (gravel drain) technique. Ground improvement by rammed granular piles (RGP) is considered one of the most reliable of these methods. This paper summarizes different mechanisms involved in the effective function of granular piles as a ground treatment method for liquefaction mitigation. Various mechanisms like: Drainage, Reinforcement, Storage, Dilation and Densification effects are briefly discussed. Generation and dissipation of the pore pressures in the granular pile reinforced ground under different earthquake conditions are quantified considering these different mechanisms. Granular piles are proved to be very effective for liquefaction mitigation.

INTRODUCTION

Ground improvement techniques are commonly employed to mitigate liquefaction hazards. Most common methods to improve the engineering properties of the soils can be classified as densification, reinforcement, grouting/mixing and drainage. Out of the various ground treatment methods, (Rammed) Granular Drains/Piles (RGP) are the most widely preferred alternative all over the world, due to technical feasibility, low energy utilization and cost effectiveness. Provision of gravel drains/granular piles/stone columns is the most commonly adopted ground treatment methodology for liquefaction mitigation which has proved its effectiveness in many instances (Mitchell and Wentz, 1991). RGP improve the ground by reinforcement, densification of the surrounding soil and by providing drainage. Different mechanisms operate in the function of gravel drains/granular piles in liquefaction mitigation. These mechanisms can be stated as Drainage, Storage, Dilation, Densification and Reinforcement. The following sections discuss each of these mechanisms in detail.

GRANULAR PILES, INSTALLATION, FUNCTIONS, MECHANISMS

Columnar inclusions such as stone columns/granular piles, sand compaction piles, lime or cement columns, etc., have been used as a ground improvement technique to increase bearing capacity, reduce settlement, increase the time rate of consolidation, improve stability and resistance to liquefaction of soft ground. Various techniques of installation have been conceived for various types of columnar inclusions in a wide variety of soils such as loose sandy to soft compressible soils depending on technical ability, efficiency and local conditions. Ground improvement by means of granular piles/stone columns/geo-piers, which is associated with partial substitution of the in-situ soil, originated in sixties. Stone columns generally use gravel or crushed stone as backfill. Effect of method of installation, cased and uncased holes, number of lifts and magnitude of compactive energy per lift given to granular piles and pile spacing were discussed by Madhav and Thiruselvam (1988). Numerous publications (e.g. Barksdale and Bachus, 1983; Munfakh et al., 1987; Baez and Martin, 1992; and Lopez and Hayden, 1992; Brennan and Madabhushi, 2002) describe the use of stone columns for ground reinforcement and their potential to mitigate the liquefaction. Liquefied and Non-liquefied subsoil conditions of two reclaimed islands in Kobe City after the 1995 Hyogoken-Nambu earthquake were investigated by Yasuda et al. (1996) who identified that subsoils treated with sand compaction piles or rod (vibro) compaction did not liquefy and nor subside even though the earthquake shaking was very strong. Ground treated by granular piles provide increased bearing capacity, significant reduction in settlement, free drainage, increase of liquefaction resistance, etc. Granular piles are installed by vibro-compaction, vibro-replacement, cased bore hole (rammed stone columns/RGP) or by simple auger boring methods (Datye and Nagaraju 1981, Balaam and Booker 1981). RGP are installed into the ground by partial or full displacement methods and by ramming in stages, using a heavy falling weight, within a 'pre-bored casing' or 'driven closed end casing', retracting the casing pipe stepwise. In the latter case, driving of closed end tube itself densifies the surrounding soil. Ramming of granular piles further densifies and reinforces the ground. Stone columns/granular piles or sand compaction piles are generally composed of compacted gravel, crushed stone or sand. Theoretical background, analysis, design aspects and installation techniques were being developed since 1970s by various researchers and practicing engineers all over the world (Hughes and Withers, 1974; Datye and Nagaraju, 1981; Engelhardt and Golding, 1975; Madhav et al. 1979, etc.).

A possible method of stabilizing a soil deposit, susceptible to liquefaction, is to install a system of gravel or rock drains so that pore-water pressures generated by cyclic loading may be dissipated almost as fast as they are generated (Seed and Booker, 1977). Granular pile inclusions improve the deformation properties of the ambient soil. Granular piles help in mitigating earthquake induced liquefaction effects through one or more of these functions.

1. Granular piles function as drains and permit rapid dissipation of earthquake induced pore pressures by virtue of their high permeability with the additional advantage that they tend to dilate as they get sheared during an earthquake event.
2. Granular piles densify and reinforce the in-situ soil;

3. Granular piles, installed in to a very dense state, are not prone to liquefaction and replace a significant quantity of in-situ liquefiable soil;
4. Granular piles modify the nature of earthquake experienced by the in-situ soil.

DRAINAGE MECHANISM OF GRAVEL DRAINS

In many cases, the installation of drainage system offers an attractive and economical procedure for stabilizing an otherwise potentially liquefiable sand deposit. Adopting ground treatment by gravel drains as a method to determine the stability of potentially liquefiable sand deposits was initiated originally by Seed and Booker (1977). In fact, better field performance of gravel drains/stone columns may be directly attributable to their capacity to dissipate pore-water pressures because of their higher permeability. Due to the installation of gravel drains, the generated porewater pressure due to repeated loading may be dissipated almost as fast as they are generated. Seed and Booker (1977) applied the one-dimensional theory of porewater pressure generation and dissipation developed by Seed et al. (1975) to the analysis of columnar gravel drains under a variety of earthquake conditions and proposed a simple radial consolidation analytical model.

In cases of high liquefaction potential the installation of columnar gravel drains may well provide an efficient method for preventing the development of excessively high pore water pressures. Generally, the horizontal permeability of a sand/gravel is several times greater than its vertical permeability. As such the spacing between vertical drains can be made less than the distance required for water to drain vertically to a free surface. Hence, the drainage mechanism by gravel drains/stone columns is attributed to their high permeability and the ability to reduce the drainage path significantly so that the developed excess pore water pressures are dissipated almost as fast as they are generated.

For flow into a gravel drain, assuming pure radial flow, and constant coefficients of permeability (k_h) and volume compressibility (m_v), the governing equation for the phenomenon can be written as (Seed and Booker, 1977):

$$\frac{k_h}{\gamma_w \cdot m_v} \left(\frac{1}{r} \frac{\partial u}{\partial r} + \frac{\partial^2 u}{\partial r^2} \right) = \frac{\partial u}{\partial t} - \frac{\partial u_g}{\partial N} \cdot \frac{\partial N}{\partial t} \quad (1)$$

Seed and Booker (1977) presented the charts (Figure 1), for the variation of maximum pore pressure ratio against time during an earthquake for different area ratios and other earthquake parameters, to aid in the design of gravel drains for liquefaction mitigation. These charts are based on the assumption that the drains are infinitely permeable so that the excess pore water pressure in the drain is effectively zero and the coefficient of permeability of the ambient soil is constant.

Tokimatsu and Yoshimi (1980), Sasaki and Taniguchi (1982) and Onoue (1988), report results similar to those of Seed and Booker (1977) taking into consideration additional factors such as well resistance (finite permeability of gravel drain) and drain slenderness ratio (slenderness ratio: L/r , where L is the length, and r is the radius of the gravel drain). Iai and Koizumi (1986), Onoue et al. (1987) and Iai et al. (1988), present design procedures for gravel drains derived analytically and verified by model or in situ tests. All of the above studies considered only the drainage effect of gravel drains (Adalier and Elgamal 2004).

Poorooshasb et al. (2000) demonstrated the effectiveness of inclusion of stone columns in reducing the risk of liquefaction of very loose to loose sandy and silty sand layers using the concept of equivalent permeability. Based on the radial consolidation theory as applicable to granular pile treated ground, Poorooshasb et al. (2000) propose an equivalent coefficient permeability, k_{eq} , for the treated soil in terms of the permeability, k_{untr} , of untreated ground, as $k_{eq} = k_{untr} \cdot t_{50}(\text{for untreated ground}) / t_{50}(\text{for treated ground})$ where t_{50} values for the untreated and granular pile treated ground are the times for 50% degree of consolidation based on one dimensional and radial consolidation theories respectively. The ratio, $r (=k_{eq}/k_{untr})$ is derived (Figure 2) in terms of the spacing ratio, $n (=S/d)$ where S and d are respectively the spacing between and diameter of granular piles. The results presented are for triangular arrangement of drains but can easily be modified for square arrangement.

Thus, the principal mechanism of granular drains/stone columns in mitigating the liquefaction potential is their drainage effect.

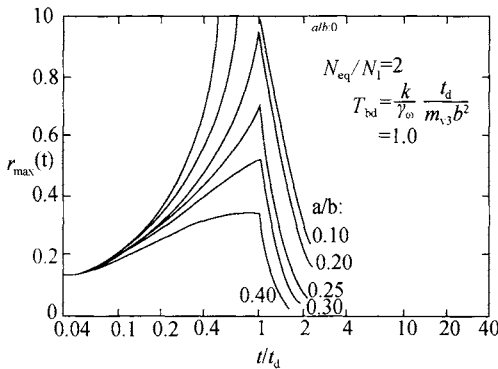


Figure 1. Effect of drain diameter and drain spacing on maximum pore pressure ratio (after Seed and Booker, 1977)

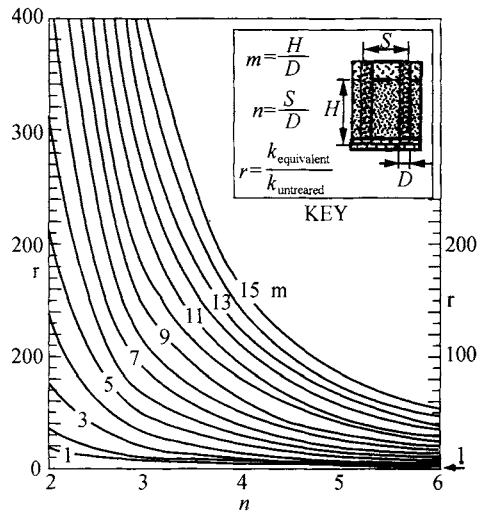


Figure 2. Equivalent permeability concept (after Poorooshasb et al., 2000)

STORAGE EFFECT, GRAVEL DRAINS

Generally, in most practical cases, the water level is at some depth below ground surface. During an earthquake, excess pore water pressure is dissipated by water discharging into the vertical drains, causing a rise in the water level within the drains. This rise in water level results in an increased “static” excess pore pressure (or backpressure) inside the drain elements, which in turn increases the excess pore pressure in the soil deposit. A reservoir (natural or man-made) with additional storage capacity above the original water table provides a buffer storage capacity and thus reduces the rate of rise of water level, thus minimizing backpressure effect in the drain (Pestana et al. 1997).

The effect of storage capacity on vertical drain performance in liquefiable sand deposits is presented by Pestana et al. (1998) by considering a two-layer soil system with a very low

permeability clay overlying the liquefiable sand layer as shown in the Figure 3. Figure 4 shows average pore pressure ratios, $Ru_z(\max)$, versus cycle ratio, r_N for perfect drain with and without the storage capacity. Here the perfect drain implied the drain with out any well resistance as that of the Seed and Booker (1977) model. If the water table in the system is not at the ground surface, there is room within the drain for water to rise that represents the storage capacity. In the figure for all storage cases, the water level in the drain was initially at 1 m depth. Ru_z is the average pore pressure ratio at depth, z , in the liquefiable layer. As the upper soil layer acts as a barrier to vertical flow, the maximum value of Ru_z , $Ru_z(\max)$, occurs at the interface between the upper and lower soil layers. The cyclic ratio, r_N , is the ratio of the number of uniform stress cycles in an earthquake versus the number of uniform stress cycles required to cause liquefaction in the soil layer in question under undrained conditions. The figure shows that at a small drain spacing ($s/d=4$), the rise in the water level in the drain forces a steady rise in the pore pressure ratios in the drain compared to the case with no storage. Similarly, in the other cases ($s/d=6, 8$ and 10), the effect of storage is to increase the maximum pore pressure ratios.

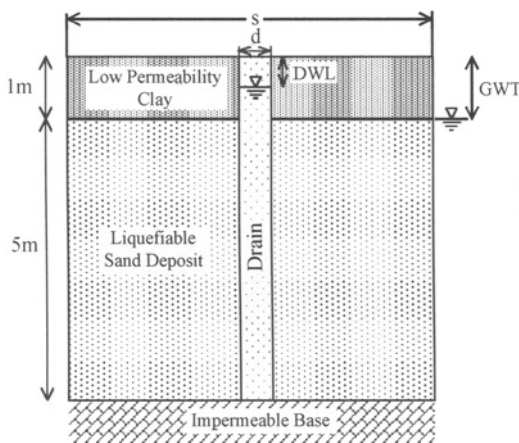


Figure 3. Unit cell with EQ drain

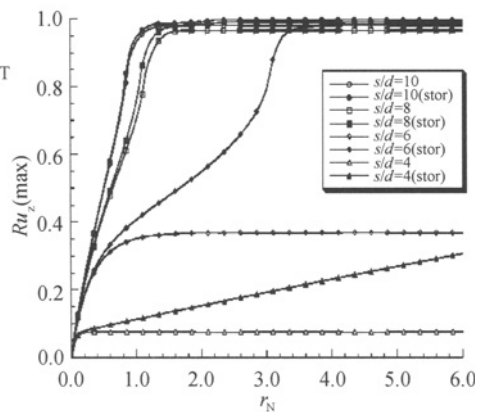


Figure 4. Pore Pressure Ratio Variation with Drain Spacing with and without storage (after Pestana et al., 1998)

Pestana et al. (1997, 1998) analysed the use of the providing the reservoir in reducing the depth of water levels within the drain and also to minimise the drain resistance to flow in to the drain. The reservoir may be formed by using a composite drainage product consisting of a perforated geopipe surrounded by a filler fabric to prevent clogging of the orifices (Pestana et al. 1998). This is achieved by a technique of auguring a hole larger than the diameter of the drain near the ground surface and filling it with crushed rock or gravel. This creates a reservoir for flow rising out of the drain during an earthquake, and at the same time, provides a means for reducing the rise in water level within the drain as the same volume of water is now spread out over a larger area (Figure 5) as the equivalent area of the reservoir is larger than that of the drain.

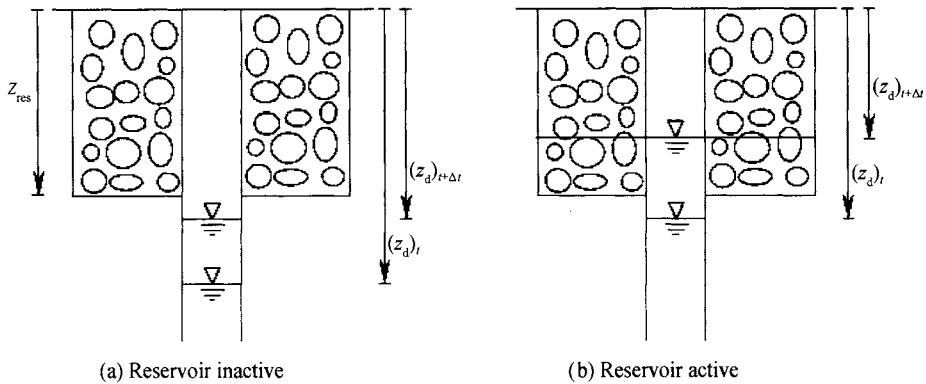


Figure 5. Rise in water level inside the drain and reservoir (after Pestana et al., 1997)

DILATION EFFECT, GRAVEL DRAINS

It has been generally recognized that the susceptibility of a given soils to liquefaction is determined to a high degree by its void ratio or relative density. In any given earthquake loose sands are very likely to liquefy but the same granular material in a denser condition would not. For example, in 1964 Niigata earthquake, liquefaction was extensive where the relative density of the sand was about 50% or less, but not in areas where the relative density exceeded about 70% (Seed and Idriss, 1971).

Shearing of dense dilative soils may generate some small positive pore pressures at small strains. However, at larger strains, the pore pressures decrease and become negative as the soil grains move up over one another, tending to cause an increase in soil volume (dilation). For dense, saturated sands sheared without drainage, the tendency for dilation or volume increase results in generation of negative pore pressure, with consequent increases in the effective stress and the shear strength of the granular material. The response of saturated sand under undrained triaxial conditions (Leonards, 1962) is shown in Figure 6. While positive pore pressures are generated in loose sands, generation of very high negative pore pressures can be observed due to suppression of the tendency for dilation in medium dense and dense sands. Figure 7 (Vaid et al., 1981) is a typical example of the volume change behaviour of granular material under drained conditions in a simple shear test at different vertical stress conditions. While initially loose samples undergo volume decrease, dense samples experience volume increase (dilation) during shearing. The rate of dilation increases with relative density. The dilation angle is one single parameter which can be readily obtained from both laboratory (drained triaxial or simple shear) and in situ (self-boring pressuremeter) tests, which can give a measure of the liquefaction resistance.

Dilation effect on the drainage function of granular piles was studied by Madhav and Arlekar (2000) by extending the Seed and Booker model (1977). It is shown that the dilation effect on pore pressure dissipation by granular piles for the range of parameters considered was marginal (Figure 8). Granular piles installed in loose sand deposits are often compacted at a relatively high density. Seismic forces which tend to generate positive pore pressures in these deposits cause an opposite effect of dilation in the dense granular piles. During the seismic event, negative pore pressures that tend to get generated therein increase

the gradient and permit rapid rates of drainage than otherwise. Madhav and Arlekar (2000) quantify this effect of dilating granular pile in mitigating liquefaction damage. The variation of maximum pore pressure ratio, W_{max} , with normalized time for different rates of dilation is depicted in Figure 9. The effect of dilation rates in reducing the peak values or the pore pressure ratio can be clearly seen in the figure.

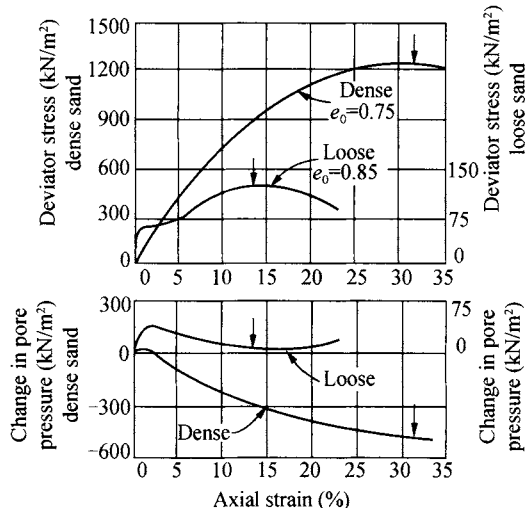


Figure 6. Response of saturated sand under undrained triaxial test conditions (after Leonards 1962)

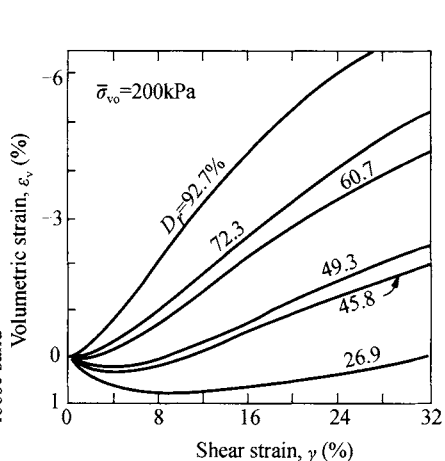


Figure 7. Volume change behavior for granular material under drained conditions (after Vaid et al. 1981)

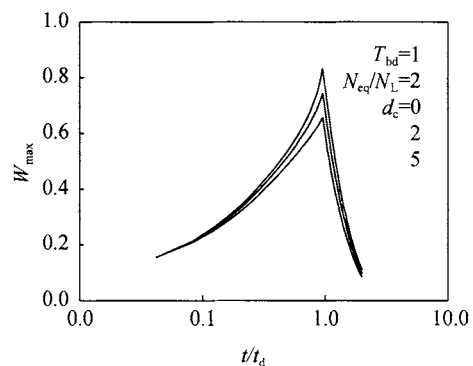


Figure 8. Effect of dilation of granular material on pore pressure generation and dissipation

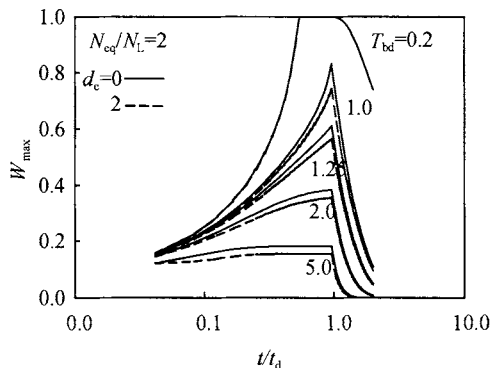


Figure 9. Maximum pore pressure versus time: Effect of dilation and T_{bd}

DENSIFICATION EFFECT OF GRAVEL DRAINS

One of the chief benefits of ground treatment with granular piles is the densification of in situ ground. The densification effect can be easily but indirectly quantified by in situ tests. The effect of densification is manifested through an increase in the coefficient of earth

pressure at rest and in the values of modulus of deformation of the soil (Ohbayashi et al. 1999). The densification is maximum close to the SCP and least at the farthest point, i.e. at the center of the grid points. Tsukamoto et al. (2000) examined the changes in the state of stress due to static sand compaction pile penetration in densifying loose to medium dense soils and presented improved or modified SPT N values (after treatment) in terms of replacement ratio, and initial SPT N (before treatment) values of the soil.

Ramming action of the falling weight tends to ram the stone into sides of the hole, densifying while reinforcing the ground in addition to compacting the stone column substantially. Thus, densification and reinforcement effects cause modifications in the properties of the in situ soil. This densification and modification effects on the soil parameters of the ground are not uniform over the entire zone of surrounding ground but are functions of the distance from the point of densification. During the process of installation of RGP, the soil adjacent to and in the vicinity of the point of treatment gets densified most. This densification effect decreases with the distance from the point of densification. Densification by RGP causes increase in deformation moduli and decrease in the coefficients of permeability and of volume change.

Murali Krishna et al. (2006) incorporated the densification effect of granular piles, with respect to the variation of flow parameters from the centre of the granular pile, in the analysis of pore pressure generation and dissipation that was originally developed by Seed and Booker (1977). The modified form of the governing Eq. 1 with the inclusion of densification is:

$$\frac{k_h(r)}{\gamma_w \cdot m_v(r)} \left(\frac{1}{r} \frac{\partial u}{\partial r} + \frac{\partial^2 u}{\partial r^2} \right) + \frac{1}{\gamma_w \cdot m_v(r)} \cdot \frac{\partial(k_h(r))}{\partial r} \cdot \frac{\partial u}{\partial r} = \frac{\partial u}{\partial t} - \frac{\partial u_g}{\partial N} \cdot \frac{\partial N}{\partial t} \quad (2)$$

Murali Krishna et al. (2006) studied the densification effect with respect to the coefficients of permeability and volume change at the near and at the farthest ends of the granular pile, individually and together, on maximum pore pressure variations during an earthquake event. Figures 10 and 11 show the densification effect on maximum pore pressure ratio with respect to coefficient of volume change at the near and farthest ends respectively. R_{ma} and R_{mb} are normalized coefficients of volume change due to densification at the near and farthest ends respectively. Figures show that densification effect minimises the pore pressure ratios. Figures 12 and 13 show the densification effect on maximum pore pressure ratio with respect to both the coefficients of permeability and volume change at the near and farthest ends respectively.

Madhav and Murali Krishna (2007) combined both the densification and dilation effects and incorporated them in the analysis of pore pressure generation and dissipation. They also verified the effect of type of variation with distance on maximum pore pressure ratios and concluded that the pore pressures ratios are not sensitive to the type of variation of permeability with distance. Figure 14 shows the effect of densification with respect to flow parameters at the near end in addition to the dilation effect. It is seen from the figure that the dilation effect reduces the negative effect of the densification effect.

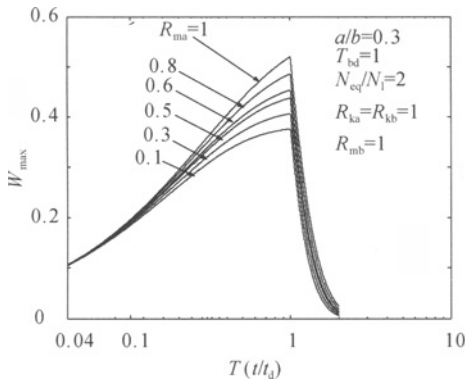


Figure 10. Effect of R_{ma} on W_{max}

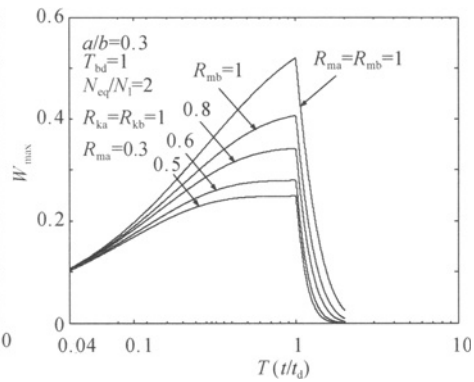


Figure 11. Effect of R_{mb} on W_{max}

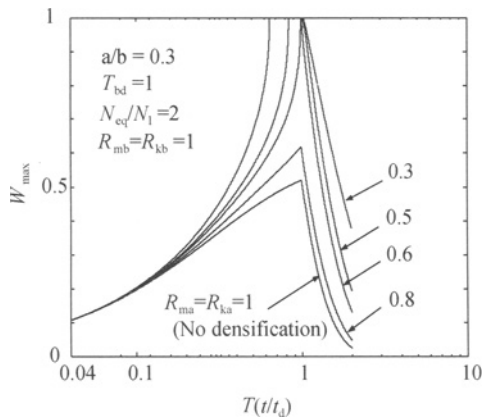


Figure 12. Effect of R_{ma} and R_{ka} on W_{max}

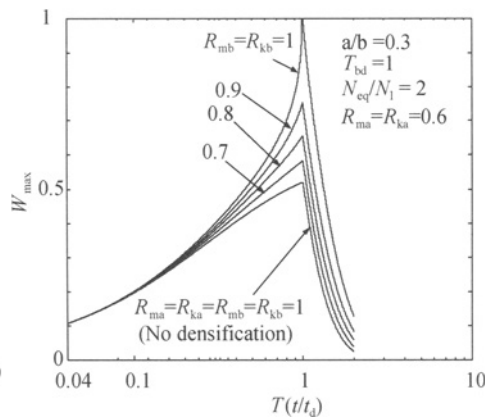


Figure 13. Effect of R_{mb} and R_{kb} on W_{max}

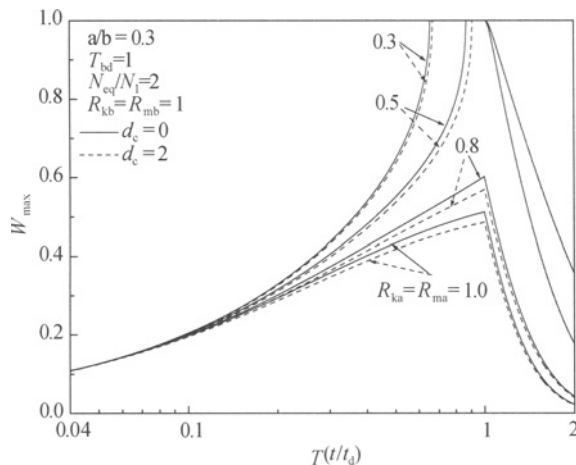


Figure 14. Effect of densification with respect to R_{ka} & R_{ma} and dilation on W_{max}

Densification effect on the coefficient of volume change is positive in that the maximum induced pore water pressure ratios get reduced and is sensitive to the type of variation

considered as pore pressure ratios are lesser for the exponential variation. Densification effect, on the coefficient of permeability alone or in addition to effect on coefficient of volume change, increases the maximum pore water pressure ratios giving a negative effect. The pore pressures ratios are not sensitive to the type of variation of permeability with distance. Densification effect on both coefficients of permeability and volume change result in a either slightly negative or positive effect depending on the degree of densification.

Dilation effect generates negative pore water pressures in the granular piles. The negative pore pressures generated in a dilating gravel drain reduce potential liquefaction induced pore pressures by permitting faster rates of dissipation, and hence enhance liquefaction mitigation. The negative effect of the densification (reduction in permeability) is offset by the dilation effect thus proving the effectiveness of granular piles in liquefaction mitigation. It is recommended that the densification and dilation effects should be considered while designing granular pile/stone column treatment for liquefaction mitigation.

REINFORCEMENT EFFECT

Granular piles, installed in to a very dense state, are not prone to liquefaction and replace a significant quantity of in situ liquefiable soil and reinforce the same. The very high deformation modulus and stiffness of the granular pile material provide reinforcement for the in situ soil and offer another mechanism to mitigate liquefaction. Stone columns installed in loose sands are effective in damage control as they are installed to a relative density (more rigid/stiff) well above the density of the surrounding soil and hence increase the ability of the layer to withstand the earthquake forces more efficiently.

Poorooshab et al. (2006) and Noorzad et al. (2007) demonstrated the reinforcement effect of stone columns while analysing their performance during an earthquake. They proposed that the seismic load imposed on the soil is shared between the stone column and the surrounding ground and stone column carries the major load. The geometry of the stone column installation is shown in the Figure 15 while the free body diagram (Figure 16) illustrates the load distribution as a result of reinforcement.

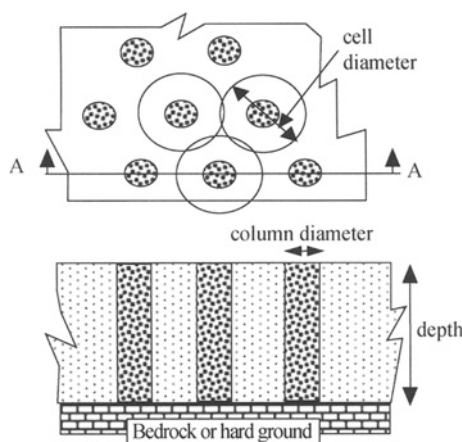


Figure 15. Definition Sketch for reinforcement effect (after Poorooshab et al., 2006)

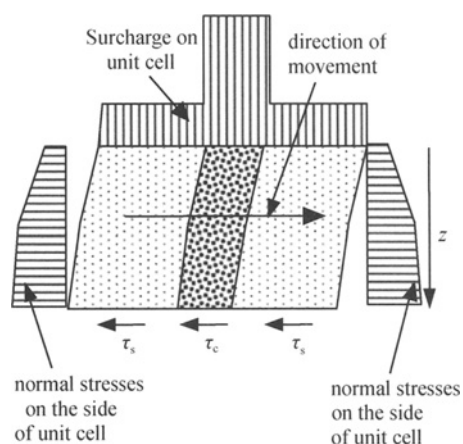


Figure 16. FBD of the Unit Cell (after Poorooshab et al., 2006)

Figure 17 shows the performance of the sand layer with void ratio at the critical state (0.9) without and with stone column against the 1989 Loma Prieta earthquake acceleration-time history. It is seen from the figure that the increase in columns diameter did have a dramatic effect on the performance of system measured in terms of the development of the excess pore water pressure and the deformations get reduced significantly.

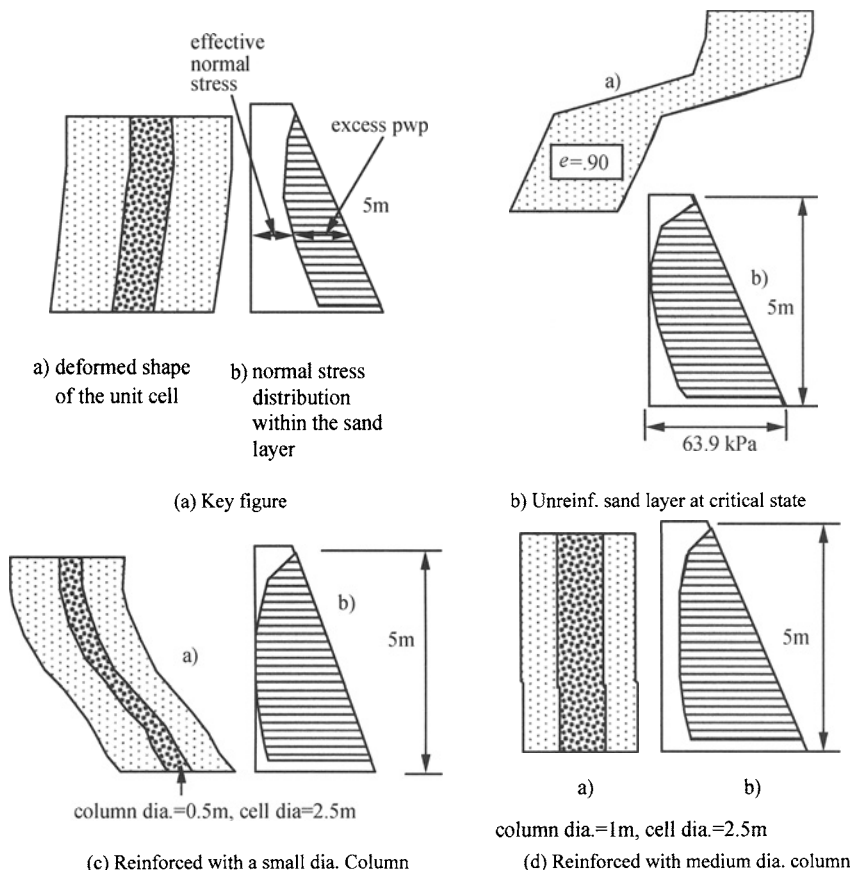


Figure 17. Performance of unreinforced and reinforced very loose sand layer with void ratio at the critical state (after Poorooshasb et al. 2006)

Noorzad et al. (2007) presented the performance of partially penetrating stone columns during earthquake on similar lines. Figure 18 shows the performance of stone columns with various lengths as a liquefaction hazard mitigation countermeasure. Here the unreinforced sand layer is 7.5 m deep and at critical state with void ratio of 0.9. The stone columns of 750 mm diameter and of different lengths are installed at a pitch of 2.5 m. It is seen from the figure that the effect of column length is obvious in mitigating liquefaction.

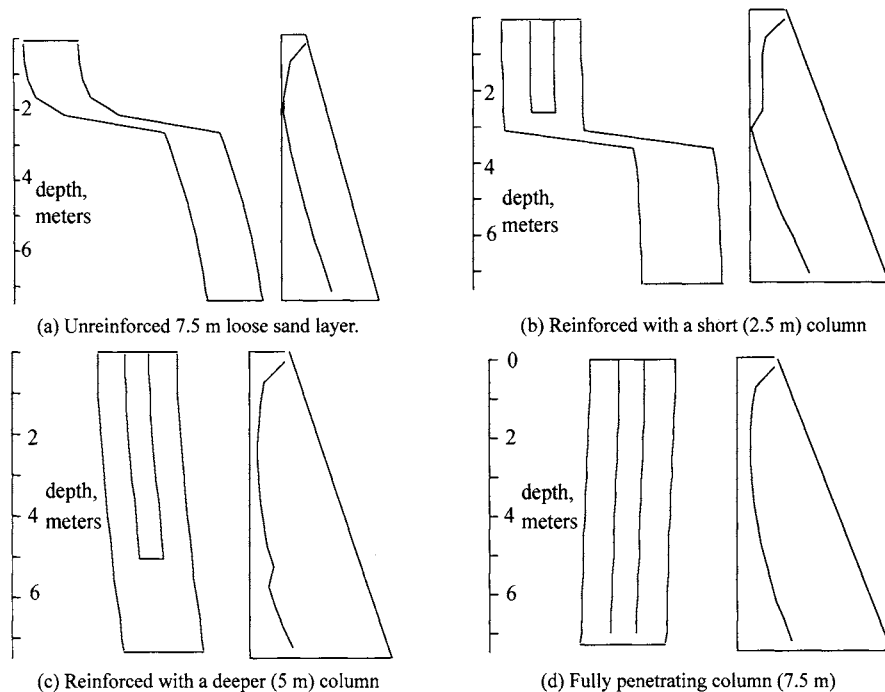


Figure 18. Effectiveness of stone columns with various lengths(after Noorzad et al. 2007)

SUMMARY

Liquefaction is the most hazardous damage during an earthquake. Among various remedial measures available, installation of gravel drains/Granular piles is the most widely adopted method for liquefaction mitigation. Granular piles provide drainage facility, densify the surrounding soil and reinforce the in-situ ground. Different mechanisms take place in the functioning of the stone columns during the process of liquefaction mitigation. The major fundamental mechanism is drainage by which developed excess pore water pressures get dissipated almost as fast as they get generated. The other mechanisms include storage, dilation, densification and reinforcement. While studying the performance of the gravel drain system all the mechanisms along with their mechanics are to be considered.

REFERENCES

- Adalier K. and Elgamal A. (2004). Mitigation of liquefaction and associated ground deformations by stone columns. *Engineering Geology*, 72: (3-4): 275-291.
- Baez J.I. and Martin G.R. (1992). Quantitative evaluation of stone column technique for earthquake liquefaction mitigation. *Proc. 10th World Conference on Earthquake Engineering*, 1477-1483.
- Balaam N.P. and Booker J.R. (1981). Analysis of rigid raft supported by granular piles. *Intl. Journal for Num. and Anal. Methods in Geomechanics*, 5: 379-403.
- Barksdale R.D. and Bachus R.C. (1983). *Design and construction of stone columns*. Report No. FHWA/RD-83/026, U. S. Department of Transportation, Federal Highway Administration, Washington, D. C., 194pp

- Boulanger R., Idriss I., Stewart D., Hashash Y. and Schmidt B. (1998). Drainage capacity of stone columns or gravel drains for mitigating liquefaction. *Proc., Geotech. Earthquake Engg. and Soil Dynamics III*, ASCE Geotechnical Special Publication. 75 (1): 678– 690.
- Brennan A.J. and Madabhushi S.P.G. (2002). Effectiveness of vertical drains in mitigation of liquefaction. *Soil Dynamics and Earthquake Engineering*, 22 (9): 1059–1065.
- Datye K.R. and Nagaraju S.S. (1981). Design approach and field control for stone columns, *Proc. 10th International Conf. on Soil Mechanics and Foundation Engineering*, Stockholm, Sweden, 3: 637-640.
- Engelhardt K. and Golding H.C. (1975). Field testing to evaluate stone column performance in a seismic area. *Geotechnique*, 25 (1): 61-69.
- Hughes J. M. O. and Withers N. J. (1974). Reinforcing of soft cohesive soils with stone columns. *Ground Engineering*, 7 (3): 42-49.
- Iai S. and Koizumi K. (1986). Estimation of earthquake induced excess pore water pressure for gravel drains. *Proc. 7th Japan Earthquake Engg. Symposium*, 679-684.
- Iai S., Koizumi K., Noda S. and Tsuchida H. (1988). Large scale model tests and analysis of gravel drains. *Proc., 9th World Conference on Earthquake Engg.*, Tokyo-Kyoto, Japan, vol. III.
- Leonards G.A. (ed.) (1962). *Foundation engineering*. McGraw-Hill, New York,
- Lopez R.A. and Hayden R.F. (1992). The use of vibro systems in seismic design. *Grouting, Soil Improvement and Geosynthetics*, Borden, R. H., Holtz, R. D., and Juran, I., eds., GSP No. 30, ASCE, 2, 1433-1445.
- Madhav M. R., Iyengar N. G. R., Vitkar R.P. and Nandia A. (1979). Increased bearing capacity and reduced settlements due to inclusions in soil. *Proc. International Conference on Soil Reinforcement: Reinforced Earth and Other Techniques*, Paris, II: 329-333.
- Madhav M.R. and Arlekar J.N. (2000). Dilation of granular piles in mitigating liquefaction of sand deposits. *12th World Conference Earthquake Engineering*, Auckland. No: 1035 (CD-ROM).
- Madhav M.R. and Murali Krishna A. (2007). Liquefaction mitigation of sand deposits by granular piles: densification and dilation Effects. *Proc. 4th International Conference on Earthquake Geotechnical Engineering*, Thessaloniki, Greece, ID No. 1119 (CD Rom).
- Madhav M.R. and Thiruselvam K. (1988). Effect of installation methods on granular pile response. *Proc. Int. Symp. on Theory and Practice of Earth Reinforcement*, I. S. Kyushu, 221-226.
- Mitchell J.K. and Wentz F.K. (1991). *Performance of improved ground during Loma Prieta earthquake*. Report No. EERC91/12, Earthquake Engineering Research Center, University of California, Berkeley.
- Munfakh G.A., Abramson L.W., Barksdale R.D. and Juran I. (1987). In-situ ground reinforcement. *Soil Improvement – A Ten Year Update*, Welsh, J. P., ed., Geotechnical Special Publication No. 12, ASCE, 1-17.
- Murali Krishna A., Madhav M.R. and G. Madhavi Latha. (2006). Liquefaction mitigation of ground treated with granular piles: Densification effect. *ISSET Journal of Earthquake Technology*, 43 (4): 105-120.
- Noorzad A., Poorooshasb H.B. and Madhav M.R. (2007). Performance of partially penetrating stone columns during an earthquake. *Proc. Tenth Symposium on Numerical models in Geomechanics (NUMOG X)*, Rhodes, Greece, 503-508.
- Ohbayashi J., Harada K. and Yamamoto M. (1999). Resistance against liquefaction of ground improved by sand compaction pile method. *Earthquake Geotechnical Engineering*, Seco e Pinto (ed.), Balkama, Rotterdam, 549-554.
- Onoue A. (1988). Diagrams considering well resistance for designing spacing ratio of gravel drains. *Soils and Foundations*, 28 (3) 160– 168.

- Onoue A., Mori N. and Takano S. (1987). In-situ experiment and analysis on well resistance of gravel drains. *Soils and Foundations*, 27 (2): 42–60.
- Pestana J.M., Hunt C.E. and Goughnour R.R. (1997). *FEQDrain: a finite element computer program for the analysis of the earthquake generation and dissipation of pore water pressure in layered sand deposits with vertical drains*. Report No. UCB/EERC-97-15.
- Pestana J.M., Hunt C.E., Goughnour R.R. and Kammerer A.M. (1998). Effect of storage capacity on vertical drain performance in liquefiable sand deposits. *Proc. Second International Conference on Ground Improvement Techniques*, Singapore, 373-380.
- Poorooshasb H.B., Madhav M.R. and Noorzad A. (2006). Performance of stone columns subjected to a seismic base excitation. *Proc. Int. Symp. on Lowland Technology-2006*, Saga, 1189-1194.
- Poorooshasb H.B., Noorzad A., Miura N. and Madhav M.R. (2000). Prevention of earthquake induced liquefaction of sandy deposits using stone columns. *Proc. Int. Symp. on Lowland Technology 2000*, Saga, 213-220.
- Sasaki Y. and Taniguchi E. (1982). Shaking table tests on gravel drains to prevent liquefaction of sand deposits. *Soils and Foundations*, 22 (3): 1–14.
- Seed H.B. and Booker J.R. (1977). Stabilization of potentially liquefiable sand deposits using gravel drains. *J. of the Geotechnical Engineering Division, ASCE*, 103 (7): 757-768.
- Seed H.B., Idriss I.M. (1971). Simplified procedure for evaluating soil liquefaction potential. *Journal of the Soil Mechanics and Foundations Division, ASCE*, 97(SM 9): 1249- 1273.
- Seed H.B., Idriss I.M., Makdisi F. and Bannerjee N. (1975). *Representation of irregular stress time histories by equivalent uniform stress series in liquefaction analyses*. Report No. UCB/EERC/75-29, Earthquake Engineering Research Center, University of California, Berkeley, California.
- Tokimatsu K., Yoshimi Y. (1980). Effects of vertical drains on the bearing capacity of saturated sand during earthquakes. *Proc., International Conference on Engineering for Protection from Natural Disasters*, Bangkok, Thailand, 643– 655.
- Tsukamoto Y., Ishihara K., Yamamoto M., Harada K. and Yabe H. (2000). Soil densification due to static sand pile installation for liquefaction remediation. *Soils and Foundations*, 40 (2): 9-20.
- Vaid Y.P., Byrne P.M. and Hughes J.M.O. (1981). Dilation angle and liquefaction potential. *Journal of the Geotechnical Engineering Division, Proceedings of the ASCE*, 107(GT7): 1003-1008.
- Yasuda S., Ishihara K., Harada K. and Shinkawa N. (1996). Effect of soil improvement on ground subsidence due to liquefaction. *Special issue, Soils and Foundations*, 99-107.

ESTIMATION OF LIQUEFACTION-INDUCED SETTLEMENT OF RIVER DIKES AND THEIR EFFECT IN LOWLAND AREA DURING EARTHQUAKES

Susumu Yasuda

*Civil and Environmental Department, Tokyo Denki University, Hatoyama, Hiki-gun,
Saitama 3500394, Japan*

Lowland area in Tokyo subsided due to abstraction from about 1930 to 1970. Now, a wide area of 124 km² is below sea level. Earthquake-triggered flood in the lowland area during earthquakes is seriously concerned. Possibility of the damage was discussed based on the analyses for the deformation of river dikes. Analyzed results showed that the dikes settle dozens of cm and causes flood during strong shaking.

INTRODUCTION

Many mega-cities in the world are located in lowlands where various geotechnical problems are potentially existed, such as ground subsidence due to draw of water from wells, liquefaction during earthquakes, flood during heavy rains, etc. Individual geotechnical problem must be predicted and appropriate measures should be applied. Moreover, complex multiple geotechnical disasters must be paid attention and prevented also. One multiple problems due to liquefaction may occur in lowland where ground subsidence has occurred and there exists liquefiable sands. In general, height of river dikes is designed not to induce flood during heavy rain and flood tide. However, the design height is not sufficient if foundation ground liquefy during earthquakes, because liquefaction causes large settlement of the dikes. Then the flood during earthquakes due to liquefaction-induced settlement of river dikes must be predicted and appropriate countermeasures must be applied.

In Japan, subsidence occurred in lowlands of three big cities, Tokyo, Osaka and Nagoya, due to draw of water from wells. The maximum settlement of the ground reached 4m in Tokyo. Consequently the area where ground surface is below sea level expanded to 124 km² in Tokyo. River dikes and canal revetments have been constructed to prevent flood during heavy rain and high tide. Recently the dikes and revetments have been strengthened against earthquakes. However, many dikes and revetments are still not treated. Then, in this paper, probabilities of earthquake-triggered flood due to liquefaction during future earthquakes are discussed.

GEOMORPHOLOGIC CONDITION AND LIQUEFACTION POTENTIAL IN TOKYO

Geomorphologic condition

Tokyo is divided into four areas in geomorphologic condition from east to west: mountain, hill, terrace and lowland areas. Liquefiable loose sand layers are deposited in the lowland area. The lowland area is subdivided into four zones: a wide alluvial lowland formed by Sumida River, Ara River, Naka River and Edo River, a narrow lowland formed by Tama River, a beach along Tokyo Bay and artificially reclaimed lands constructed along Tokyo Bay. Tokyo Station is the boundary of the hill area and the large lowland zone.

Alluvial loose sand layers are deposited in the lowlands formed by the rivers and beach. Figure 1 shows a soil cross section in the wide lowland from west to east. As shown in this figure, an alluvial loose sand layer, Yu, is deposited from ground surface to the depth of about 10 m. An alluvial soft clay layer, Yl, is underlying with a thickness of about 20 to 40 m. Then diluvial loam and gravel layers are deposited. Reclaimed loose sand layers are filled in the reclaimed lands. The alluvial sand layer is loose but contains fairly much fines such as 20% to 40%.

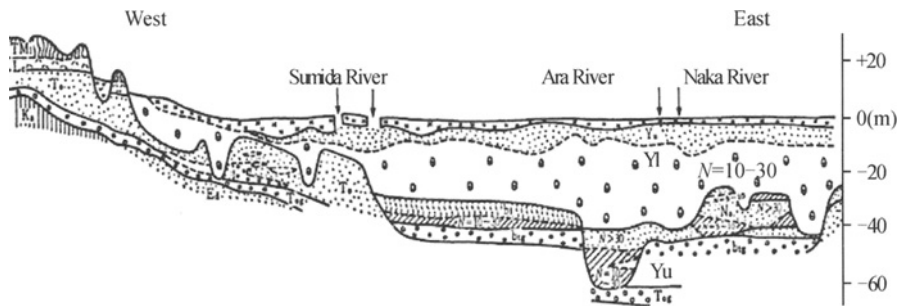


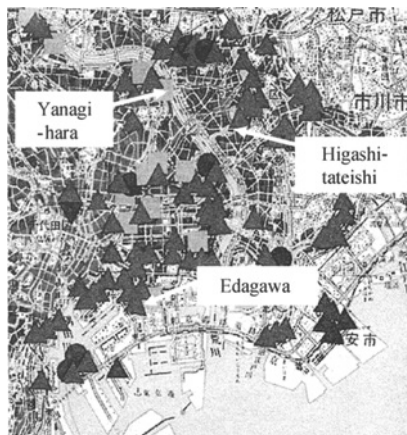
Figure 1. Soil cross section along lowland in Tokyo

There are many canals retaining by river walls in the lowland area. Moreover, reclaimed lands are protected by sea walls and quay walls.

Liquefaction potential

Though Japan is a high seismic country, big earthquakes have not hit Tokyo in these dozens of years. The latest earthquake which caused severe damage was 1923 Kanto earthquake. Figure 2 shows liquefied sites during the Kanto and other previous earthquakes (Wakamatsu, 1991). Damage to structures due to the liquefaction is not clear because the earthquake occurred dozens of years ago and widely happened fires destroyed the trace of liquefaction-induced damage. However, as shown in Figure 2, it can be seen that liquefied

sites were located in artificially reclaimed lands and along several rivers only. This implies that whole alluvial sand layer (Yu) did not liquefy, but only the sands formed by natural levee and the artificially filled sands liquefied.



▲ Liquefied sites during 1923 Kanto earthquake (Wakamatsu, 1991)

Figure 2. Liquefied sites during the Kanto and other previous earthquakes (Wakamatsu, 1991)

SUBSIDENCE AND PROTECTION BY RIVER DIKES

Subsidence due to abstraction

In Japan, industry developed rapidly from the beginning of 20th Century. Due to the lack of water many wells were excavated and ground water was drawn in lowland in Tokyo. The wells were excavated to or more than the depth of the diluvial gravel layer. This abstraction caused the decrease of pore water pressure in the alluvial soft clay layer and, consequently, induced subsidence due to the consolidation of the clay.

Settlement of the ground surface has been measured at several sites in Tokyo. Figure 3 shows the measured settlements. As shown in this figure, speed of subsidence increased from about 1930. Subsidence reached to the maximum value in about 1970, then stopped. The maximum settlement measured was about 4.5 m. Though the measurement had been started, mechanism of the subsidence had not been clarified before about 1950 because theory of consolidation had not been introduced in Japan. In 1964 abstraction was prohibited because soil mechanics proved the reason of the subsidence. Then the speed of settlement decreased as shown in Figures 3 and 4.

Due to the subsidence, very low zone named “Zero Meter Zone” where level of ground surface is lower than sea level was formed in as shown in Figure 4. Area of the “Zero Meter Zone” reached 124 km² in Tokyo. As mentioned above, the subsidence started after the 1923 Kanto earthquake. Therefore, subsidence related damage during earthquakes is a new problem in lowland in Tokyo.

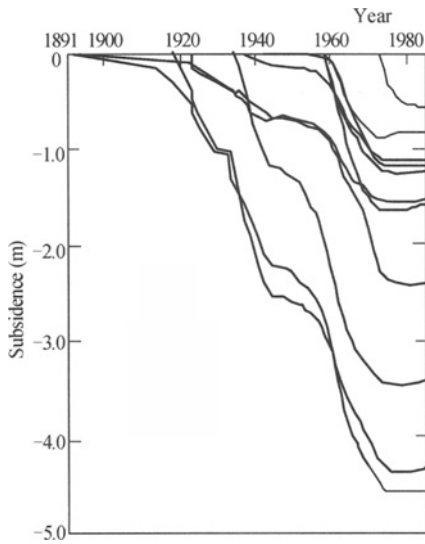


Figure 3. Measured subsidence at several sites in Tokyo

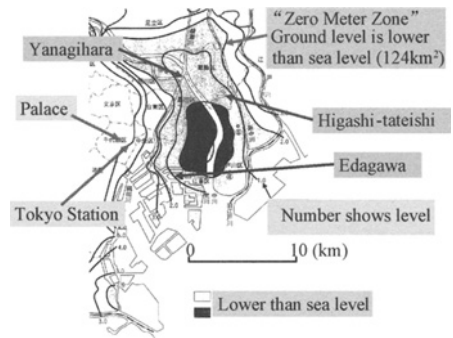


Figure 4. Zero Meter Zone in Tokyo

Reinforcing of river dikes to protect inland from flood during earthquakes

There are many rivers and canals in lowland of Tokyo. Many types of dikes or walls have been constructed to protect against flood during heavy rain. A canal revetment at Edagawa and two river dikes at Higashi-tateishi and Yanagihara are shown in Photo 1, 2 and 3, respectively. At Edagawa, inland is protected by steel sheet pile walls. Ground surface is about 1m lower than the level of canal water. At Higashi-tateishi and Yanagihara, ground surface behind a dike is about 2 m lower than the level of the water of Naka River and Ayase River, respectively.



Photo 1. Edagawa site



Photo 2. Higashi-tateishi site

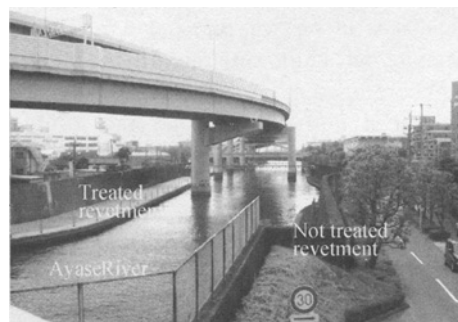


Photo 3. Yanagihara site

These canal revetments and river dikes are designed to protect inland from flood caused by mainly heavy rains and Typhoons. However, recently, some revetments and river dikes have been reinforced against the damage by liquefaction. One example of the reinforced canal revetment is shown in Figure 5 (JGS,1998). The revetment was constructed in 1969. Seismic

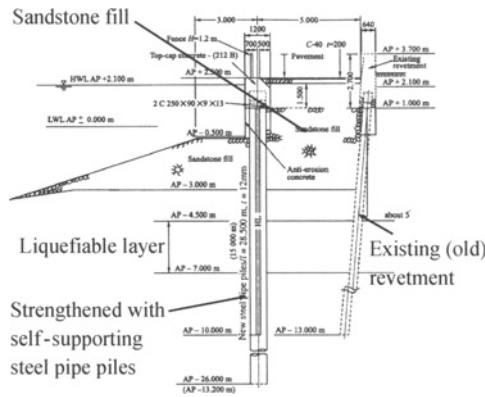


Figure 5. Reinforced canal revetment in Tokyo (JGS,1998)

inspection revealed a loose silty sand layer of 4m in thickness that was susceptible to liquefaction. As countermeasure against liquefaction, the quay wall was strengthened with self-supporting steel pipe piles, as shown in Figure 5. New steel pipe piles with a length of 28.5m were installed, sandstone fill was placed in front of the pipe piles as foot protection, and the space between the existing and newly driven piles was filled with gravel.

At Yanagihara, left side dike has been reinforced, but right side dike has not treated as shown in Photo 3. As shown in these example, many revetments and river dikes have been treated against earthquake. But dozens of dikes and revetments have not been treated. Then “earthquake-triggered flood” is seriously concerned at not treated sites. The author and his colleagues conducted several analyses to demonstrate the probability of the earthquake-triggered flood due to the deformation of non treated revetments and dikes.

APPLIED ANALITICAL METHOD

Recent evaluation methods for liquefaction-induced deformation

In Japan, very strong shaking caused severe damage to structures during the 1995 Hyogoken-nambu (Kobe) earthquake. Then it became necessary to investigate new design concepts that could withstand very strong shaking. The Japan Society of Civil Engineering organized a technical committee to deal with these problems and submitted its first proposals in 1996 (JSCE, 1996). It suggested basing earthquake-resistant design on two types of ground motion: Level 1 earthquake motion, which is likely to strike a structure once or twice while it is in service, and Level 2 earthquake motion, which is very unlikely to strike a structure during the structure life time, but when it does, it is extremely strong.

According to this concept, design accelerations for Level 1 and Level 2 earthquake motion have been introduced in several design codes. For example, in the design code for high-pressure gas facilities, the following design seismic coefficients were introduced to estimate the occurrence of liquefaction:

- i) Level 1 earthquake motion: 0.12g to 0.3g.
- ii) Level 2 earthquake motion: 0.24g to 0.6g.

As the maximum surface acceleration in the “Level 2 shaking” is very high, even medium dense sand ground is judged to induce liquefaction. However, the damage to structures in medium dense ground is not so severe. Therefore, it is necessary to evaluate not only the occurrence of liquefaction but also the deformation of structures. And the serviceability of

the structure should be considered in the design procedure, based on the evaluated deformation. This design method can be called as “Performance-based design.” in liquefaction filed.

In the estimation of liquefaction-induced deformation of structures, three grades of methods; i) empirical method, ii) static analyses (residual deformation method), and iii) dynamic analyses, are available. (e.g. Yasuda, 2005). Joint analyses for the settlement of raft foundation were carried out in 2003 in Japan (Harada et al., 2004). A hypothetical model of ground beneath a storage tank was used for the analyses. Six different cases with varying configurations in cross section were analyzed, to evaluate the improvement due to compaction. Storage tank is 10 m in width and 12 m in height. Seven different liquefaction analysis codes were used for the analyses. Among them, four effective stress analysis codes, STADAS2, LIQCA, DIANA and STADAS, were developed based on elasto-plasticity theory. Two other effective stress analysis codes, FLIP and NUW2, were developed based on multi-mechanism theory and undrained stress path model, respectively. In addition, ALID (Yasuda et al., 1999), a static method, was applied. Figure 6 shows relationships between vertical displacement of the tank and maximum acceleration of input wave. As shown in this figures, large settlements of the order of several ten centimeters could be evaluated by these codes. However, the results analyzed by the different analytical methods vary significantly, even though the same liquefaction strength is expected. The main reason for this variation is, even though liquefaction strength curves for a particular strain level are fitted, analyses do not always give acceptable results under wide range of strain.

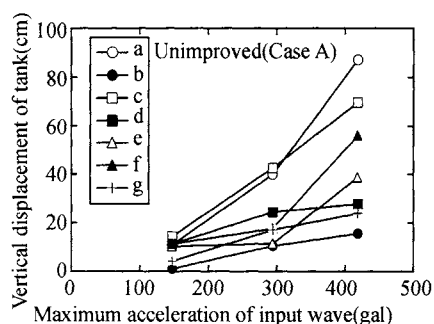


Figure 6. Relationship between maximum acceleration and calculated vertical displacement by 7 methods (Harada et al., 2004)

Brief explanation of the analytical code ALID

In this study, ALID was used to analyze the liquefaction-induced deformation of river dikes because the method is not so complex compare with dynamic analytical methods. Figure 7 shows schematic diagram of stress-strain curves of intact soil and liquefied soil. Shear strain increased with very low shear stress up to very large strain. Then, after a resistance transformation point, the shear stress increased comparatively rapidly with shear strain, following the decrease of pore water pressure. Figure 8 shows the concept of the stress-strain curves which are used in ALID. Line *l* denotes a backbone curve at the beginning of the earthquake. Point A is supposed to be initial state of a soil element in the ground. When excess pore water pressure generates, material properties, such as shear strength and elastic modulus change. Suppose that the backbone curve moves from *l* to *m* due to liquefaction, then strain should increase in order to hold the driving stress. Since driving stress, however, decreases according to the change of geometry, actual strain increment from state *l* to *m* is

from A to C. Namely, strain increment caused by the change of material property is $\gamma_C - \gamma_A$. Ground deformation stops when new material property comes to balance with a new driving stress, which is shown as point C in the figure.

By considering the concept mentioned above, a computer code “ALID/Win” was developed. In this code, static finite element method is applied in the following steps:

- i) In the first step, the deformation of the ground before earthquake is calculated by using the stress-strain relationships of not-liquefied soils.
- ii) The deformation of the ground due to liquefaction is calculated in the second step, by using the stress-strain relationship of liquefied soils. Deformation of the ground due to the dissipation of excess pore pressure is also considered.

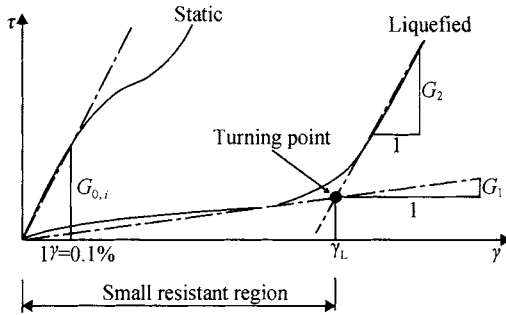


Figure 7. Schematic diagram of stress-strain curve of liquefied soil

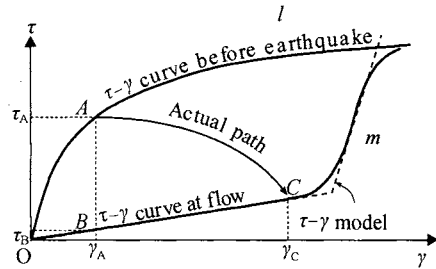


Figure 8. Concept of stress-strain curves used for analysis

Many cyclic torsional tests were conducted to obtain the stress-strain curves of liquefied sands and softened clays. In the tests, three reconstituted sands and a series of undisturbed sands were tested (Yasuda et al. (1999, 2003) at first. In the tests, samples were trimmed to become hollow cylindrical specimens. Then the specimens were saturated and consolidated. Confining pressure, σ_c' was adjusted as in-situ effective overburden pressure. After the consolidation, 20 cycles of cyclic loading with 0.1 cycles/sec. was applied to the specimens under undrained condition. Then, a monotonic loading was applied under undrained condition with a speed of 10 % of shear strain/minute. Different amplitude of cyclic loading was applied to several specimen to induce different severity of liquefaction. The severity of liquefaction was indicated as safety factor against liquefaction, F_L . Stress-strain curves before and after the resistance transformation point can be presented approximately by a bilinear model with G_1 , G_2 and γ_L as shown in Figure 9 (a). Then relationships among shear modulus ratio G_1/G_0 , fines content F_c and F_L , and relationships among G_1 , G_2 and γ_L were proposed. Where G_0 is shear modulus of intact sand without apply cyclic loadings. Based on these results, settlement of river dikes were analyzed (Yasuda et al., 2003).

In addition, many undisturbed samples of sandy soils and clayey soils were taken for tests (Yasuda et al., 2004). Total number of tested samples and specimens were 53 and about 400, respectively. In clayey soils also, shear modulus decreased due to cyclic loading. However stress-strain curves of the softened clayey soils are different from those of liquefied sandy soils, as shown in Figures 9 (b). Then the authors classified the shape of the stress-strain curves into two types as shown in Figures 9 (a) and (b). In clayey ground, it seems that large shear strain does not induce due to earthquake because some amount of resistance remains

after cyclic loading. Therefore the authors defined shear modulus of softened soil, G_1 as the secant modulus at 1% of shear strain as shown in Figure 9 (b). Then test results were combined, a new unified relationship among G_1 , effective confining pressure σ_c' , undrained cyclic strength ratio (liquefaction strength ratio) R_L , and F_L , was proposed as follows:

$$G_1 / \sigma_c' = ae^{(-\exp(-b(R_L - c)))} \quad (1)$$

where,

$$a = 23.6F_L + 0.98$$

$$b = 9.32F_L^3 - 10.8F_L^2 + 13.27F_L - 0.806$$

$$c = -1.40F_L^3 + 3.87F_L^2 - 4.14F_L + 1.95$$

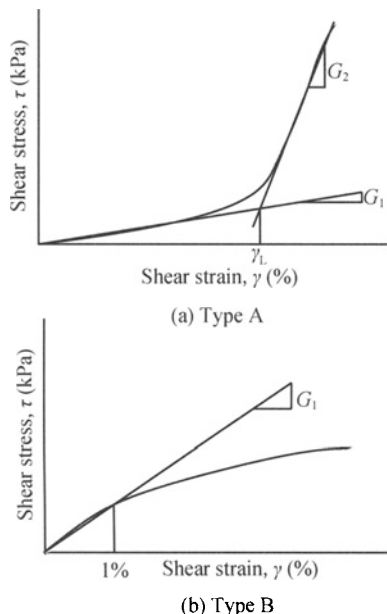


Figure 9. Classification of stress-strain curves of liquefied sandy soils and softened clayey soils

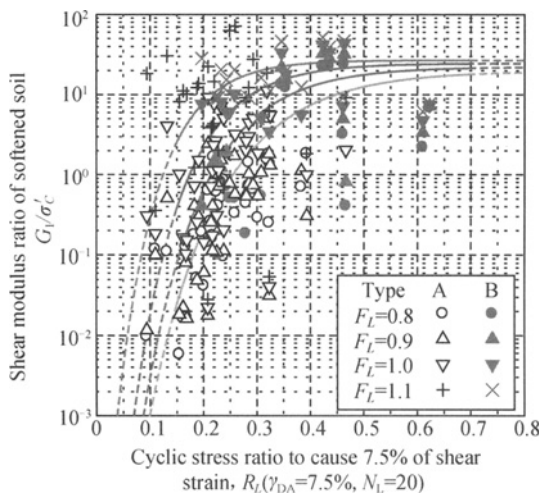


Figure 10. Relationship between G_1 / σ_c' and R_L for $F_L=0.8, 0.9, 1.0$ and 1.1 (Yasuda et al., 2004)

SOIL CONDITIONS AND LIQUEFACTION POTENTIAL AT ANALYZED SITES

Soil conditions

Two sites as shown in Photos 2 and 3 were selected to analyze the deformation of river dikes. It is estimated both sites liquefied during the 1923 Kanto earthquake. Figure 11 shows a map of existing boring data at Higashi-tateishi district. Among them the boring data at No.10 in 8-26 grid was used for the analyses. As shown in Figure 12, a loose silty sand soil layer with SPT N -value of 3 to 8 is deposited from GL-2 m to GL-8 m. A very soft clay layer with SPT N -value of zero is deposited from GL-8 m to GL-12 m. Then a loose silty sand layer with SPT N -values of 1 to 4 is underlying up to GL-25 m. Figure 13 shows the cross section of analyzed

dike. An old river dike at analyzed site had been constructed by filling soils. In 1975, a new river revetment was constructed by T-type concrete wall with steel piles. Cross section across the river dike was estimated based on design diagram during construction of the new revetment. The steel piles were 700 mm in diameter and 20 m in length. Sheet piles were driven under the concrete wall to the depth of 13 m to protect permeance. The authors measured depth of the bottom of the river and shape of the old river dike.

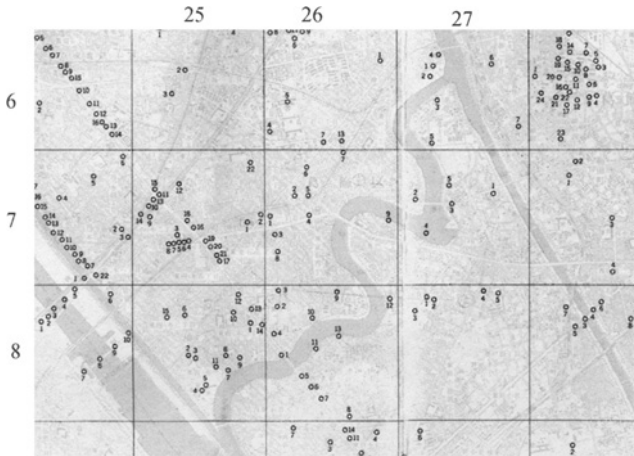


Figure 11. Sites of existing boring data at Higashi-tateishi district

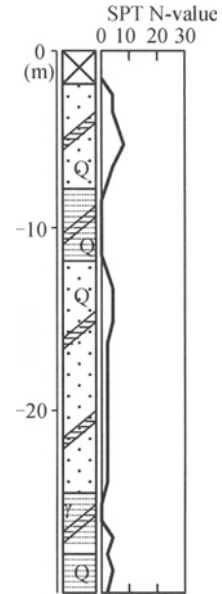


Figure 12. Soil profile at analyzed site

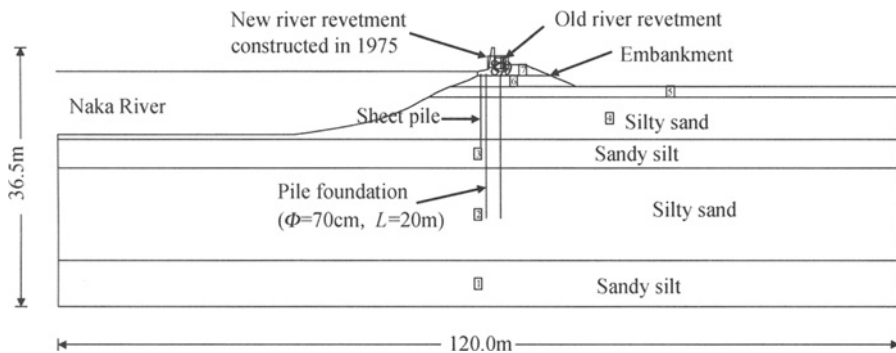


Figure 13. Cross section of analyzed dike at Higashi-tateishi

Estimation liquefaction potential

Liquefiable layers at the sites were evaluated by safety factor against liquefaction, F_L which is the ratio of liquefaction strength, R and cyclic shear stress ratio, L . In Japan, most widely used simple method to estimate R and L is the JRA method introduced in the specification

for Highway Bridges (1996). In this study, L was estimated by the JRA method. However, R was estimated by a different formula developed by the author et al. (Yasuda, Shimizu et al. (2004), Kamei et al. (2002)), because the JRA method is not appropriate to apply to the alluvial sandy soils with much fines. This method, called Tokyo Gas method hereafter, was developed based on cyclic triaxial tests and SPT N -values in Tokyo.

Figure 14 shows an example estimated F_L by the two methods at Sumida in Tokyo. In the estimation of L , 300 Gals of the maximum surface acceleration, which is almost same as the actual acceleration during the 1923 Kanto earthquake, was assumed. Square points estimated by the JRA method were far less than 1.0. This means severe liquefaction occurred during the Kanto earthquake. However, according to reports on Kanto earthquake, severe liquefaction did not occur at this site.

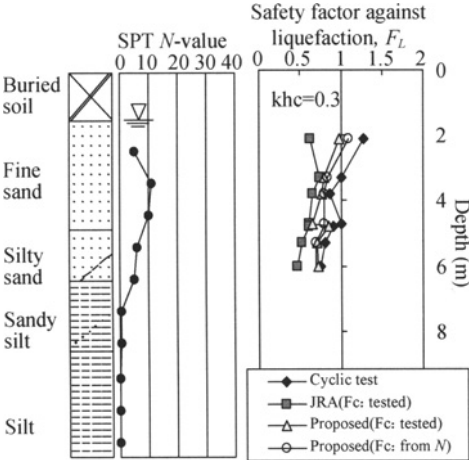


Figure 14. Soil profile, SPT N -value and F_L at Sumida site in Tokyo

One more example is zoning maps in alluvial lowland in Tokyo estimated by the JRA and the Tokyo Gas methods as shown in Figures 15 (a) and (b), respectively. Wide area between Edo River and Ara River is estimated as $P_L > 15$ by the JRA method. This means severe liquefaction occurred and would many structures damaged during the Kanto earthquake. However, again, according to the reports, severe damage occurred at several sites only. Therefore the authors judged that the JRA method underestimates the R of alluvial sands, because the sands have much fines such as $F_c = 10$ to 30 % and deposited several handed to thousands years ago. At Higashi-tateishi district, R estimated by the Tokyo Gas method for upper and lower silty sand layers were 0.26 to 0.32 and 0.27 to 0.29, respectively.

In the existing boring datum shown in Figure 12, fines content of the sandy layers are not shown. Then relationship between SPT N -value and fines content of other boring data at Higashi-tateishi district were plotted on Figure 16. A relationship proposed for alluvial sand in Tokyo (Yasuda, Shimizu et al. (2004)) was drawn in the same figure. As two relationships were coincided, fines contents at the analyzed site were estimated from SPT N -values by the proposed relationship.

As seismic force, three levels of surface acceleration were assumed:

Level 1 (old): Level 1 shaking motion designed before Kobe earthquake, $k_{hg} = 0.18$ ($A_{smax} = 176$ Gal),

Level 2 (new): Level 1 shaking motion designed after Kobe earthquake; $k_{hg}=0.24$ ($A_{smax}=235$ Gal), and

Level C: Level 2 shaking motion designed after Kobe earthquake (Type 2); $k_{hg}=0.60$ ($A_{smax}=588$ Gal)

Figure 17 (a) and Figure 18 (a) show distribution of F_L for Level A and C, respectively. In Level 1 (old), F_L at the tip of pile foundation was greater than 1.0 though the F_L in the upper silty sand layer was less than 1.0. On the contrary, F_L in whole silty sand layers was less than 1.0 in Level 2.

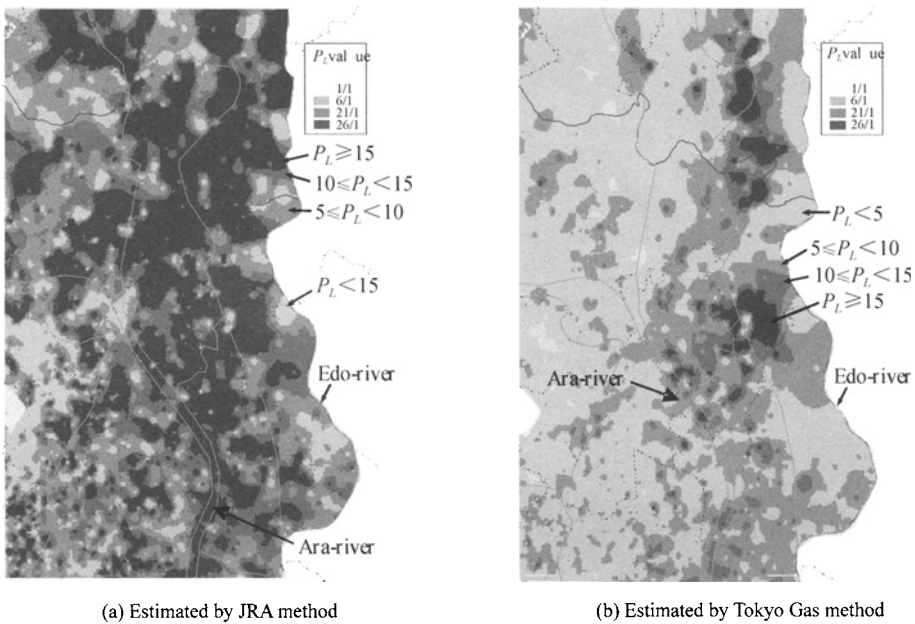


Figure 15. Zoning maps for liquefaction in alluvial lowland in Tokyo(existing boring data at Higashi-tateishi district.)

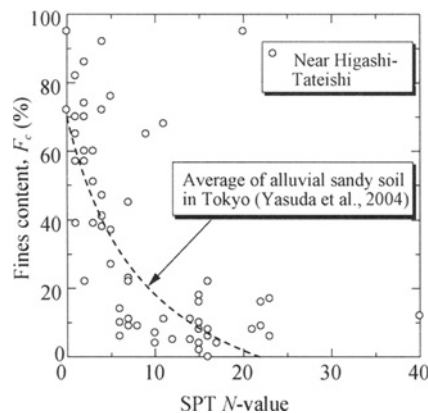


Figure 16. Relationship between SPT N -values and fines content

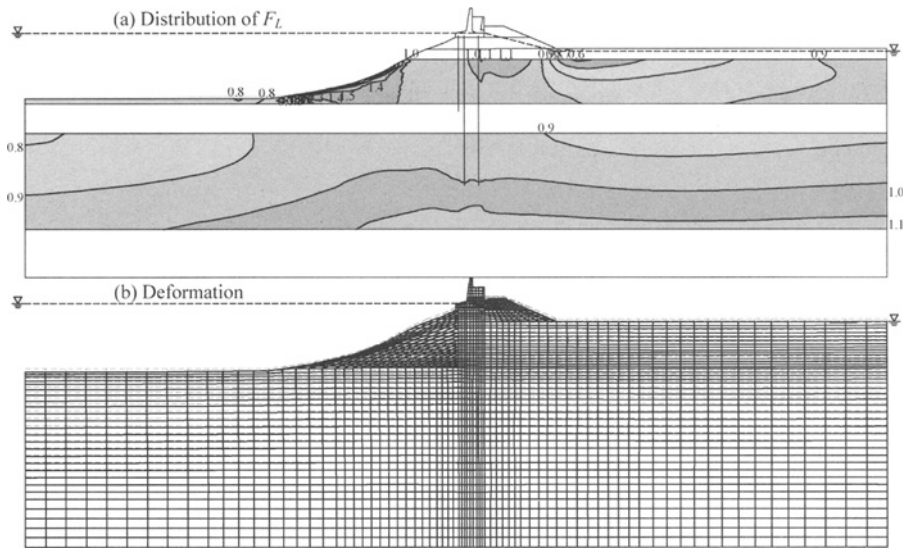


Figure 17. Analyzed F_L and deformation for Level 1 (old) at Higashi-tateishi

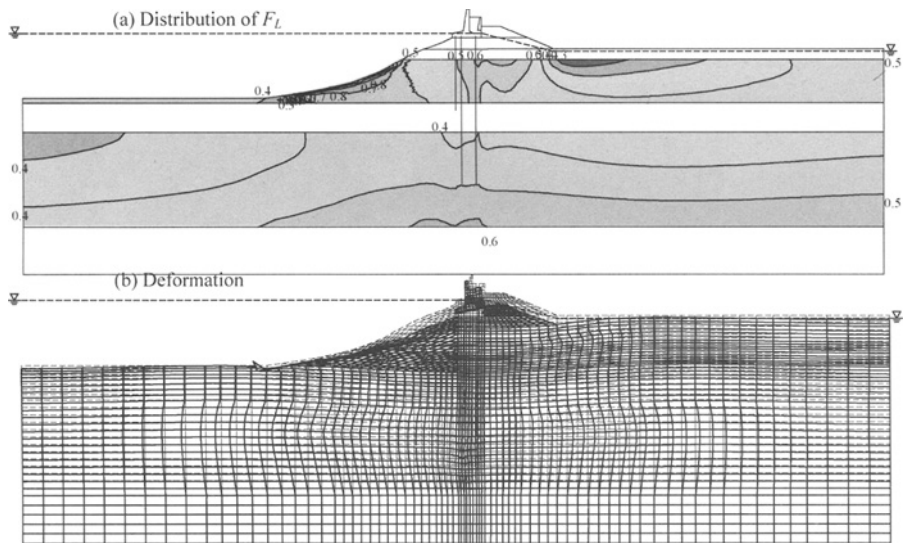


Figure 18. Analyzed F_L and deformation for Level 2 at Higashi-tateishi

ANALYZED DEFORMATION AND POSSIBILITY OF FLOOD

Analyzed deformation by ALID

Figure 17 (b) and Figure 18 (b) show deformation of the river dike at Higashi-tateishi analyzed by ALID for Level 1 (old) and Level 2, respectively. In the Level 1 (old), settlement and horizontal displacement towards river of the concrete revetment was 10 cm and 1 cm, respectively. And obvious deformation of embankment did not occur. However, large settlement and horizontal displacement of 87 cm and 76 cm, respectively, occurred in the Level 2. Moreover embankment settled 114 cm and sheet pile was bent.

Figures 19 (a) and (b) show distribution of F_L and deformation of the river dike for Level 2 at Yanagihara. Liquefiable sand layer is not thick and tip of piles supported concrete revetment is almost the same depth as the bottom of liquefiable layer. However, analyzed settlement and horizontal movement of the concrete revetment were 72 cm and 17 cm, respectively, because F_L of the sand layer was small.

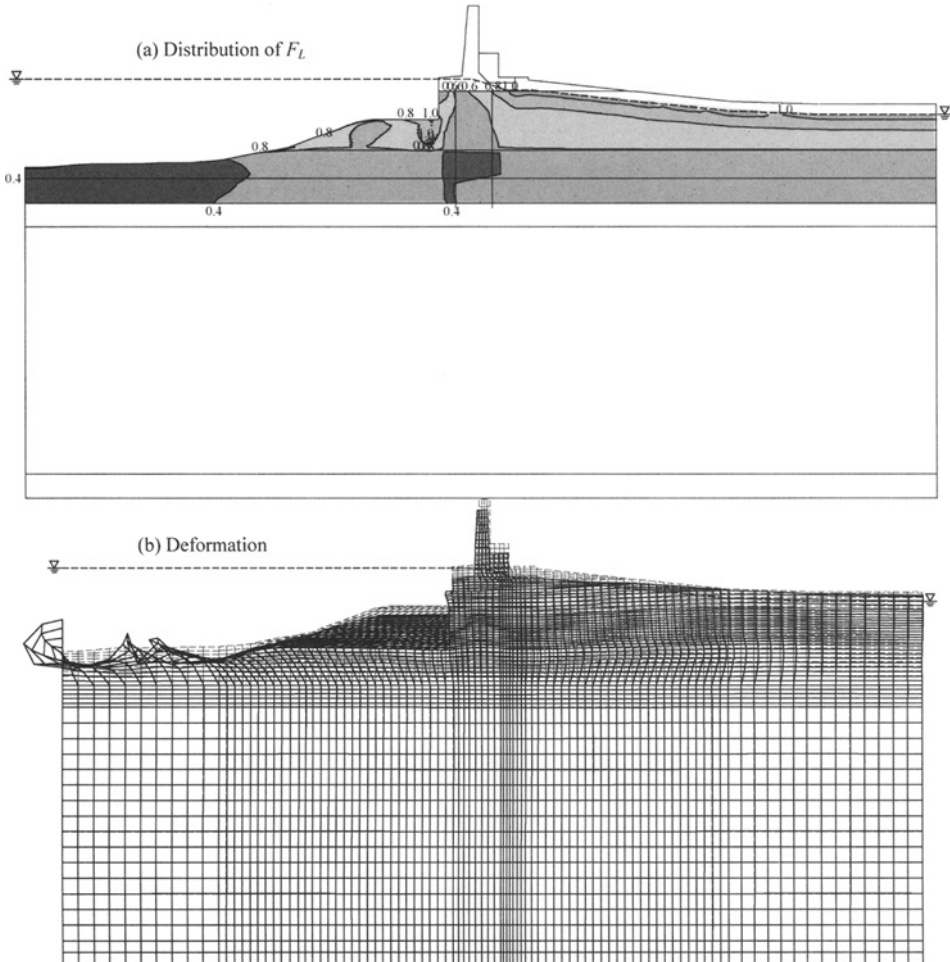


Figure 19. Analyzed F_L and deformation for Level 2 at Yanagihara

Possibility of flood due to the deformation of river dikes

Figure 20 shows relationships between maximum surface acceleration and deformation of concrete revetments at Higashi-tateishi and Yanagihara districts. As liquefaction strength ratio, R and deformation of the revetment was estimated by JRA method also, results are plotted on Figure 20. As shown in the figure, settlement and horizontal movement of the revetment is very large if liquefaction potential is estimated by JRA method even Level 1 shaking motion. However, as mentioned above, the R of silty sand is apt to underestimated by JRA method. On the contrary, deformation of concrete revetment is not large if the R is estimated by Tokyo Gas method in Level 1 shaking motion. In Level 2 shaking motion,

revetments settle dozens of cm in both sites. And, an opening of 51 cm occurred between the bottom of the slab of the revetment and the top of the embankments at Higashi-taishi site. Sheet piles which must protect permeance bend also. Moreover, joints of concrete revetments must be opened because settlement and horizontal movement of the revetments were large. Therefore, it is judged that river water invade from the openings and cause severe flood.

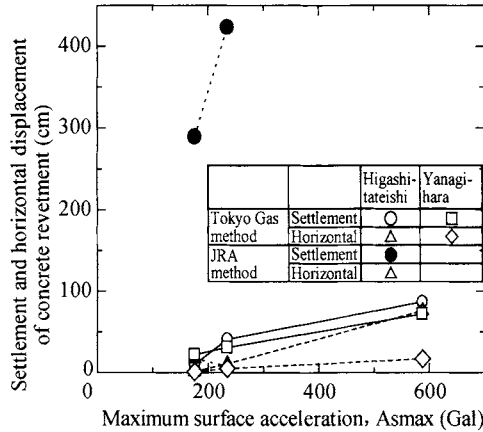


Figure 20. Relationship between acceleration and displacement of river revetment

A NEW PROBLEMS IN AND ADJACENT SUBSIDED AREA

In Tokyo the subsidence stopped from around 1970 as shown in Figure 3, because abstraction prohibited in 1964. This regulation is bringing a new problem for underground structures which were constructed before this year. Especially, two major railway stations, Tokyo Station and Ueno Station face the new problem. Big underground platforms were constructed in the stations as shown in Figure 21. Depth of the bottom of the platform is 27 m at Tokyo Station. During the construction of the platform, depth of water table was GL-35 m and it was not necessary to consider buoyancy. However, recently water level increased up to GL-15 m. Now, it is necessary worry about uplift due to buoyancy. Then, anchors were inserted to prevent uplift.

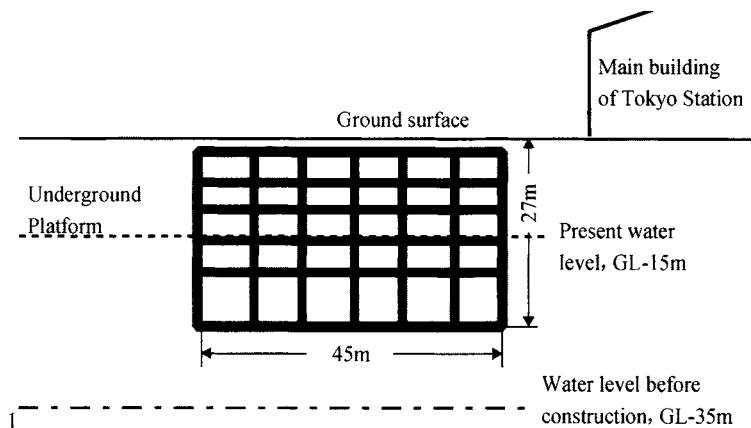


Figure 21. Change of water level around underground platforms at Tokyo Station

CONCLUSIONS

Liquefaction-induced settlement of river dikes in Tokyo during future earthquakes was estimated. Then possibility of flood due to the settlement was discussed. The following conclusions were derived from these studies:

(1) Subsidence occurred due to abstraction in lowland of Tokyo. The area where ground level is lower than sea level is 124 km² now. The area must be protected by river dikes and canal revetments. However liquefiable sandy soils are deposited under many dikes and revetments. Then the dikes and revetments have been strengthened against liquefaction. However, not treated dikes and revetments are still remained at dozens of sites.

(2) Settlements of the not treated two dikes were estimated by a static analytical method "ALID". Analyzed results showed that concrete revetments settled dozens of cm and cause flood during Level 2 shaking motion. Therefore early treatment is desired not to cause "earthquake-induced flood".

ACKNOWLEDGEMENTS

The author would like to express his thanks to Mr. M. Shimizu , graduate students at Tokyo Denki University, for his cooperation in carrying analyses.

REFERENCES

- Civil Engineering Center of Tokyo Metropolitan Government. (1977). Borehole data book, No.3.
- Harada K., Yasuda S., Yoshida N., Sato M. and Sento N. (2004). Comparative study on the effectiveness of compaction as a countermeasure against liquefaction during a strong earthquake. *Proceedings of the 3rd International Conference on Earthquake Geotechnical Engineering and 11th International Conference on Soil Dynamics & Earthquake Engineering*, 1: 56-566.
- Ishihara K., Yoshimine M. (1992). Evaluation of settlements in sand deposits following liquefaction during earthquakes. *Soils and Foundations*, 32 (1): 173-188.
- Kamei M., Morimoto I., Yasuda S., Shimizu Y., Koganemaru K. and Ishida E. (2002). A consideration on grain size of alluvial sands and relationships between fines and liquefaction resistance in Tokyo Lowland. *Journal of Japanese Geotechnical Society*, 42 (4): 101-110. (in Japanese)
- The Japan Road Association. (1996). *Specification for Highway Bridges*. (in Japanese).
- The Japanese Geotechnical Society. (1998). Remedial measures against soil liquefaction. *Balkema*, 433.
- Wakamatsu K. (1991). *Liquefaction map during past earthquakes in Japan*. Tokai University Press, 1991. (in Japanese)
- Yasuda S., Yoshida N., Adachi K., Kiku H. and Gose S. (1999). A simplified analysis of liquefaction-induced residual deformation. *Proceedings of the 2nd International Conference on Earthquake Geotechnical Engineering*, 555-560.
- Yasuda S., Ideno T., Sakurai Y., Yoshida N. and Kiku H. (2003). Analyses for liquefaction-induced settlement of river levees by ALID. *Proc. of the 12th Asian Regional Conference on Soil Mechanics and Geotechnical Engineering*, 347-350.
- Yasuda S., Inagaki M., Yamada S. and Ishikawa K. (2004). Stress-strain curves of liquefied sands and softened clays. *Proceedings of the International Symposium on Engineering Practice and Performance of Soft Deposits*, 337-342.

Yasuda S., Shimizu Y., Koganemaru K., Isoyama R. and Ishida E. (2004). Estimation of the zones susceptible to liquefaction-induced flow in Tokyo. *Proc. of the 3rd International Conference on Earthquake Geotechnical Engineering and 11th International Conference on Soil Dynamics & Earthquake Engineering*, 2: 545-552.

Yasuda S.(2005). Survey of recent remediation techniques in Japan, and future applications. *Journal of Earthquake Engineering*, 9: 151-186.

MITIGATION OF SEISMIC DAMAGE OF RIVER DIKES

Yasushi Sasaki

Professor Emeritus, Hiroshima University

Executive Advisor, Japan Institute of Construction Engineering

3-12-1 Toranomon, Tokyo 105-0001, Japan

Recent concentration of population and properties to flat low land area is being increased. River dike, though it has a long linear shape, should be evaluated of its seismic performance from a view point of its function, namely flood preventing performance for widely spread hinterland space. It is inevitable to predict the seismically induced deformation of dikes and their locations as much exactly as possible for evaluating seismic performance of dikes. It is considered necessary that not only the residual height of damaged dike, but the deformation mode including crack generation should be properly evaluated against seepage failure. In this paper, it is attempted to study the way for the geotechnical engineering to go in satisfying this requirement from three points; firstly what we should learn from past experiences of seismic damage of river dikes, secondly how to approach from geotechnical engineering to the goal of social requirement, lastly, necessity of new approach in soil mechanics to understand the seismically induced large deformation of soil structure.

INTRODUCTION

A section of the Shinano River dike was caused damage, composed of crest settlement accompanied by longitudinal fissures, during the 2007.06.16 Niigata-ken Chuetsu-oki Earthquake. Crest settlement was tentatively reported to be about 40 cm. This section was located around 0 km on left bank of the river where had occurred failure during the 1964 Niigata Earthquake. Although precise amount of the crest settlement at that occasion is not known, however it was recorded that the residual altitude became lower than the HWL by about 2 m. The repaired method for this section after the Niigata earthquake was such that re-compaction after taking out of embankment material from cracked part of the dike.

A kind of confusion was felt by the field engineers at the construction office in evaluating the residual performance of this section because there is no good guideline in judging whether the liquefiable soil layer should be treated or not for the section where settlement was limited to such amount but having had repetitive occurrence of seismic failure and one more important aspect. That is, this particular section had been designated as a section requiring careful watch against seepage phenomena from landside slope when the water level in the channel becomes high during flood.

It has already passed 43 years since the 1964 Niigata Earthquake, and there were 14 earthquakes which caused failure of river dikes among the damaging earthquakes in Japan in this period.

Efforts have been made in raising the resistance of river dikes against earthquake by utilizing the progress in earthquake geotechnical engineering in this period. However the evolution of river dike engineering is still behind the change of society due to restriction of usable resources such as investment and reliable technology. If it limits dikes in flat and lowland area, there are about 350 km long of dike sections which need improvement of their seismic performance among the dikes controlled by the central government.

The 1964 Niigata Earthquake and 1983 Nihon-kai Chubu Earthquake caused inundation at river mouth area due to tsunami effect, however luckily, no other earthquakes in these 43 years caused inundation and their inducing secondary disaster. The recent urbanization and increasing usage of underground spaces are reasons to make the inundation risk higher in densely populated urbanized district in flat lowland area, and the role of river dike becomes more important as a consequence. This tendency is thought the same globally not only in Japan. Evolution in technology to keep the river dikes in good condition becomes inevitable, irrespective the situation is noticed by the society or not. Hence after reviewing the past experiences of seismic damage to river dikes in Japan, it was attempted to find the desired direction of efforts to increase the reliability of the predicted seismic effect. This would be an inevitable contribution in mitigating seismic damage of river dike from geotechnical engineering.

WHAT SHOULD WE LEARN FROM PAST EXPERIENCE OF SEISMIC DAMAGE TO RIVER DIKES

Records of damaging earthquakes in Japan which caused failure to river dikes

River dike is a soil-structure having a long history. And as Japan is earthquake prone country, river dikes in Japan have suffered seismic damage repeatedly. However quantitative records of seismic damage to river dikes in ancient days were not left. It was since the establishment of the Investigation Committee for Earthquake Damage Prevention after the extremely disastrous event of the 1891 Nohbi Earthquake ($M=8.0$) that the results of scientific investigation on earthquake induced damage became to be left.

Table 1 shows the list of earthquakes which caused seismic damage to river dikes in Japan since the 1964 Niigata Earthquake. Geotechnical aspects of the damage will be summarized later, however, it was learned from these events that main cause of past failure of river dike was due to soil liquefaction, and ground improvement prevented damage successfully. Diagnosis on seismic performance of existing river dikes is being conducted according the recently enacted Design Guideline for River Facilities against L2 Earthquake. It is considered that potential risk of seismically induced failure of river dikes has been reduced to some extent, though quantitative records is not yet compiled.

Table 1. Earthquakes which caused damage to river dikes since 1964 Niigata EQ

Date	Earthquake	M	Affected River	Remarks
1964.6.16	Niigata EQ	7.5	Agano R., Shinano R., Mogami R.	Epoch for Liquefaction Evaluation
1968.5.16	1968 Tokachi-oki EQ	7.9	Tokachi R. Mabechi R. Kitakami R.	Preceding Rainfall
1978.1.14	1978 Izu-Ohshima Kinkai EQ	7.0	Kano T. (Mochikoshi Mine)	Revision of design manual of tailing dam
1978.6.12	1978 Miyagi-ken Oki EQ	7.4	Kitakami R. Yoshida R. Natori R.	Damage to Lifeline facilities in urbanized area
1983.5.26	1983 Nihonkai Chubu EQ	7.7	Iwaki R. Yoneshiro R. Hachiro-gata	Tsunami Drainage from dike
1993.1.15	1993 Kushiro-oki EQ	7.8	Kushiro R. 28 pls, 10.1km Tokachi R. 20 pls, 9.2 km	Damage on Peat ground Liquefaction inside dike Periodically damaged SCP
1993.7.12	1993 Hokkaido Nansei-oki EQ	7.8	Shiribeshi-Toshibetsu R. 18 pls 6.6 km	Slip plane inside dike showing Stretch Type deformation
1994.10.4	1994 Hokkaido Toho-oki EQ	8.2	Kushiro R. Abashiri R. Tokoro R.	Efficiency of ground improvement for Kushiro R.
1995.1.17	1995 Hyogo-ken Nanbu EQ	7.3	Yodo R. 18 pls 5.7 km, Ina R. 1.4 km, Kako R. 1.2 km	L2 EQ motion Major river bed reduced deformation DMM
2000.10.6	2000 Tottori-ken Seibu EQ	7.3	Hi-I R. (Naka-umi lake shore dike) 32 pls 20.7 km	Liquefaction of silty deposit Geo-grid prevented deformation SCP
2003.7.26	Miyagi-ken Hokubu EQ	6.4	Naruse R.	Preceding rainfall SMM
2003.9.26	2003 Tokachi-oki EQ	8.0	Tokachi R. 26 pls 16km	Joint opening of sluice Tsunami SCP, Geogrid
2004.10.23	2004 Niigata-ken Chuetsu EQ	6.8	Shinano R. 17 pls 19km	Ground improvement by SCP, SMM
2007.7.16	2007 Niigata-ken Chuetsu-oki EQ	6.8	Shinano R. Sabaishi R.	Same location where was damaged by 1964 Niigata EQ

Rapid urbanization

Recent urbanization, change of land use (especially usage of underground space), utilization of Information Technology in various fields, mutual dependencies of facilities and systems, globalization of economic activities, are causing increase of fragility in urban area against disaster.

Figure 1 shows the so-called zero-meter area in Tokyo along its waterfront. Table 2 shows the population inhabited in zero-meter areas in Japan and their area. Although the total number of population in zero-meter areas is limited to about 5 % of total population in Japan, industrial activities are also performed numerously there. Therefore it is concerned that, if the residual altitude of damaged dikes due to earthquake becomes lower than external water level then it may cause extensive damage to human lives, properties, and industrial activities in this area.

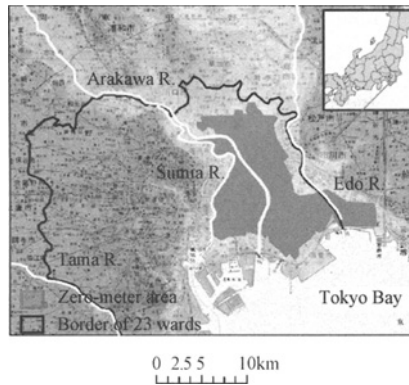


Figure 1. Zero-meter are in Tokyo

Table 2. Population and area in zero meter area in Japan

	Population	Area	Remarks (house & household property)
Tokyo Bay Area	1760 000	116 km ²	12 308 billion Yen
Ise Bay Area	900 000	336 km ²	6 601 billion Yen
Osaka Bay Area	1,380 000	124 km ²	10 204 billion Yen
Other lowland area	1350 000	1,072 km ²	10 261 billion Yen
Total	5390 000	1,648 km ²	68 485 billion Yen

On the other hand in rural area, structure of fragility against disaster is changing due to its depopulation and advancement of inhabitant's age.

In modern society, calamity in one district tends to propagate towards external society outside the affected district, and which continues long with exceeding times. It is undoubted that proper-to-each-district measures could mitigate calamity in both urban and rural areas. Proper-to-each-district measures are not yet clarified, however remediation of facilities in the district is the basic measure. Definition of seismic performance of facilities and their evaluating criteria might be different for each district and for each stage of time. Mitigating measures should be evolved in accord with the change of society.

Provision of such as fast aid, lifesavings, warning and evacuation, and rapid recovery is also required as preparedness against emergency. Concentration to urban area and depopulation in rural area cause new problem as for preparedness. Since the perfection in preparedness by public only is difficult and has a certain limit, progress of preparedness by private efforts or mutual aid are becoming more important than in the past. Volunteer's activities and philanthropy by private sector have become to play important roles in these days.

There exist so many structures controlled by public and ones owned by privately, so even part of them are unsatisfactory against possible earthquake, it is almost impossible to remediate them all in a short period.

Recognizing the difficulty in perfection of preparation by strengthening of structures and facilities in short period, local governments are making strategic plan to reduce calamity against earthquake. The strategic plan is such that: firstly predict possible amount of

calamity during a certain earthquake, next assign the reducing amount of this calamity as a targeted goal, and then make strategic action plan to reach this goal. As before mentioned, society evolves, and disaster evolves too in accord with that evolution, so this strategic action plan must be modified occasionally to fit the change of situation. It should be rated high that this strategic plan has an attitude of utilizing full ability of society synthetically.

Social requirement

It is not so easy to prioritize which facilities should be the first in remediation against future earthquake among other kind of infrastructure. This is because there is hardly a proper indicator to express the importance weight to cause fragility of an area, which should be included in technology of city planning to ease decision making for reducing damage potential. However, to drive remediation of infrastructure, it is inevitable to gain the social approval for its remediation through the interpretation on the current situation of fragility against disaster and the key structures to mitigate damage in the district. For this purpose it is unavoidable to show the unconformity between objective, namely targeted goal of mitigating damage, and the current situation of preparation to prevent damage as its means.

In other words for river dikes, it would be important to inform to society about its fragility against future earthquakes (seismic performance, as measures to reach goal) as much exactly as possible. And this should be presented by easy-to-understand manner so that communities hold same information jointly. It is heavy and large requirement from society.

ROLE OF GEOTECHNICAL ENGINEERING TO RESPOND TO SOCIAL REQUIREMENT

How can geotechnical engineering reply to the above mentioned social requirement? How it has replied in the past? Past activities to mitigate seismic damage to river dikes can be classified into three categories. Those are:

- 1) Damage investigation and emergency treatment;
- 2) Diagnosis of seismic performance, and proper maintenance;
- 3) Remediation (before earthquake, improvement during repair works).

Investigation on damage had been conducted primarily for diagnosing the residual performance of damaged sections, for prioritizing the sections for which emergency treatment should be taken to prevent secondary disaster and for selecting the proper restoration works if necessary. The investigated results gave also precious bases for clarifying the cause and mechanism of the damage which could be utilized to revise technologies in mitigating seismic damage.

Problems concerning damage investigation are the lack of experts and tools. As the ordinary engineers at field hardly happen to face earthquakes, and they do not know what kind of quantities should be looked into and what technique is proper to measure the residual performances.

Anyhow, it is true that observed facts gained from damaged sites have contributed in realizing the failure mechanism and also in rationalizing the design of mitigation. Lessons

gained from repeated study on these observed facts may lead us to a better solution. Hence it is attempted to learn again from past experiences in Japan and try to pick up several points to be reconsidered.

Observed facts during past earthquakes

Already the observed facts from the cases listed in Table 1 have been reported elsewhere (Sasaki), those facts can be pigeonholed as follows.

- (a) Main cause of large deformation of river dikes during earthquake is soil liquefaction. — This means the importance of improvement of liquefiable soil layer to mitigate seismic damage to river dikes.
- (b) Sections where failure was caused were located often on the young sediment of foundation ground such as reclaimed portion of old river bed. — This lesson could be utilized in specifying the risky portion out of long length of river dikes through deciphering geomorphologic distribution map. It was known that the thickness of reclaimed layer in the old river course was roughly equal to the current depth of main channel.
- (c) Sometimes bottom part of embankment was caused liquefaction. — This fact was known in case of 1993 Kushiro-oki earthquake. It was found that entrapped rainwater in embankment generate groundwater table inside dike when foundation ground was composed of very compressible soft layer. It was also found that when drainage function was assured to dike by installing drain system like gabion at its toe, failure was unexpectedly avoided as a consequence of preventing the generation of saturated zone inside dike. This means that countermeasure for other purpose works sometimes effectively in preventing seismic damage too to river dikes.
- (d) Seismically induced failure was such that settlement of dike top with longitudinal fissures in its deformation mode. — Figure 2 shows the deformed dike of the Yoshida River caused by the 1978 Miyagi-ken Oki Earthquake. Several longitudinal cracks were seen on its top and side slope.
- (e) Depression of top crest was sometimes caused by Stretch type deformation (Terzaghi et al. 1996) when liquefaction was caused in shallow layer in the foundation ground beneath dikes. — It is natural that liquefaction at shallow deposit beneath dike causes loss of shear resistance at bottom boundary. As a result of this change of stress state at its boundary caused redistribution of stress in dike body. And this stress redistribution caused stretch of dike width at its bottom and depression of crest as shown in Figure 3.



Figure 2. Example of large deformation

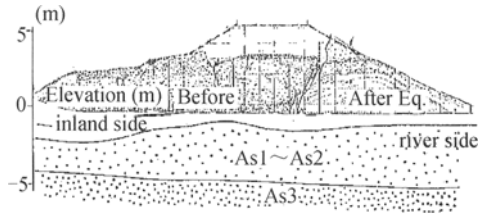


Figure 3. Kabutono Dike damaged during 1994 Hokkaido Nansei-oki Eq.

(Two orthogonal slip planes running from shoulders to bottom were clearly observed)

Therefore it should be noted that sluice pipe might be elongated in its length if it was constructed in a dike on ground where liquefiable soil deposited at shallow depth. Such threat went to real at the Tokachi River as mentioned later.

It was also experienced that trial usage of geo-grid at bottom of newly constructed dike on liquefiable ground prevented deformation of dike during 2000 Tottori-ken Seibu Earthquake. Geo-grid had been intentionally installed to prevent the stretch type deformation in case of liquefaction.

(f) Amount of crest settlement was strongly related to the depth and thickness of liquefied layer, and never exceeded 75% of original height. — Figure 4 shows the crest settlements detected since 1821 Nohbi Earthquake, and Figure 5 shows an example of the effect of non-liquefiable layer at surface on liquefiable layer to crest settlements.

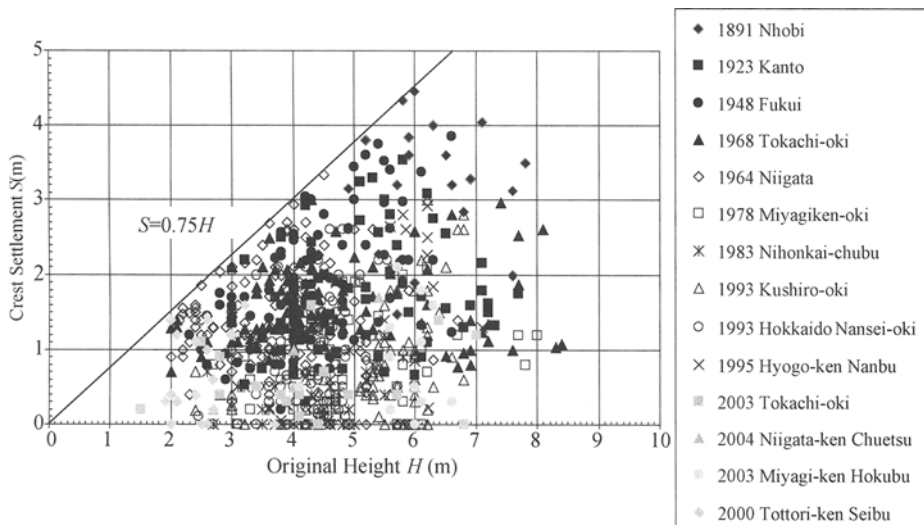


Figure 4. Crest settlement of river dikes since 1891

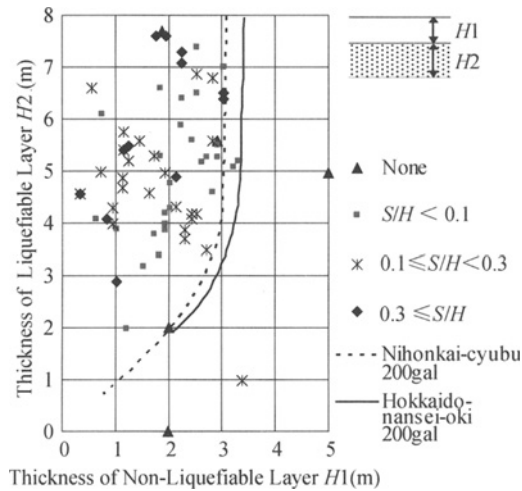


Figure 5. Depth and thickness of liquefiable layer

(g) Major river bed might reduce the crest settlement in case of the Yodo River dike in 1995 Hyogo-ken Nanbu Earthquake case. — This might be caused by the effect of initial stress state to the liquefaction inducing deformation of ground, however it is not yet clarified.

(h) Upward heaving of surrounding ground near failed slope of dike was rarely confirmed, whereas traces of sand boiling were almost always accompanied. — This implies that the liquefaction induced large deformation of ground is different from ones due to insufficiency of bearing capacity of soft and weak foundation ground.

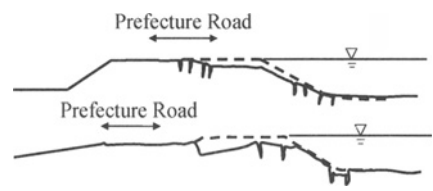


Figure 6. Damage to Machikarui dike during 1964 Niigata earthquake

(i) Occasionally revetment works of dike was caused damage by Tsunami invasion to river channel. — This kind of fact was seen in the case of 1983 Nihon-kai Chubu Earthquake. And a video record of the tsunami marching towards upstream was taken at the Tokachi River during 2003 Tokachi-oki Earthquake.

(j) Deformation amount of dike might be increased by wetting due to preceding rainfall. — In cases of the 2003 Miyagi-ken Earthquake and the 2004 Niigata-ken Chuetsu Earthquake, earthquakes hit river dikes after fairly heavy rainfall. The preceding rainfall increased the moisture of dikes. It was doubted that moist soil was a cause of increasing deformation during failure. It should be studied more about this effect on the seismic deformation of dike (Nakayama).

(k) Repetition of failure was caused at particular section where was inadequately repaired without improving liquefiable layer after the preceding earthquake. — As mentioned at the beginning of this paper, it was noticed recently that a particular section may happen to suffer damage repeatedly from the case in 2007 Niigata-ken Chuetsu-oki

Earthquake. In such a section repaired without remediation against liquefaction met shaking of another earthquake, the same section was caused failure again. This means the importance of evaluating residual performance. It is known that the dike section illustrated in Figure 6 was repaired with no ground improvement, and later it was noticed that seepage from landside toe was caused during flood. As it was concerned its stability during flood, this section was designated as a special section requiring careful watch against seepage during flood. Similar repeated failure was experienced at certain sections of the Kushiro River dike repaired without any treatment of liquefiable layer but only re-compaction was conducted during the 1994 Toho-oki Earthquake which occurred a year later after the 1993 Kushiro-oki Earthquake, whereas the treated sections with SCP method for liquefiable soil survived without any deformation against the same order of shaking felt during the Kushiro-oki Earthquake.

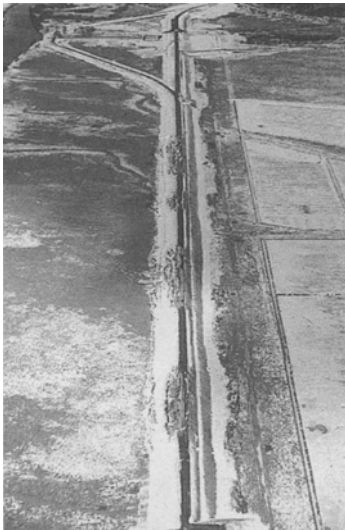


Figure 7. Aerial photo of periodical location of damaged sections on the Kushiro river dike

- (l) Periodical locations of damaged sections were found during 1993 Kushiro-oki Earthquake — From aerial photo shown in Figure 7, it is noticed that heavily damaged sections of dike appeared periodically on the Kushiro River dike. As the conditions of excitation, size and materials of dike, and the soil stratum in their foundation ground were the same, an interpretation of these peculiar locations of damage was led to be caused by the effect of three dimensional response of dike (Kano et al. 2007). It should be noted that birds-eye view is useful to grasp this kind of situation totally.
- (m) It is still unknown when dike happens to fail — Records on dike damage tell the residual shape of deformation observed after earthquakes. However there is no record left at fields about the deformation process during shaking. Though some aspect or evidences implying the deformation process of liquefied soil, the question when dike was caused its failure is still in the mist.

Repair works of damaged section of river dikes

In order to draw lessons from repair works in practice, it is attempted to summarize the past trend of repair works as below.

- (a) To recover the shape as it was before earthquake was a basic principle — Until 1993, restoring work of damaged river dike was conducted following to the basic principle for a long time. There are several reasons for this principle. Firstly, for a

long time nobody knew the real cause of failure, and effective remedial restoration method led from the deformation process was not also known. And secondarily most of hinterlands of damaged sections in the past were farm land not densely populated urban area. Further, repair works of damaged dike had been completed in short period, say about two weeks in the past experiences, and it had been thought that the dike function could be regained by recovering its shape. This point needs to be reexamined.

- (b) Failure prevention without ground improvement was contrived during repair works of damaged Hachiro-gata lake dike after the 1983 Nihonkai-chubu Earthquake — Total length of damaged sections at Hachiro-gata lake dike during the 1983 Nihonkai-Chubu Earthquake reached to about 69.1 km. This dike had been constructed to protect the reclaimed land originally in the Lake Hachiro-gata using dredged sand. Therefore the altitude of hinterland was about 4 m below MSWL.

In order to take away the threat of failure of dike by seepage force, sheet cut wall was installed at waterside toe and placed drainage pipe buried in landside slope. By this method, the groundwater level had been kept to drop by about 2 m.

Since the stretch type deformation was not known at that time, this method was not intended to prevent this type of failure. However, it is expected to reduce the amount of stretch type deformation during earthquake too. It should be noticed that there are several measures applicable to seismic remediation among techniques which are originally employed to reduce unfavorable effect of other cause except earthquake.

- (c) Classification of damaged mode is used for determining repair extent of damaged dike. — According to the deformation degree such as the crest settlement or depth and extent of generated cracks, extent of re-compaction part of dike is being decided. For this purpose, affected sections were classified into subsections in accord to their damage degree. Figure 8 shows an example of such a classification conducted for the repair works of damaged sections of the Shinano River during 2004 Niigata-ken Chuetsu Earthquake (Oshiki & Sasaki, 2006). Three sections classified “F” were repaired with remediation of liquefied layer, however 12 sections classified in the other types were recovered their original shape by partial re-compaction.

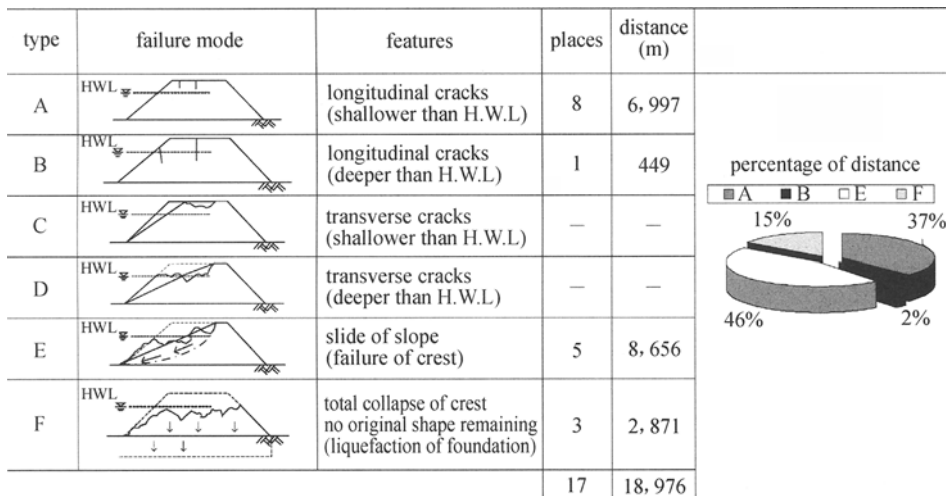


Figure 8. Classification of damaged dikes during the 2004 Niigata-ken Chuetsu Earthquake

As for the measurement of the crest settlement of irregularly deformed dike shown in Figure 9, the difference of the altitudes between original crest and one in the deformed dike which is equivalent to the same width of original crest as shown in this Figure.

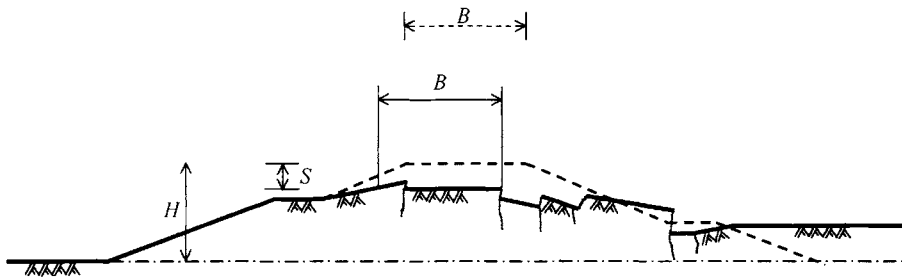


Figure 9. Amount of crest settlement

And to measure the depth of cracks, confirming pit had been often dug to detect the deepest point of reached lime milk poured from its opening at surface.

Problems in practice is that precise cross sectional shape before earthquake is hardly known exactly, it is expected to develop practical contrivance to leave better records on its shape as well as the other data such as ground condition, damage history, and maintenance history.

- (d) Ground improvement was accepted as a part of repair works from the case of 1993 Kushiro-oki Earthquake — In 1993, the river dike sections were seriously damaged at the Tokachi River and the Kushiro River in Hokkaido due to the strong shaking of the Kushiro-oki earthquake. As mentioned before this damage was caused by the liquefaction of bottom part of dike due to the subsidence of foundation ground of peat layer, it was needed to repair dike from its bottom part including subsided part into foundation ground, where the groundwater level was very high in this case. And the affected area is facing to seismically active subduction zone of the Pacific Ocean Plate, it was realized the necessity of preventing liquefaction.

Considering these site characteristics, there was no choice other than to improve the liquefiable soil layer. Therefore the Ministry of Finance at that time accepted including the cost for additional strengthening against future earthquakes in the restoration budget for these damaged dike sections for the first case in the history of restoration works in Japan. For damaged sections by Kushiro-oki Earthquake, SCP treatment was conducted at seriously damaged sections with special care, which is the sand-mat for executing the SCP was to be replaced to low permeability materials after its execution in order to prevent seepage flow through this sand-mat layer during flood.

After this event of the 1993 Kushiro-oki Earthquake, it became common to take measures for strengthening against soil liquefaction at seriously damaged sections of river dike by proper method for each site condition; solidification technique was used for the rehabilitation of seriously damaged Yodo River dike due to the Hyogo-ken Nanbu Earthquake (Figure 11); shallow mixing method (SMM) for the damaged section of the Naruse River caused by the 2003 Earthquake and similarly at the occasion during succeeding earthquakes thereafter.

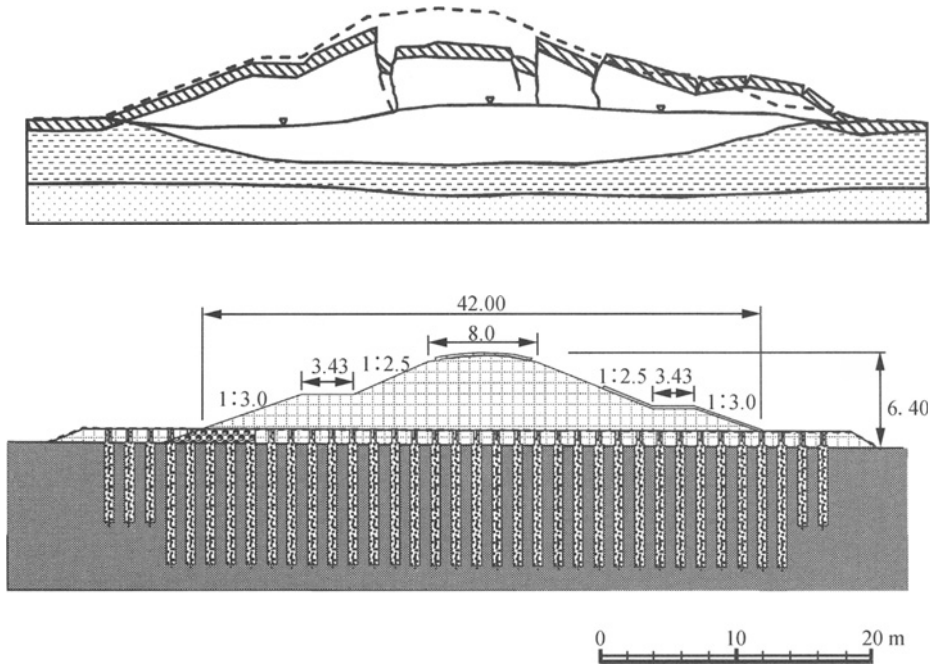


Figure 10. Deformed shape and rehabilitation on the Kushiro River dike

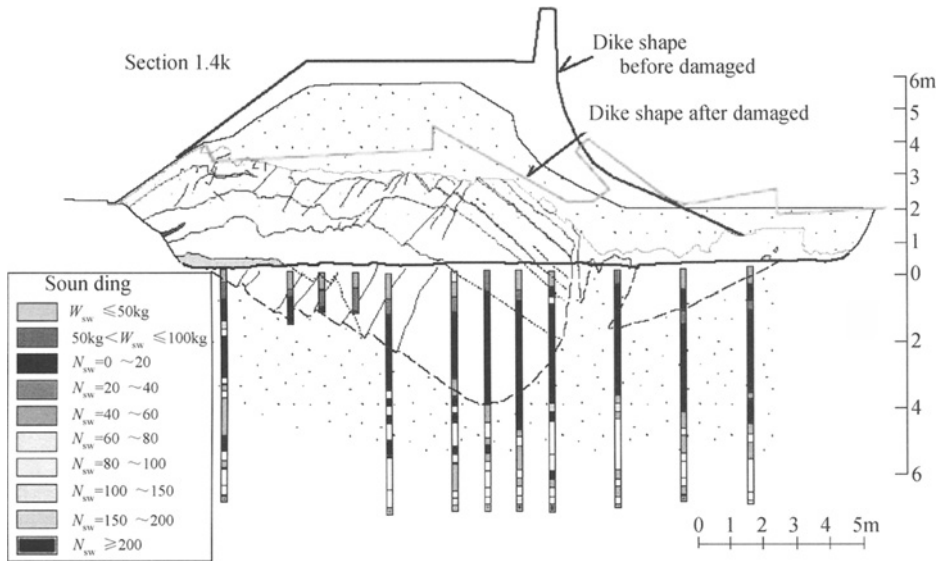


Figure 11. Damaged Torishima Dike section of the Yodo River

(e) A sluice had to be reconstructed after the 2003 Tokachi-oki Earthquake because it was found that the concrete sluice was elongated by stretching at its joints after the earthquake. — At this location of the sluice, no apparent deformation of dike was detected by eye-inspection during damage investigation after the earthquake.

However, it was found the stretch at its joints by inspection from inside of the sluice box conducted afterwards. Investigation on this sluice revealed that this elongation was caused by soil liquefaction beneath the dike (Kawai et al., 2006). It should be noticed that even at location where visible deformation is not detected, stretch type of dike deformation (not apparent visible failure) could be induced and gave unfavorable effect to buried structure when ground condition is liquefiable.

It is known from the repair practice so far in the past that only the crest settlement was focused to evaluate seismic performance. Attention was not paid for the stretched amount of base width where sluice is placed occasionally. Stretching of dike bottom width may cause elongation to the embedded sluice structure which leads to its serious damage as seen in the case of the Tokachi River sluice.

Prediction of seismically induced deformation of dike

Utilizing the accumulated knowledge on soil liquefaction and the experience of river dike failure, designating effort to pick up potentially weak section among the whole length of the dike has been made. For this purpose, division of dike into sections is ordinarily made at first considering ground condition, dike size, damage history, and construct representative model of cross section for each section. Then the seismic performance of dike at each representative section is evaluated by comparing the predicted residual crest height to external water level in the river channel. Again the stretch of bottom width had not been accounted in this evaluation.

The history of developing the predicting method of seismically induced crest settlement was briefly reviewed below, from view points such as when failure was regarded to be induced, how simplify the deformation process (deforming model), and what technique was utilized in calculation. The predicting methods used so far could be classified into three types; conventional method, pseudo-static analysis method, and dynamic analysis method.

- (a) In the conventional method, deformation is regarded to be driven by the instability of dike due to the reduction of shear strength of liquefied layer beneath dike. The full liquefaction is regarded to be brought at the end of seismic shaking, so the instability is evaluated by the reduction of soil strength due to raised pore water pressure without the application of inertia force due to shaking in conventional stability analysis. The stability analysis can only gives the equilibrium condition, however it is known that the amount of sliding is dependent to calculated safety factor, the empirical relation between the safety factor and the crest settlement is used to predict the crest settlement. — This method contributed in practical diagnosis of existing long spanned dike in Japan after the 1995 Hyogo-ken Nanbu Earthquake. As this method regards the deformation of dike is induced along the distinct slip surface, so it can not simulate the whole deformation of liquefied layer or dike deformation. There is an alternative method based on limit equilibrium concept such as the Newmark method which can calculate deformation with considering dynamic effect of inertia force. However it has same kind of limit in obtaining the deformation of dike.
- (b) In the pseudo-static analysis method here, deformation of the liquefied layer is regarded to be caused after the shaking is terminated too. The deformation process in

this method is simplified in such a manner; as the mechanical property of liquefiable layer is changed to that after liquefaction, soil in this layer is regarded to deform by the degradation of its property under the loading condition of dike weight. And simplified methods based on this concept are proposed, by regarding the liquefied layer as liquid (Towhata), or a material having softened stiffness (Yasuda). Crest settlement is obtained from vertical components of thus calculated deformation of the foundation ground and the settlement of ground due to its consolidation (dissipation of raised pore water pressure) — As this method can predict the whole deformation of liquefied layer and it was verified that both of the method proposed by Towhata and one by Yasuda can reproduce the actually caused crest settlement during the 1993 Hokkaido Nansei-oki Earthquake and the 1995 Hyogo-ken Nanbu Earthquake from a verification project (JICE). Newly enacted seismic design guideline for river facilities against L2 earthquake (MLIT) adopted the usage of these methods for evaluating seismic performance of river dikes.

- (c) In the dynamic analysis method here, time history of crest settlement of dike is given directly from the results of numerical integration of governing equation under the given initial and boundary condition. And various computer programs are proposed which employ different constitutive equations to describe nonlinear stress-strain relation of soils and pore water pressure generation. Basically in the effective analysis method, the calculated result includes deformation in liquefied layer and deformation in embankment at the same time. This method is to regard that the deformation is induced during excitation. Calculated crest settlement by this type of method ceases when earthquake shaking is terminated. — Above mentioned L2 guideline adopted the usage of computer programs named LIQCA and FLIP too, since these were verified their applicability from the above mentioned verification project. As usually for numerical integration FEM is used by modeling the dike and foundation ground as continuum, crack generation can not be reproduced. It should be noted that delayed settlement such as seepage induced strain (Sento et al. 2006) and crack generation are not obtained from ordinary program because those phenomena are not plugged in the ordinary program.
- (d) In order to evaluate remedial treatment, simplified method has been proposed for predicting crest settlement under the condition where ground improvement works are conducted under both side toe (PWRI 2003). In this method, liquefied layer is regarded as soft material layer. And the crest settlement in this method is regarded to be composed of three components shown in Figure 12.

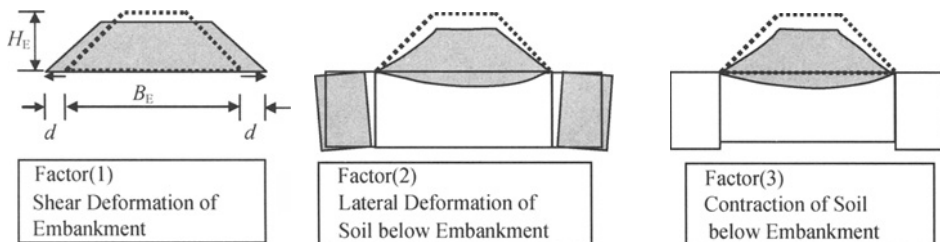


Figure 12. Three components of settlement

Necessary issues to be reexamined

Finally in this chapter, it is attempted to summarize the necessary points to be modified or advanced concerning the mitigation of dike damage during earthquake as follows.

- (a) Seismic performance of river dike — It is expected to develop a new index of seismic damage of river dike which can totally express the priority in reducing the threat to the hinterland area including effect on social and economic activities.

Seismic performance of dike is evaluated from its stability or possible deformation using representative cross section in two dimensional vertical spaces. However, as seen in the case of 1993 Kushiro-oki Earthquake, three dimensional response of river dike was doubted to cause periodical locations of failure. In this context, it is expected to reconsider about inclusion of three dimensional responses in examining conditions for the evaluation of continuing dike sections.

- (b) Effect of longitudinal cracks and stretching type of deformation to flood protection ability — Seismic performance of river dike is evaluated by its residual height only at present. However, unsatisfactory repair work of deformed dike may cause seepage flow of dike during flood as mentioned in the case of 2007 Niigata-ken Chuetsu Earthquake. In this context, the evaluation criteria should be reexamined. It is expected to develop better criteria which can evaluate the dike stability against the design force including effect of seepage flow.
- (c) Effect of stretching type of deformation of dike to buried structure such as sluice — It was experienced that stretch type of deformation of dike caused damage to buried sluice structure. Though this experience is already reflected in the L2 guideline, better method to design sluice is expected to be developed considering this effect.
- (d) Effect of infiltrated rainwater to the amount of deformation — It was experienced to have had attacks of earthquake shaking during or soon after raining, and was pointed out that the moist dike might cause larger deformation during earthquake. However the effect of moist state of dike to its deformation during seismic effect is not known. It is expected to clarify the effect of moisturized dike by rainfall.
- (e) Synthetic remedial technology — Available investment is restricted. Available spaces to raise seismic performance of river dike are limited because of highly usage of hinterland especially in zero-meter area. In that restriction of construction site, it is expected to develop effective and reasonable cost methods to reduce seismically induced deformation of dikes with considering priority index mentioned above. Further as seen in the case of gabion, it was found that remedial measure for other purpose than earthquake worked effectively to reduce seismic damage unexpectedly. In this context, it is expected to utilize all available methods for remediation synthetically. It is also expected to be flexible to be easily stepped up its performance.

NEW APPROACH IN GEOTECHNICAL ENGINEERING

In order to achieve desirable level of damage mitigating technology for river dikes considering above mentioned issues of reexamination, it is thought vital to take new approach in geotechnical engineering. One is collaboration with other field of engineering, and the other is the new approach to study soil behavior under unloading process, interaction of deformations between dike and liquefied foundation ground, and also to accumulate the knowledge on unsaturated soil behavior.

Collaboration with other field of engineering

As for the advancement of evaluation criteria of seismic performance of river dike, it is thought necessary to widen the view from a line to area. At present, the performance of a cross section of dike is examined along its length by comparing its residual height with external water height during flood. In order to develop a new index which can express the priority in preventing the damage in the hinterland area behind dike utilizing the results of this evaluation, inundation analysis and risk assessment are needed. In this context, it is inevitable to make collaboration with other field of engineering.

Soil behavior under unloading process

Figure 13 shows a demonstration of the generation of stretch type deformation of embankment.

An embankment of sand was made in a container on separable four base plates, which were pushed towards the bottom center at initial stage. By decreasing this pushing force applied to base plates, reduction of boundary shear stress at embankment bottom was reproduced. The change of boundary stress condition yielded the stretch type deformation of embankment with generating the apparent two slip surfaces running from shoulders to center of embankment bottom. This is one example of soil behavior under unloading condition. Unloading in this case is the reduction of shear stress at bottom boundary.

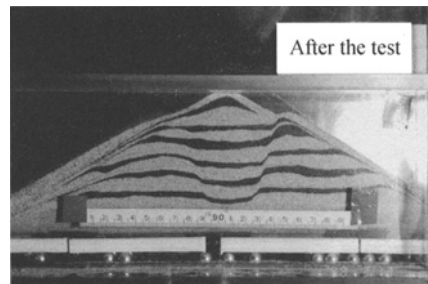


Figure 13. Stretch type deformation

Figure 14 shows an example of triaxial compression test results. A specimen of loose sand was subjected to ordinary loading process. Two more specimens were firstly applied axial stress to certain amounts in undrained condition, then confining stresses were reduced by increasing the pore water pressure of the specimens. When the stress condition reaches to the failure line, deformation of specimens abruptly increased as shown the strain path in this Figure. It should be noted that water was injected into specimen during the increasing stage of pore water pressure, this means that the deformation was not induced under completely undrained condition. Similar abrupt increase of strain was seen in the case of dense sand. This is another example of soil behavior under unloading process.

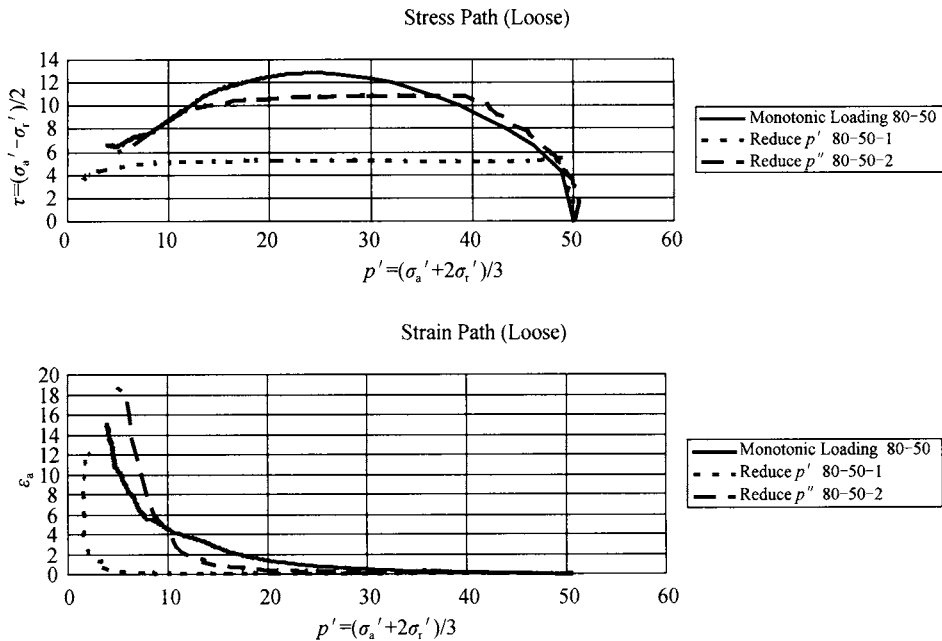


Figure 14. Deformation by reducing the confining pressure

Soil behavior has been studied mostly for conditions of increasing stress or increasing strain. Less data are accumulated for the soil behavior in unloading condition.

It should be noticed that most of deformation associated to soil liquefaction is brought by decreased effective stress regardless it is induced during excitation or after the excitation. Sento et al. (2006) pointed out that the re-distribution of raised pore water pressure causes seepage flow in soil stratum, and that inflow causes large strain in the gently sloped ground. Their result for interpreting the delayed flow deformation of ground implies that same kind of large deformation might be caused in the foundation ground of dike beneath its slope if necessary condition is satisfied. However this kind of deformation in liquefied ground is not yet taken into account in ordinary numerical analysis algorithm for predicting dike settlement. It is desired to make progress of study on this phenomenon.

Interaction between deformations of dike and liquefied layer

Stretch type deformation shown in Figure 13 and inflow inducing deformation mentioned above imply the necessity of elucidation about the interaction between deformations of dike and foundation ground.

Decrease of shear stress at dike bottom causes the change of dike shape, and dike shape change causes shear stress change in the ground. As inflow inducing strain varies with difference of initial shear stress, therefore it is inevitable to study on this interaction more in deep so that more accurately predicted deformation of dike is obtained.

It should be noted that the reason of desiring accurate deformation is to assign accurate enough initial condition for seepage analysis to examine the flood protection ability of

damaged dike. And accurate prediction of dike deformation is indispensable for checking its unfavorable influence on buried sluice.

Unsaturated soil behavior

Recently, damaging earthquakes were experienced soon after considerably intense rainfall. And it is being doubted that the moist dike was caused larger deformation. However, knowledge on mechanical properties of unsaturated soil is not accumulated enough.

Further, it is felt that necessary time to raise groundwater level inside dike for rainwater is sometimes shorter than calculated from saturated and unsaturated seepage analysis. Similar feeling is being experienced in the field of rain induced slope failure. Although it is no more than hypothesis, however the reason of unexpectedly rapid rise of groundwater level in unsaturated soil layer is being elucidated from monitoring results on rain induced change of moisture condition in the natural slope of weathered granite (Thi Ha et al., 2008).

It is well known that the rainwater infiltrates into unsaturated soil driven by potential gradient forming wetting zone. Potential in this stage is due to matric suction. The monitored results tell that once the wetting front reaches the impermeable bottom boundary, additional rainwater is pushed into the ground driven by piston flow. Potential in this stage seems to be changed from suction potential to gravity potential. Though it is needed further verification, the newer findings in other field will give better tool to get to the solution.

It is desired to accumulate the knowledge on unsaturated soil properties.

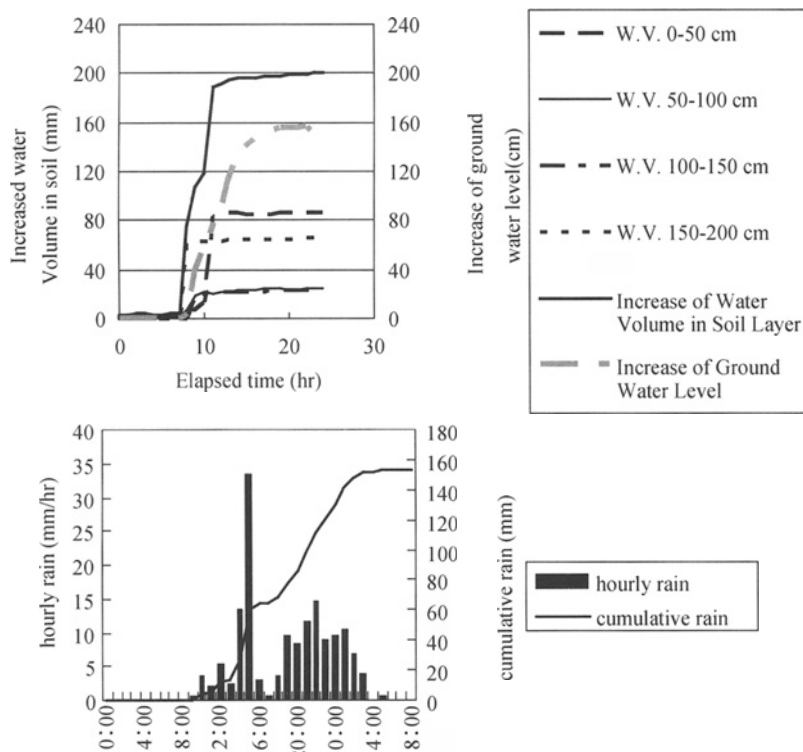


Figure 15. Rainwater infiltration and rise of groundwater level

CONCLUSION

In this paper, Japanese experiences of river dike damage in the past were reviewed to consider about the role of geotechnical engineering to mitigate seismic disaster. To solve the problems to which the society is currently facing, better indicator or method to evaluate of threat of the society is needed. And as for the approach to this goal, geotechnical engineering will have to contribute in providing better prediction of behavior during earthquake by raising its accuracy.

And it was pointed out that three issues are desired to proceed; strain increase in accordance with unloading, interaction of deformations between dike and liquefied foundation ground, deeper knowledge on unsaturated soil.

Collaboration in different field may make great advance for solving problems mentioned in this paper, such as collaboration by economics, sociology, and civil engineering for evaluation of seismic calamity in a community. And collaboration between earthquake engineering, geotechnical engineering, structural engineering and earthquake geotechnical engineering will lead to the more accurate prediction of seismic deformation of dike.

There are many unknown things in natural phenomena. Nevertheless it is a fate for engineering to mitigate disaster by utilizing measures available. That means the being used method of deformation prediction is no less than approximation of real step of phenomena reduced from simplification of complicated real manner or by limiting to a certain extent of boundary condition of problems. It is always required to examine the inconsistency between targeted goal and selected measures to realize it.

ACKNOWLEDGEMENTS

The author is grateful to Mr. Tomoyuki Abe and his colleagues of Oyo Corporation for their assistance in providing Figures 4 and 14.

REFERENCES

- Japan Institute of Construction Engineering. (2002). *Analytical methods to predict seismically induced dike deformation*. JICE Report No. 102001, (in Japanese).
- Kano S., Sasaki Y. and Hata Y. (2007). Local failures of embankments during earthquakes. *Soils and Foundation*, 47 (6): 1003-1015.
- Kawai M., Takebe T., Sato K., Minobe N., Kakubari S., Shiwa M. and Sasaki Y. (2006). Report on the sluice damage caused by the 2003 Tokachi-oki Earthquake. *Proc. Japan-Taiwan Workshop*.
- Nakayama O., Sasaki Y., Sekizawa M., Hiratsuka T. and Suzuki Y. (2007). Deformation of a river dike due to the Miyagi-ken Hokubu Earthquake. *Proc. 4th International Conference on Earthquake Geotechnical Engineering paper No.*
- Oshiki H., Sasaki Y. (2006). Damage of the shinano river dike due to the Niigata-ken Chuetsu Earthquake. *Proc. Japan-Taiwan Workshop*.
- PWRI. (2003). *Design manual of remediation for river dikes based on allowable settlement*. PWRI Report No3889.
- Sasaki Y., Kano S. and Matsuo O. (2004). Research and practices on remedial measures for river dikes against soil liquefaction. *Journal of Japan Association for Earthquake Engineering*, 4(3) (Special Issue).

- Sasaki Y., Moriwaki T. and Ohbayashi J. (1997). Deformation process of an embankment resting on a liquefiable soil layer. *Deformation and progressive failure in geomechanics, Proc. IS-Nagoya '97*, 553-558.
- Sento N., Kazama M., Uzuoka R., Ohmura H. and Ishimaru M. (2004). Possibility of postliquefaction flow failure due to seepage. *Journal of Geotechnical and Geoenvironmental Engineering, ASCE*, 130(7): 707-717.
- Terzaghi K., Peck R. B. and Mesri G. (1996). Soil mechanics in engineering practice. *John Wiley & Sons, Inc.*, 383.
- Thi Ha Sasaki Y., Kano S. (2007). Study on rainwater infiltration in subsoil of sandy slopes during rainfall by field monitoring. *Proc. 2nd ICGEDMR*.

SOME ASPECTS OF THE MITIGATIONS AND REHABILITATIONS OF NATURAL DISASTERS IN MALAYSIA

T.A. Ooi

*Director – TAO Consult Sdn Bhd, 17A, Jln Awan Hijau, Taman Overseas Union,
Batu 5, Off Jln Klang Lama, 58200 Kuala Lumpur, Malaysia*

Flooding, Landslides, Debris Flow and Tsunami are some of the disasters experienced in Malaysia. The flooding of Kuala Lumpur in the 1970s caused serious damages to lives and properties and called for the flood mitigation scheme in Kuala Lumpur. Over the years despite the repeated dredging and canalization of floodwater in Kuala Lumpur, there were repeated incidences of severe flooding of the city centre. As part of the overall solution to the frequent flooding problem, the diversion tunnel project known as SMART was constructed and has recently been completed in June 2007. The tunnel is dual-purpose designed to cater to flow of water and ease traffic congestion in the Kuala Lumpur city. In recent times, climate change has brought about severe flooding in many parts of Malaysia with increased frequencies. The Landslide that caused the collapse of Block 1 of the Highland Towers condominium in December 1993 claimed 48 lives. The landslide occurred during 10 days of incessant rainfall. In November 2002, another landslide occurred and buried the bungalow at the foothill within the vicinity of the Highland Towers site. The incidence also occurred during the period of incessant rainfall and 8 people were killed. Drainage of the Highland Towers area has been unsatisfactory as there were numerous complaints from the residents to the local authorities prior to the disastrous landslides. Debris flow occurred at the Genting Highlands area emerging from the mountainside flanking the access road and causing debris to flow onto the highway on 30th June 1995 and caused temporary closure of Kuala Lumpur-Karak highway. In the incidence 20 people were killed and 23 people were injured. Debris flow also occurred in the Gunong Tempurong area along the North-South highway, causing debris-comprising boulders, timber logs and mud to impact on the beams of a bridge, necessitating closure of a stretch of the highway. This paper reports 3 cases of tip-fill landslide including the rehabilitation of a massive landslide of a tip-fill slope that was unstable since construction. Climate change is believed to be a factor contributing to this landslide.

INTRODUCTION

The assessment of the risk of having a natural disaster and the mitigation thereof is of foremost importance in an engineering design. Failure to assess the risks appropriately could spell disaster to the completed works. Risk in Chinese means ‘danger’ and ‘opportunity’ and it aptly describes the situation of risk in the geotechnical engineering works. What is of

concern to the geotechnical engineer is the prevention and mitigation of disasters as well as rehabilitations of failures in geotechnical works.

In Malaysia, major disasters arising out of geotechnical failures in uncontrolled earthworks are: the repeated flooding of Kuala Lumpur since 1971, the collapse of Highland Towers Condominium in 1993, the Genting Highlands access road debris flow in 1995, landslide buried the bungalow at the foothill within the vicinity of the Highland Tower site in 2002, debris flow in the Gunong Tempurong Highlands area along the North South highway. The tsunami that struck Pulau Langkawi, Kuala Kedah and Penang on 26 December 2004 (Ooi & Ting 2005) was a wake up call to examine the impact of earthquake events from neighbouring country on Malaysia. Climate change has resulted in more incidences of flooding throughout Malaysia in recent years.

Mitigation, Rehabilitation and Prevention of disasters are important considerations for any geotechnical design. The SMART project was born out of the disastrous flooding of Kuala Lumpur in 1971 and the subsequent flooding events as shown in Table 1 and is believed to be the first of its kind in the world where the tunnel is used as a dual purpose tunnel for both flood control and to ease the traffic congestion of the Kuala Lumpur City Centre. Figure 1 shows the alignment and cross section of the tunnel.

The Highland Towers Condominium collapse (Figure 2) shows that it is important for designer to consider all aspect of foreseeable possible danger to the buildings in relation to the environment including future maintenance. The stability of slope and the structural foundation of the building are integral in the design analysis process. Professionals must put health and safety above all other factors in the design consideration. The need to get rid of surface and subsurface water from site is clear from this tragedy.

STORMWATER MANAGEMENT AND ROAD TUNNEL(SMART)

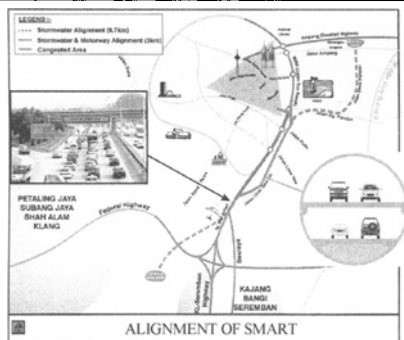


Figure 1. Schematic alignment and cross section of SMART

Figure 2. Collapse of Block 1 Highland Tower Condominium

Debris flow type of slope failures will increase with more development in the Highlands and mitigating measures recommended must consider hydraulic factors that dominate the impact of the debris flow, whilst geotechnical factors determine the formation of the natural barrier and the materials of the debris.

The tsunami catastrophe that struck the Indian Ocean on 26 December 2004 brought about the urgent need from the geotechnical community in the region and Malaysia in particular to look at the mitigation by way of design provision and consideration.

Table 1. Kuala Lumpur Flood Events

1926
4 th January 1971
1982, 1986, 1988
7 th June 1993, 21 st December 1995, 1996, 1997
30 th April 2000
26 th April 2001, 29 th October 2001
11 th June 2002
10 th June 2003
11th June 2007

The programme of public education in awareness and training in the handling of such disasters must also be implemented as has been done in Japan for Tsunami (Ohta, 2005) and Hong Kong for slopes (Mak et. al., 2007). This paper deals with some aspects of landslide disasters due to tipped fill slope in Malaysia.

THE LANDSLIDE INCIDENCES

Ooi (2004) in his special lecture on Earthwork Practice in Malaysia discussed the effect of water factor in the occurrences of landslides. Table 2 shows the case histories of major landslides in Malaysia. All these landslides occurred during the period of incessant rainfall.

Table 2. Case histories of earthwork failures due to water

Date	Location	Landslide Details
A. 4th January 1971	Bukit Gasing, Petaling Jaya	Gasing Height Development. Perimeter drains collapsed during one week of incessant rain. Tipped fill Flow slide damaged 2 Government Quarters completely. The slope reconstructed with proper compaction and quarters rebuilt. Case settlement out of court. PWD internal report (Ooi, 1971). Kuala Lumpur flooded
B. September 1988	Ulu Kelang, Ampang Jaya	Slope failure due to excavating neighbouring land during prolonged period of incessant rain Damaged to Bungalow and Swimming Pool High Court decided Engineer has a duty of care that he owed to the house owner House owner was awarded economic loss amounting to about RM360,000.00
C. December 1993	Ulu Kelang, Ampang Jaya	Collapse of Block I of Highland Towers on 11 December 1993 during prolonged period of incessant rain. 48 people were killed. Technical committee report of investigation by MPAJ (MPAJ, 1994) High Court decided Engineer failed in his duty of care he owed to the plaintiff
D. June 1995	Genting, Selangor	Debris flow, Genting Highlands on 30 June 1995 caused closure of Kuala Lumpur – Karak Highway 20 people were killed 23 people injured Economic losses, destruction of several vehicles, destruction of roadway and disruption of traffic

Date	Location	Landslide Details
E. May 1999	Ulu Kelang, Ampang Jaya	Bukit Antarabangsa filled slope failure during prolonged period of incessant rain. Access road to Bukit Antarabangsa cutoff Residents of the area were evacuated. No loss of lives but economic loss and anxieties
F. November 2002	Ulu Kelang, Ampang Jaya	Landslide occurred at 6.00am during prolonged period of incessant rain. Landslide buried the bungalow at the foothill and 8 people were killed
G. November 2003	Bukit Lanjan, NKVE	Rockslide occurred during prolonged period of incessant rain. Rockslide caused closure of NKVE Highway at Bukit Lanjan for six months. Rock slope stabilized and slided materials were blasted and removed
H. May 2006	Taman Zooview, Ulu Kelang, Ampang Jaya	Massive landslide of an old tipped filled slope with terrace houses on top of the slope. Continuous heavy rainfall in the month of April and May 2006 before the landslide. Long houses at the bottom of the slope demolished by the landslide materials and four persons in the long houses were killed. Residents of the terrace houses on top of the slope evacuated Local authority directed slope rehabilitation by the Developer for the bottom of the slope

GASING HEIGHT DEVELOPMENT

The incessant rainfall in the December 1970 and January 1971 caused the tip filled materials over the slope of the Gasing Height Development in Petaling Jaya to move down the slopes on 4th January 1971 and destroyed two government quarters at the bottom of the slopes in two separate locations of the same development as shown in Figures 3 and 4. The loose tipped fill was of residual soil of sandstone and shale origin known geologically as Kenny Hill Formation with inter-bedded quartz-veins obtained from leveling of the insitu sandstone/shale hills to create a platform for the buildings. The height of the slope was about 30m. The continuous rainfall has fully saturated the soil and the slope resulting in a debris flow down the slope and caused severe damage to the two government quarters. In Figure 3 it can be seen that the debris had entered the quarter from the back portion of the 2-storey house and emerged at the front of the house where the lounge was located. Fortunately, the incidence happened at about 6am when the family members were still sleeping in their bedrooms located on the other half of the house. Because the damaged portion of the house was not being used at that time, no lives were lost and no one was injured but the two-storey building suffered severe damages. In Figure 4 it can be seen that the debris came to rest against the single storey building and the roof was nearly overtopped. Again because the landslide event occurred at about 5am the family members were still sleeping in their rooms. The damaged portions of the building were the kitchen and storeroom that at the time of the landslide were not being used. Consequently no lives were lost and no one was injured except that the building was damaged beyond repair.



Figure 3. Landslide at quarters 1276



Figure 4. Landslide at quarters 1280

The government took the developer to the Court but the parties agreed to settle the matter out of court with the developer undertook to reconstruct the slopes with proper compaction and reinstate the damaged quarters all at its own cost.

At the same rainfall event the Kuala Lumpur city centre was flooded on 4th January 1971 with basements of banks and commercial buildings all under water. The previous recorded flooding of Kuala Lumpur happened in 1926.

THE COLLAPSE OF THE HIGHLAND TOWERS

On 11th December 1993 at 1.30pm, during a period of 10 days of incessant rain, Block 1 of Highland Towers Condominium collapsed resulting in the loss of 48 lives and the loss of use of the remaining 2 Tower Blocks that are still unoccupied. The collapsed Block 1 of the Condominium Tower is shown in Figure 2. The local authority (MPAJ, 1994) set up a Technical Committee of Enquiries and the findings as reported are as follows:

1. The Highland Towers Condominium was sited mainly on fill ground over granitic formation. The maximum depth from the ground surface to bedrock is about 19m. Granitic rocks found in and around the areas were not highly soluble minerals to adversely affect the stability of the foundations.
2. Soils overlying the granitic bedrock were very loose to loose silty sand and highly permeable.
3. The foundation for all the 3 Tower Blocks were supported on rail piles designed to take only vertical loads.
4. Surface drainage system provided was not in accordance to approved plan. Situations worsen when earthwork activities changed the drainage pattern on hill-slope behind the Condominium Blocks and available drainage systems were not maintained.
5. Clearing of trees on upper catchments resulted in increased runoff that flowed down the terraced hill-slope immediately behind the towers
6. Retrogressive slides progressively moved uphill starting from loss of toe mass at the back of the Condominium Block 1 (see Figure 5).
7. The fallen debris accumulated behind the back terrace of Condominium Tower Block 1 caused the landslide to occur beneath the entire rail pile foundation that brought down the Tower Block 1 Condominium within minutes of the landslide occurrences.

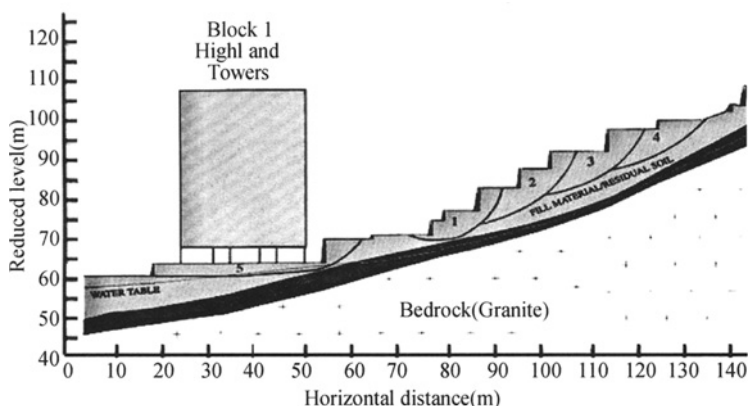


Figure 5. Retrogressive slope failure and sliding failure below building foundation

The Resident Association took the case to the High Court (Steve Phoa Chen Loon & Ors v Highland Properties Sdn Bhd & Ors, 2000) and the High Court found that the landslide that brought down Block 1 of the Highland Towers Condominium was due to a rotational retrogressive slide emanating from a high retaining wall behind the 2nd tier of the 3 tiered car parks. Water was found to be the principal factor that caused this high wall to fail.

Lessons learned from the decision of the High Court in August 2000 are as follows:

The Engineer was liable in negligence for (i) not having taken into account the hill or slope behind the Towers, (ii) not having designed and constructed a foundation to accommodate the lateral loads of a landslide or alternatively to have ensured that the adjacent hill-slope was stable, (iii) for not having implemented that approved drainage scheme, (iv) for colluding with the First (Developer) and Second (Architectural Draughtsman) Defendants to obtain CF without fulfilling the conditions imposed by the Fourth Defendant (Local Authorities) and also in nuisance as he was an unreasonable user of land. An appeal was filed by the Defendants and the Appeal Court in December 2002 maintained the fact findings of the High Court. The case went further to the Federal Court and in the judgment of February 2006; economic loss claim of the residents was rejected.

This case has several important implications for Developers, Building Professionals, Local Authorities, absentee landlords and developers of neighbouring properties in Malaysia. As the Court battle went on, the two other towers that were declared unsafe for occupation were left vacant and unattended even till today, some 14 years after the incident. The economic loss to the owners of the condominium units must have been enormous but there is no solution in sight to rehabilitate the buildings.

In general, water has been the principal cause of many slope failures as can be seen in Table 2. The design should have taken into account of suitable surface and subsurface drainage of slopes. The use of tipped fill on slope and embankment should never have been allowed under any circumstances but this practice remains unabated.

Rainfall records

Since water and poor drainage has been found to be the principal factors of the causes of collapse of the slope and one of the towers, it is important then to look at the cumulative rainfall 3 months before the collapse of the slope and the tower. Figure 6 shows the rainfall distribution from September – December 1993. On the same figure, the cumulative rainfall was also plotted. It can be seen that the cumulative rainfall on the day of the tragic event is about 900mm. The annual rainfall for 1993 was 2604mm. Thus the cumulative rainfall from September to December 11, 1993 accounts for 35% of the annual rainfall. The intensity of rainfall was severe in the month of December prior to the day when the slope and the Block 1 Tower collapsed. The seepage flow would have played a part in the collapse of the slope since water emerges from the rubble wall at the slope toe can cause loss of support as the material collapsed locally that led to the retrogressive slope failure.

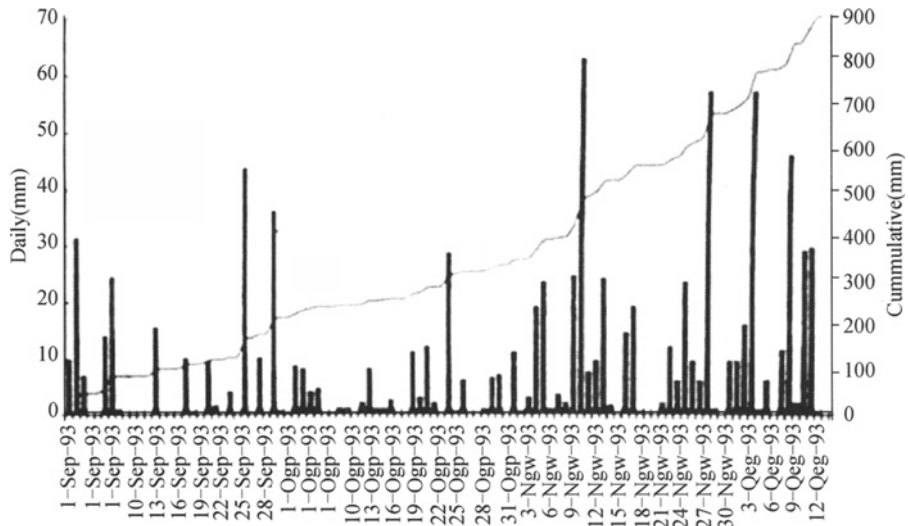


Figure 6. Daily rainfall from 1/9/93 – 12/12/93 recorded at the DID Ampang Station

TAMAN ZOOVIEW LANDSLIDE

On 31st May 2006 at about 4.30pm, a landslide occurred at the back of a row of terrace houses located on top of the slope of Taman Zooview. In the incidence, the following damages were reported to have incurred:

- a) A newly constructed Reinforced Soil Wall of 6m high and 40m long located at the boundary of the development to Taman Zooview collapsed and moved about 100m down the slope.
- b) Extensive ground movement on the down slope side of the wall resulting in the destruction of three long houses at the bottom of the slope and loss of four lives.
- c) The sixteen (16) units of terrace houses located on top of the slope in Taman Zooview were subject to evacuation order by the local authority as their houses were considered unsafe for occupation.

The geology

The geology of the entire Taman Zooview area, including the terrace houses at Taman Zooview which were affected by the landslide are underlain by graphitic schist of the Hawthorden Formation. This schist is exposed at several localities at cut slopes along the road leading up to Taman Zooview from the Zoo entrance, either as bedrock or residual soils. The same schist is also exposed in a major excavation just to the east of the said terrace houses. The Hawthorden schist can be seen intruded by weathered granite and quartz veins and dykes in the major excavation for the housing development at the adjacent site to the site of the landslide. Borehole investigation showed that the terrace houses are located on fill ground with very low SPT blow counts. Figure 7 shows a summary of the borehole results. The landslide involves the tip-fill material at the backyard of the terrace houses that was built



Figure 8. Condition of slope in 2004



Figure 9. Drainage discharging into slope in 2004

Slope stability analysis shows that the factor of safety for localized slope failure to be 1.05. The slope is thus perching precariously and failure can be expected to happen at any time, particularly with incessant rainfall and poor drainage system. The localized slope failure can propagate upwards and eventually cause the collapse of the entire slope as had happened at the Highland Towers Tragedy in December 1993 where one of the 3 blocks of Towers collapsed as a result of the initiation of localized slope failure that led to retrogressive slope failure. Fig. 10 shows the contour plan of the site after the landslide. Two parts of the slope are distinctively different; the upper slope consists of tipped fill of Hawthornden schist and the lower half where yellowish materials are visible are the original residual soil of granite origin. At both sides of the lower slope the materials were also of tip-fill over the granite residual soil. At the lower end of the lower slope there is a layer of alluvium consisting of organic material of about 1m thick overlying the weathered granite of SPT greater than 50. The geology of the site can be said to be complex. Photographs showing the various layering can be found in subsequent sections during slope rehabilitation.

The reinforced soil wall

When the residents of the terrace houses complained to the local authority on the slope movement, a site meeting was held at which the local authority directed the developer on the down slope to stabilize the slope behind the terrace houses and a 40m reinforced soil wall supported on reinforced concrete slab and piles was built by a specialist contractor. The global stability of the slope and the wall was greater than 1.4. The design was reviewed and approved by the independent reviewer appointed by the local authority. The drainage condition of the slope at the back of the houses remained the same at the time the wall was built. There was an overall plan to connect all the drains from the houses to the monsoon drains of the new development; unfortunately the plan was too early to be effected then. As there was a directive from the local authority to complete the wall urgently for fear of the raining season, the construction of the wall took about 6 weeks to reach its full height. The slope behind the terrace houses and the wall collapsed 10 days after the wall reached its full height of 6 to 7m on 31st May 2006. The landslide material travelled approximately 100m down the slope and caused massive upheaval of the ground resulting in the destruction of squatter houses and death of 4 persons. Figure 11 shows a general view of the landslide.

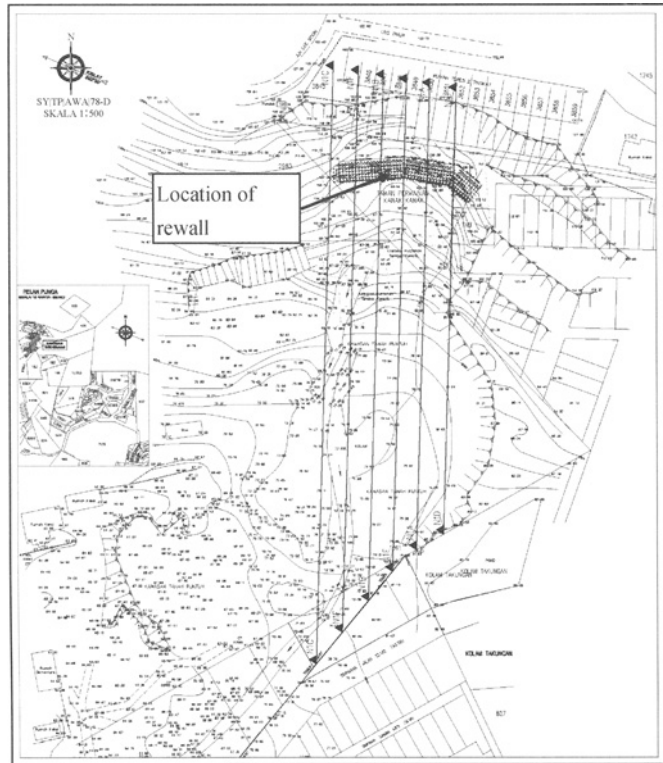


Figure 10. Contour plan of landslide area



Figure 11. General view of landslide

Rainfall record

Table 3 shows the monthly rainfall record and the cumulative rainfall at the nearby rain gauge station over the years. It can be seen that the total amount of rainfall during the consecutive months of May 2006 and the 11 months preceding it were very much higher than the long term means. It is evident that the area was exceptionally wet and registered unusually high rainfall during October 2005 to May 2006. The prolonged period of rainfall and/or the intense rainfall is common denominator in the incidence of monsoonal and flash flood, mudflow and landslide events. Such phenomenon is believed linked to climate change. Figure 12 shows the histogram of the rainfall record.

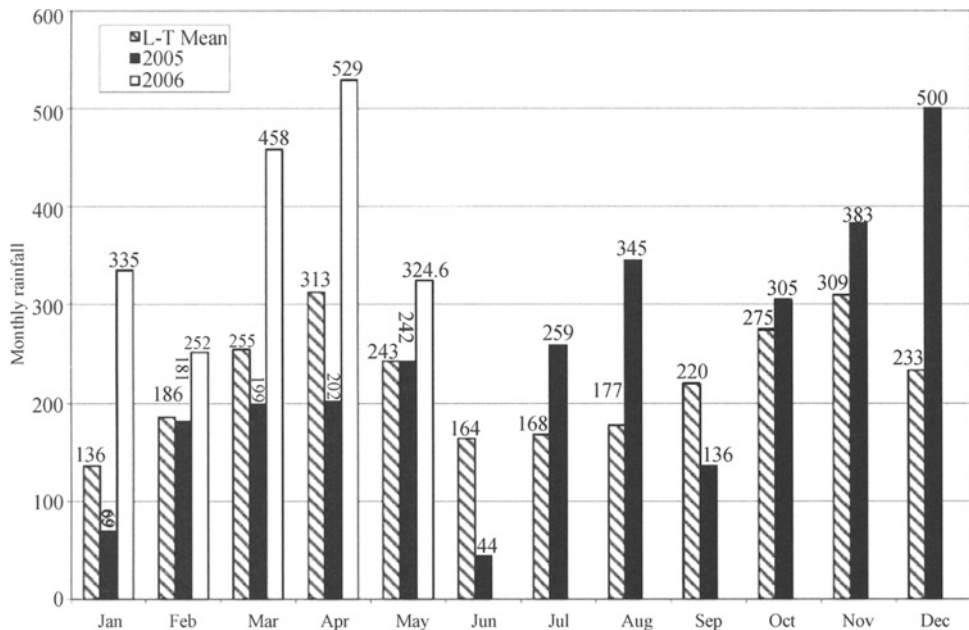


Figure 12. Histogram of monthly rainfall record

Rehabilitation of failed slope

As mentioned earlier, the 15 units of terrace houses were declared unsafe for occupation by the local authorities and the residents were evacuated. There was growing anxiety among the residents and pressure on the local authorities to restore the safety of the terrace houses so that the residents can move back to their houses. The remedial works must consider the following factors:

- the safety of the terrace houses during rehabilitation works.
- the safety of the slope.
- the design consideration of future development of the land.
- the economic consideration of the rehabilitation works.

The following were carried out prior to the commencement of rehabilitation works:

- A condition survey of the 15 units of the terrace houses was carried out.
- Owners' consent to enter the terrace houses to continue the monitoring works during the slope rehabilitation works.
- Local authorities' approvals for the proposed rehabilitation works.
- Instrumentation to monitor the movement of slope and buildings using inclinometers and settlement measuring stations.

Concept of design

A rock toe embankment with key is provided at a safe distance as shown in Figures 13 and 14. The rock-key was taken down to firm layer of weathered granite at RL 64m. Subsoil drainage

pipes were provided to take the underground water away to the open drain. It was found that above the firm layer of weathered granite there was a layer of soft organic material of about 1m thick. This layer is believed to be the sliding surface at the lower part of the slope that was responsible for the upheaval of the ground indicated by the tree as shown in Figure 11. This layer was completely removed at the lower end of the slope.

Table 3. Monthly Rainfall Record of JPS Ampang Station (Period 1953-2006)

Year	Jan	Feb	Mar	Apr	May	Jun	Jul	Aug	Sep	Oct	Nov	Dec	Total
1953	84	321	331	407	171	160	85	103	190	313	178	251	2584
1954	191	122	359	329	235	100	115	54	81	222	237	226	2271
1955	64	117	89	292	114	344	182	255	174	284	187	243	2345
1956	268	228	190	135	167	193	91	154	203	332	290	359	2610
1957	142	164	277	270	350	106	206	130	186	420	471	295	3017
1958	97	177	221	169	304	216	66	214	83	259	253	69	2128
1959	89	118	344	187	530	200	106	132	442	342	275	249	3014
1960	103	72	323	203	182	52	156	230	213	311	392	328	2565
1961	89	183	230	328	131	214	159	159	252	231	349	270	2595
1962	131	77	245	260	299	264	81	274	168	360	278	126	2563
1963	90	52	82	112	249	65	169	170	260	380	556	497	2682
1964	211	113	304	474	56	128	347	101	191	221	157	92	2395
1965	57	46	120	233	209	99	192	166	192	381	209	270	2174
1966	307	103	204	351	133	188	168	246	109	244	297	306	2656
1967	176	194	347	364	274	143	162	129	235	220	368	67	2679
1968	128	134	243	459	362	320	312	108	138	311	199	309	3023
1969	164	185	325	313	306	215	157	281	173	322	245	239	2925
1970	314	79	296	222	239	212	136	165	185	207	320	260	2635
1971	374	58	215	174	181	218	351	218	229	72	184	291	2565
1972	122	248	86	346	371	107	109	103	151	241	459	248	2591
1973	161	233	167	299	397	113	83	250	191	384	332	315	2925
1974	61	138	173	216	212	147	205	55	289	59	269	207	2031
1975	137	350	255	638	225	115	250	194	259	206	203	263	2995
1976	40	113	208	258	201	111	91	233	166	269	234	95	2019
1977	139	126	120	292	230	240	124	174	263	528	199	104	2539
1978	101	197	304	299	243	106	175	108	131	357	239	105	2365
1979	165	225	209	381	127	195	179	103	178	173	350	136	2421
1980	144	220	217	298	177	130	285	197	229	177	359	301	2734
1981	154	277	94	286	529	43	84	103	255	246	380	108	2559
1982	34	300	335	462	215	197	187	149	89	180	340	186	2674
1983	116	113	232	307	318	104	243	215	470	262	163	83	2626
1984	190	413	233	247	339	113	273	226	149	115	360	211	2869
1985	68	241	418	156	74	50	161	109	195	332	482	395	2681
1986	152	292	215	365	181	70	132	125	173	222	191	50	2168
1987	23	97	87	250	145	84	220	179	252	389	158	152	2036
1988	156	348	271	462	171	317	164	331	341	135	268	151	3115
1989	116	104	235	253	251	203	63	171	325	155	219	173	2268
1990	43	155	214	279	225	111	96	125	109	401	97	61	1916
1991	62	223	236	383	264	101	121	276	219	334	276	308	2803
1992	27	249	253	267	398	93	254	109	206	65	117	348	2366
1993	129	197	215	176	243	170	134	100	369	200	357	314	2804
1994	78	268	321	145	196	230	30	176	142	241	275	160	2262
1995	164	19	471	443	185	283	89	312	273	247	275	322	3083
1996	139	69	365	383	176	298	169	344	107	365	291	407	3113
1997	134	216	220	400	222	88	117	154	230	331	505	202	2819
1998	83	215	139	390	238	227	167	229	174	123	339	378	2702
1999	76	323	460	144	554	138	319	186	190	400	442	221	3453
2000	219	404	439	421	139	201	70	249	487	297	500	399	3825
2001	291	101	312	587	138	302	120	152	291	315	190	136	2835
2002	23	93	404	386	241	209	99	70	363	355	564	316	3123
2003	121	153	254	310	85	285	245	187	157	227	525	166	2715
2004	182	325	186	434	331	20	351	70	406	503	598	102	3508
2005	69	181	199	202	242	44	259	345	136	305	383	500	2865
2006	273	274	436	554	300								
Mean	135	186	254	313	242	164	168	177	220	275	309	233	2663
Maximum	374	413	471	587	554	344	351	345	487	528	598	500	3825
Minimum	23	19	82	112	56	20	30	54	81	59	97	50	1916
2005/ Mean	51%	97%	78%	85%	100%	27%	154%	195%	62%	111%	124%	214%	108%
2006/ Mean	203%	147%	172%	177%	124%								

The construction was therefore divided into 5 stages of excavation and at each stage the slope stability analysis is carried out. Figure 15 shows the factor of safety for the various stages of excavation. Figure 16 shows the factor of safety for the completed slope. It can be seen that the most critical stage of construction with a factor of safety of 1.25 is during stage 5 as shown in Figure 15. The reduced level for this excavation is 78.5m. At this level the second embankment starts with Tensar geogrid reinforcement that was chosen based on its rigidity, integrity and strength at the junctions of the geogrids as well as its ability to mobilize its strength at compatible low strain level of the soil.

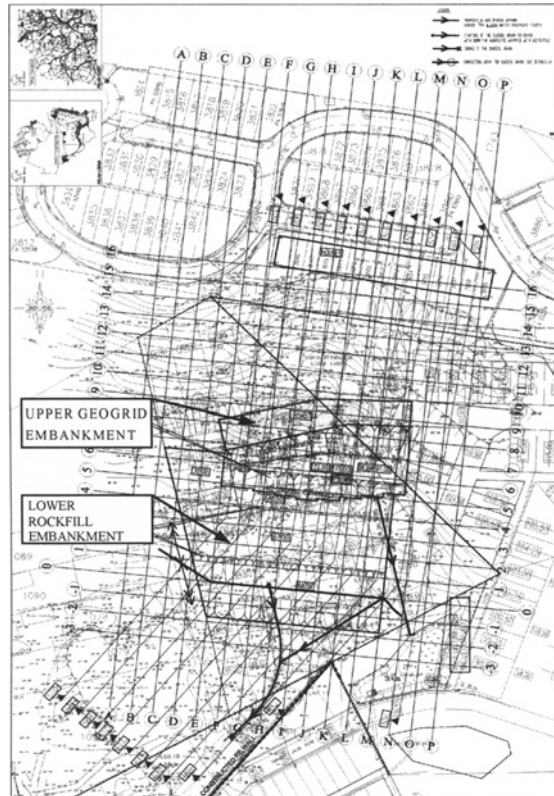


Figure 13. Plan view of lower and upper embankments

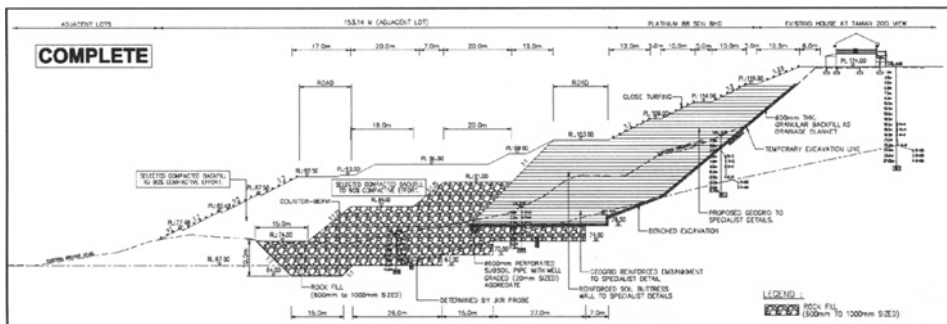


Figure 14. Typical cross section

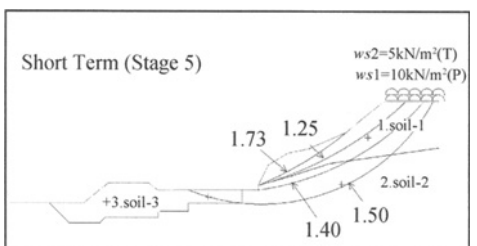
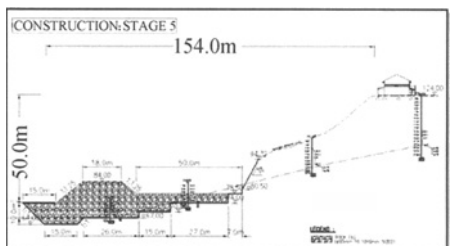
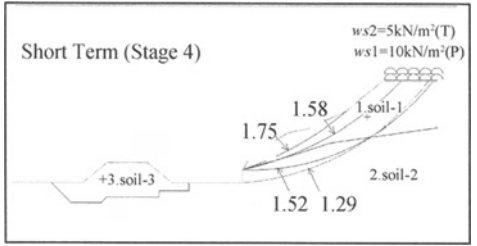
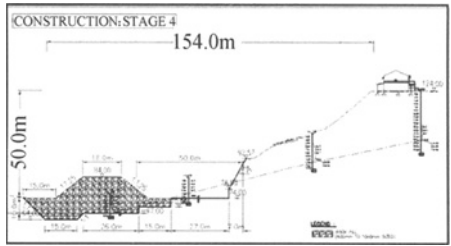
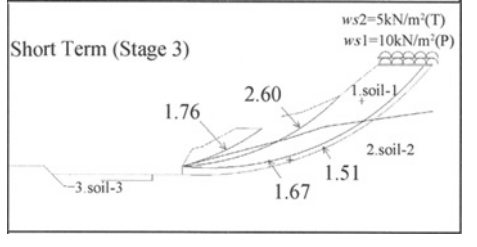
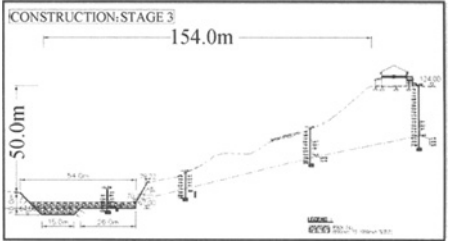
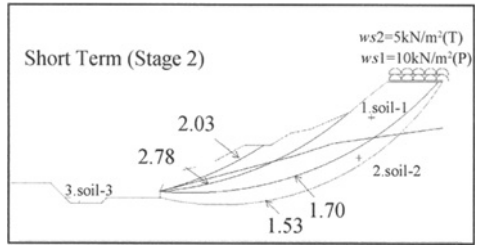
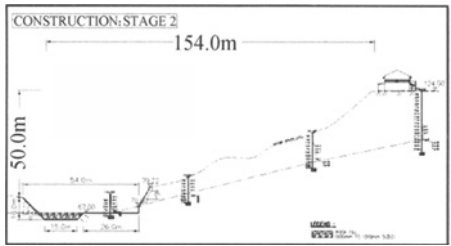
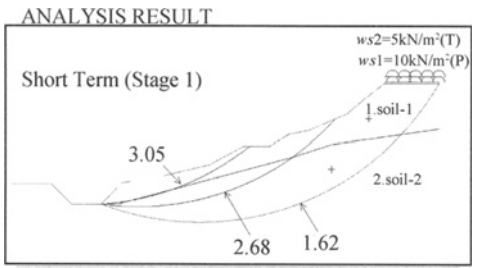
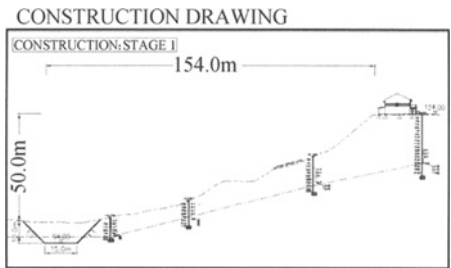


Figure 15. Factor of safety for various stage

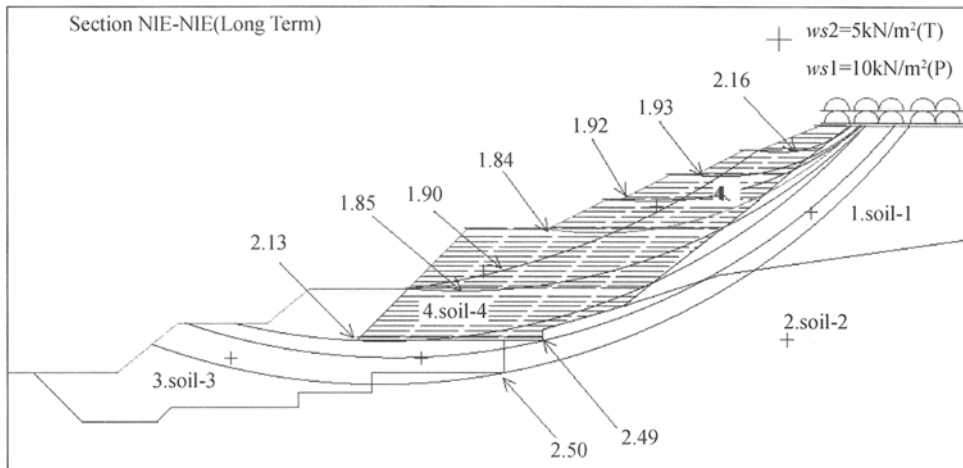


Figure 16. Factor of safety of completed slope

Construction methodology

- 1) The Site of the Landslide at the lower part of the slope was waterlogged (Figure 17) and has to be drained. Trenches at the down slope of the landslide area were excavated and the waterlogged ground drained and all water channelled to existing monsoon drain through a siltation pond within the site
- 2) All surface water were diverted and prevented from entering the valley area. All roof water from the terrace houses were piped away from the slope area.
- 3) Subsurface drainage is provided in the valley area where spring/seepage water emerges and led away from the valley (Figure 18). Suitable graded filter are provided for the intake of spring/seepage water into the piping if permanent pipe work is required (Figure 19).
- 4) All landslide materials are removed in sections and stages. Suitable materials are stockpiled for reuse. Unsuitable materials are disposed off site.



Figure 17. Waterlogged ground

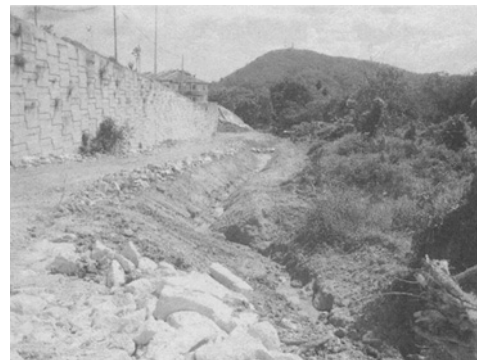


Figure 18. Subsurface drainage

- 5) Lower Rockfill Embankment was constructed first starting with the rock-key (Figure 20) and carried out in sections so as not to cause slope instability. This is an important part of the rehabilitation work and was carefully carried out and inspected. During construction, there were no undue slope movements or settlements of the houses detected by the instrumentation.



Figure 19. Intake of subsurface drainage



Figure 20. Rock-key of lower embankment

6) Rehabilitation of Landslide Area

- i) Excavate in sections to original ground, about 6m deep, stockpiled suitable material for reuse and compact the base of excavation to 90% maximum density in accordance with BS heavy compaction.
 - ii) Lay and compact 800mm thick of sand layer/aggregate layer (Figure 21). Drain all water to collector trenches. At the bottom of the trench, water is led away with suitable discharge pipes to roadside monsoon drains. Lead all water to suitable discharge outfall and the monsoon drains
 - iii) Lay and compact suitable dried landslide material on top of the sand/ aggregate layer in compacted thickness of not more than 1000mm thick; built-up in 4 layers of 250mm compacted to 90% maximum density to BS heavy compaction. Laboratory determination of maximum dry densities was carried out prior to commencement of rehabilitation work.
 - iv) Repeat with 300mm thick of sand layer/aggregate layer as in item 6(ii) above and repeat item 6(iii).
 - v) Construct alternating layers of sand/aggregate and suitable dried landslide material to suitable safe height.
 - vi) Excavate the next section and repeat items 6(i) to 6(v).
 - vii) Earthwork in the general area shall synchronize and follow closely with that of the geogrid embankment construction.
 - viii) All completed earthwork must be close turfed with cow grass immediately and watered until they are established.
 - ix) All drainage works must be constructed together with the stage completion of the earthwork.
- #### 7. Upper geogrid reinforced embankment
- x) The upper Uniaxial Geogrid Reinforced Embankment shall be founded on competent ground to be determined by boreholes and JKR probes. The JKR probes

were done in closed grids and can be carried out in advance of the rehabilitation works.

- xi) The founding level of the upper Uniaxial Geogrid embankment was inspected prior to placement of the compacted crusher run with suitable aggregate drainage channels.
- xii) Construction of the upper Uniaxial Geogrid embankment (Figure 22) shall follow the procedure in item 6 above.
- xiii) Suitable shearkey shall be provided for the Upper Geogrid Reinforced Embankment.
- xiv) Low level boundary wall shall be provided in the specialist geogrid work to avoid future excavation on the slope.

8. Instrumentation

Instrumentation such as ground water table, settlement plates and inclinometers were installed and monitored by independent party at regular interval and the results plotted and submitted to the Engineer for his necessary action throughout the construction and maintenance period.

9. Drainage of slope

Suitable overall drainage to include subsurface drains, berm drains, cascading step drains, manholes, sumps and monsoon drains all properly designed and constructed to ensure that the whole site is adequately and properly drained.



Figure 21. Laying of sand drainage layer



Figure 22. Construction of geogrid embankment

DICUSSION AND CONCLUSION

1. The knowledge in landslide controlled and management has advanced greatly over the last thirty years as shown by the achievements of Hong Kong GEO (Tang, et al., 2007). Hong Kong had its disastrous landslide of Sau Man Ping in 1972 and 1976 where 79 people died and the government of Hong Kong set up Geotechnical Control Office to address the problems of Landslide.
2. In Malaysia, the Gasing Height landslides in 1971 were just as serious as that of Hong Kong except there were no loss of lives.
3. In 1993, a retrogressive landslide caused the collapse of Block 1 of the Highland Towers Condominium in which 48 people were killed. There were public hearings of the case

and the High Court Judge concluded that drainage and its maintenance were principally responsible for the landslide and apportioned the blames on the various parties that were involved in and around the Highland Towers Development site.

4. The residents of Block 1 of the Highland Towers Condominium lost their home and that of Block 2 and 3 still look at their abandoned buildings after 14 years. Rehabilitation to Block 2 and 3 is dependent on a master drainage plan to be prepared by the local authorities and this is still not done.
5. The authorities implemented the three tiers geotechnical report systems i.e. the submitting person's geotechnical report, the reviewing geotechnical report and the independent geotechnical report by the consultant to the local authorities.
6. In 2002, again at nearby the Highland Towers site, a landslide buried the bungalow at the foothill killing 8 people in the early hour of the morning due to poor drainage.
7. In 2006, landslide occurred at Taman Zooview in Ulu Klang killing 4 people. The rehabilitation work is being carried out.
8. The landslides at Sau Man Ping in Hong Kong and the three landslide cases quoted in this paper are all tipped fill slopes. All the landslides occurred in the period of incessant rainfall with high intensities of rain. The rectification to the tip fill slope problem is to compact the fill slope with or without geogrids reinforcement with overfill trimmed back and to ensure adequate internal and external drainage.
9. The need to reinforce and compact soil started more than 2000 years ago when Qin Shi Huang Di built the 6000km Great Wall of China. Man continued to tipped fill slope and created disasters at the wrath of nature.
10. The Zooview slope rehabilitation uses the ancient philosophy of soil compaction with modern geogrids reinforcement instead of the reeds and twigs in the ancient time.

REFERENCES

- Mak S.H., Yeung Y.S.A. and Chung P.W.K. (2007). Public education and warnings in Landslide Risks Reduction. *Proc. 40th Anniversary Vol. SEAGS*, 367-375.
- MPAJ. (1994). Report of the inquiry committee into the collapse of Block 1 and the stability of Block 2 and 3 Highland Towers Condominium, Hulu Klang, Selangor Darul Ehsan. *Majlis Perbandaran Ampang Jaya*.
- Ohta H., Pipatpongsa T. and Omori T. (2005). Public education of tsunami disaster mitigation and rehabilitation performed in Japanese Primary Schools. *Proc. Int. Conf. Geotech. Engng. For Disaster Mitigation & Rehabilitation*, World Scientific Publishing Company, Singapore, 141-150.
- Ooi T.A. (1971). Report on landslides at government quarters nos 1276 and 1280 at Section 5, Petaling Jaya, Selangor. *PWD internal report*.
- Ooi T.A. (2004). Earthworks practice in Malaysia. *Proc. Conf. MGC2004*, Kuala Lumpur, 45-58.
- Ooi T.A. and Ting W.H. (2005). Report on some major geotechnical disasters in Malaysia. *Proc. Int. Conf. Geotech. Engng. For Disaster Mitigation & Rehabilitation*. World Scientific Publishing Company, Singapore, 151-164.
- Steven Phoa Cheng Loon & Ors v Highland Properties Sdn Bhd & Ors. (2000). *Current Law Journal*, 4: 508-602.

SEISMIC PERFORMANCE EVALUATION OF GEOTECHNICAL STRUCTURES

Susumu Iai, Tetsuo Tobita

*Disaster Prevention Research Institute, Kyoto University
Gokasho, Uji, Kyoto 611-0011, Japan*

The paper describes an emerging methodology for evaluating seismic performance of geotechnical structures that extend over tens of kilometers along a coastal protection line. The challenging aspect in establishing this type of methodology for performance evaluation is in the fact that site-by-site detailed study is not practical. The paper proposed a performance-based approach utilizing simplified design charts that are newly developed based on a parameter study of effective stress analyses of soil-structure systems. The coastal protection lines over a distance of 70km along Osaka Bay Area, Japan, are used as an example to demonstrate the advantages of the proposed approach.

INTRODUCTION

Rapid economic growth and urbanization in Asian countries have been noteworthy. Most of the developments are concentrated over coastal areas that are open to the sea for the advantages of development. These urban areas, however, are potentially vulnerable against earthquakes because they are developed over soft alluvial deposits. They are also vulnerable against flood due to high tide, typhoons, and tsunamis because of their proximity to the rivers and the sea. Rapid developments in these areas, far more rapid than those developments once achieved in Europe and North America, aggravate the situations against these natural hazards. A good urban planning and a solid engineering strategy are essential for preparing these areas against natural hazards. The Sumatra earthquake of 2004 reminded us the importance of our preparedness in coastal areas against natural hazards (Tobita et al., 2006).

The state-of-the-art earthquake engineering is typically based on site-by-site detailed analysis. A long coastal protection line poses a difficulty in directly applying the state-of-the-art earthquake engineering. A new methodology should be developed.

A review is provided in this paper to discuss this issue based on the previous paper by the same authors (Iai and Tobita, 2007).

OSAKA BAY AREA, JAPAN

The coastal line, along which the seismic performance of geotechnical structures is evaluated, extends over 70km along Osaka Bay Area as shown in Figure 1. As shown in this figure, northern part of the coastal protection line (designated by a blue line) is located slightly inland from the sea whereas southern part of the coastal protection line (designated

by a green line) is exposed to the sea. Geotechnical conditions along the coastal protection line were compiled based on the boring data that were obtained at every 100 to 500m originally for the construction of the Hanshin Bay Area Highway. Typical geotechnical profile consists of alternating layers of sand and clay deposit. Depth to the engineering base layer ranges from 10 to 80 m with a deepening trend toward north. Expected earthquake motions during the combined Tonankai and Nankai earthquakes of magnitude 8 class were set in four zones along the coastal protection line with a peak accelerations ranging from 0.10 to 0.18g at the base layer for evaluation of seismic performance.

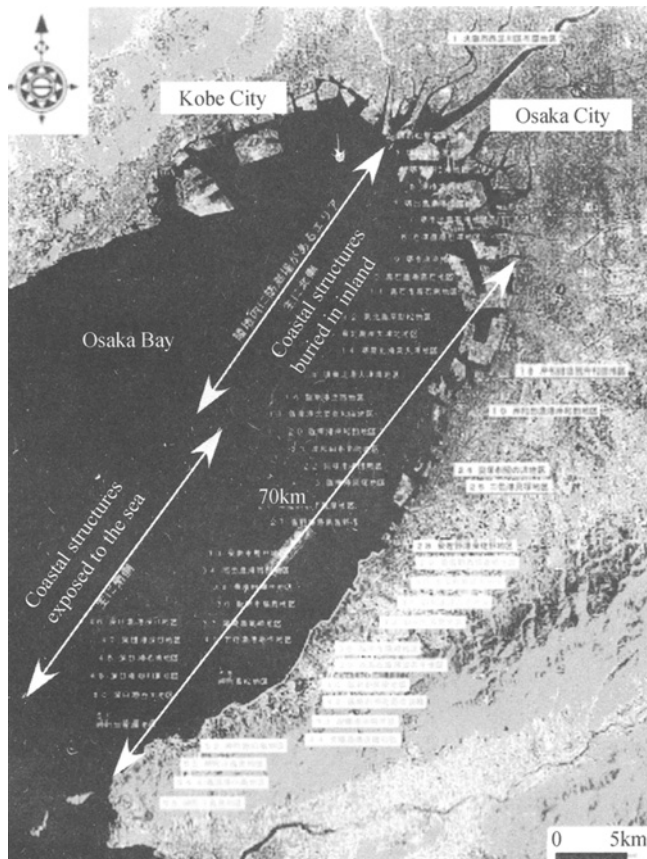


Figure 1. Investigated coastal protection line for Osaka Bay Area, Japan (Osaka_Municipal_Government, 2007)

PERFORMANCE GRADES

The performance grades of the coastal structures that reflect the consequence of failure were specified based on two factors. One is the importance categorized by the level of the use of the land behind the coastal structures. If the level of the use of the land is high such as used for residence and/or industry, the consequence of the failure of the coastal structure becomes serious. If the level of the use of the land is low such as pastures and farmland, the consequence of the failure of the coastal structure may be not so serious.

The other is the elevation of the ground relative to the sea water level and expected height of the tsunami. If the elevation of the ground is lower than the sea water level (often called below zero meter area), the flood due to the failure of the coastal structure is very difficult to recover. If the elevation of the ground is higher the sea water level, the flood due to the failure of the coastal structure might be automatically recovered when the Tsunami or high tide are gone away.

The performance grades were specified based on a combination of these two factors and are designated as S, A, B, and C as shown in Figure 2. These performance grades were used to specify the margin to allowable settlements of the coastal structures during the earthquake. For example, if the land behind the coastal structure is utilized for industry or residence and if the elevation of the land is lower than the sea level (HWL), such as shown in Figure 3, and also illustrated in Figure 2, performance grade is designated as S, the highest grade.

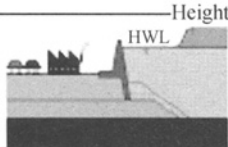
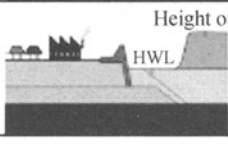
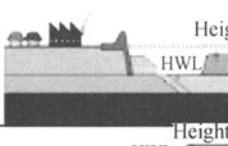
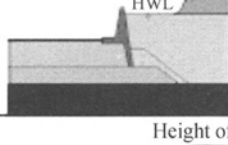
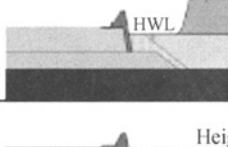
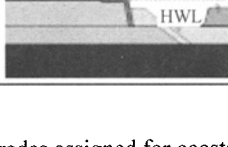
Conditions			Performance grade
Importance	Ground level	Schematic figure	
High	Low		S
	Middle		A
	High		
Low	Low		B
	Middle		
	High		C

Figure 2. Performance grades assigned for coastal structures
(Osaka_Municipal_Government, 2007)

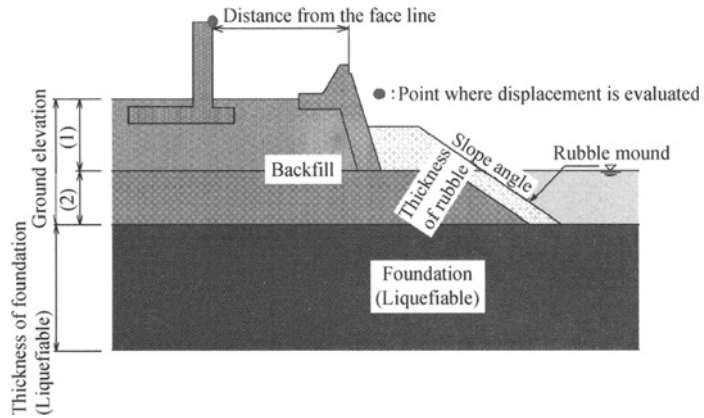


Figure 3. Seismic damage to high tide protection wall in highly industrialized area during 1995 Kobe earthquake (Kanzaki river site, Kobe, Japan)

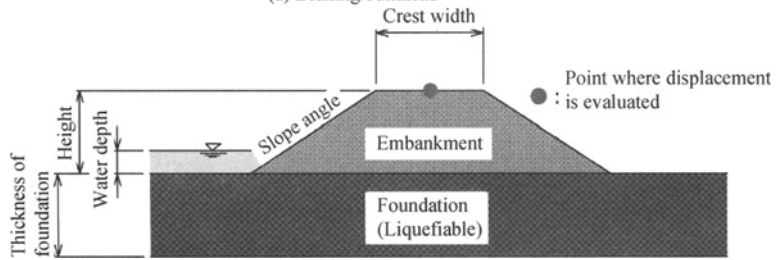
SIMPLIFIED DESIGN CHARTS

A set of design charts have been developed based on a series of parametric studies on embankments and gravity structures (Higashijima et al., 2006). The cross sections and primary dimensions used as input parameters are shown in Figure 4. Typical examples of the results of the parameter study are shown in Figure 5. These results were compiled as a comprehensive set of data for the simplified design charts. These design charts are incorporated in a spread sheet format. Input data required are (1) basic parameters defining the cross section of structures, (2) geotechnical conditions as represented by SPT N-values, and (3) earthquake data, as represented by wave form, peak ground acceleration, or distance and magnitude from the seismic source. These design charts can be conveniently used for efficiently assessing the vulnerability of coastal geotechnical structures that extends a long distance, such as tens of kilometers, over a variable geotechnical and structural conditions.

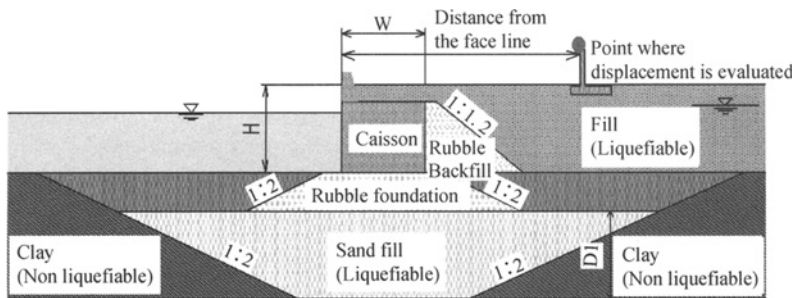
Obviously each data point shown in Figure 5 are the results of the seismic performance evaluation through an effective stress method FLIP (Iai et al., 1992); for a cross section a dike shown in Figure 6, the results as shown in Figure 7(a), having a horizontal displacement of 30cm with a settlement of 3cm at the crest, or Figure 7(b) of an idealized dike having the same cross section but with a foundation ground with SPT N-values of 10, having a horizontal displacement of 130cm with a settlement of 30cm at the crest are obtained. The failure mode of this dike can be characterized by a relatively small settlement presumably because of the small size and light weight of the dike. If other cross section with heavier structure is analyzed, the settlement will be the dominant deformation mode. The simplified charts discussed above reflects these analysis results.



(a) Leaning bulkhead



(b) Embankment



(c) Gravity type

Figure 4. Cross sections and primary parameters used for the simplified design charts (Higashijima et al., 2006)

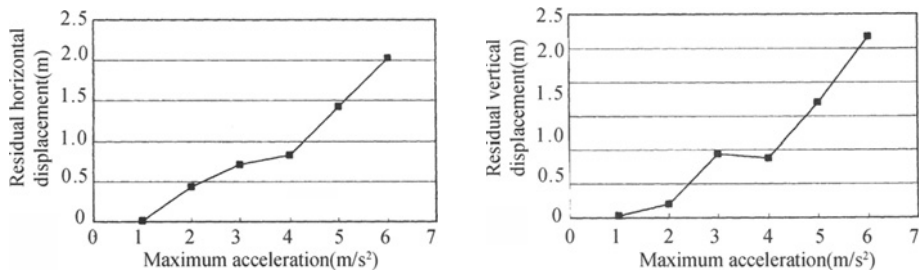


Figure 5. Parameter study of displacements of leaning bulkheads over varying maximum accelerations

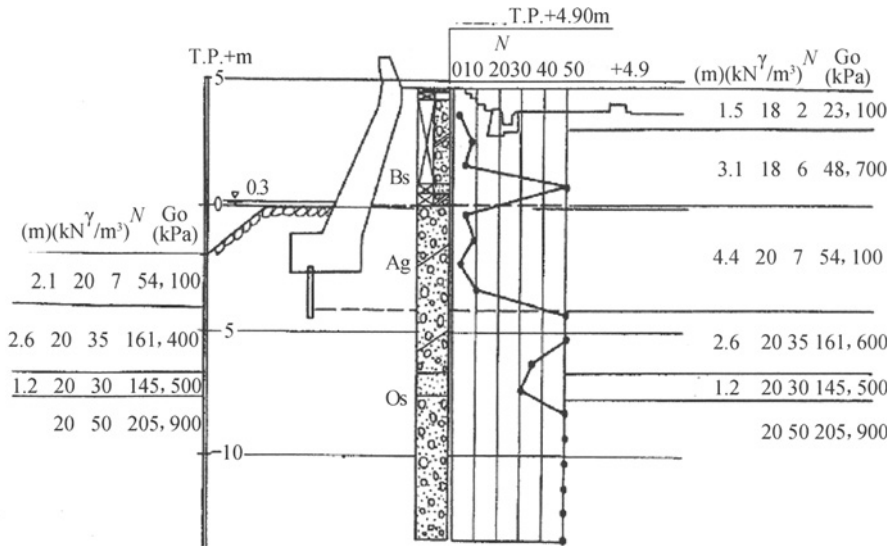
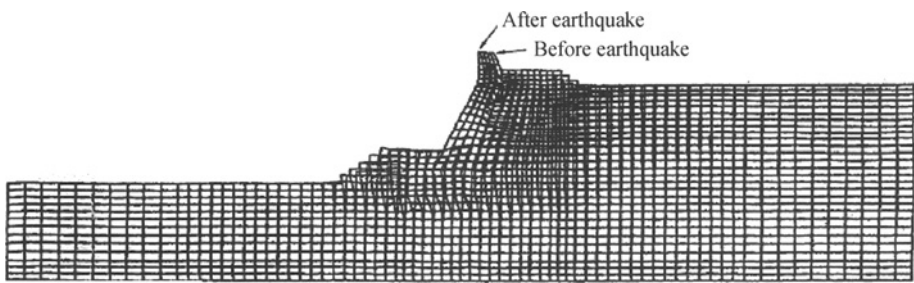
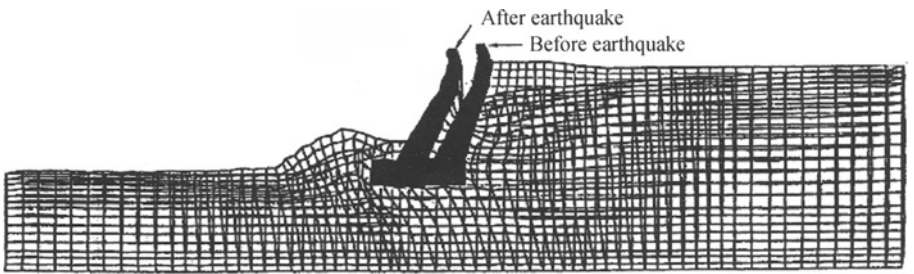


Figure 6. Example of cross section of a coastal geotechnical structure for assessment of seismic performance



(a) Results based on the current geotechnical conditions



(b) Results based on the scenario assuming the loose deposit with SPT N-values of lo

Figure 7. Computed residual deformation of a coastal geotechnical structure through effective stress analysis

RESULTS OF THE SEISMIC ASSESSMENT

The results of the seismic assessment of the coastal protection line in Osaka Bay Area are shown in Figure 8. The settlements of the coastal protection facilities due to earthquake shaking ranged from 0.2 to 1.2m as shown in Figure 8(a). Those settlements cause margin against Tsunami to be smaller. The areas that will not be able to protect the land from Tsunami and need strengthening or improvement for preparing against the Tsunami were identified from the results shown in Figure 8(c).

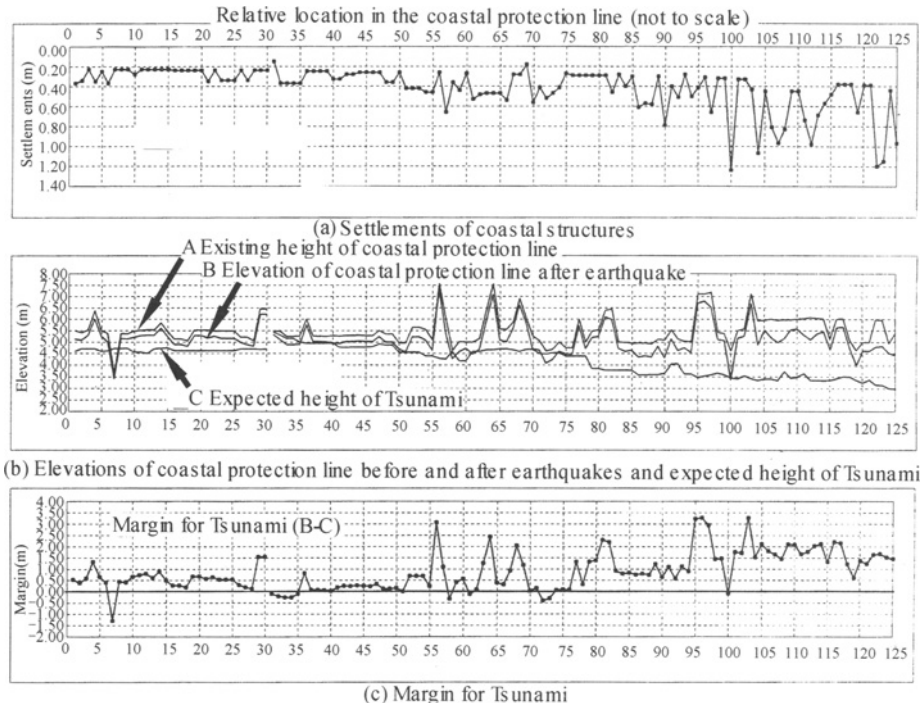


Figure 8. Results of the seismic assessment of coastal protection line
(Osaka_Municipal_Government, 2007)

CONCLUSIONS

Designing a large urban area against combined natural hazards poses a new challenge in earthquake engineering. The paper proposed the performance-based approach utilizing simplified design charts that are based on a parameter study of effective stress analyses of soil-structure systems. An application to the coastal protection line over a distance of 70km along Osaka Bay Area, Japan, demonstrates the efficiency of the proposed approach.

REFERENCES

Higashijima M., Fujita I., Ichii K., Iai S., Sugano T. and Kitamura M. (2006). Development of a simple seismic performance evaluation technique for coastal structures. *2006 Ocean Development Symposium*.

- Iai S., Matsunaga Y. and Kameoka T. (1992). Strain space plasticity model for cyclic mobility. *Soils and Foundations*, 32 (2): 1-15.
- Iai S. and Tobita T. (2007). Seismic assessment of coastal structures against combined hazard with Tsunamis. Keynote Lecture, *Proc. 8th Pacific Conference on Earthquake Engineering* (to be published).
- Osaka_Municipal_Government. (2007). Report of the technical committee for seismic assessment of coastal structures in osaka bay area. Osaka.
- Tobita T., Iai S., Chairullah B. and Asper W. (2006). Reconnaissance report of the 2004 Sumatra-Andaman, Indonesia, Earthquake - Damage to geotechnical works in Band Aceh and Meulaboh. *Journal of Natural Disaster Science*, 28 (1): 35-41.

Invited or Special Session Lectures

DEBRIS-BUDGET-BASED DEBRIS-FLOW SUSCEPTIBILITY ANALYSIS

Jia-Jyun Dong, Chyi-Tyi Lee, Kuang-Ping Lin and Yu-Hsiang Tung
*Institute of Applied Geology, National Central University, No.300, Jungda Rd.,
Jungli, Taoyuan 320, Taiwan, China*

Susceptibility analysis of debris-flow is important for mitigating the induced hazards. This research proposed a statistical model for predicting the occurrence of debris-flow in Tungshih, Taiwan. Five causative factors including steepness of creek, catchment area, form factors, potentially landslide area and debris storage index were selected in the statistical model. Based on the record of debris-flow occurrence during typhoon Toraji, the steepness of creek, potentially landslide area and debris storage index were sieved as relevant causative factors of the occurrence of debris-flow. By taking the debris budget into account, the susceptibility of debris-flow will evolve with the landslide and debris-outflow. Thereafter, the impact of geological events, such as a large earthquake, on the occurrence of debris-flow can be predicted and quantitatively evaluated.

INTRODUCTION

Debris flows are global phenomena and play an important role on the landscape evolution (Jakob and Hungr, 2005). Meanwhile, the occurrence of the debris-flow often results in enormous damage of lives and buildings. Thereafter, the researchers and government agencies make lots of efforts to the debris-flow hazard mitigation. Among others, debris-flow hazard assessment is one of the fundamental works for hazard mitigation.

In regional scale, predicting where a debris-flow will occur (susceptibility analysis) is critical. Subjective judgment of experts, statistical method, and artificial intelligent techniques are adopted to forecast the debris-flow susceptibility (DFS) on the basis of a set of relevant environmental characteristics (Su et al., 1993; Liu and Wang, 1996; Lin et al., 2000; Lin et al., 2002; Rupert et al., 2003; He et al., 2003; Liu et al., 2006; Chang and Chao, 2006; Chen, et al., 2007). In recent years, GIS technology has been increasingly used on the DFS analysis and largely enhanced the ability for spatial data processing and analysis (Lin et al., 2002; He et al., 2003). However, the generality of those susceptibility models which produce colorful DFS maps is always “suspected”. One of the critical challenges is: are the causative factors selected in the statistically-based DFS model relevant for representing the occurrence of debris flow? Besides, it is often observed lots of landslide occurred after geological events (such as earthquake or typhoon) and the number of debris-flow creeks increased. Is it possible to evaluate the potential impact of these events beforehand on the occurrence of debris-flow, quantitatively?

In this paper, factors contributing directly to the occurrence of debris-flow which correlating to the supply of run-off and debris were incorporated into a DFS model. DFS analysis was conducted in the Tungshih area in Central Western Taiwan, where many landslides and debris-flows were triggered by the 1999 Chi-Chi earthquake and followed typhoons. Utilizing discriminant analysis, a susceptibility index reflecting the DFS of the 56 studied potential debris flow torrents (PDFTs) was derived. Consequently, the evolution of the susceptibility index of PDFTs with the geological events can be predicted by the proposed DFS model. The impact of earthquake and typhoons on the occurrence of debris-flow in Tungshih area were quantitatively evaluated.

REGIONAL SETTING

In Taiwan, 1420 creeks were sieved to be PDFTs by Council of Agriculture (COA, 2003) and 64 PDFTs were located in the studied Tungshih area which is geologically in the Western Foothills geologic province (west part) and the Hsueshan Range sub-province (east part) (Figure 1).

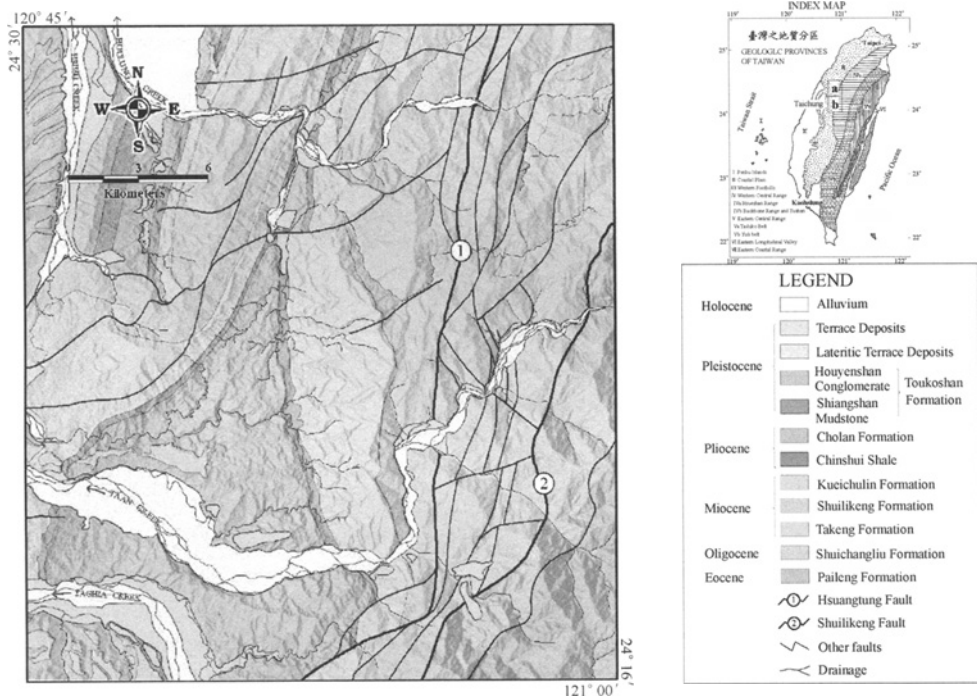


Figure 1. Location (marked a in index map) and geology of study site, Tungshih site. Index map shows the geologic provinces of Taiwan (Ho, 1975)

Following the Chi-Chi earthquake, typhoon Toraji (typhoon T) in July 2001 and typhoon Mindulle (typhoon M) in July 2004 further wounded central Taiwan. Numerous landslide and debris flow occurred in Tungshih quadrangle. The landslide areas triggered by the Chi-Chi earthquake/following typhoons and the records of debris-flow occurrence triggered by typhoon T are shown in Table 1 and will be described subsequently.

Table 1. Causative factors, landslide area triggered by earthquake and typhoons and debris flow occurrence records during typhoon T of studied PDFTs in Tungshih area

No.	S^* (°)	A^* (ha)	F^*	$A_{ls,C}$ (ha)	$A_{ls,T}$ (ha)	$A_{ls,M}$ (ha)	$A_{pls,C}$ (ha)	$A_{pls,T}^*$ (ha)	$A_{pls,M}$ (ha)	$V_{stream\ bed,AT}$ (m ³)	V_{out} (m ³)	$V_{storage,BT}$ (m ³)	$N_{v,BT}^*$	R_T
T-A001	19.8	1100.1	0.01	60.68	83.27	91.04	223.72	194.36	380.48	939000.0	74677.9	1013678	13.57	Y
T-A003	23.9	31.0	0.39	2.05	0.61	0	5.32	11.84	5.84	56000.0	10119.35	66119.35	6.53	Y
T-A004	30.2	727.4	0.05	25.48	4.95	7.79	76.96	92.48	55.16	428000.0	59235.64	487235.6	8.23	Y
T-A005	15.4	62.1	0.02	0.19	0	0.21	3.08	11.08	1.6	44500.0	14932.12	44500	2.98	N
T-A006	20.0	430.3	0.04	6.65	4.62	0.65	29.16	11.72	12	158000.0	44147.08	158000	3.58	N
T-A010	21.3	158.1	0.12	2.70	0	0	0	0	0	430000.0	25199.5	430000	17.06	N
T-A011	21.8	57.4	0.02	0.07	0	0	0	0	0	52000.0	14288.31	66288.31	4.64	Y
T-A012	18.8	64.7	0.08	0	0	0	0	0	0	245000.0	15279.05	245000	16.04	N
T-A013	13.1	179.1	0.08	0	0	0	0	0.48	0	243000.0	27022.38	270022.4	9.99	Y
T-A057	25.5	420.8	0.05	0.07	0.25	0.06	4.2	3.44	3.6	144000.0	43598.59	144000	3.30	N
T-A058	21.2	80.0	1.34	0	0	0	0.12	2.48	1.12	24000.0	17207.61	24000	1.39	N
T-A059	17.0	106.2	0.02	0	0	0	0.16	1.24	1.04	58000.0	20166	58000	2.88	N
M-011	21.9	197.8	0.64	4.36	0.15	0.29	1.44	9.44	0.68	5700.0	28567.8	34267.8	1.20	Y
M-012	23.8	1001.5	0.98	1.61	2.39	2.29	34.76	8.8	2.6	31401.0	70852.41	102253.4	1.44	Y
M-013	11.2	125.0	0.14	0.01	0.49	0.26	2.88	11.88	1.4	11550.0	22093.25	33643.25	1.52	Y
M-014	14.8	77.4	0.33	0.25	0.28	0.34	6.24	21.16	4.56	12800.0	16892.15	12800	0.76	N
M-015	15.3	61.9	0.10	0.053	0.24	0.04	0.44	1.6	0.08	3648.8	14905.17	18553.97	1.24	Y
M-016	24.4	240.3	0.23	0	0	0	8.96	13.48	4.96	19200.0	31857.54	19200	0.60	N
M-017	13.9	170.0	0.15	0.52	0	0	0.52	8.4	0.36	15650.0	26244.69	15650	0.60	N
M-018	19.8	177.6	0.56	2.44	0.41	0.16	7.48	1.68	0.08	38000.0	26895.41	38000	1.41	N
M-019	13.2	75.7	0.68	0.28	0.79	0.03	4.04	0.88	0.8	7200.0	16683.37	7200	0.43	N
M-020	17.4	454.8	0.28	0.42	0.89	1.21	4.64	1.28	2.2	44200.0	45537.54	89737.54	1.97	Y
M-021	25.5	156.1	0.31	0.44	1.31	0.79	8.08	18.76	1.48	29600.0	25020.48	54620.48	2.18	Y
M-022	20.7	211.8	0.63	0.30	1.35	0.26	0.8	22.4	0.24	40672.0	29683.06	40672	1.37	N
M-023	18.5	50.2	0.59	0.08	0.08	0	0.08	2.8	0	20700.0	13255.13	33955.13	2.56	Y
M-024	19.7	226.3	0.18	12.50	8.13	4.28	35.16	113.64	29.56	78000.0	30804.45	108804.4	3.53	Y
M-025	11.5	77.9	0.18	20.33	11.47	8.06	21.6	36.72	21.84	10300.0	16953.17	10300	0.61	N
M-026	18.5	149.9	0.28	3.36	5.96	1.13	3.04	14.88	3.08	74000.0	24459.02	98459.02	4.03	Y
M-027	17.0	52.1	0.52	3.32	2.81	0.58	1.68	6.28	1.4	5301.0	13533.78	18834.78	1.39	Y
M-028	14.2	46.7	0.11	1.74	2.28	1.37	0.32	3.8	0.32	9650.0	12729.39	22379.39	1.76	Y
M-033	23.6	567.5	0.37	1.43	2.81	0	0.16	7.76	0	19200.0	51547.9	70747.9	1.37	Y
M-A004	14.8	351.4	0.11	0.17	0.68	0	0	7.12	0	8400.0	39412.96	8400	0.21	N
M-A005	18.2	70.6	0.31	0.10	1.16	0	0	1.64	0	4900.0	16044.3	4900	0.31	N
M-A006	10.3	431.8	0.07	1.64	0.59	0.42	11.2	25.76	0.68	34200.0	44233.2	34200	0.77	N
M-A007	13.0	651.1	0.05	2.30	1.71	0.58	7.88	20.76	0.28	44120.0	55671.48	44120	0.79	N
M-A008	15.5	187.6	0.08	0	0.53	0.06	0.36	5.2	0.08	39000.0	27733.23	39000	1.41	N
M-A009	18.5	58.4	0.24	0.08	0	0.03	6.36	12.36	5.56	4200.0	14427.17	4200	0.29	N
M-A010	16.4	100.3	0.23	0.11	0.92	0.35	1.2	5.24	0.4	3600.0	19530.74	3600	0.18	N
M-A011	22.8	28.1	0.64	0	0	0	0	0	0	6358.0	9577.796	6358	0.66	N
M-A012	9.9	296.5	0.15	0.48	1.31	1.21	10.48	77.56	8.04	45600.0	35836.36	81436.36	2.27	Y
M-A013	16.3	508.7	0.09	0.08	1.16	0.23	1.88	18.2	1.92	4800.0	48485.14	4800	0.10	N
M-A014	19.2	277.1	0.06	0.27	1.36	0	0	0.08	0	7950.0	34503.77	7950	0.23	N
M-A015	19.0	510.0	0.12	0.04	1.23	0.03	2.08	19.84	2.32	42680.0	48554.49	91234.49	1.88	Y
M-A016	10.5	410.0	0.05	0.18	0.87	0	3.36	24.8	0.76	21520.0	42968.38	21520	0.50	N
M-A017	17.2	177.8	0.04	0.04	0.27	0	0.12	7.6	0	33000.0	26912.36	33000	1.23	N
M-A018	20.9	189.4	0.27	0.14	0.23	0	1.8	19.72	0.44	19570.0	27881.93	19570	0.70	N
M-A019	17.4	59.8	0.04	0.74	0.06	0	0.52	4.24	0.04	3800.0	14619.84	3800	0.26	N

continued

No.	S^* ($^{\circ}$)	A^* (ha)	F^*	$A_{Is,C}$ (ha)	$A_{Is,T}$ (ha)	$A_{Is,M}$ (ha)	$A_{pls,C}$ (ha)	$A_{pls,T}^*$ (ha)	$A_{pls,M}$ (ha)	$V_{stream\ bed,AT}$ (m^3)	V_{out} (m^3)	$V_{storage,BT}$ (m^3)	$N_{v,BT}^*$	R_f
M-A020	17.0	438.2	0.14	0.20	1.37	0	0.48	22.04	0.04	71100.0	44599.15	71100	1.59	N
M-A021	13.2	416.0	0.39	0.62	0.64	0.15	1.24	8.36	0.68	18304.0	43319.39	18304	0.42	N
M-A022	17.0	665.4	0.66	0.11	1.26	0	5.64	56.6	3.28	52000.0	56352.92	52000	0.92	N
M-A023	13.0	352.1	0.34	0.60	0.94	0	0	5.8	0	58120.0	39456.91	58120	1.47	N
M-A024	16.5	275.9	0.07	0.34	0.13	0	1.6	19.36	0.24	12100.0	34420.01	12100	0.35	N
M-A025	17.2	149.8	0.39	0.17	0	0.07	0.12	6.44	0	17000.0	24449.88	17000	0.70	N
M-A026	11.0	160.0	0.28	0	0	0	0	7.4	0	27250.0	25368.64	27250	1.07	N
M-A027	16.6	304.1	0.03	8.82	7.19	4.31	8.96	38.4	9.2	17175.0	36347.89	53522.89	1.47	Y
M-A028	21.3	123.8	0.14	0.73	0.19	0	0	0	0	1665.0	21974.23	1665	0.08	N

CAUSATIVE FACTORS OF DEBRIS FLOW

It is well known that the geology, topography and hydrogeology conditions of a creek affect the DFS. However, the selection of factors affecting the DFS is quite objective (Chen, et al., 2007). The chosen factors in the DFS model could be much different among different research groups (Lin et al., 2002; Chang and Chao, 2006; Liu et al., 2006).

Three key mechanisms are identified to be the major contributors to the occurrence of debris flow: (1) steep topography, (2) abundant loose debris, and (3) high intensity run-off. It is logical to recognize the factors reflecting the steepness of creek and affecting the debris and run-off supply as significant for the occurrence of debris-flow. Steepness can be fully represented by the slope of creeks $S(^{\circ})$ which is a commonly used causative factor in DFS analysis. The surface run-off is mainly governed by the characteristics of rainfall and watershed. Since the rain-fall is more suitable to be treated as a triggering factor, the influence of run-off on the DFS can be reflected by the catchment area A and form factor F (defined as the catchment area divided by the square of creek length) which were frequently selected in the DFS models.

Bovis and Jakob (1999) highlight the importance of debris supply on the frequency and magnitude of debris flow. The loose debris could be supplied from the deposit on the channel and from a newly occurred landslide or erosion of existing landslides. It is reasonable to classify a creek as high PDFTs if it is full of debris in the upstream and landslides occur frequently in its catchment. However, the debris supply from landslide and the effect of the sediments on the channel are difficult to be quantified, even in a specific steep mountain catchment (Schuerch et al., 2006). Fortunately, a five-year project funded in 2002 was executed in Taiwan by the Central Geological Survey (CGS, 2006). Extensive field investigation for the 1420 PDFTs was conducted. The volume of debris deposit on the upstream channel of creeks after typhoon T was estimated in the field by geologists. Besides, SPOT images are available in the studied area to identify and calculate the landslide area after the geological events. Consequently, the influence of catchment sediment budgets on the DFS can be evaluated.

Debris storage index

A debris storage index N_v is proposed to reflect the debris supply as follows:

$$N_v = V_{\text{storage}} / V_{\text{out}} \quad (1)$$

in which V_{storage} is the storage volume of debris in the catchment of a creek and V_{out} is the outflow volume for a debris-flow event. The debris storage index N_v , to certain extent, reflects how many debris-flow events can be supplied by the debris storage in the catchment of a creek. The empirical equation describing the average outflow volume V_{out} (m^3) in terms of catchment area A (km^2) (COA, 2001) is as follows:

$$V_{\text{out}} = 19498 \cdot A^{0.56} \quad (2)$$

Equation (2) is regressed from the records of debris-flow triggered by typhoon T . The debris deposits in PDFTs will increase if landslide occurred in their catchment. On the other hand, the debris deposits will decrease if the debris-flow occurs. The debris budget of a PDFT can be express as follows:

$$V_{\text{storage}} = V_{\text{stream bed}} + V_{\text{landslide}} - V_{\text{debris outflow}} \quad (3)$$

in which $V_{\text{stream bed}}$ is the volume of debris deposited in the stream bed before landslide and/or debris events, $V_{\text{landslide}}$ is the volume of debris increased after landslides, and $V_{\text{debris outflow}}$ is the volume of debris decreased after debris-flows. Assuming $V_{\text{landslide}}$ equals to $A_{ls} \cdot h_s$ and $V_{\text{debris outflow}}$ equals to $n \cdot V_{\text{out}}$, in which A_{ls} , h_s are landslide area and landslide depth; n is the event number of debris-flow. Thereafter, the volume of debris storage after landslides and/or after debris-flow events can be evaluated if the debris volume deposited on the stream bed before landslides/debris-flow is known in prior. The debris volume deposited on the stream bed ($V_{\text{stream bed}, AT}$) of 54 PDFTs in the studied area during the periods 2003-2004 (after typhoons T and before typhoon M) was estimated by geologist in-situ (CGS, 2006) and listed in Table 1.

Landslide area in the catchment of the PDFTs

Landslide area is a frequently used causative factor for DFS analysis (Lin et al., 2000; Lin et al., 2002). High correlation does exist between the occurrence of debris flow and landslide area (Chen et al., 2007). Three period of landslide area A_{ls} , which mainly triggered by Chi-Chi earthquake ($A_{ls,C}$), typhoons T and M ($A_{ls,T}$, $A_{ls,M}$), in each PDFT were identified by the processed SPOT images from 11/4/1999 to 31/10/1999, from 5/3/2001 to 10/11/2001, and from 12/4/2004 to 13/7/2004. The catchment areas A of the studied PDFTs and the areas of landslides occurred in three periods are listed in Table 1.

Since 1996, 485 hazardous PDFTs in Taiwan were mapped and published by the Council of Agriculture (COA, 1996). Following the Chi-Chi earthquake, typhoon T in 2001 triggered many landslides and debris-flows occurred in the creeks which are not classified as the PDFTs before Chi-Chi earthquake. After typhoon T The number of PDFTs in Taiwan quickly increased to 1420. Therefore, the DFS analysis should account for the influence of existed landslides, as well as the area of landslide “potentially” triggered by a geological event, in the catchment of PDFTs.

Potential landslide area in the catchment of the PDFTs

The “potential landslide area (A_{pls})” of the studied PDFTs in Tungshih were derived from the event-based landslide susceptibility analysis (EBLSA; Lee et al., 2008a; 2008b). Six causative factors (lithology, slope gradient, slope aspect, terrain roughness, slope roughness, and total curvature) were selected in the analysis. Applying the multivariate statistical method, a discriminant function is proposed to evaluate the susceptibility of landslide with event-based landslide inventory. The EBL model is capable of predicting landslides induced by a scenario event such as an earthquake or heavily rainfall. As one of the causative factors, the area of high susceptibility region is selected to represent the “ A_{pls} ”. The calculated area of high susceptibility region for scenario Chi-Chi earthquake ($A_{pls,C}$) and heavily rainfall during typhoons T and M ($A_{pls,T}$, $A_{pls,M}$) are listed in Table 1.

DEBRIS-FLOW SUSCEPTIBILITY ANALYSIS

Following the same approach as the EBLSA, a discriminant function is proposed to evaluate the DFS. Five causative factors (S , A , F , A_{pls} , N_v) are selected in the model. The coefficient vector is solved using a commercial statistical program SPSS. Thus, a discriminant score is obtained as the susceptibility index I . The possibility for the occurrence of debris-flow of a PDFT is increased with the increasing susceptibility index.

For deriving the coefficient vector of the proposed model, the records of the occurrence debris-flow during typhoons T are used. The causative factors of the proposed model are listed in Table 1 (with * marked). The $A_{pls,T}$ is derived from the scenario typhoon T. The $V_{storage}$ before debris flow events during typhoon T ($V_{storage,BT}$) is derived using the $V_{stream\ bed,AT}$ plus $V_{debris\ outflow}$. If the last column of Table 1 is “Y”, $V_{debris\ outflow}$ equals to V_{out} which imply only one debris-flow event is assumed. Therefore, the N_v before typhoon T ($N_{v,BT}$) can be calculated. Since the derived coefficient of catchment area is negative, it is removed from the model. Thereafter, the discriminant function is:

$$I = 0.083 \cdot S + 0.573 \cdot F + 0.019 A_{pls,T} + 0.08 \cdot N_{v,BT} - 2.282 \quad (4)$$

Among these four causative factors, the slope S , the potential landslide area A_{pls} and the proposed debris storage index N_v are significant than form factor F to the occurrence of debris-flow. The predicting performance of the statistical model can be demonstrated by the Relative Operating Characteristic (ROC) diagram (Chen et al., 2007). An area 0.704 under the ROC curve indicates the proposed statistical model is reasonable good.

After the 1999 Chi-Chi earthquake, the rate of expansion in landslide area grew almost 20 times in the Chenyulan River watershed in Taiwan (Lin et al., 2003). It accounts for the increasing number of creek which debris flow occurred in Chenyulan River watershed from 32 (Triggered by Typhoon Herd in 1996) to 103 (Triggered by Typhoon T in 2001) after the 1999 Chi-Chi earthquake. Lin et al. (2003) suggested that understanding the evolutions of landslides is crucial in the hazard assessment for debris flow. Based on the proposed model and the identified landslide area, the evolution of the DFS in the studied 54 PDFTs with geological events is demonstrated as follows.

The high susceptibility landslide area A_{pls} of scenario earthquake and typhoons is incorporated into the proposed model. Besides, the $V_{storage}$ before/after landslide and debris-flow events triggered by Chi-Chi earthquake and followed typhoons was estimated using Equation (3). The average thickness of landslides is assumed as 1.5 meters (shallow landslide). Consequently, the debris storage index N_v and susceptibility index I of different periods can be calculated. The evolution of I and N_v before/after Chi-Chi earthquake ($I_{BCL}, N_{v,BCL} / I_{ACL}, N_{v,ACL}$), after typhoons T ($I_{ATL,BTD}, N_{v,ATL,BTD}$ after landslide triggered and $I_{ATD,BML}, N_{v,ATD,BML}$ after debris-flow triggered), and after typhoon M ($I_{AML,BMD}, N_{v,AML,BMD}$ after landslide triggered) are demonstrated in Figure 2. It is observed in Figure 2 that N_v and I are increased after Chi-Chi earthquake. After typhoon T, N_v and I attains to the highest value but decreased with the occurrence of debris-flow during typhoon T. The N_v and I increased again after typhoon M for the triggered landslides. In addition, the evolution of the number of creek which should be classified as “debris-flow creek” (I greater than zero) is also shown in Figure 2. It is observed that the DFS is well correlates to the debris budget. Consequently, the proposed model can depict the impact of geological events on the DFS, quantitatively.

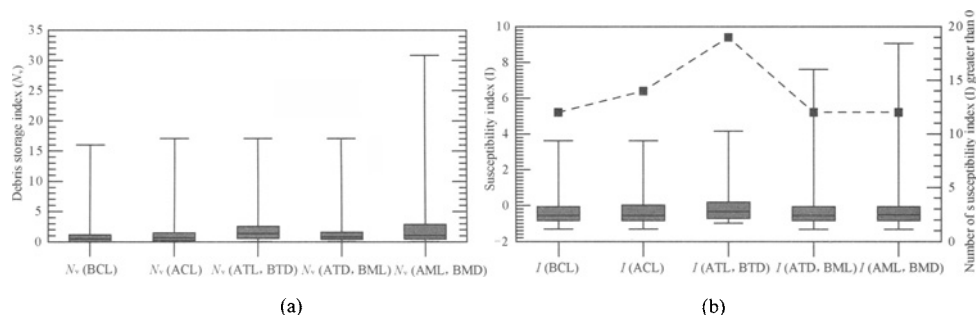


Figure 2. (a) The debris storage index N_v and (b) the susceptibility index I varies with the geological events. The squares represent the number of I greater than zero

CONCLUSIONS

This paper proposed a statistical model for predicting the DFS before and after a geological event such as an earthquake or typhoon. The proposed model fully accounts for the influence of debris budget which are key factors influencing the DFS. The slope of creek, the debris storage index, and potentially landslide area, which derived from a landslide susceptibility analysis, were identified as significant causative factors. By taking the debris budget into account, the DFS evolved with the landslide and debris-outflow was demonstrated. It is depicted that the Chi-Chi earthquake and followed typhoons which triggered tremendous landslides increase the DFS of PDFTs. The debris outflow, on the other hand, reduces the debris storage in PDFTs and reduces their DFS. The potentially landslide area of a scenario geological event can be taken into account in the DFS analysis before the occurrence of the event. Consequently, the anticipated impact of the geological event on the occurrence of debris-flow can be evaluated quantitatively.

REFERENCES

- Bovis M.J., Jakob M. (1999). The role of debris supply conditions in predicting debris flow activity. *Earth Surface Processes and Landforms*, 24: 1039-1054.
- CGS. (2006). Geological investigation of debris flow. Report of Central Geological Survey, Taiwan (in Chinese).
- Chang T.C., Chao R.J. (2006). Application of back-propagation networks in debris flow prediction. *Engineering Geology*, 85: 270-280.
- Chen C.C., Tseng C.Y. and Dong J.J. (2007). New entropy based method for variables selection and its application to the debris-flow hazard assessment. *Engineering Geology*, 94: 19-26.
- COA. (1996). *The map of hazardous debris-flow stream in Taiwan*.
- COA. (2001). *The hazard evaluation of debris-flow stream in central Taiwan after typhoon Toraji*. Report of Council of Agriculture, Taiwan (in Chinese).
- COA. (2003). *The map of hazardous debris-flow stream in Taiwan*.
- He Y.P., Xie H., Cui P., Wei F.Q., Zhong D.L. and Gardner J.S. (2003). GIS-based hazard mapping and zonation of debris flows in Xiaojiang Basin, southwestern China. *Environmental Geology*, 45: 286-293.
- Ho C.S. (1975). An introduction to the geology of Taiwan, explanatory text of the geologic map of Taiwan. *Ministry of Economic Affairs*, Republic of China, 312.
- Jakob M., Hungr O. (2005). *Debris-flow hazards and related phenomena*. Springer, New York, 739.
- Lee C.T., Huang C.C., Lee, J.F., Pan K.L., Lin M.L. and Dong J.J. (2008a). Event-based landslide susceptibility analysis (I)-earthquake-induced landslides. submitted to *Engineering Geology*.
- Lee C.T., Huang C.C., Lee J.F., Pan K.L., Lin M.L. and Dong J.J. (2008b). Event-based landslide susceptibility analysis (II)- storm-induced landslides. submitted to *Engineering Geology*.
- Liao H.W. and Lee C.T. (2000). Landslides triggered by the Chi-Chi earthquake. *Proceedings of the 21st Asian Conference on Remote Sensing 1&2*, 383-388.
- Lin C.W., Wu M.C., Shieh C.L. and Shieh Y.C. (2000). Influence of geology on debris-flows: examples from Hsin-Yi, Nantou County, Taiwan. In: Wiczorek, G.F., Naeser, N.D. (Eds.), *Debris-flow Hazards Mitigation: Mechanics, Prediction, and Assessment*, A.A. Balkema, Rotterdam, Netherlands, 169 - 176.
- Lin P.S., Lin J.Y., Hung J.C. and Yang M.D. (2002). Assessing debris-flow hazard in a watershed in Taiwan. *Engineering Geology*, 66: 295-313.
- Lin C.W., Shieh C.L., Yuan B.D., Shieh Y.C., Liu S.H. and Lee S.Y. (2003). Impact of Chi-Chi earthquake on the occurrence of landslides and debris flows: example from the Chenyulan River watershed, Nantou, Taiwan. *Engineering Geology*, 71: 49-61.
- Liu X., Wang S. (1996). Preliminary research of two-level fuzzy comprehensive evaluation on landslide and debris flow risk degree of a district. *Journal of Natural Disasters*, 5 (3): 51-59.
- Liu Y., Guo H.C., Zou R. and Wang L.J. (2006). Neural network modeling for regional hazard assessment of debris flow in Lake Qionghai Watershed, China. *Environmental Geology*, 49: 968-976.
- Rupert M.G., Cannon S.H. and Gartner J.E. (2003). *Using logistic regression to predict the probability of debris flows occurring in areas recently burned by wild land fires*. Open-file Report of 03-500US Geological Survey.
- Schuerch P., Densmore A.L., McArdeall B.W. and Molnar P. (2006). The influence of landsliding on sediment supply and channel change in a steep mountain catchment. *Geomorphology*, 78: 222-235.
- Su J., Zhou X. and Fan, S. (1993). A fuzzy set evaluation method of hazard degree of debris flow. *Journal of Natural Disasters*, 2 (2): 83-90.

GEOSYNTHETIC REINFORCEMENT FOR RIVERSIDE SLOPE STABILITY OF LEVEES DUE TO RAPID DRAWDOWN

Jie Han

*Department of Civil, Environmental, & Architectural Engineering, University of Kansas
Lawrence, Kansas 66045, USA*

Jianfeng Chen

*Department of Geotechnical Engineering, Tongji University
Shanghai 200092, China; Currently visiting scholar at the University of Kansas*

Zhenshun Hong

*Professor, Institute of Geotechnical Engineering, Southeast University,
Nanjing 210096, China*

Stability of levees depends on a number of factors. Riverside slope instability due to rapid drawdown after storms or other events is one of the factors contributing to possible failure of levees. Rapid drawdown would create difference in water head, which generates seepage force to destabilize the slope. Geosynthetics have been successfully used to stabilize natural and man-made slopes and should be able to be used for protecting the riverside slopes of levees as well. However, limited studies have been conducted so far for this application. In this study, geosynthetic layers were placed horizontally in the riverside slope to ensure its stability during rapid drawdown. The global stability of the levee is guaranteed by the installation of deep mixed walls in the core of the levee, which was investigated in another study. A finite difference method, incorporated in the FLAC (Fast Lagrangian Analysis of Continua) Slope software, was adopted. Geosynthetic layers were modeled using cable elements with grout properties between geosynthetic and soil. The riverside stability of the levee at different conditions (the average service condition, the high water surge, and drawdown from the service condition and the highest water level condition) was examined. This study clearly demonstrates that geosynthetics can enhance the riverside slope stability of the levee by providing tensile resistance to the soil.

INTRODUCTION

The recent levee breakage caused by Hurricane Katrina in August 2005 killed more than 1,000 people and were estimated to cost the U.S. Federal Government more than \$200 billion (Cristo, 2005). Preliminary investigation concluded that levee breaches due to Hurricane Katrina were caused by the water overflow and erosion of the levee and seepage under the levee and weakening of underlying soil (Cristo, 2005). Hess et al. (2006) indicated that “a major flood or earthquake and resulting levee failure in the capital region of Sacramento

alone would put at risk more than 400,000 people and 170,000 structures, with estimated potential damage of between \$7 and \$15 billion”. The Sacramento Area Flood Control Agency (SAFCA) warns that Sacramento has a higher risk of flooding than most U.S. cities including New Orleans. In addition to the erosion of the levee, the seepage under the levee, and the weakening of underlying soil, rapid drawdown after storms or other events can cause the instability of riverside slopes, which would affect the overall stability of the levee.

Ground improvement technologies, such as deep mixing (DM), vibrocompaction, compaction grouting etc., have been used to mitigate potential damage to levees. Earlier studies have demonstrated that DM columns can increase the stability of highway embankments over soft soils (Han et al., 2005). Han et al. (2008) also demonstrated that deep mixed walls installed in the core of the levee can stabilize the levee by providing more shear and bending resistance and lowering the groundwater table in the landside slope. However, deep mixed columns are difficult to be installed on the slope. Due to ease for installation, geosynthetics have been commonly placed parallel to the slope. To date, however, limited studies have been conducted to investigate the effect of geosynthetics on the riverside slope stability of levees due to rapid drawdown.

This paper presents a numerical study to demonstrate how geosynthetics can enhance the stability of levees due to rapid drawdown from the service condition and the highest water level condition.

NUMERICAL MODELING

Problems for analysis

Levees at four different conditions as listed in Table 1 and shown in Figure 1 were investigated in this study. In the analysis, a deep mixed wall was installed in the core of the embankment for the global stability of the levee. The thickness of the DM wall was assumed to be 3m, which is the same as the width of the crest. In practice, it can be formed by DM columns in wall or grid patterns. The 3m thick DM wall is considered as a composite wall treated by deep mixing. The global stability of the levee treated by the DM wall was investigated by Han et al. (2008) in another study. Details of that study can be found in that paper and are not repeated herein. The current study is focused on the stability of the riverside slope due to rapid drawdown after storms or other events. The water at the mid-height of the levee with steady seepage through the levee is considered as the average service condition in this study. The surging water at the full height of the levee but with steady seepage still at the previous average service stage is considered as a special event in which water rises suddenly

Table 1. Conditions considered in the analysis

Condition	Condition	Description
1	Average service condition	Water at the mid-height of the levee (steady seepage established)
2	Water surge to top	Surging water at the full height of the levee (steady seepage at the landside still at Condition 1)
3	Drawdown from service condition to bottom of river	Water level lowered from the mid-height to the bottom of the river (steady seepage in the levee still at Condition 1)
4	Drawdown from top water level to average service condition	Water level lowered from the top water level to the mid-height (steady seepage in the levee still at Condition 1)

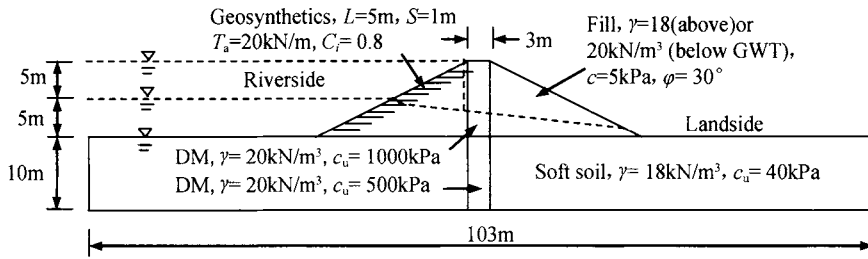


Figure 1. Cross-section of levee for analysis

from the mid-height to the full height due to flood, hurricane, etc. The water at the full height of the levee with steady seepage established at the current condition is considered unlikely thus not considered in this study because the surging water is rarely maintained at the highest level for a long period and the low permeable DM wall in the core acts as a barrier to prevent the water level from rising in the landside slope.

Geometry and material properties

Figure 1 presents the geometry and dimensions of a selected levee for analysis in this study. The cross-section of the levee meets the basic requirements by US Army Corps of Engineers (2000). The 10m high levee was built on the 10m thick soft soil underlain by a firm soil layer or bedrock. The levee had 2:1 slopes on both sides. The crest of the levee was 3m and treated by the DM wall.

Deep mixed columns were installed in continuous wall patterns, which were modeled as 2-D deep mixed walls. Mohr-Coulomb failure criteria were used for the levee, the soft soil, and the deep mixed walls. Geosynthetic layers were modeled using cable elements with grout properties between geosynthetic and soil. The physical and mechanical properties of the soft soil, the levee fill, and geosynthetics are presented in Figure 1. The soft soil was considered failing under an undrained condition. The fill below or above the ground water table had a different unit weight but the same strength values. Due to the difference in the properties of the soft soil and the fill, the DM wall within the soft soil and the fill had different strength values.

Stability analyses were conducted for unreinforced and reinforced riverside slopes using geosynthetics due to rapid drawdown. The geosynthetic layers had allowable tensile strength $T_a = 20\text{kN/m}$, length $L = 5\text{m}$, spacing $s = 1\text{m}$, and interaction coefficient between geosynthetic and soil $C_i = 0.8$.

The free surface lines shown in Figure 1 were determined based on a theoretical solution for seepage through an earth dam on an impervious base, which can be found in many geotechnical engineering textbooks, such as Das (2001). It was assumed that the soft soil had much lower permeability than the levee fill, therefore, the theoretical solution can be applied. At the riverside, there are three water table levels: bottom, mid-height, and full height.

Factor of safety

In recent years, numerical methods have been increasingly used for analyzing slope stability including the computation of its factor of safety (FoS). Han et al. (2002a) used the finite

difference software (FLAC) to obtain the identical corresponding FoS values of unreinforced and geosynthetic-reinforced slopes as the Bishop's simplified method. However, Han et al. (2005) found that the limit equilibrium method may overestimate the factor of safety for embankments over soft soil improved by DM walls, especially when the DM walls fail due to bending or rotation rather than shear. Therefore, the numerical method incorporated in the FLAC Slope 5.0 can be used for this analysis (Itasca Consulting Group, Inc., 2006).

In the finite difference program, a shear strength reduction technique was adopted to solve for the FoS value of slope stability. Dawson et al. (1999) exhibited the use of the shear strength reduction technique in this finite difference program. In this technique, a series of trial FS values were used to adjust the cohesion, c and the friction angle, ϕ , of soil. Adjusted cohesion and friction angle of soil layers were used in the model for equilibrium analysis. The factor of safety was determined by adjusting the cohesion and friction angle to make the slope become unstable from a verge stable condition or verge stable from an unstable condition.

ANALYSIS OF NUMERICAL RESULTS

Average service condition

Figure 2 presents the numerical results for the DM-treated levee at an average service condition (i.e., water at the mid-height). In this case, steady seepage was assumed for a long-term condition. No continuous slip surface can be identified, however, there was a tendency for a slide developing in front of the DM wall towards the landside. US Army Corps of Engineers (2000) recommended that new levees should have an FoS greater than 1.4 for long term (steady seepage). Therefore, the factor of safety for this case is satisfactory at the average service stage.

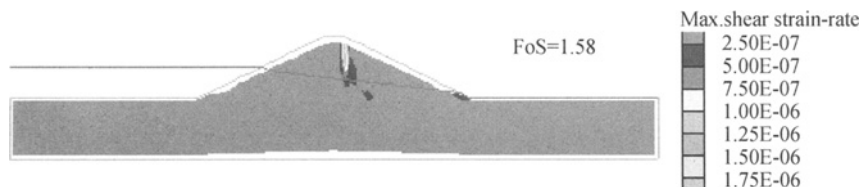


Figure 2. Stability of the levee at the average service condition (without geosynthetic)

Water surge to top

Water surging typically occurs during a special event, such as flood, hurricane, etc. so that the rise of water table is within a very short period. In this analysis, the water table at the riverside was assumed to rise from the mid-height to the full height but the water table under the crest and at the landside was assumed to remain at the same elevation as the average service condition. As shown in Figure 3, the maximum shear strain rate developed behind the DM wall and no clear slip surface formed. The factor of safety for the DM-treated levee at this stage was 1.27, which decreased from 1.58 at the average service condition. In other words, the water surging destabilized the levee. US Army Corps of Engineers (2000) did

not specify the requirements for a water surging condition, however, the required factor of safety for a rapid drawdown case is 1.0 to 1.2. Typically, a factor of safety equal to 1.1 is used in practice. Therefore, the factor of safety for this case should be high enough to ensure the temporary stability of the levee during the water surging.

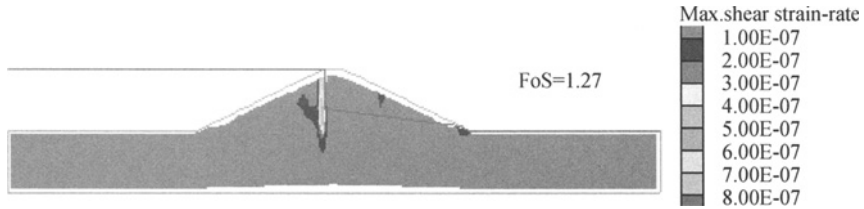


Figure 3. Stability at the water surge to top of the levee (without reinforcement)

Rapid drawdown from average service condition

Figure 4 presents the numerical results for the stability of the levee due to rapid drawdown of the water level from the average service condition to the bottom of the river. As compared with Figure 2, it is shown that the rapid drawdown reduced the factor of safety from 1.58 to 1.14 for the unreinforced riverside slope. The use of geosynthetic layers as shown in Figure 4(b) increased the factor of safety from 1.14 (unreinforced) to 1.31 (reinforced). In this case, both unreinforced and reinforced slopes are stable.

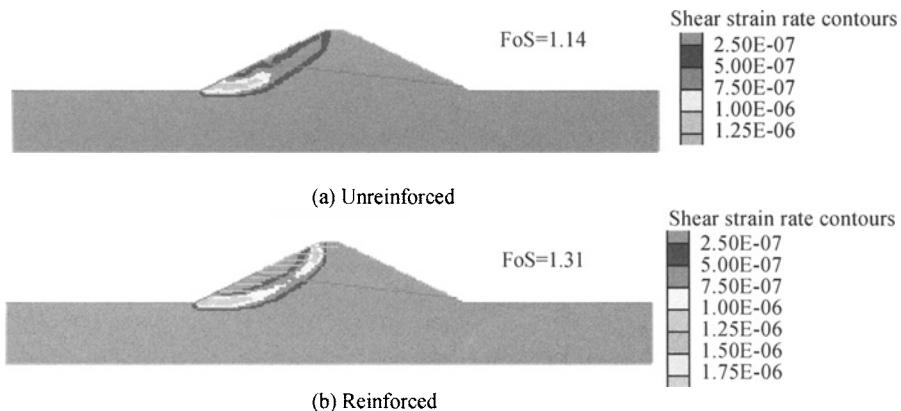


Figure 4. Stability of the levee due to rapid drawdown from the service condition

Rapid drawdown from top water level to average service condition

Figure 5 presents the numerical results for the stability of the levee due to rapid drawdown of the water level from the top water level (i.e., full-height) to the average service condition. This situation most likely happens after flood or hurricane, etc. As compared with Figure 3, the rapid drawdown reduced the factor of safety from 1.27 to 1.01, which is at a verge of failure. Figure 5(b) shows that the use of geosynthetics at the riverside slope increased the factor of safety from 1.01 (unreinforced) to 1.17, which meets the typical requirement of the factor of safety greater than 1.1.

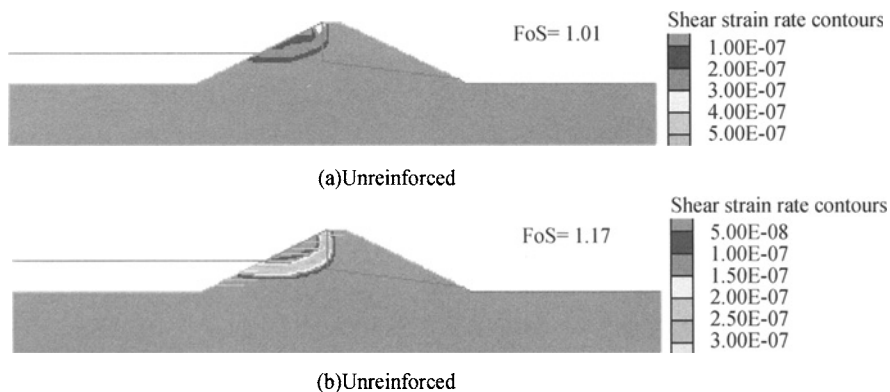


Figure 5. Stability of the levee due to rapid drawdown from the top water level to the service condition

CONCLUSIONS

This numerical analysis clearly shows that water surging would reduce the factor of safety of the levee in the overall stability. However, rapid drawdown reduced the factor of safety of the riverside slope of the levee. Geosynthetics could effectively enhance the stability of the riverside slope and protect it from failure due to rapid drawdown.

REFERENCES

- Cristo R. (2005). Researchers learn from Katrina disaster. *The Record - News*, October 19.
- Das B.M. (2001). *Principles of geotechnical engineering*. 5th edition. Thomson Learning, 589
- Dawson E.M., Roth W.H. and Drescher A. (1999). Slope stability analysis by strength reduction. *Geotechnique*. 49(6): 835-840.
- Han J., Hong Z.S. and Shen S.L. (2008). Stability of levees over soft soil improved by deep mixing technology. *Accepted for ASCE G-I GeoCongress*, New Orleans, March, 9-12.
- Han J., Leshchinsky D. and Shao Y. (2002). Influence of tensile stiffness of geosynthetic reinforcements on performance of reinforced slopes. *Proceedings of Geosynthetics – 7th ICG*, Delmas, Gourc & Girard (eds), Swets & Zeitlinger, Lisse, 197-200.
- Han J., Parsons R.J., Sheth A.R. and Huang J. (2005). Factors of safety against deep-seated failure of embankments over deep mixed columns. *Proceedings of Deep Mixing 2005 Conference*, Sweden, 1,2(23-25): 231-236.
- Hess J.R., Sills G.L., Costa R. and Shewbridge S. (2006). California's levees at risk. *Geo-Strata*, November/December, 24-28.
- Itasca Consulting Group, Inc. (2006). *FLAC/Slope User's Guide*, Version 5.0. 84.
- US Army Corps of Engineers. (2000). Design and construction of levees. *Engineering Manual*, EM 1110-2-1913, 77.

STUDY ON EARTHQUAKE AND TYPHOON INDUCED REGIONAL DEBRIS FLOWS IN TA-CHIA RIVER, TAIWAN

Ming-Chin Ho, Chien-Jung Chen and Yei-Sain Lee
Architecture and Building Research Institute, Ministry of the Interior, Taipei
23143, Taiwan, China

Cheng-Yu Ku, Sue-Yung Chi
Sinotech Engineering Consultants, Inc., Taipei, 11071, Taiwan, China

Large-scale debris flow hazards occurred in Ta-Chia River watershed during typhoons that passed through Taiwan from 2001 to 2005 without forewarning. Especially, the Minduli typhoon event in 2004 hit Taiwan which caused severe property damage and inflicted heavy casualties. Though landslide-induced debris flows present a hazard that is being increasingly recognized, such a large-scale debris flow hazard in Ta-Chia River watershed still appears to be particular. In this paper, we present a detailed study on the occurrence of regional debris flow hazard in Ta-Chia River watershed and reveal the trigger mechanism of the landslide and debris flow. Our findings indicate that the regional debris flow hazards were mainly caused by the huge amount of sparsely deposited materials from landslides triggered by Chi-Chi earthquake. Rapidly increasing water pressure caused by typhoon events provided a powerful force that moved the sparsely deposited materials into gullies and then triggered the debris flow movement. A strong coupling between the spatial distribution of rainfalls and the occurrence of regional debris flows is also addressed.

INTRODUCTION

Observations of landslides and debris flows have been reported for many decades. Historically typhoon events with high-intensity, long-duration rainfall often triggered shallow, rapidly moving landslides, i.e. debris flows, resulting in casualties and property damage in Taiwan along the past decades. It is widely recognized that slope instability can be caused by increased subsurface pore pressures during periods of intense rainfall, which reduce the shear strength of hillslope materials. A number of studies have demonstrated that rainfall-induced landslides can be transformed into debris flows as they move downslope.

Large-scale debris flow hazards occurred in Ta-Chia River watershed during typhoons that passed through Taiwan from 2001 to 2005 without forewarning. Especially, the Minduli typhoon event in 2004 hit Taiwan which caused severe property damage and inflicted heavy casualties. Though landslide-induced debris flows present a hazard that is being increasingly recognized, such a large-scale debris flow hazard in Ta-Chia River watershed still appears to be particular. On September 21, 1999, the Chi-Chi earthquake was triggered near Chi-Chi in central Taiwan. Though this earthquake triggered numerous landslides and severely

disturbed montane slopes, the debris flow hazard did not appear in the first two years after this earthquake. Post-earthquake watershed restoration works progressed without disruptions until several typhoon events with intense rainfall, such as (1) Toraji in 2001, (2) Minduli in 2004, (3) Airi in 2004, and (4) Hytarn in 2005, hit Taiwan and triggered numerous debris flows in central Taiwan and caused significant property damage and inflicted heavy casualties in regional scale.

In this paper, we present a detailed study on the occurrence of regional debris flow hazard in Ta-Chia River watershed and reveal the trigger mechanism of the landslide and debris flow. To explore the coupling between the Chi-Chi earthquake and sequential regional debris flow hazards in Ta-Chia River watershed, the remote sensing data, Digital Elevation Model (DEM), historical landslides, and rainfall data were adopted in this study. For characterizing temporal aspects of the hazard, aerial photographs and satellite images of multi-temporal stages were adopted. Spatial distribution of landslides and rainfall characteristics were also discussed.

MAJOR DEBRIS-FLOW STORM EVENTS IN THE STUDY AREA

The study region includes a major river, named Ta-Chia river, one of the abundant water resources in central Taiwan as shown in Figure 1. The watershed area is about 1,236 km². The elevation of the highest mountain in the watershed is around 3,875 m. The river stretch extends 124 km from upstream to the sea. There are also many tributaries along the Ta-Chia river. In our study region, about 20 tributaries were found between Te-Chi dam and Ma-An dam. Since severe debris flow hazards were occurred in this region, the following discussion focused on it.

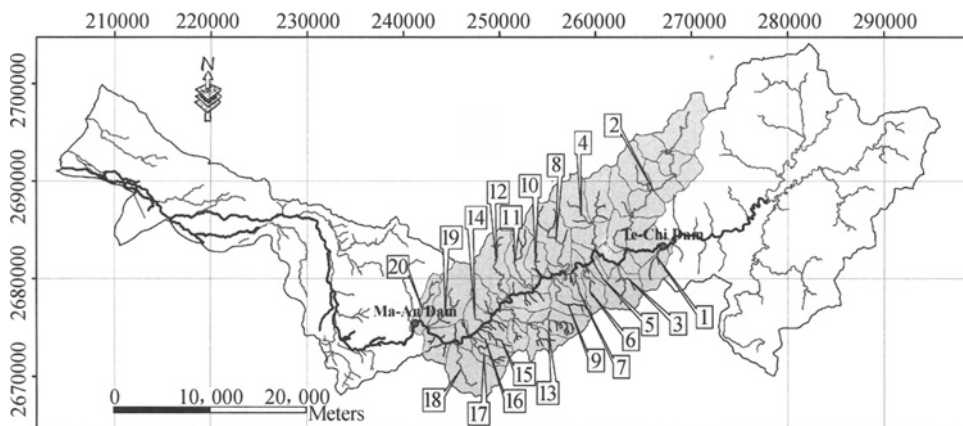


Figure 1. Study region and tributaries

During 1996 to 2005, according to the Central Weather Bureau of Taiwan, the following storm events including typhoon Herb in 1996, typhoon Toraji in 2001, typhoon Minduli in 2004, typhoon Airi in 2004, and Hytarn in 2005 have hit the study area. Within this period, the Chi-Chi earthquake on 21 September 1999 which is the largest in Taiwan for 50 years, was also occurred. This typhoon-earthquake-typhoon sequence represents a natural

experiment that provides quantitative information about the impact of a large earthquake on landslides and transfer of sediment to debris flows.

OCCURRENCE OF REGIONAL DEBRIS FLOW HAZARDS

Landslide mapping

Multi-temporal remote sensing data including aerial-photograph and SPOT satellite imagery were used for landslide mapping. For characterizing temporal aspects of the debris flows, remote sensing data include aerial photographs and satellite images of five temporal stages which are the stage before and after Chi-Chi earthquake, the stage after typhoon Toraji, the stage after typhoon Minduli, the stage after typhoon Airi and Hytarn. Table 1 shows before and after the Chi-Chi earthquake (1989) the landslide rates are 0.68% and 7.54% respectively. After typhoon Toraji in 2001, typhoon Minduli in 2004, and typhoon Airi in 2004, the landslide rates are 6.05%, 7.80%, and, 6.92% respectively. Comparing the landslide rate from these events, it is found that the Chi-Chi earthquake has caused significant landslides in the study region.

Table 1. Landslide area mapping from multi-temporal remote sensing data

	Landslide area (km ²)	Landslide rate	Increase area (km ²)	Increase rate
Before Chi-Chi earthquake	2.69	0.68%	-	-
After Chi-Chi earthquake	29.91	7.54%	28.34	7.15%
After typhoon Toraji	23.99	6.05%	6.68	1.68%
After typhoon Minduli	30.94	7.80%	14.04	3.54%
After typhoon Airi	27.43	6.92%	6.68	1.69%

Note: The landslide rate is the landslide area divided by watershed area.

Furthermore, we computed the new landslides triggered by each event and found that the increase rates of slope failures occurred by these events are 7.15%, 1.68%, 3.54%, and, 1.69% for four events including the Chi-Chi earthquake, typhoon Toraji, typhoon Minduli, and typhoon Airi, respectively. Accordingly, we have revealed that the Chi-Chi earthquake with the landslide increase rate of 7.15% is the major event for inducing the landslides and typhoon Minduli with the landslide increase rate of 3.54% is the second. From the results of landslide mapping as shown in Figure 2, we found that the landslides were most located in the areas between Te-Chi dam and Ma-An dam.

Analysis of rainfall characteristics

Precipitation data from more than 20 rainfall stations operated by Water Resources Agency of the Taiwan Ministry of Economic Affairs and other government agencies in the watershed were adopted for conducting the rainfall frequency analysis. The results of the frequency analysis were represented as the return period of rainfall. The return period of a storm event is the expected value of its average value measured over a very large number of occurrences. We plotted contours of the 200-year return period of rainfall for each gauging station in Ta-Chia river watershed as shown in Figure 3. Results demonstrated that the spatial

distribution of the precipitation in the study region mainly concentrated around the upper Gu-Gang rainfall station.

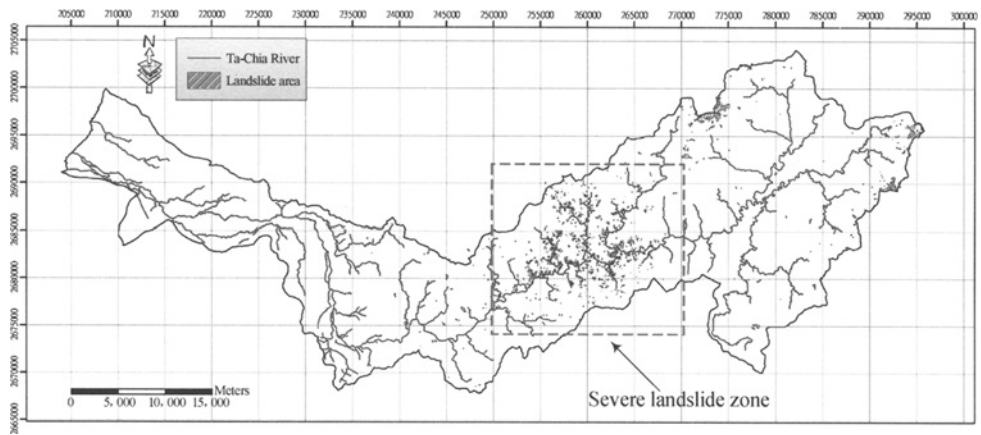


Figure 2. Spatial distribution of landslide areas

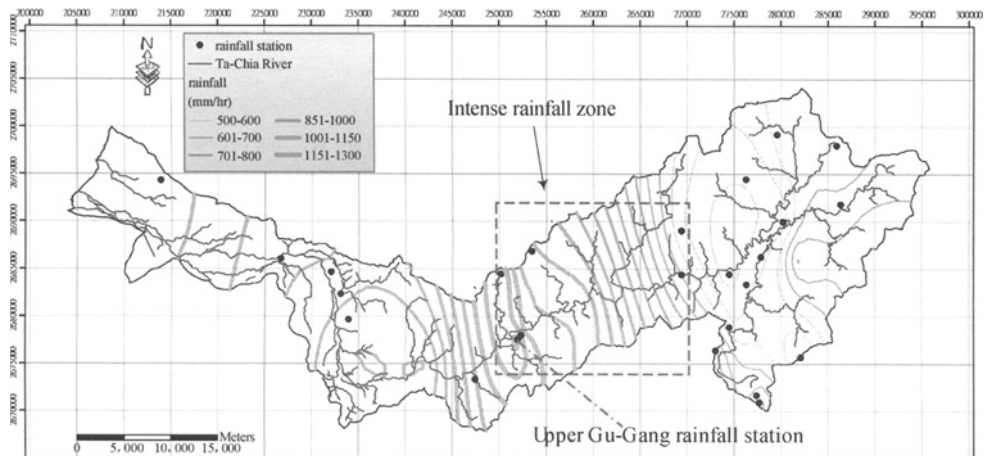


Figure 3. Spatial distribution of rainfall characteristics

Characteristics of major debris flows

Before the Chi-Chi earthquake, no observations of debris flows have been reported for decades. After the Chi-Chi earthquake and the first typhoon Toraji hit the region in 2001, three branch rivers (# 13, #14, and #17, shown in Figure 1) with the occurrence of debris flow have been reported. Severe debris flow hazards have been reported during the typhoon Minduli in 2004. The occurrence of debris flow was found in almost all of the branches, except one in the downstream. The following two typhoon events such as Airi in 2004 and Hytarn in 2005 also moved huge amount of debris sediment from these branch rivers into the main Ta-Chia river.

A debris flow is usually triggered by heavy rainfall over mountainous areas. It is made up of mud, soils, gravels, rocks, and water. Solids or soils on steep slopes slide downward due to weathering processes and mechanical influence such as gravity. From the occurrence of the debris flow hazard in the study area, it is obvious that the weathering process is not the major cause for creating such a large scale of the debris flow hazard. The mechanical influence from the Chi-Chi earthquake disturbed montane slopes, thus setting the conditions for the occurrence of the regional debris flows.

From the results of landslide mapping as shown in Figure 2, we found that the landslides were most located in the areas between Te-Chi dam and Ma-An dam. Comparing Figures 2 and 3, it is found that the regional debris flow hazards in Ta-Chia river watershed are strong related to the spatial distribution of rainfalls.

FORMATION OF DEBRIS FLOW

Figure 4 shows multi-temporal aerial-photographs of the formation of a debris flow. In this figure, the four stages including before and after Chi-Chi earthquake, after typhoon Toraji, and after typhoon Minduli of aerial-photographs were presented. Before the Chi-Chi earthquake (1998), it was clear that the branch # 14 was just a regular gully that the water flow only presents in precipitation. In 1999 (after the Chi-Chi earthquake), landslides initiated from the source areas but no debris flow occurred. In 2001, typhoon Toraji hit this region. Field reconnaissance of this study area revealed that the trigger mechanism of this debris flow took place in two stages: the primary slope failure was due to the Chi-Chi earthquake from the source area. The hydraulic movement was transferred to the landslide mass of the source area flowing into brook track, following slope surface exposure to the action of running water.

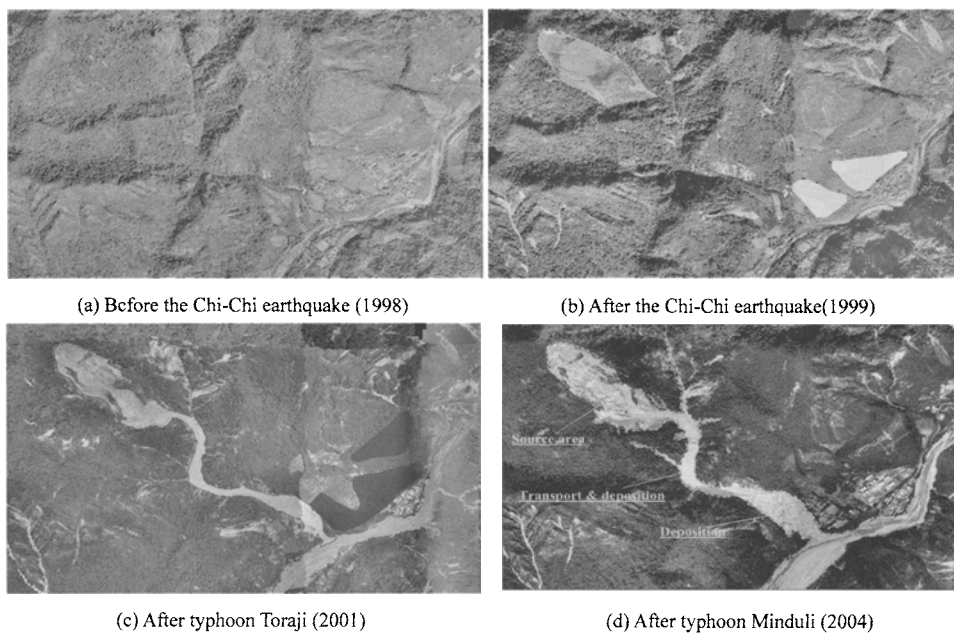


Figure 4. Trigger mechanism of the debris flow occurrence in the study area

Debris flows are commonly triggered by the sudden increase in pore water pressure on the material. This rapid increase in pore water pressure, however, may not always be attributable to the infiltration of precipitation. In this study case, the debris flow resulted from the mixing of rock fragments, fine fractions and water, moving together down gully, and finally deposited in downstream of the gully in which the slope angles for each phase is ranging from about 35, 11.5, and 9.5 degrees, respectively.

CONCLUSIONS

In this study, we have revealed that the Chi-Chi earthquake with the landslide increase rate of 7.15% is the major event for inducing the landslides and typhoon Minduli with the landslide increase rate of 3.54% is the second in the study area. From the occurrence of the debris flow hazards in the study area, it is obvious that the weathering process is not the major cause for creating such a large scale of the debris flow hazard. The mechanical influence from the Chi-Chi earthquake disturbed montane slopes, thus setting the conditions for the occurrence of the regional debris flows. Analysis results from the spatial distribution of rainfall in the study region demonstrated that the regional debris flow hazards in Ta-Chia river watershed are strong related to the spatial distribution of rainfalls.

REFERENCES

- Ku C. Y., Kao H. C., Weng M. C. and Lin C. C. (2006). *Study on rockfall hazard mitigation for hillside resident communities*. Architecture and Building Research Institute, Ministry of the Interior, Taiwan.
- Taiwan Power Company. (2006). *Investigation and strategy study of landslide and debris flows in ta-chia reiver basin between Te-Chi to Ma-An*.
- Keefer D. K., Wilson R. C., Mark R. K., Brab E. E., Brown W. M., Ellen S. D., Harp E. L., Wieczorek G. F., Alger C. S. and Zarkin, R. S. (1987). Real-time landslide warning during heavy rainfall, *Science*, 238: 921-925.
- Iverson R.M. (2000). Landslide trigger by rain infiltration. *Water Resour Res.*, 36(7): 1897-1910.
- Chen Hongey, Dadson Simon and Chi Yi-Guan. (2006). Recent rainfall-induced landslides and debris flow in northern Taiwan, *Geomorphology*, 77: 112-125.

INSTRUMENTED FULL SCALE TEST AND NUMERICAL ANALYSIS TO INVESTIGATE PERFORMANCE OF BAMBOO PILE-MATTRESS SYSTEM AS SOIL REINFORCEMENT FOR COASTAL EMBANKMENT ON SOFT CLAY

Masyhur Irsyam, Sugeng Krisnanto

Civil Engineering Department, Faculty of Civil and Environmental Engineering, Bandung Institute of Technology, Jl. Ganesha 10, Bandung 40132, Indonesia

S. P. R. Wardhani

Civil Engineering Department, Faculty of Engineering, Diponegoro University, Jl. Prof. Soedarto, S. H., Tembalang, Semarang 50239, Indonesia

Bamboo pile-mattress is a system that combines both bamboo piles and bamboo mattress for reinforcement embankment on soft clay. This system utilizes bamboo piles to act as friction piles and bamboo mattress to distribute embankment load uniformly, to alter critical failure surface, and to provide upward buoyancy pressure. The system has been utilized in several projects for coastal embankment on soft clay in Indonesia and has been proven reliable and durable. To investigate the performance of the system, instrumented full scale test was conducted at near shore area at Tambak Oso, Surabaya. At the area, very soft to medium clay layer was found until 30 m below ground surface. Stability analysis and settlement prediction was performed using analytical and numerical methods. The numerical method analysis was conducted using finite element method utilizing a commercial program package. Trial embankment was performed in several fill stages followed by observation of embankment stability and ground settlement. Field observation indicated that embankment using bamboo pile-mattress system showed adequate stability against slope failure and bearing capacity failure and actual settlement was also close to predicted settlement. Hence, bamboo pile-mattress system is proven to be reliable as ground reinforcement and to distribute settlement more uniformly and the calculation method was fit with actual condition.

INTRODUCTION

Several treatments have been used to reinforce coastal embankment on soft clay. Bamboo pile-mattress system was proposed as a reliable and cheap alternative of ground reinforcement for coastal embankment on soft clay for coastal area of Java. This system utilizes bamboo piles to act as friction piles and bamboo mattress to distribute embankment load uniformly, to alter critical failure surface, and to provide upward buoyancy pressure. This system was used in several projects of embankment on soft clay and has been proven reliable and durable. However the previous designs were based on an assumed calculation method. Full scale test program was performed to investigate the performance of the system and to check the calculation. The test was performed at near shore area at Tambak Oso, Surabaya.

SOIL CONDITION AT FIELD TEST LOCATION

First layer at field test location has characteristics of 25 to 45 m thickness of very soft soil layer having $q_c = 0-15 \text{ kg/cm}^2$ and N-SPT value 1 to 2. Stiff to very stiff clay was found below the first layer (PT Citra Marga Nusaphala Persada Tbk., 1998). Soil properties used for analysis are presented in Table 1.

Table 1. Soil properties at test location (PT. Utama Karya (Persero), PT. Citra Marga Nusaphala Persada Tbk, LPPM Institut Teknologi Bandung, 2005)

Depth (m)	Soil Type	c (kN/m ²)	ϕ (°)	γ (kN/m ³)	e_o	C_c
0-23	very soft clay	6-15	1	14	2	0,9
23-25	soft clay	15-35	1	15	1,8	0,8
25-30	médium clay	35-55	1	16	1	0,75
below 30	stiff to very stiff clay	55-150	1	16		

STABILITY AND SETTLEMENT ANALYSIS BEFORE TEST

Embankment stability and ground settlement analysis was performed before field test to ensure that ground soil has adequate bearing capacity, to ensure that the trial embankment stable against slope failure and to predict immediate and consolidation ground settlement. Stability and settlement analysis was performed using analytical and numerical methods. The numerical method analysis was conducted using finite element method utilizing a commercial program called PLAXIS (Brinkgreve & Vermeer, 1998). The analysis was performed for the first stage fill until an embankment height of 2.5 m and for the second stage fill until a final embankment height of 3.25 m.

In analytical method, immediate settlement was calculated by modeling soil as elastic material whereas consolidation settlement was calculated using Terzaghi's one dimensional consolidation theory (Terzaghi, 1967). Modulus elasticity for immediate settlement calculation was obtained from correlation of modulus elasticity with overconsolidation ratio and plasticity index from Jamiolkowski (1979). In consolidation analysis, bamboo piles were modeled as group of piles and stress increase due to embankment load was assumed to follow load transfer of friction pile proposed by Tomlinson (1977). In finite element analysis, subsurface soil and embankment were modeled as elastic-plastic solid material using Mohr-Coulomb failure criteria whereas bamboo piles and mattress were modeled as elastic-plastic springs and elastic plastic beams respectively. Stability analysis was performed using $c-\phi$ reduction method provided in the program and settlement analysis was performed using modulus elasticity of soil in undrained and drained condition and by modeled pore water pressure dissipation.

Stability analysis showed that safety factor of the embankment at end of construction was 1.6 (for embankment height 2.5 m) and 1.3 (after additional fill to 3.25 m). Using analytical method, immediate settlement was predicted to be approximately 35 cm and consolidation settlement was predicted to be approximately 54.5 cm, whereas using finite element method, immediate settlement was predicted to be approximately 40 cm and consolidation settlement was predicted to be approximately 58 cm. Output of settlement analysis using finite element method is presented in Figure.

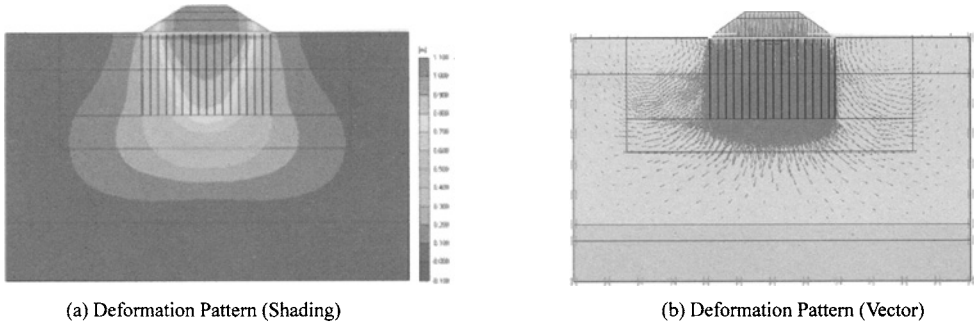


Figure 1. Settlement prediction using finite element method

Construction of trial embankment

The trial embankment was 58 m long, 16.5 wide and 3.25 m high as shown in Figure 2. Ground soil was reinforced by 10 m depth bamboo piles and 4 layers bamboo mattress. Bamboo used for the trial embankment had 5 to 10 cm diameter. Woven geotextile having tensile strength 50 kN/m was used as separator between fill material and bamboo mattress. There was no special treatment on bamboos before used since after construction bamboos were always in soaked condition and therefore were preserved (Frick, 2004). As shown in Figure 2 (a) and Figure 2 (b) seven settlement plates and three piezometers were installed to monitor ground settlement and pore pressure dissipation below embankment respectively.

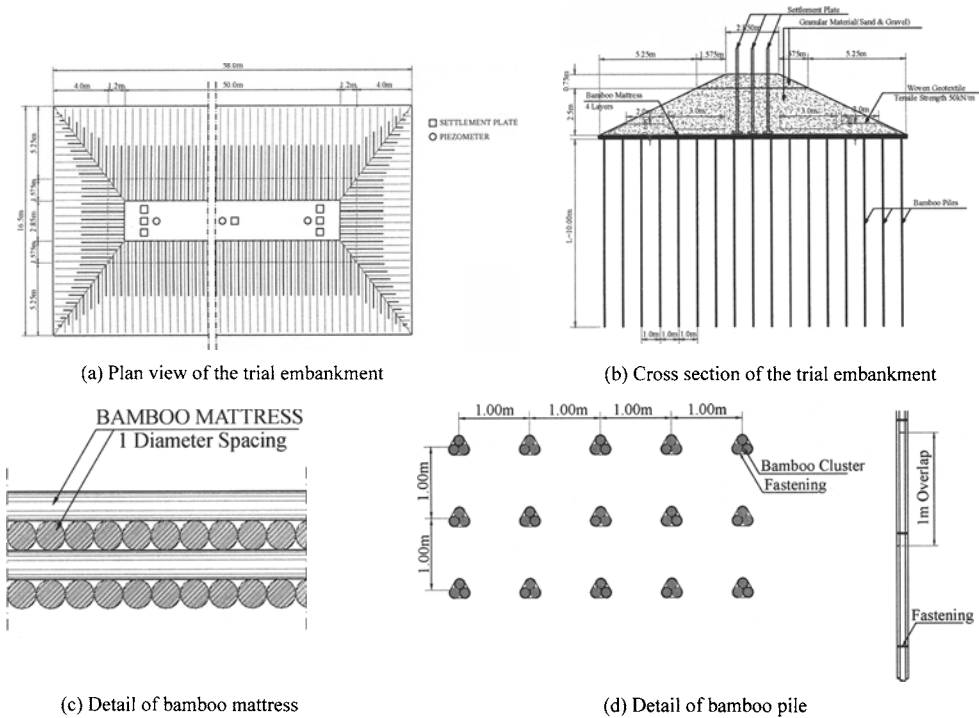


Figure 2. Detail of the trial embankment

Construction of trial embankment was performed by installing bamboo piles and then placing bamboo mattress above the piles. After geotextile was laid above bamboo mattress, granular material as fill material was placed and compacted layer by layer. Embankment fill was performed in two stages, first stage until embankment height of 2.5 m and second stage was to add fill until final height of embankment was 3.25 m. Construction of the trial embankment is presented in Figure 3.



(a) Installation of bamboo piles



(b) Installation of bamboo mattress



(c) Embankment fill



(d) Trial embankment at final condition

Figure 3. Construction of trial embankment

Monitoring

Monitoring of embankment stability and ground settlement was performed from May 26, 2005 to September 6, 2005. Stability monitoring showed that trial embankment did not exhibit slope failure as well as bearing capacity failure that was conformed to prediction analysis. Ground settlement monitoring showed that consolidation settlement until the end of observation was relatively uniform and close to calculated settlement. Average rate of consolidation for the settlement plates decreased from 9 mm/day at the beginning of consolidation process to 0.9 mm/day at the end of observation. Based on tamerate consolidation settlement calculation, after 3 months (at the end of observation) the amount of consolidation settlement reached 30 % of total consolidation settlement. Summary of settlement observation for all settlement plates and predicted tamerate consolidation is presented in Figure 4. From the observation it is proven that pile-mattress system reliable to

act as ground reinforcement and to distribute settlement more uniformly and the calculation method was also fit with actual condition.

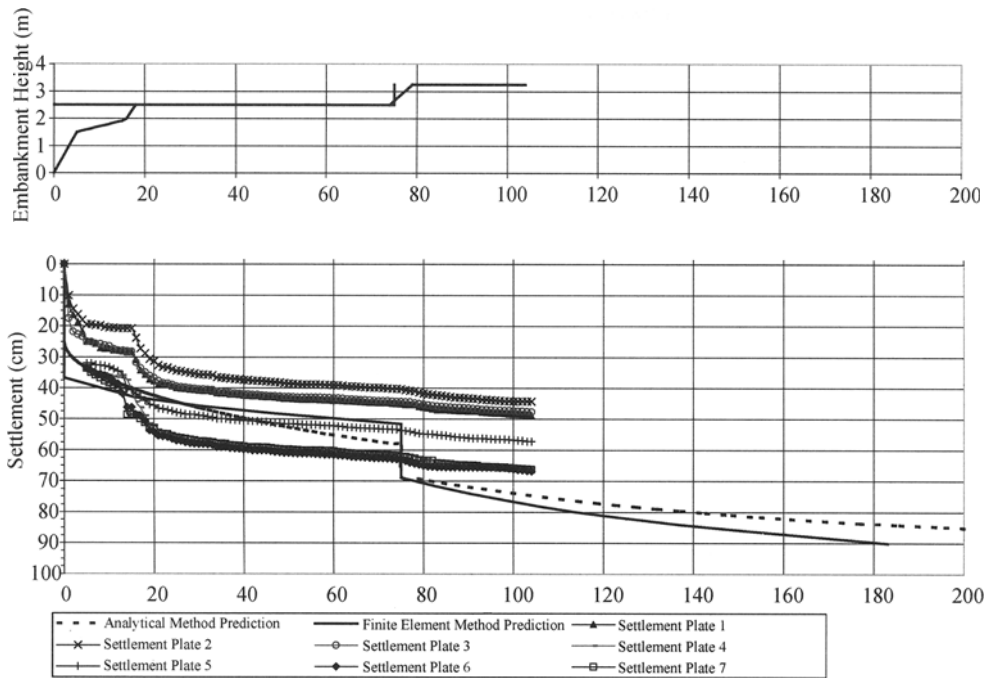


Figure 4. Monitoring and prediction settlement result

CONCLUSION

1. From the observation, it is concluded that using bamboo pile-mattress system:
 - Reinforced soil has adequate bearing capacity to sustain embankment load
 - Embankment has adequate slope stability
 - Consolidation settlement is relatively uniform (14.9 cm to 17.5 cm after 3 months observation)
 - After 3 month, average rate of consolidation is decreased from 9 mm/day to 0.9 mm/day and when compared to settlement prediction, at 3 month, timerate consolidation has reached 30%.
2. Bamboo pile-mattress system is proven to be reliable and hence can be used as ground reinforcement for coastal embankment having height 3.25 m on a thick soft soil layer.

ACKNOWLEDGEMENT

The full scale test was performed by PT. Hutama Karya (Persero), PT Citra Marga Nusaphala Persada Tbk., and Lembaga Penelitian dan Pengabdian Masyarakat (LPPM) of Bandung Institute of Technology as a collaborative research in 2005. Construction of trial embankment was performed by PT. Hutama Karya (Persero).

REFERENCES

- Brinkgreve and Vermeer. (1998). *PLAXIS: finite element code for soil and rock analyses*. A. A. Balkema, Rotterdam.
- Frick H. (2004). *Ilmu konstruksi bangunan bambu, pengantar konstruksi bambu (Introduction to Bamboo Construction)*. Penerbit Kanisius – Soegijapranata University Press, Semarang.
- Jamiolkowski M., Lancellotta R., Marchetti S., Nova R. and Pasqualini E. (1979). Design parameters for soft clays. *Proc. 7th Eur. Conf. on Soil Mech. Found. Engng.*, 5: 21-54, Brighton.
- PT. Citra Marga Nusaphala Persada. (1998). *Laporan geoteknik tahap I ruas waru – tambak oso – akses juanda, rencana teknik akhir proyek jalan tol simpang susun waru – tanjung perak surabaya surabaya eastern ring road (geotechnical report phase I for waru – tambak oso – juanda access, final engineering design surabaya eastern ring road project)*.
- PT. Hutama Karya (Persero), PT. Citra Marga Nusaphala Persada Tbk, Lembaga Penelitian dan Pengabdian Masyarakat (LPPM) Institut Teknologi Bandung (2005), *Trial Matras Bambu pada Tanah Lunak, Lokasi Tambak Oso, Jawa Timur (Trial Bamboo Mattress on Soft Soil at Tambak Oso, East Java)*.
- Terzaghi K. (1967). *Soil mechanics in engineering practice, second edition*. Wiley, New York.
- Tomlinson M. J. (1977). *Pile design and construction practice*. A Viewpoint Publication, London.

PROGRESSIVE DAMAGE SIMULATION OF FOUNDATION PILE OF THE SHOWA BRIDGE CAUSED BY LATERAL SPREADING DURING THE 1964 NIIGATA EARTHQUAKE

Motoki Kazama, Noriaki Sento, Ryosuke Uzuoka
*Department of Civil Engineering, Tohoku University, Aoba 6-6-06, Aoba-ku
Sendai, 980-8579, Japan*

Makoto Ishimaru
*Central Research Institute of Electric Power Industry
1646 Abiko, Abiko-shi, Chiba-ken 270-1194, Japan*

The authors analyze a progressive pile damage of the Showa-bridge caused by post-liquefaction phenomena during the 1964 Niigata earthquake. In the analysis, using time histories of ground displacement and excess pore water pressure calculated, the authors conduct an elasto-plastic analysis of a pile subjected to external force from ground displacement. Simulation results provide a reasonable explanation not only of the observed plastic deformation of the pile, but also the progressive damage of the pile.

INTRODUCTION

Residual lateral displacements of several meters as a result of liquefaction were observed in the 1964 Niigata earthquake (Hamada et al., 1992). During the earthquake, it is reported that the Showa Bridge collapsed a few minutes after termination of the main seismic motion (JSCE report, 1966). The cause of the collapse is inferred to be that steel pipe pile piers of the bridge deformed by lateral spreading caused by liquefaction. This damage is considered as typical post-liquefaction progressive damage. To date, the final structural damage of the pier pile has been studied using a seismic deformation method (e.g., Mori, et al., 1989), but there is still explanation for the progressive damage.

In this paper, a seepage failure mechanism of a gently inclined slope during the dissipation process of the excess pore water pressure generated by seismic shearing (Sento et al., 2004) is used. Using time histories of ground displacement and excess pore water pressure calculated, the authors conducted an elasto-plastic analysis of a pile subjected to external force from ground displacement.

DAMAGE PROCESS OF THE SHOWA-BRIDGE

The Showa Bridge is located at the river mouth of the Shinano River in Niigata city. Figure 1 shows a schematic diagram to explain the bridge damage (JSCE report, 1966). According to an eyewitness account, the collapse of girders proceeded as G6→G7→G5→G4→G3 one to

two minutes after the end of the main shock. He said his impression was that the seismic motion might cause the toppling of G6 girder, but the other girders slowly collapsed, regardless. On the toppling of G6 girder, there is an opinion that large displacement amplitude due to the following the motion after main motion might be the cause, which is based on the reconsideration of the witness accounts (Wakamatsu et al., 2004).

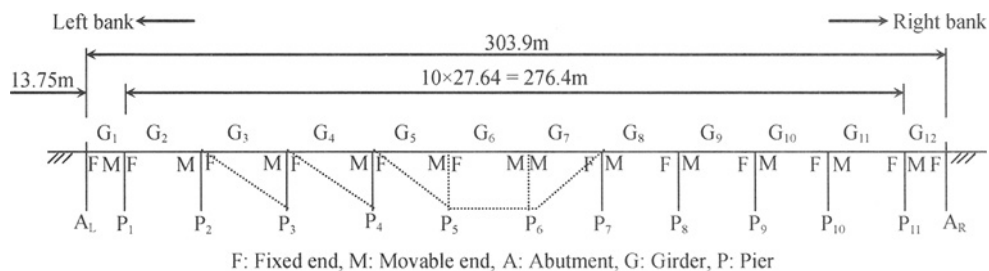


Figure 1. Schematic diagram to explain damage to the Showa Bridge

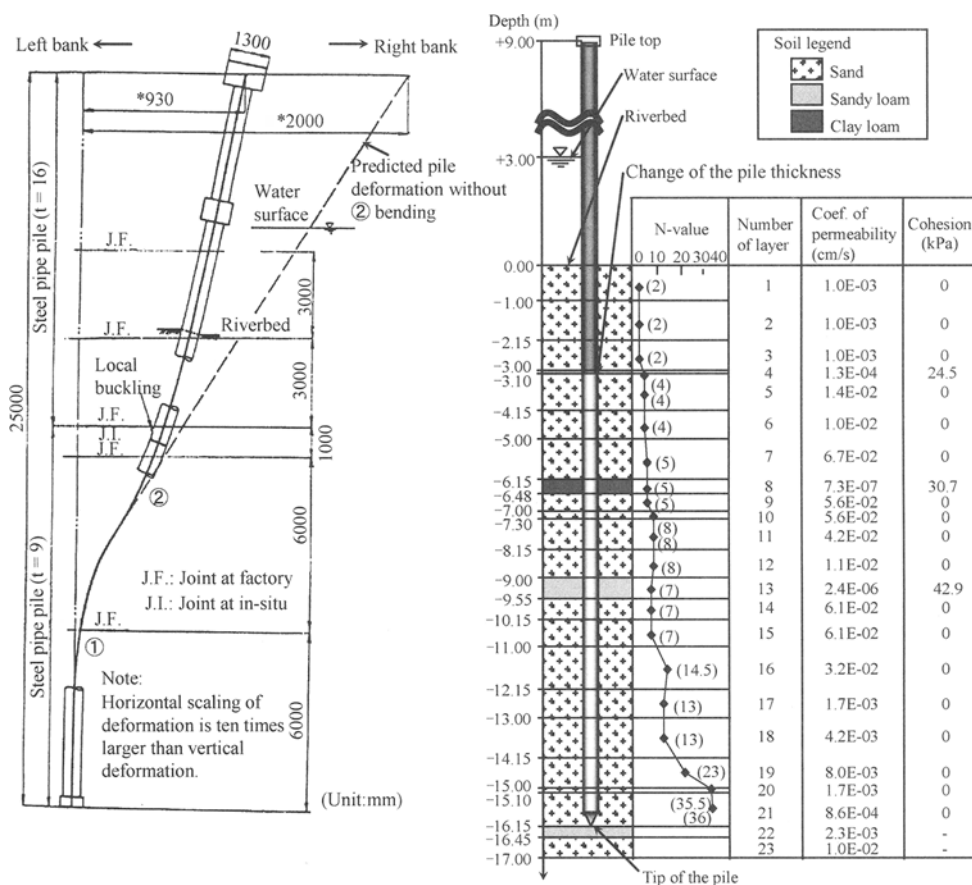


Figure 2. Damage of the P4 pier pile after the report (JSCE, 1966) and modeling of the soil-pile structure system

After the earthquake, the pile in the downstream side of the P4 pier was pulled out for restoration work. A schematic figure of damage to the P4 pier pile is shown in the left hand side of Figure 2. It was reported that there were bend deformations in the P4 pier pile ① that approached the river center at around upper 6 m from the pile lower tip and those ② that returned to the left bank side at around 9 m up from the pile lower tip (JSCE report, 1966). Consequently, 93 cm was displaced towards the river heart at the pile top. Also, a local buckling was found at the ② position.

Mori et al. (1989) made an attempt to explain the bending damage of the P4 pier pile by a seismic deformation method. They assumed a triangular and a rectangular shape as a ground displacement distribution model and calculated the coefficient of subgrade reaction models, by which they considered the effect of liquefaction by introducing a reduction coefficient (0.01-1.0). According to their analysis, bend deformation ① could be explained using triangle ground displacement distribution, but on bend deformation ② they inferred that displacement of the pile top to the river heart might be restricted because the fallen girder (G5 girder) worked as a strut. They called it the "strut effect". It is conceivable that, because of the observation in the remedial work, that P5 pier was deformed involving the lower G5 girder. Consequently, they concluded that the pile might have sustained severe damage by lateral spreading.

However, because their analysis was a static one and considered only the final deformations of the ground and pile, the time-dependent damage process could not be explained. The purpose of this study is to explain such post-earthquake damage. The authors ignore the dynamic effects of seismic shaking and address only the post-earthquake damage in this study.

OUTLINE OF THE PILE DAMAGE SIMULATION

We address the behavior of a single pile subjected to external force caused by lateral spreading. As described above, the deformation during seismic shaking is ignored. The soil-pile system analyzed in this study is idealized as a single beam supported on nonlinear Winkler-type springs, as shown in Figure 3. Our analysis consists of the following two parts.

Post-earthquake shear deformation analysis of gently inclined layered ground caused by pore water migration

The post-earthquake shear deformation analysis of a gently inclined layered ground caused by pore water seepage: This portion calculates the distribution of lateral displacement of layered ground in depth direction $u_g(z,t)$, where z is the vertical coordinate and t is time. In analysis, the distribution of initial excess pore water pressure, soil permeability, volume change properties and a shear strength parameter of soils in the depth direction are necessary. Details are available in the literature (Sento et al., 2004).

Interaction analysis between pile and ground

Using lateral displacement of layered ground obtained and spring constants between the free field ground and pile, pile deformation $u_p(z, t)$ is calculated by loading external force evaluated from incremental ground displacements and subgrade reaction, where the spring constant is presumed to depend on the effective stress of soil, which is a time dependent value during pore water migration. This nonlinear time incremental analysis can be performed if site conditions, such as soil profiles and items related to the pile, are given.

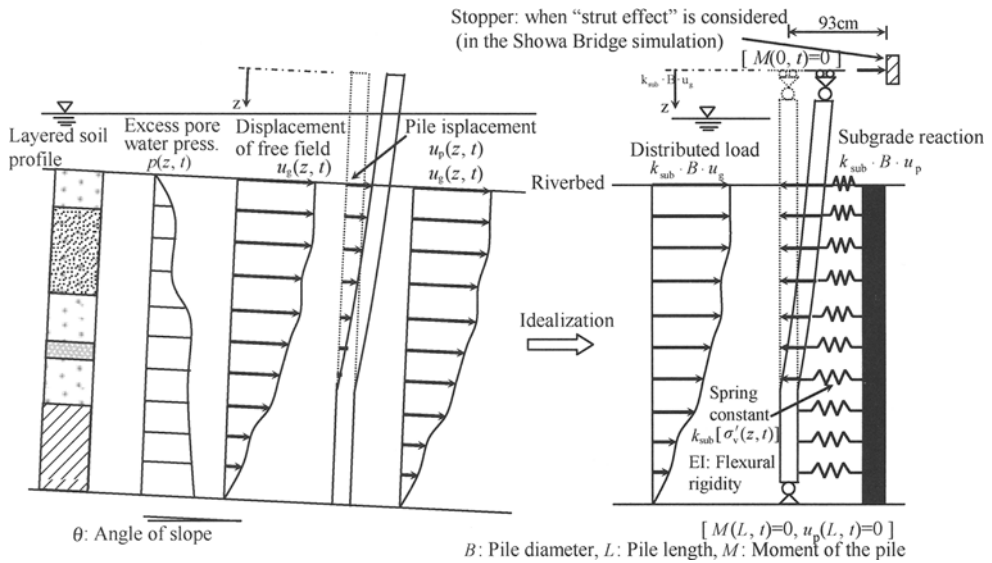


Figure 3. Schematic of load-displacement analysis model subjected to lateral spreading during pore water migration

SIMULATION RESULTS

Ground displacement

Example time histories of the ground displacement distribution and the excess pore water pressure distribution of certain case are shown in Figure 4. Layers 4, 8, 13, and 22 are loam, as shown in right hand side of Figure 1, and the initial excess pore water pressure in those layers right after the earthquake is smaller in comparison with the sand layers. The water pressure of the fourth layer increases immediately as a result of the inflow of pore water from the lower layers because the layer thickness is thin, even though it has low permeability. On the other hand, the water pressures of layers 8 and 13 do not increase significantly. This is because of the low permeability of the loam layers and also, the pore water accumulates in the layers under these layers. In addition, the shear strain develops when the pore water pressure of the layer reaches the critical pore water pressure. Ground displacement stops at the point when the water pressure becomes less than the critical pore water pressure.

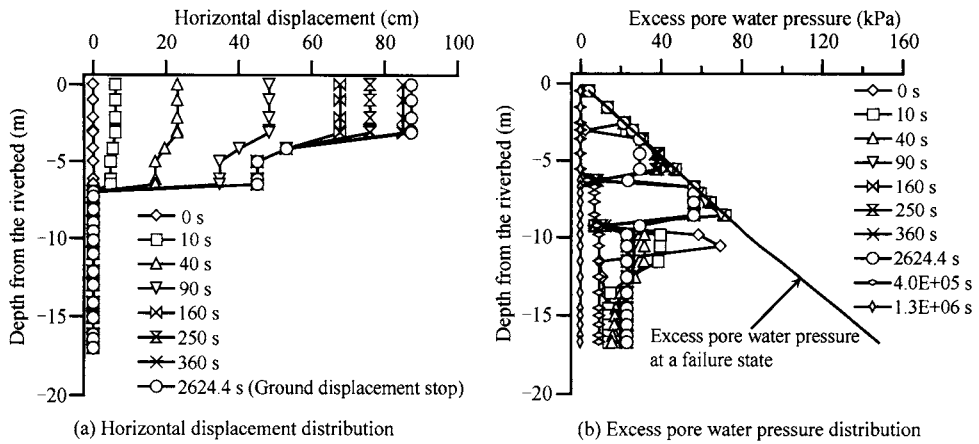


Figure 4. Simulation results of the free field ground

Deformation and stress of the pile

The final deformation and moment of the pile with the consideration of the "strut effect" are shown in Figure 5. In final deformation, the deformation pattern in the case of $\alpha = 0.4$ agrees well with that of the damaged pile, and the deformation pattern in the case of $\alpha = 0.0$ is similar to the ground deformation. However, in the case of $\alpha = 1.0$, the pile hardly deformed at all after the "strut effect" came into consideration. Where α is a power coefficient which represents the effect of liquefaction on the coefficient of subgrade reaction. That is, the subgrade reaction of liquefiable layer is assumed to be in proportion to $(\sigma'_v / \sigma'_{v0})^\alpha$. The result indicates that a deformation pattern, like the damaged pile, is not explained unless great force affects the pile from the time when the pile top is fixed by the "strut effect". The final moment distribution shows that pile moments in the cases of $\alpha = 0.0$ and $\alpha = 0.4$ reach fully plastic moment not only near -19 m, but also near -12 m. This

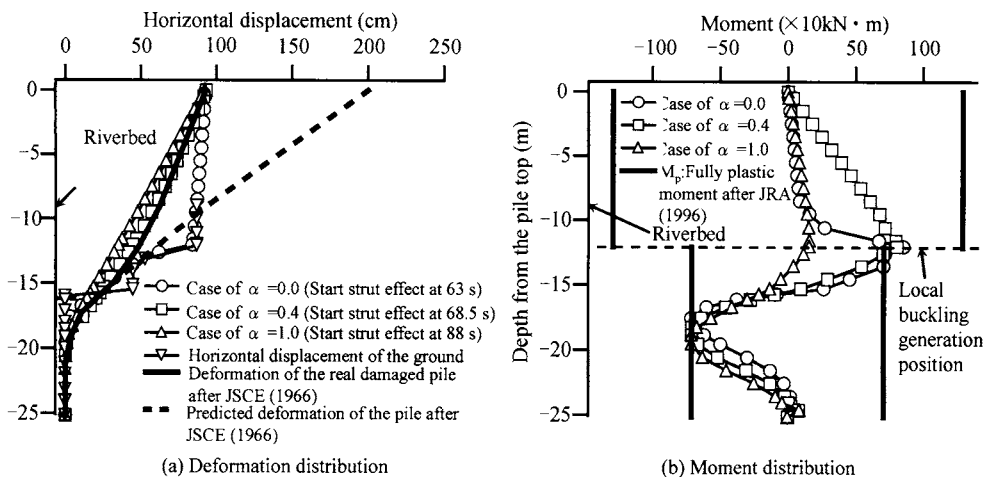


Figure 5. Simulation results of the pile with the "strut effect"

position (-12 m from the pile top) agrees with the position where local buckling in the damaged pile was observed. From the time history of the pile top displacement (in the case of $\alpha = 0.4$), the time that the "strut effect" came into consideration is 68.5 seconds from the earthquake end; this concurs well consistent with the time at which the witness reported the collapse of bridge girders occurring 1-2 minutes after the main earthquake motion end.

From the above discussion, this simulation seems to be a reasonable explanation of the post-earthquake progressive damage of the Showa Bridge P4 pier pile considering lateral spreading and the effect of the collapsed bridge girder.

CONCLUDING REMARKS

In this study, the authors have analyzed the progressive damage of the pile induced by lateral spreading. The following conclusions are obtained:

1. On the basis of the analysis using soil properties estimated from boring data, the possibility was proven that shear deformation developed in the riverbed ground under the Showa Bridge during pore pressure migration. The generated ground displacement was sufficiently large to cause pier pile damage.
2. Final deformation of the pile was explained reasonably by considering the "strut effect", which was caused by a toppled girder. Fully plastic moments observed at two points in the damaged pile were reproduced reasonably by simulation.
3. Simulated progressive damage agreed well with an eyewitness story, which reported the collapse of a bridge girder occurring after one to two minutes after earthquake motion ended.

REFERENCES

- Hamada M. (1992). Large ground deformations and their effects on lifelines: 1964 Niigata earthquake. *Case studies of liquefaction and lifeline performance during past earthquakes, 1, Japanese case studies*, Technical report NCEER-92-0001.
- Japanese Society of Civil Engineering. (1966). The report of damage investigation in the 1964 Niigata Earthquake. (in Japanese).
- Kazama M., Shimizu Y., Mori T., Sento N. and Uzuoka R. (2007). Trace of Liquefaction under the Shinano river bank during the 1964 Niigata Earthquake. *Earthquake Geotech. Eng.*, KYRIAZIS D. PITILAKIS Editor, Paper No. 1209.
- Mori S., Shimizu K., Suzuki N., Takagi M. and Nakamura S. (1989). Measurement and discussion of permanent ground displacement due to liquefaction. *20th Japan earthquake engineering symposium*, 25-28 (in Japanese).
- Sento N., Kazama M., Uzuoka R., Ohmura H. and Ishimaru M. (2004). Possibility of postliquefaction flow failure due to seepage. *J. of Geotechnical and Geoenvironmental Engineering*, ASCE, 130(7): 707-716.
- Wakamatsu K., Tazoh T., Yasuda S., Towhata I., Yoshida N., Kanatani M., Kiku H. and Nakazawa H.(2004). Report of the special session on the 40th anniversary of Niigata earthquake, *Tsuchi-to-Kiso*, JGS, 52(12): 15-20 (in Japanese).

EARTHQUAKE-INDUCED SUBMARINE LANDSLIDES IN VIEW OF VOID REDISTRIBUTION

Takaji Kokusho

*Faculty of Science & Engineering, Chuo University, 1-17-23 Kasuga, Bunkyo
Tokyo, Japan*

Tetsuya Takahashi

Ex-Graduate Student, ditto

Submarine slides occurring near-shore in non-cohesive sandy deposits are first discussed in view of void redistribution effect. Model tests demonstrate that formation of water film beneath silt seam plays a key role in liquefaction-induced sliding failure in gentle slope. Considering that soil deposits are naturally stratified with sandwiched low permeability seams, it seems quite reasonable to recognize the water film effect as a major mechanism for seismically induced submarine slides in gently sloped sandy sea-bed near coasts. Analogous void redistribution effect on the submarine slides occurring in clayey sea floor far from coasts is then studied by cyclic loading tests to find out large volumetric strain after strong cyclic loading. Simple consolidation plus seepage analysis considering the earthquake-induced large volumetric strain indicates that excess pore water may accumulate beneath less permeable seams sandwiched in relatively permeable clayey layer, possibly causing delayed shear strength reduction due to excessive swelling just beneath the seam.

INTRODUCTION

One of geotechnical hazards on which geotechnical engineering has not focused so much is submarine slides. Various causes are considered as the triggers; earthquakes, high ocean waves during storms, tidal changes, etc., among which earthquake-induced slides are focused here. The slides may be classified into two types. The first is the ones which occur near coasts, affecting coastal areas in deltaic lands or man-made fills. The slopes in those slides are relatively steep compared to the other type. For example, Valdez and Seward, port cities in Alaska, USA, suffered great loss of human lives and properties by large scale submarine slides involving coastal areas (Coulter et al., 1966; Lemke et al., 1967). As shown in Figure 1, the inclination of the sea bed was 30° at most near the beach, but actually 5° or less on average considering the long span of the slip surface of more than 2 km offshore, which is considerably less than the internal friction angle of the soil. Analogous submarine failure occurred during the 1999 Kocaeli earthquake along the southern coast of the Izmit bay in Turkey (The Japanese Geotechnical Society, 1999). The slope of the seabed originally

about 5°-10° consisting of coarse sand and gravel became very steep at the scarp after the earthquake as shown in Figure 2. In the world, there remain quite a few coastal zones with high seismicity and relatively steep sea floor consisting of loose sand or gravel where submarine slide is likely to occur.

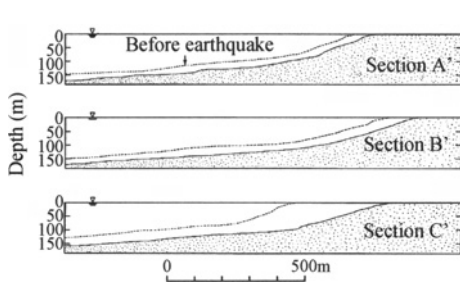


Figure 1. Cross-sectional change of sea bed at Valdez before and after the 1964 Alaskan earthquake (Coulter 1966)

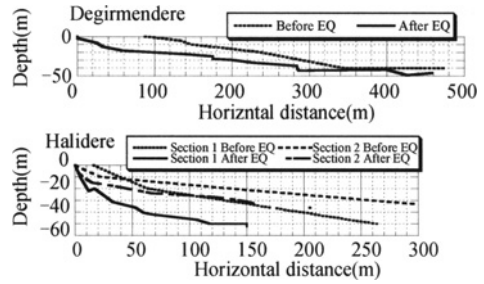


Figure 2. Cross-sectional change of sea bed at Valdez before and after the 1999 Kocaeli earthquake (JGS 2000)

The second type is the submarine slides which occur offshore in the deep sea bottom. The slope is normally gentler than a few percent or even less than 1% (Hampton and Lee, 1996). A typical example of this type occurred 60 km off the California Coast during a 1980 medium magnitude earthquake (Field et al., 1982).

In this case, 2 by 20 km sea floor consisting of sand and mud of only 0.25 degrees slipped and became much more flat with some evidence of liquefaction such as sand boils on the sea bottom of 30 to 70 m depth as sketched in Figure 3.

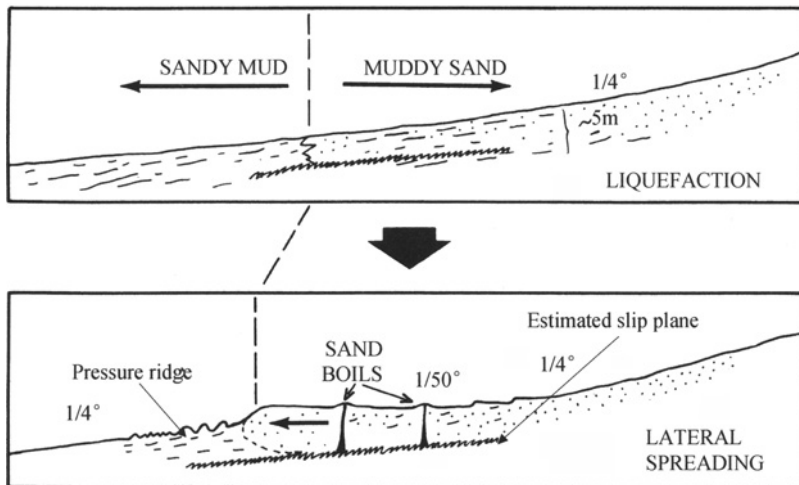


Figure 3. Cross-sectional change of sea bed off the California Coast before and after a 1980 medium magnitude earthquake (Field et al., 1982)

As one of possible mechanisms to explain sliding failures of low-gradient sandy slopes, void redistribution effect may be considered. In this view, fine soil sublayers sandwiched in sand deposits are considered to play a key role in flow failure. The formation of water interlayers (Seed, 1987) or water films between liquefied sand and overlying lower-permeability seams has been observed under level ground conditions in a number of model tests. For sloping ground conditions it has been demonstrated, based on model tests, that the water film or void-redistribution effect plays an important role in post-earthquake large lateral flow in liquefied ground.

Thus, liquefaction may be highly responsible in earthquake-induced submarine slides, particularly in near-shore sites where the seabed is composed of liquefiable loose sand or gravel. However, in off-shore slides far from coasts, sea floors are normally very gently sloped and composed of cohesive fine soils, in which liquefaction seems to hardly occur. Nevertheless, slumps and scars of off-shore submarine slides are often found and sometimes really huge in scale and suspected as potential causes of tsunami other than fault dislocations. Thus, a concern on submarine slides from geotechnical point of view is necessary as one of potential natural disasters for coastal structures, offshore explorations for natural resource and even for tsunami. Needless to say, much more research is needed to understand the mechanism correctly.

In the first part of this article, the void redistribution effect in liquefied sand slopes will be addressed as one of the key mechanism of submarine slides particularly near coastal areas where seabed is mostly sandy and non-cohesive. Then, off-shore conditions far from coastal areas will be studied to examine a relevance of a similar void redistribution mechanism in cohesive soils for major cause of submarine slides.

VOID REDISTRIBUTION MECHANISM IN LIQUEFIED SAND SLOPE

Kokusho (1999) demonstrated, by model tests, soil element tests and site investigations, that water film or void-redistribution effect plays an important role in post-earthquake large lateral flow in liquefied ground. This concept had been introduced in a committee report in US (National Research Council, 1985) and also discussed by Seed (1987) by using a special term, water interlayer.

In this view, fine soil sublayers sandwiched in sand deposits are considered to play a key role in flow failure. A sand layer, which is classified as a single uniform layer in normal engineering practice, may also be composed of sublayers with different grain size and, hence, different permeability. Thus, soil stratification may be able to

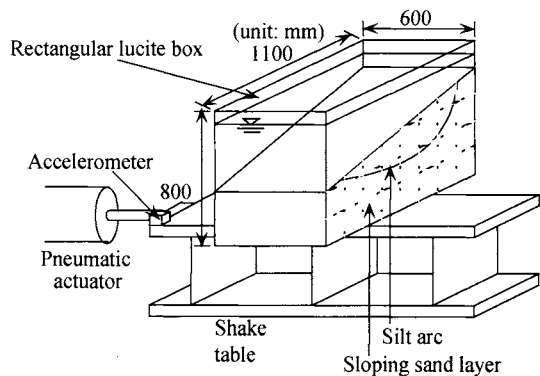


Figure 4. Shake table test for 2D saturated sand slope sandwiching silt arc

explain, as Seed (1987) already pointed out, why steady-state strength of uniform sand leads significantly higher values of residual strength than those estimated by case studies in the field.

Liquefaction-induced lateral flow in gentle slopes have been studied by the present author and his research group (Kokusho, 1999, 2000, 2003, Kokusho and Kojima, 2002; Kokusho and Fujita, 2002). focusing on the significant effect of void redistribution or water film by utilizing various investigation methods such as soil investigations of insitu deposits, 1-D liquefaction tests in a tube, 1G shake table tests, laboratory soil tests, field survey, numerical analyses etc. Among them, 2-dimensional shaking table tests were performed as shown in Figure 4. Clean fine sand was rained in water to make saturated loose sand slope in a rectangular soil box in which an arc-shape silt seam was sandwiched. The model was subjected to 3 cycles of sinusoidal shaking perpendicular or parallel to the sloping direction and the sliding was observed through the transparent side wall. It was demonstrated that soil mass flows along a continuously formed water film beneath the arc-shaped fine soil seam still after the end of shaking, while in a uniform sand without a silt seam a major slide takes place only during shaking. Video movies of the tests are accessible at the web site;

<http://www.civil.chuo-u.ac.jp/lab/doshitu/index.html>

Figure 5(a) indicates that the slide occurs not only during shaking but also after the end of shaking quite discontinuously along the silt arc beneath which thin water film could be recognized. In contrast, Figure 5(b) indicates that flow deformation in a uniform sand

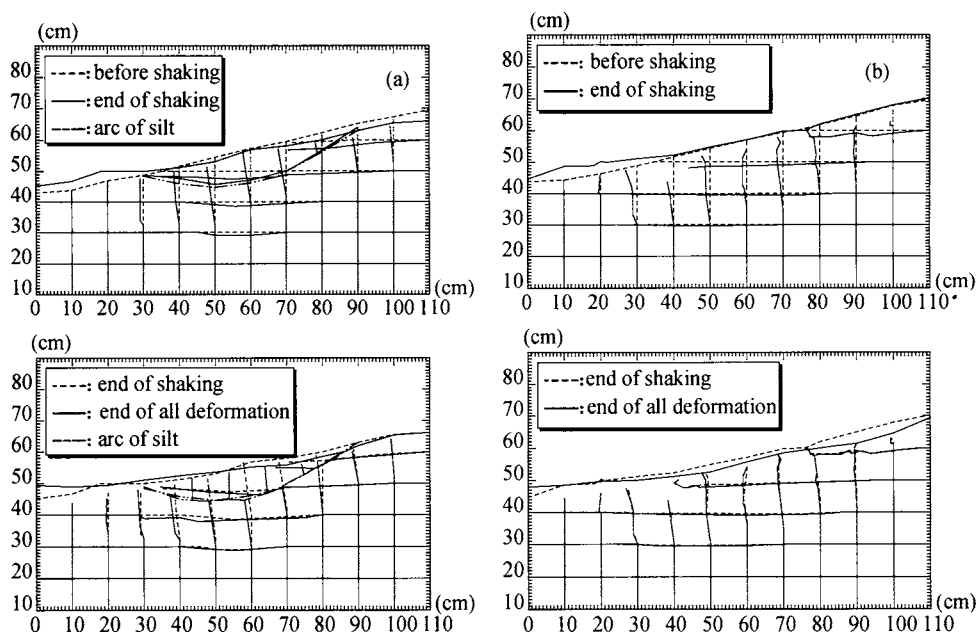


Figure 5. Cross-sectional deformation for slopes with silt arc (a) and without silt arc (b) Top of (a) and (b): during shaking, Bottom of (a) and (b): after shaking

model occurs mostly during shaking continuously in the cross-section. Time histories of the same test results are shown in Figure 6. In Figure 6(a) without the silt seam, flow is

restricted during shaking, while in Figure 6(b) with the silt arc large flow also occurs after shaking. The target points on the charts are shown in Figure 6(d) by the same symbols. These results are for the input acceleration of 0.31 G. In Figure 6(c), the time histories of the flow deformation of the same model subjected to weaker input acceleration of 0.18G. Interestingly enough, much larger post-shaking flow occurs than the case of the larger input acceleration of 0.34, and only minimal deformation takes place during shaking. This is because in the weaker motion, the slope remains steep leaving larger driving force for the post-shaking flow along the water film, if it is formed.

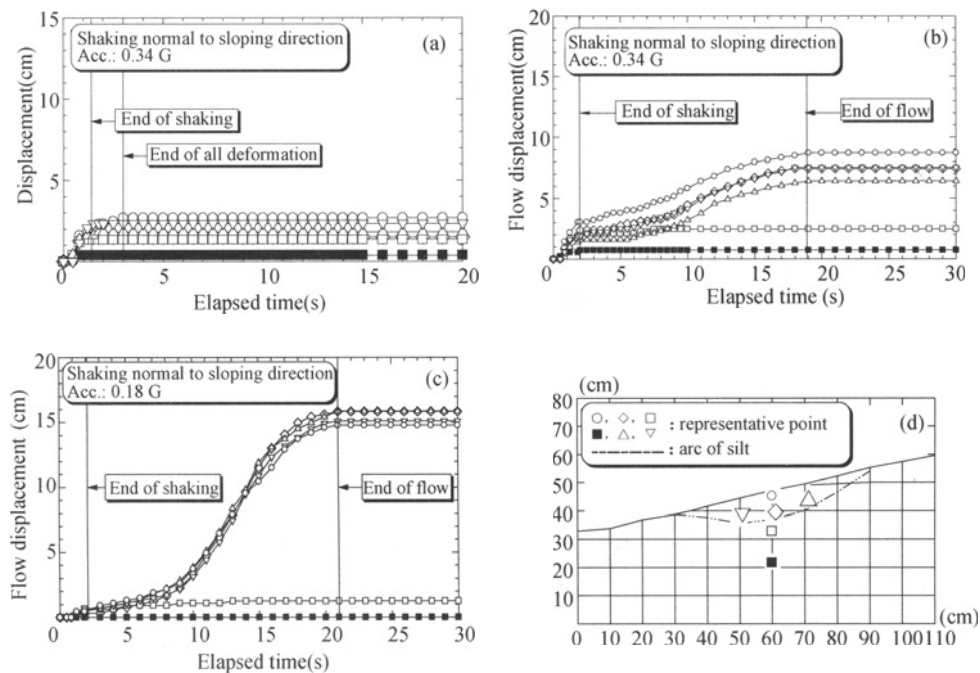


Figure 6. Time-dependent sliding displacement at target points shown in (d); without silt arc by Acc. 0.34 G (a), with silt arc by Acc. 0.34 G (b) and with silt arc by Acc. 0.18 G(c)

A basic question may arise that sand which can be so dilative if sheared under a low confining stress may absorb ambient excess pore water and hence block the water film development. It was pointed out, however, based on the comparative observation of the cases with and without a silt seam that a water film formed beneath the seam serves as a shear stress isolator which shields the deeper soil from the development of shear strain and dilatancy (Kokusho, 2000). Consequently, sand can experience large shear strain beneath the silt seam without suffering from the dilatancy effect, whereas it stops moving after the end of shaking if the sand is uniform.

In another shaking table test, a soil mass slid even on a very gently inclined water film, which broke at weak points of the overlying sublayer, triggering the boiling failure in the sand above and a mud avalanche of the upper layer (Kokusho, 1999; Kokusho, 2000). A video movie of the test is also accessible at the web site. Considering that no such drastic sliding failure occurs in the uniform sand slope, a significant effect of the void

redistribution or water film formation has been demonstrated. Considering that soil deposits are naturally stratified with sandwiched low permeability seams, it seems quite reasonable to identify the water film effect as a major mechanism for seismically induced submarine slides in gently sloped sandy seafloor near coast.

If water films are formed continuously, they will tremendously reduce the residual strength. If sliding occurs all the way through a continuous water film, the strength ratio becomes zero. This however seems unrealistic because water films may be neither

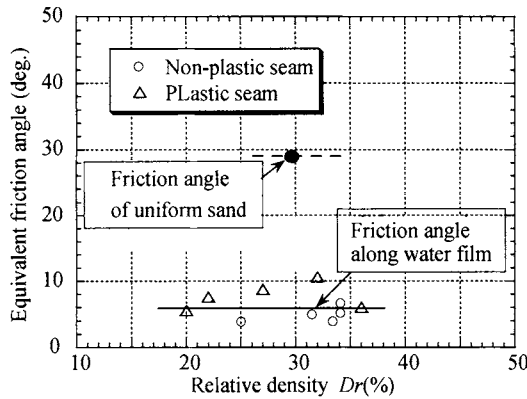


Figure 7. Residual strength along water film evaluated from model shake table tests with different conditions (Kabasawa & Kokusho, 2005)

continuous nor straight but winding with rough faces. Based on model shaking table tests, Kabasawa and Kokusho (2003) quantified the residual strength exerted during the delayed flow along a water film by using the balance between potential energy and dissipated energy along the slip surface. The result shown in Figure 7 indicates that the residual strength along the water film is almost independent of sand density and other test parameters and remains around 20% that of the uniform sand.

POST-EARTHQUAKE VOID REDISTRIBUTION IN COHESIVE SEABED

Figure 8(a) and (b) show relationships of water depth versus water content (a) and water content versus clay content (b) for submarine soils in Japan Sea (Ikehara, 1989). By combining the two charts, a clear trend can be recognized that the soil is changing from sandy silt to clay with increasing water depth or increasing distance from coast. Geotechnical properties of top sediments in Korea Plateau margin in Japan Sea are exemplified in Table 1 (Lee et al., 1991), which clearly indicates again that soils are changing from sandy silt to clay with increasing water depth from near-shore continental shelf (<200 m) to offshore continental slope (>1500 m). Water content and plastic index tend to increase accordingly toward the offshore direction, being consistent with the change in soil type. Quite a few slump scars can be found in lower continental slope in Japan Sea where the slope inclination is 1° - 2° . This indicates that multiple massive submarine landslides had occurred from time to time presumably by earthquakes (Lee et al., 1991). Thus, it is not exceptional that submarine slides occur not only near the coast but also at continental slopes of deep sea where the seabed deposits are predominantly clayey soils.

Table 1. Physical properties of topmost sediments in Japan Sea (Lee et al., 1991)

Province	Solcontent(%)			Water content W(%)	Plasticity index Ip	Sensitivity ratio
	Sand	Silt	Clay			
Shelf (<200m)	28	56	16	60	29	2.4
Upper slope (200-700m)	10	55	35	96	68	2.8
Middle slope (700-1500m)	1	41	58	170	79	2.6
Lower slope (>1500m)	4	29	67	176	69	

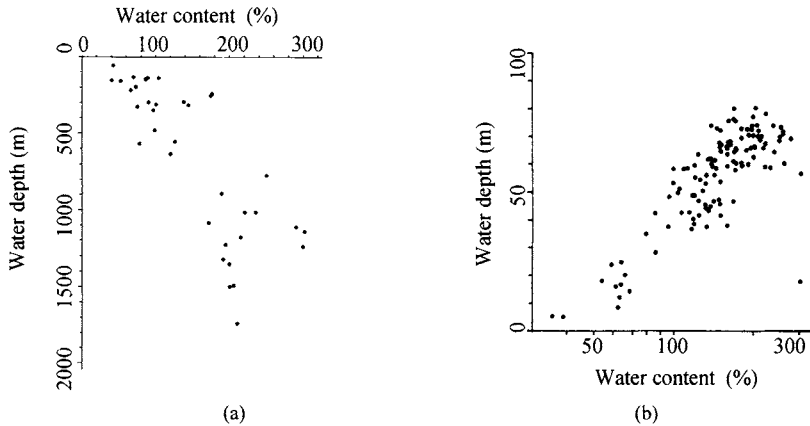


Figure 8. Relationships of water depth versus water content (a) and water content versus clay content (b) measured for seabed soils in Japan Sea (Ikehara, 1989)

In order to investigate the cyclic loading effect during strong earthquakes on submarine soft clay, undrained cyclic triaxial tests were performed for intact soil samples recovered from Japan sea off West Japan. The basic properties of tested specimens are listed in Table 2. The depth of the sampled soils are from 60 to 100 cm from the sea floor. Judging from the water content of the sample, $w=73\%-90\%$, it is estimated from previous research results (Ikehara, 1989) that the soil is from continental slope. The initial void ratio is $e=1.7-2.5$ and the plasticity index is $I_p=45-50$.

The test specimen of 50 mm in diameter and 100 mm in height was set in the triaxial apparatus shown in Figure 9. It was first consolidated by the confining stress $\sigma'_c=29$ kPa corresponding to the shallow sampling depth and then loaded in 30 cycles under undrained condition by cyclic axial stress σ_d with frequency of 0.05 Hz. The stress ratio ($R=\sigma_d/2\sigma'_c$) was varied from 0.23 to 0.73. In Figure 10(a), pore-pressure ratio $\Delta u/\sigma'_c$ at the end of cyclic loading is plotted against the stress ratio R . The pore

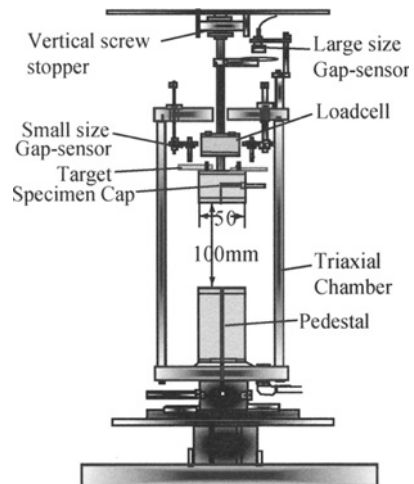


Figure 9. Triaxial apparatus used for cyclic loading tests of submarine clay

pressure builds up to $\Delta u/\sigma'_c \approx 90\%$ for the stress ratio around $R \approx 0.5$ and then approaches to an asymptote.

After the cyclic loading of 30 cycles, the specimen was drained and the volumetric strain ε_v was measured by excessive pore water. Figure 10(b) shows the plots of volumetric strain ε_v against stress ratio R . It is noted that if the stress ratio attains $R=0.4-0.5$, the post-earthquake volumetric strain reaches $\varepsilon_v=4\%-5\%$. This magnitude of volumetric strain is almost equivalent to that of loose sand after liquefaction, which actually occurred during the 1964 Niigata earthquake or the 1995 Kobe earthquake, indicating that the effect of the excess pore-water may not be ignored in view of the void redistribution even in cohesive submarine clay.

Table 2. Physical properties of specimens for cyclic triaxial tests

Depth(cm)	Void ratio before test e	Water content $W(\%)$	Particle density ρ_s (t/m^3)	LL(%)	PL(%)	PI(%)
60-75	2.308	87.4	2.591	86.3	38.2	48.1
	2.334	90.2				
75-87.5	2.209	76.9	2.662	81.7	35.5	46.2
	1.746	72.5				
	2.370	79.7				
87.5-100	2.362	79.7	2.611	93.7	29.6	64.1
	2.219	84.0				

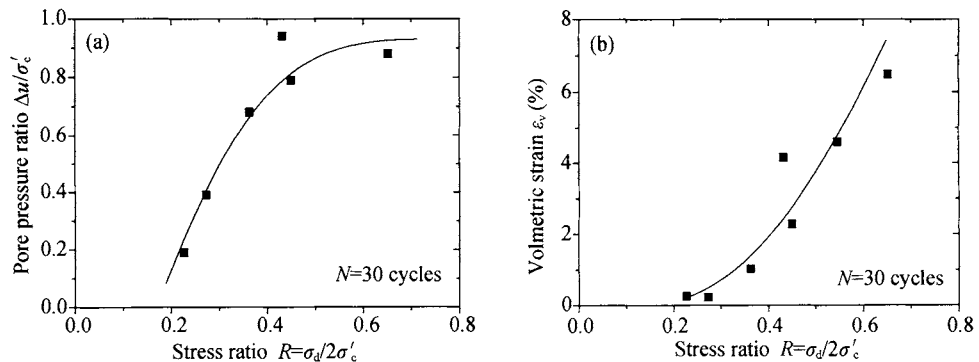


Figure 10. Stress ratio plotted versus pore pressure ratio (a) and volumetric strain (b) for submarine soft clay by cyclic triaxial tests

Analogous to sandy deposits in which the soil is normally stratified as demonstrated by Kokusho (2003), it may well be estimated that submarine clay layer is also strongly stratified. Sonic profiles of submarine clay layer normally show a set of reflection boundaries indicating such stratification. It further implies that clay layer similar to sand layers consist of sublayers with different properties and different permeability.

In order to know the role of the excess pore-water seismically squeezed in stratified clayey submarine deposits, a simple model shown in Figure 11, which is basically the same as in the previous research for analyzing water film effect in liquefied sand (Kokusho 2000), was chosen for consolidation analyses. The model consists of upper and lower clay layers of low permeability sandwiching a seam of still lower permeability in between.

Linear consolidation by self weight is assumed to occur in parallel in the two layers from the initial excess pore-pressure of triangular shape corresponding to 100% pore pressure buildup due to cyclic loading as shown in Figure 11. In the process of consolidation, excess pore-water in the lower layer migrates upward and accumulates beneath the seam developing a narrow band of higher water content. The pore-pressure there is sustained equal to the effective overburden, while the pore pressure at the bottom in the upper layer continues to decrease with the progress of consolidation, introducing seepage flow through the intermediate seam. Even after the completion of the consolidation in the lower layer, the seepage flow continues until all the accumulated pore-water beneath the seam goes out to the surface. In the analysis, the consolidations in the individual layers are computed in parallel assuming impermeable lower boundary and then seepage velocity is calculated from hydraulic gradient in the seam. The seepage velocity and pressure are superposed together to evaluate the accumulation of excess pore-water beneath the seam during the consolidation and seepage process.

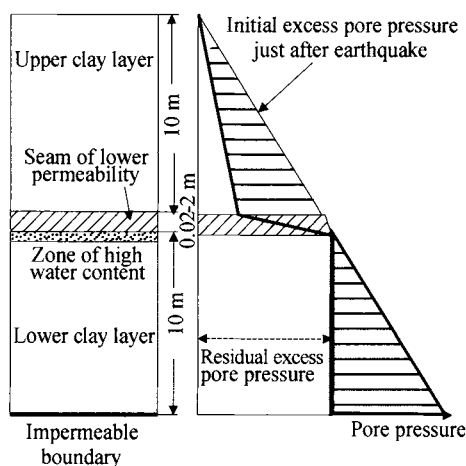


Figure 11. Analytical model for void redistribution in clay deposit sandwiching seam of lower permeability

Eight cases, Case1-8, were analyzed, the parameters of which are listed in Table 3. The thickness of intermediate seam was assumed 0.2 m in most cases but also changed as 0.2 m or 2.0 m in Case 7 and Case 8, respectively. Permeability in the upper/lower layer and the seam was systematically changed in the range of 10^{-5} - 10^{-8} cm/s as listed in the table based on consolidation tests conducted on the same soil (Takahashi 2007), so that the seam always has a lower value than the sandwiching upper and lower layers by the ratio of 10^{-1} ~ 10^{-3} . In all the cases, the thickness of the upper and lower layers were set as 10 m and the post-earthquake volumetric strain was prescribed as 5% based on the test results shown in Figure 10(b) corresponding to large cyclic stress ratio of $R=0.5$. Consequently, the compressibility coefficient was evaluated as $m_v = 0.0025 \text{ kPa}^{-1}$. The buoyant unit weight of the clay was assumed as 4.0 kN/m^3 .

Table 3. Analytical cases for clay seafloor sandwiching more impermeable silt seam considering void redistribution effect

Case	Upper layer		Intermediate seam		Lowerlayer	
	Thickness(m)	Pemeability (cm/s)	Thickness(m)	Pemeability(cm/s)	Thickness(m)	Pemeability(cm/s)
1	10	1×10^{-5}	0.2	1×10^{-6}	10	1×10^{-5}
2	10	1×10^{-5}	0.2	1×10^{-7}	10	1×10^{-5}
3	10	1×10^{-5}	0.2	1×10^{-8}	10	1×10^{-5}
4	10	1×10^{-6}	0.2	1×10^{-7}	10	1×10^{-6}
5	10	1×10^{-6}	0.2	1×10^{-8}	10	1×10^{-6}
6	10	1×10^{-7}	0.2	1×10^{-8}	10	1×10^{-7}
7	10	1×10^{-5}	0.02	1×10^{-7}	10	1×10^{-5}
8	10	1×10^{-5}	2	1×10^{-7}	10	1×10^{-5}

Figure 12 shows major results of the analysis; time-dependent variation of excess pore-water accumulation beneath the intermediate seam expressed in terms of equivalent pure water thickness. It is obvious that no meaningful water accumulation occurs in Cases 1, 4, 6 where the permeability ratio between the seam and the sandwiching layers is 10^{-1} , while Cases 2, 3, 5 indicate that the permeability ratio lower than 10^{-2} leads to water accumulation equivalent to or more than 10 cm water thickness and it becomes thicker for the permeability ratio getting smaller from 10^{-2} to 10^{-3} . It should be noted that the pore-water accumulation sustains very long, 150 days (Case 2), 400 days (Case 3) and 1600 days (Case 5) if the total soil system becomes more impermeable at the same time keeping their ratios constant. It is also obvious by comparing Case 2, 7, 8 that the duration of the water accumulation very much reflects the thickness of intermediate seam.

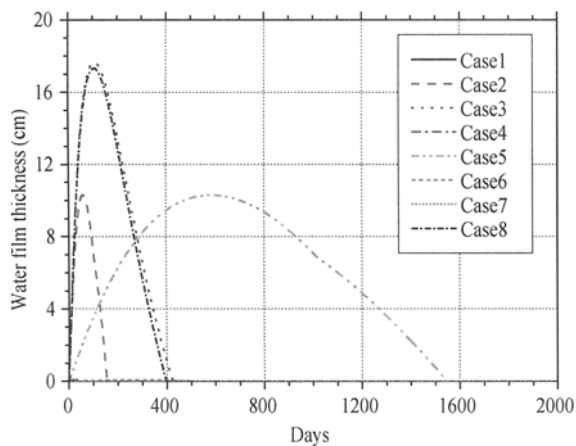


Figure 12. Time-dependent variation of excess pore-water accumulation beneath the intermediate seam expressed in terms of equivalent pure water thickness

Thus, the simple analyses on the sea-bottom clay layers sandwiching lower permeability seam indicate the occurrence of void redistribution which may be equivalent to more than 10 cm water thickness and sustain for hundreds of days in the condition given here. The thickness and time duration may vary according to various conditions such as seismic stress

ratio, thickness and compressibility of the seabed soft clay, etc. However, the effect seems great enough to affect the post-earthquake stability of submarine gentle slope.

A big question here is how the excess pore-water will be accumulated beneath the seam. If the soil is non-cohesive, it is clear that a thin water-interlayer will be formed causing sliding failure along it as demonstrated by Kokusho (1999). If the soil is highly plastic and cohesive as observed in many field research, the cohesion will prevent the formation of water film and swelling of clay will occur. As the quantity of the accumulated pore water gets larger, the soil will excessively swell leading to very large void ratio and very small shear strength. More research is certainly needed to clarify what will happen in submarine clays and how the strength is affected beneath a very low permeable seam if excessive pore-water is supplied from below.

CONCLUSIONS

In the first part, the mechanism of submarine slides occurring near-shore in cohesionless sandy deposits was discussed. Model tests demonstrated that the void redistribution or water film effect plays a key role in sliding failure in liquefied gentle slope. The residual strength along the water film evaluated in the model was found very much reduced down to 20% of the original strength due to the effect. Considering that soil deposits are naturally stratified with sandwiched low permeability seams, it seems quite reasonable to identify the water film effect as a major mechanism for seismically induced submarine slides in gently sloped sandy or gravelly sea-bed near coastal areas.

Analogous void redistribution effect on the submarine slides occurring in clayey sea floor was investigated on samples from Japan Sea to find out that the volumetric strain after strong cyclic loading was almost equivalent to that in liquefiable loose sand. A simple analysis combining consolidation and seepage flow revealed that large quantity of excess pore water accumulates beneath a more impermeable seam sandwiched in clay deposits, causing swelling of clay just beneath the seam. More research is needed whether or not the excessive swelling gives significant effect on delayed instability of submarine slope consisting of plastic soft clay.

ACKNOWLEDGMENTS

Dr. Ken Ikehara of Geological Survey and Applied Geo-Science, AIST, Tsukuba, Japan, who kindly provided submarine soil samples from Japan Sea and also valuable advice on marine geology is gratefully acknowledged.

REFERENCES

- Coulter H. W., Migliaccio R. R. (1966). Effects of the Earthquake of March 27, 1964 at Valdez, Alaska. *Geological Survey Professional Paper 542-C*, U. S. Department of the Interior, p.36.
- Field M. E., Gardner J. V., Jennings A. E. and Edwards B. D. (1982). Earthquake-induced sediment failures on a 0.25° slope, Klamath River delta, California. *Geology*, 10: 542-546.
- Hampton M. A., Lee H. J. (1996). Submarine landslides. *Reviews of Geophysics*, 34: 33-59.

- Ikehara K. (1989). Some physical properties of shelf to basin deposits off San'in and Hokuriku district, southern part of Japan Sea. *Bulletin of Geological Survey of Japan*, 40 (5): 239-250 (in Japanese).
- Kabasawa K. and Kokusho T. (2003). Energy analysis and model tests on lateral flow induced by water film effect in liquefied ground. *Journal of Japan Society for Civil Engineers*, N0.771/III-68, 135-145 (in Japanese).
- Kokusho T. (1999). Formation of water film in liquefied sand and its effect on lateral spread. *Journal of Geotechnical and Geoenvironmental Engineering*, ASCE, 125(10): 817-826.
- Kokusho T. (2000). Mechanism for water film generation and lateral flow in liquefied sand layer. *Soils and Foundations*, 40(5): pp.99-111.
- Kokusho T., Fujita K. (2002). Site investigation for involvement of water films in lateral flow in liquefied ground. *Journal of Geotechnical and Geoenvironmental Engineering*, ASCE, 125(10): 817-826.
- Kokusho T., Kojima T. (2002). Mechanism for post-liquefaction water film generation in layered sand. *Journal of Geotechnical and Geoenvironmental Engineering*, ASCE, 128(2): 129-137.
- Kokusho T. (2003). Current state of research on flow failure considering void redistribution in liquefied deposits. *Soil Dynamics and Earthquake Engineering*, Elsevier, 23: 585-603.
- Lee H. J., Clough S. S., Chun S. S. and Han S. J. (1991). Sediment failures on the Korea Plateau slope, East Sea (Sea of Japan). *Marine Geology*, 97: 363-377.
- Lemke R. W. (1967). Effects of the Earthquake of March 27, 1964 at Seward, Alaska. *Geological Survey Professional Paper 542-E*, US Department of Interior.
- National Research Council. (1985). Liquefaction of soils during earthquakes. *Committee of Earthquake Engineering, Commission of Engineering and Technical Systems*, National Academy Press, Washington, D.C.
- Seed H.B. (1987). Design problems in soil liquefaction. *Journal of Geotechnical Engineering*, 113(8): ASCE.
- Takahashi T. (2007). Geotechnical properties of submarine sediments and basic study on submarine landslide mechanism. *Master's Thesis*, Graduate School of Chuo University (in Japanese).
- The Japanese Geotechnical Society. (1999). Investigations of the 1999 Kocaeli earthquake. *Reports on the Investigations of the 1999 Kocaeli Earthquake in Turkey and the 1999 Chi Chi Earthquake in Taiwan*, JGS (in Japanese).

LANDSLIDE HAZARD MAPPING USING MONTE CARLO SIMULATION- A CASE STUDY IN TAIWAN

Chia-Nan Liu

*Civil Engineering Department, National Chi Nan University,
No. 1, University Road, Nantou, Taiwan 545, China*

Taiwan's slope disasters resulted from heavy rains happen frequently due to its geographic, weather and topographic conditions. Therefore, the slope disasters in Taiwan cannot be neglected. With the development of GIS, the infinite slope analysis method which uses deterministic concept will confront two major problems when it is used in evaluating landslide susceptibility: first, the various engineering parametrics can't be determined easily. second, the mutual independent between grids will cause the unreal conditions such as the low landslide potential grids surrounded by high ones. This study chooses route Tou-71—from Puli to Ren-Ai as the main research area and typhoon Toraji as the rainfall event of analysis. The study also use the wide-range slope stability analysis software—TRIGRS, and Monte Carlo simulation which considers the uncertainty in parametrics to replace traditional single factor of safety with probability ones. The landslide susceptibility of study area is described by potentially failure probability.

INTRODUCTION

Taiwan is an island with about 70 % of its area is mountainous. The mountainous geography and young geology provide a developing environment for the occurrence of landslides. Moreover, the subtropical climate brings an average of 3.5 typhoons to Taiwan every year. The intense rainfall gives rise to severe landslide problems. Rainfall-triggered landslides are a recurring problem in Taiwan. They cause traffic disruption and economic damage or even claim catastrophic losses of human casualty. Therefore assessment susceptibility of landslide is important. A rational regional mapping of susceptibility of rainfall-triggered landslide is especially necessary to provide information for the hazard reduction and community development, such as mitigation facilities and warning system, regulation and management of land use, etc. There are a lot of sources of uncertainty associated with mapping landslide susceptibility. For example, the accuracy of information about past landslides and contributing parameters (elevation, slope angle, aspect, rainfall, etc) for the statistical approach is significantly dependent on the precision and version of remote sensing results. The parameters (strength properties, pore water pressure, failure surface, etc) applied in analytical approach for estimating the factor of safety of slope is also with inherent heterogeneity spatially. The quality and quantity of available data affect the exactness of generated landslide hazard map. A deterministic map showing the spatial distribution of level (class, or factor of safety, etc) of landslide hazard is not sufficient to take the uncertainties

into consideration. It is more appropriate to present a map showing landslide occurrence potential (or probability) which includes the spatial and temporal uncertainties of these data into the map generation. The goal of this study is to conduct probabilistic analysis to evaluate the probability of landslide occurrence that is triggered mainly by rainfall. In this paper, the analysis procedures including the application of analytical method, calculation of factor of safety, conduction of Monte Carlo simulation, evaluation of slope failure probability, and generation of hazard map are introduced. The landslide susceptibility map of a case site is built to demonstrate the manipulation of proposed methodology.

METHODOLOGY

The approach of mapping regional landslide hazard starts from the calculation of factor of safety of each pixel. The Monte Carlo method is incorporated in the calculation of factor of safety by simulating multiple times until the failure probability of each pixel is obtained.

The factor of safety is an index of the level of stability. The intent of a factor of safety is to account for uncertainty in design and analysis. Uncertainty in the factor of safety arises from uncertainty in the individual variables. The sources of uncertainties include shear strength (c' , ϕ'), the fluid pressure (u), the unit weight of soil (γ), slope angle (α), and sliding depth (Z). Further, the uncertainty in fluid pressure comes from uncertainties in conductivity (K_z), diffusivity (D_o), and initial infiltration rate (I_z). Therefore, the actual landslide reliability is not known from a deterministic value due to uncertainty in the calculation of factor of safety.

Monte Carlo simulation repeatedly samples the values from the probability distributions for the uncertain variables then put them into model to calculate the corresponding outcome. It is a useful tool to approximate the probability when the analytical results are difficult to obtain. For example, Gui et al. (2000) implemented it into SWMS_2D program to consider the significant uncertainty of hydraulic conductivity in soil to analyze the dam stability. Liu and Chen (2006) also applied it to simulate spatial distribution of CPT measurement to map the liquefaction potential over Yuanlin town in Taiwan. Monte Carlo simulation is also popular in mapping slope stability. For example, Zhou et al. (2003) use it to simulate the strength parameters to build the map of landslide probability. Wang et al. (2006) based on 3D slope-stability analysis models and on Monte Carlo simulation to identify the spots of potential landslides.

In this analysis, the Monte Carlo simulation technique is implemented into the TRIGRS program. The mean value and variance of random variables of each element are input to form specific probability distribution. The information of mean value and standard deviation is to provide the most possible value of a variable and its variation, respectively. Randomly sampled values from these probability distributions along with deterministic variables are input into TRIGRS to calculate the fluid pressures as a function of time and location while the factor of safety of each pixel corresponding to these parameters is calculated using infinite slope method. The procedures for generating random numbers, calculation of fluid pressures, evaluation of factor of safety, are repeated multiple times in one set of Monte-Carlo simulations. The failure probability for pixel i , $P_{F,i}$ is calculated from the simulation results as follows:

$$P_{F,i} = \left(\sum_{j=1}^{N_{\text{realization}}} I_j \right) / N_{\text{realization}}$$

where $N_{\text{realization}}$ is the number of realizations conducted; I_j is an indicator function with a value of 1.0 if factor of safety is smaller than unity and a value of 0.0 otherwise.

RESULTS AND DISCUSSIONS

Nantou 71 road locates in the center of Taiwan, connecting Puli town and Fachi village as the only transportation line for the Fachi villagers. The section between WuJai tribe and Fachi village suffered severe damage due to landslide during Typhoon Toraji on 2001/07/30. Rainfall data from WuJai station reveal that one daily (07/29-07/30) total rainfall of 372 mm was recorded during this typhoon event. There were two peak rainfall intensity occurred at the morning on 07/30. The maximum hourly rainfall was 55.5 mm/hr. A great amount of landslide phenomena was observed along Nantou 71 road after the strike of Typhoon Toraji. These landslides were characterized as shallow, planar slope failure. The failure surface was not deep seated nor circular. The occurrence of these landslides is directed induced by the heavy amount of rainfall. The landslide susceptibility of this region corresponding to this storm event will be mapped using the approach proposed in this study.

To prepare the landslide susceptibility map, the study region was divided into pixels. The size of the pixels is basically based on the resolution of the potential map and computing time. The study area is meshed into 8064 pixels for landslide potential mapping. The dimension of each pixel is 10 m (length) \times 10 m (width). The GIS system was used for data input, storage, capture, query, layout, and analysis. The data layers of potential sliding depth and fluid pressure, as described in the previous paragraphs, were prepared for the GIS system to capture values for each pixel. Digital elevation model data were used to layout topographical parameters. To achieve more accurate calculations, the original 40m \times 40m Digital Elevation Model (DEM) published by Agriculture and Forestry Aerial Survey Institute in 1994 is refined into 10m \times 10m by using Inverse distance weighting (IDW) model which is embedded in Arcview 3.2.

The attributes and statistical properties of parameters input for analysis are listed in Table 1. According to Central Limit Theorem, the shear strength parameters (c' , ϕ') and soil unit weight (γ) were treated as normally distributed random variables (Lumb, 1966). The hydraulic conductivity (K_z) was treated as lognormally distributed random variables (Freeze, 1975; Hoeksema and Kitanidis, 1985; Sudicky, 1986; Yang et al., 1996). As described in the previous section, initial infiltration rate (I_z) and diffusivity (D_o) were assumed to be 0.01 and 200 of K_z . Therefore their probabilistic distributions were also lognormal. The slope angle and sliding surface were assumed to be deterministic but not homogeneous. They were spatially distributed over study region thus the potential failure surface and slope angle were different for each pixel. These values were captured from data layers by using GIS system. Though the statistical properties of each parameter listed in Table 1 refer to the test results, site investigation results, and information collected from previous researches, it is worthy noted that certain extent of uncertainty exist in these parameters because of the insufficiency, subjective judgment or even erroneousness in the process of data preparation.

The effects of these design parameters on the landslide susceptibility will be discussed later.

Following the procedures presented in the previous section, the randomly generated numbers were assigned into the cumulative density function of c' , ϕ' , γ , and K_z to generate the values for these random variables and corresponding I_z and D_o variables.

Table 1. Characteristic of design parameters in this study

parameter	unit	type	mean value	cov
cohesion, c'	(kPa)	Normal	24.5	7 %
friction angle, ϕ'	(°)	Normal	30	18 %
soil unit weight, γ	(kN/m ³)	Normal	19.6	2.5 %
hydraulic conductivity, K_z	(m/s)	Log-normal	10 ⁻⁴	74 %
initial infiltration rate, I_z	(m/s)	Log-normal	0.01 K_z	-
diffusivity, D_o	(m ² /s)	Log-normal	200 K_z	-
sliding surface, Z	(m)	Deterministic	exploration	

These hydrological parameters along with the topographical data of each pixel, and the hourly rainfall histogram recorded in WuJai station were input into TRIGRS program to simulate the resultant spatial distribution of transient fluid pressure. The infinite slope method imbedded in TRIGRS is used to calculate the factor of safety of landslide of each pixel for this realization. The simulated statistical estimators of four random variables, c' , ϕ' , γ , and K_z for different number of simulations (N) are compared with the input statistical properties. The results show that 2000 simulations are appropriate as N value in this analysis. Therefore the above procedures of evaluating factor of safety of all pixels were repeated for 2000 realizations. The 2000 factors of safety of each pixel were collected to calculate the failure potential by using Equation (1).

The landslide potential map at 15 hours after rainfall initiation (the most critical status) is compared with the field records of landslides triggered by this rainfall event (Figure 1). It shows that locations of clusters of higher landslide potential are comparable to the location and shape of the observed landslide phenomena after Typhoon Toraji. The average landslide probability of the 911 pixels which landslide did occur is 48.4 %, while it is 8.8 % for the 7153 pixels which landslide did not occur.

There are some clusters is not consistent with the field observation. This inconsistency is attributed to the initial status. As shown in Figure 1, the significantly grey dark pixels indicate high landslide potential at these locations though no rainfall occurs. Landslide potentials at those locations are further increased when the rainfall begins to infiltrate into soil profile. The initial high landslide potential is ascribed from large slope and deep failure surface which was retrieved from the topographical data (DEM). The DEM applied in this study is issued in 1994. It may not show the accurate terrain in 2001 because this region has been suffered from severe weathering process, landslide, and strong earthquake (Chi-Chi Earthquake in 1999). This inconsistency reveals the quality of initial information is very important to the accuracy of landslide susceptibility map.

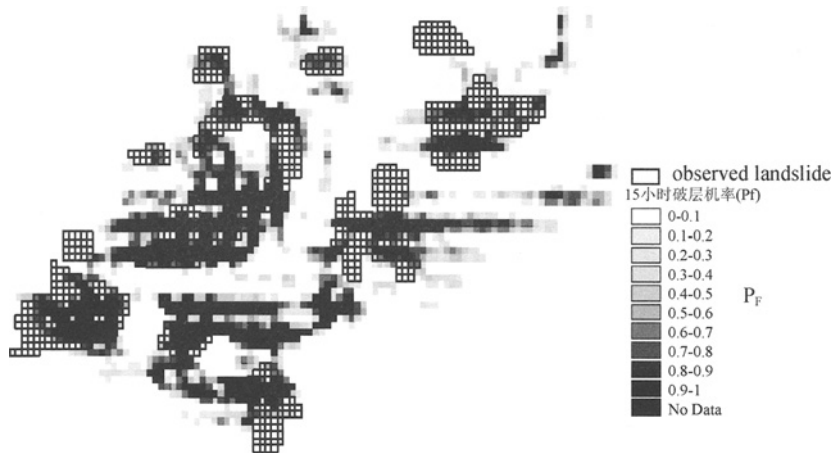


Figure 1. Comparison between the most critical (2001/07/30/0500) status of simulated landslide probability of study area and field records of landslides

CONCLUSIONS

To build a region having sustainable development as a goal, the mapping of the potential hazardous area is important to assess the possible location of risk, to develop a reliable and practical mitigation program, and to plan hazard management. Landslides cause significant economic loss or even life every year in mountainous areas. Therefore, landslide susceptibility mapping is important in such regions. Several methodologies have been suggested for landslide susceptibility mapping. This paper has provided a practical approach for mapping landslide susceptibility of each pixel. Compared with the defects of subjectivity embedded in qualitative approach and the imperfect or limited historical landslide data in quantitative approach, this approach bases on solid consideration of analytical analysis. A case history of landslide triggered by Typhoon Taraji in Taiwan was used to demonstrate how to manipulate the approach. It shows the landslide probability over study region getting higher with the accumulation of rainfall. The simulated potential map is generally comparable to the field observations. Some inconsistencies exist between the simulated potential map and field observation because part of the DEM data does not accurately reflect the initial status of landslide susceptibility. The probabilistic approach implemented in the TRIGRS software relies on grid-based data. The accuracy of output is heavily dependent on the accuracy of the digital elevation model (DEM) data input.

REFERENCES

- Freeze R.A. (1975). A stochastic-conceptual analysis of one-dimensional groundwater flow in nonuniform homogeneous media. *Water Resources Research*, 11: 725-741.
- Gui S.X., Zhang R. and John P.T. (2000). Probabilistic slope stability analysis with stochastic soil hydraulic conductivity. *Journal of Geotechnical and Geoenvironmental Engineering*, 126: 1-9.

- Hoeksema R.J., Kitanidis P.K. (1985). Analysis of the spatial structure of properties of selected aquifers. *Water Resource Research*, 21: 563-572.
- Liu C.N., Chen J.H. (2006). Mapping liquefaction potential considering spatial correlations of CPT measurements. *Journal of Geotechnical and Geoenvironmental Engineering*, 132: 1178-1187.
- Lumb P. (1966). The variability of natural soils. *Canadian Geotechnical Journal*, 3: 74-97.
- Sudicky E.A. (1986). A natural gradient experiment on solute transport in a sand aquifer: Spatial variability of hydraulic conductivity and its role in the dispersion process. *Water Resource Research*, 22: 2069-2083.
- Wang C., Esaki T., Xie M. and Qiu C. (2006). Landslide and debris-flow hazard analysis and prediction using GIS in Minamata–Hougawachi area. Japan. *Environmental Geology*, 51: 91-102.
- Landslide prediction. *Earth Surface Processes and Landforms*, 27: 1285-1297.
- Yang J., Zhang R., Wu J. and Allen M.B. (1996). Stochastic analysis of adsorbing solute transport in two-dimensional unsaturated soil. *Water Resource Research*, 32: 2747-2756.
- Zhou G., Esaki T., Mitani Y., Xie M. and Mori J. (2003). Spatial probabilistic modeling of slope failure using an integrated GIS Monte Carlo simulation approach. *Eng Geol*, 68: 373-386

STATISTICAL EVALUATION FOR STRENGTH OF PILE BY DEEP MIXING METHOD

Yong Liu, Junjie Zheng and Jia Guo

*School of Civil Engineering and Mechanics, Huazhong University of Science and
Technology, Wuhan 430074, China*

This paper presents a statistical method to evaluate the strength of heterogeneous stabilized pile by deep mixing method using cement as an additive reagent. The cross-section of stabilized shaft is conceptually divided into small elements in order to examine the characteristics of its heterogeneity due to imperfect mixing. The properties of each element are treated as independently identical. Typically, the unconfined compressive strength of cemented clay is regarded as a random variable of which the probability density distribution is assumed as log-normal. Based on probabilistic and statistic theory, another random variable, denoted as the factor of mixing uniformity, is proposed to quantitatively assess the influences of mixing quality on the strength of pile shaft. The probability density function of this factor is studied, and its applications in conventional design and Reliability-Based Design (RBD) method are analyzed as well.

INTRODUCTION

The deep mixing stabilizing process typically takes place by mechanical dry mixing, wet mixing or, grouting (Rathmayer, 1996; Porbaha, 1998; Bruce, 2003). Dry mixing is usually preferred in project sites where water tables are high and close to the ground surface. Wet mixing is recommended for dry and arid environments or sites with deep water table locations. Grouting with or without jets has been used for ground strengthening, excavation support and ground water control in construction projects (Kamon, 1996; Porbaha, 1998).

The strength of cemented clay of deep mixing method (DMM) has been extensively investigated (Gallavresi, 1992; Nagaraj et al., 1996; Lee et al., 2005). Many of them are conducted via treating the unconfined compressive strength as invariable for given curing days. However, taking into account the non-uniformity of deep soil mixing, variation of natural soil properties and changes of some conditions during construction, the stabilized pile shaft by DMM has some heterogeneity in strength, and the range of strength variation is much larger than that of natural cohesive soils. In design, this heterogeneity in the material properties of the stabilized soil makes it difficult to treat its strength as a mass. It is possible to take core samples from the stabilized ground by boring and evaluate strength of each specimen by such as unconfined compression test (e.g. Lesson 2001, 2005a, 2005b). Nevertheless, the strength of stabilized soil as a mass cannot thoroughly be evaluated from that of specimens. Therefore very conservative value has been used for design strength in practical design.

Some probabilistic methods are studied to deal with this problem (e.g. Honjo, 1982; Porbaha, 2002). The formulations of these probabilistic methods are based on the following three basic assumptions:

- (a) A non-homogeneous pile cross-section, V , is composed of N pieces of smaller elements, v , which are assumed to be individually homogeneous and independently contribute to V .
- (b) Each element, v , is a perfectly elastic body that fails simultaneously with yielding, but no residual strength occurs.
- (c) The elastic shear modulus, G , and the strain at failure, γ , of v , are random variables, with the joint probability density function defined as

$$\text{Prob}[G \leq G \leq G + dG, \gamma \leq \gamma \leq \gamma + d\gamma] = \iint f_{G,\gamma}(G,\gamma) dG d\gamma \quad (1)$$

As for the assumption (c), however, it is quite difficult to determine the joint probability density function, $f_{G,\gamma}(G,\gamma)$. The present paper has proposed a probabilistic approach to estimate the strength of pile shaft based on the above assumptions (a) and (b).

PROBABILISTIC CHARACTERISTIC OF CEMENTED ADMIXED SOFT SOIL

With regard to the strength of cemented admixed soft soil, Lee et al (2005) proposes an empirical formula to predict the unconfined compressive strength q as follows

$$q = q_0 [e^{m(s/c)} / (w/c)^n] \quad (2)$$

in which q_0 , m and n are experimentally fitted values, w = mass of water in cemented admixed soft soil, c = mass of cement, s = mass of soil.

As for a given pile cross-section, the unconfined compressive strength of the i -th element, q_i , can be predicted by using Eq.(2). In order to make it amenable to statistical analysis, we transform Eq.(2) as

$$\ln q = \ln q_0 + m(s/c) - n \ln(w/c) \quad (3)$$

In order to figure out the probability density distribution (PDF) of q , it is necessary to investigate the effect of each term in Eq. (3) on q in terms of variation.

In concrete technology, strength development in cement-based composites, in which cement is the only interacting material, is often analyzed using Abrams' law (Abrams 1918, Horribulsuk et al., 2005). The law states that for a given set of ingredients, strength development is solely dependent upon the w/c ratio. Considering this, s/c in Eq. (3) may be taken as invariable for its relatively less influence on q , and w/c viewed as a random variable. It is obvious that the domain of w and c can be respectively estimated as $[a, b]$ and $[d, e]$, where $a, d > 0$ and $b, e < +\infty$. As a result, the domain of w/c is restricted to $[0, +\infty]$. For this reason, the PDF of w/c is reasonably assumed to follow a log-normal distribution. Upon analyzing Eq. (3), the PDF of q can also be regarded as log-normal. Accepting log-normal distribution as a reasonable fit to the q , the next task is to estimate parameters of the fitted distribution

$$f(q) = \frac{1}{\sqrt{2\pi}\sigma_{\ln\delta}q} \exp\left\{-\frac{1}{2}\left(\frac{\ln q - \mu_{\ln\delta}}{\sigma_{\ln\delta}}\right)^2\right\}, 0 \leq q < +\infty \quad (4)$$

where the parameters $\sigma_{\ln \delta}$, $\mu_{\ln \delta}$ may be obtained from the relations

$$\mu_{\ln \delta} = \ln(\mu_q) - \frac{1}{2} \sigma_q^2 \quad \sigma_{\ln \delta}^2 = \ln(1 + \sigma_q^2 / \mu_q^2) \quad (5)$$

in which μ_q and σ_q^2 represent the mean value and variance of q respectively. Therefore, two parameters of fitted lognormal distribution may be determined by the values of μ_q and σ_q^2 . Some researches have been conducted on evaluating these two parameters (e. g. Larsson 2001, 2005 a&b). Larsson's (2001) approach involves extraction of soil samples from field deep mixing columns using split-tube-sampler. Larsson's (2001, 2005a&b) researches demonstrate the feasibility of studying the uniformity of binder contents in deep mixing treated pile using statistical analysis. The mean value and variance is given by

$$\begin{cases} \mu_q = \sum_{j=1}^3 \sum_{i=1}^{n_s} (a_{ij} \times \alpha_i) / 3 \times \sum_{i=1}^{n_s} \alpha_i \\ \sigma_q^2 = \sum_{j=1}^3 \sum_{i=1}^{n_s} [(a_{ij} - \mu_q)^2 \times \alpha_i] / (3 \times \sum_{i=1}^{n_s} \alpha_i - 1) \end{cases} \quad (6)$$

The samples are numbered from the centre of the column, $i = 1$ to n_s where $n_s = 6$ for the small scale, $n_s = 4$ for the medium scale and $n_s = 2$ for the large scale. The samples are drawn in three directions from the centre of the column, numbered $j = 1$ to 3. The coefficient α represents the area ratio which the samples represent.

FACTOR OF MIXING UNIFORMITY

When the pile is under loading, some elements in the cross-section will fail. Denote $p(q(v_i))$ as the probability that an element v_i survives under a certain load. Based on assumption (b), $p(q(v_i))$ can be calculated as

$$p(q(v_i)) = \text{Porb}[q(v_i) \geq q_0] = \int_{q_0}^{+\infty} f(q) dv \quad (7)$$

in which q_0 = failure value of unconfined compressive strength, $f(q)$ = PDF of q , which is assumed to follow a log-normal distribution.

Providing that the number of elements on a cross-section is N , probability of n elements survive under the given load can be given by binomial distribution from the assumption (a)

$$p(n) = \binom{N}{n} p(q(v_i))^n [1 - p(q(v_i))]^{N-n} \quad (8)$$

If N is sufficiently large, the Eq.(8) is approximated by normal (Gaussian) distribution from the Demoiver-Laplace Theorem

$$p(n) = \frac{1}{\sqrt{2\pi N p(q(v_i))(1 - p(q(v_i)))}} \exp \left[-\frac{(n - N p(q(v_i)))^2}{\sqrt{2\pi N p(q(v_i))(1 - p(q(v_i)))}} \right] \quad (9)$$

Here the factor of mixing uniformity μ is introduced. It is defined as the ratio of number of elements on cross-section of mass V which survives under the given load to the total number of elements on the surface

$$\mu = n/N \quad (10)$$

From Eqs.(7-10), the PDF of μ is

$$p(\mu) = \frac{1}{\sqrt{\frac{2\pi p(q(v_i))(1-p(q(v_i)))}{N}}} \exp \left[-\frac{(\mu - p(q(v_i)))^2}{\frac{2p(q(v_i))(1-p(q(v_i)))}{N}} \right] \quad (11)$$

This is a normal distribution with mean value $p(q(v_i))$ and variance $\frac{p(q(v_i))[1-p(q(v_i))]}{N}$.

APPLICATIONS OF FACTOR OF MIXING UNIFORMITY

Application in conventional design

In conventional design, it is not uncommon to calculate the strength of pile using the following formula

$$R_a = \eta q A \quad (12)$$

in which R_a = strength of pile, η = reduction factor, q = unconfined compressive strength of cemented admixed soil, A = cross-section area of pile.

For a specific engineering problem, the value of η is determined differently due to different experiences or/and experts, and ranges roughly from 0.2 to 0.5. Due to such large a domain of η , the conventional design tends to relatively subjective. In this study, μ is used to replace η as

$$R_a = \mu q A \quad (13)$$

As for a practical design, the mean value of μ is a specific value which may be obtained from sampling. Therefore, it is reasonable using the mean value of μ to predict the strength of pile as

$$R_a = p(q(v_i)) q A \quad (14)$$

Application in reliability based design

In this study, a simple Reliability Based Design (RBD) methodology is introduced for controlling mixing quality. By denoting the minimum required strength of deep mixing pile as R_0 , a limited state equation can be given as follows based on Eq.(13)

$$Z = R_a - R_0 \quad (15)$$

in which Z = safety margin of strength. Considering the above limited state equation, apart from increasing the content of cement, there are two approaches enhancing the safety margin

Z to meet an acceptable reliability index value of 3.2 (Phoon 2003, 2005). On the one hand, A may be enlarged to increase the strength of pile, on the other hand, according to Eq.(7), (15) and (16), the safety margin may be enhanced by increasing $p(q(v_i))$ (i.e. the mean value of μ). This process can be achieved by reducing the variance of q . The latter method reflects the uniformity of mixing, for the variance of q tends to be small when the process of mixing is conducted with high quality, and relatively large for poor mixing. If A is fixed, the reliability index of Eq.(15) will be a function of $p(q(v_i))$. Therefore, the reliability of pile strength may be guaranteed through improve the mixing quality, of which the result is reflected in the value of $p(q(v_i))$.

CONCLUSION

This paper presents a statistical method to evaluate the strength of heterogeneous stabilized pile by DMM using cement slurry as an additive reagent. The PFD of the strength of cemented admixed soft soil may be assumed to follow a log-normal distribution due to its domain ranging from 0 to $+\infty$. The factor of mixing uniformity is introduced as a random variable, and its mean value is suggested to estimate the mixing quality. Therefore, the calculation of strength of pile can be conducted in a relatively subjective manner. Furthermore, the factor of mixing uniformity is expected to be applied in the RBD method, for its relationship of mixing quality and reliability index.

REFERENCES

- Abrams D. A. (1918). Design of concrete mixtures. *Bulletin 1 Structural Materials Research Laboratory*, Lewis Institute, Chicago.
- Bruce D. A., Bruce M. E. C. The practitioner's guide to deep mixing. *Proc. 3rd International Conference on Grouting and Ground Treatment*, New York, 1: 474-488.
- Gallavresi F. (1992). Grouting improvement of foundation soils. *Proc. Grouting, soil improvement and geosynthetics*, ASCE, New York, 1: 1-38.
- Honjo Y. (1982). A probabilistic approach to evaluate shear strength of heterogeneous stabilized ground by deep mixing method. *Soils and foundations*, 22(1): 23-38.
- Horpibulsuk S., Miura N. and Nagaraj T. S. (2005). Clay-water/cement ratio identity for cement admixed soft clays. *Journal of Geotechnical and Geoenvironmental Engineering*, 131(2): 187-192.
- Kamon M. (1996). Effects of grouting and DMM on big construction projects in Japan and the 1995 Hyogoken-Nambu earthquake. *Proc. 2nd International Conference on Ground Improvement Geosystems*, Tokyo, 1: 807-824.
- Larsson S. (2001). Binder distribution in lime-cement columns. *Ground Improvement*, 5(3): 110-122.
- Larsson S., Dahlstrom M. and Nilsson B. A. (2005a). Uniformity of lime-cement columns for deep mixing: a field study. *Ground Improvement*, 9 (1): 1-15.
- Larsson S., Dahlstrom M. and Nilsson B. A. (2005b). A complementary field study on the uniformity of lime-cement columns for deep mixing. *Ground Improvement*, 9(2): 67-77.
- Lee F. H., Lee Y. and Chew S. H. (2005). Strength and modulus of marine clay-cement mixes. *Journal of Geotechnical and Geoenvironmental Engineering*, 131(2): 178-186.
- Nishida K., Koga Y. and Miura N. (1996). Energy consideration of the dry jet mixing method. *Proc. 2nd International Conference on Ground Improvement Geosystems*, Tokyo, 1: 643-648.

- Phoon K. K., Kulhawy F. H. and Grigoriu M. D. (2000). Reliability-based design for transmission line structure foundations. *Computers and Geotechnics*, 26(4): 169-185.
- Phoon K. K., Kulhawy F. H. and Grigoriu M. D. (2003). Multiple resistance factor design for shallow transmission line structure foundations. *Journal of Geotechnical and Geoenvironmental Engineering*, 129(5): 807-818.
- Probaha A. (1998). State of the art in deep mixing technology, Part 1: Basic concepts and overview of technology. *Ground Improvement*, 2 (2) 81-92.
- Probaha A. (2002). State of the art in quality assessment of deep mixing technology. *Ground Improvement*, 6(3): 95-120.
- Rathmayer H. (1996). Deep mixing methods for soft subsoil improvement in the Nordic countries. *Proc. 2nd International Conference on Ground Improvement Geosystems*, Tokyo, 2: 869-878.

LIMITED FLOW BEHAVIOUR OF SAND WITH FINES UNDER MONOTONIC AND CYCLIC LOADING

S. R. Lo, M. D. Mizanur Rahman
*University of New South Wales, ADFA Campus
Canberra, ACT 2600, Australia*

D. Bobei
*Austrass Menard Pty Ltd, 13-15 Lyon Park Road, Macquarie Park
Sydney, NSW 2113, Australia*

Experimental studies on a sand with 10% fines were conducted to establish the linkage between monotonic and cyclic instability under undrained loading, in particular for the case of limited flow. Results of special strain path testing were presented to offer a theoretical explanation on the lack of clear field evidence of limited flow.

INTRODUCTION

Significant progress has been made, since the 80s, in linking liquefaction to instability; and as such the strain softening behaviour under monotonic undrained loading provides the key for understanding cyclic liquefaction behaviour. Mohamad and Dorby (1986) reported that the monotonic behaviour of soil must be considered in analyzing the undrained cyclic behaviour of saturated sand. Georgiannou et al. (1991) demonstrated that the monotonic bounding envelope of Ham river sand as determined in undrained loading was also applicable in determining cyclic response. Konrad (1993) found that the undrained peak strength envelope in the effective stress space could be used to define the triggering of strain softening in both monotonic and cyclic undrained loading. This envelope could be taken to be a unique line for samples at similar void ratio. Yamamuro and Covert (2001) confirmed that cyclic liquefaction in loose Nevada sand with 40% silt was triggered by “crossing” the instability line. Vaid and Sivathayalan (2000) reported that strain softening under undrained cyclic loading occurred at the instant when the mobilized friction angle attained the value that triggered strain softening under static loading. Gennaro et al. (2004) suggested that the response in undrained monotonic shearing contribute to the prediction of undrained response in cyclic loading.

Based on the above studies, the conceptual framework for linking liquefaction under cyclic loading to static liquefaction is presented in Figure 1. Unless stated otherwise to the contrary, shearing is performed under an undrained mode. In this framework liquefaction is a manifestation of instability and this is different from cyclic mobility. We can define an instability stress ratio, η_{IS} , by the effective stress state at peak undrained strength under monotonic loading. When the effective stress state crosses the line defined by η_{IS} as a result of pore water pressure generation due to either monotonic or cyclic loading, instability will be triggered. It is evident from Figure 1 that the stress pulse required to trigger instability under cyclic loading is less than that in monotonic loading. Furthermore, the effective stress

path of monotonic loading defines the boundary of admissible stress state during cyclic loading.

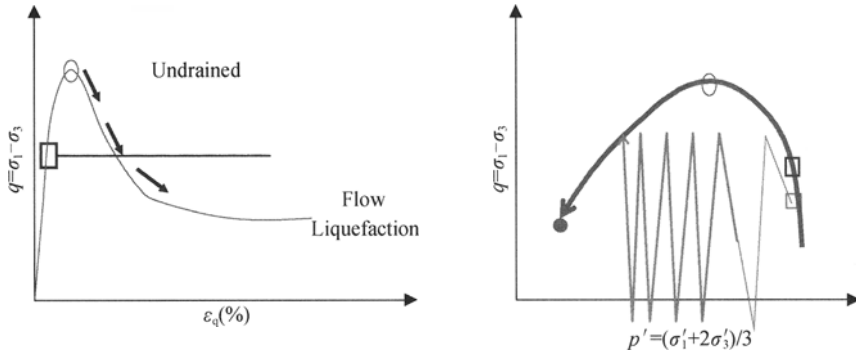


Figure 1. Instability under static and cyclic loading

However, experimental evidence directly verifying the above conceptual framework is relatively limited. There are also issues related to limited flow. First is how the above framework be applied to the case of limited flow. Second is whether limited flow is a real soil behaviour (Zhang and Garga, 1997). Although laboratory evidence indicates that limited flow can be real (Chu, 1999; Vaid et al., 1999a; Yoshimine, 1999), there has been a lack of clear field evidence on the existence of limited flow (Zhang and Garga, 1997). It is also recognized that most loose sandy soil have some fines, whereas experimental studies addressing the issue of limited flow has largely based on clean sand. The objective of the paper is to present experimental evidence that demonstrates the linkage between monotonic and cyclic instability in the case of limited flow, and explain via strain path testing the absence of clear field evidence of limited flow.

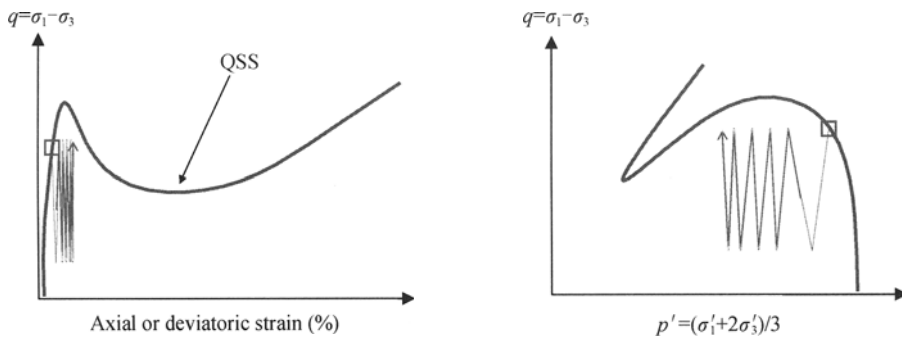


Figure 2. Limited flow

EXPERIMENTAL STUDY

Material tested

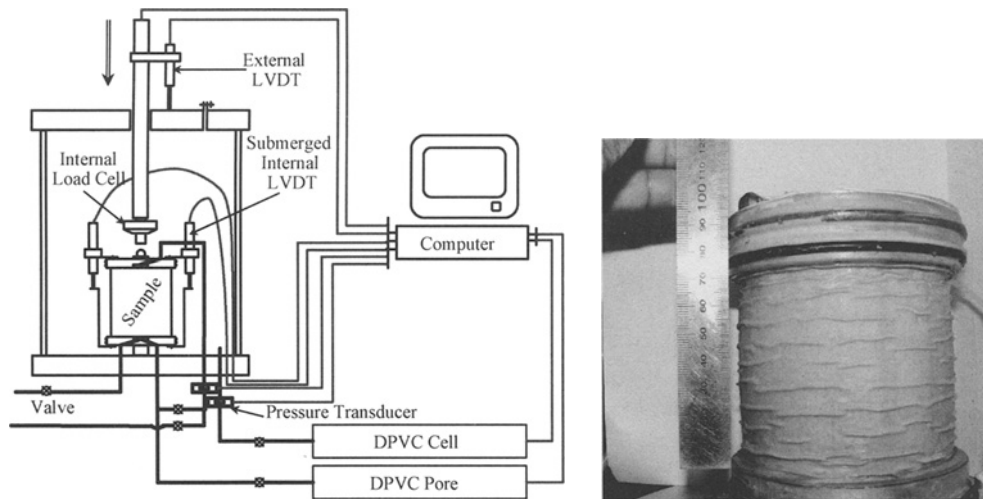
The material tested is a uniform quartz sand with 10% fines. The host sand is Sydney sand, a clean uniform size quartz sand (SP) with a mean size of 0.30mm and it's index properties can be found in Lo et al. (1989). The fines is a low plasticity fines (PI=11, LL=28) with a uniformity coefficient of 12.56. It is composed of 2/3 of well-graded silt from the Majura River and 1/3 commercial kaolin.

Specimen preparation

A specimen was formed by a modified moist tamping method. A pre-determined quantity of moist soil was carefully placed and then tamped lightly into a prescribed thickness using a standardized plastic strip with a tamping area of 8.5mm×20 mm. A total of 10 layers were placed in forming a specimen with a dimension of 100mm in both diameter and height. Free ends with enlarged platens were used to minimize end restraint. This technique has been proven to be successful in achieving essentially uniform deformation for a range of soil type (Chu et al., 1993; Lo and Wardani, 2002; Lo and Chen, 1999). Bedding and membrane penetration errors were reduced to an insignificant value by using the liquid rubber technique developed by Lo et al. (1989). Saturation was achieved by vacuum flushing with a low head followed by back pressure saturation. Details of the specimen preparation method are contained in Bobei (2005).

Experiment procedures

A schematic diagram of the experimental setup is shown in Figure 3(a). A triaxial testing system with PC-controlled data logging and stress/strain control capabilities was used for this study. Axial load was measured with an internal load cell. The axial deformation was measured with a pair of internal LVDTs mounted directly across the top platen plus an external LVDT. The former was used in the early stage of shearing whereas the latter was used at large deformation. Cell pressure was controlled by a large capacity Digital Pressure Volume Controller (DPVC). The pore pressure line was connected to a small capacity DPVC which served three purposes: i) controlling back pressure and measurement of volume change in drained stage, ii) ensuring nil volume change and measuring pore water generation in undrained shearing, and iii) controlling the ratio $d\varepsilon_v/d\varepsilon_q$ in a strain path test. The concept and implementation of a strain path test will be discussed at a later section. Pressure transducers were mounted at both the top and bottom platens to verify pore pressure equilibrium.



(a) Schematic diagram of experimental setup (b) Photo of specimen after loaded to an axial strain > 35%

Figure 3. Experimental methodology

COMPARISON BETWEEN MONOTONIC AND CYCLIC INSTABILITY

Monotonic loading and limited flow

A monotonic loading test that clearly manifested limited flow was used as the benchmark for comparison. This test, denoted as B_0 , was isotropically consolidated at an effective confining stress pressure of 600 kPa from which monotonic shearing began. Its behaviour in undrained shearing was shown as dotted line in Figures 4a-b. As evident from Figure 4a, the resultant effective stress path (ESP) clearly showed limited flow behaviour. However, the ESP did not show a sharp peak and η_{1S} was in the range of 0.75 to 0.81.

A distinct peak was, however, manifested in the stress strain curve of Figure 4b. The peak deviator stress, q_{peak} , of 390 kPa was mobilized at $\sim 3\%$ axial strain and the specimen strain softened to a q_{QSS} of 190 kPa, where subscript “QSS” denotes quasi-steady state. Although the minimum deviator stress point occurred at an axial strain of $\sim 10\%$, clear strain hardening resumed after axial strain exceeded 15%. This means unless the deformation of the specimen remains essentially uniform deformation when sheared well beyond 15%, QSS cannot be clearly differentiated from SS. This specimen, as shown in Figure 3b, did not show any sign of platen restraint even after the specimen was loaded to an axial strain of $\sim 35\%$ and therefore limited flow and QSS could be reliably confirmed.

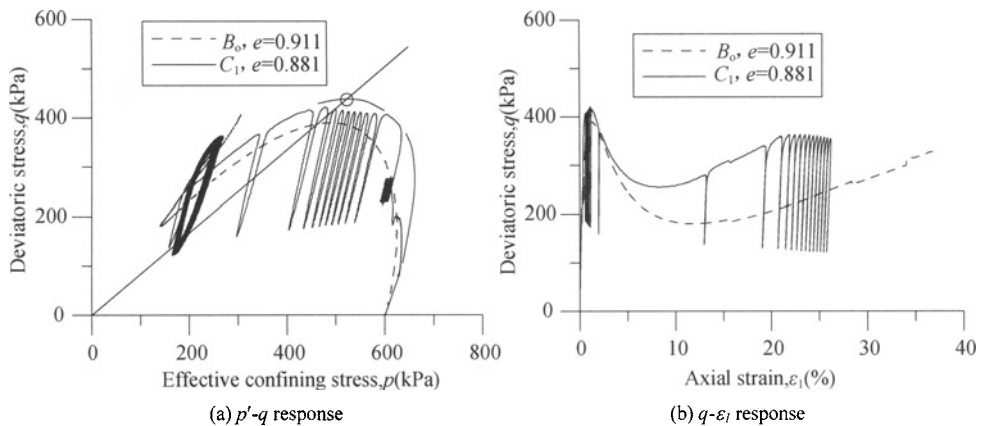


Figure 4. Comparison of tests B_0 & C_1

Cyclic loading and limited flow

Two one-way cyclic loading tests were conducted in a load-controlled mode. For both tests, the specimen was first brought to a non-zero deviator stress via undrained monotonic loading prior to the application of cyclic loading. For the first test C_1 , cyclic loading commenced prior to attaining q_{peak} . For the second test C_2 , the specimen was sheared beyond QSS prior to application of cyclic loading. The consolidated states of both C_1 and C_2 are closed to that of B_0 (in monotonic loading) so thus a meaningful comparison can be made.

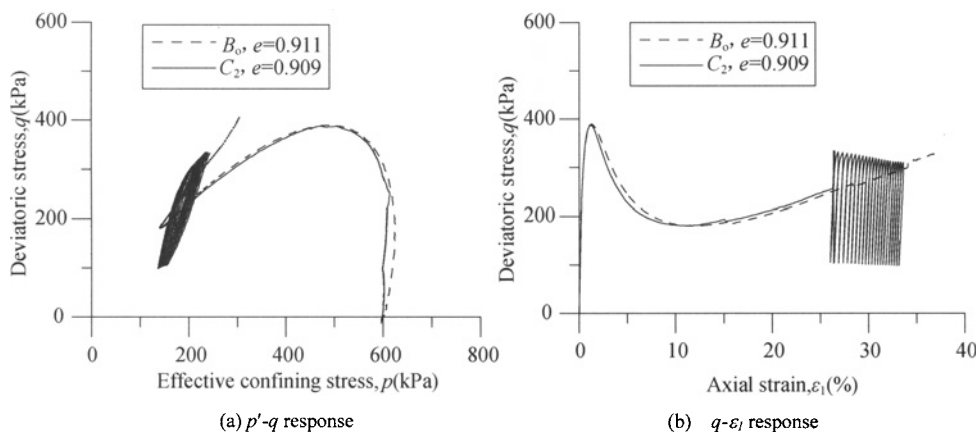


Figure 5. Comparison of tests B_0 & C_1

Test C1: This test had two stages of cyclic loading and the test results are shown as solid lines in Figures 4a-b. The first stage of cyclic loading was conducted with the deviator stress, q , cycling between 220 to 270 kPa. It is pertinent to mention that ESP manifested in bring the specimen from the isotropic stress state to $q = 270$ kPa essentially followed that of B_0 , thus confirming that the responses of these two tests could be compared meaningfully. During the first stage of cycling, the ESP moved slightly to the left (ie increase in p') with load repetition. There was also minimal accumulation of permanent strain. Therefore, the specimen showed no sign of approaching instability. This specimen was then brought in undrained mode to a high deviator stress and cycled between a cycle-trough of 190 kPa to a cycle-peak of 410 kPa. Despite the imposed cycle-peak of 410 kPa was higher than q_{peak} of 390 kPa (for B_0 in monotonic loading), the corresponding stress ratio η @ cycle-peak was less than η_{IS} because p' at cycle-peak was higher. The higher p' (due to lower pore water generation) was most likely to be due to the fact that C_2 had a lower void ratio. Thus a “projected” ESP for monotonic loading at an “identical” void ratio was shown as dashed line in Figure 4a. This projected ESP has η_{IS} of 0.81, which is the upper bound estimation of η_{IS} for B_0 . During the first 7 load cycles, the ESP moved gradually to the left and the shift per cycle is about the same. However, the leftward shift of the ESP increased for the 8th cycle. It is noted that η_{IS} was exceeded in the 8th cycle. For the 8th to 10th load cycles, the ESP shifted left considerably. Furthermore, the maximum deviator stress cannot reach the prescribed cycle-peak of 410 kPa. Instead, it traced a downward path that followed closely, but located above, the downward (instability) segment of the resultant ESP in monotonic loading. From the 11th cycle onwards, the ESP traced a closed and stable loop and with the cyclic-peak located approximately on the post-QSS segment of B_0 . A similar behaviour was also manifested in the stress-strain plot of Figure 4b, the cycle-peak traced a stress-strain curve that showed strain softening to a minimum deviator stress followed by strain hardening. However, the stress strain curve formed by the cycle-peak of cyclic loading was located considerably above the corresponding monotonic response of B_0 .

Test C_2 : This test had a void ratio very close to that of B_0 . As cyclic loading was applied only after the specimen had been sheared to beyond QSS, the equivalence of these two

specimen was assured. The test results of C_2 are shown as solid lines in Figures 5a-b. The imposed cyclic loading was from a cycle-trough of 105 kPa to a cycle-peak of 335 ka. The ESP during cyclic loading manifested a close loop with minimal shifting of location with load cycles. Furthermore, the stress state of cycle-peak was close to the last (upward) segment of the ESP of B_0 . However, the stress strain curve of C_2 during cyclic loading was different from the monotonic curve of B_0 . Initially, the cycle-peak was located well above the monotonic stress strain curve of B_0 . With load repetition, it eventually merged back to the monotonic stress strain curve of B_0 . Whether this difference is due to a load rate effect or due to some other mechanisms is unclear.

IN-SITU LIQUEFACTION MECHANISM

The occurrence of limited flow behaviour has been well established in element testing, but why this has not been clearly observed under field scale needs investigation. The so-called “Mechanism C” proposed by NCR (1985), in conjunction with behaviour under strain path testing, offers an explanation. The principle of “Mechanism C” is illustrated in Figure 6. Liquefaction in the field is not element behaviour as the in-situ stress states, say within a slope, are not uniform. Liquefaction initiates within the slope. This will leads to void ratio and pore water pressure re-distribution, with the soil above the initially liquefied zone having increase in void ratio. As this re-distribution is a continuous process, it can be represented by shearing under the condition of $d\varepsilon_v/d\varepsilon_q < 0$.

Independent of the NRC report, Lo and co-worker initiates an experimental program of studying the behaviour of sandy soil in strain path testing (Chu and Lo 1991). In essence, strain path testing is shearing along a constant strain increment ratio path, with the strain increment ratio, $d\varepsilon_v/d\varepsilon_q$, being controlled to a prescribed value. This is achieved by having the DPVC connected to the pore water line controlled by special software developed in-house. Strain path control can be activated at any stage, and the strain increment ratio can be change during shearing. Undrained shearing is a special form of strain path testing with $d\varepsilon_v/d\varepsilon_q=0$. The re-distribution of void ratio can be simulated as a process by strain path testing.

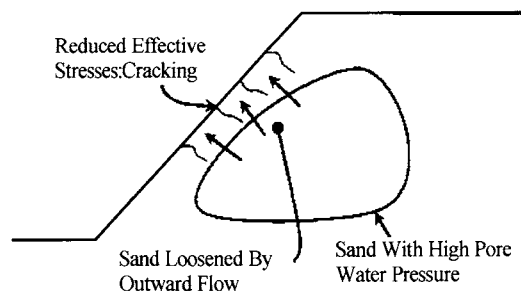


Figure 6. “Mechanism C” proposed by NCR (1985)

An undrained test B_1 was compared to a strain path tests SP in Figure 7. The strain path test was conducted in 4 stages, therefore denoted as SP_1 to SP_4 , and each stage was prescribed a different $d\varepsilon_v/d\varepsilon_q$ value. SP_1 was conducted with $d\varepsilon_v/d\varepsilon_q = 0$ and should showed a response identical to B_1 . As shown in Figure 7, B_1 manifested a limited flow response, with QSS attained at $\sim 10\%$ axial strain and strain-hardening re-commenced clearly at an axial strain of 15%.

Since the responses of B_1 and SP_1 are essentially identical over a strain range of $\sim 15\%$, the two specimens can be considered as replicate. Strain path control was activated on test SP at an axial strain of $\sim 15\%$ where the behaviour of clearly returned to strain hardening. A slight dilative strain path control defined by $d\varepsilon_v/d\varepsilon_q = -0.05$ was prescribed. This simulates a slight void ratio redistribution. As evident from Figure 7, the behaviour of SP_2 for $d\varepsilon_v/d\varepsilon_q = -0.05$ was strain softening! By any means, $d\varepsilon_v/d\varepsilon_q = -0.05$ is very small and more significant void ratio re-distribution can occur. Therefore, the prescribed value of $d\varepsilon_v/d\varepsilon_q$ was changed to -0.10 (for SP_3) and then -0.20 (for SP_4). As he test result showed that the more dilative the prescribed strain increment ratio, the more significant is the strain softening. This means, for the soil above the initially liquefied zone, the occurrence of a slight void ratio re-distribution will change the behaviour from limited flow for undrained shearing to that of strain softening. This change will be more significant for higher void ratio re-redistribution. This offers a plausible and theoretically sound explanation on why limited flow has not been clearly observed in the field.

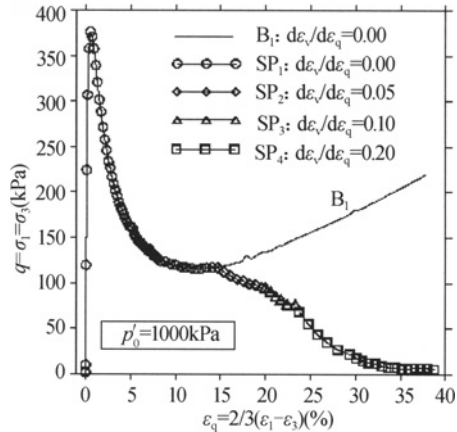


Figure 7. Simulation of void ratio re-distribution by strain path testing

CONCLUSION

This paper synthesizes some of the test results on the instability behaviour of sand with a small amount of low plasticity fines. The findings are:

- The effective stress conditions for triggering strain softening in cyclic and monotonic undrained loading is essentially identical: an effective stress ratio exceeding η_{IS} . This criterion also applies to the strain softening segment of limited flow.
- Once instability commenced, the cycle-peak appears to trace along the effective stress path of monotonic undrained loading. This applies to both the pre-QSS strain softening segment and the post-QSS strain hardening segment of the response, and irrespective of whether cyclic loading commenced from a pre-QSS state or a post-QSS state.
- “Mechanism C” as proposed by NCR (1985) can be simulated by strain path testing. Strain path tests that simulate a slight void ratio re-distribution in the soil above the

initially liquefied zone will turn a limited flow behaviour (for undrained mode) into continued strain softening. This offers a plausible and theoretically sound explanation on why limited flow has not been observed in the field.

ACKNOWLEDGEMENT

The second author is currently supported by the Endeavour International Postgraduate Research Scholarship. The last author was supported by the University College Postgraduate Award while conducting his research on instability of sand with fines. The opinions expressed in this paper are, however, solely those of the authors.

REFERENCES

- Bobei D. C., Lo S. R. (2001). Static liquefaction of Sydney sand mixed with both plastic and non-plastic Fines. *14th South East Asian Geotechnical Conference*, A.A Balkema, Hong Kong, 485-491.
- Bobei D. C., Lo S. R. (2007). Is conventional laboratory testing a reflection of field behaviour? *10Th Australia New Zealand Conference on Geomechanics*, Brisbane, Australia, 674-679.
- Chu J., Lo S-C.R.(1991). On the implementation of strain path testing. *10th European Conference on Soil Mech and Foundation Engg*, Florence, Italy, May 1991, Balkema Publishers, 53-56.
- Chu J., Lo S-C.R. and Lee I.K. (1993). Instability of granular soils under strain path testing. *J of Geot Engr J*, ASCE, 119(5): 874-892.
- Chu J. (1999). Quasi-steady state: A real behaviour?: Discussion / reply. *Canadian Geotechnical Journal*, 36(1): 190-191.
- Gennaro V. D., Canou J., Dupla J. C. and Benahmed N. (2004). Influence of loading path on the undrained behaviour of a medium loose sand. *Canadian Geotechnical Journal*, 41(1): 166.
- Georgiannou V. N., Hight D. W. and Burland J. B. (1991). Behaviour of clayey sands under undrained cyclic triaxial loading. *Géotechnique*, 41(3): 383-393.
- Ishihara K. (1993). Liquefaction and flow failure during earthquakes. *Géotechnique*, 43(3): 351-415.
- Konrad J. M. (1993). Undrained response of loosely compacted sands during monotonic and cyclic compression tests. *Géotechnique*, 43(1): 69-89.
- Ladd R. S. (1978). Preparing test specimens using undercompaction. *Geotechnical Testing Journal*, 1(1): 13-23.
- Lade P. V., Yamamuro J. A. (1997). Effects of nonplastic fines on static liquefaction of sands. *Canadian Geotechnical Journal*, 34(6): 918-928.
- Lo S. R., Chu J. and Lee I. K. (1989). A Technique for reducing membrane penetration and bedding errors. *Geotechnical Testing Journal*, 12(4): 311-316.
- Mohamad R., Dobry R. (1986). Undrained monotonic and cyclic triaxial strength of sand. *Journal of Geotechnical Engineering*, 112(10): 941-958.
- NCR. (1985). *Liquefaction of soils during earthquakes*. National Research Council CETS-EE-001, National Academy Press, Washington, D.C.
- Rahman M. M., Lo S. R. (2007). Equivalent granular void ratio and state parameters for loose clean sand with small amount of fines. *10Th Australia New Zealand Conference on Geomechanics*, Brisbane, Australia, 674-679.
- Vaid Y. P., Eliadorani A., Sivathayalan S., Uthayakumar M., et al. (1999a). Quasi-steady state: A real behaviour?: Discussion / reply. *Canadian Geotechnical Journal*, 36(1): 182-183.

- Vaid Y. P., Sivathayalan S. (2000). Fundamental factors affecting liquefaction susceptibility of sands. *Canadian Geotechnical Journal*, 37(3): 592-606.
- Vaid Y. P., Sivathayalan S. and Stedman D. (1999b). Influence of specimen-reconstituting method on the undrained response of sand. *Geotechnical Testing Journal*, 22(3): 187-195.
- Yamamuro J. A., Covert K. M. (2001). Monotonic and cyclic liquefaction of very loose sands with high silt content. *Journal of Geotechnical and Geoenvironmental Engineering*, 127(4): 314-324.
- Yoshimine M. (1999). Quasi-steady state: a real behaviour?: discussion / reply. *Canadian Geotechnical Journal*, 36(1): 186-187.
- Zhang H., Garga V. K. (1997). Quasi-steady state: a real behaviour? *Canadian Geotechnical Journal*, 34(5): 749.

TRAVEL DISTANCE OF DEBRIS FLOWS TRIGGERED BY SLOPE FAILURES

Hideki Ohta

*Department of International Development Engineering, Tokyo Institute of Technology,
Oh-okayama 2-12-1
Meguro, Tokyo 152-8550, Japan*

Hirohiko Kusaka

*Tohoku Branch, East Nippon Expressway Company,
Chuo 3-2-1
Aoba, Sendai 980-0021, Japan*

Yutaka Miura

*Hachioji Branch, Central Nippon Expressway Company,
Utsugi 231
Hachioji 192-8648, Japan*

*Katsumi Ohkubo, Masaru Takemoto and Kiyoyuki Amano
Nippon Expressway Research Institute,
Tadao 1-4-1
Machida 194-8508, Japan*

The travel distance of debris flow is known as a function both of volume of failed rock mass and height difference as empirically shown by Scheidegger (1973) and Hsu (1975). The authors additionally plotted the travel distance of debris flows which took place in Japan and the Philippines in 2006 on the graph proposed by Scheidegger and Hsu. As the results, the authors obtained a band of data points similar to but somewhat different from the tendency given by Scheidegger and Hsu.

INTRODUCTION

Slope failures triggered by heavy rainfall (and/or earthquakes) usually result in debris flows which sometimes hit residential areas and kill many people. A debris flow at Guinsaogon in Layte Island, the Philippines, traveled about 3.7km and killed about 1,500 people in 2006. A debris flow at Betto Valley near Mt. Hakusan, Japan, traveled 2.8km in 2004. A debris flow at Mt. Ontake, Japan, traveled 13km in 1984. It is intuitively understandable that a bigger slope failure at a higher altitude causes longer travel distance. However it is not very easy to predict the travel distance of a debris flow possibly caused by a potential slope failure.

The travel distance of debris flow is known as a function both of volume of failed rock mass and height difference as empirically shown by Scheidegger (1973) and Hsu (1975). Okuda (1984) plotted his data obtained in Japan in addition to Hsu's data and found that his data are in accordance with the data plotted by Hsu (1975). The authors additionally plotted the travel distance of debris flows which took place in Japan and the Philippines in 2006 on the graph proposed by Scheidegger (1973) and Hsu (1975). As the results, the authors obtained a band of data points similar to but somewhat different from the tendency given by Scheidegger (1973), Hsu (1975) and Okuda (1984).

Ashida, Takahashi and Michiue (1983) introduced theoretical interpretations on the travel distance of debris flows which are not necessarily reliable on the case by case basis. Iketani (1999) mentioned that the debris flows in many cases start depositing at the location where the gradient of the valley becomes gentler than 10 degrees and stop travelling when the ground gradient becomes about 3 degrees.

NEARBY SLIDES ALONG CHUO EXPRESSWAY

During a period from 18th through 20th July of 2006, 11 slides took place resulting in debris flows which hit Chuo Expressway in the central part of Japan. The slides were caused by two days (18th and 19th July) heavy rain of about 230mm preceded by another one day (17th July) heavy rain of about 100mm. The authors have inspected the sites, surveyed along the route of the debris flows and collected the data needed in plotting data points on the graph proposed by Scheidegger (1973) and Hsu (1975).

Figure 1 is an overlooking view of a tentative protection wall installed at the edge of Chuo Expressway that was swept by a debris flow a few days before this Figure was taken. A debris flow and its scars are shown in Figures 2 and 3 where sandbags are tentatively placed to fix the stream route. Quickest opening of the mortorway to the traffic was urgently needed immediately after the disaster.

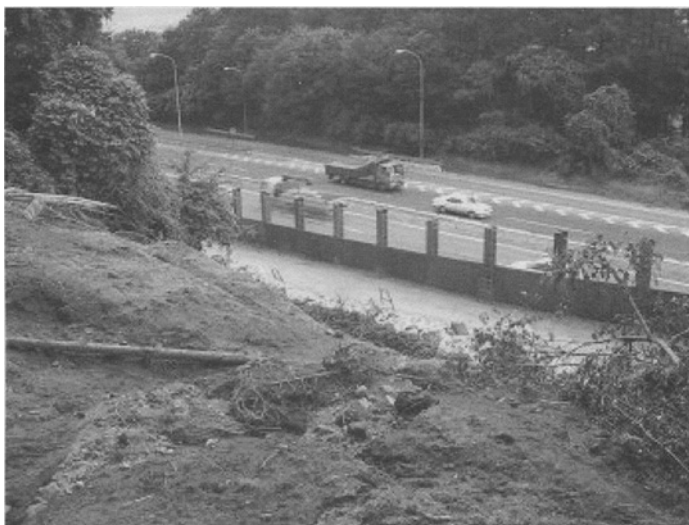


Figure 1. Tentative protection wall at a site

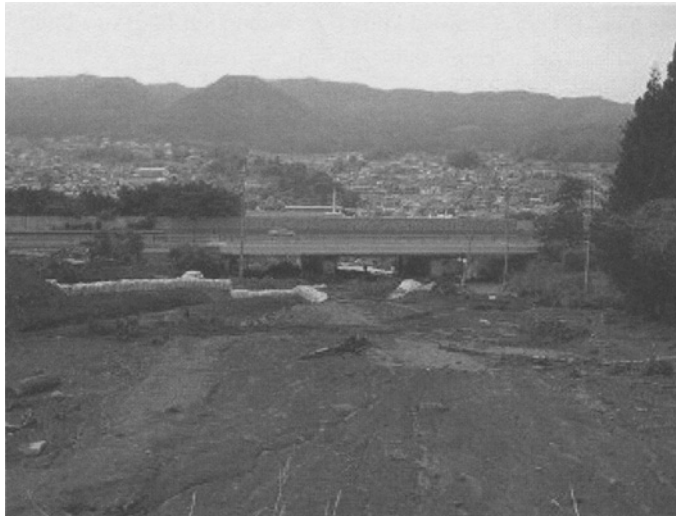


Figure 2. Debris flow passing under the mortorway



Figure 3. Scars of debris flow coming down the valley

Figures 4 show a tunnel found at the uppermost part of failed slope. The surface of the tunnel was smooth and clean indicating that it must have been a passage of the underground stream during the time of heavy rainfall. Existence of such a natural tunnel through which the water flows quite rapidly suggests some possibility of detecting the possible danger of slope failure by placing a microphone in the ground near the surface to hear the sound of water flow at the time of heavy rainfall. It would also be possible to detect the existence of such a natural tunnel by hearing the sound of water flow and make a man-made water outlet. The ground water coming out to the ground surface through the man-made water outlet will give no pore pressure to the soil anymore. This could be an economical countermeasure to stabilize a potentially dangerous slope.



Figures 4. Uppermost stream flowing out from a natural tunnel of about 1m diameter

CATASTROPHIC SLOPE FAILURES

A slope failed on 17th May in 2004 at Betto Valley near Mt. Hakusan, Japan, and debris flow traveled 2.8km. The failure took place after 2days heavy rain of about 200mm. The reported volume of failed rock mass was about $176,000\text{m}^3$. Another nearby slope failed on 7th and 15th September in 2006 resulting in the failed rock mass of about 4000 and 1000m^3 respectively.

A colossal slope failure took place on 17th February in 2006 at Guinsaugon in Leyte, Philippines as seen in Figure 5. Huge area was swept by the debris flow as seen in Figure 6. The first author visited the site in September, 2006. It was really a pity to see many of houses destroyed by the debris flow in the area of Guinsaugon village which disappeared in a very short moment.



Figure 5. Colossal slope failure at Guinsaugon, Leyte



Figure 6. Debris flow covering a huge area

TRAVEL DISTANCE OF DEBRIS FLOWS

The authors plotted all the data points collected from the sites described above on a graph of Scheidegger and Hsu. The results are shown in the upper figure of Figure 7 where the

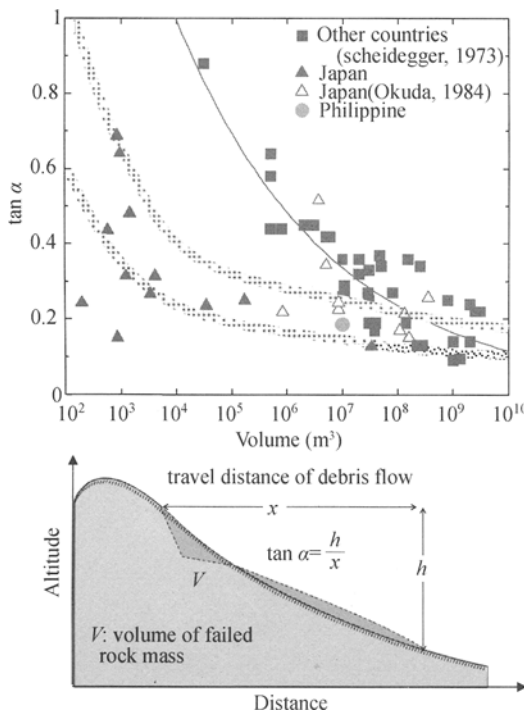


Figure 7. Travel distance of debris flow

vertical axis of the graph is a parameter indicating the travel distance of debris flow as defined in the lower figure of Figure 7 and the horizontal axis is the volume of the failed rock mass.

As seen in Figure 7, the authors obtained a band of data points similar to but somewhat different from the tendency given by Scheidegger and Hsu. The band obtained by the authors gives travel distance longer than that given by Scheidegger and Hsu. This difference may be due to the water content of the failed rock mass since the data points plotted by the authors are obtained from the slides in the Philippines and Japan where the annual precipitation is relatively high compared to many of the other regions of the world.

In Southeast Asian Region and in Japan, the intensity of rainfalls caused by typhoons seems to have increased year by year probably due to typhoons

getting stronger in average because of the temperature rise of the sea water in Pacific Ocean. If this is correct, there will be more danger of having debris flows more often than before in these regions . The findings obtained by the authors may make it less difficult to predict the travel distance of debris flows possibly caused by potential slope failures in the future.

ACKNOWLEDGEMENTS

The first author wishes to thank Heiwa Nakajima Foundation for the financial support during the execution of this study.

REFERENCES

- Ashida K., Takahashi T. and Michiue M. (1983). *Debris disasters in the rivers and countermeasures*. Morikita-Shuppan. (in Japanese)
- Ikeya H. (1999). *Debris flow disaster*. Iwanami-Shinsho. (in Japanese)
- Hsu K.J. (1975). Catastrophic debris streams (Sturzstroms) generated by rockfalls. *Geological Society of America Bulletin*, 86: 129-140.
- Okuda S. (1984). Characteristics of mudflows caused by historic rock collapses. *Disaster Prevention Research Institute Annuals, Kyoto University*, 27(B-1): 353-368. (in Japanese)
- Scheidegger A.E. (1973). On the prediction of the reach and velocity of catastrophic landslides. *Rock Mechanics*, 5: 231-236.

SOME NUMERICAL CONSIDERATIONS IN UNSATURATED SLOPE STABILITY ANALYSIS DUE TO RAINFALL INFILTRATION

Kok Kwang Phoon

*Department of Civil Engineering, National University of Singapore
Blk E1A #07-03, 1 Engineering Drive 2, 117576, Singapore*

Yonggang Cheng

*Department of Civil Engineering, National University of Singapore
Blk E1A #07-03, 1 Engineering Drive 2, 117576, Singapore*

Accurate prediction of the propagating wetting front arising from rainfall infiltration into an unsaturated soil slope is of considerable importance to stability analysis of the slope. However, difficulties exist in numerical simulations of unsaturated flow analyses because of the highly nonlinear soil hydraulic properties. This paper emphasizes the slow convergence of calculated pressure heads with the refinement of mesh sizes and time steps, and discusses possible solutions.

INTRODUCTION

Shallow failures of slopes due to rainfall infiltration are quite usual in Singapore. During the rainfall, a wetting front goes deeper into the slope, which results in a gradual increase of the water content and a decrease of the negative pore water pressure. As this negative pore water pressure, referred to as matric suction when referenced to the pore air pressure, is recognized to contribute towards the stability of unsaturated soil slopes, the loss of suction causes a decrease in shear strength of the soil on the potential failure surface and finally triggers the failure (Rahardjo et al., 1995; Ng and Shi, 1998). Thus, the accurate prediction of the propagating wetting front arising from rainfall infiltration into the unsaturated soil is of considerable importance to slope stability analysis, especially when unusual heavy and prolonged rainfall becomes more frequent due to the global climate changes.

Due to the limitations often exhibited by analytical solutions, to obtain realistic representations of the ground water condition under a transient rainfall situation, numerical methods such as finite element method are often necessary for such unsaturated flow simulations. Many commercial finite element packages are available for such analyses. Among them, SEEP/W, developed by Geoslope (2004) is one of the most popular programs among engineers (e.g., Rahardjo et al., 2001; Tsaparas et al., 2002). We observe in passing that the Green-Ampt and similar simplified models are popular in soil sciences (Green and Ampt, 1911; Cho and Lee, 2002; Kim et al., 2004), but there are fundamental difficulties in these models.

In the literature, the effect of different mesh sizes and time step sizes is not well emphasized and systematic convergence studies are quite rare. Usually, coarse meshes and big time steps were used in their studies. For example, Rahardjo et al. (2001) used only 424 triangular or quadrilateral elements in a slope stability analysis with the slope height of 35m and width of around 60m. Few of the studies discussed whether the solutions generated with such meshes and time steps were accurate or not. Some studies have already shown that slow convergence problem existed in unsaturated seepage analysis using SEEP/W. It is found that the calculated pressure heads converged to a correct solution very slowly with progressive refinement of the element size and time step. For slope stability problems in unsaturated residual soils, errors made in the position of the wetting front seriously affect the location of the failure surface and the eventual factor of safety. Thus, the correctness of numerical solutions obtained using reasonable spatial and temporal discretization schemes based on limited convergence studies is of direct practical concern.

NUMERICAL OSCILLATION

Numerical oscillation describes a phenomenon that the calculated solution oscillates around the correct value. This oscillated pore-water pressure distributions do not appear realistic, as they indicate drying of the soil, which is unlikely with an influx boundary condition.

In SEEP/W 2004, the lumped-mass scheme is applied to curb such oscillations. However, it is found that the assumption of the mass-lumped scheme that the neighboring node response is always positive may be physically incorrect in a dry medium and may cause smearing of the wetting front, i.e., less accurate compared to consistent-mass scheme. It is also found that quadratic/cubic elements could cause oscillation even with lumped mass scheme. Effect of lumped-mass scheme is shown in Figure 1. It clearly shows that for linear 2-node elements, the oscillation can be removed by lumped-mass scheme; while for quadratic 3-node elements, oscillations can be observed in both consistent-mass scheme and lumped-mass scheme.

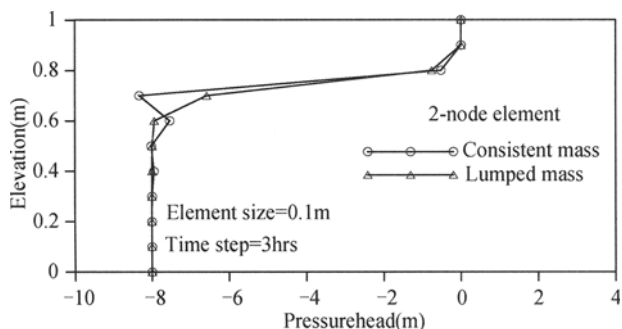
On the other hand, several authors (e.g., Karthikeyan et al., 2001) concluded that the oscillation was caused by using a time step which was too small relative to the element size. Karthikeyan et al. (2001) showed that a simple minimum time step criteria were adequate for ensuring non-oscillatory solutions, with various element types. These simple criteria are of considerable practical value as they allow engineers to remove numerical oscillations using their existing software without any modifications. The practical disadvantage is that a large time step satisfying these minimum time step criteria compromises accuracy. The minimum time step can be reduced by mesh refinement, but this solution increases runtime.

SLOW CONVERGENCE PROBLEM

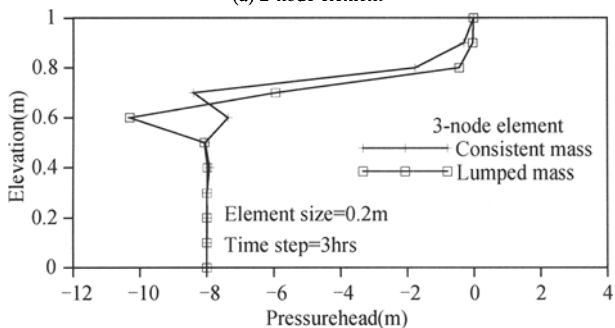
Slow convergence and under relaxation

Slow convergence problem has been observed by numerous researches (Celia et al., 1990; Tan et al., 2004; Cheng et al., 2007). While some authors (Celia et al., 1990) attributed such slow convergence problem to the mass imbalance error when pressure head based equation is used, Tan et al. (2004) showed that even with mass balance, slow convergence could still be

observed. They demonstrated that this slow convergence problem is an indirect result of the under relaxation technique (UR1) used in SEEP/W. This relaxation evaluates the hydraulic conductivity for the new iteration using an average of pressure heads calculated from the preceding time step and most recent iteration of the current time step. It is showed that UR1 ensures that the solution converges to a stable solution quickly within a time step, but may converge to a wrong wetting front unless a sufficiently dense mesh is used. An alternative under relaxation technique (UR2) is recommended that the material properties for the new iteration are defined at the average of the pressure heads computed from the two most recent iterations of the current time step. Their study showed that UR2 does not require very small time steps to produce reasonably accurate results, but does so at a price of increasing the number of iterations within each time step when dealing with soils with highly nonlinear hydraulic properties.



(a) 2-node element



(b) 3-node element

Figure 1. Effect of lumped-mass scheme

Transformation with under relaxation

Recently, Cheng et al. (2007) proposed a combination approach (TUR1) consisting of a rational function transformation method and the UR1 under relaxation scheme to solve the h-based form of Richards equation. Numerical studies (Figure 2) show that this combined method has the advantages of both UR1 and UR2. Firstly, like UR2, TUR1 can use coarser mesh and larger time step to produce acceptable results. Secondly, like UR1, TUR1 can converge to a stable solution quickly in each time step. In general, TUR1 appears more

superior to UR1 and UR2 in the sense that a more realistic solution can be obtained using a practically reasonable spatial and temporal discretization eventually.

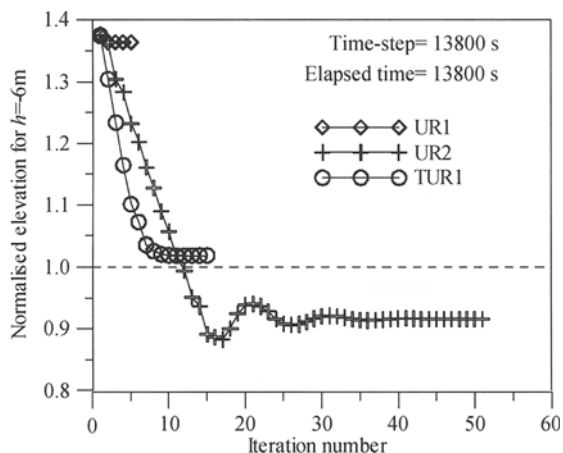


Figure 2. Convergence of the solution within a time step (correct solution is achieved at normalized elevation = 1)

Numerical example

In the following, numerical simulations are carried out to show the effects of different mesh sizes on the calculated pore water pressure response during rainfall infiltration in a slope and also the influence on the calculation of slope stability.

A 10m high slope at an inclination of 26.6° (inclination 2H:1V) is adopted in this study (Figure 3). The soil properties are defined in Table 1. The four parameter van Genuchten model is used here to define the soil water characteristic curve. And the Mualem model is used to define the conductivity function. As the initial condition, a constant negative pressure head of -8m is defined for the whole domain. To define the boundary condition, a zero pressure head is imposed at the slope surface. This type of boundary condition is representing a rainfall greater than the saturated permeability of the soil with the non-infiltrating water taken as runoff. To avoid the oscillation problem, 4-noded quadrilateral element is adopted.

Table 1. Summary of soil properties

Hydraulic parameters	θ_s	θ_r	a	n	K_s
	0.363	0.186	1.000 m^{-1}	1.53	$1.0 \times 10^{-6} \text{ ms}^{-1}$
Strength parameters	Saturated unit weight	Unsaturated unit weight	c'	φ'	φ^b
	20 kN/m^3	19 kN/m^3	1 kN/m^3	25°	25°

Notes: θ_s , θ_r , a , n , K_s : hydraulic parameters in van Genuchten and Mualem model;
 c' , φ' : effective cohesion and effective angle of internal friction;
 φ^b : friction angle with respect to the matric suction.

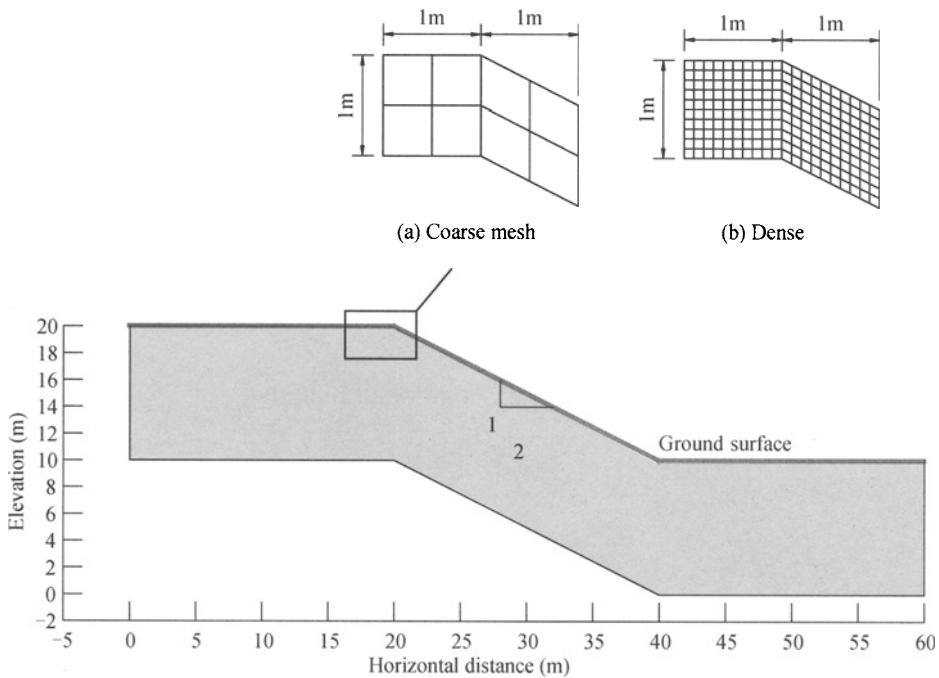


Figure 3. Geometry and finite element mesh of the slope used for stability analysis

Two different meshes are compared in the following study, as a coarse one with mesh size of $0.5 \times 0.5\text{m}$ (2400 elements) and a dense one of mesh of $0.1 \times 0.1\text{m}$ (60000 elements). It is worth to note that coarser mesh means less number of degrees of freedom (2541 DOFs for coarse mesh vs. 60701 DOFs for dense mesh). This results in a smaller set of FEM equation to solve, which further implies much less number of operations required for the direct matrix solver in each iteration, as it is reported that for large 2D and 3D problems involving matrices with significant bandwidth, the number of operations required for the direct matrix solver will approach $O(N^3)$ (Press et al., 1986), where N is the number of DOFs. For the specific problem we studied here, it is observed that the solution of linear system grows with $N^{1.3}$ because the global matrix is sparse. Therefore, the penalty on total run time becomes significantly heavier for denser mesh, which can be seen from the results of runtime in Table 2.

The result of pore water pressure profiles at the crest of the slope with different mesh sizes is shown in Figure 4. It clearly shows that with a coarse mesh of $0.5 \times 0.5\text{m}$, elevations of the wetting fronts are largely over predicted compared to the dense mesh of $0.1 \times 0.1\text{m}$. And this overprediction has serious influence on the slope stability calculations, which can be seen in Table 2 and Figure 5. For example, after 48 hours of rainfall, the wetting front reaches to the elevation of 18.2m with the dense mesh, compared to 19.0m with the coarse mesh. The corresponding factors of safety (FOS) are 1.137 for the dense mesh and 2.295 for the coarse mesh.

Note that the “coarse” mesh – $0.5 \times 0.5\text{m}$ – is already fine for most analyses undertaken by practicing engineers. Hence, the error in prediction of wetting front is not artificially

produced by the choice of an unrealistically coarse mesh. In fact, given that the mesh used by most engineers can be coarser than that shown in Figure 3(a), the error can be viewed as an optimistic estimate.

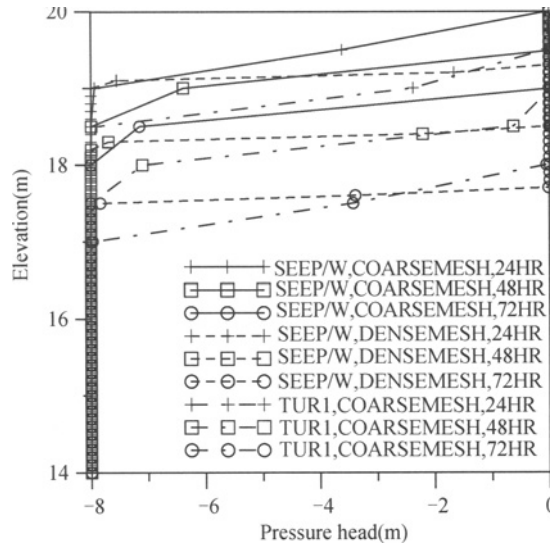


Figure 4. Pore water pressure profiles at the crest of the slope with different mesh sizes

Table 2. Slope safety factors and total runtime

Real time (hours)		Initial	12	24	36	48	60	72
Coarse mesh (SEEP/W)	Total runtime (seconds)	0	9	15	21	31	39	47
	Safety factor	2.768	2.726	2.704	2.675	2.295	1.856	1.023
Dense mesh (SEEP/W)	Total runtime (seconds)	0	368	848	1668	3448	5200	7080
	Safety factor	2.768	2.727	1.874	1.149	1.137	1.095	1.074
Coarse mesh (TUR1)	Total runtime (seconds)	0	10	20	31	42	53	64
	Safety factor	2.768	2.658	2.213	1.273	1.126	1.125	1.086

It also can be seen from Figure 4 that with the same coarse mesh, the TUR1 method generates much more accurate results than SEEP/W which adopts the UR1 under relaxation technique. Actually, the calculated depths of wetting fronts from TUR1 are quite close to the dense mesh solution from SEEP/W. And this is also true for the calculation of FOS of the slope, which can be seen in Table 2 and Figure 5. It clearly shows that with a “reasonable” mesh, TUR1 method can generate approximately correct solutions for unsaturated seepage flow problem, and hence more accurate computation of the factor of safety of the slope. A minor disadvantage of TUR1 is that it may requires a little more iterations per time step to get a stable solution, thus more runtime than UR1 with the same mesh (Table 2). But considering the accuracy and efficiency of solutions, the superiority of TUR1 is undoubted.

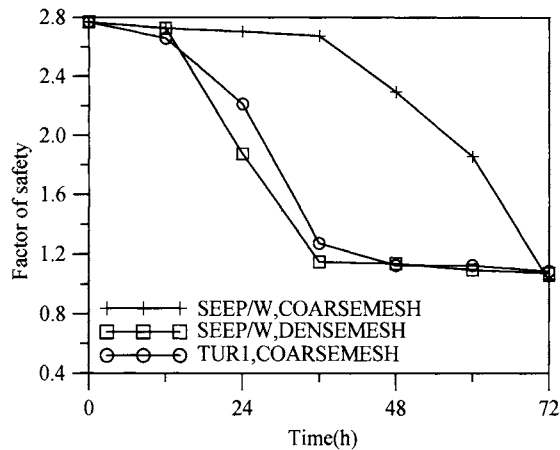


Figure 5. Change of FOS of the slope with time

CONCLUSION

SEEP/W is one of the most popular finite element commercial software used to simulate unsaturated seepage flow problems. However, numerical difficulties are found in such analyses such as the slow convergence of calculated pressure heads with reducing time step and mesh size. This overprediction of the wetting front has serious influence on the slope stability calculations. Studies show that this slow convergence is an indirect result of the under relaxation technique adopted by SEEP/W. To accelerate the convergence, an alternative under relaxation technique or a combination approach consisting of a rational function transformation method and the original under relaxation technique is recommended.

REFERENCES

- Celia M.A., Bouloutas E. and Zarba R.L. (1990). A general mass-conservative numerical solution for the unsaturated flow equation. *Water Resour. Res.*, 26(7): 1483-1496.
- Cheng Y.G., Phoon K.K. and Tan T.S. (2007). Unsaturated soil seepage analysis using a rational transformation method with under-relaxation. *Int. J. Geomech.*, submitted.
- Cho S.E. and Lee S.R. (2002). Evaluation of surficial stability for homogeneous slopes considering rainfall characteristics. *Journal of Geotechnical and Geoenvironmental Engineering, ASCE*, 128: 756-763.
- GEO-SLOPE. (2004). *Seepage modeling with SEEP/W: An engineering methodology*. GEO-SLOPE International Ltd., Calgary, Alberta, Canada.
- Green W.H., Ampt C.A. (1911). Studies on soil physics: Flow of air and water through soils. *Journal of Agricultural Science*, 4: 1-24.
- Karthikeyan M., Tan T.S. and Phoon K.K. (2001). Numerical oscillation in seepage analysis of unsaturated soils. *Can. Geotech. J.*, 38: 639-651.
- Kim J., Jeong S., Park S. and Sharma J. (2004). Influence of rainfall-induced wetting on the stability of slopes in weathered soils. *Engineering Geology*, 75: 251-262.
- Ng C.W.W., Shi Q. (1998). A numerical investigation of the stability of unsaturated soil slopes subjected to transient seepage. *Computers and Geotechnics*, 22(1): 1-28.

- Press W.H., Flannery B.P., Teukolsky S.A. and Vetterling W.T. (1986). *Numerical recipes*. Cambridge University Press, Cambridge, U.K.
- Rahardjo H., Li X.W., Toll D.G. and Leong E.C. (2001). The effect of antecedent rainfall on slope stability. *Geotech. and Geological Engrg.*, 19: 371-399.
- Rahardjo H., Lim T.T., Chang M.F. and Fredlund D.G. (1995). Shear-strength characteristics of a residual soil. *Can. Geotech. J.*, 32: 60-77.
- Tan T.S., Phoon K.K. and Chong P.C. (2004). Numerical study of finite element method based solutions for propagation of wetting fronts in unsaturated soil. *J. Geotech. and Geoenviron. Engrg.*, 130(3): 254-263.
- Tsaparas I., Rahardjo H., Toll D.G. and Leong E.C. (2002). Controlling parameters for reinfall-induced landslide. *Computers and Geotechnics*, 29: 1-27.

PROBABILISTIC SEISMIC AND TSUNAMI HAZARD ANALYSIS FOR DESIGN CRITERIA AND DISASTER MITIGATION IN REHABILITATION AND RECONSTRUCTION OF A COASTAL AREA IN CITY OF BANDA ACEH

I. Wayan Sengara

*Geotechnical Engineering Division - Civil Engr Department and Center for Disaster
Mitigation, Institut Teknologi Bandung, Jl. Ganesha 10, Bandung-40132, Indonesia*

Hamzah Latief, Syahril B. Kusuma

*Center for Disaster Mitigation, Institut Teknologi Bandung,
Jl. Ganesha 10, Bandung-40132, Indonesia*

A Rehabilitation and reconstruction process for coastal area of city of Banda Aceh post Great Sumatra ($M_w = 9.3$) earthquake requires both seismic and tsunami hazards design criteria. A case study to develop design criteria of a coastal sub-district site in the effort of disaster mitigation is presented. The case study consists of probabilistic seismic and tsunami hazard analysis. The potential of both subduction and shallow crustal faults is considered in the seismic hazard analysis. The subduction source zones are considered as a seismic source for the tsunami hazard analysis. Some site-classification analyses were conducted to estimate level of ground surface acceleration. The analyses were based on collection of shear wave velocity data from a set of geotechnical subsurface exploration and spectral analysis of surface wave survey. Likewise, tsunami inundation maps generated from probabilistic tsunami hazard analysis was also developed. The maps were developed through tsunami and run-up numerical modeling associated with its earthquake probabilities. Both the seismic and tsunami hazard criteria are recommended as a basis for design criteria as part of the disaster mitigation effort in the currently undergoing rehabilitation and reconstruction process, as well as for long-term development of the case-study site.

INTRODUCTION

Coastal areas of City of Banda Aceh has experienced catastrophic damages due to earthquake ($M_w = 9.3$) and tsunami of December 2004. More than two hundred thousands people had loss their life and many buildings, infrastructures, and lifelines have been completely destroyed. Almost all the residential houses in the coastal area were destroyed by the tsunami. The earthquake had caused many buildings completely collapse and some buildings experienced only slight damage. Many roads and embankments were identified to collapsed and damaged due to liquefaction and lateral spread.

Rehabilitation and reconstruction is currently undergoing, consisting of construction of thousands of residential houses and many infrastructures and lifelines as well as some critical facilities. Both seismic and tsunami hazard criteria is essential as a basis for rehabilitation, reconstruction, and long-term development of the city.

PROBABILISTIC SEISMIC HAZARD ANALYSIS

PSHA for city of Banda Aceh has been conducted herein to recommend the level of peak baserock acceleration (PBA). The PSHA also resulted in the associated uniform hazard spectra at the reference base-rock (site-class S_B that represents geotechnical profile with shear wave velocity of a value higher than 720 m/s). Total probability theorem assuming earthquake magnitudes (M), hypocenter distances (r) as continuous independent random variables that affected the intensity (I), in this case PGA, is adopted in this PSHA. The total probability theorem methodology is adopted in EZ-FRISK computer program (Risk Engineering, 2004) used in the PSHA in this case study. Subduction earthquake sources characterization consists of separate identification of megathrust and benioff seismic source zones. In addition, shallow crustal seismic source zone considered to affect the site have also been identified. Recurrence models for each zone and appropriate attenuation functions are adopted in the PSHA.

Seismic source model

There have been many large earthquakes reported and recorded originated from subduction source zone along south-west of Sumatra Island. Many earthquakes occurred along megathrust of the subduction zone and the rate of this subduction is estimated about 60–70 mm/year. The latest large earthquake originated from the megathrust was the Great Sumatra 2004 earthquake. Due to the in-perpendicular movement direction of Indo-Australian plate to the basin structure then Sumatra Fault Zone (SFZ) was formed along the Sumatra Island. SFZ activities were indicated by occurrence of earthquakes at shallow depths (< 60 km) along the faults. Compared to subduction earthquake activities, the SFZ activities activity triggered relatively smaller earthquakes. However, the earthquake hypocenters from this SFZ were shallower (usually less than 30 km), therefore earthquakes of the SFZ has often caused large earthquake. Aceh and Simeuleum fault segments are part of the SFZ that are only a few kilometers distance from city of Banda Aceh. Therefore, this shallow crustals are the main faults that is considered potential to generate large earthquakes in the future, since the subduction earthquake would need much longer time to accumulate its energy post 2004 earthquake for another large earthquake.

The subduction earthquakes are modeled by area sources with segments in conjunction with the geological input. Likewise, the SFZ earthquakes are modeled by thin area sources with segments also in conjunction with the geological input that referred from Sieh, 2000, and Natawidjaja, 2002. Figure 1 presents seismic source model for the PSHA. Each seismic source zone is assigned seismic parameters representing seismic characteristics of the source.

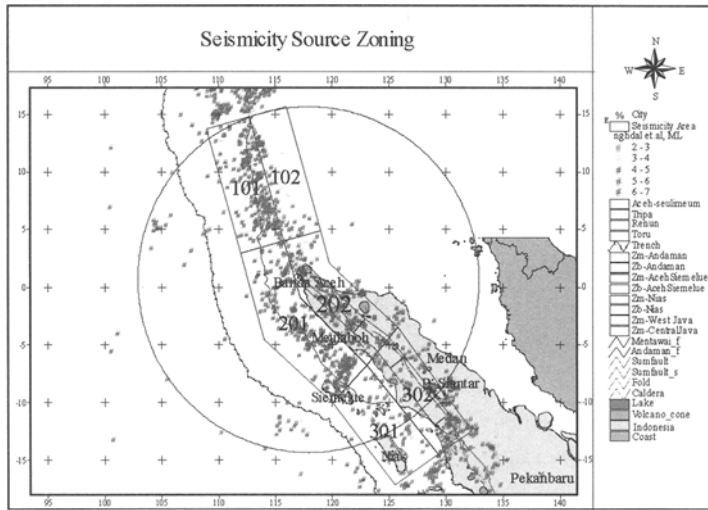


Figure 1. Seismic source zoning representing both subduction and shallow crustal faults

Earthquake recurrence model and attenuation functions

Recurrence model is adopted and is input in the PSHA in the form of seismic parameters for each seismic source zone. The seismic parameters from use of the recurrence model for each source zone are obtained from both instrumental and historical data, as well as information on its maximum moment magnitude (M_w). Maximum magnitude for each source zone is assigned based on both historical and potential magnitude estimated from geometry and slip rate of the plates or faults. Maximum magnitude (M_{max}) assigned for subduction zone is 9.3. Meanwhile, Aceh and Seumeleum faults are assigned a value from its potential to generate maximum magnitude of 7.7 and 7.5, respectively (Natawidjaja, 2002). In this PSHA, earthquake recurrence model parameters have been calculated based on seismicity and slip data to be used in exponential and characteristic recurrence models.

Young's et al. (1997) attenuation function has been adopted to represent the subduction earthquake source. While, Sadigh et al. (1997) and Idriss (2004) attenuation functions have been adopted for shallow crustal seismic sources. Attenuation functions of Sadigh et al (1997), and Idriss (2004) are assigned a relative likelihood of 0.5, respectively.

Result of PSHA

Results of PSHA on PBA with probability level of 200, 475, and 1000 years return period are 0.18, 0.3, and 0.41g, respectively. Hazard level recommended is probability hazard level of 475 years earthquake return period, as commonly adopted in many building codes. In this case, PBA of 0.3g is resulted from PSHA. De-aggregation curve in the PSHA determines the controlling earthquake magnitudes and distances. It is indicated in the analysis that for 475 years return period earthquake, the dominant event is originated from shallow crustal SFZ. Since there are some uncertainties in seismic parameters, particularly for Aceh and

Simeuleum fault segments that are still need to be verified, therefore characteristics of these segments still need further detail investigation.

SITE-CLASSIFICATION ANALYSIS

Site-classification analysis was conducted based on various geotechnical investigation programs that have been conducted within a sub-district in coastal area of Banda Aceh city as a case study. Several geotechnical investigation consisting of Cone Penetration Test (CPT), auger boring, and spectral analysis of surface wave (SASW) have been conducted. The SASW provide shear wave velocity profile at several points within the site. The site-classification was based on the International Building Codes (IBC2006).

Results of the geotechnical site investigation show that the site-classification of the area varies from Soft, Medium, and Hard. This site-classification analysis suggest that microzonation map of the area need to be developed and different seismic criteria need to be provided for each different site-class. Figure 2 shows site-classification mapping of the case-study coastal site. Each site-class will be subjected to different PGA, that is 0.33g, 0.36g, and 0.36g for Hard, Medium, and Soft site class, respectively. Although level of PGA for different site-class does not vary significantly, seismic design criteria with respect to its design response spectra, however, could differ significantly. For structures or buildings, seismic design criteria in the form of design response spectra need to be provided either from building codes or more accurately through site-specific response analysis and recommend design response spectra considering appropriate seismic input motions.

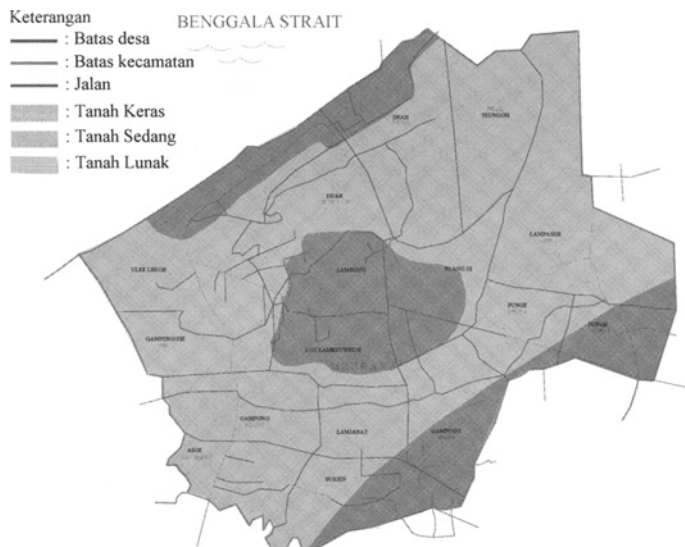


Figure 2. Site-classification map for case study coastal site

PROBABILISTIC TSUNAMI HAZARD ASSESSMENT

Tsunami potential post the great 2004 Sumatra earthquake was evaluated to recommend tsunami hazard criteria. The earthquake generated tsunami potential to city of Banda Aceh is the subduction zones. This subduction zones are the same source that was used for PSHA. Therefore, for tsunami hazard potential the subduction source zones and seismic parameters were used for probabilistic tsunami hazard analysis (PTHA). The analysis was made by activating only the subduction seismic source zones (Aceh-Seumelue-Andaman segments). The analysis was done using EZ-FRISK computer program to provide hazard curve correlating earthquake return periods and the potential moment magnitudes considering the seismic parameters adopted in the recurrence models. The analysis was conducted by Sengara and Hendarto, 2006. Result of the analysis is presented in Figure 3. It is indicated the 2004 earthquake is approximately predicted to be of 520 years return period earthquake.

Based on hazard curve presented in Figure 3, several earthquake magnitude scenarios associated with its return periods were developed and these scenarios are adopted for earthquake generating tsunami wave propagation and inundation modeling.

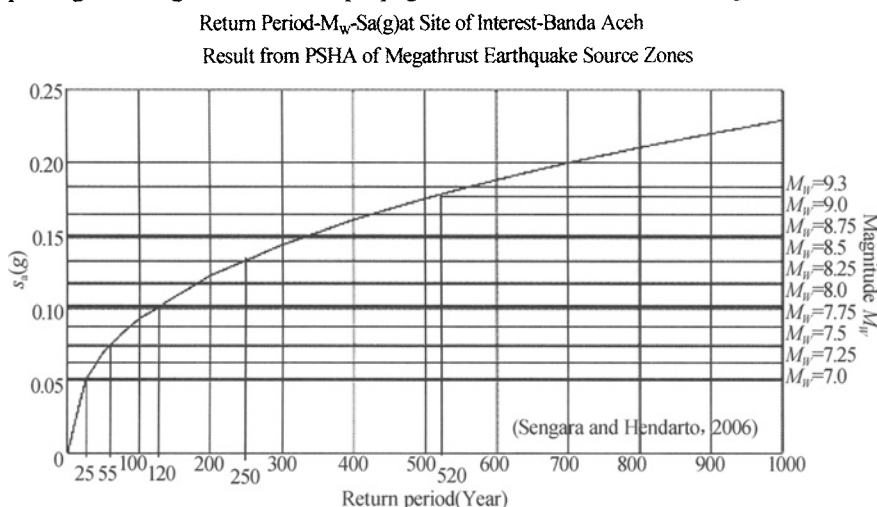


Figure 3. Hazard curve correlating earthquake return period, peak acceleration, and earthquake moment magnitude considering Aceh-Seumelue-Andaman segments

Tsunami wave propagation analysis

The result of PTHA was used as an input in tsunami wave propagation modeling to estimate the tsunami height at the shoreline of the site of interest. The earthquake generating tsunami hazard curve (Figure 3) is adopted and five different earthquake scenarios were developed for tsunami modeling. Each scenario with associated earthquake moment magnitude and return period will correspond to particular potential of sea-bed deformation as the tsunami generation input. The sea-bed deformation was calculated by using Masinha and Smylie method (1971) with the fault parameter which has been determined from focal earthquake mechanism results from Harvard-CMT solution. Results of the tsunami modeling for various

scenarios correlating the return period or moment magnitude potential and maximum tsunami height at coastline of the case-study site is summarized in Table 1.

Table 1. Summary on results of tsunami wave propagation modeling

Scenario	Moment Magnitude	Return Period (years)	Tsunami Height at Case-Study Site (m)
1	9.3	520	9.1
2	8.5	250	7.2
3	8.0	120	3.4
4	7.5	55	1.5
5	7.0	25	0.5

Tsunami inundation modeling

The tsunami inundation model was later developed to recommend the distribution of tsunami height and distance onshore based on the tsunami velocity and height along the shorelines, topographical data and surface friction condition of the case-study site. One scenario tsunami inundation map is presented in Figure 4, that is for scenario 3 for earthquake moment magnitude of 8.0 (return period 120 years) with maximum tsunami height of 3.4 meters.

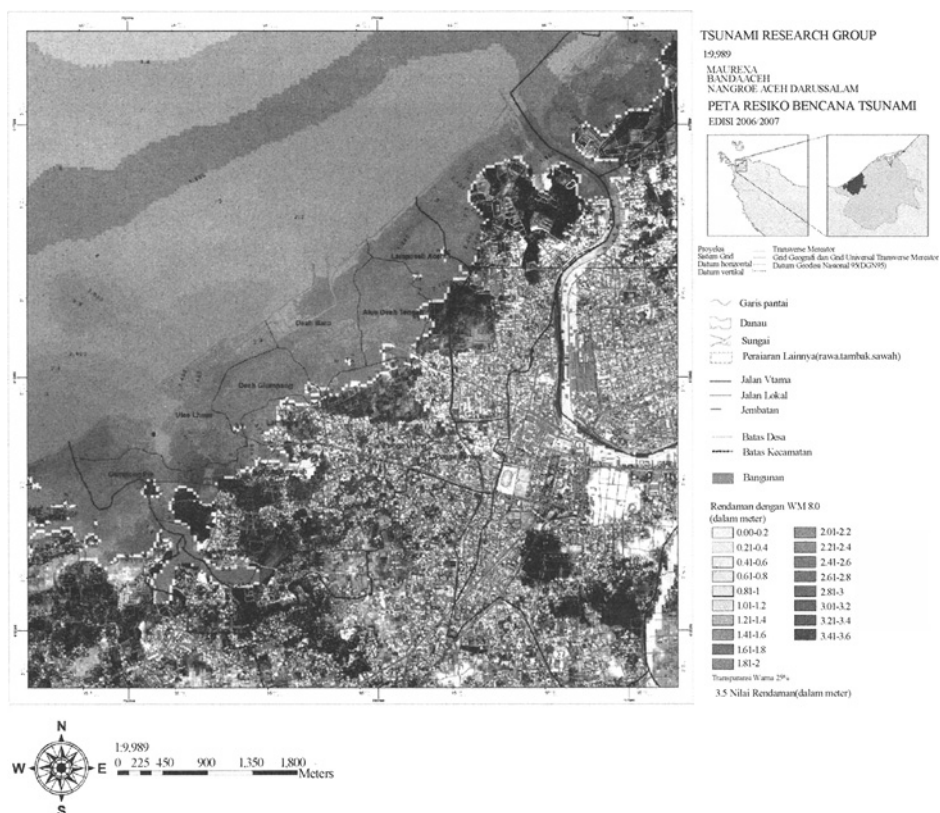


Figure 4. One scenario tsunami inundation map ($M_w=8.0$, return period 120 years)

CONCLUSIONS AND RECOMMENDATIONS

Probabilistic seismic hazard analysis (PSHA) for city of Banda Aceh indicated that PBA of approximately 0.3g is potential to occur in Banda Aceh for probability level of 475 years return period earthquake. This level of PBA is dominant to be originated from shallow crustal fault (SFZ) potential which is of relatively very close distance from the city. Some geotechnical characterization involving spectral analysis of surface wave survey at a site along coastal area indicated variation from hard to soft site-classification. This variation in geotechnical site condition has to be considered for potential amplification of baserock motion to the ground surface. Tsunami inundation map has also been developed based on probabilistic hazard assessment with scenario on probability of earthquake generated tsunami potential, that is correlating subduction earthquake magnitude with return period and tsunami height distribution to the coastal area.

The level of baserock and its variation on ground surface motions as well as the distribution of tsunami height potential resulted from this study are recommended as the basis for design criteria in the currently undergoing rehabilitation and reconstruction process and for long-term development of buildings, housings, and infrastructures in the coastal area of the city.

ACKNOWLEDGEMENTS

The seismic and tsunami hazard analysis was conducted at Center for Disaster Mitigation-Institut Teknologi Bandung which is partially sponsored by Rehabilitation and Reconstruction Agency of NAD-Nias and Indonesian Ministry of Research and Technology. The support is highly appreciated. The authors thankful to Dr. Munirwansjah, Mr. Hendarto, and Mr. P. Sumiartha who assisted and provided contribution in conducting some of the hazard analysis. Contribution by Dr. Natawidjaja is appreciated for input on geologic setting provided for the analysis.

REFERENCES

- Mansinha L. and Smylie D.E. (1971). The displacement field of inclined faults. *Bulletin of the Seismological Society of America*, 61(45): 1440-1443.
- Natawidjaja D.H. (2002). Ph.D Thesis, California Institute of Technology.
- Risk Engineering, Inc. (2004). EZFRISK, Software for In-depth Seismic Hazard Analysis, Boulder, Colorado, USA.
- Sadigh K., et al. (1997). *Attenuation relations for shallow crustal earthquakes based on california strong motion data*. Seismological Research Letters, Seismological Society of America, 68(1): 180-189.
- Sengara I.W. et al. (2005). Geotechnical engineering aspects related to aceh's tsunami and earthquake disaster and the need for its mitigation strategy. *International Conference on Geotechnical Engineering for Disaster Mitigation & Rehabilitation, Singapore*.
- Sengara I.W., Hendarto. (2006b). *Probabilistic seismic hazard analysis for city of banda aceh*. Research Report (unpublished), Institut Teknologi Bandung.
- Sieh K., Natawidjaja D. (2000). *Neotectonic of the sumatra fault indonesia, journal of geophysical research*, 105(B12): 28295-28326.
- Youngs R. R., Chiou S. J., Silva W. J. and Humphrey J. R. (1997). *Strong ground motion attenuation relationship for subduction zone earthquake*. Bulletin of Seismological Society of America, 68(01): 58-73.

SOME CASE STUDIES ON DEBRIS FLOW IN PENINSULAR MALAYSIA

B.K. Tan

Consultant Engineering Geologist, Petaling Jaya, Malaysia

W.H. Ting

Consulting Geotechnical Engineer, Kuala Lumpur, Malaysia

Debris flow is a natural geohazard in mountainous terrains showered with high annual rainfalls. This paper presents three case studies of debris flow in Peninsular Malaysia based on published literature/reports and personal involvement in one of the case studies by the principal author (Ting). The special features of debris flow, in contrast to other naturally occurring geohazards, are highlighted.

INTRODUCION

Debris flow is a natural phenomenon in mountainous terrains where uphill valleys or streams are fed by high annual rainfalls. The occurrences of debris flows have been well documented in some countries such as Canada, U.S.A, New Zealand, Taiwan, etc., for e.g. Hungr et al. (1987), Moh & Yao (2005) where the mountainous terrains combined with heavy rainfalls provide ideal settings or predispositions for the development of debris flow.

In Malaysia, the occurrences of debris flow in the mountainous terrains must, undoubtedly, have taken place from time to time, albeit away from man's view and unreported so long as they do not impact on human lives or infrastructures. It is when human lives and/or infrastructures are impacted that such debris flow incidents are investigated and reported. This paper presents three such incidents of debris flow in Peninsular Malaysia which had resulted in loss of lives and damage to infrastructures.

CASE STUDIES

The three case studies presented below are: 1) the Genting Sempah debris flow which involved a large number of fatalities and casualties, 2) the Kampung Dipang debris flow which practically wiped out a small village settlement, and 3) the North-South Highway debris flow which caused severe damage to the highway but, fortunately, no casualties/fatalities.

Genting sempah debris flow, selangor

The Genting Sempah debris flow was investigated and reported by, among others, the Geological Survey Department (now Department of Minerals and Geoscience), Malaysia.

The findings of the investigation were also presented in the Forum on “Geohazards: Landslide & Subsidence” organized by the Geological Society of Malaysia in 1996. The following account is extracted from the paper by Chow, et al. (1996). Further details can be referred to in the paper mentioned.

The Genting Sempah debris flow occurred on 30th June 1995, in the popular Genting Highlands resort area just north of Kuala Lumpur. The incident occurred after heavy rainfall, and involved a series of sequential events which are typical of debris flows.

According to Chow, et al. (1996) : The heavy downpour triggered a series of landslides, followed by a debris flow which swept away 19 vehicles, resulting in the loss of 20 lives with one missing and 23 others injured.

The disastrous debris flow occurred along a stream, and was the culmination of three landslides occurring near the headwaters of the stream. Debris from two landslides, with one on the western bank near the middle reaches of the stream and the second occurring near the headwaters of the stream, were deposited on the valley floor, causing an impounding of the stream waters. It was debris from the third landslide at the headwaters of the stream which breached these two debris barriers on the valley floor, causing a debris flow of water, mud, boulders and fallen trees.

The stream along which the debris flow occurred has an average gradient of about 45°, with waterfalls of 5 to 15m height. It has a narrow valley of 0.3-2m wide. The hill slopes on both banks of the stream generally have gradients between 30° to 45°. Near the headwaters of the stream, the hill is very steep, with gradient reaching 60°.

Geology consists of rhyolite and metasediments (metasandstone and metaconglomerate). Residual soil cover is thin along the river bank and side slopes, i.e. 0.5- 1.5m thick, with colluvium and old landslide debris.

Thus, the Genting Sempah debris flow is the result of breaching of two earlier “landslide dams” by a later, third landslide during a heavy downpour. The steep gradients of the valley/stream concerned, and the existence of colluvium and old landslide deposits all contributed to the total amount of debris that was finally transported downstream, adding to its destructive power.

Kampung dipang debris flow, perak

The Kampung Dipang debris flow would have been one of those naturally occurring debris flows in the highlands that would have gone un-noticed or un-reported if not for the existence of a small village settlement at the base of the hill/valley.

The debris flow occurred down a steep valley/stream on the western flank of the Main Range near Kuala Dipang, Perak, during heavy storm. Materials transported consist of mud to boulders and tree trunks as are typical of debris flows, and swept through a small village settlement and practically wiped out the entire village, with numerous fatalities and casualties.

The aftermath of the incident is shown in the Figure 1 below, Tan (2006). Interestingly, this debris flow occurred not far from the North-South Highway debris flow which occurred some years later (third case study).



Figure 1. Debris flow deposit comprising boulders, tree trunks and soil materials, Kampung Dipang, Perak. (photo taken from helicopter)

North-south highway debris flow, perak

The third case study of debris flow which occurred at a bridge site on part of the North-South Highway just south of Ipoh, Perak, has been investigated by the principal author (Ting), and documented in Ting and Moh (2007). The following brief summary of the North-South Highway debris flow is based on the above reference/paper. Further details of this debris flow can be referred to the paper mentioned.

The trigger event for this debris flow was, again, a period of intensive rainfall. The debris comprising boulders and mud with sand and gravel together with tree trunks and branches is “hydraulically” transported, travelling rapidly along a long straight ravine that normally conveys a stream. The ensuing debris quickly accumulates if an obstruction such as an undersized opening through a road embankment is encountered.

Another important associated visual phenomenon is the large volume of water involved in the flow together with the high velocity. In the case cited for the North-South Highway, triggered by a storm flow, a “dam-break” phenomenon has been deduced that is due to the breach of a naturally formed barrier. The views of the debris flow are as shown in Figures 2 and 3 below. The debris flow reached a bridge site and partially flowed over the bridge, after a substantial amount of debris went through the bridge opening.

The two important features for this case study are a backbone mountain range (Main Range) with generally steep and straight gradients (average gradient of flow channel was about 10% in this case study) and copious rainfall. As was also the case in the Genting Sempah case study above, the “dam-break” phenomenon here involves pre-existing or newly formed “landslide-dams” in the valley concerned which were eventually breached during the heavy downpour.



Figure 2. Aerial view of debris flow toward Bridge site



Figure 3. Accumulation of debris at bridge opening

A distinctive topographical feature in the flow process is a defined catchment area feeding into a single long straight channel. There is usually an abrupt change in flow section from the catchment into the receiving channel. The channel carrying the flow is largely straight and narrow and has generally a steep uniform gradient along its length, thus effecting rapid flow. With a sizeable catchment area, large volume of water is available to convey the flow.

The debris in the flow typically comprises boulders and mud with sand and gravel together with tree trunks and branches. The geotechnical component is generally loose material from colluviums, meta-stable slopes and sometimes man-made fills derived from the side slopes of the ravine; with the larger material ranging from boulder to sand typically originating from the stream bed.

Back analysis from hydraulic calculation shows that total volume of water in the catchment area and velocity of water in the affected channel during normal stream flow, is not sufficient to account for the volume and velocity of the deposited debris that have been physically observed. It may therefore be deduced that a natural barrier is first formed across the channel acting as a dam that impounds a large volume of water upstream, accounting for the height of the debris at the bridge site, and the significant volume of water observed during the debris flow phenomenon.

The formation of the natural barrier is facilitated by: deposition and accumulation of the loose flanking side slopes material into the channel carrying the flow. The boulders in the channel bed together with tree trunks branches is gradually infilled with smaller size stream bed as well as side slope slide materials, easily forming the barrier to flow. The barrier could gradually develop in size as long as no dam break occurs.

A period of intensive rainfall can then trigger breach of the natural barrier and a dam-break phenomenon occurs; causing the large volume of impounded water at the given head to rush down the steep gradient of the channel, carrying with it the original material forming the barrier as well as other material in its flow path until a barrier is reached or until the flow material is deposited in a basin, where its energy is dissipated.

The configuration in this case study is typical of many reported debris flows in the country, and therefore it may be possible that the formation of a natural barrier (“landslide dam”) is a prerequisite of Malaysian debris flow in the majority of cases.

CONCLUSIONS

Debris flow is a natural phenomenon in mountainous terrains with high rainfalls. Typically, it involves the breaching of a “landslide dam” (un-engineered, unstable) during heavy downpour, either by another landslide or by the excessive amount of water impounded during the downpour. Materials transported would include mud to boulders and tree trunks, hence adding to the destructive power of debris flow. Survey for potential “landslide dams” in mountainous terrains, say by aerial means, could be one of the mitigation measures to reduce debris flow hazard.

REFERENCES

- Chow W.S., Jadid M.S.M. and Yaacob S. (1996). Geological and geomorphological investigations of debris flow at Genting Sempah, Selangor. *Proc. Forum on “Geohazards: Landslide & Subsidence”*. Working Group on Engineering Geology & Hydrogeology, Geological Society of Malaysia, 22 Oct. 1996, Kuala Lumpur, 5.1-5.15.
- Hungr O., Morgan G.C., VanDine D.F. and Lister, D.R. (1987). Debris flow in British Columbia. Review in Engineering Geology. *Geological Society of America*, 7: 201-222.
- Moh Z.C., Yao T.C. (2005). Natural disasters in Taiwan. *Proc. Int. Conf. Geotechnical Engineering for Disaster Mitigation and Rehabilitation*. Dec. 2005, Singapore, 23-48.
- Tan B.K. (2006). On boulders and boulder-problems in construction. *Proc. GSM-IEM Oktoberforum 2006 on “Engineering Geology and Geotechnical Engineering”*. 31st Oct. 2006, Petaling Jaya, paper no. 6, 13
- Ting W.H., Moh Z.C. (2007). The role of debris flow in hazardous ground movement. *Proc. 16th Southeast Asian Geotechnical Conf.* 8-11 May 2007, Kuala Lumpur, Keynote Lecture , 153-160.

GPS/GIS INTEGRATION USED TO ESTABLISH A DISASTER RISK MAPPING SYSTEM FOR NANTOU COUNTY IN CENTRAL TAIWAN

Kuang-Jung Tsai

*Department of Land Management and Development, Chang Jung Christian University,
Taiwan, China*

Kun-Ting Chen, Chin-Chuan Lin

*Department of Civil Engineering, National Pingtung University of Science and Technology,
Taiwan, China*

The Administration of Nantou County, located at the central part of Taiwan island, includes 13 townships with 410644 ha in total area. Lots of slope land became instable induced by the 921 Chi-Chi earthquakes since 1999. Serious sediment related disaster such as soil erosion, landslide, soil mass movement and debris flow resulted from high rainfall intensity and steep geomorphology after Chi-Chi earthquake has been recognized as major detrimental factors. As a matter of fact, sediment disasters damaging public facilities were seriously concerned by Nantou county government. Residential properties and human lives attacked by Chi-Chi earthquake and sediment related disaster were also considered as an important issue of Nantou County. To identify large-scale soil mass movement and debris flow by using satellite image processing system and aerial photography interpretation should be required in this project. Applications of GIS integrated with GPS and RS technology would be also necessary for this research. However, establishing disaster auto-mapping system used to estimate the disaster risk occurrence of hill slope environment at Nantou County would be critical. This mapping system was setup by using disaster risk analysis on the basis of GIS/RS integration and disaster database establishment. This can give a positive guideline of sediment disaster prevention on hill slope. Also, we expect this auto-mapping system can help Nantou county government renew their disaster prevention program and keep well development of Nantou County in the near future.

INTRODUCTION

Large scale landslide and soil mass movement have attracted the attention of human in the same way as other uncontrollable natural disaster, such as earthquake, volcanism, floods and debris flow, which threaten human lives and their properties. Slope failures are usually related to human activity such as deforestation, hillslope development and surface mining operation. In general, when slope stability is disturbed, a great variety of sliding movements take place. Because of the great damage caused by landslides to forest stands, farmland, buildings, transportation facilities and other engineering structures, they also can be recognized as a serious economic problem such as the sediment disasters occurred at Nantou County in central Taiwan.

Sediment disasters occurred at Nantou hillslope have been recognized as a big issue which was serious concerned by the resident at Nantou County. The administration of Nantou contains the area of 410,644 ha. However, Most of land areas are located at hillslope with 390,372 ha in total. Highly weathered geological formation, uneven distribution of rainfall intensity, steep geomorphology and intensive human activities have been identified as the predominated factors contributing to the sediment disasters occurred at Nantou slopeland.

Applications of GIS integrated with GPS and RS technology should be necessary for this research. This project was also critical to establish a disaster risk mapping system for Nantou hillslope. All results can give a fundamental guideline of disaster prevention program. Hopefully, this guideline can help Nantou County government set up his own sediment disaster prevention system to keep urban safe and well development of rural and city in the future.

Nantou hillslope is one of the main regions for the slopeland development in central Taiwan. The effect of Chi-Chi earthquake in 1999 on the growth of Nantou area is strong related to the development of Nantou rehabilitation and reclamation. Actually, large-scale landslide and debris flow after Chi-Chi event does have a detrimental effect on the natural environment and public facilities in Nantou County. Factors governing these sediment related disasters are complicate. Various studies have shown that most landslides and debris flow in Nantou area are natural environment related. The great diversity of factors and complexity of interrelationships, as well as the practical relevance of large scale landslide and debris flow, can be recognized only by systematic field studies. Therefore, the possible approaches used to work out these hazards was to intensively perform the field investigations by using GPS (Global positioning system) and conduct the laboratory experiments based on the soil mechanical properties determination and disaster database established by GPS/GIS integration. In this study, the best results can be achieved by the combination of both these approaches and GPS/GIS/RS integration. Since the field investigations can provide a clear picture of the origin, cause, and nature of disaster processes by checking their information against the result of static analysis and soil mechanical laboratory studies. From what has been said above, a sound treatment for the soil mass movement on Nantou County is based on careful observations for possible site of landslide before, during and even after carrying out stabilization measures. Indispensable geological survey, hydrological analysis, slope failure investigations by means of GPS/GIS/RS integration shall serve this purpose during the period of this research. Besides purely theoretical considerations, the practical aspects also play an important part in this study. Hence, the reorganization of the cause, nature and development of landslide and debris flow occurred at Nantou area can make it possible to appreciate the extent of any danger and find an adequate solution to control these disasters. Hopefully, this study can give a reference on the futural planning of hillslope development and rehabilitation for Nantou area in central Taiwan.

METHODS AND PROCEDURES

Site characterization

Nantou County has total area of 410,644 ha (Figure 1), of which more than 95% is classified as slopeland including 13 townships. Significant high central mountain range runs from north to south. The highest peak is the Yu-Shan central range mountain with the elevation of 3937 meters above sea level.

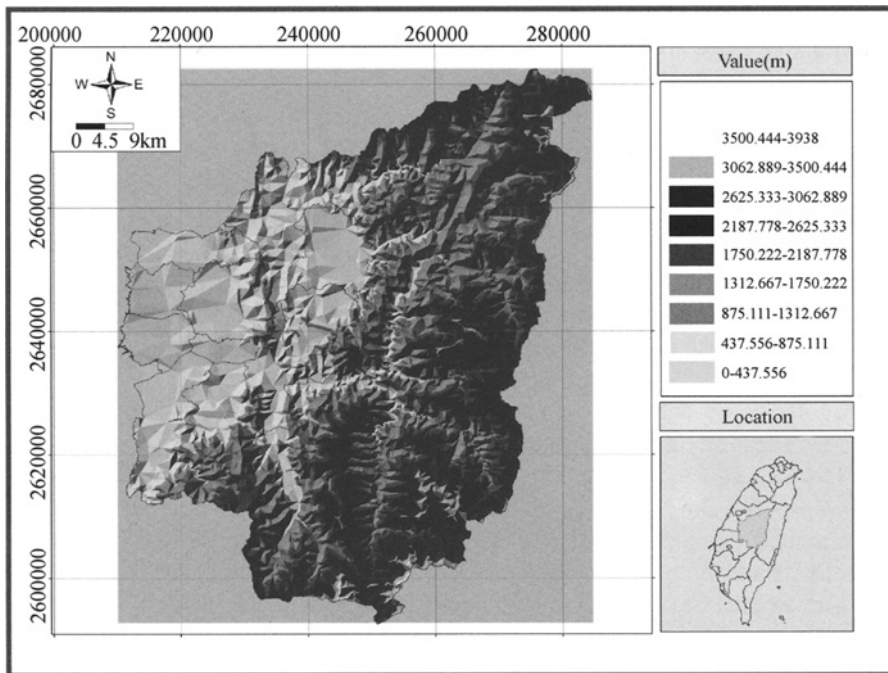


Figure 1. Location of Nantou area in Taiwan

Nantou area is located within the western foothills geologic province of Neocene classic sediments. The predominant underlying rock is LuShan and Szoleng sandstone formation that is composed of sandstone and shale. LuShan and Szoleng sandstone formations are the important rocks that are distributed sparsely in the Pliocene rocks of central Taiwan. These sandstone and shale reefs are whitish gray, massive and fracture with significant evidence of stratifications.

The soil of Nantou area lies in the zone of Ultisols, Alfisols and Inceptisols. Properties observed in these soils resulted from the interaction of five soil forming factors, such as climate, organism, parent material and relief, combine to create a set of processes which modify soils through time (Morgan & Rickson, 1995). The soils in the study area are weakly developed and usually silty loam or sandy loam in texture. Rapid penetration of water into shale is due to the formation of many coarse-textured soils coming from the weathering of sandstone and colluvium. This subsurface flow not only aggravates soil erosion but also induces slope failure in this area. Therefore, hydrological factors play an important part on controlling slope failure of the region. Most of soils have a thermic temperature regime. Inceptisols are locally common due to steep slope and high weathering process of LuShan and Szoleng sandstone formations. Some of them are infertility in soil profile.

The climate of Nantou area is humid and subtropical. The annual precipitation ranges from 1405 to 3143mm. High rainfall amount are intensively concentrated on storm season during summer time. They trigger the soil erosion and induce large scale debris flow within the region. The extreme temperature range fluctuated from 14°C to 23 °C which is characterized the subtropical climate of the region. The warmest month is June with mean monthly

temperature of 23 °C, but the coldest month occurred at December with temperature of 14°C. The mean relative humidity of whole year is 84%. Average annual precipitation for the period 1960-2006 is 2691mm, about 2100mm of this occurs as heavy rainfall during the period of May to August. Summer precipitation comes as showers, typhoon and high intensity thunderstorms. Approximately 80% of the annual precipitation falls in the months June to August. In general, the temperature is warm during the summer season but is cold in the winter time (Table 1).

Table 1. The meteorological data of study area (period: 1999-2006)

Month	1	2	3	4	5	6	7	8	9	10	11	12
Average Temp.(°C)	14.1	19.1	20.7	22.7	22.5	23	21.9	21.3	19	14.4	15.4	13.5
Maximum Temp.(°C)	25	27.9	28.2	30	30.1	30	29	29.1	24.9	24.9	28	22
Minimum Temp.(°C)	2.5	12.6	15.7	18.1	17.6	18.2	19.2	16.3	13.3	1	6.4	4.1
Relative Humidity.(%)	78	78	84	83	87	87	90	88	85	84	85	81
Average Temp.(°C)	62.3	71.6	103	207	322	387.6	512.4	453.8	227.3	97.8	72.5	67.9

The primary land use in Nantou area is native forestry, tea farm and rangeland. An increasing amount of land within the region is being used for recreation development including vocational dwellings, roads and commercial activities such as big hotel and resort area (Figure 2).

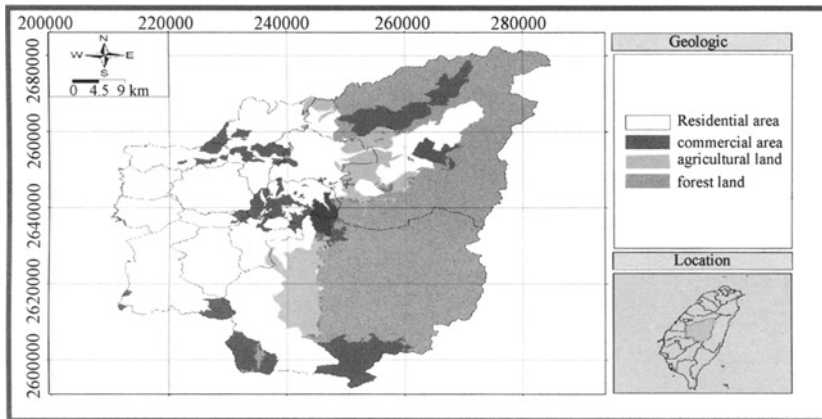


Figure 2. Land use map of study area

Field investigations

No matter what methods are used, it is necessary to conduct an overall geologic appraisal of landslide sites, followed by a planned subsurface investigation or topography survey. The purpose of field investigations is to determine the nature, cause, and extent of each type of material that may have a negative effect on the stability of landslide (Huang, 1984; Das, 2002). The scope of field investigations should include topography, erosion, vegetation, geomorphology and history of hillslope changes (Veder 1981; Zaruba, 1982). Several disaster sites located at Nantou hillslope, were investigated by using GPS to allocated their coordination in situ. The topography of landscape is an overt clue to past landside activity and potential sloopeland instabilization. Satellite image processes and aerial photograph

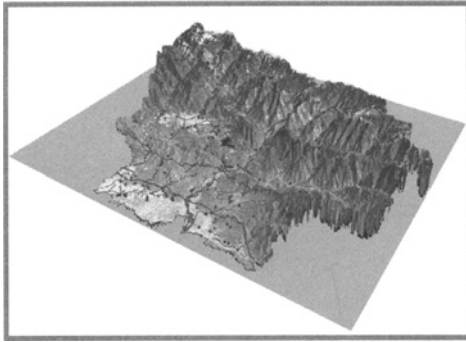


Figure 9. Satellite image overlap with investigated sites at Nantou area

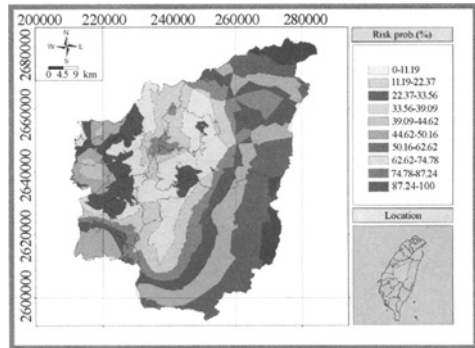


Figure 10. Disaster risk map (2-dimension) of Nantou area

The effects of climatic factors can seldom be evaluated analytically because the relations are too complex. Empirical correlations of one or more of these factors, particular rainfall amount and intensity with movement rates can point out their influences that must be controlled to minimize the soil mass movement. Three analytic techniques, based on the meteorological data collected from rainfall station in the field, including Gumbel's Extremal-Value-Type I, Log-Pearson Type III and Normal Distribution method were used to set up the regressions which describe the correlation between rainfall and frequent year. This will provide information, such as groundwater fluctuation, seepage force increases, poor drainage systems, vegetative recovery, and history of soil mass movement, were also essential in this program.

Laboratory analysis

Laboratory tests complement field investigations are to give more complete picture of soil materials within the slope and their engineering properties. Furthermore, it is possible in the laboratory to establish the changes in soil behavior due to the changes in environment. For example, the construction of an embankment will certainly affect the shear strength in the foundation soils. Field tests before construction can't establish these changes, while laboratory tests can simulate these changes they occur in the field.

The major laboratory analysis (McCarthy, 2002) for determining the characteristics of environmental disaster include topography analysis and soil physical properties determinations. Satellite image analysis combined with GIS technology is used to determine the attribute data of disaster area. Soil physical properties can provide the information to evaluate the causes of debris flow and landslides. These analyses were conducted in the laboratory during the period of this study.

Sediment disasters occurred at Nantou area are greatly affected by the non-homogeneity and anisotropy of soil mass and rock formation within the slope as well as by the conditions in the surrounding environment (Lee et al., 2002 and Liu, 2004). Consequently, the validity of result analyses depends on the ability of investigator who can give a true picture of the geological properties at disaster site in relation to the mechanical properties of rocks and soils. The initial stresses present in the ground are also important, as well as the hydrogeological

condition, the fluctuation of groundwater or other climatic factors that trigger the landslide and debris flow in the region. However, each of these factors is a function of complex interrelations between each other.

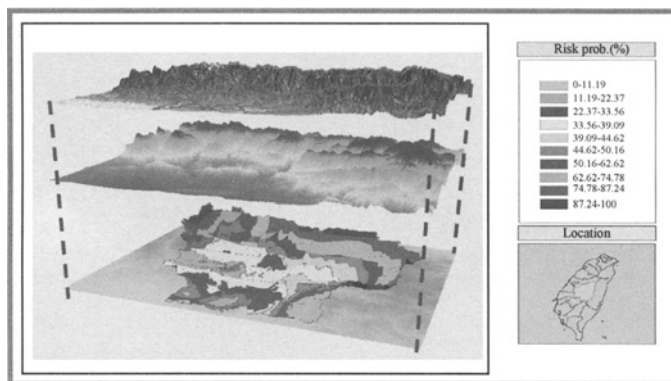


Figure 11. Disaster risk map (3-dimension) of Nantou area

Tables 1 and Figures 3 through 11 illustrate the typical results of this research. These accompanying tables, satellite images and GIS map layers show how various physical parameters affect the results. (Dunn, 1980). Table 1 shows the metrological data collected from disaster area are uneven distribution. Much more important is the influence of low vegetative cover and organic matter content due to the soil erosion resulted from high velocity of runoff on slopeland. Unfavorable effect of biological slope protection may generate serious soil erosion by runoff on ground surface. This caused a further decrease of soil shear strength within the slope. Quite general, any significant deviation from normal soil erosion has an unfavorable effect on shear strength. Hence, soil erosion in these areas has a detrimental effect on the slope stability of Nantou hillslope.

Figures 4 through 11 give the results of auto mapping system by using the GPS/GIS/RS integrated technology that have been computerized by the GPS/GIS database system developed at National Pingtung University of Science and Technology. At this point, an automatic search program has been developed to further refine the location of the most critical risk zone of disaster occurrence in this research. Figures 10 & 11 also show the two and three dimensional overlap of disaster map layers by using GPS/GIS integration. Therefore, the prediction of disaster risk can be effectively controlled by the disaster database system developed from GPS/GIS/RS integrated technology. The risk analysis of sediment disaster can also be reasonably suggested by the results of potential risk analysis. Figures 10~11 can give a general information related to the geo-environmental hazard automatically mapped by using GPS/GIS/RS integration. These GPS/GIS risk maps of sediment disaster can help Nantou County government design a good environment for the well management and development of rural and city at Nantou area.

CONCLUSION AND RECONMENDATION

All factors governing sediment disasters of Nantou area include highly weathering of rock formation, frangible geological structure, lose soil formation induced by Chi-Chi earthquake,

surface drainage system, soil mechanical properties, uneven distribution of rainfall and improper human activities. As a result, the following conclusions and recommendations can be summarized:

1. Serious soil erosion resulted from high accelerated runoff has an unfavorable effect on the slope stability in this region. Soil erosion effect increases the instabilization of Nantou hillslope environment and decreases the shear strength of soil layers in the sliding zone.
2. The major factors contributing to the sediment disaster of Nantou slopeland are predominated by weak geological structure, high rainfall intensity, weak developed soil formation, soil erosion caused by high speed runoff on slope, highly weathering of shale formation and intensive human activities.
3. The distributions of potential disaster risk area are presented graphically as Figures 10-11 that can be used to identify the possible extent of disaster risk zone in Nantou county.
4. Further research should make it possible to develop accurate instruments that can be set up in the field for monitoring the stability of highly sensible disaster environment on Nantou slopeland.
5. This disaster risk auto-mapping system developed on the basis of GPS/GIS/RS integration can help Nantou County government renew his sediment disaster prevention program and allocate the disaster risk area used for the city/rural planning and management.

REFERENCES

- Das B. M. (2002). *Fundamentals of geotechnical engineering*. 5th ed., Brooks/Cole, CA., 445-500.
- Dunn L.S., Anderson C.R. and Kiefer F.W. (1980). *Fundamentals of geotechnical analysis*. John Wiley & Sons Inc., N.Y., 235-259.
- Huang Y.H. (1984). *Stability analysis of earth slopes*. McGraw-Hill book Co., 71-122, 223-225.
- Lee W. A., Lee T. S. and Sharma G. E. Boyce. (2002). *Slope stability and stabilization methods*. 2nd ed. John Wiley & Sons Lnc., 329-598.
- Liu Cheng. (2004). *Soils and foundations*. 6th ed, Prentice Hall, 9-255.
- McCarthy D. F. (2002). *Essentials of soil mechanics and foundations*. 6th ed. Prentice Hall, NJ., 396-440.
- Morgan R.P.C. and Rickson R.J. (1995). *Slope stabilization and erosion control, a bioengineering approach*. E & FN Spon London UK., 221-248.
- Veder C. (1981). *Landslides and their stabilization*. Prentice-Hall Inc. Englewood Cluffs, N.J. P1.7-17, 22-27, 29-39.
- Zaruba O., Mencl V. (1982). *Landslides and their control*. 2nd ed, Czechoslovak Academy of Science, 187-201.

TYPES OF FLOWSLIDE FAILURES AND POSSIBLE FAILURE MECHANISMS

Dariusz Wanatowski

*School of Civil Engineering, The University of Nottingham,
University Park, Nottingham, NG7 2RD, United Kingdom*

Jian Chu

*School of Civil and Environmental Engineering, Nanyang Technological University,
Blk N1, 50 Nanyang Avenue, Singapore 639798*

Robert S.C. Lo

*School of Aerospace Civil and Mechanical Engineering, UNSW at ADFA,
Canberra, ACT 2600, Australia*

Flowslide is a common type of failure of granular soil slopes. Although many flowslides can be explained using static liquefaction or instability behaviour of sand under undrained conditions, some of the failure might have occurred under essentially drained conditions. In this paper, some flowslide case histories are reviewed. Typical flowslides and the possible failure mechanisms behind each flowslide are identified. Based on the laboratory studies, new failure mechanisms are proposed and used to offer new interpretations to some of the failure cases.

INTRODUCTION

Landslides are commonly classified as falls, topples, spreads and flowslides based on their ways of movement (Sassa, 1989). Since flow failures are characterised by a sudden loss of strength followed by a very rapid development of large deformations, their effects are often much more dramatic and devastating than other types of landslides. Examples of such flow failures include Fort Peck Dam (Casagrande, 1965), Helsinki Harbour (Andresen and Bjerrum, 1976), the Mississippi river bank (Torrey and Weaver 1984), Nerlerk berm (Sladen et al., 1985), Wachusett Dam (Olson et al., 2000), and the failures of some tailings dams such as the Merriespruit Tailings Dam in South Africa (Fourie et al., 2001). Most of these failures are considered to be triggered by static liquefaction or instability of granular soils occurring under undrained conditions. Here, static liquefaction is defined as a phenomenon in which loose sand loses a large percentage of its shear resistance and flows in a liquid manner when it is subjected to undrained monotonic loading, and instability as a behaviour in which large plastic strains are generated rapidly due to the inability of a soil element to sustain a given stress. Under undrained conditions, failure occurs at a stress state much lower than that

determined by the effective failure envelope. For this reason, most of the above mentioned flowslides should have remained stable according to conventional slope stability analysis.

Although it is a common understanding that static liquefaction or instability only occurs for loose granular material under undrained conditions, this may not be the case in practice. Slope failure in dilating soil has been observed in several cases by Been et al. (1988). The Fort Peck Dam (Casagrande 1965) case is one of such failures. Flow failures in Mississippi riverbanks occurring in dense sand were also described by Torrey and Weaver (1984). Furthermore, Been et al. (1987) argued that a well-documented Nerlerk berm case (Sladen et al., 1985) might also have occurred for dilating sand. Therefore, liquefaction type of unstable behaviour may occur for sand that is not loose or there are other than liquefaction failure mechanisms of dense granular soil slopes.

Furthermore, numerous failures in granular slopes under other than undrained conditions have been reported in the past. In the reanalysis of the Wachusett Dam case in 1907, Olson et al. (2000) concluded that the failure was caused by static liquefaction under completely drained conditions. In laboratory model tests of stockpiled coal, Eckersley (1990) also observed that the pore water pressure increase in a gentle granular slope was a result, rather than the cause of flowslide. In other words, the flowslide in the slope occurred under a drained condition. In fact, the possibility of static liquefaction occurring under other than undrained conditions has been recognised for a long time. The failure mechanisms related to the re-distribution of void ratio within a globally undrained sand layer [Figure 1(a)] or spreading of excess pore water pressure with global volume changes along a slope [Figure 1 (b)] have been suggested by the National Research Council (NRC, 1985). Adalier and Elgamal (2002) also observed from a series of centrifuge model tests that there is a potential strength loss in the dense sand zone as a result of pore water migration into the dense area from the adjacent loose ground. These observations further indicate that flowslides can also take place under other than undrained or fully drained conditions. However, the failure mechanisms of granular soils under these conditions have seldom been studied.

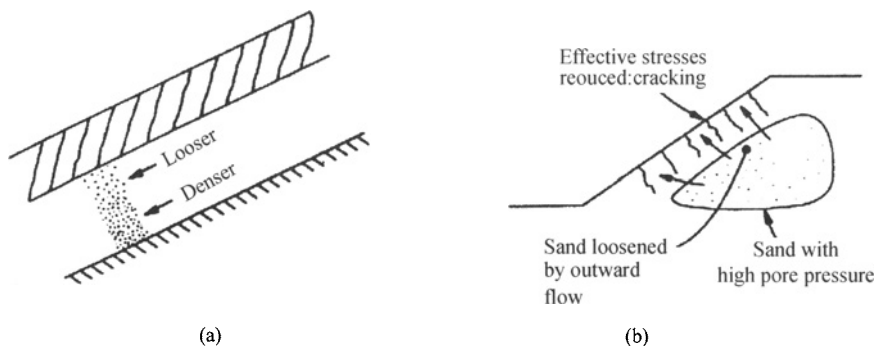


Figure 1. Failure mechanisms identified by NRC: (a) mechanism B: situation for void redistribution within a globally sand layer; (b) mechanism C: situation for failure induced by spreading of excess pore pressure with global volume changes (after NRC 1985)

The objectives of this paper are to review some flowslide case histories that cannot be explained using conventional slope stability analysis and suggest new possible failure

mechanisms and a framework for interpreting some of the slope failures. This can improve our understanding of flowslide initiation mechanisms which is essential in order to propose counter measures to slope failures or landslides in the future.

REVIEW OF CASE STUDIES

Nerlerk berm

The failure of Nerlerk berm in Beaufort Sea is a well-documented case history (Sladen et al., 1985; Been et al., 1987; Lade, 1993) that can be used to illustrate the phenomenon of flowslides and to demonstrate the inability of the conventional slope stability analysis for such cases. The Nerlerk berm in the Canadian Beaufort Sea was constructed over two seasons at the location where the sea depth was approximately 45 m. The top 1-2 m of the seabed consisted of soft clay overlying dense sand (Lade, 1993). The subsoil stratigraphy of the Nerlerk berm consisted of Ukalerk sand core overlaid by Nerlerk sand.

At the turn of July and August 1983, four flow slides occurred at the Nerlerk berm within two weeks and a fifth slide was intentionally triggered on the 4th of August. All the slides involved only the Nerlerk sand and were almost evenly distributed around the berm. The slide material came to rest beyond the berm at very flat slopes of about 1 to 2 degrees. The original slope angle was approximately 13 degrees. The Nerlerk sand was assumed to have a relative density of 30% (Lade, 1993) and effective friction angle of $\phi' = 31^\circ$ (Sladen et al., 1985). According to the conventional stability analysis, the safety factor for the slope was found to be 2.60, indicating a stable slope.

Sladen et al. (1985) concluded that Nerlerk berm slides were liquefaction-induced flow slides triggered by essentially static loading. Lade (1993) proposed a slightly different interpretation to link the flow slides to pre-failure instability of the sand, which occurs for very loose sand under undrained conditions. On the other hand, Been et al. (1987) argued that the slope failures at Nerlerk berm might have been caused by other failure mechanisms rather than static liquefaction.

Wachusett dam

The slope failure at the North Dike of Wachusett Dam is a unique case history because the failure was likely to have occurred under completely drained conditions according to Olson et al. (2000).

Construction of the Wachusett Dam situated on the south branch of the Nashua River in Clinton, Massachusetts was completed in 1907. On April 11, 1907, the upstream slope of the eastern section of the North Dike, consisting of relatively dense sands, gravels and non-plastic silts overlying natural soils, failed during the initial reservoir filling. The failure involved approximately 46,500 m³ of material from a 213 m long section of the North Dike.

Based on the back analysis of the Wachusett Dam failure Olson et al. (2000) concluded that the failure most likely has occurred as a result of static liquefaction as no seismic or dynamic activity was reported in the vicinity of the failure. However, the loading was probably completely drained prior to liquefaction. This is because the elapsed time and the

high permeability of the soils suggested that it is highly unlikely that any excess pore water pressures existed in the upstream fill at the time of failure.

Mississippi riverbanks

Since 1939 numerous flow slides have occurred along the banks of the lower Mississippi River, South of Memphis (Torrey and Weaver 1984). The flow slides at the Reid-Bedford Revetment Reach and at the Plaquemine Bend, Montz in Louisiana are two typical examples among many others.

The typical soil profile of the Mississippi riverbanks consists of a cohesive overburden overlying a fine sand layer, which in turn overlays a layer of coarser sand. Numerous standard and cone penetration tests along the river banks indicated that a vast majority of sands exceed 40% relative density with some reaching to as high as 80%. Furthermore, the effective stress paths from the loosest of the soil samples obtained from Montz showed a tendency for dilative behaviour at all confining pressures and depths. All these data suggest that the failures of the Mississippi riverbanks were unlikely to be initiated by static liquefaction as they had to occur in dilative sands (i.e. under other than undrained conditions).

NEW EXPERIMENTAL OBSERVATIONS

Instability of sand under drained conditions

It has been established by several researchers that instability will not occur for loose or dense sand under a drained condition if the stress state imposed into a soil element does not change. Therefore, it is commonly believed that the soil behaviour is always stable under a fully drained condition. However, the stress state of a soil element along a slope can be changed. For example, during water infiltration, a soil element along a slope may follow a constant shear drained (CSD) effective stress path, as suggested by Brand (1981). Along this stress path, the shear stress is considered constant but the mean effective stress is reducing. As such, the stress state of a soil element may be brought above the instability line and instability under fully drained conditions becomes possible.

The instability behaviour of sand along a CSD path has been examined experimentally in triaxial and plane-strain compression by Leong (2001) and Wanatowski (2005), respectively. The results of typical tests, IND01 and IND03, conducted on loose ($e_c = 0.902$) and dense ($e_c = 0.679$) sand under plane-strain conditions, are shown in Figure 2. The effective stress paths resulting from the two tests together with the instability lines, the failure line and the CSL are plotted in Figure 2a. The details of the testing setup and the determination of the CSL, instability line (IL) and failure line (FL) are described in Wanatowski and Chu (2007). Both specimens were first anisotropically consolidated to points A_1 and A_3 , respectively. After that the vertical load was maintained at a constant level and the back pressure was increased at a constant rate of 0.5 kPa/min. Consequently, the mean effective stresses reduced and the effective stress paths moved towards the FL. It can be observed from Figure 2(b) that between points A_1, A_3 and I_1, I_3 the change in axial strains was very small. Furthermore, axial

deformation of both specimens was increased at a constant rate (Figure 2(b)). However, when the effective stress paths reached points I_1 and I_3 , acceleration in the axial strain was evident. Therefore, upon reaching points I_1 and I_3 , instability occurred in both tests. Using points I_1 and I_3 , the instability line can be determined, as shown in Figure 2(a).

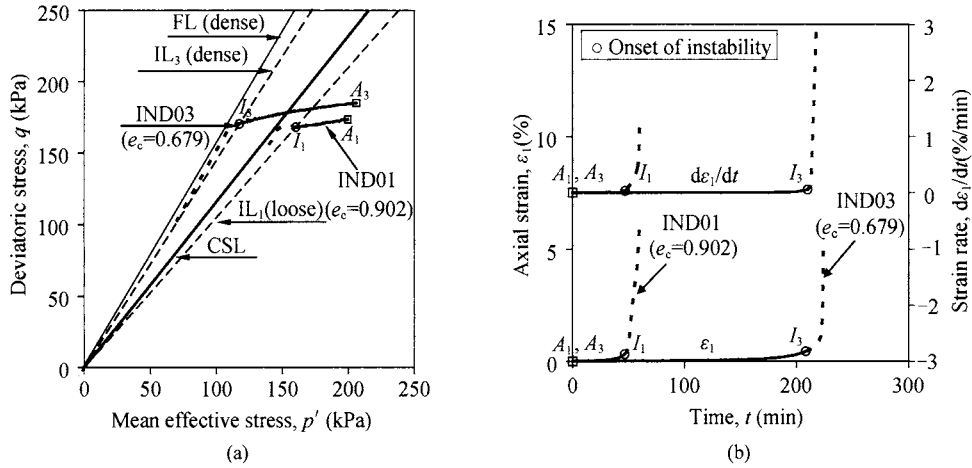


Figure 2. Instability of loose and dense sand under drained conditions

It can be seen from Figure 2(a) that instability occurred much earlier in the loose specimen than in the dense specimen. The loose specimen became unstable before reaching the CSL. On the other hand, the medium dense specimen became unstable after the CSL, but before reaching the FL. However, the CSL is also the FL for loose sand. Therefore, pre-failure instability occurred in both tests. As can be observed from Figure 2(a), the mean effective stress in Test IND01 reduced about 40 kPa from the initial state to the unstable state. In Test IND03, the mean effective stress had to be reduced about 90 kPa. This corresponds to an increase in pore water pressure equivalent to a rise water head in the field of 4 m and 9 m, respectively. It shows that the loose granular slopes are more susceptible to the occurrence of pre-failure instability. Nevertheless, the pore water pressure did not change during the entire tests (Wanatowski, 2005). Therefore, instability in a form of a rapid increase in plastic strains occurred in loose and dense sand under fully drained conditions.

It should also be pointed out that the specimen does not collapse instantly during a drained instability (tests IND01 and IND02), even though the strain rate increased at an accelerating rate. Therefore, the instability occurring under drained conditions is not a runaway type. Furthermore, instability under drained conditions can only take place along a stress path with a reduction in the mean effective stress. As a result, the drained instability has been called the conditional instability (Chu et al., 2003).

Instability of sand under non-undrained conditions

It has been established by Chu et al. (1993) and Chu and Leong (2003) that for dense sand, instability will not occur under undrained conditions. However, an undrained condition may not be a necessary condition for instability to occur as a soil element could be subjected to

conditions in which pore water pressure and volume can be changed simultaneously. This non-undrained condition can be modelled experimentally by strain path with the strain increment ratio ($d\varepsilon_v/d\varepsilon_1$) controlled. When $d\varepsilon_v/d\varepsilon_1 > 0$ is imposed on dense sand, the pore water pressure will decrease and instability will not occur. However, when an adequate dilative $d\varepsilon_v/d\varepsilon_1$ is imposed, the pore water pressure will increase and instability becomes a possibility.

Figure 3(a) presents the effective stress paths resulting from an instability test, IST01 conducted on dense sand (Loke, 2004). In this test, the specimen was first sheared along a drained path from $p'_0 = 150$ kPa to a stress ratio of $q/p' = 1.13$. The external loads, i.e., the axial load and the cell pressure, were then maintained constant to conduct an instability check along a strain path of $d\varepsilon_v/d\varepsilon_1 = -0.67$. Under these conditions, instability occurred at point B and the axial strain and the pore-water pressure increased suddenly, as shown in Figure 3b. Physically, it was observed that the specimen collapsed suddenly, i.e., pre-failure instability had occurred. This behaviour resembles the runaway instability that occurs in loose sand under undrained conditions. This observation shows that dense sand, despite exhibiting strain hardening behaviour under an undrained condition, can become as vulnerable as loose sand when it is subjected to a non-undrained condition.

It needs to be pointed out that the instability shown in Figure 3 was not only due to the control of a negative strain increment ratio but also due to the stress state upon the instability check, as reported by Chu et al. (1993) and Chu and Leong (2001). Also, the observed instability was not due to strain localization or rate/time effect, as explained by Chu et al. (1993). Instability only occurs when appropriate conditions are met (i.e. adequate strain increment ratio and stress state).

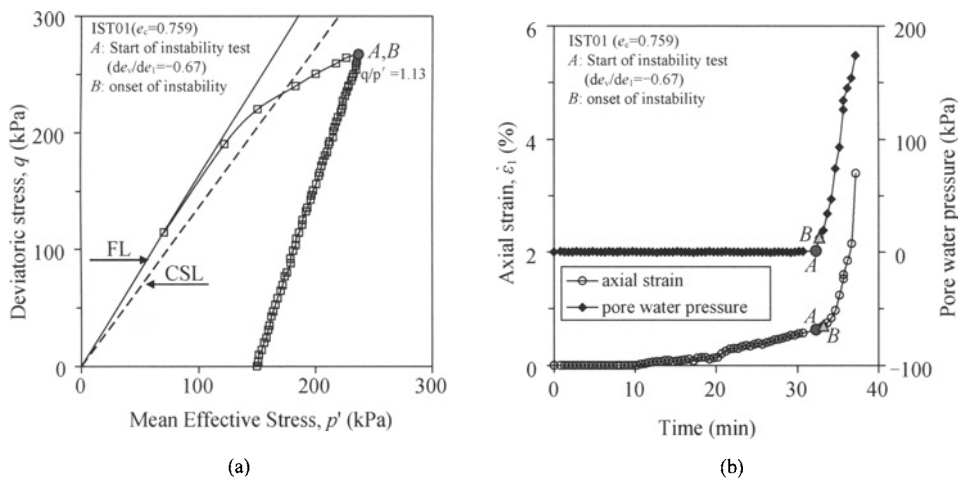


Figure 3. Instability of dense sand under non-undrained conditions

NEW FAILURE MECHANISMS

The above new experimental findings have suggested two new possible failure mechanisms: (a) instability of sand under drained conditions when there is a reduction in the mean

effective stress and (b) instability of sand under non-undrained conditions. For the former, Chu et al. (2003) have pointed out that although instability may start under an essentially drained condition in the form of a rapid increase in the axial strain and volumetric strain rate, it is likely to evolve into an undrained instability when the amount of pore water resulting from the large volumetric strain is too large to be dissipated. This explains why the pore pressure increase was only observed after flowslide in Eckersley's model tests (Eckersley, 1990). The failure cases reviewed in this paper may be reinterpreted using the new failure mechanisms.

Sladen et al. (1985) and Lade (1993) interpreted the failure of the Nerlerk berm as caused by static liquefaction or instability of loose sand under undrained conditions. However, Been et al. (1987) pointed out that the soil was not loose enough to cause liquefaction. Furthermore, an undrained condition might not be the case as the static load was not applied very rapidly. Knowing now that instability of sand, either loose or dense, can occur under drained conditions, one possible interpretation of the Nerlerk berm failure could be that the instability was initiated under drained conditions and evolved into undrained liquefaction. There could be reduction in the lateral stress caused by the tendency of lateral spreading as a result of settlement of the underlain soft clay, which was considered as a factor causing the failure by Been et al. (1987). The same mechanism can be used to explain the Wachusett dam failure (Olson et al., 2000).

The non-undrained instability that occur for dilating granular soil can be used to justify the two failure mechanisms envisaged by the National Research Council (NRC, 1985), as shown in Figure 1.

For the first mechanism shown in Figure 1a, failure will take place in the looser soil zone. In order for failure to be initiated, this zone must become even looser, thus, the soil needs to absorb water from the surrounding soil, or the denser soil zone. In other words, the soil needs to dilate. However, it needs to be pointed out that dilation alone does not trigger instability, as has been shown by Chu et al. (1993) and Chu and Leong (2001). The soil needs to dilate at a dilatancy ratio, $(d\varepsilon_v/d\varepsilon_1)$; that is more negative than the maximum ratio $(d\varepsilon_v/d\varepsilon_1)_s$, obtained from drained tests. In addition, the stress ratio at which instability can take place has to be higher than the peak stress line as established based on the experimental data obtained in this study.

Further experimental evidence of the this type of failure mechanism is given by Adalier and Elgamal (2002) in their dynamic centrifuge model tests. From the series of model tests, Adalier and Elgamal (2002) observed that there is a potential strength loss and sliding in dense sand as a result of pore pressure increase due to migration of pore water into the dense zone from the surrounding liquefied ground.

An example of the second type of failure mechanism proposed by NRC is the delayed liquefaction failure that has been studied by Boulanger and Truman (1996), Kokusho (2003) and Sento et al. (2004). Some slope failures were observed only a few hours or a few days after earthquake. This type of failure is related to the non-undrained instability which is caused by water seepage due to excess pore pressure gradients and restricted flow.

The Mississippi riverbanks case is another example of failure caused by volumetric change in dilative sand, as postulated by Torrey and Weaver (1984). This dilation in the sand may be

related to the volume change simulated by imposing a dilative strain increment ratio, $d\varepsilon_v/d\varepsilon_1 < 0$ during the instability tests under non-undrained conditions. When a non-undrained condition is imposed to force the specimen to dilate more than the sand would under a drained condition, extra water will have to flow into the specimen to generate the required dilation. As a result, positive pore water pressure will develop and the specimen will become unstable in a similar way as in an undrained test. This mechanism can explain slope failures such as the Mississippi riverbanks that cannot be explained by conventional slope stability analysis. However, the study on the instability behaviour of dilative granular soil is still at the initial stage. The amount of data published in the literature is still insufficient to construct a clear picture of the instability behaviour of dilative granular soil. Therefore, further studies are required to achieve a better understanding of such failures.

SUMMARY AND CONCLUSIONS

In this paper, some flowslide case histories were reviewed. Based on the experimental studies carried out under axisymmetric and plane-strain conditions, some of the possible causes for the flow failures of granular slopes were identified. These are: (1) instability of sand under drained conditions, and (2) instability of sand under non-undrained conditions.

The failure of the Nerlerk berm in Beaufort Sea might have been caused by pre-failure instability (or static liquefaction) of loose sand under undrained conditions. As a result, the failure took place rapidly and the sand mass generally moved a distance of approximately 150 to 200 m (Lade, 1993). However, as the load was not applied rapidly and the sand might not have been in a very loose state, instability under a drained condition or instability that was initiated under a drained condition and eventually evolved into an undrained condition could have been the other possible mechanism that triggered the failure.

The failure of the Wachusett dam occurred most likely due to the instability of granular soil under fully drained conditions. In this case, a very slow filling of the reservoir ensured a fully drained condition and also led to a reduction in the effective stresses. This in turn initiated mechanism of drained instability leading to the failure.

The flowslides along the Mississippi riverbanks are examples of failure caused by volumetric change in dilative sand, which can be simulated by imposing a dilative strain increment ratio, $d\varepsilon_v/d\varepsilon_1 < 0$ during the instability tests under non-undrained conditions. Although the experimental data on instability under non-undrained conditions can explain the failure mechanisms of some failures of dilative sandy slopes, a method to consider this mechanism in design had not been proposed yet. Therefore, further studies are required to achieve a better understanding of the failure mechanisms of dilative sandy slopes.

ACKNOWLEDGMENTS

The first author wishes to thank the British Council for the financial support of his Visiting Fellowship at University of New South Wales, Australian Defence Force Academy in Canberra.

REFERENCES

- Adalier K., Elgamal A.W. (2002). Seismic response of adjacent dense and loose saturated sand columns. *Soil Dynamics and Earthquake Engineering*, 22: 115-127.
- Andresen A., Bjerrum L. (1976). Slides in subaqueous slopes in loose sand and silt. *Proc. the Int. Research Conf. on Marine Geotechnique*, Chicago, 221-237.
- Been K., Conlin B.H., Crooks J.H.A., Fitzpatrick S.W., Jefferies M.G., Rogers B.T. and Shinde S. (1987). Back analysis of the Nerlerk berm liquefaction slides: Discussion. *Canadian Geotechnical Journal*, 24: 170-179.
- Been K., Crooks J.H.A., Colin B.H. and Horsfield D. (1988). Liquefaction of hydraulically placed sand fills. *Proc. Conference on Hydraulic Fill Structures, ASCE Geotechnical Special Publication*, 21: 330-345.
- Boulanger R.W. and Truman S.P. (1996). Void redistribution in sand under post-liquefaction loading. *Canadian Geotechnical Journal*, 33: 829-833.
- Brand E.W. (1981). Some thoughts on rain-induced slope failures. *Proc. 10th Int. Conf. on Soil Mechanics and Foundation Engineering*, Stockholm, 3: 373-376.
- Casagrande A. (1965). Role of calculated risk in earthwork and foundation engineering. *Journal of the Soil Mechanics and Foundation Division, ASCE*, 91(SM4): 1-40.
- Chu J., Lo S-C. R. and Lee I.K. (1993). Instability of granular soils under strain path testing. *Journal of Geotechnical Engineering, ASCE*, 119(5): 874-892.
- Chu J., Leroueil S. and Leong W.K. (2003). Unstable behaviour of sand and its implications for slope instability. *Canadian Geotechnical Journal*, 40: 873-885.
- Chu J., Leong W.K. (2001). Pre-failure strain softening and pre-failure instability of sand: a comparative study. *Géotechnique*, 51(4): 311-321.
- Chu J., Leong W.K. (2003). Recent progress in experimental studies on instability of granular soils. *Proc. International Workshop on Bifurcation and Instability of Geomaterials, J.F. Labuz and A. Drescher (Eds.)*, Minneapolis, 175-192.
- Eckersley J.D. (1990). Instrumented laboratory flowslides. *Géotechnique*, 40(3): 489-502.
- Fourie A.B., Blight G.E. and Papageorgiou G. (2001). Static liquefaction as a possible explanation for the Merriespruit tailings dam failure. *Canadian Geotechnical Journal*, 38: 707-719.
- Kokusho T. (2003). Current state of research on flow failure considering void redistribution in liquefied deposits. *Soil Dynamics and Earthquake Engineering*, 23: 585-603.
- Lade P.V. (1993). Initiation of static instability in the submarine Nerlerk berm. *Canadian Geotechnical Journal*, 30(6): 895-904.
- Leong W.K. (2001). *Instability behaviour of a granular fill material*. Ph.D. Thesis Nanyang Technological University, Singapore.
- Loke W.L. (2004). *Failure mechanisms of gentle granular soil slopes*. M.Eng. Thesis Nanyang Technological University, Singapore.
- National Research Council (1985). *Liquefaction of soils during earthquakes*. Committee on Earthquake Engineering, National Academies Press, Washington, D.C.
- Olson S.M., Stark T.D., Walton W.H. and Castro G. (2000). 1907 static liquefaction flow failure of the north dike of Wachusett dam. *Journal of Geotechnical and Geoenvironmental Engineering, ASCE*, 126(12): 1184-1193.
- Sassa K. (1989). Geotechnical classification of landslides. *Landslides News*, 3: 21-24.

- Sento N., Kazama M., Uzuoka R., Ohmura H. and Ishimaru M. (2004). Possibility of postliquefaction flow failure due to seepage. *Journal of Geotechnical and Geoenvironmental Engineering*, ASCE, 130(7): 707-716.
- Sladen J.A., D'Hollander R.D., Krahn J. and Mitchell D.E. (1985). Back analysis of the Nerlerk berm liquefaction slides. *Canadian Geotechnical Journal*, 22: 579-588.
- Torrey V.H., Weaver F.J. (1984). Flow failures in Mississippi riverbanks. *Proc. 3rd International Symposium on Landslides*, Toronto, 2: 335-360.
- Wanatowski D. (2005). *Strain-softening and instability of sand under plane-strain conditions*. Ph.D Thesis, Nanyang Technological University, Singapore.
- Wanatowski D., Chu J. (2007). Static liquefaction of sand in plane-strain. *Canadian Geotechnical Journal*, 44: 299-313.

DISASTER MANAGEMENT IN CENTRAL JAVA PROVINCE, INDONESIA

S.P.R. Wardani

*Research and Development Centre for Disaster Prevention and Rehabilitation,
Diponegoro University
Jl. Prof Soedarto SH, Semarang-50239, Indonesia*

R.J. Kodoatie

*Civil Engineering Department, Engineering Faculty, Diponegoro University
Jl. Prof Soedarto SH, Semarang-50239, Indonesia*

Recent disasters in Indonesia have brought disaster management as the first priority of actions as government's responsibility role. A pro-active approach to elucidate the problem through concentrating on post-disaster and pre-disaster phases in addition to disaster phase has become very important management pertaining to disaster. Disaster management must be applied as an integrated and comprehensive activity. It is a continuing process not temporary action. Integration means and implies linkage in all aspects as well as dimensions and comprehensive implies broad coverage. This paper will discuss the disaster management in Central Java Province and inherent aspects of environment in Central Java Province. Besides that, this paper emphasizes the role of Diponegoro University, Indonesia along with Joint Working Group on Geotechnical on Geotechnical Engineering for Disaster Mitigation and Rehabilitation (JWG-DMR) and Ministry of Public Works of the Republic of Indonesia conducting specific program in evolving suitable programs for preventing, rehabilitating and mitigating future disaster.

INTRODUCTION

Indonesia faces numerous natural disasters such as floods, landslide, and drought. These disasters always occur along the year as a forever threat. Drought disaster occurs in the dry season, flood and landslide occur in the rainy season. These disasters tend to increase in recent years. Other natural disasters include tsunami, earthquake, volcano eruption, etc. The recent disaster in Indonesia (i.e. tsunami in Aceh in December, 2004) followed by earthquake in Nias, Yogyakarta, tsunami in Pangandaran, landslide in Banjarnegara Regency, fast flood in Jember Regency and other disasters such as volcanic eruption, flood, landslide etc, have brought into high priority of disaster management in Indonesia.

Disaster management is complex in all aspects. However, the management is a very much continuous urgent requirement that is very needed and important by the province government, people and all stakeholders. The Government has done many actions, but due to limited budget and complexity of the problems, the disasters still exist. Therefore, disaster

management must be applied as an integrated and comprehensive activity. It is a continuing process not temporary action. Integration means and implies linkage in all aspects as well as dimensions and comprehensive implies broad coverage (Kodoatie and Syarief, 2006). The management substances are: human (human resources), nature (natural resources), infrastructure, institution, financial, policy, legalization and management capability. All of management substance must be applied as an integrated and comprehensive activity to get the main objective of the disaster management (raising the awareness of all stakeholders and society to reduce the disaster impact). The guideline characteristics must be open and applicable to the central, regional and local governments due to the different characteristics, situation, and condition areas.

We construct the paper into several sections. In the second section, we briefly describe the disaster management. We identify the stakeholders that may be affected by the disasters in the third section. The fourth section describes the typology of Central Java geography and its government's policy supporting for disaster rehabilitation, mitigation and prevention. Finally, we discuss the role of Diponegoro University in disaster management.

DISASTER MANAGEMENT

Flood, landslide and drought cycle overall year and phase of disaster management activity
 Flood, landslide, and drought are influenced by two season conditions along the year, rainy and dry season. Flood, landslide and drought cycle overall year and phase of disaster management activity are shown in Figure 1.

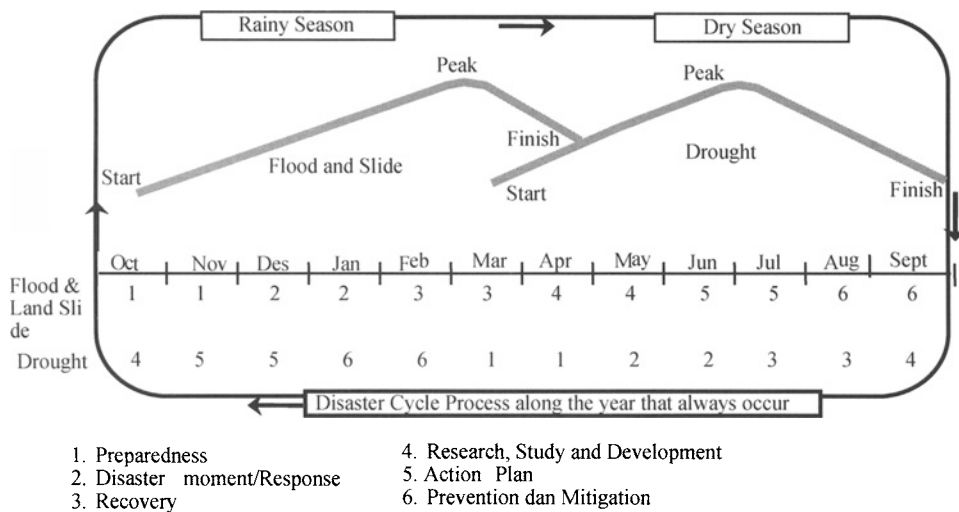


Figure 1. Flood, landslide and drought disaster cycle diagram

Institutions that handling disaster

Several descriptions:

- BAKORNAS PBP is abbreviation from Badan Koordinasi Nasional Penanggulangan Bencana dan Penanganan Pengungsi, representing non-structural organization for handling of disaster and refugee which is under and hold responsible directly to President.

- SATKORLAK PBP is non-structural institute, which is coordinated, control the execution of handling disaster and refugee, domicile in Central Java Province, known by Governor, and is responsible to Chief of BAKORNAS PBP.
- SATLAK PBP is abbreviation from Satuan Pelaksana Penanggulangan Bencana dan Penanganan Pengungsi, representing non structural organization that executing effort handling disaster before, at the time and also hereafter disaster happened in Regency region and or Town and hold responsible to Governor / Chief of SATKORLAK PBP and Chief of BAKORNAS PBP.
- Posko Banjir is abbreviation from Pos Komando Banjir, representing non structural organization that assistive some of operational duty Institution of Central Java Water Resources Management (PSDA) and Regional Office of Water Resources Management (Balai PSDA) to handle floods in Central Java and hold responsible to the Head of Dinas PSDA.
- Posko Longsor is non structural organization that assistive some of operational duty of Mining and Energy Institution and Mining Regional Office for handling landslide in Central Java and hold responsible to Head Mining and Energy Institution Central Java Province.

The procedure of satkorlak PBP

Under decree of Governor's Central Java Province No. 65 /2003 about "Forming Set of Coordination of Execution of Handling Disaster and Refugee (Satkorlak PBP) Central Java Province.

RELATED STAKE HOLDERS

There are many related stakeholders, including elements: government, university, non government organization, private/investor, contractor, consultant, communities and other. Type of stakeholders may be categorized into 5 groups, including: service provider, regulator, planner, support organizations, user.

DESCRIPTION OF CENTRAL JAVA

Geography location

- The province is divided into 35 regents/cities: 29 regents and 6 cities According to geography, Central Java is on 05°40' – 08°30' South Latitude to 108°30' – 111°30' East Longitude. The area is bonded by Java Sea to the North, East Java Province to the East, Special Region of Yogyakarta Province and Indonesian Ocean to the South, and West Java Province to the West (Balai Pusat Statistik Jawa Tengah, 2004).
- The province is divided into 35 regents/cities: 29 regents and 6 cities

Topography

Central Java Province has variety of topography, including low plain, high plain, hill, mountain and coastal. Approximately 53,30 percent are 0 - 100 meter above sea level, 27,40

percent are 100 – 500 meter above sea level, 14,70 percent are 500 – 1.000 m above sea level, and 4,60 percent are more than 1.000 m above sea level. Central Java has many kind of river from small to big rivers , lakes and reservoir.

Climate

- Climate in Central Java influence of Monsoon. There are two seasons in Central Java: rainy season (October – March) and dry season (April – September)
- According the data of Meteorology Station Class I Semarang, mean of weather temperature in Central Java is between 25°C and 29°C (Year 2003) (Balai Pusat Statistik Jawa Tengah, 2004).

Demography and administration

Population of Central Java according to types of gender can be seen in Table 1.

Table 1. Amount of Central Java population according to types of gender (Balai Pusat Statistik Jawa Tengah, 2004)

Year	male	female	Total
2003	15.957.412	16.095.428	32.052.840
2002	15.767.143	15.904.723	31.691.866
2001	15.445.400	15.618.418	31.063.818
2000	15.253.438	15.522.408	30.775.846

Government policy

The strategic plan of Central Java Province is translated into law as the Regional Legislation of Central Java Province No. 11/2003. There are three approaches used in the strategic plan including participation, system integration and regionalization. The policy and strategic development focuses on three strategic aspects including economy, social-culture and government, as well as physicals and infrastructure. The policy related to the disaster management stated clearly as part of the third strategic aspect, includes: to increase the action plan at vulnerability hazard areas and implement the early warning system, to increase the control and supervision of the land-use according to the regional space plan, to increase the recovery of damage and natural resources and environmental conservation.

ROLE OF DIPONEGORO UNIVERSITY

After the devastating disaster caused by the tsunami on 26 December 2004, disaster mitigation, prevention and rehabilitation has become one of the pressing topics to be discussed among geotechnical engineers and related professions. To share information relevant to geotechnical engineers on issues pertaining to the mitigation of natural disaster and to pool our expertise together to provide technical support on reconstruction and rehabilitation works, a Joint Working Group on Geotechnical Engineering for Disaster Mitigation and rehabilitation (JWG-DMR) has been form among the national geotechnical

societies of Australia, China, India, Indonesia, Japan, South Korea, Southeast Asia (comprising Malaysia, Singapore, Taiwan, and Thailand) and Sri Lanka.

The immediate work plan of the JWG-DMR was to organize International conference related to disaster prevention, mitigation and rehabilitation in the region. The 3rd International Conference on Geotechnical Engineering combined with the 9th Yearly Meeting of the Indonesian Society for Geotechnical Engineering at Semarang – Indonesia, on 3-4 August 2005 was the first action to respond to tsunami disaster in Indonesia. The theme of the conference was Geotechnical Engineering for Disaster Prevention and Rehabilitation, organized by Diponegoro University, Department of Public Works and Indonesian Society for Geotechnical Engineering and supported by Centre for Soft Ground Engineering, National University of Singapore, Geotechnical Research Institute (Hohai University – China), University College of Technology Tun Hussein Onn (KUITHO) and JWG-DMR. This conference was chaired by Dr. SPR. Wardani from Diponegoro University. 14 countries participated in this conference.

Before that, since 2003 this University also already took an important role in disaster management, include: Involve in setting up guideline, standard, manual related to disaster; Writing book about disaster; Conducting workshop and training. On 13 June 2005, Diponegoro University, in collaboration with BAPPEDA and supported by France Government (through Fran's Embassy in Jakarta) conducted workshop and training for development of coastal region post tsunami in Aceh Besar. This workshop and training for 60 staff (for high level). On 14 - 25 June 2005 conducted training for about 40 staff of middle and low level. They also helped to translate the application of blue print for post disaster, reconstruction, reconciliation and model. They conducted field trip, identification of the problem, went to studio to analyze and solve the problem. Other group from Diponegoro University, in collaboration with Province and Regency BAPPEDA, conducted training in Aceh with activities: field trip, collected data, gave report, presentation and doing training / workshop. They also gave information for disaster prevention by Mangrove planting. Beside that, Diponegoro University proposed to BRR as Technical Audit for Post Disaster building in NAD and Nias and it has approved for 2007. Diponegoro University is also as adviser for Development of Earthquake resistance building in Central Java Province. Diponegoro University with Ministry of Public Works also organized trainings on prevention, mitigation, preparedness and rehabilitation of flood, landslide, riverbank slide and marine abrasion in Central Java on 6-10 August 2007 and 20-24 August 2007. The programs are fully supported by the government of the Republic of Indonesia from APBN 2007.

Universities and other research organizations in the country have a major role in evolving suitable programs for preventing, rehabilitating and mitigating future disaster. Lack of pre-disaster preparation led a large number of human casualties and massive destruction in the past tragedy. Integrated disaster management should take into account the risks caused by all conceivable natural hazards. To fulfill that requirement, the 4th International conference on Disaster Prevention and Rehabilitation and 1st International workshop on Disaster Prevention and Rehabilitation was held at Diponegoro University, during 10th and 11th September 2007. International Conference was organized jointly by Diponegoro University and Ministry of Public works of the Republic of Indonesia, which was supported by the Joint

Working Group on geotechnical engineering for disaster Prevention and Rehabilitation and also Technical committee TC -39 of ISSMEGE. During the same time, launching of a new center of Disaster Prevention and Rehabilitation was done at Diponegoro University. The chair of the conference was Dr. SPR Wardani. The establishment of this Centre at Diponegoro University make a Plan of Operation inline with Ministry of Public Works of the Republic of Indonesia program. This centre is fully supported by TC-39 of ISSMGE and JWG-DMR. Furthermore, one of executive members of JWG-DMR and member of TC-39 is from Diponegoro University. It also builds up connections and supports funding from international organizations. At the time moment, this group already actively involves in flood management provided by Municipality and Provincial Government.

Diponegoro University proposed to BRR as Technical Audit for Post Disaster building in NAD and Nias and it has approved for 2007. Diponegoro University is also as adviser for Development of Earthquake resistance building in Central Java Province. Diponegoro University with Ministry of Public Works also organized trainings on prevention, mitigation, preparedness and rehabilitation of flood, landslide, riverbank slide and marine abrasion in Central Java on. The programs are fully supported by the government of the Republic of Indonesia from APBN 2007. Diponegoro University will also contribute in the following area: Need assessment surveys and data processing, Community health service, Environmental impact assessments, Counseling and trauma management, Locating and sizing of infrastructure facilities, Condition surveys of structures, Design of infrastructure facilities and construction supervision, Technical training on planning and enterprise development, Provide GIS services and preparation of maps for town and settlement planning, Socio-economic studies pertaining to the affected areas and impact assessment.

REFERENCES

- Balai Pusat Statistik Jawa Tengah. (2004). Jawa Tengah Dalam Angka Tahun 2004.
- Kodoatie R.J., Sjarief Roestam. (2006). *Pengelolaan bencana terpadu*. Penerbit Yarsif Watampone, Jakarta.

ON THE RELATIONSHIP BETWEEN RELIABILITY INDICES FOR ULTIMATE AND SERVICEABILITY LIMIT STATES OF BUILDING FOUNDATIONS

Yu Wang

*Department of Building and Construction, City University of Hong Kong
Tat Chee Avenue, Kowloon, Hong Kong, China*

Fred H. Kulhawy

*School of Civil and Environmental Engineering, Cornell University
Hollister Hall, Ithaca, NY 14853, USA*

This paper presents a simplified relationship between the reliability indices (β_{SLS} and β_{ULS}) for the serviceability limit state (SLS) and ultimate limit state (ULS) of building foundations. Under certain conditions, β_{SLS} is a linear function of the β_{ULS} that is specified already in reliability-based design (RBD) codes. For illustration, the relationship is used to estimate β_{SLS} for augered cast-in-place (ACIP) piles designed in accordance with the RBD methodologies in the National Building Code of Canada.

INTRODUCTION

Over the last two decades, reliability-based design (RBD) methodologies gradually have gained popularity in geotechnical engineering. Several RBD codes have been developed and implemented around the world, such as the load and resistance factor design (LRFD) code adopted by the American Association of State Highway and Transportation Officials (Aashto 1997), the Canadian National Building Code (Becker, 1996), Eurocode 7 [European Committee for Standardization (CEN), 2001], and the Japanese Geo-Code 21 (Honjo and Kusakabe, 2002). A review of these RBD design codes shows that, although they apply reliability principles for ultimate limit state (ULS) designs and calibrate the designs for a target ULS reliability index (β_{ULS}), the serviceability limit state (SLS) designs still are evaluated using conventional deterministic approaches with an unknown SLS reliability index (β_{SLS}).

This paper presents a simplified relationship that can infer the β_{SLS} from the β_{ULS} that is specified already in design codes. The derivation considers the limiting tolerable foundation settlement (y_{ft}) as a random variable and accounts for the uncertainties associated with the calculation models. First, β_{ULS} is defined, which is followed by derivation of the relationship between β_{SLS} and β_{ULS} . A key variable in this relationship is the ratio (R) of the SLS capacity (Q_{SLS}) to the ULS capacity (Q_{ULS}). Capacity herein refers to the maximum soil resistance mobilized by a loaded foundation unit when it reaches either the ultimate limit state (Q_{ULS}) or serviceability limit state (Q_{SLS}). Closed-form approximations are used to characterize R

probabilistically. Then, for illustration, the relationship is used to estimate β_{sls} for augered cast-in-place (ACIP) piles that are designed in accordance with the National Building Code of Canada (NBCC), as described by Becker (1996).

RELIABILITY INDEX (β_{uls}) FOR ULTIMATE LIMIT STATE DESIGNS

In RBD, design quantities, such as the load (F) and the ULS capacity (Q_{uls}), are modeled as random variables, as shown in Figure 1. For simplicity herein, it will be assumed that all components of both F and Q_{uls} can be lumped into the single distributions shown. In addition, since F and Q_{uls} must be positive, and for mathematical convenience, they commonly are assumed to be lognormally distributed (Ang and Tang 1975). The basic reliability problem is to evaluate the probability of ULS failure p_{fuls} (or β_{uls}) from some pertinent probabilistic characterizations of F and Q_{uls} , which frequently include the mean (m_F and $m_{Q_{uls}}$), standard deviation (s_F and $s_{Q_{uls}}$), coefficient of variation (COV_F and $COV_{Q_{uls}}$), and even probability density function.

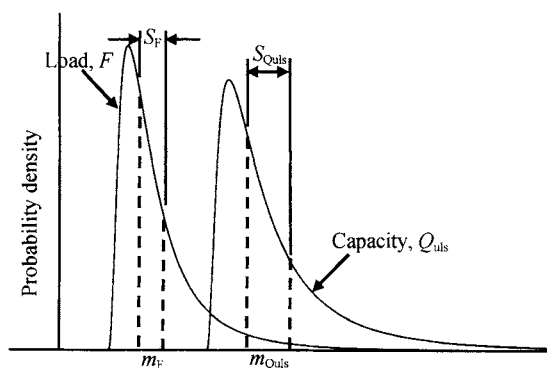


Figure 1. Lognormally distributed load and capacity

For lognormally distributed F and Q_{uls} , the p_{fuls} can be evaluated as:

$$\begin{aligned} p_{fuls} &= \text{Prob}(Q_{uls} < F) = \text{Prob}(Q_{uls}/F < 1) = \text{Prob}[\ln(Q_{uls}/F) < \ln(1)] \\ &= \text{Prob}[\ln(Q_{uls}) - \ln(F) < 0] = \text{Prob}[Q_{uls}^N - F^N < 0] \end{aligned} \quad (1)$$

in which Q_{uls}^N and F^N = equivalent normal random variables for Q_{uls} and F , respectively. For this condition, the equivalent safety margin $M_{uls} = Q_{uls}^N - F^N$, and it is normally distributed with the mean ($m_{M_{uls}}$) and standard deviation ($s_{M_{uls}}$). The β_{uls} then can be expressed as:

$$\beta_{uls} = \Phi^{-1}(1 - p_{fuls}) = \frac{m_{M_{uls}}}{s_{M_{uls}}} = \frac{\ln\left[\frac{m_{Q_{uls}}}{m_F} \sqrt{\frac{1 + COV_F^2}{1 + COV_{Q_{uls}}^2}}\right]}{\sqrt{\ln[(1 + COV_{Q_{uls}}^2)(1 + COV_F^2)]}} \quad (2)$$

in which Φ^{-1} = inverse standard normal probability distribution function.

Eq.(2) has been used as the basis for RBD (e.g., Barker et al. 1991, Becker 1996, Phoon et al. 2003a, b). Using a set of calibrated resistance factors, the RBD codes ensure that all ULS designs have a nominally consistent p_{fuls} or β_{uls} . Consider, for example, the National Building Code of Canada (Becker, 1996), in which the proposed resistance factors result in a nominal

$\beta_{uls} = 3.4$ for pile axial compression capacity obtained from semi-empirical analysis using in-situ and laboratory test data.

RELATIONSHIP BETWEEN β_{uls} AND β_{sls}

If the ratio of SLS capacity (Q_{sls}) to Q_{uls} is defined as R , the SLS probability of failure (p_{fsls}) can be expressed as:

$$\begin{aligned} p_{fsls} &= \text{Prob}(Q_{sls} < F) = \text{Prob}(Q_{sls} / F < 1) = \text{Prob}\{\ln[(Q_{sls} / Q_{uls})(Q_{uls} / F)] < \ln(I)\} \\ &= \text{Prob}[\ln(R Q_{uls} / F) < \ln(I)] = \text{Prob}[\ln(R) + \ln(Q_{uls}) - \ln(F) < 0] \end{aligned} \quad (3)$$

Using Monte Carlo simulations and hypothesis tests, Wang and Kulhawy (2007) showed that, for augered cast-in-place (ACIP) piles, R is lognormally distributed and uncorrelated with Q_{uls} . Therefore, Eq.(3) can be rewritten as:

$$p_{fsls} = \text{Prob}[R^N + Q_{uls}^N - F^N < 0] = \text{Prob}[M_{sls} < 0] \quad (4)$$

in which R^N = equivalent normal random variable for R , and $M_{sls} = R^N + Q_{uls}^N - F^N$ = normally distributed equivalent safety margin with the mean (m_{Msls}) and standard deviation (s_{Msls}). Then β_{sls} can be expressed as:

$$\beta_{sls} = \frac{m_{Msls}}{s_{Msls}} = \frac{\ln\left[\frac{m_R}{\sqrt{1 + \text{COV}_R^2}}\right] + \ln\left[\frac{m_{Q_{uls}}}{\sqrt{1 + \text{COV}_{Q_{uls}}^2}}\right] - \ln\left[\frac{m_F}{\sqrt{1 + \text{COV}_F^2}}\right]}{\sqrt{\ln(1 + \text{COV}_R^2) + \ln(1 + \text{COV}_{Q_{uls}}^2) + \ln(1 + \text{COV}_F^2)}} \quad (5)$$

Combining Eqs.(2) and (5) results in:

$$\beta_{sls} = C_0 + C_1 \beta_{uls} \quad (6)$$

in which C_0 and C_1 = intercept and slope of this linear function, respectively, given by:

$$C_0 = \frac{\ln\left[\frac{m_R}{\sqrt{1 + \text{COV}_R^2}}\right]}{\sqrt{\ln[(1 + \text{COV}_R^2)(1 + \text{COV}_{Q_{uls}}^2)(1 + \text{COV}_F^2)]}} \quad (7)$$

$$C_1 = \sqrt{\frac{\ln[(1 + \text{COV}_{Q_{uls}}^2)(1 + \text{COV}_F^2)]}{\ln[(1 + \text{COV}_R^2)(1 + \text{COV}_{Q_{uls}}^2)(1 + \text{COV}_F^2)]}} \quad (8)$$

Since β_{uls} is specified in the RBD codes, β_{sls} can be estimated directly using Eq.(6) with m_R , COV_R , $\text{COV}_{Q_{uls}}$, and COV_F .

PROBABILISTIC CHARACTERIZATION OF $R = Q_{sls}/Q_{uls}$

A key random variable in the relationship between β_{uls} and β_{sls} is $R = Q_{sls}/Q_{uls}$ and its probabilistic characteristics, such as m_R and COV_R . Probabilistic characterization of R requires a load-displacement model that relates the foundation displacement to load capacity

and probabilistic characterization of the limiting tolerable foundation settlement (y_{lt}). The load-displacement model and its associated uncertainties are described below, followed by probabilistic characterization of y_{lt} . Then, closed-form approximations are used to characterize R probabilistically.

Foundation load-displacement model

For ACIP piles under compression, Chen (1998) and Kulhawy and Chen (2005) compiled a database that includes load tests of 56 piles from 31 sites and found that the load-displacement curves can be represented reasonably well by the following hyperbolic model:

$$\frac{Q}{Q_{uls}} = \frac{y}{a + b y} \quad (9)$$

in which Q_{uls} = ULS capacity, y = axial butt displacement, and a and b = hyperbolic model parameters. Phoon et al. (2006) further found that the parameters a and b are correlated random variables that follow a lognormal distribution and have the following statistics: mean ($m_a = 5.15$ mm and $m_b = 0.62$), standard deviation ($s_a = 3.07$ mm and $s_b = 0.16$), and coefficient of correlation ($\rho_{a,b} = -0.67$).

Limiting tolerable settlements for building foundations

The limiting tolerable foundation settlement (y_{lt}) is the maximum settlement that a building foundation can sustain before causing any serviceability failure, and it corresponds to the SLS capacity Q_{sls} , expressed as:

$$R = \frac{Q_{sls}}{Q_{uls}} = \frac{y_{lt}}{a + b y_{lt}} \quad (10)$$

The y_{lt} for building foundations has been examined by many researchers (e.g., Skempton and MacDonald 1956, Grant et al. 1974, Wahls 1981, and Zhang and Ng 2005), and deterministic y_{lt} values for buildings have been proposed and adopted in design codes around the world. Zhang and Ng (2005) synthesized the y_{lt} values reported in the literature into a database and found that, for pile foundations, y_{lt} is lognormally distributed with $m_{y_{lt}} = 96$ mm, $s_{y_{lt}} = 56$ mm, and $COV_{y_{lt}} = 0.583$. These y_{lt} statistics are significantly larger than the allowable settlement limit of 25 mm that is used frequently in deterministic SLS designs of most foundation types (e.g., Peck et al. 1974). However, these pile statistics are used as a starting point in the example below. The effect of y_{lt} on β_{sls} is discussed later.

Closed-form approximations

With the load-displacement model and probabilistic characterization of y_{lt} , the probabilistic characteristics of R , given by m_R and s_R , can be approximated by a Taylor series expansion as follows:

$$m_R \approx \frac{m_{y_{lt}}}{m_a + m_b m_{y_{lt}}} \quad (11)$$

$$\begin{aligned}
s_R^2 &\approx \left(\frac{\partial R}{\partial a}\right)^2 s_a^2 + \left(\frac{\partial R}{\partial b}\right)^2 s_b^2 + \left(\frac{\partial R}{\partial y_{lt}}\right)^2 s_{y_{lt}}^2 + 2\frac{\partial R}{\partial a}\frac{\partial R}{\partial b}\rho_{a,b}s_a s_b \\
&\quad + 2\frac{\partial R}{\partial a}\frac{\partial R}{\partial y_{lt}}\rho_{a,y_{lt}}s_a s_{y_{lt}} + 2\frac{\partial R}{\partial b}\frac{\partial R}{\partial y_{lt}}\rho_{b,y_{lt}}s_b s_{y_{lt}} \\
&= \frac{m_{y_{lt}}^2 s_a^2 + m_{y_{lt}}^4 s_b^2 + m_a^2 s_{y_{lt}}^2 + 2\rho_{a,b} m_{y_{lt}}^3 s_a s_b}{(m_a + m_b m_{y_{lt}})^4} \tag{12}
\end{aligned}$$

For ACIP piles, m_R and s_R can be estimated as 1.484 and 0.317, respectively. Therefore, $COV_R = s_R / m_R = 0.317 / 1.484 = 0.214$.

SLS RELIABILITY INDEX ESTIMATED FOR NBCC

Becker (1996) described the development of RBD methodologies for the NBCC and summarized the calibration process, corresponding ULS reliability index (β_{uls}), and proposed resistance factors. For example, the proposed resistance factor is 0.4 for the axial compression capacity of a pile foundation, when calculated from semi-empirical analysis using in-situ and laboratory data. The corresponding $\beta_{uls} = 3.4$, and the coefficient of variation of Q_{uls} ($COV_{Q_{uls}} = 0.40$).

Using Eq.(6), the SLS reliability index (β_{sls}) can be estimated directly. Figure 2 shows the estimated β_{sls} as a function of the coefficient of variation for load effects (COV_F) for ACIP piles designed in accordance with the NBCC. As COV_F increases from 0 to 1.0, β_{sls} remains relatively constant at about 3.75 with slight variation between 3.83 and 3.71. As illustrated in Figure 2, the COV_F of various load effects for on-land and offshore foundations lies in the range of 0.05 to 0.6 (Meyerhof 1995). Figure 2 also includes the variations of the intercept C_0 and slope C_1 . As COV_F increases from 0 to 1.0, C_0 decreases from 0.85 to 0.40, while C_1 increases from 0.88 to 0.97. The opposing effects of C_0 and C_1 result in a β_{sls} that remains relatively constant at about 3.75.

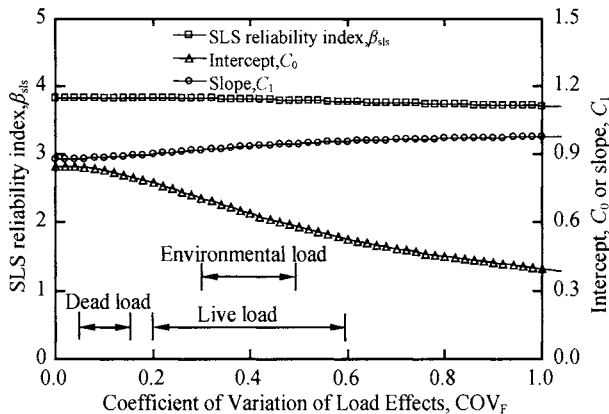


Figure 2. Estimated SLS reliability index β_{sls} for $m_{y_{lt}} = 96$ mm and $s_{y_{lt}} = 56$ mm

The estimated β_{sls} is larger than the $\beta_{uls} = 3.4$ specified in the NBCC. This result indicates that, for the axial compression capacity of ACIP piles designed in accordance with the NBCC, the designs automatically satisfy the SLS design requirements and have a $\beta_{sls} = 3.75$, which is

larger than the $\beta_{uls} = 3.4$. This result can be attributed to the probabilistic characterization of R , which shows that R is larger than 1 (e.g., $m_R = 1.484$), and therefore the SLS capacity Q_{sls} is larger than Q_{uls} . Consequently, the probability of $Q_{sls} < F$ is smaller than the probability of $Q_{uls} < F$, and β_{sls} is larger than β_{uls} .

The y_{lt} statistics (i.e., $m_{y_{lt}} = 96$ mm and $s_{y_{lt}} = 56$ mm) reported by Zhang and Ng (2005) and used herein are significantly larger than the displacement limit of 25 mm that is used frequently in deterministic SLS designs (e.g., Peck et al. 1974, Wahls 1994). To explore the effect of y_{lt} on the estimated β_{sls} , a sensitivity study was performed using a $m_{y_{lt}} = 25$ mm in combination with the $COV_{y_{lt}} = 0.583$ reported by Zhang and Ng (2005). Under this condition, $s_{y_{lt}} = 15$ mm, $m_R = 1.211$, $s_R = 0.249$, and $COV_R = 0.205$. Then, β_{sls} is estimated using these m_R , s_R , and COV_R values. Figure 3 shows the estimated β_{sls} as a function of the COV_F for $m_{y_{lt}} = 25$ mm. As COV_F increases from 0 to 1.0, β_{sls} remains relatively constant at about 3.45 with slight variation between 3.40 and 3.50. Figure 3 also includes the variations of the intercept C_0 and slope C_1 . As COV_F increases from 0 to 1.0, C_0 decreases from 0.39 to 0.18, while C_1 increases from 0.88 to 0.98. The estimated β_{sls} is larger than the $\beta_{uls} = 3.4$ specified in the NBCC. This result indicates that, even with $m_{y_{lt}} = 25$ mm and $s_{y_{lt}} = 15$ mm, the NBCC design of ACIP piles still is acceptable for the SLS design requirements.

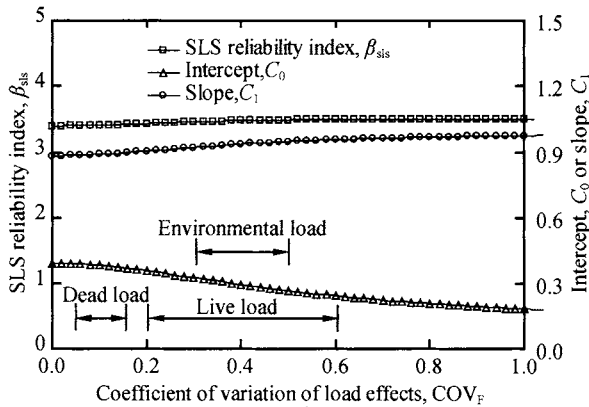


Figure 3. Estimated SLS reliability index β_{sls} for $m_{y_{lt}} = 25$ mm and $s_{y_{lt}} = 15$ mm

SUMMARY AND CONCLUSIONS

In this paper, a relationship was developed to relate the SLS reliability index (β_{sls}) to the ULS reliability index (β_{uls}) that is specified already in RBD codes. The derivation considers the limiting tolerable foundation settlement (y_{lt}) as a random variable and accounts for the uncertainties associated with the empirical load-displacement models. The resulting relationship between β_{sls} and β_{uls} is linear, and its intercept (C_0) and slope (C_1) are functions of m_R , COV_R , $COV_{Q_{uls}}$, and COV_F .

The developed relationship was used to estimate β_{sls} for ACIP piles designed in accordance with the NBCC. For assumed input variables consistent with recent data summaries ($m_{y_{lt}} = 96$ mm and $COV_{y_{lt}} = 0.583$), it was found that, for COV_F ranging from 0 to 1.0, β_{sls} remains relatively constant at about 3.75, with a slight variation between 3.83 and 3.71. This estimated β_{sls} is larger than the $\beta_{uls} = 3.4$ specified in the NBCC. This result

indicates that, for the axial compression capacity of ACIP piles that are designed in accordance with the NBCC, the design automatically satisfies the SLS design requirements. Even if the $m_{y/t}$ was changed to the frequently used value of 25 mm, the estimated β_{sls} is larger than the $\beta_{uls} = 3.4$ specified in the NBCC, and the NBCC design of ACIP piles still is acceptable for the SLS design requirements.

ACKNOWLEDGMENTS

This research was supported by a grant from the Research Grants Council of the Hong Kong Special Administrative Region, China [Project No. 9041260 (CityU 121307)]

REFERENCES

- American Association of State Highway and Transportation Officials (AASHTO) (1997). *LRFD Highway Bridge Design Specifications*. AASHTO, Washington, DC.
- Ang A.H-S., Tang W.H. (1975). *Probability concepts in engineering planning & design, Vol. 1: basic principles*. Wiley, New York.
- Barker R.M., Duncan J.M., Rojiani K.B., Ooi P.S.K., Tan C.K. and Kim S.G. (1991). Manuals for design of bridge foundations. *NCHRP Report 343*, Trans. Research Board, Washington, DC.
- Becker D.E. (1996). Limit state design for foundations – part II: development for national building code of Canada. *Canadian Geotech. J.*, 33(6): 984-1007.
- Chen J.R. (1998). Case history evaluation of axial behavior of augered cast-in-place piles and pressure-injected footings. *MS Thesis*, Cornell University, Ithaca.
- European Comm. for Standardization (CEN) (2001). *Eurocode 7 Pt 1: geotech. design: general rules (final draft)*. European Comm. for Standardization (CEN), Brussels.
- Grant R., Christian J.T. and Vanmarcke E.H. (1974). Differential settlement of buildings. *J. Geotech. Eng.*, ASCE, 100(9), 973-991.
- Honjo Y. and Kusakabe, O. (2002). Proposal of comprehensive foundation design code: Geocode 21 ver.2. *Proc. Intl. Workshop on Foundation Design Codes & Soil Investigation in View of International Harmonization & Performance Based Design*, Tokyo, 95-103.
- Kulhawy F.H., Chen J.R. (2005). Axial compression behavior of augered cast-in-place (ACIP) piles in cohesionless soils. *Advances in Designing & Testing Deep Foundations (GSP 129)*, ASCE, Reston, 275-289.
- Meyerhof G.G. (1995). Development of geotechnical limit state design. *Canadian Geotech. J.*, 32(1): 128-136.
- Peck R.B., Hanson W.E. and Thornburn T.H. (1974). *Foundation engineering, 2nd Ed.*, Wiley, New York.
- Phoon K.K., Chen J.R. and Kulhawy F.H. (2006). Characterization of model uncertainty for augered cast-in-place (ACIP) piles under axial compression. *Foundation Analysis & Design: Innovative Methods (GSP 153)*, ASCE, Reston, 82-89.
- Phoon K.K., Kulhawy F.H. and Grigoriu M.D. (2003a). Development of a reliability-based design framework for transmission line structure foundations. *J. Geotech. & Geoenv. Eng.*, ASCE, 129(9): 798-806.
- Phoon K.K., Kulhawy F.H. and Grigoriu M.D. (2003b). Multiple resistance factor design (MRFD) for shallow transmission line structure foundations. *J. Geotech. & Geoenv. Eng.*, ASCE, 129(9): 807-818.

- Skempton A.W., MacDonald D.H. (1956). Allowable settlement of buildings. *Proc. Institution of Civil Engineers*, 5(Part 3): 727-768.
- Wahls H.E. (1981). Tolerable settlement of buildings. *J. Geotech. Eng.*, ASCE, 107(11): 1489-1504.
- Wang Y., Kulhawy F.H. (2007). Reliability Index for Serviceability Limit State of Building Foundations. *J. Geotech. & Geoenv. Eng.*, ASCE, (under review).
- Zhang L.M., Ng A.M.Y. (2005). Probabilistic limiting tolerable displacement for serviceability limit state design of foundations. *Geotechnique*, 55(2): 151-161.

PLANNING SLOPE STABILIZATION ACTIONS

Limin Zhang

*Department of Civil Engineering, the Hong Kong University of Science
and Technology, Clear Water Bay, Hong Kong, China*

Dianqing Li

*State Key Laboratory of Water Resources and Hydropower Engineering Science,
Wuhan University, 8 Donghu South Road, Wuhan 430072, China*

The risk posed by slopes may be taken as the intersection of slope hazards and vulnerability of elements at risk. Slopes deteriorate over time. The elements at risk also develop over time. Therefore, the slope risk evolves over time and proper slope maintenance or stabilization actions are needed to keep the slope risk within a tolerable level. This paper outlines a procedure for planning slope stabilization works considering changes of slope safety and elements at risk over time. An example is presented to illustrate the proposed procedure. The results indicate that as a slope deteriorates the risk of slope failure increases with time and may reach an unacceptable level at a certain time even though the elements at risk remain the same. In addition, the risk of slope failure may reach an unacceptable level due to a change of elements at risk.

INTRODUCTION

The risk posed by slopes may be taken as the intersection of slope hazards and vulnerability of elements at risk, as shown in Figure 1. Slopes deteriorate over time. Environmental loads

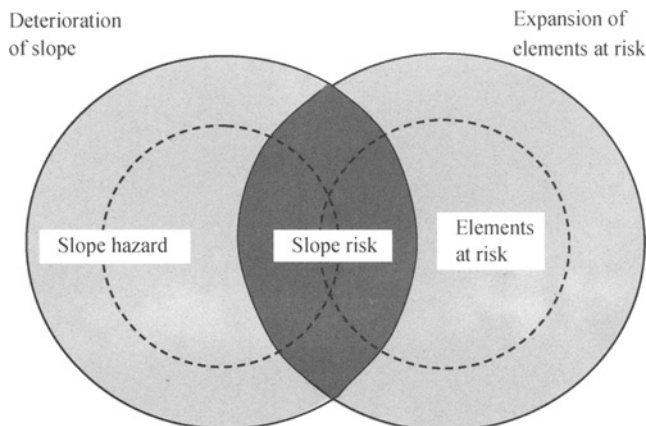


Figure 1. Slope risk changes due to changing slope safety and elements at risk

on slopes may vary with time [e.g., a large number of natural terrain slopes in the Three-Gorge Reservoir zone, which are submerged in the reservoir and subjected to hydrodynamic forces when the reservoir water level draws down (Tang et al., 2006; Chen and Zhang, 2005)]. Both slope deterioration and changes of environmental loads will lower the slope safety level and increase the hazard level. The elements at risk also develop over time as the community affected by the slopes grows, which increases the vulnerability. In Figure 1, the increased slope hazard and vulnerability will finally lead to increased slope risk over time. Proper slope maintenance or stabilization actions are needed to keep the slope risk within a tolerable level. This paper outlines a procedure for planning slope stabilization works considering the changes of slope safety and elements at risk over time. An example is presented to illustrate the proposed procedure.

DETERIORATION OF SLOPES

The stability of slopes deteriorates over time due to several reasons: degradation of surface cover, blockage or damage of surface drainage systems, surface or internal erosion, reduction of the shear strength of slope materials, and large changes in pore pressure (e.g., GEO 2003; Cheung 2004).

In a previous research program by Cheung (2004) and Cheung and Tang (2005), approximately 16,000 from a population of 21,000 soil cut slopes with observed performance records during 208 rainstorms in the period from 1984 to 2002 were selected for study. Most of these slopes were formed before the implementation of geotechnical control in 1977. The rainfall intensity, $i_{24\max}$, was divided into three categories: 0–200 mm/day, 200–400 mm/day, and > 400 mm/day. For each of the rainstorms, relevant landslides in response to the three rainfall intensity categories were also identified and grouped. The grouping of slope failures for the 208 rainstorms under different categories of rainfall intensity and slope ages is shown in Figure 2. Although the number of rainstorm hits $i_{24\max} > 400$ mm/day is the smallest, a large number of landslides have still been resulted.

Based on the dataset in Figure 2, the conditional annual probability of failure as a function of age t can be estimated as (Cheung and Tang, 2005):

$$\hat{h}(t, i_{24\max}) = \frac{\text{Number of } t\text{-year-old slopes that failed at a rainstorm of intensity } i_{24\max}}{\text{Number of rainstorm hits of intensity } i_{24\max} \text{ on } t\text{-year-old slopes}} \quad (1)$$

The conditional rate of failure given by Eq. (1) is equivalent to the hazard function that is commonly used in reliability analysis to denote the instantaneous rate of failure for an operating system. The hazard function $h(t)$ for a Weibull-distributed time to failure t is expressed as

$$h(t) = \lambda\gamma(\lambda t)^{\gamma-1} \quad (2)$$

where γ = shape parameter that governs the rate of change of the hazard function; and λ = scale parameter that dictates the spread of the distribution.

In addition to the hazard function, a designer may want to know the probability of failure over a given future service time. One can integrate the probability density function of the time to failure and obtain the probability of slope failure for a service period t as follows:

$$P_f(t) = 1 - \exp(-\lambda t)^\gamma \quad (3)$$

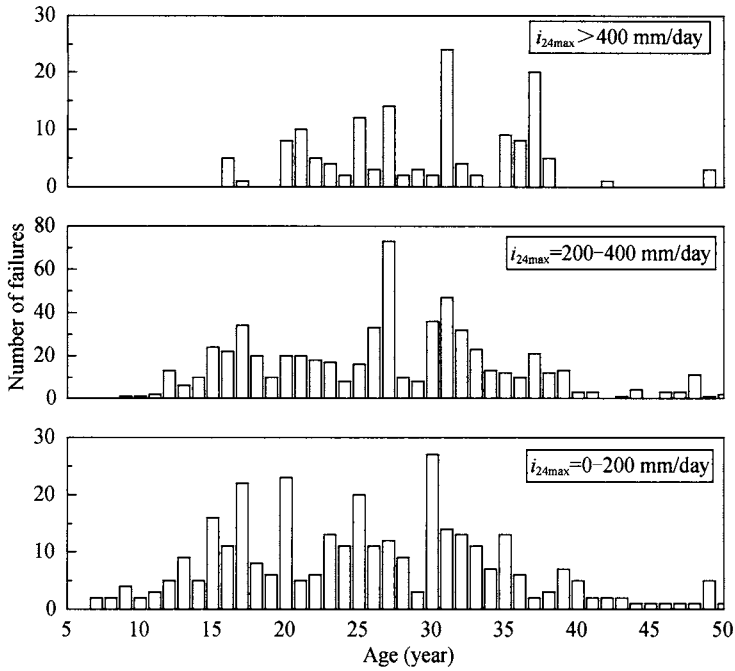


Figure 2. Number of old cut slope failures during 1984-2002 (After Cheung and Tang, 2005)

Applying Eq. (3), the probabilities of slope failure for the three categories of rainfall intensity can be obtained. If the chances of different rainstorm intensities are taken into account, one can determine the probabilities of slope failure for various service periods by virtue of the total probability theorem (e.g., Ang and Tang 2007),

$$P_{ft}(t) = \sum_{i=1}^3 P_{fi}(t)P_i(i_{24max}) \quad (4)$$

where $P_i(i_{24max})$ = occurrence probability of the i th category of rainstorm intensity; and $P_{fi}(t)$ = probability of slope failure for a service period t shown in Eq. (3). Lam and Leung (1994) established the occurrence probability of different rainstorm intensities based on past rainfall records. The occurrence probabilities of rainstorm categories $i_{24max} = 0-200$, $200-400$, and > 400 mm/day in a given year are found to be 43%, 50%, and 7%, respectively. Based on these data, the probability of slope failure over any given service period can be determined, and the annual probability of slope failure in year t can be calculated by

$$P_{fa}(t) = P_{ft}(t) - P_{ft}(t-1) = \sum_{i=1}^3 (P_{fi}(t) - P_{fi}(t-1))P_i(i_{24max}) \quad (5)$$

Figure 3 shows the annual probability of failure in any year t within the given service period. It is evident that the rate of slope deterioration increases significantly when the service time is longer than a decade. For example, the annual failure probability increases from 0.01% at a service time of 5 years to 0.4% at a service time of 15 years. This means that the time of slope maintenance should be smaller than a decade in order to alleviate the rate of slope deterioration efficiently. After maintenance works were initiated in the 16th year, the annual probability of failure after $t = 16$ years has been reduced substantially and changes

with time more slowly. As reported by Cheung and Tang (2005), a public campaign on slope maintenance was initiated in 1992 to increase public awareness of the importance of slope maintenance and the owners' liability to keep their slopes in good condition. The youngest slopes in the population were 16 years old in 1992. Maintenance of many of these slopes has been carrying out since then and the rate of slope failure after $t = 16$ years has therefore been retarded.

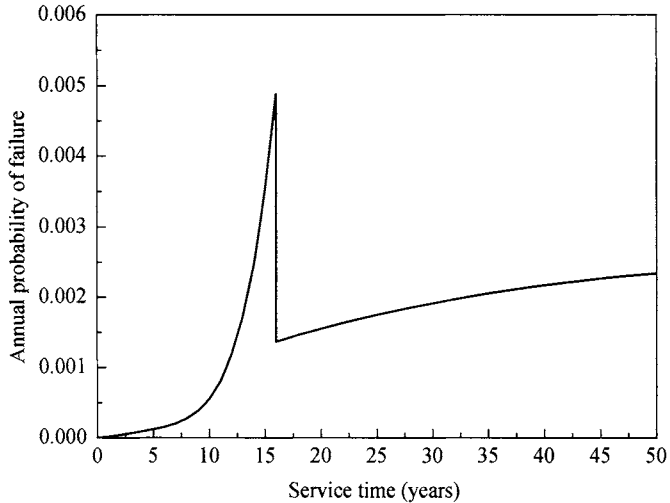


Figure 3. Annual probability of slope failure for various service periods

CHANGE OF ELEMENTS AT RISK

The risk posed by a particular slope may change when the population and economic activities in the affected area expand. The risk level of the slope may therefore reach a limit that triggers stabilization actions. The construction of new towns in hilly terrains in the Three-Gorge Reservoir zone is one example for this. Before the construction of a new town at a site, the slopes near or at that site only affect a limited number of people. After the construction of the new town, the population and properties at risk grow rapidly. The risks of these slopes should accordingly be re-evaluated and the safety levels of these slopes enhanced. A risk analysis example will be presented in the later sections to illustrate how a change of elements at risk triggers slope stabilizations actions.

TOLERABLE RISK IN TERMS OF FATALITY

As a slope deteriorates or as the community grows, the risk increases with time and may reach an unacceptable limit at a certain time. The time for slope stabilization can be determined when the risk-time relation is found and appropriate risk acceptance criteria are selected. Fell and Hartford (1997), GEO (1998), Song et al. (2007) and several others have recommended acceptable risk levels for landslides. The guidelines published in the Hong Kong Planning Standards and Guidelines (HKGPD 1994) are reproduced in Figure 4 in the form of an $F-N$ curve (Frequency vs. Number of fatalities). An $F-N$ curve provides a measure of the probability of fatality by plotting the frequency of accidents that affect the

public against the possible fatality number. There are three regions indicated in Figure 4; namely, unacceptable region, as low as reasonably practicable (ALARP) region and acceptable region. If the risks lie wholly or partly within the unacceptable region, then risk mitigation measures must be implemented to lower the risks to the ALARP region.

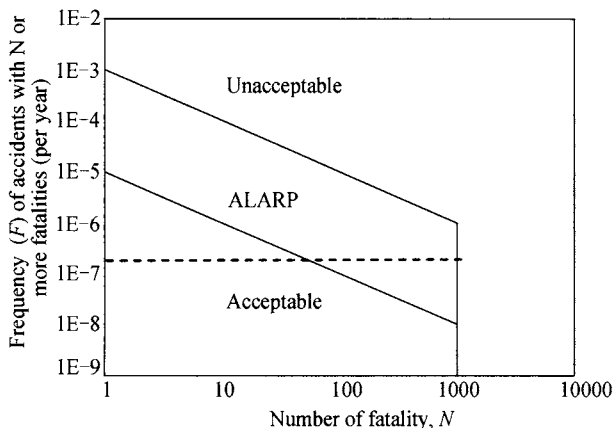


Figure 4. Risk acceptance criteria for a potentially hazardous installation adopted in Hong Kong (After HKGPD, 1994)

PLANNING SLOPE STABILIZATION AND WORKED EXAMPLE

The risk of slope failure can be expressed in terms of annual fatality. For simplicity, only one consequence for all slope failure modes is considered in this study. In this case, an F - N curve becomes the same as an f - N curve (Fell and Hartford 1997). According to Figure 4, if the consequence is only one fatality associated with the slope failure concerned, the annual risk of fatality larger than 10^{-3} will be unacceptable and the annual risk of fatality in the ALARP region ranges from 10^{-5} to 10^{-3} . If the annual risk of fatality of a slope is larger than 10^{-3} , stabilization actions should be activated. Similarly, for the consequence of 100 fatalities, the annual risk of fatality larger than 10^{-5} will be unacceptable and the annual risk of fatality in the ALARP region ranges from 10^{-7} to 10^{-5} . Consider a deteriorating slope with the relationship between annual probability of failure and service time shown in Figure 3. For simplicity, the failure consequence of the slope is expressed in terms of potential loss of life (PLL). Before the construction of a new town at the slope site, the slope only affects a limited number of people and the potential number of fatality is assumed to be one. Based on this assumed fatality number and the annual probability of failure in Figure 3, the slope risk can be calculated as the product of the probability of slope failure and the consequence of failure in terms of PLL. The calculated annual fatality is plotted in Figure 5 against the service time. It can be seen from Figure 5 that the annual fatality increases from 1.2×10^{-4} at the 5th year to 1.2×10^{-3} at the 12th year. According to Figure 4, the time for slope stabilization should be 11 years or shorter to keep the slope risk within the ALARP region. This indicates that, as a slope deteriorates, the risk of slope failure increases with time and reaches an unacceptable level at a certain time although the elements at risk remain the same.

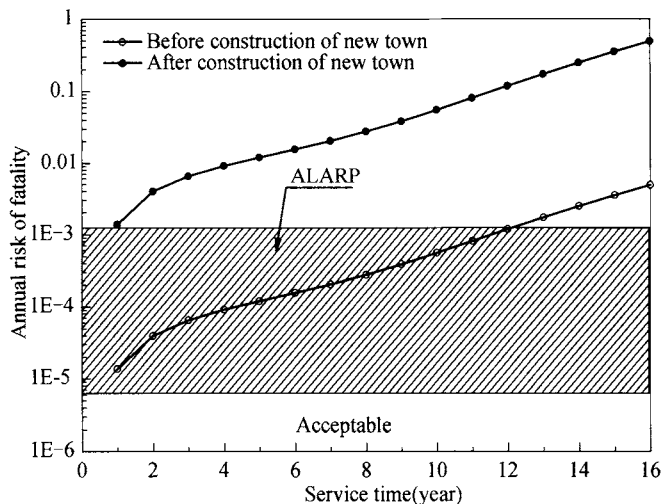


Figure 5. Annual risk of fatality for slope failure

The risk posed by a particular slope may also change due to changes of elements at risk. Now consider again the deteriorating slope with the annual probability of failure as shown in Figure 3. Suppose a new town will be constructed at the 5th year at a site affected by the slope. Before the town is constructed, the risk of fatality is only 1.2×10^{-4} at the 5th year, which lies within the ALARP region in Figure 5 and does not require stabilization effort. After the new town is constructed in the 5th year, the number of people affected by the slope will increase substantially. For illustrative purposes, the potential number of fatality is assumed to be 100 to account for the growth of population at risk. Accordingly, the risk of fatality will increase from 1.2×10^{-4} before the construction of the new town to 1.2×10^{-2} after the construction of the new town. The latter annual fatality exceeds the ALARP limit and suggests that the slope has to be properly stabilized before the residents move into the affected area. In addition, the slope safety in terms of annual probability of failure should be enhanced substantially (say by at least one order of magnitude) and the slope has to be properly maintained after construction so that the slope risk always falls into the ALARP or acceptable zone. This example indicates that the risk of slope failure may reach an unacceptable limit due to a change of elements at risk.

CONCLUSIONS

A procedure for planning slope stabilization works has been developed in this paper considering changes of slope safety and elements at risk. The risk for slope failure is taken as the intersection of slope hazards and vulnerability of elements at risk. Both slope safety and elements at risk change over time. As a slope deteriorates, the risk of slope failure increases over time and may reach an unacceptable level at a certain time even though the elements at risk remain the same. The risk of slope failure may also reach an unacceptable level due to the growth of elements at risk. The proposed procedure considers the time-dependency of risk of fatality from both slope deterioration and growth of elements at risk. Slope

stabilization actions should be activated when the risk of fatality is envisaged to be outside the ALARP or acceptable range.

ACKNOWLEDGMENTS

This research was substantially supported by a grant from the NSFC/RGC Joint Research Scheme between the National Natural Science Foundation of China and the Research Grants Council of the Hong Kong SAR (Project No. N-HKUST611/03).

REFERENCES

- Ang H.S., Tang, W.H. (2007). *Probability concepts in engineering: emphasis on applications to civil and environmental engineering*. 2nd edition, John Wiley and Sons, New York.
- Chen Q., Zhang L.M. (2005). Stability of a gravel soil slope under reservoir water level fluctuations. *Proc. ASCE Geo-Frontiers*, Austin, Texas, Jan. 2005. ASCE *Geotechnical Special Publication No. 140*, Gabr M., Bowders J.J., Elton D. and Zomberg J.G. (eds.), in CD Rom.
- Cheung R.W.M., Tang W.H. (2005). Realistic assessment of slope reliability for effective landslide hazard management. *Geotechnique*, 55(1): 85-94.
- Fell R., Hartford D. (1997). Landslide risk management. *Proceedings of the International Workshop on Landslide Risk Assessment*, Honolulu, Hawaii, USA, 19–21 February, D.M. Cruden and R. Fell (eds.), A.A. Balkema, Rotterdam, 51-109.
- GEO. (1998). *Landslides and boulder falls from natural terrain: interim risk guidelines*. GEO Report No. 75, Geotechnical Engineering Office, Hong Kong.
- GEO. (2003). *Guide to slope maintenance (Geoguide 5)*. third edition, Geotechnical Engineering Office, Hong Kong.
- HKGPD. (1994). *The Hong Kong planning standards and guidelines, Chapter 11: potentially hazardous installations*. Hong Kong Government Planning Department (HKGPD), Hong Kong, 12–19.
- Lam C.C., Leung Y.K. (1994). *Extreme rainfall statistics and design rainstorm profiles at selected locations in Hong Kong*. Technical Note No. 86, Royal Observatory, Hong Kong.
- Song Q.H., Liu D.S. and Wu Y.X. (2007). Study on acceptable and tolerable risk criteria for landslide hazards in the Mainland of China. *Proc. First international symposium on geotechnical safety & risk*. Shanghai, 18-19 Oct., 2007, H.W. Huang and L.M. Zhang (eds.), 363-374.
- Tang W.H. and Cheung R.W.M. (2004). Performance-based modelling of slope reliability. *Proc. 3rd Asian-Pacific Symposium on Structural Reliability and Its Applications*, Seoul, Korea, 19–21 August, Cho. H.N., Yun C.B. and Kim S.H. (eds.), 65–79.
- Tang W.H., Zhang L.M. and Zheng Y.R. (2006). Dealing with uncertainty in engineering design for large-scale gravel soil slopes in the Three Gorges Reservoir Zone. *Geohazards - Technical, Economical and Social Risk Evaluation*, Lillehammer, Norway, 18-21 June 2006, F. Nadim (ed.), Berkeley Electronic Press, in CD Rom.

Earthquakes and Soil Dynamics

MODELING OF STRESS-STRAIN BEHAVIOR OF SOFT CLAY UNDER CYCLIC LOADING

Yuanqiang Cai

*Architecture and Civil Engineering College, Wenzhou University,
Wenzhou 325027, China*

Institute of Geotechnical Engineering, Zhejiang University, Hangzhou 310027, China

Jun Wang

*Architecture and Civil Engineering College, Wenzhou University,
Wenzhou 325027, China*

Iwan models often used in modeling the non-linear and hysteretic behavior of soils under cyclic loading conditions, are unreliable when there is significant cyclic degradation and residual strain accumulating of the stress-strain curves. Especially, for soils with initial shear stress which the cumulative residual strain increase significantly, Iwan models often fail to simulate. In the present paper, the stiffness reduction and residual strain accumulating behavior of Hangzhou soft clay with different initial static shear stresses under stress-controlled undrained cyclic triaxial conditions are researched. Based on the test results, empirical models for cyclic degradation and residual strain accumulating are proposed. The empirical models are further incorporated into Iwan model to simulate the cyclic stress-strain relationship of soft clay. A comparison between experimental and predicted stress-strain curves shows good agreement.

INTRODUCTION

During ocean wave storms, earthquakes, traffic vibrations, and similar phenomena, fully saturated clays are often subjected to cyclic loading conditions. Geotechnical problems involving cyclic loading often require information on dynamic properties of soil, i.e. the constitutive relationship (Puzrin and Shiran, 2000). In practice, perhaps the most widely used models simulating nonlinear stress-strain behavior are those satisfying the extended Masing rules such as the ones proposed by Iwan(1967). While the model appears to simulate the stress-strain characteristics under cyclic loading at different strain levels, it does not, however, account for a substantial degradation in the modulus of the soil with the progression of loading cycles. To take into account the effect of cyclic stiffness degradation, Rao and Panda (1999) proposed a approach to modify Iwan's series-parallel model by incorporating into it the degradation index as suggested by Idriss et al.

However, the modified Iwan's series-parallel models can not take into account the residual strain increase of soft clay. Hence, the models can only agree well with the test results within the first few cycles. Studies also show residual strain will increase greatly when soft clay subjected to cyclic loading with initial static shear stress which the models fail to

simulate. In this paper, the cyclic degradation and residual strain accumulating models for soft clay subjected to initial shear stress are established respectively based on the undrained cyclic triaxial tests. Then the Iwan model is further modified by introducing into it cyclic degradation and residual strain accumulating models. In such a case, the Iwan's model can be extended to predict the undrained cyclic stress-strain behavior of soft clay with initial static shear stresses.

SOIL SAMPLE

Soil samples were taken at the construction site of Xiaoshan, Hangzhou. The soil is about 35m thick at this site. In order to ensure homogeneity, all samples were taken from the same layer, about 5~10m. All samples were undisturbed and normally consolidated with water content $\omega=48.4\%$, void ratio $e=1.225$, specific gravity $G_s=2.744$, liquid limit $w_L=58\%$, plastic limit $w_p=25\%$, plastic index $I_p=33$, liquid index $I_L=0.709$, cohesive force $C=18.5\text{kPa}$ and friction angle $\phi=18.8^\circ$.

TEST PROCEDURE

The tests were performed using GDS bidirectional dynamic triaxial testing system. The cylindrical specimens (3.91 cm diameter and 8 cm height) were backpressure saturated to a minimum B-value of 0.96. Following this, samples were subjected to an isotropic effective confining pressure p_0' of 60kPa for more than 24 h to produce normally consolidated specimens. The initial shear stress was ramped up to the target value for 1 min. Then cyclic loading was imposed in the vertical direction with a sine wave. Different cyclic stress levels and initial shear stresses were used to define the effects on cyclic behavior. In this paper, the cyclic stress q_{cyc} and initial static shear stress q_s will be given as cyclic stress ratio τ_c , and initial static shear stress ratio τ_{st} respectively, where $\tau_c = q_{cyc} / C_u$ and $\tau_{st} = q_s / C_u$, in which C_u is the undrained shear strength of soft clay.

MODELING CYCLIC DEGRADATION

In Figure 1, the cyclic loops obtained at cycle 1 and cycle N in the cyclic triaxial test with a constant cyclic stress amplitude are shown. In the figure, N is cycle number, q is deviator stress ($q = \sigma_1 - \sigma_3$), $\varepsilon_{aN, \max}$ and $\varepsilon_{aN, \min}$ are the maximum and minimum axial strains at cycle N , respectively, and G_N is secant shear modulus at cycle N . To quantify such degradation, Idriss et al. (1976,1978) introduced the concepts of the degradation index δ , which is redefined as follows:

$$\delta = \frac{G_N}{G_1} = \frac{2q_{cyc} / (\varepsilon_{aN, \max} - \varepsilon_{aN, \min})}{2q_{cyc} / (\varepsilon_{a1, \max} - \varepsilon_{a1, \min})} = \frac{(\varepsilon_{a1, \max} - \varepsilon_{a1, \min})}{(\varepsilon_{aN, \max} - \varepsilon_{aN, \min})} \quad (1)$$

The relationship between degradation index δ and $\log N$ for different cyclic stress ratios is shown in Figure 2. It can be seen the degradation index δ decreases with an increasing in the number of cycles. The value of δ changes linearly with a change in $\log N$ for specimens with initial shear stress (Yasuhara, 1997). However, for specimen without initial shear stress, the relationship between δ and $\log N$ shows nonlinear.

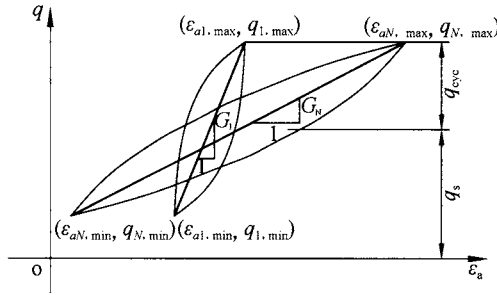


Figure 1. Definition of degradation index

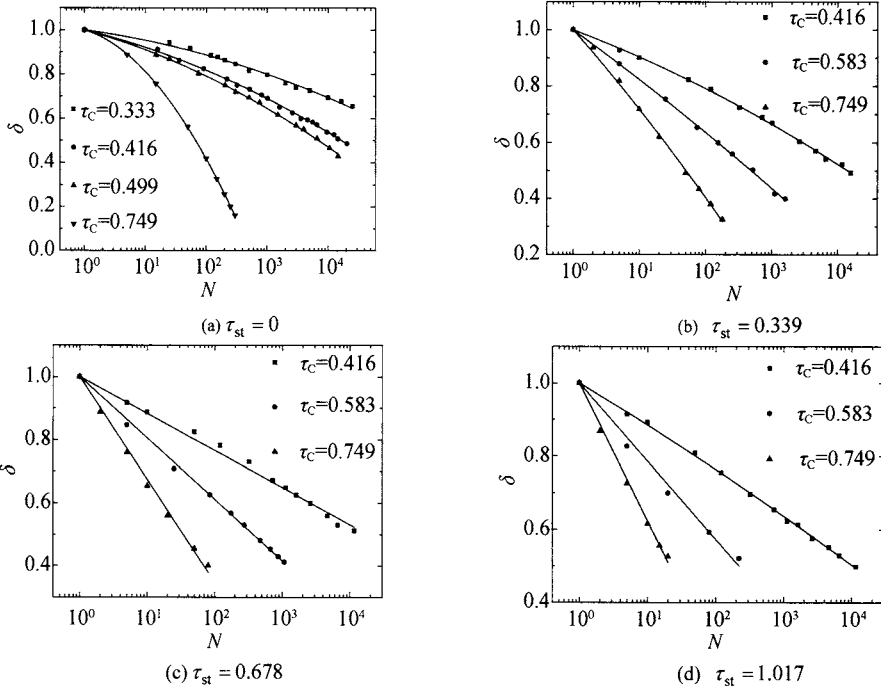


Figure 2. Relationship between degradation index and the number of cycles

Based on these experimental results shown in Figure 2, the following relationships for stiffness degradation in terms of number of cycles can be proposed:

$$\delta = \frac{G_N}{G_1} = 1 - \alpha \lg N - \beta (\lg N)^2 \quad (2)$$

The parameters α and β have a similar meaning to the degradation parameter originally proposed by Idriss et al.(1976,1978). By regression analysis, α and β are expressed as follows

$$\alpha = a_1 + a_2(\tau_c - \tau_t) \quad (3)$$

$$\beta = b_1 + b_2(\tau_c - \tau_t) + b_3(\tau_c - \tau_t)^2 \quad (4)$$

where a_1, a_2, b_1, b_2 and b_3 are curve-fitting constants, and τ_t is the threshold cyclic stress ratio(Vucetic, 1994).The test constants a_1, a_2, b_1, b_2 and b_3 for different initial shear stress

ratios are given in Table 1. The substitution of Eqs. (3) and (4) into Eq. (2) gives the cyclic degradation model:

$$\delta = 1 - [a_1 + a_2(\tau_c - \tau_i)] \lg N - [b_1 + b_2(\tau_c - \tau_i) + b_3(\tau_c - \tau_i)^2] (\lg N)^2 \quad (5)$$

Table 1. Constants for degradation and residual strain models

τ_{st}	a_1	a_2	b_1	b_2	b_3	c_1	c_2	c_3	d_1	d_2	d_3
0	0.021	0.022	0.039	0.168	0.190	0.044	0.218	0.147	0.979	3.408	3.372
0.339	0.056	0.229	0.012	0.045	0.043	0.209	0.742	0.523	1.597	5.310	5.611
0.678	0.113	0.368	0.005	0.036	0.050	0.474	1.636	1.038	1.265	3.846	4.326
1.017	0.128	0.426	0.012	0.027	0.005	0.229	0.713	0.019	0.355	0.301	0.575

MODELING RESIDUAL STRAIN ACCUMULATION

In Figure 3, the residual strain ε_p ($\varepsilon_p = (\varepsilon_{N,max} + \varepsilon_{N,min})/2$) for each loop is plotted against $\log N$. A number of empirical equations have been proposed to predict the permanent deformation of cohesive soil under repeated load. However, the most commonly used is the following power model proposed by Monismith et al. (1975):

$$\varepsilon_p = AN^b \quad (6)$$

where ε_p is the cumulative plastic strain, A and b are parameters depending on soil type, soil properties, and stress state.

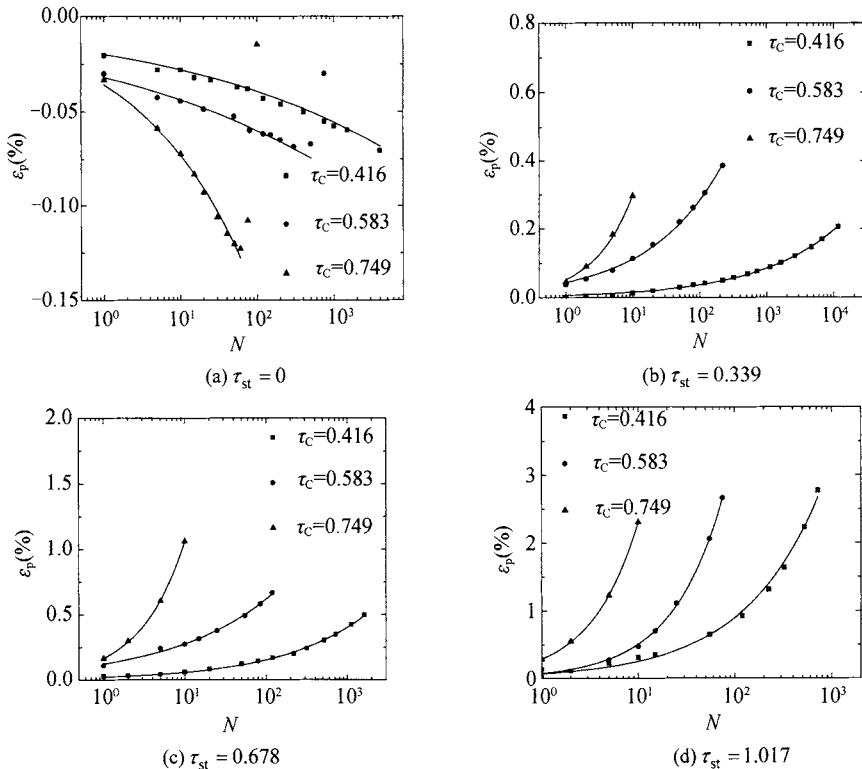


Figure 3. Relationship between residual strain and the number of cycles

To use Eq. (6) for estimating residual strain, parameters A and b needs to be quantified. By regression analysis the curves shown in Figure 3, a relationship between parameters A and b and cyclic stress ratio is respectively assumed to be:

$$A = c_1 + c_2(\tau_c - \tau_t) + c_3(\tau_c - \tau_t)^2 \quad (7)$$

$$b = d_1 + d_2(\tau_c - \tau_t) + d_3(\tau_c - \tau_t)^2 \quad (8)$$

where c_1, c_2, c_3, d_1, d_2 and d_3 are curve-fitting constants. Constants c_1, c_2, c_3, d_1, d_2 and d_3 for different initial shear stress ratios are given in Table 1.

The substitution of Eqs. (7) and (8) into Eq. (6) gives the cumulative residual strain model:

$$\varepsilon_p = [c_1 + c_2(\tau_c - \tau_t) + c_3(\tau_c - \tau_t)^2] N^{[d_1 + d_2(\tau_c - \tau_t) + d_3(\tau_c - \tau_t)^2]} \quad (9)$$

MODIFIED IWAN'S MODEL

An important feature of Iwan models is that the strains may be easily separated into elastic and plastic components, as required by incremental plasticity. The model consists of one spring with corresponding elastic coefficient E and series of sliding elements with the slip stresses (yield stresses) σ_i^* as indicated in Figure 4.

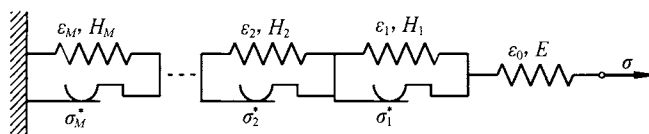


Figure 4. Iwan's series-parallel model

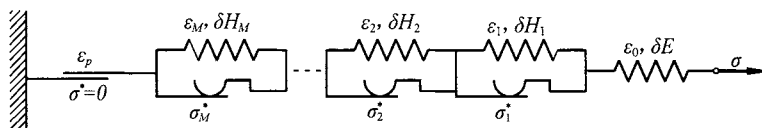


Figure 5. Modified Iwan's series-parallel model

The adoption of the Iwan model requires that the parameters of the model such as elastic coefficients E and H_i are made to degrade proportionally with the number of cycles. This is achieved by multiplying each of the elastic coefficients by the factor δ , to comply with the stiffness degradation of normally consolidated clays with the progression of loading cycles.

In addition, a pure plastic spring is also introduced into the Iwan's model to simulate the accumulation of residual strain as shown in Figure 5. The pure plastic spring is characterized as follows:

- (1) The yield stress σ_i^* is zero.
- (2) After yielding, the pure plastic spring gives plastic strain ε_p , which exhibits the cumulative residual strain of preceding cycling.

Then, the total strain can be expressed as follows:

$$\varepsilon = \varepsilon_p + \sum_{i=0}^m \varepsilon_i = \varepsilon_p + \sum_{i=0}^m \frac{\sigma - \sigma_i^*}{\delta H_i} \quad (10)$$

where, elastic coefficient E is written as H_0 . The substitution of Eqs. (5) and (9) into Eq. (10), the total strain can be obtained.

MODELING CYCLIC STRESS-STRAIN BEHAVIOR

The predicted results by the proposed model (Eq.(11)) are also compared with that of Rao's modified model in Figure 6 and Figure 7. Figure 6 gives the experimental and predicted stress-strain loops by different models for tests without initial shear stress at different number of cycles at cyclic stress ratios of 0.416. It can be observed that the proposed normalized stress-strain curve at number of cycle $N=1$ lies near the Rao's curve. However, at higher cyclic numbers, the proposed curves show better agreement than the corresponding Rao's curves.

In Figure 7, the predicted loops for tests with initial stress are also given. It shows that Rao's model fail to simulate the hysteresis loops favorably even at number of cycle $N=1$. However, the proposed curves can also agree with the experimental data better.

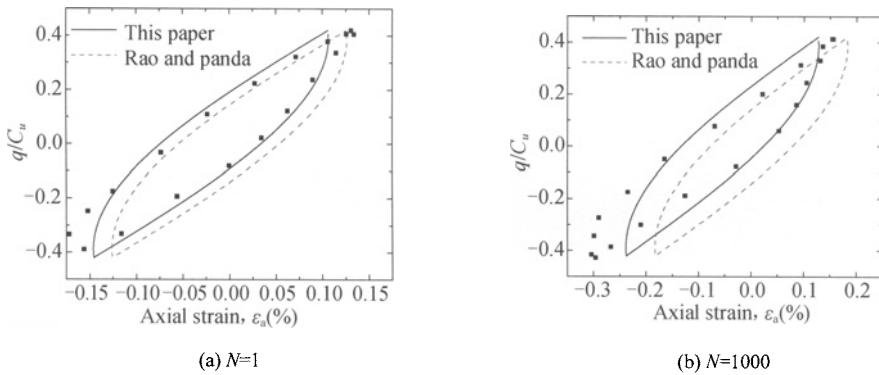


Figure 6. Comparison of recommended normalized stress-strain curves and curves by Rao and Panda, without initial shear stress

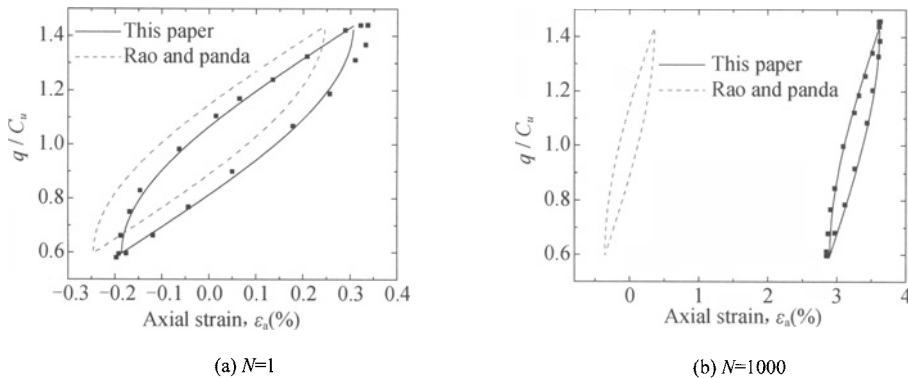


Figure 7. Comparison of recommended normalized stress-strain curves and curves by Rao and Panda, with initial shear stress

CONCLUSIONS

Degradation of soil properties in undrained cyclic loading is considered to be the main reason for deviation of the cyclic behavior of soft clays from the pattern described by the Iwan models. However, for the cyclic behavior of soft clay with initial shear stress which the Iwan models often fail to simulate, the accumulating residual strain is another important factor should be considered. The cyclic degradation and residual strain accumulating behavior are both studied by stress-controlled cyclic triaxial test. Based on the test results, empirical models for cyclic degradation and residual strain accumulating are proposed. Incorporation of degradation and residual strain models, the Iwan model can be extended to predict the undrained cyclic stress-strain behavior of soft clay with initial static shear stresses. The predicted results by proposed model are also compared with those of Rao's modified model. It may be concluded that for clay without initial shear stress, the proposed curve at number of cycle $N=1$ lies near Rao's curve. However, at higher cyclic numbers, the proposed curves show better agreement than the corresponding Rao's curves. For soft clay with initial stress, the proposed curves can agree with the experimental data well. However, Rao's model fail to simulate the hysteresis loops favourably even at number of cycle $N=1$.

REFERENCES

- Idriss I.M., Dobry R., Doyle E.H. and Singh R.D. (1976). Behavior of soft clays during earthquake loading conditions. *In Proceedings of the Offshore Technology Conference*, Houston, Texas, OTC 2671, Vol.3
- Idriss I.M., Dobry R. and Singh R.D. (1978). Nonlinear behaviour of soft clays during cyclicloading conditions. *Journal of the Geotechnical Engineering*, ASCE, 104: 1427-1447.
- Iwan W. D. (1967). On a class of models for the yielding behavior of continuous and composite systems. *J Appl Mech*, ASME, 34(3): 612-617.
- Monismith C. L., Ogawa N. and Freeme C. R. (1975). Permanent deformation characteristics of subgrade soils due to repeated loading. *Transp. Res. Rec.* No. 537, Transportation Research Board, Washington, D. C., 1-17
- Narasimha Rao S., Panda A. P. (1999). Non-linear analysis of undrained cyclic strength of soft marine clay. *Ocean engineering*, 26: 241-253.
- Puzrin A. M. and Shiran A. (2000). Effects of the constitutive relationship on seismic response of soils. Part I. Constitutive modeling of cyclic behavior of soils. *Soil Dynamics and Earthquake Engineering*, 19(5): 305-318
- Vucetic M. (1994). Cyclic threshold shear strain in soils. *Journal of Geotechnical Engineering*, ASCE, 120(12): 2208-2228.
- Yasuhara Y., Hyde A. F. L., Toyata N. and Murakami S. (1997). Cyclic stiffness of plastic silt with an initial drained shear stress. *Proc., Geotechnique Symp.* In print(SIP) on Prefailure Deformation Behavior of Geomaterials, R. J. Jardine et al., eds., London, 373-382

ANALYSIS AND EVALUATION OF GROUND VIBRATION RESPONSE INDUCED BY RAPID RAIL TRANSIT

Bin Chen

*Institute of Geotechnical Engineering, Nanjing University of Technology, 200N Zhongshan
Road, Nanjing, China*

*Shaoxing Quality Supervision and Management Station of Civil Defense Engineering,
Shaoxing, China*

Guoxing Chen, Xiaomei Su

*Institute of Geotechnical Engineering, Nanjing University of Technology, 200N Zhongshan
Road, Nanjing, China*

With the fast development of urban rapid rail transit, the environmental vibration problem induced by urban rapid rail transit has aroused broad attentions of the scholars and the society. Based on the ABAQUS finite-element software and track irregularity theory to simulate the train vibration load, the nonlinear dynamic visco-elasto-plastic constitutive model which is based on Davidenkov model is used to describe the dynamic character of the soils. The characters of ground vibration induced by rapid rail transit are analyzed by taking Nanjing representative sites as research object. Ground surface vibration responses with different sites and different train speeds are also obtained. Ground surface acceleration vibration level is used to describe the intensity of ground surface vibration. The intensity of ground surface vibration is evaluated and analyzed to give basic information to the further research and control of ground surface vibration induced by rapid rail transit.

INTRODUCTION

With the fast development of modern transportation technologies, the rail transits, such as intercity passenger train, urban light train and subway, connect big cities and have many advantages like large transport ability, high speed, low energy cost, little pollution and less land. The Chinese 6th railway speedup has been outspreaded in the main railway network from April 2007. The train speed has reached 200 km/h, and some railway sections like Beijing to Harbin, Beijing to Guangzhou, Beijing to Shanghai have reached 250 km/h. The high-speed railway, such as Beijing to Shanghai, Beijing to Wuhan, Guangzhou to Zhuhai and Shanghai to Nanjing have been layout, and this is the symbol that China has come into the “High-speed rail transit” age.

However, the urban rapid rail transit course will inevitably through or draw near the residential area or industrial park that are sensitive to the vibration. The effect on the daily life of the nearby residents, buildings, underground pipes, precision apparatus and equipments induced by ground vibration and strong noise can not be neglected. Thereby, the ground vibration induced by rapid rail transit must be analyzed and researched. For example,

Taiwan high speed railway passes through south-Taiwan high-tech zone, which is very sensitive to the foundation vibration. The vibration influence of the high speed railway to the high-tech zone has aroused increasing attention and research.

FEM MODEL OF GROUND VIBRATION

MS-Word simulation of rail transit load based on track irregularity theory

Track irregularity is the main cause of the vehicle-track system vibration. The mass theory research and experiment work of Great Britain railway technology center indicates track irregularity is the main cause of the contacting forces between railway wheels and tracks. The vertical contacting forces include three frequency spectra: low frequency part: 0.5~10Hz; middle frequency part: 30~60Hz; and high frequency part: 100~400Hz. The contacting forces between railway wheels and tracks are mainly low and middle frequency part, but the high frequency part is mainly to effect the vehicle dynamic response. The main effect factors of the forces between railway wheels and tracks are track irregularity and track surface wave shape wasting effect.

Japanese track irregularity maintaining and managing standard is as follows: comfort index standard is 7mm/10m, safety target value is 10mm/10m. Table 1 shows the Great Britain geometry track irregularity maintaining and managing standard for 200km/h rail transit.

Table 1. Management values of railway geometric irregular condition (GB)

Control condition	Wave length(m)	vector height (mm)
According to traveling placidity(I)	50	16
	20	9
	10	5
	5	2.5
According to the dynamic added load to the track (II)	2	0.6
	1	0.3
	0.5	0.1
Wave shape waste (III)	0.05	0.05

Thus, the vibration force function can be used to simulate the random vibrating train load, which contains the dead load part and the dynamic load part which is formed by a series of sine functions. The experiment, based on track irregularity theory, uses the vibration force function to simulate the contacting forces between railway wheels and tracks, namely rail transit load, with the expression

$$F(t) = P_0 + P_1 \sin \omega_1 t + P_2 \sin \omega_2 t + P_3 \sin \omega_3 t \quad (1)$$

where P_0 represents wheel dead load; P_1 , P_2 , P_3 represent a certain representative value of the vibration load within the control standard I, II, III in the Table 1.

Defining the train quality below the spring as M_0 , thus accompanying vibration load amplitude is

$$P_i = M_0 a_i \omega^2 \quad (2)$$

where a_i represents a certain representative vector height within the control standard I, II, III in the Table 1; ω_i represents the circular frequency of the irregularity vibration wave length within the control standard I, II, III.

The circular frequency is given by

$$\omega = 2\pi \frac{v}{L_i} \quad (3)$$

where v represents the train speed, L_i represents the representative wave length within the control standard I, II, III.

Seven different train speeds (50km/h, 80km/h, 150km/h, 200km/h, 250km/h, 300km/h and 350km/h) are chosen in the experiment. According to the request of rapid rail transit, choose single side dead wheel load $P_0=80\text{kN}$, the quality below the spring $M_0=750\text{kg}$, higher standard are chosen based on the control standard I, II, III in the table 1.

$$L_1=10\text{m}, \quad a_1=3.5\text{mm};$$

$$L_2=2\text{m}, \quad a_2=0.4\text{mm};$$

$$L_3=0.5\text{m}, \quad a_3=0.08\text{mm};$$

Based on the function (1), (2), (3), the curve of track vibration force F_t in the first 0.5s with the train speed 300km/h is as Figure 1.

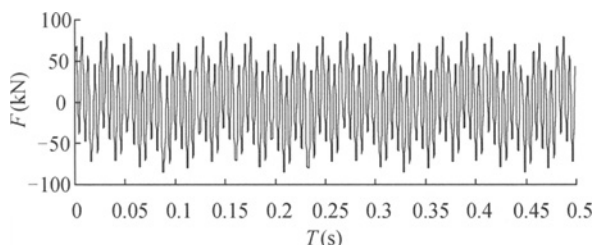


Figure 1. The curve of rail excitation load (first 0.5s)

Calculating model and the parameter choice

The incidence of the ground vibration induced by urban rapid rail transit in the vertical direction to the railway is commonly within 40m, the influence depth of the foundation soil is within 5m. Therefore, calculating model size as 200m×30m is chosen, and half of the structure is modeled according to the symmetry, as shown in Figure 2.

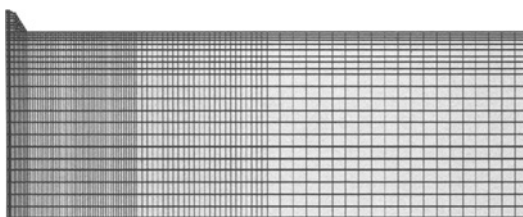


Figure 2. FEM analysis model of the ground vibration due to rapid rail transit (200m×30m)

Partial data of Qinghuangdao-Shenyang passenger train and Pioneer style train are used, single side dead wheel load $P_0=80\text{kN}$ is chosen, the length of the sleeper is 2.6m, the height is 0.20m, the linear elastic model is used; the thickness of the ballast is 0.35m, the thickness of the embankment is 3m, both the ballast and embankment use Mohr-Coulomb elasto-plastic model, as shown in Table 2.

Table 2. The parameters of sleeper, ballast and embankment

Material	ρ (kN/m ³)	E (MPa)	ν	V_s (m/s)	C (MPa)	φ (°)	G (MPa)
sleeper	25	30000	0.16	-	-	-	-
ballast	25	200	0.30	-	200	40	-
embankment	20.2	-	0.42	310	-	-	190

The foundation soil is numerically simulated with the background of three representative sites in Nanjing city. The soil dynamic visco-elasto-plastic constitutive model based on Davidenkov model is used to simulate the dynamic characters of the soils, as shown in Table 3.

In order to simulate the boundary condition, the field surface is chosen as free boundary; the field side is chosen as $\Delta x = 0$; as the influence depth of the train load is less than 5m, the field bottom boundary is chosen as full constraint.

Table 3. Fitting parameters A , B , γ_0 of the Nanjing city site

Stratum	$\gamma_0 (\times 10^{-4})$	A	B
plain fill (flow-plastic)	3	1.09	0.36
silt clay (soft-plastic to plastic)	3.2	1.09	0.37
silt clay (plastic to stiff-plastic)	3.4	1.09	0.38
silt clay (plastic)	3.7	1.09	0.38
silt clay (flow-plastic)	2.6	1.02	0.35
silty sand contain with fine sand (loose)	1.5	1.05	0.35
silty sand contain with fine sand (intermediated dense – dense)	4	1.08	0.35
silty fine sand (intermediated dense)	3.5	1.1	0.35
silty fine sand(dense to intermediated dense)	2.7	1.1	0.35

Three representative sites in Nanjing city are chosen to investigate the ground vibration induced by rail transit. Site No.1 is the geological represent from Xingjiekou station to Xuanwumen station, which is formed with soft-plastic to plastic and silt clay, as shown in Table 4.

Table 4. The soil parameters of the No.1 site in Nanjing city

No.	Stratum	Thick-ness (m)	ν	ρ (kN/m ³)	V_s (m/s)	φ (°)
1	surface is plain fill, under layer is silt clay	2.7	0.35	19.9	171	26
2	silt clay, brown gray-lark, soft-plastic to plastic	2.5	0.35	19.5	192	22.2
3	silt clay, lark-brown gray, soft-plastic-plastic	3.3	0.35	19.9	236	20
4	silt clay, green gray-brown yellow, plastic to stiff-plastic	3.5	0.35	19.3	235	15.8
5	silt clay, brown yellow-lark, contain with silt, silty fine sand	4	0.32	18.8	197	21
6	silt clay、brown gray-gray, part mucky silty clay	6.5	0.38	18.2	191	21
7	silt clay、brown yellow-gray, contain silty fine sand, soft-plastic to plastic	3.5	0.40	19.9	219	19.4
8	silt clay, lark-gray, plastic	4	0.40	20	240	20.7

Site No.2 is the geological represent from Xufuxiang station to Nanjing Railway station, which is formed with intermediated dense silty fine sand、silty sand contain with fine sand and soft-plastic silt clay. Site No.3 is the geological represent from Nanjing Railway station to Sanshan street station, which is formed with soft-plastic silt clay, flow-plastic mucky silty clay and loose silty sand contain with fine sand.

CALCULATING RESULTS AND ANALYSIS

The time-history curve of ground vibration

Based on the ABAQUS software, the time-history curve of ground vibration acceleration induced by different speed trains with different distances to the rail center line is obtained, as shown in Figures 3 and 4 is the contour of ground vibration acceleration by 300km/h rail transit.

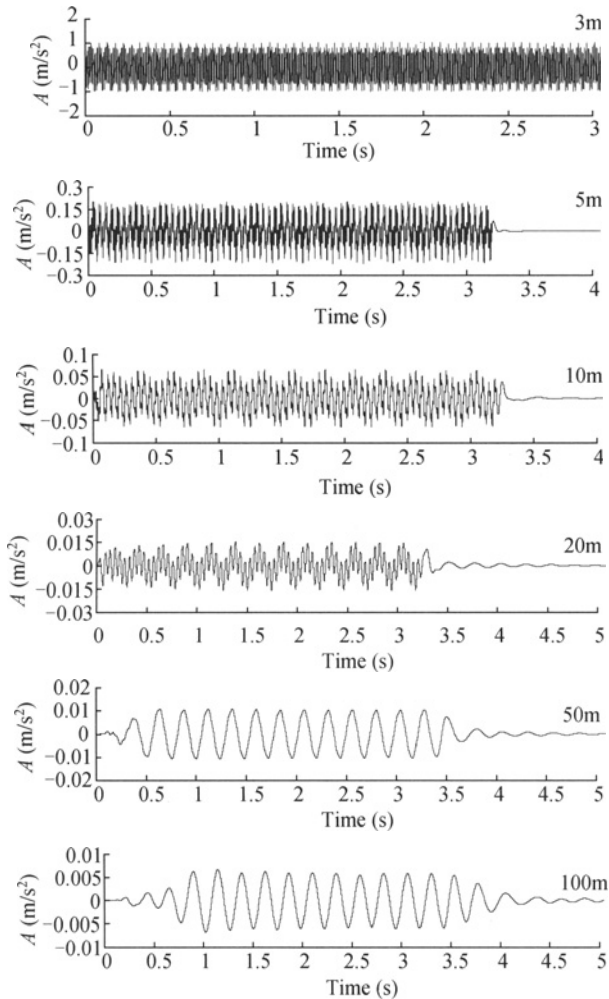


Figure 3. The time-history curve of ground surface vibration acceleration with 150km/h speed train

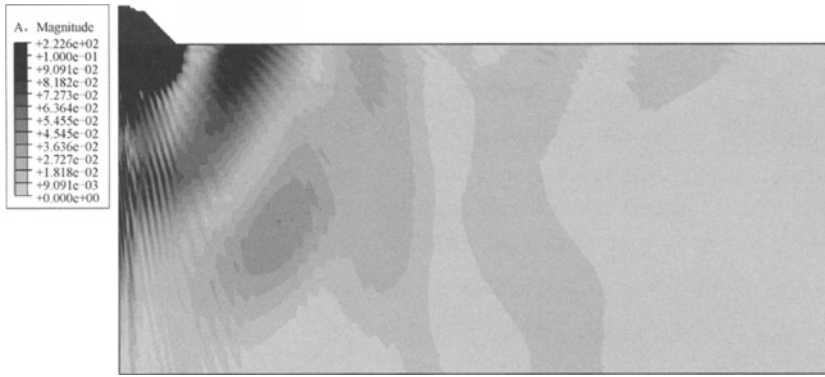


Figure 4. The contour of ground vibration acceleration due to 300km/h rail transit

Analysis of the ground surface vibration acceleration

The intensity of ground surface vibration acceleration

As the time effect of train load is not long, about 3-5s, so 3.2s is chosen as the time effect. Table 5 is the peak value of the ground surface vibration acceleration with different train speeds at different distances to the rail.

Table 5. Peak values of ground surface vibration acceleration with different train speeds

Speed(m/s ²) <i>D</i>	50	80	150	200	250	300	350
3	0.088	0.314	1.057	2.108	3.630	5.831	8.594
5	0.038	0.086	0.219	0.323	0.422	0.528	0.597
10	0.014	0.025	0.066	0.076	0.087	0.137	0.181
20	0.0041	0.010	0.016	0.019	0.031	0.048	0.061
50	0.0018	0.0025	0.011	0.015	0.016	0.018	0.023
100	0.0008	0.001	0.006	0.006	0.006	0.009	0.009

The moving transit induces strong motion near the rail, when the train speed is 350km/h, the peak value of vibration acceleration at 3m to the rail achieves 8.59m/s^2 , and this vibration will produce strong effect to surrounding buildings. The peak value of vibration acceleration at 10m to the rail achieves 0.18m/s^2 , and it will also produce strong effect to nearby residents. It is evidently unbecoming to set up the buildings which are strict to the environmental vibration.

The character of the ground surface vibration acceleration time-history

The shape and the changing direction of the time-history curve of ground surface vibration acceleration are basic identical as the train speed changes from 150km/h to 350km/h.

The period of the curve of ground surface vibration acceleration is short at 3m to the rail, but at 10m, the vibration period is evidently longer, the vibration assumes periodic rule. At 100m to the rail, the curve assumes sine wave shape, as shown in Figure 3. The vibration period achieves at 0.2s.

The effect of the train speed to the peak value of ground vibration acceleration

Train speed is the main effect factor to the ground vibration. Based on track irregularity theory, both the train load and ground vibration increase as the train speed increases.

The peak value of vibration acceleration at 3m to the rail is 0.088m/s^2 when the train speed is 50km/h , but when the train speed is 350km/h , the peak value achieves at 8.594m/s^2 , which is 97 times than that the train speed is 50km/h . Thus, the train speed has strong effect on the ground vibration intensity, it is the main effect factor on the ground vibration.

The attenuation rule of the ground vibration acceleration

The ground vibration induced by rail transit spreads in the form of three kinds of waves, which are P wave, S wave and surface wave (Rayleigh wave and Love wave). As the soil damp absorbs the vibration energy, the intensity of the vibration reduces as the distance increases, as shown in Figure 5.

The ground vibration acceleration attenuates obviously within 10m to the rail. When the train speed is at 350km/h , the peak value achieves 8.594m/s^2 , but this value attenuates to 0.181m/s^2 rapidly at 10m to the rail. At 100m to the rail, the value is 0.00914m/s^2 , at this time, the vibration can be ignored.

As shown in Figure 4 and Figure 5, the ground surface vibration rebounds at a certain distance to the rail, this phenomena is consistent with other studies, but the rebound area has some difference. The position of this area is related to the embankment size, the depth of the rock and the character of the site.

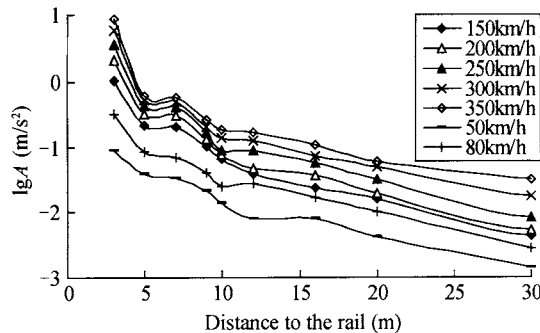


Figure 5. The attenuation curve of ground surface vibration peak acceleration

THE EVALUATION OF GROUND VIBRATION INTENSITY

The standard and calculating method of city area environmental vibration of China

ISO, USA, Japan, Germany, Great Britain and Canada all have founded the Standard and calculating method of city area environmental vibration.

In order to control the impaction of the environmental vibration to the surrounding buildings, China also has set up *The standard and calculating method of city area environmental vibration* (GB10070-88) to prescribe the degree of Z direction vibration (L_a) of all kinds of city area, as shown in Table 6.

Table 6. The control standard of city area environmental vibration
(Degree of Z direction vibration L_a : dB)

Belt area	daytime	night
Special uptown	65	65
Uptown, culture and education area	70	67
Mix area, emporia area	75	72
Industry area	75	75
Along the traffic line	75	75
Along the railway	80	80

Ground surface vibration acceleration degree L_a is used to denote the intensity of environmental vibration, it is the comparative value of acceleration virtual value \bar{a} with benchmark acceleration ($a_0 = 10^{-5} \text{ m/s}^2$), with the expression

$$L_a = 20 \log_{10} \frac{\bar{a}}{a_0} \quad (4)$$

where \bar{a} (m/s^2) can be gained with the expression

$$\bar{a} = \sqrt{a^2(t)} = \sqrt{\frac{\int_0^T a^2(t) dt}{T}} \quad (5)$$

where $a(t)$ represents field tested (or numerical simulated) acceleration time history (m/s^2); T represents the action time of acceleration (s).

The evaluation of ground vibration intensity induced by rapid rail transit on Nanjing representative site

In the coming 40 years, plenty of rapid rail transit and across-river tunnel will be built in Nanjing. Thus, it is necessary to estimate the ground vibration induced by rapid rail transit on Nanjing representative site. According to Chinese national standard *The standard and calculating method of city area environmental vibration* (GB10070-88), the ground surface vibration acceleration degree L_a should not be larger than 80 dB within 30m to the railway.

The grade of ground surface acceleration vibration induced by different speed trains on the No.1 site in Nanjing city is shown Table 7.

Table 7. The grade of ground surface acceleration vibration induced by different speed trains on the No.1 site in Nanjing city (dB)

distance (m)	150km/h		200km/h		250km/h		300km/h		350km/h	
	virtual value	L_a	virtual value	L_a	virtual value	L_a	virtual value	L_a	virtual value	L_a
3	0.591	95.42	1.162	101.3	2.043	106.2	3.240	110.2	4.677	113.4
5	0.100	80.02	0.144	83.18	0.183	85.26	0.209	86.40	0.244	87.76
10	0.031	69.77	0.030	69.45	0.041	72.22	0.065	76.31	0.094	79.43
20	0.0076	57.68	0.010	60.07	0.0178	64.97	0.0285	69.08	0.0396	71.97
50	0.0069	56.76	0.0069	56.76	0.0064	56.12	0.0062	55.87	0.0078	57.82
100	0.0037	51.53	0.0037	51.53	0.0035	48.12	0.0041	52.19	0.0038	51.63

As shown in Table 7, the grade of ground surface acceleration vibration is less than the control standard 80dB with the distance larger than 10m, but in Nanjing, as the rail transit

cross the whole city, many buildings were built within 10m to the rail, some of these are even within 3m to the rail. These buildings are located at residential, cultural and educational areas or mixed areas as shown in Table 7, where the control standard are 70dB(daytime), 67dB(night) and 75dB(daytime), 72dB(night). But at 3m to the rail, the vibration level is larger than 95dB when the train speed is 150km/h. When the train speed is 350km/h, the vibration level even reaches 113dB. At 20m to the rail, the vibration level reaches 71dB when the train speed is 350km/h, which is also beyond the control standard. The vibration level attenuates rapidly as the distance to the rail increases. When the train speed is low, the vibration level is about 50~60dB in the area which is over 20m to the rail, it is receivable for the residents nearby.

Therefore, it is necessary to take effective measures to control and decrease the effect of the ground vibration within 10-20m to the rail.

The effect of site condition to the ground surface vibration acceleration

Site condition is one of the important effects to the ground vibration. Figure 6 is the curves of the degree of ground acceleration vibration induced by different speed trains on different Nanjing sites. At 3m to the rail, the vibration level is 95.42dB, 106.21dB and 113.40dB when the train speed is 150km/h, 250 km/h and 350 km/h respectively. The vibration level increases rapidly as the train speed increases. As shown in Figure 6, the same situation happened in Site 2 and Site 3, the strong vibration area is within 20m to the rail.

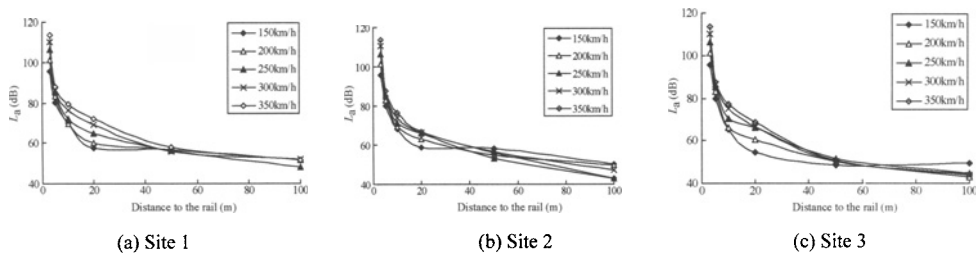


Figure 6. The curves of the degree of ground acceleration vibration induced by different speed trains on different sites

RESULTS

Based on the ABAQUS software, the finite-element model of rapid rail transit induced ground vibration is built and the ground vibration response is numerically simulated with the background of three representative sites in Nanjing city. The soil dynamic visco-elasto-plastic constitutive model based on the Davidenkov model is used to simulate the dynamic characters of the soils. The main results are as follows:

The rapid rail transit induces strong ground vibration, which will bring strong effect on the nearby buildings. The period of the curve of ground surface vibration acceleration increases as the distance to the rail increases.

The ground vibration increases as the train speed increases. The breadth of the vibration acceleration attenuates rapidly as the distance to the railway increases.

The vibration rebound takes place at same distance, but the position of this area is related to the embankment size, the depth of the rock and the character of the site.

Strong ground vibration is induced by moving rail transit within the 20m region from the rail. It is suggested that do not build any style or functional buildings in this area otherwise the effective vibration reduction and isolation measures should be considered.

REFERENCES

- Chen Guoxin, Zhuang Haiyang. (2005). Developed nonlinear dynamic constitutive relations of soils based on Davidenkov skeleton curve. *Chinese Journal of Geotechnical Engineering*, 27(8): 860-864
- Ha11, Lars. (2003). Simulations and analyses of train-induced ground vibrations in finite element models. *Soil Dynamics and Earthquake Engineering*, 23(5): 403-413.
- Jenkins H, et al. (1974). The Effect of Track and Vehicle Parameters on Wheel/Rail Vertical Dynamic Forces. *Railway Engineering*, 3(1).
- Liang Bo, Caiying. (1999). Dynamic analysis on subgrade of high speed railways in geometric irregular condition. *Journal of the China Railway Society* , 21(1): 84-88.
- Pan Changshi, G. N. (1984). Pande. Preliminary deterministic finite element study on a tunnel driven in loess subjected to train loading. *China Civil Engineering Journal*, 17(4): 54-55.
- Xia He, Zhang Nan and Cao Yanmei. (2004). Experimental Study of Train-induced Vibrations of Ground and Nearby Building. *Journal of the China Railway Society*, 24(6): 93-98.
- Yan Weiming, Nie Han, Ren Ming, et al. (2006). In situ experiment and analysis of ground surface vibration induced by urban subway transit. *Journal of Railway Science and Engineering*, 3(2): 1-5.
- Yang Y. B. (2003). Ground vibration induced by high-speed trains over viaducts. *Proc ISEV*. Hangzhou: Zhejiang University, 147-157.

DYNAMIC SHEAR MODULUS AND DAMPING RATIO OF RECENTLY DEPOSITED SOILS IN THE COASTAL REGION OF JIANGSU PROVINCE

Guoxing Chen

*Institute of Geotechnical Engineering, Nanjing University of Technology,
Nanjing 210009, China*

Binghui Wang, Jianda Liu

*Institute of Geotechnical Engineering, Nanjing University of Technology,
Nanjing 210009, China*

Jiangsu Province Institute of Earthquake Engineering, Nanjing 210014, China

Many important engineering projects such as digital strong-motion observation stations, ports or wharfs, wind power stations have been constructed because of the unique locations and rapid development of economy in the coastal region of Jiangsu province. And the dynamic shear modulus and damping ratio of soil are indispensable basic data for the seismic design on important engineering projects. For the construction of these important engineering projects, the free vibration column tests of 134 undisturbed soil samples were conducted which took about 3 years and the free vibration column test system developed by Nanjing University of Technology was used. Those undisturbed soil samples are 5 type soils of muddy soils, clay, silt clay, silt and fine sand. Due to the transgressions after the late Pleistocene Epoch, the marine deposited soils have existed in the coastal region of Jiangsu province extensively. Therefore, 3 type marine deposited soils of silt clay, silt and fine sand were also screened. The results show that it is suitable to use the Martin-Davidenkov model and the damping ratio empirical formula recommended by Chen Guoxing et al to fit the results of the normalized dynamic shear modulus ratio $G/G_{\max} - \gamma$ and damping ratio $\lambda - \gamma$ curves respectively. By comparing marine deposited soils with continental deposited soils, the following results can be found. For silt clay, the dynamic shear modulus ratios and damping ratios are very close to each other. And for silt and fine sand, however, the dynamic shear modulus ratios and damping ratios have obvious differences.

INTRODUCTION

The dynamic shear modulus and damping ratio are important parameters of dynamic characteristics of soils and they are indispensable basic data for the seismic response analysis of important project sites. The coastal region of Jiangsu province mentioned in this paper is stand for 3 cities, namely Nantong city, Yancheng city and Lianyungang city, where exist the marine deposited stratum. The Chinese researchers generally considered that there are 3 times transgressions after late Pleistocene Epoch, and the marine deposited stratum which

deposited in Holocene Epoch is the thickest. Based on the research of Wang qiang et al, the whole thickness of marine soil stratum approach 80m in the southern Dongtai city area, and gradually reduce in the northern Dongtai city area, as shown in Figure 1. It is impossible to classify all soil samples into marine deposited or continental deposited in that the information of the distribution of marine soil stratum in the coastal region of Jiangsu province is insufficient. However, some of marine deposited soil samples are screened by observing the remains of marine animals and by comparing the depth from which samples were taken with the distribution information of marine deposited soil stratum and the location of the drill holes as shown in Figure 1. With these relevant materials, the samples which the overburden depth is lower than 80m in these areas are marine deposited soil samples. However, the marine deposited soils have the different physical and mechanical properties. For example, the marine deposited soft soils in Lianyungang city have high compactibility, high thixotropy, high creep and low water permeability etc.

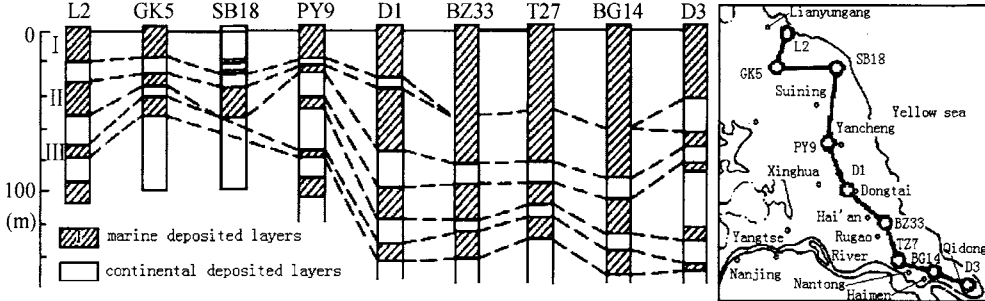


Figure 1. The marine deposited layers in the coastal region of Jiangsu province

For the further works of protecting against and mitigating earthquake disasters, the digital strong-motion observation stations are being built and spread over the province. ‘Jiangsu digital strong-motion observation network’ is an important part of ‘China digital strong-motion observation network’. For the construction of digital strong-motion observation stations in the coastal region of Jiangsu province, it is necessary to conduct experimental study on the dynamic modulus and damping ratios of recently deposited soils in the region which will obtain the propagation properties of earthquake waves and the spatial distribution of ground motion field.

The study of the dynamic modulus and damping ratios will benefit to the estimating work of important projects in the coastal region of Jiangsu province and it will get the reference data for seismic design of important projects. The coastal region of Jiangsu province is rich in port and sea wind resources. The port resource is the best and core strategic resource of the economy and development in the region. The coastal region of Jiangsu province has been taken for as an example base of wind power generation in China. As we know, the sea wind power is a green resource and the wind power generation will be a new and important industry along the coastal region of Jiangsu province. However, the ground of ports or wharfs and wind power station requires high resistance of seismic (or shake). With the development of the economy in the region, the important projects, which require seismic design, will be built.

For reasons mentioned above, the study on the dynamic shear modulus and damping ratios were carried out. It took about 3 years and used 134 undisturbed recently deposited soil samples taken from different places of a few project types. They are mainly digital strong-motion observation stations, power stations, ports or wharfs, as shown in Table 1 which also show the classification of samples by the engineering properties and deposited environment.

Table 1. statistical chart table of the classification of soils

By the background projects			By the deposited environment and engineering properties			
Types of projects	Number of samples	Notes	Marine or continental deposited	Number of samples	Marine deposited	Number of samples
Digital strong-motion observation stations	52	From 17 cities or towns	Muddy soils	10	Silt clay	11
Wind power stations	32	From 8 towns	Clay	19	Silt	6
Other kind of power stations	21		Silt clay	37	Fine sand	17
Ports or wharfs	14		Silt	29		
Other projects	15		Fine sand	39		

Test equipment and testing method

The GZZ-1 free vibration testing system developed by Nanjing University of Technology was employed in this experiment research, the operation manual can be seen in the reference. This system can investigate the dynamic characteristics of soils in the strain amplitude range of 10^{-6} - 10^{-4} and the method of soils column free vibration was applied to determine the dynamic shear modulus and damping ratios.

The testing samples are 3.91cm in diameter and 8.00cm in height. The confining pressures applied on the samples are effective mean consolidated pressures, identified by following equation. $\sigma'_m = (\sigma'_v + 2\sigma'_h)/3$. In which σ'_v is effective overburden pressure, σ'_h is effective lateral pressures. The tests started after consolidated for 8-12h. The dynamic shear modulus and damping ratios were calculated on the basis of the attenuation curves of free torsion shear vibration of the samples measured in the tests.

TESTING RESULTS AND ANALYSIS

All of the dynamic shear modulus of each undisturbed soil were standardization by the maximum dynamic shear modulus, and then the data points of dynamic shear modulus ratios visa shear strain amplitudes were collected and reorganized with all soil types mentioned above.

Figure 2-Figure 6 are the results of the relationships of dynamic shear modulus ratios G/G_{max} and damping ratios λ with the shear strain amplitudes γ_a increasing for all types of soils mentioned above. The equation (1) of Martin-Davidenkov model was used to fit the data points of $G/G_{max} - \gamma_a$, and the empirical formula (2) recommended by Chen Guoxing et al was also used to fit the data points of $\lambda - \gamma_a$.

$$\frac{G}{G_{\max}} = 1 - \left[\frac{(\gamma/\gamma_0)^{2B}}{1 + (\gamma/\gamma_0)^{2B}} \right]^A \quad (1)$$

$$\lambda = \lambda_{\min} + \lambda_0(1 - G/G_{\max})^n \quad (2)$$

In which, A 、 B 、 γ_0 、 λ_{\min} 、 λ_0 、 n are regression coefficient obtained by the least-square method. The reference values of regression coefficients are given in Table 2.

Table 2. Fitting parameters of $G/G_{\max} - \gamma_a$ and $\lambda - \gamma_a$ curves for recently deposited soils in the Coastal region of Jiangsu Province.

Regression coefficients		A	B	γ_0	λ_{\min}	λ_0	n
Types of soils							
Marine or continental deposited	Muddy soils	1.15	0.68	5.95	1.77	20.41	1.45
	Clay	1.19	0.72	5.96	2.01	19.95	1.19
	Silt clay	1.05	0.83	4.31	1.92	18.58	1.17
	Silt	1.15	0.81	3.68	1.76	15.36	1.14
	Fine sand	1.31	0.71	3.75	1.02	15.55	1.08
Marine deposited	Silt clay	1.22	0.80	3.22	1.40	19.50	1.11
	Silt	1.00	1.00	3.72	1.76	18.56	1.10
	Fine sand	0.86	1.00	4.99	0.86	17.16	1.05

The test results of marine or continental deposited soils are plotted in Figure 2-Figure 6 and the test results of marine deposited soils are also plotted in Figure 4-Figure 6 in order to conveniently compare the properties of soils with different deposited environment.

In the test, all undisturbed samples were separated into continental deposited soils and marine deposited soils. Comparing the differences of dynamic shear modulus ratios and damping ratios between marine deposited soils and marine or continental deposited soils in Figure 4-Figure 6, it can be found that the dynamic shear modulus ratios and damping ratios of marine deposited silt clays are almost no difference with continental deposited silt clays. But the dynamic shear modulus ratios of marine deposited silt and fine sand are obviously smaller than those of continental deposited silt and fine sand, and the damping ratios of marine deposited silt and fine sand are obviously larger than those of continental deposited silt and fine sand. Those differences are more obvious in the vicinity of shear strain amplitude $\gamma_a = 1.0 \times 10^{-3}$. Two facts should be noticed here. First, those differences of dynamic characteristics between marine deposited soils and continental deposited soils are statistically general differences for a large number of tests. For single marine deposited soils, the differences of dynamic characteristics may not appear. Secondly, due to the equipment limitation in measurement, the dynamic shear modulus and damping ratios can not be measured when the shear strain exceeds the range of 1.0×10^{-3} , and the credibility of the test results will be reduced in the range of $1.0 \times 10^{-4} < \gamma_a < 1.0 \times 10^{-3}$. The significant differences between the dynamic shear modulus ratios and damping ratios in vicinity of $\gamma_a = 1.0 \times 10^{-3}$ as shown in Figure 5 and Figure 6 are still a question which needs further investigation.

Table 3 shows the reference values of the dynamic shear modulus ratios and damping ratios of all types of soils mentioned above in the coastal region of Jiangsu province. So it will be convenient to use SHAKE91 or other similar program to carry out the seismic response analysis.

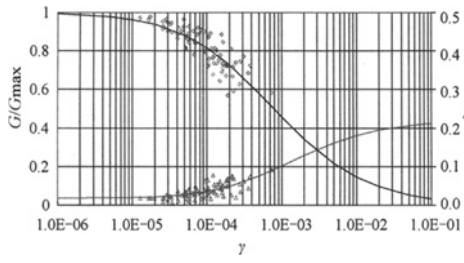


Figure 2. $G/G_{\max} - \gamma_a$ and $\lambda - \gamma_a$ curves for muddy soils

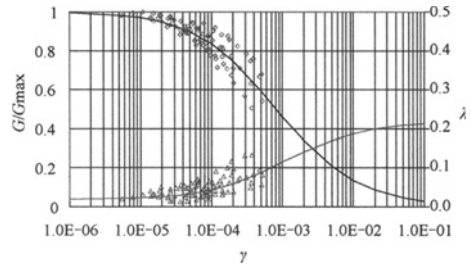


Figure 3. $G/G_{\max} - \gamma_a$ and $\lambda - \gamma_a$ curves for clays

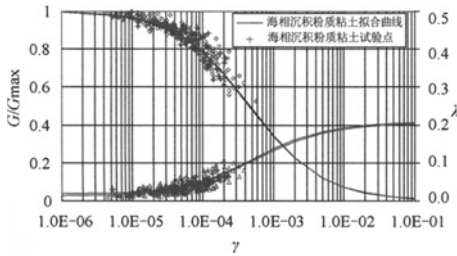


Figure 4. $G/G_{\max} - \gamma_a$ and $\lambda - \gamma_a$ curves for silt clay

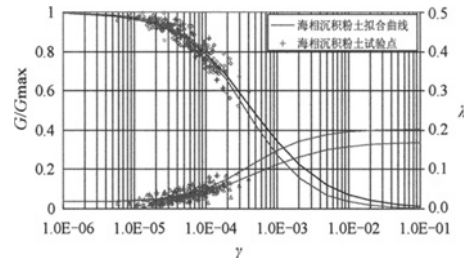


Figure 5. $G/G_{\max} - \gamma_a$ and $\lambda - \gamma_a$ curves for silt

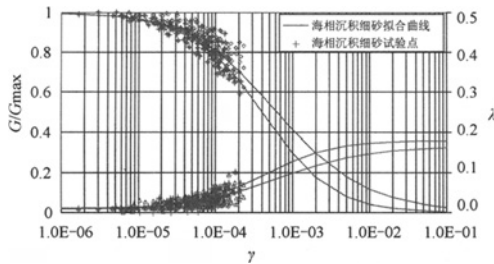


Figure 6. $G/G_{\max} - \gamma_a$ and $\lambda - \gamma_a$ curves for fine sand

Table 3. Recommended values and standard deviation of $G/G_{\max} - \gamma_a$ and $\lambda - \gamma_a$ curves on recently deposited soils for the coastal region of Jiangsu province

Types of soils	parameters	Shear strain amplitudes γ_a						
		1×10^{-6}	5×10^{-6}	1×10^{-5}	5×10^{-5}	1×10^{-4}	5×10^{-4}	1×10^{-3}
Muddy soils	G/G_{\max}	0.993	0.978	0.962	0.882	0.817	0.580	0.457
	λ	1.79	1.85	1.95	2.69	3.51	7.58	10.19
Clay	G/G_{\max}	0.996	0.983	0.971	0.899	0.836	0.593	0.463
	λ	2.03	2.15	2.30	3.31	4.32	8.85	11.52
Silt clay	G/G_{\max}	0.995	0.980	0.964	0.870	0.787	0.485	0.345
	λ	1.96	2.12	2.31	3.65	4.99	10.49	13.26
Silt	G/G_{\max}	0.996	0.983	0.967	0.874	0.789	0.483	0.343
	λ	1.79	1.91	2.07	3.20	4.35	8.98	11.26

continued

Types of soils	parameters	Shear strain amplitudes γ_a						
		1×10^{-6}	5×10^{-6}	1×10^{-5}	5×10^{-5}	1×10^{-4}	5×10^{-4}	1×10^{-3}
Fine sand	G/G_{\max}	0.996	0.983	0.969	0.884	0.810	0.542	0.412
	λ	1.06	1.21	1.39	2.55	3.61	7.71	9.79
Marine deposited silt clay	G/G_{\max}	0.996	0.983	0.968	0.873	0.786	0.478	0.340
	λ	1.44	1.61	1.82	3.38	4.92	10.87	13.70
Marine deposited silt	G/G_{\max}	0.997	0.987	0.974	0.881	0.788	0.426	0.271
	λ	1.79	1.92	2.10	3.53	5.12	11.82	14.86
Marine deposited fine sand	G/G_{\max}	0.995	0.981	0.966	0.873	0.786	0.449	0.295
	λ	0.92	1.12	1.35	2.82	4.25	10.02	12.75

CONCLUSION

For the important projects of Jiangsu digital strong-motion observation stations, ports or wharfs, power stations etc, the dynamic shear modulus ratios and damping ratios of recently deposited soils in the coastal region of Jiangsu province were studied. And the soils are divided into 5 types of marine or continental deposited soils and marine deposited soils. It is suitable to use the Martin-Davidenkov model and the experience equation considered by Chen Guo-xing et al to fit the results of dynamic shear modulus ratios G/G_{\max} and damping ratios λ visa shear strain amplitudes γ_a for all types of soils. The reference values of regression coefficients are given and for the convenience in engineering applications, the reference values of the dynamic shear modulus ratios and damping ratios corresponding to shear strain amplitudes are also given.

By analyzing and comparing the test results of dynamic characteristics between marine deposited soils and continental deposited soils, it can be concluded as follows. For silt clays, the dynamic shear modulus ratios and damping ratios of marine deposited and continental deposited are very close to each other. For silt and fine sand, the dynamic shear modulus ratios and damping ratios of marine deposited and continental deposited are obviously different. It indicates that the dynamic characteristics of silt and fine sand in the coastal region of Jiangsu province are affected by the deposited environment.

This testing study will benefit seismic researchers and designers to understand the dynamic properties of soils in the coastal region of Jiangsu province and the construction of 'Jiangsu digital strong-motion observation network' and other important projects.

REFERENCES

- Chen Yi'nan, Liu Songyu. (2001). Engineering geological analysis of problems of soft-soil foundation for expressway in coastal area of Jiangsu province. *Journal of China Three Gorges University. (Natural Sciences)*. 6: 507-511.
- Chen Guoxing, Zhu Dinghua and He Qizhi. (2003). Development and property test of GZZ-1 free vibration column test system. *Earthquake Engineering and Engineering Vibration*. 1: 110-114.
- Chen Guoxing, Liu Xuezu. (2005). The preliminary study on dynamic characteristics of recently deposited soils in southern area of Jiangsu Province, China. *Proceedings of The International*

Symposium on Innovation & Sustainability of Structures in Civil Engineering-including Seismic Engineering, Nanjing, China. 20-22.

Deng Yongfeng, Wu Yankai, Liu Songyu and Hong Zhenshun. (2005). Sediment environment of shallow marine clays deposited in lianyungang area and their physical and mechanical properties. *Journal of Engineering Geology*. No.1:29-33.

Martin P.P., Seed H. B. (1982). One dimension dynamic ground response analysis. *Journal of Geot.Eng. ASCE*. 7: 935-952.

Wang Qing, Tian Guoqiang. (1999). The neotetonic setting of late quaternary transgressions on the eastern coastal plan of China. *Journal of Geomechanics*. 4: 41-48.

Zhao Songling. (1986). *The researches of sea level alteration in coastal region of eastern china in recent hundred years. the sea level alteration of China*. Ocean press. Beijing.

Zhao Songling, Zhang Hongcai and Cang Shuxi. (1987). Studies of quaternary magnetostratigraphy in the coastal region of Jiangsu. *Oceanologia Et Limnologia Sinica*, 2: 173-180.

EXPERIMENT ON EARTHQUAKE-INDUCED PERMANENT DEFORMATION OF NANJING RECENTLY DEPOSITED MUDDY SOIL

Guoxing Chen, Dinghua Zhu, Junjian Shi and Xuezhu Liu

*Institute of Geotechnical Engineering, Nanjing University of Technology, 200N Zhongshan
Road, Nanjing, China*

The analysis of earthquake-induced ground settlement is based on study of soil permanent strain under ground motion. So far, some experiential formulas have been established to estimate the permanent strain of soils. But the parameters of the established experiential formulas are too much and a lot of tests must be done to determine these parameters. A series of permanent deformation of Nanjing recently deposited muddy soil under cyclic load were completed by WFI cyclic triaxial apparatus and the soil permanent strain experiential formula with three parameters is given. The experimental results show that the permanent strain of Nanjing recently deposited muddy soil increased suddenly when permanent strain is over 4%. So, the permanent strain value 4% may be as the failure standard of soil element under cyclic load. The relationship of axial cyclic stress amplitude and cyclic number under different confining pressure and consolidation ratios in the system of double logarithm coordinates could be normalized by dynamic shear stress ratio based on the concept of maximum cyclic shear plane. So permanent strain parameters of Nanjing recently deposited muddy soil can be determined by test under one confining pressure and consolidation ratio. The soil permanent strain experiential formula with three parameters could predict the earthquake-induced ground settlement of Nanjing recently deposited muddy soil. For application purposes, the permanent strain parameters of Nanjing recently deposited muddy soil are given under cyclic load.

INTRODUCTION

The analysis of earthquake-induced ground settlement is based on the study of the soil permanent strain under seismic load. Seed H.B. began to research the permanent strain of soil in 1970s, and presented the concept of permanent strain. The experiment results of soil dynamic strength showed that the consolidation soils will have an additional deformation under cyclic loading and the additional deformation depends on three factors under invariant loading frequency and duration: the magnitude of consolidation pressure, cyclic stress amplitude and the cycle numbers of dynamic loading. Lee K.L. (1974) used dynamic triaxial apparatus to make a systemic study on the permanent strain of soils under cyclic loading. He recommended an experiential formula to forecast the permanent strain of soils and earthquake-induced ground settlement of earth dam was calculated by using this experiential formula. However, the experiential formula has seven parameters relating to the properties of

soils and these parameters must be determined through experiment. Xie Jun-Fei and Shi Zhao-Ji(1988) ,Yu Shou-Song and Shi Zhao-Ji(1989) presented a five parameter-experiential formula to forecast the permanent strain based on experiential formula recommended by Lee, separately. Moreover, these parameters involve some principal factors such as dynamic stress, confining pressure and consolidation ratio. Zhang Ke-Xu and Chen Guo-Xing (1992) set up an experiential formula to calculate permanent strain of cohesive soil and the difference between the stress state of soils in the dynamic triaxial experiment and its practice stress state subjecting to ground motion was considered reasonably in this formula. Zhou Jian and Yasuhara(1992) recommended an experiential formula for calculating undrained permanent strain based on the quantitative relation between vibration pore water pressure and permanent strain under cyclic loading. Meng Shang-Jiu and Liu Han-Long et al. (2004) used irregular cyclic load in stead of sine cyclic load to make dynamic triaxial experiments and presented a permanent strain increment formula. Based on undrained dynamic triaxial test of Shanghai saturated soft clay and critical state theory, Huang Mao-Song and Li Jin-Jun et al.(2006) provided an experiential formula to calculate cumulative plastic strain of saturated soft clay in consideration of the relation between the speed rate of cumulated plastic strain and the numbers of cyclic loading.

So far, many experiential formulas of soil permanent strain to calculate earthquake-induced ground settlement have been presented, but they mostly have many parameters. In order to provide these parameters, a large number of tests must be completed. In addition, processing test data is also a complicated problem and some professional software are indispensable for such aim. However, many project survey and design corporations are lack of tools to process test data. So, considering Nanjin recently deposited muddy soil as a study object, by means of dynamic triaxial tests, this paper studies the characteristics of earthquake-induced soil permanent strain, and tries to find a simple and convenient method of earthquake-induced soil permanent strain test. Furthermore, an experiential formula recommended with less-parameters for calculating permanent strain of recently deposited muddy soil can be applied expediently for project survey and design corporations.

TEST METHOD

Description of soil properties

The physical and mechanical parameters of Nanjing recently deposited muddy soil are provided in Table 1. Sampling sites are located in ① The western segment project of Nanjing expressway, ② The fourth Nanjing Yangtze River Bridge, ③ New city project of Nanjing Shi-Mao bund, ④ Eastern extension line project of No.2 line of Nanjing metro and ⑤ Heating and power plant project of Nanjing chemical industry park.

Test Program

The aim of earthquake-induced soil permanent strain test is to study the relationship between soil permanent strain and confining pressure, consolidation ratio, axial cyclic stress amplitude, number of cyclic, and to present a corresponding experiential formula to calculate

earthquake-induced ground settlement. In this paper, the WFI cyclic triaxial apparatus is used to study permanent strain of Nanjing recently deposited muddy soft. The test process is controlled by the computer, and the data of axial cyclic stress, deformation and vibration pore water pressure are all gathered and treated by the computer. The soil sample size is 3.91cm in diameter and 8.0cm in high. The cyclic stress wave is sine wave and its frequency is 1Hz. The soil samples are all saturated by vacuum at first, and then saturated under reverse compression in pressure chamber. The last, drainage consolidation is completed. The test consolidation conditions are determined depend on the stress state of soil element and the drain condition on project site. In order to simulate the stress state of soil element on project site the consolidation ratio value K_c is 1.05-1.5 and the confining pressure σ_{3c} is 100, 150 and 200 kPa. In addition, the axial cyclic stress amplitude σ_d employs 30, 40, 50, 60, 70, 80 and 90 kPa, separately. The cyclic triaxial test of 43 soil samples is completed, the results of test showed as following in Table 2.

Table 1. physical and mechanical parameters of Nanjing recently deposited muddy soft

Project	W (%)	Γ (kN/m ³)	W_L (%)	W_p (%)	I_L	e	φ	C (kPa)	E_s (MPa)
①	41.8	17.3	38.5	21.5	1.19	1.22	12.8	17.4	2.6
②	42.1	17.7	38.4	21.5	1.22	1.18	11.6	18.3	2.8
③	39.7	17.6	39.6	23.1	1.03	1.13	10.5	16.2	2.7
④	40.3	17.6	38.8	24.1	1.1	1.17	11.3	19.1	2.5
⑤	46.1	17.2	41.1	23.4	1.28	1.33	12.1	18.6	2.1

Table 2. Program of cyclic triaxial experiments

σ_{3c} (kPa)	K_c	1.05			1.2			1.5		
		σ_d (kPa)								
100		30	40	50	30	40	50	30	50	60
150		50	60	80	50	60	80	50	60	80
200		60	70	90	60	70	90	60	70	90

The determination method of soil permanent strain

The soil permanent strain is irrecoverable strain of soils after unloading cyclic stress, and in the test, that is, the ratio of high difference to original high of the soil sample. So it can only be measured after the cyclic stress is stopped. In order to save quantities of soil samples and experiment time, the soil permanent strain ε_p is defined depend on cyclic stress $\sigma_d = 0$ of the last-cycle number so that the soil permanent strain determined by this method is a bit more than the actual permanent strain of soils. According to relevant research results, the difference between the permanent strain of Nanjing recently deposited muddy soil determined by the method mentioned above and the actual permanent strain should be smaller than 10% of the actual permanent strain of soils.

ANALYSIS OF TEST RESULTS

The results of cyclic triaxial tests on Nanjing recently deposited muddy soil under different test condition are shown as Figure 1, Figure 2 and Figure 3. The test results show that the

permanent strain increases with the vibration number. And under the same cyclic number, the axial cyclic stress amplitude increases with the soil permanent strain increasing, but the bigger the consolidation ratio is, the smaller the soil permanent strain is. When the permanent strain value of soil samples is more than 4%, the permanent strain increases sharply with the cyclic number. So the permanent strain value 4% can be taken as the failure standard of Nanjing recently deposited muddy soil under cyclic load.

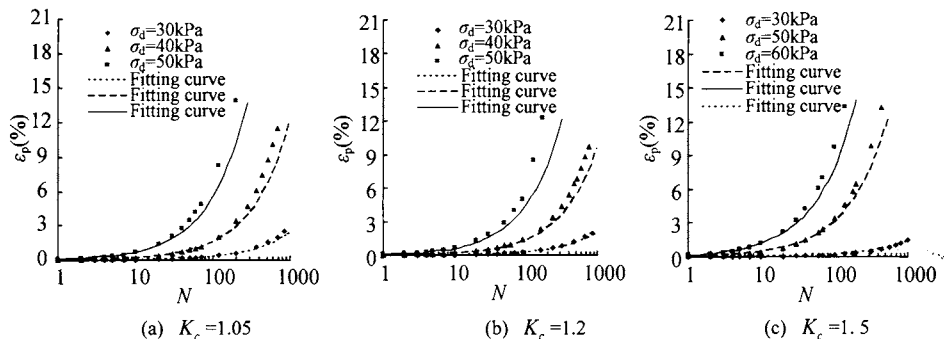


Figure 1. Curves of $\varepsilon_p - N$ under $\sigma'_{3c} = 100\text{kPa}$

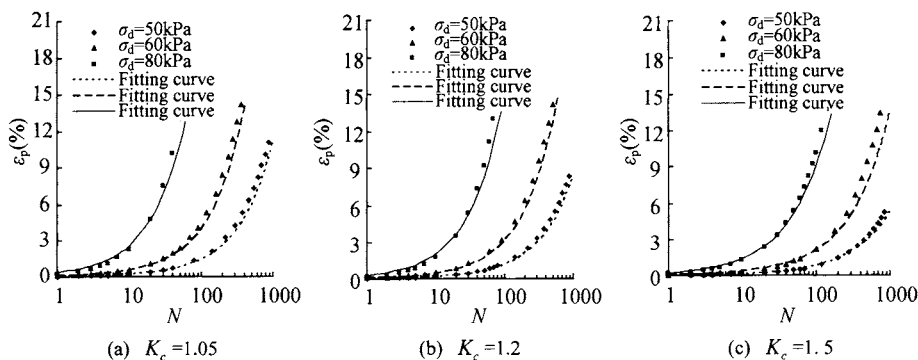


Figure 2. Curves of $\varepsilon_p - N$ under $\sigma'_{3c} = 150\text{kPa}$

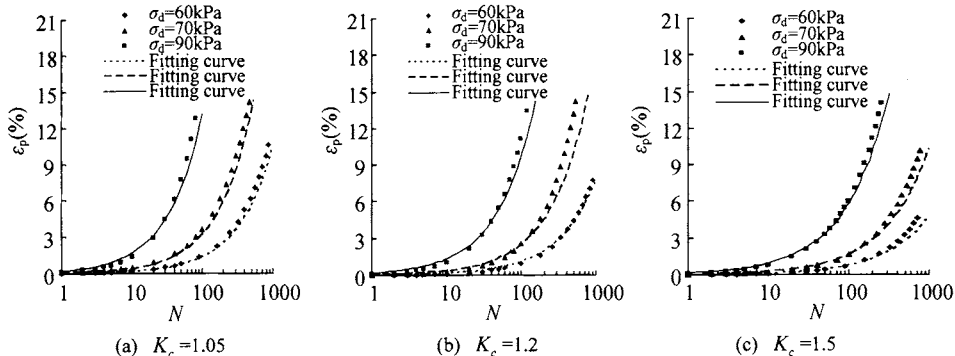


Figure 3. Curves of $\varepsilon_p - N$ under $\sigma'_{3c} = 200\text{kPa}$

The parameter calculation of the residual strain exponential formula

Zhang Ke-Xu and Chen Guo-Xing(1992) recommended permanent strain exponential formula of soils, and the difference between the stress state of soils in the cyclic triaxial experiment and its actual stress state subjected to earthquake ground motion was considered reasonably in this exponential formula suggested. The exponential formula is expressed as follows:

$$\varepsilon_p = 0.1 \times \left[\frac{2}{C_5} \sqrt{K'_c} \alpha_d \left(\frac{N}{10} \right)^{-S_5} \right]^{\frac{1}{S_5}} \quad (1)$$

$$C_5 = C_6 + S_6(K'_c - 1) \quad (2)$$

$$S_5 = C_7 + S_7(K'_c - 1) \quad (3)$$

$$K'_c = \frac{\sigma'_{e1} + \sigma_a}{\sigma'_{3c} + \sigma_a} \quad (4)$$

$$\alpha_d = \frac{\sigma_d}{2\sqrt{K'_c}(\sigma'_{3c} + \sigma_a)} \quad (5)$$

$$\sigma_a = c \cdot \text{ctg} \varphi \quad (6)$$

where S_1 、 C_6 、 S_6 、 C_7 、 S_7 are test parameters. N is the cyclic number of dynamic load; K'_c is a generalized consolidation ratio; σ_a is the binding stress of soils; α_d is the dynamic shear stress ratio of maximum cyclic shear plane; c and φ denote cohesion stress and internal friction angle, respectively, and In this paper, $c = 17.9$, $\varphi = 11.7$.

Based on the exponential formula mentioned above, the process method of test data suggested by Yu Shou-Song and Shi Zhao-Ji(1989) is used in this paper. The dynamic shear stress ratio α_d and the cyclic number N under the same permanent strain ε_p are plotted in a double-logarithmic coordinates, shown as Figure 4. The results show that the relation between α_d and N is approximately linear under different confined pressure, consolidation ratio and axial cyclic stress amplitude. It is expressed as Eq. (7). With the soil permanent strain ε_p changing, a group of approximate parallel line can be obtained, as shown in Figure 4.

$$\alpha_d = C_1 \left(\frac{N}{10} \right)^{S_1} \quad (7)$$

where C_1 is the value of α_d when the cyclic number N is 10.

Considering $\lg C_1$ as longitudinal coordinate and taking $\lg \varepsilon_p$ as horizontal coordinate, it is founded that the relation between $\lg C_1$ and $\lg \varepsilon_p$ is approximately linear, as shown in Figure 5. The relation between C_1 and ε_p can be expressed as:

$$C_1 = C_2 \left(\frac{\varepsilon_p}{0.1} \right)^{S_2} \quad (8)$$

where C_2 is the value of C_1 when ε_p is 10%.

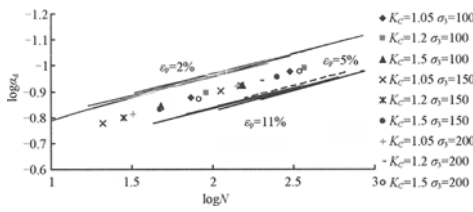


Figure 4. Curves of $\lg \alpha_d - \lg N$

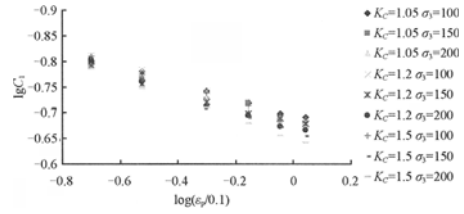


Figure 5. Curves of $\lg C_1 - \lg(\frac{\epsilon_p}{0.1})$

Figure 4 shows that the relationship between $\lg \alpha_d$ and $\lg N$ under different consolidation ratio and confining pressure can be normalized by dynamic shear stress ratio α_d . In other words, through a group of dynamic triaxial tests on Nanjing recently deposited muddy soils under a consolidation ratio and a confining pressure, the seismic subsidence parameters S_1 can be obtained. The slopes of curves of $\lg \alpha_d - \lg N$, S_1 , are provided in Table 3.

Table 3. Values of S_1

σ'_{3c} (kPa)	S_1				C_1			
	1.05	1.2	1.5	Mean value	1.05	1.2	1.5	Mean value
100	-0.159	-0.148	-0.153		0.158	0.154	0.155	
150	-0.165	-0.168	-0.169	-0.163	0.162	0.161	0.161	0.159
200	-0.165	-0.168	-0.176		0.161	0.157	0.164	

Attention: The value of C_1 is the value of intercept of the line when $\epsilon_p = 2\%$ in Figure 4.

Figure 5 shows that the relation curves of $\lg C_1 - \lg \epsilon_p$ under different consolidation ratio and confining pressure are almost parallel, and the distances between these curves are very short. The slope S_2 and the intercept C_2 are shown in Table 4.

Table 4. Values of S_2 and C_2

σ'_{3c} (kPa)	S_2				C_2			
	1.05	1.2	1.5	Mean value	1.05	1.2	1.5	Mean value
100	0.155	0.099	0.166		0.202	0.207	0.208	
150	0.15	0.151	0.189	0.160	0.185	0.209	0.216	0.208
200	0.148	0.185	0.195		0.204	0.218	0.225	

Since the variation of the slope S_2 and the intercept C_2 is very small as shown in Table 4, their mean values can be taken as the soil permanent strain parameters. They can be normalized by dynamic shear stress ratio α_d . Similarly, according to a group of cyclic triaxial tests on Nanjing recently deposited muddy soils under a consolidation ratio and a confining pressure, the soil permanent strain parameters S_2 and C_2 can be obtained. So, by substituting Eq. (8) into Eq. (7), the permanent strain ϵ_p can be expressed as Eq.(9).

$$\epsilon_p = 0.1 \times \left[\frac{\alpha_d}{C_2} \cdot \left(\frac{N}{10} \right)^{-S_1} \right]^{\frac{1}{S_2}} \quad (9)$$

where S_1 , S_2 and C_2 are test parameters.

Based on the analysis above, the permanent strain parameters of Nanjing recently deposited muddy soil can be obtained as shown in Table 5.

Table 5. Soil permanent strain parameters

Parameters	S_1	C_2	S_2
Value of parameter	-0.163	0.160	0.208

The comparison of fitting value and experiment value

The axial cyclic stress amplitude and consolidation ratio of the fitting curves and experiment curves under different confining pressure are shown in Figure 1, Figure 2 and Figure 3. They demonstrate that the fitting curves with Eq. (9) are in accordance with the experiment curves. So, the characteristics of earthquake-induced ground settlement of Nanjing recently deposited muddy soil can be well reflected with Eq. (9), and it also indicates that Eq. (9) is reasonable. The test method on soil permanent strain and the experimental equation of calculating soil permanent strain can all be simplified by normalizing with dynamic shear stress ratio α_d of maximum cyclic shear surface.

CONCLUSIONS

- (1) The characteristics of earthquake-induced ground settlement on Nanjing recently deposited muddy soil are studied systematically through cyclic triaxial tests. A simplified experimental equation of calculating soil permanent strain, only including three test parameters, is provided by analysis of the test results. And test parameters can be obtained from cyclic triaxial tests.
- (2) The relationship between axial cyclic stress amplitude and cyclic number can be normalized by dynamic shear stress ratio. So, the soil permanent strain parameters can be obtained only through a group of cyclic triaxial tests on Nanjing recently deposited muddy soil under a consolidation ratio and a confining pressure.
- (3) The simplified experimental Eq. (9) can well reflect the characteristics of earthquake-induced ground settlement on Nanjing recently deposited muddy soil and the permanent strain parameters of Nanjing recently deposited muddy soil are also presented for convenient application in engineering projects.
- (4) For Nanjing recently deposited muddy soil, the permanent strain value 4% may be as the failure standard of soil element under cyclic load.

REFERENCES

- Huang Maosong, Li Jinjun and Li Xingzhao. (2006). Cumulative deformation behaviour of soft clay in cyclic undrained tests. *Chinese Journal of Geotechnical Engineering*, 28(7): 892-896.
- Lee K. L. (1974). *Seismic permanent deformation in earth dams*. Mechanics and Structures Department, School of Engineering and Applied Science, University of California, Los Angeles, California.
- Meng Shangjiu, Liu Hanlong, Yaun Xiaoming, et al. (2004). Earthquake-induced differential settlement of buildings in Tanggu area. *Journal of Hehai University*, 32(2): 175-178.

- Xie Junfei, Shi Zhaoji, Yu Shousong, et al. (1988). Hazard analysis of liquefaction. *Earthquake Engineering and Engineering Vibration*, 8(1): 61-77.
- Yu Shousong, Shi Zhaoji. (1989). *Experimental investigation of soil settlement due to earthquake. Chinese Journal of Geotechnical Engineering*, 11(4): 35-44.
- Zhang Kexu, Chen Guoxing and Wang Yi. (1992). The analysis on residual deformation of building foundation with piles. *Colloquia of Earthquake Engineering research*, Beijing: China seismic press.
- Zhou Jian, Yasuhara K. and Hirai. (1992). A model for predicting the cyclic behavior of clay with initial static shear stress. *Proc. of 47th annual meeting of Japanese society of civil engineering*.

PROBABILISTIC EVALUATION OF EARTHQUAKE-INDUCED LIQUEFACTION POTENTIAL FOR LARGE REGION SITE BASED ON TWO-DIMENSIONAL GIS TECHNIQUE

Guoxing Chen, Hao Tang

*Institute of Geotechnical Engineering, Nanjing University of Technology, North Zhongshan
Road 200, Nanjing 210009, China*

The empirical equation of cyclic resistance ratio *CRR* of saturated sands with different probability levels is utilized to evaluate the earthquake-induced sand liquefaction for 2D (two-dimensional) large region site. Based on GIS technique, the evaluation results of earthquake-induced liquefaction potential at the observation boreholes can be adopted as the “elevation” in digital elevation model, therefore the identification of liquefaction locality for 2D large region site can also be evaluated by Kriging interpolation method. The research in this paper shows that: (1) The Kriging interpolation is an effect method for evaluating the latent distribution of the site liquefaction potential beyond the observation boreholes. Thus, it is a preferable way to evaluate the possible liquefaction range for 2D large site. (2) Based on ArcGIS software, the Kriging method embedded in the “Spatial Analyst” extension module can be utilized to evaluate the liquefaction potential of the unidentified points by the evaluated results of the reconnaissance boreholes. Therefore, the 2D distribution map of the liquefaction potential for the large region site can be generated.

INTRODUCTION

As the saturated sandy soil liquefaction is one of the most important earthquake-induced geologic disasters. It is necessary to evaluate the earthquake-induced site liquefaction potential to prevent and mitigate the seismic site disasters. The general methods of liquefaction potential evaluation, which based on the test results of SPT (standard penetration test), CPT (cone penetration test) and V_s (shear wave velocity) etc., can just evaluate the actual boreholes. With these evaluated results, the liquefaction potential of the stratum that among the actual boreholes can also be estimated cursorily. However, as the number of reconnaissance borehole in geotechnical investigation is usually limited and the stratum characteristics among these boreholes are unknown. It is uncertain to evaluate the liquefaction extent of the whole engineering site according to the evaluated results of these actual boreholes. Thus, the problem that how to evaluate the earthquake-induced liquefaction potential of the whole engineering site based on the limited boreholes is put forward.

To solve the above problem, two aspects are considered in this paper.

(1) The empirical equation of cyclic resistance ratio *CRR* of saturated sandy soil with different probability levels is utilized to evaluate the earthquake-induced sandy soil liquefaction of the large engineering site region.

(2) Kriging interpolation method is adopted to evaluate the liquefaction potential of the unidentified stratum based on the evaluated results of these observation boreholes. Also, the 2D plot plan of the site liquefaction potential can be given supported by GIS according to the Kriging interpolation results.

PROBABILITY EVALUATION MODEL OF THE EARTHQUAKE- INDUCED SITE LIQUEFACTION POTENTIAL

Based on 344 liquefaction site data in 25 strong earthquakes, the limit state function CRR_{cri} (Critical Cyclic Resistance Ratio) is constructed to estimate the sandy soil liquefaction based on RBF (radial basis function) neural network method (Chen G. X. et al., 2006). Therefore, the critical cyclic resistance ratio CRR_{cri} can be calculated by the following formula:

$$CRR_{cri} = 0.0002N_1^2 + 0.005N_1 + 0.03 \quad (1)$$

where, N_1 is the SPT blow count normalized to an overburden pressure of approximately 100 kPa (1 ton/sq ft) and a hammer energy ratio or hammer efficiency of 60%.

When the equivalent cyclic stress ratio CSR of sandy soil layer caused by the earthquake ground motion is greater than CRR_{cri} determined in formula (1), the saturated sandy soil layer will be liquefaction case, otherwise non-liquefied case.

Thus, the probability function to estimate the sandy soil liquefaction can also be set up according to the relationship $F_s = CRR_{cri}/CSR$, F_s is the cyclic resistance safety factor and P_L is liquefaction probability.

$$P_L = 1/(1 + F_s^{4.297}) \quad (2)$$

Combine formula (1) and (2), sandy soil liquefaction resistance stress curve under the different probability can be shown as the follows:

$$CRR = [P_L / (1 - P_L)]^{0.233} \cdot CRR_{cri} \quad (3)$$

As the Table 1 shows, three grades are classified to identify the liquefaction potential of saturated sandy soil according to the different liquefaction probability level. Therefore, the probabilistic estimation of earthquake-induced site liquefaction can be done as the follows: Firstly, one acceptable liquefaction probability level must be confirmed according to the importance of the engineering project. Secondly, the estimation criteria of sandy soil liquefaction (CRR) with different probability can be calculated by formula (3). Thus, the calculated CRR can be compared with the CSR .

Table 1. Standard for probability evaluation

Liquefaction probability level P_L	Sand liquefaction safety factor F_s	Liquefaction potential evaluation
$0.00 \leq P_L < 0.30$	$F_s \geq 1.2$	non-liquefaction
$0.30 \leq P_L < 0.70$	$0.81 < F_s < 1.2$	possible liquefaction
$0.70 \leq P_L < 1.00$	$F_s \leq 0.81$	liquefaction

2D GIS EVALUATION OF LIQUEFACTION POTENTIAL BASED ON PROBABILITY MODEL

DTM (Digital Terrain Model) is the digital expression of terrain surface information. Also, it is the digital description of spatial location characteristics and terrain attribute. DTM can describe the spatial terrain information by ordinal array of numerical value. When the terrain

attribute is adopted as “elevation” in DTM, it is called DEM (Digital Elevation Model). DEM is utilized to describe the terrain surface in numeric form, and its construction is necessary to the GIS analysis. Based on DEM idea, the probability evaluation results are adopted as the “elevation” in DEM in this paper. Sustained by GIS software-ArcGIS, the 2D distributing plan of earthquake-induced liquefaction potential can be obtained by Kriging interpolation method.

Kriging method applied in the interpolation of liquefaction potential

Based on Kriging interpolation method, the variogram function is utilized to simulate the spatial characteristics of earthquake-induced site liquefaction potential. Therefore, the liquefaction potential of unidentified site points can be evaluated by the original observation boreholes.

(1) Basic interpolation principle

Soil property presents to be special variant. However, there is still certain relativity between the different soil points, viz. the vertical or horizontal relativity and variability. Therefore, the attributes of site soil liquefaction potential can be generally expressed by regional variable $z(x)$.

$z(x_i)(i = 1, 2, \dots, n)$ is assumed as a set of scattered liquefaction potential value of sampling points, and these values are second-order stationary. In order to estimate the true liquefaction potential value at arbitrary point x_0 in the identified region, the best appraisal value $z^*(x_0)$ is assumed as the linear combination of $z(x_i)$:

$$z^*(x_0) = \sum_{i=1}^n \lambda_i z(x_i) \quad (4)$$

Where, λ_i is the weight coefficient; $z^*(x_0)$ is the appraisal value at the position x_0 ; i is the serial number of the borehole.

(2) Kriging Interpolation Equations

The principle of Kriging interpolation is to make sure this appraisal value $z^*(x_0)$ is unbiased estimator, and the estimated variance is less than the value of any other linear combination. Therefore, Kriging interpolation equations can be shown as the follows:

$$\sum_{i=1}^n \lambda_i \gamma(x_i, x_j) + \mu = \gamma(x_j, x_0) \quad (i, j = 1, 2, \dots, n)$$

$$\sum_{i=1}^n \lambda_i = 1$$

Viz.

$$\begin{vmatrix} \gamma_{11} & \dots & \gamma_{1n} & 1 \\ \dots & \dots & \dots & \dots \\ \gamma_{n1} & \dots & \gamma_{nn} & 1 \\ 1 & \dots & 1 & 0 \end{vmatrix} \begin{vmatrix} \lambda_1 \\ \dots \\ \lambda_n \\ \mu \end{vmatrix} = \begin{vmatrix} \gamma_{01} \\ \dots \\ \gamma_{0n} \\ 1 \end{vmatrix} \quad (5)$$

where, $\gamma_{ij} = \gamma(x_i, x_j)$ is the variogram function value between x_i and x_j ; μ is the Lagrange multiplier.

When the weight coefficient λ_i and Lagrange multiplier μ are obtained after resolving the Kriging equations (5), the best appraisal value $z^*(x_0)$ can also be estimated according to the formula (4).

Flow analysis of 2D numeric modeling

Figure 1 shows the follow of building the 2D numeric modeling of liquefaction potential and the realization steps are as the follows:

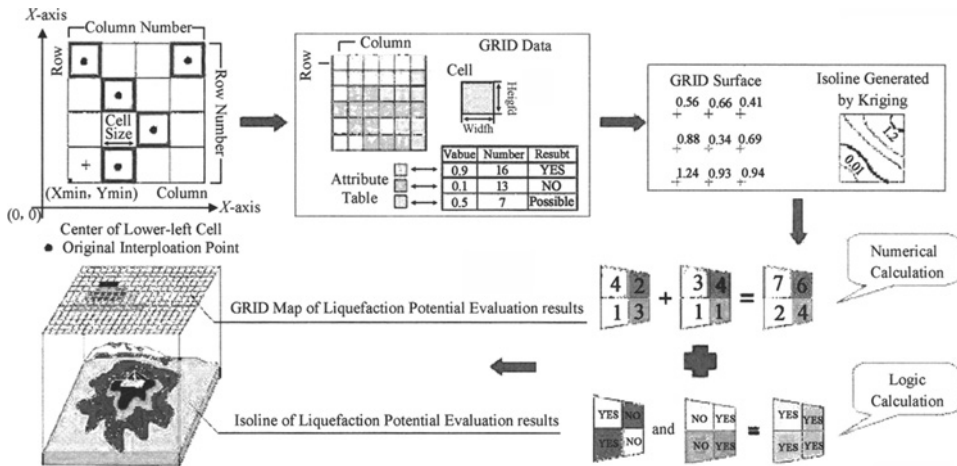


Figure 1. The flow chart of the digital model for the site liquefaction potential

- (1) The probability evaluation result of liquefaction potential is adopted as the “Elevation” in DEM, and the GRID model is generated by GIS.
- (2) The isoline of liquefaction potential is given by Kriging interpolation.
- (3) Based on the GRID model, the logic inquiring and algebraic calculation can be operated on multi-cell data.
- (4) According to the standard for probability evaluation of liquefaction, several limiting data are chosen accordingly. Thus, the whole site can be divided into several districts with the different liquefaction potential grade.

2D evaluation of liquefaction potential based on ArcGIS

The extension module “Spatial Analyst” embedded in ArcGIS, which is developed by ESRI (Environmental Systems Research Institute, U.S.A), is often utilized to extract and analyze DEM. Based on this extension module, the probability evaluation results of liquefaction potential (F_s or P_L) is adopted as the “Elevation” in DEM. The 2D distributing plot of site liquefaction potential can be given by the spatial interpolation when Kriging method, which is attached in the extension module, is utilized.

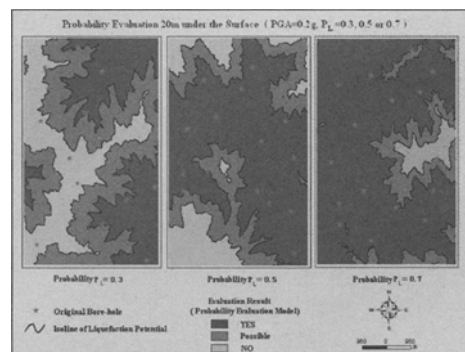
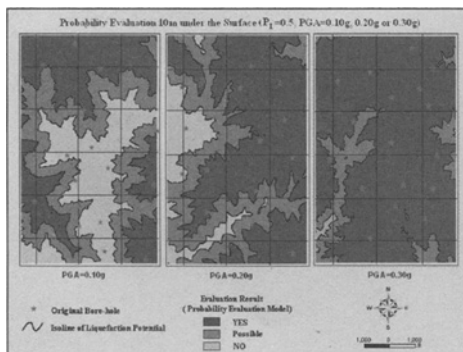


Figure 2. The map of site soil liquefaction potential at depth 10m under different PGA ($P_L = 0.5$) Figure 3. The map of site soil liquefaction potential at depth 20m under different P_L (PGA = 0.20g)

According to the standard for probability evaluation in Table 1, the site liquefaction potential can be classified into three grades, viz. liquefaction, possible liquefaction and non-liquefaction. Figures 2, 3 are the 2D plot plan of site soil liquefaction potential at depth 10m and 20m under certain probability or PGA.

Iwasaki et al. (1978) proposed a quantitative value of site liquefaction potential index I_{LE} to classify the liquefaction potential grade at a site. The bigger I_{LE} value is, the higher the liquefaction risk grade will be.

Therefore, the soil liquefaction potential index I_{LE} value of every actual borehole at site can be calculated according to Chinese Code for Seismic Design of Buildings, and the site liquefaction risk grade can also be classified synthetically into 4 grades. Thereby, the 2D risk evaluation map of liquefaction potential expressed in I_{LE} is shown as Figure 4.

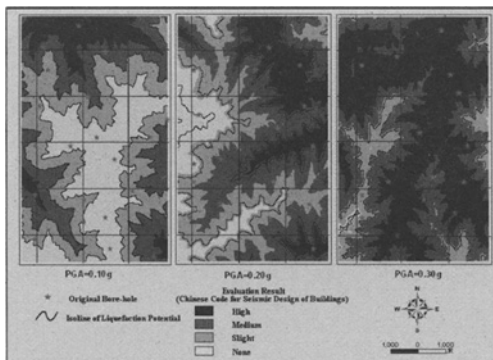


Figure 4. The synthetic map of the soil liquefaction potential I_{LE} for large site

CONCLUSIONS

(1) When the probability evaluation results are adopted as the “elevation” in DEM, the Kriging interpolation method can be utilized to evaluate the liquefaction potential of the unidentified points by the evaluated results of the observation boreholes. Thus, it is a preferable way to estimate the possible liquefaction risk for engineering site and it is worth to study further in the spatial visibility aspect of liquefaction potential.

(2) GIS can be adopted to realize the Kriging interpolation and generate the isoline of the liquefaction potential. Also, the advanced analysis can be done to give the 2D plot plan of earthquake-induced site liquefaction potential. Thereby, GIS is a preferable method to realize the spatial visibility of earthquake-induced site liquefaction potential.

ACKNOWLEDGMENTS

This research is financially supported by the Talent Summit in Six Fields of Jiangsu Province under the grant number 06-F-008 and the PhD Innovation Foundation of NJUT under the grant number BSCX200613.

REFERENCES

- Chen G. X., Li F. M. (2006). Probabilistic estimation of sand liquefaction based on neural network model of radial basis function. *Chinese Journal of Geotechnical Engineering*, 28(3): 301-305.
- Tang H., Chen G. X. and Liu J. D. (2007). Probabilistic estimation of seismic liquefaction potential for large region site based on two-dimensional GIS technique. *Journal of Disaster Prevention and Mitigation Engineering*, 27(3): 296-301.

- Tang H., Chen G. X. (2007). Probabilistic estimation of seismic liquefaction potential for 2.5 dimensional site based on GIS. *Journal of Natural Disasters*, 16(2): 86-91.
- Tang H., Chen G. X. (2007). GIS and ANN model applied in risk evaluation of earthquake-induced site liquefaction potential. *Geomatics and Information Science of Wuhan University*, 32(8): 727-730.
- Youd T. L., Idriss I. M. (2001). Liquefaction resistance of soils: summary report from the 1996 NCEER and 1998 NCEER/NSF workshops on evaluation of liquefaction resistance of soils. *Journal of Geotechnical and Geoenvironmental Engineering*, ASCE, 4: 297-313.

EVALUATION OF LIQUEFACTION POTENTIAL OF POND ASH

Ashim Kanti Dey

Civil Engineering Department, NIT Silchar, Assam, India – 788 010

S. R. Gandhi

Civil Engineering Department, IIT Madras, Chennai, Tamil Nadu, India – 600 036

India is facing a serious problem of effective disposal of huge quantity of fly ash generated from thermal power plants. Fly ash is highly susceptible to liquefaction and thus the rehabilitation of ash ponds requires a detailed study on evaluation of liquefaction potential so that suitable densification measures can be adopted. This paper contains various steps of evaluation of liquefaction potential of pond ash.

INTRODUCTION

Huge quantity of ash is generated in India as a waste from thermal power plants annually. It is estimated that the production of ash is more than 100 million tonnes now. The disposal of this huge quantity of ash is a major problem. At present the ash is dumped in the adjacent low lying areas which are also getting filled up day by day. Rehabilitation of these filled up areas needs a proper analysis of dynamic properties of pond ash, particularly its liquefaction potential.

Number of theories on evaluation of liquefaction potential of cohesionless soil has been developed since the Alaska and Niigata earthquakes in 1964. Most of these theories are based on laboratory investigation on pore pressure rise, whereas, some are based on in-situ properties. Whatever may be the method of analysis, the basic reason for liquefaction is the generation of excess pore pressure under undrained loading condition.

In the field, the liquefaction phenomena can occur in two ways: flow liquefaction and cyclic mobility. Kramer (1996) reported that flow liquefaction can occur when the shear stress required for static equilibrium of a soil mass (the static shear stress) is greater than the shear strength of the soil in its liquefied state. Cyclic mobility, on the other hand, occurs when the static shear stress is less than the shear strength of the liquefied soil.

All soils are not susceptible to liquefaction. A uniform, fine grained, loose, round shaped soil deposit of recent origin is highly susceptible to liquefaction. A shallow depth of ground water increases the liquefaction susceptibility. Pond ash is fine grained, uniformly graded and round grained and thus is highly susceptible to liquefaction. In addition to it, the pond ash, used in the present study, exhibits a gradation curve, which falls within the boundary of liquefiable soil proposed by Tsuchida (1970) as shown in Figure 1. Hence a detailed study on liquefaction potential of pond ash is to be studied.

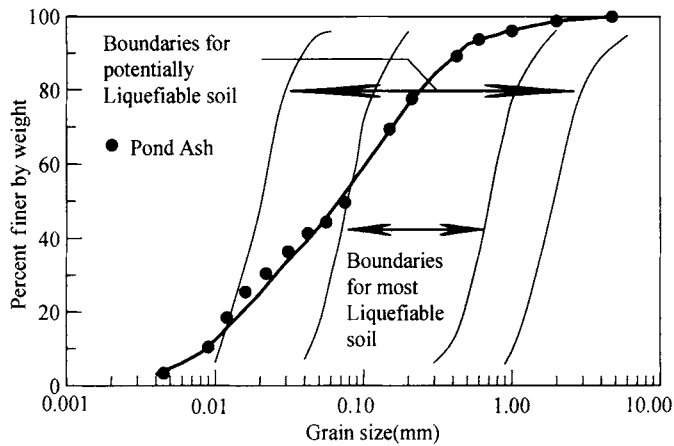


Figure 1. Boundaries for potentially liquefiable soil

TEST SET UP

The conventional triaxial test set up with a little modification to the triaxial cell was used in the present study. A nylon loading plunger with diameter equal to the sample diameter was used. As such the top cover of the triaxial cell was modified to accommodate the larger diameter plunger. Figure 2 shows the fabricated top cover. To minimise friction, lubricating grease was applied on the contact surface between the plunger and the top cover. It was observed that the plunger slides down the top cover under its own weight ensuring negligible friction. This modification permits individual variation of cell pressure and axial stress. Figure 3 shows the total test set up used for the present research work. For axial stress dead loads were placed directly over the loading plunger and for lateral stress cell pressure was applied through a regulatory valve connected to the air compressor. One linear variable differential transformer (LVDT) of +20 mm range was placed over the dead loads to measure the axial deformation. The four outlets of the triaxial cell were connected as follows :

- i) One outlet from the sample was directly connected to a 5 kg/cm^2 (=500 kPa) dynamic pore pressure cell with a digital indicator.
- ii) Another outlet from the sample was connected with a common system of volume measurement and back pressure unit. The back pressure unit consists of a pair of mercury pots as well as a screw control cylinder along with a pressure gauge.
- iii) One outlet from the cell was connected to the loading plunger for top drainage
- iv) Another outlet from the cell was connected to the closed air/water chamber. An air compressor was connected to this chamber. The regulating valve marked 17 in Figure 3 was used to increase the cell pressure and a release valve marked 18 was used to decrease the cell pressure. This increase and decrease of cell pressure contributed one loading cycle to the sample.

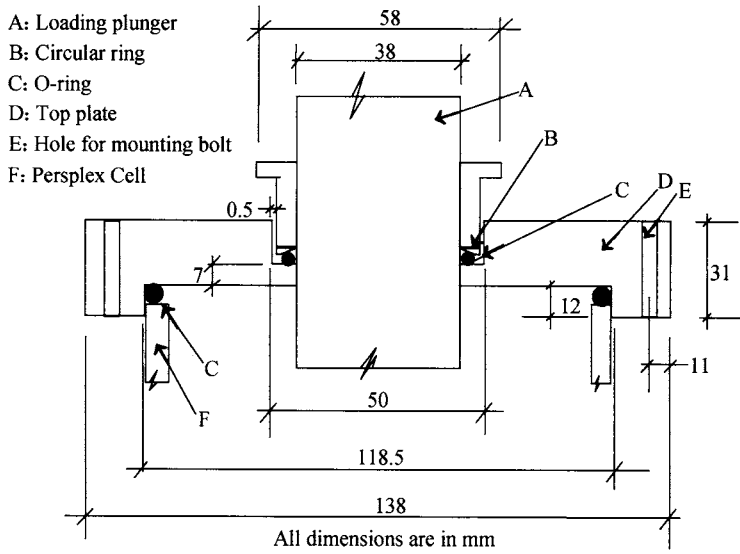
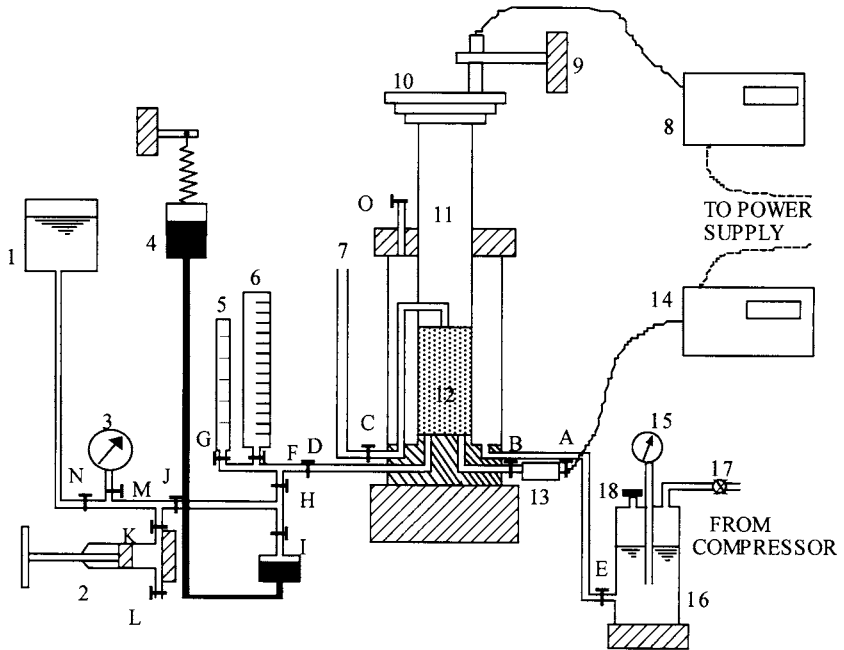


Figure 2. Details of top cover



- 1 . water reservoir 2 . screw control cylinder 3 . pressure gauge 4 . mercury pot
 5 . 0 – 1.5 cc burette 6 . 0 – 25 cc burette 7 . overflow tube 8 . read out unit
 9 . LVDT 10 . weights 11 . loading plunger 12 . sample 13 . pore pressure transducer gauge
 14 . read out unit 15 . pressure gauge 16 . air/water chamber 17 . regulating valve 18 . release valve

Figure 3. Modified Triaxial test set up

Sample preparation

Oven dried sample was taken in five parts, the weight of each part was predetermined depending on the desired relative density. Each of the five parts of the sample was poured one by one inside the mould. Each part was compacted with a 12-mm diameter tamping rod. The nylon plunger was placed over the compacted specimen. The ends of the rubber membrane were slipped off the membrane stretcher. A slight vacuum was applied while the rubber membrane was rolled off. The final size of the cylindrical specimen is around 38-mm diameter and 80 mm height. The top cover of the triaxial cell was placed in position through the plunger and was tightly clamped. The cell was then filled with water.

Saturation of sample

The sample was saturated with distilled water under a small head of 1 cm. The saturation took about an hour. The 'B' value was then measured by noting the rise in pore pressure under a certain confining pressure. When the B value was found to be less than 98%, a little negative pore pressure was applied and maintained for 5~6 minutes. After complete saturation, the sample was consolidated under isotropic condition at different confining pressures. Isotropic condition was achieved by simultaneous application of cell pressure and an equivalent axial load.

Cyclic load application

The cyclic load was applied by increasing and decreasing the cell pressure from the isotropic condition by the same amount. Time period for the cyclic loading was maintained at 1 s. Figure 4 shows the stress path for cyclic load application. The increase in cell pressure depends upon the chosen values of CSR, where CSR indicates the cyclic stress ratio, a ratio of cyclic shear stress to initial effective confining pressure.

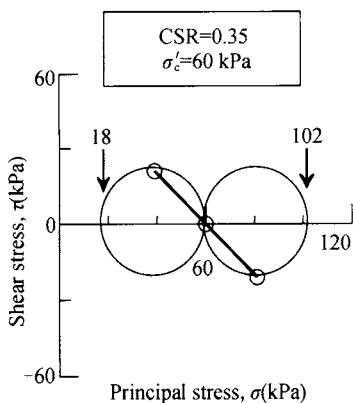


Figure 4. Stress path for cyclic load application

Test results

Number of cycles causing liquefaction under different CSRs was noted. A plot as shown in Figure 5 between CSR and number of cycles causing liquefaction was obtained. The

liquefaction was considered to have occurred when the rise in pore pressure became equal to the initial effective confining pressure.

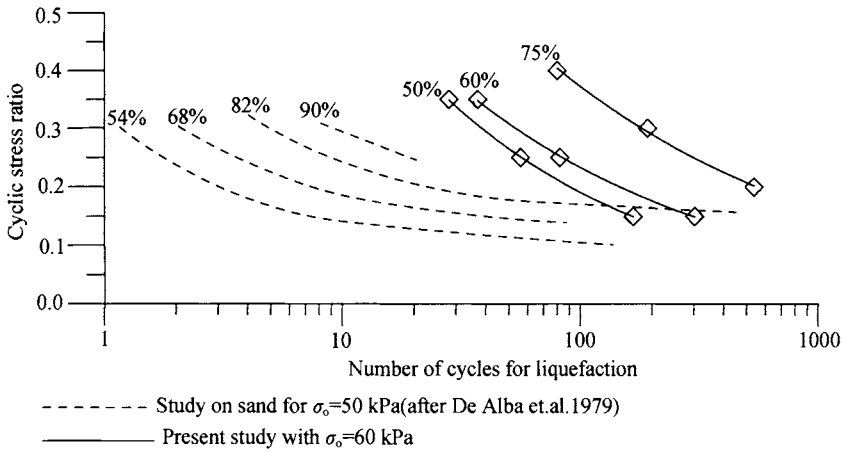


Figure 5. Cyclic shear strengths of pond ash at different relative densities

EVALUATION OF LIQUEFACTION POTENTIAL

Cyclic stress approach (Seed and Idriss, 1971) was adopted to evaluate the liquefaction potential of pond ash. In this approach, cyclic shear stresses induced by earthquakes are compared with the cyclic shear strengths obtained from the laboratory after a certain number of loading cycles. An earthquake magnitude is also represented by an equivalent number of uniform loading cycles. The depths where the shear stress exceeds shear strength, liquefaction will occur. The cyclic shear stress is given by

$$\tau_{cyc} = 0.65 \frac{a_{max}}{g} \sigma_v r_d \quad (1)$$

The cyclic shear strength is given by

$$\tau_{cyc} = (CSR)_{lab} \sigma_v' C_r \quad (2)$$

where, a_{max} is the maximum ground acceleration due to an earthquake;

σ_v and σ_v' are the total and effective stress at any depth;

r_d is a reduction factor obtained.

C_r is a correction factor. Both r_d and C_r are adopted from the tables given by Seed and Idriss (1971). Saturated and bulk unit weights of pond ash were found to be 15.5 kN/m^3 and 13.5 kN/m^3 respectively at 50% relative density. a_{max} for seismic zones IV and V in India are found to be $0.354g$ and $0.459g$ respectively (Dey, 1999). Figure 6 shows the comparison of cyclic shear stress and cyclic shear strength. It can be seen that fully saturated pond ash is highly susceptible to liquefaction whereas the zone of liquefaction decreases as the water table is lowered. It is observed that the zone of liquefaction extends from 1.0 m to 10.5 m in zone V.

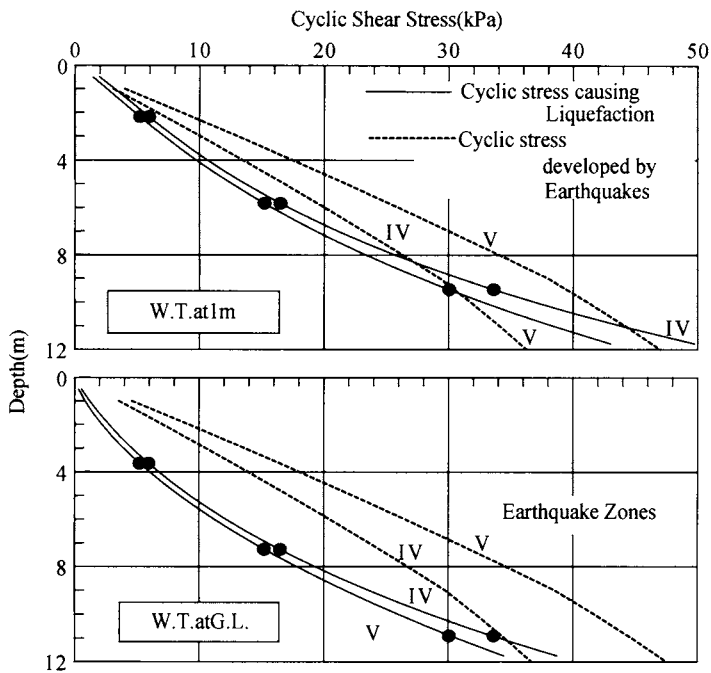


Figure 6. Comparison of shear stresses at earthquake zones IV and V of India

CONCLUSIONS

Following conclusions are drawn from the present study:

1. Cell pressure and axial stress can be varied independently by using a loading plunger equal to the diameter of the sample.
2. Pond ash is susceptible of liquefaction.
3. The liquefaction zone increases with increase in water table.
4. Cyclic stress approach can be used to determine the liquefiable zone at different places in India under different magnitudes of earthquakes.

REFERENCES

- De Alba, P., Seed H.B. and Chan C.K. (1976). Sand liquefaction in large scale simple shear tests. *Journal of the Geotechnical Engineering Division*, 102, GT9, 909-927.
- Dey A.K. (1999). *Liquefaction evaluation and blast densification of pond ash*. Ph.D. Thesis submitted to IIT Madras, India
- Kramer S. L. (1996). *Geotechnical earthquake engineering*. Pearson Education Pvt. Ltd. Delhi, India.
- Seed H. B., Idriss I.M. (1971) Simplified procedure for evaluating soil liquefaction potential. *Journal of Soil Mechanics and Foundation Division*, 97, SM9, 1249-1273.
- Tsuchida H. (1970). Prediction and countermeasure against the liquefaction in sand deposits. *Abstract of the Seminar in the Port and Harbour Research Institute*, 3.1-3.33 (in Japanese)

ANALYSIS ON DYNAMIC RESPONSE OF CAST-IN-PLACE CONCRETE THIN-WALL PIPE PILE COMPOSITE FOUNDATION UNDER LATERAL SEISMIC EXCITATION

Xuanming Ding, Hanlong Liu

*Key Laboratory of Ministry of Education for Geomechanics and Embankment Engineering,
Hohai University, Nanjing 210098, China*

Geotechnical Research Institute, Hohai University, Nanjing 210098, China

A new form of driven Cast-in-place Concrete thin-wall Pipe pile (referred as PCC pile) developed independently by GeoHohai has recently been patented in China. In this paper, the dynamic responses of PCC pile composite foundation under lateral seismic excitation have been analyzed with three dimensional nonlinear finite element method (3DFEM). The soil initial stress field is computed by static calculation, in which the nonlinear elastic Duncan-Chang constitutive model has been adopted to simulate soil behavior. In dynamic calculation, the soil is considered to be viscoelastic material and the equivalent linearization dynamic constitutive model is also applied for simulation. The viscous-elastic boundary is set along the model boundaries. According to the analyses on numerical results of absolute acceleration, relative dynamic displacement and dynamic stress, some conclusions are obtained as follows: The maximal acceleration response locates at the top of reinforced area. That in reinforced area is greater than unreinforced area. The acceleration response at the top of natural foundation is smaller than the composite foundation. The deformation of PCC pile composite foundation is smaller than solid pile composite foundation. The maximal shear stress in pile is greater than in soil. That in PCC pile is greater than in solid pile. The maximal tension stress locates nearby the depth of 1/4 to 1/3 pile length. The distribution of seismic force is changed by PCC pile composite foundation which made the reinforced area participate more seismic force. The contrastive results of several different models show that the dynamic response of PCC pile composite foundation is smaller than that of the solid pile composite foundation with the same cross section to PCC pile, which indicates that the PCC pile composite foundation is more effectively anti-seismic.

INTRODUCTION

The composite foundation technique is widely applied to soft ground improvement. As one of the most cost-effective soft ground improvement techniques, PCC pile composite foundation is rapidly increasing in popularity in China since its first application (Liu et al. 2003, (Liu et al. 2003a, Liu et al. 2004, Liu et al. 2004a). The static characteristic of PCC pile composite foundation was lucubrated in the past (Liu et al. 2005, Xu et al. 2006). However, there was little dynamic characteristic research (Zhu, 2006).

Analytic method or numerical method can be used for analysis. Numerical method was adopted in the paper and the dynamic response of PCC pile composite foundation has been computed with 3DFEM. The dynamic response of solid pile composite foundation has also been calculated and compared to that of PCC pile composite foundation. Some important conclusions are obtained which have some referenced value for aseismic design in engineering.

THREE DIMENSIONAL NONLINEAR DYNAMIC FINITE ELEMENT METHOD

The FEM dynamic analysis on soil consists of static computation and dynamic computation. The soil initial stress field is computed by static computation before dynamic computation, in which the nonlinear elastic Duncan-Chang constitutive model has been adopted to simulate soil behavior. In dynamic calculation, soil is considered to be viscoelastic material and the equivalent linearization dynamic constitutive model is applied for simulation. The dynamic balance equation is:

$$[M]\{\ddot{\delta}\} + [C]\{\dot{\delta}\} + [K]\{\delta\} = -[M]\{\ddot{\delta}_g\} \quad (1)$$

where $[M]$ —diagonal mass matrix;
 $[C]$ —global damping matrix, Reyleigh' damping matrix is adopted in this paper;
 $[K]$ —symmetric stiffness matrix;
 $\{\ddot{\delta}\}, \{\dot{\delta}\}, \{\delta\}$ —relative nodal acceleration, velocity and displacement;
 $\{\ddot{\delta}_g\}$ —seismic acceleration array.

The acceleration, velocity and displacement at any time are calculated by Wilson- θ step-by-step integration method. The dynamic shear modulus G and damping ratio λ are variable as the variety of shear strain γ . Dynamic shear modulus G is calculated by Seed' formula:

$$G = KP_a^{1-n} \sigma_m^n \frac{G}{G_{\max}} \quad (2)$$

where K, n —experimental constant of G_{\max} ;
 σ_m —average effective stress;
 G/G_{\max} —the function of shear strain γ .

Two typical seismic wave—Kobe seismic wave and Nanjing artificial wave are used for calculation (as shown in Figure 1 and Figure 2), the amplitude acceleration of which is 0.2g.

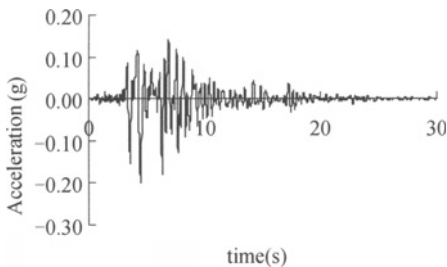


Figure 1. Kobe seismic wave

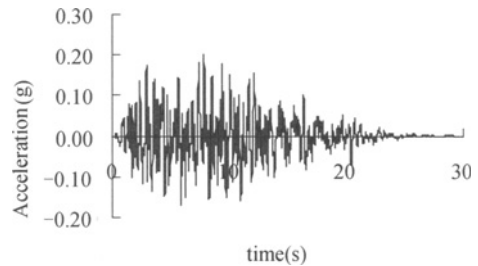


Figure 2. Nanjing artificial wave

The parameter used in computation is excerpted from the paper of Zhu(2006). The 8-node solid element is used in the model. The FEM mesh is shown in Figure 1. The length of piles is 20 m. The height of both underlying soft layer and superstructure is 10m and that of the cushion is 0.5m. The distance between piles is 3m. Take advantage of symmetry(as shown in Figure 3), only a section of the whole model is considered and the y direction of boundary is fixed. Similarly, take advantage of anti-symmetry, only a half of the actual model is considered.

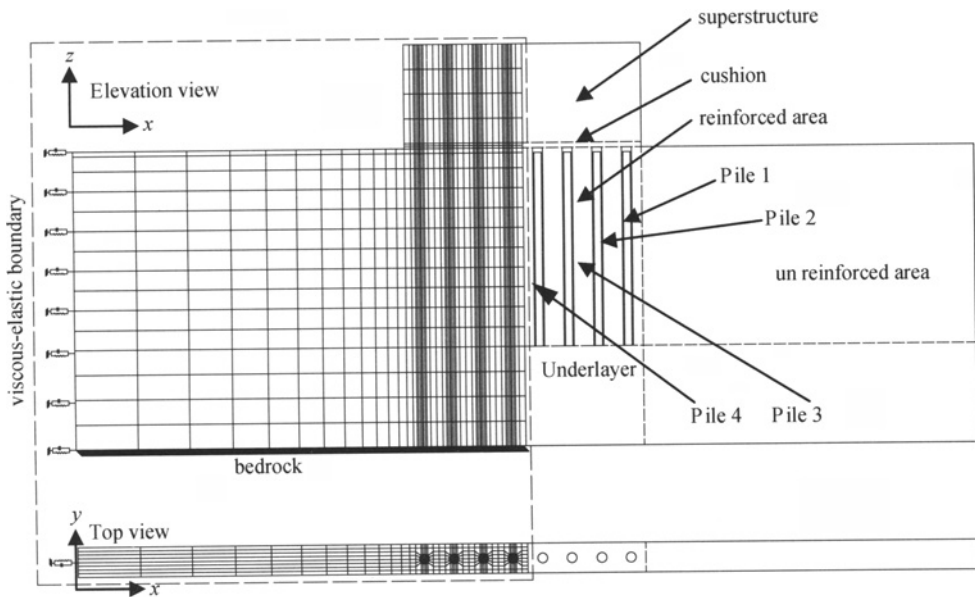


Figure 3. FEM mesh The meaning of three models mentioned afterward is:

Model 1:PCC pile composite foundation;

Model 2: solid pile composite foundation with the same cross-sectional area to PCC pile;

Model 3: natural foundation.

NUMERICAL RESULTS AND ANALYSIS

Maximal acceleration response

The acceleration response is more and more larger from bottom to top(as shown in Figure 4 and Figure 5). The maximal acceleration response locates at the top of reinforced area. That in reinforced area is greater than in unreinforced area. It indicates that the distribution of seismic force is influenced by the pile which made the reinforced area participate more seismic force. The acceleration response of Nanjing wave is greater in unreinforced area but smaller in reinforced area than that of Kobe wave.

The stiffness of composite foundation is larger than natural foundation which enhanced the passing of seismic force, as a result, the acceleration response at the top of natural foundation is smaller than composite foundation (as shown in Figure 6 and Figure 7).

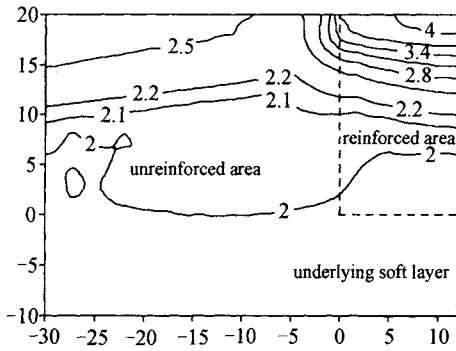


Figure 4. Acceleration response isoline in model 1 of Kobe wave.

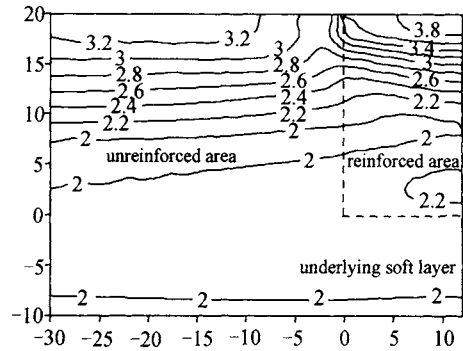


Figure 5. Acceleration response isoline in model 1 of Nanjing wave

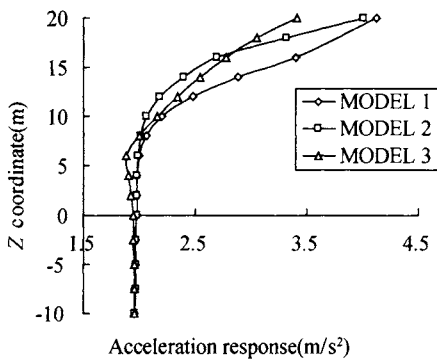


Figure 6. Acceleration response in reinforced area of Kobe wave

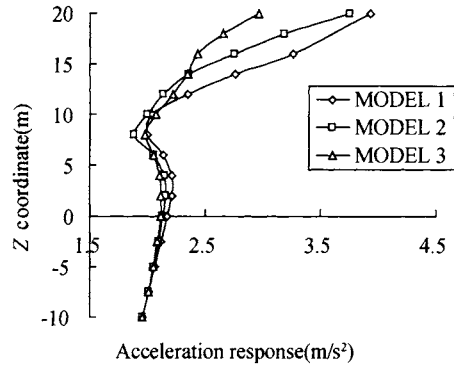


Figure 7. Acceleration response in reinforced area of Nanjing wave

The acceleration response of model 1 is greater than model 2, which shows that the PCC pile composite foundation is more effective to reinforce natural foundation than solid pile composite foundation with the same cross section to PCC pile.

Maximal relative dynamic displacement response

The distributing characteristic of relative dynamic displacement response is similar to that of acceleration response. The relative dynamic displacement response is more and more larger as the increase of node's height(z coordinate). In unreinforced area, the relative dynamic displacement of 3 models has little distinction, but in reinforced area, the relative dynamic displacement at the top of model 1 is smaller than model 2(as shown in Figure 8 and Figure 9). Obviously, the diameter of PCC pile is larger than that of solid pile with the same cross-sectional area, therefore both the flexural rigidity and soil resistance of PCC pile are greater than solid pile. As a result, PCC pile composite foundation has smaller deformation.

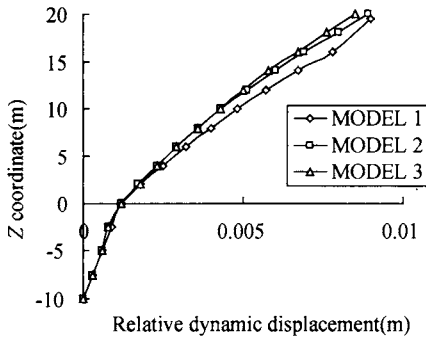


Figure 8. Relative dynamic displacement response in unreinforced area of Kobe wave

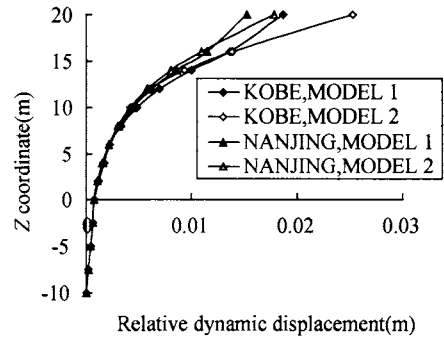


Figure 9. Relative dynamic displacement response in reinforced area of Kobe wave and Nanjing wave

Maximal dynamic stress response

The dynamic shear stress is very small in soil but large in pile (as shown in Table 1). The dynamic shear stress in soil of model 3 is greater than model 1 and model 2, which indicates that composite foundation made soil participate fewer seismic force and the pile support more. The maximal dynamic shear stress in piles of model 1 is greater than model 2. The maximal dynamic shear stress in piles at the edge of reinforced area is greater than that at the central of reinforced area.

Table 1. The maximal dynamic shear stress (kPa)

Model	Model 1		Model 2		Model 3	
	Kobe	Nanjing	Kobe	Nanjing	Kobe	Nanjing
Soil in unreinforced area	125	120	130	120	150	130
Soil in unreinforced area pile	70	65	80	75	110	105
underlying soft layer	1591	1566	1350	1273	—	—
	105	100	110	105	130	125

The maximal dynamic tension stress (σ_z) in piles of model 1 is greater than that of model 2 (as shown in Figure 10 and Figure 11). As for model 1, the maximal tension stress in pile 1

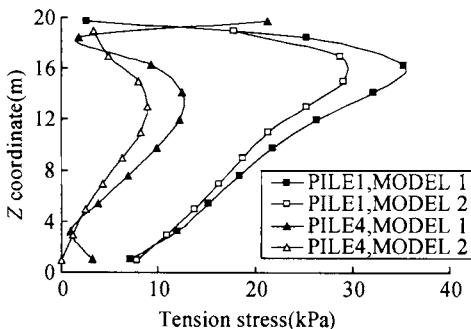


Figure 10. Maximal dynamic tension stress in pile 1 and pile 4 of Kobe wave

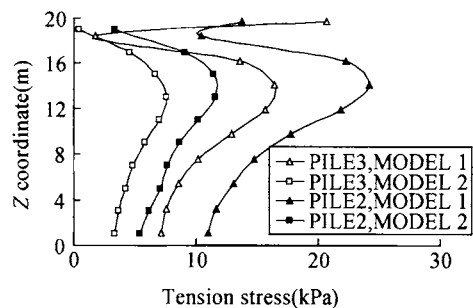


Figure 11. Maximal dynamic tension stress in pile 2 and pile 3 of Nanjing wave

locates nearby the depth of 1/4 pile length. In pile 2, it locates nearby the depth of 1/3 pile length. In pile 3 or pile 4, it locates nearby the top of the pile and the position of 1/3 pile length also has comparatively large tension stress.

CONCLUSIONS

By above research on dynamic responses of PCC pile composite foundation and other two models, some conclusions have been obtained as follows:

- (1) The maximal acceleration response locates at the top of reinforced area. That in reinforced area is greater than unreinforced area. The acceleration response at the top of natural foundation is smaller than composite foundation.
- (2) PCC pile composite foundation has smaller deformation than solid pile composite foundation.
- (3) The maximal shear stress in pile is larger than in soil. That in PCC pile is larger than in solid pile.
- (4) The maximal tension stress locates nearby the depth of 1/4 to 1/3 pile length.
- (5) The distribution of seismic force is changed by PCC pile which made the reinforced area participate more seismic force.

ACKNOWLEDGMENTS

Thanks for the help of the national natural science foundation of China(50679017).

REFERENCES

- Liu H. L., Fei K., Ma X. H. and Gao Y. F. (2003). Large-diameter driven cast-in-place concrete thin-wall pipe pile (I) Research and Development. *Journal of Rock and Soil Mechanics*, 24: 164-198.
- Liu H. L., Fei K., Ma X. H. and Gao Y. F. (2003a). Large-diameter driven cast-in-place concrete thin-wall pipe pile (II) Application. *Journal of Rock and Soil Mechanics*, 24: 372-375.
- Liu H.L., Ma X. H., Chu H. Y., Chen Y. H. and Gao Y. F. (2004). *Cast-in-place pipe pile construction equipment for soft ground improvement*. Patent Number: ZL 02219218.X.
- Liu H.L., Ma X. H., Chu H. Y., Chen Y. H. and Gao Y. F. (2004a). *Cast-in-place pipe pile construction technology for soft ground improvement*. Patent Number: ZL 021125384.4.
- Liu H.L., Fei K., Xu X.T. (2005). Development and application of the large-diameter driven cast-in-place concrete thin-wall pipe pile. *Proceeding of the 16th international conference on soil mechanics and geotechnical engineering*, Osaka, Japan: 2137- 2140.
- Xu X.T., Liu H.L., Lehane, B.M. (2006). Pipe pile installation effects in soft clay. *Geotechnical Engineering, Issue GE4*, 285-296.
- Zhu X.C. (2006). *Dynamical analysis of the cast-in-situ concrete thin-wall pipe pile composite foundation*. The paper for master's degree of Hohai university, Nanjing, China.

THE ANALYSIS OF COMPOSITE FOUNDATION WITH CFG AND GRAVEL PILES TO RESIST SOIL LIQUEFACTION

Yuqin Feng, Yinghao Wang and Chunmei Zhang

The school of Architecture and Civil Engineering, Inner Mongolia University of Science & Technology, Baotou 014010, China

Based on a practical engineering project (in Inner Mongolia), which uses composite foundation with CFG & gravel piles to deal with the soil liquefaction, the composite foundation's capacity and function mechanism are analyzed in the paper. And the design, construction effect and test results of the composite foundation are also discussed. The test results presented in the paper can be applied to the similar projects in the region of Inner Mongolia. These include the experimental parameters of the composite foundation, the test results of the carrying capacity of single pile vertical static load and heavy dynamic touch test, the test results of the pile's quality affected by low stain dynamic test and the test results of standard penetration experiment. The following conclusions can be reached from the analysis of the test results mentioned above: (1) That the engineering project involved in the paper has gotten good reinforcement effect shows that the application of the composite foundation to resisting soil liquefaction is successful, which sets an example for widely application of the composite foundation with CFG and gravel piles to treating the soil liquefaction of foundations; (2) The composite foundation with CFG and gravel piles has the functions of quickening up the soil's drainage and consolidation; and (3) During the construction of the composite foundation, the dynamical load and the shock absorption function of the piles can increase soil's density, and thereby abate or clear up soil liquefaction.

INTRODUCTION

It is common all over the world that many buildings will be destroyed because of groundsill soil liquefaction when the earthquake occurs. Whether the groundsill soil liquefaction can be treated properly is related to the engineering's quality, investment and finish date, so that more and more attentions are paid to its importance. At the moment, the single composite groundsill such as dynamic compaction, compaction pile, grouting and gravel pile is used widely. This method has sound theory and is used successfully in practical engineering. But the further study needs to be done for the method of the composite foundation with CFG and gravel pile against liquefaction. To compare with single foundation, multi pile composite foundation consists of at least two piles. And the piles which can bear main load are called main piles, the others are named auxiliary piles. When the loads are very great and groundsill's design capacity is high, the single pile can't meet demand, multi pile composite foundation can be used to resist liquefaction and enhance groundsill's capacity.

DESCRIPTION OF THE PROJECT

This project is of a office building in Inner Mongolia. The main structure is twenty-two stories, and part of the structure is twenty stories. The whole structure is poured-in place reinforced concrete and with shear walls. The foundation is of the type of raft. Its depth is 4.5meters. The relief of area is like a intersection alluvial fan and alluvial plain. The depth of the groundwater is 5.8 meters. The results of in-situ soil tests are listed in Table 1.

Table 1. The results of stratum

No.	stratum	thickness (m)	compaction	humidity	capacity(f_{ak}) (kPa)
1	miscellaneous fill	0.8-1.2	incompact	dry	
2	silt clay	1.2-2.7	little close-grained	wet	130
3	silt fine sand	1.0-7.2	incompact	dampish-saturated	135
4	medium fine sand	6.5-13.5	little close-grained	dampish-saturated	180
5	medium sand	>8.5	medium close-grained	dampish-saturated	200

The earthquake intensity of this area is eighth. The bearing stratum is silt、 fine sand and its f_{ak} is 135KPa. The f_{ak} which the project requested is 300kPa and the maximal deformation is 50 mm.

According to Table 1, the stratum which is under bearing stratum occurs liquefaction easily and can only bear some plate load. If the static load or force of earthquake exists, the sand will liquefy. So we should make proper ground treatment to avoid liquefaction and to meet the demand of capacity. By comparisons of all kinds of treatments, the composite foundation with CFG and gravel piles is adopted. The gravel piles can resist liquefaction while CFG piles can increase capacity. At first, the gravel piles are driven into stratum by hammering diving casting cast-in-place pile, then the CFG piles are driven into stratum by bobbing diving casting case-in-place pile. The parameters of the composite foundation are listed in Table 2. The materials of gravel piles include gravel with diameter 20-50mm、 detritus contains less than 7% mud or medium sand. The mix proportion of the gravel piles is 75% of gravel and 25% of detritus. The dry unit weight should be more than 20kN/m^3 . The materials of CFG pile include portland cement、 gravel、 grime and medium、 coarse sand. The strength of pile should be more than 9.0MPa. Furthermore, it is necessary to pave bed course to make composite ground sill. The bed course is concerned with the success of the composite foundation. Its functions are as follows: making piles and soil bear loads jointly; reducing stress concentration of the base of the foundation; adjusting the ratio of horizontal and vertical loads. The bed course's thickness is 200mm, and the material for the bed course is gravel with diameter 5-10mm.

Table 2. Parameters of composite ground sill

kind	diameter (mm)	length (m)	pile spacing (m)	bed course's thickness (mm)
CFG pile	400	9-16	1.6	200
gravel pile	420	4-5	1.6	

THE PRINCIPLES OF SOIL LIQUEFYING AND THE FUNCTIONS OF THE COMPOSITE FOUNDATION WITH CFG AND GRAVEL PILES

The principles of saturated sands' liquefying are as follows: when the earthquake occurs, the soil with different weight and array in saturated sands will endure inertial force whose size

and direction are different. Then the new stress will bring about on the interfaces of soil. The stress will destroy intrinsic structure of soil when it increases and overrun a limit. So the soil will be loose. At the same time, the pore water stress can't lift, so it increases continually that strength of soil falls even loses. Three conditions are necessary for soil liquefying: incompact、saturated sand、drain ill and vibrant loads. The use of composite ground sill with CFG and gravel pile can control above-mentioned three adverse conditions. As many projects which use gravel piles show that the functions of reducing or eliminating liquefaction are as follows: ①increase the soil's compactness ②control the pore water stress to rise by draining ③ share horizontal shear coming from earthquake (shock absorption).

THE METHODS OF EXPERIMENT AND THE ANALYSIS OF THE RESULTS

In order to prove the efficiency of composite foundation to resist liquefaction, the capacity and settlement are measures in site

Standard penetration test(SPT)

《Aseismic Code》 (GB50011-2001,China) suggests that the soil liquefaction occurs or not can be differentiated by SPT. If $N_{63.5}$ is more than N_{cr} (critical figure) which is counted according to code, the soil won't liquefy, or else occurs. N_{cr} should be counted as follows:

$$N_{cr} = N_0[0.9 + 0.1(d_s - d_w)]\sqrt{3/\rho_c} (d_s \leq 15)$$

$$N_{cr} = N_0(2.4 - 0.1d_s)\sqrt{3/\rho_c} (15 \leq d_s \leq 20)$$

Where: N_{cr} is critical figure comes from SPT. N_0 is based figure; d_s is penetration, d_w is ground water's depth. ρ_c is percent of clay, when it is less than 3, or the soil is sand, ρ_c should be regard as 3. 10 holes with up to 30 test points were selected for liquefaction test. The test and results are listed in the Table 3.

Table 3. The subsoil of pile standard penetration experiment result

hole	depth (m)	stratum	practical $N_{63.5}$	revised $N_{63.5}$	N_{cr}	liquefy or not	hole	depth (m)	stratum	practical $N_{63.5}$	revised $N_{63.5}$	N_{cr}	liquefy or not
K1	1.2-2.5	silt	18	18.0	10.5	not	K16	1.2-2.5	silt	20	19.5	9.9	not
K2	2.5-4.5	silt	21	20.5	11.2	not	K17	2.1-3.6	silt	22	21.3	10.2	not
K3	3.3-5.5	silt	28	27.0	13.5	not	K18	2.8-4.0	silt	32	30.9	12.3	not
K4	2.4-4.5	silt	34	32.5	10.5	not	K19	2.3-3.5	silt	30	29.4	13.3	not
K5	3.0-5.5	silt	41	40.6	11.2	not	K20	3.0-5.0	silt	35	34.6	12.0	not
K6	3.5-6.5	silt	45	44.6	13.5	not	K21	4.0-5.0	silt	40	38.9	11.8	not
K7	3.5-4.0	silt	33	32.3	10.5	not	K22	1.8-2.9	silt	28	27.5	12.6	not
K8	4.0-5.5	silt	36	35.4	11.2	not	K23	2.6-3.5	silt	25	24.3	13.5	not
K9	5.5-6.0	silt	45	44.8	13.5	not	K24	3.5-5.5	silt	34	33.5	11.6	not
K10	2.4-3.5	silt	30	29.2	10.5	not	K25	2.4-3.4	silt	33	32.4	13.5	not
K11	3.5-4.5	silt	32	30.9	11.2	not	K26	3.0-4.8	silt	38	37.6	12.1	not
K12	4.5-5.5	silt	42	40.2	13.5	not	K27	4.6-5.7	silt	40	39.4	11.5	not
K13	5.0-6.0	silt	26	25.7	10.5	not	K28	4.0-5.6	silt	41	40.5	10.4	not
K14	6.0-7.5	silt	38	37.4	11.2	not	K29	5.3-6.5	silt	42	41.6	13.1	not
K15	6.5-3.5	silt	40	38.8	13.5	not	K30	6.0-7.5	silt	43	42.2	12.4	not

According to above test results in Table 3, it is clear that the composite groundsill with CFG and gravel pile eliminates liquefaction of intrinsic sand soil.

The values of the soil capacity (fak)

Three plate loading test machines is set up in both sides and midst of building. The Figure 1 shows P-S curve comes from experiment. In accordance with the appendix C of *Groundsill Code* (GB5007-2002), the fak of soil which should be disposed is 169kPa. It is 34kPa more than before. Because the soil is compacted by gravel and CFG piles. In the course of driving piles, the sand soil accepts transverse stress coming from piles and getting dense, and when the gravel is put into piles, its vibration and recoil make soil dense too. So the shear strength of soil is raised and the result of resisting liquefaction is good.

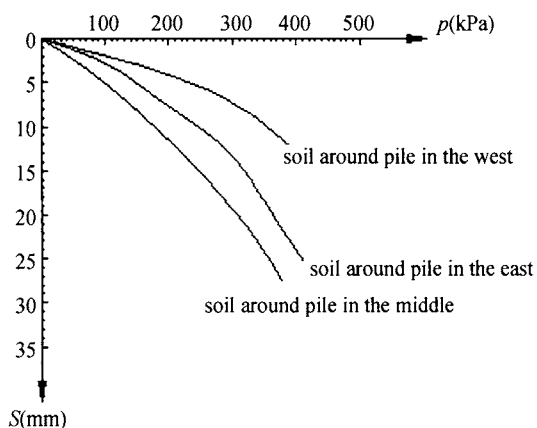


Figure 1. P-S curve

Vane shear test

The vane shear test is made after reinforce. The experiment shows: the vane strength of the third soil gets an increase from 16kPa to 26kPa, while the fourth one from 13kPa to 37kPa, the percent of enhance is 62.5% and 184.6% respectively. This result shows: the drainage of gravel pile gets consolidation quickly, i.e. decompression by drainage. The pile's water permeability is good because some coarse soils such as gravel are filled in it, so the artificial vertical drainage shaft with good permeability is made. It is effective to prevent the pore water pressure from enhancing, and the sandy soil from liquefying. When the earthquake happens, the pore water pressure can decrease and the liquefaction won't occur. The capacity of resisting liquefaction is great.

Furthermore, gravel and CFG piles can absorb shock. Because the rigidity of piles is much bigger than the natural soil's, when the primary rigidity and stress changes, the earthquake loads will be distributed again. So when the soil and piles deform together, the earthquake shear which is on the gravel and CFG piles with large rigidity will concentrate. At the same time, the shear on the soil is light. So it is proved that the gravel and CFG piles can absorb shock.

The low strain dynamic test experiment

To measure the pile's quality, the low strain dynamic test was made with reverberation. The test results show that piles can meet the loads. The quantity of the piles which were measured is 10 percent. The results are listed in table 4 and show the pile's quality meets the design.

Table 4. The results of the low strain dynamic test

total	test quantity	wave speed (m/s)	I pile		II pile		III pile
			quantity	ratio	quantity	ratio	quantity
1045	105	3200	95	95.6%	10	4.4%	—

The test of loading capacity of composite ground sill

At first the silt、fine sand are treated by gravel piles. When the project finished, we made the test of loading capacity of composite ground sill on both sides of building. The f_{ak} of composite ground sill is 180 kPa which is 33.3% more than natural ground sill's. Then CFG pile near gravel pile was put to make composite ground sill. The test of loading capacity of composite ground sill was made again according to the rules of *Ground Treatment regulation* (JGJ79-2002). During the test, the load board is contacted firmly with bed course, the counter force comes from heavy object which is placed on the platform, the loads from hydraulic jack was 500KN. The pressure was measured by pressure gauge. The result is listed in Table 5.

Table 5. The result of SPT on composite ground sill with many kinds pile

Type	No.	parameters			results		
		diameter (mm)		design f_{ak} (kPa)	ultimate load (kPa)	total settlement (mm)	practical f_{ak} (kPa)
		gravel	CFG				
Composite piles	3	420	400	300	800	20.20	360
	5	420	400	300	600	19.45	360
	7	420	400	300	400	18.60	360
	9	420	400	300	200	12.20	360

The test shows: the practical f_{ak} is bigger than design f_{ak} after the ground sill was dealt with CFG and gravel piles. The former f_{ak} is 2.7 times as big as the latter f_{ak} . At the same time, it is 2 times as big as the f_{ak} of the composite ground sill using single gravel pile.

Analysis of the settlement

During the construction, we observed the settlement when each structure was finished. The observation points were located at the four corners and midpoints of the structure. The average settlement of the eight observation points is regarded as the final settlement and is listed in Table 6. When the whole structure was finished, the average settlement is 18.9mm which is 6.22 percent of the final settlement. According to the estimation, the final settlement isn't more than 50mm. The results show the CFG and gravel pile is used successfully.

Table 6. The settlement when the whole structure is finished (mm)

Date	observe points							
	1	2	3	4	5	6	7	8
2006.3.6	16.1	18.5	17.2	19.5	21.5	19.2	18.4	20.8

CONCLUSION

- ① CFG and gravel piles can accelerate the soil consolidation;
- ② CFG and gravel piles can increase the soil's density and absorb shock to alleviate or eliminate liquefaction;
- ③ For the composite groundsill with CFG and gravel piles, its capacity is 2.7 times as big as natural groundsill's, and 2 times as big as single gravel pile's;
- ④ The settlement is within allowable deformation;

REFERENCES

- Aseismic Code*. Beijing, China Architecture and Building Press.
- Ground Treatment Code*. Beijing, China Architecture and Building Press, 2002
- Yan Mingli, Zhang Donggang. (2001). *the technique and example on composite groundsill with CFG and pile*. Beijing, China Waterpower Press
- Ye Shulin, Ye Guanbao. *Ground treatment (the second edition)*. Beijing, China Architecture and Building Press.

COMPUTATION OF PASSIVE EARTH PRESSURE OF COHESIVE BACKFILL ON RETAINING WALL CONSIDERING EARTHQUAKE FORCE

Zhen Feng ^{1,2}, Na Wang ¹ and Lianjun Wang ²

¹ *Institute of Disaster Prevention Science and Technology*

Beijing 101601, China

² *School of Civil Engineering and Architecture, Beijing Jiaotong University,*

Beijing 100044, China

This paper based on having research conclusion, according to the Coulomb's earth pressure theory, from the condition of the equilibrium of the force when the slide wedge was in limit equilibrium, thinking about most infaust condition to retaining wall stability during earthquake, a formula was derivated for the calculation of passive earth pressure of cohesive or non-cohesive backfill soils. This formula could be used in the calculation of earth pressure with superimposed load uniformly distributed on any location of ground surface behind retaining wall. Some suggestions were proposed to the calculation of earth pressure in gravity retaining wall design in high frequency earthquake region considering earthquake force.

PREFACE

Passive earth pressure computation method about Gravity style retaining wall (Chen Xizhe, 1998) is very much, but all this methods have default. There is little error used the Coulomb's earth pressure theory to cohesive-less soil; about passive earth pressure of cohesive soil, reference (GB50007-2002, 2002) fits for the situation that uniformly distributed load act from top of retaining wall, about the situation that uniformly distributed load act from a distance to top of retaining wall, reference (Li Juwen, et al, 2006) gives a formula that was derivated for the calculation of active earth pressure of cohesive or non-cohesive backfill soils, but it can not consider earthquake force. To the question of retaining wall earth pressure computation, reference (Matsuo H, 1941; Mononobe N and Matsuo H., 1929; Prakash S. and Basvanna B.M., 1969; Prakash S. and Saran S., 1966) do some useful research; but the conclusion of reference (Matsuo H, 1941; Mononobe N. and Matsuo H., 1929) only can be used to cohesive-less soil; reference do some research about cohesive soil, but only fit for uniformly distributed load act from top of retaining wall (Prakash S. and Basvanna B.M., 1969; Prakash S. and Saran S., 1966). About the situation that uniformly distributed load act from a distance to top of retaining wall considering earthquake force (Figure 1), there is no precise simple computation to now. This paper based on researches (Feng et al 2007; Li Juwen. et al 2006; Prakash S., 1984), give a formula of passive earth pressure computation considering earthquake force and uniformly distributed load q acting from a distance d to top of retaining wall, do some necessary expansion to researches done by FENG et al (2007) and LI Ju-wen et al (2006).

EARTH PRESSURE ABOUT LEVEL BACKFILL SURFACE

Suppose there is a retaining wall, the angle between wall back and vertical axis is (Figure 1), the response of retaining wall to ground movement under earthquake force is like Figure 2. The backfill surface is level, from a distance d to top of retaining wall, there is uniformly distributed load q acting on the earth wedge ABC , the forces acting on earth wedge is like Figure 1. Let backfill surface is x axis, and through wall heel vertical line to x axis is y axis.

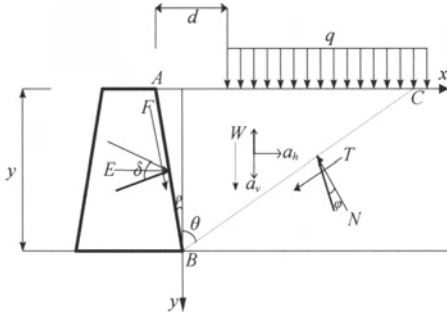


Figure 1. Force acting on the soil wedge

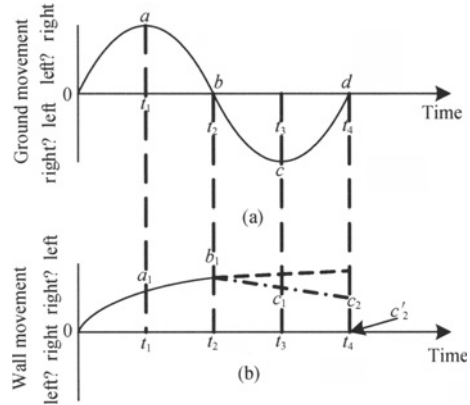


Figure 2. Response of retaining wall to ground vibration

Expression of earth wedge self-weight:

$$W = \frac{1}{2} \gamma y^2 (\tan \theta + \tan \rho) \quad (1)$$

in which: γ - earth gravity density. If horizontal acceleration of earth wedge is a_h , then earthquake force is $W a_h / g$, If vertical acceleration of earth wedge is a_v , then earthquake force is $W a_v / g$, in actual earthquake, the most infaust condition to passive earth pressure is $W a_h / g$ act to earth direction, so choose the direction that can increase earth pressure in actual (Figure 1).

Now let:
$$\frac{a_h}{g} = \alpha_h, \quad \frac{a_v}{g} = \alpha_v$$

where α_h —horizontal earthquake coefficient;
 α_v —vertical earthquake coefficient.

When the earth wedge in limit equilibrium condition, resistance of retaining wall and static earth to earth wedge is:

$$F = \frac{1}{\cos \rho} (c'y + E \tan \delta) \quad (2)$$

$$T = cl + N \tan \varphi \quad (3)$$

in which: δ - friction angle of wall back to earth, φ - inner friction angle of earth; c' - viscous force of wall back to earth, c - viscous force of earth. l - length of BC .

Resistance of retaining wall to wedge F is made of viscous resistance and friction resistance. Thinking about every kind of factor (for example: decline of wall back,

coarseness), this paper let: $\tan \delta = \eta \tan \varphi$, $c' = \eta c$, η - coefficient in 0-1. So, resistance of retaining wall back is:

$$F = \frac{\eta}{\cos \rho} (cy + E \tan \varphi) \quad (4)$$

According to situation of earth body standing force, x , y direction equilibrium formula of force is:

$$\sum y = Q + W + F \cos \rho + T \cos \theta - N \sin \theta - E \tan \rho \pm (W + Q)\alpha_v = 0 \quad (5)$$

$$\sum x = -T \sin \theta - N \cos \theta + (W + Q)\alpha_h + E + F \sin \rho = 0 \quad (6)$$

in which: Q - sum of uniformly distributed load superimposed on wedge surface, so

$$Q = qy(\tan \theta + \tan \rho) - qd \quad (7)$$

take formula (1)、(3)、(4)、(7) to equilibrium formula(5)、(6), remove N , get:

$$\frac{qy(\tan \theta + \tan \rho) - qd + \frac{1}{2}\gamma y^2(\tan \theta + \tan \rho) + cy - E \tan \rho + \eta(cy + E \tan \varphi)}{E + \eta(cy + E \tan \varphi) \tan \rho - cy \tan \theta} \rightarrow$$

$$\pm \frac{\left[\frac{1}{2}\gamma y^2(\tan \theta + \tan \rho) + qy(\tan \theta + \tan \rho) - qd \right] \alpha_v}{\left[\frac{1}{2}\gamma y^2(\tan \theta + \tan \rho) + qy(\tan \theta + \tan \rho) - qd \right] \alpha_h} = \frac{\tan \theta - \tan \varphi}{1 + \tan \varphi \tan \theta}$$

clean up then get:

$$\begin{aligned} & \left(\frac{1}{2}\gamma y^2 + qy \right) (\tan \theta + \tan \rho) \tan \varphi \tan \theta + \left(\frac{1}{2}\gamma y^2 + qy \right) (\tan \theta + \tan \rho) \\ & - qd(1 + \tan \varphi \tan \theta) - cy[\eta \tan \rho(\tan \theta - \tan \varphi) - 1 - \eta - \tan^2 \theta - \eta \tan \varphi \tan \theta] \\ & \pm \left[\frac{1}{2}\gamma y^2(\tan \theta + \tan \rho) + qy(\tan \theta + \tan \rho) - qd \right] \alpha_v (1 + \tan \varphi \tan \theta) \\ & + \left[\frac{1}{2}\gamma y^2(\tan \theta + \tan \rho) + qy(\tan \theta + \tan \rho) - qd \right] \alpha_h (\tan \theta - \tan \varphi) \\ & = [(1 - \eta \tan^2 \varphi)(\tan \theta + \tan \rho) + (1 + \eta)(\tan \varphi \tan \theta \tan \rho - \tan \varphi)] E \end{aligned}$$

so, in limit equilibrium condition, we get the force acting on retaining wall in direction x is:

$$E = \frac{1}{2} \omega \gamma y^2 + \omega qy - \zeta qd - \psi cy \quad (8)$$

where

$$\omega = \frac{(\tan \theta + \tan \rho) [1 + \tan \varphi \tan \theta - \alpha_h (\tan \theta - \tan \varphi) \pm \alpha_v (1 + \tan \varphi \tan \theta)]}{(1 - \eta \tan^2 \varphi)(\tan \theta + \tan \rho) + (1 + \eta)(\tan \varphi \tan \theta \tan \rho - \tan \varphi)}$$

$$\zeta = \frac{1 + \tan \varphi \tan \theta - \alpha_h (\tan \theta - \tan \varphi) \pm \alpha_v (1 + \tan \varphi \tan \theta)}{(1 - \eta \tan^2 \varphi)(\tan \theta + \tan \rho) + (1 + \eta)(\tan \varphi \tan \theta \tan \rho - \tan \varphi)}$$

$$\psi = \frac{\eta \tan \rho (\tan \theta - \tan \varphi) - 1 - \eta - \tan^2 \theta - \eta \tan \varphi \tan \theta}{(1 - \eta \tan^2 \varphi)(\tan \theta + \tan \rho) + (1 + \eta)(\tan \varphi \tan \theta \tan \rho - \tan \varphi)}$$

Differentiate formula(8) to θ , and let $\partial E / \partial \theta = 0$, because denominator can not be 0, numerator must be 0, can get slim craze angle corresponding to least passive earth pressure. reader can derivate it referring to Li Juwen et al (2006).

The natural condition can give great effect to soil property, and can make fissure on soil surface. This paper use uniformly distributed load replacement referring to LI Ju-wen et al (2006). Look the soil upper intension zero point as uniformly distributed load $q_0 = \gamma y_0$, the force acting on soil is like Figure 3.

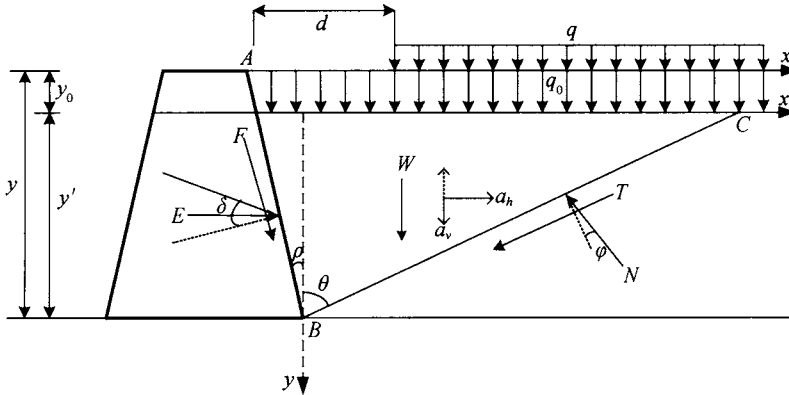


Figure 3. Forces acting on the soil with uniform load substituted

Move axis x to zero point of positive pressure intension, use x' to express, and let $q' = q + q_0$ as uniformly distributed load, $y' = y - y_0$, take to equilibrium formula(5)、(6), then

$$E = \frac{1}{2} \omega \gamma y'^2 + \omega q' y' - \zeta q d - \psi c y' = \frac{1}{2} \omega \gamma (y - y_0)^2 + \omega q' (y - y_0) - \zeta q d - \psi c (y - y_0) \quad (9)$$

where ω 、 ζ 、 ψ same as formula(8).

EARTH PRESSURE ABOUT DECLINING BACKFILL SURFACE

Suppose there is angle β between declining backfill surface to level(look Figure 4), still let backfill surface is x axis, and through wall heel vertical line to x axis is y axis, according to the forces acting on earth wedge (look Figure 4), x 、 y direction equilibrium formula of force is:

$$\sum y = (Q + W) \cos \beta + F \cos \rho + T \cos \theta - N \sin \theta - E \tan \rho + (W + Q) \alpha_h \sin \beta \pm (Q + W) \alpha_v \cos \beta = 0 \quad (10)$$

$$\sum x = -T \sin \theta - N \cos \theta + E + F \sin \rho - (Q + W) \sin \beta + (W + Q) \alpha_h \cos \beta \mp (Q + W) \alpha_v \sin \beta = 0 \quad (11)$$

where W 、 T 、 F 、 Q same as formula(1)、(3)、(4)、(7)。

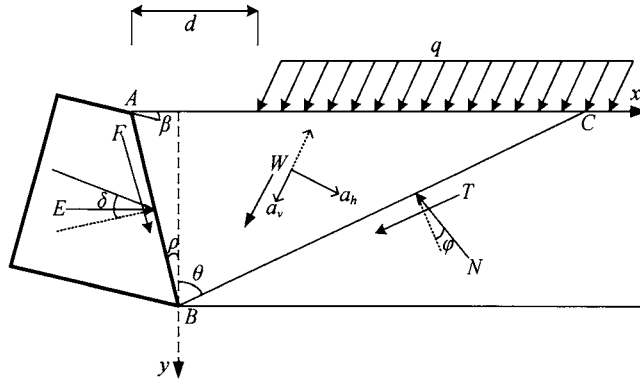


Figure 4. Forces acting on the soil wedge

so, in limit equilibrium condition, we get the force acting on retaining wall in direction x is:

$$E = \frac{1}{2} \omega \gamma y^2 + \omega q y - \zeta q d - \psi c y \quad (12)$$

in which:

$$\omega = \frac{(\tan \theta + \tan \rho)[(1 + \tan \phi \tan \theta \pm \alpha_v(1 + \tan \phi \tan \theta) - \alpha_h(\tan \theta - \tan \phi)) \cos \beta \rightarrow}{(1 - \eta \tan^2 \phi)(\tan \theta + \tan \rho) +$$

$$\leftarrow \frac{+(\tan \theta - \tan \phi + \alpha_h(1 + \tan \theta \tan \phi) \pm \alpha_v(\tan \theta - \tan \phi)) \sin \beta]}{(1 + \eta)(\tan \phi \tan \theta \tan \rho - \tan \phi)}$$

$$\zeta = \frac{(1 + \tan \phi \tan \theta \pm \alpha_v(1 + \tan \phi \tan \theta) - \alpha_h(\tan \theta - \tan \phi)) \cos \beta \rightarrow}{(1 - \eta \tan^2 \phi)(\tan \theta + \tan \rho) +$$

$$\leftarrow \frac{(\tan \theta - \tan \phi + \alpha_h(1 + \tan \theta \tan \phi) \pm \alpha_v(\tan \theta - \tan \phi)) \sin \beta}{(1 + \eta)(\tan \phi \tan \theta \tan \rho - \tan \phi)}$$

$$\psi = \frac{\eta \tan \rho(\tan \theta - \tan \phi) - 1 - \eta - \tan^2 \theta - \eta \tan \phi \tan \theta}{(1 - \eta \tan^2 \phi)(\tan \theta + \tan \rho) + (1 + \eta)(\tan \phi \tan \theta \tan \rho - \tan \phi)} \circ$$

If $\beta = 0$, formula(12) change to formula(8). Let $\partial E / \partial \theta = 0$, people can get slim craze angle corresponding to least passive earth pressure, reader can derivate it referring to Li Ju-wen et al (2006).

The natural condition can give great effect to soil property, and can make fissure on soil surface. This paper use uniformly distributed load replacement referring to Li Ju-wen et al (2006). Look the soil upper positive intension zero point as uniformly distributed load $q_0 = \gamma y_0$, the force acting on soil is like Figure 5.

Move axis x to zero point of positive pressure intension, use x' to express, and let $q' = q + q_0$ as uniformly distributed load, $y' = y - y_0$, take to equilibrium formula(10), (11), then

$$E = \frac{1}{2} \omega \gamma y'^2 + \omega q' y' - \zeta q d - \psi c y' = \frac{1}{2} \omega \gamma (y - y_0)^2 + \omega q' (y - y_0) - \zeta q d - \psi c (y - y_0) \quad (13)$$

where ω 、 ζ 、 ψ same as formula(12).

To non-cohesive soil, let $c = 0$, use above formula can solve. Reader can derivate it self.

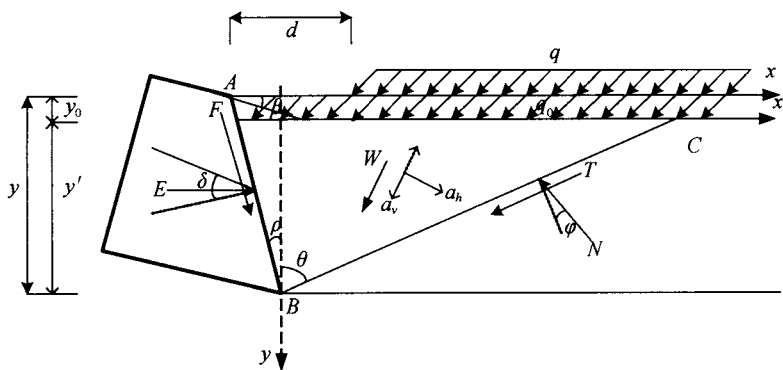


Figure 5. Forces acting on the soil with uniform load substituted

CONCLUSIONS

Based on having research conclusion, according to the Coulomb's earth pressure theory, this paper gets the following results:

- (1) Do some necessary expansion to computation formula of references (Li Juwen, et al., 2006; Prakash, et al., 1984);
- (2) The method of this paper mainly fit for cohesive soil, also fit for non-cohesive soil, especially to the situation that uniformly distributed load act from a distance to top of retaining wall considering earthquake force, use this paper's method, can make computation of passive earth pressure is feasible and simple;
- (3) This paper only can supply a approximate method to computation of earth pressure, because the factor affecting soil property is very complex;
- (4) About the question of earth pressure considering layer soil or ground water and inertial force, the author write another article to express it.

REFERENCES

- Chen Xizhe. (1998). *Soil mechanic ground and foundation*. Beijing: Tsinghua university Press, 169-200.
- Feng Zhen, Li Juwen and Wang Na. (2007). Computation of passive earth pressure of cohesive backfill on retaining wall. *Journal of Institute of Disaster-Prevention Science and Technology*, 9(2): 79-81.
- GB50007-2002 *Code for design of building foundation*.
- Li Juwen, Wang Chong, Liang Yongduo and Feng Zhen. (2006). Computation of earth pressure of cohesive backfill on retaining wall. *Chinese Journal of Geotechnical Engineering*, 28(5): 650-652.
- Matsuo H. (1941). Experimental study on the distribution of earth pressure acting on a vertical wall during earthquakes. *Japanese Society of Civil Engineers*, 27(2)
- Mononobe N., Matsuo H. (1929). On determination of earth pressure during earthquakes. *Proc. World Engineering Congress, Tokyo*.
- Prakash S., Basvanna B.M. (1969). Earth pressure distribution behind retaining walls during earthquakes. *Proc. Fourth World Conference on Earthquake Engineering*, Chile, 3: 133-148.
- Prakash S., Saran S. (1966). Static and dynamic earth pressure behind retaining walls. *Proc. Third Symposium on Earthquake Engineering*, Roorkee, 1: 277-288, November.
- Prakash S. (1984). *Soil dynamic*. Beijing: Water and Electric Power Press, 12: 91-112.

APPLICABILITY OF NEWLY-DEVELOPED INSTRUMENT FOR MICROTREMOR MEASUREMENTS TO ESTIMATE THE LOOSENED ZONE IN SHALLOW GROUND

Taiji Hanakawa, Seiji Kano

*Department of Social and Environmental Engineering, Hiroshima University
4-1, Kagamiyama 1 chome, Higashi-Hiroshima 739-8527, Japan*

Toshikazu Sawamatsu

*Independent Administrative Institution Public Works Research Institute
1-6, Minamihara, Tsukuba City, Ibaraki-Pref, Japan*

Koji Ichii

*Department of Social and Environmental Engineering, Hiroshima University
4-1, Kagamiyama 1 chome, Higashi-Hiroshima 739-8527, Japan*

After large earthquakes, slope failures induced by a small rainfall were often reported. However, such a failure could not be caused in usual situation. The reason why such failures are caused is that the instabilities of ground (looseness of ground) are caused due to a seismic motion. Such a loosened ground causes troubles in many construction cases. It is possible to estimate the looseness of the ground qualitatively, but it is hard to estimate it quantitatively. It has reported that microtremor measurement is useful for estimating looseness of ground by Seiji Kano etc. However, the conventional microtremor is not suitable to get information of shallow ground. To know the properties of shallow ground, a newly method of microtremor measurement with pile-shaped instrument has been proposed in this paper.

MICROTREMOR MEASUREMENT USING THE PROPOSED INSTRUMENT

In the conventional microtremor measurement, the microtremor is set on the ground directly and the microtremor running through the ground surface is measured. But this is not good for getting information of shallow ground. Therefore a new method using a pile-shaped instrument intruded into ground was proposed. The microtremor was measured on the top of this instrument. The stiffness of the ground supporting the pile is focused in the proposed method, and the predominant period of the ground - pile - microtremor system is observed. The predominant period of the ground - pile - microtremor system depends on the ground condition, so we think the proposed microtremor measurement can detect information about earth pressure, void ratio and so on.

DESIGN AND DEVELOPMENT OF PILE-SHAPED INSTRUMENT

The optimum shape of the proposed instrument was investigated by numerical analyses with the mass system model as shown in Figure 1. This mass system model was constituted with ground springs, pile spring, pile mass and microtremor mass. According to the specifications for highway bridges, the ground spring was calculated from the static spring as follows.

$$B_H = \sqrt{D/\beta} \quad (1)$$

$$\beta = \left(k_H D / 4EI \right)^{\frac{1}{4}} \quad (2)$$

$$k_1 = k_H \cdot B_H \cdot Le \quad (3)$$

where B_H : an equivalent loading width of foundation, D : pile diameter, β : foundation characteristics, k_H : horizontal coefficient of subgrade reaction, EI : flexural rigidity of pile, k_1 : horizontal ground springs against to pile, Le : pile length intruded into the ground. Assuming that the horizontal coefficient of subgrade reaction k_H is depth-independent and constant, and pile length in the ground is long enough, spring constant of perpendicular direction of pile axis is decided as it of head of the hinged pile, based on Hayashi-Chang concept.

The predominant period of the obtained microtremor records is used as the index of stiffness of the ground. When the ground springs k_1 is estimated by the predominant period of microtremor records with the ground - pile - microtremor system, in this research, first predominant period is used. According to results of various parametric studies, it is cleared that the predominant parameters of this system are a pile diameter D , a pile length intruded into the ground Le and microtremor mass m_2 . Based on this, the instrument that has a basic structure was developed as shown in Figure 2. Then, pile is 80cm in length, and top plate is

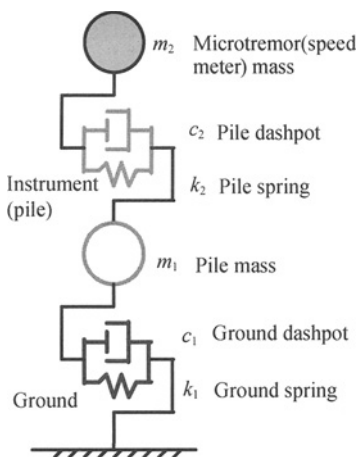


Figure 1. ground - pile - microtremor system

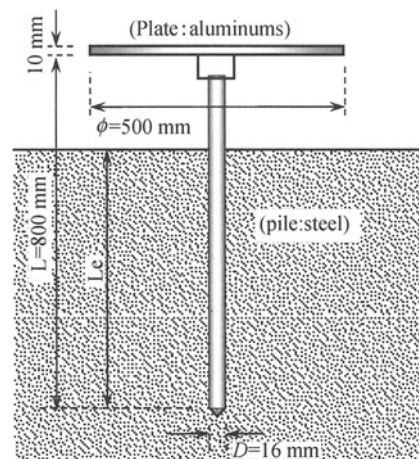


Figure 2. Newly-developed Instrument

56 N in weight. And conventional microtremor measurement was done in a place of 1m away from proposed method point for comparison. The relationships between the predominant period of this system and the elastic modulus of ground are shown in Figure 3. In this figure, ground elastic modulus was calculated using the pile length intruded into the ground and mass.

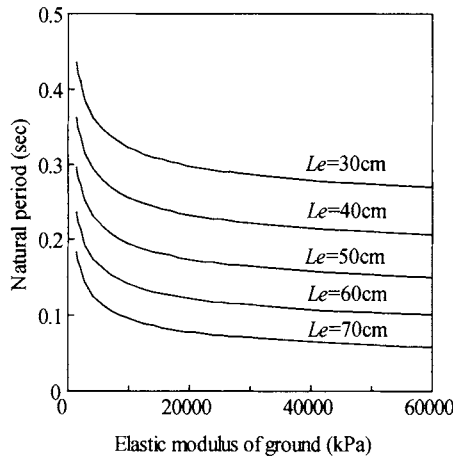


Figure 3. Relationship between elastic modulus of ground and predominant period

LABORATORY EXPERIMENT OF CHANGING GROUND CONDITIONS IN MODEL GROUND

A series of laboratory tests were conducted to examine the influence of decreasing of earth soil pressure on microtremor measurement. Figure 4 shows the test equipments. Model ground was compacted with 6 size siliceous sand in acrylic chamber. Stick balloons were set inside the chamber to reduce the lateral earth pressure.

At first, the pile instrument was penetrated. And microtremor measurements with the pile instrument were conducted before. Then the balloons were deflated in order to decrease the lateral pressure. After that, the microtremor was measured again. To check the decreasing of lateral pressure, strain gauges were put on the outside wall of chamber. In these tests, pile that its diameter D is 1.6cm and is 50 cm in length was used. The pile was penetrated in 30 cm. Table 1 shows test conditions.

Ground settlement induced by deflating balloons was not observed. It means that ground moved to balloons area horizontally.

Figure 5 shows Fourier spectrum in the north-south direction of microtremor was measured with newly-developed instrument. It was found that the predominant period changed to longer with the change of the volume strain.

Figure 6(a) shows the distribution of the volumetric strain. According to this, it is found that the volumetric strain became larger in the deeper position except the 0.4m.

In the case that both inside pressure and outside pressure were acted, the radial stress is derived as following equation (4) (Timoshenko and Goodier).

$$\sigma_{\theta} = -\frac{r_i^2 (P_o - P_i)}{r_o^2 - r_i^2} + \frac{P_i r_i^2 - P_o r_o^2}{r_o^2 - r_i^2} \quad (4)$$

σ_{θ} : a radial stress at the outside of the cylinder, r_i , r_o : an inner and outer diameter, p_i , p_o : an inside and outside pressure. In this study, outside pressure, p_o is zero and inside pressure, p_i is lateral earth pressure. Figure 6(b) shows the distribution of lateral earth pressure calculated by formula (4) and strains. The theoretical overburden pressure without the friction of the cylinder surface is also shown in this figure.

Figure 6(c) shows the coefficient of earth pressure calculated from the earth pressure, the strain and the theoretical overburden pressure without the friction. It is cleared that the coefficient of earth pressure was decreased when the balloons were deflated.

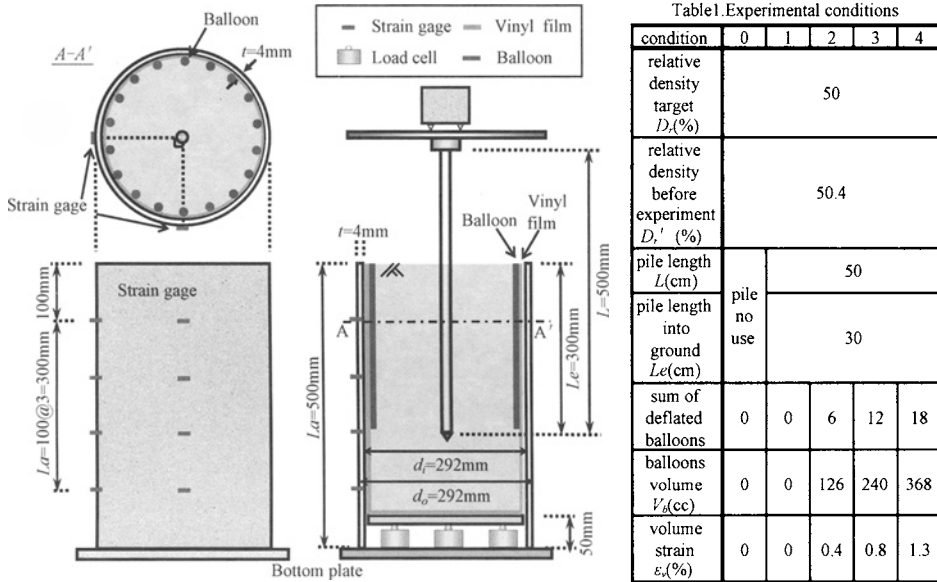


Figure 4. Experiment

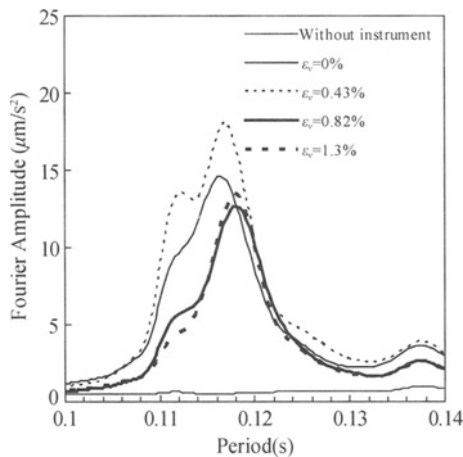


Figure 5. Fourier spectrum of the microtremor records

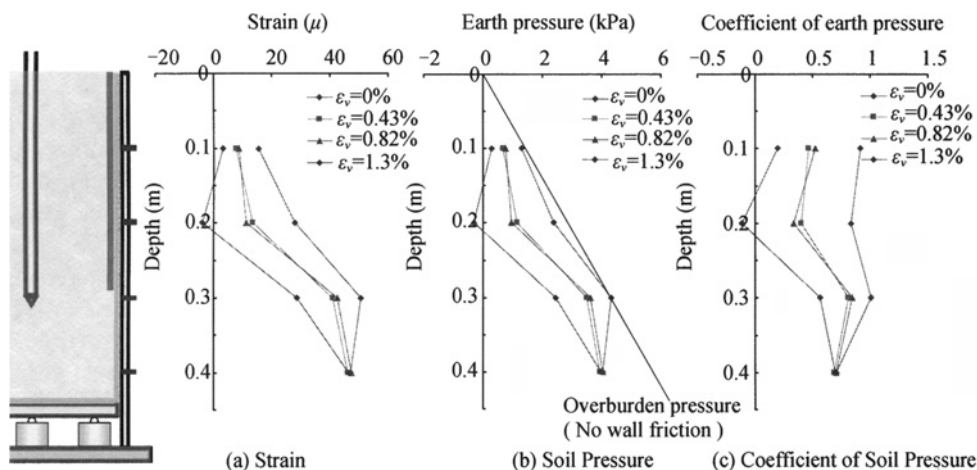


Figure 6. Distribution of depth component of strain, soil pressure, and coefficient of soil pressure

Figure 7 shows the relationships between the coefficient of earth pressure and the measured predominant period. It is found that the predominant period changed to longer when the coefficient of earth pressure became smaller.

Therefore, it was cleared that the decreasing of the earth pressure can be observed by microtremor measurement with newly-developed instrument.

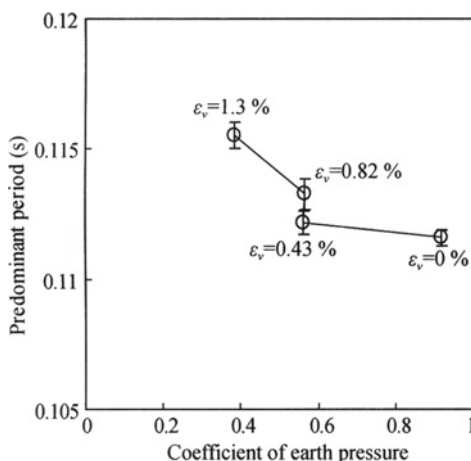


Figure 7. Relationship between the predominant period and the coefficient of soil pressure

FIELD TESTS ON EVALUATION OF AN APPLICABILITY OF THE PROPOSED METHOD

The field tests using the proposed technique were conducted in order to examine its applicability. The field tests were carried out as follows.

Simplified penetration test was conducted to know the ground strength first. After the penetration test, the pile of the proposed equipment was intruded into the ground and microtremor was measured by using this system. To compare with it, the microtremor on the ground was also measured near the equipment.

The ground excavation was conducted to 1m depth and the ground was backfilled again. After the backfilling, the simplified penetration test was conducted to know the ground strength near the equipment. Then the microtremor with and without the proposed pile equipment were measured. In the second excavation, the ground was backfilled by tamping. Figure 8 shows the method of field tests. Figure 9 shows the Fourier spectrum of microtremor measurement with the proposed method. The periods were converted into the value at 30cm penetration of the equipment in this figure. It is found from this that the predominant periods were varied with the ground conditions.

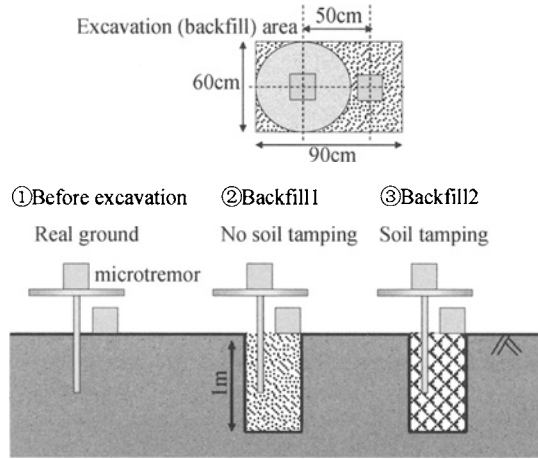


Figure 8. Experimental overview

Figure 10 shows the predominant periods before excavation and after backfilling. In this figure, the numbers near the marks are average value of N_d -value from top to 50cm depth. It is clarified from this figure that the predominant periods becomes longer when the ground strength becomes smaller.

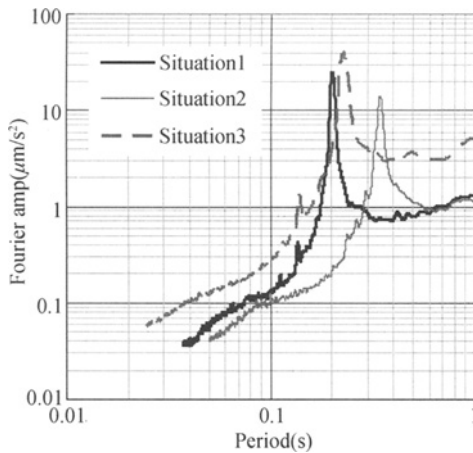


Figure 9. Fourier amplitude spectrum of microtremor measurement with instrument

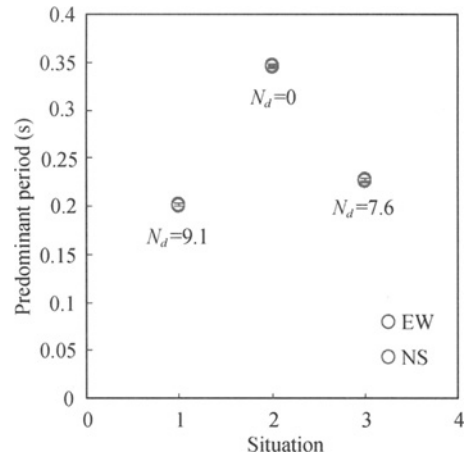


Figure 10. Peak of Fourier amplitude spectrum and foundation strength (N_d -value) in 3 pattern ground conditions

This result indicates that the predominant period of microtremor measurement with the equipment becomes longer when the ground is loosened. It can be said that this proposed method with the equipment is available to evaluate the ground strength.

CONCLUSIONS

1. To obtain the properties of a shallow grounds, a newly method of microtremor measurement with pile-shaped instrument has been proposed in this paper. This method uses the vibration characteristics that depend on the stiffness of the ground supporting the pile.
2. According to the results of microtremor measurement in the field tests and laboratory tests, very remarkable peak in the Fourier spectrum is observed by using pile-shaped instrument.
3. Decreasing of earth pressure could be detected by microtremor measurement with newly-developed instrument in laboratory tests.
4. According to the results of field tests, it was confirmed that the predominant period from microtremor measurement with this instrument became longer when the ground strength became smaller.

Therefore the proposed microtremor measurement using newly-developed instrument is available to know the looseness of shallow ground by monitoring the change of predominant period.

REFERENCES

- Timoshenko S. and Goodier J.N. Theory of elasticity 2nd edition. *Kogakusya Company, Ltd*, 55-60.
- Seiji Kano. (2004), Microtremor measurement at the ridge and the estimation of loosened zone in foundation due to an earthquake. *Proceedings of the 49th geotechnique symposium*, 407-414.
- The Japanese Geotechnical Society (2000). *Shinpen Tsuchi to kiso no sekkei keisann ennsyuu*. 96-112. (in Japanese).

EXPERIMENTAL STUDY ON THE RELATIONSHIP BETWEEN DEGREE OF SATURATION AND P-WAVE VELOCITY IN SANDY SOILS

Munenori Hatanaka

*Department of Architectural and Civil Engineering, Chiba Institute of Technology, Professor,
2-17-1, Tsudanuma, Narashino, Chiba 275-0016, Japan*

Takemi Masuda

*Department of Architectural and Civil Engineering, Chiba Institute of Technology, graduate
student, 2-17-1, Tsudanuma, Narashino, Chiba 275-0016, Japan*

A series of laboratory tests were performed to investigate the effects of the size and roundness of soil particles, relative density, and air bubbles in pore water within sandy soils on the relationship between the degree of saturation (S_r) and P-wave velocity (V_p). We also considered the effect of the degree of saturation on the liquefaction strength of sand. We arrived at the following conclusions based on the test results: (1) the size of soil particles in sand has a strong influence on the B -value- V_p relationship, but a weak influence on the S_r - V_p relationship; the P-wave velocity increases rapidly with increasing degree of saturation from 90 to 100 % for all tested sands; (2) relative density (D_r) has a negligible effect on the S_r - V_p relationship; (3) air bubbles in pore water have a significant effect on both the B -value- V_p relationship and S_r - V_p relationship; (4) based on comparisons of the liquefaction strengths obtained in undrained cyclic triaxial tests on Futtsu sand, we propose that the method of reducing the degree of saturation by injecting air bubbles into sandy ground will prove to be a useful method in terms of mitigating disasters induced by the liquefaction of sand.

INTRODUCTION

Most of the liquefaction countermeasures used in practice are difficult to utilize in situations with pre-existing structures. In such cases, two approaches may be employed in reducing the degree of saturation as a countermeasure to liquefaction: to pump up ground water, or inject air bubbles into the ground. The former method has an inherent disadvantage in that it induces settlement of the foundation and surrounding ground.

The objective of this study is to investigate the potential of the latter method, i.e., increasing liquefaction strength by reducing the degree of saturation of the ground via the injection of air bubbles. Three basic technologies are required to develop this method to completion: i) a technology to generate air bubbles of a suitable size and amount, and to inject the bubbles into the ground without disturbing the structure of in situ soils; ii) a

technology to evaluate the degree of saturation of in situ sandy soils; and iii) a technology to evaluate the liquefaction strength from the degree of saturation. In this paper, the last two of these technologies were investigated.

The background to the development of the second of the above technologies is as follows. It is difficult to precisely evaluate the degree of saturation for in situ soils that lie beneath the water table because of difficulties in accurately measuring the in situ dry density and water content. In the present study, V_p was investigated as an index property to estimate the degree of saturation of in situ soils. In previous studies, useful correlations between the degree of saturation and the P-wave velocity have been observed in laboratory tests using Toyoura sand (Tamura et al. 2002; Yongnan et al. 1999); however, the applicability of such a correlation to other kinds of in situ sands with different sizes and shapes of soil particles, relative densities, and conditions of pore water remain unknown. The present study investigates the effects of the size and roundness of soil particles, relative density, and pore water characteristics on the relationship between the degree of saturation and P-wave velocity.

The background to the development of the third technology is as follows. Many studies describe the effect of the degree of saturation on the liquefaction strength using reconstituted samples such as Toyoura sand (e.g., Soga et al. 2005); however, the applicability of such quantitative correlations between the degree of saturation and liquefaction strength to in situ sandy soils has yet to be demonstrated. In the present study, we conducted tests using undisturbed samples obtained by the in situ freezing sampling method. Based on these test results, we consider the potential of the method in terms of mitigating disasters induced by sand liquefaction by injecting air bubbles into the ground.

TEST METHOD AND TEST SAMPLES

Test samples of 100 mm in height and 50 mm in diameter were prepared using an air pluviation method to ensure a specified relative density. Test samples were then isotropically consolidated at a cell pressure of 50 kN/m². Thereafter, a specified pore water was poured into the test samples through a burette, and the P-wave velocity was measured for each degree of saturation. The degree of saturation of test samples was controlled by the difference of the water head between the test sample and the burette, and also by the back pressure. A back pressure (maximum of 800 kN/m²) was used to obtain a high degree of saturation.

Figure 1 provides an outline of the system used to measure the P-wave velocity. The bender elements were used to both generate and receive P-waves with a sinusoidal form and frequency range of 5,000 to 150,000 Hz. Figure 2 shows a typical time history of a P-wave for both transmitted and received waves. The P-wave velocities were determined based on the sample height and the time lag between the transmitted and received waves.

We tested four kinds of sand (Toyouura sand, Futtsu sand, Keisa-sand No. 2, and Keisa-sand No. 3), three relative densities ($D_r=45\%$, 55% and 70%), and three kinds of pore water (tap water, de-aired water, and groundwater). Table 1 lists the test parameters.

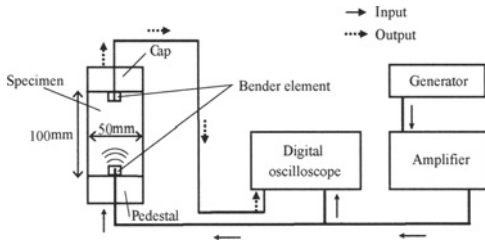


Figure 1. P-wave measurement system

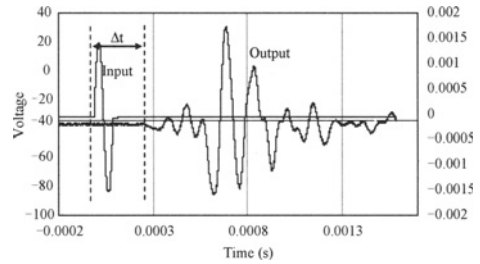


Figure 2. Typical P-wave time history

Table 1. Test parameters

Sample name	Toyoura sand			Futtsu sand		Keisa-sand No.2	Keisa-sand No.3	
	Relative density(%)	70	70	70	45	70	70	55
Pore water	Tap water	De-aired water	Groundwater	Tapwater	Tapwater	Tapwater	Tapwater	Tapwater
Backpressure (Kn/m ²)	400	850	800	850	850	500	600	700
Confining pressure (kN/m ²)	50							

TEST RESULTS

Effects of the size and roundness of soil particles on the relationship between the degree of saturation and P-wave velocity

Figure 3 shows the B -value- V_p relationships for samples with a relative density of 70% and tap water as pore water. Also shown are the mean grain size (D_{50}), the uniformity coefficient (U_c), the roundness coefficient (R_c) of tested samples, and the test results reported by Tamura et al. (2002). The B -value- V_p correlation obtained in the present study for Toyoura sand agreed well with those presented by Tamura et al., except for the lower range of B -values. The P-wave velocity increases with increasing B -value for all tested sands; however, the quantitative B -value- V_p correlation depends on the type of sand. Fine sand, such as Toyoura sand and Futtsu sand, shows a continuous relationship, whereas Keisa-sand No. 2 and Keisa-sand No. 3 show a discontinuous relationship at a B -value of approximately 0.6. The discontinuity in the B -value- V_p relation reflects the effects of grain size and shape.

Figure 4 shows the degree of saturation (S_r)- V_p relationships determined for each sample, along with the test results presented by Yongnan et al. (1999). All of the samples show similar quantitative relationships between S_r and V_p , indicating negligible effects of the size and roundness of soil particles on the S_r - V_p relationship. All of the samples show the same tendency in that the P-wave velocity increases rapidly from 90 % saturation. The observed differences between the B -value- V_p relation and the S_r - V_p relation may reflect differences in the sensitivity of the B -value at high degrees of saturation.

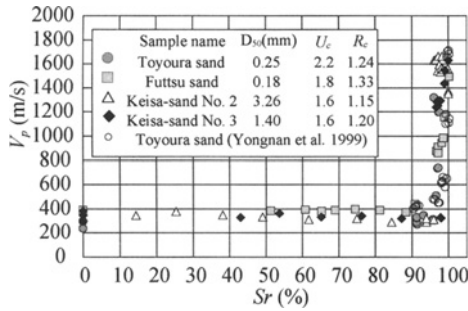


Figure 3. Effects of the size and roundness of soil particles on the B -value- V_p relationship

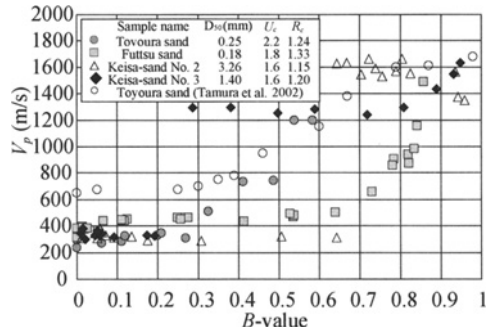


Figure 4. Effects of the size and roundness of soil particles on the Sr - V_p relationship

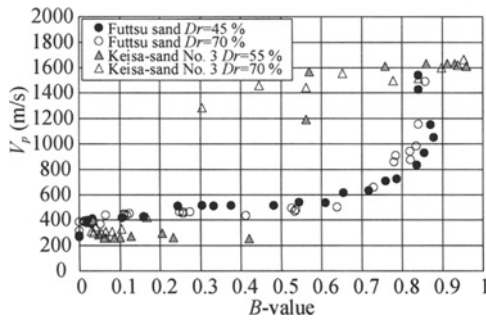


Figure 5. Effects of relative density on the B -value- V_p relationship

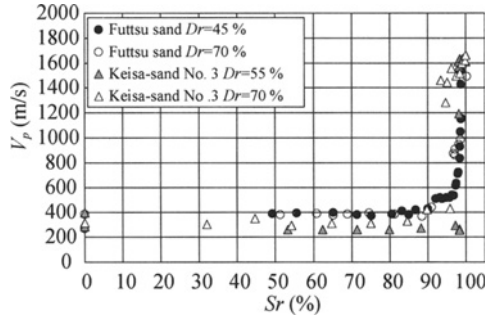


Figure 6. Effects of relative density on the Sr - V_p relationship

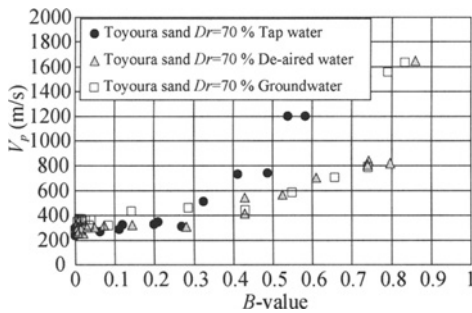


Figure 7. Effects of air bubbles in pore water on the B -value- V_p relationship.

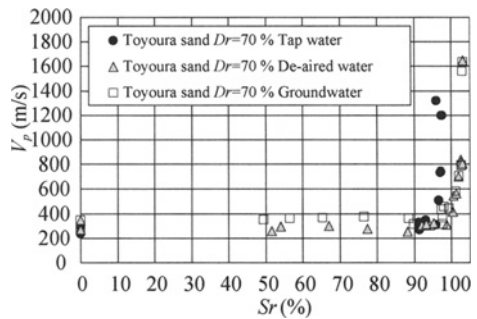


Figure 8. Effects of air bubbles in pore water on the Sr - V_p relationship

Effects of relative density on the relationship between degree of saturation and P-wave velocity

Figure 5 compares the B -value- V_p relationships for both Futtsu sand (relative density(Dr) =45 % and 70 %) and Keisa-sand No. 3 (Dr =55 % and 70 %). The results indicate that the effects of relative density are minor.

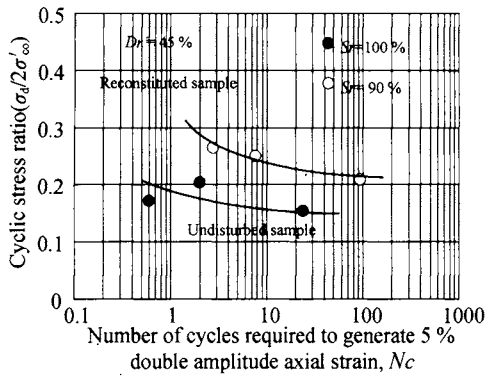


Figure 9. Liquefaction strength curves (Futtsu sand)

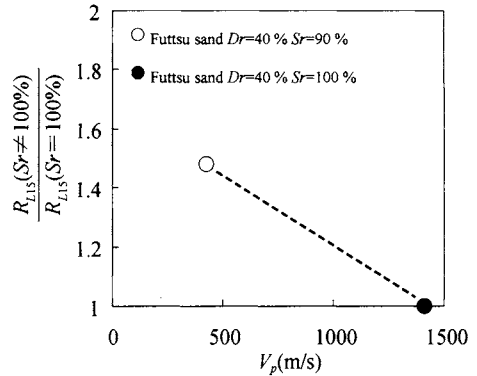


Figure 10. Relationship between the liquefaction strength ratio and P-wave velocity (Futtsu sand)

Figure 6 shows equivalent data for the $Sr-V_p$ relationship. The effects of relative density on the $Sr-V_p$ relationships are minor. Again, the P-wave velocity showed a rapid increase from 90 % saturation.

Effects of pore water characteristics on the relationship between degree of saturation and P-wave velocity

Figure 7 shows the B -value- V_p relationships of Toyoura sand with a relative density of 70 % for different kinds of pore water (tap water, de-aired water, and ground water). The use of de-aired water and ground water yields similar quantitative B -value- V_p relationships. The test results suggest that the ground located deeper than the ground water level is almost fully saturated. In contrast, the use of tap water yielded a different quantitative relationship: air bubbles in the pore water had a pronounced effect on the B -value- V_p relationship. The details of this effect are the focus of ongoing study.

Figure 8 shows the effects of air bubbles in pore water on the $Sr-V_p$ relationship, showing a similar trend to that for the B -value- V_p relationship.

Effects of the degree of saturation on liquefaction strength

The results of liquefaction tests of Futtsu sand are shown in Figure 9. The test samples with 90 % saturation are reconstituted samples, and the test data with 100 % saturation were obtained from undisturbed samples recovered by the in situ freezing sampling method (Hatanaka et al. 2006). Both sets of test results were obtained via undrained cyclic triaxial tests. The initial effective confining stress was 50 kN/m^2 , the relative density was about 45 %, and the frequency of the cyclic stress was 0.1 Hz. The liquefaction strength of the samples with 90 % saturation was approximately 1.5 times that of the fully saturated samples (Figure 9).

Figure 10 shows the relationship between the liquefaction strength ratio (the ratio of the liquefaction strength with any degree of saturation below 100 % to that of fully saturated

samples) and the P -wave velocity of Futtsu sand. A decrease in V_p from 1500 to 400 m/s brought about an approximately 50 % increase in liquefaction strength.

CONCLUSIONS

Based on a series of laboratory tests, we obtained the following conclusions.

- (1) The effect of the size of soil particles of sand on the $Sr-V_p$ relationship is minor.
- (2) The effect of relative density on the $Sr-V_p$ relationship is negligible. For all tested sands, the P -wave velocity increased rapidly with increasing degree of saturation from 90 to 100 %.
- (3) Air bubbles in pore water have a significant effect on both the B -value- V_p relationship and the $Sr-V_p$ relationship.
- (4) A decrease in V_p from 1500 to 400 m/s brought about an approximately 50 % increase in liquefaction strength.

Based on the above test results, the method of injecting air bubbles into sandy ground to decrease the degree of saturation is expected to be a useful method in mitigating disasters induced by the liquefaction of sand.

REFERENCES

- Hatanaka M., Abe A. and Masuda T. (2006). Effect of degree of saturation on the liquefaction strength of in-situ sandy soils. *Proceeding of the 4th Asian Joint Symposium on Geotechnical and Geo-Environmental Engineering*, 1: 59-62.
- Soga Y., Okamura M. and Yatabe R. (2005). Liquefaction resistance of a partially saturated sand with reference to air compressibility. *Proceedings of the 40th Annual Meeting of JGS*, 511-512. (in Japanese)
- Tamura S., Tokimatsu K., Abe A. and Sato M. (2002). Effects of air bubbles on B -value and P -wave velocity of a partly saturated sand. *Soils and Foundations*, 42(1): 121-129.
- Yongnan H., Hisashi T. and Kenji I. (1999). Estimation of partial saturation effect on liquefaction resistance of sand using P -wave velocity. *Symposium on Liquefaction Mechanism Prediction and Design Method*, 430-434. (in Japanese)

EFFECTS OF ANISOTROPIC CONSOLIDATION AND INITIAL SHEAR LOAD ON LIQUEFACTION RESISTANCE OF SAND IN SIMPLE SHEAR CONDITION

Yasuyo Hosono

*Department of Architecture and Civil Engineering, Toyohashi University of Technology
Hibarigaoka 1-1, Tempaku-cho, Toyohashi-shi, Aichi 441-8580, Japan*

Mitsutoshi Yoshimine

*Department of Civil and Environmental Engineering, Tokyo Metropolitan University
Minami-Osawa 1-1, Hachioj-shii, Tokyo 192-0397, Japan*

Undrained triaxial test is commonly used in laboratory for evaluating liquefaction resistance of sand. The principal stress components are fixed vertical and horizontal in triaxial tests, thus it is impossible to examine the effects of initial consolidation stress ratio ($K_c = \sigma_h / \sigma_v$) and initial stress ratio ($\alpha = \tau / \sigma_v$) independently. This study utilized hollow cylindrical specimen and mutual effects of these two stress conditions are researched in detail. The outer and inner diameter of the hollow specimens were maintained constant during undrained cyclic loading to realize exact simple shear condition. It was found that the liquefaction resistance ratio to the initial vertical stress increased with increasing consolidation stress ratio (K_c) and initial stress ratio (α). It was also shown that the effect of initial stress ratio (α) was smaller for larger initial consolidation stress ratio (K_c).

INTRODUCTION

Previously the authors compared undrained behaviors of sand in triaxial compression and triaxial extension tests under monotonic loading conditions, and we found that the two responses were completely different from each other (Yoshimine et al., 1998; Yoshimine & Hosono, 2000, 2001; Yoshimine et al., 1999). In the triaxial tests, it was observed that the undrained shear behavior of sands was dilative and highly stiff in triaxial compression tests, whereas considerably large excess pore water pressure was developed and the behavior was much softer in triaxial extension tests under monotonic loading conditions for the same materials of the same density. In addition, we also compared undrained behaviors of sand with different initial shear stress in triaxial cyclic tests, and it was shown that the liquefaction strength was strongly affected by the direction of the initial share stress. Cyclic strength of sandy soils has been generally evaluated by means of the undrained cyclic triaxial test in which triaxial compression and extension are repeatedly applied on the specimen. These stress conditions repeated in the cyclic triaxial tests are the two extremes in terms of the direction of maximum principal stress and the magnitude of intermediate principal stress, which are scarcely true in real ground.

Initial static torsional shear stress ($\tau_s = \tau_{ini}$) was also applied to the specimens during consolidation. The ratio of torsional static shear stress to the vertical effective stress was $\alpha = \tau_{ini} / \sigma'_{v\ ini} = 0$ to 0.4.

After waiting about one hour to complete consolidation, the specimen was subjected to cyclic torsional shear load with constant amplitude under undrained simple shear condition with constant volume of the inner confining cell and constant height of the specimen, as afore mentioned. Initial liquefaction was defined by either excess pore water pressure ratio of 1.0 or residual torsional strain of 5 % that was achieved earlier than another, and the number of cycles causing initial liquefaction was recorded. The testing conditions for the simple shear tests were summarized in Table 1.

Table 1. List of undrained cyclic simple shear tests

test No.	Relative Density, D_r (%)	Initial stress state					Cyclic stress ratio, $\tau_d / \sigma'_{v\ ini}$	Number of cycles causing initial liquefaction, N
		$\sigma'_{v\ ini}$ (kPa)	σ'_h (kPa)	τ_{ini} (kPa)	$K_c = \sigma'_h / \sigma'_{v\ ini}$	$\alpha = \tau_{ini} / \sigma'_{v\ ini}$		
HC013	39.1	200	100	0	0.5	0	0.13	125
HC015	38.1	200	200	0	0.5	0	0.20	7
HC017	42.4	200	100	40	0.5	0.2	0.18	80
HC018	41.6	200	100	40	0.5	0.2	0.20	20
HC019	39.2	100	50	40	0.5	0.4	0.38	30
HC027	39.7	100	50	30	0.5	0.3	0.35	2
HC032	40.5	100	50	30	0.5	0.3	0.3	14.75
HC037	42.1	100	50	20	0.5	0.2	0.29	6.25
HC038	40.8	100	50	30	0.5	0.3	0.25	>1700
HC046	40.3	100	100	0	1.0	0	0.35	2.5
HC048	39.7	100	100	0	1.0	0	0.2	18.5
HC049	40.8	100	100	0	1.0	0	0.19	17.5
HC051	39.7	200	50	0	0.25	0	0.14	4.5
HC052	40.3	200	50	0	0.25	0	0.08	25
HC055	41.1	100	50	0	0.5	0	0.19	10
HC056	40.3	200	50	0	0.25	0	0.07	136
HC069	39.7	100	150	0	1.5	0	0.22	161
HC070	42.4	100	150	0	1.5	0	0.27	23
HC073	41.3	50	200	0	4.0	0	0.38	105
HC074	40.8	100	150	0	1.5	0	0.30	22
HC077	41.3	50	200	0	4.0	0	0.40	54
HC078	41.1	50	200	0	4.0	0	0.44	16
HC079	40.0	50	100	0	2.0	0	0.31	18
HC096	40.8	100	100	0	1.0	0	0.30	3
HC097	39.5	100	100	0	1.0	0	0.16	71
HC103	40.3	100	100	10	1.0	0.1	0.21	24
HC104	39.2	100	100	10	1.0	0.1	0.24	9.5
HC105	41.8	100	100	10	1.0	0.1	0.31	3.5
HC106	43.2	100	100	20	1.0	0.2	0.23	12
HC107	42.9	100	100	20	1.0	0.2	0.2	30.75

TESTS RESULTS

Results of the simple shear tests

Firstly examples of time history of the direction of maximum principal stress and intermediate principal stress coefficient during undrained cyclic simple shear loading are shown in Figures 2, because these stress parameters have been shown to have strong effects on the undrained shear behavior of sands (Yoshimine et al., 1998; Uthayakumar and Vaid 1998; Nakata et al., 1998). Such an accurate measurement of stress conditions is one of the most prominent features of this series of simple shear tests. The time histories of the torsional shear stress $\tau_d = \sigma_{z\theta}$, the direction of the maximum principal stress from the vertical α_σ , and the intermediate principal stress coefficient b were plotted in this figure. If there was no static torsional shear stress, the direction of σ_1 was vertical ($\alpha_\sigma = 0$) and the magnitude of σ_2 was equal to σ_3 ($b = 0$) at the initial anisotropic consolidation that is exactly the same as the triaxial compression state. Then the amplitude of α_σ was increased with accumulation of cycles, and it became about $\pm 40^\circ$ at initial liquefaction and the following larger deformation. The b -value was also increased from 0 and settled around 0.3 when liquefaction was achieved. The specimens consolidated under the initial shear stress with larger α and K_c values also showed the same tendency of α_σ and b after liquefaction. Thus it may be said that the same stress condition that is characterized by parameters $\alpha_\sigma = 40^\circ$ and $b = 0.25$ to 0.3 was mobilized at larger undrained deformation during cycle shear loadings irrespective to the magnitude of initial static shear stress levels. The same values of stress parameters were observed in monotonic loading condition in simple shear tests of the previous studies (Yoshimine et al. 1998, 1999a). In the case of tests with initial shear stress, the shear strain was accumulated into the same direction of the initial shear.

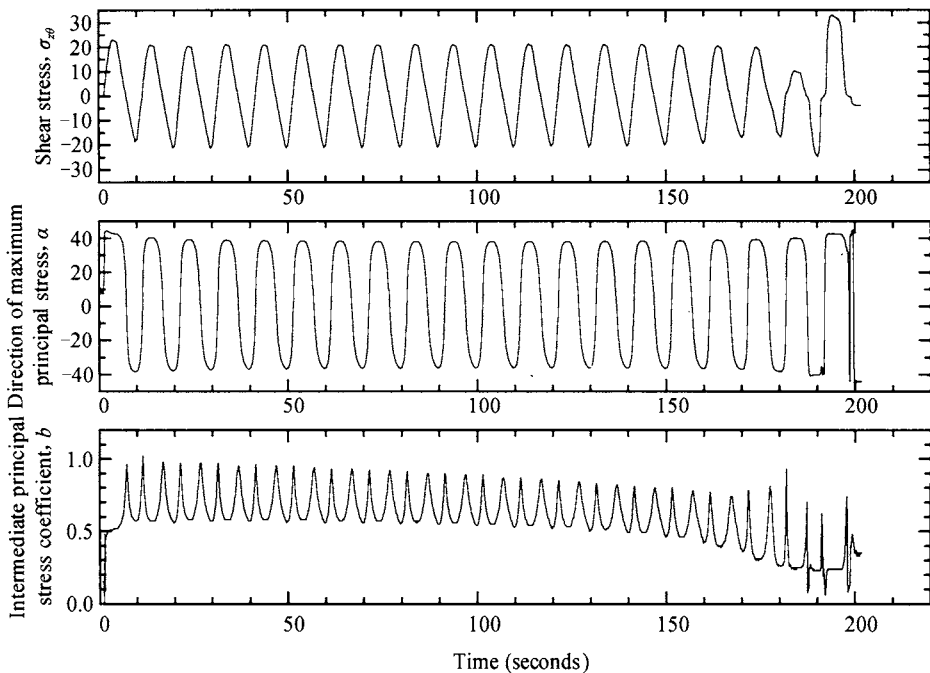


Figure 2. Typical result of cyclic simple shear test without initial static shear stress ($\alpha = 0$)

All of the cyclic simple shear tests were summarized and the cyclic stress amplitude was plotted versus number of cycles for initial liquefaction on Figure 3. It can be seen that the resistance for liquefaction at $N = 20$ increased by application of initial shear stress. When the initial shear stress ratio of $\alpha = 0.1, 0.3$ were applied on the specimens, the strength of liquefaction were 1.1 times, and 1.3 times larger than the strength of liquefaction without initial shear stress, respectively. Data from the undrained cyclic triaxial tests were also plotted on this figure. The liquefaction strength evaluated from the simple shear tests was slightly larger than that of from triaxial tests. In the same way, the liquefaction strength curves of the sand with several levels of initial anisotropic consolidation stresses were shown in Figure 4. The initial consolidation stress ratio K_c also influenced the liquefaction strength. When the initial consolidation stress ratio of $K_c = 0.25, 0.5, 1.5, 2.0, 3.0, 4.0$ were applied on the specimens, the strength of liquefaction were 0.5 times, 0.8 times, 1.4 times, 1.5 times, 1.9 times and 2.2 times larger than the strength of the isotropically consolidated sample, respectively.

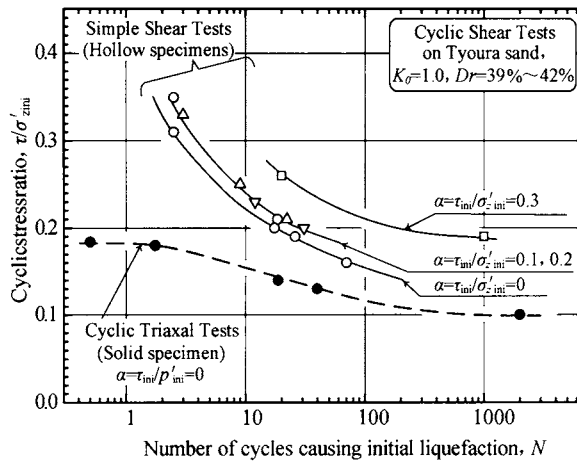


Figure 3. Effect of initial shear stress on the liquefaction strength

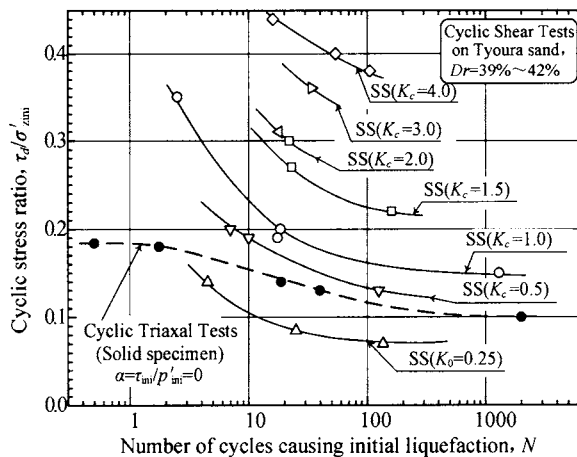


Figure 4. Effect of consolidation stress ratio on the liquefaction strength

Combined effect of the initial shear stress and the initial anisotropic consolidation

Cyclic strength correction factor, namely $K_a = CSR(\alpha) / CSR(0)$, is plotted in Figure 5, where $CSR(\alpha)$ is the liquefaction strength of sand under initial shear stress ratio of α , and $CSR(0)$ is the strength of sand without initial shear stress. From this figure, it is understood that the cyclic strength correction factor is larger for larger initial shear stress conditions as well as larger K_c -value. The result from triaxial tests is also indicated on Figure 5. To visualize the combined and mutual effects of initial shear stress and initial anisotropic consolidation, contour lines of strength correction factor is plotted in Figure 6, where K_{α,K_c} is given by $K_{\alpha,K_c} = CSR(\alpha, K_c) / CSR(0, 1)$.

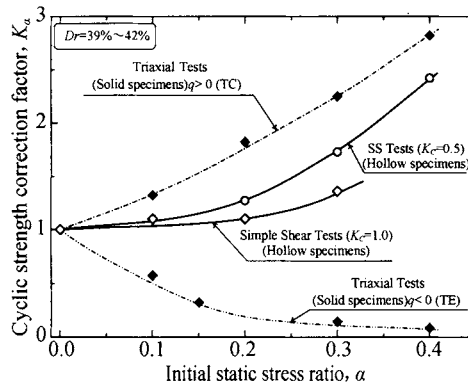


Figure 5. Effect of initial shear stress ratio on the strength correction factor

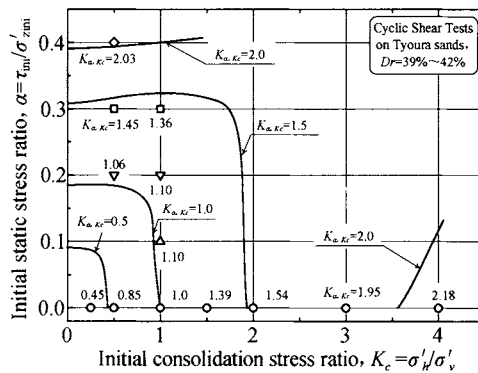


Figure 6. Effect of combined effect of K_c and α on the strength correction factor

From this figure, it is understood that the liquefaction resistance became larger with larger K_{α,K_c} value as the increasing initial shear stress within the range of smaller value of K_c . On the other hands, within the range of larger value of K_c , the contour lines of K_{α,K_c} are more or less vertical which indicate that the discrepancy of the liquefaction resistance due to the difference of initial shear stress is little.

CONCLUSION

The undrained simple shear tests were conducted by means of hollow cylindrical torsion shear apparatus, and the mutual effects of anisotropic consolidation and initial shear stress conditions are researched in this study. It was found that the cyclic liquefaction resistance ratio to the initial vertical stress increased with increasing consolidation stress ratio (K_c) and initial stress ratio (α). It was also shown that the effect of initial stress ratio (α) was smaller for larger initial consolidation stress ratio (K_c).

REFERENCES

- Hosono H., Yoshimine M.(2003). Liquefaction of sand in simple shear condition. *Cyclic Behaviour of Soils and Liquefaction Phenomena*, 129-136.
- Nakata Y., Hyodo M., Murata. S. and Yasufuku N.(1998). Flow deformation of sands subjected to principal stresses rotation. *Soils and Foundations*, 38(2): 115-128.
- Pradhan B.S., Tatsuoka F. and Horii N.(1988). Simple shear testing on sand in a torsional shear apparatus. *Soils and Foundations*, 28 (2): 95-112.
- Riemer M.F., Seed H.B.(1997). Factors affecting apparant position of steady-state line. *Journal of Geotechnical and Geoenvironmental Engineering*, 123 (3): 281-288.
- Uthayakumar M., Vaid Y.P.(1998). Static liquefaction of sands under multiaxial loading. *Canadian Geotechnical Journal*, 32(2): 273-283.
- Yoshimine M., Hosono Y.(2000). Effect of anisotropy of sand on results of undrained triaxial test. *Memoirs of Graduate School of Engineering, Tokyo Metropolitan University*, 50: 158-169.
- Yoshimine M., Hosono Y.(2001). Effects of anisotropy of sand on the liquefaction resistance evaluated by triaxial tests. *The Second Japan-Philippine Workshop on Safety and Stability of Infrastructure against Environmental Impacts*, Diliman, Manila, Philippines, 133-142.
- Yoshimine M., Ishihara K.(1998). Flow potential of sand during liquefaction. *Soils and Foundations*, 38 (3): 187-196.
- Yoshimine M., Ishihara K. and Vargas W. (1998). Effects of principal stress direction and intermediate principal stress on undrained shear behavior of sand. *Soils and Foundations*, 38 (3): 177-186.
- Yoshimine M., Robertson P.K. and Wride C.E.(1999). Undrained shear strength of clean sands to trigger flow liquefaction. *Canadian Geotechnical Journal*, 36 (5): 891-906.

THE RESEARCH ON DYNAMIC RHEOLOGICAL MECHANICAL RESPONSE AND RHEOLOGICAL DYNAMIC MODEL OF GEOLOGICAL DISASTER OF SOFT ROCK-SOIL

Hua Hu, Hengxing Gu and Dengrong Yu
*College of Architecture and Civil Engineering, Xiamen University,
Xiamen 361005, China*

The practice and theoretic analysis indicate that the dynamic loading (such as earthquake, tsunami, raging billow, vibration) are the important factor and mainly power of inducing geological disaster of soft rock-soil. The objective factors (such as climate and weather, Geotechnical Engineering and geological terms, landform and physiognomy, the disturbness of building project) and inducing power of bursting out geological disaster in our country are analyzed and summarized. The research countermeasure of rheological dynamics of geological disaster of soft rock-soil is put forward, the research clue and potential application are discussed. The rheological mechanics response and rheological parameters of soft rock-soil are tested and analyzed under dynamic loading, the viscoelastic-plasticity rheological dynamic model is established, and new rheological equation is deduced. The research results settle better foundation for us to research deeply critical mechanics terms of bursting out geological disaster and dynamic key indexes of forecast geological disaster. All these have important theory and actual signification for us to reveal the rheological dynamic mechanism of bursting out Geotechnical Engineering and geological disaster under dynamic loading, perfect the monitoring theory of disaster, improve the science and veracity of forecasting.

INTRODUCTION

The objective factors such as landform and physiognomy, Geotechnical Engineering and geological terms, climate and weather in our country are prerequisite condition of bursting out Geotechnical Engineering and geological disasters, meanwhile, most of civil engineering such as industry and civil architecture, road and bridge, irrigation and hydroelectric engineering, flood control dams are constructed on soft rock-soil foundation or highland, these engineering activities impact and deteriorate further geological environment; on the other hand, exterior dynamic loading such as earthquake, tsunami, raging billow, flood erosion, various vibration made by human activities accelerate the rheological behavior of soft rock-soil and induce Geotechnical Engineering and geological disasters such as foundation settlement and slippage, engineering incline and crack, destabilization and collapse, more easy to trigger serious cataclysm of geological environment such as landslide, debris flow, slide of embankment, ground subsidence (Xu Qiang, Huang Runqiu, et al., 2002). It is obvious that the strong dynamic loads accelerate rheology of soft rock-soil, and

become the main and direct external dynamic power that lead to Geotechnical Engineering and geological disasters. Accelerated rheology of soft rock-soil is external expression patterns of bursting out disasters.

According to geological environment gazette of the Ministry of Land and Resources : all kinds of geological disasters occurred 102804 times in whole country in 2006, 663 person are died, 111 person are lost, 453 person are injured, and direct economic losses reach 44.2 billion yuan. Moreover, every year the whole country occurred thousands of Geotechnical Engineering and geological disasters and security accidents such as foundation settlement and inclination, unstable sliding, building collapse and crack, underground engineering cave in, and result in enormous casualty and property loss. It is obvious that the geological disasters are frequent in our country, the damage is the most serious, it bring tremendous economic losing to the national basic construction and people's life safety, and the position is still austerity.

Therefore, the research on various influencing factors of sudden Geotechnical Engineering and geological disasters, the probe of dynamic rheological mechanical behaviour of soft rock-soil, the establishment of rheological model and rheological equation, all of these have important theory and actual signification for us to reveal the rheological dynamic mechanism of bursting out Geotechnical Engineering and geological disasters, keep the stability and security of Geotechnical Engineering, prevent and reduce Geotechnical Engineering and geological disasters as well as to discuss the dynamic key indexes of monitoring and forecasting geological disasters, improve the science and veracity of monitoring and forecasting geological disasters .

ANALYSIS ON FACTORS OF INDUCING GEOTECHNICAL ENGINEERING AND GEOLOGICAL DISTASTERS

Natural objective factors

Chinese territory is vast, there are developed drainage system such as rivers, lakes, long coastline, distributed over all hills and basins, varied landform and physiognomy, complicated geological terms, widely covered soft rock-soil. According to statistics (Li Xiuzhen, 2003) that the proportion of mountain area is 69%, and there are 1500 debris flow gullies along highways in the national territory. The natural climate and geological terms are varied in the whole country, In the Yangtze drainage area, the rainy season is long, rainfall intensity is great, rain precipitation is concentrated, climate is hot and humid, and weathering is strong, all these lead to sedentary product developed in slope, and strong erosion effect of hilly mountains and rivers; Most of northwest areas are loess plateau and gobi desert with loose state, its natural bearing capacity and stability are weak, and unsuitable every kind of civil engineering construction. In southeast coastal areas, large rivers are linked crisscross, embankment and civil engineering adjacent to seacoast are marinated and washed away in the water, stroke by billow, all these result in reduced of mechanics strength and stability declined of rock soil mass. Therefore, multivariate objective factors such as varied topography, complicated geological conditions, widely covered soft rock- soil, natural climate differences are prerequisite condition of bursting out geological disasters, and these

factors make our country become one of the countries in the world, of which geological disasters frequently occur (Liu Chuanzhen, 2001).

Factors of engineering building

The economy and social development are new periods in our country, national infrastructure is further perfected and equipped, and new town's expansion, urban old areas' transformation, various large engineering project, etc, All these accelerate the development of geotechnical engineering. Southeast coastal area march towards higher goal by unprecedented speed, and most of civil engineering are constructed on soft rock-soil foundation or typical region of highland, such as industry and civil architecture, road and bridge, irrigation and hydroelectric engineering. The stratagem of middle area grow up is actualized, and many engineering and project are built. In the implementing of West development Strategy, a lot of infrastructure and engineering are constructed on sand soil, loess and unconsolidated layer. Many projects that relate to the national economy and the people's livelihood have been carried out all over China, such as Three Gorges Project of the Yangtze river, West-to-East Gas Transmission, South-to-North Water Transfer Project, West-to-East Electricity Transmission, Tibet Railroad. Soft rock-soil has serious potential threat to both engineering security and stability under external strong dynamic disturbances, and it is more easily to break out serious Geological disasters such as landslide, collapse, debris flow, ground subsidence. It is visible that mass construct increase the possibility of bursting out Geotechnical Engineering and geological disasters.

Dynamic factors

Soft Rock-soil has rheology character, it will accelerate rheology and cause geotechnical engineering security accidents under external dynamic loading, such as earthquake, tsunami, raging billow, flood erosion, various vibration made by human activities. At the same time, compared with stable loading, dynamic loading will accelerate easily rheology of soft rock-soil, and induce various geological disasters. According to the material from geologicalal environment gazette of the Ministry of Land and Resources, mining actions are more easily to induce and cause geological disasters such as ground collapse, ground subsidence, landslide, debris flow, collapse, ground fissures and soil erosion. The gazette material indicated, above 90% Geotechnical Engineering and geological disasters are induced and caused by dynamic load such as earthquake, flood erosion, external vibration. Therefore, dynamic loading become direct and main factor which accelerate rheology of soft rock-soil and cause Geotechnical Engineering and geological disasters.

Static loading way is used to research the characters of the soft rock-soil rheology and effect on projects' stability, this traditional way neglects the existence of stimulation character of dynamic loading in real world, so the research results have a great deviation with the practical case. But it is these objectively dynamic loading that result in various Geotechnical Engineering and geological disasters and serious engineering security accident. Accordingly, we should combine with the dynamic loading produced in nature to research

the basic theory such as the dynamic mechanism that result in serious Geotechnical Engineering and geological disasters.

COUNTERMEASURE FOR RESEARCH ON THE RHEOLOGIC DYNAMICS OF GEOTECHNICAL ENGINEERING AND GEOLOGIC DISASTER

Objective factor can't be obviated, the dynamic loading in nature as external factor can't be eliminated, the development and construction of country will not stop ever, therefore, we must contact with the practice tightly, think and scan from the new point of view, find out the new law by the new theory and way of study, settle scientific and technical problems. As the medium-term and long term layout of the development of science and technology (2005—2020) constituted by the Ministry of Land Resource about preventing the geologic disaster pointed out (Hu Hua, 2005; Wu Shuren, 2004), the inducing mechanism and forming mechanism of the bursting out Geotechnical Engineering and geologic disaster has no advance in breakthrough, the basis of theory is weak relatively, and these make the theory of forecasting break through difficultly. The index system and criterion of forecasting the bursting out Geotechnical Engineering and geologic disaster are still in the first time step, and the key index of monitoring and sign are not still established. Therefore, the mechanism of the bursting out geologic disaster, the criterion of forecasting the disaster, the technique of monitoring and forecasting become the tackle key problem for science and technology.

Based on the reasons above, the research subject about the rheologic dynamics mechanism of the soft rock-soil bursting out geologic disaster under dynamic loading is put forward, and surround the center of the rheologic dynamics mechanism of the soft rock-soil bursting out geologic disaster, some theory such as the Geotechnical engineering mechanics, the Engineering Geology, the Dynamic Rheologic mechanics, the Geotechnical engineering Microstructure, and the reducing and preventing disaster are synthesized and use to research the mathematic mode of dynamic loading, the rheologic mechanics response of soft rock-soil, the rheologic dynamics model and the rheologic equation, the change of rheologic process of soft rock-soil from slowness to speediness and the process of sliding collapse under dynamic loading, the critical mechanics condition, the accelerating rheologic dynamics equation, the characteristic and law of the rheologic parameters of soft rock-soil vary as the multi-factor of dynamic loading (different loading mode, the value of acting force, frequency and so on), the characteristic of interior microstructure of soft rock-soil vary as dynamic loading, the process and the characteristic of the micro-evolvement of rheologic collapse from the stable solidity to the slipping flow pattern and so on. The research results have important theory signification for us to find out the rheologic dynamic mechanism of accelerating rheologic process of soft rock-soil and leading to grave disaster under dynamic loading, perfect the monitoring and forecasting theory of geologic disaster, improve the traditional method of monitoring and forecasting disaster; and it have also actual signification on the preventing and control of rock-soil rheologic slipping, maintaining the slid slope and the stability and security of other Engineering, reducing the disaster of Geotechnical Engineering, protecting the geologic environment and so on.

CHARACTERISTIC OF DYNAMIC RHEOLOGIC MECHANICS RESPONSE OF SOFT ROCK- SOIL UNDER DYNAMIC LOADING

In the special environment and condition, such as earthquake, quick vibration, dynamic impact and dynamic shearing, elasticity effect of soft rock-soil will be obvious, and it will represent the mechanics characteristic of elastic body. Therefore, it can be regarded as viscoelastic-plasticity body.

Taking typical muddy soft soil in Xiamen area as sample, test the viscoelasticity parameter of soft soil with 24% of the water ratio in the dynamic condition using type of MCR-300 rheometer. In the condition of dynamic frequency 10Hz, test the storage modulus G' of soft rock-soil and the loss modulus G'' vary as dynamic shearing strain. The curve of viscoelasticity parameter varying as dynamic shearing strain refer to the Figure 1. It is obvious that muddy soft soil behave as viscoelasticity-plasticity body in the rheologic process under the dynamic loading (Hu Hua, 2007).

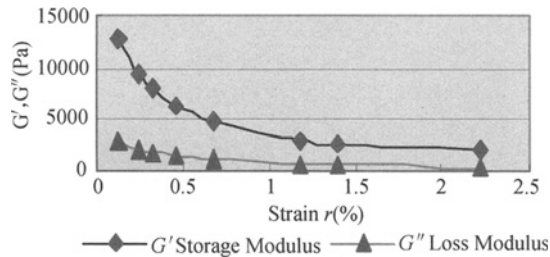


Figure 1. 10Hz, viscoelasticity parameter

RHEOLOGIC DYNAMICS MODEL AND EQUATION OF SOFT ROCK-SOIL UNDER DYNAMIC LOADING

Viscoelastic-plasticity rheologic model of soft rock-soil

Under the dynamic loading, the soft rock-soil behave as the characteristic of viscoelasticity solid and the flow deforming don't occur before yielding, therefore, in the model, the elastic element and viscous element with parallel connection are used to form the viscoelasticity solid model. After yielding, it serves as viscoelastic-plasticity body and behaves as the characteristic of viscoelastic-plasticity, and the plasticity deforming flow begins to occur. So, in the basis of former model, using a gliding block and a viscous jar with parallel connection and connecting in series with former solid model, in this way, the rheologic mechanics model reflecting the viscoelastic-plasticity of the soft rock-soil under the external dynamic loading can be built, as Figure 2 shows. τ_0 serves as the initial yielding shearing stress; η_1 serves as the elastico-viscosity of soft rock-soil under the external dynamic loading; η_2 serves as plastic viscosity of soft rock-soil under the external dynamic loading.

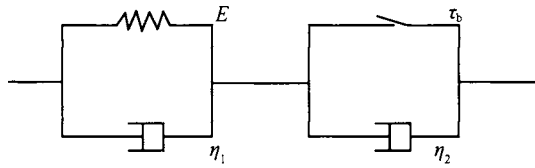


Figure 2. the viscoelastic-plasticity rheologic mechanics model of soft rock-soil under dynamic loading.

RHEOLOGIC EQUATION EQUATION OF SOFT ROCK-SOIL UNDER DYNAMIC LOADING

When $\tau > \tau_b$, the viscoplastic body enter into the rheologic state, $\tau - \tau_b$ force the viscoplastic body to take place plastic flow. It represent as viscoelastic-plasticity body. Given the individual displacement of elastic body and viscoplastic body as γ_1 、 γ_2 , the individual shearing stress as τ_1 、 τ_2 , the displacement of whole system as γ , the shearing force as τ , then:

$$\tau = \tau_1 = \tau_2; \quad \gamma = \gamma_1 + \gamma_2; \quad \dot{\gamma} = \dot{\gamma}_1 + \dot{\gamma}_2; \quad \ddot{\gamma} = \ddot{\gamma}_1 + \ddot{\gamma}_2$$

For the viscoelastic part:

$$\tau = E\gamma_1 + \eta_1 \dot{\gamma}_1^n \tag{1}$$

For the viscoplastic part:

$$\tau - \tau_b = \eta_2 \dot{\gamma}_2^n \tag{2}$$

When index “n” is 1, the equation is (Hu Hua.2007):

$$\eta_1 \eta_2 \dot{\gamma} = (\eta_1 + \eta_2) \dot{\tau} - E \eta_2 \dot{\gamma} + E(\tau - \tau_b) \tag{3}$$

The dynamic rheologic model and deducing of the new rheologic equation of soft rock-soil under dynamic loading are built, and it settle foundation for the study on the law of large displacement flow deforming for bursting out Geotechnical Engineering and geologic disaster, accelerating rheologic dynamic equation, critical mechanics condition for rheologic collapse, and dynamic key index of bursting out disaster.

The mechanics of bursting out Geotechnical Engineering and geologic disaster is a difficult problem for our country and even for the world. This article brings forward some thinking and exploring from the point of view of the dynamic rheologic mechanics, supplying use for reference. Although the present study is in the prior period phase, a mass of work is about to put into effect, some research findings with more scientific theory significance and use value are wished to achieve.

CONCLUSIONS

- (1) The complicated geological conditions and natural climate are the objective precondition of bursting out Geotechnical Engineering and geologic disaster. The

corporate effect of various objective factors makes our country to become one of the multiple Geotechnical Engineering and geologic disaster countries. Therefore, it is no time to delay to enhance the study for reducing and preventing geological disaster.

- (2) Soft rock-soil have the rheologic characteristic, the rheological process behaves slowly under steady loading in general, but it will accelerate rheologic under external dynamic loading. Therefore, the intensive effect of the external dynamic loading is the most chief and direct external dynamic factor for geologic disaster. Seizing the dynamic factor of dynamic loading firmly, developing study from the point of view of the dynamic rheologic mechanics and evolving microstructure is a new way of thinking and attempt, and this is a supplement and perfecting for the traditional study, and the research countermeasure and the way of thinking accord with objective practical situation much more.
- (3) The intensive effect of external dynamic loading makes the microstructure of soft rock-soil evolve, and accelerates the rheological process of leading to the bursting out geologic disaster. The fast rheological process of soft rock-soil is the external representing way of the bursting out geological disaster. It accords with the deformation damage characteristic of soft rock-soil rheological disaster, and has more pertinence and meaning of practical instruction that we study the law of large displacement flow deforming, critical mechanics condition for rheologic collapse, rheologic dynamic equation from the point of view of the dynamic rheologic mechanics.
- (4) By the way of experimental testing and theoretical analysis, the rheologic dynamics model of soft rock-soil under dynamic loading is established and new rheologic equation is deduced. All these settle stable foundation for us to find out the rheologic dynamic mechanism of soft rock-soil bursting out Geotechnical Engineering and geologic disaster, critical mechanics condition for rheologic collapse, and dynamic key index of bursting out disaster.
- (5) The preventing and defending the Geotechnical Engineering and geologic disaster is a difficult problem for our country and even for the world. This article brings forward some countermeasure to supply new approach to maintain the stability of the Geotechnical Engineering, prevent and control the rheologic slipping of rock-soil, and it supply new technique method for the design of the Geotechnical Engineering, also supply reference for researcher.

ACKNOWLEDGEMENT

Project funded by National Natural Science Foundation of China (50678155) and Fu Jian province new century excellence person with ability plan.

REFERENCES

- Geological environment gazette of the Ministry of Land Resource of China*, 2003—2006 year.
- Hu Hua. (2005). He analysis on dynamic rheologic mechanics for soft rock-soil to burst out geologic disaster. *Journal of catastrophology*, 20(4): 13-17.

- Hu Hua. (2007). The rheological model and rheological equation of sillage soft soil under dynamic loading. *Rock and Soil Mechanics*, 28(2): 237-240.
- Li Xiuzhen. (2003). Research on prediction criterion for temporary prediction of landslide. *The Chinese Journal of Geological Hazard and Control*, 14(4):5-11.
- Liu Chuanzhen.(2001). Study on the early warning of the abrupt geo-hazards. *Hydrogeology & Engineering Geology*, 2: 1-4.
- Wu Shuren. (2004). Important scientific and technological problems in the field of geological hazard prevention and control—a discussion. *Journal of Geomechanics*, 1: 1-6.
- Xu Qiang, Huang Runqiu, et al. (2002). Mechanism analysis on geological hazards triggered by external disturbance . *Chinese Journal of Rock Mechanics and Engineering*, 21(2): 280-284.

SEISMIC RESPONSES OF BRIDGE PIER CONSIDERING THE EFFECT OF HYDRODYNAMIC PRESSURE

Furong Li

*College of Civil Engineering, Yancheng Institute of Technology, No.20,
Huanghai Road Yancheng, China*

Guoxing Chen, Zhihua Wang

*College of Civil Engineering, Nanjing University of Technology, No.200,
Zhongsan North Road, Nanjing, China*

The bridge pier structure in deep water on the group piles is taken as the research object, the ABAQUS software is used as the computation platform, based on the Morison equation, using the added mass of water to consider the effect of water on bridge pier, establishing the mechanical model of water-soil-piles-pier structure multi-medium coupled, researching responses of the acceleration, relative displacement and inner force of the pier under the condition water-free and water-full, analyzing the effect of hydrodynamic pressure on the seismic responses of acceleration and relative displacement on the top of pier and the inner force under the bottom. The result indicates that, considering hydrodynamic pressure, the peak-acceleration, relative displacement, inner force are all increased, the increased amplitude is related to the strength and the spectrum character of the earthquake motion input.

INTRODUCE

As transport cause develops continually, China's bridge construction has been in a rapid development, and in China's major rivers, many big span- bridge piers are always in the deep water. Under the earthquake, pier in the deep water will happen in a certain vibration and deformation, causing the surrounding water rocks, and the water again in the form of hydrodynamic pressure is counterproductive to the pier, changing the bridge pier vibration and deformation state, and this role has always been counterproductive accompanied by the earthquake. Therefore, the issue of hydrodynamic pressure is very complex.

Some domestic and foreign scholars have done some studies on hydrodynamic pressure over the seismic response of bridge pier. On the basis of the pile with offshore oil platform, using a finite element analysis and considering dynamic interaction of the upper water and structure, for example Peter Arnold et al. (1977). Raising theory based on cantilever vibration equation, which can only be applied to the pier all submerged in the fluid, for example Yoshihiro et al. (1988). The result of Li Yucheng shows that interaction of structure and fluid on the dynamic response of structure has been in a greater impact (1993). Based on the semi-analytical and semi-numerical methods, analyzing hydrodynamic pressure of

flexible bridge pier structure, for example Lai Wei et al. (2004). Based on the assumption of rigid foundation, studying the seismic hydrodynamic pressure on the pier in deep water, for example Gao Xuekui et al. (2006). Analyzing the seismic responses of the bridge pier structure in deep water has not only to consider the role of hydrodynamic pressure, but also to consider the pile - soil interaction. This paper based on Morison equation, uses the added mass of water to consider the effect of water, adopts the finite element method to analyze seismic response of bridge pier, and takes a full consideration in hydrodynamic pressure and pile-soil interaction.

ANALYSIS METHOD

To cylinder bridge piers, the hydrodynamic pressure of the pier can be calculated approximately with Morison equation. With assumption that water incompressible, analyzing the seismic response of the pier as water in the form of added mass to the pier.

Overlooking the effect of pier on water movement, and assumed the role of water to pier was caused by undisturbed acceleration field and velocity field, and caused by the inertia and damping force along from water movement to bridge, adopt simplified Morison equation to show hydrodynamic pressure of bridge pier caused by earthquake, which is expressed as:

$$P_w = \rho V \ddot{u} + (C_M - 1) \rho V (\ddot{u} - \ddot{x} - \ddot{x}_g) + \frac{1}{2} C_D \rho A_p \left[(\dot{u} - \dot{x} - \dot{x}_g) |(\dot{u} - \dot{x} - \dot{x}_g)| \right] \quad (1)$$

Where ρ is the density of water, V is the volume of the pile underwater, A_p is the cross section area of the pile, \ddot{u} 、 \dot{u} is the absolute acceleration and absolute speed respectively, \ddot{x} 、 \dot{x} is the relative acceleration and relative velocity respectively, \ddot{x}_g is the earthquake acceleration, C_M is hydrodynamic inertial coefficient, C_D is hydrodynamic viscous damping coefficient.

Bridge pier is in the hydrostatic hypothetically, that is $\ddot{u} = \dot{u} = 0$, Eq. (1) is simplified as:

$$P_w = -(C_M - 1) \rho V (\ddot{x} + \ddot{x}_g) - \frac{1}{2} C_D \rho A_p \left[(\dot{x} + \dot{x}_g) |(\dot{x} + \dot{x}_g)| \right] \quad (2)$$

The second subquadratic of is nonlinearity, treat it to the linear, get the linear Morison equations.

$$P_w = -(C_M - 1) \rho V (\ddot{x} + \ddot{x}_g) - \frac{1}{2} C_D \rho A_p \sigma_{\dot{x} + \dot{x}_g} \sqrt{8/\pi} (\dot{x} + \dot{x}_g) \quad (3)$$

where $\sigma_{\dot{x} + \dot{x}_g}$ is the standard deviation of structure absolute velocity.

Order $M_w = (C_M - 1) \rho V$ is the hydrodynamic additional quality coefficient, $C_w = \frac{1}{2} C_D \rho A_p \sigma_{\dot{x} + \dot{x}_g} \sqrt{8/\pi}$ is the hydrodynamic additional damping coefficient

Balance equation of bridge pier system under the earthquake can be expressed as

$$[M + M_w] \{\ddot{x}\} + [C + C_w] \{\dot{x}\} + [K] \{x\} = -[M + M_w] \{I\} \ddot{x}_g - [C_w] \{I\} \dot{x}_g \quad (4)$$

Dynamic response change rate of bridge pie the hydrodynamic resistance pressure caused is little, to simplify the calculation, the impact of C_w can be ignored, then Eq. (4) can be simplified

$$[M + M_w] \{\ddot{x}\} + [C] \{\dot{x}\} + [K] \{x\} = -[M + M_w] \{I\} \ddot{x}_g \quad (5)$$

Time-history analysis uses the method of gradual integration to solve the equation of motion, seen from the above, consider the hydrodynamic pressure effects, the form of dynamic equation has no change, and matrix $[M_w]$ is only imposed on the quality matrix $[M]$, so the dynamic response equation can be solved by the method of solving structural equation of motion with no-water.

Assume that relative velocity of the Water and Pier is unchanged between the mid-point of Pier two adjacent units, the force value on the node i is half of the total force connected component with node i . That is, each node is only bear half the force of unit, equivalent additional water quality of the node i is

$$M_{iw} = \sum (C_M - 1) \rho A_p l_{ij} \quad (6)$$

where j is the node with adjacent of node i , l_{ij} is the half effective length of ij unit, C_M is took 2.0 referenced to "standardize the construction of the sea fixed platforms" (1982).

CALCULATION EXAMPLES

The single-column pier is used on a rigid frame bridge; the pier is the high pier with the round cross-section, the diameter is 3m, the height is 36m, the depth of water is 30m, the square cap has the height of 1.5m and the width of 4.5m under the pier, four drilled caisson piles are under the cap, the height of pile is 18m, the diameter is 1m, the spacing is 3m. The bridge deck is Four lanes for two-way, the width is 12m, the quality of pier top is a cross-quality on the bridge deck, it is 7.8×10^5 kg. Figure 1 is the sketch map of the single-column pier with piles-supported.

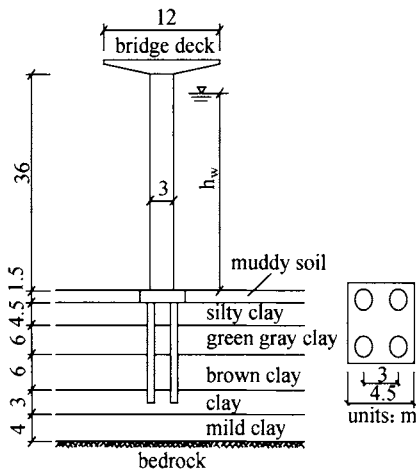


Figure 1. The sketch of the single-column pier with piles foundation

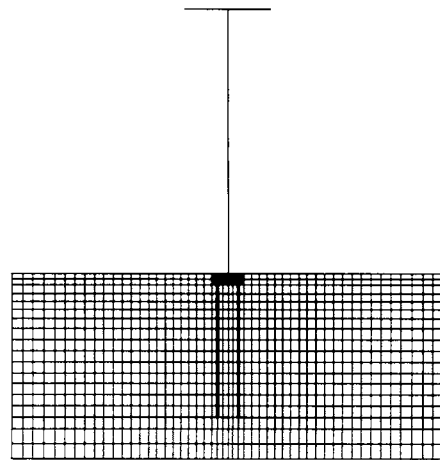


Figure 2. The finite element model of the single-column pier with piles foundation

The soil covers on the bedrock with the level layered soil, using the viscous-plastic memorial nested yield surface model of soil to describe the soil nonlinear. Table1 shows the model parameter values of soils. In the dynamic calculation, don't consider pore water

discharge, soil Poisson's ratio is 0.49 generally. The pier and piles are made of concrete, using the plastic-damage model of concrete to describe the concrete nonlinear.

Table1. Model parameters of soils

soils	$\nu_0(\times 10^{-4})$	Density (kg/m ³)	shear wave velocity(m/s)	friction angle (°)
①muddy soil	4.0	1800	170	16
②silty clay	4.0	1890	190	16
③green gray clay	3.7	1900	210	24
④brown clay	3.7	1960	260	24
⑤clay	3.8	1970	320	21
⑥mild clay	4.4	2030	380	21

In this paper, the foundation border is large enough to eliminate the border impact on the structural dynamic response, the width of foundation is 60m, the width ratio of foundation and pier cap is 13.3, This width is sufficient to eliminate border effects on the seismic response of structures according to the study, The finite element mesh of the overall system is in Figure 2, by the additional water quality consider the impact of water on the pier, don't consider the role of waves and currents.

In this paper, using El centro earthquake wave as the inputting the bedrock earthquake ground motion. Figure 3 shows the acceleration time-history and spectrum.

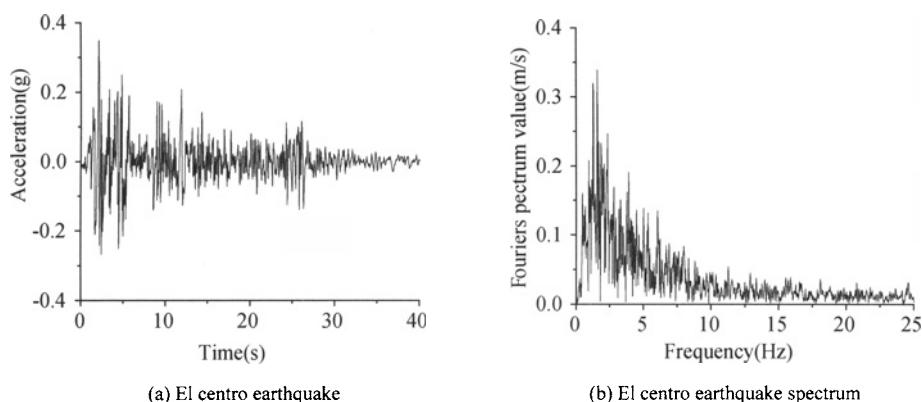


Figure 3. The acceleration time-history and spectrum of bedrock earthquake ground motion

CALCULATION RESULTS AND ANALYSIS

Displacement and acceleration response of the pier

In the seismic analysis of the pier, the absolute acceleration of pier top and displacement relative the bottom of pier are the analysis basement on evaluating seismic stability of pier structure. The displacement of Pier Top relative the bottom of the pier is the important contents of checking the bridge piers earthquake deformation one in the seismic design of pier. Under the bedrock ground motion, the absolute acceleration of Pier Top is the key factor related to Deck Motion.

Bridge Pier body displacement reaction peak relative the bottom is presented on Figure 4, seen from it, the hydrodynamic pressure changes the response of the bridge pier, relative peak displacement of Pier is changed. The relative displacement is increased except inputting

the 0.2g peak acceleration, and reaches the maximum peak at the Pier Top. Figure 5 shows the relative displacement reaction time history between the top and bottom of piers under non-water and water, seen obviously that, relative displacement changes significantly after considering the effect of hydrodynamic pressure.

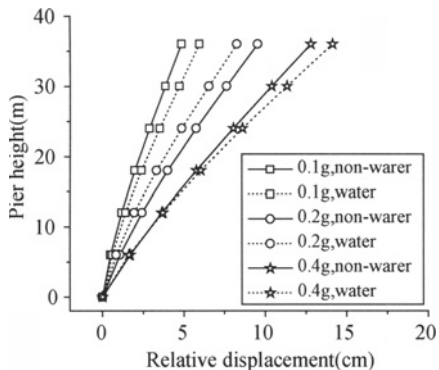


Figure 4. Peak displacement of the pier relative to the bottom of the pier

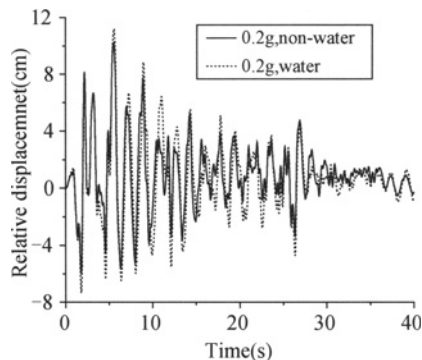


Figure 5. Relative displacement responses between the top and bottom of the pier

Figure 6 shows the peak acceleration of the pier, we can see that, the acceleration is reducing and then increasing from the bottom to the top, because the pier bottom is subject to the larger earthquake force, the concrete is cracking and forming the plastic hinge, the flexural rigidity of the pier bottom section is lower, which leading to the pier acceleration is decreasing and the relative displacement is increasing. The acceleration of the pier in the upper region is increasing, because of the upper structure of the inertial effect, the acceleration at the top pier and at the end of pier is homology.

Figure 7 shows the absolute acceleration response time history at the different behaviors. From seen it, with the increase of input peak accelerations, acceleration at the top of the pier is also have increasing with different degrees regardless of the water or non-water situation, acceleration response of the pier top has the increasing trend after considering the effects of hydrodynamic pressure.

Figure 8 shows the β spectrum of absolute acceleration response spectrum on the top of the pier. From seen it, the acceleration response of the pier is changing considering the effects of hydrodynamic pressure; the major reflection is that the value of the β spectrum in the mid-cycle and long-cycle has the decreasing trend, especially in the mid-cycle.

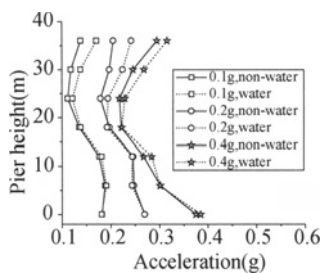


Figure 6. Peak acceleration of the pier

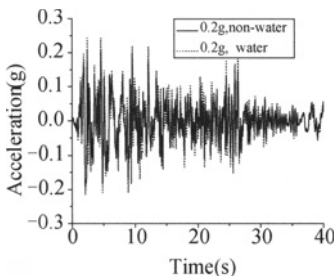


Figure 7. Acceleration responses of the pier top

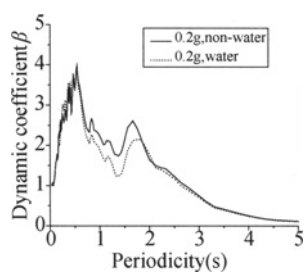


Figure 8. β spectra of acceleration of the pier top

Internal force response of the pier

Because the internal forces response value of a certain part exceeds its bearing capacity, the pier is damaged and generating the plastic hinge under the earthquake. The bottom region of the pier is the potential plastic hinge region for the single-column pier. Therefore, this article compares the shear force and moment of the pier bottom under the condition of water and non-water to consider the effect on the internal force of the pier of under the earthquake hydrodynamic pressure.

Figure 9 shows the peak shear reaction of the pier body. Seen from it, the shear of the pier bottom is bigger than upper region of the pier bottom obviously. The pier bottom is subject to much larger force and this region is very easy to create the plastic hinge under the bedrock earthquake.

Figure 10 shows the moment reaction peak of the pier body; we can see that the moment of the pier bottom within 10 m at is obviously greater than the other sites.

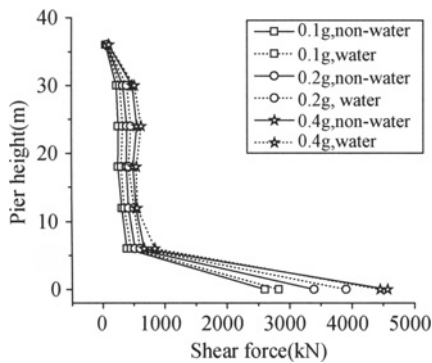


Figure 9. Peak shear force of the pier

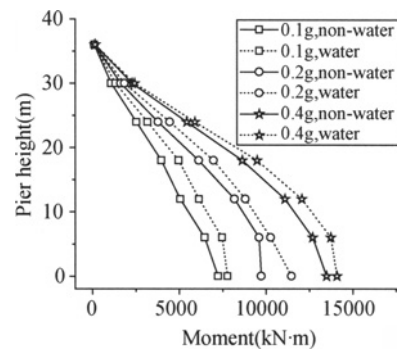


Figure 10. Peak moment response of the pier

Earthquake hydrodynamic pressure influence coefficient

The hydrodynamic pressure influence coefficient of the pier seismic response peak is definite as follows:

$$K = \frac{\text{earthquake response peak with water} - \text{earthquake response peak with non-water}}{\text{earthquake response peak with water}} \times 100\%$$

The K_d 、 K_a 、 K_f and K_m shows the hydrodynamic pressure influence coefficient of the relative displacement, acceleration on the top of pier and the shear force, moment at the bottom of pier separately.

Table 2 shows the hydrodynamic pressure influence coefficient. As can be seen, the degree of the effect on the seismic response of the pier by hydrodynamic pressure is varying differently, but the effect is not so obvious. Therefore, it is also necessary to consider the effect of hydrodynamic pressure for the bridge safety.

Table 2. Hydrodynamic pressure influence coefficient

The peak accelerations of bedrock earthquake	K_d (%)	K_a (%)	K_f (%)	K_m (%)
0.1g	9.7	-0.4	8.5	7.4
0.2g	9.3	0.0	15.1	17.9
0.4g	11.1	7.0	-2.6	4.5

CONCLUSION

Through analyzing, the conclusion is that there has some influence on the relative displacement, acceleration, shear force and moment response of the pier with piles foundation by the hydrodynamic pressure, The influence degree is relative to the earthquake wave, peak acceleration input, the pier structure and other factors, is may also relative to the ratio between the additional water quality and bridge structure quality.

Therefore, it is necessary to consider the effects of hydrodynamic pressure for the high pier bridge structure seismic design. If the hydrodynamic pressure is neglected, it may underestimate its dynamic response, it is not safe. At the same time, because of the differences of the bridge structural system and the impact of random earthquake vibration, the effect of the hydrodynamic pressure need to further research and study, so that the earthquake response and seismic analysis of the bridge is more reasonable and accurate.

ACKNOWLEDGMENTS

Universities Special Fund of the Ministry of Education P.R.China Dr. disciplines point(20060291007); General Project of Jiangsu Provincial Natural Science Research (06KJB560042)

REFERENCES

- Arnold P., Bea R.G. and Idriss L.M. (1977). A study of soil-pile-structure systems in severe earthquakes. *Proc.The 9th Annual Offshore Technology Conference*, 1: 2749.
- Chen G. X., Zhuang H. Y. (2005). Developed nonlinear dynamic constitutive relations of soils based on davidenkov skeleton curve. *Jourual Geotechnical Engineeriug*, 27(8): 860-864.
- Gao X. K., Zhu X.(2006). Hydrodynamic effect of bridge pier on seismic response in deep water. *Journal of Beijing Jiaotong University*, 30(1): 55-58.
- Gao X. K, Zhu X. and Li H.(2006). Seismic response analysis of bridge pier in deep water excited by near-fault earthquakes. *Earthquake Resistant Engineering and Retrofitting*, 28(3): 83-87.
- Jeeho Lee and Gregory L. Fenves. (1998). Plastic-damage model for cyclic loading of concrete structures. *Journal of Engineering Mechanics*, 4: 892-900.
- Lai W., Wang J. J. and Hu S.D.(2004). Earthquake induced hydrodynamic pressure on bridge pier. *Journal of Tongji University*, 32(1): 1-5.
- Li Y. C., Teng B.(1993). *Wave Action to Maritime Structure*. 1st edition, China Ocean Press.
- Morison J.R., O'Brien M.P., Johnson J.W. and Schaaf S.A.(1950). The force exerted to surface wave on piles. *Petroleum Transaction, AIME*, 189: 149-154.
- Yoshihiro T., Robert T. H. (1988). Restoring forces on vertical circular cylinders forced by earthquakes. *Earthquake Engineering and Structural Dynamics*, 16(5): 98-102.
- Yuan Y. C., Lai W., et al. (2005). The effects of hydrodynamic damping on seismic response of bridge piles. *World Earthquake Engineering*, 21(4): 88-94.

NUMERICAL STUDY ON SANDPILE FORMATION OF GRANULAR MATERIALS WITH DIFFERENT GRAIN SIZE DISTRIBUTIONS

Jun Liu, Jing Zhou

*Key Laboratory of Ministry of Education for Geomechanics and Embankment
Engineering, Hohai University, Nanjing 210098*

Geotechnical Research Institute, Hohai University, Nanjing 210098, China

The dynamic sandpile formation process and the angle of repose of granular particles with different grain size distribution are studied by numerical simulation. The modified Discrete Element Method (DEM) has been employed in current simulation. Four kinds of pad materials were placed on ground to vary the friction coefficient between particle and ground and the effects were analyzed in detail in simulation. The simulated results show that the angle of repose increases with grain size and friction coefficient between particle-to-ground.

INTRODUCTION

Granular geomaterials widely exist in nature. Geomaterials are essentially composed of granular particles or blocks, for example, soil is deposit of particles, rock mass is also made up of blocks which are formed by structural plane. The packing characteristics of granular geomaterials are widely used in geotechnical engineering, such as deposition of mud and sand, embankment and slope stability analysis and flow of railway ballast under loading of running train etc. Thus, the heap of granular geomaterials is one of the most important and basic problems in rock and soil mechanics.

In the past, numerous studies have been carried out on heap formation related to packing, Trojan et al. (2003), segregation, Jullien et al. (1990), stress distribution, Elperin et al. (1998), avalanching, Frette et al. (1996), self-organization, Ruskin et al. (1997), and stratification, Baxter et al. (1998). Some new computer simulation techniques have been used to simulate sandpile formation process or analyze problems related to sandpile formation. The main numerical techniques which include Monte Carlo simulation, Elperin et al. (1997), cellular automaton, Mehta et al. (1994), and DEM, Cundall et al. (1979) have been adopted. The former two methods focus on geometrical factors and ignore the mechanical process of sandpile formation. The DEM is probably most realistic, because it explicitly takes into account not only the geometrical factors but also the forces involved. DEM has been adopted by a number of researchers to simulate two dimensional sandpile formations. However, some of those simulations involved arbitrary or unrealistic assumptions. For examples, Lee and Herrmann, Lee et al. (1993), and Luding, Luding (1997), ignored the rotation of particles or tangential forces, and Elperin and Golshtein, Elperin et al. (1997), set the velocities of all particles to zero after every 5000-15000 iterations. Some of the above shortcomings were overcome by Zhou et al. (1999), by incorporating rolling friction in their simulation to obtain stable sandpile configuration.

In the studies mentioned above, mono-sized and polydisperse (i.e., only one kind of or several kinds of size distribution) particles were used. Thus, the effect of different grain size distributions on the angle of repose was not studied systemically.

The objectives of this study are to establish the relationship between the angle of repose and the grain size distribution and the effect of friction coefficients of particle-to-ground on the formation of sandpile and angle of repose by simulation. The modified DEM similar to Zhou's model, Zhou et al. (1999), was applied in this research.

SIMULATION METHOD

In this study, the simulations were carried out in the following three steps. First, loosely packed particles with random size distribution were generated by regular lattice (named as reference lattice) within a container. Second, the loosely packed particles were allowed to fall under gravity into the container to form a stable packing so to avoid the particle velocity effect on the angle of repose. Finally, the vertical walls of the container were slowly lifted to allow the particles to collapse and form a stable sandpile.

MODIFIED DEM

In this study, the modified DEM similar to Zhou's model, Zhou et al. (1999), has been employed to simulate the second and third step above-mentioned. DEM is a finite difference scheme. It is used to study assemblies of individual particles. The behavior of the material can be derived by monitoring the interaction between particles. The amplitude of normal contact force F_{ij}^N and shear contact force F_{ij}^T (the corresponding vectors are F_{ij}^N and F_{ij}^T , see equation (3)) can be expressed by

$$F_{ij}^N = k_n \delta_{ij} + c_n V_{ij} \cdot n_{ij}, \quad (1)$$

$$F_{ij}^T = k_t \tau_{ij} + c_t V_{ij} \cdot t_{ij}, \quad (2)$$

where k_n and k_t represent the normal and shear spring constant, c_n and c_t are the normal and shear damping coefficient due to the dissipative force, and n_{ij} and t_{ij} are the unit vector in normal direction and tangential direction, respectively.

The motions of particles are simulated using Newton's second law, i.e.

$$m_i \ddot{X}_i = \sum_{l=1}^{k_i} (F_{il}^N + F_{il}^T) + m_i g, \quad (3)$$

$$I_i \ddot{\theta}_i = \sum_{l=1}^{k_i} (M_{il}^T + M_{il}^N), \quad (4)$$

where m_i and I_i represent the mass and moment of inertia of particle i , l is a particle which contact with particle i ($l=1,2,\dots,k_i$, $l \neq i$, where k_i is the amounts of particles contacting with particle i), \ddot{X}_i and $\ddot{\theta}_i$ are the acceleration and angular acceleration of particle i . g is the acceleration of gravity. For a spherical particle of radius R_i , $M_{il}^T = R_i \times F_{il}^T$, is a torque generated by tangential forces, R_i is a vector of magnitude R_i pointing from the mass center of the particle to the contact point, M_{il}^N is a torque due to the asymmetric distribution of normal contact force. Its effect is equal to exert a rolling friction

between particles in contact. The asymmetry leads to a non-zero portion which can be described by using the rolling friction

$$M_{il}^N = \min \left\{ \mu_r \left| F_{il}^N \right|, \mu_r' \left| \theta_{il}^n \right| \right\} \hat{\theta}_{il}^n \quad (5)$$

where μ_r and μ_r' are the rolling friction coefficient and the rotational stiffness constant (mainly related to material properties), and $\hat{\theta}_{il}^n = \theta_{il}^n / \left| \theta_{il}^n \right|$, θ_{il}^n is the vector of the relative tangential rotation of particle i and l , i.e. $\theta_{il}^n = \dot{\theta}_i \times (R_i n_{ij}) - \dot{\theta}_j \times (R_j n_{ji})$.

The equations of particle motion (3) and (4) are solved by means of Verlet integrator. In this study, the conditions where the static, sliding and rolling friction will occur and how the different components are distinguished from each other have been taken into consideration using the method developed by Zhang and Whiten, Zhang et al. (1999).

Loosely packed structure

A loosely packed structure was generated by allowing particles of a given size distribution. A loose packing means there were no overlap between particles- particles and particles-boundaries of container. A simple scheme was applied to generate a loosely packed structure.

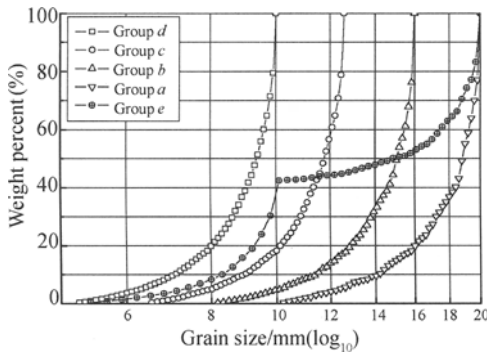


Figure 1. The grain size distribution of 5 groups used in simulation

Reference lattices were generated within or above the container. The reference lattice was used to generate coordinates of the central point for a spherical particle and its radius to ensure no overlap between particles. Five series of particles within different size range have been generated, named them Group a, b, c, d and e, respectively. The size range, average size and amounts for each group see Table 1. The grain size distributions of five groups see Figure 1. The five loosely packed structures and their reference lattices for 5 groups are shown in Figure 2.

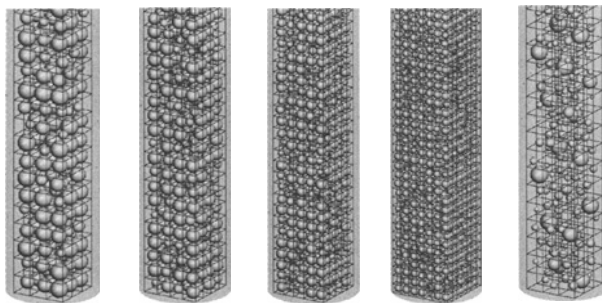


Figure 2. The loosely packed configurations of 5 groups by reference lattice. From left to right: Group a, b, c, d and e, respectively

Table 1. Size distribution, average size and amounts for particles of each group¹

Group label	Size range (mm)	Average size (mm)	Amounts
a	10-20	16.334	454
b	8-16	13.138	1000
c	6.4-12.6	10.35	2000
d	5-10	8.182	4000
e	5-20	9.321	2720

Formation of densely packed configurations

The densely packed configurations were formed within a cylindrical container by particles in loose structure falling under gravity. The parameters used in these simulations are given in Table 2. The dense configurations of the 5 groups are shown in Figure 3.

Table 2. Parameters used in the simulations²

Variable	Value
Particle density ρ	2500kg/m ³
Normal elastic constant k_n	107N/m
Tangential elastic constant k_t	107N/m
Particle-particle friction coefficient μ_s	0.4
Rolling friction coefficient μ_r	5×10^{-4} m
Rotational stiffness constant μ_r'	5×10^{-3} s/rad
Normal damping coefficient c_n	0.4
Tangential damping coefficient c_t	0.4

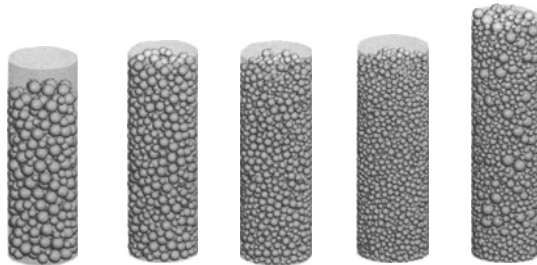


Figure 3. The formation of 5 densely packed configurations within cylindrical container, from left to right: Group *a*, *b*, *c*, *d* and *e*, respectively

Sandpile formation

The sandpiles were formed by slowly elevating the cylinders (shown in Figure 4) to allow the particles to collapse to the ground. The same modified DEM and the parameters (see Table 2) as used in the second step. The time step was chosen to be small enough (10^{-6} s) to ensure the

¹ The Group *e* is made up of 389 particles of Group *a* and 2331 ones of Group *d*.

² It is assumed that the wall is rigid and only deformation of particle considered and the parameters for contacts between particle and wall are the same with those between particles except for friction coefficient.

numerical stability was achieved in all the simulations. The simulation lasted until a stable heap was reached.

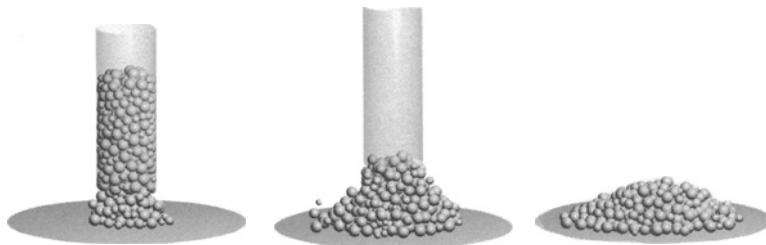


Figure 4. The method of simulated sandpile formation

SIMULATED RESULTS

Twenty simulations have been completed for 5 groups packing on 4 kinds of pad materials, respectively. In this paper, only are simulation results of glass and coarse sand paper pad listed. Figure 5 and Figure 6 are the heap configurations on glass pad and coarse sand paper pad.

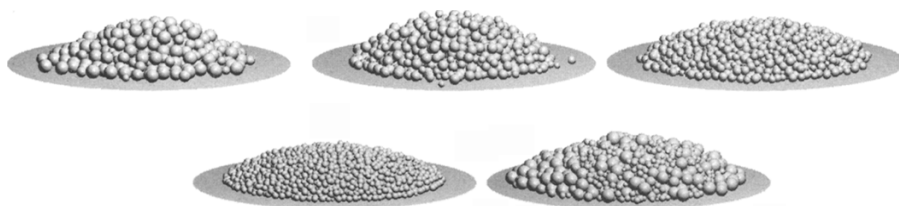


Figure 5. The finally simulated sandpile formed by 5 groups on glass pad (the order as follows: Group *a*, *b*, *c*, *d* and *e* in turn, and the corresponding angle of repose 28.3, 26.9, 24.5, 22.8 and 24.3 degree, respectively)

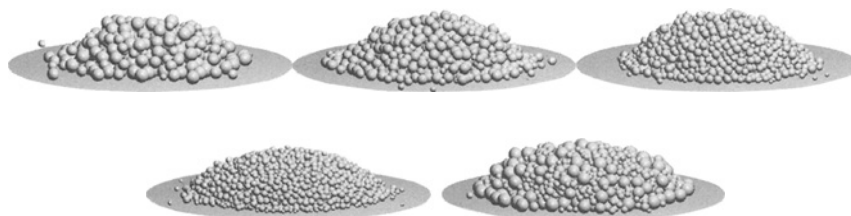


Figure 6. The finally simulated sandpile formed by 5 groups on coarse sand paper pad (the order as follows: Group *a*, *b*, *c*, *d* and *e* in turn, and the corresponding angle of repose 32.4, 30.8, 29.5, 26.6 and 27.2 degree, respectively)

DISCUSSION

As discussed in the Introduction, there are many factors that affect the angle of repose. These include the density, the shape, the friction coefficient between particle-to-particle, the friction coefficient between particle-to-ground, the size and the property of the particles and the way the heap is formed etc. In the following, the effect of grain size distribution and friction

coefficient between particles and different pad materials are discussed. For this purpose, other factors were kept the same in numerical simulation. For the convenience of comparison, all results (20 simulated results, respectively) were shown in Figure 7 and Figure 8.

It can be seen from Figure 7 and Figure 8 that the angle of repose gradually increases with grain size for a certain friction coefficient between particle-to-pad. At the same time, the repose angle of a sandpile formed on the pad with higher friction coefficient is larger than that on the pad with lower friction for a certain Group. It indicates that a larger repose angle can be obtained in the case of bigger grain size or higher friction coefficient between particle-to-ground for the particles with the similar shape and the same materials. For the Group e (mixture of Group a and d), the angle of repose is larger than that of Group a, but less than that of Group d under a certain pad, i.e. the repose angle of the mixture of two kinds of size distribution is between that of smaller and larger particles.

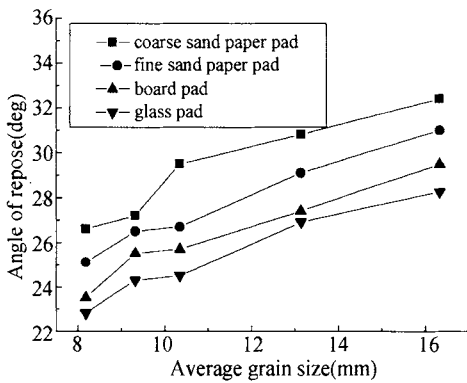


Figure 7. The relations between the angle of repose and the average grain size of each Group for each pad

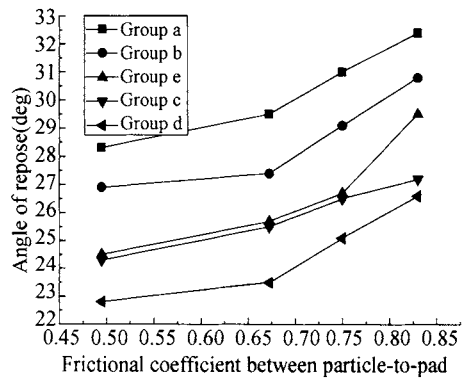


Figure 8. The relation between the angle of repose and the friction coefficient for each group

CONCLUSION

In this paper, the relationship between repose angle of sandpile formed by non-cohesive particle and different grain size distribution, and the relationship between different grain size and friction coefficient of different pad materials are analyzed. The results indicate that the modified DEM applied in this paper is very effective on simulating flow and heap problems of non-cohesive particles. Based on numerical simulation of 5 series of different grain size, with the other influencing factors kept the same, repose angle gradually increases with the increment of grain size and friction coefficient between particle and pad. Besides that, repose angle of mixture of two kinds of different size distribution is analyzed; the results show that the repose angle of mixture is larger than that of smaller grain size distribution, while smaller than that of larger size distribution.

REFERENCES

- Mehta A. and Barker G.C. (1994). Disorder, memory and avalanches in sandpiles. *Europhysics Letters*, 27: 501-506.
- Zhang D., Whiten W.J. (1999). A new calculation method for particle motion in tangential direction in discrete element simulations. *Powder Technology*, 102: 235-243.
- Ruskin H. J. and Feng Y. (1997). Self-organised criticality in some dissipative sandpile models. *Physica A*, 245: 453-460.
- Matuttis H.G., Luding S. and Herrmann H.J. (2000). Discrete element simulations of dense packings and heaps made of spherical and non-spherical particles. *Powder Technology*, 109: 278-292.
- Lee J. and Herrmann H.J. (1993). Angle of repose and angle of marginal stability: molecular dynamics of granular particles. *Journal of Physics A*, 26: 373-383.
- Baxter J., Tuzun U., Heyes D., Hayati I. and Fredlund P. (1998). Stratification in poured granular heaps. *Nature* 391: 136-137.
- Li Y. J., Xu Y. and Thornton C. (2005). A comparison of discrete element simulations and experiments for “sandpiles” composed of spherical particles. *Powder Technology* 160: 219-228.
- Trojan K., Ausloos M. (2003). Magnetically controlled ballistic deposition. A model of polydisperse granular packing. *Physica A*, 326: 492-510.
- Liffman K., Nguyen M. and Metcalfe G. (2001). Forces in piles of granular material: an analytic and 3D DEM study. *Granular Matter*, 3: 165-176.
- Cundall P. A., Strack O. D. L. (1979). A discrete numerical model for granular assemblies. *Geotechnique*, 29: 47-65.
- Jullien R., Meakin, P. (1990). A mechanism for particle size segregation in three dimensions. *Nature*, 34: 425-427.
- Luding S. (1997). Stress distribution in static two-dimensional granular model media in the absence of friction. *Physics Review E*, 55: 4720-4729
- Elperin T., Vikhansky A. (1998). Stress distribution in sandpiles-A variational Approach. *Physica A*, 260: 201-217.
- Elperin T., Golshtein E. (1997). Comparison of different models for tangential forces using the particle dynamics method. *Physica A*, 242: 332-340.
- Frette V., Christensen K., Malthesorensen A., Feder J., Jossang T. and Meakin P. (1996). Avalanche dynamics in a pile of rice. *Nature*, 379: 49-52.
- Zhou Y.C., Wright B.D., Yang R.Y., Xu B.H. and Yu A.B. (1999). Rolling friction in the dynamic simulation of sandpile formation. *Physica A*, 269: 536-553.
- Zhou Y.C., Xu B.H., Yu A.B. and Zulli P. (2002). An experiment and numerical study of the angle of repose of coarse spheres. *Powder Technology*, 125: 45-54.

ANALYSIS OF SEISMIC DISASTER OF MASONRY PAGODAS

Junlong Lu, Yin Zhang and Qianfeng Yao

College of Civil Engineering, University of Architecture And Technology Xi'an, China

Many strong earthquakes happened in the past in China and numerous houses were destructed heavily by earthquakes. As ancient high-rise buildings, the existent masonry pagodas suffered from earthquakes seriously too. They can provide a lot of information to study the historical earthquakes and seismic mechanics of masonry high-rise buildings. In light of seismic calculation by model analysis method, the capacity of Xingjiao Pagoda which is a national cultural relic in Chang'an, Shaanxi Province was discussed. Associated with the results of calculation, seismic disasters of masonry pagodas were analyzed. It can be conclude that the seismic disasters of masonry pagodas can be impacted by the followings: the soil conditions of subsoil, the characters of structures and responses to earthquakes. At the same time, some seismic disasters such as tops of towers falling or flection, tops of towers collapsed by shake and split along middle axis can be explained according to seismic response of masonry pagodas. Therefore, to protect the existent masonry pagodas from earthquakes, seismic check calculations must be involved. Based on results of seismic calculation, some suggesting seismic reinforcement for masonry pagodas are put forward viewed from culture relic protection and seismic engineering.

INTRODUCTION

Many strong earthquakes happened in the past in China and most of them brought remarkable disasters to people and made a large amount of buildings collapsed. However, many masonry pagodas preserved until today were suffered from earthquakes as production of national and international civilization and crystal of wisdom of the laboring people. To protect them from collapse, one of the key points is to analyze the seismic capacity of the structure to probe the seismic safety. The seismic protective methods have not been mature yet and it is difficult to bring forward some reasonably safeguards to masonry pagodas. The facts lie in the follows (Chen P., et al., 1999): On the one hand, scarce necessary theories of destroy mechanism, it is difficult to bring forward actually computing models and analysis methods. On the other hand, some traditional safeguards need rebuilding or changing the structure. They are difficult to carry out for colliding with the principle of culture relic maintenance of "revamps the old as the ancient". In this paper, some matters involved those are discussed.

ANALYSIS OF SEISMIC DAMAGE OF PAGODAS

By investigations to historic earthquake disaster, the characters and laws are analyzed as follows (Chen P., Zhao D., Yao Q.F., 1999).

Tops of towers falling or flected by shake

The tops of towers are concentrated in mass and usually standing high. The tops of towers also response heavily for whipping effect in earthquake. As a result, the tops of towers always are demolished in earthquake. A case in point, the top of the Big Wild Goose Pagoda in Xi'an, Shaanxi province, China was falling in an eight-grade earthquake in 1556.

Tops of towers collapsed by shake

In earthquake, the middle or bottom of towers is seldom parted; even an "X" oblique crack is singularly. But there are many pagodas whose top are collapsed and scattered. A case in point, the Small Wild Goose Pagoda in Xi'an lost its two stories collapsed by earthquake in 1556 and the stories lessened from 15 to 13(Figure 1). The brick masonry pagodas are small, with shrinkages in section areas, the top towers are influenced by high vibration mode heavily. Furthermore, the felt material of masonry is low in intensity; that is liable for the top to scatter in strong motions. Therefore, changes of section areas of brick masonry pagodas from bottom to top are facts leading the tops to scatter and fall.

Split along middle axis of pagodas

In strong motions, it is a prevalent and important law for brick masonry pagodas splitting along middle axis. That is not only a key reason why brick masonry pagodas are destroyed heavily and collapsed but also research basis of mechanism of masonry destroyed by earthquake. Based on the traditional theories, the critical section area of the tower should be in bottom. And the capacity of shear resistant is perfect than that of bend resistant. In earthquake, the tower might be destroyed for moment and break down toward one side. In fact, the bottom of towers is destroyed not at all; the vertical cracks and shaking scatters are appeared in the top where the stresses of moment and shear are very less. That is contradicting with traditional viewpoints. It is indicated that brick masonry pagodas were demolished by vertical axial cracks, which are evoked by shear stresses. The structure of brick masonry pagodas can be seen as a cantilever bar whose bottom is fixed. Impacted by earthquake, the maximum shear stress can appear around the neutral axis. For window and door holes are settled along the neutral axis, that gives more chance to pagodas destroyed by shear. Viewed from some earthquake damages, shear dislocations happens to form crevices along the neutral axis of brick masonry pagodas at first. Then the shear deformation is repeated back and forth impacted by last shake. Sometimes the deformations are regressed and the vertical crack closed. As indicated by related history, the Small Wild Goose Pagoda was "still exact as if the gods made it closed" in the earthquake in 1556. However, vertical cracks closed only happen in well subsoil or site with elastic. If the subsoil were not well enough, vertical cracks could be extended when large deformation appears and makes pagodas to collapse. For example, the Famen Pagoda in Fufeng County, Shaanxi Province was split for bad subsoil and one half was collapsed(Figure 2).



Figure 1. Small Wild Goose Pagoda

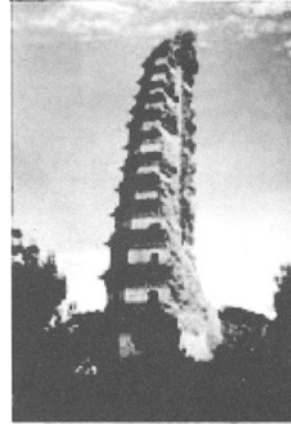


Figure 2. Famen Pagoda

Method to seismic check of masonry pagodas

The related research shows that masonry pagodas can be seen as a multi-particle structure system (Chen P., Zhao D., Yao Q.F., 1999). The earthquake action and response are calculated with model analysis method. Then the internal force can be combined with SRSS(Square Root of Sum Square) from no less than 3 modes. At the same time, calculation of the shear strength of connecting beams along the neutral area is a key point to safety of pagodas whose structure is hole-opened. That can be expressed in

$$\eta Q_i \leq [Q_i] \quad (1)$$

Where Q_i =shear force under intensity of seismic evaluation;

$[Q_i]$ =shear strength;

η = adjusting coefficient, to ordinary pagodas defined as 0.8, to important pagodas defined as 1.0.

Based on theoretical analysis and seismic disasters of masonry pagodas, shear stress in neutral area is enlarged because of holes in structure. It makes the shear strength of link wall beam insufficient and weakness points come into being. Associated to the characters of pagodas, a brief and convenient method was adopted to check the seismic strength. And the seismic safety of masonry pagodas can be analyzed based on disasters and calculating results.

EXAMPLE OF SEISMIC CHECK OF MASONRY PAGODA

Structure of the pagoda

Xingjiao Pagoda is the tomb of Xuanzhuang, a famous hierarch in Tang Dynasty. It lies in Chang'an County, Shaanxi Province, China. It is a brick masonry rectangle and five-floor pagoda. The pagoda and its size are shown in Figure 3 and Table 1.

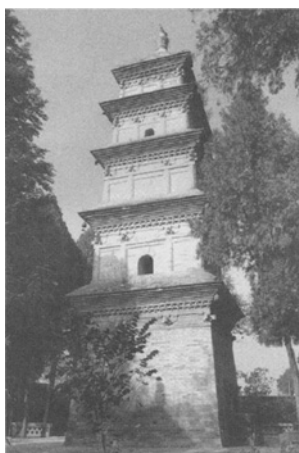


Figure 3. Xingjiao Pagoda

Table 1. Structure size of Xingjiao Pagoda

Item Floor	Size of sides (m)	Height of floors (m)	Height (m)	Size of holes			Extend size (m)
				height	broad	depth	
0	5.60	/	±0.00	/	/	/	/
1	4.95/5.12	5.40	5.40	1.76	1.20	1.80	0.70
2	3.96/4.13	3.75	9.15	0.96	0.66	0.60	0.60
3	3.63/3.80	3.38	12.53	0.70	0.52	0.50	0.50
4	2.97/3.30	2.78	15.31	0.50	0.40	0.40	0.40
5	2.97	2.48	17.79	/	/	/	0.30
Top of tower	0.68/29.7	1.73	19.52	/	/	/	/
Tip of tower	/	2.24	21.76	/	/	/	/

Calculating principles

The follows are considered when the sketch was defined.

1. Excluding the deviation of the pagoda, it was still think as vertical.
2. Excluding the torsion, the center of mass was inosculated.
3. Excluding the co-interaction of subsoil and structure, the pagoda was consolidated with subsoil.
4. The horizon earthquake action was disassembled along two main directions. Considering the pagoda is symmetrical in two directions and the NS direction is the weaker, we only calculated the earthquake action in NS.
5. For short floor height of the pagoda, the calculating elements were plot in each floor.
6. The ratio between height and width is high to each floor (more than 0.8). To enhance the calculating precision, the bend and shear was considered together.

Calculation and analysis

Xingjiao Pagoda is the first-group national relic. Based on the *Seismic Code for Seismic Design of Buildings* (GB 20011-2001) the grade of the pagoda is defined as Grade Two. Its earthquake resistant constructional measures can be reached 9 degree, one degree higher than that of Xi'an area. The site classification can be III based on soil conditions.

Equivalent gravity load

The pagoda can not be entered because of solid. So the variable loads were not included. The equivalent gravity load was characteristic value of permanent load.

The horizontal earthquake action of the first mode can be determined by the following:

$$F_{li} = \alpha_1 \gamma_1 x_{li} G_i = \alpha_1 \gamma_1 x_{li} m_{ig} \tag{2}$$

Earthquake action and seismic bearing capacity of each story

By SRSS, the seismic shear of drift can be acquired. Based on investigation and related materials, the index of bricks of the pagoda can be define as Mu15, sand pulp M0.4, the strength of the masonry can be determined as 0.04MPa according to *Code for Design of Masonry Structures* (GB 50003-2001). So the shear strength requires

$$V \leq \frac{f_{vE} \cdot A}{\gamma_{RE}} \tag{3}$$

By calculation, We check the strength at the spot of half the story height, the strength of each story can be showed in Figure 4.

From Figure 4 we can see that earthquake-resistant strength of each story is not sufficient, so the necessary measures should be taken.

Vertical earthquake action

Total characteristic value of vertical earthquake action is

$$F_{Evk} = \alpha_{v1} \cdot G_{eq} = 0.208 \times 417.70 \times 9.8 = 851.4 \text{ kN}$$

So vertical earthquake action of particle i is

$$F_{vi} = \begin{Bmatrix} 205.5 \\ 195.7 \\ 176.8 \\ 148.8 \\ 124.7 \end{Bmatrix} \text{ kN; and } 1.3 \times F_{vi} = 1.3 \times \begin{Bmatrix} 205.5 \\ 195.7 \\ 176.8 \\ 148.8 \\ 124.7 \end{Bmatrix} = \begin{Bmatrix} 267.2 \\ 254.2 \\ 229.8 \\ 193.4 \\ 162.1 \end{Bmatrix} \text{ kN.}$$

The tensile strength of masonry can be determined as 0.04MPa, that is

$$f_t = 40 \text{ kN/m}^2$$

So tensile strength of the pagoda is

$$[F_{vi}] = f_t \cdot A_i = 40 \times \begin{Bmatrix} 24.86 \\ 20.78 \\ 15.06 \\ 12.04 \\ 8.82 \end{Bmatrix} = \begin{Bmatrix} 994.4 \\ 831.2 \\ 602.4 \\ 481.6 \\ 352.8 \end{Bmatrix} \text{ kN}$$

For $F_{vi} < [F_{vi}]$, the tensile strength can be fulfilled.

Check of split along vertical neutral area

The calculation formulation is (Chen P., Zhao D., Yao Q.F., 1999)

$$\tau_s = Q_1 S_s / I_s B_s \quad (\text{Solid Part}) \quad (4)$$

$$\tau_k = Q_2 S_s / I_k B_k \quad (\text{Hollow Part}) \quad (5)$$

That can be shown in Figure 5.

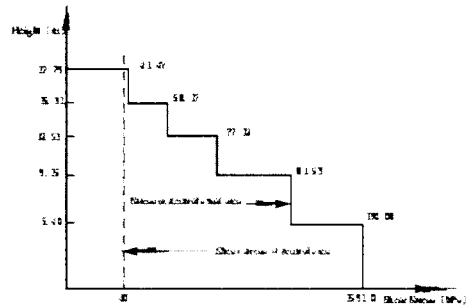
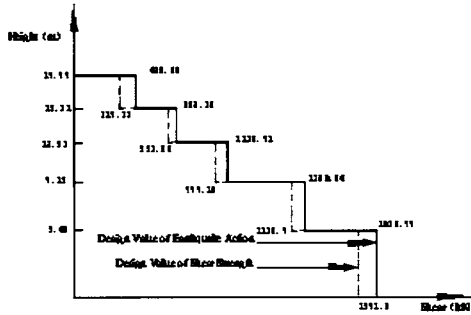


Figure 4. Check of horizon shear of the pagoda Figure 5. Check of vertical split of the pagoda

We can see that the shear strength of neutral area is 40 kPa, obviously it is not sufficient. So it is necessary to take some measures to protect the pagoda.

CONCLUSIONS AND SUGGESTIONS

By analysis we can see that seismic protection to masonry pagodas involves a lot of content such as the renovation of appearance, maintenances of culture relic and deviation rectification to pagodas. While the main topic lies in to avoid vertical splitting, collapse of tops of towers and deviation rectification. To solve those problems, some seismic measures of reinforcement can be taken as follows:

1. Setting hoops around pagodas. The hoops can be made of steel plate, reinforced concrete or reinforced masonry materials. The functions of hoops are to prevent extending of cracks, enhancing the shear strength of masonry and improvement of seismic performance by integration.
2. Felting cracks. Cracks in walls not only affect the appearance but also weaken structural integration of pagodas. It makes the seismic performance of structures weakened heavily. So pressure grouting can be applied to remedy it.
3. Aiming at the actuality and calculating result of Xingjiao Pagoda, following measures are suggested to take: Steel plate hoops are adhered along broad cracks at eaves and body of the pagoda. There is some thickness from exterior to hoops. After hoops set, bricks are applied to cover outside and that can not affect the appearance of the pagoda.

REFERENCES

- Chen P., Yao Q. F. and Zhao D. (1999). An exploration of the seismic behavior of Xi'an Big Wild Goose Pagoda. *Journal of Building Structures*, 20(2): 46-49.
- Chen P., Zhao D. and Yao Q.F. (1999). An exploration of the seismic behavior of Xi'an Xiaoyan Pagoda. *Journal of Xi'an University of Architecture and Technology*, 31(2): 149-151.

LIQUEFACTION OF SAND UNDER BI-DIRECTIONAL CYCLIC LOADING

Maotian Luan, Dan Jin, Zhendong Zhang and Qiyi Zhang

*State Key Laboratory of Coastal and Offshore Engineering, Dalian University
of Technology, Dalian 116024, China*

*Institute of Geotechnical Engineering, School of Civil and Hydraulic Engineering, Dalian
University of Technology, Dalian 116024, China*

A laboratory study is presented of liquefaction behavior of saturated loose sand subjected to bi-directional cyclic loading under isotropic consolidated conditions using the soil static and dynamic universal triaxial and torsional shear apparatus, which can apply axial pressure W and torque M_t individually. Tests were performed following the stress path that is controlled by shape of ellipse in terms of axial component $\sigma_d/2$ and torsional component τ . In this type of loading pattern the progressive rotation of orientation of principal stress axis and the unequal transverse and longitudinal cyclic components can be realized for simulating the complex stress condition induced by wave or earth embankments. For equivalent ratio of $\sigma_d/2$ to τ , the cyclic loading resistance decreases with the increasing area bounded by the elliptical stress path. And for the same area of the elliptical stress path, the sample exhibits the highest resistance to liquefaction when the ratio of $\sigma_d/2$ to τ reaches a critical value which equals to 0.6~0.75. The deformation behavior of sand is also considerably associated with the proportion of $\sigma_d/2$ to τ .

INTRODUCTION

Until recently, the major concern during earthquake loading of saturated sands was to avoid the occurrence of liquefaction. Saturated granular materials, such as sands and silts, when subjected to cyclic loading, the tendency of compact and decrease in volume will occur, and thus will generate excess pore water pressure if the drainage is prevented. The pore water pressure reaches the effective stress, what is known as liquefaction occurs.

Many studies have been done concerning with the characteristics of deformation and strength of sands in liquefaction. However, most of them are restricted in the behaviors of sands under narrow loading conditions, and cannot explain the characteristics under complex stress condition such as the cyclic stress induced by wave loading which characterized by the

fact that the orientation of principal stress axis rotates progressively. Cyclic simple tests such as triaxial shear test and torsional shear test are not able to reproduce the above-mentioned complex stress condition and cyclic loading pattern (Fu, 2000). Therefore, the efforts have been made by several researchers to well develop the soil experimental technology.

Seed (1975) has revealed that the multidirectional cyclic resistance is less than one-directional cyclic resistance by multidirectional shaking tests on dry sand. Boulanger (1995) has researched the liquefaction of sand under bi-directional loading and pointed out that the perpendicular cyclic loading resistance is lower than parallel cyclic loadings. Pyke et al. (1975) also accomplished bi-directional simple shear loading to evaluate the effects of bi-directional shaking on the deformation of dry sands. All the researches show that the rotations of principal stress axis influence the behavior of sand remarkably. Since the valuable laboratory data is extraordinary rare and not comprehensive, especially in the field of bi-directional cyclic loading with unequal peak value separately. This paper is aim to find some useful information about this issue by implementing sets of laboratory tests using the advanced soil static and dynamic universal triaxial and torsional shear apparatus.

The soil static and dynamic universal triaxial and torsional shear apparatus, which was accomplished in the Institute of Geotechnical Engineering, Dalian University of Technology after importing from Seiken Corp., Inc, was used in this paper. The apparatus enables simultaneously exertion and individually control of axial pressure W , torque M_T , outer chamber pressure p_o and inner chamber pressure p_i and combination of these components. Therefore the consolidation and loading paths under different complex stress conditions of soils can be implemented. It constitutes a well-performed universal test system that makes possible to conduct a great deal of experimental tests of soil under various complex stress conditions. Furthermore comprehensive and systematic analyses on deformation and strength characteristics of saturated loose sand under monotonic and cyclic shear loading are carried out.

EXPERIMENTAL TECHNIQUE

Hardware

The soil static and dynamic universal triaxial and torsional shear apparatus used for the experiments is composed of five components including main unit, air-water unit (air compressor and vacuum pump), analogue control unit, data acquisition and automatic control system and hydraulic servo loading unit (hydraulic actuators and hydraulic supply). The details concerning this comprehensive system were given by Luan et al. (2003).

Material and sample preparation

Please preserve the style of the headings, text font and line spacing in order to provide a uniform style for the proceedings volume. The materials used for this experimental study is

the Chinese Fujian Standard Sand. The basic properties were as follows: specific gravity $G_s = 2.643$; granular size $d_{50} = 0.34\text{mm}$; uniformity coefficient $C_u = 1.542$; the maximum and minimum void ratios $e_{\max} = 0.774$ and $e_{\min} = 0.537$; and the maximum and minimum dry unit weights $\rho_{\max} = 1.72\text{g.cm}^{-3}$ and $\rho_{\min} = 1.49\text{g.cm}^{-3}$.

The sand sample is prepared by pluviation through air. Saturation of the sample is fulfilled by pouring both CO_2 and de-air water and by exerting backpressure. Consolidation and cyclic stress-controlled tests are carried out on the hollow cylinder soil samples with height of 150mm, outer diameter of 100mm and inner diameter of 60mm. All samples are tested undrained with pore pressure measurement and consolidated in the triaxial cell under a backpressure of 200kPa to ensure full saturation and rapid pore pressure response. The average B value (Skempton, 1954) for all samples was 0.98, and any samples that did not have a B value of at least 0.96 were discarded. The stress state on the hollow cylinder sample is shown in Figure 1.

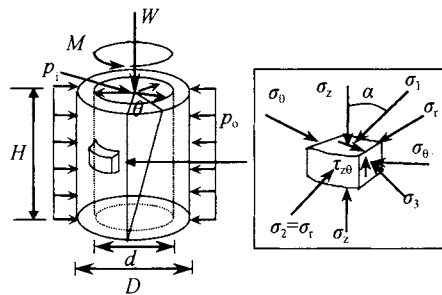


Figure 1. Stress state of soil element in hollow-cylinder soil sample

Test characteristics

To simulate the cyclic stress induced by wave loading which characterized by the fact that the orientation of principal stress axis rotates progressively, the phase different of the axial pressure and the torque are kept with 90° in the bi-directional cyclic loading tests. Figure 2 shows both the two cyclic components recorded in the test.

A total of 19 bi-directional cyclic loading tests will be discussed. Three various areas bounded by the elliptical stress path followed during the test in terms of $\sigma_d/2$ and τ are employed. And for each area the amplitude of the axial and shear stresses are kept changing to research the effect of each component on the strength and deformation behavior of saturated loose sand. To discuss the effect of each component on behavior of dynamic shear on sands, the specific value of the amplitude of dynamic axial stress and shear stress is defined as $(\sigma_d/2)/\tau = \lambda$. Furthermore, a radius $\sigma^* = \sqrt{(\sigma_d/2) \times \tau}$ of the circle whose

area is equal to the elliptical area is evaluated to study the effect of elliptical area on strength of sands in liquefaction. There are two methods to be applied in the tests.

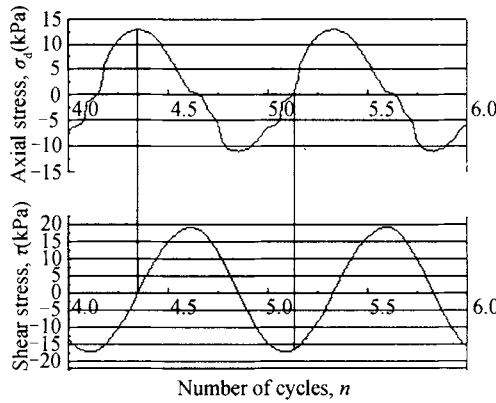


Figure 2. Cyclic components recorded in the test

(1) Several samples are subjected to cyclic loading following the elliptical stress path with constant ellipse area, but with λ varied. In this type of tests there are total three different ellipse areas employed, and at least four samples tested with different specific value λ for each ellipse area. When λ is much less than 1, the bi-directional shearing could be simplified to torsional shearing approximately. And when λ is much larger than 1, the bi-directional shearing could be simplified to triaxial shearing approximately. Figure 3 shows the loading patterns changing from similar cyclic triaxial shearing to similar cyclic torsional shearing.

The tests are investigated to simulate the decreasing ratio of vertical to horizontal accelerated speed occurring from near field earthquake to far field earthquake. The similar cyclic triaxial test is shown in Figure 3(a), in which the axial stress is much larger than shear stress as near field earthquake condition.

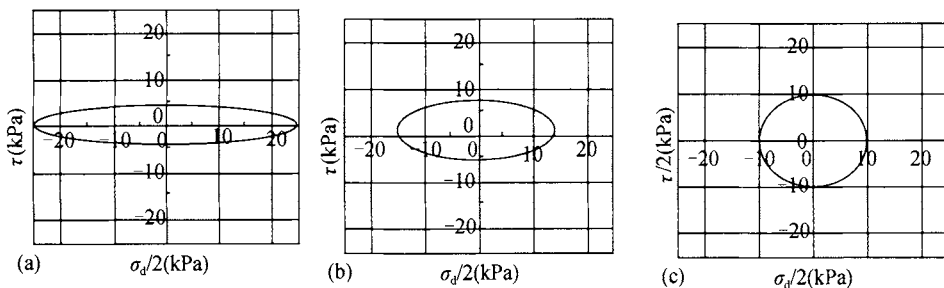


Figure 3. Stress paths in bi-directional cyclic shearing under isotropic consolidation

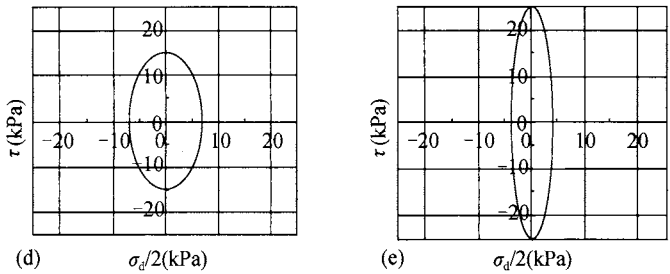


Figure 3. Stress paths in bi-directional cyclic shearing under isotropic consolidation (continued)

(2) Several samples are subjected to cyclic loading following the elliptical stress path with different ellipse area, but with λ constant. In this type of tests there are total five different values of λ employed, and at least two samples tested with different ellipse area for each λ .

The two actual stress paths recorded in tests shown in Figure 4 represent the specific value of λ larger and less than one respectively. It can be seen that the tests methods are valid, for which can realize the principal stress rotating progressively and the alteration of each cyclic component.

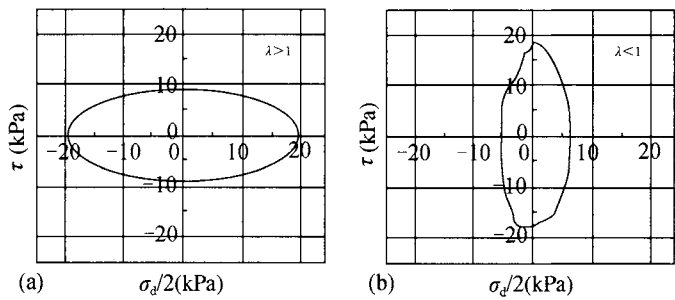


Figure 4. Stress paths recorded in vertical-torsional coupling shear tests under isotropic consolidations

TEST RESULTS AND DISCUSSION

Liquefaction

When a sand is subjected to cyclic shear loading under undrained conditions, the pore-water pressure rises, and consequently, the effective stresses decrease. If loading is continued, the pore water pressure may develop to the initial effective confining pressure and the effective stresses may be reduced to zero, resulting in what is known as liquefaction, as shown in Figure 5. Failure due to cyclic loading is defined by development of the pore-water pressure reaches its initial effective confining pressure.

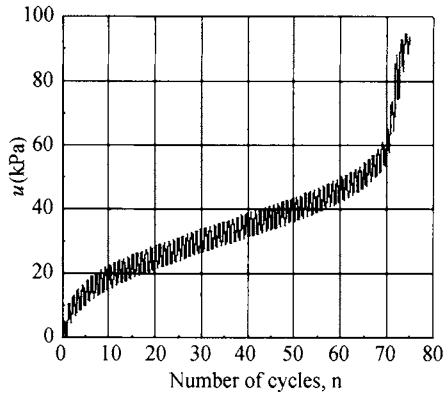


Figure 5. Pore pressure recorded in bi-directional cyclic loading

Strength

The liquefaction strength of saturated sand is commonly evaluated by undrained cyclic triaxial test with two-way loading in compression and extension (Hyde 2006). That is because the laboratory testing equipment is not generally available for performing tests which model multidirectional loading conditions (Boulanger, 1995). This paper considered more complex stress conditions of bi-directional cyclic shearing than one-directional cyclic shearing such as cyclic triaxial shearing. Thus bi-directional cyclic testing is capable of providing comprehensive conclusions in liquefaction. Using bi-directional cyclic loading tests the writers have therefore attempted to provide qualitative guidance on the effects of the two orthogonal cyclic components.

Figure 6 shows the relationships between λ and number of cycles to cause failure for each area of the elliptical stress path. Figure 7 shows the relationships between σ^* and number of cycles to cause failure for each identical λ .

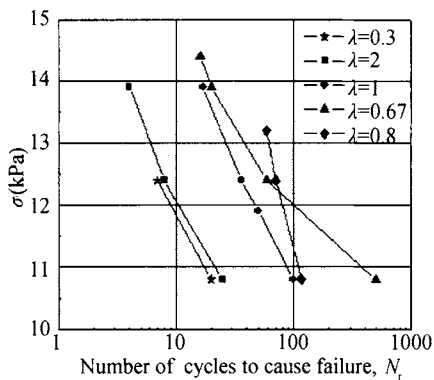


Figure 6. Relationship between λ and N_f

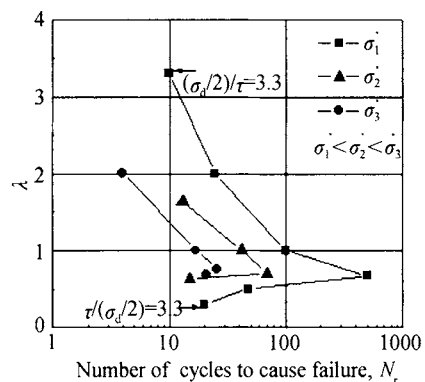


Figure 7. Relationship between σ^* and N_f

The tests results show that the strength of sand is closely associated with both the area of elliptical stress path and the ratio of two stress components λ . The specimen has a lower resistance to liquefaction if tested under elliptical stress path of a greater area. For the same area of elliptical stress path, sand behaves the highest cyclic loading resistance at a critical value of λ , which equals to 0.6~0.75. The cyclic loading resistance of sand increases with the decrease of λ when λ is larger than the critical value, whereas the resistance increases with the increase of λ when λ is less than the critical value. Moreover, for two types of stress combination with the same value of $(\sigma_d/2)/\tau$ and $\tau/(\sigma_d/2)$, the former one will result in the failure of sand more rapid, as shown in Figure 6. It shows that the cyclic loading resistance of saturated loose sand under similar cyclic torsional test is larger than that under similar cyclic triaxial test, which is uniformity with results of Guo (2003) and Boulanger (1995).

It can be clarified from Figure 7 that the cyclic resistance to liquefaction of sand decreases with the increase of ellipse area when λ is invariable. Moreover, the critical value of λ is increasing gradually with the ellipse area.

As a result, it should be comprehensively considered about in evaluating the cyclic resistance of sand to liquefaction, that both the area of elliptical stress path and the amplitude ratio of two orthogonal cyclic components.

Deformation

Figure 8, 9 (a), (b), (c) represent the undrained cyclic response of sand subjected to bi-directional cyclic loading with different λ but same ellipse area bounded by elliptical stress path. For isotropically consolidated samples, strain amplitude suddenly increased at an occasion and the sample failed within a few cycles. Such a rapid accumulation of strain, characteristic of loose sands, is now more commonly known as liquefaction failure.

The relationships between cyclic axial stress (σ_d) and axial strain (ε_v) are illustrated in Figure 8. Regarding to Figure 8 (a), (b), (c), sand exhibits softer behavior in extension side although the amplitude of cyclic stress is the same both in the compression and extension sides. Axial deformation in extension side is also considerably larger. In the first case of λ less than the critical value, the sample undergoes cumulative permanent axial strain on single extension side, as shown in Figure 8 (a). Conversely, in other cases of λ larger than the critical value, sample undergoes cyclic permanent axial strains both in the extension and the compression side, of which the extension side occurs more remarkable strain, as shown [Figure 8 (b), (c)].

It also can be seen from Figure 8 (a) that major axial strain occurs during the phase axial stress unloading for λ less than the critical value. And converse feature that major axial strain occurs during axial stress loading can be observed for the case of λ larger than the critical value, as shown in Figure 8 (b), (c).

The relationships between cyclic shear stress (τ) and shear strain (γ_θ) are illustrated in Figure 9. Almost all the shear strains exhibit double directional cyclic nature. For the first case of λ less than the critical value [Figure 9 (a)], the sample undergoes symmetric cyclic permanent shear strains. Conversely, for other cases of λ larger than the critical value [Figure. 9 (b), (c)], the sample undergoes asymmetric cyclic permanent shear strains.

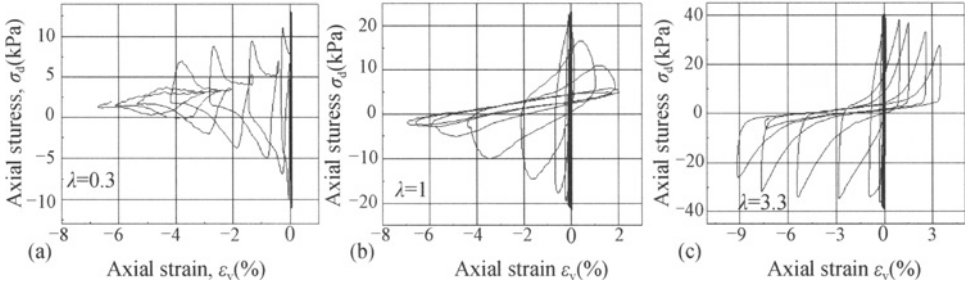


Figure 8. Relationships between axial stress and axial strain

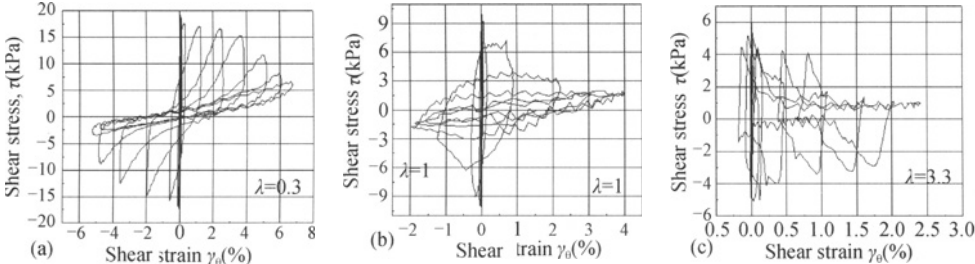


Figure 9. Relationships between shear stress and shear strain

Cyclic stress paths

Figure 10, 11 show typical effective cyclic stress paths corresponding to the cyclic stress-strain behaviors illustrated in Figure 8, 9. The rate of reduction in effective stress during cycling was approximately constant at the beginning of a test. However, as soon as the strain amplitude increased, the rate of reduction became increasing and the samples liquefied within 2-4cycles, characterized by transient excursions of the stress path through the origin (Ghionna and Porcino, 2006).

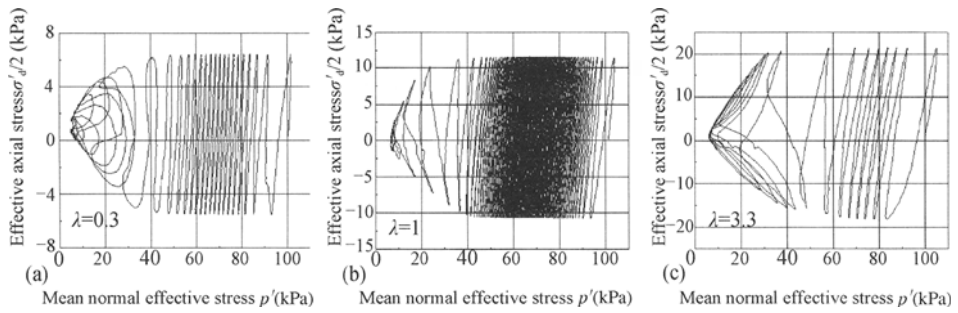


Figure 10. Relationships between effective axial stress and mean normal effective stress

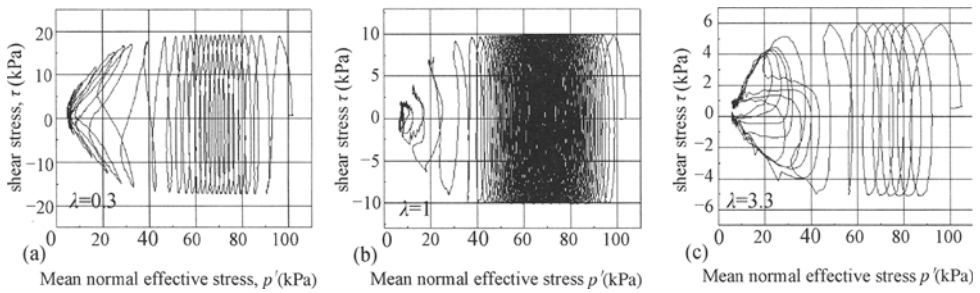


Figure 11. Relationships between shear stress and mean normal effective stress

Pore water pressure

Figure 5 depicts a trend with a number of cycles (N_f) cyclically induced pore water pressures (u). It can be observed that both the peak and valley values of u appear in one cycle, which means both dilative and contractive deformation occurs in the sample. But the extent of contraction is eventually greater than dilatation, which represented in the curve is that the residual pore water pressure develops gradually. Figure 12 (a), (b) illustrate $\sigma_d/2$, τ and u versus N_f curve. As marked in the figure, the pore water pressure and axial stress achieve their peak values at the same occasion in one cycle while the shear stress reaches the valley value.

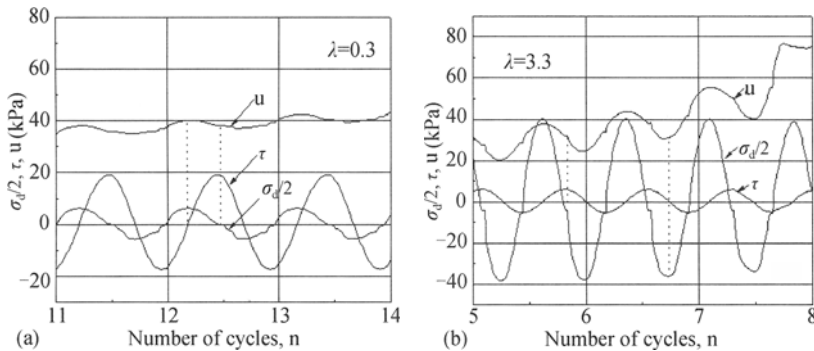


Figure 12. u , $\sigma_d/2$, τ - n curve

CONCLUSIONS

Undrained cyclic stress-strain-strength behavior of the Chinese Fujian Standard Sand has been investigated through cyclic bi-directional elliptical coupling shear tests. The main conclusions that can be drawn from the study may be summarized as follows:

(1) The cyclic resistance of sand is closely associated with both the area bounded by the elliptical stress path followed in terms of $\sigma_d/2$ and τ , and the ratio of $\sigma_d/2$ to τ . For the same λ , the resistance of sand decreases with the growth of ellipse area. There exists a critical value of λ . The sand may exhibit the highest resistance to liquefaction at this value for the same area of the elliptical stress path.

(2) When λ is less than the critical value, sample undergoes cumulative permanent axial strain only on the extension side and symmetric cyclic permanent shear strains on double direction.

(3) When λ is larger than the critical value, sample undergoes significant cyclic permanent axial strain both on the extension and the compression side, and much smaller asymmetric cyclic shear strains on double direction.

(4) The pore water pressure and axial stress achieve their peak values at the same occasion in one cycle while the shear stress reaches the valley value.

ACKNOWLEDGEMENTS

The authors wish to express their gratitude to Professor Dahong Qiu of Dalian University of Technology, who is a CAS's member, for his continuing support and invaluable advice for the investigation. The financial support for this study through the grant 50579006 and 50639010 from National Natural Science Foundation of China is mostly grateful.

REFERENCES

- Boulanger R. W., Seed R. B. (1995). Liquefaction of sand under bi-directional monotonic and cyclic loading, *J. Geotech. Eng.*, 121 (12), 870-878.
- Fu L., Wang H. J. and Zhou J. X. (2000). Effect of the initial rotation angle of principal stress on the dynamic properties of soil, *Chinese Journal of Geotechnical Engineering*, 22 (4): 435-440.
- Ghionna V. N., Porcino D. (2006). Liquefaction resistance of undisturbed and reconstituted samples of a natural coarse sand from undrained cyclic triaxial tests, *J. Geotech. Geoenviron. Eng.*, ASCE, 132 (2): 194-202.
- Hyde Adrian F. L., Higuchi T. and Yasuhara K. (2006). Liquefaction, cyclic mobility, and failure of silt, *J. Geotech. Geoenviron. Eng.*, ASCE, 132 (6): 716-735.
- Luan M. T., Guo, Y., Li M. G., Wang J., Wang D. and Chong J. Z. (2003). Discussions on related key issues in development of soil static and dynamic universal triaxial and torsional shear apparatus, *Chinese Journal of Dalian University of Technology*, 43 (5): 670-675.
- Pyke R. M., Seed H. B. and Chan, C. K. (1975). Settlement of sands under multidirectional shaking, *J. Geotech. Engrg. Div.*, ASCE, 101 (4): 370-398.

- Seed H. B., Pyke R. M. and Martin G. R. (1975). Effect of multidirectional shaking on liquefaction of sands, Rep. No. EERC 75-41, University of California, Berkeley.
- Skempton, A. W. (1954). The pore-pressure coefficients A and B, *Geotechnique*, 4 (4): 143-147.
- Vaid, Y. P. and Chern, J. C. (1983). Effect of static shear on resistance to liquefaction, *Soils Found.*, 23 (1): 47-60.

EARTHQUAKE SHOCKS AND LIQUEFACTION THREAT TO DHA AND CLIFTON AREAS, KARACHI PAKISTAN. A CASE STUDY

Syed Amir Mahmud, Shamim Ahmed Sheikh
Department of Geology, University of Karachi,
Karachi 75270, Pakistan

Coastal zones are always vulnerable to natural hazards while earthquakes and resulting liquefaction remains to be the most devastating phenomenon in urban areas. The residents of Defence Housing Authority and Clifton areas, part of Karachi coast have been experiencing jolts produced due to local seismic activity. As there are no seismographs installed, these jolts remain unrecorded and the local seismic behavior remains unexplained. In September, 2006 a water tank in DHA Karachi, vertically submerged into the ground. An investigation was made in this context; samples were collected and analyzed which revealed that liquefaction induced by local seismic activity resulted in the submergence of the tank structure. The threat of liquefaction is increasing in the coastal belt of Karachi as new buildings of ever increasing heights are being constructed recently. The threat of liquefaction can be minimized by applying geo-technical methods both by treating the soil layers and structure.

INTRODUCTION

The Defence Housing Authority came into existence through presidential order No. 7 of 1980 and was later approved by the National Assembly of Pakistan .The area is spread over 8852 acres and provides civic facilities to millions of residents.

In order to provide the residents with water, water tanks had been built through out the area, one of which collapsed and sunk vertically into the ground. This tank was constructed in mid seventies, by a joint venture with a Chinese company. According to the residents of the area, subsidence of the tank took 8 minutes causing the 80 feet high tank to submerge 70 feet in the ground, the remaining 10 feet left above the surface. This event that took place on the 8th September 2006 and resulted in destruction on a small scale, in the area, as water with high velocity gusted out of the tank.

A technical investigation was made to ascertain the causes of the collapse of the structure. The studies done in this context revealed that the major cause of subsidence of the tank could be liquefaction, possibly triggered by localized shocks which result in jolts in DHA and Clifton areas. The soil of the area has high tendency to liquefy as it is rich in water with increased salinity and very poor cementation of the particles.

GEOLOGICAL SETTING

The Karachi city and its surroundings have diverse geological conditions, with deformed Kirthar foothills in the North; Pab and Mor ranges in the West, Indus Delta in the East and

Arabian Sea in the South. Rocks ranging in age from Eocene to Recent, deposited under shallow marine to deltaic conditions, are exposed.

Karachi is a part of major synclinorium stretching from the Ranpathani River in the East to Cape Monze in the West, Mehar and Mol Jabals (mountains) in the North. Within the synclinorium a number of structures as Pipri, Gulistan-e-Jauhar, Pir Mango and Cape Monze are exposed (Quraishi et al., 2001).

Defence Housing Authority is part of Southern coastal strip of Karachi (Figure 1), covering an area of 8852 acres, with Arabian Sea in the South and South West, Gizri Creek in the East and South East, and Karachi Harbor and Clifton in the West. The topography of the area is flat with very low relief. Exposures of inter-bedded yellow and grey sandstone and limestone (Gulistan-e-Jouhar member of Gaj Formation, Miocene) and Grey sandstone (Manchar Formation, Pliocene) are present in the Northern part. Structurally this is the Southern most extremity of a low angled anticline known as the Gulistan-e-Jouhar anticline.

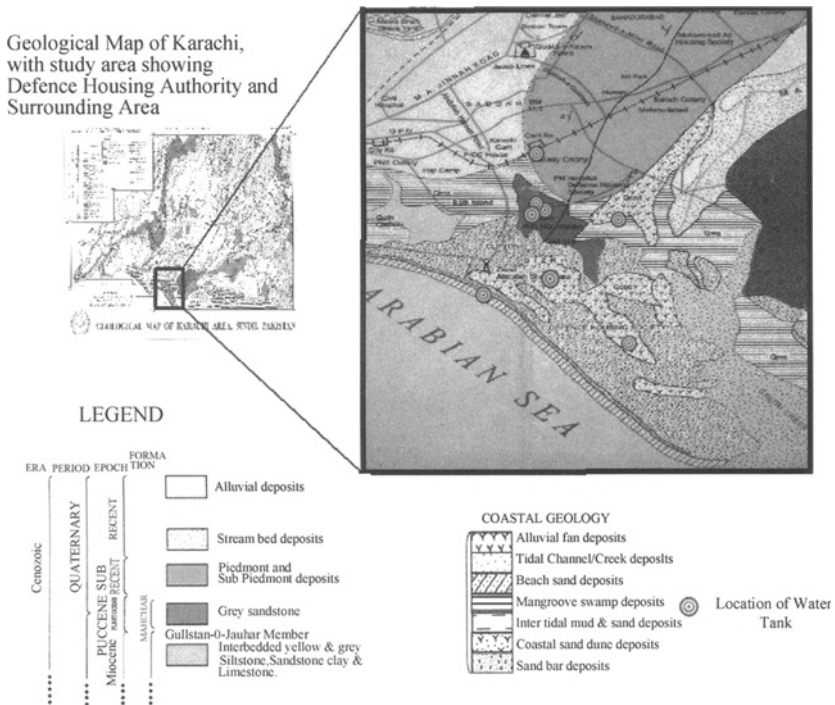


Figure 1. Geological Map of Study Area

The Southern part of DHA is influenced by Coastal geology with Beach Sand Deposits (Qbs) found along the Arabian Sea. The Sand Bar Deposits (Qsb) and Coastal Sand Dune Deposits (Qcsd) are widely distributed through out the area, while the Mangrove Swamp Deposits (Qms) in the North East.

Several water tanks have been constructed in the area, the sub surface geology is mainly influenced by recent coastal deposits, details of the sub surface geology of each tank and location is given in Table 1.

Table 1. Locations of water tanks and the sub surface lithology

Serial	Co-ordinates	Location & Remarks	Subsurface Lithology
1	N24°47.886,E67°48.387	Phase 5 Extension <i>The collapsed tank</i>	Beach sand deposits ,Sand bar deposits
2	N24°48.199,E67°03.732	Phase 6	Coastal Sand dune deposits ,Sand bar deposits
3	N24°49.120,E67°03.180	Phase 5	Manchar formation ,mangrove swamp deposits
4a	N24°49.128,E67°03.172	Phase 5	Manchar formation ,mangrove swamp deposits
4b	N24°49.128,E67°03.172	Phase 5	Manchar formation ,mangrove swamp deposits
5	N24°49.552,E67°04.166	Phase 7	Gaj formation, Mangrove swamp deposits.
6	N24°50.537,E67°03.432	Adjacent to Phase 2 and 1.	Gaj Formation
7	N24°47.610,E67°04.092	Phase 6, Ittehad	Coastal sand dune deposits ,Sand bar deposits

MATERIALS AND METHODS

Sediment samples were collected from the tank site located using Global Positioning System (GPS), from a depth of 3 feet .These samples were analyzed in the laboratory for the following parameters.

Grain size

200 grams of each sample was taken for sieving using the sieve shaker set. The grain size data obtained is given in Table 2. The cumulative curves drawn from this data are illustrated in the following two graphs.

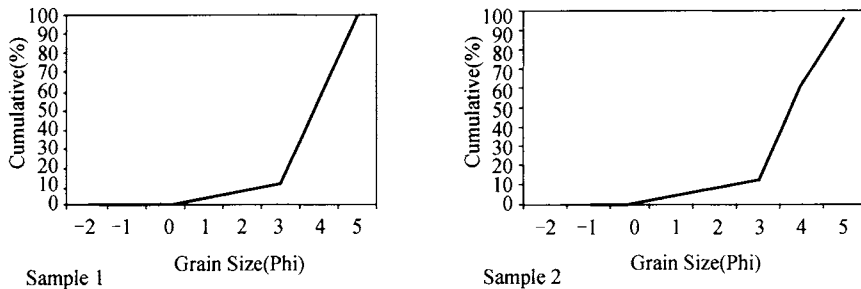


Figure 2. Sample Size distributions

Table 2. Result of Grain size analysis

Grain Size		Sample 1			Sample 2		
Φ	Mesh #	Weight (gm)	Weight (%)	Cumulative (%)	Weight (gm)	Weight (%)	Cumulative (%)
-2	5	0	0.0	0.0	0	0.0	0.0
-1	10	0.2	0.1	0.1	0.2	0.1	0.1
0.0	18	1.2	0.6	0.7	0.9	0.45	0.55
1	35	5.4	2.7	3.4	6.4	3.2	3.75
2	60	5	2.5	5.9	4.8	2.4	6.15
3	120	11.2	5.6	11.5	9.5	4.75	10.9
4	230	91.3	45.65	57.15	103.4	51.7	62.6
5	Pan	84.7	42.35	99.5	70.7	35.35	97.95

Sorting

The samples were found to be moderately sorted, it was determined by the formula

$$(\Phi_{84} - \Phi_{16})/4 + (\Phi_{95} - \Phi_5)/6.6 \quad (\text{Folk, 1980})$$

The Standard Deviation determined is 0.84 Φ .

Water content

10 grams of each sample was taken after coning and quartering, and was placed over night in an electric oven at 100°C. The difference in the weight revealed that the average water content present is 17.85%.

Mineralogy

The samples were observed under a binocular microscope, the major mineral observed was quartz with subordinate amounts micas and some calcareous grains. The grains were moderately to well rounded, poorly packed with cementation almost absent.

Soil classification

The grain size data reveals that the samples contain an average 38.67 % Silt and 59.77 % of Sand. The samples were classified as Silty Sand, (zS) (Folk, 1980) (Figure 3).

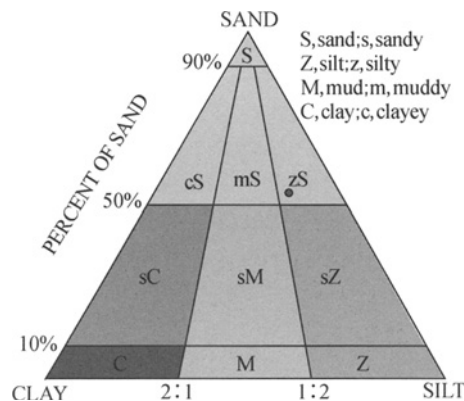


Figure 3. Fols Classification of soil (Folk, 1980)

Core density

A 2 liter cylinder weighed in the laboratory was taken to the site and drawn 2 feet inside the ground, it was again weighed and the mass of the soil collected was calculated, the density of the soil was calculated to be 1.39 gm/ltr.

Clay content

10 grams of each sample was taken and 100 ml of water was added, the sand was allowed to settle and was separated by decantation process, the remaining solution was dried in the oven. After the water had evaporated the clay left was weighed which was found to be 0.1% to 0.2 % in mass.

DISCUSSION AND CONCLUSIONS

Different parameters and analyzed results have been discussed below which reflect the behavior of ground which includes: location of ground water table, soil type, soil relative density, particle size gradation, particle shape, depositional environment of soil, soil drainage conditions, confining pressures, aging and cementation of the soil deposits, the intensity of ground shaking and its duration.

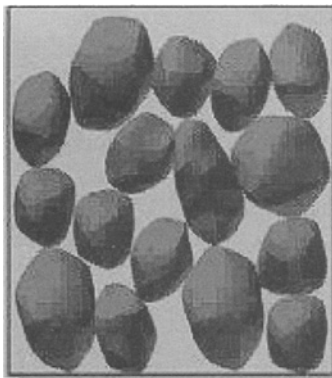
The soil may lose its strength and liquefy due to the loss of effective stress during earthquake vibrations if it is uniformly graded with a grain size less than 0.7mm (Tony, 1994). The analyzed samples of soil revealed that 99.37 % of the grains are of the size less than 0.7mm.

Sandy and silty sands are most prone to liquefaction (Environment Canterbury fact sheet, 2006), the samples collected from the collapsed tank site are classified as Silty-sand.

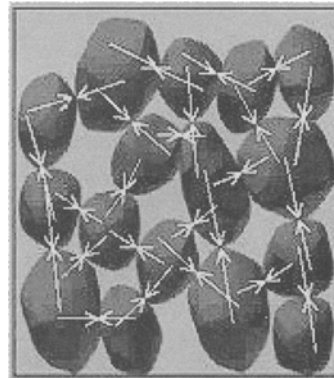
The density of soil is an important factor in the evaluation of its strength. Saturated, low density soils have the highest potential to liquefy (Moffat, 2007). Poorly packed sands with low relative density are more susceptible to liquefy (Tony, 1994). The soil samples collected are saturated and have a low density i.e. 1.39 gm/lt.

The liquefaction potential of soil is greatly influenced by the particle arrangement. Poorly graded, well rounded grains increase the pore water pressure which increases the susceptibility of soil to liquefy (Moffat, 2007). The soil samples analyzed were moderately sorted, rounded to well rounded, poorly packed with cementation almost absent.

A soil deposit consists of an assemblage of individual soil particles, the weight of the overlying soil particles produce contact forces between the particles - these forces hold individual particles in place and give the soil its strength (Figure 4 a, b).

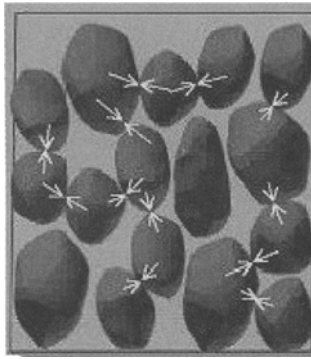


(a) Soil grains in a soil deposit, with blue color showing the pore water pressure



(b) The lengths of the arrows represent the size of the contact forces between individual soil grains. The contact forces are large when the pore water pressure is low

Figure 4. (After Jorgen, 2000)



(c) Arrows showing Small contact force between the grains

Figure 4. (After Jorgen, 2000) (continued)

An increase in water pressure which reduces the contact forces between the individual soil particles, thereby softening and weakening the soil deposit. Contact forces become small because of the high water pressure. (Figure 4c), in some cases, the pore water pressure may become so high that many of the soil particles lose contact with each other; the soil will have very little strength, and will behave more like a liquid than a solid (Jorgen, 2000).

The samples collected from the tank site contained average 17.85 % water, with the Arabian Sea coast at a distance of 300 meters. Saline water also plays an important role in the soil behavior. The water contents are high due to the close proximity of the sea as well as the rain water that may have also changed the soil salinity. The local conditions are favorable for the increase in the pore water pressure .Water table in the area is as shallow as 3-4 meters. Liquefaction has been abundant in areas where ground water lies within 10 meters of the ground surface (Hussain et al., 2004)

Reclaimed lands, wind-deposited soils, or sites comprised primarily of sedimentary deposits are all at a higher risk to liquefy. (Moffat, 2007).The Coastal zones of Karachi specially DHA and Clifton areas have been developed on reclaimed land, this un-natural process of regressing the coast is still underway with an efficient pace. Unconsolidated loose sand deposits are found to an average depth of 35 meters in these areas.

Sands may liquefy during periods of earthquake due to the propagation of seismic waves through the grains (Tony, 2002), the residents of Defence Housing Authority and Clifton have been experiencing seismic jolts in which the energy propagates from South to North, Due to un-availability of seismic stations no records are present but the residents have felt intense shaking produced due to the unknown phenomenon responsible for producing these jolts.

During an earthquake, significant damage can result due to instability of the soil in the area affected by internal seismic waves. The soil response depends on the mechanical characteristics of the soil layers, the depth of the water table and the intensities and duration of the ground shaking. If the soil consists of deposits of loose granular materials it may be compacted by the ground vibrations induced by the earthquake, resulting in large settlement and differential settlements of the ground surface. This compaction of the soil may result in the development of excess hydrostatic pore water pressures of sufficient magnitude to cause

liquefaction of the soil, resulting in settlement, tilting and rupture of structures (Bertero,1997).

In recent times, shocks have been felt in the area of DHA and Clifton which seems to be responsible for causing liquefaction, synchronized with collapse of the tank. Significant damage can result due to instability of the soil in the area affected by internal seismic waves. The soil response depends on the mechanical characteristics of the soil layers, the depth of the water table and the intensities and duration of the ground shaking, as discussed above. If the soil consists of deposits of loose granular materials as of the coastal deposits it may be compacted by the ground vibrations induced by seismic shocks, resulting in large and differential settlements of the ground surface. It is concluded that the subsidence of the water tank took place due to the liquefaction which was triggered by the local seismic activity which is being felt by the residence of Defence Housing Authority and Clifton areas.

RECOMMENDATIONS

Several hundred of thousand people live in Defence Housing Authority and Clifton areas along the coastal belt of Karachi. High rise residential buildings of Clifton and The Sea View Apartments Township are the most venerable localities to natural hazards specially to liquefaction. It is recommended that the following steps should be taken immediately.

- A network of seismographs should be installed through out the area in order to record the local seismic activity.
- Studies should be under taken in order to exploit the ground strength for various layers through out the area which should include the Standard Penetration Test (SPT), Cone Penetration Test (CPT) and a data-base should be developed for these geo-technical information which should be applied while planning the construction.
- Liquefaction hazard maps should be developed and made public followed by public awareness programs.
- Standards for constructions should be designed and implemented.
- The buildings constructed in the past should be inspected and checked thoroughly for strength and the subsoil conditions, reinforcements should be applied to the buildings or the soil as necessary.
- It had been observed that old buildings and water storage tanks were fitted with advertising hoardings and cellular phone antennas which might be responsible for extra load on the structure and may become fatal.

REFERENCES

- Bertero V. V. (1997). *An illustrated introduction to earthquake engineering principles*. Web version by Virian Isaradharm. National Information Service for Earthquake Engineering University of California, Berkeley http://nisee.berkeley.edu/bertero/html/damage_due_to_liquefaction.html
- Environment Canterbury.2006. *Environment canterbury fact-sheet*.
www.ecan.gov.nz/our+environment/liquefactionfactsheet.htm
- Folk R. L. (1980). *Petrology of sedimentary rock*. Austi, Tex.Hemphill

- Hussain V., Sheikh S. A., Tabrez A. R. and Anjum S. (2004). Liquefaction effects of bhuj earthquake on thar-indus delta region of sindh. Pakistan. *SEGMITE international: A journal of Resource, Industrial and Environmental Geology*. Volume 1.
- Jorgen J. (2000). Soil liquefaction website. Department of Civil Engineering, University of Washington ,www.ce.washington.edu/liquefaction
- Moffat B.S., (2007). Soil remediation techniques for reduction of earthquake-induced liquefaction. *In proceedings of the ASCE/SEI Structures Congress* .Long beach, California
- Quraishi I. H.,Shah S. A. A., Tariq M. A., Khan M. S., Ahsan S. N. and Khanzada M. I. (2001). *Geological map of karachi area, sindh Pakistan*. Geological Survey of Pakistan, Map series number 3.
- Tony W. (2002). *Foundation of engineering geology*. 2nd Edition, Spon Press, London, USA, Canada.

STUDY ON DYNAMIC PROPERTIES OF SATURATED CLAY AND UNDISTURBED SILTY CLAY

Ying Nie

*School of Civil and Hydraulic Engineering University Department, Dalian University of
Technology, Dalian 116085, Liaoning Province, China*

Maotian Luan^{1,2}, Qi Shao^{1,2}, Shujie Liu^{1,2}, Meng Wang^{1,2}

*State Key Lab. of Coastal and Offshore Engineering, Dalian University of Technology,
Dalian 116085, China*

*School of Civil and Hydraulic Engineering, Dalian University of Technology
Dalian 116085, China*

The testing is employed to perform cyclic torsional shear test under isotropic consolidated condition. The authors conducted three dynamic torsional with single sample achieving dynamic properties under three confining pressures with saturated clay and undisturbed silty clay in Dalian. Special attention was paid to the maximum dynamic shear modulus G_{\max} and ξ obtained from single sample of cyclic simple shear test was basic approximated with traditional method of dynamic torsional test. Based on the test results and theoretical analysis, the confining pressure had a significant influence on the dynamic shear modulus and feeble influence on the dynamic damping ratio. It was also found that the G of two soils decreases when the confining pressure decreases from 400kPa to 100kpa and the decreasing gradient of G is less than the increasing gradient of G from 100kpa to 400kPa. This paper indicates that $G/G_{\max} - \gamma$ and $\xi/\xi_{\max} - \gamma$ of two soils fall in a narrow band. The relation of G and ξ can be fitted by logarithm equations in this paper. Furthermore, this method can diminish the difference of the sample during experiment and effectively provide convenience with authentic experimental results.

INTRODUCITON

As an important aspect on the research of the soil dynamics, the dynamic shear modulus and damping ratio are the two principal parameters, which can be required to set up the model of Hardin-Drnevich (1972), to describe the stress-strain relationship. In order to investigation on the dynamic shear modulus and damping ratio of soil, free vibration method by resonant column apparatus were carried for different soils by Gu et al. (1995) and Yuan et al. (2000). It was shown by Xie et al. (1988) that on occasion of small strain; one sample could be loaded progressively, according to the test of measuring module and damping ratio. Through the dynamic triaxial test by Guo et al. (2006), it proved that to load multilevelly on one sand sample could be practicable. After many years of experimental investigation, according to many types of soil sample, dynamic properties under triaxial test by He et al.

(1997) use one specimen on 20 level loads after changing confining pressure or consolidation ratio and keeping on consolidation and revibration.

Recognized as the perfect test on research of soil dynamic property, the dynamic torsional test is the ideal method to measure dynamic property, according to which, the dynamic property of dynamic torsional tests on clay and silty clay were discussed in this paper. Guo et al. (2006), He et al. (1997) and WANG et al. (2005) have measured the module and damping ratio using one sand sample on the dynamic triaxial apparatus, and demonstrated the reliability of test results, without the discussion of feasibility to get dynamic shear modulus and damping ratio through the dynamic torsional test of progressive loading after changing confining pressure of single sample under the small strain. Therefore, it is discussed that the method of getting dynamic shear modulus and damping ratio curve of saturated clay and undisturbed silty clay through changing the confining pressure (including imposed and reduced pressure) by single sample, the result of which was compared with the result of the dynamic torsional test under three different consolidation pressures by three independent samples respectively.

TEST APPARATUS AND EXPERIMENTAL PROCEDURE

The clay and silty clay for test were all taken from Dalian. The clay was made into the specimen by vacuum suction method. Considering the Poisson ratio at initial state of undisturbed silty clay approached to 0.44 and the problems of losing water of the specimens in transportation and preservation, the pore water pressure coefficient of each sample was assured to reach more than 0.98 by the saturation of applying backpressure deaired water. The basic physical property indices of the samples are listed as Table 1.

Table 1. Physical property of the clay and silty clay samples

	ρ ($t \cdot m^{-3}$)	w (%)	G_s	w_p (%)	w_l (%)	I_p	S_r (%)
saturated clay	1.95	29	2.67	18	36	18	>98
Silty clay	1.92	17	2.65	14.03	23.1	9.07	>98

Put one sample of saturated clay and another sample of undisturbed silty clay respectively into 100kPa consolidated pressure firstly, and then applies about 20 level different loading at frequency of 0.1Hz with 5 cycles per load level. Due to the same samples, keep on the consolidation respectively at 200kPa and 400kPa consolidation pressure and apply cyclic loading sectional; to the same sample, reduced the consolidation pressure to 200kPa and 100kPa and then reconsolidate it by applying cycle loading sectional, measuring the G and ζ of soil when rebounding under degressive consolidation pressure relevantly. Compared with the result of dynamic torsional test about dynamic property by adopting three independent samples of two kinds of soil samples at 100, 200 and 400kPa confining pressure, the former kind of curve went around the later one within 20%. It can make sure the reliability of experimental results and analyses to use the method of getting dynamic property of different consolidated pressures (including imposed and reduced pressure) with single sample.

The soil static and dynamic universal triaxial and torsional shear apparatus was jointly designed by Dalian University of Technology and Seiken Corp., Inc., Japan in 2001. The hollow cylindrical sample was used in this experimentation, with external diameter of 70mm, inner diameter of 30mm and height of 100mm. The sinusoid cycle load was adopted in the cycle torsion shear test, with frequency of 0.1Hz and applying equal confining pressure both inside and outside at same time

THE EXPERIMENTAL RESULT ANALYSES OF SHEAR MODULUS

The $G-\gamma$ relation curve of single sample with imposed pressure

Based on the curve of hysteric relationship of τ and γ in the condition of cyclic stress, the dynamic shear modulus of different strain levels can be gotten. In the condition of avoiding pore water pressure raise obviously, the changing law of G with γ of single sample due to two kinds of soil samples consolidated in different confining pressures, as Figure 1. G and G_{max} are both growing with the increase of confining pressure, the reason of which is that when applying confining pressure, the grains inside the sample come to a thickening trend continually, the void ratio decreases and the grain contact point of soil increases, which makes the dynamic strain less and the slope of skeletal curve increase. It is also shown in the picture that the G of undisturbed silty clay is larger than that of saturated clay and the G of silty clay increases more when confining pressure increases, that is, the shear modulus of silty clay is more sensitive than that of clay.

The $G-\gamma$ relation curve of single sample with imposed and reduced pressure

According to each single sample of two kinds of soil, reduced the consolidation pressure to 200kPa and 100kPa, and then apply cyclic loading to get the reduced rebound $G-\gamma$ relation curve of the two soil in the degressive consolidation pressure as Figure 2. It is also shown in the picture that the dynamic shear modulus of two kinds of soil decreases after confining pressure reduced, but can be little larger than that of increase confining pressure. That is, the G decreases as the pressure reduced and the descending gradient is smaller than that of imposed gradient with increasing pressure.

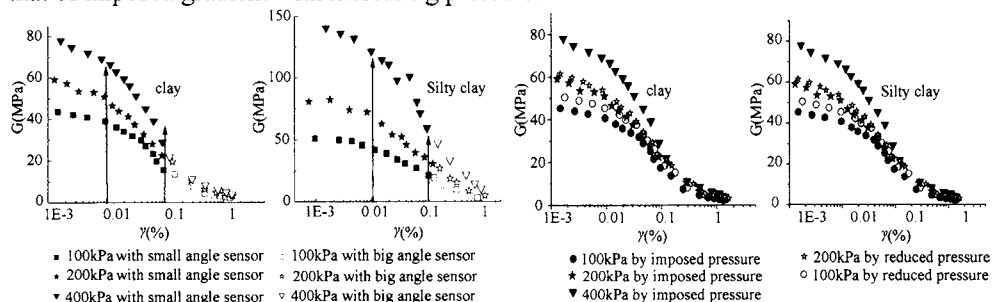


Figure 1. Variation of $G-\gamma$ by imposed and reduced pressure

Figure 2. Variation of $G-\gamma$ of single sample with three pressure

The $G-\gamma$ relation curve measured by two methods

The experimental result of measuring G by one sample of multiple consolidations can be compared with the one by three single sample, from which the $G-\gamma$ relation curve should be gotten as Figure 3 (In the picture, the solid icon stands for Method 1: the result of single sample by multiple consolidation; the hollow icon stands for Method 2: the result of three samples by respective consolidation). As is analyzed from Figure 4, the trend change of the two $G-\gamma$ relation curve are affected a lot by the two methods, especially when $\gamma < 10^{-3}$, that is, the influence in minute shearing strain amplitude value is very particular, but not when $\gamma > 10^{-3}$ at all. The dynamic shear modulus of multiple consolidation by one sample is a little lower than the one of consolidation by three single samples, but when confining pressure comes to 400kPa, the difference between two curves enlarges, which shows that although the variant level increases as confining pressure increases, it can also ensure the reliability of experimental result basically, compared with the result of routine dynamic torsional test, especially in the confining pressure of 100kPa and 200kPa. As is also shown in Figure 4, the difference of undisturbed silty clay is larger than the one of clay when confining pressure is 400kPa, which probably relates to the internal structure of the two kinds of soil samples.

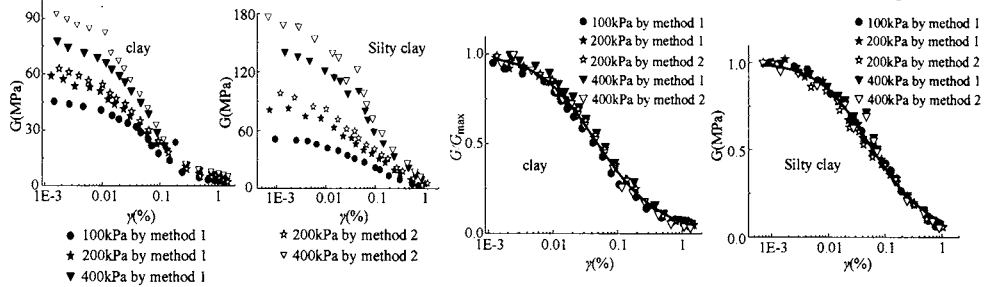


Figure 3. Variation of $G-\gamma$ by two test method Figure 4. Variation of $G/G_{max}-\gamma$ by two test method

G_{max} and G/G_{max} acquired by different experimentations

When the maximal shear modulus is ascertained from test information, dynamic stress-strain relation is supposed to meet the Hardin – Drnevech hyperbola model, which expression can be written as:

$$\tau_m = \gamma_m / (a + b\gamma_m) \quad (1)$$

where $a=1/G_{max}$, G_{max} is the initial slope coefficient of skeletal curve; $b=1/\tau_{max}$, τ_{max} is the maximum shear stress. Through the coordinate transformation of equation (1), it can be written as:

$$\gamma_m / \tau_m = 1/G = a + b\gamma_m = 1/G_{max} + \gamma_m / \tau_{max} \quad (2)$$

After $1/G_{max}-\gamma$ linear relation is acquired, the initial slope coefficient of skeletal curve can be gotten as G_{max} by taking reciprocal of the straight line's intercept. The G_{max} taken by two different methods are shown as Table 2, from which it can be seen that the dynamic shear stress-shearing strain relation satisfy Hardin-Drnevech hyperbola model in small strain amplitude and it is reliable to get the G_{max} by increasing the measuring accuracy of small strain.

Table 2. Result of $1/G-\gamma$ by two test methods with two soils

	single clay sample imposed			three clay sample imposed		
p_{m0} (kPa)	100kPa	200kPa	400kPa	100kPa	200kPa	400kPa
a (MPa ⁻¹)	0.0220	0.0176	0.0123	0.0220	0.0159	0.0104
b (MPa ⁻¹)	0.3273	0.2370	0.2091	0.3273	0.2646	0.2265
G_{max}	45.45	56.81	81.30	45.45	62.89	95.96
	single silty clay sample imposed			three silty clay sample imposed		
p_{m0} (kPa)	100kPa	200kPa	400kPa	100kPa	200kPa	400kPa
a (MPa ⁻¹)	0.0193	0.01225	0.00744	0.0193	0.0107	0.0056
b (MPa ⁻¹)	0.3906	0.23163	0.06775	0.3906	0.2081	0.1108
G_{max}	51.89	81.63	134.41	51.89	93.15	178.57

The G acquired by two methods can be divided by each G_{max} and the changing law of normalization shear modulus $G/G_{max}-\gamma$ is shown as Figure 4. It is can be seen from the Figure 4 that the $G/G_{max}-\gamma$ relation curves of different consolidated pressure by two methods basically fall into a narrow banding range. Since the scatter of points tally well with fitted curves, a suggested fitting curve can be expressed in this paper as:

$$\text{clay: } G/G_{max} = 1/(1 + 28.22\gamma)^{0.7974} \quad \text{silty clay: } G/G_{max} = 1/(1 + 37.28483\gamma)^{0.6493}$$

Analyses to the experimental result of damping ratio

Damping ratio of soil can express the viscous behavior of soil. It is hardly to perfectly fit the complicated changing law of damping ratio and shearing strain with Hardin-Drnevich and Davidenkov model, according to which the logarithmic formula used in this paper fit well:

$$\xi = \xi_{max} - (\xi_{max} - \xi_{min}) / [1 + (\gamma/a)^b] \quad (3)$$

Where ξ_{min} is the minimal damping ratio; ξ_{max} is the maximal damping ratio; a and b are match parameter of experimentation.

It can be seen in Figure 5 that neither of clay or undisturbed silty clay is affected particularly by confining pressure, but there is still a trend of damping ratio reducing with increase of confining pressure. The damping ratio ξ fitting result of two soil samples by experimentation of continuance consolidation to single sample, respectively, is shown in Figure 5.

As important curves of soil dynamic property, $\xi/\xi_{max}-\gamma$ curve is shown in Figure 6 from which it can be seen that all the testing point fall into a narrow banding area. Since the scatter of points well tally with the fitted curve, the fitted curve can be expressed as:

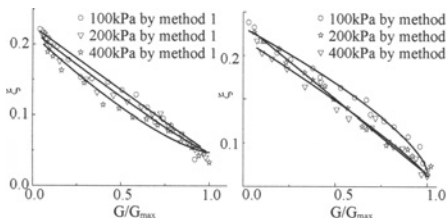


Figure 5. Fit plot of $G/G_{max}-\xi$ curve

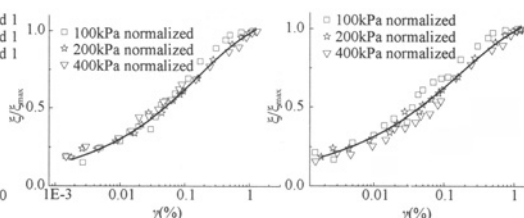


Figure 6. Variation of $\xi/\xi_{max}-\gamma$ by normalized

$$\text{Clay : } \xi / \xi_{\max} = 1.431 * (\gamma(1+2.039\gamma))^{0.335} \text{ silty clay: } \xi / \xi_{\max} = 1.353 * (\gamma(1+1.737\gamma))^{0.3148}$$

CONCLUSIONS

In this paper the method of acquiring G and ξ through changing confining pressure (including imposed and reduced pressure) on single sample is compared with the method of the conventional dynamic torsional test by different respective confining pressure on different samples:

- (1) Although the result of dynamic shear modulus by multiple consolidations on single sample is a little lower than that by respective consolidation on three single samples, it is still reliable to adopt the experimentation of multiple consolidations on one sample in this paper, for the trial curves of two methods are so closed. To use such a method as mentioned above could save amount of sampling, solve the problems of soil texture nonuniformity and supply a lot of advantages on base of reliable experimental result.
- (2) It is shown that the dynamic shear modulus measured with impose and reduce pressure. The G and G_{\max} decreased as the reduction of consolidation pressure and the gradient of reducing is smaller than gradient of imposition.
- (3) The experimental result gained by continuance consolidation on single sample of clay and silty clay is satisfied, since the $G/G_{\max} - \gamma$ and $\xi/\xi_{\max} - \gamma$ after normalization of two soil samples both fall into a narrow range basically.

ACKNOWLEDGEMENTS

The financial support for this study through the grant 50579006, 50639010, 50439010 from National Natural Science Foundation of China is mostly grateful.

REFERENCES

- Gu Yaozhang. (1995). Shear Modulus of the marine clay. *Chinese Journal of Geotechnical Engineering*, 7(2): 29-35.
- Guo Ying, Liu Yang, et al. (2006). Study on experimental technology obtained dynamic modulus and damping ratio. *Proc. The 7th National Conference on soil dynamics*, Bei Jing: The Publishing of Tsinghua University, 266-269.
- Hardin B. O., Drnevich V. P. (1972). Shear modulus and damping in soils: Design equations and curves. *Soil and Foundations*, 98 (SM7): 667-691.
- He Changrong. (1997). Dynamic Triaxial test on modulus and damping. *Chinese Journal of Geotechnical Engineering*, 19(2): 39-48.
- Luan Maotian., Guo Ying, Li Muguoguo, et al. (2003). Development and application of soil static and dynamic universal triaxial and torsional shear apparatus. *Journal of Dalian niversity of Technology*, 43(5): 670-675.
- Wang Quanmin, Li Gang, Chen Zhenghan, et al. (2005). Research on dynamic characteristics of sands in Xiamen city. *Rock And Soil Mechanics*, 26(10): 1628-1632.
- Xie Dingyi. (1988). *Soil Dynamics*. Xi 'an: The Publishing of Xi 'an Jiaotong University.
- Yuan Xiaoming, Sun Rui, Sun Jing, et al. (2000). Laboratory experimental study on dynamic shear modulus ratio and damping ratio of soils. *Earthquake Engineering and Engineering Vibration*, 20(4): 133-139.

NUMERICAL SIMULATION OF DYNAMIC COMPACTION USING LS-DYNA

Xiayong Qin, Maotian Luan and Qing Yang
*School of Civil and Hydraulic Engineering, Dalian University of Technology,
Dalian 116023, China*

Xiaojie Li, Zheng Zhao
*Department of Engineering Mechanics, Dalian University of Technology, the State Key
Laboratory Of Structural Analysis for Industrial Equipment, Dalian 116023, China*

In the process of dynamic compaction, large deformation occurs at some rammed points and their surrounding areas. In this paper, the vibration of dynamic compaction is analyzed with the large deformation theory and LS-DYNA finite element software is employed to simulation the process of dynamic compaction. The velocity-time data acquired in the analysis are close to the actual data measured in dynamic compaction. Using dimension analyzing method reasons a relational formula between vibration velocity and weight of the hammer. And the author uses the actual measured data to imitate the relationship of the vibration velocity. The formula provides a new method to forecast the vibration of dynamic compaction, which makes sense for the similar construction work to forecast the impact for adjacent buildings.

INTRODUCTION

Owing to the simple equipment, easy working process, low construction cost and un-demanding operational conditions in dynamic compaction, this method is extensively employed in the foundation of incompact sandy soil, miscellaneous fill, clayey soil and collapsed loess (Ouyang Lisheng and Wang Dijie, 2004). During the foundation reinforcement through dynamic compaction, the speed of the falling hammer from 20 m height can reach 720 km/h. This will result in intensive shock to the ground and produce earthquake wave in the foundation. The buildings near the rammed points will sway and jounce and sometimes the buildings will be damaged. Therefore, the research on the vibration caused by the dynamic compaction is very important to the building safety.

The Rayleigh wave is the main part in the transmission of the earthquake wave produced by the dynamic compaction, taking about 67% of the total energy. The foundation particles near the dynamic compacted points will vibrate at X , Y and Z directions and the Z direction which is perpendicular to the ground is the main factor resulting in damage. The intensity of the vibration can be determined by the particle speed or acceleration. In this article, the vibration of the nearby $10 \times 104\text{m}^3$ crude coil tank is evaluated in its welding and pressure test on the basis of the foundation particle vibration speed while the 40t hammer falls down from 20 m height. Meanwhile, LS-DYNA finite element software is employed to simulate such vibration to provide a new numerical simulation method for the later estimation of the vibration in the dynamic compaction.

ELASTIC/PLASTIC DYNAMIC FORMULATION FOR LARGE DEFORMATION IN DYNAMIC COMPACTION

During the foundation reinforcement through dynamic compaction, intensive shock of the hammer to the foundation results in large local deformation at the rammed points and the nearby foundation and the permanent plastic deformation also occurs. Thus, the geometric nonlinearity of the large deformation and the nonlinearity of the elastic/plastic materials shall be taken into account. In the consideration of the deformation history, e.g. the time effects such as the elastic/plastic material model and its inertia, the increment method must be employed. The time variable is dispersed into a time sequence $t = 0, t_1, t_2, \dots, t_m, t_{m+1}, \dots$ to obtain the numerical solutions to such discrete points. The process from t to $(t + \Delta t)$ will be described with matter or Lagrange method. In LD-DYNA3D, the Updated Lagrange Formulation is employed to obtain the solution, that is, the object configuration at time t will be taken as the reference configuration and the Euler stress and the infinitesimal strain σ_{ij} of the real configuration ε_{ij} are used to describe the stress and strain in the calculation of all variables in $[t, t + \Delta t]$.

Matter description

Taking the occupied space (initial configuration) of the object as the reference configuration at the moment $t=0$ and the occupied space of the object as the real configuration at the moment $t=t$, the radius vector of the particle in the object in the initial configuration can be expressed as

$$X = X_i e_i, \quad i = 1, 2, 3 \quad (1)$$

where, e_i - the basic vector in rectangular coordinate; X_i - the component of the particle radius vector X in the reference configuration; X - irrelevant of time. X_i - matter coordinate or Lagrange coordinate of particle. Taking matter coordinate X_i and time t as the independent coordinates is called matter description or Lagrange description. In the solid mechanics, Lagrange description is the main method, that is, the object configuration at time t is (Gao Guangyun, Gu Zhonghua and Zhou Qunli, 2004):

$$x_i = x_i(X_j, t) \quad (i, j = 1, 2, 3) \quad (2)$$

Equation (2) also shows a single value continuous mapping from the initial configuration V_0 to the real configuration V and

$$J = \begin{bmatrix} \frac{\partial x_1}{\partial X_1} & \frac{\partial x_1}{\partial X_2} & \frac{\partial x_1}{\partial X_3} \\ \frac{\partial x_2}{\partial X_1} & \frac{\partial x_2}{\partial X_2} & \frac{\partial x_2}{\partial X_3} \\ \frac{\partial x_3}{\partial X_1} & \frac{\partial x_3}{\partial X_2} & \frac{\partial x_3}{\partial X_3} \end{bmatrix} = e_{ijk} \frac{\partial x_i}{\partial X_1} \frac{\partial x_j}{\partial X_2} \frac{\partial x_k}{\partial X_3} \neq 0 \quad (3)$$

where, $\partial x_i / \partial X_i$ is called deformation gradient and an unsymmetrical second order tensor and J is Jacobian determinant. Based on the change of the micro hexahedron dV_0 in initial configuration, there will be $J = \frac{dV}{dV_0} = \frac{\rho_0}{\rho}$. Where, ρ_0 and ρ mean the media densities in initial configuration and real configuration respectively. If incompressible, $J=1$.

Updated lagrange formulation

Formulation of conservation of matter

$$\rho(X, t)J(X, t) = \rho_0(X) \quad (4)$$

Formulation of conservation of momentum

$$\frac{\partial \sigma_{ij}}{\partial x_j} + \rho b_i = \rho \ddot{u}_i \quad (5)$$

Formulation of conservation of energy

$$\rho \dot{w}^{\text{int}} = D_{ji} \sigma_{ij} \quad (6)$$

$$\text{Deformation } D_{ij} = \frac{1}{2} \left(\frac{\partial v_i}{\partial x_j} + \frac{\partial v_j}{\partial x_i} \right) \quad (7)$$

$$\text{Constitutive equation } \overset{\nabla}{\sigma} = \overset{\nabla}{\sigma}(D_{ij}, \sigma_{ij}, \dots) \quad (8)$$

$$\text{Boundary condition } \begin{cases} (n_j \sigma_{ji})|_{A_i} = \bar{t}_i \\ v_i|_{A_i} = \bar{v}_i \end{cases} \quad (9)$$

$$\text{Initial condition } \begin{cases} \dot{u}(X, 0) = \dot{u}_0(X), \sigma(X, 0) = \sigma_0(X) \\ \dot{u}(X, 0) = \dot{u}_0(X), u(X, 0) = u_0(X) \end{cases} \quad (10)$$

Taking the virtual speed as the weighted coefficient, the weak form of the momentum formulation can be changed to

$$\int_V \delta v_i \left(\frac{\partial \sigma_{ij}}{\partial x_j} + \rho b_i - \rho \ddot{u}_i \right) dV = 0 \quad (11)$$

where, $\delta v_j(X) \in R_0, R_0 = \left\{ \delta v_j \mid \delta v_j \in C^0(X), \delta v_j|_{A_r} = 0 \right\}$ is virtual speed. And through frictional integral, the above formulation can be changed to

$$\int_V \frac{\partial(\delta v_i)}{\partial x_j} \sigma_{ji} dV - \int_V \delta v_i \rho b_i dV - \int_{A_r} \delta v_i \bar{t}_i dA + \int_V \delta v_i \rho \ddot{u}_i dV = 0 \quad (12)$$

The above formulation, called formulation of virtual power, is the weak form of the formulation of conservation of momentum and planar force conditions. To solve this formulation, firstly disperse the structure. The space coordinate $x_i(X, t)$ of the particle X at any time t is

$$x_i(X, t) = N_I x_{iI}(t) \sqrt{2} \quad (13)$$

where, N_I is the form function of the node I . Then, the displacement of any point in the cell is

$$u_i(X, t) = x_i(X, t) - X_i = N_I(x) u_{iI}(t) \quad (14)$$

where, $u_i(X, t) = x_{iI}(t) - X_{iI}$ is the displacement of the node I . Similarly, the speed, acceleration, deformation and virtual speed of any point in the cell can be expressed as

$$\begin{cases} \dot{u}_i(X, t) = N_I(x) \dot{u}_{iI}(t) \\ \ddot{u}_i(X, t) = N_I(x) \ddot{u}_{iI}(t) \\ D_{ij} = \frac{1}{2} \left(\frac{\partial \dot{u}_i}{\partial x_j} + \frac{\partial \dot{u}_j}{\partial x_i} \right) = \frac{1}{2} \left(\dot{u}_{iI} \frac{\partial N_I}{\partial x_j} + \dot{u}_{jI} \frac{\partial N_I}{\partial x_i} \right) \\ \delta v_i(x) = N_I(x) \delta v_{iI}(x) \end{cases} \quad (15)$$

Organize the above formulations into matrix structure and put it into formulation of virtual power, there will be

$$M\ddot{U} + f^{\text{int}} = f^{\text{ext}} \quad (16)$$

$$\begin{aligned} \text{where, } f^{\text{int}} &= \int_V B^T \sigma dV \\ f^{\text{ext}} &= \int_V N^T \rho \sigma dV + \int_{A_i} N^T \bar{t} dV \\ M &= \int_V \rho N^T N dV = \int_{V_0} \rho_0 N^T N \sigma dV_0 \end{aligned}$$

Solve the formulation (16) to obtain the node displacement at the current time. Then the structural strain and stress can be obtained.

PROJECT EXAMPLE AND ACTUAL MEASUREMENTS

Project profile

Dalian Harbor Liquid Tank Dock Company constructed a stockyard for the liquid chemical tank in Dalian New Harbor. The area was seaside slope before construction and after the backfilling, the elevation and the relative height difference of the stockyard ground were 2.92-5.17 m and 2.25 m respectively. From the surveying, the stratum comprise, from the top to bottom, plain fill, mucky clay, silty clay, fine sand, coarse sand, crushed gravel, completely weathered slate, intensively weathered slate, medium weathered slate, completely weathered diabase and medium weathered diabase. The dynamic compacted area for the newly constructed liquid chemical tank stockyard neighbored the as-constructing 39# tank $10 \times 10^4 \text{ m}^3$. At that moment, the water tightness testing and welding of the 39# tank and other $10 \times 10^4 \text{ m}^3$ tanks were in process and their individual construction period was extremely tight. To ensure the construction without sacrificing the safety and the normal operation of the two projects, Dalian University of Technology, under the consignment of the employer, carried out the testing and evaluation for the vibration of the $10 \times 10^4 \text{ m}^3$ tanks in South Sea Tank Stockyard Project resulting from the dynamic compaction of the liquid chemical tank foundation and forwarded the safety working area and measures for the dynamic compaction.

Upon the testing and calculation, it is safe in case of the 43 m distance between the rammed points and the 39# tank. The practice witnessed the 39# tank which is nearest to the rammed point is in good function, without any unfavorable consequences.

Measured data

As longer distance away from the hypocenter, the maximum amplitude of the earthquake attenuates gradually and the vibration frequency also decreases as shown in Figure 1.

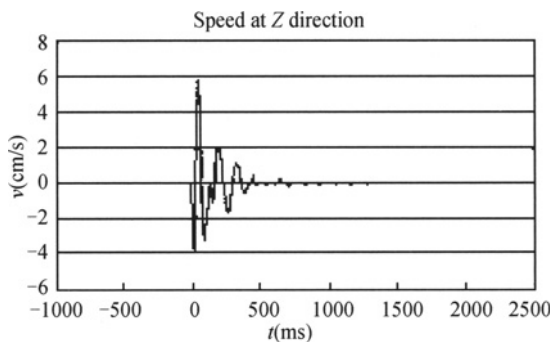


Figure 1. Vibrtion curve measured by tester No.192

Because the relationship between the structural damage and the particle vibration speed is closer than that between the displacement and the acceleration and such speed is less affected by the type and thickness of the earth overburden, this speed is usually taken as the criterion for the safety evaluation of the structure. For 39# crude oil tank ($10 \times 10^4 \text{m}^3$), the circular wall foundation was used, including circular wall reinforced concrete, tar sand insulation layer, sand cushion and packing layer. The inside diameter, height, design level and design temperature of the tank were 80m, 21.8m, 20.2m and 65°C respectively. The dynamic compacted point was 43m away from the 39# tank. To evaluate the effect of the vibration in the dynamic compaction to the tank, IDTS vibration testers were employed to monitor such vibration. Four testers numbered 97, 98, 191 and 192 were used synchronously as shown in Figure 2.

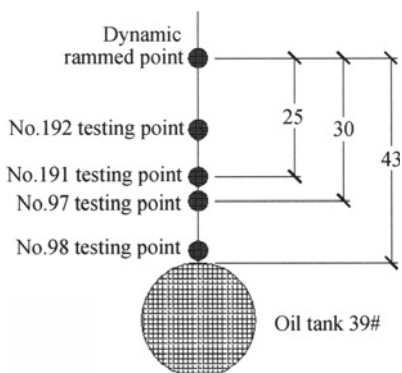


Figure 2. Vibration and testing

The weight and height of the hammer were 40t and 20m respectively and the vibration speed of the foundation particle was shown in Table 1. The effective area of the dynamic compaction is shown in Figure 3.

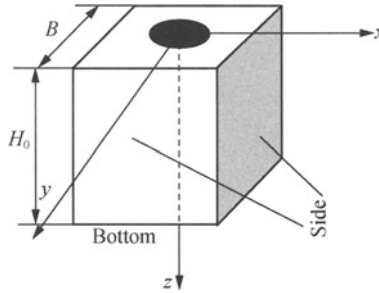


Figure 3. Effective area of dynamic compaction

Table 1. Vertical vibration speed of foundation particle

Tester no.	192	191	97	98
Distance to dynamic compacted point (m)	15	25	30	43
Vertical vibration speed (cm/s)	5.7975	2.3343	0.8142	0.6430

The vibration speed curve measured by the tester no.192 is shown in Figure 3.

The vibration speed of the foundation particle attenuated gradually to zero after about 0.5s. The foreshock period was not clear and lasted for about 0-0.1s and the main shock period and the tail shock period lasted for about 0.1-0.3s and about 0.3-0.8s individually. The vibration speed curves measured by other three testers were similar by the tester

no.192 . In engineering, the approximate formulation $v = k \left(\frac{1}{\sqrt[3]{R}} \right)^\alpha$ is usually employed to calculate the vibration speed. After fitting the data in Table 1, the relationship between the distance R and the vertical vibration speed is obtained as: $v = 2074.3 \left(\frac{1}{\sqrt[3]{R}} \right)^{6.5}$. With comparison to the actual measured data, the relative error reached 50% and therefore a new formulation or method must be found to estimate the vibration speed. In Zhou Tingqing's research on the vibration of the collapsed building ground, the vibration speed at the point with the distance R from the hammer hitting center is observed. Given hammer weight W, falling height h, acceleration of gravity g, ground media density ρ_0 and wave speed c_0 , the vibration of the media is

$$v = f(W, h, \rho_0, c_0, R) \quad (17)$$

Taking R, ρ_0 and c_0 as basic dimensional unit, the following relationship can be obtained after the nondimensionalization of formulation (17):

$$\frac{v}{c_0} = f \left(\frac{W}{\rho_0 c_0^2 R^2}, \frac{h}{R}, \frac{gR}{c_0^2}, 1, 1, 1 \right) \quad (18)$$

$$\text{It can be changed to: } v = c_0 f_1 \left(\frac{W}{\rho_0 c_0^2 R^2}, \frac{h}{R}, \frac{gR}{c_0^2} \right) \quad (19)$$

The falling hammer test showed the intensity of the ground vibration is only relevant to the impulse $I = \frac{W}{g} \sqrt{gh}$ of the hammer to the ground. Thus, formulation (19) can be transferred to

$$v = c_0 f_2 \left(\frac{W \sqrt{gh}}{\rho_0 c_0 g R^3} \right) = c_0 f_2 \left(\frac{W}{\rho_0 c_0 R^3} \sqrt{\frac{h}{g}} \right) \quad (20)$$

By fitting the curve, the following approximation can be reached:

$$v = k'_B \left[\frac{1}{R} \left(\frac{W}{g} \sqrt{gh} \right)^{1/3} \right]^2 \quad (21)$$

where, k'_B is the coefficient; for sand clay media, $k'_B = 0.30 - 0.40$; for the site conditions and measured data in this example, the fitting formulation is:

$$v = 0.19 \left[\frac{1}{R} \left(\frac{W}{g} \sqrt{gh} \right)^{1/3} \right]^2 \quad (22)$$

LS-DYNA DISPLAY ANALYSIS

In LS-DYNA software, the central difference method is employed to carry out the display analysis to avoid the rigidity matrix inversion. It is especially suitable for the nonlinearity dynamic solution to high speed collision, penetration, explosion and metal forming. LS-DYNA includes nearly 200 material models and 16 cells and can carry out the 2D or 3D analysis for various materials and simulate the complicated conditions in reality.

In this paper, LS-DYNA finite element software is employed to perform the display analysis for the dynamic compaction and simulate the relationship between the foundation surface particle vibration speed and the distance from the tested point to the rammed point to provide an estimation basis to the vibration in dynamic compaction. The FEA model is shown in Figure 4. To simplify the calculation and taking the axial symmetry in consideration, 1/4 model is used. The foundation radius is 60m and its height is 30 m. The fixed boundary is provided in four sides and the transmission boundary is provided in the ground to stimulate the definite domain. The hammer diameter is 2.52 m and its height is 1.05 m. The foundation is divided into hexahedron cells with a total number of 81750. For the foundation body, the *MAT_SOIL_AND_FOAM_FAILURE constitutive model is selected. The hammer is in little deformation in the dynamic compaction and it is considered as a rigid object approximatively. Therefore, the *MAT_RIGID constitutive mode is selected for the hammer (Bai Jinze 2005, Li Yuchun 2006, Shi Danyong 2005 and Shang Xiaojiang 2006).

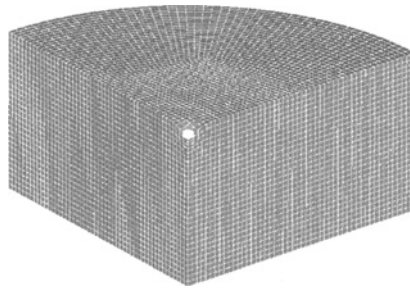


Figure 4. FEA model

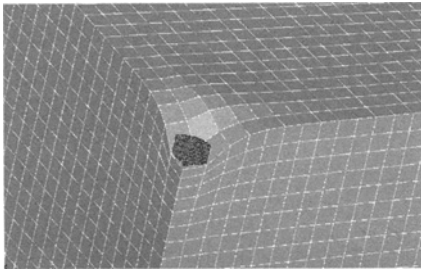


Figure 5. Soil deformation

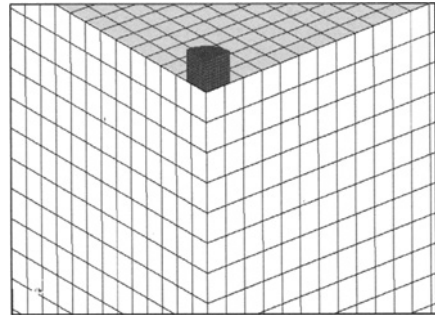


Figure 6. Soil deformation at $t=0$

The hammer collided with the soil mass at a 20 m/s speed and the plastic deformation of the soil mass was shown in Figure 5. The instant deformation was shown in Figure 6 and Figure 7. Through the calculation, the time-vibration speed curves at the positions on the foundation at 15 m, 25 m, 30 m, 43 m and 50 m away from the rammed point were shown in Figure 8. The calculated curve nearly fitted the measured curve (Figure 3) and the calculated vibration wave was more regular because the soil mass was considered as isotropy. The relative error between the calculated value and the measured data was no greater than 5%. This proved the LS-DYNA calculations was more accurate and can serve for the estimation of the vibration in dynamic compaction. In case of 50 m distance, the estimated vibration speed was 0.56 cm/s.

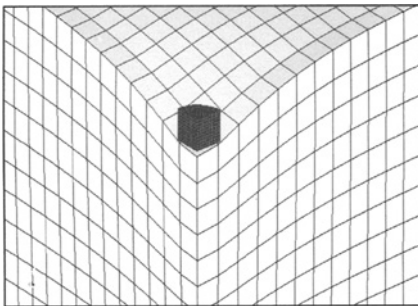


Figure 7. Soil deformation at $t=0.5s$

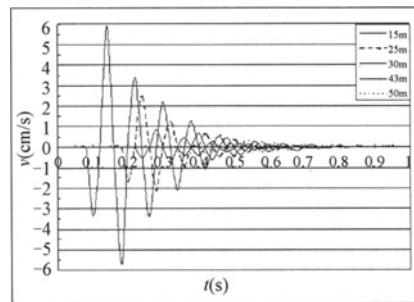


Figure 8. LS-DYNA calculated vibration speed curve

CONCLUSIONS

1. In this paper, LS-DYNA software was employed to carry out the display analysis of the dynamic compaction and through the comparison between the vibration speed curve and the measured curve of the foundation surface, the LS-DYNA calculations was accurate. The calculations can be used for the vibration estimation for the later dynamic compaction and had an important effect on the tank protection and the preparation of the dynamic compaction plan.
2. From Figure 8, the speed of the hammer decreased quickly at the moment it touched the ground. About 97.5% of the ramming energy was utilized for the soil mass compaction. However, the subsequent speed attenuation slowed down.
3. Through the calculation and testing of soil mass with different density, the higher density resulted in the lower ramming depth, and vice versa.

REFERENCES

- Ouyang Lisheng, Wang Dijie. (2004). An analysis on earthquake effect of dynamic compaction. *South China Earthquake*, 24(3): 96-102.
- Gao Guangyun, Gu Zhonghua and Zhou Qunli.(2004). FEA Dynamic Numerical Simulation of Large Deformation in Dynamic Compacted Foundation Reinforcement. *Underground Space*, 24: 2.
- Zhou Tingqing. (2001). *Explosive dynamics and its application*. USTC M/E Press Hefei.
- Bai Jinze. (2005). *LS-DYNA 3D Theoretical Basis and Example Analysis*. Beijing, Science Press.
- Li Yuchun, Shi Danyong and Zhao Yuan. (2006). *ANSYS 10.0/LS-DYNA basic theory and engineering practice*. Beijing, China Water Resource & Hydro Power Press.
- Shi Danyong, Li Yuchun and Zhang Shengming. (2005). *Display Analysis Based on ANSYS/LS-DYNA 8.1*. Beijing, Tsinghua University Press.
- Shang Xiaojiang, Su Jianyu. (2006). *Dynamic analysis method and engineering example by ANSYS/LS-DYNA*. Beijing, China Water Resource & Hydro Power Press.

AXIAL VIBRATION OF FLOATING PILE GROUPS WITH FLEXIBLE CAPS

Q. Ren, M.S. Huang

*Department of Geotechnical Engineering, Tongji University
Shanghai 200092, China*

In this paper, a hybrid formulation is developed for the axial harmonic response of floating pile groups with flexible caps in homogeneous soil deposits. Based on pile-pile interaction factors, sub-structure method is used to form the global stiffness matrix of pile-cap-soil system, and the pile is treated as a dynamic Winkler beam. A comprehensive parameter study focuses on the influence of cap thickness and pile spacing on the dynamic response of pile groups. It can be concluded that the present method can give more reasonable and reliable prediction on the dynamics response of pile groups.

INTRODUCTION

Pile foundations as a kind of reliable and effective foundation has been widely used in civil engineering. As for pile groups, the complexity of their dynamic behavior stemming from the pile-soil-pile interaction has restricted further research in this field. Over the past 35 years, amount of theoretical methods have been developed for the dynamic analysis of piles and pile groups subjected to axial loads. All of these methods can be divided into: (1) direct methods (e.g. continuum models, finite element methods, boundary element techniques), and (2) superposition methods based on interaction factors (e.g. Winkler models). A comprehensive review of the above methods has been presented by Novak (1991) and Pender (1993). Unfortunately, most of them adopted rigid cap assumption. This assumption was preferred to be simplification of the analytical formulation. However, in practical situations it could lead to unsafe prediction when the thickness of caps is relatively small.

Tajimi (1966) firstly calculated the dynamic vibration of pile groups with floating rigid caps, from then on several researchers paid attention to study influence of caps stiffness on the dynamics response of pile groups. Mamoon (1988) analyzed the influence of ground-contacting cap inertia on the stiffness of pile group. Yan and Huang (2004, 2005) proposed a simplified method to calculate the contribution of cap to the dynamic response of pile groups in half space and layered soil deposits.

The work reported here was motivated by the need to find the influence of flexible cap on the response of pile groups under harmonic loads. To this end, a hybrid formulation is presented, based on the sub-structure method and dynamic Winkler beam model. The dynamic Winkler beam model is formulated by considering the interaction between passive piles and surrounding soils.

DYNAMIC INTERACTION BETWEEN TWO PILES

Gazetas et al. (1991) proposed an approximate method to calculate axial vibration of pile groups in half space based on the Beam-on-Winkler-Foundation (BWF) model, in which the interaction between the passive pile and surrounding soils was taken into account. The proposed method was further improved for layered soils by Mylonakis and Gazetas (1998), as well as Wu and the authors (2007).

The pile-soil-pile system is shown in Figure 1. Two identical piles embedded in the layered soil with length L and diameter d under harmonic load $Pe^{i\omega t}$. Obviously, the response of the receiver pile (Pile 2) to the oscillations of the source pile (Pile 1) is not identical to the response of the free-field soil at the location of the receiver pile due to the interaction between the passive pile and surrounding soils. Let s be the distance between two piles, the free-field displacement at the location of Pile 2 can be expressed as

$$w_s(z, t) = w_s(z) e^{i\omega t} = \psi(s) w_{11}(z) e^{i\omega t} \quad (1)$$

where w_{11} is displacement amplitude of pile1 and $\psi(s)$ is the attenuation function of the vertical soil displacement with radial distance from the pile

$$\psi(s) \approx \sqrt{\frac{r_0}{s}} \exp[-(\beta_s + i)\omega(s - 0.5d)/V_s] \quad (2)$$

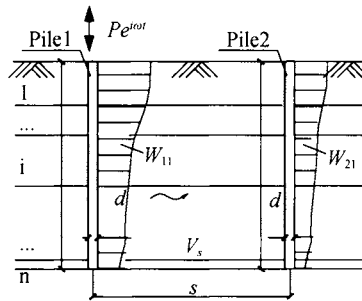


Figure 1. Schematic illustration of pile-pile interaction

in which d is the diameter of the pile, β_s and V_s are the damping ratio and shear wave velocity of soil. Obviously, the receiver pile does not follow exactly the free-field movement. Thereby, the pile displacement will be different than that given by equation (1). For a receiver pile, the dynamic equilibrium produces the following equation governing the axial displacement $w_{21}(z, t) = w_{21}(z) e^{i\omega t}$ of the pile:

$$\frac{d^2 w_{21}(z)}{dz^2} + \frac{\lambda^2}{h^2} w_{21}(z) = \frac{-(k_z + i\omega c_z) \psi(s) w_{11}(z)}{E_p A_p} \quad (3)$$

with λ given by $\lambda = h[(m_p \omega^2 - k_z - i\omega c_z)/E_p A_p]^{1/2}$ where $E_p I_p$ and m_p are the flexural rigidity and mass per unit length of the pile, respectively; $(k_z + i\omega c_z)$ is the complex soil impedance encompassing the stiffness, inertia, radiation, and hysteretic action of and in the soil. Based on the transfer matrix, the axial force and displacement between the passive pile top and tip can be written as

$$\begin{Bmatrix} w_{21}(L) \\ N_{21}(L) \end{Bmatrix} = [T^1] \begin{Bmatrix} w_{21}(0) \\ N_{21}(0) \end{Bmatrix} + [T^2] \begin{Bmatrix} w_{11}(0) \\ N_{11}(0) \end{Bmatrix} \quad (4)$$

where $[T^1]$ and $[T^2]$ is the transfer matrix for the pile-soil interaction and pile-pile interaction, respectively

According to the definition of interaction factor, the interaction factor can be expressed as

$$\alpha(s) = \frac{w_{21}(0)}{w_{11}(0)} = -\frac{T_{11}^2 K_b + \Re^s K_b T_{12}^2 + T_{21}^2 + \Re^s T_{22}^2}{T_{11}^1 K_b + T_{21}^1} \quad (5)$$

where $K_b = G_b(C_{w1} + iC_{w2})$ in which G_b is the shear moduli of soil below the pile tip, C_{w1} and C_{w2} are the impedance functions of the soil deposit at the pile tip.

The displacements vector of piles $\{w\}$ can now be expressed by the production of interaction factors matrix $[\alpha]$ and loads vector $[N]$ distributed onto the individual pile heads.

$$\begin{Bmatrix} w_1 \\ w_2 \\ \dots \\ w_n \end{Bmatrix} = \frac{1}{K_p^s} \begin{bmatrix} 1 & \alpha_{12} & \dots & \alpha_{1n} \\ \alpha_{21} & 1 & \dots & \alpha_{2n} \\ \dots & \dots & \dots & \dots \\ \alpha_{n1} & \alpha_{n2} & \dots & 1 \end{bmatrix} \begin{Bmatrix} N_1 \\ N_2 \\ \dots \\ N_n \end{Bmatrix} \quad (6)$$

or

$$[N] = K_p \{w\} \quad (7)$$

in which $[K_p] = K_p^s [\alpha]^{-1}$ is the stiffness matrix of pile groups in the whole pile-cap system.

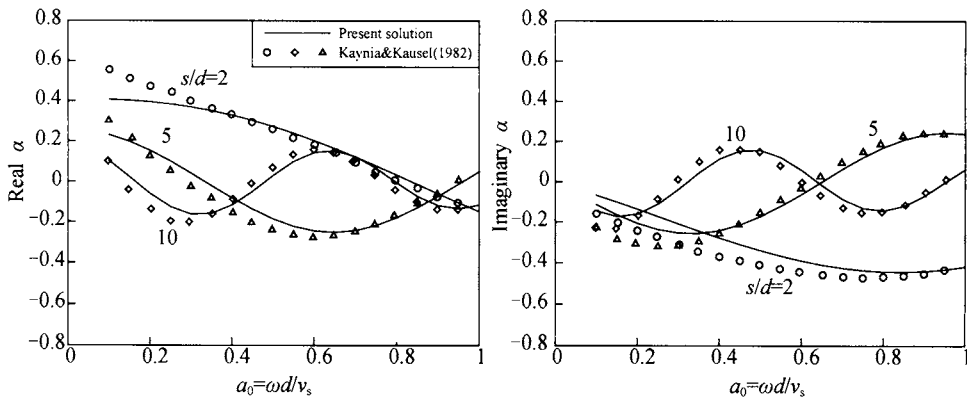


Figure 2. Vertical interaction factor in homogeneous half-space
($L/d=20; E_p/E_s=1000; \nu_s=0.4; \rho_p/\rho_s=1.5; \beta_s=0.05$)

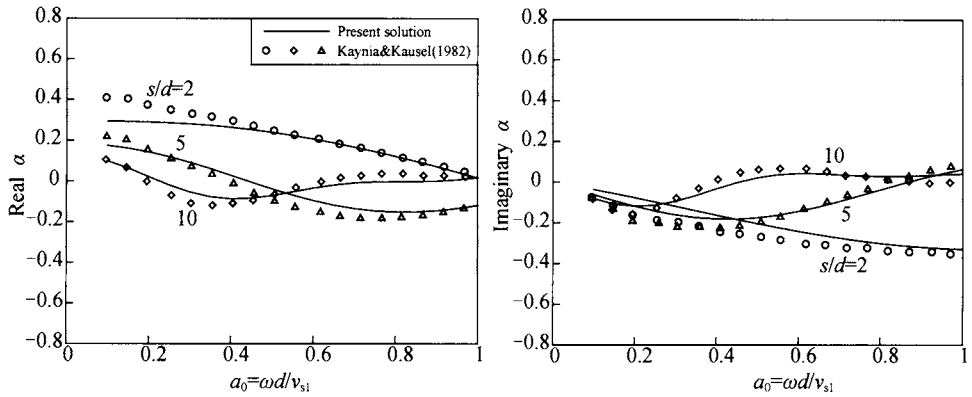


Figure 3. Vertical interaction factor in layered soil
 ($L/d=20; h_1/L=1/3, E_p/E_s=1000; \nu_s=0.4; \rho_p/\rho_{s2}=1.5; \rho_{p1}/\rho_{s2}=0.8; \beta_{s1}=0.1, \beta_{s2}=0.05$)

In Figures 2 and 3, the interaction factors α in homogeneous and non-homogeneous soils by the proposed simplified method are plotted against results of Kaynia and Kausel(1982). Notice the oscillatory behavior of the interaction factors with frequency. The performance of the proposed simplified method has a good accordance with rigorous solution in the whole range of frequencies. Therefore, if the accuracy of interaction factors and dynamic impedance of single pile were good enough, the solution of dynamic impedance of pile group will be very close to rigorous solution.

CAP-PILE GROUP INTERACTION

In the traditional methods (Kaynia and Kausel, 1982; Dobry and Gazetas, 1988), geometry and mass of rigid floating caps are omitted, enforcing boundary condition of pile atop to satisfy the rigid cap assumption. However, the cap has limited mass and dimensions. It is therefore important to study the interaction between flexible cap and pile group.

According to the classical theory of Mindlin plate, each node of plate has three degrees of freedom: translational displacement w , and rotation angle around x axis and y axis, θ_x and θ_y . The nodal displacement vector is then formed as

$$\{\delta\}_i = \{w_i, \theta_{xi}, \theta_{yi}\}^T \quad (8)$$

The finite element equation for a flexural plate subjected to dynamic load can be written as

$$[M]\{\ddot{\delta}\} + [C]\{\dot{\delta}\} + [K]\{\delta\} = \{P\} - \{\bar{N}\} \quad (9)$$

where

$$\{\bar{N}\} = [\bar{K}_p]\{\delta\} \quad (10)$$

and

$$[C] = \alpha[M] + \beta[K] \quad (11)$$

in which α and β are the coefficients for Rayleigh damping.

Combining with Equation (8), Equation (9) can be written in the case of harmonic loading as

$$-[M]\omega^2 \{\delta\} + i[C]\omega \{\delta\} + ([K] + [\bar{K}_p])\{\delta\} = \{P\} \quad (12)$$

where ω is the circular frequency of the applied load. The dynamic response of the whole system can be obtained by solving Equation (12).

DYNAMIC RESPONSE OF PILE GROUPS

The superposition method, based on pile-pile interaction factors, is one of the most effective approaches to calculating dynamic response of floating pile groups with rigid caps. The boundary integration method proposed by Kaynia and Kausel(1982) is often treated as a rigorous solution. In what follows, a parametric study, which is focused on the effects of pile spacing and cap thickness on the impedance of pile groups, is presented. Comparison with well-known results by Kaynia and Kausel(1982) is also given.

In Figure 4, the axial dynamic impedance of a 3×3 pile group is plotted in terms of the so-called group efficiency factor (defined as the dynamic impedance of the pile group divided by the sum of the individual static stiffness of the pile). It is evident that the thickness of cap has great influence on the group factor. The impedance function of pile groups is weakened with the decreasing of cap thickness, especially when the cap is too thick ($B/H=12$). But the differences between two approaches can be omitted when the ratio larger than 6.

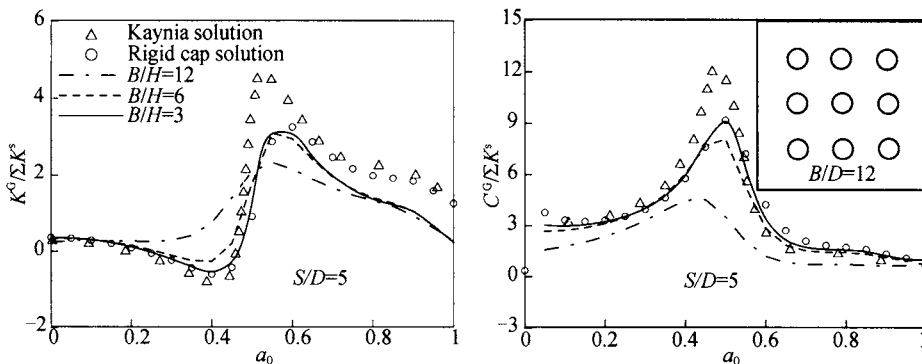


Figure 4. Axial dynamic stiffness and damping of 3×3 pile group in homogeneous half-space ($L/d=15$, $E_p/E_s=1000$, $\rho_s/\rho_p=0.7$): Comparison of proposed method with rigorous solutions of Kaynia and Kausel (1982) and rigid cap solution

CONCLUSIONS

A hybrid method has been proposed for the analysis of pile groups with flexible caps subjected to vertical dynamic loading. Based on pile-to-pile interaction factors, sub-structure method is used to form the global stiffness matrix of pile-cap-soil system, while the pile is treated as a Winkler beam. Through comprehensive parameter study, it is pointed out that the

thickness of cap has significant influence on the dynamic response of pile groups. It is in fact very important for engineers to understand properly the distinction between rigid cap and flexible cap in practical design. Despite of the simplified assumptions on which this procedure is based, a good agreement has been found between the results obtained using it and those derived from rigorous solution.

REFERENCES

- Gazetas G., Fan K. and Kausel E. (1991). Dynamic interaction factors for floating pile groups. *Journal of Geotechnical Engineering*, 117(10): 1531-1548.
- Novak M. (1990). Piles under dynamic loads: State of art. *Proceedings 2nd international conference on recent advances in geotechnical earthquake engineering and soil dynamics*. St. Louis, 3: 2433-2456.
- Pender M. (1993). A seismic pile foundation design analysis. *Bulletin of the New Zealand National Society for Earthquake Engineering*, 26(1): 49-160.
- Tajimi H. (1966). Dynamic analysis of a structure embedded in an elastic stratum. *Proc. 4th World Conf. Earthquake Eng. Santiago*. 3: 53-69.
- Mamoon S.M. (1991). *Dynamics and seismic behavior of deep foundations*. State University of New York at Buffalo.
- Yan B., Huang Y. (2005). Dynamic interaction of axial vibration between pile groups and raft foundations. *Journal of Building Structures*, 26(5): 125-129.
- Gazetas G., Makris N. (1991). Dynamic pile-soil-pile interaction: Part I : Analysis of axial vibration. *Earthquake Engineering and Structure Dynamics*, 20: 115-132.
- Mylonakis G., Gazetas G. (1998). Vertical vibration and additional distress of pile groups in layered soil. *Soils and Foundations*, 38(1): 1-14.
- Wu Z.M., Huang M.S. and Ren Q. (2007). Vertical vibration and internal forces of pile groups in layered soil. *J. Tongji University (Natural Science)*, 35(1): 21-26.
- Dobry R., Gazetas G. (1988). Simple method for dynamic stiffness and damping of floating pile groups. *Geotechnique*, 38(4): 557-574.
- Kaynia A.M., Kausel E. (1982). *Dynamic stiffness and seismic response of pile groups*. Research Report, Dept. of Civil Engineering., MIT, Cambridge, Mass.

ESTIMATION OF GROUND MOTION PARAMETERS FOR MUZAFFARABAD EARTHQUAKE, PAKISTAN ON 8th OCTOBER 2005

D. Neelima Satyam

*Assistant Professor, Department of Civil Engineering
VNR Vignana Jyothi Institute of Engineering and Technology
Hyderabad 500072, India*

K.S. Rao

*Professor, Department of Civil Engineering
Indian Institute of Technology Delhi, New Delhi 110016, India*

M.R. Madhav

*Professor Emeritus, JNTU College of Engineering
Hyderabad 500072, India*

An important problem in earthquake engineering is the prediction of ground motions from possible future large earthquakes. Seismological input that describes the amplitude, frequency content and duration of the expected motions are required to assess the seismic performance of the structures. Several empirical relationships are available in the literature for the estimation of these ground motions. In this study, the stochastic finite fault simulation technique which implements the concept of fault discretization wherein the sub-events are represented as stochastic point sources is used. The detailed description of the method is given by Beresnev & Atkinson (1997 & 1998a). Using the seismic source data of the earthquake occurred on Saturday, October 8th, 2005 with a 7.6 magnitude near Muzaffarabad which is 80 km north-east of Islamabad and using the FINSIM program the PGA at bedrock is estimated. This value can be used as input for microzonation of ground motion at the surface by incorporating the local soil/ground conditions.

INTRODUCTION

The damage resulting from earthquakes may be influenced in a number of ways by the characteristics of ground in the affected area. Earthquake engineers are interested in strong ground motion i.e., the motion of sufficient strength to affect people and their environment. It is important to describe the characteristics of the ground motion that are of engineering significance and to identify the ground motion parameters that reflect those characteristics. The three important characteristics of earthquake ground motions are amplitude, frequency and duration of the motion. There are various other ground motion parameters, which

provide information about these ground motion characteristics. The most commonly used amplitude parameters are peak acceleration, peak velocity and peak displacement. Peak acceleration is a very useful parameter to characterize amplitude. This peak acceleration can be peak horizontal acceleration (PHA) or peak vertical acceleration (PVA). The peak horizontal acceleration for a given component of motion is simply the largest value of horizontal acceleration obtained from the accelerogram of that component. The maximum resultant PHA which is commonly used to describe ground motions can be obtained by taking the vector sum of two orthogonal components. The variation of intensity of ground motions with distance from the source i.e., attenuation relationships has been studied for many years. Plots of attenuation relationships of peak acceleration and velocity as a function of distance have been presented by numerous researchers in the seismology and earthquake engineering.

A discrete finite fault model that captures the salient features of radiation from large earthquakes has been a popular seismological tool for the last two decades. Hartzell (1978) introduced this first as a finite fault plane which is subdivided into smaller elements. The contributions from all the independent sub-faults are summed up in estimating the ground motions parameters from a large earthquake. Generally, rupture starts at hypocenter and propagates radially triggering the sub-faults as it passes them. The fields from all sub-events are geometrically delayed and added together at the observation point. Beresnev & Atkinson (1997) extended the original method and developed a finite fault simulation model code termed as FINSIM. The applicability of the program to predict ground motion parameters has been tested by numerous authors in various countries. In this study an attempt is made to estimate the peak ground acceleration (PGA) at some places in Pakistan like Muzaffarabad, Islamabad, Balakot, Tarbela, and Abbottabad due to the October 8th 2005 Kashmere earthquake.

SEISMICITY OF THE AREA

The Muzaffarabad earthquake, which affected severely many places in India and Pakistan is associated with the great plate boundary region, where the Indian Plate is subducting the Asian Plate. The tectonic movement in the region is responsible for the creation of the Himalayan mountain ranges through compressive and bending stresses. The subduction mechanism has triggered a few great and several intermediate earthquakes in a band of about 50-80 km width and an arc length of about 2500 kms. The recent event lies at the western side of the active subduction Himalayan belt.

The earthquake occurred at 8:50:40 am local time on October 8th, 2005. The USGS estimated the magnitude as $M_w=7.6$, and the coordinates of the location are 34.493N and 73.629E, with a focal depth of 26 kms. Large number of aftershocks more than 1000 in number were recorded, in the first few weeks of magnitudes of up to 6. It is stated that the fractures reported in the literature are secondary and not associated directly with the fault rupture. Also, extensive landslides observed are also not directly associated with the fault rupture. The direction of the fault, being N27E to N30E, is confirmed by several researchers. The length of the rupture is reported by Harvard Seismology to be about 90 km, with a width of about 50 km. The fault plane dips about 37 degrees and the mechanism is mostly thrust

with the average slip between 2-4 meters. Figure 1 shows the location of the rupture region which clearly indicates the axis running through Muzaffarabad and Balakot.

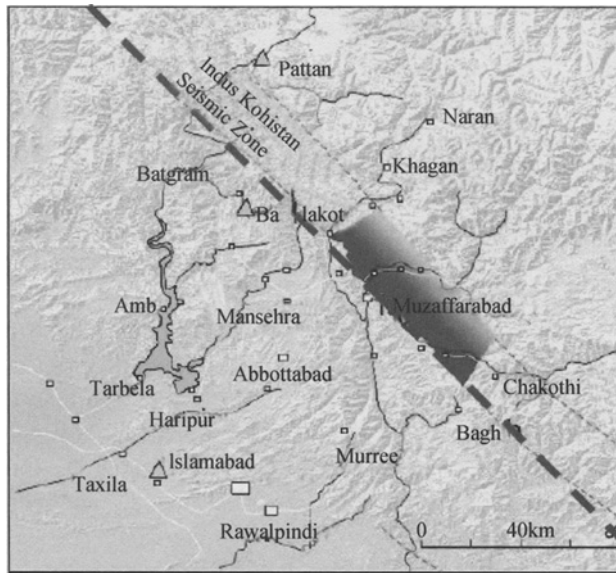


Figure 1. Location of the rupture region (www.cires.colorado.edu/~bilham/Kashmir 2005.htm).

FINSIM APPROACH

Ground motion at a particular site is influenced by three main elements, viz., source, travel path, and local site conditions. Source factors include size, depth, stress drop, rupture process and fault geometry. Travel path factors include geometrical attenuation, dissipation of seismic energy due to inelastic properties of the earth and scattering of elastic waves. Local site factors include the properties of the upper most rock/soil and the effect of the surface topography near the recording site.

The computer code FINSIM, a finite fault simulation technique is used in this study to generate the peak ground acceleration map at bedrock for five different potential earthquake sources in and around Delhi region. The applicability of this method in predicting the ground motions has been verified by several researchers (Hartzell et al., 1999; Beresnev and Atkinson, 2002; Roumelioti and Kiratzi, 2002; Hough et al., 2003; Singh et al., 2003). As stated earlier, the method implements the concept of discretization of the major fault plane into minor faults and estimation of the earthquake response by summing the contributions from all the sub-elements. In general, the rupture starts at the hypocentral point on the fault plane and triggers all sub-faults by propagating in the radial direction. The information on the orientation and dimension of the fault plane, location of the hypocenter and the dimensions of the sub-faults are the major inputs for its analysis. The fault plane can be discretised using the empirical equation developed by Beresnev and Atkinson (1999) as:

$$\log \Delta l = 0.4 M - 2 \quad (1)$$

where Δl is the sub-fault dimension in km and M is the earthquake magnitude.

The depth to the top of the fault plane surface is assumed a value of 1 km in this study. The other important input is the stress parameter ' $\Delta\sigma$ '. This stress parameter is unknown with

large uncertainties, but a constant average value of 50 bars is recommended by the authors. Lower values are possible but higher values should not generally be used. In this study also a value of 50 bars is used. The authors of this program cleared that a fixed value of this parameter primarily affects the number of elementary sources that need to be summed in order to conserve the seismic moment of the target event and not the radiation amplitudes. The material properties like shear wave velocity and crustal density are taken values of 3.6 km/sec and 2.8 g/cc respectively as recommended by Singh et al. (2003) for the Indian shield. The other input is the factor controlling the strength of sub-fault radiation. This parameter controls the amplitudes of the radiation at frequencies higher than the corner frequency of the subfaults and reflects the maximum velocity of slip on the fault (Beresnev and Atkinson, 1997). A value of 1 is taken in this study, which corresponds to the standard rupture while the recommended range is from 0.7 to 2.0.

In the implementation of the stochastic method, the attenuation effects of the propagation path are modeled through the empirical ‘ Q ’ and geometric attenuation models. The ground motions are strongly influenced by the value of ‘ Q ’ factor, the strength of the subfault radiation and $\Delta\sigma$. For the geometric attenuation, the geometric spreading operator of $1/R^b$, where $b=1.0$ for R less than 50 km, $b=0$ for $50 \leq R < 150$ km, and $b=0.5$ for R greater than or equal to 150 km is assumed. The frequency dependent ‘ Q ’ is interpreted as a tectonic parameter and regions of high seismic activity are characterized by less value compared to stable regions. The relationship for this factor will be in the form of $Q(f) = Q_0 f^n$. Generally Q_0 is $Q(f)$ at a frequency of 1 Hz and n , power of frequency dependence, represents the level of tectonic activity of the region. Higher n value shows that the regions with high seismic activity and vice versa. Various researchers (Gupta et al., 1995; Gupta, 1999; Paul et al., 2001; Singh et al., 2003 & 2004) estimated the Q_0 and n values for the Indian seismic regions.

The frequency dependent quality factor ‘ Q ’ estimated by Singh et al. (2004) for the Indian shield is used in this analysis as given in the Eq. 2. This equation is based on a larger data and was modeled for a wide frequency range of 1 to 20 Hz. Based on the Jabalpur data, Singh et al. (2003) proposed the Q_0 and n values as 508 and 0.48. The number of iterations made is 6 in the present study. Table 1 shows the values of the input parameters used in the FINSIM program.

$$Q(f) = 800 f^{0.42} \quad (1 \text{ Hz} < f < 20 \text{ Hz}) \quad (2)$$

Table 1. Input parameters used in the analysis

Parameter	Value
Depth of the upper edge of the fault (km)	1
Subfault dimensions (km)	10 × 4
Stress parameter $\Delta\sigma$ (bars)	50
Radiation strength factor	1.0
$Q(f)$	$800 f^{0.42}$
Geometric spreading	$1/R^b$ $b=1$ for $R < 50$ km $b=0$ for $50 \leq R < 150$ km $b=0.5$ for $R \geq 150$ km
Crustal shear wave velocity (km/s)	3.6
Crustal density (g/cm^3)	2.8
Rupture velocity (km/sec)	0.8 × (shear wave velocity)
No of iterations	6

Table 2. Estimated peak ground acceleration at bedrock

Location	Epicentral Distance (km)	PGA (gals)
Muzaffarabad	4	0.790
Islabamad	95	0.104
Balakot	10	0.532
Tarbela	80	0.116
Abbottabod	40	0.257

The program is executed for all the selected places in Pakistan e.g. Muzaffarabad (4 km), Islabamad (95 km), Balakot (10 km), Tarbela (80 km), and Abbottabod (40 km) and the distances in the parenthesis give the epicentral distances from the source. Table 2 gives the PGA values estimated for the five locations. Figure 2 shows the distribution of the PGA with epicentral distance for these locations.

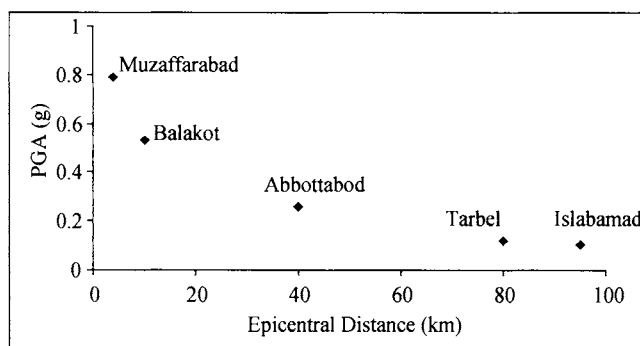


Figure 2. PGA with epicentral distance for the five locations

CONCLUSIONS

The value of peak ground acceleration at Muzaffarabad is very high (0.79g) as it is close to the epicenter and it is less at Islamabad which is at around 95 km from the source location. The PGA value ranges from 0.1g to 0.8g at all the locations which are within 5 to 100 km from the source point. Thus PGA value depends not only on the epicentral distance but also on site conditions, which is an important input parameter in seismic design of structures and liquefaction hazard analysis. Thus, this stochastic method has become a popular and very useful tool in estimating ground motion parameters like PGA for the regions with insufficient instrumental data.

REFERENCES

- Hartzell S. (1978). Earthquake aftershocks as Green's functions. *Geophys. Res. Lett.* 5: 1-14.
- Beresnev I., Atkinson G. (1997). Modeling finite fault radiation from the ω^n spectrum. *Bull. Seism. Soc. Am.*, 87: 67-84.
- Beresnev I., Atkinson G. (1998). FINSIM - a FORTRAN program for simulating stochastic acceleration time histories from finite faults. *Seism. Res. L.*, 69: 27-32.
- Beresnev I., Atkinson G. (1999). Generic finite fault model for ground motion prediction in eastern north America. *Bull. Seism. Soc. Am.*, 89: 608-625.

- Beresnev I., Atkinson G. (2002). Source parameters of earthquakes in eastern and western north america based on finite fault modeling. *Bull. Seism. Soc. Am.*, 92: 695-710.
- Hartzell S., Harmsen S., Frankel A. and Larsen S. (1999). Calculation of broadband time histories of ground motion: comparison of methods and validation using strong ground motion from the 1994 northridge earthquake. *Bull. Seism. Soc. Am.*, 89: 1484-1504.
- Hough S.E., Martin S., Bilham R. and Atkinson G.M. (2003). The January 26, 2001 M7.6 Bhuj, India Earthquake: Observed and Predicted Ground Motions. *Bull. Seism. Soc. Am.*, 92(6): 2061-2079.
- Roumelioti Z., Kiratzi A. (2002). Stochastic simulation of strong motion records from the 15 April 1979 (M 7.1) montenegro earthquake. *Bull. Seism. Soc. Am.*, 92: 1095-1101.
- Singh S. K., Bansal B. K., Bhattacharya S. N., Pacheco J. F., Dattatrayam R. S., Ordaz M., Suresh G., Kamal and Hough S. E. (2003). Estimation of ground motion for bhuj (26 January, 2001; $M_w = 7.6$) and for future earthquakes in india. *Bull. Seism. Soc. Am.*, 93(1): 353-370.

EFFECTIVE STRESS ANALYSIS FOR THE EFFECTS OF LIQUEFACTION CONDITION ON GROUND MOTIONS

J. Z. Sun

*Key Laboratory of Rock and Soil Mechanics, Chinese Academy of Sciences,
Wuhan 430071, China.*

G. L. Shi

*School of Civil and Architectural Engineering, Wuhan University of
Technology, Wuhan 430070, China*

Based on the representative soil layer distribution in Shanghai and its mechanical parameters, the authors select and build a number of computation profiles, the effects of ground water level, silty sand deposit thickness and its depth on the ground surface peak acceleration and its displacement are calculated by means of drained effective stress analysis method incorporating Biot dynamic consolidation equations and a bounding surface hypoplasticity model. Some results are useful.

INTRODUCTION

The effects of Site conditions on the ground motion is a key factor to find the design load, it decides directly our estimation of design seismic action, and so, studies in the field is paid a wide attention to in recent years, such as. Bo, J.S. et al.. (2003), Qian S.G.(1994) and Tu H.Q. et al.. (1994), etc.

The equivalent linear fluctuation approach is used widely for the engineering site, but it is rather approximate, because when amplitude of input motion from bedrock becomes greater more, its nolinear computation effect will be strengthened, furthermore this characteristic will be more obvious when the soil layer contains soft soil. In addition this method does not incorporate ground water. Liquefaction is the first factor of earthquake disasters of engineering site, but the ground water lever, thickness and depth of silty sand despoit are the most important factors to affect liquefaction. The effect of all these on ground dynamic responses is analyzed with effective stress method in the paper.

DYNAMIC ANALYSIS EQUATION

Under the seismic loading originating from bedrock, dynamic response of horizontal soil layer can be considered as one-dimensional boundary value problem, only a part of the stress and strain components are engaged in the formulation. Referring to the coordinate convention shown in Figure 1, horizontal soil deposits are subjected to vertically propagating compression and shear waves, it is assumed that the viscous damping is uncoupled and the

damping coefficients are the same for all the shear components, then the stress-strain relation of soil skeleton may be written in the following incremental form

$$\begin{Bmatrix} \Delta\sigma_{13} \\ \Delta\sigma_{23} \\ \Delta\sigma_{33} \end{Bmatrix} = \begin{bmatrix} d_{11} & d_{12} & d_{13} \\ d_{21} & d_{22} & d_{23} \\ d_{31} & d_{32} & d_{33} \end{bmatrix} \cdot \begin{Bmatrix} -\Delta u_{1,3} \\ -\Delta u_{2,3} \\ -\Delta u_{3,3} \end{Bmatrix} + \begin{Bmatrix} -\eta_s \cdot \partial(\Delta u_{1,3})/\partial t \\ -\eta_s \cdot \partial(\Delta u_{2,3})/\partial t \\ -\eta_s \cdot \partial(\Delta u_{3,3})/\partial t \end{Bmatrix} \quad (1)$$

Biot dynamic consolidation equation can be obtained from Eq. (1) as the following

$$\rho \partial^2 \Delta u_1 / \partial t^2 - \eta_s \partial(\Delta u_{1,33}) / \partial t - d_{11} \Delta u_{1,33} - d_{12} \Delta u_{2,33} - d_{13} \Delta u_{3,33} = 0 \quad (2)$$

$$\rho \partial^2 \Delta u_2 / \partial t^2 - \eta_s \partial(\Delta u_{2,33}) / \partial t - d_{21} \Delta u_{1,33} - d_{22} \Delta u_{2,33} - d_{23} \Delta u_{3,33} = 0 \quad (3)$$

$$\rho \partial^2 \Delta u_3 / \partial t^2 - \eta_c \partial(\Delta u_{3,33}) / \partial t - d_{31} \Delta u_{1,33} - d_{32} \Delta u_{2,33} - d_{33} \Delta u_{3,33} + \Delta p_{,3} - \rho g = 0 \quad (4)$$

$$k / g \cdot \partial^2 \Delta u_{3,3} / \partial t^2 + k / (\rho_w g) \cdot \Delta p_{,33} - \Gamma^{-1} \cdot \partial \Delta p / \partial t - \partial \Delta u_{3,3} / \partial t = 0 \quad (5)$$

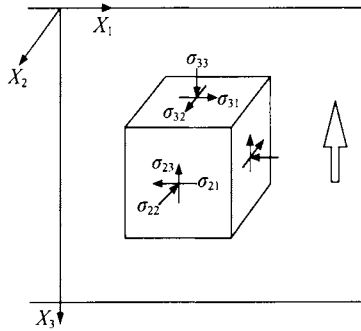


Figure 1. Coordinate system for ground response analysis

Where ρ = bulk density of soil mass; p = pore pressure; $u_i (i=1-3)$ = displacements of the soil skeleton; $\sigma_{ij} (i=1-3, j=1-3)$ = effective stress components of the soil skeleton; $d_{ij} (i=1-3, j=1-3)$ = elements of elastoplastic modulus matrix; ρ_w = density of pore fluid; g = gravitational acceleration; k = coefficient of permeability; η_s and η_c = viscous coefficients for shear and compressive vibration; and Γ = combined bulk modulus of pore fluid and solid particles. hypoplasticity bounding surgence model is used in Li X.S. (1996), dynamic equation group (Eq. 2-5) can be solved by finite element space discretization based on Galerkin's approximation and the Newmark-Hilber time integration scheme.

SOIL LAYER PROFILE AND COMPUTATION PARAMETERS

Regarding to the geological significance and factual engineering, based on investigation of all covering soil layer down towards to bedrock in Shanghai, representative site profile is constructed, which is a thickness of 140 m and consists with Shanghai. All soil layers are numbered as depth (Table 1), computation profiles are made up of ten soil layers with different thickness, their physical and mechanical parameters are listed in Table 1 and 2, a

detailed description can be read in Huang y. et al. (2002), Wang T.L et al. (1992), Cai H.Y. et al. (2000), Li X. S. et al. (1998) and Li X.S. (1996).

Table 1. Physical parameters of Shanghai soils in its urban area.

Number	Soil name	Thickness (m)	Unit weight (kN/m ³)	Permeability (m/s)
①	Deep yellow silty clay	3	19.0	1.5E-8
②	Mucky silty clay	7	17.5	1.5E-9
③	Mucky clay	10	17.4	1.5E-9
④	clay	5	18.0	1.2E-8
⑤	Silty clay	5	18.2	5.8E-7
⑥	Silty fine sand	15	19.2	1.2E-5
⑦	Silty clay containing sand	30	19.0	5.8E-7
⑧	fine medium sand	20	19.5	6.0E-5
⑨	Silty clay	15	20.0	5.8E-7
⑩	medium coarse sand	30	20.2	2.3E-4

Table 2. Model parameters of all soil layers

Soil layer number	②③	①④⑤⑦	⑨	⑧	⑥⑩
ϕ	13.0	24.0	28.0	33.0	35.0
G_0	165.7	229.4	296.1	401.0	489.0
λ	0.0050	0.0088	0.0053	0.0026	0.0026
κ	0.0010	0.0018	0.0017	0.0005	0.0005
h_r	0.456	0.143	0.456	0.143	0.143
d	100.0	1.5	100.0	3.6	3.6
R_p/R_f	1.00	0.75	1.00	0.75	0.75
k_r	100.0	0.60	100.0	1.20	1.20
b	2.0	2.0	2.0	2.0	2.0
h_p	35.0	35.0	35.0	35.0	35.0

First 15 second horizontal acceleration time history during 1971 San Fernando earthquake is taken as the input motions (shown in Figure 2), and it is scaled to obtain peak ground acceleration of 0.1 g, in accordance with VII degree antiseismic demand.

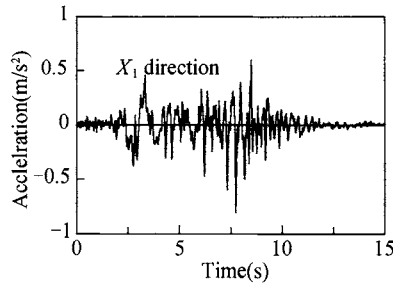


Figure 2. Input motion time history

ANALYSIS RESULTS

Influence of ground water level

Soil deposits from the number 1 to 10 are chosen to construct the base profile, water level is set on the top of soil layers number from 1 to 7; ground peak acceleration and displacement are computed at different water levels, the results are shown in Figure 3.

It can be found from Figure 3 that when the ground water drops, the ground peak acceleration increases slightly, but the ground peak displacement decreases obviously. The former shows that soil becomes harder, the latter - the liquefaction potential reduces.

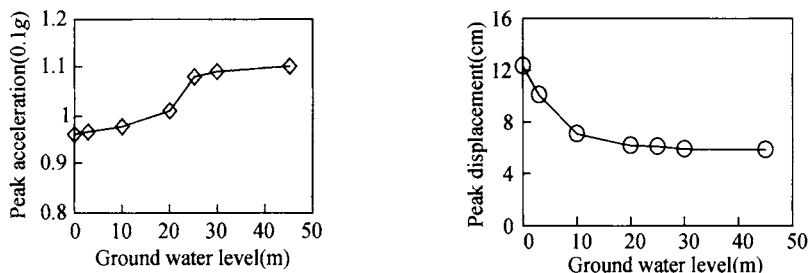


Figure 3. Effect of ground water level on peak acceleration and displacement

Influence of embedded depth of silty fine sand layer

In order to compute the effect of fine sandy layer on ground acceleration, when sandy layer depth changes, the seepage condition of its covering and underlying soil deposits do not change, six soil deposits from the number 4 to 10 are chosen to construct the base profile, but the thickness of soil deposit 4 is changed to 30m. The fine sand deposit is 2m thick and located from 0 to 30m below the surface, soil layer 4 is divided into two parts and distributed on and under it, then the new computation profiles are created, the calculation results are shown in Figure 4.

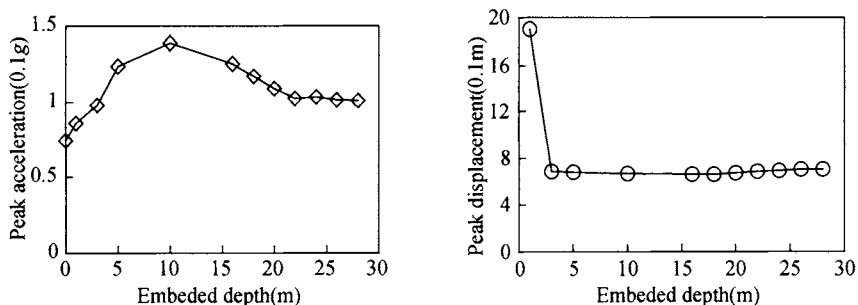


Figure 4. Effect of embedded depth of fine sandy layer on ground horizontal peak acceleration and displacement

It can be seen from Figure 4, under this geology profile and boundary condition, the ground peak acceleration does not increase infinitely, if embedded depth of fine sand layer decrease. When the embedded depth reduced from 28m to 12m, the ground peak acceleration increase; but the depth decreases continuously, it decreases instead. This is because the depth increases, its liquefaction potential drops monotonically, so energy loss of earthquake wave is little; at the same time the ground soft soil become harder due to pore pressure dissipating, in addition its amplification becomes weaker due to its own thickness increasing. When the depth is small, the former predominates, so the ground peak acceleration increases; instead, the latter predominates, the ground peak acceleration decreases. If the embedded depth of

fine sandy layer decreases, the ground peak displacement increases, this is related to the drop of its liquefaction potential.

Influence of thickness of fine sand layer

The base profile in section 3.1 is chosen, the thickness of fine sand layer is set as 2m, 4m, 6m, 8m, 10m, 12, 13m, 14m, 15m respectively, at the same time the thickness of its covering soil layer is scaled down to make total thickness unchangeable, then 9 new profiles are constructed. The calculation results are shown in Figure 5.

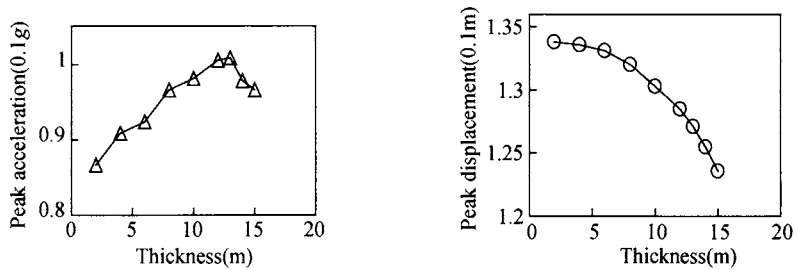


Figure 5. Effect of thickness of fine sand layer on ground horizontal peak acceleration and displacement

It can be seen from Figure 5, the ground peak acceleration does not increase infinitely, if the thickness of fine sand layer increases. When the thickness increasing within 13m, the ground peak acceleration increases; but beyond 13m, it decreases instead. This is because the thickness of fine sand layer increases, its liquefaction potential also increases monotonically, so energy loss of earthquake wave is much. At the same time the ground soil becomes softer due to the buildup of pore pressure, in addition its amplification becomes more noticeable. When the thickness is small, the latter predominates, so the ground peak acceleration increases; instead, the former predominates, the ground peak acceleration decrease. If the thickness of fine sand layer increases, the ground peak displacement decreases, it is related to the thickness reduction of upper soil layers.

CONCLUSIONS

Based on the representative soil layer distribution in Shanghai, the author select and build a number of computation profiles. The effects of ground water level, silty sand deposit thickness and its depth on the ground peak acceleration and displacement are calculated by means of drained effective stress analysis method incorporating Biot dynamic consolidation equations and a bounding surface hypoplasticity model. If ground water drops, ground peak acceleration increases slightly, but displacement decreases noticeably; when the embedded depth and thickness of sandy layer increases, the ground peak acceleration increases first and decreases later. Seismic responses of ground are devoted to dynamic characteristics and geological condition of all underlying soil layers, and related to input motion nearly. The effect of only three sandy soil liquefaction factors on ground acceleration and displacement are studied in the paper, soil layer interaction and its dynamic parameters need to be investigated deeply.

REFERENCES

- Bo J.S., Li X.L. and Liu H.S. (2003). Effects of soil layer construction on peak accelerations of ground motions. *Earthquake engineering and engineering vibration*, 23(3): 35-40.
- Qian S.G. (1994). Seismic responses study of site containing soft soil. *Earthquake resistant engineering*, 23(1): 32- 36.
- Tu H.Q., Zhou J. (1994). Liquefaction potential analysis induced by ground water rising. *Earthquake resistant engineering*, 23(4): 31-35.
- Huang Y., Ye W.M. and Tan Y.Q. (2002). Coupled seismic response analysis of deep saturated soil covering layer in Shanghai. *Rock and Soil Mechanics*, 23(4): 411- 416.
- Wang T.L. and Hu W.Y.(1992). Seismic response analysis of covering soil layer in Shanghai. *Theory and practice of soft foundation*. edited by Gao D.Z., China construction industry press, 55-61.
- Cai H.Y., Zhou J. and Li X.S.(2000). Elasto-Plastic dynamic response of horizontal layered sites under multi-directional earthquake shaking. *Journal of Tongji university*, 28(2): 177-182.
- Li X.S., Shen C.K. and Wang Z.L. (1998). Fully coupled inelastic site response analysis for 1986 LOTUNG earthquake. *Journal of Geotechnical and Geoenvironment Engineering*, 124(7): 560-573.
- Li X.S. (1996). Reduced-order sand model for ground response analysis. *Journal of Engineering mechanics*, 122(9) 872-881.

INFLUENCE OF CUSHION ON DYNAMIC RESPONSE OF CAST-IN-PLACE CONCRETE THIN-WALL PIPE PILE COMPOSITE FOUNDATION UNDER LATERAL SEISMIC EXCITATION

Huiming Tan, Hanlong Liu

*Key Laboratory of Ministry of Education for Geomechanics and Embankment Engineering,
Hohai University, Nanjing 210098, China*

Geotechnical Research Institute, Hohai University, Nanjing 210098, China

With the rapid development of construction in the coastal areas of China, the composite foundation has been widely adopted to reinforce the soft ground. The cushion which lies between pile-reinforced foundation and superstructure is a pivotal part of composite foundation and keeps the piles and soils co-work together to support the static and dynamic loads. Considering the different requirements of constructions, many forms of piles can be applied in composite foundation, such as Cast-in-place Concrete thin-wall Pipe pile (referred as PCC pile). The PCC pile is developed independently by Geohohai and the PCC pile composite foundation has been increasingly adopted on account of its advantages in suitability and economy. In view of the importance of cushion and the necessity of PCC pile composite foundation application, the influences of cushion on dynamic response of PCC pile composite foundation under seismic excitation have been analyzed with non-linear three dimensional FEM in the paper. The computation is consisting of static computation and dynamic computation: the initial soil stress is calculated in static computation, in which the non-linear elastic constitutive model (Duncan Chang model) has been adopted to simulate the behavior of soil, and in dynamic computation the soil is considered to be visco-elastic material and the equivalent linearization dynamic constitutive model is also applied for simulation. In the computation the viscous-elastic boundary is set along the model boundaries. The cushion modulus and thickness have been changed to check the effects of cushion on dynamic response. Based on the computation results, the cushion has effects on the dynamic responses of reinforced-foundation and superstructure. The cushion works as a load transfer platform between foundation and superstructure. With the increase of cushion thickness and the decrease of cushion modulus, the transfer platform becomes softer and its deformation is larger, which leads to max acceleration of superstructure decreased. It shows that the existing of cushion in composite foundation is helpful to reduce the force acted on the superstructure under seismic loads. According to the comparison, the influence of cushion on dynamic response of superstructure is greater than that of reinforced-foundation.

INTRODUCTION

With the rapid development of constructions in China, the composite foundation has been increasingly adopted. The composite foundation mainly consists of pile, soil and cushion. The cushion lying above the piles and soils is a key part of composite foundation, which makes the piles and soils co-work together to support the above loads.

According to the different requirements, the different kinds of piles can be adopted in composite foundation. In the recent years, the PCC pile has been widely applied in composite foundation on account of its advantages in suitability and economy. The PCC pile abbreviated for Cast-in-place Concrete thin wall Pipe pile is developed by Geohohai (Liu et al., 2003, Liu et al., 2003a). Some researches have been done on this new type of pile, which mainly focus on the behavior of PCC pile under static loads, such as the load transfer mechanism, the influences of cushion (Liu et al., 2005; Xu et al., 2006, Tan et al., 2006) and so on. The performances of PCC pile under seismic loads are seldom considered, and Zhu (2006) has made a dynamic analysis on the response of PCC pile composite foundation, but the influences of cushion have not been referred. On account of the importance of cushion, the influences of cushion in PCC pile composite foundation under seismic excitation have been discussed in the article. The characteristics of cushion, such as thickness and modulus, are changed in different computation with FEM to check the influences of cushion on the dynamic responses of PCC pile composite foundation.

COMPUTATION MODEL

The FEM dynamic analyses on soil include static computation and dynamic computation. The soil initial stress field is computed by static computation before dynamic computation, in which the nonlinear elastic Duncan-Chang constitutive model has been adopted to simulate soil behavior (Duncan et al., 1970). In dynamic calculation, soil is considered to be viscoelastic material and the equivalent linearization dynamic constitutive model is applied for simulation. The acceleration at any time is calculated by Wilson- θ step-by-step integration method. The dynamic shear modulus is calculated by Seed formula:

$$G = KP_a^{1-n} \sigma_m^n \frac{G}{G_{\max}}$$

where, K, n — experimental constant of G_{\max} ;

σ_m — average effective stress;

G/G_{\max} — function of shear strain γ .

The typical seismic wave—Kobe seismic wave is used for computation (as shown in Figure 1), the amplitude acceleration of which is 0.2g.

The computation model is illustrated in Figure 2. The three dimensional problem has been simplified, and the unit length of the model has been taken along the Y direction. The PCC pile length is 20.0m, the diameter of PCC pile is 1.0m, the wall thickness of pile is 0.12m, and the pile space is 3.0m; the height of the superstructure is 10.0m; the fixed bedrock is 10 meters away from the bottom of pile. Considering the symmetry of the model, half of it has been taken for computation and the Y direction of boundary is fixed. The viscous-elastic boundary has been set in X direction, which is 62-meter away from the

symmetry axis. The thickness of cushion which lies between superstructure and reinforced foundation is 0.5m in the basic computation model.

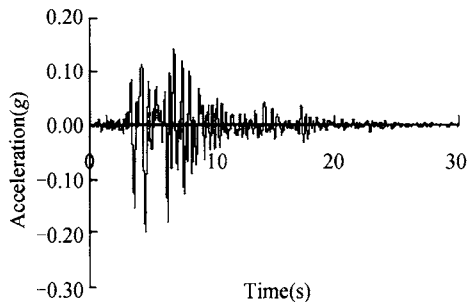


Figure 1. Kobe seismic wave

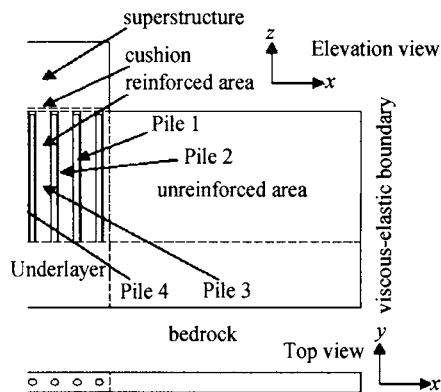


Figure 2. Computation model

The 8-node solid element has been used in the model, and there are 4680 elements and 5682 nodes in the whole model. The material parameters for static and dynamic computation have been listed in Table 1, Table 2 and Table 3.

Table 1. Parameters for static computation

Item	k	n	R_f	C	φ	μ
Soil	300	0.35	0.78	54	27	0.33
pile	300000	0	0	3000	50	0.17
Superstructure	3000	0.3	0.9	40	30	0.33
cushion	850	0.22	0.81	0	35	0.20
Under layer	550	0.34	0.80	50	29	0.33

* The meanings of parameters k , n , and so on listed in Table 1 are shown in reference (Duncan *et al.*, 1970).

Table 2. Parameters for maximal shear modulus calculation

	soil	pile	Under layer	cushion	Superstructure
K	600	128000	1500	2000	8000
N	0.88	0	0.87	0.69	0.72

Table 3. Value list of dynamic shear modulus and damping ratio for different shear strain

Shear strain		10^{-6}	5×10^{-6}	10^{-5}	5×10^{-5}	10^{-4}	5×10^{-4}	10^{-3}	5×10^{-3}	10^{-2}	0.05^{-6}
soil	G/G_{ma}	1	0.998	0.965	0.874	0.782	0.448	0.236	0.088	0.065	0.037
	λ	0.023	0.026	0.03	0.0345	0.036	0.065	0.099	0.197	0.223	0.241
pile	G/G_{ma}	1.0	1.0	1.0	1.0	1.0	1.0	1.0	1.0	1.0	1.0
	λ	0.05	0.05	0.05	0.05	0.05	0.05	0.05	0.05	0.05	0.05
under layer	G/G_{mx}	1	0.998	0.965	0.874	0.782	0.448	0.236	0.088	0.065	0.037
	λ	0.023	0.026	0.03	0.0345	0.036	0.065	0.099	0.197	0.223	0.241
cushion	G/G_{ma}	1	0.977	0.910	0.788	0.543	0.343	0.276	0.155	0.095	0.038
	λ	0	0.039	0.048	0.080	0.082	0.112	0.130	0.160	0.230	0.257
superstructure	G/G_{ma}	1	0.921	0.788	0.576	0.500	0.342	0.274	0.121	0.065	0.024
	λ	0	0.042	0.054	0.062	0.071	0.111	0.164	0.188	0.220	0.258

INFLUENCES OF CUSHION ON DYNAMIC RESPONSE

Effects of cushion modulus

In order to consider the influences of cushion modulus on PCC pile composite foundation dynamic responses, the parameter K , which reflects the cushion modulus and is listed in Table 2, is variable from 1000 to 4000, and the other computation parameters are unchangeable.

The influence of cushion modulus on the max acceleration of the top of superstructure is illustrated in Figure 3. With the increase of cushion modulus, the max acceleration of the top of superstructure is increased in X direction with the same distance from the center of the model. It also shows that the max acceleration is decreased with the distance from the center increased. In the computation the cushion modulus ($K=1000-4000$) is always less than superstructure ($K=8000$), the cushion works as a load transfer platform to transfer seismic loads from the bottom of the model to the superstructure. With the increase of cushion modulus, the deformation resistance of cushion is increased and the cushion is stiffer, which leads to the more dynamic loads applied on the superstructure and the max acceleration is increased.

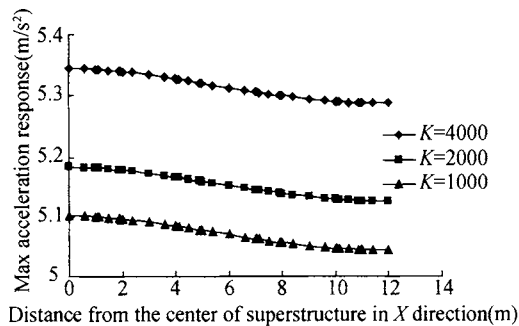


Figure 3. influence of cushion modulus on max acceleration of superstructure

Figure 4 shows the influence of cushion modulus on max acceleration of the whole model along the symmetry axis. The zero point of Z coordinate is set at the bottom of the pile. When the cushion modulus is varied from 1000 to 4000, the basic transferring regular of the max acceleration along the symmetry axis is almost the same, especially in the reinforced foundation and under layer. From the bottom of under layer to the midpoint ($Z=10$) of the pile, the max accelerations are changed slightly, and the max accelerations are a bit different in the cushion and superstructure areas. With the increase of cushion modulus, the max accelerations are increased. Compared to the influence of cushion modulus on the max acceleration, the influence on reinforced foundation is relatively inconspicuous from Figure 4.

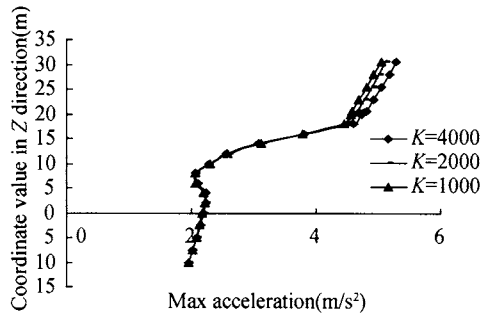


Figure 4. influence of cushion modulus on max acceleration along the symmetry axis

Effects of cushion thickness

In order to consider the influences of cushion thickness on PCC pile composite foundation dynamic responses, the thickness of cushion has been changed from 0.1m to 0.5m in different computation, and the other computation parameters are kept the same.

The influence of cushion thickness on the max acceleration of the top of superstructure is illustrated in Figure 5. With the increase of cushion thickness, the max acceleration of the top of superstructure is decreased in X direction with the same distance from the center of the model. It also shows that the max acceleration is decreased with the distance from the center increased. In the computation model, the cushion modulus ($K=2000$) is always less than that of superstructure ($K=8000$), and the cushion works as a softer load transfer platform to transfer seismic loads from the bottom of the model to the superstructure. With the increase of cushion thickness, the deformation of cushion is increased and more energy is absorbed in the cushion, which leads to the less dynamic loads applied on the superstructure and the max acceleration is decreased.

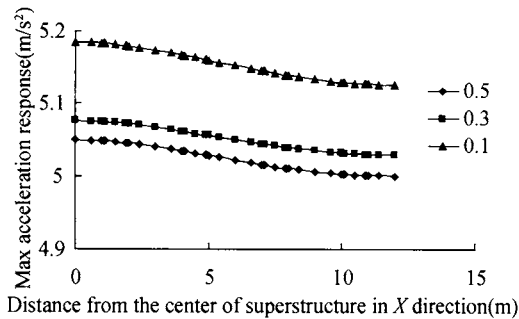


Figure 5. Influence of cushion thickness on max acceleration of superstructure

Figure 6 shows the influence of cushion thickness on max acceleration the whole model along the symmetry axis. The zero point of Z coordinate is set at the bottom of the pile. When the cushion thickness is varied from 0.1m to 0.5m, the basic transferring regular of the max acceleration along the symmetry axis is almost the same. From the bottom of under layer to the midpoint ($Z=10$) of the pile, the max accelerations are changed slightly, and the max accelerations are a bit different in the cushion and superstructure areas. With the

increase of cushion thickness, the max accelerations of the whole superstructure are decreased. Compared to the influence of cushion thickness on the max acceleration, the influence on reinforced foundation is much smaller from Figure 6.

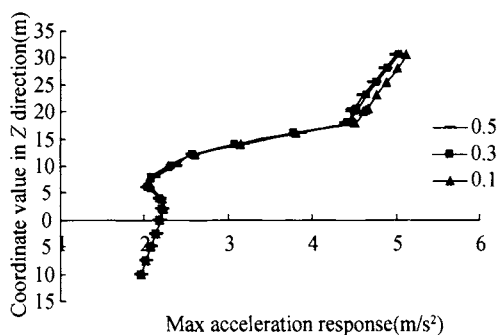


Figure 6. influence of cushion thickness on max acceleration along the symmetry axis

CONCLUSIONS

Cushion is a pivotal part of composite foundation, and it works as a soft load transfer platform between reinforced foundation and superstructure. The influences of cushion characteristics (such as modulus and thickness) on the dynamic responses of PCC pile reinforced foundation and superstructure under seismic loads have been computed and analyzed with non-linear three dimensional FEM. Some conclusions can be drawn as follows:

- (1) The max acceleration of superstructure is always at the center of the structure and the acceleration is decreased with the distance away from the center increased.
- (2) With the increase of cushion modulus, the max acceleration of whole model is increased, and the influence of cushion modulus on the max acceleration of superstructure is greater than that of pile-reinforced foundation. The max acceleration is changed rapidly from the top to the middle pint of pile.
- (3) With the increase of cushion thickness, the max acceleration of whole model is decreased, and the influence of cushion modulus on the max acceleration of superstructure is greater than that of pile-reinforced foundation. The max acceleration is changed rapidly from the top to the middle pint of pile.
- (4) The existing of cushion in PCC pile composite foundation is helpful to reduce the forces acted on the superstructure under seismic excitation.

REFERENCES

- Duncan J. M., Chang C. Y. (1970). Nonlinear analysis of stress and strain in soils. *J. Soil Mech. Found Div.*, 96(5): 1629-1652
- Liu H. L., Fei K., Ma X. H. and Gao Y. F. (2003). Large-diameter driven cast-in-place concrete thin-wall pipe pile (I) Research and Development. *Journal of Rock and Soil Mechanics*, 24: 164-198.
- Liu H. L., Fei K., Ma X. H. and Gao Y. F. (2003a). Large-diameter driven cast-in-place concrete thin-wall pipe pile (II) Application. *Journal of Rock and Soil Mechanics*, 24: 372-375.

- Liu H.L., Fei K. and Xu X.T. (2005). Development and application of the large-diameter driven cast-in-place concrete thin-wall pipe pile. *Proceeding of the 16th international conference on soil mechanics and geotechnical engineering*, Osaka, Japan, 2137-2140.
- Xu X.T., Liu H.L. and Lehane B.M. (2006). *Pipe pile installation effects in soft clay*. Geotechnical Engineering, Issue GE4, 285-296.
- Tan H.M, Liu H.L. and Zhang T. (2006). Numerical analysis on cushion in PCC pile composite foundation. *Chinese Journal of Geotechnical Engineering*, 28: 1489-1492.
- Zhu X.C. (2006). *Dynamical analysis of the cast-in-situ concrete thin-wall pipe pile composite foundation*. The paper for master's degree of Hohai university, Nanjing, China.

NUMERICAL MODELLING OF SEISMIC PERFORMANCES OF PASSIVE PILE GROUPS ADJACENT TO SOIL SLOPE

Mingwu Wang

*School of Civil Engineering, Hefei University of Technology,
Hefei 230009, China*

Li Li

*School of Resources and Environmental Engineering, Hefei University of Technology,
Hefei 230009, China*

The seismic performance of pile groups founded on the lateral spreading soils is a complex problem. Based on the effective stress analysis method using a multiple shear plasticity model and a concept of liquefaction front, and combined with a practical example, seismic responses of pile groups adjacent to soil slope was investigated in this paper. The numerical predications show that the values of lateral displacements in pile groups decreased with the increase of the distance between the pile and soil slope, and also decreased with increase of the buried depth along the pile. The values of bending moments are smaller inside the pile groups than outside of pile groups at the same depth. At the same time, the dynamic earth pressure in the soil is smaller in the core of pile groups than beneath the slope at the same depth.

INTRODUCTION

Extensive damage to pile-supported structures in areas of lateral spreading has been observed in many earthquakes around the world. As soft soil moves laterally past piles due to adjacent to soil slope during earthquakes, passive lateral pressure may be applied to the piles. This may lead to serious problems, such as much larger bending moment and deflection of pile, or even failure of pile, then results in the instability and destruction of superstructures. Consequently, the passive pile foundations adjacent to soil slope not only needs to undergo the load of superstructures, but also undergo the additional load resulted from the lateral spreading of soils during earthquakes. However, the performances of passive pile groups adjacent to soil slope are not yet well understood, especially the seismic behavior of passive pile groups, although researches in recent years have begun to clarify certain aspects of behavior. Thus research on seismic performances of passive pile groups adjacent to slope during earthquakes is of great significance to improve and perfect the seismic design theory of passive pile groups.

Previous design methods have employed pile load-transfer curves usually described as active loading, to predict passive lateral pressures and deflections. Liyanpathirana and Poulos (2005) presented a pseudostatic approach using the spring coefficients of the Winkler

model to compute the maximum bending moment and shear force developed in pile founded in liquefying soil. However, those methods are either of a semiempirical nature or employ approximate analysis which often involves considerable simplifications. This makes it difficult for practicing engineers to effective application. Consequently, analytical closed form solutions become very difficult and numerical techniques are use to investigate the seismic behaviors of passive pile groups. Fraser et al. (1999), Li et al. (2007) analyzed the performances of passive pile subjected to the static loading by the means of the FEM method. The post earthquake observations and results from numerical simulations indicate that the response of passive pile can be significantly influenced by the behavior of the larger deformation of liquefiable soils.

The objective of this study is to investigate the seismic response of passive pile foundation adjacent to soil slope by the means of numerical simulations, and to provide a basis for the seismic design of passive pile group during earthquakes.

EFFECTIVE STRESS ANALYSIS METHOD

Numerical modeling for analysis of seismic behaviors of the passive pile groups adjacent to slope has been conducted using the program FLIP (Finite element analysis program for LIquefaction Process) developed by Iai et al. (1990, 1992).

The constitutive model of soil mass incorporated in the FLIP is composed of a multiple shear plasticity model and a model for generating excess pore water pressure. The constitutive model used for the analysis, which can take into account the effect of rotation of principal stress axis directions and can behave the large deformation of liquefiable soils during motions, is based on multiple inelastic shear springs defined in the deviator strain space. The multiple-spring model is composed of virtual simple shear mechanisms in arbitrary orientations, which is assumed to follow the hyperbolic stress-strain relation. And the model uses the extended Masing's rule to reproduce more realistic hysteresis loop for cyclic loading. The excess pore water pressure generation due to dilatancy is modeled using the concept of liquefaction front proposed by Iai et al. (1992), which is defined in the normalized stress space with the isotropic stress ratio and the deviatoric stress ratio.

NUMERICAL MODELING

Computed model

The practical example is a pile foundation project adjacent to a soil slope which was reinforced by bolting and shotcrete lining system. The soil profile is consisted of 5 soil layers. The type and thickness of each soil layer are listed in Table 1. The soil layers of number 4

Table 1. Parameters of soil layer for the numerical modeling

Soil No.	Soil type	ρ (g·cm ⁻³)	G_{ma} (kPa)	K_{ma} (kPa)	ϕ_r (°)	S_1	W_1	P_1	P_2	C_1
1	Silty clay	1.93	9.419×10^4	2.456×10^5	40.04	0	0	0	0	0
2	Sandy silt	1.96	7.917×10^4	2.056×10^5	39.46	0	0	0	0	0
3	Silty clay	1.96	1.201×10^4	3.131×10^5	40.98	0	0	0	0	0
4	Fine sand	2.02	4.976×10^4	1.298×10^5	38.22	0.005	4.858	0.5	1.016	1.805
5	Medium sand	2.03	1.034×10^5	2.697×10^5	40.38	0.005	4.757	0.5	0.939	2.779

and 5 are liquefiable soils. The finite element mesh used in the analysis is shown in Figure 1. The finite element model consists of 2 796 nodes and 4 666 elements. The number of pile groups from left to right is labeled as from number 1 to 14 in turn. The length, diameter and spacing of pile are 2.0 m 0.41m and 1.8 m, respectively. The pile and anchor are simulated with linear beam elements. The soil is modeled with a multiple spring element. The pore water pressure is modeled with pore water element. The super-structure mass is treated as a rigid body and is represented by a concentrated mass. The soil-pile interaction spring element is used to simulate the pile-soil interaction. The water table is at the buried depth of 1.3 m. The locations of output elements indicated as shown in Figure 1.

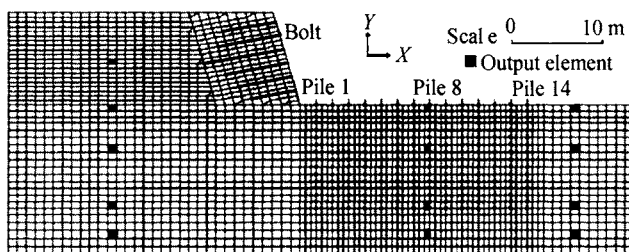


Figure 1. Mesh of computed model

Soil parameters and computed conditions

The parameters of soil profile used for the numerical analysis are listed in Table 1. The parameters were determined based on the laboratory test results and a simple determination method (Wang et al., 2005a, 2005b).

To simulate the conditions of practical end-bearing pile, the multiple point constraint are set for the pile end and soil. A fixed bottom boundary was set at the base of soil layer 5. The horizontal ground motions were applied at the bottom boundary. Vertical roller condition and viscous boundary was assigned for the both side boundaries for the step of static analysis due to gravity and dynamic analysis, respectively. The input earthquake motions performed for 30 s is the El Centro earthquake wave. The numerical integration is done by Wilson- θ method ($\theta=1.4$) at time step of 0.02 seconds. Rayleigh damping ($\alpha=0$, $\beta=0.002$) was used for ensure the stability of the numerical solution process.

RESULTS AND DISCUSSIONS

Deflections

The maximum lateral displacements along pile are depicted in Figure 2. It may be seen that the value at pile top decreased with the distance from the pile to the slope toe, and also the deflection of each pile decreased when the buried depth increased. The numerical predications indicate that the bigger the deflection, the bigger the distance to slope toe.

Accelerations

The relation between the crest amplitude of horizontal acceleration in soils and elevation is illustrated in Figure 3. The amplitude of acceleration decreased in the liquefiable soil layers

during the motion. Then it increased in the non-liquefiable soils. Meanwhile, the acceleration of soil at the elevation of 0.0 m is bigger within the pile groups than in free field and beneath the slope.

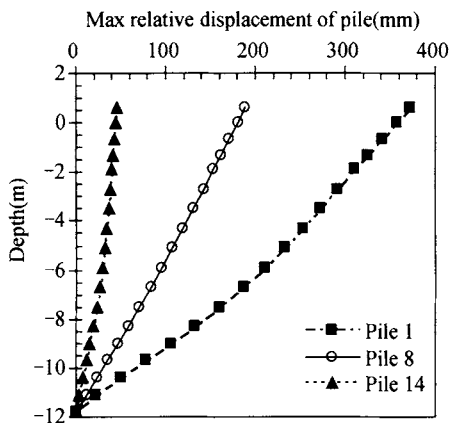


Figure 2. Lateral displacements of pile

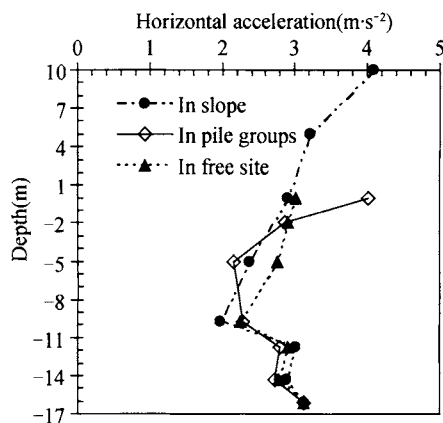


Figure 3. The crest amplitude of acceleration in soil

Blending moments

The max bending moments and bending moment at time of max displacement of pile top are illustrated in Figure 4. It may be seen that the value of bending moments changed with the distance to the slope toe. The value of pile 1 is biggest due to the most influence of lateral spreading of soils. The value of bending moments in pile 8 is smaller. This may be due to the effect of pile groups. However, the maximum bending moment happened all at about 8m from the pile top. And the maximum of bending moments didn't occur at time of maximum lateral displacement of pile. Those observations are of significant for the design of piles adjacent to slope during earthquakes.

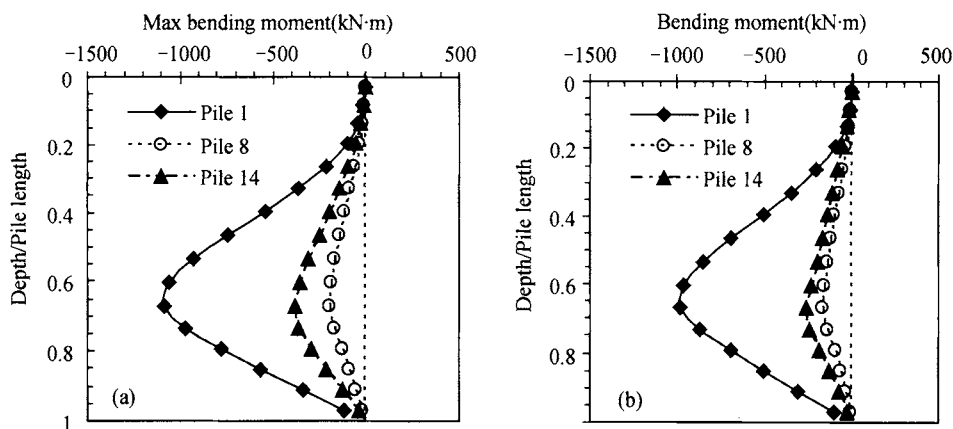


Figure 4. Maximum bending moments of piles

Normal stress and EPWP

The normal stress and excess pore water pressure (EPWP) time histories are obtained as shown in Figure 5, in which the alphabets shown in the figures indicate the locations shown in Figure 1. Difference in the phases of the responses can be recognized among those response normal stress and EPWP. The values of total normal stress after shaking are bigger than those before shaking. And the value in soils beneath the slope is bigger than in the pile groups. The EPWPs gradually increase as the shaking continues while the effective normal stress decreases. But the value of EPWP in the liquefiable soil beneath the slope is biggest. The value of EPWP is less in pile groups than in free field in spite of the equal buried depth. This may be due to the energy translation through pile groups during motions.

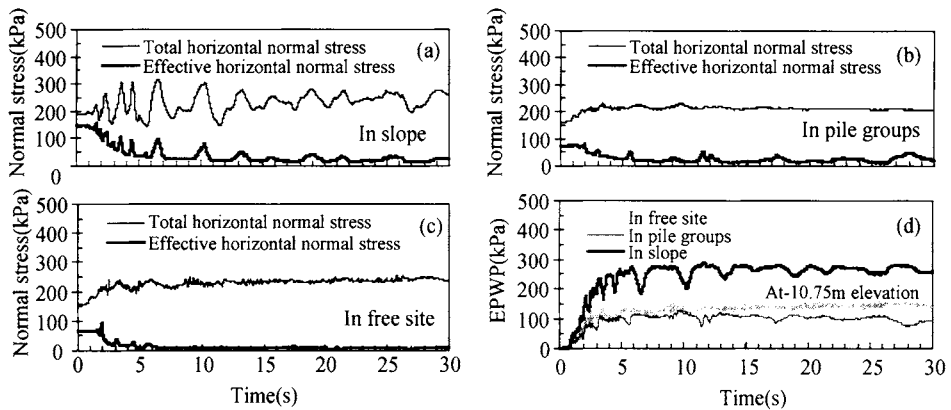


Figure 5. Normal stress time histories and excess pore water pressure time histories

CONCLUSIONS

This paper presents numerical simulations of seismic responses of passive pile groups adjacent to soil slope on liquefiable soils. These results provide a foundation and reference for the seismic design of passive pile groups on a liquefiable soil foundation. The main results are presented as follow,

- 1) It is concluded that the presented analysis method is capable of predicting the behaviors of passive pile group during earthquakes. And it is very helpful to understand better the liquefaction process and seismic behaviors of pile foundation under strong shaking condition.
- 2) The deflections of passive pile decrease with increase of the distance of the pile top to the slope toe. When the buried depth increases, the deflection along the pile decreases. The maximum bending moment is smaller inside pile groups than outside pile groups. However, the dynamic earth pressure in soils is bigger beneath soil slope than in the pile groups at the same depth.
- 3) The behaviors of passive pile groups during earthquakes are much more complex in liquefiable soils than in non-liquefiable soils. And the non-linear behavior of the liquefiable soil has a significant influence on the response of the passive pile to

seismic excitation. Thus extensive and further studies are needed to evaluate further the performance and validity of numerical modeling, such as the comparison of results between centrifuge tests and numerical predications.

ACKNOWLEDGEMENTS

Financial supports provided by the National Natural Sciences Foundation, China (No. 40702049) are gratefully acknowledged.

REFERENCES

- Liyanpathirana D.S., Poulos H.G. (2005). Pseudostatic approach for analysis of piles in liquefying soil. *Journal of Geotechnical and Geoenvironmental Engineering*, 131(12): 1480-1487.
- Fraser M., Bransby M.F. and Springman S.M. (1999). Selection of load-transfer functions for passive lateral loading of pile groups. *Computers and Geotechnics*, 24(3): 155-184.
- Iai S., Matsunaga Y. and Kameoka T. (1990). Parameter identification for a cyclic mobility model. *Rep Port Harbour Res Inst*, 29(4): 57-83.
- Iai S., Matsunaga Y. and Kameoka T. (1992). Strain space plasticity model for cyclic mobility. *Soils Foundations*, 32(2): 1-15.
- Li L., Wang M.W. and Zhang H. (2007). Effective stress analysis of deformations of passive pile groups adjacent to soil slope. *China Civil Engineering Journal*, 40(S1): 95-99. (in Chinese)
- Wang M.W., Iai S. and Tobita T. (2005a). Effective stress analysis of underground RC structures during earthquakes. *Annals of Disaster Prevention Research Institute, Kyoto University*, 47(B): 371-382.
- Wang M.W., Iai S. and Tobita T. (2005b). Numerical modeling for dynamic centrifuge model test of the seismic behaviors of pile-supported structure. *Chinese Journal of Geotechnical Engineering*, 27(7): 738-741.(in Chinese)

DYNAMIC BEHAVIOUR OF RIGIDLY-CAPPED PILE GROUPS OF VERTICAL AND ROCKING OSCILLATIONS

Bin Yan, Lihua Liu and Xiaotong Peng

*School of Civil Engineering & Architecture, University of Ji'nan,
Ji'nan 250022, China*

Mingdong Wang

*Department Civil Engineering, Shandong Communications College,
Ji'nan 250022, China*

The behaviours of soil layers in a different depth are presented mainly. The pile group and the surrounding soil are discretized into horizontal layers, which meet a plane strain assumption. By means of that the single pile dynamic impedance is developed using a transfer matrix method, the pile-to-pile dynamic interaction factor is derived. Then, the paper introduces the dynamic impedances of rigidly-capped pile groups with due consideration to pile-soil-pile interaction for vertical and rocking oscillations.

INTRODUCTION

Piles are often used in a group in a foundation system. When the grouped piles are closely spaced, pile-soil-pile interaction modifies the pile response leading to group effects. Now it has been found that group effects are far more significant and complex under dynamic loading than static loading, for example Nogami (1983), Novak et al (1978).

Pile foundations are sufficiently rigid against axial loads, and most piles are designed for load-bearing capacities and for lateral deflection criteria only. However, there are many cases in which dynamic axial pile responses become one of the key considerations in foundation design. For example, the pile foundation for tall buildings and fixed offshore platforms must resist dynamic overturning moments due to winds, earthquakes, and waves. The design of pile-supported machine foundations is another typical example for which dynamic axial pile responses play an important role.

Responses of axially loaded pile have been studied by several techniques. Wolf et al (1978) used a finite-element method. Nogami et al (1983) and Ettouney et al (1983) used solutions obtained from the equations of wave propagation in a three-dimensional continuum in their analyses of pile groups. Nogami et al (1983), Sheta et al (1982), Gazetas et al (1991) and Poulos (1994) developed a Winkler soil model for grouped piles, which can account for dynamic pile-soil-pile interaction. The finite-element and boundary-element methods may not be readily available to design engineers. Mathematical solutions are limited to idealized soil-pile conditions. The Winkler soil model neglects the interaction between soil springs.

This paper presents a semi-analytical solution of the dynamic behavior of pile groups, including the interaction between the piles through the soil medium. The pile-to-pile dynamic interaction

factors are studied in layered soils. Then dynamic impedances of rigidly-capped pile groups for vertical and rocking oscillations are conveniently solved.

DYNAMIC AXIAL IMPEDANCE OF A SINGLE PILE

The soil in a model is composed of horizontal layers. The soil properties are constant within each layer but may be different in individual layers. The soil material is assumed to be linear and isotropic with hysteretic type damping. The pile group is composed of a set of vertical piles assumed to behave according to the conventional beam theory. They are also assumed to have a circular cross-section. The piles and soil are bonded together. Now, the soil stiffness is to be calculated by using the plane-strain method. The plane-strain method is based on subdividing the soil media into sets of layers, each layer with a unit thickness, and with a single pile with radius r_0 at the origin.

The amplitude of vertical vibration in soil, $W_s(r)$, produced by unit harmonic force, is quoted from Ettouney's paper. Then, the amplitude of vertical vibration in l th soil can be obtained to be

$$W_{sl}(r) = -\frac{K_0(sr)}{2\pi G_l sr_0 K'_0(sr_0)} \quad (1)$$

where $K_0(\)$ = modified Bessel function of zeroth order and the second kind, $K'_0(\) = dK_0(\)/dr$, $s = \omega/V_s$, V_s = complex shear wave velocity of soil layer.

The vertical stiffness of l th soil layer correspondingly a single pile with radius r_0 is

$$k_{sl} = \frac{1}{W_{sl}(r_0)} = -\frac{2\pi G_l sr_0 K'_0(sr_0)}{K_0(sr_0)} \quad (2)$$

A homogeneous layer is assumed to be composed of an infinite number of uncoupled horizontal layers in which each layer is the plane strain model previously described. If the pile is not an end-bearing pile, the model of the pile is assumed that the pile extends to the rigid layer with the same cross section, but different materials are reinforced concrete and soil respectively. Extending pile is viewed as a integrate pile except that the modulators of reinforced concrete and soil are distinct. A harmonic vertical excitation is exerted on the pile top, the displacement of the pile is written as $w(z,t) = W(z)\exp(i\omega t)$, in which $W(z)$ is the amplitude of vertical vibration.

The differential equation of motion in the vertical direction is

$$E_p^i A_p^i \frac{d^2 W_p^i(z)}{dz^2} - (k_s^i - m_p^i \omega^2) W_p^i(z) = 0 \quad (3)$$

$$\alpha_i^2 = (k_{sl} - m_p \omega^2) / E_{pl} A_{pl} \quad (4)$$

According to the elastic equation of the axial force and the displacement, the solution is

$$\begin{bmatrix} W_p^1 \\ N_p^1 \end{bmatrix} = [T_p] \begin{bmatrix} W_p^{m+1} \\ N_p^{m+1} \end{bmatrix} \quad (5)$$

in which $[T_p]$ is 2×2 matrix. Let

$$\begin{bmatrix} T_p \end{bmatrix} = \begin{bmatrix} T_{p11} & T_{p12} \\ T_{p21} & T_{p22} \end{bmatrix} \quad (6)$$

According to the boundary conditions, the vertical displacement of the bottom resting on a rigid layer is zero, $W_{p(m+1)} = 0$. Then the dynamic axial impedance of a single pile can be expressed as

$$K_{pv} = \frac{N_p^1}{W_p^1} = \frac{T_{p22}}{T_{p12}} \quad (7)$$

PILE –TO-PILE DYNAMIC INTERACTION FACTOR

Two piles with same long and diameter is a distance R between their centers. If one of them is loaded with an axial harmonic force on its top, its dynamic displacement of the top, $w_{p11}(z,t) = W_{p11}^1(z) \exp(i\omega t)$, and the dynamic displacement fields in soil, $w_s(z,t) = W_s^1(z) \exp(i\omega t)$, are produced. Since the displacement fields in soil, the dynamic displacement of another pile top can be written as $w_{p21}^1(z,t) = W_{p21}^1(z) \exp(i\omega t)$. Then the dynamic equation of another pile in l th layer is expressed as

$$E_p A_p \frac{\partial^2 w_{p21}^i}{\partial z^2} - m_p \frac{\partial^2 w_{p21}^i}{\partial t^2} - k_s (w_{p21}^i - \bar{w}_s) = 0 \quad (8)$$

The solution is obtained as

$$\begin{bmatrix} W_{p21}^1 \\ N_{p21}^1 \end{bmatrix} = \begin{bmatrix} T_p \end{bmatrix} \begin{bmatrix} W_{p21}^{m+1} \\ N_{p21}^{m+1} \end{bmatrix} + \begin{bmatrix} \xi \\ \zeta \end{bmatrix} W_{p11}^1 \quad (9)$$

where

$$\begin{bmatrix} \xi \\ \zeta \end{bmatrix} = \begin{bmatrix} t_p^1 \end{bmatrix} \begin{bmatrix} t_p^2 \end{bmatrix} \cdots \begin{bmatrix} t_p^{m-1} \end{bmatrix} \begin{bmatrix} \lambda_m \\ \eta_m \end{bmatrix} + \cdots + \begin{bmatrix} t_p^1 \end{bmatrix} \begin{bmatrix} t_p^2 \end{bmatrix} \cdots \begin{bmatrix} t_p^{i-1} \end{bmatrix} \begin{bmatrix} \lambda_i \\ \eta_i \end{bmatrix} + \cdots + \begin{bmatrix} \lambda_1 \\ \eta_1 \end{bmatrix} \quad (10)$$

$$\begin{bmatrix} \lambda_i \\ \eta_i \end{bmatrix} = \begin{bmatrix} \frac{-k_s^i W_s^i(R) (\text{ch} \alpha_i \ell_i - 1) b_i}{W_s^i(r_0) \alpha_i^2} \\ \frac{-k_s^i W_s^i(R) (\text{sh} \alpha_i \ell_i) b_i}{W_s^i(r_0) \alpha_i^2} \end{bmatrix} \quad (11)$$

According to the boundary conditions, $N_{p21}^1 = 0$, $W_{p21}^{m+1} = 0$, then the dynamic interaction factor of two piles are solved. Hence,

$$\alpha_{12} = \alpha_{21} = \frac{W_{p21}^1}{W_{p11}^1} = \xi - \zeta \frac{T_{p12}}{T_{p22}} \quad (12)$$

DYNAMIC IMPEDANCES OF PILE GROUPS FOR VERTICAL AND ROCKING OSCILLATIONS

Dynamic axial impedances of pile groups

A massless rigid cap excited by dynamic force $N(t) = N_0 \exp(i\omega t)$, where N_0 is amplitude of the force, is supported by n piles. Then each pile is subjected to dynamic force N_i . Due to the constraining role of the rigid cap, the axial amplitude of vibration of the rigid cap W is equal to the displacement of each pile W_i . The equation is written as

$$W = W_i^0 \quad (i = 1, \dots, n) \quad (13)$$

Due to dynamic interactions, the axial displacement of i th pile is

$$W_i^0 = W_{i1}^0 + \dots + W_{ii}^0 + \dots + W_{ij}^0 + \dots + W_{in}^0 \quad (14)$$

Introducing Eq. (7) and Eq. (12) into Eq. (14) yields

$$W = W_i^0 = \frac{1}{K_{pv}} (\alpha_{i1} N_1 + \dots + \alpha_{ii} N_i + \dots + \alpha_{in} N_n) \quad (i = 1, \dots, n) \quad (15)$$

Also the force N_0 applied on the rigid cap is shared by n piles, hence

$$N = \sum_{i=1}^n N_i \quad (16)$$

According to Eq. (15) and Eq. (16), the displacement of the rigid cap and the force of each pile subjected can be calculated. Then the axial dynamic impedance of pile group can be written as

$$K_{pv}^G = \frac{N}{W} \quad (17)$$

Dynamic impedances of pile groups for rocking oscillations

A massless rigid cap excited by rocking moment $M(t) = M_0 \exp(i\omega t)$, where M_0 is amplitude of the moment, is supported by n piles. Then each pile is subjected to dynamic force N_i . The rotations of rigid caps about the coordinate axis, y , bring an angle, ϕ . The x coordinate of each pile is expressed as x_i . The vertical displacement of each pile and moment equations are written as

$$W_i^0 = \frac{1}{K_{pv}} (\alpha_{i1} N_1 + \dots + \alpha_{ii} N_i + \dots + \alpha_{in} N_n) \quad (18)$$

$$M = \sum_{i=1}^n x_i N_i \quad (19)$$

where

$$W_i^0 = x_i \phi \quad (20)$$

According to Eq. (18), Eq. (19) and Eq. (20) , the rocking dynamic impedances of pile groups are obtained,

$$K_r^G = \frac{M}{\phi} \tag{21}$$

EXAMPLE

Poulos gave an example of 2×2 pile groups, the slenderness ratio $L/d = 15$, comparing the space between piles with the diameter of piles $s/d = 5$ or 10 . The modular ratio of the pile and the soil, E_p/E_s , was 1000. The vertical impedances can be expressed as $K_{pv}^G = \bar{K}_{pv}^G + i\omega C_{pv}^G$. The rocking impedances also can be written as $K_r^G = \bar{K}_r^G + i\omega C_r^G$. In Figure 1 the predictions of the developed simple analytical method compare very well with the rigorous solution of Poulos. Figure 2 shows rocking dynamic stiffness and damping group factors as a function of frequency for a 2×2 pile groups.

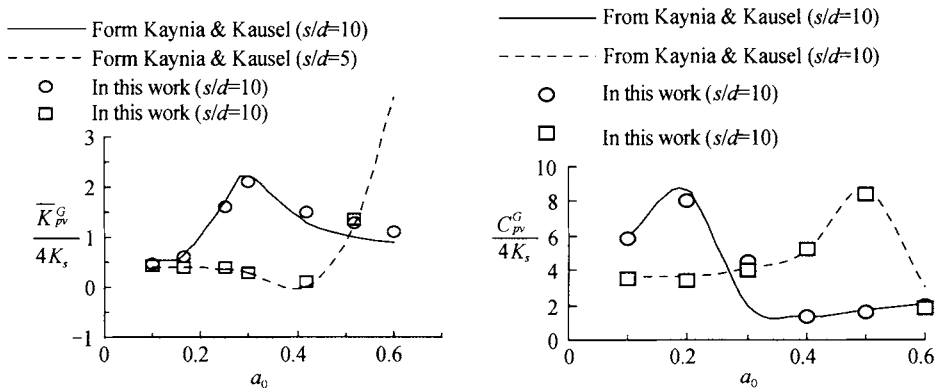


Figure 1. Vertical dynamic stiffness and damping group factors as a function of frequency for a 2×2 pile groups

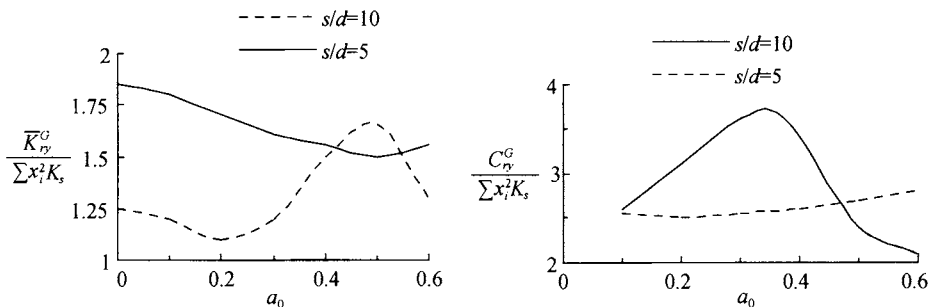


Figure 2. Rocking dynamic stiffness and damping group factors as a function of frequency for a 2×2 pile groups

CONCLUSIONS

The behaviours of soil vary with distance from ground level. In many cases, the soil properties can be viewed as constant within each layer but may be different in individual layers. Hence, the pile groups

and the surrounding soil are discretized into many horizontal layers, which well meet a plane strain assumption. By means of that the single pile dynamic impedance is developed using a transfer matrix method, the pile –to-pile dynamic interaction factor is derived. Then, the paper introduces the dynamic impedances of rigidly-capped pile groups with due consideration to pile-soil-pile interaction for vertical and rocking oscillations. A companion paper deals with interaction under vertical and rocking loading.

ACKNOWLEDGMENTS

The support from Natural Science Foundation of Shandong Province by award # G0637 is appreciated. The study was supported by a grant in aid of research from University of Jinan (B0421).

REFERENCES

- Ettouney M., Brennan A. (1983). Dynamic behavior of pile groups. *Journal of Engineering Mechanics Division*, ASCE, 109(3): 301-317.
- Gazetas G., Makris N. (1991). Dynamic pile–soil–pile interaction. part I : Analysis of Axial Vibration. *Earthquake Eng. Struct. Dyn.*, 20(1): 115-132.
- Nogami T., Chen H.L. (1983). Behavior of pile groups subjected to dynamic loading. *Proc.4th Canadian conf. Earthquake Eng.*, Vancouver, 1: 413-423.
- Nogami T. (1983). Dynamic group effect in axial responses of grouped piles. *Journal of Engineering Mechanics Division*, ASCE, 109(3): 228-243.
- Novak M., Aboul-Ella F. (1978). Impedance functions of pile in layered media. *Journal of Engineering Mechanics Division*, ASCE, 104(3): 643-658.
- Poulos H.G. (1994). An approximate numerical analysis of pile-raft foundation. *J. Num. Anal. Mechs. In Geomechs.*, 18(1): 73-92.
- Sheta M., Novak M. (1982). Vertical vibration of pile groups. *Journal of Engineering Mechanics Division*, ASCE, 108(4): 570-590.
- Wolf J., Von Arx G.A. (1978). Impedance foundation of a group of vertical piles. *Proc. ASCE geotech. Eng. Apediality conj.*, Pasadena, 2: 1024-1041.

EFFECTS OF SINGLE JOINT WITH DIFFERENT NONLINEAR NORMAL DEFORMATIONAL BEHAVIORS ON P-WAVE PROPAGATION

J. Yu

*Geotechnical Engineering Department, Nanjing Hydraulic Research Institute
Nanjing 210024, China*

The classical exponential elastic model and the *BB* hyperbolic elastic model are used to investigate the effects of nonlinear normal deformation on elastic P-wave normal incidence without the shear deformation considered. A theoretical research is presented on normally incident P-wave transmission across single dry joint with these different nonlinear normal deformation behaviors. Based on the classical and the *BB* nonlinear models, the different nonlinear displacement discontinuity models are established. Numeric difference resolution and analytic resolution of reflected and transmitted coefficients for normally incident P-wave propagates across single joint with different nonlinear normal deformation behaviors are obtained. Then parametric studies are conducted, in terms of the quantitative ratio of the joint current maximum closure to the joint maximum allowable closure, the joint initial normal stiffness and the incident wave frequency. Comparisons between the results of different nonlinear behaviors are drawn and the conclusions have theoretical meaning.

PREFACE

Extensive studies have been conducted to investigate the effects of joints on stress wave propagation in fractured media, for such effects are important subjects in solving problems of rock mass dynamics and shelter engineering. The theories of wave scattering at cracks have been developed with the considerations of linear contact conditions of crack faces (e.g., Hudson, 1981, Angle and Achenbach, 1985) and nonlinear contact conditions of crack faces (Achenbach and Norris, 1982, Smyshlyaev and Willis, 1994). The objects investigated are mainly cracks of small size relative to wavelength. In comparison with the micro-cracks, the macro-joints may be more dominant in a fractured rock mass on most occasions (Zhao, 2001). A planar macro-joint, which is assumed to be large in extent and very thin in thickness relative to a wavelength (hereafter termed simply as joint), can be physically viewed as a planar collection of collinear micro-voids and asperities in contact. When waves propagate across such a joint, the stress field is continuous, but the displacement field is discontinuous due to the joint deformation. To account for the effects of joints on wave propagation, the joint deformational behaviors are treated as displacement discontinuity boundary conditions in the wave equation, which is termed as displacement discontinuity theory. Linear elastic displacement discontinuity models for dry joints have been established by Schoenberg (1980) and Kitsunozaki (1983). The linear elastic displacement discontinuity models for dry joints

are valid, provided that the magnitude of the seismic stress is insufficient. However, it has been found that the complete deformational behaviors of rock joints are generally nonlinear. Zhao (2001) promote the famous static normal nonlinear deformation behaviors of joints, the *BB* model in the dynamic condition, and the numerical resolution of transmitted and reflected coefficients are obtained by finite-difference methods when the normal incident P-wave propagates to single joint with nonlinear normal deformation behaviors.

The normal deformational behavior of rock joints has been widely investigated. As different considerations of joint deformational behaviors generate various displacement discontinuity models, the choice of nonlinear deformation behaviors of joints becomes the key in analyzing the transmissions characters of elastic p-wave across rock joints. So the studies on the effects of different deformation models on stress wave propagation laws have great significance in theory. The analytic resolution and numeric resolution of transmitted and reflected coefficients are obtained in this paper, considering the joints with different nonlinear normal deformation behaviors, and parametric studies and comparisons are conducted on the effects of initial normal stiffness and the ratio of current maximum closure to maximum allowable closure of the joints, as well as the incident wave amplitude and frequency on reflected and transmitted coefficients.

ROCK JOINTS WITH NONLINEAR DEFORMATION BEHAVIORS

The normal deformational behaviors of rock joints have been widely proposed by predecessors under static and quasi-static loading conditions. In rock mechanics and engineering, hyperbolic model (Bandis et al., 1983; Barton et al., 1985) and logarithmic (exponential) model (Shehata, 1971, Malama and Kulatilake, 2003) are commonly used. In this paper, we choose the commonest *BB* model and typical exponential model to discuss.

If the joint closure (opening) and compression (tension) are assumed to be positive (negative), the *BB* hyperbolic elastic model is.

$$d_n = \frac{\sigma_n}{k_{ni} + (\sigma_n / d_{ma})} \quad (1)$$

where σ_n is the joint normal stress, d_n is the joint normal closure, d_{ma} is the maximum allowable closure of the joint, and k_{ni} is the normal stiffness of the joint at initial stress.

The derivative expression of Eq. (1) is the joint stiffness k_n of *BB* model.

$$k_n = \frac{\partial \sigma_n}{\partial d_n} = \frac{k_{ni}}{1 - (d_n / d_{ma})^2} \quad (2)$$

The typical exponential model relation is:

$$d_n = d_{ma} \left[1 - \exp\left(-\frac{\sigma_n}{k_i d_{ma}}\right) \right] \quad (3)$$

The derivative expression of Eq. (3) is the joint stiffness k_n of exponential model.

$$k_n = \frac{\partial \sigma_n}{\partial d_n} = \frac{k_{ni}}{1 - (d_n / d_{ma})} \quad (4)$$

Figure 1. schematically illustrates *BB* hyperbolic model and typical exponential model with the same d_{ma} and k_{ni} . In comparison with the two models, joint stiffness increases with the joint normal closure, and the curvilinear trend of *BB* model is faster than that of the typical exponential model.

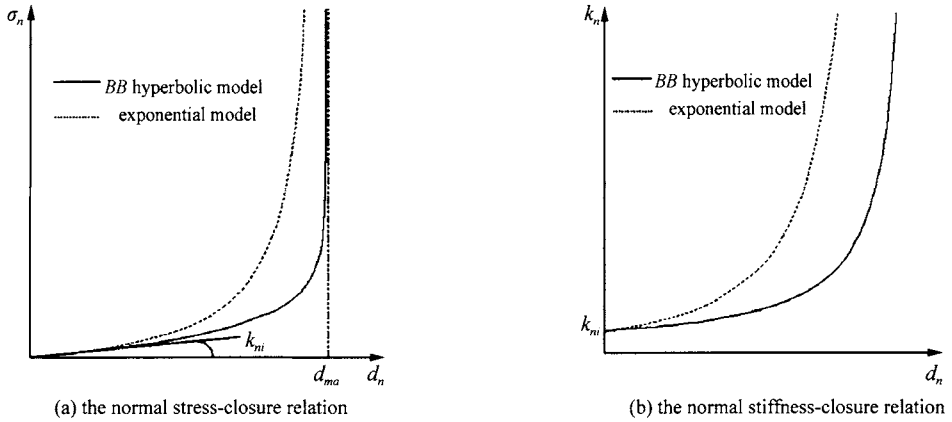


Figure 1. Illustration of *BB* hyperbolic model and classical exponential model of normal deformation behavior of a joint

ANALYTIC METHODS AND NUMERIC METHODS

The analytic resolution of transmitted and reflected coefficients

Exact resolutions of reflected and transmitted coefficients are obtained when the normal incident P-wave propagates to single joint with linear deformation behavior at arbitrary angles, as Eq. (5), (6).

$$|R_{lin}| = \sqrt{1 / \left[4 \left(\frac{k}{z\omega} \right)^2 + 1 \right]} \quad (5)$$

$$|T_{lin}| = \sqrt{4 \left(\frac{k}{z\omega} \right)^2 / \left[4 \left(\frac{k}{z\omega} \right)^2 + 1 \right]} \quad (6)$$

where $|R_{lin}|$ is reflected coefficients, $|T_{lin}|$ is transmitted coefficient, z is the wave impedance, k is the joint stiffness, ω is the angular frequency.

To obtain the analytic resolution of transmitted and reflected coefficients of elastic waves across single joints with nonlinear deformation behaviors with the *BB* hyperbolic model, Wang (2006) borrows the hypothesis of equivalent strain Lemaître in damage mechanics, by using equivalent stiffness, the nonlinear joint stiffness is represented by the form of linear deformation behaviors. According to such method, the analytic resolution with the typical exponential model can be gained easily.

$$|R_{exp}| = 1 / \sqrt{1 + 4 \left[\frac{k_{ni}}{z\omega(1 - d_n / d_{ma})} \right]^2} \quad (7)$$

$$|T_{exp}| = 2 / \sqrt{4 + \left[\frac{z\omega(1 - d_n / d_{ma})}{k_{ni}} \right]^2} \quad (8)$$

where R_{exp} is reflected coefficient, T_{exp} is transmitted coefficient, z , ω and k_{ni} are the same as defined for Eq. (5) and Eq. (6).

Numeric resolution of reflected and transmitted coefficient

The numeric resolution of reflected and transmitted coefficients has been obtained when elastic P-wave propagates to joints with normal deformation behaviors of BB hyperbolic curve. Now to solve the transmitted and reflected coefficients of the elastic wave with the typical exponential model according to the idea offered in (Zhao, 2001).

Now suppose that there is a joint at $x=x_1$ in a half-space of a linear elastic, such space is subject to a normally incident planar P-wave, which is expressed as waveform histories of particle velocity $p(t)$. During the wave transmission across the joint, the displacement discontinuity boundary conditions of the joint at $x=x_1$ are defined by the BB model of joint normal behavior,

$$\sigma^-(x_1, t) = \sigma^+(x_1, t) \quad (9)$$

$$u^-(x_1, t) - u^+(x_1, t) = d_{ma} \left\{ 1 - \exp \left[-\frac{\sigma(x_1, t)}{k_{ni}d_{ma}} \right] \right\} \quad (10)$$

The derivative expression of Eq. (10) with respect to time domain is

$$v^-(x_1, t) - v^+(x_1, t) = \frac{\partial \sigma(x_1, t)}{\partial t} \frac{\exp \left[-\frac{\sigma(x_1, t)}{k_{ni}d_{ma}} \right]}{k_{ni}d_{ma}} \quad (11)$$

where σ_x is seismic stress normal to joint, u is seismic displacement normal to joint; v is the particle velocity; superscripts “-”, “+” refer to the wave fields before and after the joint, and d_{ma} and k_{ni} are the same as defined for Eq. (1).

The left and right running characteristic line equation can be easily derived using the method of eigenfunction, and in combination with Eq. (11), the differential equation with respect to $v^+(x_1, t)$ can be derived:

$$\frac{\partial v^+(x_1, t)}{\partial t} = \frac{[2p(t - x_1/\alpha) - 2v^+(x_1, t)]k_{ni}d_{ma}}{z \exp \left[-\frac{zv^+(x_1, t)}{k_{ni}d_{ma}} \right]} \quad (12)$$

The time interval $[0, t]$ is divided into j equal time steps, the time increment Δt for each time step can always be selected as $\Delta t = T_e/m$. Where T_e is the period of the incident wave, and

m is the number (integer) of time steps within one period of the incident wave. The difference recurrence equation for calculating $v^+(x_1, t)$ is obtained:

$$\frac{\partial v^+(x_1, t_{j+1})}{\partial t} = \frac{T_e [2p(t_j - x_1/\alpha) - 2v^+(x_1, t_j)] k_{ni} d_{ma}}{mz \exp\left[-\frac{zv^+(x_1, t_j)}{k_{ni} d_{ma}}\right]} + v^+(x_1, t_j) \quad (13)$$

When the wave input, $p(t)$, and the initial particle velocity condition, $v^+(x_1, 0)$, are specified, $v^+(x_1, t)$ can be determined in an iterative calculating process using Eq(13). In the calculation, if m is selected to be large enough, a sufficiently small Δt can be obtained, so the numeric results of $v^+(x_1, t)$ with sufficient accuracy can be gained. Then $v^-(x_1, t)$ can be derived through the method of eigenfunction, so as to obtain the particle velocity of the reflected wave across the joints.

PARAMETRIC STUDIES

Parametric studies are conducted in terms of initial normal stiffness k_{ni} and the ratio of maximum closure to maximum allowable closure of the joints $\gamma = d_n/d_{ma}$, as well as the incident wave amplitude and frequency. To make a comparison with the results made by predecessors, the parametric combinations are all from passage [10, 20]. The concrete parametric combination can be seen in Table 1. The rock density is $2.4 \times 10^3 \text{ kg/m}^3$, the wave frequency is 50Hz and 150Hz respectively, and the P-wave propagation velocity α is 4500m/s. The seismic impedance $z = \text{density} \times \text{wave velocity} = 1.08 \times 10^7 \text{ kg/(m}^2 \cdot \text{s)}$.

Table 1. d_{ma} and k_{ni} (Zhao and Cai, 2001)

Curve	Maximum allowable closure of the joints $d_{am}(\text{mm})$	Normal stiffness of the joint at initial stress $k_{ni}(\text{GPa} \cdot \text{m}^{-1})$
①	0.61	1.25
②	0.57	2.00
③	0.53	3.00
④	0.50	3.80
⑤	0.40	5.50

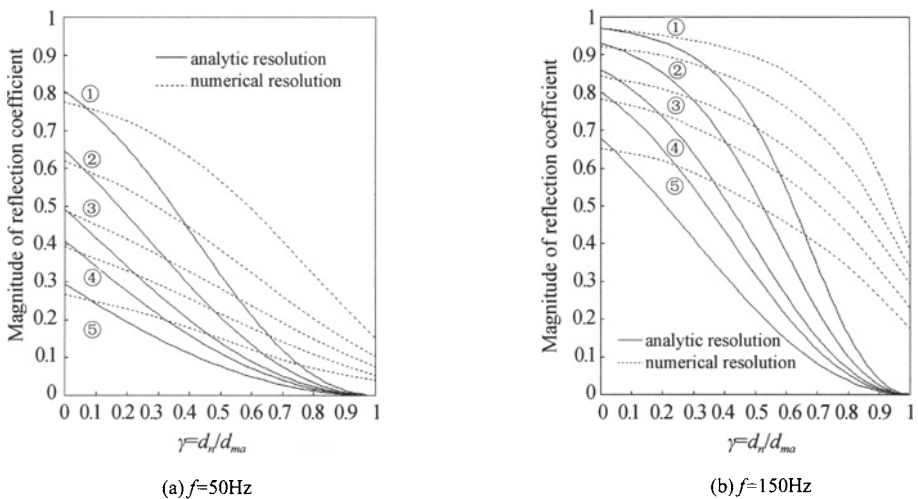
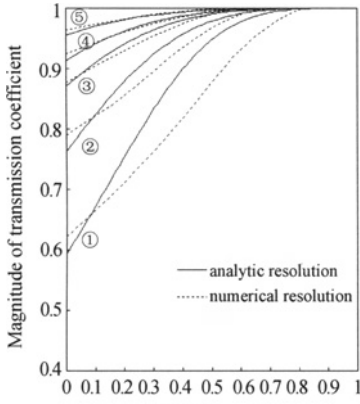
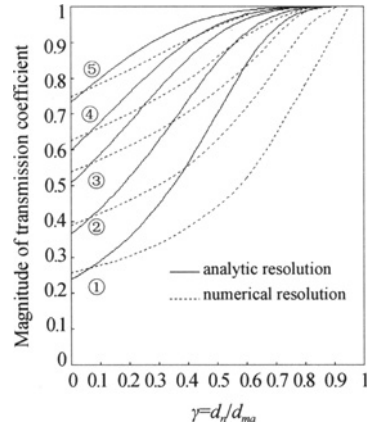


Figure 2. Numerical solutions and analytic solutions of reflection coefficients (hyperbolic model)

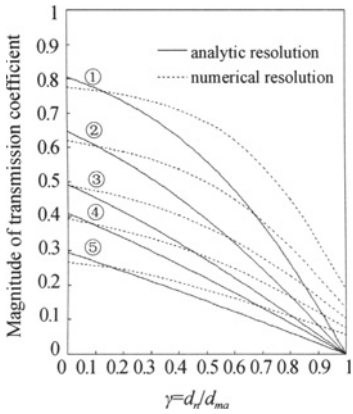


(a) $f=50\text{Hz}$

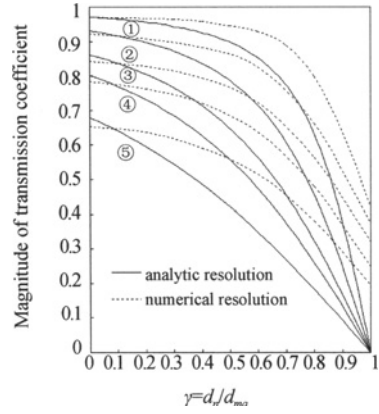


(b) $f=150\text{Hz}$

Figure 3. Numerical solutions and analytic solutions of transmission coefficients (hyperbolic model)

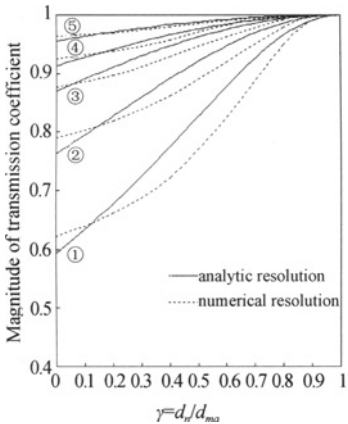


(a) $f=50\text{Hz}$

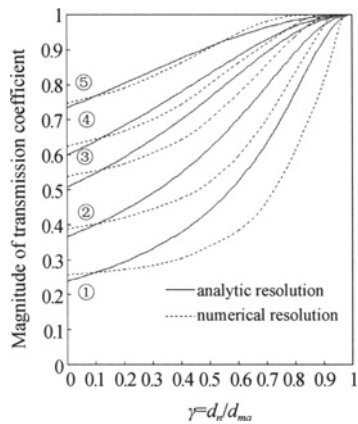


(b) $f=150\text{Hz}$

Figure 4. Numerical solutions and analytic solutions of reflection coefficients (exponential model)



(a) $f=50\text{Hz}$



(b) $f=150\text{Hz}$

Figure 5. Numerical solutions and analytic solutions of transmission coefficients (exponential model)

The differential numerical solutions and analytic solutions of reflected and transmitted coefficients are obtained respectively when elastic wave propagates joints with *BB* hyperbolic model respectively in (Wang, 2006), as shown in Figure 2 and Figure 3. We can conclude from Figure 2(a) that when $\gamma=0$, the analytic solution of reflected coefficient is slightly larger than the numerical solution, both of the analytic and numerical solution decrease with the increased value of y , when $\gamma=1$, the analytic solution is 0, however the numeric solutions are not to 0. In contrast with the parameters, the transmitted coefficient decreases with the increased value of initial joint stiffness, which implies that an initially stiffer joint produces more wave transmission across the joint; the transmission coefficient decreases with d_{ma} , indicating that the joint with smaller aperture generates more wave transmission across the joint, Figure 2(b) shows the calculating value of the elastic wave(150Hz), from which we can draw that the incident wave frequency is increased, and reflected coefficient is also increased correspondingly, proving that the hindrance of joints on high-frequency waves.

On the whole, there's a degree of error between the analytic solution and numeric solution, which is different from the cognition in (Wang, 2006), as the analytic solution is gained on the basis of hypothesis idea of equivalent strain, it has essential differences from numeric method in theory, so that there are sensible differences in calculating results between analytic and numeric solutions, Figure 3(a) and (b) shows the curve of transmitted coefficient, from which we can easily conclude that the curves have the opposite change trend from those in Figure 2.

The differential numeric and analytic solutions of reflected and transmitted coefficients are shown in Figure 4 and Figure 5 when elastic waves propagate joints with typical exponential model. We can draw that the change trend of the two figures is consistent with that with the *BB* model conditions, as in the case that y is the same, the joint stiffness of typical exponential model is lower than that of *BB* model, so for the *BB* model., the reflected coefficient is large, while the transmitted coefficient is small with the exponential model conditions.

CONCLUSIONS

In this paper the analytic and numeric resolution of reflected and transmitted coefficients are obtained in relation to *BB* hyperbolic model and typical exponential model, when the elastic wave propagates to single joints with exponential model deformation behaviors, considering the joints with different nonlinear normal deformation behaviors Based on the analytic results of predecessors, parametric studies and comparisons are conducted on initial normal stiffness and the ratio of current maximum closure to maximum allowable closure of the joints, as well as the effects of incident wave amplitude and frequency on reflected and transmitted coefficients. The results show that different deformation behaviors have different degrees of influences on elastic wave transmission, to *BB* model, the reflected coefficient is large, while the transmitted coefficient is small in the condition of exponential model. However, the change trend of reflected and transmitted coefficients of elastic wave tend to be the same in the conditions of the two models.

REFERENCES

- Hudson J.A. (1981). Wave speeds and attenuation of elastic waves in material containing cracks. *Geophysical Journal of the Royal Astronomical Society*, 64(1): 133-150.
- Angle Y.C., Achenbach J.D. (1985). Reflection and transmission of elastic waves by a periodic array of cracks. *Journal of Applied Mechanics*, 52(1): 33-46.
- Achenbach J.D., Norris A.N. (1982). Loss of specular reflection due to nonlinear crack-face interaction. *Journal of Nondestructive Evaluation*, 3(4): 229-239.
- Smyshlyaev V.P., Willis J.R. (1994). linear and nonlinear scattering of elastic waves by microcracks. *Journal of Mechanics and Physics of Solids*, 42(4): 585-610.
- Schoenberg M. (1980). Elastic wave behavior across linear slip interfaces. *Journal of Acoustic Society of America*, 68(5): 1516-1521.
- Kitsunezaki C. (1983). Behavior of plane elastic waves across a plane crack. *Journal of Mining College of Akita University*, 6(3): 173-187.
- Yi W., Nihei K.T., Rector J.W., et al. (1997). Frequency-dependence seismic anisotropy in jointed rock. *International Journal of Rock Mechanics and Mining Science*, 34(3/4): 349-360.
- Zhao J., Cai J.G. (2001). Transmission of elastic P-wave across single joints with a nonlinear normal deformational behavior. *Rock Mechanics and Rock Engineering*, 34(1): 3-22.
- Goodman R.E. (1974). The mechanical properties of joints. *Proceedings of 3rd International Congress of Rock Mechanics*, Denver, 127-140.
- Goodman R.E. (1976). *Methods of geological engineering in discontinuous rocks*. New York, West, 472-490.
- Bandis S.C., Lumsden A.C. and Barton N.R. (1983). Fundamentals of rock joint deformation. *International Journal of Rock Mechanics and Mining Sciences and Geomechanics Abstracts*, 20(6): 249-268.
- Barton N.R., Bandis S.C. and Bakhtar K. (1985). Strength, deformation and conductivity coupling of rock joints. *International Journal of Rock Mechanics and Mining Sciences and Geomechanics Abstracts*, 22(3): 121-140.
- Shehata W.M. (1971). *Geohydrology of mount vernon canyon area*. Golden: Colorado school of mines, Ph.D.Thesis.
- Malama B., Kulatilake P.H.S.W. (2003). Models for normal joint deformation under compressive loading. *International Journal of Rock Mechanics and Mining Sciences*, 40(6): 893-901.
- Wang W.H., Li X.B. and Zuo Y.J. (2006). Effects of single joint with nonlinear normal deformation on P-wave propagation. *Chinese Journal of Rock Mechanics and Engineering*, 25(6): 1218-1225.(in Chinese)

GEOTECHNICAL AND SEISMIC HAZARD STUDY FOR A MARINE SITE DEVELOPMENT IN SOUTHERN CALIFORNIA

Endi Zhai, *PhD, PE, GE*

Kleinfelder West, Inc., 8 Pasteur, Suite 190 Irvine, CA 92614, USA

Liping Yan, *PhD, PE, GE*

*Earth Mechanics, Inc., 17660 Newhope Street, Suite E
Fountain Valley, CA 92708, USA*

This paper presents results of a geotechnical and seismic hazard study for a marine site development consisting of four main structures, which are up to 12-story high over a two- to three-level parking structure in Marina Del Ray, California, U.S.A. The site encompasses approximately 6.5-acre area bounded by two channels and is underlain by typical marine soils including soft clay and liquefiable sand. Extensive field exploration and laboratory testing were performed to investigate site-specific geotechnical conditions. After developing site-specific design ground motion parameters, liquefaction potential, liquefaction-induced settlements and lateral spreading were evaluated. Several site retrofit measures to mitigate liquefaction-induced ground deformations were discussed and recommendations were made.

INTRODUCTION

A marine site development consists of approximately four main structures that are up to 12-story high over a two- to three-level parking structure. The site will encompass approximately 6.5-acre area bounded by two channels in Marina Del Ray, California, U.S.A.. The site location map is shown in Figure 1. Extensive field exploration and laboratory testing were performed to investigate site-specific geotechnical conditions. The subsurface soils encountered during our field exploration consisted of fill underlain by native costal alluvial soils. Design groundwater level was 5 feet below grade. Based on the 2001 California Building Code (CBC), the site was classified as Type F, requiring a site-specific seismic hazard evaluation.

There are several active faults within 15 km to the site including the Santa Monica fault, Newport-Inglewood (L.A. Basin) fault, Palos Verdes fault, Malibu Coast fault and Hollywood fault. We performed a site-specific probabilistic seismic hazard analysis (PSHA) to determine the seismic parameters for the Design Basis Earthquake (DBE), which is an event having 10% probability of exceedance in 50 years as required in the 2001 CBC. This resulted in a peak ground acceleration (PGA) of about 0.5g associated with a moment magnitude of 6.7. After ground motion parameters were determined, we evaluated liquefaction potential, liquefaction-induced settlements and the nearby main marina and Ballona Creek channel slope lateral spreading using the standard procedures commonly used

by qualified geotechnical engineers in California. More rigorous numerical modeling approaches and nonlinear site response analyses using the finite difference computer program FLAC were also performed for this site and were presented elsewhere (Zhai, 2008).

It was concluded that the primary hazards for site development are seismic deformations of the main marina and Ballona Creek channel slopes; seismically-induced settlement of loose and medium dense sand, silty sand, and sandy silt layers; and compressible clay soils. Due to the magnitude of the estimated lateral seismic displacement of about 6 to 9 inches of the main marina and Ballona Creek channel slopes and the potential for flow slides, we recommend that the channel slopes be reinforced with a ground improvement program. Several options including deep soil mixed buttress, and/or vibro-replacement were discussed.

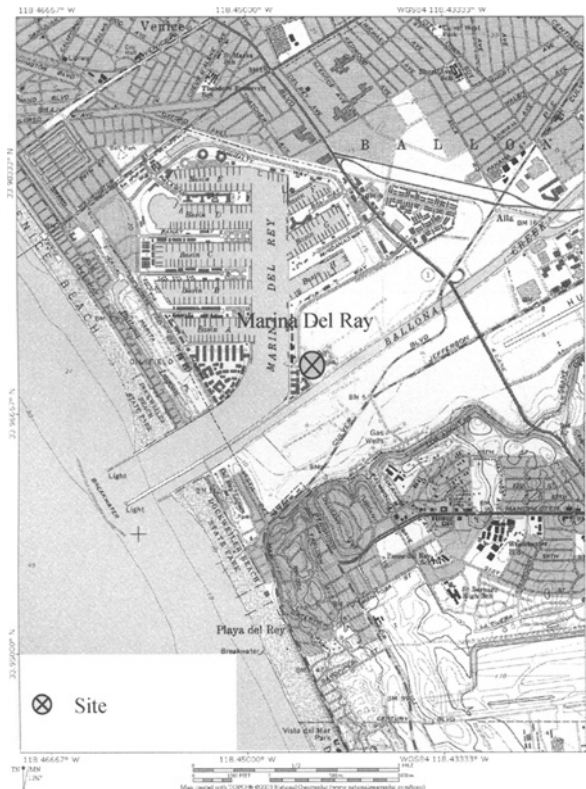


Figure 1. Site location map

GEOTECHNICAL INVESTIGATIONS FOR THE SITE

A field exploration program consisting of 7 borings and 8 Cone Penetration Test (CPT) soundings was performed to evaluate site-specific geotechnical and geological conditions. The borings were drilled to depths of approximately 81 to 101 feet below the existing ground surface. The CPTs were advanced to depths of approximately 70 to 100 feet. Shear wave velocities were also obtained from one of the CPTs. Laboratory tests were conducted to determine relevant physical characteristics and engineering properties of soils that exist at the site. In addition to our field exploration program and laboratory testing, we also reviewed the

existing logs of 13 borings, 6 CPTs and 2 piezometers for the site. A site visit was performed including observation of the main marina and Bollona Creek channels which bound the site to the west and to the southeast, respectively. Detailed channel slope configurations were investigated by reviewing costal drawings from the United States Army Corps of Engineers.

As presented in a typical cross section in Figure 2, the soil stratigraphy defined by the subsurface explorations consists of primarily 10 to 15 feet of fill underlain by 15 to 25 feet of very soft to medium stiff clay. Below the clay layer is about 20 to 30 feet of loose to medium dense silty sand to sand susceptible to liquefaction subjected to the DBE. Dense to very dense sand to gravelly sand layer is present below the liquefiable sand layer. Groundwater was encountered in the borings advanced during our subsurface explorations at depths ranging from between 8 and 22 feet below ground surface. The water level readings in the borings were taken after completion of drilling and after bailing the drilling mud from the boreholes. Groundwater information was also available from the previous existing geotechnical data. The historical high groundwater table is about 5 feet deep and recommended for the design of the site.

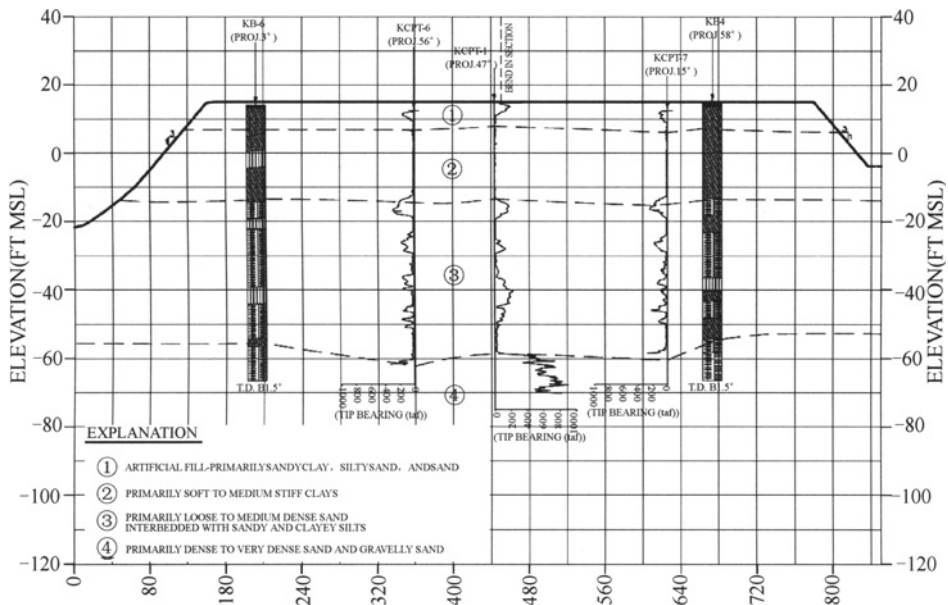


Figure 2. Geotechnical cross-section

GEOLOGIC AND SEISMIC HAZARDS

The State of California has developed state-wide hazard maps for fault ruptures, landslides and liquefaction potential. The site is not located within a State of California- or Los Angeles County-designated Earthquake Fault Rupture Hazard Zone for active faulting. However, the site is located within a State-designated seismic hazard zone for liquefaction. The site is not located within a State-designated hazard zone for Earthquake-Induced Landsliding. However, the main marina and Ballona Creek channels are judged to be subject to seismic deformation. Due to the site's coastal location, tsunami or seiches may represent potential hazards to the

proposed development, but tsunami or seiches hazards will not be addressed in this paper due to space limitation. The most significant geologic hazard to the project site is the potential for moderate to strong ground shaking resulting from earthquakes generated on the faults within the vicinity of the site. In the vicinity of the site, approximately 46 known active faults have been mapped with a 100-km radius of the site. We performed a site-specific seismic hazard analysis to develop Uniform Hazard Spectrum (UHS) for a firm-ground condition. Detailed equivalent-linear and nonlinear effective-stress site response analyses were performed to evaluate effect of liquefaction on wave propagation from the firm-ground to ground surface. The site response analyses were provided in a separated paper (Zhai, 2008).

The PSHA approach is based on the earthquake characteristics and its causative fault. These characteristics include such items as magnitude of the earthquake, distance from the site to the causative fault, and the length and activity of the fault. The effects of site soil conditions and mechanism of faulting are accounted for in the attenuation relationship used for the site. Our seismic source model is based on the seismic source model used in developing probabilistic seismic hazard maps by United States Geological Survey (USGS) and California Geological Survey (CGS) for the State of California. We used the commercial computer program EZ-FRISK V7.2 to perform the PSHA. The attenuation relationships selected in our analysis were the same as used by CGS for the 2002 Southern California Hazard Map. The results were obtained by taking an average of the hazard results from these attenuation relationships. The peak ground horizontal acceleration was computed to be 0.5g. The results of our deaggregation analysis to estimate the controlling earthquake magnitude and distance associated with the DBE event are M_w 6.7 and 8.5 km, respectively.

LIQUEFACTION POTENTIAL AND SEISMIC SETTLEMENT

To assess the potential for liquefaction of the subsurface soils at the site, we used the simplified liquefaction analysis procedure (Youd et al., 2001). For estimating the resulting ground settlement, we used the method proposed by Tokimatsu and Seed (1987). Both these methods utilize the standard penetration test (SPT) blow counts data to characterize the liquefaction resistance of sandy soils to evaluate the triggering of liquefaction and estimate the amount of volumetric compaction or settlement during an earthquake. We evaluate the liquefaction potential at the site using equivalent SPT blow counts from the CPT data (see Figure 2). CPT data were used primarily because they provide a continuous measurement of equivalent blow counts and accurate stratigraphy of the site. In addition, good correlations between measured SPT blow counts and CPT-derived blow counts have been established for the site from a number of soil borings performed adjacent to CPT sounding locations. Based on our analyses, it was estimated that seismically-induced settlement of saturated sandy soils due to strong ground shaking during a design level seismic event could be on the order of 2 to 4 inches. Because of variations in distribution, density, and confining conditions of the soils, seismic settlement is generally non-uniform and can cause serious structural damage due to differential settlement. Using the different borings and CPT data at the site, it was estimated that the differential settlement over 2 column locations could be 1 to 2 inches.

GROUND DEFORMATIONS OF CHANNEL SLOPES

For screening or estimating seismic slope performance, it has been either to use a pseudo-static representation of seismic loading in a conventional limit-equilibrium analysis, or to perform a displacement analysis based on the analogy of a rigid block on an inclined plane (i.e., Newmark-type displacement analysis). Nonlinear effective-stress numerical modeling using FLAC was also performed (not included in this paper) and resulted in generally similar conclusions.

Our deformation analyses consisted of first evaluating the yield acceleration for each channel slope and then evaluating the seismic displacement using the simplified procedures from Bray and Rathje and Makdisi and Seed and a Newmark-type time history analysis as documented in the Special Publication No. 117 (Blake et al., 2002). The shear strengths were conservatively estimated from the laboratory test results, SPT blow counts, and CPT data. Post-liquefaction residual shear strengths were used for potentially liquefiable layers identified in the liquefaction analysis described in the previous section. The yield acceleration was determined by applying various values of horizontal pseudostatic acceleration until the factor of safety against sliding reaches unity. A yield acceleration of 0.15 was calculated for both channel slopes. The calculated seismic deformations using the Bray and Rathje method, Makdisi and Seed method and the mean value of the Newmark time history integration method are 9 inches, 5.5 inches and 5 inches. The Newmark time history analysis method utilized 5 acceleration time history records selected from the PEER/COSMOS database which were recorded under compatible geologic and seismic conditions and further scaled to the peak ground acceleration developed for this site. The results are presented in Figure 3.

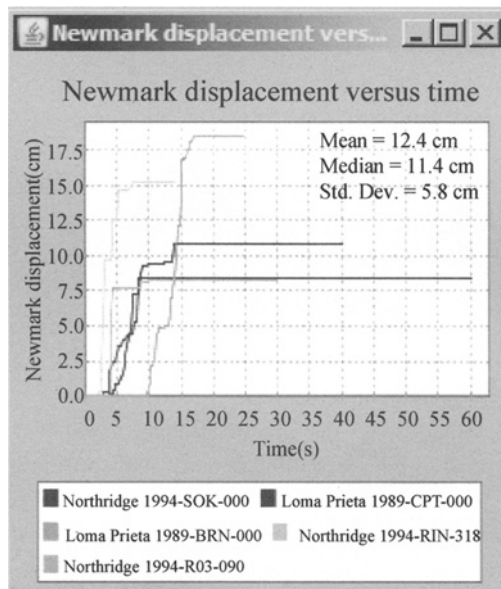


Figure 3. Newmark displacements

DISCUSSIONS AND RECOMMENDATIONS

Due to the magnitude of the estimated lateral seismic deformations of the main marina and Ballona Creek channel slopes and the potential for flow slides, we recommend that site mitigation be performed to reinforce the channel slopes. Reinforcement may consist of a continuous deep soil mixed buttress, approximately 10 to 15 feet wide and 60 to 65 feet deep, or a narrower continuous deep soil mixed buttress reinforced with steel members such as I-beams to improve its rigidity. A preliminary analysis (not included in this paper due to space limitation) indicates that the above retrofit measures could mitigate the potential for lateral spreading. Regarding mitigation of liquefaction-induced settlement and compressible clay soils for building foundations, there are 3 foundation options including 1) driven piles with large diameter and relatively deep penetration; 2) ground improvement, such as deep soil mixing or a combination of deep soil mixing and stone columns (vibro-replacement), so that the structure may be supported on structural mat or spreading footings; and 3) a combination of deep foundations with shorter and smaller piles and ground improvement with stone columns. The decision to select which foundation and mitigation option would likely be dictated at least partially by economics, and should be made by the owner in consultation with the design team.

ACKNOWLEDGMENTS

Mr. Brian Crystal and other Kleinfelder staff are highly appreciated for their assistance in the field and laboratory investigations.

REFERENCES

- Blake T.F. (2002). Recommended procedures for implementation of DMG special publication 117 guidelines for analyzing and mitigating landslide hazards in California. *Document published by the Southern California Earthquake Center.*
- Tokimatsu K., Seed H.B. (1987) Evaluation of settlements in sands due to earthquake shaking. *Journal of Geotechnical Engineering*, 113(8): 861-878.
- Youd T. L., et al., (2001). Liquefaction resistance of soils: summary report from the 1996 NCEER and 1998 NCEER/NSF workshops on evaluation of liquefaction resistance of soils. *Journal of Geotechnical and Geoenvironmental Engineering*, 127(10): 297-313.
- Zhai E. (2008). Developing site-specific design response spectra for a Type-F site due to liquefaction. *Proc. 4th decennial Geotechnical Earthquake Engineering and Soil Dynamics Conference*, Sacramento, California, May 18-22.

NUMERICAL ANALYSES OF DYNAMIC RESPONSE OF SATURATED POROUS SEABED-PIPELINE INTERACTION UNDER SEISMIC LOADING

Xiaoling Zhang, Maotian Luan

*Institute of Geotechnical Engineering, School of Civil and Hydraulic
Engineering, Dalian University of Technology, Dalian 116023, China*

Based on the Biot's theory of consolidation, the model of the seabed-pipeline interaction is established using viscous-elastic artificial boundary in this paper. The distribution of the pore pressure in seabed soil and the dynamic response of submarine pipeline are studied under El Centro seismic wave by virtue of the general-purpose FEM analysis package ADINA. The effects of the elastic anisotropic soil and two-layered seabed behaviors on the seismic-induced pore pressure and internal stresses are discussed emphatically. It actually shows the validity and practicality of dynamic response of submarine pipeline under seismic loading.

INTRODUCTION

Recently, people intensify the exploitation of submarine petroleum and natural gas because the need of energy sources increases, it makes submarine pipeline applied widely (Sun et al., 2006). Submarine pipelines in the shallow seabed carry not only wave loading but also seismic loading. China is a country with many earthquakes, so we must consider the influence of earthquakes during laying the submarine pipelines. At present, some experimental and theoretical research has been done about dynamic response of submarine pipelines under wave loading. J H DeFree hydraulic laboratory did model tests on submarine pipelines (Turcotte et al., 1984). Wang (Wang et al., 2000) compared the numerical analysis results with the experimental results, discussed the effects of elastic anisotropic soil and geometry of cover layer on wave -induced pore pressure. Qu peng (Qu et al., 2006) took the interaction between seabed and pipeline and the inertia effects of both seafloor soil and pipeline into account through studying dynamic response of seabed-pipeline interaction under wave loading. Zou de-gao (Zou et al., 2004) et al simulated the shaking table model test on pipelines buried in saturated sand foundation, showed that the effective stress FEM can be effectively used to simulate the process of build-up and dissipation of pore pressure in foundation around the pipelines.

But in most of the previous investigations, the equivalent disposal of seabed boundary and the interaction between seabed and pipeline under seismic loading have not been taken into consideration. Aimed at this, the model of the seabed-pipeline interaction is established based on the Biot's theory of consolidation using viscous-elastic artificial boundary in this paper. The distribution of the pore pressure in seabed soil and the dynamic response of

submarine pipeline are studied under El Centro seismic wave by virtue of the general-purpose FEM analysis package ADINA. The effects of the elastic anisotropic soil and two-layered seabed behaviors on the seismic-induced pore pressure and internal stresses are discussed emphatically.

DYNAMIC ANALYSIS METHOD

Dynamic analysis equations

According to Biot's dynamic consolidation theory, if porous liquid is compressible, the law of conservation of mass of saturated liquid is that

$$\frac{n}{K_w} \frac{\partial p}{\partial t} + \frac{\partial \varepsilon_{ii}}{\partial t} + \frac{1}{\gamma_w} \nabla^\top \cdot (-K \cdot (\nabla p)) = 0 \quad (1)$$

where K is the permeability matrix of the soil, ε_{ii} is the bulk strain of soil skeleton, n is soil porosity, K_w the bulk modulus of porous liquid, p is pore pressure, γ_w is the weight of pore water.

Neglecting the effects of relative acceleration and between pore fluid and solid and the compressibility of soil grains, the equations governing the overall equilibrium of porous medium can be expressed as

$$\sigma'_{ij,j} + p_{,j} \delta_{ij} + \rho b_i = \rho \ddot{u}_i \quad (i, j = 1, 2, 3) \quad (2)$$

where σ'_{ij} is effective stress, δ_{ij} is Kronecker sign, ρ and b_i is the density of soil and the acceleration of bulk force respectively, \ddot{u}_i is the acceleration of soil skeleton.

Based on elastic theory, the governing equation for buried pipeline is given by

$$\sigma_{pij,j} + \rho_p b_{pi} = \rho_p \ddot{u}_{pi} \quad (i, j = 1, 2, 3) \quad (3)$$

where σ_{pij} represents the inner stress of pipeline, ρ_p is the density of the pipeline, b_{pi} is the bulk force acceleration of the pipeline, \ddot{u}_{pi} is the acceleration of the pipeline.

THE MODEL AND SIMULATION METHOD

The modeling

Considering a soil column in a porous seabed of finite thickness (h), a fully buried pipeline (with a radius R) is located in the saturated seabed surrounding by two impermeable walls (see Figure 1). The z -direction is measured positive upward from impermeable rigid bottom, while y -direction is the vertical direction to the axes of pipeline.

The elastic modulus of pipeline, poisson ratio and density respectively is $E_p = 30\text{GPa}$, $\nu_p = 0.2$ and $\rho_p = 2.4\text{t/m}^3$; the thickness of porous seabed is $h = 40\text{m}$, the length is $l = 205\text{m}$; The seabed is sandy and its elastic modulus, poisson ratio and density respectively is $E = 70\text{MPa}$, $\nu = 0.25$, $\rho = 1.9\text{t/m}^3$; The soil porosity is $n = 0.4$, the permeability of the soil is $k = 10^{-4}\text{m/s}$. Because the concentration of stresses is to be expected, the local refinement of the finite-element mesh always has to be taken into account in the region near a structure. To improve the accuracy of the solution in this region, a

four-node iso-parametric element is used in the region near the pipeline. Outside this region, a four-nodal rectangular element is used.

Boundary conditions

Displacement boundary conditions

It is impossible to include infinite ground in dynamic model, so we can cut off it and substitute the part for the whole. But essentially, an artificial boundary technique is applied to the model to insure the transmission of scattered waves. In this study, viscous-elastic boundaries based on viscous boundaries (Liu and Lv, 1998) is adopted, these boundaries (Lysmer and Kuhlemeyer, 1969) have advantage over viscous boundaries.

Viscous-elastic boundaries belong to local artificial boundary conditions in time field; the springs and dampers are set at the node along the boundaries to simulate the radiant damping. As seen in Figure 1 and Figure 2, the coefficients of the spring and damper is that $K = \frac{G}{2r}$, $C = \rho c_s$, Where C represents the damping coefficients of damper, K is the elastic coefficients of spring, ρ is the density of seabed, c_s is the velocity of seismic wave, G is the shear modulus of the seabed.

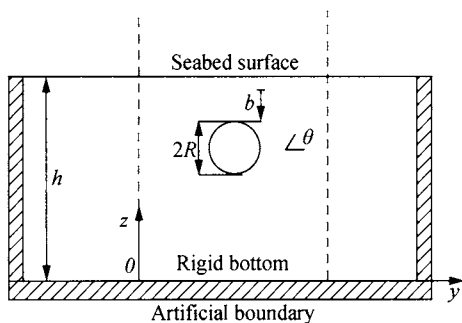


Figure 1. The seabed-pipeline system

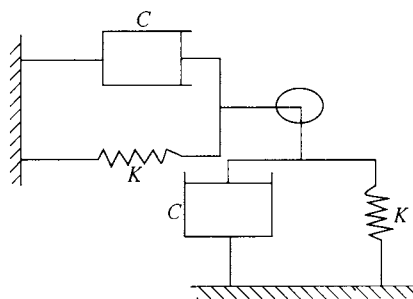


Figure 2. Schematic view of artificial boundaries

Pore pressure boundary conditions

We assume that the seabed is permeable and the pore pressure at the surface is zero firstly; secondly, the surface along the pipeline is impermeable and the pore pressure grad is zero. Because the time of seismic loading is very short, it can be assumed that the seabed bottom and lateral is impermeable.

RESULTS AND DISCUSSIONS

The comparisons of isotropic and anisotropic soil behaviors

In general, an isotropic material can be described by two elastic constants: Young's modulus E and Poisson's ratio μ . However, most marine sediments display some degree of anisotropy, possessing different properties in different directions. The elastic behavior of a cross-anisotropic material is described by five independent elastic parameters. They are: E_z ,

$E_x, \mu_{xx}, \mu_{zx}, G_z$. In this paper, we assume that the seabed soil is isotropy and anisotropy respectively and compare the results of them. The isotropic soil parameters are in 3.1, The isotropic ones can be computed from above formulas, where $\mu_{xx} = 0.45, \mu_{zx} = 0.45, n=0.8, m=0.6$, the others have no change.

Figure 3 shows the distribution of the seismic-induced pore pressure p and radial normal stress σ_{pr} as well as shear stress $\tau_{pr\theta}$ along the pipeline circumferential outer surface and circumferential normal stress $\sigma_{p\theta}$ along the pipeline circumferential inner surface with isotropic and anisotropic soil behaviors. The horizontal axis represents the node coordinate along pipeline at the beginning of the middle of the right end, the solid lines show the results of isotropic soil and the dotted lines show the anisotropic ones. As seen in Figure 3, the two results have some difference in value, particularly the pore pressure along the pipeline outer surface. At the same time, the effects of anisotropic soil behaviors on pore pressure at the bottom ($180^\circ \leq \theta \leq 360^\circ$) is greater than the top ($0^\circ \leq \theta \leq 180^\circ$). This is similar to Wang's conclusion (Wang et al., 2000). Besides, the effects of anisotropic soil behaviors on radial normal stress σ_{pr} along the pipeline circumferential outer surface and circumferential normal stress $\sigma_{p\theta}$ along the pipeline circumferential inner surface are great at the bottom, the top, the end of left and right, but reversibly on shear stress $\tau_{pr\theta}$ along the pipeline circumferential outer surface.

The comparisons of homogeneous and two-layered seabed behaviors

In ocean ground, the soil is formed with all kinds of sediments which have different behaviors each other. To simulate this, the sandy seabed is divided into two layers at the boundary of pipeline in the paper. The dynamic response of two-layered seabed under seismic loading is studied and it is compared with that of homogeneous seabed. Table 1 shows the two-layered seabed parameters, the homogeneous seabed behaviors are the same with the under soil behaviors of two-layered seabed.

Table 1. Material parameters of two-layered seabed

	Thickness (m)	Elastic modulus (MPa)	Passion ratio	Density (t/m^3)	permeability (m/s)
upper layer	2.5	50	0.30	1.7	1×10^{-3}
below layer	37.5	70	0.25	1.9	1×10^{-4}

Figure 4 shows the distribution of the seismic-induced pore pressure p and radial normal stress σ_{pr} as well as shear stress $\tau_{pr\theta}$ along the pipeline circumferential outer surface and circumferential normal stress $\sigma_{p\theta}$ along the pipeline circumferential inner surface with homogeneous and two-layered seabed behaviors. The horizontal axis is the same with the one in Figure 3; the solid lines show the results of homogeneous seabed and the dotted lines show two-layered seabed ones. As seen in Figure 4, the dynamic responses of the two behaviors are different in value, particularly pore pressure along the pipeline outer surface, but they are the same of change tendency. It is related to the parameters of submarine soil. For the inner stresses of pipeline, there are only a little different because the pipeline stiffness is bigger than submarine soil and this match with the facts.

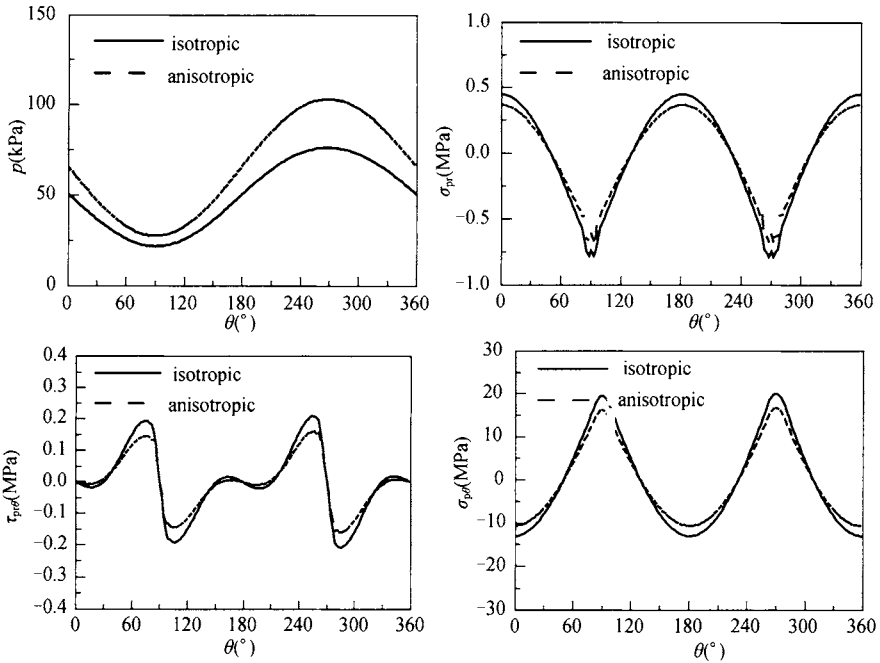


Figure 3. Distribution of the seismic-induced pore pressure p and inner stress σ_{pr} , $\tau_{pr\theta}$, $\sigma_{p\theta}$ of the pipeline with isotropic and anisotropic soil behaviors

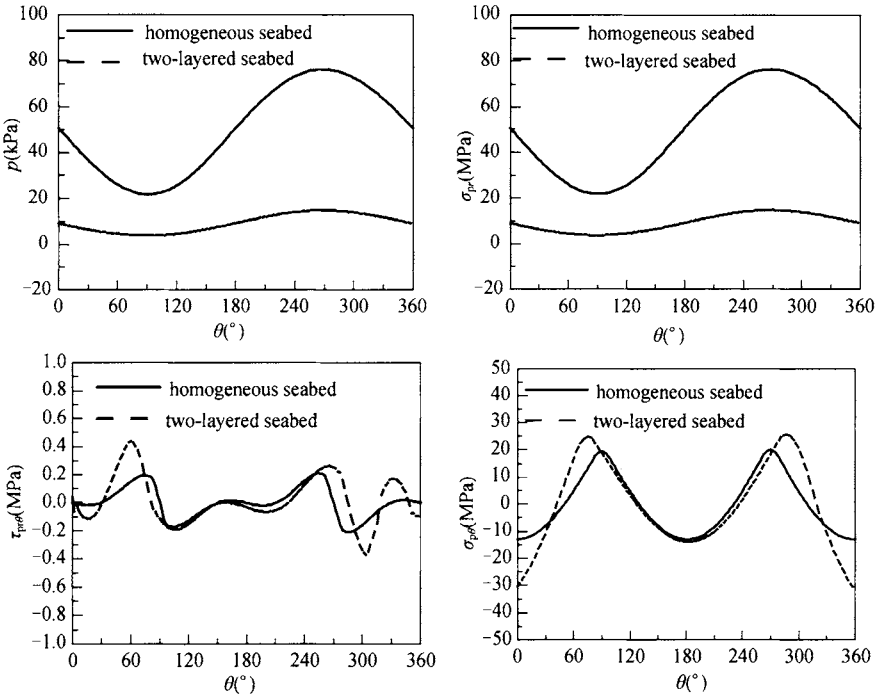


Figure 4. Distribution of the seismic-induced pore pressure p and inner stress σ_{pr} , $\tau_{pr\theta}$, $\sigma_{p\theta}$ of the pipeline with single-layered and two-layered seabed behaviors

CONCLUSIONS

The main contribution of this paper is to establish the model of the seabed-pipeline interaction based on the Biot's theory of consolidation using viscous-elastic artificial boundary, study the distribution of the pore pressure in seabed soil and the dynamic response of submarine pipeline under El Centro seismic wave and discuss the effects of the elastic anisotropic soil and two-layered seabed behaviors on the seismic-induced pore pressure and internal stresses in detail. Through numerical analysis by virtue of the general-purpose FEM analysis package ADINA. It is valid to simulate dynamic response of submarine pipeline under seismic loading.

ACKNOWLEDGEMENTS

The authors wish to express their gratitude to Professor Dahong Qiu of Dalian University of Technology for his continuing support and invaluable advice for the investigation. The financial support for this study through the grants 50439010 and 50639010 from National Natural Science Foundation of China is mostly grateful.

REFERENCES

- Sun Z. C., Duan M. L. and Zhang W. (2006). Method for evaluating ultimate subsea pipeline stress in anti-seismic design. *Chinese Journal Of Applied Mechanics*, 23(3): 440-446.
- Turcotte B. R., Liu P. L. F. and Kulhawy F. H. (1984). Laboratory evaluation of wave tank parameters for wave-sediment interaction. *School of Civil and Environmental Engineering*, Cornell University. New York, Cornell University.
- Wang X., Jeng D. S. and Lin Y. S. (2000). Effects of a cover layer on wave-induced pore pressure around a buried pipe in an anisotropic seabed. *Ocean Engineering*, 27: 823-839.
- Qu P., Luan M. T., Guo Y., et al (2006). FEM analysis of dynamic response of saturated porous seabed-pipeline interaction system under wave loading. *The 7th National Conference on Soil Dynamic*, Beijing, 446-453.
- Zou D. G., Kong X. J., Lou S. L., et al (2004). Numerical simulation of shaking table test on pipelines buried in saturated sand foundation. *Journal of Hydraulic Engineering*, 12: 112-119.
- Liu J. B., Lü Y. D. (1998). A direct method for analysis of dynamic soil-structure interaction. *China Civil Engineering Journal*, 31(3): 55-64.
- Lysmer J., Kuhlemeyer R. L. (1969). Finite dynamic model for infinite media. *Journal of Engineering Mechanics Division (ASCE)*, 95: 859-877.

Landslides and Slopes

DEFORMATION AND STABILITY ANALYSES OF A PILE SUPPORTED T-WALL WITH DEEP MIXED SHEAR PANELS IN PLAQUEMINES PARISH, LOUISIANA

Tiffany E. Adams, George M. Filz

*Department of Civil and Environmental Engineering, Virginia Tech
Blacksburg, VA 24061, USA*

Peter R. Cali, Mark L. Woodward

*U.S. Army Corps of Engineers, P.O. Box 60267
New Orleans, LA 70160, USA*

The U.S. Army Corps of Engineers recently completed reconstruction of flood protection walls adjacent to the Gainard Woods Pump Station. Shear panels were installed on the protected side of the pile-supported T-wall to improve the stability of the system. The walls were created using the deep-mixing method (DMM) by overlapping wet-mixed, triple-axis columns. Numerical analyses were completed to evaluate the performance of the T-wall under design loads and to calculate the factor of safety for the system. Numerical methods were selected for the analyses for their ability to capture the complex soil-structure interaction and to account for potential racking of the DMM columns due to slipping along vertical joints between adjacent triple-axis installations in the shear panels. Numerical analyses were completed for a range of joint strength values to evaluate the sensitivity of the results to this factor. The results show that, for the conditions used to represent this project, the potential for slippage along vertical joints in the DMM shear panels does not reduce the factor of safety of the system.

INTRODUCTION

The U.S. Army Corps of Engineers (the Corps) recently completed reconstruction of flood protection walls adjacent to the Gainard Woods Pump Station along the Mississippi River in Plaquemines Parish, Louisiana. The project included a 27.4 m long section of new T-wall construction, consisting of a reinforced-concrete retaining wall supported on two steel H-piles. The top of the T-wall is at elevation 5.2 m. The flood side pile was installed at a 1H:4V batter to a tip elevation of -21.6 m and the protected side pile was installed at a 1H:3V batter to a tip elevation of -28.3 m. The design includes a sheet-pile cutoff underneath the T-wall to elevation -3.2 m for seepage control. A zone of deep-mixed shear panels was installed on the protected side of the T-wall, between the wall and an existing drainage canal, to improve the stability of the system. The shear panels, which are oriented perpendicular to the T-wall alignment, were constructed using the deep-mixing method (DMM) by overlapping wet-mixed, triple-axis columns. The shear panels are 91m long, 16.8 m deep,

and positioned at a 1.8 m center-to-center spacing in the direction of the levee alignment. The columns are 91cm diameter, and the overlap between adjacent columns is 30.5 cm, which produces a center-to-center spacing of 61 cm and a chord length of 68 cm at the overlap. The DMM shear panels were located 9.1 m ft away from the toe of the T-wall at the ground surface in order to provide a minimum clearance between the bottom of the shear panels and the battered piles of 3.05 m. This geometry leaves a gap between the DMM shear panels and the pile-supported T-wall. The gap created uncertainty about the effectiveness of the shear panels in improving stability of the T-wall.

The depth, length, and spacing of the shear panels, as well as the required spacing of the improved ground, were established by the Corps to achieve a factor of safety of 1.3 using a simplified design procedure that includes limit-equilibrium stability analyses of the cross-section without the T-wall by means of the “Method of Planes” and structural analyses of the T-wall using loads derived from the Method of Planes analysis. The T-wall geometry and the subsurface conditions are described below.

The purpose of this study was to evaluate the deformation of the T-wall under design loads and assess the stability of the design section using numerical methods for the same conditions analyzed by the Corps.

ANALYSIS SECTION AND MATERIAL PROPERTIES

The geometry of the design section was established by the Corps and it includes the configuration of the soil-cement columns. The design Section is shown in Figure 1, in which “Stratum 1” is the floodwater on the left-hand side and the water in the drainage canal on the right side, “Stratum 2” is a low-height embankment near the T-wall and stability berm near the canal, and “Stratum 4” through “Stratum 13” are existing layers of soil at the site. The location of the DMM columns that comprise the shear panels is also shown in Figure 1.

The material property values for the soil strata were provided by the Corps. The strengths and unit weights used in their Method of Planes limit equilibrium analyses are listed in Table 1. Linear interpolation was used to model the horizontal variation in strengths and unit weights between verts 1 and 2 and between verts 2 and 5. Shear modulus and poisson’s ratio values required for numerical analyses, as well as properties for the T-wall structural elements and the pile coupling springs for connecting the piles to the soil grid, were determined based on previous numerical analyses of T-walls in New Orleans provided by the Corps. The shear modulus/shear strength ratios, G/s_u , listed in Table 1 for the soil strata were based on pressuremeter testing in the New Orleans area. All soil strata were assigned a poisson’s ratio of 0.49.

The strength and unit weight for the DMM zone listed in Table 1 were provided by the Corps. The cohesion value of 48 kN/m² is based on a design unconfined compressive strength of 552 kN/m² for the DMM treated soil, a 40% replacement ratio, and two partial factors of safety of 1.5, which are part of the Corps’ design process for DMM material. The Corps conservatively did not include the strength of the soil between DMM panels in its evaluation of the strength of the DMM zone because of the much higher strain to failure expected for the untreated soil compared to the DMM material. The resulting calculation of the shear strength of the DMM zone is $((0.4)(552 \text{ kN/m}^2))/((2)(1.5)(1.5)) = 49 \text{ kN/m}^2$.

Statistical analyses of 280 unconfined compressive tests on cores taken from the DMM columns during construction resulted in a mean unconfined compressive strength of 2085 kN/m² with a coefficient of variation of 50%. A G/s_u ratio of 103 and a poisson's ratio of 0.45 was assigned to the DMM zone based on information provided in Filz and Navin (2006).

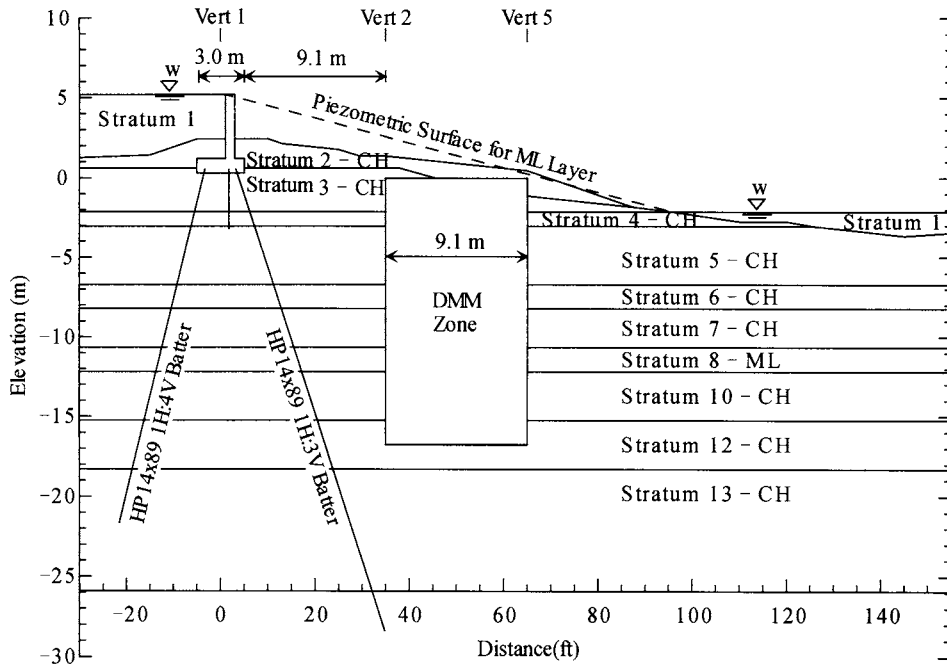


Figure 1. Design cross-section

Table 1. Summary of material property values

Stratum	γ_t (kN/m ³)			c^b (kN/m ²)			ϕ (deg)	G/s_u
	Vert 1	Vert 2	Vert 5	Vert 1	Vert 2	Vert 5		
1	9.8			0			0	0
2	17.3			19			0	130
3	13.5			14	10	7.2	0	100
4	15.4	13.5	15.4	14	10	7.2	0	130
5	15.7	14.5	15.7	14 to 20	10 to 16	7 to 13	0	130
6	18.1	15.7	15.7	20 to 23	16 to 18	13 to 15	0	130
7	18.1	15.7	15.7	23 to 26	18 to 22	15 to 19	0	130
8	18.4			200			15	130
10	18.1	15.7	15.7	29 to 34	25 to 29	22 to 26	0	160
12	16.5			34 to 38	29 to 34	26 to 31	0	160
13	16.5			38+	34+	31+	0	160
DMM	Varies ^a			48 ^c			0	103

^a The unit weight equals that assigned to the corresponding existing soil layers.

^b Cohesion for CL strata increases with depth below El -3.05 m at a rate of 1.57kN/m.

^c Representative DMM cohesion is a weighted average for the column/soil matrix within the DMM zone, see discussion in text.

Four vertical joints were included in the DMM improved zone in order to model potential weak joints between triple-axis installations at the Gainard Woods site. In addition to a reduction in the composite strength due to the reduced width of the wall at the overlap locations, the strength at the column overlap could be further reduced by misalignment during construction. The influence of strength achieved at the column overlap on stability of the system was evaluated by varying the joint strength from that corresponding to the full design mixture strength applied to the full design column overlap (100% efficiency) and that corresponding to no overlap between the columns (0% efficiency). The vertical joint strength corresponding to 100% joint efficiency is 80% of the full DMM zone composite strength of 48 kN/m^2 , based on the ratio of the width of the shear panel at the location of the design column overlap (68 cm) to the average width of the shear panel (84 cm). The joint strength corresponding to 0% efficiency is the representative soil strength of 17.6 kN/m^2 in the DMM treated zone.

NUMERICAL ANALYSIS

Numerical analyses were completed using the finite difference computer code FLAC (ITASCA 2005). Deformation analyses were completed at the design loads for 0% and 100% efficiency of the DMM vertical joints. Slippage along vertical joints was not observed for the 0% joint efficiency analyses at design loads and as such, the results for the 100% and 0% joint efficiency analyses are essentially the same. The deformation analyses under design loads show a lateral displacement of the base of the retaining wall of 4.3 cm towards the right and a slight vertical uplift at the top of the retaining wall equal to 0.1 cm due to rotation effects.

Factors of safety were calculated using a manual strength reduction procedure that was developed based on the automatic factor of safety procedure in the FLAC program. The automated procedure reduces the shear strength of all of the materials in the model by a uniform strength reduction factor (SRF) until the program is not able to satisfy convergence criteria in a limited number of iterations. The factor of safety is the largest SRF at which convergence is still achieved. Because the automatic factor of safety procedure in the FLAC program does not reduce the strength of the pile coupling springs that connect the piles to the two-dimensional soil elements, the manual procedure was developed using the same methodology to allow for this reduction.

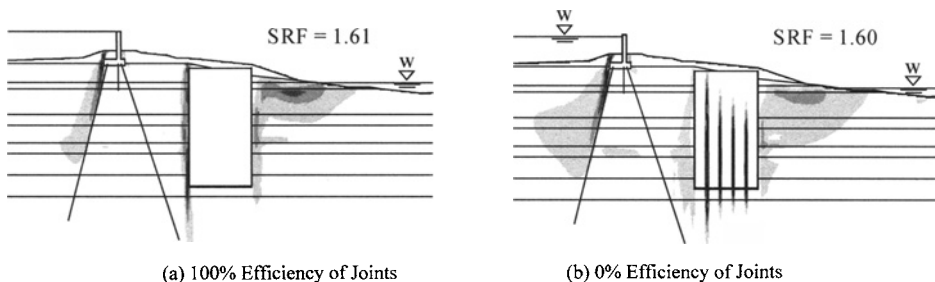


Figure 2. Shear strain contours at failure, 0% and 100% efficiency of Joints

The computed factors of safety and shear strain contours that illustrate the failure modes for the analyses with 100% and 0% efficiency of vertical joints are shown in Figure 2. For the case with 100% efficiency of vertical joints, the DMM zone rotates as a rigid block, as illustrated by the shear strain contours in Figure 2(a). For the case with 0% efficiency of vertical joints, a racking failure occurs within the DMM zone, as shown in Figure 2(b). The reduction in the factor of safety due to the occurrence of racking is minimal. The factor of safety for the system is approximately 1.6.

Pile response for joint efficiencies of 0% and 100% are shown in Figure 3 at design loads with $SRF = 1.0$ and at strength reduction factors corresponding to failure. The axial and normal pile displacements are positive for pile pullout and movement to the right. Pile deformations and loads for 0% joint efficiency are essentially the same as those for 100% joint efficiency at design loads. For conditions corresponding to failure, the deformations and loads in the piles are greater for 0% efficiency of joints than for 100% efficiency of joints.

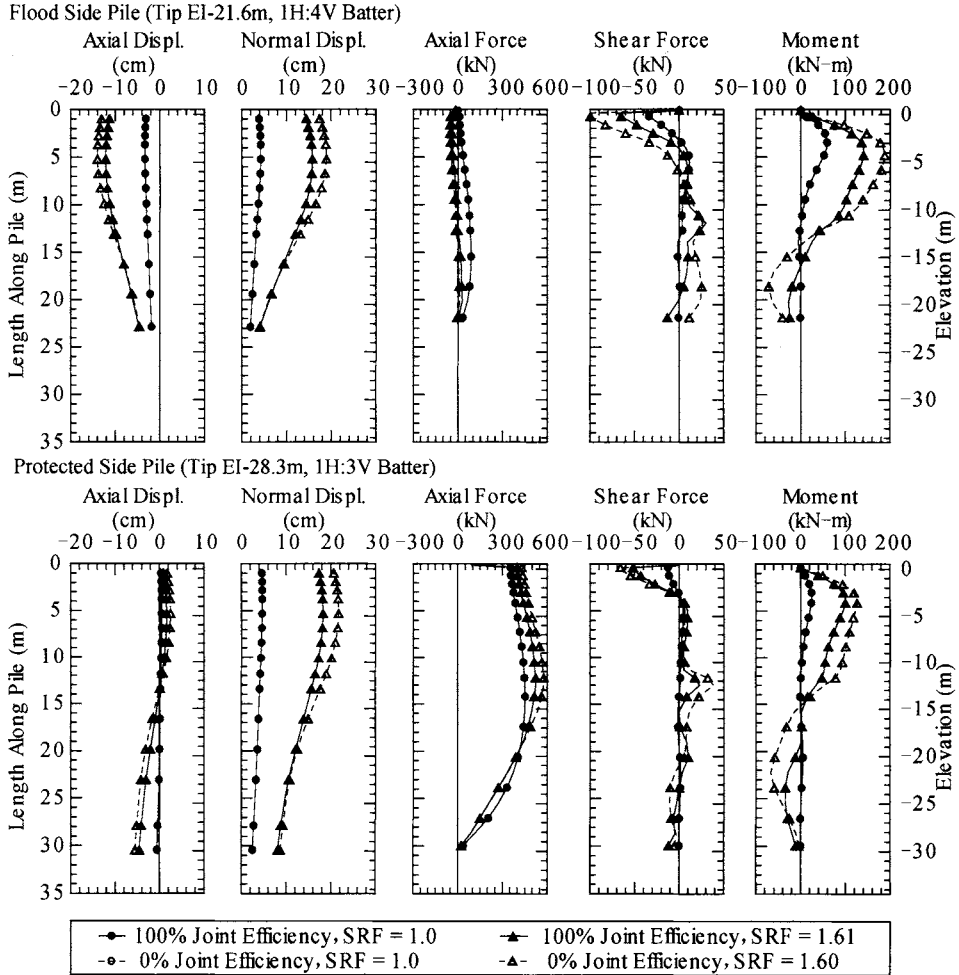


Figure 3. Pile response curves

CONCLUSIONS

The following conclusions can be drawn from the analyses described above, for the conditions used to represent the Gainard Woods T-wall:

- Displacements of the T-wall at design loads with SRF = 1.0 are independent of DMM vertical joint efficiency. Racking does not occur in the DMM zone for SRF = 1.0 regardless of vertical joint efficiency.
- The factor of safety value is only very slightly dependent on vertical joint efficiency. For 100% vertical joint efficiency, the factor of safety is 1.61. For 0% vertical joint efficiency, the factor of safety is 1.60.
- The failure mode is dependent on the joint efficiency. For 100% efficiency of joints, the DMM zone rotates as a rigid block at failure. For 0% efficiency of joints, racking of the DMM shear panels occurs along the vertical joints at failure.
- The factor of safety for the pile-supported T-wall with the DMM zone is about 1.6, according to the numerical calculations. This value is substantially higher than the design factor of safety of 1.3 used by the Corps in their method-of-planes analyses. For this cross-section, the Corps method-of-planes analyses are conservative compared to the numerical analyses.

REFERENCES

- Filz G.M., Navin M.P. (2006). *Stability of column-supported embankments. Virginia*. Transportation Research Council Report No. 06-CR13, Richmond.
- ITASCA Consulting Group. (2005). *FLAC2D fast lagrangian analysis of continua*. ITASCA Consulting Group, Minneapolis.

ANALYSIS OF TYPICAL EXPANSIVE SOIL SLOPE PROJECT

Liang Chen, Pei Zhang and Sheng Lu

*Key Laboratory of Ministry of Education for Geomechanics and Embankment Engineering,
Hohai University, Nanjing 210098, China*

Geotechnical Research Institute, Hohai University, Nanjing 210098, China

Lots of slope engineering problems take place for expansive soils. The progress and the characteristic of the expansive soils landslide are introduced and analyzed in the paper. The safety factor analysis of an expansive soils slope in Zhenjiang is also given considering the real basic physical property of the slope. Calculated with the Sweden Slice Method, considering that there are crannies in the slope, the safety factor is close to the real result. Other similar engineering can consult the result from contrasting the analysis result with the data from the field.

INTRODUCTION

The expansive soil is widely distributing in China, and it is greatly harm to the engineering for its special characteristics: expanding and shrinking, crannies, over-consolidation, slaking, weathering and strength retrogression (Lu Tinghao, 2002). The expansive soil is unsaturated ordinarily and the pore water pressure in it is negative, which leads to the characteristics different from the saturated soil. Many researching difficulties are result from these characteristics. The theory and the calculating method of the unsaturated soils are drawing board as well (Bao Chengang, 2004).

As the society and economy development of China, more and more expansive soils problems are occurring in constructions. The stability of the expansive soils slope is not as good as the ordinary slope, so whose analysis method can not use to the expansive soils slope directly. Then the expansive soils slope needs more and deeper researches (Wu Haitao, 2006).

The simple and applied method to analyze the stability of the slopes is Slice-Method. In this method, some shearing-and-sliding faces are presumed in the slopes, and then soils beyond the faces are divided into some vertical bars. The safety factor can be obtained by analyzing the force and moment balances among the bars. By some tentative calculations, the most dangerous shearing-and-sliding face and the minimum safety factor can be determined. There is not possible to get the result of the safety factor if the unknown quantities do not be cut down for that the slope stability problem is statically indeterminate. The different simplifying can calculating method can lead to different results, and the Sweden Slice Method is in common use, which is the oldest and simplest method. It presumes the sliding face is a column face and the sliding soils are rigid body. The forces on the side faces of the bars are not considered in the method, too. The calculating formula is as follow:

$$F_s = \frac{cL + rbtg\varphi \sum h_i \cos \theta_i}{rb \sum h_i \cos \theta_i} \quad (1)$$

Where,

F_s is the safety factor; c is the soils cohesive force; ρ is the bulk density; L is the length of the sliding arc; b is the width of a bar; φ is the internal friction angle; h_i is the height of the No.i bar; θ_i is the angel between normal of the bottom face of the No.i bar and the vertical line.

Considering the pore water stress , Formula (1) can be overwritten by Formula (2):

$$F_s = \frac{\sum [c'_i l_i + (W_i - u_i b_i) \cos \alpha_i \text{tg} \varphi'_i]}{\sum W_i \sin \alpha_i} \quad (2)$$

Because the forces among the bars are ignored, the safety factor is about 10%~20%'s lower than the result from the other rigid method. And if the central angle of the sliding arc and the pore water stress are relatively great, the safety factor may 50% lower than the result from the other rigid method (Li Huaizhen, Zhu Wenxiao, 2006; Drucker, 1967; Prager, 1964; W F.chen, 1975; Gray, Donald H, Sotir, Robbin B, 1992)

BACKGROUND OF THE ENGINEERING

Huang-Mountain is next to the Nan-Xu Street of Zhenjiang. A typical expansive soil slope, whose slope ratio is 1:3-1:5, length is about 500m, and width is 100m-200m, have formed for that the soils of the Huang-Mountain are fetched to build the Nan-Xu Street after suffering a unusual rainstorm in 2002. The main phenomena of the sliding are cranny and collapse. There are 11 extensive crannies with the width of 5cm-6cm and depth of 0.5m-2m and 3 obvious collapses in the slope. The sliding was fathered in Apr. to Aug. 2004. However, the sliding is beginning again from Jun. 2006, which shows that the past safety factor calculation need to be mended.

SLIDING PROGRESS

At the beginning of the sliding, some crannies and collapses emerge in the top of the slope (Figure 1).

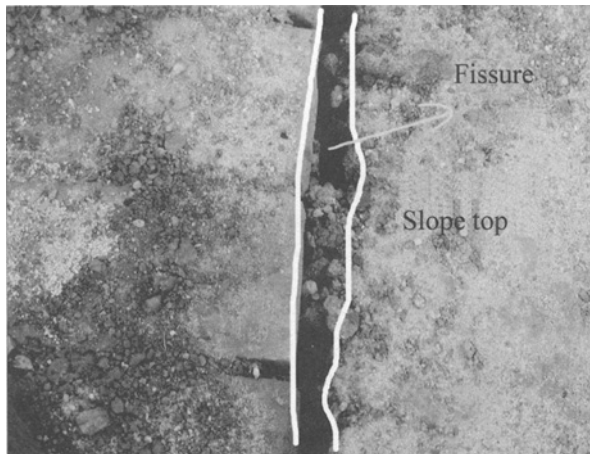


Figure 1. Location of the crannies

Then the biggish lateral displacement and hunching are appearing in the slope foot, which like the coated tongue (Figure 2).



Figure 2. Lateral displacement and hunching

With the developing of the crannies in the top and the lateral displacement in the foot of the slope, a part of soils sharply sliding down along a sliding-face, which is the slope sliding (Figure 3).



Figure 3. Slope sliding

SAFETY FACTOR CALCULATION

Basic data

The earth layers of the field are very complex(List 1), the free expanding rate of the soils δ_e is 11.5%-78.5%.The residual strength C is 6-8kPa, and the inner friction angel φ is 8° .

Table 1. physical parameters of the soils

Characteristic	Water content W (%)	unit weight (KN/m ³)	void ratio (e)	liquid limit I _L	plastic limit I _p	compressibility α_{1-2} (MPa ⁻¹)	compressibility E_{s1-2} (MP)	shear strength C_k (kPa)	shear strength ϕ_k (degree)
Silty clay	25.9	19.3	0.79	0.34	16.8	0.39	5.8	37.3	14.4
Gravel clay	21.8	20.0	0.67	0.05	19.4	0.17	10.3	39.7	13.7
Silty clay	22.5	19.9	0.68	0.15	16.8	0.17	11.0	59.5	14.1

The sliding slope is divided into 13 bars, height, arc of each bar and center of the most dangerous arc are showed in Figure 4.

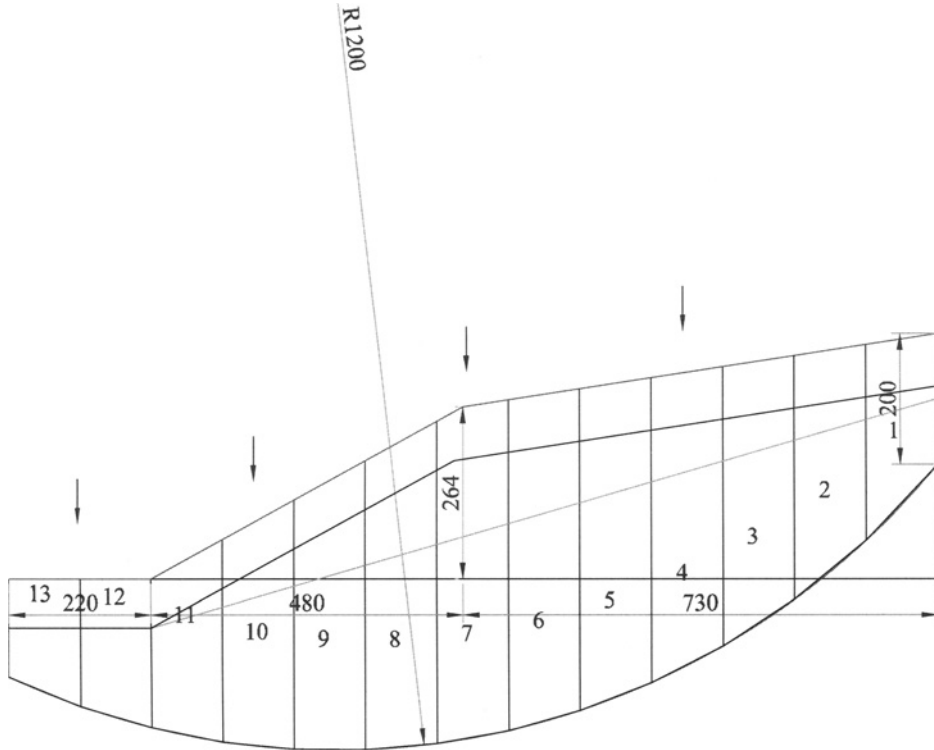


Figure 4. Center of the most dangerous arc

Calculating result

The safety factor calculating progresses are as follow:

$$F_s = \frac{\sum \text{skid resistance}}{\sum \text{glide force}} = \frac{206.35}{205.0} = 1.01 \quad (3)$$

The safety factor calculated by the Sweden Slice Method is 1.01. And the slope is sliding now, so the theoretical safety factor is 1, which shows the safety factor calculated by the Sweden Slice Method is closer to the fact.

CONCLUSION AND ANALYSIS

The shrinking and expanding of the expansive soils are not even as a result of the composition mineral, the water content and the climate such as the evaporation and the rainfall infiltration, which leads to the emerging of the crannies. In rain season, the rainfall seeps to the inner of the slope along the crannies, which leads to the strength decrease of the slope soils. And the sliding moment is reinforced by the water pressure, and then the slope is instable. So the crannies must be considered in the slope stability analysis.

Crannies can not to be ignored in stable analysis of the unsaturated expansive soil slope, or the result will depart from the fact.

The researches of the expansive soil slope are relatively complex, and the methods are faultiness, too. The geometric parameters of the cranny: length, width and depth can not be detected accurately. So the cranny developing can not be observed really. More rigid calculating method is deficient to calculate and simulate the whole status of the slope while determining the slope safety factor.

The workload of the Sweden Slice Method is relatively minor, and the result towards to the engineering above is close to the fact, so the method and result can be adopted in other similar engineering.

ACKNOWLEDGEMENT

Supported by Natural Science Foundation of Hohai University (2084/407185).

REFERENCES

- Bao Chengang. (2004). Behavior of unsaturated soil and stability of expansive soil slope. *Chinese Journal of Geotechnical Engineering*, 26(1): 1-15.
- Drucker. (1967). Progressive failure in slopes of over consolidated plastic clay. *Mechanics and Found Div, ASCE*, 93(5): 3-50.
- Gray Donald H, Sotir Robbin B. (1992). Biotechnical stabilization of highway cut slope, *Journal of Geotechnical Engineering*, 118 (9): 1395-1409.
- Li Huaizhen, Zhu Wenxiao. (2006). Instability mechanism and stability analysis of expensive soil slope. *Gui Zhou Geology*, 23(2): 132-135.
- Lu Tinghao. (2002). *Soil Mechanics*. 2nd edition. Hohai University Press.
- Prager. (1964). Long term stability of clay slope. *Geotechnique*, 14(2): 231-242
- Take W.A. (2003). *Physical modeling of seasonal moisture cycles and progressive failure in embankments*: [PhD Thesis] 1Univer2sityofCambridge.
- W F.chen. (1975). *Limiting analysis and soil plasticity*, 23-25.
- Wu Haitao. (2006). *Slope stability analysis and comprehensive treatment in expensive soil* [PhD Thesis]. WUHAN University of Technology.

STUDY ON PARAMETERS SENSIBILITY ANALYSIS MODEL OF LANDSLIDE STABILITY CONSIDERING CORRELATION

Shengguo Cheng, Xianqi Luo

*China Three Gorges University, Key Laboratory of Geological Hazards on Three gorges
Reservoir Area, Ministry of Education, 8 university avenue, Yichang 443002, China*

It is key problem to study parameters sensibility of landslide stability analysis, especially correlation of soil parameters should be considered in the research. A new model of landslide stability sensibility considering of parameter correlation was advanced by analyzing existed results. The model is composed of uniform design, limit equilibrium method and partial least squares method. Uniform design is better than orthogonal design etc. in multifactor and multi-level sensibility analysis of landslide stability. Safety factor of landslide stability can work out by limit equilibrium method. Partial least squares method can solve the correlation of parameter on landslide stability sensibility. The model may apply to geologic hazards especially in Three Gorges reservoir area, and has extensive adaptability and theory value.

INTRODUCTION

Landslide is result of internal and external factors. Though causes is complex and comprehensive, each landslide has own specific and key triggering factors. So parameter sensitivity analysis of landslide stability has been attended by researchers. The criterion of geological disasters controlling feasibility study report on the Three Gorges reservoir area in Chongqing Municipality emphasized that sensitivity analysis of landslide stability must be made. In recent years, the research has been developed from the traditional single-factor analysis to multi-factor and multi-level evaluation. The latest development is the introduction of orthogonal design which is a type of multi-level and multi-factor test design method. The earliest user of orthogonal design sensitivity analysis of landslide stability is Ni H. et al. (2002), and later Zhang X.H. et al. (2003), Ge H. et al. (2003) and others have been carrying out the research. The prospects and significance of the multi-factor sensitivity analysis method was recognized. But the correlation between the parameters wasn't considered and, the number of test times of orthogonal design is the square of the number of test level at least, which limited numbers of level of sensitivity analysis and impacted the accuracy. Based on the research results, the parameters sensitivity analysis method of landslide stability considering of correlation was advanced. The method is the combined use of orthogonal design or uniform design, Landslide stability calculation methods and partial least squares regression. The analytical model overcomes the shortcomings of single-factor sensitivity analysis, and takes into account correlation of the parameters. The sensitivity analysis method is important for us to analysis sensitivity of landslide stability, especially to control geological disasters in the Three Gorges reservoir area.

BASIC THEORIES OF LANDSLIDE STABILITY SENSITIVITY ANALYSIS

The applications of experimental techniques are very quickly since the 1950s, and in the 1960s attended to a peak. The technology has played a major role in increasing productivity and creating economic benefits. Test design method includes the traditional all factors design, orthogonal design, uniform design and mixture experiment design. In these experimental design theories, each has its own characteristics and the field of application. For Multi-factor test design, orthogonal design and uniform design are usually choice. Orthogonal design is the most widely used multi-factor and multi-level design method that its numbers of test is square of the test level at least and data processing is very simple. Uniform design that overcomes these shortcomings was proposed by Fang Kai-tai and Wang Yuan in 1978. Test numbers of the design method equals to the test level. It can be properly applied to multi-factor and multi-level test design. Both methods can be used to landslide sensitivity analysis, orthogonal design is obviously not conducive to the more level and uniform design can overcome the shortcoming, and particularly for multi-level uniform design should be preferentially used.

Landslide stability analysis can be divided into theoretical calculation, physical model test and field monitoring, and ultimate equilibrium theory is most widely used method and can provide a direct safety factor of the stability. Calculation results of various strict slices method are close. Though approximate Sweden slices method is the most widely used, it has been gradually replaced by simplified Bishop Method. The standards and norms in our country has recommended Unbalanced Thrust Method to calculation safety factor of landslide. Simplified Bishop is chosen in the paper.

The viewpoint is uniform that soil parameters have correlation. The correlation have a greater impact on the stability of landslide. The key problem of multi-level and multi-factor landslide stability sensitivity analysis is correlation between parameters at present. Principal component analysis, least-squares regression analysis and correlation analysis are often used to deal with in the past and burdensome. Partial least squares regression(PLS) which were first introduced by s.wold and c.albano in 1983 is a new multivariate statistical method. PLS can apply variedly methods of data processing. It can organically combine the multiple linear regression analysis, principal component analysis and correlation analysis. In one algorithm, regression analysis, simplify analysis of data structure and the correlation analysis between two variables can be carry out. However, because of well-known statistical software have yet not to achieve this function, users must take the function through their own programming. So the application of partial least squares regression is not very wide. In the paper, partial least squares regression was completed by the author's programming with Matlab.

SENSITIVITY ANALYSIS CONSIDERING OF PARAMETER CORRELATION

The basic idea of landslide sensitivity analysis considering of correlation is first to determine the actual impact factor of landslide stability, and gives the scope of factors, Then chooses a suitable orthogonal design table or uniform design table, and calculates the corresponding safety coefficients of landslide stability. Finally partial least squares regression analysis is used to determine the sensitivity of parameters.

- (1) To determine factor and their scope of landslide stability analysis: Factors are complex to affect landslide stability, and including rock itself characterizes (cohesion, friction angle, bulk density), the affecting of water to Landslide (uplift of the water, pore pressure, penetration, softening coefficient), Earthquake (the horizontal seismic forces, the vertical seismic forces), topography (landslide height, landslide angle) and human factors (the design of slope, crest load). Landslide sensitive analysis of the factors used the cohesive force, friction angle, bulk density, groundwater level, the water level of the reservoir, seismic, slope ratio, overload. After determining the specific factors, the scope of the parameters and the level of various factors are chosen.
- (2) To select appropriate uniform design table: According to the numbers of factors and levels, appropriate uniform design tables are selected. For multi-factors and the fewer level tests, we usually make repeat test for increasing the sensitivity of degree of freedom. The numbers of test is three times of factors.
- (3) To calculate the safety factor: By Bishop method the safety factor of landslide stability can be determinate.
- (4) To determine the parameter sensitivity sequencing using partial least squares regression analysis.

ENGINEERING APPLICATION

The downstream slope of earth dam: Imbankment filled clay and a minor amount of grave. Natural moisture of clay was 21.9%-26.1%. The natural porosity was 0.47-0.72. Dry density was 1.52-1.76g/cm³. The optimum water content was 16.6%. Maximum dry density was 1.77g/cm³.

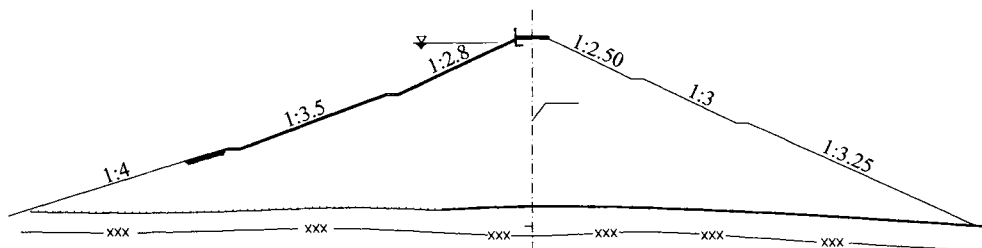


Figure 1. Dam cross-sectional

Table 1. Dam stability analysis parameter table

Material kind	Dry density (g/cm ³)	Gravity(γ) (kN/m ³)	Friction Angle(ϕ) (°)	Cohesion(<i>c</i>) (kPa)
Clay filling imbankment	1.67	19	16	32
Dam foundation	1.68	21.21	20.0	40

Table 2. factors and levels

factor	Gravity(γ) (kN/m ³)	Friction Angle(ϕ) (°)	Cohesion(<i>c</i>) (kPa)	Slope angle(<i>a</i>) (°)
scope	17-20	8-20	24-36	14-20

Table 3. The results of orthogonal design calculation

The numbers	1(γ)	2(φ)	3(c)	4(a)	Safety factor(K)
1	17	8	24	14	1.647
2	17	12	28	16	1.898
3	17	16	32	18	2.038
4	17	20	36	20	2.149
5	18	8	28	18	1.406
6	18	12	24	20	1.366
7	18	16	36	14	2.471
8	18	20	32	16	2.295
9	19	8	32	20	1.452
10	19	12	36	18	1.821
11	19	16	24	16	1.757
12	19	20	28	14	2.266
13	20	8	36	16	1.601
14	20	12	32	14	1.938
15	20	16	28	20	1.481
16	20	20	24	18	1.695

Table 4. Correlation

correlation	1(γ)	2(φ)	3(c)	4(a)
1(γ)	1.000	0.244	0.149	-0.179
2(φ)	0.244	1.000	-0.433	0.521
3(c)	0.149	-0.433	1.000	0.317
4(a)	-0.179	0.521	0.317	1.000

Correlation coefficient table shows that there is a certain correlation between the parameters. the general analysis model was used and didn't taking into account the correlation between parameters, the main conclusions are as follows:

Table 5. Variance analysis of orthogonal design

items	Sum of Squares (SS)	Degree of Freedom (DF)	Mean Square(MS)	F Value
γ	SS γ	a-1	SS γ /(a-1)	MS γ /MSE
φ	SS φ	a-1	SS φ /(a-1)	MS φ /MSE
c	SS c	a-1	SS c /(a-1)	MS c /MSE
a	SS a	a-1	SS a /(a-1)	MS a /MSE
error	SSE	a-1	SSE/(n-1)	
Total	SST	n-1		

Table 6. Test results and analysis

items	Sum of Squares	Degree of Freedom	Mean Square	F	critical value (F_a)	significance
γ	0.146	3	0.0487	11.32	F _{0.05} (3,3)=9.28 F _{0.01} (3,3)=29.45	**
φ	0.730	3	0.2433	56.59		***
c	0.372	3	0.1240	28.84		**
a	0.487	3	0.1623	37.75		***
error	0.013	3	0.0043			
Total	1.748	15				

Typical regression equation is as follows:

$$k = -0.278\gamma + 0.644\Phi + 0.457c - 0.525\alpha \quad (1)$$

Table 6 shows and typical the regression equation (1) both show that ϕ , a are especially significant to the stability of the landslide, and γ , c are certain significant to the stability of the landslide. According to sensitivity, their orders are $\phi > a > c > \gamma$.

Using partial least squares regression and considering of the correlation between the parameters, standard regression equation was as follow:

$$k = -0.616\gamma + 0.8047\Phi + 0.4417c - 0.4998\alpha \quad (2)$$

The order of sensitivity is $\phi > \gamma > a > c$. According to the above analysis and the basic theory of mathematical model, conclusions considering of correlation between these parameters is better than other methods. We can see that the analysis model should be more comprehensive in landslide stability sensitivity analysis and be better to stimulate the actual situation of slope. The method will have important value to control geologic hazard in the Three Gorges reservoir area.

CONCLUSIONS

- (1) Sensitivity analysis is a important topics of geologic hazard mechanism, prediction and controlling, and its development has been from single factor to multiple factors.
- (2) The new analysis method are made up of orthogonal design (uniform design), stability calculation and partial least squares regression. It can consider the correlation between parameters and contribution of each factor.

REFERENCES

- Cheng S.G., Luo X.Q. and Fang K.H.(2002). The test and design theory of the similar materials of soil-type landslide and the study on its assessment method. *China Water Powder*, 21(4): 21-22,29.
- Fan M.Q. and Sheng J.B.(1997). The correlation between soil strength ϕ c. *Journal of Geotechnical Engineering*, 19(4): 100-104.
- Fang K.T.(1994). *Uniform design and uniform design table*. 1st edition, China Science Press
- Ge H. and Liu H.C(2003). Sensitivity analysis on influence factors for stability of Caojiezi Shuangyantang Landslide in Wanzhou. *China Journal of Geological Hazards and prevention*, 14(2): 15-18
- Ni H. and Liu R.R.(2002). Applications of orthogonal design to sensitivity analysis of landslide. *Chinese journal of rock mechanics and engineering*, 21(7): 989-992.
- Zheng Y.R. and Shi W.M.(2005). Several issues of landslide stability analysis in the Three Gorges reservoir area. *Chongqing construction*, 6: 34-41.
- Zhang X.H., Gong X.N. and Xu R.Q.(2003). Orthogonally analysis method of sensibility on factor of slope stability. *China Journal of Highway and Transport*, 16(1): 36-39.

EVALUATION OF BIANLOO LANDSLIDE USING CELLULAR AUTOMATA

A. Fahimifar

*PhD, Professor, Department of Civil and Environmental Engineering,
Amirkabir University of Technology, Hafez Ave, Tehran, Iran*

M. A. Bahri

MSc, in Soil Mechanics and Foundation Engineering

Cellular Automata (CA) is an effective method for simulating complex natural and artificial systems, which is able to evaluate various processes. For the Purpose of analyzing Bianloo landslide, and to determine its sliding characteristics (height of run-up, sliding surface, length of sliding and movement, and so on), a two dimensional CA model with square shape cells was selected as the analytical tool, together with an algorism pertinent to this approach. Bianloo landslide occurred in 1995 after a heavy rainfall which made it saturated. This landslide is located near a village in Bijar city in kordestan province in Iran. This landslide is predominantly composed of clay and fine sand. For determining mechanical and physical properties of the landslide a back analysis was carried out using Slope/w program, and C , ϕ and γ were estimated 8 kpa, 20° and 18 kn/m^3 respectively. For simulation of the landslide by CA, the landslide cross-section was divided to 10×10 cells (in meters) and using the selected algorism, the sliding soil of each central cell was distributed to the neighboring cells, and finally, the simulated cross section was determined which is comparable to the true landslide cross-section. The effect of cell dimension was also examined in this study and the appropriate dimensions were proposed. A computer program was prepared for the performing the analysis on the basis of CA method. The results obtained in this analysis showed a very good agreement with the reality.

INTRODUCTION

A landslide is a phenomenon in which soil mass on a slope moves slowly along the slip surface downward the slope under the influence of ground water and other causes. Since landslides occur over an extensive area and a large amount of soil mass is moved in general, it can cause serious damages.

A debris/mud/soil flow can be physically described by fluid-dynamic equations and can range rheologically from approximately Newtonian liquids to brittle solids. Forecasting the movement process of landslide may meet serious difficulties, since it is extremely arduous to solve the governing flow equations without making substantial simplification, S.Di.Gregorio et al. (1998). In order to overcome these difficulties CA (Cellular Automata) models have been tried for simulation of a debris/mud flow with two dimensional cells, by research

group , ,S.Di.Gregorio et al. (1994,1995,1998,2000,..). (e.g., the simulation of Tessina and Mount Ontake landslides based on CA).

In this essay, based on Di.Gregorio CA method, hypothesis, concept and computer program is given for simulating slope landslides. the type of slope landslide is composed of sliding and flowing with mechanism of shear movement of saturated soil.

SUMMARY DISCRPTION OF CA METHOD

Cellular Automata is a regular grid of cells with certain state, that according to fixed model, each cell communicates with its neighboring cells. This connection is local and equal for all cells. The cell and all cells which were related to it, make collection of neighboring cells. Any cell at any time can choice one of the exist state. The state set is equal for all cells in any time. All cells state change synchronizing and based on one law. After each step system update and this process is continued to reach a dynamic equilibrium condition. Applications of CA are very broad; they range from microscopic simulations of physical phenomena to macroscopic simulations of geological and social processes, Wolfram, S. (1996).

An extension of the definition of homogeneous CA is introduced by , Di. Gregorio and Serra .(1998), the primary and main class of CA, which is most commonly used in modeling and simulation. Such an extension is useful in order to model macroscopic phenomena .

CA is defined:

$$CA = \langle R, X, Q, P, \sigma \rangle \quad (1)$$

R : is a finite cellular d-dimensional region where the phenomenon evolves; it is defined by means of a D-dimensional vector of integers, which denotes the limits of this finite region.

X : The set X identifies the geometrical pattern of the cells which influence the cell state change; they are respectively the cell itself and "north", "south", "east", and "west" cells.

Usually a neighborhood is chosen for a two –dimensional CA such that two cells are defined as neighboring cells when they have common edge. A usual neighborhood for a three-dimensional CA is such that two neighboring cells have a common face.

Q : is the finite set of the CA state.

P : is the finite set of global parameters of the CA.

σ : is the deterministic state transition for the cells in R . in each step σ function is applied for all cells.

Each characteristic, relevant to the evolution of the system and relative to the portion of the space corresponding to the cell, is defined as a substate. The allowed values of the substate form a finite set. The set of possible states of the cell is given by the Cartesian product of the sets of substates, ie, $Q = Q_1 \times Q_2 \times \dots \times Q_n$.

The first assumption is that the values of the substates are constant in the space occupied by the cell.

The second assumption prescribes that the interactions in the neighborhood (local interaction) must/may be described in terms of flows of some quantity in the central cell (expressed as substate) towards its neighbors.

The third assumption is that the fragmentation of the complex phenomenon in internal transformations and local interactions may be applied, calculating sequentially the change of the values of the substates, Di. Gregorio et al .(2000).

In this method the cross-section of landslide is divided in two manner to square cells with dimensions of 5m×5m and 10m×10m. Sliding soil of each central cell is distributed to its neighboring cells by using this process is continued step by step, and the height of each cells is obtained with updates the cells soil content and finally the cross-section of the simulated is compared with the true landslide cross-section.

The important points of this method is that calculate the height of velocity gradient and run-up effect, with using new method and based on primary concepts of physics.

Since the existence of friction and cohesion between soil grains, only a portion of the soil in the cell can be distributed. Therefore it is assumed that soil can be distributed between the central cell and neighbor if the tangent of local slope angle between the central cell and the neighbor is larger than the coefficient of friction, see Figure 1.

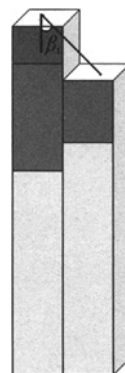


Figure 1. Local slope angle (β_i)

COMPUTER PROGRAM FOR ANALYSIS OF LANDSLIDE PROCESS

In this research a computer program was prepared for the performing the analysis of landslide movement process, on the basis of CA method (Di.Gregorio algorism). The following structure, sketch the algorism method:

A: φ (friction angle) condition, angle β_i (local slope angle between two neighboring cells) is obtained from height difference of central cell and neighboring cells. If $\tan(\beta_i) < \tan(\varphi)$, then the i -th cell were eliminated from distribution algorism. In the other hand, if $\tan(\beta_i) > \tan(\varphi)$, then the distribution of soil from central cell to neighboring cells is possible.

$$\text{tg}\beta_i = \{(Q_a[0] + Q_{th}[0] + h_k) - (Q_a[i] + Q_{th}[i])\} / a \quad (2)$$

a : is equal to cell dimension size.

$Q_{th}[0]$: correlated to the height of soil changeable part in central cell.

$Q_a[0]$: correlated to the height of soil fixed part in central cell.

$Q_a[i]$: correlated to the height of soil fixed part in I-th neighboring cell.

$Q_{th}[i]$: correlated to the height of soil changeable part in I-th neighboring cell.

Q_i : correlated to the height of soil in I-th neighbor cell.

h_k : correlated to the height arising from kinetic energy.

B: A is the set of cells not eliminated. Its initial value is set of the number of its neighbors.

C: average height for A set include of undeleted cells which is defined as followed:

$$\text{Average} = (p + \sum q[i]) / A \quad (3)$$

D: cells which have been height greater than average height were eliminated from A set.

E: come back to B stage, until there are no more cells to be eliminated.

F : with distracting the quantities of Q_i from average height quantities, distributed soil height of central cell were obtained.

SUMMARY DESCRIPTION OF BAYANLOO LANDSLIDE

This landslide occurred in 1995 after heavy rainfall, which made it saturate. The landslide is located near a village in kordestan province in iran. this landslide is predominately composed of clay and fine sand. The slope of cross-section before landslide was estimated about 20° . width of sliding mass in average is about 200 meter.

SIMULATION OF BIANLOO LANDSLIDE BASED ON CA

In this simulation a neighboring include of one central cell and eight neighbor, see Figure 2.

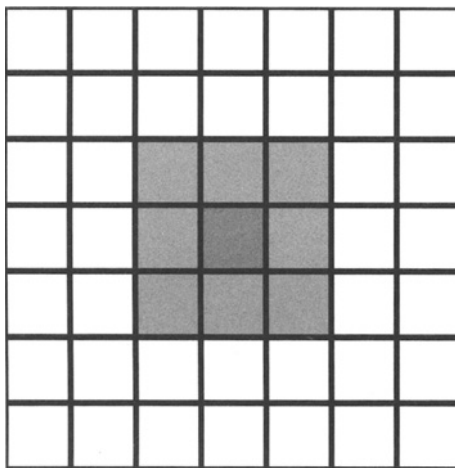


Figure 2. Definition of neighboring

It is supposed that, the soil of each cell divided in two separated section:

1. fixed soil part (part of soil under the sliding surface).
2. slidable soil part (part of soil above the sliding surface).

THE EFFECT OF COHESSION PARAMETER AND RUN_UP

In fact the cohesion parameter is considered as thickness of soil. The cohesion parameter is assumed according to the following formula:

$$P_{adh} = C/\gamma \quad (4)$$

C : (kN/m^2).

γ : is the special weight (kN/m^3).

In this method in order to investigate the height effect arising from kinetic energy, the basic formula of physics ($h_k = v^2/2g$) is used.

DISCUSSION AND CONCLUSION

The exact cross-section of bianloo, reality landslide has compared with simulated landslide with square cells in dimension of (10×10) and (5×5) meter, see Figures 3 and 4. According to compute the total length of simulated landslide has obtained 123 meter which in compared with 130 (m) reality length it has simulated development of landslide length with good approximation in this way. With increase of compaction of grid and decrease of cells dimension the results were obtained in this analysis showed more agreement with the reality.

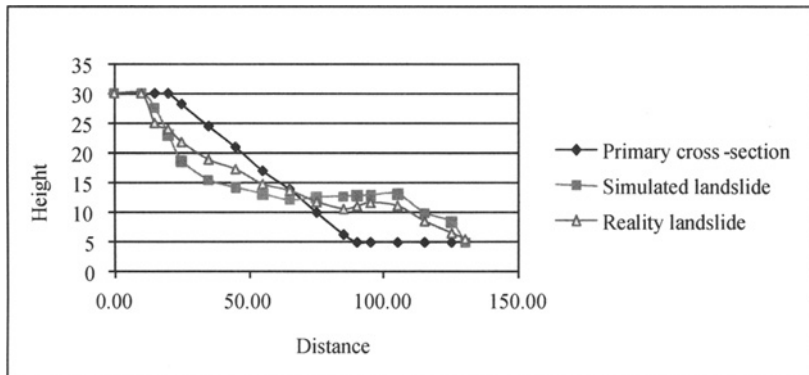


Figure 3. Compare the results for 10×10 meter

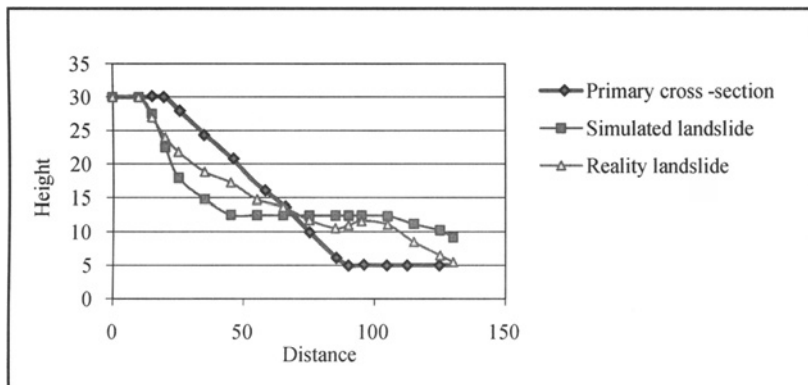


Figure 4. Compare the results for 5×5 meter

REFERENCES

- Gregorio S.Di, et al. (1998). Mount ontake landslide simulation by the cellular automata model SCIDDICA-3. *Physc. Chem. Earth(A)*, 24(2): 131-137.
- Gregorio S.Di, et al. (2000). Simulation of the tessina landslide by a cellular automata model and future hazard scenarios. *JAG. Volume2-issue 1-2000*.
- Wolfram S. (1996). *Theory and application of cellular automata*. world publishing Co. PTE. LTD.

THE LIMIT ANALYSIS OF REINFORCED SLOPES

Xiaojing Feng, Qing Yang

*Department of Civil Engineering, Dalian University of Technology,
Dalian 116024, China*

Based on the fundamental theory of Upper-bound limit analysis of plasticity, the change of the slip surfaces with is shown. Also the limit heights and stability coefficients of the reinforced steep slope with different slope angle, top slope angle, internal friction angle, cohesive, reinforcement tension strength, reinforced spacing, reinforcement arrangement, seismic intensity and additional load were calculated in this paper based on a code written by the authors. The sequence of sensibilities was listed, and the results showed that the internal friction angle and earthquake were the key factors that influenced the critical heights of the reinforced steep slope.

INTRODUCTION

Reinforced soil retaining structures have been widely used because they offer economic benefits compared to conventional retaining systems (Desai et al., 2005). However, their destruction under various complex conditions confused designers and managers which slow down the spread of this technique. Among dozens of factors that influence the stability of reinforced slopes, the emphasis should be placed on the more sensitive factors. (Zhang et al., 2003)

The factors influencing the stability of the reinforced slopes are more than dozens of and most of them are random, variable and fuzzy. So it is necessary to find out their sensibility sequence, then the emphasis can be placed on the more sensible factors in designing. Such researches based on the limit equilibrium methods (Ji et al., 2003) which are widely used in the design show that the cohesive and internal friction are the most sensitive factors. Since the limit equilibrium-based approaches do not account for the constitutive equations, another kind of simple and practical methods, limit analysis of plasticity, which involve a perfect plasticity model was developed. And then they have been spread to the reinforced soil structures (Wang et al., 2005; Xiao et al., 2005; Cui et al., 2007). Based on the Upper-bound limit analysis of plasticity, this paper probes into the limit height of the steep slopes considering ten variable factors, and gives their sequence by using the orthogonal table.

UPPER-BOUND LIMIT ANALYSIS

The upper-bound limit analysis for slopes can be described as: for a rigid plasticity soil slope, if an existent kinematical admissible velocity field made the power of external load equal to the inner energy dissipation, the slope will be destroyed, and the relative height will be the

The Quasi-static method is used to simplified the complex earthquake that the earthquake force here is just supposed as a constant horizontal force which is proportional to the gravity of the soil. The constant is $K_H W$, where K_H is the coefficient of horizontal seism related to earthquake intensity, see Table 1.

Table 1. Coefficient of horizontal seism, K_H

Design intensity K_H	None	VIII	IX
	0	0.2	0.4

The power of the earthquake force is calculated just like the self-weight, whereas the orientation is changed. So the expression of the earthquake power is:

$$\dot{W}_e = \dot{W}_{eADC} = \dot{W}_{eOAC} - \dot{W}_{eODC} - \dot{W}_{eOAD} = \gamma R_0^3 \omega K_H (f_{e1} - f_{e2} - f_{e3}) \quad (4)$$

where

$$f_{e1} = \frac{1}{3(1+9 \tan^2 \varphi)} \{ (\cos \theta_0 - 3 \tan \varphi \sin \theta_0) + (3 \tan \varphi \sin \theta_1 - \cos \theta_1) \exp[3(\theta_1 - \theta_0) \tan \varphi] \}$$

$$f_{e2} = \frac{1}{6} \frac{L}{R_0} \sin(\theta_0 + \alpha) \left(2 \sin \theta_0 + \frac{L}{R_0} \sin \alpha \right)$$

$$f_{e3} = \frac{1}{6} \exp[(\theta_1 - \theta_0) \tan \varphi] \cdot \left[\sin(\theta_1 - \theta_0) - \frac{L}{R_0} \sin(\theta_1 + \alpha) \right] \\ \times \left\{ \sin \theta_1 \exp[(\theta_1 - \theta_0) \tan \varphi] + \sin \theta_0 + \frac{L}{R_0} \sin \alpha \right\}$$

Inner energy dissipation of reinforcement W_r

The equation of Inner energy dissipation of reinforcement is given by:

$$W_r = \frac{R_0^2 \omega}{\cos \varphi} \int_{\theta_0}^{\theta_1} k_r \sin \theta \cos(\theta - \varphi) \cdot \exp[2(\theta - \theta_0) \tan \varphi] d\theta = \frac{k_{r0} R_0^2 \omega}{2} \cdot f_r \quad (5)$$

k_r will vary with the limit strength, spacing and arrangement of the reinforcement, so does the inner energy dissipation W_r .

a. Uniformly arranged

When the reinforcement is arranged uniformly, the reinforcement force per height will be:

$$k_r = k_{r0} = \frac{T_r}{S}, \text{ where } T_r \text{ and } S \text{ are the strength and spacing of reinforcement.}$$

b. Top half sparse and bottom half dense

When the reinforcement is sparse in top half and dense in bottom half, for convenient, k_r is supposed to be distributed linearly and continuingly, the equation is given as (Cui et al., 2007):

$$k_t = k_{t1} = 2k_{t0} \frac{e^{(\theta-\theta_0)\tan\varphi} \sin\theta - \sin\theta_0}{e^{(\theta_1-\theta_0)\tan\varphi} \sin\theta_1 - \sin\theta_0}$$

c. Top half dense and bottom half sparse

Similar to the above, k_t is given as:

$$k_t = k_{t2} = 2k_{t0} \frac{e^{(\theta_1-\theta_0)\tan\varphi} \sin\theta_1 - e^{(\theta-\theta_0)\tan\varphi} \sin\theta}{e^{(\theta_1-\theta_0)\tan\varphi} \sin\theta_1 - \sin\theta_0}$$

Limit height of reinforced slope

Combing the equation(1), (2), (3), (4) and (5), and supposed that $c \neq 0$, the limit height of reinforced slope can be deduced:

$$H^{rs} = \frac{c}{\gamma} f^{rs}(\theta_1, \theta_0) \quad (6)$$

where

$$f^{rs}(\theta_1, \theta_0) = \frac{f_4 \sin\beta}{2\sin(\beta-\alpha)} \cdot \frac{\left(\frac{f_3}{\tan\varphi} + \frac{k_{t0}}{c} f_r - \frac{2q}{c} f_q \right)}{\left[f_1 - f_2 - f_3 + K_H (f_{e1} - f_{e2} - f_{e3}) \right]}$$

As $q=0$, $K_H=0$, and the reinforcement arranged uniformly, equation(6) will be identical to equation(1). The limit height of reinforced slope is calculated by substituting the extreme angles θ_{1cr}^{rs} and θ_{0cr}^{rs} which are deduced by the extreme conditions, $\frac{\partial f^{rs}}{\partial \theta_1} = 0$ and $\frac{\partial f^{rs}}{\partial \theta_0} = 0$, to the equation (6).

THE CHANGE OF THE SLIP SURFACE

The rotational failure mechanism used in the analysis is known to be the most adverse failure mode, and the log-spiral failure surface is proved to be the most proper one in the limit equilibrium zone by Chen(1975). Also, Chen(1975) indicated that the upper-bounded limit analysis can be used to estimate the critical height of slopes, this technique seems to be more convenient sometimes and logical.

The position of the slip surfaces are change with the vary of slope angle, top slope angle, internal friction angle, cohesive, reinforcement tension strength, reinforced spacing, reinforcement arrangement, seismic intensity and additional load. Here the emphasis will be focused on the amount of reinforcement, the others have been discussed by Chen(1975). The change of critical factors such as: θ_1 , θ_0 , L/R_0 , L/H of failure surface are showed in diagrams(Figure 2). Calculations were performed assuming that the reinforcement are all ruptured but not pulled out. The diagrams revealed that θ_1 increases with the increasing of K_t , however, the θ_0 is decreased. The change of L/R_0 is similar to L/H , the ascent of the ratio of L/H indicates that the failure surfaces go further for the slopes with more reinforcement. This phenomena has been discovered in a model test by Ji(2003).

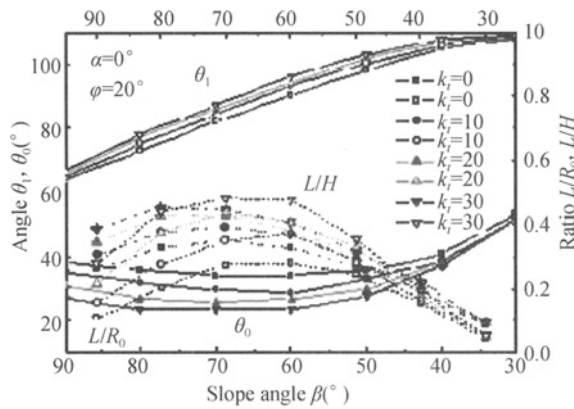


Figure 2. Critical slip surface factors

MULTI-FACTOR ORTHOGONAL ANALYSIS

Using the codes which were written by author , this paper probes into the limit heights of slopes influenced by slope angle β , top slope angle α , bulk density γ , internal friction angle ϕ , cohesive c , reinforcement tension strength T , reinforced spacing S , reinforcement arrangement Ty , seismic intensity Q and additional load q . Each factor has 3 levels considering the practice (Table 2), all of them are arranged in the orthogonal test table ,and the calculation results are given in Table 3.

Table 2. The range and level of the factors

level	parameter									
	Slope angle β ($^{\circ}$)	Top slope angle α ($^{\circ}$)	Internal friction angle ϕ ($^{\circ}$)	Cohesive c /kPa	Reinforcement tension trength T /kN/m	Reinforced spacing S /m	Bulk density γ / KN/m^3	Surcharge q /kPa	Seismic intensity Q	Arrangement Ty
I	90	0	5	5	5	0.5	15	0	none	1(1)
II	75	5	15	10	10	0.8	18	10	VIII	2(2)
III	60	10	25	20	30	1.0	20	30	IX	3(3)

Notes: (1) 1 represent the uniform arrangement; (2) 2 represent the top sparse and bottom dense;(3) 3 represent the top dense and bottom sparse.

Table 3. Range analysis of the factors for the Limit Height

Factor	β ($^{\circ}$)	α ($^{\circ}$)	ϕ ($^{\circ}$)	c (kPa)	T (kN/m)	S (m)	γ (KN/m^3)	q (kPa)	Q	Ty
I /9	3.8	6.3	2.0	3.5	3.7	9.0	8.1	6.6	9.0	4.6
II /9	6.4	7.0	6.7	6.8	6.0	4.4	5.1	5.7	3.1	7.2
III /9	7.5	4.5	9.0	7.4	8.1	4.4	4.5	5.5	5.6	5.9
Range for H_{cr}	3.7	2.5	7.0	3.9	4.4	4.6	3.5	1.1	5.8	2.6
Sensibility	$\phi > E > S > T > c > \beta > \gamma > Ty > \alpha > q$									
Optimal policy	$T_3, \phi_3, E_1, \beta_3, S_1, c_3, \alpha_2, \gamma_1, q_1, Ty_2$									

The sensibility sequence of cohesive in table 4is just the 5th, however, this result is different from the former studies by Ji et al.2003, Chen et al.2006, Tan et al.2007 whose

conclusion showed the cohesive was the most sensible factor. Doing the same research to the slope angle of 45°, 60° and 75°, the sensibility sequence of cohesive go forward to the 2nd. Therefore, it can be said that the cohesive for the steep slope is less sensible. Meanwhile, reinforcement spacing and strength are quite effective factor for limit height.

CONCLUSIONS

- a. The sensibility sequence for the steep reinforced slope is: ϕ , E , S , T , c , β , γ , Ty , a and q .
- b. For the steep reinforced slopes, the sensibility of cohesive descends, but the sensibility of reinforcement parameters ascend.
- c. The top sparse and bottom dense is the best arrangement type of reinforcement, but its sensibility is weak.
- d. The failure surface of the reinforced slopes go further from the surface when the amount of the reinforcement increased.

Except the factors mentioned in this paper, there are still other influence factors, like underground water, rain seepage etc. are not taken into account in this paper. Also the supposed slippage is through the toe of slope, whereas it is unfit for the low slope angle. So a lot of problem need the further study.

REFERENCES

- Chen W F. (1975). *Limit analysis and soil plasticity*. New York: Elsevier Scientific Publishing Company.
- Chen Z.B., Jian W.B. (2006). Sensibility analysis of slope stability based on grey correlation analysis. *J. Journal of Disaster Prevention and Mitigation Engineering*, 26(4): 473-477.
- Cui X.Z., Yao Z.Y. (2007). Limit analysis of critical heights of reinforced soil slope. *J. China Journal of Highway and Transport*. 20(1): 1-6.
- Desai C. S., El-Hoseiny K. E. (2005). Prediction of field behavior of reinforced soil wall using advanced constitutive model. *Journal of Geotechnical and Geoenvironmental Engineering. ASCE*, 131(6):729-739.
- Ji D.X., Yang Q. (2004). Studies on sensibilities of factors influencing on reinforced uniform slope stability. *J. Rock and Soil Mechanics*, 25(7): 1089-1092.
- Qian J.H., Yin Z.Z. (1996). *Soil engineering principle and calculation*. China Water Power Press. Beijing.
- Tan X.H., Wang J.G., Liu X.R., Liu D.J. and Wu D.X. (2007). Finite element reliability computation and sensitivity analysis of slope stability. *J. Chinese Journal of Rock Mechanics and Engineering*. 26(1): 115-122.
- Wang Z., Qiao L.P. (2005). Critical height of reinforced slope based on limit analysis upper bound method. *J. Engineering Journal of Wuhan University*, 38(5): 67-69.
- Xiao C.Z. (2005). A study on rheologic properties of geogrids and long-term performance of reinforced earth walls. *D.Ph.D.Dissertation*. Dalian University of Technology. Dalian..
- Zhang X.H., Gong X.N. and Xu R.Q. (2003). Orthogonality analysis method of sensibility on factor of slope stability. *J. China Journal of Highway and Transport*. 16(1): 36-39.

STUDY ON RAINWATER INFILTRATION IN SUBSOIL OF SANDY SLOPES DURING RAINFALL BY FIELD MONITORING

Thi Ha

*Research & Development Center, Nippon Koei Co., Ltd.
2304, Inarihara, Tsukuba City, Ibaraki300-1259, Japan*

Yasushi Sasaki

*Japan Institute of Construction Engineering,
3-12-1 Toranomon, Minato Ward, Tokyo 105-0001, Japan*

Takashi Tsuchida, Seiji Kano

*Engineering Department, Hiroshima University
1-4-1 Kagamiyama, Higashi Hiroshima City, Hiroshima 300-1259, Japan*

To accurately predict the time and place of sediment-related disasters, an urgent ongoing problem is to clarify the behavior of rainfall infiltration in the top 1-2 m thickness of subsurface layers. Normally, rainwater infiltration on hill slopes is determined by unsaturated and saturated numerical analysis using FEM, FDM, or similar methods. But, insufficient verification studies means that it is unclear whether modeled results show good agreement with behaviors on in-situ slopes. Therefore, here is an attempt to elucidate the mechanism of rainfall infiltration by field monitoring.

INTRODUCTION

Most of land areas in Japan are covered by hilly and mountains areas and it has repeatedly experienced rain-induced failures causing severe damages to both life and property. Hiroshima Prefecture, located at western part of the Honshu Island of Japan, is also one of the regions where such disasters frequently occur. When counting such events during recent 62 years in 1945 - 2007, 19 times of disasters caused severe damage to both life Most of failures in this region are caused by shallow failure of slope which is covered by comparatively thin surface layer of heavily-weathered granite soil called Masado and its induced debris flow. Among them, a disastrous case occurred in the prefecture causing 32 deaths and damage to 4,785 houses on June 29, 1999 (Figure 1).

It is almost impossible to completely prevent such sediment related disasters by hardware system such as Sabo dam only, at all susceptible natural slopes to rain-induced failures. However, it is important to be secured at least human lives and for this purpose, a better software system should be established to mitigate this kind of disasters by early predicting and warning system to the related community. For early predicting, the authors had already proposed a newly rainfall index from on-going rainfall records to apply for warning to evacuate from possible slope failures (Sasaki et al.,2001).



Figure 1. Transported mud, rock and fallen trees attacked to residential areas during 1999 disaster

However, the critical rainfall due to rainfall indices should be reasonable from the view of geotechnical engineering and, to satisfy this requirement, elucidation of the mechanism of rainwater infiltration and failure is still urgent problem. Therefore, the authors carried out a series of research by conducting small-scale model slope tests in order to know the mechanism of rain-induced failure, and the long term monitoring of rainfall infiltration on in-situ slope to know rain water infiltration on in-situ slopes. The results and detail discussions for model tests are presented in Thi Ha et al. (2002). In this paper, field monitoring of rainfall infiltration will be discussed.

FIELD MONITORING SYSTEM FOR RAINFALL INFILTRATION

Position of monitoring site

The heavy rainfall of June 29, 1999 caused slopes failures in and around Hiroshima University. One of the debris-flow sites on university premises where the field monitoring was carried out was on the northern slope of Mount Gagara, with an elevation of about 330 m above mean sea level (MSL). More detailed explanations about the flow-site are presented in Thi Ha et al. 2002 and in Thi Ha et al. 2003.

In this field monitoring, two sites were selected near the debris-flow, namely Sites A and B, as shown in Figure 2. Six positions were instrumented-- three at each site - and a rain gauge was setup in an open space between the two sites.

Measuring system

The measuring system consisted of an array of tensiometers and TDRs (Time Domain Reflectometry)&ADRs (Amplitude Domain Reflectometry) to measure suction and volumetric water contents, a piezometer to measure groundwater level, a rain gauge, and an automatic data-acquisition system. The schematic layout diagram of the measuring system at location B3 and detailed lists of instrumentations at each point are shown in Figure 3 and Table 1. The required power for functioning of the monitoring system is supplied by solar power. The measuring data at each place are filled into a data logger and sampling interval can be selected from 1 second to 60 minutes; here, it was actually set at 10 minutes for all

monitoring. The detailed description of each instrument, the calibration method, installation, and maintenance has been presented in Thi Ha et al. (2001).

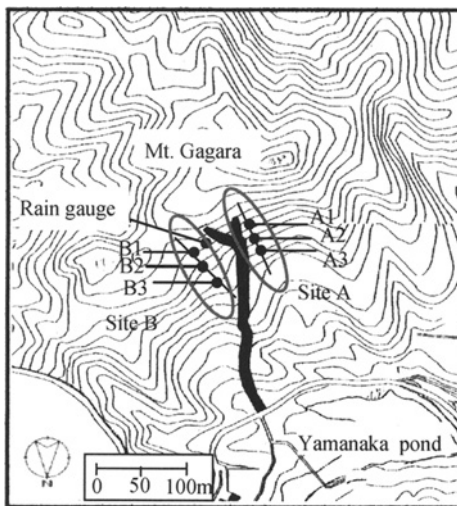


Figure 2. Position of monitoring sites

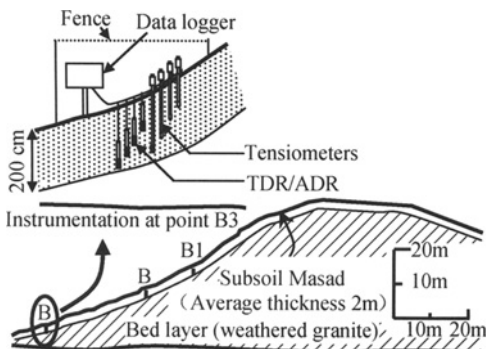


Figure 3. Instrumentation at site B

Table1. Details of instrumentation

Pt.	Depth below ground level (cm)	
	Tensiometer	ADR•TDR
A1	58, 96, 114, 185	100, 150
A2	56, 93, 122, 193	50, 90, 145, 200
A3	44, 98, 115, 174	45, 155
B1	10, 30, 37, 97, 135	10, 30, 50, 150
B2	10, 30, 59, 88, 136, 176	10, 30, 50, 140
B3	10, 30, 60, 97, 159, 172	10, 30, 50, 100, 155, 195
Piezometer	Installed at depth 200cm of point A2	
Rain gauge	Installed at mid point of site A and B	
Date of Installation at depth 10cm、30cm→		
B1•B3 (2006/6)、B2 (2007/7)		

DISCUSSION OF THE RESULTS

Variations of water content and suction during rainfall

Figure 4 shows an example of moisture change in the monitored slope during July 2006. It can be seen from the figure that suction decreases with increasing volumetric water content during rainfall. And then, suction increases again with decreasing of volumetric water content after rainfall cease. During the rainfall from July 1st to 2nd, the tensiometer show positive pressures at deep places (97 cm- 172 cm) on July 1, and at shallow places (30 cm, 60 cm) on July 2. At the same time, the volumetric water content increases rapidly and then enters a very narrow range of variation at each depth. It indicates that the formation of groundwater has occurred at this point.

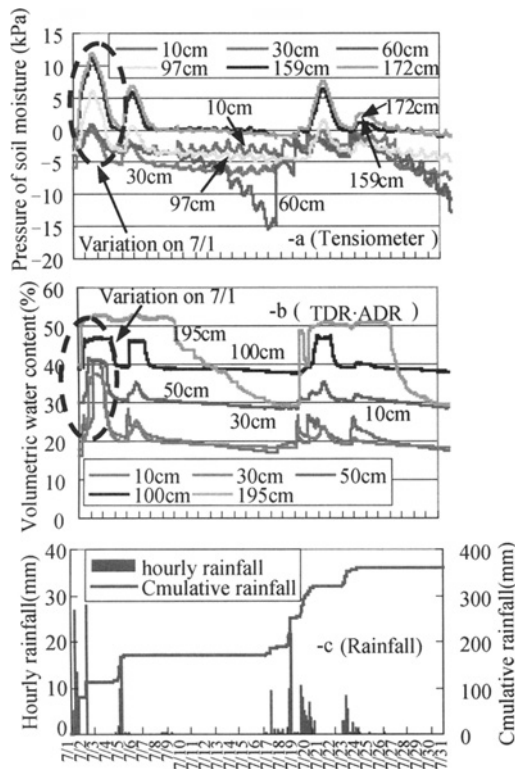


Figure 4. Example of monitoring results of July 2006 at point B3

Descending behaviors of wetting front

Figure 5 shows time history of vertical rainwater infiltration during rainfall. Here, the phenomena will be examined by using the data of rainfall events when the amount of (initial) soil moisture is very low and very high period. Therefore, the data of 2002, when the lowest values of volumetric water content were recorded during monitoring period of 2001 to 2006, would be used. First, in case of the driest period of September 16 to 18 of

figure (a) (average value of initial volumetric water content of 4 installed depths - $\theta_{av_0}=23.3\%$), even though 85 mm of rainfall is fallen, only the volumetric water content of 50 cm depth (θ_{50cm}) increase from 13 to 21 %, and there are no responses of TDR at down to 50 cm in depth. But in case of June 25 rainfall event ($R=43.5\text{ mm}$) with $\theta_{av_0}=32.5\%$, θ_{50cm} increase from 29 to 33 %, and after that the responses of TDR at depth of 100 cm can be seen. Here, θ_{100cm} increase from 37 to 40 % in this event. Next, in case of May 10 rainfall with the smallest amount of rainfall ($R=35\text{ mm}$) and the largest value of moisture content ($\theta_{av_0}=33.4\%$), the rainwater infiltrate to dept of 200 cm.

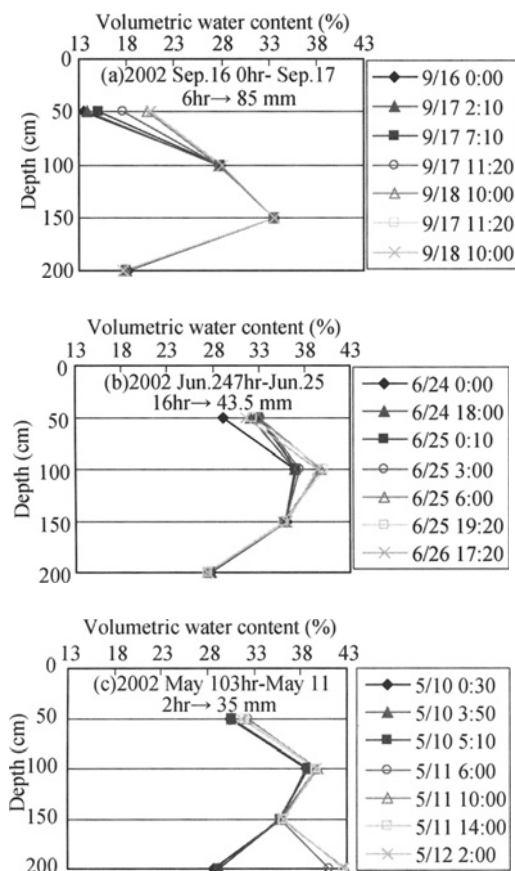


Figure 5. Changes of distribution of volumetric water content during rainfall

Figure 6 shows the required time to infiltrate rainwater to each monitored depth. As shown in the figure, the required time becomes long in order of monitored depth and, it indicates the vertical infiltration of rainwater to bottom of layer. Besides, infiltration time varies in each rainfall event and it can be considered that infiltration speed depends on moisture contents before rainfall and rainfall conditions such as intensity and cumulative time.

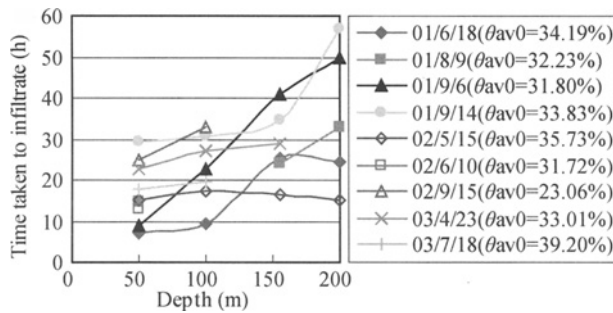


Figure 6. Required times of infiltration to each depth

From those monitored results, downward progress of wetting front to bottom of subsoil layer can be confirmed. Then, average value of increased volumetric water content when it reaches to bottom of layer is around 36 % ($\theta_{50cm}=32\%-33\%$, θ_{100cm} = approx. 40 %, θ_{150cm} = approx. 36 %). It is around 70%-75 % in degrees of saturation (Sr) and that means, the area of wetting front is not fully saturated in this monitored sandy slope. This value of $Sr=70\%-75\%$ can be considered as a critical value of moisture content to keep rainwater in the void of soil and when the amount of water in void exceeds this critical value, the water will move to deep place as free gravity water.

Descent depth of wetting front and precipitation

As above explained, wetting front descends while raising the amount of moisture content to a critical state. Figure 7 is a relationship between amount of precipitation and descent depth of wetting front at point B3. The rainfalls used in this figure were observed data in wet season (May to July) and dry season (August to September) of 2002. The initial water contents are the average values of 4 depths (50 cm, 100 cm, 155 cm, 195 cm) of observed results of TDR at point B3 just before rainfall start. And the amount of precipitation was the cumulative value from the beginning of rainfall until the wetting front reach to each monitored depth. The prospect relationship between descent depth and amount of rainfall can be drawn as dotted line of the figure.

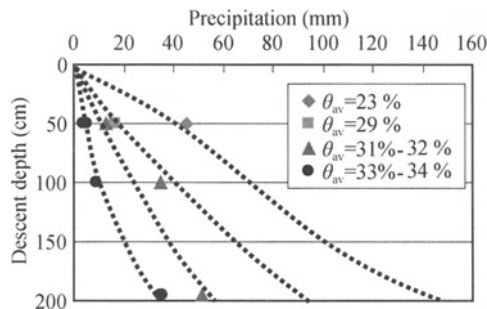


Figure 7. Relationship between descent depth and precipitation

The above observation fact is considered the descent depth of wetting front depends not only on the amount of precipitation but also initial moisture content. That means, rainwater until wetting front descends to bottom of the permeable layer, is supplied to unsaturated layers and that supplied water will be ineffective rainfall to generation of groundwater. Therefore, in cases where cumulative rainwater exceeds the ineffective rainfall, wetting front reach to bottom of permeable layer and then groundwater generation will be started.

Figure 8 is proofing this observation fact. Here, the amount of rainfall in Figure 8 is cumulated values from the start of rainfall until the results of tensiometer at a depth of 172 cm showed positive pressures. As shown in the figure, even though large amount of rain was fallen, wetting front did not reach to bottom when the initial moisture content was small. The reason can be considered that a dry condition of soil with small θ_{av_0} leads to a large amount of ineffective rainfall and therefore supplied rainwater to unsaturated layers will be increase.

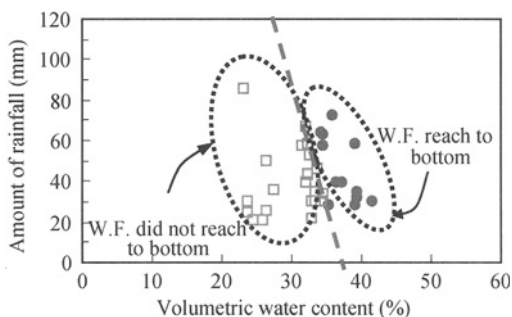


Figure 8. Amount of rainfall and water content which caused formation of groundwater

Groundwater behavior after wetting front reach to bottom of subsoil layer

Figure 9 shows rise up of groundwater level and the amount of rainfall which is cumulative value after wetting front reach to bottom of subsoil layer. As shown in the figure, groundwater level rises up rapidly almost in proportion to the amount of rainfall cumulated since wetting front had hit the bottom.

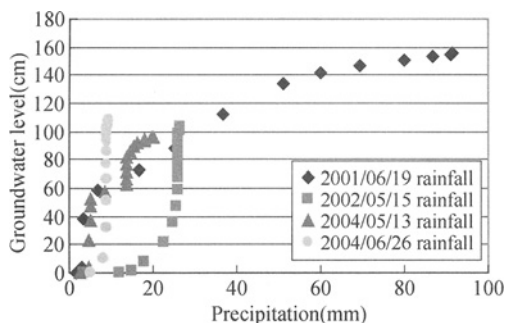


Figure 9. Precipitation and rises of groundwater after wetting front reach to bottom of layer

Therefore, it can be considered that rainwater infiltration after wetting front hit to bottom of layer is similar to piston flow of pushing out. That means, the risk of rain-induced failure rapidly increases after wetting front descends to bottom of layer.

CONCLUSIONS

From continuous monitoring of moisture content, suction and groundwater level, the behaviors of soil moisture became elucidated as below.

- (1) Wetting front descends while raising the amount of moisture content to a critical state. That supplied water can be considered as ineffective rainfall to generation of groundwater and that critical value in this monitored slope is round 70%-75 % in *Sr*.
- (2) Descent depth of wetting front depends not only on rainfall but also initial moisture content. Then, after it reaches to bottom of layer, groundwater generation is started.
- (3) Rainwater infiltration after wetting front reach to bottom of layer is similar to piston flow of pushing out and groundwater level rapidly rises up.

REFERENCES

- Sasaki Y., Moriwaki T., Kano S. and Shiraishi Y. (2001). Characteristics of precipitation-induced slope failure disaster in Hiroshima Pref. on June 29, 1999, and a rainfall index for warning against slope failure disaster. *Tsuchi-to-Kiso, JGS*, 49(7): 16-18.
- Thi Ha, Moriwaki T., Sasaki Y., Kano S. and Dissanayake A.K. (2001). Field measurements of moisture content and suction in masa slope at hiroshima university campus. *Journal of Ground Engineering, JGS*, 19-1: 37-48.
- Thi Ha, Moriwaki T., Sasaki Y., Kano S., Dissanayake A.K., Desiree A.U. and Yamamoto M. (2002). Study on the mechanism of slope failures induced by rainfall. *Proceeding of International Conference on Civil and Environmental Engineering ICCEE*, 99-108.
- Thi Ha, Moriwaki T., Sasaki Y., Dissanayake A.K. and Kano S. (2003). The change in suction and water content in natural masado slopes due to rainfall. *Int. Sym. on Grounwater Problems Related to Geo-Environment, IS Okayama*, 181-187.

ACID MINE DRAINAGE EROSION AND EARTHQUAKE COUPLING ACTION TO SLOPE IN RICH SULFIDE OPEN PIT

Lichun Jiang

*Institute of Safety Engineering, South China University of Technology
Guangzhou 510640, China*

Jilong Zhang

*School of Resources and Safety Engineering, Central South University
Changsha 410083, China*

*Science & Technology Department, China Aluminum Corp.
Beijing 100088, China*

The coupling action by Acid Mine Drainage erosion and earthquake is one of the major inducements of slope instability in chemical (metal) mine. The tests shown that the affected distance by AMD erosion is about 60~100m to slope inner in general; The natural frequency in slope area is small under the influence of steps free face; in earthquake field, the natural frequency of shear stress at fault section is obviously higher than other sections, high stress area mostly distributes at the bottom of slope and fault section; The stress is parallel to the dominant joints direction at the free face of steps; under the coupling action of AMD and earthquake, enrichment area of high stress comes up nearby the free face of the slope; Stress enrichment area of AMD erosion is enlarged, while strength is enhanced, and the crest value of displacement change is increased by 10% comparing with single earthquake stress filed. The sections are ranked from the greater to smaller one based on crest value of displacement inner the slope: the fault section, the centre of slope, the top of steps, and the footing of the slope.

INTRODUCTION

Coast and collapse inducted by earthquake are common engineering geology disasters (JIANG Li-chun, 2005; ZHANG ChuanHeng et al, 2007; Keh-Jian Shou, Cheng-Fung, 2003). The major effects are accumulative action and inspire action (O.Sracek, M.Choquette, et al, 2004; M.M.Vandiviere, VP. Evangelou, 1998), on one hand, it brings out that the structure of slope rock mass loosens, bursting surface & weakness plane displacement and accumulative increasing of pore water pressure; on the other hand, it impels thixotropy liquefaction of slope soft layer and leads slope at critical state to become unstable instantly.

The major damage methods of slope by water are power osmosis and Acid Mine Drainage (AMD) erosion in open pit (Jiang Lichun, 2005; O.Sracek, M.Choquette, et al., 2004; M.M.Vandiviere, VP. Evangelou, 1998; Jiang Lichun, Chen Jiasheng. 2007; Yang Zhifa et al., 1999). Damage effect by AMD is obvious especial for the slope with rich sulfur ore.

There are different scale slopes with rich sulfur in Chinese chemical (metal) mine. For special acid environment, slope endures erosion of acid water solution and action by the earthquake load. It suffers the both actions more obvious along with the extension of mining; it is easy to take place partial collapse even entire instability. At current, the scholars are mostly focused on the slope damage by water power osmosis, but the deformation and mechanics effect of slope rock mass induced by AMD erosion have not been paid high attention (Jiang Lichun, 2005; Zhang Chuanheng et al., 2007; Kehjian Shou, Chengfung, 2003; O.Sracek,M.Choquette, et al., 2004; M.M.Vandiviere, V.P. Evangelou, 1998; Jiang Lichun, Chen Jiasheng. 2007; Yang Zhifa et al., 1999). Few literature reports the coupling actions by earthquake load and AMD action Jiang Lichun, 2005; Zhang Chuanheng et al., 2007; Kehjian Shou, Chengfung, 2003; O.Sracek, M.Choquette, et al., 2004; M.M.Vandiviere, V.P. Evangelou, 1998; Jiang Lichun, Chen Jiasheng. 2007; Yang Zhifa et al., 1999; Wu Shimin. 1997; Liu Yaqun, et al., 2004). This article is to carry on frontier researches on this area with the engineering example at Xinqiao Pyrite mine, based on volumes of experiment investigation (Jiang Lichun, 2005; Zhang Chuanheng et al., 2007; Kehjian Shou, Chengfung, 2003; O.Sracek,M.Choquette, et al., 2004; M.M.Vandiviere, V.P. Evangelou, 1998; Jiang Lichun, Chen Jiasheng. 2007).

ENGINEERING SURVEY

Xinqiao mine located in Anhui province is a deep-concave open pit which is mostly pyrite ore. The design elevation of slope footwall is +426-180m, it is -72 m depth at present. The slope footwall is mostly made of quartz sandstone, arenaceous shale, limestone, feldspar, etc. Faults and joints are filled with a great amount of mudstone; major compositions are illite, chlorite and kaolinite, etc...The average annual precipitation is about 1330mm in mine field. Because the drainage system can not meet the requirement of production schedule so that part of precipitation is constantly gathered to the bottom of mining pit(top of ore body along with extension of mining). With the disturbance from explosion and mechanical vibrating, the original close texture of exposed pyrite body had been damaged, ore lump size is changed to small, and contact area with air and water is increased, the pyrite is constantly oxidized, bringing out a mass of acid solution which ceaselessly reacts with the Gaolishan sandstone, shale, changing the rock microstructure, and decreasing the macroscopic mechanics strength of slope, it induces large area collapse and footwall instability, therefore brings out great economic loss to the mine. The exterior of serious erosion at the slope footwall is shown in Figure 1.



Figure 1. The exterior of slope footwall at Xinqiao mine

AMD EROSION TEST

Multiple tests had been carried out to analyze mechanics change characteristics of quartz sandstone before and after AMD erosion, such as shear test at home position, point loading test and environmental test of AMD action simulation (Jiang Lichun 2005; Yang Zhifa et al., 1999), parts of test result are set out in Table 1.

Table 1. Point loading data of C_{1g} sandstone [$\sigma_c = 24I_s(50)$, $\sigma_t = 2.2I_s(50)$]

Item	Test position	Sample quantity	Intensity index $I_{s(50)}/\text{MPa}$	Compressive strength (σ_c/MPa)	Tensile strength (σ_t/MPa)	Remark
Quartz sandstone	PD-1、PD-2	19	4.35	93.21	9.71	fresh
Quartz sandstone	Inside stope (-16m)	28	3.05	73.21	6.71	light erosion
Siltstone	Inside stope (-16m)	38	3.36	80.64	7.39	light erosion
Quartz sandstone	Drill #5	47	2.64	63.36	5.81	light erosion
Quartz sandstone	Drill #10 (bottom)	29	3.49	83.98	7.70	light erosion

Before and after AMD erosion, the test results indicated:

- (1) The shear strength between layers of rock mass is between 0.351 to 0.642MPa, cohesion is between 0.426 to 0.589MPa, friction strength is 0.039 to 0.07MPa, and internal friction angle is 37.57° to 41.96° . After AMD, shear strength between layers of rock mass and cohesion has obviously change, value is decreased by 13.2% to 21.3%, internal friction angle between layers is reduced by 5.0% to 7.5%.
- (2) The shear strength and cohesion between layers decrease with the increasing of dipping time, reaction between acid water and rock mass become weaker with the increase of inner distance of vertical slope, it approximately followed negative linear relation, and the affected distance by AMD is 60 to 100m inside of vertical slope.

EARTHQUAKE ACTION

Predominant period test

The researches indicate (Wu Shimin. 1997) that field dynamic behavior directly affects the loss in earthquake disaster. In general, each field has respective predominant period, once the predominant period of ground shock is close to period of the structure, the structure would seriously damaged. The foundation in the certain range of observation site can be approximately regarded as a linear system, the source of earth microseism is taken as input, and earth microseism of observation point is as output. The earth microtremor spectra $Y(\omega)$ are product of earth microtremor source spectra $X(\omega)$ and transfer function $H(\omega)$:

$$Y(\omega) = H(\omega)X(\omega) \quad (1)$$

In order to find out more about the slope characteristics of earth microseism in Xinqiao mine, preventing the disturbance by human factor, the test was arranged at night 1:00 AM~3:00AM; there were no traffic vibration and engineering vibration close to the test point, and also noise free. The test point is at +144m bench of #19 geologic exploration line at the bottom of slope, the major composition is quartz sandstone, there are six test points separately set at the bench, three vibration pickups for each test point recorded signal at three directions of south-north, east-west, and perpendicularity. The test equipment is DH5935N dynamic signal test system, the test position is shown in Figure 2, and the result is shown in Table 2.

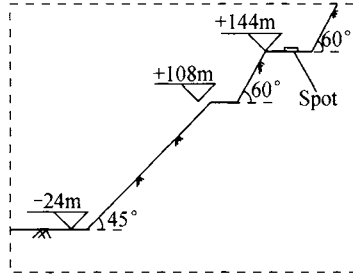


Figure 2. Test points position of predominant period

Table 2. Results of slope natural frequency and period

points	predominant period (s)	predominant frequency (Hz)	Max. period (s)	perk value of frequency (Hz)
1	0.259	3.86	0.435	2.3
2	0.229	4.35	0.313	3.2
3	0.201	4.97	0.208	4.8
4	0.215	4.65	0.27	3.7
5	0.183	5.45	0.294	3.4
6	0.193	5.18	0.294	3.4
7	0.189	5.29	0.303	3.3

The test result indicates: the natural frequency of slope in Xinqiao is 3.86-5.29Hz, predominant period is 0.189-0.259s. On account of removal of surface soil tectum in Quaternary Period, groundwork of step almost appears rigid, magnification effect is obviously weakened. Due to the effect of step free face, the natural frequency of slope area is small.

Earthquake loading

The choice of earthquake waveform is a complicated issue; lots of literatures have relative reports (Liu Yaqun, et al., 2004; Researches Team of Three Gorges Project Engineering in the Great River, 1992). Science academe of Changjiang water conservancy committee had a characteristic comparison between national earthquake wave in Qianan and Sanxia artificial earthquake wave (Researches Team of Three Gorges Project Engineering in the Great River. 1992), analyzed the dynamic response of Sanxia dam to different earthquake waveform. The relation formula between the acceleration of ground peak value and earthquake intensity was summarized as :

$$a = 10^{(I \log 2 - 0.01)} \quad (2)$$

Where a is the acceleration of ground peak value, and I is earthquake intensity.

Based on the history record, the maximum earthquake scale is 6.25 at Xinqiao mine since A.D.294; the maximum acceleration peak value is then 1.86m/s^2 according to equation (2).

Input acceleration time path of earthquake wave is $a = 0.2g \cos(\frac{2\pi}{T}t)$, the main period T of earthquake is 0.2s. Based on transmit theory of earthquake elastic wave, the transmit velocity of longitudinal wave and transverse wave in the medium of slope are:

$$\left. \begin{aligned} V_p &= \sqrt{\frac{E(1-\mu)}{\rho(1+\mu)(1-2\mu)}} \\ V_s &= \sqrt{\frac{E}{2\rho(1+\mu)}} = \sqrt{\frac{G}{\rho}} \end{aligned} \right\} \quad (3)$$

where E is medium modulus of elasticity, G is medium shear modulus, ρ is medium density, and μ is medium Poisson ratio.

Velocity time path integral of earthquake wave is translated into relative stress time path equation:

$$\sigma_s = 2 \sqrt{\frac{E}{2\rho(1+\mu)}} \cdot \rho \frac{0.2g}{2\pi} T \sin\left(\frac{2\pi \cdot t}{T}\right) = \frac{0.2g}{\pi} \sqrt{\frac{E\rho}{2(1+\mu)}} \sin\left(\frac{2\pi \cdot t}{T}\right) \quad (4)$$

NUMERICAL CALCULATION

According to slope topographic survey at Xinqiao mine slope, model is built upon the section crossed by the #19 exploratory line which is located special instability slope (see Figure 4.), the elevation of the lowest point in pit is -72m, the highest elevation of slope is +324m, and the elevation of pit closure is +36m. The ultimate pit slope angle by design is 41° to 42.9° , actual slope is 41.5° , and cross section angle of step is 47° above 0m and 50° below 0m, respectively. Reverse face of mining pit is initial form, closed with the earth's surface at +36m. Exploit method at Xinqiao mine is movable roof type carried out by motor vehicle transportation, hangingwall of orebody always keep movement, the stability is ignored here, steps can be simplified as one bench, and cross section angle is 60° . There were two faults at the section of #19 exploratory line at slope footwall, there into, initial position of F4 fault is 97m, prolonged 170m, section projection length of F4 is 125m, fault displacement is 1.0m, dip angle is 30° , filling is clay; initial position of fault F11 is +50m, prolonged 120m, section projection length is 80m, fault displacement is 1.2m, dip angle is clay also. Length of exposed joint is about 1.0~10.0m, width is quite small, fillings were mud, calcium film and pyrite vein. UDEC is applied for relative numerical calculation.

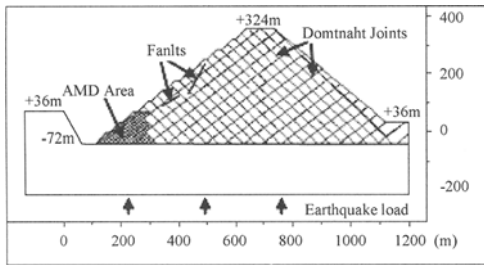


Figure 3. Distribution of fault and AMD inside slope as well as earthquake wave

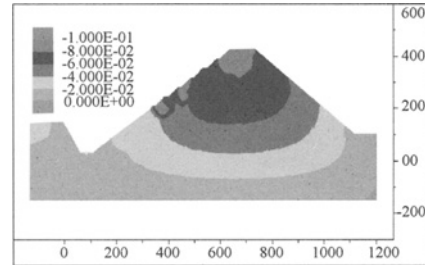
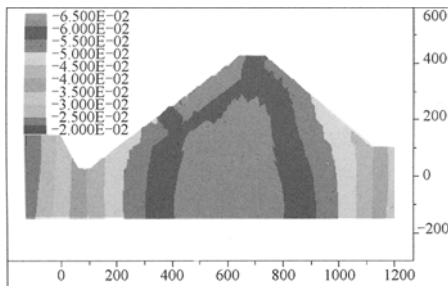


Figure 4. Slope displacement distribution at y direction (m)

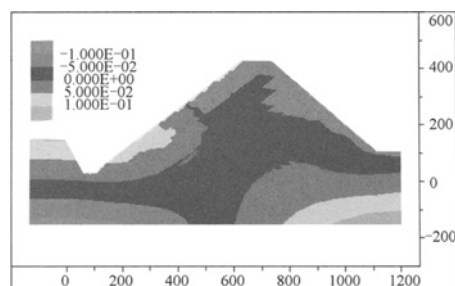
Initial condition

In order to simplify the calculation model, based on the investigation analysis of joints distribution, only dominant joints of group 1) & 2) have been taken into account.

- **Initial stress.** Initial stress is from actual measurement on the spot, the initial slope stress at Xinqiao is most of deadweight, stress in the vertical direction is -8.279MPa , stresses in remaining horizontal directions are 2.76MPa and 5.193MPa , respectively.
- **Active region of AMD.** #1 ore body at Xinqiao clings to super stratum of slope footwall, average thickness is 20m above, embedding height of orebody is between +36 and 180m. At current, the mining is close to -72m . According to exposure status of adit PD-1 and PD-2, home position shear tests and point load tests, AMD is mostly focused on $-72\text{--}+36\text{m}$ position of slope, 60-100m range of vertical slope is weaken area (Figure 5).



(a) y axis



(b) x axis

Figure 5. Slope displacement distribution in y and x axis (m)

- **Rock mechanics parameters.** Based on test result on the spot (JIANG Li-chun. 2005), rock mechanics parameters of pit wall are presented in Table 3.
- **Response time.** The vertical height of slope at Xinqiao mine is about 500m, by earlier research results (JIANG Li-chun. 2005; LU Xiao-bing, et al. 2002; QI Lian-sheng. 2000), 0.75s is adopted for the dynamical response time of slope. Response time to AMD is result of slope achieving balance time.

Table 3. Characteristics parameters of slope

Rock	Bulk density ($\gamma/\text{kN}\cdot\text{m}^{-3}$)	Poisson ratio/ μ	Coefficient of rigidity (GPa)	Compressive strength (σ/MPa)	Tensile strength (σ/MPa)	Modulus of elasticity (E/GPa)	Cohesion (c/MPa)	Internal friction angle ($\varphi/^\circ$)
Quartz sandstone	26.8	0.28	26.6	93.2	4.9	38.3	0.576	36.7
Sandstone etched by AMD	24.6	0.23	23.6	68.3	3.8	28.3	0.556	32.6
Clay (filling)	18.0	0.35	0.389	0.46	0.019	4.0	0.026	21-25

RESULTS AND ANALYSIS

(1) AMD erosion

After slope achieved balance in the condition of deadweight, it is attacked by AMD; colorful plot of slope displacement distribution at y direction is shown in Figure 4.

Results shows after gravity stress field of slope realized balance, initial disturbance increased obviously in the AMD weak area, the shear stress at the bottom of slope and AMD centre area were reduced by 52.0% and 64.7%, respectively, range of displacement disturbance increased in y axis, crest value of variety increased by around 10%. The shear stresses in top of slope and fault position were decreased by 22.0%~31.4%, slope displacement in Y axis had not obvious change; AMD erosion mostly performed to alter mechanics behavior of rock body in AMD weakened area.

(2) Earthquake load (0.75s)

After slope achieved deadweight balance, colorful plot of slope displacement at y and x direction under earthquake load are shown in Figure 5.

Results shows, under the earthquake stress field, the slope displacement disturbance in y direction submitted symmetric gradient distribution at left and right terminal, top of slope had bigger disturbance than bottom. The displacement disturbance in x direction submitted symmetric distribution along vertical axis, bottom is bigger than top. Curves of shearing stress with time are similar for each of points in slope, it submitted sine wave variation, and natural frequency of shear stress in fault position is obviously higher than other positions. High stress concentration areas were mostly distributed on the bottom of slope and fault position. The stress is mainly parallel to $192^\circ\text{-}243^\circ < 61^\circ\text{-}78^\circ$ dominant direction of joints nearby the steps with free face; the stress is mainly parallel to $131^\circ\text{-}141^\circ < 38^\circ\text{-}67^\circ$ dominant direction of joints on the reverse of slope. The fault area had biggest disturbance crest value based on the displacement curve of record unit with time.

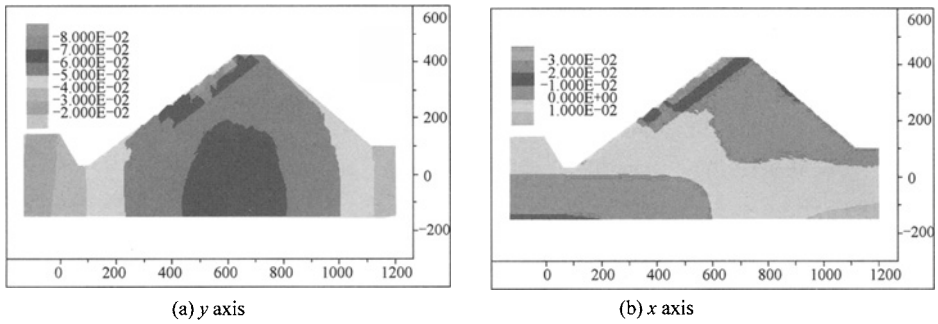


Figure 6. Displacement distribution of slope at y and x axis (unit: m)

(3) Coupling action by AMD and earthquake loading (0.75s)

After slope reached deadweight balance, under the coupling actions by AMD and earthquake load, colorful plots of slope displacement at y and x direction are shown in Figure 6; displacement and shearing stress of record unit at y axis with time are shown in Figure 7 and Figure 8.

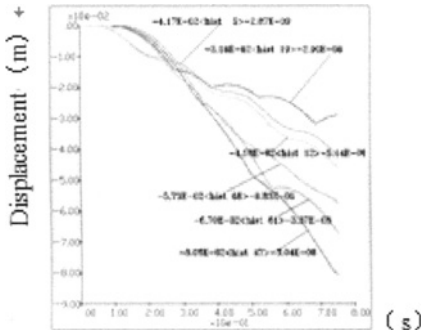


Figure 7. Displacement curves of record unit with time at y axis

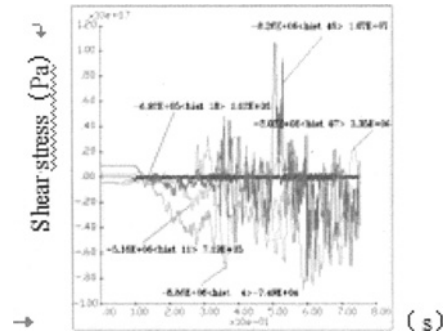


Figure 8. Shearing stress curves of record unit with time

Under coupling action by AMD and earthquake, stress enrichment area in weak area by AMD is enlarged, intensity increased, crest value of stress change is increased by 10% comparing with single earthquake stress field. Density of stress enrichment area along free surface neighborhood of slope is increased; weakened along boundary of slope bottom. The maximum shear stress is increased 3.45 times in the toe of step, the max shear stress in the centre of AMD is increased 1.52 times; the max. Shear stress at the top of step is increased 0.64 times; the max shear stress at the fault position is increased 1.81 times. Crest value of displacement change from the great one to smaller one are: fault position, centre of slope, top of step and bottom of slope. Under the coupling action, the maximum shear stress is enlarged by AMD weaker area and fault position; stress enrichment phenomenon came up along free surface neighborhood of slope.

CONCLUSIONS

- (1) The shear strength and cohesion between layers decrease with the increasing of dipping time, reaction between acid water and rock mass become weaker with the increase of inner distance of vertical slope, it approximately followed negative linear relation, and the affected distance by AMD is 60 to 100m inside of vertical slope.
- (2) Test result shown that natural frequency of slope is about 3.86-5.29Hz at Xinqiao mine slope, predominant period is about 0.189-0.259s. For the surface soil tectum in Quaternary Period had been removed, groundwork of slope is rigid; the natural frequency in slope area is small under the influence of steps free face.
- (3) In earthquake field, the natural frequency of shear stress at fault section is obviously higher than other sections, high stress area mostly distributes at the bottom of slope and fault section. The stress is parallel to the dominant joints direction at the free face of steps.
- (4) Under the coupling action of AMD and earthquake, enrichment area of high stress comes up nearby the free face of the slope. Stress enrichment area in AMD weak area is enlarged, while strength is enhanced, and the crest value of displacement change is increased by 10% comparing with single earthquake stress filed. The sections are ranked from the greater to smaller one based on crest value of displacement inner the slope: the fault section, the centre of slope, the top of steps, and the footing of the slope.

ACKNOWLEDGEMENT

Foundation item: Project (50574099) supported by National Natural Science Foundation of China ;Project (2004CB619200) supported by National Key Fundamental Research and Development Program of China.

REFERENCES

- Jiang Lichun, Chen Jiasheng. (2007). Erosion characteristic of slope sandstone soaking in acid mine drainage. *J.Cent.South Univ. Technol*, 14(2): 236-242.
- Jiang Lichun. (2005). Safety environmental analysis and engineering control researches on unstable high & steep slope in deeper concave open mine. *Central South University*.
- KehJian Shou, Chengfung. (2003). Analysis of the chiufengershan landslide triggered by the 1999 Chi-Chi earthquake in Taiwan. *Engineering Geology*, 3(68): 237-250.
- Liu Yaqun, et al. (2004). UDEC Simulation on dynamic response of rock slope of huangmailing phosphorite mine under explosion. *Chinese Journal of Rock Mechanics and Engineering*, 23(21): 3659-3663.
- Lu Xiaobing, et al.(2002). Dispersion analysis on longitudinal cofferdam under earthquake loading during the third period of three gorges project. *Rock Mechanics and Engineering Journal*, 21(2): 158-163.
- Vandiviere M.M., Evangelou VP. (1998). Comparative testing between conventional and micro encapsulation approaches in controlling pyrite oxidation. *Journal of Geochemical Exploration*, 64: 161-176.
- Sracek O., Choquette M., et al.(2004). Geochemical characterization of acid mine drainage from a waste rock Pile,Mine Doyon,Quebec,Canada. *Journal of Contaminant Hydrology*, 69: 45-71.

- Qi Liansheng. (2000). Dynamical response analysis and application of slope. *Chinese Academy of Science*.
- Researches Team of Three Gorges Project Engineering in the Great River. (1992). *Researches on Important Geology and Earthquake Problems of Three Gorges Project in the Great River*. Geology Press.
- Wu Shimin. (1997). *Wave in Soil Medium*. China Technology Press.
- Yang Zhifa et al. (1999). *The Slope Stability Researches in China Open Mine*. China Technology Press.
- Zhang Chuanheng, et al. (2007). Earthquake-induced soft-sediment deformation structures in the Mesoproterozoic Wumishan Formation, North China, and their geologic implications. *Sci China Ser D-Earth Sci*. 50(3): 350-358.

DANGER OF THE LANDSLIDE ACTIVITY OF SLOPES ON THE RAILWAY LINE CHINA – KYRGYZSTAN – UZBEKISTAN ON SITE KARASU-TORUGART

K.Ch. Kojogulov, O.V. Nikolskay
Institute of physics and mechanics of rocks
National Academy of Science of Kyrgyz Republic,
Bishkek, Kyrgyzstan

Construction and operation of roads in seismologically active mountain-folded areas are connected by a number of specific problems, one of which is maintenance of long stability of directly slope and engineering constructions in a pedigree file. The most typical infringements of slopes stability of road dredging are slipping and falling of the riding and local slopes, less often - slipping of all road dredging.

INTRODUCTION

The modern relief of the area of the projected railway line passage was generated in the newest stage of geological history of Tien Shan. The area is carried to regions of high seismicity. The line of passage of railroad line Karasu - Torugart (on border of Kyrgyz Republic and the Peoples Republic of China) is characterized by complex tectonics and crosses a number of ridges. The internal structure of each such structures - is complicated by earlier folded movements. The territory of laying lines of the railway is characterized by a wide range of relief forms, amplitude relative exceedings and hypsometric levels.

Explosive infringements of significant extent and amplitude are rather numerous. The majority of them has sublitudes and the east-northeast the prodeleting conterminous with prodeleting of the basic structures of the area.

Studying features of a rock massif within the limits of the passage of the railroad line China-Kyrgyzstan-Uzbekistan (Karasu - Torugart) on territory of Kyrgyzstan the qualitative and quantitative estimation of tangential pressure of compression, sizes of a horizontal component and average speeds' gradients has been lead. Calculations and map of a horizontal component and average speeds' gradients of the territory of Kyrgyz Tien Shan (Figure 1) (Lemzin I.N., Institute of seismology NAS KR) have been put in a basis of this estimation.

The analysis of a horizontal component of total deformations of a bend of tangential compression on structures has shown, that the line of the railroad line passes as through sites with the abnormal (raised) sizes of compression with values within the limits of (0,05-0,40 m/years), through sites with background (0,01-0,05) m/years and average values (0,005-0,01) m/years, and through sites with the minimal values of compression size (<0,001¼/year). The line of the railroad line passes through three sites with the raised sizes of compression (with factor from (0,05 up to 0,40) m/year with their general extent of 27 km (or 10 % from the general extent of a considered railroad line).

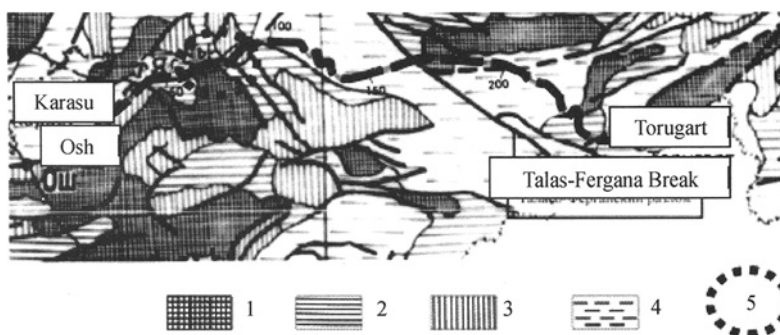


Figure 1. A map of horizontal making tangential pressures on the railroad line. 1 – abnormal sizes of compression 0,05-0,40; 2 - background sizes of compression 0,01-0,05; 3 - average sizes of compression 0,005-0,01; 4 - the minimal sizes of compression; 5 railroad line's most dangerous site.

On these sites the landslide phenomena are intensively developed exogenous processes in the form of wind erosion, lateral and ground erosion of constant and temporary water-currents, landslide and falling phenomena.

On the basis of the lead analysis of deformations sizes, speeds of an earth's crust and display exogenous geodynamic processes communication between these phenomena is established. Thus, the most complex site is the site of a railroad line of km 55-70 which passes on the territory having the maximal parameters both horizontal contenting deformation of a surface, and average gradients of speeds and revealed the greatest quantity of displaying slope processes in the form of landslides.

LANDSLIDE POTENTIAL

Geological background

Landslide is the most typical and widespread process on the majority of positive forms of a relief. These are modern and ancient landslips in a classical variant:

- precise contours of the take-off in a back part;
- steep and hillside character of wall of the landslide circus;
- cascade-ledged character of a surface of the shifted weights in the top and average part of the landslide body;
- fanlikely split and convex fronts and flanks of the landslide bodies;
- various till extents of a transit way and volumes of the shifted masses.

Morphologically are dated in most cases for the bottom half of slope of eminences, less often - grasp a slope up to a local watershed. And, the last have the maximal volume of the shifted masses.

Except for landslips of the classical type there are the numerous landslips dated to foothill part of eminences slopes. The landslide phenomena in the area develop, basically, on clay cretaceous and paleogene age, inclined to sliding. It is promoted by higher watering of the slopes of the northern exposition, concurrence of a bias of a radical slope to falling thickness of breeds secondary Paleozoic, long use of the grounds under irrigated agriculture, since an

extreme antiquity, and also existing irrigational system in aggregate with intensive irrigational and road construction of last time. Except for it the important factor of infringement of integrity of a slope is the dense network of tracks subparallel to the general prodeleting of the radical slope, promoting penetration of a moisture in soils and to formation of cracks of lateral repulse and take-off. - obvious preconditions for formation of massif yield and active landslide processes in the long term.

Practically on all surface of the slopes predisposed to display landslide processes, numerous hillocks of crippling. Here numerous cracks of lateral repulse and take-off. The effect of the landslide processes amplifies presence numerous tracks subparallel to prodeleting of slopes on which cracks of take-off and repulse are formed.

Except for it essential influence on soaking integumentary of soil slopes there are channels and aryks, submitting water on the flat watersheds of an eminence used under irrigation arable lands.

The estimation of landslide dangers of hillsides on sites of passage of the line of new China - Kyrgyz - Uzbek railway-trunk in territory of Kyrgyz Republic was made by two variants:

- on the left board of the river Jassy (further a variant 1), and
- on the right board of the river Jassy (further a variant 2) on a site of the railroad line of 40-70 km.

By variant 1 road passes on the left board of the river Jassy.

The railroad line is laid in the bottom part and along bottom of the radical slope in a zone of emerging modern active landslide forming process.

Landside site covers by river-bed part of the left board of valley Jassy from a mouth of stream Kulduk up to village Kaakkyr. In a ledge middle-quarter terraces on this site are fixed traces upper-quarter landslips in the form of fixed take-off crater and landslide masses. In 2003 as a result of long storm rains in a mouth of stream Kolduk on 12km of motorways the Myrza-Ake-Kara-Shoro in 25km from Uzgen the powerful landslip which has captured a loessial cover of the terrace and cretaceous clay with prolayers of limestones has descended. The volume of a landslip has made 5,5 mln m³. Thus 9 cattle which for a moment of landslip going down were on the given site were lost. The landslip has closed a traffic part of the road in width of 750 m, the height of a blockage reaches 10 meters. 15 supports of an electric main and communications are destroyed. The bed of the river Jassy was blocked by a landslide body for short time. In this connection without the transport message there were some settlements Kuldukskoj and Salam-Alikskoy rural administratives of Uzgen area, Osh region with the population more than 15 thousand people.

At repeated survey of this landslide in the autumn 2003 revealed presence of cracks of the take-off on a slope above the crater of the take-off, that threatens a new going down of landslide, possible a larger one.

Predisposition to slipping of thickness of covering formations promote higher watering of the northern slope of a water-separate massif, long use of the grounds under irrigated agriculture, since an extreme antiquity, and also intensive irrigational and road construction.

This board of a valley of the river Jassy lengthened and strongly watering, it is generated by a series lengthened terraces of quarter age. Radical breeds (limestones, sandstones, marl) are blocked by integumentary loams.

In a slopes' relief precisely traced ancient and modern landslips and collapses which are fixed on walls of failure and traces of the displaced soil masses. Fresh landslides have take-off cracks, displaced on various distances of landslide masses, short earth flows.

Revealed landslide processes on the railway line

AK30-AK40. In a relief traces of ancient landslips (Paleo-landslides) are shown. On the slope traces of the subsidence, the displaced soils masses are everywhere visible. In the basis of the slope shaft of heavings of modern landslips are traced. On the western slope landslips gravitate to breaks zones of northeast prodeleting in an middle part of the slope to the West from village Lenin. On the east slope uneven-age landslips on Paleogene and quaternary sediments form large Uzgen landslide with total area more than 5km². The failure and slipping of unstable masses of the ground begins from a crest of the basic watershed and reaches a modern channel of Kara-Dar'ya River.

In 1990 in this area there was an earthquake by force of 5 points under the Richter scale that has led to activization of landslide process. In 1993-1995 precipitations in the form of rains and snows have dropped out in total 2830 mm. In a combination to the begun activization of slope process, action of precipitations and overwatering of the ground has led mass going-down of the landslide during 2 km on prodeleting of the slope.

In 1998 after incessant rains there was a repeated motion of the landslide. In the basis of a slope passes a break tracing puddles and springs. A principal cause of landslides on this site is underground waters. Rocks in which landslides are formed are loams pale-yellow.

AK45 +400. The landslide was generated in loess-like rocks, a wall of failure of 10 m. Volume of a landslide $\approx 500\ 000\ \text{m}^3$. Are visible first cracks above the edge of failure, repeated activization is not excluded.

AK49+300-AK69. Slope of ancient landslide. Borders of ancient landslides (Paleo-landslides) are visible. On separate sites of a slope the phenomena of subsidence and first cracks of preparation for formation of landslides are noted. A slope on all extent has danger of landslide.

On the western slope landslides gravitate to breaks zones of northeast prodeleting in the middle part of a slope. On east slope uneven-age landslips on Paleogene and quaternary sediments form large Uzgen with total area more than 5km². Failure and slipping of unstable masses of the ground begins from a crest of the basic watershed and reaches a modern channel of the River Kara-Dar'ya.

On this site on AK62+200 - AK62+500 in 2003 the landslide in volume 5,5 million m³ has descended. On a tentative estimation the wall of failure of a landslip makes 15-17 m, width of a landslip in its top part - 200-250 m, in the bottom 750 m. Length of the landslide massif 800-850 m. Landslide masses have blocked road and a channel of the river Jassy (Figure 2).

At repeated survey of this landslide in the autumn 2003 presence of cracks separations a on the slope above the crater of separation is revealed, that threatens going-down of a new, possibly larger landslide.



Figure 2. A landslide on the left board of the River Jassy on the average current

By *variant 2* line of the railway passes on the right board of the river Jassy. The line crosses the slopes combined by radical breeds (limestones conglomerates sandstones), the integumentary formations blocked by a cover (loams coarse-grained) capacity of 1-5 meters. The bottom part of the slope (10-15m from a highway) is crossed with a break (?). On a slope mud-stream traces in the width of 15-20 meters crossing a highway, fine earth flows (width 20-50sm) and small taluses are visible.

Principal causes of formation and activization of landslides on hillsides by a *variant 2* are:

- a) trim of landslide slope of highway,
- b) atmospheric precipitation.

Large first cracks, traces of active landslide activity within the limits of the surveyed site it has not been revealed. On separate sites of a line infringement of stability of breeds on slopes proceeds in the form of failure of separate blocks of insignificant volumes, mass failure of rock blocks has not been revealed. Traces of landslides-streams of insignificant volumes in loess-like loams are revealed.

Within the limits of this site on km 55+000 - km 55+750 the zone of failure in sandstones was generated by extent of 100-150 meters. Failure proceeds in the form of failure of separate rock blocks of insignificant volumes, mass failure of rock blocks has not been revealed.

On a site of km 59+000 - km 59+400 are revealed traces of landslides-streams in loess-like loams. The reason of such streams, most likely, is having watered the fields of sunflower located on a slope. At inspection of a slope it has been revealed ditch, passed directly on top of the slope which serves as the reason of accumulation of water and seepage it in soils of the slope.

km 60 - km 74. The line crosses gentle slopes without obvious attributes landslide activity and traces of ancient landslips. On a site of 73 km pale-yellow loams lie on conglomerates and watered. In bottom of a slope traces of the landslip which has descended in the last years of the small sizes are visible (Figure 3).



Figure 3. Landslide slopes on the right board of the River Jassy on the average current

Prominent feature of this site is that by a variant 1 and 2 line of a railroad line crosses a geodynamic zone with active horizontal and vertical displacement .

SUMMARIZATION

On the basis of the comparative analysis of display landslide activity of hillsides of the line of the projected railway by a variant offered by the First Design and Survey Institute (of Lanchow) of the Ministry of Railways of the Peoples Republic of China and by a variant offered by Open Companies " Transproekt" (Almaty) the following is established:

1. On a geological structure the right and left boards of valleys of the Rivers Jassy (Jazzes) and Kara-Dar'ya have no basic distinctions.
2. On the left and right boards of a valley the maximal values of deformation factor of a bend and development geodynamic processes in the form of landslides are established.
3. A geomorphological structure of the right and left board of valleys of the rivers Jassy (Jazzes) and Kara-Dar'ya noticeably differ. On the left board there are ancient and modern landslides, a part from them is active.
4. The left board of a valley more watering in comparison with the right board that leads to high landslide activity.

In the result of the comparative study of the geological condition of the right bank and left bank variants of the passing railway line, the right bank variant has advantages of:

- passing railway line through dryer slopes of the South exposition,
- less rivers' flow and streams from this slope,
- a big comparative resistance of slopes (practical absence of large landslides).

In connection with high landslide activity on the left board of the River Jassy (Jazzes), construction of the trunk-railway China-Kyrgyz-Uzbek on site AK30-AK69 is inexpedient from the economic point of view and from the point of view of a safety of construction and operation of the trunk-railway.

Construction and operation of the trunk-railway China-Kyrgyz-Uzbek on the right board of the River Jassy (Jazzes) is economically justified and provided stability of slopes, even when presence active technogenic loadings.

REFERENCES

- Trofimov, V. T. (1976). Engineering Geology of USSR - Moscow, MGU V.7.
- Sidorenko, A.V., Pomazkov, K. D. (1972). "Geology of USSR", Nedra, Vol. 2, 15.
- Gataulin F. S., Kojogulov K.Ch., Nikolskay O.V. (2004). "Geodynamic processes on the railway line China-Kyrgyzstan-Uzbekistan (on the site Karasu-Torugart) //Geodynamics and Stress State of the Earth's Bowels". *Proceeding of the International Conference Novosibirsk*, Institute of Mining Siberian Branch Russian Academy of Science. p. 348-354.
- Masadikov, E. K., Kojogulov, K. Ch., Nikolskay O. V., Gataulin F. C., Kurenkov Y. V. and Trutnev G. R. (2002). "*Eurasian railway corridor through Kyrgyzstan*". - Bishkek: Ilim. - p. 118.

STUDY ON UPLIFT TEST OF PRESSURE-DISPERSIVE PRESTRESSED CABLE IN SLOPE REINFORCEMENT PROJECT

Wei Li, Haigui Kang

*The state key laboratory of coastal and offshore engineering, Dalian University of
Technology, Dalian 116024, China*

With the background of a reinforcement slope project in the Wan-Ping expressway (Henan, China), this paper studies the uplift test of the non-adhesive pressure-dispersive prestressed cable. The determination method of test parameters and the whole test process are expatiated. The result shows that there are elasticity phase and plastic phase in the P-S curve relating the tensile strength to the end displacement of the cable. Some problems on the test are also analyzed. The results obtained from the study enrich the data and experience of uplift test for this kind of anchorage cable and have important reference value.

INTRODUCTION

In recent years, the pressure-dispersive prestressed cable has broad application in the deep foundation project and the slope reinforcement project. The most notable characteristic of this type of anchorage cable is that the prestressing force is dispersed in the form of pressure in different soil layers by the supporters which belong to different cable elements. Because of the pressure on the anchored cement paste is more homogeneous; that is to say, the strain concentration is much less obvious than that in the traditional tensile cable, the crack in the anchored cement paste can be reduced relatively. Based on the structure of the pressure-dispersive prestressed cable, more attentions should be paid to the load control and some other aspects during the uplift test. Owing to the test data on the capability of the pressure-dispersive prestressed cable under different geology condition in different area are much more insufficient, it becomes necessary and important to enrich our experience through more test.

Uplift test is a conventional test of prestressed cable which helps to ascertain the relevant parameters of the cable and provides the necessary science basis for the choice of scheme during the design phase. The present paper expatiates the whole test process and studies the characteristic of the cable in this kind of geology condition and enriches the data on the design, application and uplift test control of pressure-dispersive prestressed cable.

GEOLOGY

The test slope, with the attitude of stratum 190° - 210° and the stratigraphic dip 30° - 40° , is located in low mountain area at an altitude of 244.43-339.83m. The angle of strike line between the road and the stratum is about 14° . The slope, whose main lithology are thin

sandstone, mudstone and glutenite, consists of mantlerock (5.0-6.0m) and loam (7.4-9.0m), with the shear strength parameters unit weight $\gamma = 20.0\text{kN/m}^3$, cohesion $c = 25\text{kPa}$ and friction angle $\Phi = 20^\circ$. And the interstitial water level is 0.8~3.0m.

GENERAL SITUATION OF PROJECT

A supporting system named “combined supporting system with non-adhesive pressure-dispersive prestressed cable and concrete lattice beam” is used. The cable, with the diameter 130mm and standard intensity 1860MPa, is consisted of high-strength, low-relaxation strands ($6 \times 7\Phi 5$) without cohesion combined. This project is estimated to accomplish about 244 pressure-dispersive prestressed cables that have the single length from 20m to 33m and whose axis makes an angle of 20° with the horizontal line. The strength of the anchored cement paste water with the cement ratio 0.45-0.50 is 42.5MPa. The lattice beam and compression supporter under the anchor head are concreted using concrete grade C40.

UPLIFT TEST

The purpose of uplift test is to ascertain the maximum bearing force of the cable and then to control the choice of design parameters or optimize the construction technology and ensure the effect of the slope reinforcement project. (ZhuHuan-chun et al., 1999)

After thinking synthetically about the economy and reinforcement effect, three full-size grouted cables (11m, 13m, 15m) are constructed.

YDC1100 hydraulic jack, with Y-150 pressure gauge (Scale 60MPa, precision class 1.6), is used as the loading device.

Table 1 shows the relevant parameters of anchorage cable in the uplift test.

Table 1. Parameters of test anchorage cable

Test cable No.	Depth (m)	Number of supporter	Space between supporters (m)
SM_1	11.0	3	3.6
SM_2	13.0	3	4.3
SM_3	15.0	3	5.0

Structure of anchor

The pressure-dispersive prestressed anchor cable is usually divided into three parts: interior bond section, free-segment, external bond section. Three inequality cable units are fixed to three rigid supporters so that the pressure is dispersed in different soil layers. (Jia Jinqing et al., 2004)

The structure of test cable is as shown in Figure 1.

Technical route for uplift test

Theory of compensate stretching method

Integral tension method is improper in the test because of the length difference of the cable unit. Otherwise, the prestressing force acting on different cable unit is inhomogeneous which

may result in the extension difference among the cable units. Compensate stretching method is used to solve this problem.

Figure 2 shows the units of the test cable.

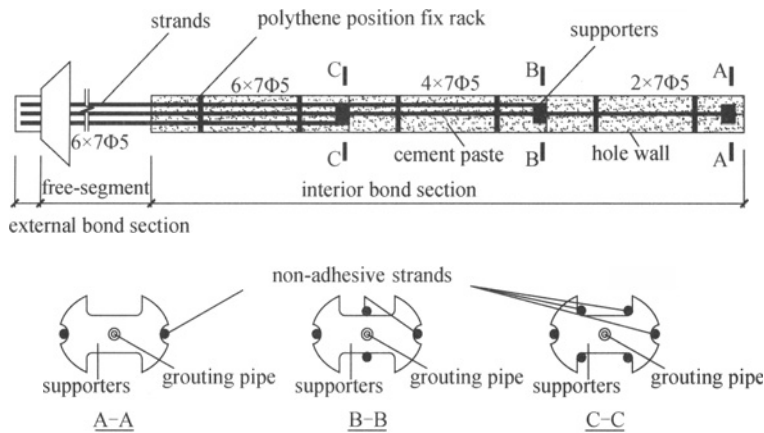


Figure 1. Structure of pressure-dispersive prestressed anchor

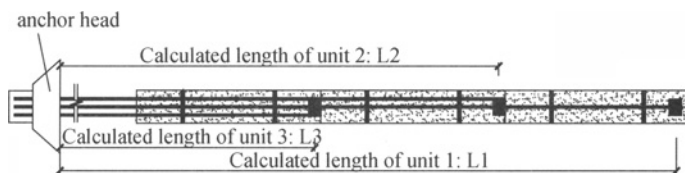


Figure 2. Diagrammatic sketch of the unit length

The determination method of compensate stretching parameters is expatiated as follows. (15m test cable)

$$s_i = \frac{P_n L_i}{E_s A_s} \quad (1)$$

$$P_i = P_{i-1} + [(i-1)P_n - P_{i-1}] \cdot \frac{s_{i-1} - s_i}{s_{i-1}} \quad (i=1,2,3) \quad (2)$$

Substituting (1) into (2), we have:

$$P_i = P_{i-1} + [(i-1)P_n - P_{i-1}] \frac{L_{i-1} - L_i}{L_{i-1}} \quad (i=1,2,3) \quad (3)$$

where

n = the number of cable units;

L_i =calculated length of unit i (mm);

E_s = elastic modulus of steel stranded wire (N/mm²);

A_s = cross section area of steel stranded wire (mm²);

P_i = prestressing force of unit i (kN);

The total test prestressing force can be defined as follows:

$$P_t = 1.50N_t = 1.50 \times 780\text{kN} = 1170\text{kN}$$

where

N_t = the design maximum bearing force of the cable

So, the force acting on every unit is

$$P_n = 1/3P_t = 390\text{kN} ;$$

The threshold value is given by

$$P_0 = 0\text{kN} ;$$

According to Eq.3, the total compensate stretching value of unit 1,2,3 can be defined as follows:

$$P_1 = 1/3P_n = 130\text{kN} \quad (6.7729\text{MPa})$$

$$P_2 = P_1 + 5/6P_n = 455\text{kN} \quad (23.5917\text{MPa})$$

$$P_3 = P_2 + 11/6P_n = 1170\text{kN} \quad (>60\text{MPa})$$

note: To coincide with the measurement unit of the loading device, the values calculated above are converted as shown in the round-parenthesis base on the relationship between f (kN) and p (MPa) in the testing report of the hydraulic jack. The relationship between f and p is shown in Figure 3 by curve fitting. And the regression equation is

$$p = 0.05175 \times f + 0.04545$$

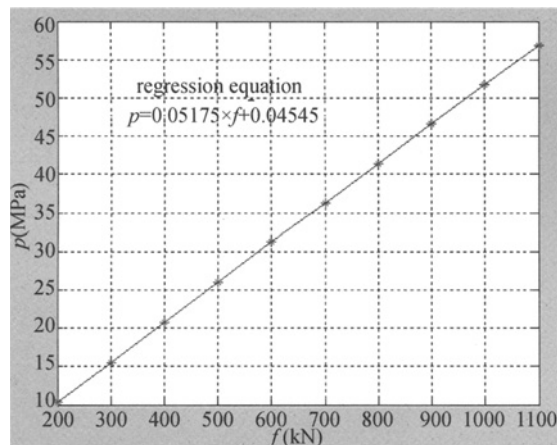


Figure 3. f-p curve of pressure gauge

Test process

Progressive loading method is used in the test; the threshold step size is 5MPa and decreases gradually with the increasing of load. 5 to 10 minutes are necessary between every two steps. And during this time, the end displacement of cable is measured three times and the average value is noted.

The test device is shown in Figure 4.

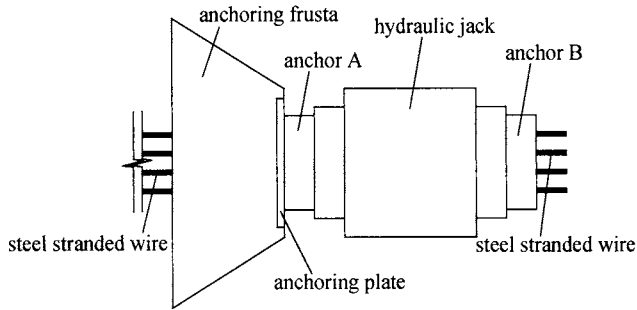


Figure 4. Test device of the anchorage cable

(1) Install the test device based on Figure 4

(2) Progressive loading

① Fix the whole 6 steel stranded wires with clips in anchor B (No clips in anchor A.) and 5MPa tension is implemented;

② Fix the unit 1 with clips in the anchor A; tension with the load step until 7MPa and note the end displacement of each step based on the method illuminate above;

③ Fix the unit 2 with clips in the anchor A (Keep the clips of ②); tension with the load step until 24.2MPa and note the end displacement of each step;

④ Fix the unit 3 with clips in the anchor A (Keep the clips of ② and ③); tension with the load step until 60MPa and note the end displacement of each step;

The purpose of ① is to make sure that the cables are straight; and ②~③ is the progressive loading process.

Test result analysis and conclusions

P-S curve

Figure 5 shows the typical curve of load P (kN) and end displacement S (mm).

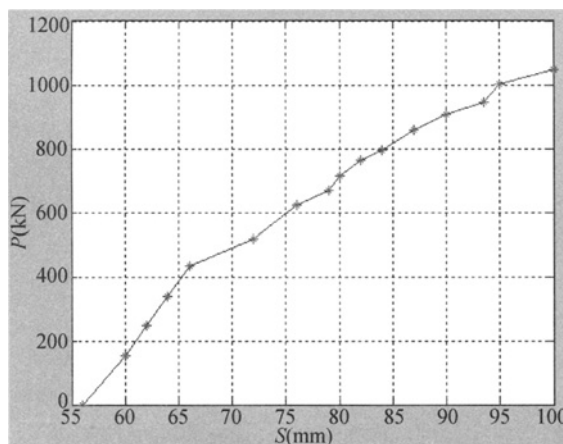


Figure 5. P-S curve of anchorage cable SM_1

An important observation highlighted in Figure 5 is that there are two phases during the whole loading process: the elasticity deformation phase in the range of $0 < P < 450 \text{ kN}$ where P - S curve shows the linear relationship between P and S ; and the plasticity deformation phase in the range of $P > 450 \text{ kN}$. In the later phase, the shearing strength between the anchored cement paste and the borehole reaches the limit equilibrium state and some shear failure planes are formed along the borehole direction.

In fact, the second phase can be divided into two phase farther by the point when P is about 1000 kN as is shown in the Figure 5. That is to say, when $P > 1000 \text{ kN}$, with the increase of load, the plasticity area extends along the borehole direction and the little increase of load will lead a large end displacement. This phase is named plastic failure phase.

The result of the test shows that the elasticity deformation and the plasticity deformation are 66.2 mm and 29.1 mm respectively for the test cable (15 m). And the cable can bear the design prestressing force of 780 kN .

Test result

Table 2. Destructive test table

Cable Number	Test cable length (m)	ultimate resistance capacity (kN)	elasticity deformation (mm)	plasticity deformation (mm)
SM_1	11	1117.9	66.2	29.1
SM_2	13	1123.7	73.0	31.2
SM_3	15	1193.3	85.3	38.6

CONCLUSIONS

The reasonable determination of test parameters and the choice of loading step guarantee the success of the uplift test. Two obvious phases, named the elasticity deformation phase and the plasticity deformation phase, or three further phases, together with the plastic failure phase, are shown clearly in the P - S curve.

The elasticity deformation and the plasticity deformation of the three test cable are determined. The results also prove that the cables used in this slop reinforcement can bear the design prestressing force well.

The test results enrich the data on the design, application and uplift test control of pressure-dispersive prestressed cable and have important reference value.

The findings of this research get the following conclusions:

- (1) Three rigid supporters make it possible to disperse the pressure in different soil layers which decrease the strain concentration and reduce the crack in the anchored cement paste relatively.
- (2) Compensate stretching method is used to reduce the influence of the length difference of the cable unit. We can also use several hydraulic jacks to achieve the test and in this situation, the results are the summation of data of the whole cable units.

REFERENCES

- Barely A. D.(1997). The single bore multiple anchor system. *Ground Anchorages and Anchored Structures*. London: Thomas Telford.
- Jia Jinqing, Song Erxiang et al., (2004). Study on prestressed anchor flexible retaining method. *Industrial Construction*, 53-59.
- Zhu Huanchun, Xiaoming et al., (1999). Study on bearing shear strength capability by in-situ test of anchor. *Chinese Journal of Rock Mechanics and Engineering*, Aug, 18: 1126-1128.

APPLICATION OF IN SITU STRESS REGRESSION METHOD IN ROCK SLOPE STABILITY ANALYSIS

Yao Liang, Depei Zhou, Tao Yang

*Department of Civil Engineering, SouthWest JiaoTong University,
Chengdu 610031, China*

Gang Zhao

Sichuan Dashuan Expressway CO., Ltd, Chengdu 610031, China

A detailed study about the application of in situ stress field in engineering slope has been carried out. To take the in situ stress into account in analysis of slope stability, the parent-model with coarse grids and sub-model with fine grids was established. In order to determine the in situ stress field of slope, the regional stress field calculated by stress regression method was converted to stress boundary of sub-model. The analysis of slope stability based on the in situ stress field is accurately to reflect the effect of natural factors.

INTRODUCTION

The construction of stable geotechnical engineering in and on rock masses requires knowledge of in situ stress field. The in situ stress field is initial condition of rock masses before disturbance. It is an important parameter in the design of structures and supports. Ideally, in situ stress field changes over geological time. However, to a particular engineering and time, the in situ stress field is considered as constant which is independent of time. Knowledge of in situ stresses in the rock masses relates with a lot of factors, such as gravity, tectonic movements, earthquakes temperature, groundwater. Because of small magnitude, the stresses caused by temperature and groundwater are ignored. Practically, the in situ stress are thought to be the sum of self-weight stress and tectonic stress resulting from crustal movements.

During the past decades, increasing interest has been shown in the determination of in situ stress field (C. Fairhurst, 2003). A lot of experimental and numerical methods of stress determination have been proposed and applied in design and construction of underground engineering, slope engineering, water conservancy and hydroelectric power engineering. The field test is carried out at several individual points to obtain displacement, stress, strain measurements. It is performed by means of hydraulic fracturing method (Klee et al., 1999), Kaiser effect method (C. A. Tang, et al., 1997; C. Li, et al., 1993) and so on. To determine the magnitude and orientation of in situ stress field by field test of several points, too much manpower and material resource are wasted. The numerical methods based on the information of field test are applied, such as displacement back analysis method (G. Gioda et al., 1987; S. Sakurai et al., 1983; Zhifa et al., 2001) and stress regression method. The

displacement back analysis method was first applied in underground engineering by Sakurai. It aims to determine the in situ stresses and elastic modulus according to displacement of surrounding rocks. The stress regression method is designed to determine in situ stress field by means of regression method, least-squares method and other mathematic methods. Recent research shows that neural network and gray forecast are developed in determination of in situ stresses.

The analysis of slope stability is carried out with hypothesis of self-weight stress field caused by gravity. Little attention has been focused on in situ stress field including self-weight stress field and tectonic stress field. None of these studies has attempted to take the tectonic stresses into consideration. For the areas with high tectonic stresses, like canyon, alpine and river drainage areas, the tectonic stresses may take more than a half part of in situ stresses, and cannot be ignored.

The main focus of this study was take in situ stress field into consideration in slope stability analysis. There were some efforts to perform it. (1) Firstly, a three dimension (3D) parent-model of Pusiluo (PSL) ditch has been established considering geomorphology characteristic, region terrain, rock properties. (2) Consequently, based on field test, in situ stress field has been determined by stress regression method. In order to reflect the influence of tectonic movements, tectonic movement factors including horizontal compressive movements and shear movements were simulated. (3) Then, sub-model with fine grids were involved in. The stress boundaries which derived from parent-model have been initialized on sub-model. The in situ stress field of sub-model was determined when the slope had been equilibrium. (4) Lastly, slope stability analysis was performed with consideration of in situ stress field. The results of stress and displacement were outlined.

THEORY OF IN SITU STRESS FIELD

Review of stress regression method

The stress regression method is suggested to determine the regional in situ stress field, based on field test of a few measurement points. The basic procedure of the stress regression method is introduced as following.

- (1) Establish 3D regional model with effort to reflect joints, fractures and terrain.
- (2) Take in situ stress as dependent variable σ_k , the stresses caused by regression factor i as independent variables σ_k^i . The effect of factor i is evaluated by regression coefficients b_i . The stress regression equation is assigned as following.

$$\sigma_k = \sum_{i=1}^n b_i \cdot \sigma_k^i \quad (1)$$

To a particular measurement point k , where σ_k is the regression stress, b_i is the regression coefficient of factor i , σ_k^i is the calculation stress related to factor i .

- (3) The optimal solution of regression coefficients is solved with principle of the minimum residual square sum. Assuming there were k measured points in total, the residual square sum of regressed stress is mentioned in Eq. (2).

$$S_{\text{残}} = \sum_{k=1}^m \sum_{j=1}^k (\sigma_{jk}^* - \sigma_{jk})^2 \quad (2)$$

where σ_{jk}^* is field test stress of point k , σ_{jk} is regression stress of point k .

The influence of regression factors are monitored by regression coefficients b_i . If the regression coefficient is too small, the correlated factor should be deleted. It means that the factor has played no important role in the regression. In the same way, the factor which is important in regression would be added. This is so called stepwise regression. Repeat two steps introduced before until the residual square sum is minimum.

The in situ stress field of engineering slope

The stress regression method aims to determine regional in situ stress field based on field test. But the model of region is too big to reflect the construction and excavation area exactly. Stability analysis of engineering slope based on regional model is inaccurately and unpractically. Further attempts of determining local in situ stress field fit into design of engineering slope were conducted.

The in situ stress field of engineering slope could be achieved by applying stress boundary. First of all, the regional parent-model with coarse grids was established. The parent-model which ignored tiny characteristics was modeled to reflect the whole regional terrain. The in situ stress field had been determined by the stress regression method, so did the stress of elements. Then, to model slope we concerned with fine grids, called sub-model. The sub-model was more accurate than parent-model in reflecting terrain and geological characteristic. Because of different element size, an element of parent-model may corresponded with several fine elements of sub-model. Some elements of parent-model were concerned, which located on boundaries of sub-model. To query regression stresses of those parent-elements, and applied on sub-model as stress boundaries instead of the boundary constraint. When sub-model was equilibrium under the stress boundaries, the stress field in sub-model was the in situ stress field suitable for slope stability analysis.

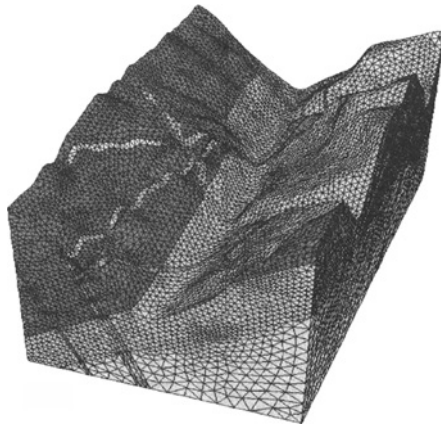


Figure 1. Parent-model with coarse grids of PSL ditch

APPLICATION OF IN SITU STRESS FIELD IN SLOPE STABILITY ANALYSIS

Regional in situ stress field determination of PSL ditch

We regressed the in situ stress field of Pu Si Luo (PSL) ditch by means of stress regression method. The parent-model was established on purpose of reflect topographical and rock characteristics, shown in Figure 1. In order to minimize boundary effects, the model was 2650m in x-component, 1530m in y-component, elevation from 1000m to 2500m. The horizontal axis x was along the river from upstream to downstream, while horizontal axis y was cross the river from left to right.

After the screening of regression factors, there were three natural factors simulated to determine the in situ stresses: (1) the S62°E uniform compressive movement, (2) the N28°E uniform compressive movement, (3) the shear movement in horizontal plane. Consequently, three types of unit displacement corresponded to three factors were applied on parent-model. We arranged 21 test points. The regressed in situ stress field should coincide with test stress field. The coefficients of natural factors would be optimal when residual square sum came to be minimum. The multiple correlation coefficient was calculated out as 0.73 to evaluate the accuracy of regression stresses. The regression equation is shown as following:

$$\sigma_k = \sigma_k^g + 1.2032\sigma_k^{u1} + 0.1477\sigma_k^{u2} + 0.3601\sigma_k^{u3} \quad (3)$$

To point k , Where σ_k is the regression stress, σ_k^g is the self-weight stress, σ_k^{u1} is the stress caused by S62°E uniform compressive movement, σ_k^{u2} is the stress caused by N28°E uniform compressive movement, σ_k^{u3} is the stress caused by shear movement in horizontal plane.

Local in situ stress field determination of engineering slope

After in situ stress field of PSL ditch had been determined, the procedure changing in situ stress field from regional to local was conducted. The sub-model was modeled, which located from 2060m to 2110m in x-axis of parent-model, at the size of 50m×1530m×1500m. To make sure the stress field of sub-model coincided with the regression stress field, the stress boundaries of 2060m and 2110m were initialized to instead of displacement boundaries which we usually done. The application of stress boundaries was mean to simulate in situ stress field of sub-model. The stress derived from regional parent-model elements, were applied on center of sub-model boundary elements.

The characteristics of slope stress distribution coincided with which we known about the deeply cut valley. The stress distribution is characterized by strong inhomogeneity with a maximum to minimum principal stress ratio of up to 5:1 approximately. The principal stresses zoned into three regions by depth: stress released region, stress concentration region, and stress stationary region, like the contour of maximum principal stress shown in Figure 2. The stress released region was in shallow bank slope because of weathering relaxation and valley cutting. The bottom region of valley was stress stationary region which hadn't been

REFERENCES

- Tang C. A., Chen Z. H., Xu X. H. and Li C. (1997). A theoretical model for kaiser effect in rock. *Pure and applied geophysics*, 150(2): 13.
- Li C. and Nordlund E. (1993). Experimental verification of the Kaiser effect in rocks. *Rock mechanics and rock engineering*, 26(4): 333-351.
- Fairhurst C. (2003). Stress estimation in rock: a brief history and review. *International Journal of Rock Mechanics and Mining Sciences*, 40: 957-973.
- Gioda G. and Sakurai S. (1987). Back analysis procedures for the interpretation of field measurements in geomechanics. *international Journal for Numerical and Analytical Methods in Geomechanics*, 11: 28-33.
- Klee G., Rummel F. and Williams A. (1999). Hydraulic fracturing stress measurements in Hong Kong. *International Journal of Rock Mechanics and Mining Sciences*, 36(6): 731-741.
- Sakurai S. and Takeuchi k. (1983). Back analysis of measured displacement of tunnel. *Rock mechanics and rock engineering*, 16(3): 173-180.
- Zhifa Y., Zhiyin W., Luqing Z., Ruiguang Z. and Nianxing X. (2001). Back-analysis of viscoelastic displacements in a soft rock road tunnel. *International Journal of Rock Mechanics and Mining Sciences*, 38(3): 331-341.

DISPLACEMENT CHARACTERISTIC OF SOIL SLOPE IN SHEAR STRENGTH REDUCTION METHOD BASED ON MOHR-COULOMB MODEL

Hang Lin, Ping Cao, Jiangteng Li, Xueliang Jiang
*School of Resources & Safety Engineering, Central South University,
Changsha 410083, China*

During implementation of strength reduction method (SRM) in Mohr-Coulomb model, the magnitude of some particles' displacement will become abruptly large with the increasing of reduction factor K , which indicates the failure of slope. And this displacement characteristic is named as the 'displacement mutation criterion' in SRM. But it is not widely used for some problems still remain such as which monitoring points and which displacement modes are available to be chosen to reflect the mutation characteristic. First of all, a simple homogeneous slope model is built by FLAC^{3D}; then, according to the location slip plane, several monitoring points are located inside and outside of slip plane. Relationship of displacement for these points and reduction factor K is obtained by hyperbola fitting equations, which shows that points inside slip plane can reflect the displacement mutation characteristic while points outside can not. And in many cases, vertex of slope locates inside the slip plane, so it is recommended to be chosen as the monitoring point. Then the displacement modes like horizontal displacement, vertical displacement and total displacement mode are discussed to find that they can obtain the same safety factor.

INTRODUCTION

In the assessment of slopes, factor of safety F still remain the primary indexes for determining how close or far slopes are from failure. Traditional limit-equilibrium techniques are the most commonly-used analysis methods, which consider slope material as rigid body (Abramson LW et al., 2002). Recently, however, rapid advances in computer technology and sustained development have pushed the numerical analysis like the method of fast lagrangian analysis of continua three dimensions (FLAC^{3D}) (Itasca Consulting Group, 2002) to the forefront of geotechnical practice. In numerical analysis, shear strength reduction method (SRM) (Duncan J.M., 1996; Griffiths D. V. and Lane P. A., 1999; Colby C. Swan and Young-Kyo Seo, 1999; Song Erxiang, 1997; Y.M. Cheng et al., 2007) is mainly adopted to calculate factor of safety for slopes based on Mohr-Coulomb model. As Duncan (Duncan J.M., 1996) points out, F is the factor by which the soil shear strength must be divided to bring the slope to the verge of failure. Since it is defined as a shear strength reduction factor, an obvious way of computing F with a finite element program or finite difference program is simply to reduce the soil shear strength until collapse occurs. So how

to define the critical failure state of slope is the most important step in SRM. During implementation of SRM, magnitude of some particles' displacement will become abruptly large with the increasing of reduction factor K , which indicates the failure of slope. And this displacement characteristic is named as the 'displacement mutation criterion' in SRM (Griffiths D V and Lane P A., 1999; Song Er-xiang, 1997). But it is not widely used for some questions still exist such as which monitoring points and which displacement modes are available to be chosen to reflect the mutation characteristic. In this paper, we will try to answer these questions by a simple homogeneous numerical model, then, the displacement characteristic of soil slope is recorded, and quantified.

NUMERICAL MODEL

A numerical model is founded in plane strain mode by FLAC^{3D} for homogeneous soil slope, shown in Figure 1, with 20 meters of slope height, 45° of slope angle, and 1 meter of model thickness. Model element will affect the calculation result by FLAC^{3D}. After comparing time consumed and calculation precision, the whole model is divided into three parts which consists of 816 elements and 1176 grids, part I with 12×8 elements, part II with 40×8 elements, part III with 40×10 elements. The size of model will also affect the result, so model is built large enough to reduce the size effect, with the length from slope toe to the left boundary of 30 meters, length from slope vertex to the right boundary of 55 meters, and length from slope toe to the bottom boundary of 20 meters which is equal to slope height. Soil parameters are as follows, 25kN/m³ for unit weight, 10MPa for elastic modulus, 0.3 for Poisson's ratio, 42kPa for cohesion, 17° for internal friction angle, and 10kPa for tensile strength. Numerical model is fixed in both horizontal and vertical direction on bottom boundary, in horizontal direction on both sides, and the upper boundary is free. The tolerance for calculation is 10⁻⁵, which is sufficiently accurate for the present study.

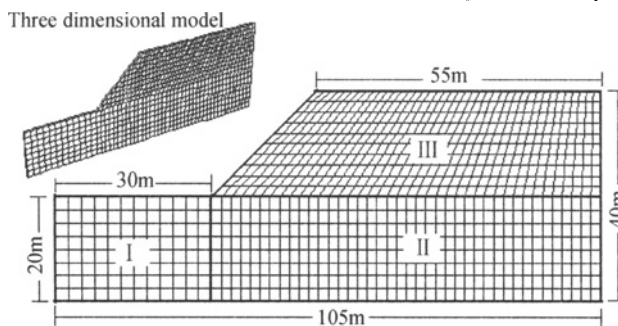


Figure 1. Numerical model

RESULT AND DISCUSSION

Displacement mutation criterion

When slope reaches the verge of failure, the whole model can be divided into two parts, one is the stable part, the other is the unstable part, shown in Figure 2. From Figure 2, we can also see the obvious boundary between two parts, which is believed to be the critical slip plane.

And displacement of unstable part is extremely large when comparing to that of stable part, shown in Figure 3, the closer the particle is near slope surface the larger the displacement is.

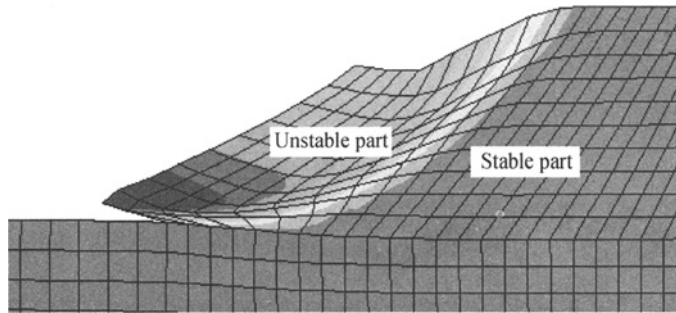


Figure 2. Failure of slope

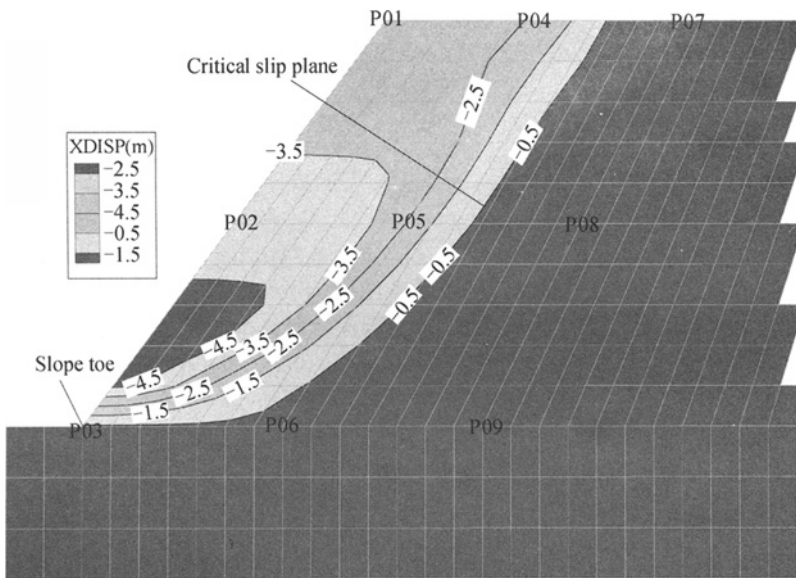


Figure 3. Location of monitoring points

Monitoring point and displacement mode

In order to choose appropriate points to reflect the displacement mutation characteristic, some monitoring points are located inside and outside slip plane, shown in Figure 3, from P01 to P09. Vertical distances between P01-P02, P02-P03 are 10 meters. Horizontal distances between P01-P04, P04-P07 are 10 meters. It is obvious that points P01, P02, P04 and P05 are located inside the slip plane, while the others are located outside slip plane.

Calculated by FLAC^{3D}, magnitudes of displacement can be recorded with the increase of reduction factor K . Relationships of reduction factor K and displacement δ for different monitoring points and different displacement modes are shown in Figure 4, which shows that points outside slip plane do not represent the displacement mutation characteristic. And curves of displacements for point P01, P02, P04 and P05 which are inside the critical slip line

all represent the mutation phenomenon, so it is proper to choose these points as the monitoring points. In the present calculation model, the slip plane does not run through the toe of slope, it run through certain place of slope plane, which is at a few distance from the toe of slope, shown in Figure 3. Then, it is not proper to choose slope toe as the monitoring point in some cases. As we know, critical slip plane can not be drawn before calculation, so it is difficult to determine the appropriate monitoring points. But for many cases, the vertex of slope locates inside the critical slip plane, so it is recommended to be chosen for monitoring the displacement characteristic. From Figure 4, we can also see that, all of the three displacement modes, δ_t , δ_h , δ_v can reflect the displacement mutation characteristic.

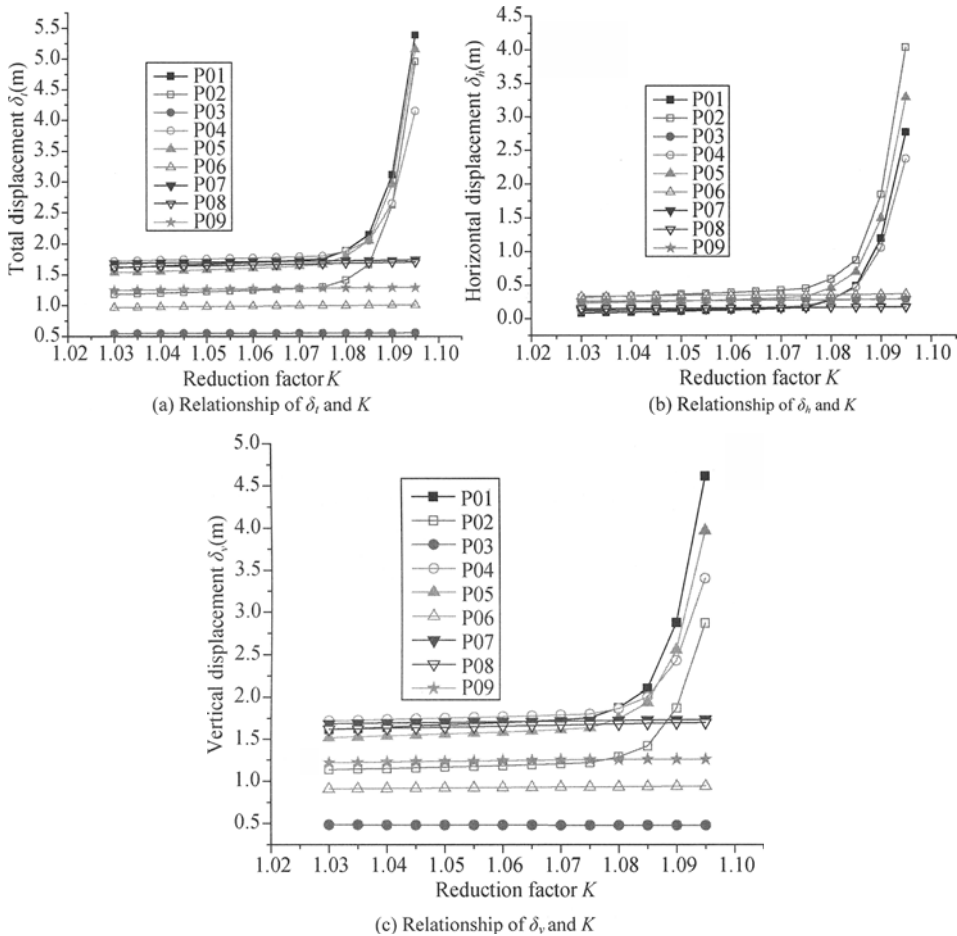


Figure 4. Relationship between displacement and reduction factor

Data fitting

From the above discussion, we know that monitoring points inside slip plane as well as the three displacement modes can reflect the mutation characteristic, and the relationship of reduction factor K and particles displacement δ are recorded in Figure 4. Then furthermore we are interested in another problem: how to quantify their relationship so as to obtain the

safety factor of slope. In order to solve this problem, we have to do some additional work. And the most effective way is to fit the relationship curves like P01, P02, P04, P05 which can reflect the mutation characteristic in Figure 4. Then, some equations are tried for fitting. At last, hyperbola equation is proved to fit them well, which has the form as follow,

$$\delta = (\xi + \omega K) / (1 + \zeta K) \quad (1)$$

where ζ , ξ and ω are the parameters to be determined.

When $1 + \zeta K = 0$, $\delta \rightarrow \infty$, slope goes on slipping, failure of slope starts to occur, then K for critical state of slope can be obtained by,

$$K^{cr} = 1 / \zeta \quad (2)$$

According to the definition of SRM, K^{cr} is the global safety factor F .

Table 1. The fitting result of δ - K curves

Displacement modes	NO	ζ	ξ	ω	R^2	Safety factor F
Total displacement δ_t	P01	-0.9108	1.3919	-1.2578	0.9896	1.0980
	P02	-0.9109	0.9575	-0.8630	0.9890	1.0978
	P04	-0.9109	1.5849	-1.4376	0.9903	1.0978
	P05	-0.9108	1.3159	-1.1891	0.9902	1.0980
	P01	-0.9106	-0.1006	0.0992	0.9873	1.0981
Horizontal displacement δ_h	P02	-0.9107	0.0749	-0.0579	0.9884	1.0981
	P04	-0.9106	-0.0440	0.0466	0.9878	1.0982
	P05	-0.9106	0.0206	-0.0102	0.9884	1.0983
	P01	-0.9105	1.4265	-1.2902	0.9898	1.0983
Vertical displacement δ_v	P02	-0.9105	1.0272	-0.9302	0.9899	1.0983
	P04	-0.9105	1.6139	-1.3645	0.9901	1.0983
	P05	-0.9104	1.3593	-1.2303	0.9905	1.0984

Curve fitting results are summarized in Table 1 for P01, P02, P04 and P05 with different displacement modes. Correlation coefficients R^2 of the fitting results are close to 1, which indicate that fitting results are in good correlation with the monitoring data, and the hyperbola equation can do good fitting to the curves. The maximum and minimum of the safety factors differ by 0.00059, vary in a very small range. So it is proved that safety factors obtained by different points inside slip plane and different displacement modes are equal to each other. Safety factor obtained by displacement mutation of SRM is 1.10, when compared to that of 1.09 by Janbu method shown in Figure 5, it is a little larger, but displacement mutation criterion takes into consideration of stress-strain relationship and deformation process of slope.

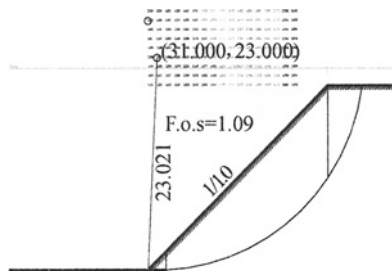


Figure 5. Calculation result by Janbu method

CONCLUSIONS

- (1) Hyperbola equation built in this paper can do good fitting to the relationship of displacement-reduction factor, safety factors can be obtained for different monitoring points and different displacement modes according to the fitting results.
- (2) In order to reflect the displacement mutation characteristic, monitoring points should be located inside the slip plane. In many cases, it is difficult to draw the critical slip plane before calculation, but the vertex of slope locates inside the slip plane, so it is recommended to be chosen as the monitoring point. Different displacement modes reflect the same displacement characteristic and safety factor by curves fitting method.
- (3) Safety factor obtained by displacement mutation is 1.10, when compared to that of 1.09 by Janbu method, it is a little larger, but displacement mutation criterion takes into consideration of stress-strain relationship and deformation process of slope.

REFERENCES

- Abramson L.W., Lee T.S., Sharma S. and Boyce G. M. Slope stability and stabilization methods. *Second ed. USA: Wiley.*
- Colby C. Swan, Young-Kyo Seo. (1999). Limit state analysis of earthen slopes using dual continuum/FEM approaches. *Int.J.Numer.Anal.Meth.Geomech*, 23: 1359-1371.
- Duncan J.M. (1996). State of the art: limit equilibrium and finite-element analysis of slopes. *J Geotech Eng, ASCE*, 122(7): 577-596.
- Griffiths D.V., Lane P. A. (1999). Slope stability analysis by finite elements. *Geotechnique*, 49(3): 387-403.
- Itasca Consulting Group. (2002). *User's guid.* Minnesota: itasce consulting group.
- Song Erxiang. (1997). Finite element analysis of safety factor for soil structures. *Chinese Journal of Geotechnical Engineering*, 19(2): 1-7.(in Chinese).
- Cheng Y.M., Lansivaara T. and Wei W.B. (2007). Two-dimensional slope stability analysis by limit equilibrium and strength reduction methods. *Computers and Geotechnics*, 34: 137-150.

AN INTERFACE MODEL TO PREDICT THE STABILITY OF LANDSLIDE WITH WEAK INTERCALATED LAYER

Yulong Luo, Hua Peng

*School of Civil and Architectural Engineering, Wuhan University,
Wuhan 430072, China*

The landslide always consists of a lot of weak intercalated layers; the distribution and seepage-stress coupled effect of weak intercalated layer are the key factors affecting the landslide stability. In order to predict the stability correctly and mitigate the disaster maximumly, a new type of seepage-stress coupled interface model based on the Goodman joint was proposed, which is based on the Biot's consolidation theory and interpenetration control method proposed by Desai. An elastic visco-plastic constitutive model was adopted to simulate the creep behavior, and a relevant FE program was developed to analyze the Dayeping landslide with weak intercalated layers, whose stability is attached important to the construction of Linxihe hydropower station. The calculated groundwater free surface is consistent well with the in-situ testing data, and the displacements and stresses suggest that the landslide may slide along with the weak intercalated layer from the elevation of 230m to 370m, especially when the water level downriver falls suddenly. The results provide theoretical bases for the landslide disaster forecast, prevention and construction decision of Linxihe hydropower station. The proposed interface model can predict the stability of landslide with weak intercalated layer correctly.

INTRODUCTION

With the increasing of population, the extension of human activities and the influence of engineering activities on geological environment disturbance, the landslide disasters have become the most frequent and serious geological hazards. So predicting the stability of landslide and mitigating the disasters are very important and meaningful. It is well known that the distribution and seepage-stress coupled effect of weak intercalated layer are the key factors affecting the landslide stability, Oda. (1986). Thus modeling the coupled effect correctly is necessary, but the relevant studies are seldom reported.

Generally, there are two methods modeling the weak intercalated layer now: (1) solid element, Chai et al. (2004). The materials at the top and bottom of weak intercalated layer are very different, and the relative sliding or opening may occur between the top and bottom, and yet the solid element can't model the discontinuous displacement of the weak intercalated layer. (2) Goodman joint or Desai element, Goodman et al. (1968) and Desai et al. (1984). The two elements can't consider the pore pressure, they can only take the seepage force or pore pressure as the external load to do the stress analysis, Samtani et al. (1996). In addition, the Goodman joint is difficult in deciding reasonable normal stiffness; though the

Desai element introduces the interpenetration control method to overcome the node penetration, it is short of theoretical bases on deciding the mechanical parameters of interface. It can be concluded that the above methods will occur large errors, and some improvements need to do for them. Thus this paper proposed an interface model based on the original Goodman joint and Biot's consolidation theory.

FE FORMULATION

Key assumptions

The proposed interface model is shown in Figure 1. Every node has three freedoms: u , v and p . Two key assumptions are made here: (1) there are only two components of stress σ_n, τ_s , and the relative effective stress, $\sigma'_n = \sigma_n - p, \tau'_s = \tau_s$; (2) the velocity of seepage flow can only occur in the tangential direction, that is, $p_1=p_3, p_2=p_4$.

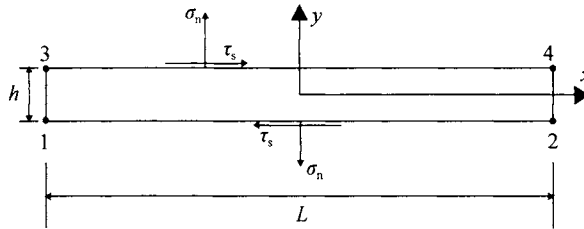


Figure 1. Interface model (local coordinate system)

FE approximation

Based on Biot's consolidation theory, introduce the boundary conditions into the stress equilibrium equations and water continuity equation, the FE equations can be derived

$$\int \sigma'_i \delta u_i dV + \int p \delta u_n dV + \int T_i \delta u'_i dS = 0 \quad (1)$$

$$-\int \frac{k_x h}{r_w} \frac{\partial p}{\partial x} \frac{\partial \delta p}{\partial x} dV - \int \frac{\partial u_n}{\partial t} \delta p dV = 0 \quad (2)$$

where $\delta u_i, \delta u'_i$ represent any arbitrary change in relative and absolute displacements, respectively; δu_n is the arbitrary change in the relative normal displacement; T_i are the components of traction along the boundary S .

To obtain an approximate solution of Eqns (1) and (2), it is necessary to first relate the displacements and water pressures to the nodal values. According to the Goodman joint, we gained a set of coupled equations in the global coordinate

$$\begin{bmatrix} K & -L^T \\ -L & -\alpha \Delta t K_s \end{bmatrix} \begin{Bmatrix} \Delta \delta_u \\ \Delta \delta_p \end{Bmatrix} = \begin{Bmatrix} \Delta m \\ \Delta t K_s p_t \end{Bmatrix} \quad (3)$$

where p_t are the pore pressures at time t , α is the integrating factor, a value of 0.5 was adopted to ensure unconditional stability with respect to time. The stiffness submatrices in Eqn (3) can be expressed

$$K = \int R^T B^T D B R dx \quad (4)$$

$$L^T = \int R^T V a^T dx \quad (5)$$

$$K_s = \frac{k_x h}{r_w} \int E_x^T E_x dx \quad (6)$$

$$m = \int R^T N^T T dS \quad (7)$$

$$B = \begin{bmatrix} -N_1 & 0 & -N_2 & 0 & N_1 & 0 & N_2 & 0 \\ 0 & -N_1 & 0 & -N_2 & 0 & N_1 & 0 & N_2 \end{bmatrix} \quad (8)$$

$$V = [0 \quad -N_1 \quad 0 \quad -N_2 \quad 0 \quad N_1 \quad 0 \quad N_2]^T \quad (9)$$

$$a^T = \frac{1}{2} [N_1 \quad N_2 \quad N_1 \quad N_2] \quad (10)$$

$$E_x = \frac{1}{2} \begin{bmatrix} \frac{\partial N_1}{\partial x} & \frac{\partial N_2}{\partial x} & \frac{\partial N_1}{\partial x} & \frac{\partial N_2}{\partial x} \end{bmatrix} \quad (11)$$

$$N = \begin{bmatrix} N_1 & 0 & N_2 & 0 & N_1 & 0 & N_2 & 0 \\ 0 & N_1 & 0 & N_2 & 0 & N_1 & 0 & N_2 \end{bmatrix} \quad (12)$$

where D is the constitutive matrix; D_e is the elastic matrix, Desai et al. (1984), the elastic visco-plastic matrix D_{vp} will be discussed later. R is the transform matrix; N_i is the interpolation function, $N_1=N_3=(1-2x/L)/2$, $N_2=N_4=(1+2x/L)/2$.

Interpenetration control method

The interpenetration control method proposed by Desai was introduced to overcome the node penetration. The steps for two typical adjacent nodes p and q are given below.

- (1) Compute normal displacement u_n^i at the end of the last iteration i , and the increment of displacement Δu_n for the two nodes as $(u_n^i)_p, (\Delta u_n)_p, (u_n^i)_q, (\Delta u_n)_q$.
- (2) Compute $A = [(u_n^i)_p + (\Delta u_n)_p + h - \{(u_n^i)_q + (\Delta u_n)_q\}]$.
- (3) If $A \geq 0$, penetration does not occur and proceed to next pair of nodes.
- (4) If $A < 0$, penetration occurs, $\alpha = [\varepsilon h - h - \{(u_n^i)_q - (u_n^i)_p\}] / [(\Delta u_n)_q - (\Delta u_n)_p]$.
- (5) Compute the equivalent or correction load vector $\{\Delta Q\} = \int [D][B]\{\Delta q\} dV$, where $\{\Delta q\}^T = [(\Delta u^1)_p, (\Delta v^1)_p, (\Delta u^1)_q, (\Delta v^1)_q]$.
- (6) Repeat the above steps for all pairs of interface nodes and accumulate the correction load vectors for all nodes that have experienced penetration.

- (7) Perform finite element iterative analysis with the accumulated correction load until convergence, defined by $|A - \varepsilon h| \leq \lambda$, where λ is a small number, Desai et al. (1984).

Constitutive model

The elastic visco-plastic matrix in Δt^n can be expressed

$$D_{vp}^n = \left[(D_e)^{-1} + \Theta \Delta t^n (\partial \dot{u}_{vp}^n / \partial \sigma')^n \right]^{-1} \quad (13)$$

According to the Perzyna theory, Perzyna (1966)

$$\dot{u}_{vp} = \gamma \langle \Phi(F/F_0) \rangle \partial Q / \partial \sigma' \quad (14)$$

$$\Phi(F/F_0) = (F/F_0)^n \quad (15)$$

where F, F_0 represent the material yield criterion and reference value, respectively. The Mohr-Coulomb yield criterion and associated flow rule were adopted, and $F_0 = c \cos \varphi$. The D_{vp} can be obtained, then a relevant FE program was developed.

ENGINEERING APPLICATION

The Dayeping landslide lies on the Loushui River, it is nearby the Linxihe hydropower station, which is preparing to construct. Its stability affects the safety and operation of Linxihe hydropower station seriously. So predicting the stability is necessary. According to the drill test and geology analysis, it is primarily estimated that the plane shape of the landslide is round-backed armchair, and its elevation is about from 230m to 480m.

Calculation model and parameters

The material zone is shown in Figure 2. The material parameters are shown in Table 1. The weak intercalated layer adopted the interface model, and the other materials adopted the $Cpe4p$, Hibbitte et al. (2002). The constitutive law is the elastic visco-plastic model.

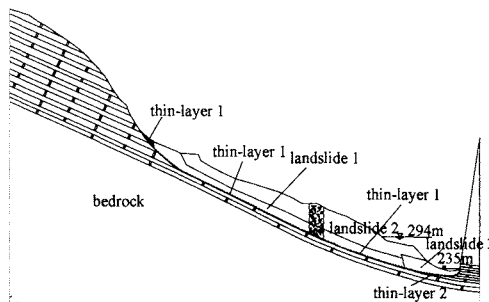


Figure 2. Material zone of landslide

Table 1. Material parameters

Material	ρ (kN/m ³)	E (MPa)	μ	k (m/s)	c (kPa)	ϕ (°)
Bedrock	26.5	8000.0	0.26	4.98×10^{-6}	300.0	50.0
Thin-layer 1	19.5	λ_s (MPa/m)	λ_n (MPa/m)	0.6(<i>shear</i>)	30.0	19.8
		7.28	133.0	0.0(<i>normal</i>)		
Landslide 1	22.0	10.0	0.35	2.3×10^{-7}	55.0	25.0
Landslide 2	21.0	9.8	0.33	2.0×10^{-3}	58.0	27.0
Landslide 3	20.5	9.5	0.31	3.2×10^{-4}	60.0	31.0
Thin-layer 2	19.8	λ_s (MPa/m)	λ_n (MPa/m)	2.0(<i>shear</i>)	28.0	20.3
		5.34	105.0	0.0(<i>normal</i>)		

The water level upriver is 500m; the water level downriver of load case 1 is 235m, and yet that of load case 2 falls suddenly from 259m to 255.72m in four hours. Because of short of coupled test data, supposed the permeability of materials were constant.

Results and discussions

It is seen in figure 3 that the calculated groundwater free surfaces are consistent well on the drill holes, and some discrepancies are also observed at the top bedrock in Figure 3(a) and the stepwise weak intercalated layer in Figure 3(b), the reasons may be few drill holes and the error fitting the in-situ testing data, so these discrepancies are reasonable, and they are in the permission range of engineering. Therefore adopting the interface model to simulate the seepage-stress coupled effect of the weak intercalated layer is feasible.

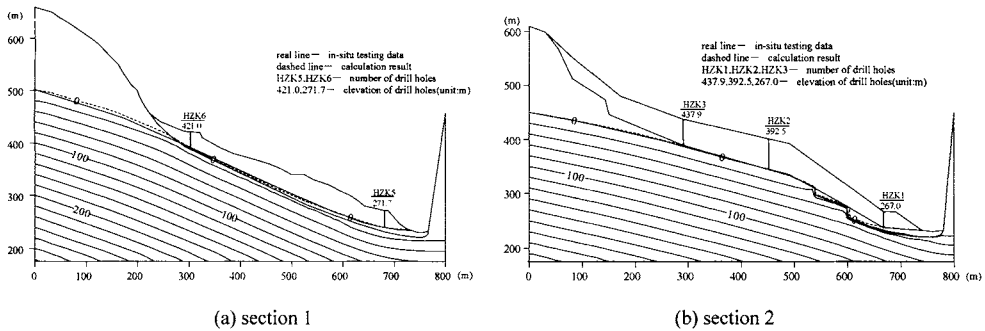


Figure 3. Groundwater free surface comparisons (load case 1)

The displacement results indicate that the displacement on the surface is very large, and it decreases gradually with the increase of depth. The maximum occurs on the first and second platform, the elevation is 421m and 340m, respectively. Figure 4 shows that the vectors have the trend of sliding along with the weak intercalated layer, especially from the elevation of 230m to 370m in load case 2, the sliding trend is very evident.

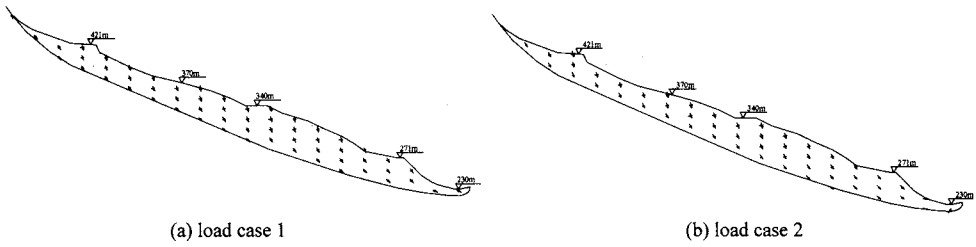


Figure 4. Displacement vectors (section 1)

The stress results show that the first and third principal stresses (S_1 and S_3) are mainly compressive stress. The plasticity zone in load case 2 is shown in Figure 5, the S_1 and S_3 in load case 2 are shown in Figure 6. It is seen that the maximum of S_1 and S_3 are 0.2MPa and 0.1MPa, respectively; the minimum of S_1 and S_3 are -1.0MPa and -2.0MPa, respectively. The maximum of Tresca stress in load case 1 and 2 are 1.1MPa, 1.3MPa, respectively, which lie on the front of weak intercalated layer. These suggest that the water level falling suddenly results in the expansion of plasticity zone along the weak intercalated layer, and load case 2 is more dangerous than load case 1.

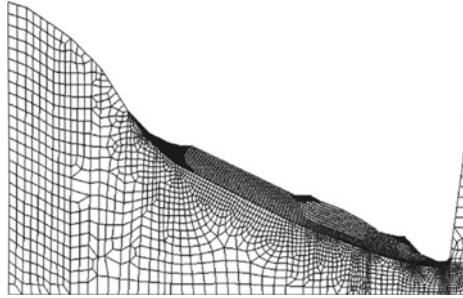


Figure 5. Plasticity zone (load case 2)

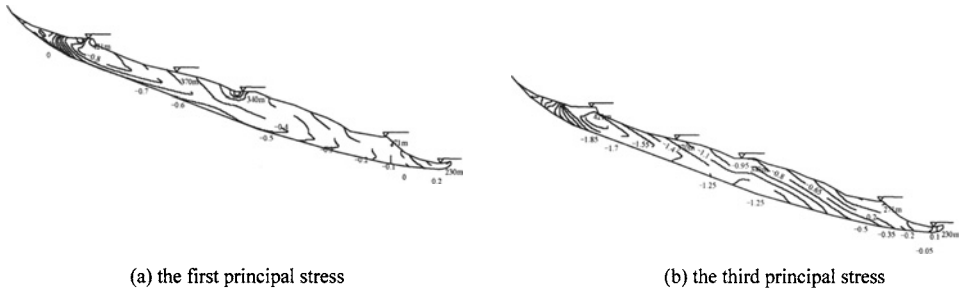


Figure 6. The principal stress (load case 2)

It can be concluded that the landslide will occur partial broken-line slide along with the weak intercalated layer from the elevation of 230m to 370m in load case 2.

CONCLUSIONS

This paper proposed an interface model to simulate the coupled effect of the weak intercalated layer in landslide stability analysis. The interface model follows the formulation

of original Goodman joint, introduces the Desai's interpenetration control method, and the pore pressure is considered as an unknown variable simultaneously. Thus the new model makes up the faults of Goodman and Desai element, and has the ability of coupled analysis.

A relevant FE program was developed to analyze the Dayeping landslide; the calculated groundwater free surface is consistent well with the in-situ testing data, the displacement and stress results present the stability in detail. These results provide theoretical bases for the landslide disaster forecast, prevention and construction of Linxihe hydropower station. The proposed interface model can predict the stability of landslide with weak intercalated layer correctly.

REFERENCES

- Chai J.R., Li S.Y. (2004). Coupling analysis of seepage and stress fields in Xietan Landslide in Three Gorges region. *Chinese Journal of Rock Mechanics and Engineering*, 23(8): 1280-1284.
- Desai C.S., Lightner J.G. and Siriwardane H.J, et al. (1984). Thin-layer element for interfaces and joints. *International Journal for Numerical and Analytical Methods in Geomechanics*, 8: 19-43.
- Goodman R.E., Taylor R.L. and Brekke T.L. (1968). A model for the mechanics of jointed rock. *Journal of the Soil Mechanics and Foundations Division Proceedings of the American Society of Civil Engineers*, 94(SM3): 637-659.
- Hibbitte, Karlsson, Sorenson, Inc. (2002). *ABAQUS/Standard user's manual*.
- Oda M. (1986). Equivalent continuum model for coupled stress and fluid flow analysis in jointed rock masses. *Water Resources Research*, 22(13): 1845-1856.
- Perzyna P. (1966). Fundamental problems in visco-plasticity. *Advances in Applied Mechanics*, 9: 243-377.
- Samtani N.C., Desai C.S. and Vulliet L. (1996). Interface model to describe viscoplastic behavior. *International Journal for Numerical and Analytical Methods in Geomechanics*, 20: 231-252.

CATASTROPHE EVALUATION OF LANDSLIDE INSTABILITY

Qiang Ren, Weiya Xu

*Key Laboratory of Ministry of Education for Geomechanics and Embankment Engineering,
Hohai University, Nanjing 210098, China*

Geotechnical Research Institute, Hohai University, Nanjing 210098, China

The slope movement is a complex process related to landslide stability and huge surge. With respect to physical, structural and environmental condition of landslide, the limiting equilibrium method based Monte-Carlo reliability calculation was applied to analyze the stability of landslide under rain and earthquake, and the empirical formula was employed to evaluate consequences induced by surge wave. In the case of understanding degree of catastrophe and grade of risk, according to evaluation results, engineering treatments were proposed and the catastrophe evaluation of landslide instability system was established. The application to an example demonstrates the feasibility and practicability of risk evaluation-consequence evaluation-treatment evaluation system, thus the case can provide reference to study on catastrophe evaluation of slope instability.

INTRODUCTION

Landslids from massive rock slope failure are a major geological hazard in many parts of the world and have been responsible for some of the most destructive natural disasters.

Catastrophe caused by landslide being not only oneself, but also associated significant secondary disaster, such as landslide surge phenomenon. It is necessary to establish catastrophe evaluation of landslide instability coupled with quantitative and qualitative analysis.

Catastrophe evaluation of landslide instability system is composed of three sub-systems: risk evaluation, consequence evaluation and treatment evaluation system.

RISK EVALUATION OF GEOLOGIC LANDSLIDE

The method for the evaluation of slope stability includes engineering geology analogism method, limit equilibrium method, stress-strain analysis and reliability method. However, the utilization of reliability methods offer a systematic way of treating uncertainties and of quantifying the reliability of a design, thus gains widespread application for the design of rock slopes in practice.

In this paper, limit state function based a simplified Bishop method and Monte-Carlo reliability calculation are used to evaluate rock slope stability.

Reliability analysis

The slope stability problem can be considered as a system with many potential failure surfaces the probability of the most critical slip surface is commonly used as the estimate of the system failure probability, such as JC method, midpoint method, first-order reliability method and Monte-Carlo method. These approaches assume the probability of failure along different slip surfaces is highly correlated (Mostyn and Li, 1993; Chowdhury and Xu, 1995).

In Monte Carlo method, discrete values of the component random variables are generated in a fashion consistent with their probability distribution, and the performance function is calculated for each generated set. The process is repeated many times to obtain an approximate, discrete probability density function of the performance function (Sung Eun Cho, 2007).

Limit state function

The limit state of structure is described by performance function $Z(X)$. A vector, $X=[X_1, X_2, X_3, \dots, X_n]$, represent a set of random variables, In n -dimensional hyperspace of the basic variables, $Z(X)=0$ is the boundary between the region in which the target factor of safety is not exceeded and the region which it is exceeded.

$$Z = g(x_1, x_2, \dots, x_n) = R(x) - S(x) \quad (1)$$

In Eq. (1), $R(x)$ is resistance force, $s(x)$ is driving force. Among the various factors contributing to slope stability, only the rock mechanical index and physical index are taken into consideration, thus can be expressed as (x_1, x_2, \dots, x_n) . Consequently, the limit state function denoting limit failure state of slope is as follows (H. S. B. Duzgun, 2003):

$$Z = g(x_1, x_2, \dots, x_n) \quad (2)$$

We assume that the slope is unstable when $Z < 0$, stable when $Z > 0$, and limit state when $Z=0$. For the purposes of illustration of slope reliability, we take simplified bishop method for example to establish limit state function as:

$$g(x) = \sum_{i=1}^n \frac{c_i l_i + \gamma_i b_i h_i \tan \phi_i}{\cos \theta_i + \sin \theta_i \tan \phi_i} - \sum_{i=1}^n \gamma_i b_i h_i \sin \theta_i \quad (3)$$

In Eq. (3), b_i, h_i is the width and height of block, c_i, ϕ_i, γ_i respectively represent the cohesion, friction angle and weight of block. θ_i is the angle of gravity vertical and base plane radius.

Minimum reliability index

In this study, we use a deterministic method to search minimum safe factor with the aim that find a critical failure plane and compute its reliability index called minimum reliability index β_{\min} .

CATASTROPHE EVALUATION OF LANDSLIDE SECONDARY DISASTER

Influence and hazard of surge

Surge as a phenomenon consequent to slope failures involves two conceivable movements. First is the ground motion which can be explained by kinematics and landslide dynamics. Second is the submarine motion. When rock masses enter into reservoir at a high speed in very short time and keep moving with each interfacial extrusion, increasing volume underwater results in a huge surge, which get landslide as center and spread toward bank and upper lower reaches.

Among the factors influencing scope and strength of surge, sliding speed and height of surge is the key factor (S.G. Evans et al., 2006). At the present time, three categories of analysis have been developed to compute sliding velocity and height of surge: model testing, numerical simulation and empirical equations.

Forecasting of surge scope

The ASCE recommend method is put forward to calculate surge scope. It is assumed that (a) landslide movement is Centrobatic particle motion and the landslide startup speed is obtained according to gravity acceleration; (b) surge height of a certain distance from failing slope is computed based on thickness of landslide, water height, centre of gravity position and experience curve; (c) wave of the upriver area and downriver area of the river is calculated by maximal surge at start point.

Failing slope speed

Landslide failing speed can be expressed as formula 4, which can be established by energy conservation law.

$$v = \sqrt{2gH \left(1 - \cot \alpha \tan \phi - \frac{cL}{mg \sin \alpha} \right)} \quad (4)$$

In Eq. (4), α is gradient of slide surface, m is mass, c , ϕ represent the cohesion, friction angle of slide surface is distance from gravity to water surface, L is length of contact surface.

The ASCE recommend method simply sliding mass into a mass point and not take into account the actual behavior of a landslide movement. Actually, when sliding mass entering reservoir, the parts underwater have no impact on water surface and no influence on surge upper water. So, it is recognized to employ the modified distance from gravity of sliding mass underwater to water surface H' in Eq. (5)

$$v = \sqrt{\left(1 - \cot \alpha \tan \phi - \frac{cL}{mg \sin \alpha} \right) \sqrt{2gH'}} \quad (5)$$

Maximum surge of failing slope

The maximum surge of failing slope is controlled by the nondimensional relative landslide speed V_r in Eq. (6), Where v is failing slope speed, H_w is water depth .

$$V_r = v / \sqrt{gH_w} \tag{6}$$

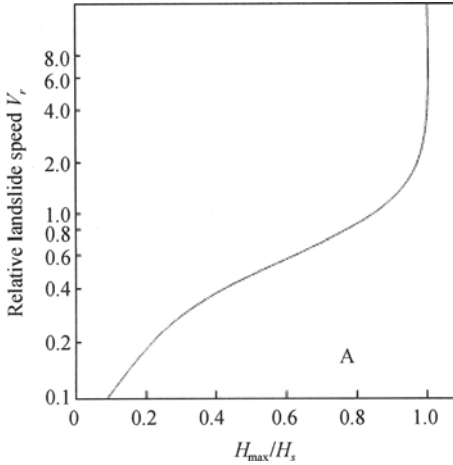


Figure 1(a). Maximum surge of failing slope

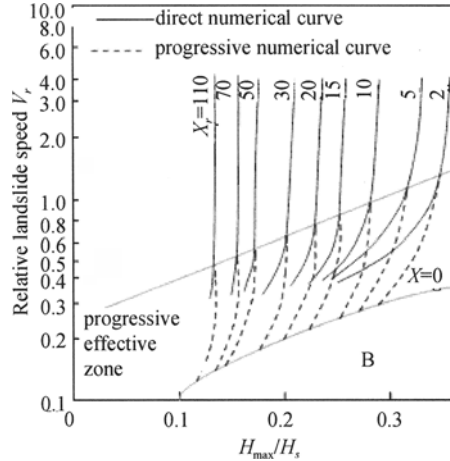


Figure 1(b). Maximum surge height

Surge at a certain distance

The maximum surge can be estimated from empirical graph in Figure 1. Relative distance

$$X_r = X / H_w \tag{7}$$

where, X is the distance from failing slope, H_w is water depth of channel. It comes to conclusion that surge height decrease in the direction of landslide wave propagation and little increase with river roughness.

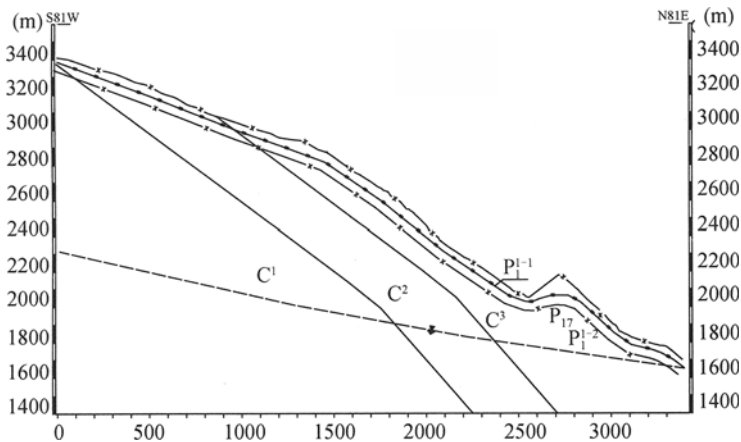


Figure 2. A typical slope section of slope

EXAMPLE ANALYSIS

In this section, application of the presented procedure is illustrated through an analysis of example problems to the stability of the left bank of the upper Tiger Leaping Gorge of the Jinsha rivers slope. The slope consists of several ladders of slide surface. The deposit is highly heterogeneous. A typical slope section showing is presented in Figure 2.

Reliability analysis of slope stability

Geologic analysis indicates the rock slope stability controlled by structural plane and exhibit local traction failure. Table 1 presents the results obtained from a Monte Carlo method. It shows that failure probability of landslide mass approach to safe factor. Slope safe factor reach to 1.1 under natural and rainy work condition and means slope basic stable; safe factor fall down 1.0 under seismic condition when slope in limit equilibrium state; safe factor below 1.0 under mal-condition and slope in risk state.

The failure probability obviously gradually increases at disadvantageous environment. Unfortunately, probabilistic slope stability analysis methods do not considered in design code. Thus, the similar probabilistic engineered slopes results are referenced. It is suggested reliability up to 96%(failure probability 4% below) means integral safety. So, the given slope in risk state under mal-condition.

Table1. The results of slope failure probability

Work condition	Slide surface	Safe factor	Failure probability	Reliability index
Natural	Most dangerous	1.276	3.24%	1.85
slope	rain	1.137	3.75%	1.78
Naturalslope	Most dangerous	1.062	4.09%	1.72
+earthquake	rain	0.957	4.55%	1.69

Landslide surge analysis

The modified ASCE recommend method talked in the previous section is adopted to estimate landslide scope. According to initial computed sliding speed is 4.72m/s, Table 2 presents the height of surge at a certain distance from the failing location.

It can be observed from results the low sliding speed could induce high surge height. Therefore, any form of failure would damage to up and downstream and trsurement should be put inforwd to landslide.

Treatment evaluation

The principle of treatment evaluation is adaptation to local conditions and acclimatization to the environment. Thus, by considering the slope properties, deform regularity, feasibility and practicability involved in the technology, design treatment scheme should conducted based on protection idea.

The upper Tiger Leaping Gorge slopes are characterized by structural plane controlled local traction failure and sagging slopes in which movement may result in huge surge. The

mechanics of landslides are influenced by the lithology and hydrogeology. The subsequent reduced shear strength was induced by the additional water supplied by the rainfall. In order to reduce the threat of landslide to environment, important treatment evaluation to rock slope is proposed (a) drainage arrangement at slope surface; (b) anti-slide pile at base of slope; (c) prestressed anchor rope at the top of slope.

Table 2. Maximum height of surge at a certain distance ($V_r=4.72\text{m/s}$)

Location	Falling Slope	Upstream 800m	Upstream 1300m	Downstream 900m
Distance $X(\text{m})$	0	1250	790	840
Depth water $H_w(\text{m})$	38.6	38.5	39.3	38.2
Effective distance $X_r(\text{m})$	0	20.67	32.338	22.432
Max surge H_{max}	45.3	10.25	8.13	9.54

CONCLUNTION

The landslide is a complex process which involves lithology, hydrogeology aspects(R. COUTURE,2006). The probility analysis based on limiting equilibrium method was applied to appreciate slope stability under rain and earthquake condition. The empirical formula was employed to evaluate consequences induced by surge wave. In the case of understanding degree of catastrophe and grade of risk, engineering treatments system were proposed and catastrophe evaluation of landslide instability was established.

REFERENCES

- Chowdhury R.N., Xu D.W.(1995). Geotechnical system reliability of Slopes. *Reliability Engineering and Systems Safety*, 47: 141-151.
- Duzgun H. S. B., Yucemen M. S. and Karpuz C. (2003). A methodology for reliability-based design of rock slopes. *Rock Mech. Rock Engng.* 36(2): 95-120.
- Mostyn G.R., Li K.S. (1993). Probabilistic slope stability-state of play. *Conf. on Probabilistic Methods in Geotechnical Engineering*, Balkema, Rotterdam, The Netherlands, 89-110.
- Courtire R., Evans S.G. (2006). Slow-moving disintegrating rockslides on moutain slopes. *Landslides from Massive Rock Slope Failure*, 2006 Springer. Printed in the Netherlands, 377-393.
- Evans S.G., Scarascia Mugnozza G. Storm A.L. et al. (2006). Landslides from massive rock slope failure and associated phenomena. *Landslides from Massive Rock Slope Failure*, 2006 Springer. Printed in the Netherlands, 3-52.
- Sung Eun Cho. (2007). Effects of spatial variability of soil properties on slope stability. *Engineering Geology*, 92: 97-109

NONLINEAR FINITE ELEMENT RELIABILITY ANALYSIS OF SLOPE STABILITY

Xiaohui Tan

*School of Resource and Environmental Engineering, Hefei University of Technology,
Hefei 230009, China*

Jianguo Wang

School of Civil Engineering, Hefei University of Technology, Hefei 230009, China

A method of nonlinear finite element reliability analysis (FERA) of slope stability based on slip surface stress analysis is proposed in this paper. The main effort of this method lies in the calculation of gradient of stress and gradient of plastic matrix with respect to basic variables. Supposing the soil mass is elasto-plastic and meets Mohr-Coulomb yield criterion, the formulae of these gradients are deduced. The advantage of this method is that it can calculate both the reliability index and the corresponding position of slip surface.

INTRODUCTION

There are several kinds of methods which can be used to analyze slope stability, such as limit equilibrium method and finite element method (FEM). Finite element analysis of slopes can be mainly divided into two categories: one is called strength reduction method (SRM), which can get the factor of safety (F_s) by continually reducing the values of strength parameters to such a critical state that the running of finite element code cannot converge anymore (Swan et al., 1999); the other is called slip surface stress analysis method (SSA), which gets the value of F_s according to the value of stress obtained from the finite element analysis (Kim et al., 1999). Many authors have studied the technique of using various kinds of limit equilibrium methods to conduct the reliability analysis of slopes. However, the research work of using FEM to conduct the reliability analysis of slopes is very limited. Griffiths et al. (2004) used strength reduction method to calculate the reliability index and of the failure probability of a slope. Mellah et al. (2001) used stochastic finite element method to calculate the reliability index of each finite element and draw the contour of reliability index of soil slope, but they didn't calculate the overall reliability index and the corresponding position of the critical slip surface.

Although it is important to calculate the reliability index of a slope, it is also necessary to calculate the position of the slip surface corresponding to the overall reliability index of a slope, especially when the slope is unstable. Only if the position is known, can we design a suitable supporting system for the slope. Therefore, this paper proposes a nonlinear finite element reliability analysis (FERA) method of slope stability based on SSA technique which can calculate both the reliability index and the corresponding position of slip surface. The

main difficulty of this method is the calculation of gradient of stress and plastic matrix with respect to basic variables. Then, the detail formulae are deduced based on the assumption that the soil mass is elasto-plastic and meets Mohr-Coulomb yield criterion.

PRINCIPLE OF NONLINEAR FINITE ELEMENT RELIABILITY ANALYSIS OF SLOPE STABILITY BASED ON SSA TECHNIQUE

Methods of reliability evaluation

There are several methods for the evaluation of the reliability of structures, such as mean first order reliability analysis method (MFORM), first order reliability analysis method, Monte Carlo simulation method, and response surface method (Gong et al.,2003). Among these methods, MFORM is very simple and it's widely used in geotechnical engineering. Hence, this paper uses MFORM for the calculation of reliability index. The formula can be expressed as follows:

$$\beta = \frac{\mu_z}{\sigma_z} = \frac{g(\mu_{x_1}, \mu_{x_2}, \dots, \mu_{x_n})}{\left[\sum_{i=1}^n \sum_{j=1}^n \frac{\partial g(\mu_x)}{\partial X_i} \frac{\partial g(\mu_x)}{\partial X_j} \rho_{X_i, X_j} \sigma_{x_i} \sigma_{x_j} \right]^{1/2}} \quad (1)$$

where μ_z and σ_z are the mean value and standard deviation of the limit state function $Z=Z(\mathbf{X})$, respectively; $\mathbf{X}=(X_1, X_2, \dots, X_n)$ is basic random variables; μ_{x_i} and σ_{x_i} ($i=1, \dots, n$) are the mean value and standard deviation of the basic random variable X_i , respectively; ρ_{X_i, X_j} ($i=1, \dots, n$; $j=1, \dots, n$) is the correlation coefficient of basic stochastic variables X_i and X_j ; $\partial g(\mu_x)/\partial X_i$ ($i=1, \dots, n$) is the gradient of the limit state function with respect to the basic stochastic variable X_i at the value of μ_x .

Nonlinear FERA of slope stability based on SSA

The framework nonlinear FERA of slope stability based on SSA is similar to the method of deterministic finite element analysis of slope stability based on SSA. The main steps for the calculation of the overall factor of safety (Fs_{\min}) and its position in deterministic finite element analysis of slope stability based on SSA are as follows. Firstly, a potential slip surface is selected, and the value of Fs of this surface can be derived according to the value of stress obtained from the finite element analysis. Secondly, lots of slip surfaces are tested, and the minimum value of Fs will be the overall factor of safety of the slope. Correspondingly, the main steps for the calculation of β_{\min} and its position in nonlinear FERA of slope stability based on SSA are the same. The difference of these two methods is that in the nonlinear FERA of slope stability, what is needed to be calculated is β instead of Fs . Then, not only stress but also the gradient of stress with respect to basic variables are needed in the finite element analysis.

Let's define the limit state function on a slip surface is as follows (Tan, 2007):

$$Z = g(\mathbf{X}) = \sum_{i=1}^{ne} Z_i \Delta_i = \sum_{i=1}^{ne} g_i(\mathbf{X}) \Delta_i \quad (2)$$

where

$$Z_i = g_i(\mathbf{X}) = -\left(\frac{\sigma_x + \sigma_y}{2} - \frac{\sigma_x - \sigma_y}{2} \cos 2\theta + \tau_{xy} \sin 2\theta\right) \tan \varphi + c - \left(\frac{\sigma_x - \sigma_y}{2} \sin 2\theta + \tau_{xy} \cos 2\theta\right) \quad (3)$$

where ne represents the number of elements on a special slip surface, $Z_i = g_i(\mathbf{X})$ and Δl_i represent the limit state function and the length of the slip surface of the i th element; $\sigma_x, \sigma_y, \tau_{xy}$ are stress components at the central point of the slip surface; c and φ are cohesion and internal friction angle; θ means the angle of the slip surface to the horizontal plane.

Form Eqs. (2-3) we can get the gradient of Z_i with respect to basic variables as follows:

$$\frac{\partial Z}{\partial \mathbf{X}} = \sum_{i=1}^{ne} \frac{\partial Z_i}{\partial \mathbf{X}} \Delta l_i = \sum_{i=1}^{ne} \left[\frac{\partial g_i(\mathbf{X}, \boldsymbol{\sigma}^*)}{\partial \mathbf{X}} + \frac{\partial g_i(\mathbf{X}^*, \boldsymbol{\sigma})}{\partial \boldsymbol{\sigma}} \cdot \frac{\partial \boldsymbol{\sigma}}{\partial \mathbf{X}} \right] \Delta l_i \quad (4)$$

where $\boldsymbol{\sigma} = (\sigma_x, \sigma_y, \tau_{xy})^T$, T means transpose of a vector. The superscript asterisk means the correspondent variable should be considered as a constant in the calculation of partial derivatives. From Eq. (3) we can find that it is easy to calculate the value of $\partial g_i(\mathbf{X}, \boldsymbol{\sigma}^*)/\partial \mathbf{X}$ and $\partial g_i(\mathbf{X}^*, \boldsymbol{\sigma})/\partial \boldsymbol{\sigma}$. However, it is difficult to calculate the value of $\partial \boldsymbol{\sigma}/\partial \mathbf{X}$, which will be discussed in detail in the next section.

GRADIENT OF STRESS AND PLASTIC MATRIX WITH RESPECT TO BASIC VARIABLES

Gradient of stress with respect to basic variables

The authors use the direct differentiation method to calculate the gradient of stress with respect to each variable. Supposing the calculation method of equilibrium equations is incremental tangent stiffness method, the iterative equilibrium equation will be

$$(\mathbf{K}_0)^{k+1} \Delta \mathbf{d}_{i+1}^{k+1} = \mathbf{F}^{k+1} + \mathbf{R}_i^{k+1} \quad (5)$$

where k ($k=1,2,\dots,N$; N is the number of total load steps) and i ($i=1,2,\dots$) represent the number of load increment and the number of iteration of nonlinear equations, respectively; \mathbf{K}_0 is the initial tangent stiffness matrix; $\Delta \mathbf{d}$ is displacement increment; \mathbf{R} is the vector of internal force. Form Eq. (5), we can get

$$\Delta \mathbf{d}_{i+1}^{k+1} = [(\mathbf{K}_0)^{k+1}]^{-1} (\mathbf{F}^{k+1} + \mathbf{R}_i^{k+1}) \text{ and } \left(\frac{\partial \Delta \mathbf{d}}{\partial \mathbf{X}} \right)_{i+1}^{k+1} = [(\mathbf{K}_0)^{k+1}]^{-1} \left[\left(\frac{\partial \mathbf{F}}{\partial \mathbf{X}} \right)^{k+1} + \left(\frac{\partial \mathbf{R}}{\partial \mathbf{X}} \right)_i^{k+1} - \left(\frac{\partial \mathbf{K}_0}{\partial \mathbf{X}} \right)^{k+1} \Delta \mathbf{d}_{i+1}^{k+1} \right] \quad (6)$$

Based on the relationship of stress increase ($\Delta \boldsymbol{\sigma}$) and displacement increase ($\Delta \mathbf{d}$) and the general expression of elasto-plastic matrix \mathbf{D}_{ep} , we can get

$$(\Delta \boldsymbol{\sigma})_{i+1}^{k+1} = \mathbf{D}_e \mathbf{B} (\Delta \mathbf{d})_{i+1}^{k+1} - (1-m) (\mathbf{D}_p)_{i+1}^{k+1} \mathbf{B} (\Delta \mathbf{d})_{i+1}^{k+1} = (\Delta \boldsymbol{\sigma}_e)_{i+1}^{k+1} - (\Delta \boldsymbol{\sigma}_p)_{i+1}^{k+1} \quad (7)$$

where \mathbf{B} is strain matrix; m is a factor of proportionality. By differentiation, we can get

$$\left(\frac{\partial \Delta \boldsymbol{\sigma}}{\partial \mathbf{X}} \right)_{i+1}^{k+1} = \left(\frac{\partial \Delta \boldsymbol{\sigma}_e}{\partial \mathbf{X}} \right)_{i+1}^{k+1} - \left(\frac{\partial \Delta \boldsymbol{\sigma}_p}{\partial \mathbf{X}} \right)_{i+1}^{k+1} \quad (8)$$

$$\left(\frac{\partial \Delta \sigma_e}{\partial X}\right)_{i+1}^{k+1} = \frac{\partial D_e}{\partial X} B \Delta d_{i+1}^{k+1} + D_e B \left(\frac{\partial \Delta d}{\partial X}\right)_{i+1}^{k+1} \quad (9)$$

$$\left(\frac{\partial \Delta \sigma_p}{\partial X}\right)_{i+1}^{k+1} = (1-m) \left(\frac{\partial D_p}{\partial X}\right)_{i+1}^{k+1} B \Delta d_{i+1}^{k+1} + (1-m) (D_p)_{i+1}^{k+1} B \left(\frac{\partial \Delta d}{\partial X}\right)_{i+1}^{k+1} - \frac{\partial m}{\partial X} (D_p)_{i+1}^{k+1} B \Delta d_{i+1}^{k+1} \quad (10)$$

Because D_e is simply the function of soil parameters, the expression of $\partial D_e / \partial X$ can be obtained easily. However, D_p is the function of X , m and σ , so the gradient of D_p with respect to X will takes the form of Eq. (11) by the use of chain rule of differentiation:

$$\frac{\partial D_p}{\partial X} = \frac{\partial D_p(X, \sigma^*)}{\partial X} + \frac{\partial D_p(X^*, \sigma)}{\partial \sigma} \cdot \frac{\partial \sigma}{\partial X} \quad (11)$$

Gradient of plastic matrix with respect to basic variables

Assuming the soil mass is elasto-plastic and meet Mohr-Coulomb criterion, the expansion form of plastic matrix D_p will take the form of Eq.(12) (Smith et al., 2003)

$$D_p = \frac{E}{2(1+\mu)(1-2\mu)(1-2\mu+\sin\phi\sin\psi)} A \quad (12)$$

where E and μ means elastic module and poisson ratio, respectively; A is a matrix:

$$A = \begin{bmatrix} R_1 C_1 & R_1 C_2 & R_1 C_3 & R_1 C_4 \\ R_2 C_1 & R_2 C_2 & R_2 C_3 & R_2 C_4 \\ R_3 C_1 & R_3 C_2 & R_3 C_3 & R_3 C_4 \\ R_4 C_1 & R_4 C_2 & R_4 C_3 & R_4 C_4 \end{bmatrix}, \begin{cases} C_1 = \sin\phi + k_1(1-2\mu)\sin\alpha \\ C_2 = \sin\phi - k_1(1-2\mu)\sin\alpha \\ C_3 = k_2(1-2\mu)\cos\alpha \\ C_4 = 2\mu\sin\phi \end{cases}, \begin{cases} R_1 = \sin\psi + k_1(1-2\mu)\sin\alpha \\ R_2 = \sin\psi - k_1(1-2\mu)\sin\alpha \\ R_3 = k_2(1-2\mu)\cos\alpha \\ R_4 = 2\mu\sin\psi \end{cases},$$

$$\alpha = \arctan \left| \frac{\sigma_x - \sigma_y}{2\tau_{xy}} \right|, \quad k_1 = \begin{cases} 1 & \text{if } (\sigma_x \geq \sigma_y) \\ -1 & \text{if } (\sigma_x < \sigma_y) \end{cases}, \quad k_2 = \begin{cases} 1 & \text{if } (\tau_{xy} \geq 0) \\ -1 & \text{if } (\tau_{xy} < 0) \end{cases}$$

For simplicity, let's define $X=(c, \phi, \psi, \gamma, E, \mu)^T$ (where $c, \phi, \psi, \gamma, E, \mu$ means cohesion, internal friction angle, expansive angle, unit weight, poisson rate, respectively) and $BB = 2(1+\mu)(1-2\mu)(1-2\mu+\sin\phi\sin\psi)$. Then, $D_p = (E/BB)A$.

The calculation of $\partial D_p(X, \sigma^*) / \partial X$

From Eq. (12), we can get

$$\frac{\partial D_p(X, \sigma^*)}{\partial X_i} = \frac{1}{BB^2} \cdot \left(\frac{\partial E}{\partial X_i} \cdot A \cdot BB + E \cdot \frac{\partial A}{\partial X_i} \cdot BB - E \cdot A \cdot \frac{\partial BB}{\partial X_i} \right) \quad (13)$$

where

$$\frac{\partial E}{\partial X} = [0 \ 0 \ 0 \ 0 \ 1 \ 0]^T$$

$$\frac{\partial BB}{\partial X} = \{0, 2(1+\mu)(1-2\mu)\sin\phi, 2(1+\mu)(1-2\mu)\sin\phi, 0, 0, 2[-3(1-4\mu^2) - \sin\phi\sin\psi(1+4\mu)]\}^T$$

$$\frac{\partial \mathbf{A}}{\partial X_i}(j, k) = \frac{\partial R_j}{\partial X_i} C_k + \frac{\partial C_j}{\partial X_i} R_k \quad (j, k=1, \dots, 4) \text{ and}$$

$$\begin{cases} \frac{\partial \mathbf{R}}{\partial X_3} = \frac{\partial \mathbf{R}}{\partial \phi} = [\cos \phi \quad \cos \phi \quad 0 \quad 2\mu \cos \phi]^T \\ \frac{\partial \mathbf{R}}{\partial X_6} = \frac{\partial \mathbf{R}}{\partial \mu} = 2[-k_1 \sin \alpha \quad k_1 \sin \alpha \quad -k_2 \cos \alpha \quad \sin \phi]^T \end{cases}$$

$$\begin{cases} \frac{\partial \mathbf{C}}{\partial X_2} = \frac{\partial \mathbf{C}}{\partial \phi} = [\cos \phi \quad \cos \phi \quad 0 \quad 2\mu \cos \phi]^T \\ \frac{\partial \mathbf{C}}{\partial X_6} = \frac{\partial \mathbf{C}}{\partial \mu} = 2[-k_1 \sin \alpha \quad k_1 \sin \alpha \quad -k_2 \cos \alpha \quad \sin \phi]^T \end{cases}$$

The calculation of $\partial \mathbf{D}_p(\mathbf{X}^*, \boldsymbol{\sigma}) / \partial \boldsymbol{\sigma}$

From Eq. (12), we can get

$$\frac{\partial \mathbf{D}_p(\mathbf{X}^*, \boldsymbol{\sigma})}{\partial \boldsymbol{\sigma}} = \frac{E}{BB} \cdot \frac{\partial \mathbf{A}}{\partial \boldsymbol{\sigma}} \quad (14)$$

where

$$\begin{cases} \frac{\partial C_1}{\partial \boldsymbol{\sigma}} = \frac{\partial R_1}{\partial \boldsymbol{\sigma}} = k_1(1-2\mu) \cos \alpha \cdot \begin{bmatrix} \frac{\partial \alpha}{\partial \sigma_x} & \frac{\partial \alpha}{\partial \sigma_x} & \frac{\partial \alpha}{\partial \tau_{xy}} \end{bmatrix} \\ \frac{\partial C_2}{\partial \boldsymbol{\sigma}} = \frac{\partial R_2}{\partial \boldsymbol{\sigma}} = -k_1(1-2\mu) \cos \alpha \cdot \begin{bmatrix} \frac{\partial \alpha}{\partial \sigma_x} & \frac{\partial \alpha}{\partial \sigma_x} & \frac{\partial \alpha}{\partial \tau_{xy}} \end{bmatrix} = -\frac{\partial C_1}{\partial \boldsymbol{\sigma}} \\ \frac{\partial C_3}{\partial \boldsymbol{\sigma}} = \frac{\partial R_3}{\partial \boldsymbol{\sigma}} = -k_2(1-2\mu) \sin \alpha \cdot \begin{bmatrix} \frac{\partial \alpha}{\partial \sigma_x} & \frac{\partial \alpha}{\partial \sigma_x} & \frac{\partial \alpha}{\partial \tau_{xy}} \end{bmatrix} \\ \frac{\partial C_4}{\partial \boldsymbol{\sigma}} = \frac{\partial R_4}{\partial \boldsymbol{\sigma}} = [0 \ 0 \ 0] \\ \frac{\partial \alpha}{\partial \sigma_x} = \frac{2k_3 \tau_{xy}}{4\tau_{xy}^2 + (\sigma_x - \sigma_y)^2} \\ \frac{\partial \alpha}{\partial \sigma_y} = -\frac{2k_3 \tau_{xy}}{4\tau_{xy}^2 + (\sigma_x - \sigma_y)^2} = -\frac{\partial \alpha}{\partial \sigma_x} \\ \frac{\partial \alpha}{\partial \tau_{xy}} = \frac{-2k_3(\sigma_x - \sigma_y)}{4\tau_{xy}^2 + (\sigma_x - \sigma_y)^2} \end{cases}$$

SAMPLE EXAMPLES

A two-layer slope (Figure 1) (Crum,2001; Xu et al., 2006) is adopted to validate the proposed approach. The soil strength parameters, cohesion, and friction angle, are treated as random variables whose statistical moments are presented in Table 1. The unit weights of the two soil layers are assumed to be 19kN/m^3 . In the nonlinear FERA of this slope, the boundary conditions are: the bottom of the slope is fixed, and the horizontal displacements on the left and right sides are fixed. The overall reliability index obtained by this study is listed in the last row in Table 2.

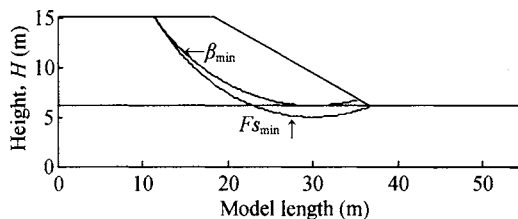


Figure1. Cross section and slip surfaces of two-layer slope

Table 1. Soil strength parameters for two-layer slope

Basic variables	Mean value	Standard deviation	Coefficient of variation
$c_1(\text{kPa})$	38.31	7.66	0.2
$c_2(\text{kPa})$	23.94	4.79	0.2
$\varphi_2(\text{deg})$	12	1.2	0.1

Table 2. Results of reliability analysis from different methods

Method	Reliability index
Crum [20]	2.23
Xu et al. (2006), Spencer's method with circular slip surface	2.22
Xu et al. (2006), Spencer's method with noncircular slip surface	2.06
Xu et al. (2006), FERA based on strength reduction method	2.18
This study (FERA based on SSA)	2.33

From Table 2, we can know that the reliability index obtained from the nonlinear FERA of slope stability based on SSA proposed in this paper is 2.33, which is slightly larger than those of Crum's method and Xu's methods. Since this study assumes the slip surface is circular, the reliability index is more close to Crum's method and Xu's method Spencer's method with circular slip surface. As to Xu's Spencer's method with noncircular slip surface and Xu's FERA based on SRM (without the assumption of circular slip surface), the difference of reliability indices between the two methods and this study are a little larger. Xu's FERA based on SRM cannot obtain the position of the critical slip surface. However, the method proposed in this paper can easily get the position of the critical slip surface (β_{\min}), which is plotted in Figure 1. For comparison, the position of the slip surface corresponding to Fs_{\min} obtained from deterministic finite element analysis is also plotted in Figure 1. We can find that the positions of this two slip surfaces are different: the slip surface of β_{\min} is tangent to

the interface of the two soil layers, but the bottom of slip surface of Fs_{\min} is already in the second layer.

CONCLUSIONS

The method of nonlinear FERA of slope stability based on SSA is similar to deterministic FEM of slope stability analysis based on SSA. The difference is that in deterministic FEM of slope stability, only stress is needed for the calculation of Fs . However, in FERA, not only stress but also the gradient of stress with respect to basic variables is needed. Therefore, the main effort of nonlinear FERA of slope stability based on SSA lies in the calculation of the gradient of stress and plastic matrix with respect to basic variables. Supposing the soil mass is elasto-plastic and meets Mohr-Coulomb yield criterion, the formulae of gradients are deduced. The features and advantages of the method of nonlinear FERA based on SSA were demonstrated by an example, from which we can find it can calculate both the reliability index and the corresponding position of the critical slip surface, the latter of which is very important for the design of supporting system if the slope is unstable.

ACKNOWLEDGEMENTS

The study was supported in part by National Natural Science Foundation of China (No.50748033), Youth Foundation from Education Department of Anhui province, China (No.2005jq1021) and the Specific Foundation for Doctor's degree of HFUT, China (No.2007GDBJ044). These supports are gratefully acknowledged.

REFERENCES

- Crum D.A.(2001). Discussion of 'Search algorithm for minimum reliability index earth slopes. *Journal of Geotechnical and Geoenvironmental Engineering*, 127(2): 194-195.
- Gong J.X.(2003). *Computational Methods for Reliability of Engineering Structures*. Dalian: Dalian University of Technology Press.
- Griffiths D.V., Fenton G.A.(2004). Probabilistic slope stability analysis by finite elements. *Journal of Geotechnical and Geoenvironmental Engineering*, 130(5): 507-518.
- Kim J.Y., Li S.R.(1997). An improved search strategy for the critical slip surface using finite element stress fields. *Computer and Geotechnics*, 21(4): 295-313.
- Mellah R., Auvinet G. and Masrouri F. (2001). Stochastic finite element method applied to non-linear analysis of embankments. *Probabilistic Engineering Mechanics*, 15: 251-259.
- Swan C.C., Seo Y.K.(1999). Limit state analysis of earthen slopes using dual continuum/FEM approaches. *International Journal for Numerical and Analytical Methods in Geomechanics*, 23: 1359-1371.
- Smith I.M., Griffiths D.V. (2003). *Programming the Finite Element Method*. Beijing: Publishing House of Electronics Industry.
- TAN X.H. (2007). *Nonlinear finite element reliability analysis of slope stability*. PhD. Thesis, School of Civil Engineering, HeFei University of Technology.
- Xu B., Low B.K. (2006). Probabilistic stability analyses of embankments based on finite-element method. *Journal of Geotechnical and Geoenvironmental Engineering*, 132(11): 1444-1454.

FINITE ELEMENT ANALYSIS OF STRAIN LOCALIZATION PROBLEMS FOR SLOPE BASED ON COSSERAT CONTINUUM MODEL

Hongxiang Tang

*School of Civil and Hydraulic Engineering, Dalian University of Technology,
Dalian 116023, China*

Daguo Wang

*Research Center for Numerical Tests on Material Failure, Dalian University,
Dalian 116622, China*

In the present work, the Cosserat micro-polar continuum theory is introduced into the FEM numerical model, which is used to simulate the strain localization phenomena due to strain softening. The numerical studies on progressive failure phenomena, which occur in slope, characterized by strain localization due to strain softening and its development, are numerically simulated by two types of Cosserat continuum finite elements, i.e. $u_8\omega_8$ and $u_8\omega_4$ elements, and classical continuum finite element, i.e. u_8 . It is indicated that both two Cosserat continuum finite elements possess better performance in simulation of strain localization, and the effectiveness in preserving the well-posedness of the localization problems and simulating the progressive failure phenomena characterized by strain localization due to strain softening.

INTRODUCTION

As strain softening constitutive behavior is incorporated into a computational model in the frame of classical plastic continuum theories, the initial and boundary value problem of the model will become ill-posed, resulting in pathologically mesh-dependent solutions. To correctly simulate strain localization phenomena characterized by occurrence and severe development of the deformation localized into narrow bands of intense irreversible straining caused by strain softening, it is required to introduce some type of regularization mechanism into the classical continuum model to preserve the well-posedness of the localization problem.

One of the radical approaches to introduce the regularization mechanism into the model is to utilize the Cosserat micro-polar continuum theory, in which high-order continuum structures are introduced. Among the typical work, are contributions of de Borst et al. (1991,1993). In the present work, two types of Cosserat continuum finite elements, i.e. $u_8 \omega_8$ (8-noded element interpolation approximations for both displacements u and microrotation ω) and $u_8 \omega_4$ (8-noded and 4-noded element interpolation approximations for u and ω respectively) elements are developed to study the progressive failure phenomena,

which occur in slope, characterized by strain localization due to strain softening and its development.

THE GOVERNING EQUATIONS OF ELASTIC COSSERAT CONTINUUM

Each material point in the two dimensional Cosserat continuum has three degrees-of-freedom, i.e. two translational degrees-of-freedom u_x, u_y and one rotational degree-of-freedom ω_z with the rotation axis orthogonal to the two dimensional plane,

$$\mathbf{u} = [u_x \ u_y \ \omega_z]^T \quad (1)$$

Correspondingly, the strain and stress vectors are defined as

$$\boldsymbol{\varepsilon} = [\varepsilon_{xx} \ \varepsilon_{yy} \ \varepsilon_{zz} \ \varepsilon_{xy} \ \varepsilon_{yx} \ \kappa_{zx} l_c \ \kappa_{zy} l_c]^T \quad (2)$$

$$\boldsymbol{\sigma} = [\sigma_{xx} \ \sigma_{yy} \ \sigma_{zz} \ \sigma_{xy} \ \sigma_{yx} \ m_{zx}/l_c \ m_{zy}/l_c]^T \quad (3)$$

where κ_{zx}, κ_{zy} are introduced as micro-curvatures in Cosserat theory, m_{zx}, m_{zy} are the couple stresses conjugate to the curvatures κ_{zx}, κ_{zy} , l_c is defined as the internal length scale.

It is assumed that the strain vector $\boldsymbol{\varepsilon}$ is additively decomposed into both the elastic and the plastic parts, i.e. $\boldsymbol{\varepsilon}_e$ and $\boldsymbol{\varepsilon}_p$, and the elastic strain vector $\boldsymbol{\varepsilon}_e$ is linearly related to the stress vector,

$$\boldsymbol{\sigma} = \mathbf{D}_e \boldsymbol{\varepsilon}_e \quad (4)$$

in which the elastic modulus matrix \mathbf{D}_e for isotropic media can be given in the form

$$\mathbf{D}_e = \begin{bmatrix} \lambda + 2G & \lambda & \lambda & 0 & 0 & 0 & 0 \\ \lambda & \lambda + 2G & \lambda & 0 & 0 & 0 & 0 \\ \lambda & \lambda & \lambda + 2G & 0 & 0 & 0 & 0 \\ 0 & 0 & 0 & G + G_c & G - G_c & 0 & 0 \\ 0 & 0 & 0 & G - G_c & G + G_c & 0 & 0 \\ 0 & 0 & 0 & 0 & 0 & 2G & 0 \\ 0 & 0 & 0 & 0 & 0 & 0 & 2G \end{bmatrix} \quad (5)$$

with the Lamé constant $\lambda = 2G\nu/(1-2\nu)$, G and ν are the shear modulus and Poisson's ratio in the classical sense, while G_c is introduced as the Cosserat shear modulus. Li and Tang(2005) formulated a consistent algorithm of the pressure-dependent elastoplastic model in the framework of Cosserat continuum theory, which is used in the present work.

THE FINITE ELEMENTS FOR COSSERAT CONTINUUM

Requirements of element performance

Modelling strain localization caused by strain softening and characterized by weak discontinuities requires the efforts in the following two aspects. The first aspect is to incorporate some type of regularization mechanism into the classical continuum to preserve

the well-posedness of the localization problem. The second aspect is to develop a finite element formulation, which possesses, in addition to the usual requirements to element intrinsic properties, the capability to capture the pronounced localized failure mode and to simulate the reduction of the load-carrying capability due to strain softening.

The second aspect requires that the finite element adopted in the analysis has the ability of eliminating the difficulties associated with the treatment of incompressible materials. Low-order elements, when applied to incompressible materials, tend to exhibit volumetric locking. In volumetric locking, the displacements are underpredicted by large factors, 5 to 10 is not uncommon for otherwise reasonable meshes. Although incompressible materials are quite rare in linear stress analysis, in the nonlinear regime many materials behave in a nearly incompressible manner. For example, Mises elastic-plastic materials are incompressible in their plastic behavior, and an element that locks volumetrically will not perform well for Mises elastic-plastic materials. For another example, Drucker-Prager elastic-plastic materials are incompressible in their plastic behavior as the plastic potential angle is closed to zero. To be applicable to a large class of nonlinear materials, an element must be able to treat incompressible materials effectively. However, most elements have shortcomings in their performance when applied to incompressible or nearly incompressible materials. The detailed analysis can be seen from Ted et al. (2000).

Two types of cosserat continuum finite elements

As the properties of volumetric locking for low-order elements still exist despite the introduction of microrotation ω , the high-order elements with reduced integration, which possess better performance in this issue, are used in the present work.

Firstly, the eight noded displacement-based quadrilateral isoparametric element interpolation approximation is simply employed for the three degrees-of-freedom in the 2D Cosserat continuum, as illustrated in Figure 1(a). Both the displacements u and microrotation ω are approximated over the element area by the quadratic polynomials

$$u_x(u_y) \cong \sum_{K=1}^8 N_K^u \bar{u}_{xK} (\bar{u}_{yK}) = N^u \bar{u}, \quad \omega \cong \sum_{K=1}^8 N_K^\omega \bar{\omega}_K = N^\omega \bar{\omega} \quad (6)$$

This element is marked as $u8\omega$ (8-noded element interpolation approximations for both displacements u and microrotation ω) in following analysis.

Next, the eight noded displacement-based quadrilateral isoparametric element interpolation approximation is employed for the two degrees-of-freedom u , while the four noded displacement-based quadrilateral isoparametric element interpolation approximation is employed for the degree-of-freedom ω in the 2D Cosserat continuum, as illustrated in Figure 1(b). The displacements u are approximated over the element area by the quadratic polynomials

$$u_x(u_y) \cong \sum_{K=1}^8 N_K^u \bar{u}_{xK} (\bar{u}_{yK}) = N^u \bar{u} \quad (7)$$

The microrotation ω is approximated over the element area by the bilinear polynomials

$$\omega \cong \sum_{K=1}^4 N_K^\omega \bar{\omega}_K = N^\omega \bar{\omega} \quad (8)$$

This element is marked as $u8\omega4$ (8-noded and 4-noded element interpolation approximations for u and ω respectively) in following analysis.

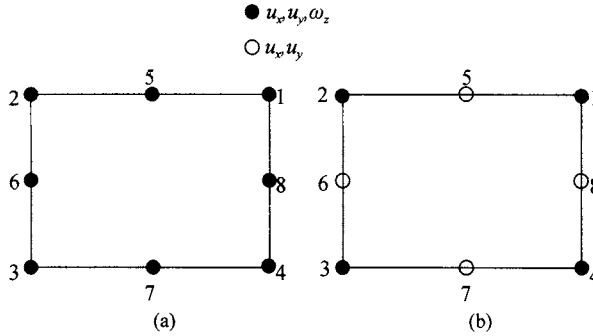


Figure 1. Two types of cosserat continuum finite elements: (a) $u8\omega8$; (b) $u8\omega4$.

FINITE ELEMENT ANALYSIS OF STRAIN LOCALIZATION PROBLEMS FOR SLOPE BASED ON COSSERAT CONTINUUM MODEL

The slope stability problem in the plane strain condition is considered to illustrate the performance of these two finite elements for Cosserat continuum model. The slope is loaded by a footing resting on its crest illustrated in Figure 2. The contact between the footing and the slope is assumed to be perfectly adhesive. The increasing load is applied to the slope via the increasing vertical displacement prescribed to the nodal point A of the element mesh, so that the footing is also allowed to rotate around the point A.

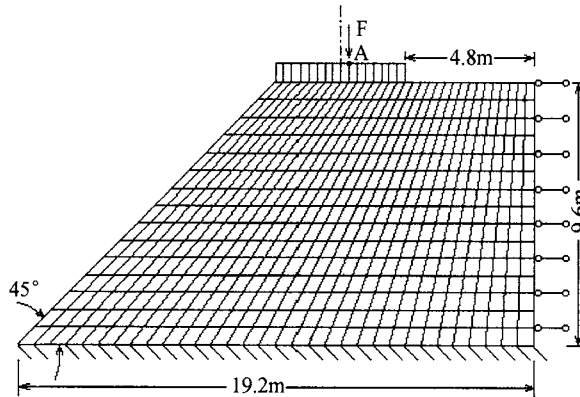


Figure 2. The slope stability problem: geometry, boundary conditions and finite element mesh.

The pressure dependent elastoplastic constitutive behavior of the medium and the Drucker-Prager yield criterion are particularly considered. With the piecewise linear softening assumption for the cohesion, we have

$$c = c(\bar{\epsilon}_p) = c_0 + h_p^c \bar{\epsilon}_p \quad (9)$$

where c_0 is the initial cohesion, h_p^c the softening parameter for cohesion, $\bar{\epsilon}_p$ the equivalent plastic strain. The material parameters used in this example are chosen as: elastic modulus $E=5.0E+7\text{Pa}$, Poisson's ratio $\nu =0.3$, Cosserat shear modulus $G_c =1.0E+7\text{Pa}$, initial cohesion $c_0 =0.5E+5\text{Pa}$, softening parameter $h_p^c =-0.2E+5\text{Pa}$, internal frictional angle

$\varphi = 25^\circ$, plastic potential angle $\psi = 5^\circ$. Different values of internal length scale l_c are used in the analysis.

Generally speaking, the material parameter l_c defined as internal length scale in the Cosserat continuum has the meaning of “characteristic length”. The equivalent plastic strain distributions in the slope corresponding to different values of l_c and to the above two finite elements are given in Figure 3(a) and (b), respectively, which show the correlation of the width of the shear band to the internal length scale l_c , i.e. a smaller value for l_c implies a smaller width of the localization zone for the same finite element; and a little bigger width of the localization zone for $u8\omega4$ element than for $u8\omega8$ element as the same l_c is used.

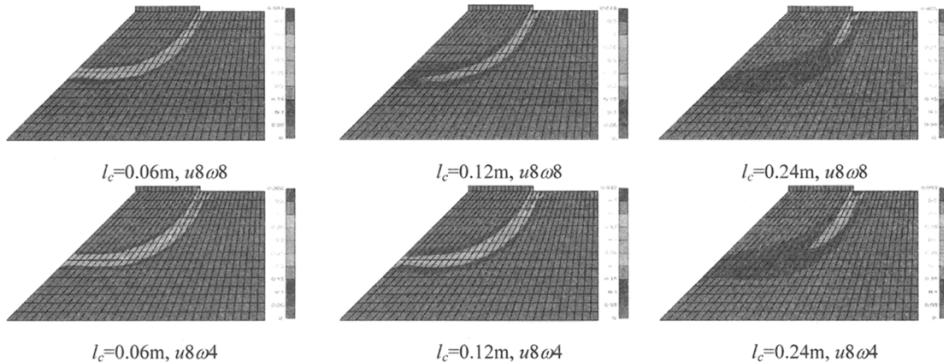


Figure 3. Equivalent plastic strain distribution in the slope: (a); (b) $u8\omega8$.

Figure 4 illustrates gradual reduction of the load-carrying capability of slope due to strain softening with the development of plastic strains. It shows that the load-displacement curves with different values of the internal length scale l_c have different post peak response, i.e. a less peak and a steeper reduction of the load-carrying capability of slope relating to a smaller value for l_c ; and that the load-displacement curves for $u8\omega8$ and $u8\omega4$ have different post peak response, i.e. a less peak and a steeper reduction of the load-carrying capability of slope relating to $u8\omega8$ element. It also shows that these two finite elements for Cosserat continuum model possess better performance in simulation of strain localization and post peak response during progressive failure process than that($u8$) for classical continuum does.

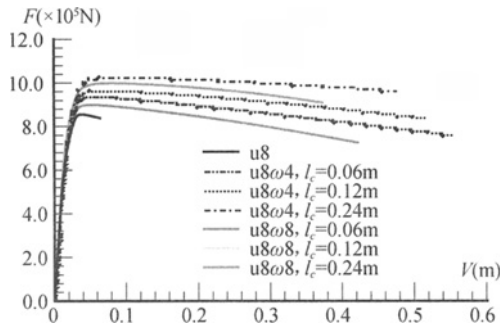


Figure 4. Load-displacement curves for the slope stability problem with different internal scales l_c and different interpolation functions.

By this token, the above numerical results of the slope stability illustrate the capability and performance of these two finite elements for Cosserat continuum model in keeping the well-posedness of the boundary value problems with strain softening behavior incorporated and in reproducing the characteristics of strain localization problems, i.e. intense plastic straining development localized into the narrow band and a significant reduction of the load-carrying capacity of the structure in consideration.

REFERENCES

- de Borst R. (1991). Simulation of strain localization: a reappraisal of the Cosserat continuum. *Eng. Comput.*, 8: 317-332.
- de Borst R. (1993). A generalization of J2-flow theory for polar continua. *Comp.Meth. Appl. Mech. Eng.*, 103: 347-362.
- Li X.K., Tang H.X. (2005). A consistent return mapping algorithm for pressure-dependent elastoplastic Cosserat continua and modeling of strain localization. *Computers & Structures*, 83(1): 1-10.
- Ted B., Wing K., Brian M. (2000). *Nonlinear finite elements for continua and structures*. 1st edition, London: John Wiley & Sons.

EVALUATION OF IN-SITU SHEAR STRENGTH OF NATURAL SLOPES VULNERABLE TO HEAVY RAINFALL BY LIGHTWEIGHT DYNAMIC CONE PENETROMETER

Takashi Tsuchida

*Graduate School of Engineering, Hiroshima University, 1-4-1 Kagamiyama
Higashi Hiroshima, 739 8527, Japan*

A.M.R.G. Athapaththu

*Department of Civil and Environmental Engineering, Ruhuna University,
Hapugala, Galle, Sri Lanka*

Seiji Kano

*Graduate School of Engineering, Hiroshima University, 1-4-1 Kagamiyama
Higashi Hiroshima, 739 8527, Japan*

Kazuaki Suga

Shimizu Corporation, Tokyo, Japan

Shallow slope failures, induced by torrential rainfall, are common in the western Japan, where Masado, a regional soil made of decomposed granite, is widely distributed in natural slopes. There is quite a few information on the geotechnical conditions, because of the difficulty of ground investigation on steep slopes with lush vegetation. The lightweight dynamic cone penetration test (LWDCPT) has been used for geotechnical survey of natural Masado slopes in the region. Based on the results of direct shear tests and the laboratory calibration tests of LWDCPT, a method of determining shear strength parameters from the data of q_d was proposed. The applicability of the proposed method was examined by comparing the strength parameters predicted by of q_d values and those measured in the laboratory shear strength test with undisturbed samples at the same sites.

INTRODUCTION

Shallow slope failures, induced by torrential rainfall, are common in the western Japan, where Masado, a regional soil made of decomposed granite, is widely distributed in natural slopes. The occurrence of these failures is mainly due to the rise of ground water table and the loss of inbound shear strength of soils, which were decomposed granite called "Masado". The present regional risk assessment system, which was developed by Hiroshima prefecture government, thoroughly based on rainfall data and past records of failures, is not adequate for correct prediction of failures in the region. Therefore, this study was proposed to enhance the present risk assessment system by incorporating strength properties of Masado soils for

better prediction of slope failure. There has been quite few information on the geotechnical conditions of Masado slopes because of the difficulty of ground investigation on steep slopes with lush vegetation. Recently developed lightweight dynamic cone penetration test (LWDCPT) has been used for geotechnical survey of natural Masado slopes in the region. The use of LWDCPT is convenient and practical due to its simplicity in handling by one person and its high accuracy.

Lightweight dynamic cone penetrometer and portable dynamic cone penetrometer

LWDCPT has been designed and developed in France since 1991(Langton D.D., 1999). The schematic view of LWDCPT is shown in Figure 1. It weighs 20 kg, and can be operated by one person at almost any location to a depth of 6 m. It mainly consists of an anvil with a strain gauge bridge, central acquisition unit (CAU), and a dialogue terminal (DT). The hammer is a rebound type and weighs 1.73 kg. The stainless steel rods are 14 mm in diameter and 0.5 m in length. Cones of 2, 4, and 10 cm² in area are available, and a cone holder is used to fix the 2cm² cone to the rod.

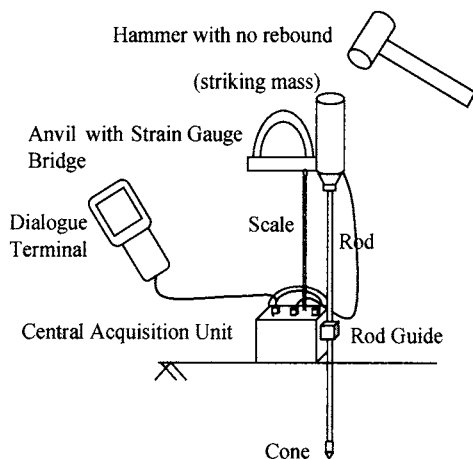


Figure 1. Schematic view of LWDCPT

The blow from the hammer to the anvil provides energy input, and a unique microprocessor records the speed of the hammer and depth of penetration. The dynamic cone resistance (q_d) is calculated from the modified form of Dutch Formula as shown in (1) (Cassan M., 1988). It should be noted that the expression for energy used in this formula ($\frac{1}{2}MV^2$) is for kinetic energy, as the energy input is variable and is delivered manually by the blow of the hammer. On the screen, dialogue terminal displays not only real time data both graphically and in tabular form but also dynamic cone resistance and penetration depth.

$$q_d = \frac{1}{A} \cdot \frac{\frac{1}{2}MV^2}{1 + \frac{P}{M}} \cdot \frac{1}{x_{90^\circ}} \quad (1)$$

where,

x_{90° = penetration due to one blow of the hammer by 90° cone,

A = area of the cone,
 M = weight of the striking mass,
 P = weight of the struck mass, and
 V = speed of the impact of the hammer.

In Japan, the portable dynamic cone penetration test (PDCPT), which consists of a guide rod, a series of rods, hammer, and a cone, has been used for geotechnical investigation of slopes as a practical substitution for the standard penetration test (SPT). Comparing the efficiency of LWDCPT with that of PDCPT in natural slopes in Mt. Gagara, LWDCPT showed the advantages with about 30% labor saving and 40% less time consuming.

LABORATORY SHEAR TEST OF MASADO SOIL

Masado is a sandy residual soil of decomposed granitic rocks of igneous origin. Due to differential weathering process over the years, Masado exhibits variable composition of secondary minerals and unchanged primary minerals such as quartz result in variable material properties even within the same weathering grade. The gradation curves of Masado soils are shown in Figure 2. Masado mainly consists of sand with considerable amount of gravel particles interconnected with small fraction of fine particles.

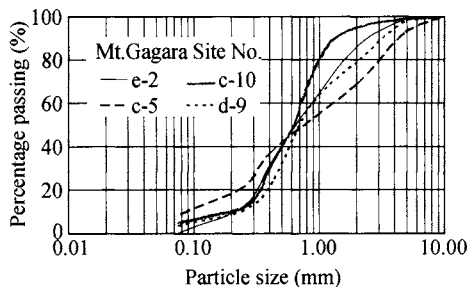


Figure 2. Grading curves of Masado soils

A series of direct shear tests of Masado soil were carried out (Athapaththu et. al., 2007). A ceramic disk of 200 kPa air entry value was sealed onto the bottom half of the shear box facilitates the measuring of negative pore water pressures due to the suction in specimen.

Soil samples, collected at Gagara Mountain, in Hiroshima University, were fairly air dried and pass through 2 mm sieve. Reconstituted specimens were prepared applying small compaction energy to ensure avoiding crushing of individual particles and to achieve normally consolidated state in the specimens.

Direct shear tests were conducted at void ratios ranging from 0.7 to 1.0 at different degrees of saturation varying from 40% to 80%. All tests were conducted at 9.8, 19.6, 39.2, 78.4 kPa normal stresses. Shearing was achieved by horizontally displacing the bottom half of the direct shear box relative to the top half at constant rate of shear displacement 0.2 mm/min as described in Japanese geotechnical standards. Pore pressure was measured through the high air entry disk mounted below the sample by transducer connected to the data logger at sample preparation, consolidation, and shearing stages. For the full saturated condition, the consolidated drained (CD) triaxial compression tests were carried out because the direct shear test of saturated sample was not available due to the mechanical difficulties.

The internal frictional angle tends to be varied with the void ratios are shown in Figure 3. The apparent cohesion ' c_d ' are developed as almost linear functions of void ratios at different degrees of saturation, and the relationships are shown in Figure 4. It appears that the apparent cohesion decreases as the degree of saturation increases. It can be observed that the apparent cohesion reduces more than 50% when the degree of saturation varies from 40% to 100% in all range of void ratios. The appearance of ' c_d ' of sandy Masado is mainly due to the suction in unsaturated conditions, while it seems to be due to the effect of particle crushing in fully saturated condition.

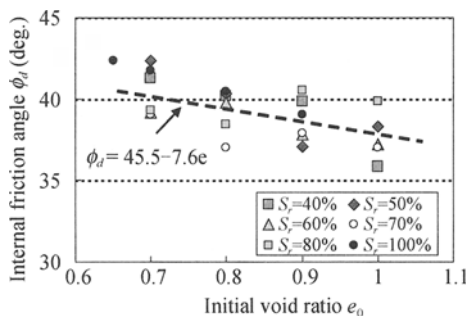


Figure 3. Initial void ratio of reconstituted Masado and internal frictional angle

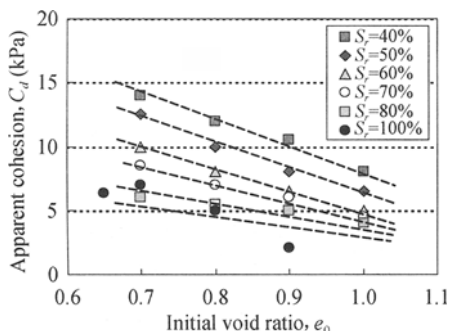


Figure 4. Initial void ratio of reconstituted Masado and apparent cohesion

CALIBRATION TEST ON q_d (LWDCPT) AND STRENGTH PARAMETERS

In order to develop strength correlations between q_d (LWDCPT) and shear strength parameters, a series of LWDCPT were performed under void ratios ranging from 0.6 to 1.1, and degrees of saturation ranging from 50% to 90% in the calibration chamber.

Acryl cylinders each 30 cm in diameter and 20 cm in height were fastened through nuts and bolts and porous plate was sealed to the bottom cylinder. A Number of acryl cylinders used for each test varies from six to two and some tests were conducted by applying surcharge weights. Masado soils, which having maximum particle sizes 2 mm, were mixed with the calculated amount of water and immediately fill into four consecutive layers. Light compaction was given to each layer and care was taken to avoid crushing of individual particles. Two to three trials of LWDCPT were performed at each preparation and specimens

were taken at each cylinder for water content and void ratio measurements in order to compare the values before and after the tests.

All data collected at different void ratios and degrees of saturation were reanalyzed to examine the effect of overburden in determining the cone resistance. It has been observed that the variation of cone resistance with overburden stress is almost in similar rate irrespective of void ratios and degrees of saturation. The linear ascent gradient (0.01MPa/1kPa) was observed the graphs drawn between cone resistance with overburden stress (Athapaththu, Tsuchida, Suga, and Kano, 2007)

Relationship between cone resistance and void ratio at different degrees of saturation

Figure 5 shows the correlations developed between cone resistance and data pertaining to all range of void ratios and degrees of saturation calculated for 5 kPa overburden stress. The correction for overburden stress has to be done using Eq. 4 and q_{d5} should be used when calculating void ratios from Figure 5.

$$q_{d5} = q_d - 0.01 \times (\gamma z - 5) \quad (2)$$

where: γ = the bulk density of soil kN/m^3 , and z = depth in m.

The cone resistance is drastically decreased at higher void ratios. The graphical correlations shown in Figure 5 can be approximated to the formula shown in Equation 5.

$$e = \left\{ (S_r / 10 - 2) q_{d5} \right\}^{\left(\frac{7}{5-100} \right)} \quad (3)$$

where: q_{d5} is given by Eq.2 in MPa, and S_r = degree of saturation in percentage.

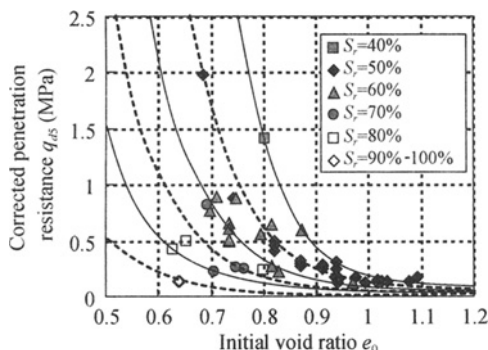


Figure 5. initial void ratios, degree of saturation and q_{d5} (reconstituted Masado)

FIELD INVESTIGATION BY LWDCPT AND APPLICABILITY OF CALIBRATION OBTAINED IN LABORATORY TEST

In order to apply the laboratory findings to the natural slopes, a series of in-situ LWDCPT were conducted at the northern slope of Gagara Mountain in Hiroshima University, where Hiroshima University installed the field observation facility in 2000, and since then the continuous measurements of ground volumetric water, ground suction and the rainfall have been carried out (Thi-Ha et al., 2003).

Lightweight dynamic cone penetration tests were conducted at 3 locations (b-7,c-5,e-2) twice under the fine weather conditions and immediately after the rainfall. The average degree of saturation calculated during the fine weather conditions at the site was from 40% to 60% depending on void ratios and the depth, while the average degrees of saturation calculated after the rainfall was from 60% to 90%. Figure 6 shows the q_d with the depth measure under both conditions. The void ratio was predicted by Equation 3, and the internal frictional angle and the apparent cohesion were predicted with using Figure 3 and 4, respectively. Further, the un- disturbed soil samples were taken at 0.5m depth of three sites and the strength parameters were measured with CD triaxial compression tests. Figure 7 shows the comparison between the predicted and the measured strength parameters. As shown in Figure, the agreement was fairly well on the internal frictional angle, however, the measured apparent cohesion were smaller than the predicted ones.

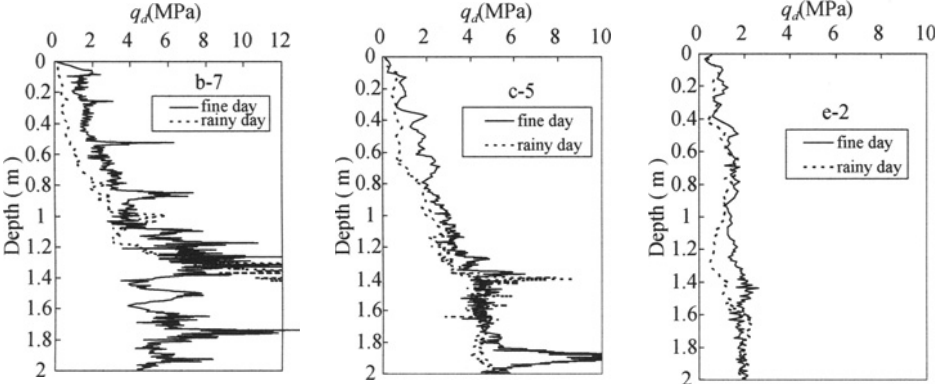


Figure 6. q_d with depth measured during fine weather condition and after rainfall

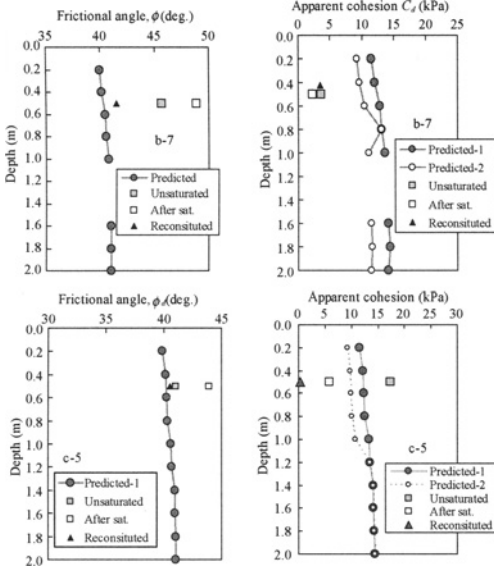


Figure 7. Predicted and measured shear strength parameters (Mt. Gagara, Site b-7, c-5,e-2)

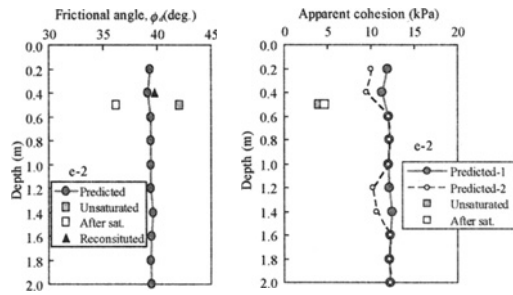


Figure 7. Predicted and measured shear strength parameters
(Mt. Gagara, Site b-7, c-5,e-2).(continued)

CONCLUSIONS

The method to predict shear strength parameters of natural Masado slopes with lightweight dynamic cone penetration test (LWD/CPT) is newly developed. The applicability of proposed method was examined by the field and laboratory triaxial tests, and it revealed that the prediction on ϕ_d was fairly good, but the apparent cohesion, “ c_d ” seemed to be underestimated.

REFERENCES

- Athapaththu A.M.R.G., Tsuchida T., Suga K. and Kano S.(2007). A lightweight dynamic cone penetrometer for evaluation of natural masado slopes. *Journal of Japanese Society of Civil Engineers-C* , 63(2): 403-416.
- Cassan M.(1988). Les essais in situ en mecanique des sols. *Realization et interpretation*, Eyrolles, Paris, 2nd ed. 1: 146-151.
- Langton D.D.(1999). The PANDA-lightweight penetrometer for soil investigation and monitoring material compaction. *Ground Engineering*, September, 33-37.
- Thi Ha, Takeo Moriwaki, Yasushi Sasaki, Seiji Kano and Dissanayake A. Kamalnath.(2003). The change in suction and water content in natural Masado slopes due to rainfall. *The International Symposium on Groundwater Problems related to Geo-environment*, Okayama, Japan, 181-187.

THE VISUALIZATION STUDY OF A GREEN SLOPE SYSTEM

Baocheng Wei, Zhende Zhu and Qing Wang

*Key Laboratory of Ministry of Education for Geomechanics and Embankment Engineering,
Hohai University, Nanjing 210098, China*

Geotechnical Research Institute, Hohai University, Nanjing 210098, China

The traditional slope engineering often destroy vegetation and had some bad effects on our environment which is not fit the sustainable policy, however the Green Slope System(GSS) has more environmental and economic advantages. Computer aided design on GSS can make it used much more widely. This paper developed a system (VGSS) which includes friendly interactive user-interface, efficient data-manage and high integration. The Object Oriented Programming (OPP), visual interface design and graphics-processing technique were analyzed based on the theory of visualization, parameterization theory and the design criterion of slope and retaining wall, an optimization design method of genetic algorithm about retaining wall was also analyzed. It will play an important role to promote this emerging environmental technology.

INTRODUCTION

With the development of geo-environmental engineering, ecological slope engineering also received extensive attention. In order to meet the requirements of sustainable development developed a new environmental protection slope structure, it is primarily through standard fastener linked to the various eco-filled bags connected together to form a very strong interlocking structure. To promote the technology and facilitate the designer, the development of a system for the visualization of application software is necessary.

At the beginning of 1980s, based on the DOS platform with Basic or Fortran language of the computer program can meet basic computing needs, but the input method is still cumbersome, the graphics capabilities is especially hard to meet the design needs. The 90's, appear based on the Windows platform in slope engineering analysis software, such as Slope-CAD, providing a variety of before and after processing function, enhanced graphics capabilities accordingly, but it still use traditional text data to manage data which caused the input process is too cumbersome. The international impact of slope stability analysis software are Geoslope, Slide and so on, the notable feature are their powerful calculation abilities, a high degree of visualization of before and after handling process. The Hydropower Planning and Design Institute of China's Ministry of Electricity and Water in the early 1980s, it launched earth dam slope stability analysis procedures for planning and development. Currently, the slope stability analysis procedures used widely in domestic are Stab95 (1982), Tongji Qiminxi Slope (1997.12), and the Lizheng is rock slope stability analysis software (2002.2), they are all unique in many aspects of the project and after years of practice and constantly improved. The objective of this study is to develop a green slope visualization system (VGSS, Green Slope of Visualization System) based on the visualization of digital thinking.

The software user interface is similar to the Windows style, it has an onboard graphics system, and it can build a calculation model automatically according to the input data. So it is a good design staff aide.

ECOLOGICAL SLOPE ENGINEERING SYSTEM

Ecological slope engineering system is a standard fastener linked to various ecological filled bags connected together to form a very strong interlocking structure, as shown in Figure 1. The system is an engineering patent which can replace the high-energy, high-polluting construction materials, such as steel, cement and concrete. The materials of the system have never degradation in soil, anti-aging, anti-UV, nontoxic, anti-microbial salt, and acid-base characteristics of erosion; 100% recovery and can truly achieve the goal of zero pollution. With the late growth of vegetation, it will form a permanent, full of vitality ecological engineering which will not have the high maintenance costs.

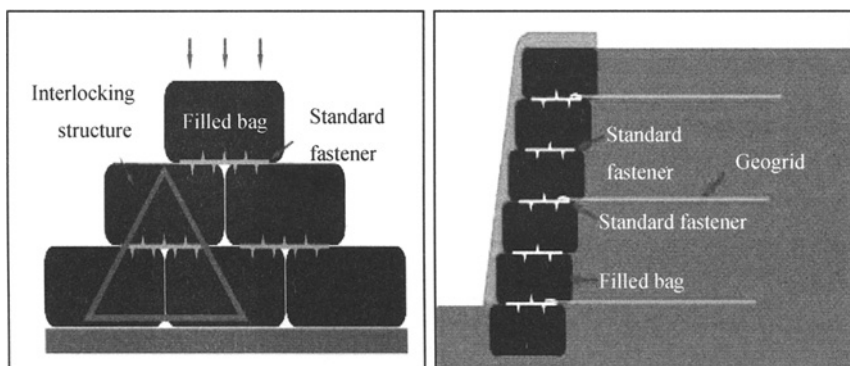


Figure1. Ecological slope engineering system

The features of this system include: the angle of slope can freely build in 0 to 90 degrees; the ratio of slope is lower, thereby reducing the land occupied; no cement, steel, concrete, the project will reduce the project cost 10-15%; adaptation of complex geological environment; good flooding impenetrable soil filter performance; construction fast, simple processing foundation can be implemented; a wide range of plant species can plant; long-term resistance to natural disasters such as droughts and floods; all the materials in full compliance with environmental standards and recyclable reuse; in water conservancy, transportation, urban construction, military, in areas such as flood can be widely used.

CALCULATE MODEL AND MAIN PROGRAM ALGORITHM

Calculate model

The green slope system is a gravity retaining wall structure, relying on weight to resistant the static and dynamic load, then to achieve stability. Shear capacity of the ecosystem is formed through the side stress sent between one to another bag, the wall structure as a whole when the ecological bags linked by fastener, then the shear capacity will be stronger. For retaining structure, the stability of the wall is often the controlling factor in design .The stability of retaining structure including the stability against sliding and overturning. The retaining

structure set up in soft ground or on the slope should check the overall stability including retaining walls, foundation and filling. The wall calculation model is shown in Figure 2.

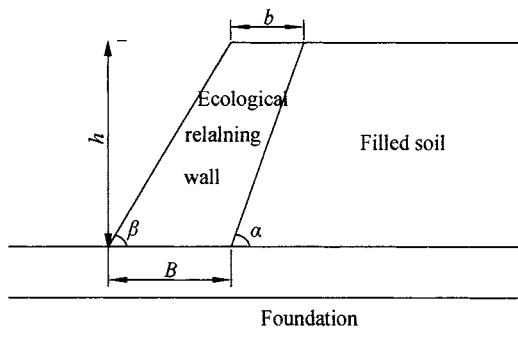


Figure 2. Calculate model

Genetic algorithm of ecological retaining wall

The objective function:

$$S_{\min} = Bh - \frac{1}{2}h^2m + \frac{1}{2}h^2n \quad (1)$$

Constraint conditions:

$$K_c > [K_c] \quad (2)$$

$$K_0 > [K_0] \quad (3)$$

$$e \leq [e] \quad (4)$$

$$p < [\sigma] \quad (5)$$

$$p_{\max} < 1.2[\sigma] \quad (6)$$

Among them, K_c is anti-slip coefficient; K_0 is anti-overturning stability coefficient; e is eccentricity of basement; p is basement stress; p_{\max} is the biggest basement stress; [...] is the allowable value of corresponding.

Main algorithm of slope stability

In engineering practice, slope stability analysis often are accustomed to use the limit equilibrium theory, in which Swedish circle is the most traditional and extensive method; Bishop method is not only simple and accurate, but also commonly used in the projects. Therefore, the visualization system adopts this two limit equilibrium analysis methods. The determination of the dangerous arc is one of the key issues in slope stability analysis. Determining the smooth arc need for three variables, that is the center coordinates and the

radius of the circle, this system uses 0.618 optimization method to determine the position of arc.

VISUALIZATION RESEARCH

Visualization system on the green slope

According to the design process, which involves slope stability calculation and the design of retaining structures. There are two major software packages system components: One is the green slope stability calculation package, mainly used to calculate the general slope stability and the overall stability of the ecological system; the other is the retaining wall of ecological package, mainly for the design of ecological wall. Figure 3 for the window of ecological slope stability calculation packet, Figure 4 for the window of ecological wall calculation packet.

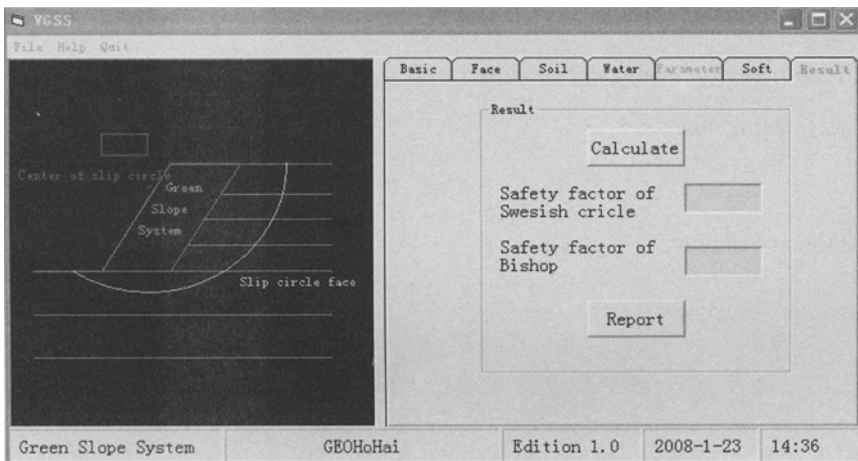


Figure 3. Initialize Window for VGSS

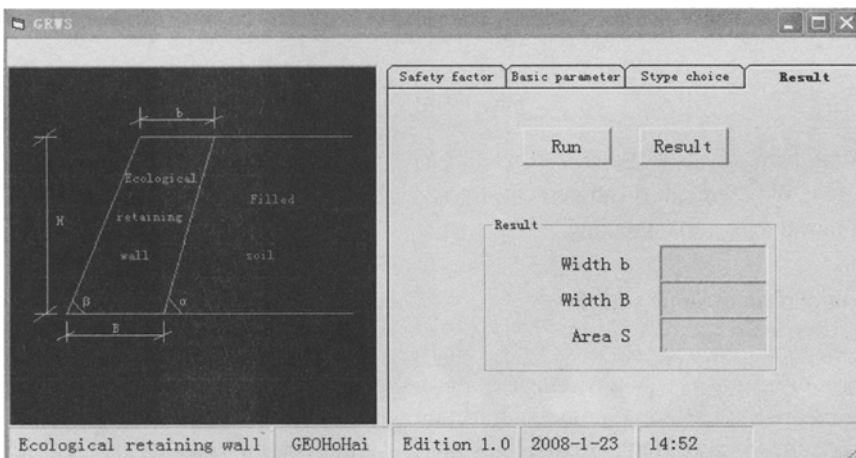


Figure 4. Initialize Window for GRWS

Key technologies of visualization

Graphic display of system parameters

When designers input the basic parameters, the system automatically mapping plane model. The results can be enhanced by visual design and designer can understand the design data deeper. Use of VB's picture frame object handling graphics, the system default of origin coordinates its work in the upper left corner, the right level for the x -axis, y -axis vertical downward. We can set a new coordinate system from the methods used are as follows Scale:

Object.Scale $(x_1, y_1)-(x_2, y_2)$

Among: object for the picture frames or windows such as graphics objects;

$(x_1, y_1), (x_2, y_2)$ for the upper left and upper right coordinates of the mapping regional.

In VB environment for graphics processing, graphical objects used methods are shown in Table 1.

Table 1. Graphical methods of VB

Method	Ability
Pset	Paint points in window or picture frame
Line	Paint lines in window or picture frame
Circle	Paint circle, ellipse and arc in window or picture frame
Print	Display text in window or picture frame
Cls	Clear graphic or text in window or picture frame

Data access technology

Visual Basic has a powerful data management capabilities, the single data can use TextBox directly, the handling of large amounts of data used mainly MSFlexGrid object, make full use of MSFlexGrid can display better than DataGrid object. However, MSFlexGrid Control can only display data, can not input and modify data. To solve this problem, we use TextBox controls as intermediate transition process which store data changes, then gave the data to MSFlexGrid show them.

SYSTEM TEST

To ensure a smooth test, the better the performance of the software, a test question from ACADS is selected which attribute data as shown in Table 2, examples of spatial data as shown in Figure 5.

Table 2. Material attribute of slope

$C(\text{kN/m}^2)$	φ ($^\circ$)	γ (kN/m^3)	ν	$E(\text{kN/m}^2)$
0	38.0	19.5	0.25	1.0E4
5.3	23.0	19.5	0.25	1.0E4
7.2	20.0	19.5	0.25	1.0E4

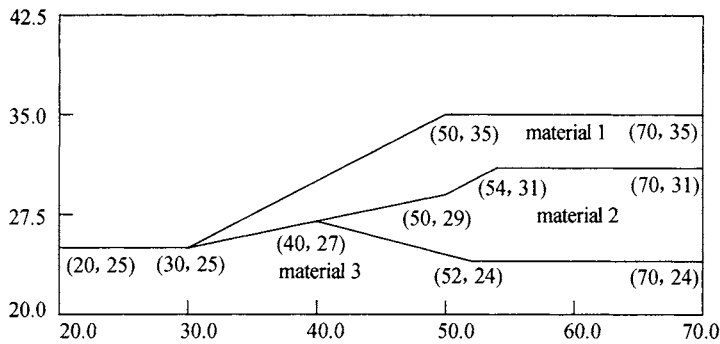


Figure 5. Spatial data

The original test results with the results of this software compared to Sweden circle calculations errors, Sweden circle itself with this assumption, since Sweden circle is only applicable to heterogeneous slopes, if for complex slopes will be a larger error. The calculation results of Bishop method is high precise, have small error, as shown in Table 3.

Table 3. Comparison of the results

Method	ACADS recommended result	Result of VGSS	Discrepancy percent
Swedish	1.39	1.243	10.6%
Bishop		1.416	1.9%

CONCLUSION

- (1) Parameter graphics technology avoids the complex pre-treatment process modeling, model will automatically establish after you input parameters;
- (2) Control over data access technology can reduce data entry errors, the amount of data validation provides a powerful means;
- (3) The green slope visualization system, including retaining wall and slope stability calculation packages, and the calculation results can meet the needs of project through the ACADS test questions.

REFERENCES

- Zhang Luyu, Ouyang Xiaoxiu and Zhen Yingren.(2003). Problems and thoughts of development of slope stability analysis software in China. *Chinese Journal of Rock Mechanics and Engineering*, 22(1): 166-169.
- Goh A.T.C.(1999). Genetic algorithm for critical slip surface in multi-wedge stability analysis. *Canadian Geotechnical Journal*, 36:(2): 383-391.
- Donald I.B., Giam P. (1992). The ACADS slope stability programs review. Proc.6 *The International Symposium on Landslides.*, 3: 1665-1670.
- Bai Shiwei, Wang Xiaohai and Cheng Jian.(2002). Geotechnical engineering information and visualization. *Geothmical Engineering World*, 4(8): 16-17.

APPLICATION OF NONLINEAR TIME SERIES ANALYSIS IN SLOPE DEFORMATION ANALYSIS AND FORECAST

Jia Xu

School of Geomatics, Liaoning Technical University, Fuxin 123000, China

Fenghai Ma

Dalian University, Dalian 11662, China

The slope is a nonlinear dissipative dynamic system, which is controlled by the condition of rock mass and influenced by the terrain, groundwater, earthquake and human projects. So its deformation takes on nonlinear feature. In this paper the method of phase space reconstruction is discussed including the method of mean mutual-information used to determine the delay time-delay and the method of the nearest neighbors to the embedding dimension. Based on the nonlinear feature, the radial basis function is selected to build neural network for forecasting the deformation and compared with the BP neural network. The results show that the radial basis function model has well generalization ability. It is much better than BP network in the convergence speed and predicting accuracy.

INTRODUCTION

The slope is a complex system whose deformations show complex nonlinear behavior. Most engineering practices show that it is more accurate that the time series are established using partial displacements to predict the intending displacements Liu et al. (2005). In the past research on prediction, however, the forecasting results are always unreliable with this method. Because once the slope evolution has be in the chaos state, the traditional time series model may not work and cannot predict the direction of evolution Huang et al. (2005). The chaos is of certain property and has the limited ability for forecasting. Thus, with some single component we can reconstruct phase space to determine predicting space Huang et al. (1999).

PHASE SPACE RECONSTRUCTION

For any time variable deciding the long-term evolution of the system, each of them contains the long-term evolution information of all variables. So we can extract the helpful information from the time series of single variable which contains all variable traces participating in system activity Fu et al. (2003). The basis of method is phase space reconstruction that the complex system is researched based on the chaos time series acquired from the observations. Its principle is that the trajectory generated from the chaos system will act regularly after a period of change and form a chaotic attractor finally. To reconstruct an

equal state space only one component is enough, the observations of which on some fixed time-delay points are worked with as a new dimension. This means the time-delay is considered as the new coordinates to establish a point in multidimensional space. Thus it can be seen that the phase reconstruction is to create a multidimensional space based on the time series Lv et al. (2002).

Suppose that there is a set of time series with length of N showed as $\{x_i, i = 1, 2, \dots, N\}$. Based on the embedding theory of Takens, the “trajectory” formed by reconstruction phase space in embedding space is dynamically equal to its original space in topology sense, as long as m, τ are properly selected Liu et al. (2003). The phase space with m dimensions can be reconstructed as follow:

$$X_n = \{x_n, x_{n-\tau}, \dots, x_{n-(m-1)\tau}\} \quad (n = N_0, N_0 + 1, \dots, N) \quad (1)$$

In Eq.(1), X_n are called phase points of m dimensions phase space and n is the number of phase points. This set describes the evolutive trajectory of the system in the phase space.

Time-delay determination

The mutual-information function is the degree of the general stochastic correlation of two stochastic variables. It is a nonlinear analyzing method and excels the auto-correlation method in computing the time-delay τ through computing the first minimum of the mutual-information function Han (2007). To the time series $\{x_n\}$, the mean mutual-information of the measurements between n timing and $n + \tau$ is:

$$I(\tau) = \sum_{n=1}^N P(x_n, x_{n+\tau}) \log_2 \left[\frac{P(x_n, x_{n+\tau})}{P(x_n)P(x_{n+\tau})} \right] \quad (2)$$

In Eq.(2), $P(x_n)$ and $P(x_{n+\tau})$ are the probabilities, which can be acquired by computing the histogram of the time series and the $P(x_n, x_{n+\tau})$ by two dimensions histogram. Then the τ is the best time-delay interval while $I(\tau)$ is in the first local minimum. Because in this case the redundancy generated is minimal and the independence is maximal.

Embedding dimension determination

In this paper, the method of nearest neighbors is adopted to compute the m . When the embedding dimension changes from m to $m + 1$, the neighboring points of X_n are checked to determine which are the true neighboring points and which the false. Until there is no false neighboring point, the geometry structure can be thought to be open entirely. In the m dimensions space, X_n is the phase point and its nearest neighbor point is $X_{\eta(n)}$. So the distance between them is:

$$\begin{aligned} R_m(n) &= \left\| X_{\eta(n)} - X_n \right\|_2^{(m)} = \min_{j=N_0, \dots, N, j \neq n} \left\| X_n - X_j \right\|_2 \\ &= \sqrt{\sum_{l=1}^{m-1} (x_{\eta(n)+l\tau} - x_{n+l\tau})^2} \end{aligned} \quad (3)$$

While the embedding dimension changes from m to $m+1$, the distance will be:

$$R_{m+1}^2(n) = R_m^2(n) + \|x_{\eta(n)+mr} - x_{n+mr}\|^2 \quad (4)$$

Compared with $R_m(n)$, if $R_{m+1}(n)$ varies greatly, it can be thought that two adjoining points in the high dimension attractor change into false neighboring points while projecting on the low dimension phase space. Suppose that

$$S_m = \frac{\|x_{\eta(n)+mr} - x_{n+mr}\|}{R_m(n)} \quad (5)$$

If $S_m > S_\tau$, $X_{\eta(n)}$ is the nearest false neighboring point to X_n and the threshold can be selected within the range of [10,15].

RADIAL BASIS FUNCTION NEURAL NETWORK FOR PREDICTION

Based on the theory of phase space reconstruction, the nonlinear time series from certainty system can be used for short-term prediction. Because a feed-forward neural network with three layers can approximate any complex continuous function, the artificial neural network is the important predicting tool to approximate nonlinear function Zhang et al. (2003). Usually, the BP neural network is applied for predicting. It adopts the gradient decent algorithm to adjust the weights for universal approximation. So the BP network has the disadvantages including lower speed in Convergence, local minimum etc. However, the radial basis function (RBF) neural network has local approximation property and only adjusts few weights of inputs and outputs. So it excels BP neural network in the ability of approximation and training speed. The prediction model of RBF Wang et al. (2006) is as following.

$$x_{n+1} = \hat{G}_1(x_n) = \sum_{j=1}^{N_c} \lambda_j \varphi_j(\|x_n - c_j\|), n = N_0, N_0 + 1, \dots, N$$

$$\varphi_j(r) = \exp\left(-\frac{r^2}{2\sigma_j^2}\right) \quad (6)$$

In Eq.(6), $\varphi_j(r): R^+ \rightarrow R$ is the radial basis function σ_j are constants called width. $c_j (j = 1, 2, \dots, N_c)$ are the centers of RBF neural network and $\lambda_j (j = 1, 2, \dots, N_c)$ are the indeterminate constants.

EXAMPLE ANALYZING

In this paper, the displacements of the slope by the sixth prism were analyzed with the theory above, and those were observed before 20th Feb, 2005 in Constructing District, Danba County. Danba slope lied in the back of the hill in Ganzi Tibetan autonomy in Sichuan. This area presented the cliff and valley physiognomy due to the interaction of intensively later uplift of Qinghai-Tibetan plateau and glacier activity. Till August, 2002, the Danba slope

took on obvious distortion. The displacements monitored were shown in Table 1 and the noise had already been reduced by the wavelet method. In this paper the Matlab7.0 is selected as program environment for reconstructing phase space and building the neural network.

Table 1. Displacements of the sixth prism in Danba slope

Date (m.d)	Displacement (mm)	Date (m.d)	Displacement (mm)	Date (m.d)	Displacement (mm)
1.24	7.7629	2.3	9.4765	2.13	14.712
1.25	6.6774	2.4	10.879	2.14	16.079
1.26	7.248	2.5	12.173	2.15	17.688
1.27	9.1737	2.6	13.351	2.16	19.088
1.28	9.2187	2.7	13.8	2.17	20.289
1.29	6.3837	2.8	13.239	2.18	20.501
1.30	7.0207	2.9	13.371	2.19	22.222
2.1	9.1285	2.10	14.007	2.20	24.679
2.2	9.348	2.11	14.193	2.21	27.134
2.3	8.8097	2.12	14.175	2.22	29.547

Firstly, the data needed to be stabilized for acquiring the stationary series to reconstruct the phase space and the result showed as Figure 1. Then the maximal time-delay interval $\tau = 3$ by the method of mutual-information and the embedding dimension $m=2$ by the method of false neighboring point. So the series reconstructed is $X_n = (x_n, x_{n-3}) \quad (n = 4, 5, \dots, 30)$.

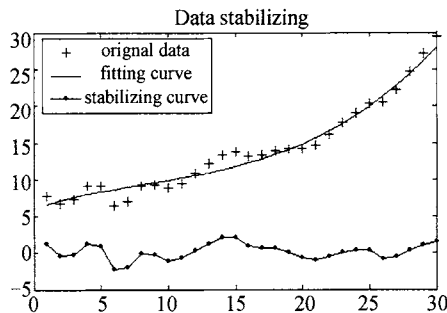


Figure 1. Data stabilizing

At last, both the methods of BP neural network and RBF neural network are applied for predicting. In this process, the first twenty displacements are used as the training net and the last ten as the testing net. The graphs of error performance of predicting values acquired were shown as Figure 2 and Figure 3. It was shown that both BP and RBF network could be used for predicting displacement of the slope. But the whole precision of prediction by RBF network was higher than BP network and the curve of error performance more stable. During training, to same error index, the time and steps taken for training RBF network was far few than BP network whereas the fitting precision was acceptable. This showed the advantage of the method of RBF network for predicting in the deformation monitoring. The detailed predicting values were shown in Table 2.

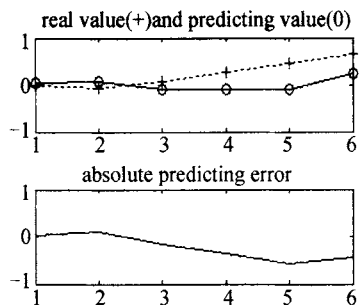


Figure 2. Result by the method of BP

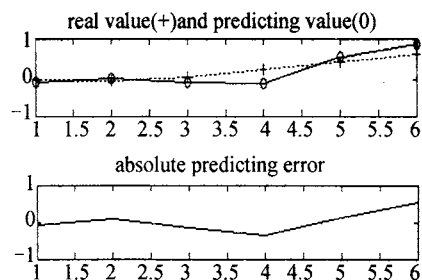


Figure 3. Result by the method of RBF

Table 2. Predicting values of the sixth prim on Danba slope

Date (m.d)	Original value (mm)	Method of BP network		Method of RBF network	
		Displacement (mm)	Difference (mm)	Displacement (mm)	Difference (mm)
2.17	20.289	20.163	0.126	20.210	0.079
2.18	20.501	20.025	0.476	20.142	0.459
2.19	22.222	19.857	2.465	20.526	1.696
2.20	24.679	20.793	4.086	21.278	3.401
2.21	27.134	21.629	5.505	26.486	0.648
2.22	29.547	23.835	5.712	31.925	-2.348

CONCLUSION

In this paper, the method of reconstructing phase space for analyzing and predicting slope deformation is discussed. That is used for determining the chaotic property and to approximate the observation data for predicting. The example shows that RBF can improve the accuracy of prediction compared with BP network. The construction of RBF network is simple and avoids prolix computation as BP network and overcomes the problem of local minimum. Its study speed is beyond comparison with BP neural network. So there is great significance for RBF neural network used in the slope monitoring.

ACKNOWLEDGMENTS

This paper supported by the National Natural Science Foundation of China(50604009); the Open Research Fund Program of the Geomatics and Applications Laboratory, Liaoning Technical University (Grant No.06-268); Liaoning Technical University Fund for Distinguished Younger(07-98) and Enterprise Post Doctor Fund of Liaoning

REFERENCES

- Fu Y.X., Liu Z.Q. (2003). Analytic method and application about chaotic slope deformation destruction time-series. *Journal of Wuhan University of Technology(Transportation Science & Engineering)*, 27(4): 473-476.
- Han M. (2007). *Prediction theory and method of chaotic time series*. 1st edition, China WaterPower Press.

- Huang Z.Q. (1999). *The theory and application of nonlinear analyzing for slop engineering*. 1st edition, Yellow River Water Conservancy Press.
- Huang Z.Q., Fan J.L. (2005). A prediction method of chaotic time series for slope deformation. *Journal of Engineering Geology*, 13(2): 252-256.
- Liu H.M., Qi H. and Cai Z.Q. (2003). Nonlinear chaotic model of landslide forecasting. *Chinese Journal of Rock Mechanics and Engineering*, 22(3): 434-437.
- Liu X., Zeng X.H. and Liu Y.C. (2005). Research on artificial neural network-time series analysis of slope nonlinear displacement. *Chinese Journal of Rock Mechanics and Engineerin*, 4(19): 3499-3504.
- Lv J.H., Lu J.A. and Chen Sh.H. (2002). *Chaos time series analysis and its application*. 1st edition, Wuhan University Press.
- Wang H.Y., Lu SH. (2006). *nonlinear time series analysis and its application*. 1st edition, Science Press.
- Zhang X.Ch., Xu H., Zheng N.W. and Chen R.X. (2003). Application of a radial basis function neural network model to data processing technique of dam safety monitoring. *Engineering Journal of Wuhan University*, 36(2): 33-36.

THE 3-D STOCHASTIC ANALYSIS OF PROGRESSIVE FAILURE OF ROCK SLOPES

Lingqiang Yang

*Civil Engineer School, University of Jinan, Jiwei Road 106
Jinan 250022, China*

Jing Ma

Control Engineer School, University of Jinan, Jiwei Road 106, Jinan 250022, China

Zuping Chen

Shougong Institute of Technology, Beijing 100041, China

Interface element style was used to simulate the fault zone in arch-dam zone. The entire fault zone in the dam location, 22-fault zone, has been simulated. The Mohr-Coulomb criterion function and the most-pull-stress law have been selected as yield function in plastic analysis. The stochastic distribution of rock and fault zone has been considered. Cracking analysis has been used to search for critical slip surface based on gradually cracking theory and credibility theory and elastic-plastic theory. Then the probability of slip has gain according to reliability theory. Through three thousand times calculation, the location of slip surface, the form of surface and the sequence of cracking have been found.

INTRODUCTION

Structure fault zone is place developing in rock mass with slow obliquity and soft rock scraping or mud. How to simulate it in rock basement engineer, slope engineer and underground work engineer is a puzzle for long time. Rock slope is stochastic field. The slipping (or cracking) processor is 3-D progressive failure, for example Wang (1996). All these are not ignored when study the slope's stability. Slope progressive failure processor is the failure occurs at some location at first, then spread along a track, at last the slope slip. The result already tested by experimentation, for example Chowdhury (1982). The key factor is local failure's occur, expand and the effect to slope's safety with considering the fault zone's randomness.

CONCEPT OF SLOPE PROGRESSIVE FAILURE

Based on the continuous mechanics, the failure of slope is the gather of infinite failure part (dot). But, when the finite element method was used to study the slope, the failure of slope is changed into the gather of finite failure part (element). Because different part's stress state is different, the part whose stress is largest will failure firstly. So the processor of slope's

failure is progressive. At first, the stress field, strength function and credibility index field is studied using finite element method. Then the element whose credibility index is minimum can be founded. Then the element was forced to failure. The stress, which the element bears, will transfer to neighbor elements. The stress state of slope is redistributed. The element's stiff matrix and the whole stiff matrix are calculated again. So the stress field, strength criterion function and credibility index field can be calculated again. Another element whose credibility index is minimum can be founded again. Then the element is forced to failure again. The stress state of slope is redistributed again. The element's stiff matrix and the whole stiff matrix are calculated again. So the stress field, strength function and credibility index field can be calculated again. Another element whose credibility index is minimum can be founded again. And so on. At last there are n element that is forced failure. The slope slips. Or slope's displacement is too large to affect the usage. The location of the n element forms the maximal possible slipping surface. The condition probability of the n element forms the probability vector to depict the slipping surface, for example Yang et al. (2003).

$$P_f = [p_{f1} \quad p_{f2} \quad \dots \quad p_{fn}] \quad (1)$$

where the p_{fk} can expressed as:

$$p_{fk} = \prod_{i=1}^k p_{f0i} \quad (2)$$

If $k=1$, p_{f1} is the original slipping probability. If the phenomenon of slope slip is seen as parallel system, the above vector was the maximal possible one.

Stochastic analyses

The method of solving credibility index of element is based on invalidation probability. The method is first-order matrix reliability approximation. The arithmetic as follow: suppose the base variable $X=(x_1, x_2, \dots, x_n)$ is a group independents variable one another. If a variable is unnormal variable, it will be transfer to normal one. Command $Y_i = (x_i - \mu_{xi}) / \sigma_{xi}$, the variable $Y=(y_1, y_2, \dots, y_n)$ is a group independents variable one another. Command $Y=T(X)$. Suppose the function is $g(X)=g(R(X), S(X))$. In normal interspaces it will be $G(X)=g(R(T^{-1}(Y)), S(T^{-1}(Y)))$. According to the repeatedly format calculate Y_j^i , for example Zhang et al. (1999).

$$Y_j^{(i+1)} = \frac{\partial G(Y)}{\partial Y_j} \Big|_{Y^{(i)}} \frac{-G(Y^{(i)}) + \sum_{j=1}^n \partial G(Y) / \partial Y_j \Big|_{Y^{(i)}} \cdot Y_j^{(i)}}{\sum_{j=1}^n \left[\partial G(Y) / \partial Y_j \Big|_{Y^{(i)}} \right]^2} \quad (3)$$

The credibility index can be resolved by $\beta = \sqrt{Y^T Y}$. If the credibility index less than 0.0 , the element will failure. In the paper, the cohesion force and friction coefficient are stochastic variable. $X=(c, f)$.

ELASTIC-PLASTIC ANALYSES OF INTERFACE ELEMENT

The equal thickness interface element was used to simulate fault zone in rock mass, for example Zhu (1998). Supposed the interface element is elastic-plastic. The elastic

deformation is calculated by normal stiff coefficient λ_n and tangent stiff coefficient λ_s . Mohr-Coulomb criterion function was adopted in program, for example Yu (2002).

$$F_n = \sigma_n = 0 \quad (4)$$

$$F_s = |\tau| + \sigma_n \text{tg}\varphi - c = 0 \quad (5)$$

Relating flow law was used. If pull crack occur, the plastic strain increment is calculate according to:

$$\begin{Bmatrix} d\varepsilon_n^p \\ d\gamma^p \end{Bmatrix} = \lambda \begin{Bmatrix} \partial F_n / \partial \sigma_n \\ \partial F_n / \partial \tau \end{Bmatrix} = \lambda \begin{Bmatrix} 1 \\ 0 \end{Bmatrix} \quad (6)$$

If shear yield failure occur, the plastic strain increment is calculate according to:

$$\begin{Bmatrix} d\varepsilon_n^p \\ d\gamma^p \end{Bmatrix} = \lambda \begin{Bmatrix} \partial F_n / \partial \sigma_n \\ \partial F_n / \partial \tau \end{Bmatrix} = \lambda \begin{Bmatrix} \text{tg}\varphi \\ 1 \end{Bmatrix} \quad (7)$$

CASE STUDY

A hydraulic-electricity station locates on Jinsha River. The dam basement that is made up of Emei mountain basalt only was divided into 14-rock layers. The thickness is about 25 to 40m. No big fault was found. But structure fault zone between layers was popular. The thickness of structure fault zone is 5 to 10cm. The structure fault zone affects neighbor layer into about 50cm. The structure fault zone is made up of gravel, rock scraps or mud. The geologic status was shown as Figure 1. The mechanics parameter of rock layer and structure fault zone was shown as Table 1.

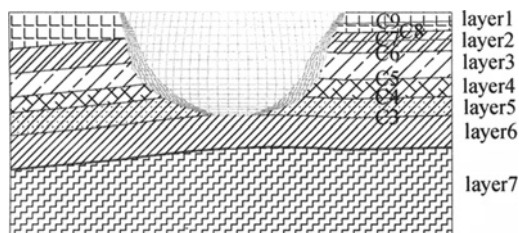


Figure 1. Geologic distribution

Table 1. Parameters of material in dam and foundation.

	Density kN(m ³)	Deform model(GPa)	Possion' ation	Height (m)	Cohesion force(MPa)	Friction coefficient (MPa)
dam	24.0	24	0.17		2.50	1.00
Layer 7	26.0	15	0.22		1.20	1.10
Layer 6	28.5	19	0.20		2.50	1.35
Layer 5	28.0	12	0.25		1.70	1.18

(continued)

	density kN(m ³)	Deform model(GPa)	Possion' ation	height (m)	Cohesion force(MPa)	friction coefficient (MPa)
Layer 4	27.5	8	0.28		0.80	1.00
Layer 3	28.5	23	0.20		2.50	1.35
Layer 2	28.0	15	0.25		1.70	1.18
Layer 1	27.5	10	0.28		0.80	1.00
fault zone	22.0	0.50	0.30	0.5	0.10	0.40

The differentiation coefficient of cohesion force and friction coefficient in structure fault zone are 0.5 and 0.3 respectively. The differentiation coefficient of cohesion force and friction coefficient in rock layer are both 0.5. The dam is concrete double-curving arch dam.

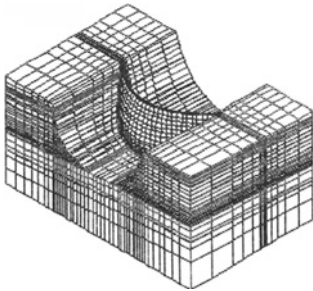


Figure 2. The mode of EFM

The maximal dam height is 278m. The hexahedron element and equal thickness interface element was used to cut the dam, rock layer and structure fault zone. The finite element model was shown in Figure 2. The load combination is all static loads.

Firstly the stress state field, displacement field and credibility index field of arch dam and rock basement was calculated by stochastic finite element method program to gain slope's stress state and displacement state and credibility index. The original state of slope can be calculated by adding stress state that caused by rock deadweight. There are two kind type failure elements. One is that cannot be dissatisfy with strength criterion, the other is that is forced to failure to find the slipping surface although satisfying with strength criterion, whose credibility index is minimum.

The failure sequence in fault zone was shown in Figure 3 to Figure 9(the number in Figure is the number of failure sequence). The result show the common boundary of layer 3, layer 6, layer 7, layer 5 and layer 8 with dam failure firstly where the element is not satisfy with strength criterion. So the failure probability is about 90%(shown in Figure 10). Then the element whose credibility index is minimum found. Then the element was forced to failure. The stress state and credibility index of the element was saved. Then the stress state field, displacement field and credibility index field of slope was calculate again. Another element whose credibility index is minimum found. Then the element was forced to failure. And so on. In the processor, the failure probability of first 56 elements is very little. After the 286th element failure, some rock element start cracking. When the 1457th element failure occurs, the layer 3 will crack to transfixion. When the 2000th element failure occurs, the layer 4 will crack to transfixion. The stress state is very bad. The failure probability is large. When the 3500th element failure occurs, the slope will collapse. The credibility index is 24.69 at the time.

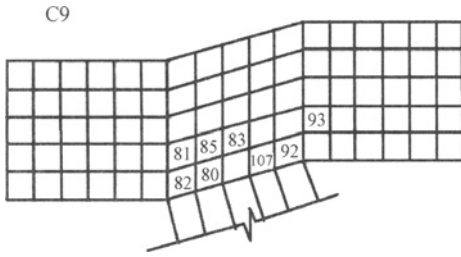


Figure 3. C9 failure place & sequence



Figure 4. C8 failure place & sequence

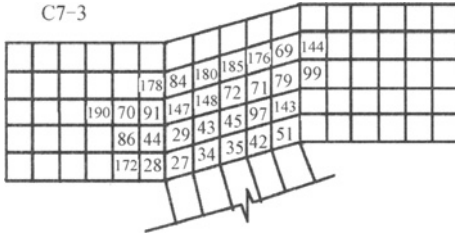


Figure 5. C7 failure place & sequence

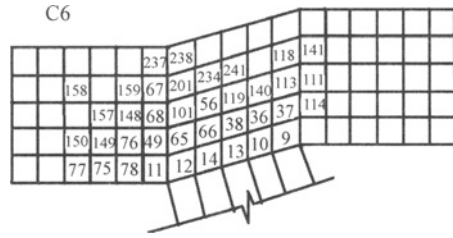


Figure 6. C6 failure place & sequence

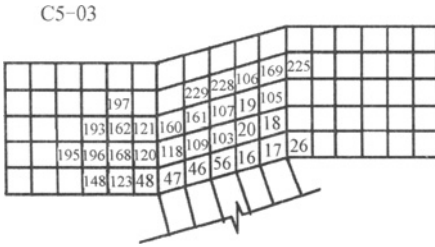


Figure 7. C5 failure place & sequence

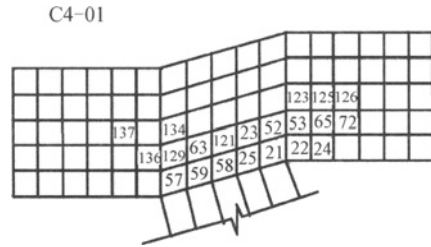


Figure 8. C4 failure place & sequence

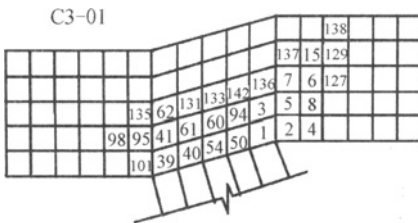


Figure 9. C3 failure place & sequence

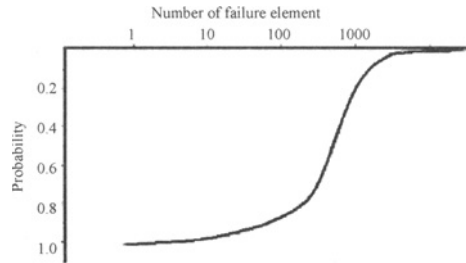


Figure 10. Slope globe failure probability

CONCLUSION

The method to simulate the 3-D rock slope stochastic slip processor has clear physics sense. The arithmetic is simply. The stress state field, displacement state field and credibility index field in any failure degree condition can be gain. So the method is feasible.

The failure mode of rock slope with structure fault zone can describe as: the failure began at structure fault zone. With the developing of structure fault zone failure, the stability descends. And the stress of element increases. Rock layer is changed into board with different support. Then the board cracks. The slope began slip. The slope collapse in the end.

REFERENCES

- Wang J.C. (1996). *Stochastic theory in slope*. Chinese Coal Engineer Press.
- Chowdhury R. N. (1982). probability model of progressive failure of slopes. *J. Geotech. Eng.* 108(6): 803-819.
- Yang L.Q, Lian J. J. and Zhang S. R.(2003). Analysis of creaking and overloading of arch dam. *Chinese Journal of Hydraulic Engineering.* 3: 55-63.
- Zhang S. R, Guo H. Z. (1999). credibility analysis of rock slope. *Journal of Soil Engineering.* 20(2): 57-61.
- Zhu B. F, (1998). *Finite element method theory and applications*. Chinese Water Press.
- Yu M. H. (2002). *Engineer strength theory*. Chinese High Education Press.
- Yang L. Q. (2003). *Cracking analysis and safety evaluation for high arch dam*. Tianjin University.

NUMERICAL SIMULATION ANALYSIS ON STABILITY OF A SURROUNDING ROCK OF UNDERGROUND CAVITIES

Yisi Zhuge

*School of Water Resources and Hydropower, Wuhan University
Wuhan 430072, China*

Xiutong Chen

Ertan Hydropower Development Company, LTD. Chengdu, China

Based on the data of geological reconnaissance, combining with the practice of a hydropower project, the article deeply analyzes the circumstance of geomechanics for engineering region, and creates a mechanical model which could represent topography, rock mass construction and circumstance of ground stress. According to measuring results of ground stress, adopting inversion of linear method of finite element to analyze initial ground stress field, using non-linear method of finite element to model the stress of surrounding rock and the stability of underground cavities, the author demonstrates the feasibility for excavation scheme, and shows concentrated site of stress and potential failure point in surrounding rock during different excavate phases.

OVERVIEW

Presently, China at high tide of hydropower project construction. But most key projects are seated on south west China, mountainous region. Limited to terrain and space, it's a better choice to dispose important constructions such as generator groups and house buildings underground, furthermore, sometime it's the only choice. Consequently, the stability study for surrounding rock of underground cavities is significant.

Because of the large-scale of underground cavities excavation, it's a efficacious method that adopting numerical simulation to model the course of excavation. For such method, first step is to confirm the field of stress of surrounding rock, secondly to simulate the course of excavation of underground cavities, then to get a well-regulated cognition of stability and deformation failure of surrounding rock, last to judge the validity of consolidation measures for surrounding rock and optimize the scheme. The author expatiates on each above-mentioned steps, and takes a example of a hydropower project practice, using method of finite element in three-dimensional to simulate the stability of surrounding rock.

PRINCIPLES OF INVERSION ANALYSIS AND METHODS FOR INITIAL GROUND STRESS

Principles of FEM

FEM is one of numerical methods which is more prior and popular at present. With the development of computing technology, the usage of FEM in civil engineering and other

engineering area is more and more extensive. The basic thought of FEM is dividing the continue solving area into a set of elements which are of finite number and connected with a kind of rule. It could model solving area with complex geology shape because the element can connected with different rules and the shape of element can be different. The displacement in element can be interpolated by shape function with node displacement. The method creates node displacement equation with the variation and principle of virtual work. And the strain and stress in elements are calculated by node displacements. The general equilibrium equation of FEM is:

$$[K]\{\delta\} = \{F\} \quad (1)$$

where: $[K]$ is stiffness matrix; $\{\delta\}$ is displacement vector; $\{F\}$ is load vector.

Back-analysis method

Some data indicates that, the maximum of difference value is about 10% between elastic and plastic conditions when analysis with FEM. Therefore, it can be assumed that initial stress is linear superposed by several simple stress fields. It can be written as:

$$\sigma = a_1\sigma_g + a_2\sigma_x + a_3\sigma_y + a_4\sigma_{rxy} + a_5\sigma_{ryz} + a_6\sigma_{rxz} \quad (2)$$

where: σ is the fitting stress field;

$a_1 - a_6$ are the parameters;

σ_g 、 σ_x 、 σ_y 、 σ_{rxy} 、 σ_{ryz} 、 σ_{rxz} are gravitation stress field, X direction formulation stress field, Y direction formulation stress field, Z direction formulation stress field, XY shearing formulation stress field, YZ shearing formulation stress field, ZX shearing formulation stress field.

After creating FEM model, 6 stress fields could be got when gravitation, X direction unit displacement, Y direction unit displacement, Z direction unit displacement, and shearing unit displacement are applied on the model. From measured value and 6 computing values of stress fields, the linear equation can be created by using formula (2). The parameters $a_1 - a_6$ could be got from the equation, and the stress field could be defined.

ENGINEERING SITUATION AND GEOLOGICAL CONDITION IN HOUSE DISTRICT

Engineering situation

The hydropower project locates in Sichuan province, limited to especial geological condition, disposing the house building underground. The principal part of underground cavities is the main power house (344.4m×25.8m×68.7m) with sub-house and assembly room, combining with the main transformer power house (314.95m×19.8m×33.0m). The direction of power house's axis is N35°E, and the thickness of the dyke between cavities is 45m.

Engineering geological environment in house district and physical mechanics parameter of mass of rock

The lithology of rocks in house district is mainly marmoreal. Based on the texture and the character of rocks, the marble can be divided into five forms including cinereous marble,

canescence marble, banded marble, granophyre, marl and faults. In the model, actualities of geological structure and project had been considered comprehensively. The model take some main faults which pass the house district, such as f7,f14, f16,f17,f25 and f30 into consideration. The distributional characteristics of space for each fault were confirmed by geological section map and ground observation, and also were generalized.

Through times of fitting and correction, the parameters of physical mechanics for rocks and faults were verified, as listed in table1.

Table 1. Macroscopic parameters of physical mechanics for rocks and faults

Rock and Fault	Modulus of Elasticity	Tensile trength	Poisson ratio	Wet weight	Cohesion	Internal friction angle
Banded Marble (T_{2y}^4 、 $T_{2y}^{5-(1)}$)	56600	1.75	0.34	28.3	0.35	45
Cinereous Marble ($T_{2y}^{5-(1)}$)	49500	2.64	0.21	27.0	0.32	40
Canescence Marble ($T_{2y}^{5-(2)}$)	57200	2.74	0.22	27.1	0.52	48
Granophyre ($T_{2y}^{5-(2)}$)	57200	2.88	0.22	27.1	0.4	42
Marl (T_{2y}^6)	48800	2.2	0.27	27.0	0.17	35
Fault 1	1100		0.37	20	0.06	21
Fault 2	1000		0.4	20	0.05	20

THE FITTING OF ORIGINAL GROUND STRESS FIELD

The observed values of ground stress showed that the level of stress in house district is medium. The direction of maximum primary stress approximately is NWW. Combining the analyses of observed datum with geological structure coactions, boundary condition can be got as showed in Figure 1. The north-west profile in computing model is boundary of load, laid on horizontal stress superimposed by tectonic stress and stress of dead weight. The distribution pattern and magnitude of stress is verified by fitting and inversion of the field of stress. Because of small displacement caused by the extrusion in both sides of rocks, the lateral face close with river bed and below the waterline of river is setting as restriction boundary, while the lateral face above the waterline of river is as free boundary.

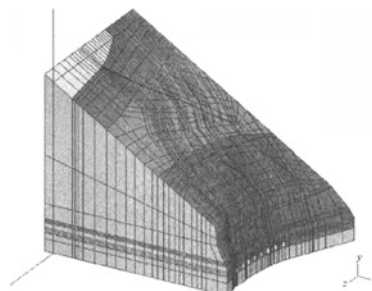


Figure 1. The FEM computing model

To adopt 3D-σ which is a soft for finite element analysis, computing parameters are listed in Table 1. Through iterative analysis for fitting and inversion, the result indicates that boundary of load in north-west profile is pertained to trapezium distribution, and the magnitude of stress is about 2-7MPa. Original ground stress field as Figures2-4 showed.

Integrating observed values of ground stress and computed result, we can get a conclusion that maximum primary stress is about 10-17MPa, and medium primary stress is about

4-10MPa, and minimum primary stress is 3-8MPa. The level of ground stress in house district is medium.

CHARACTERS OF THE FIELD OF STRESS FOR THE EXCAVATION OF UNDERGROUND POWERHOUSE

Through the finite element simulation for excavation, ultimate production of the field of stress gained as Figures 5-7.

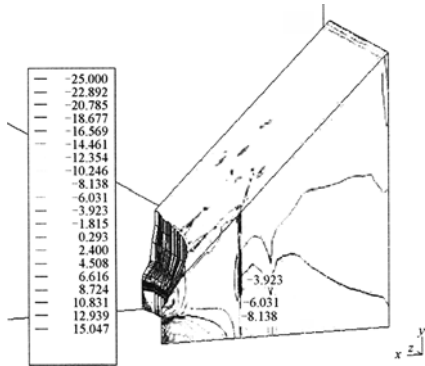


Figure 2. Maximum original primary stress

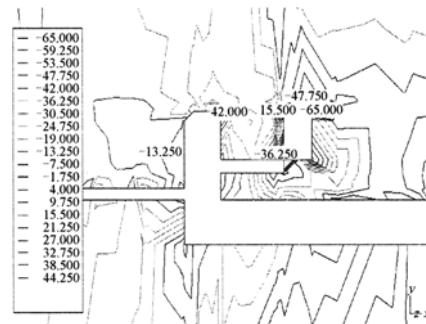


Figure 3. Medium original primary stress

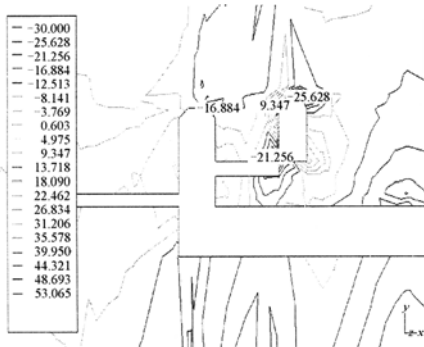


Figure 4. Minimum original primary stress

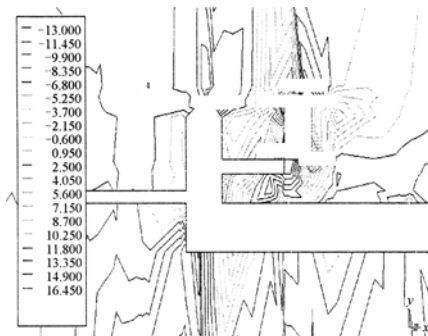


Figure 5. Maximum original primary stress

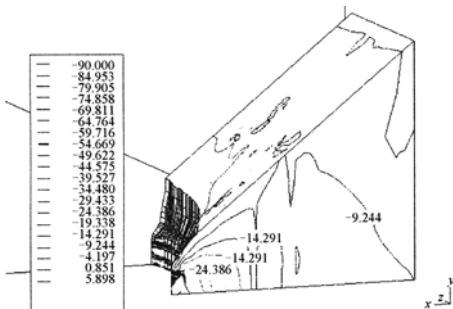


Figure 6. Medium original primary

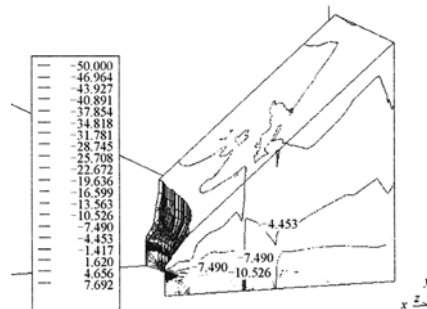


Figure 7. Minimum original primary stress

After the excavation of underground powerhouse, the distribution of second stress produced by surrounding rock has regular patterns as following:

(1) The magnitude of maximum stress (σ_1) around cavities is from 2 to 65 MPa, concentrated district for compressive stress includes the top arch of outer side wall, nether angular point of inner side wall. The magnitude of stress in main power house and main transformer power house is about 7-36MPa. The magnitude of stress in upper angular point of inner side wall and nether angular point of outer side wall is lesser, about 15MPa.

(2) The magnitude of medium stress (σ_2) around cavities is from 0 to 30 MPa. Concentrated district for compressive stress includes the top arch of outer side wall, nether angular point of inner side wall. The magnitude of stress in above district is about 10-30 MPa. The magnitude of stress in upper angular point of inner side wall and nether angular point of outer side wall is lesser, about 9 MPa. Tensile stress concentrate in inner side wall of main power house, about 0.6 MPa.

(3) Concentrated district for maximum stress (σ_3) includes the angular points of side wall. Concentrated district for compressive stress includes the top arch of outer side wall, nether angular point of inner side wall, about 12 MPa. Concentrated district for tensile stress in main power house includes the Middle and Upper part of inner side wall, nether angular point of outer side wall, about 12-16 MPa.

CONCLUSION

The result of stress calculating for excavation and the geological condition of surrounding rocks show that the surrounding rocks are stable in the main. But it is also likely to jitter in some local place. Based on the results of stress analysis, following advises for supporting are listed: the direction of primary stress in surrounding rocks deflect obviously, generally, as ordinary character of distortion in excavation. The maximum stress (σ_1) contact with of the peripheral place of cavities, for example arches. The σ_1 also has the trend to parallel with side wall. The deflection of stress direction appeared most obviously in angular points. There brings tension stress in the nether angular point of channels and cavities. The sites mentioned above should be supported.

REFERENCES

- Fu Chenghua, Wang Weiming and Chen Shenghong. (2006). Back analysis study on initial geostress field of dam site for XiLuoDu hydropower project. *Chinese Journal of Rock Mechanics and Engineering*. 25(11): 2305-2312.
- Sun Hongyue, Shang Yuequan and Zhang Chunsheng. (2004). Numerical modeling analysis for surrounding rockmass stability of large underground cavities. *Journal of Zhejiang University (Engineering Science)*, 38(1).
- Yu Weiping, Wang Xiaogang, Yang jian and Wang yufang (2005). Stability analysis of surrounding rock of underground excavations and visualization of its results. *Chinese Journal of Rock Mechanics and Engineering*. 24(20).
- Jiang Xiaolan, Chen Jin, Cao Jianguo and Sun Shaowen. (2006). Geo-mechanics model experiment on underground cavities of Jingping hydro-power station class-1. *Journal of Yangtze River Scientific Research Institute*. 22(1).

- Jiang Zhenwei, Wang Qiyao and Shi Yuling. (2005). Study on stability of surrounding rock of huge underground openings in layered rock with steep dip angle. *Journal of Highway and Transportation Research and Development*. 22(6).
- Jiang Zhongming, Xu Weiya and Shao Jianfu. (2005). ANN-Based 3-D back analysis of initial stress in rock masse. *Journal Of Hohai Universit*. 30(3): 52-56.

Mitigation and Rehabilitation

RECOVERY OF ANISOTROPIC SLOPE AFTER THE LANDSLIDE

Rysbek Baimakhan, Nargozy Danaev, Aigerim Baimakhan, Gulnaz Salgaraeva, Gulaym Ylyasova, Nurgul Kurmanbekkizy, Ainagul Kozhebayeva, Zhumazhan Kulmaganbetova and Beket Zhakashbayev

Scientific Center of Fundamental Researches near the Kazakh State Woman's Pedagogical University, Almaty, Kazakhstan

Sarandulam Dashdorj
Hokkaido University, Sapporo, Japan

The algorithm of finite-element simulation of some sides of effect is adduced. These sides are uneven saturation of grounds with water, not uniform structure of the ground thickness and bounded with this fact the slope anisotropy. The details of reduced anisotropy and its influence on the value of the limit stresses at the places of geometric fractures and at the slide line are given.

INTRODUCTION

The South and South-East of Kazakstan are bordered with the mountains of Zailiisky Alatau, Jongary and Altai. The largest city of Republic – Almaty, with the population numbering one and half million, is located at the foot of the hills. A lot of different buildings, such as sanatoriums, rest homes, children camps, sport centers, etc., are situated in pre-mountain gorges. Building fever compels the city to climb higher and higher, closer to the mountains. The adopted decision about carrying of the Winter Asian games of 2011 requires building in Almaty on a large scale. At that the sport constructions will be built closely to the mountains and directly in the mountains.

The main danger for building at the slopes is the landslide effects. There is a lot of data about happened landslides both bygone and recent. The probability of them grows because of intense thawing of glaciers and more often raining. The region belongs to the traditionally high-seismic zone with force 9-10. Thus, all three rules of non-lead to landslide - “don't wet, don't shake, don't cut” - are broken.

In order to reach safety and strengthen the hills the scientific system approach is necessary. It ought to clear up the mechanism of landslide beginning and generalize the rules of landslide process developing, to determine their peculiarities for specific geological-geomorphic and nature-climate conditions, to take into account influence of technogeneous processes, i.e. the technology of building of the own strengthening constructions and so on.

CALCULATION OUTLINE

At the Figure 1(b) the proposed variant of rehabilitation of slope stability with the aim of all the constructions keeping is shown. According to the Figure 1a the height and width of the hill by the base are equal to 185 m and 300 m correspondingly. It conforms to the contour EZD. It is proposed to hew the top of the hill with the height 35 m till the level of JC (dwelling construction). At the bottom, beginning from the mark AE, it is necessary to construct the inclined support wall by the way of filling up with geosynthetic materials and their ramming. As the geosynthetic materials the cut grounds, conglomerate BZC and broken-stone pebble grounds may be. The last ones may be brought from the valley of the river, running below. Filling up begins from the bottom by the layers of ground, conglomerate, broken rocks, pebble with boulders with gradual growth of the height till the mark BJ. Below the line BC the part of the slope mass (it is shown by number 1 and dotted lines and circles) is cut till the straight line. Because of it an angle of the left slope incline is decreased from 75 to 60 degrees and it becomes equal to the incline angle of the right slope. The width of the new building site for erecting of the engineering constructions (BC) will be equal to 120 m. The width of the cross-section of the support wall $ABJE$: $BJ = 35$ m; $AE = 50$ m.

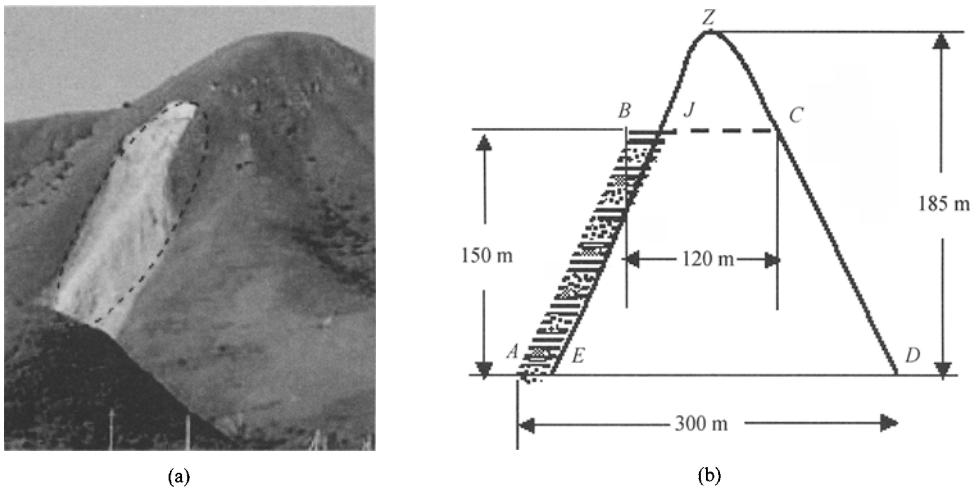


Figure 1. The landslide slope and its geometric characteristics

The calculating scheme of the problem of stability investigation of the safety construction of geosynthetic materials with application of the finite-element method (FEM) is shown at the Figure 2.

The investigated area consists of five different materials, which differ from each other by physical-mechanical properties and geometrical dimensions: I – the surface concrete plate with the thickness of 1 m; II – the inclined strengthening construction, created by layering of boulders, ground, conglomerate and pebble with the thickness of 1 m each; III – solid clay of the sediment thickness; IV – nature stratified rocky massif; V – the covering loam. The widths of the inclined layers at the top are 35 m, 25 m, 25 m, 26 m, 9 m, and by the base – 50 m, 60 m, 90 m, 37 m, 63 m correspondingly; φ_1 and φ_2 - the angles of the isotropic planes incline concerning the horizontal axe Ox .

The physical-mechanical properties: $\gamma, 1 \times 10^2 \text{ MN/m}^3$ - the volume weight, $E, 1 \times 10^4 \text{ MPa}$ - Young's modulus, ν - Poisson's ratio for isotropic materials; $E_1, 1 \times 10^4 \text{ MPa}, E_2, 1 \times 10^4 \text{ MPa}, G_2, 1 \times 10^4 \text{ MPa}, \nu_1, \nu_2$ - modulus of Young, shear and Poisson for the transtropic materials.

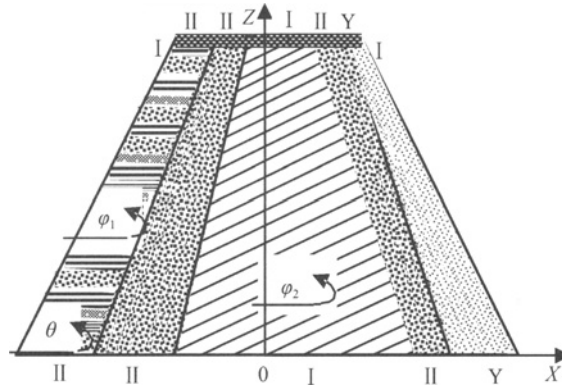


Figure 2. The calculating scheme of the problem of the anisotropic slope stability.

θ – an angle of the slope

As the strengthening inclined layer is created by layering of the different isotropic materials it will have the property of directed anisotropy. Within the invariable geometric dimensions they may be layered under the different incline angles φ_1 . That is why the anisotropic mechanical properties for them were obtained by the formulas of the reduced anisotropy according to the work, Minchev. (1969). Taking into account the data about the physical-mechanical properties of the pre-mountain zone of Zailiisky Alatau, Kolotilin. (1967). the values of the equivalent anisotropic elastic properties have been obtained.

The values of the physical-mechanical properties of five different materials, adopted for calculation, are added to the table.

Table 1. Physical-mechanical properties the materials of slope

Parameters	Sub-areas of the massif				
	I	II	III	IV	V
$E_1, 1 \times 10^4 \text{ MPa}$	–	0.014	–	1.074	–
$E_2, 1 \times 10^4 \text{ MPa}$	–	0.009	–	0.523	–
$G_2, 1 \times 10^4 \text{ MPa}$	–	0.382	–	0.413	–
ν_1	–	0.318	–	0.198	–
ν_2	–	0.100	2.30	0.120	–
$\gamma, 1 \times 10^2 \text{ M} \cdot \text{N/m}^3$	2.70	2.400	0.010.00	2.300	2.200
$E, 1 \times 10^4 \text{ MPa}$	2.50	–	0.32	–	0.005
ν	0.28	–	–	–	0.260

THE FINITE ELEMENT METHOD AND CALCULATIONS

The equations of the generalized Hook's law for incline-stratified transtropic medium concerning the components of the stress tensor are written in the view, Erzhanov. (1980).

$$\begin{aligned}
 \sigma_x &= b_{11}\varepsilon_x + b_{12}\varepsilon_y + b_{13}\varepsilon_z + b_{15}\gamma_{xz} \\
 \sigma_y &= b_{12}\varepsilon_x + b_{22}\varepsilon_y + b_{23}\varepsilon_z + b_{25}\lambda_{xz} \\
 \sigma_z &= b_{13}\varepsilon_x + b_{23}\varepsilon_y + b_{33}\varepsilon_z + b_{35}\gamma_{xz} \\
 \tau_{yz} &= b_{44}\gamma_{yz} + b_{46}\gamma_{xy} \\
 \tau_{xz} &= b_{15}\varepsilon_x + b_{25}\varepsilon_y + b_{35}\varepsilon_z + b_{55}\gamma_{xz} \\
 \tau_{xy} &= b_{46}\gamma_{yz} + b_{66}\gamma_{xy}
 \end{aligned} \tag{1}$$

The main solving equation of FEM for geostatic field of stresses for non-uniform medium can be written in the view, Baimakhan. (2002).

$$[R]\{U\} = \{yH\} \tag{2}$$

where $[R]$ – the matrix of the system rigidity, $\{U\}$ – the vector of unknown movements, $\{yH\}$ – the vector of geostatic pressure loads.

The deformation components after the system (2) solving are calculated with a help of expression:

$$\{\varepsilon\} = [B]\{U\} \tag{3}$$

where $[B]$ – the matrix of the basic functions of FEM. The components of stresses in the internal points of the finite elements integration are calculated by the formula (1).

The area, shown at the Figure 2, is divided into 1260 isoparametric elements of quadrangular form with the total quantity of layout – 1334.

Depending on acting stresses shear may be happened at the slide line between the inclined slopes II and III with the normal n in accordance with Coulomb-Moor condition of strength, Erzhanov. (1980).

$$|\tau_n| < \sigma_n \operatorname{tg} \rho + C \tag{4}$$

where ρ and C are an angle of internal friction and coefficient of cohesion.

For the contact knots on the former slide line, the normal tangent stresses $|\tau_n|$ are determined by formulas of the Erzhanov works. (1980).

$$\tau_n = 0.5(\sigma_z - \sigma_x) \sin 2\varphi + \tau_{xz} \cos 2\varphi \tag{5}$$

where φ – is an angle of the isotropy plane incline. The values of the isotropy plane incline angle φ_1 were varied from $\varphi_1 = 0$ to $\varphi_1 = 30^\circ$ and $\varphi_1 = 60^\circ$ by invariable $\varphi_2 = 0$. It was supposed that we have hard, but rough contact on the slide line EJ by the Figure 1 or between the inclined slopes II and III at the Figure 2. It means that the contact line had zigzag form.

RESULTS

Because of the paper volume limitation in the Figure 3 only the diagrams of normal tangent stresses $|\tau_n|$ for the contact knots on the former slide line, calculated by the formula (5).

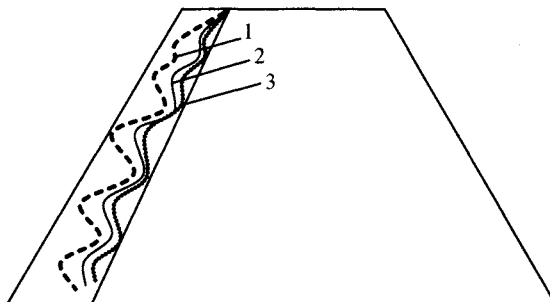


Figure 3. The diagrams of normal tangent stresses $|\tau_n|$ on the contact by the slide line in the points of the strengthened layer. By $\theta = 60^\circ$ the lines correspond to:

$$1 - \varphi_1 = 0; 2 - \varphi_1 = 30^\circ; 3 - \varphi_1 = 60^\circ$$

CONCLUSION

Analysis of the results shows that moving tangent stress will be the lowest with increase of the angle φ_1 , i.e. it is possible to control stability of the supporting construction of the anisotropic building by the geosynthetic materials.

Thus there were shown the starting results of the research and the new algorithms to investigate the stressed-deformed state of anisotropic slope with the isotropic covering stratum and artificially created multivendor anisotropic inclined protective construction from geosynthetic materials.

REFERENCES

- Minchev I.T. (1969). *Mechanica na naplastenite sredy*. Sofia: Derzhavno izdatelstvo. Technica
- Kolotilin N.F., Bochkarev V.P., Antonenko E.M. Novitzsky S.A. (1967). *Engineering-geological conditions of the pre-mountain zone of Zailiisky Alatau*. Alma-Ata.
- Erzhanov Zh.S., Aitaliev Sh.M. and Masanov Zh.K. (1980). *Seismic stressed state of the underground constructions in layered anisotropic massif*. Alma-Ata: Nauka.
- Baimakhan R.B. (2002). *Calculation of seismic stressed state of the underground constructions in non-uniform thickness by the finite-element method*. Almaty.

MINING ENVIRONMENT REGENERATION AND INDUCED CAVING TECHNOLOGY IN MINE ENGINEERING

Feng Gao

*School of Resources and Safety Engineering, Central South University,
Changsha 410083, China*

Keping Zhou, Qingfa Chen

*Hunan Key Lab of Mineral Resources Exploitation and Hazard Control for Deep Metal
Mines, Changsha 410083, China*

Considering the understanding on the idea of environmental protection and sustainable development in recent years, limitation of traditional concepts of people was beoked to realize the changes and innovation for the thinking of mining technology. The science conception of mining environment regeneration is put forward to accord with the situation and needs at present. The meaning of this conception that the geological environment of mineral deposit is regarded as structure environment and boundary condition. By using special technical ways of mining and geotechnical engineering, we can improve mining conditions, reframe mining space and satisfy the needs of security and high efficiency of exploitation. Based on continuous mining technology, induced caving technology adopts artificial advance disturbance to induce roof failure and build a safe workspace. It can avoid the great disaster as well as guarantee the trouble-free execution of continuous mining technology. Moreover, this technology decreases the negative domino effect of mining action on environment which accord with the essence of mining environment regeneration. In addition, new technology develops the passive modification into the active regeneration of mining environment.

INTRODUCTION

With advancement of civilization of human society, many new industry and modern technology develop rapidly, while the space of development of mining industry and technology is relatively slow. However, mining technology in nowadays is much different form that of 1990's ago. The development of modern science and technology brings opportunities to mining engineering, such as equipments upsizing, intelligentizing, application of computer science and information technology. All of these are the source and power of development of mining technology. The developing trend of mining science and technology is moved progressively towards high efficiency, waste free, continuing, harmless, deep and unmanned mining. Whereas, a persistent goal for conventional mine exploitation is to obtain economic benefit without considering the destruction to environment. Moreover,

the goal for high efficiency is only order to reduce the cost and increase economic benefit. Therefore, the negative effects of serious global environment and ecological problems, as well as continual occurrence accidents have become the criticism and attention focus by all over the world.

As we know, mining engineering is a greatly complex system because of complicated structure condition and underground surroundings. At the same time, the development of mining technology lies on the development of other science technologies in a certain extent. Considering the idea of environmental protection and sustainable development in recent years, the limitation of traditional concepts of people was broke to realize the changes and innovation for the thinking on mining technology. Therefore, the conception of mining environment regeneration is put forward to accord with the requirement of mining, which embodies the development tendency of international mining technology. It breaks the limitation among the conventional mining methods, advocates unconventional mining, accelerates development of mining industry to security, high efficiency and sustainable development.

CONNOTATION OF MINING ENVIRONMENT REGENERATION

Revealing the essential attribute of mining science

During the process of mining, the changing of stress state in rock mass brings the deformation and failure in stope. In order to hold the stability of mining engineering, many supporting measures are used to prevent deformation and failure. The main mechanism is to improve initial stress state and stability of rock mass after excavation by reducing principal stress difference. In deep mining, ground temperature is a very important controlling factor. The temperature reduces because of ventilation, which lead the reducing of stress in rock mass and bring troubles to mining tasks significantly. Therefore, whether in the past or the future, the process of mining is to reconstruct environment substantively. The difference of mining methods and techniques is always the difference of mining environment regeneration actually.

Valuing protection and restoration of mine environment

The acts of focusing on economy benefits while ignoring the capability of environment or only protecting environment without exploiting nature resources actively are not approved for scientific and rational exploitation of mineral resources. The relationship between exploitation and environment protection can be regulated effectively. Measures are adopted in some mines in order to hold harmonious development together between human and nature, such as circular economy, ecological compensation, industrial ecological garden and whole process non-pollution control, etc. It is also possible to realize harmonious development between mining industrial production and ecological environment based on industrial ecology. The transition from mining industry to industrial ecological economy has become an urgent issue.

ENGINEERING APPLICATION

Kelatongke Copper-Nickel Mine is the only complex corporation in mining, mineral processing and smelting and it is one of the backbone enterprises of nonferrous metal industrial company in Sinkiang. Panel horizontal downward slicing cut-and-fill mining method was used for many years. Some outstanding problems exist as follows:

- low mining efficiency and complex process
- bad work condition because of bad roof-contacted filling
- high cost of mining and filling

In order to change these obstacles, we innovate in techniques and invent a new mining method named method of mining environment regeneration with deep-hole induced caving and filling.

PROCESS OF METHOD

The difference between basal processes of mining environment regeneration with deep-hole induced caving and filling and traditional method is steps of mining environment regeneration after ore deposit was partition to ore block. Figure 1 shows the simplified process of this kind of mining method.

Application steps of mining environment regeneration

In the middle of roof pillar of ore section, 1 and 2 slice stopes should be mined by conventional method of horizontal downward slicing cut-and-fill. Then artificial roof pillar could be formed by using high strength concrete. In sill pillar of ore section, first, a certain height space was mined by using the short hole bringing-down method, then artificial sill pillar with ore drawing system formed by concrete.

If the mineral deposit construct with unstable ore body, top wall or foot wall, artificial intervening pillar which along or plumb the trend of ore body must be formed by consolidated fill in cutting. A relative stability confined space formed around the ore section before mining activities, and this called mining environment regeneration which shows it in Figure 2 (b).

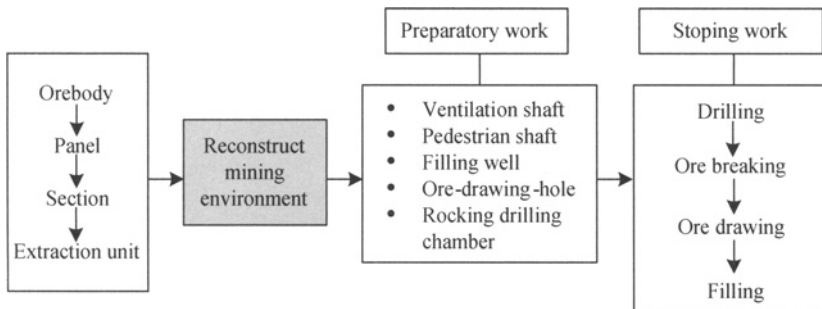


Figure 1. Simplified process of mining environment regeneration with deep-hole induced caving and filling

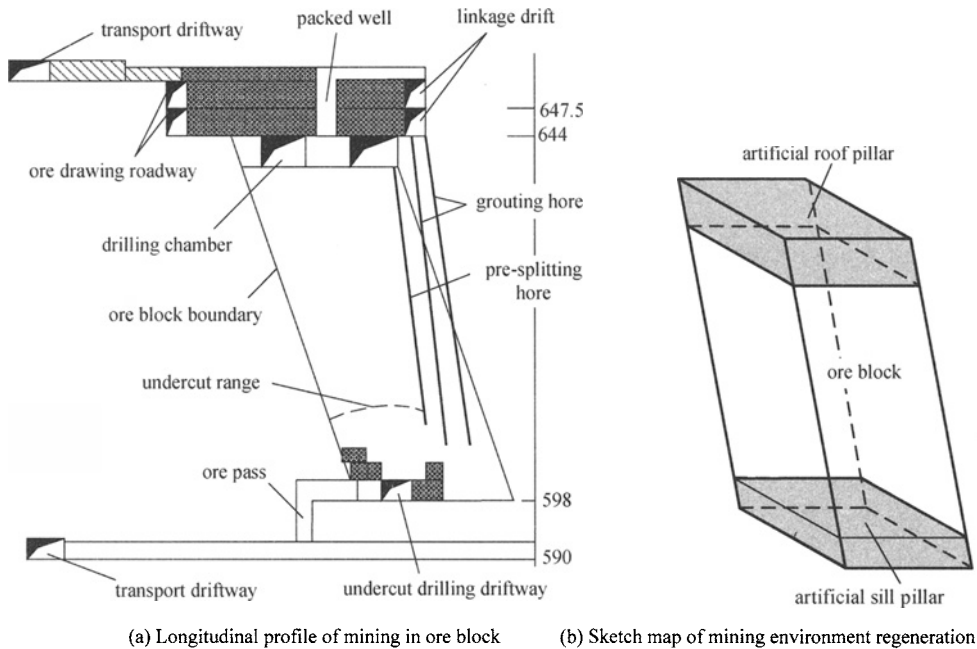


Figure 2. Mining environment regeneration with deep-hole induced caving and filling

Induced caving technology

With fusion of mining environment regeneration, induced caving based on continuous mining technology is a non-traditional, safe and high-efficiency method, which used for mining and processing to mined stope. This technology is that uses the instable status formed by development of discontinuity and changes the strain condition in rock mass by the activities with man-made intervention. This operation induces an irreversible mechanical destabilization and fracture the process in orebody or rock mass. The advanced prediction perturbation forms a safe mining site through inducing instability and failure of rock mass. It can avoid the great disasters as well as guarantee the favoring implement of continuous mining technologies.

Figure 3 presents the basic technology of induced caving continuous mining, which adopts rock strength weakening by middle-depth explosive bores. Fan-shaped middle-deep holes are drilled in subsection drilling roadway. The diameter of the bore is 165mm and the space between bores is from 1.0 to 1.5m. Extraction sequence from one side to another side or from center to both sides of the ore block is put in practice according to the field situation. When the exposed area of roof in mined-out areas arrive to some extent, artificial induced caving of roof and surrounding rock mass should be done by using blasting. Pre-splitting holes are arranged on the two sides of stope. Imperative blasting in the centre of stope is put in force, which called one-off millisecond-delay blasting technique.

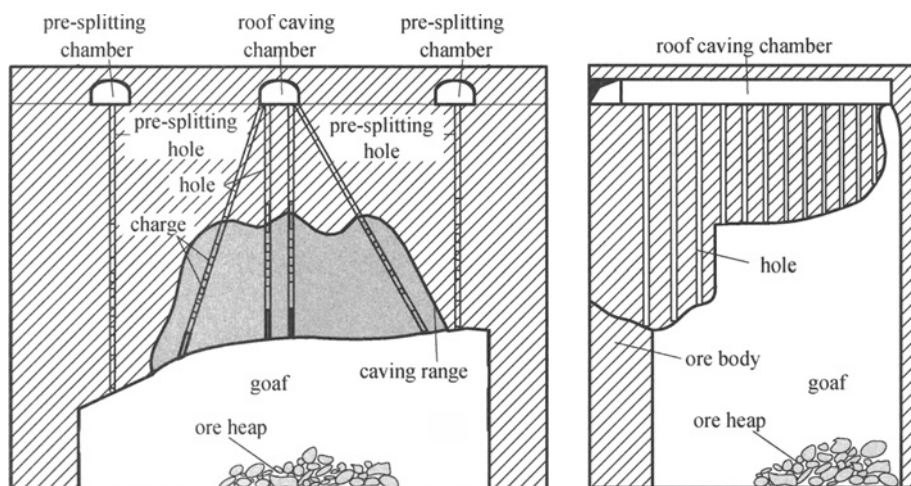


Figure 3. Sketch map of induced caving technology

Advantages and disadvantages

Because of providing with flexibility of downward back fill method and characteristics of high-efficiency mining method, mining environment regeneration with deep-hole induced caving and filling has breached the shackle of sub-level mining technique in high-cost and soft-fractured ore body. It is a revolution to sub-level mining technology and its advantages are as follows:

- It is of great significance for increasing of resource utility to construct artificial roof and sill pillar before stoping. On the one hand, hard recovery work of roof and sill pillar can be avoided and mineral resources can be completely utilized. On the other hand, safety is improved greatly and working intensity is reduced obviously under artificial roof.
- It is an innovation and precedent for using deep or middle-deep holes to ore production under unstable ore-rock by mining environment regeneration. Mining efficiency is improved greatly comparing to that of traditional short holes bringing-down sub-level backfill method. The main technical and economical parameters are given in Table 1.

Table 1. Main technical and economical parameters

Sl no.	Attributes	Unit	New method	Traditional method
1	Stope capacity	t/d	600	120~400
2	Stripping ratio	m ³ /kt	25.8	15~30
3	Dilution ratio	%	7	10~40
4	Loss ratio	%	6	11~44

Some high requirements for construct craft of artificial sill pillar of ore drawing system and quality of backfilling body are the disadvantages. However, these problems can be conquered effectively by using some particular measures under present technique condition.

CONCLUSIONS

With the increasing depth of mining, special environmental conditions in deep mining such as high stress, high temperature and large underground depth will be more serious than ever before. Not only the cost will be increased, but also the safety problem of working is a big challenge. Hence, it is significant to develop a high-efficiency, low cost and safe mining method. Mining environment regeneration in induced caving technology accelerates the mining technology. On one hand, it accords with the developing trend of mining in the future, other hand, it also has irresistible effect on disasters controlling and accidents decreasing.

ACKNOWLEDGMENTS

This work is supported by National Key Project of Scientific and Technical Supporting Programs Funded by Ministry of Science & Technology of China (No. 2006BAB02A02), the Doctor Degree Paper Innovation Engineering of Central South University (No. 1343-77236)

REFERENCES

- Adisa A. (2003). Developing a framework for sustainable development indicators for the mining and minerals industry. *Journal of Cleaner Production*. 12 (6): 639-662.
- Brown E.T. (2003). *Block caving geomechanics*, 1st edition, Julius Kruttschnitt Mineral Research Centre.
- Graedel T.E., Allenby, B.R. (2004). *Industrial ecology*, 2nd edition, Tsinghua University Press.
- Gu D.S. (2004). The development tendency of mining science and technology of underground metal mine, *Gold*. 25 (1): 18-22.
- Malmgren L., Nordlund, E. (2006). Behaviour of shotcrete supported rock wedges subjected to blast-induced vibrations. *International Journal of Rock Mechanics and Mining Sciences*. 43 (4): 593-615.
- Zhou K.P., Gao F., Hu J.H., Su J.h., Zhang S.C. and Deng H.W. (2007). Monitoring and analysis of fracture development in pre-splitting hole of cave inducement of roof. *Chinese Journal of Rock Mechanics and Engineering*., 26 (5): 1034-1040.

VIBRATION ISOLATION BEHAVIOR OF EPS REINFORCED HIGHWAY EMBANKMENTS

Hongmei Gao, An Deng and Hanlong Liu

*Key Laboratory of Ministry of Education for Geomechanics and Embankment Engineering,
Hohai University, Nanjing 210098, China; Geotechnical Research Institute, Hohai
University, Nanjing 210098, China*

As a kind of light-weight embankment fill, EPS can lighten the self-gravity of embankment and diminish the additional stress to the subgrade. The settlement of embankment can be controlled without treating soft foundation. As a kind of fill material behind the abutment, EPS can reduce differential settlements and avoid bump at bridge-head. Otherwise, one of the most important properties of EPS is bigger damping ratio, so it plays certain role in vibration isolation. The deformation properties of general fill material and EPS under self-gravity and vehicle dynamic loads are respectively analyzed through commercial finite element computer program ABAQUS in this paper. From the result, we can conclude that settlement of the subgrade is reduced much more using EPS material than using general fill material. Under vehicle dynamic loads, the incidence of dynamic deformation gets smaller and EPS has certain vibration isolation property. EPS fill material with light weight plays certain role in diminishing the differential settlement of embankment, releasing bump at bridge-head and reducing the dynamic deformation induced by dynamic loads. So EPS has certain application value and will be used widely in highway construction.

INTRODUCTION

Bump at bridge-head is a hard worldwide problem. Especially in soft foundation area, the embankment fill is easy to produce greater settlement under loads. But, the abutment will produce less because the pile foundation of abutment lied on hard bedrock. So the differential settlements between abutment and embankment in the bridge-head area induce the bump problem at bridge-head. As common disease of different kinds of highway, bump at bridge-head always results in thrashing of vehicles and indirectly influences the safety of traveling. It makes passengers uncomfortable, makes vehicles ruined, causes traffic accident and results in tremendous life casualty and economic losses (Wang, 2007). However, dynamic load induced by bump at bridge-head results in damage to road and greater differential settlement. Such a vicious circle does harm to road surface traffic. In recent years, people decline to use light-weight EPS as embankment fill material.

As embankment fill material, EPS block is provided with lots of advantages (Ge, 2006):

- 1) Super-lightweight: Its gravity is only from one sixtieth to one hundred and fiftieth.
- 2) Property of compressive strength: The compressive strength of EPS is about 100kPa to

300kPa. Generally, the overlying pressure of embankment is smaller than 100kPa, so the stability of embankment is guaranteed.

3) Self-steady: Because of smaller poisson's ratio, lateral pressure and deformation of EPS block is smaller, and it can be steady by itself.

4) Vibration isolation behavior: As fill material, EPS block differs from other general fill material because of its bigger damping ratio. Firstly, vibration liquation phenomenon will not arise like saturated sand. Secondly, because of small mass, the pressure to adjacent other constructions induced by mass force of EPS can be alleviated. Thirdly, because of bigger poisson's ratio, EPS can effectively absorb and obstruct the vibration energy which the vibration load of road surface conveys downwards. As fill material of embankment, EPS can play a role on the vibration isolation because it can buffer the dynamic loads.

Concerned conference (Liu et al., 2005) concludes that young's modulus, density and poisson's ratio of embankment all affect the sedimentation. The deformation properties of general fills and EPS fills under the deadweight and dynamic load induced by automobiles are compared and analyzed in the paper by merchant ABAQUS finite element program.

MODELING

Dynamic load

Vehicle loads, seismic loads and wave loads are one kind of dynamic loads, but they differ from each other in properties. Vehicle load is a kind of short-lived and repeating dynamic load acting on road surface. This paper emphasizes on different responses utilizing different fill material under self-weight and dynamic load, so dynamic load is simplified as temporal uniform surface load lasting for 0.01 second.

Constitutive equation

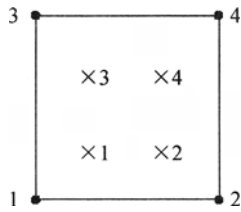
According to involved reference (Ding and Chen, 2004), in the normal condition, the road is at the stage of elastic deformation. So, constitutive model of embankment and foundation material in this paper all choose ideal linear elastic model confirming to Hooke's Law.

Integration method

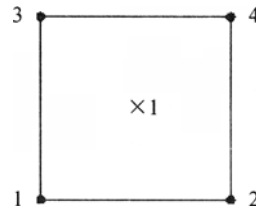
Explicit integration method of ABAQUS is suitable for solving complex contact problem (Shi and Zhou, 2006). In this paper, in order to balance initial geostatic stress, we can only choose implicit integration method in the subsequence step.

Meshing

In order to diminish dimensional effect, generally speaking, we choose the area as large as possible. Moreover, it takes much time to calculate dynamic problem. Using reduced integration which is lack of an integration point in each direction can save time instead of complete integration. Complete and reduced integration element is shown in Figure 1 (a) and (b).



(a) linear complete integration element(like:CPS4)



(b) linear reduced integration element(like: CPS4R)

Figure 1. Two-dimensional linear integration point of complete and reduced integration

GEOMETRY MODELING

Because loads are established as uniform area loads, the model is simplified as two-dimensional plane stress finite element model in terms of longitudinal section. The boundary and constraint conditions are shown in Figure 2.

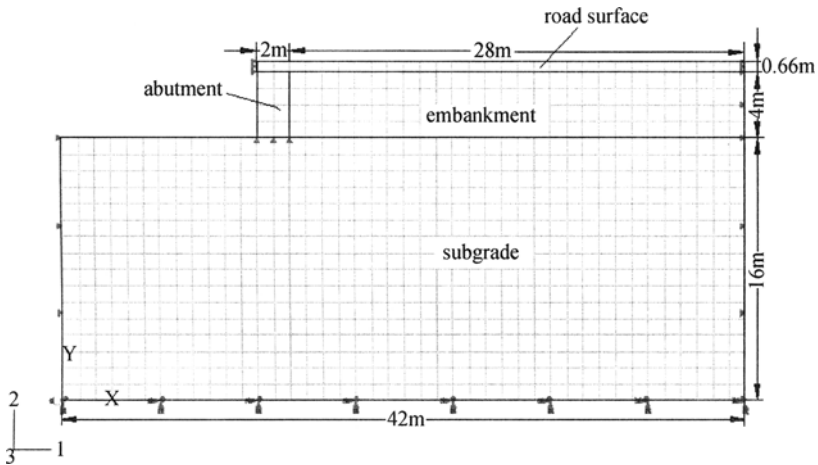


Figure 2. Plane finite element model

CALCULATION AND ANALYSIS

Relevant calculation parameter

According to the mentioned above, in the normal condition, the road is at the stage of elastic deformation, so constitutive models of material in this paper all choose ideal linear elastic model. The material parameters of the main parts in the model are shown in Table 1. In order to simulate responses of the model under dynamic loads, we have to calculate the inherent fundamental frequency. Rayleigh damping is chosen in the model. Mass matrix parameter α and stiffness matrix parameter β are respectively required from the product and quotient of damping ratio and inherent fundamental frequency (Yin et al., 2007).

Table 1. Material parameters of the main parts in the model.

Roadbed structure	Thickness (m)	Elastic modulus (MPa)	Poisson's ratio μ	Density (kg/cm^3)	Damping ratio ζ
subgrade	16	30	0.4	1800	0.1
abutment	4	35000	0.35	2430	0.05
road surface	0.66	1000	0.35	2200	0.05
general fill	4	50	0.4	1900	0.05
EPS block	4	5	0.1	20	0.2

Analysis step

Three analysis steps are established in both models. The first step in the model is to balance initial geostatic stress. It is very important to balance initial geostatic stress for simulating interaction problem and material yielding problem which depends on confining pressure. In civil engineering, the material yielding has close relation with confining pressure, so to balance initial geostatic stress is the first step to analyze geotechnical engineering problem. The second step is gravity step of embankment fill. The third step is dynamic load step of vehicles. The dynamic load lasts for 0.01 second and time period sets for 1 second.

Results and analysis

Balance of initial geostatic stress

In initial geostatic stress, the displacement is about 2 centimeters in small range of bilateral boundaries in the model. However, the displacement value of the main parts we care about is about 10^{-5} meter, so initial deformation can be ignored.

Deformation analysis in gravity step

Vertical displacement of road surface and subgrade surface in gravity step is shown in Figure 3. Although gravity of EPS is only one twentieth to one fiftieth of that of general fill, it only occurs elastic displacement when above load is lower than 100kPa. Road loads are lower than 100kPa, so strength of EPS satisfies the need. Under the gravity of embankment, vertical displacements of road surface and subgrade surface increase and finally incline to be gentle with the distance to abutment. In spite of road surface or subgrade surface, the vertical displacement of model E is absolutely smaller than that of model G. The maximum settlement of road surface is only about 1.5 centimeters and that of subgrade surface is no more than 1 centimeter in model E. And the settlement inclines to be gentle when the distance to abutment is only about 6 meters. However, the maximum settlement of road surface reaches to 4.5 centimeters and it inclines to be gentle until the distance to abutment gets 16 meters. Utilizing EPS with light weight as embankment fill material can effectively diminish the settlement value of road surface and subgrade surface. It can diminish the differential settlements between embankment and abutment and so play an important role in releasing bump at bridge-head.

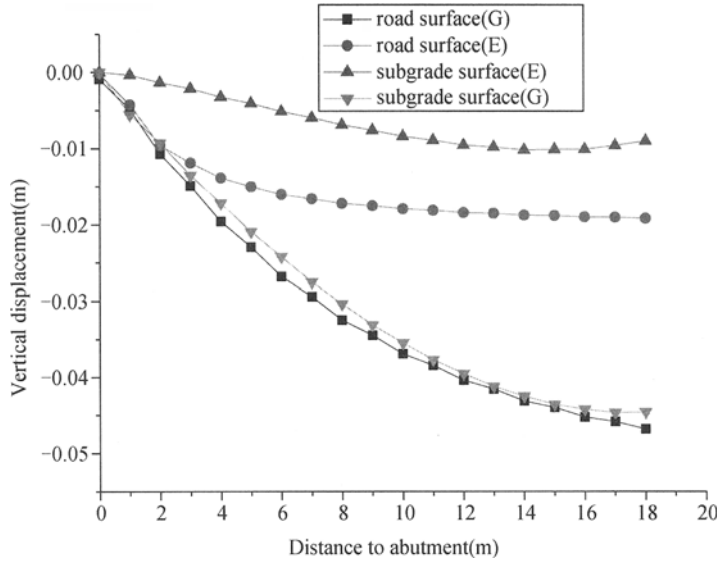


Figure 3. Settlement value of road surface and subgrade surface in gravity step.

Displacement contour chart

Of full analysis process, the maximum vertical displacement appears respectively after applying dynamic loads for 0.1286 second and 0.147 second in model G and model E. Displacement contour chart appearing maximum displacement is shown in Figure 4. From the figure we know that the maximum settlement of road surface respectively is 2 centimeters and 6 centimeters in model E and model G. It shows that using EPS as embankment fill material actually diminishes the settlement value. In model G, the settlement whose magnitude is centimeter widely distributes in the subgrade. However, in model E, the settlement whose magnitude is centimeter almost distributes in shallow embankment. Only few parts of displacement whose magnitude is centimeter spread to the subgrade in shape of inverse triangle. This is because EPS with big damping ratio displays the vibration isolation functions and it makes dynamic loads reduced when it transports to the subgrade.

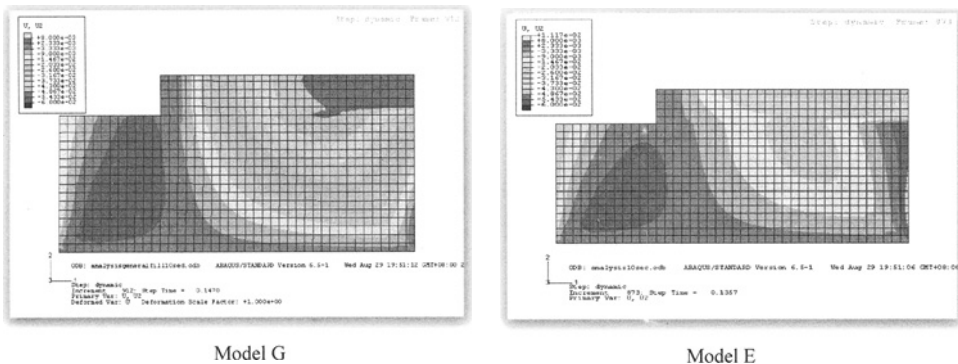


Figure 4. Displacement contour chart.

Settlement of road surface

Change chart of settlement of road surface with the distance to abutment in gravity step, dynamic load step and final settlement step is shown in Figure 5.

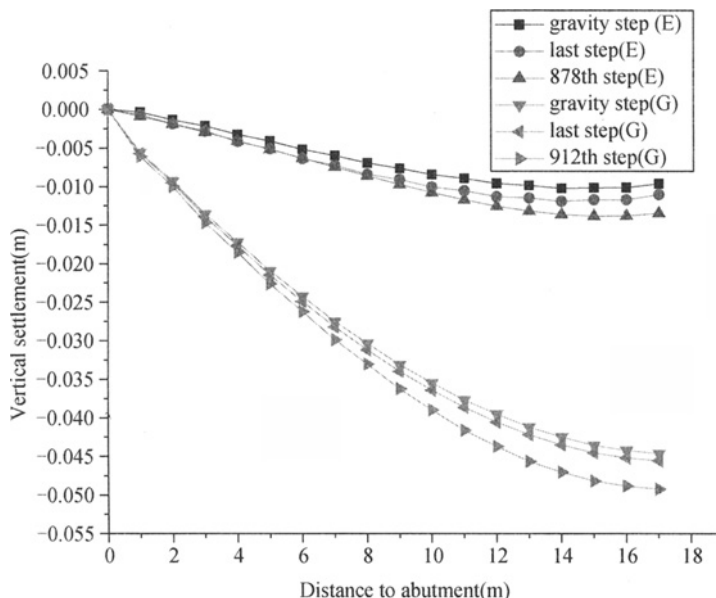


Figure 5. Settlement of road surface.

From the figure, settlement of road surface in these three steps is about 1.5 centimeters to 2.5 centimeters in model E, and it declines to be gentle when the distance to abutment is about 6 meters. The maximum vertical displacement induced by dynamic is about 3 millimeter in model E. Compared with model E, in model G, settlement of road surface reaches 5 to 5.5 centimeters and it declines to be gentle until the distance to abutment reaches about 20 meters. The maximum vertical displacement induced by dynamic is about 5 millimeters in model G. The final settlement induced by dynamic load is smaller, not more than 1 millimeter in these two models.

Time-travel curve of road surface and subgrade surface whose distance to abutment is 6 meters.

The first to the second step is set for gravity step. The second to the third step is set for dynamic load step.

From Figure 6, the vertical displacement values are all negative that explains dynamic load induces vibration of subgrade up and down, but upward displacement induced by dynamic load is smaller than downward settlement induced by gravity load. In gravity step, settlements of road surface and subgrade surface in model E are largely smaller than that in model G. Settlement of subgrade is about 3 millimeters because the self-gravity of EPS is small which induces smaller additional stress to the subgrade. In model E, vertical displacement of road surface changes suddenly under dynamic loads in first half period. In embankment construction with EPS, they are connected by connecting piece with claw shape

of both sides (Dong et al., 2006). In the model, ignored contact relation may results in that vibration amplitude of road surface increases widely. After half period, amplitude of vertical vibration displacement declines to be steady. Differential vibration displacement between subgrade surface and road surface is great, and it illuminates that EPS plays an important role in shock absorption in transmitting process of dynamic load. General fill with small damping ratio has no effect on shock absorption, so differential vibration displacement between subgrade surface and road surface is small.

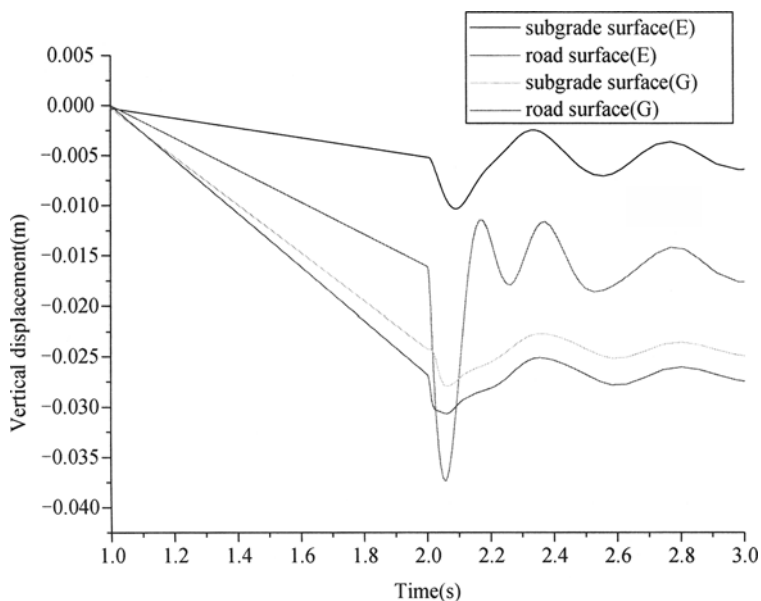


Figure 6. Time-travel curve of road surface and subgrade surface.

CONCLUSION

(1) Settlement of road and subgrade surface induced by self-gravity using EPS as fill material is smaller than that of general fill material.

(2) EPS block possesses certain shock absorption effect because of great damping ratio. Compared with general fill material, the dynamic load is partly weakened by EPS fill material when vehicle load transmits to the subgrade.

(3) Lateral stress of EPS block to abutment is smaller due to its light weight and small Poisson's ratio. The lateral displacement of abutment using EPS as fill material under the self-gravity of embankment and dynamic load is absolutely smaller than using general fill material.

Using EPS block as embankment fill material can diminish settlement of road and subgrade surface induced by self-gravity and dynamic load. So it can diminish differential settlement between road surface and abutment and has certain effect on slowing up bump at bridge-head. EPS is more expensive than general material, but its cost of freight is much lower than that of general material. And labor fee in the construction of EPS is low and the

expensive fee for piling can be saved. As a kind of embankment fill material, EPS has a great application prospect in highway.

ACKNOWLEDGEMENTS

This work is supported by National Natural Science Foundation of China (Grant No 50708031) and Scientific Research Foundation for the Returned Overseas Chinese Scholars, State Education Ministry (SRF for ROCS, SEM).

REFERENCES

- Ding G.H., Chen L.Z. (2004). Vibration isolation analysis of EPS cushion at bridge-head, *HIGHWAY*, (3): 30-33. (in Chinese)
- Dong Y., etc. (2006). The Applications of Expanded Polystyrene (EPS) Foam in Road Engineering, *Communications Standardization Issue*, 150/151: 117-121. (in Chinese)
- Ge X.H. (2006). Applying super-light embankment fill material EPS to deal bridge pier soft subgrade, *Fujian Architecture & Construction*, 97(1): 186-188. (in Chinese)
- Liu M.C., etc. (2005). Influence factors on post-construction settlement of high backfills adjacent to abutment, *Journal of Traffic and Transportation Engineering*, (5) 3: 36-40. (in Chinese)
- Shi Y.P., Zhou Y.R. (2006). *Particular Case Interpretation of ABAQUS*, China Machine Press. (in Chinese)
- Wang J.C., Chen Y.K. (2006). *Application of ABAQUS in Geotechnical Engineering*, Zhejiang University Press. (in Chinese)
- Wang X.J. (2007). Reason analysis and prevention and cure countermeasure to bump at bridge-head, *Shanxi Energy and Conservation*, 45 (2): 28-29. (in Chinese)
- Yin Z.Z., etc. (2007). *Geotechnics Principle*, Chinese Water Conservation and Hydroelectricity Press. (in Chinese)

A REPAIRING METHOD FOR THE CLAY LANDSLIDE IN SHAOGUAN OF GUANGDONG PROVINCE

Jian Gao, Jiaoli Zhu and Jian Pan

*School of Civil and Traffic Engineering, South China University of Technology,
Guangzhou 510640, China*

A slope in Shaoguan of Guangdong province is composed of soils with high water adsorption. Rainstorms usually decrease strength parameters of soils and lead to great landslide with severe soil disturbance. A popular unloading and anti-sliding supporting method usually couldn't achieve a good treatment effect. The closely spaced steel-tube and compressive grouting method, with two or more line steel flower tubes drilling into anti-sliding section of sliding mass and compressive grouting, can reinforce the soil around steel tubes. The steel tubes and around soil can form a solid continuous integrality acts as a retaining wall. Steel-tube and compressive grouting improve the mechanical capability of soil obviously so that the stability of slope is recovered with special unloading along slope and drain measures together.

INTRODUCTION

Landslide is a geological hazard. Its frequent occurrence is often followed by sudden traffic block, waterway obstruction and village destruction, causing great losses. Thus the prevention of landslide has always been a world-wide concern. Measures like retaining wall, anti-sliding piles, stabilizing piles with prestressed anchor cables, prestressed anchor cable pier, anchor-rope and ground sill, anchor cable frame and micro-piles group (Xie Xiao hua, 2001; Xia Xiong, 2002; Wei Shi zhuo, 2003; Zhao Wei chu, 2005; Zhu Bao long, 2005; Deng Jian tiao, 2006; Zhou Bei, 2006), have turned out to be effective in prevention against landslide. However, improvements have to be made to face landslides in complex geological conditions of various projects. Some landslides are too poor in soil conditions to be prevented by one anti-sliding retaining structure; therefore the combination of two or more techniques may become a necessity.

This paper studies a new landslide treatment method: a new supporting structure—Steel-tube Bored Grouting Anti-sliding Retaining Wall by the joint use of steel-tube micro-piles (group) and grouting, with the remediation of landslide in Shaoguan of Guangdong Province as an example.

THE STEEL TUBE BORED GROUTING ANTI-SLIDING RETAINING WALL (SBGARW)

SBGARW is the joint use of grouting and steel-tube micro-piles group. The combination of

the steel-tube piles and grouting can be regarded in the stress analysis as an anti-sliding wall. What is most striking is that part of sliding mass is reinforced to be an anti-sliding mass to achieve the landslide treatment effect. With two or more line steel flower tubes drilling into anti-sliding section of sliding mass and compressive grouting, SBGARW can reinforce the sliding mass around steel tubes, rocks and soil on the surface of slide and under it. The closely spaced steel flower micro-tubes and around soil can form a solid integrality acting as a retaining wall. The distribution of steel-tube piles in the section and on the plane of landslide is illustrated respectively in Figure 1 (a) and (b).The advantages are as follows: (Zhu Bao long, 2005).

(1) Retaining: steel-tube pile and the cement grout around it form a micro-pile. Multi steel-tubes closely spaced at a landslide, crossing the sliding surface embedded in a rock bed, become anchor piles, which retain the sliding mass and reinforce it stability. (2) Resistance: Root Pile is formed by splitting grouting. The solidifying grout, cohesive and absorbent, bonds the sliding mass and stable mass forming a proliferation of the complex, in this way improves the mechanical capability of sliding soils, enhances the value of c and ϕ , and increases friction, thereby improves the anti-sliding ability of the rocks and soils on the sliding surface. (3) Strengthening and compaction: with cement grout filled and compaction, the rocks and soils become higher in density, lower in porosity and permeability. Less surface water would infiltrate and the stability of the sliding mass would improve. (4) Anti-sliding: with the reinforcement of soils around and between the piles, lateral resistance of the rocks and soils is raised. and two lines of steel-tube piles and the soils between them are reinforced to become an integral anti-sliding mass, acting as retaining wall in the treatment of landslide; meanwhile, a robust integral anti-sliding mass is formed by the steel-tube piles, sliding mass around them, and the stable mass under sliding zone and sliding bed reinforced by steel-tubes and bored grouting. What's more, part of sliding mass in the front of the landslide is reinforced to become anti-sliding mass, as a part of the retaining wall against sliding. (5) Such a wall is easily constructed, with little damage to environment and no great consumption of steel and cement. (6) It applies to the management of soft clay landslide with high water adsorption such as avalanche slope accumulation and residual slope accumulation.

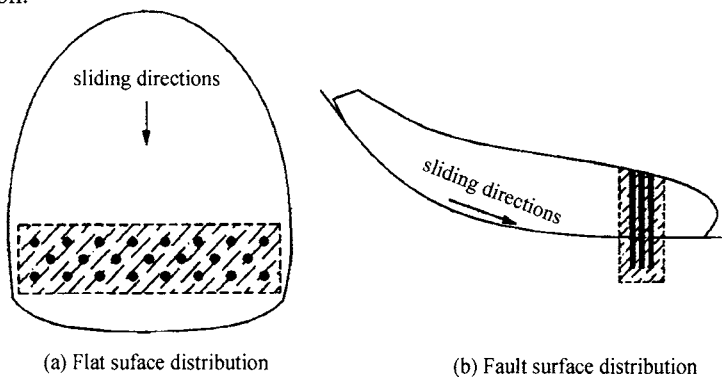


Figure 1. Schematic diagram of steel-tube bored grouting anti-sliding retaining wall

ENGINEERING BACKGROUNDS (Pan Jian, 2006)

In the southern district of an institution in Shaoguan of Guangdong Province, there is a six-storey dormitory in-built. In the west side of the dormitory, the site and outlying of the slope is erosive low hills, with a elevation of 76.00–108.00m. The site in the east part of the hills has a very complicated geological condition: the upper layer of slope is silty clay soil, with a considerable amount of low-purity kaolin that has a mineral composition of montmorillonite. It inflated like robber-mud when comes across water. The layer below is composed of carbonaceous silty clay, or carbonaceous clay, with coal seam occasionally. The depth of bedrock varies greatly: in most cases bedrock can't be seen in the depth of nearly 16m whereas some bedrock heaves up (but the surrounding places are still low). Originally the hill is not steep, with a gradient only about 20 degrees, but with the latter construction, artificial slope raise to 35 degrees. The slope angle at the foot of the hill is about 55 degrees to 60 degrees. The hill is covered by the Q4 fill, artificial soil, with specially high water adsorption. A large amount of rain infiltrates, which decreases the shear strength of soil and may leads to soil collapse or landslide, especially in more than one sliding surfaces.

Because of the rainy season, there is a great decrease in the shear strength of soil and a continuous expansion of landslide. During the construction, new landslide emerges and the soil can not maintain homeostasis. The landslide can not be prevented by retaining structure of anchor and grille groundsill according to the condition of the site and the regional geotechnical characteristics. Neither will a single anti-slide pile or gravity retaining wall do because of the continuous landslide and release of gas, like sulfurated hydrogen.

REPAIRING METHOD FOR THE LANDSLIDE

The main point of the landslide control is: firstly to remove the loose soil in order to solidify sliding surface and flatten the slope, and then to use steel-tubes and compressive grouting retaining wall for supporting, in the process of which the ground must be well drained and soil parameters accordingly changed. The detailed measures are as follows:

(1) Unloading on sliding surface and reducing load in slope. After unloading, the average rate of slope is flattened to 1:2.75 to 1:3.0, equivalent to the original ground slope of 20 °, reaching stability by itself.

(2) On the surface of slope, bind ditch is supported with grille stone tablet to avoid the collapse. The bottom of the channel, being below the surface of slope, could be reinforced and avoid seepage, thus become a good channel for both supporting and drainage.

(3) Make sure channels of side ditch, gutter ditch and platform ditch are well prepared. In the lowest slope, drainage channel of the plastic blind ditch on the vertical retaining wall should be done, to dredge hidden water at the foot of slope and improve geotechnical parameters of the slope.

(4) Make steel-tube piles stratified for supporting: Due to the softness of sliding mass and the low shear strength of the sliding surface, it is essential for landslide remediation to reinforce sliding surface and rocks and soils on the landslide and improve the stability of sliding mass. Thus Steel-tube bored grouting anti-sliding retaining wall composed of closely spaced steel-tube and compressive grouting micro-piles is used on this slope to prevent the

landslide. Cement grout should be grout both in the steel-tubes and between the steel-tube and drilling hole. Splitting sub-grouting technology is used to grout the cement grout in the rocks and soils among the steel-tubes, therefore the rocks and soils among the piles was cementation and reinforced. Rows of piles and the rocks and soils between them become a whole, equivalent to a continuous wall. In other words, because of the construction of steel-tube and compressive grouting micro-piles, sliding mass surrounded by micro-piles in slope at different heights was reinforced to become an integral part of the retaining wall, to prevent against sliding together with the micro poles. All the steel-tube and compressive grouting piles are 5.0–9.0 m below the sliding surface, so that the cement grout could be grout in the sliding surface and be effective in reinforcement. Furthermore, steel-tube has certain shear strength itself. The distribution of Micro-piles on the plane and profile section in the landslide can be illustrated in Figure 2.

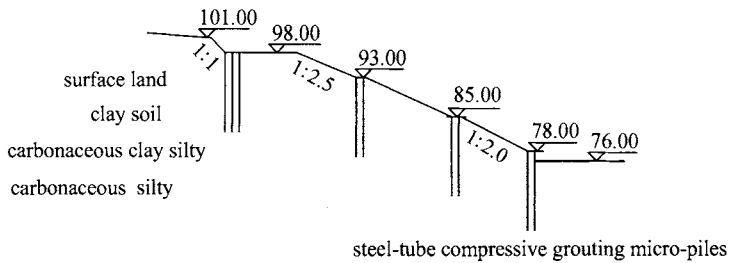


Figure 2. Section plan of the slope

In this project, the elevation of the slope is 76.0m at foot and 101.0m at top, and the biggest height of slope is 25.0m. The entire slope contains three steps at 85.0m, 93.0m and 98.0m elevation; the first step and the second step are both 2.0m in wide, and the third step is 15.0m. The rate of slope from foot to top is 1:2.0, 1:2.25, 1:2.5 and 1:1.0, respectively.

The process of compressive grouting piles is shown in Figure 3, concrete designing as follows:

① requirements to set the piles.

A, foot of the slope: $\phi 90$ mm steel-tube, $\phi 90$ mm aperture, two lines, the length of 12 m, the distance between lines is 1.5 m, the distance between holes is 2 m.

B, the first platform: $\phi 90$ mm steel-tube, $\phi 130$ mm aperture, two lines, the length of 15 m, the distance between lines is 1.5 m, the distance between holes is 2m.

C, the second platform: $\phi 90$ mm steel-tube, $\phi 130$ mm aperture, two lines, the length of 15 m, the distance between lines is 1.5 m, the distance between holes is 2m.

D, the third platform: $\phi 90$ mm steel-tube, $\phi 130$ mm aperture, three lines, the length of 25 m, the distance between lines is 1.5 m, the distance between holes is 2m.

② grouting parameters.

A, Figure 3 shows the process of steel-tube compressive grouting micro-piles. The holes on the steel flower tube are drilled in the wall with drill at a diameter of 4 to 5 mm, spiral set spacing of 30 cm and there is only one hole in the same section. The structure of grouting tube can be illustrated in Figure 4.

B, the water-cement ratio: 0.45 to 0.50 for the first grouting, 0.6–0.7 for the second

grouting.

C, grouting pressure: normal grouting not exceeding 3 MPa largest.

D, quantity of grouting: the quantity of grouting should reach to 200 kg / m.

E, splitting grouting: use splitting sub-grouting for the second grouting. The grouting mouth of each piles should be located in sliding zone and 1.0 m below and up it, each of 1.5 to 2.0 m; 10–12 after the first grouting, the second grouting should begin.

F, cement grout: cement grout for grouting should be pure at 42.5R.

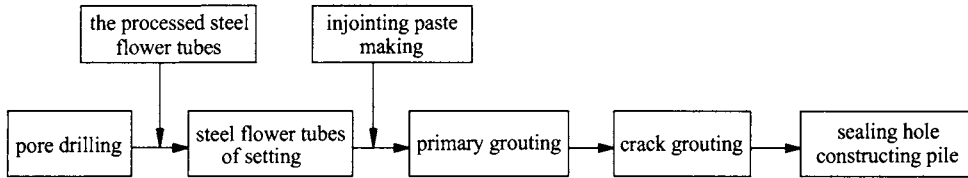


Figure 3. Flow chat of steel-tube bored grouting micropiles

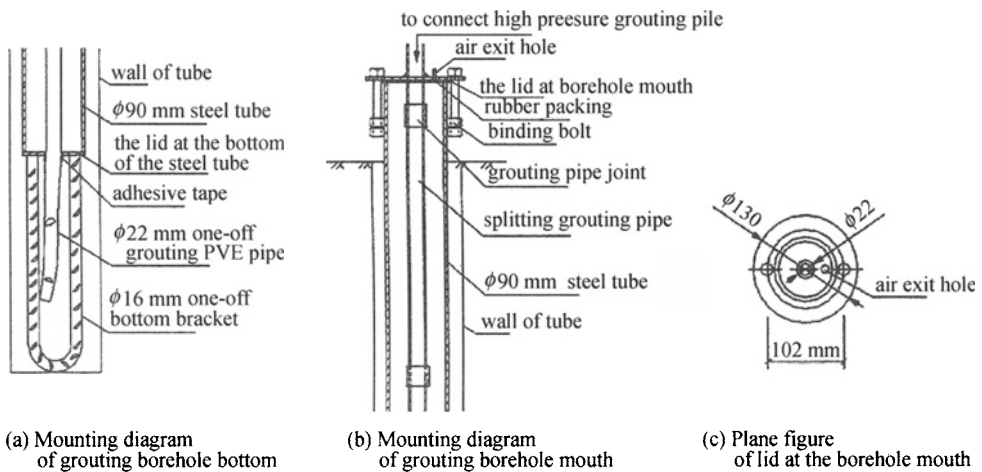


Figure 4. Structure of grouting tube

EVALUATIONS ON STABILITY OF THE LANDSLIDE

The stability of the slope has been analyzed before the slope is supported by steel-tube compressive grouting piles. The slope is considered as uniform and sliding surface passes through the foot of slope. Make a qualitative check about the stability of the sliding surface and the local slopes at the elevation of 101.00–98.00, 98.00–93.00, 93.00–85.00 and 85.00–78.00, admitted to checking parameters shown in Table 1.

An analysis by the slope by strength reduction FEM(Zhao Shangyi, 2002; Zheng Yingren, 2004), the safety index is 0.89 before reinforcement. After the application of steel-tube compressive grouting piles, value of c and ϕ is obviously improved, so does the strength of the weathered carbonaceous mudstone. It is analyzed that, after reinforced with Steel-tube bored grouting anti-sliding retaining wall, the safety index of the landslide reach 1.565, suggesting the effectiveness of the treatment.

Table 1. Essential parameter of the landslide

types of soil	gravity of soil (kN/m ³)	cohesion (kpa)	friction angle (°)	thickness of soil (m)
surface land	20.0	26.0	15.0	1.80~ 2.10
clay soil	20.2	32.3	16.3	2.00~12.90
carbonaceous clay silty	20.1	27.4	14.9	2.00~10.35
carbonaceous silty	19.0	10.8	17.9	2.60~ 7.08

CONCLUSIONS

(1) Some slopes are composed of complex, highly absorbent soils, the strength parameters of which would be greatly decreased after heavy rain. For these slopes with great slide and severe soil disturbance, the usual unloading and anti-sliding supporting method will not improve the strength parameters of soils, therefore could not achieve a good treatment effect.

(2) Good treatment effect can be achieved by unloading the slope to its rate of stability and setting drainage channel to improve the strength parameters of rocks and soils.

(3) The steel-tube and bored grouting micro-piles, which can prevent sliding in itself, can reinforce soils around sliding zone, micro-piles and between rows of micro-piles. Micro-piles rows and the soils between them are reinforced to become an integral part of anti-sliding mass, acting as a retaining wall in the treatment of landslide. It applies to soft clay landslide with high water adsorption such as avalanche slope accumulation and residual slope accumulation.

(4) The landslide treatment can be evaluated afterwards by PS wave test hole and pressuremeter test, examining the change of the soil parameters. Meanwhile, necessary monitoring is also of great importance, in that further sliding can be observed in time by the test hole and further treatment should follow as well.

REFERENCES

- Deng Jiantiao.(2006). Analysis on function of prestressed anchor cable in slopes remediation and slope engineering protection. *Railway Engineering*, 6: 36-38.
- Pan Jian, Zhang Naiji. (2006). A project of some clay landslide measures in Shaoguan of Guangdong province. *Journal of Shantou University (Natural Science)*, 21, 3: 70-74.
- Wei Shizhuo. (2003). Remediation of slope side at highway cuts. *Central South Highway Engineering*, 28(4) 92-94.
- Xia Xiong, Zhou Depei.(2002). Application of prestressed anchor-rope and ground sill to slope stability. *Rock and Soil Mechanics*, 23(2): 242-245.
- Xie Xiaohua, Liu Jifu and Pang Qisi. (2001). Application of m icropiling in a landslide treatment engineering . *West China Exploration Engineering*, 13(2):110-111.
- Zhao Shangyi, Zheng YingRen, Shi WeiMin.(2002). Analysis of safety factor of slope by strength reduction FEM. *Journal of Geotechnical Engineering*, 24 (3):343 - 346.
- Zhao Weichu, He Pi yuan and Xu Bian. (2005). Anti-slide pile treat the ancient landslide of Gan-ding highway Longnan intercommunication. *Journal of Highway and Transportation Research and Development*, 22 (9): 19-22.

- Zhou Bei, Zhao Minghua and Liu Xiaoping. (2006). The applications of stabilizing piles with Pre-stressed anchor cables in highway slopes remediation works. *Central South Highway Engineering*, 31 (2):89-92.
- Zhu Baolong. (2005). Study on engineering characteristic of similar soft soil slope and steel-tube bored grouting anti-sliding retaining wall [Ph. D. Thesis][D]. Chengdu: Southwest Jiaotong University.
- Zhu Baolong, Yang Ming and Hu Houtian.(2005). Testing study on internal forces for prestressed anchor cable frame in reinforced soil slope. *Journal of Rock Mechanics and Engineering*, 24 (4):697-702.
- Zheng Yingren, Zhao Shangyi. (2004). Application of strength reduction FEM to soil and rock slope. *Journal of Rock Mechanics and Engineering*, 23(19):3381-3388.

IMPROVING SOFT SOIL USING CONCRETE-CORED SAND-GRAVEL PILE COMPOSITION FOUNDATION

Yunfei Guan, Jin Yu

*Geotechnical Engineering Department, Nanjing Hydraulic Research Institute,
Nanjing 210098, China*

A new type of composite foundation, named concrete-cored sand-gravel pile composite foundation for thick and soft ground treatment is introduced in this paper. The new style composite foundation is composed of the concrete-cored sand-gravel pile, the soil between piles and the cushion. This paper describes its design and construction technology, and analyzes its load transfer mode and improvement mechanism. Field test results indicate that the new type combined pile is sufficient in satisfying the stability and the post-construction settlement of embankment and foundation.

INTRODUCTION

In eastern China, most of the areas consist of soft subsoil with high compressibility, poor intensity and low permeability. The soft ground was always caused by marine, lake or river. In recent years, with the rapid development of highway construction, many highways can not but pass the soft soil distributed area. For the construction of highway embankment, the soft subsoil need to be treated at an earlier stage, which bring the challenge to the engineers and technicians.

In the past practice, the reinforce methods of saturated soft clay foundation included accumulation load preloading and Deep Mixing Method (DMM). If the soft subsoil is treated by preloading method of accumulation load, the advantage is the low construction cost and available experience, the major disadvantage is the long construction period, the shallow reinforcement depth and the excessive post-construction settlement. On the other side, the long DMM column length is limited by the ability of the construction machines, and the quality of the long column cannot easily be controlled. If use the rigid column composite foundation, the ground treatment cost will dramatically increase.

In some areas, thick soft subsoil (20m or more) may be encountered. Either preloading method or DMM can not satisfy the requirement of the highway's post-construction settlement. In the past practice, we must increase cost to construct rigid column composite foundation or pile foundation. It is well-known that the rigid pile's major resistance to load is derived by side friction, So its cross-section must have sufficient size. However, at the same time, the compressive strength of the pile usually play only 30% ~ 40%. Besides, the sand column in soft clay foundation plays the role of drainage, but its strength is lower. We

may conceive a plan to insert a little diameter rigid pile in the middle of the sand column to enhance the strength of the sand column. Based on these ideas, Zhao (2006) suggested a new type of composite foundation, named concrete-cored sand-gravel pile composite foundation. This new style composite foundation is composed of the concrete-cored sand-gravel pile, the soil between piles and the cushion. In this proposed composite foundation, prefabricated concrete pile is vertical reinforcement, sand-gravel shell is vertical drainage body and accumulation earthwork is pre-loading. Under the load, the sand-gravel shell speeds up the consolidation of soil between piles in construction and preloading periods to reduce the post-construction settlement in applied periods.

PILE COMPOSITION AND CONSTRUCTION SEQUENCES

PILE composition

The concrete-cored sand-gravel pile is composed by the prefabricated concrete pile and the sand-gravel shell, which are inner-core and outer-core respectively. Figure 1 depicts the composition of this new type pile.

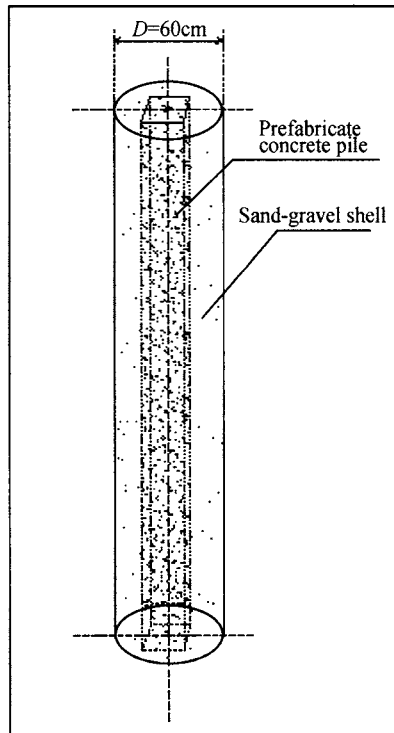


Figure1. The prefabricated concrete-core sand-gravel pile

The prefabricate concrete-core

The grade of the prefabricate concrete pile is generally C20, and its cross-section is square, that the length of the side is 50mm. We use prefabricated reinforcement concrete pile as

inner-core because of its high strength, lower compressibility and the easily controlled quality.

To convenient for transportation, the prefabricated concrete piles need to be produced and transported segment by segment. At the construction site, we lift the first prefabricated pile, and then place it in the hole, which is excavated by vibratory immerse tube driver in advance, then assembly the second pile with the first one. By this method, the concrete-cored sand-gravel pile can reach 25m or more.

The sand-gravel shell

The outer diameter of the sand-gravel shell is decided by the geological condition and the type of drill tool, is usually 50cm. The sand or gravel to be used must be chosen with extreme care in order to have good drainage property.

Construction sequences

The construction sequences of the concrete-cored sand-gravel pile are as following:

- Putting the vibratory immerse tube driver to the designated location
- Immersing tube by vibration to the designed level
- Placing the prefabricated piles in the hole and assembling them segment by segment
- Filling granular substance such as sand or gravel in the inter space
- Pulling out the tube by vibration
- Repeating the above steps and constructing the next combined pile

THE IMPROVEMENT MECHANISM OF THE CONCRETE-CORED SAND-GRAVEL PILE

The concrete-cored sand-gravel pile is composed by the prefabricated concrete inner-core and the sand gravel outer-core. The new style combined pile, the soil between piles and the cushion made up to composite foundation, which is effectively to improve soft subsoil. The functions are as following:

(1) Replacement: After carrying out the concrete-cored sand-gravel pile, the equivalent volume soft clay is replaced.

(2) Drainage: The sand-gravel shell, like a hollow granular column, shortens the drainage paths, speeds up the soft clay's consolidation process, enhances the bearing capacity of the composite foundation.

(3) Reinforcement: The prefabricated concrete pile, as inner-core, reinforces the foundation's stability.

As mentioned above, the concrete-cored sand-gravel pile composite foundation is sufficient in satisfying the stability and the post-construction settlement.

LOAD TRANSFER

By the results of field monitoring, in the shallow foundation, the load from embankment and traffic mainly transfer to the precast concrete-core. The load carried by the concrete-core is transferred downward and outward. When load transfer from the

concrete-core to the soil, it must pass through the sand-gravel shell. That is the double-layer load transfer mode: form the concrete pile inner-core to the sand outer-core and form the sand outer-core to the soil.

The axially load of the concrete-core is partial transferred to the sand-gravel shell by frictional resistance along the concrete pile. The other is transferred downward till the pile tip. This is the first layer of the load transfer. Except the frictional resistance coming from the concrete inner-core, the sand-gravel outer-core carries the side friction, which came from the soil between piles. This is the second layer of the load transfer. The double-layer load transfer mode insures that the composite foundation can bear enough embankment load.

FIELD TEST

A field test research for the concrete-cored sand-gravel pile composite foundation was taken by CHEN (2007) in a section of Zhen-Li expressway bridge approach. The depth of the soft subsoil at the test site was 20m. The formerly ground treatment plan was DMM column composite foundation. However, the quality of the long column was limited by the ability of the construction machines. Then, the concrete-cored sand-gravel pile composite foundation was used. The composite pile length was 22m. The space of the pile was 2.1m. After finishing the construction of the composite pile, a 50cm sand layer was spread over the ground as the embankment cushion, and a 7.9m earth fill was covered on the cushion (including 2.6m earth fill as overloading). The construction period was 4 months. When the preloading had continued for about 6 months the surcharge can be removed and the road can be paved.

After carrying out the concrete-cored sand-gravel pile, a static load test of single pile and a in-situ plate loading test of the composite foundation were undertaken. The static load test result indicated that the bearing load capacity of the single pile was 300kN. The in-situ plate loading test showed that the bearing pressure capacity of the composite foundation was 150kPa. After preloading 6 months, the composite foundation's settlement speed was less than 5mm per month. According to this result, post-construction settlement should be less than 10cm, which satisfied the stipulated criteria of load-bearing capacity and post-construction settlement.

CONCLUSION

In summary, following conclusions can be drawn.

(1) The concrete-cored sand-gravel pile composite foundation is an alternative for the improvement of the thick soft subsoil in the highway embankment construction. It has the merits of drainage preloading and vertical column.

(2) The improvement mechanism of the concrete-cored sand-gravel pile is its actions of replacement, drainage and reinforcement.

(3) The load of the new type combined pile has double layer transfer form, concrete-core to sand-gravel shell and sand-gravel shell to soil.

(4) Field test results indicate that the new type combined pile can meet the requirement of the stability and the post-construction settlement of the embankment and foundation.

ACKNOWLEDGMENT

The authors gratefully acknowledge the support of Nanjing Hydraulic Research Institute, which is providing the funding for this research.

REFERENCES

- Chen J.S., Zhao W.B (2007). Field test study on concrete-cored sand-gravel pile composite foundation, *Chinese Journal of Geotechnical Engineering*, 29(7): 957-962.
- Zhao W. B (2006). Composite foundation technology of concrete-cored sand-gravel pile, *Proceedings of the 9th Chinese Conference of Soil Improvement*, Taiyuan, Zhejiang University Press, 83-88.

STUDY ON RELATIONSHIP BETWEEN WHEEL LOAD AND RUT DEPTH OF GEOGRID-REINFORCED UNPAVED ROAD

Youchang Hu

*School of Transportation, Wuhan University of Technology, Heping Road,
Wuhan 430063, China*

The behavior under working conditions of a temporary road, serving for rescue, with a geogrid on soft ground is studied. Taking into account of the model test results, the surface rutting of such reinforced road is analyzed under wheel load. The relationship between the rut depth and the contact pressure of tire is derived, which can be used to estimate the bearing capacity corresponding to a given surface rut depth for a given geogrid-reinforced unpaved road, or to calculate the proper thickness of the granular fill layer for a selected geogrid, the tensile modulus of which is known. Therefore, the theoretical method proposed in this paper is a guide to design the geogrid-reinforced unpaved road on soft ground.

INTRODUCTION

The temporary road is necessary once a natural disaster, such as earthquake, occurs. When the road has to be built on soft ground, using geogrid to reinforce the temporary road structure is a good selection because a geogrid-reinforced unpaved road not only meet the requirement of the rescue traffic due to the high tensile strength and tensile stiffness of the geogrid, but also can be constructed quickly with less cost. Such temporary road usually consists of granular fill and a geogrid at the fill – soft ground interface.

Several researchers have conducted experimental studies on such a system (Love et al. 1987; Fammin and Sigurdsson, 1996). A number of procedures have been proposed for geotextile-reinforcement unpaved roads, notably by Giroud and Noiray (1981). For geogrid-reinforced unpaved roads, a theoretical method has been proposed by Giroad and Han (2004). All of them are based on the assumption that general shear failure will occur in the soft subgrade soil while the surface load is big enough. This idea is supported by the observations in laboratory tests performed by Love et al. (1987). However, when such a failure occurs, the displacement of the system is usually unacceptable. If the deformation of the reinforcement layer is small, a solution has been proposed by Wan tao and Wang Zhao (2003).

The purpose of this paper is to analyze the load-rut depth relationship of an unpaved road that consists of a layer of granular fill overlying soft subgrade soil with a geogrid at the fill-subgrade interface under working conditions. In this situation of such a system, the general shear failure is not permissible in the soft subsoil, and the deformation of the geogrid is commonly not small. So the analytical method by Giroud and Noiray (1981) or that by Wan Tao and Wang Zhao (2003) mentioned above is not rational to explain the problem

discussed here. Therefore, the behavior under working conditions for the above system is to be studied in order to get the load-rut depth relationship. Once the load-rut depth curve is obtained, the bearing capacity under permissible rut depth of this system can be evaluated, or for a given load, the geogrid with suitable tensile strength and stiffness is easily selected for the structure; or an appropriate thickness of the fill is determined for a supplied geogrid.

The similar idea mentioned above has been discussed under plain strain conditions in another paper (Hu, 1996a). So, the analysis presented herein is to be focused on axis symmetrical problem, taking into account the model test results (Hu, 1996b), which will be introduced briefly in the following sections.

BRIEF DESCRIPTION OF MODEL TESTS

Hoping to provide some further data concerning the behavior of unpaved road with a geogrid inclusion, the author has carried out a series of model tests under plane conditions with a 0.2 m wide footing on a 0.09 m thick layer of gravel fill over a 0.4 m thick stratum of soft clay with or without a geogrid at the gravel-clay interface.

Details of the apparatus and the test procedures have been given by Hu (1996b). Briefly, the tests were carried out in a rigid box of internal length 0.8 m, width 0.26 m, and depth 0.6 m. On the back of the front wall, which was made of Plexiglas and stiffened by two angle bars, a coordinate system was engraved slightly. The subsoil, which was reconstituted clay, with basic properties presented in Table 1, was compacted in three layers. On the surface of every layer, small markers, which were the sharp-end parts of pins, were embedded close to the Plexiglas. A plastic grid produced by Netlon Ltd. Was used with a mass per unit area of 660 g/m², and tensile strength of 5.4 kN/m at 10% strain. The material of the fill layer was a crushed stone with an average grain diameter of 20 mm, and unit weight of 21.0 kN/m³.

Table 1. Properties of clay used in tests

Property	Value
Plastic limit, w_p /%	19.7
Liquid limit, w_L /%	31.2
Water content, w /%	31.0
Unit weight, γ /kN/m ³	18.9
Apparent cohesion, c_v /kPa	5.0
Apparent angle of internal friction, ϕ_w °	2.5

The footing load applied by a lever in increment of 11.3 kPa, and the resulting footing displacement measured by two dial gauges, placed at opposite corners of the footing. When the displacement varied less than 0.05 mm per hour at one level of pressure, another increment was added. The process is repeated for several increments of load until the footing displacement exceeded 60 mm or failure occurred in the subsoil. Before every incremental load was applied, the positions of the small markers mentioned above were recorded by means of the coordinate system on the Plexiglas and a coordinate microscope with 0.01 mm sensitivity. Thus the displacement field of the subsoil can be obtained. Such a displacement tracing method was first brought into use in laboratory by Liu et al. (1989).

In order to determine the load-spread angle in the gravel fill, the shape of the geogrid after tests was examined after removing the gravel fill.

The displacement fields with and without geogrid and the footing pressure-rut depth curves for reinforced and unreinforced systems were given in detail in another paper (Hu 1996b). The test results confirmed the following effects of the geogrid-reinforcement: (1) load-spreading effect; (2) tensioned-membrane support; and (3) lateral restraint. It was found that the lateral restraint effect was so strong to lead the subsoil vertically below the footing nearly no lateral moving. That is to say the subsoil is confined by the geogrid. In addition, the load-spread angle of the gravel fill, found in the experiment, is about 38°.

THEORETICAL ANALYSIS

Based on the above test results, a model, shown in Figure 1, for an aggregate-geogrid-soft subgrade system is suggested here, in which the load-spreading effect and the tensioned-membrane support are included after Giroud and Noiray's approach (Giroud & Noiray 1981), and the lateral restraint of the subgrade is taken into account by assuming the subgrade soil vertically below the wheel-road contacting area is in confined conditions. In the model, the wheel load is assumed a uniform circular pressure. From the model showing in Figure 1, we get the following relationships.

$$D = d + 2H \tan \theta \tag{1}$$

$$p_s = p \left(\frac{d}{D} \right)^2 + \gamma_0 H - \frac{4T \cos \beta}{D} \tag{2}$$

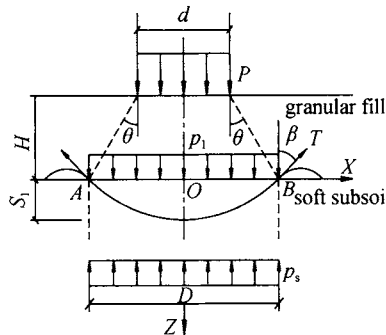


Figure 1. model for the reinforced road

In Figure 1, p = contact pressure between wheel and aggregate layer, which is approximately equal to the internal pressure of the wheel; d = diameter of wheel-ground contacting area; p_1 = pressure on geogrid-reinforcement layer; p_s = contact pressure between geogrid-reinforcement layer and subgrade; θ = load-spread angle in aggregate layer; and T = tension force in geogrid.

The shape of the deformed geogrid is assumed to represent portions of parabolas connected at A and B according to the model test results noted above (see Figure 1), and it has the following equation

$$Z = -\frac{4S_1}{D^2}x^2 + S_1 \quad (3)$$

T is calculated by the following equation:

$$T = E_g \varepsilon_g \quad (4)$$

where ε_g is the geogrid strain; and E_g is the geogrid modulus.

According to Eq. (3), ε_g and $\cos \beta$ are respectively expressed as follows:

$$\varepsilon_g = \frac{1}{2} \sqrt{1+m^2} + \frac{1}{2m} \ln(m + \sqrt{1+m^2}) - 1 \quad (5)$$

$$\cos \beta = \frac{1}{\sqrt{1+m^2}} \quad (6)$$

$$m = \frac{4S_1}{D} \quad (7)$$

where γ_0 = aggregate unit weight.

In Eq. (2), $4T \cos \beta / D$ is the upward force provided by geogrid (Bai 1994).

The additional vertical stress induce in the subgrade soil due to p_s is derived from Boussinesq solution. And the relationship between p_s and S_1 is determined by the uniaxial compression assumption. Therefore, the following equations are obtained.

$$\sigma_z = p_s \left[1 + \frac{8}{3} \left(\frac{Z}{D} \right)^2 \right]^{-1} \quad (8)$$

$$S_1 = \frac{1}{E_s} \int_0^{z_0} \sigma_z dz \quad (9)$$

or

$$S_1 = \sqrt{\frac{3}{8}} \frac{D}{E_s} \arctan \left(\sqrt{\frac{8}{3}} \frac{z_0}{D} \right) p_s \quad (10)$$

where σ_z = additional vertical stress due to p_s at the depth of Z below the center of the area of p_s ; E_s = mean constrained modulus of subsoil; Z_0 = settlement calculation depth, which is calculated from the following equation by assuming it is approximately equal to the depth in subgrade affected by wheel load P .

$$z_0 = \sqrt[3]{\frac{0.5nP}{\gamma}} \quad (11)$$

where $n = 5 \sim 10$; γ = unit weight of subsoil. Generally, $P = 100$ kN; $\gamma = 18$ kN/m³; $n = 10$ for soft subsoil, so Z_0 is commonly about 3 m.

Eq. (10) is based on the assumption that the subgrade soil is in confined conditions. But this assumption is a little different to the observation in model tests (Hu 1996b). According to Hu (1996a), Eq. (10) is modified as

$$S_1 = \psi \sqrt{\frac{3}{8}} \frac{D}{E_s} \arctan \left(\sqrt{\frac{8}{3}} \frac{Z_0}{D} \right) p, \quad (12)$$

where ψ is a coefficient related to the constrained modulus of the subgrade soil. For soft subsoil, $\psi = 1.2$ (Hu 1996a).

In order to find out the relationship between the surface rut depth, S , and the soft ground deflection, S_1 (see Figure. 1), an assumption, showing in Figure. 2, is proposed here that V , which is the volume of the pit in the fill surface induced by the wheel pressure, p , is equal to V_1 , which is the volume of pit in the soft ground surface. The shape of V is taken as cylinder with diameter d , and V_1 as a space formed by spinning parabola AB (see Figure 1). Then the following equation is derived.

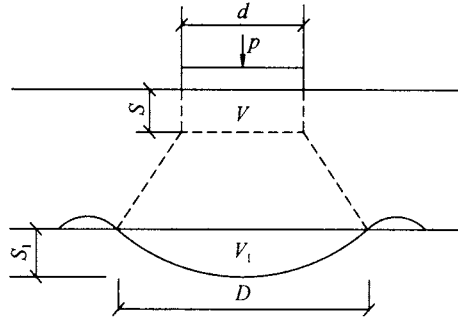


Figure 2. model for relationship of S and S1

$$S_1 = 2 \left(\frac{d}{D} \right)^2 S \quad (13)$$

Combining Eqs. (2), (12) and (13), the following relationship is given

$$p = 4 \sqrt{\frac{2}{3}} \frac{E_s \cdot S}{\psi D \arctan \left(\sqrt{\frac{8}{3}} \frac{z_0}{D} \right)} - \gamma_0 H \left(\frac{D}{d} \right)^2 + \frac{4DT \cos \beta}{d^2} \quad (14)$$

For a given unpaved road on soft ground with geogrid reinforcement as described in this paper, the volume of H , γ_0 , E_s in Eq. (14) and E_g in Eq. (4) are known, d is determined by the wheel load P and the internal pressure of the wheel, p . Therefore, when the surface rut depth S is certain, S_1 and D can be deduced from Eq. (1) and Eq. (13). Then m is calculated by Eq. (7), $\cos \beta$ is determined by Eq. (6), and T is derived from Eq. (5) and Eq. (4). At last, the volume of p corresponding to the given S is obtained. According to such a procedure, the p - S curve is determined. On the other hand, if the thickness of the granular fill, H , is given, the corresponding permissible minimum of the geogrid modulus, E_{gmin} , can be determined by the equations presented in this paper.

CONCLUSION

For an unpaved road on soft ground with geogrid reinforcement, how to calculate rut depth induced by wheel load is a key issue. The method presented in this paper is an answer of the problem. When the permissible surface rut depth is given, the corresponding thickness of

granular fill can be determined by the method if a certain geogrid is applied. On the other hand, while the thickness of granular fill is set, a geogrid with proper tensile modulus can be selected using the method noted here.

REFERENCES

- Bai Bing (1994). Bearing capacity of soft subgrade soil reinforced with geotextile under three dimensional conditions. . *East China Highway*, 6: 54-57.
- Fammin R. J., Sigurdsson O. (1996). Field observations on stabilization of unpaved roads with geosynthetics. *J. Geotech. Engrg., ASCE*, 122(7): 544-553.
- Giroud J. P., Noiray L. (1981). Geotextile-reinforced unpaved road design. *J. Geotech. Engrg, ASCE* , 107(9): 1233-54.
- Giroud J. P., Hna, J. (2004). Design method for geogrid-reinforced unpaved roads. I. Development of design method. *J. Geotechnical and Geoenvironmental Engineering*, 130 (8) 775-786.
- Hausman M. R. (1987). Geotextiles for unpaved roads—A review of design procedures. *Geotextiles and Geomembranes*, (5): 201-233.
- Hu Youchang (1996a). Bearing capacity of geogrid-reinforced subgrade soils. *Soil Engineering and Foundation*, 10 (3): 14-18.
- Hu Youchang (1996b). Experimental study on highway soft ground treatment with geogrid. *Rock and Soil Mechanics*, 17 (2): 76-80.
- Liu Zude, Z. Wang and H. Xia (1989). Application of displacement tracing method with microscope in model tests of soil engineering. *Chinese Journal of Geotechnical Engineering*, 11 (3): 7-10.
- Love J. P., Burd H. J. Milligan G.W.E. and Houlsby G. T. (1987). Analytical and model studies of reinforcement of a layer of granular fill on a soft clay subgrade. *Canadian Geotechnical Journal*, (24): 611-622.
- Wang Tao, Wang Zhao (2003). Model of geosynthetics reinforced pavements based on membrane effect. *Chinese Journal of Geotechnical Engineering*, 25 (4): 706-709.

RESEARCH ON THE CHARACTERISTICS OF THE SUBSIDENCE OF SOFT SOIL FOUNDATION IN YANGTZE RIVER DELTA AREA BASED ON ORIGINAL POSITION MONITOR

Chenguang Jiang

*College of Civil Engineering, Jiangnan University, Lihu Dadao 1800,
Wuxi 214122, China*

Yong He

*Construction Management Office, Qingdao Agricultural University, Chengyang
Qingdao 266109, China*

The sedimentation of soft-soil road of speedways directly influences the project quality. To scientifically calculate the velocity of fill placement, the completion time of pre-loading and pavement time of road surface, can effectively control the sedimentation during the construction of road surface and sedimentation after the construction, save investment on projects and enhance the utility quality of roads. While, the accurate calculation of fill replacement velocity, completion time of pre-loading and pavement time of road surface, must depend on reliable in situ motoring data and rational calculation method. Taking plenty of in situ motoring data of the speedways in the Yangtze River Delta area as the basis, we preliminarily sum up the statistic form of rules of soft-soil roadbed sedimentation in the Yangtze River Delta area.

INTRODUCTION

Soft clays, the glutinous soil sediment or river wash of sea facies, lagoon facies, delta facies, drowned-valley facies and limnic facies which are formed in the late quaternary, belongs to sediment of modern era among which the silts and silt earth are the flabbiest. It is the characteristics of soft soil that it has high moisture, high void ratio, low intensity, weak water permeability, low bearing capacity, low shear strength, high compressibility and high sensitiveness. Under the effect of load, the soft-soil groundwork's sedimentation deformation is great; its asymmetrical sedimentation is great; it takes longer time for the stabilization of sedimentation; and the dis-stability accidents occur easily (Asaoka A. 1978).

Stabilization and sedimentation are the leading two restriction elements in the process of construction of speedways in soft-soil areas. Regarding the construction of speedways in soft-soil areas, the high filled road dyke on thick soft roadbeds is usually adopted, and when the project is completed, there are strict requirements on sedimentation. If there is a tight time limit for the construction of speedways, due to increase of expected pre-loading time and comparatively shortening of fill replacement time, the stability of roadbed is definitely exerted stricter requirements on.

MOTORING METHOD OF SOFT-SOIL ROADBED SEDIMENTATION

The observation result of sedimentation is gained through setting boundary line points, setting sedimentation boards underground and setting inclinometer casings. The boundary line points which should be determined in accordance with the conditions of groundwork and road embankment, are generally set at the road embankment section where the filling is relatively higher, including the two ends of filling section of soft-soil groundwork and structure objects. The points collocated should be parallel with midline; the position of points should reflect the sedimentation characteristics of this section; and generally, the boundary line points should be set symmetrically along the two sides of roadbed. The sedimentation boards are generally buried along the two sides of boundary, with their pedestals buried in the sand cushion, should be buried after the silt clearance and should be observed for the first time. Observation points of layered sedimentation should be set in the soils of different layers, following the direction of plumb line, with the number of points and depth determined according to distribution condition of delamination. In principle, a point is set in each layer of soil, with the lowest point set under the base and the deepest point exceeding the theoretical thickness of compressed layer or on the gravel or rock layers which are of low compressibility. The layered sedimentation instrument is made up of layered sedimentation tubes, magnetic rings, corrugation tubes and sedimentation instrument. Make holes in the middle of roadbed to the bearing layer, and install magnetic rings at corresponding depth according to geological condition; after descending the sedimentation tubes, seal holes with expansive soils to enable magnetic rings and stratum to make synchronous sedimentation; and use layered sedimentation instrument to measure the positions of each magnetic ring and calculate the sedimentation quantity of each layer respectively.

EXPERIENCE FORMULA OF FINAL SEDIMENTATION QUANTITY OF SOFT-SOIL ROADBED IN THE YANGTZE RIVER DELTA AREA

By use of computers, through the analysis of a large number of motoring data of about 20 roads in the Yangtze River Delta area, the writer, together with the scientific research team, has made preliminary sum-up of the experience formula of final sedimentation quantity of soft-soil roadbed in the Yangtze River Delta area, that is

$$h=A \times W \times \ln (e+t \times 10^{-3}) \times \ln [(D_1 \times \rho_1) / (D_2 \times \rho_2)]+B \quad (1)$$

In formula (1), W refers to the average content of stratum clay which is between roadbed and the hard rock underground with W less than 1; e refers to the base of natural logarithm; t refers to the time after the completion of road construction with the unit of year; D_1 refers to the stratum thickness between the roadbed and hard rock underground, with the unit of m; ρ_1 refers to the weighted average dry density of stratum rock between roadbed and hard rock underground, with the unit of kN/m^3 ; D_2 refers to the thickness between roadbed and road surface, with the unit of m; ρ_2 refers to the weighted average dry density of stack carrier which is between roadbed and road surface, with the unit of kN/m^3 . A and B refer to experience coefficients. The simulation result of data from field tests done by the writer and scientific research team who has studied about 20 roads for more than ten years, show that the

fluctuation range of A is between 0.1673 and 0.1711 while the fluctuation range of B is between -0.0006 and 0.0030; generally, $A=0.1692$ and $B=0.0012$.

DEMONSTRATIONS

Ring-road of Tai Lake of Wuxi locates on the alluvial lake plain, the underground of which is extensively accumulated with the forth loose sediment soils which mainly include glutinous soils, powder soils and fine powder sands, with the total thickness of 100-190m and the total thickness at the motoring spot exceeding 80m.

For the purpose of scientific research, it is necessary to prospect for the roadbeds, making drilling to fetch soils with machines as the central tasks and combining static cone survey. In the process of drilling with machines, soil samples are fetched to make soil tests and standard penetration tests within the holes. The drilling on the spot is conducted with four G-1A type drilling machines, making omegatron whorl drilling as the main drilling approach, with diameter of opening holes of 135mm and the diameter of bores of 110mm. In order to guarantee the quality of fetched soils and meet the requirement of standard penetration test, all the holes are filled with the upside separated by bushings and the drilling is conducted with slop protecting the wall. The soil catcher of take-up double-prick movable valve is adopted to fetch soil sample of the original state, using the method of impact sampling with soil catcher or static press method. The soil samples are sealed on the spot and delivered to the lab. The standard penetration test adopts the liberal weight drop which is automatically unhooked. Fifteen cm after the penetrator is stroked into the earth, the number of strikes of each 10cm that is stroked into the earth is recorded, and the number of hammer strike that is used to strike 30cm into the earth accumulatively is called the standard penetration strike number. The recorder is responsible for the differentiation, compilation and record of the drilling core, and responsible for the records of samples and the strike number of standard penetration test. The single bridge probe, adopted in the static cone survey, and penetrates continuously. After an interval of 10cm, the data is measured and read. The single bridge static cone survey adopts JC-H1 type of measurement instrument for static cone survey to record data, make tests on moisture, specific gravity and thickness to sample tests and conduct grain assaying to powder soil and sand soil. In order to acquire the mechanics index, concretion tests, direct shear tests and the unconsolidated-undrained triaxial shear tests are carried on.

The surrounding stratum of the ring-road of Tai Lake belongs to south of Yangtze stratum area, Xiushui-Qiantang River sub-area and Suzhou-Changxing community, and its bedrocks mainly show themselves in southern mountain areas. From old to new, there are stratums belonging to Palaeozoic era's Silurian period, Carboniferous period and Permian, Mesozoic's Triassic and Cretaceous, and Cenozoic's Tertiary and Quaternary. Except the stratum of Devonian that shows itself on the earth's surface and forms mountains, others all lie concealed under the stratum of the Quaternary.

The reconnaissance result shows that within the survey depth, the stratums are all alluvium of the Quaternary, belonging to the alleviation of middle and lower reaches of the Yangtze River. Within the maximum revealment depth of 20.5 meters, there are totally six layers of soil layer from top to the bottom, among which the ②、③、⑥ layers are divided into two

sub-layers respectively. The character description of each rock and soil layer as well as the project characteristics are remarked as follows:

① Surface soil layer, brown and gray, is made up of rubbles and gravels on the top and gray and lark cohesive plain backfill in the bottom in the sections of villages, factories and roads; and it is the cultivation soil in the section of farmland. This soil layer, the thickness of which is generally 0.7-2.5m, is loose and of bad equality.

②-1 is powder claypan, and partially is clay, taking on the color of lark. It is in the state of plasticizing and stiff-plastic, contains iron-manganese nodules and green and grey kaolin streaks and has not shaking and rocking reaction. It is sheeny, of high dry intensity and of high tenacity. The powder claypan, whose layer thickness is generally 4.1-4.6m, distributes partly. It belongs to the medium compactable soil and has good project characteristics.

②-2 is powder claypan, and partially is clay, taking on the color of lark. It is in the state of plasticizing and stiff-plastic, contains iron-manganese nodules and green and grey kaolin streaks and has not shaking and rocking reaction. It is sheeny, of high dry intensity and of high tenacity. The powder claypan, whose layer thickness is generally 3.2-5.8m, is of no distribution at part of places. It belongs to the medium compactable soil and has good project characteristics.

③-1 is the powder soil layer, taking on the color of lark. It is in the slightly dense and mediumly dense state, containing a few glutinous soils, and is quite wet. It is of bedding structure, has rapid shaking and rocking reaction, has no sheen, is of low dry intensity and is of low tenacity. The powder soil layer, whose thickness is 0.0-3.6m, distributes at part of places. It belongs to medium compactable soil and has ecumenic project characteristics.

③-2 is powder clay containing powder soil, taking on the color of filemot-taupe with the bottom turning gray. It is mainly of plasticizing state and has bedding structure. Part of the bottom of this layer is mainly of powder soil. It has medium shaking and rocking reaction, slightly sheen, of medium dry intensity and of medium tenacity. This layer of soil, whose thickness is generally 0.0-5.2m, spreads in the full field. It belongs to medium compactable soil and has ecumenic project characteristics.

④ is powder clay layer of soil, gray, taking on the state of soft plastic—flowing plastic, containing a few lamina of powder soils. It is of slightly bedding structure, of no shaking and rocking reaction, of slightly sheen, of medium dry intensity and of medium tenacity. This layer of soil, whose thickness is 0.0-2.5m, spreads in the full field. It belongs to medium and slightly high compactable soil and has relatively bad project characteristics.

⑤ is powder soil layer, gray, taking on the state of slightly dense—mediumly dense, containing a small quantity of glutinous soils in the bottom, quite wet. It is of bedding structure, of rapid shaking and rocking reaction, of no sheen reaction, of low dry intensity and low tenacity. This layer of soil, whose thickness is generally 4.8m, spreads in the full field. It belongs to medium and slightly low compactable soil and has ecumenic project characteristics.

⑥-1 is powder clay layer, taking on the color of dark ashy green and gradually turning into yellow green. It is in the state of plasticizing—soft plastic, with slightly worse state on the top. It is of no shaking and rocking reaction, sheeny, of high dry intensity and medium

tenacity. This layer of soil, whose thickness is 0.0–1.8m, distributes at part of places. It belongs to medium compactable soil and has ecumenic project characteristics.

⑥-2 is powder clay layer of soil and part of this layer is clay, taking on the color of dark ashy green and gradually turning into yellow green and then into ashy yellow. It is in the state of plasticizing–hard plastic, of no shaking and rocking reaction, of sheen, of high dry intensity and high tenacity. In the process of this reconnaissance, this layer hasn't been fully penetrated. It belongs to medium and slightly low compactable soil and has good project characteristics.

According to reconnaissance result, comprehensively analyzing soil layer condition within the field and regional geological materials, we find out that the thickness of the coverage layer within the field is more than 50m, and the type of soil within the field is medium soft soil. According to wave velocity test result, the sort of the field is determined as the III grade.

According to the drilling exposure, it is estimated that within 20 meters of prospecting depth of the field, the main layers that contain water include surface soil on the top of ① layer which belongs to backwater–phreatic water type, powder soil on the middle and top of ③-1 layer which belongs to feeble confined water, powder clay containing powder soil of the ③-2 layer and powder soil of the ⑤ layer.

The type of ground water in the shallow part of the field belongs to phreatic water. In the process of reconnaissance, it is measured that the comparatively stable ground water in every holes is generally 0.60–1.40m apart from the earth's surface and the Yellow Sea Datum is 1.65–2.50 meters.

Around the field, bad geological effects such as new active rupture structure and terra cracks haven't been discovered yet. According to regional geological materials and geological materials of surrounding projects, there are not bad geological phenomenons such as new active rupture structures and terra cracks and son on in the surrounding area of ring-road of the Tai Lake. And there are also not possible liquefacient soil layers within the field. The seismic fortification intensity of Wuxi areas is six degrees. According to historical records, earthquakes that are over five magnitude have never happened within the range of forty kilometers in recent one hundred odd years. Therefore, this field is stable.

As for the place that is thirty five kilometers apart from ring-road of the Tai Lake, the relevant calculation parameter is $A=0.1692$, $W=63\%=0.63$, $t=1.8$ years, $D_1=97$ m, $\rho_1=16.31$ kN/m³, $D_2=3.6$ m, $\rho_2=23.46$ kN/m³, $B=0.0012$. According to formula (1), we can get the result is that $h=0.3138$ m.. the actual total sedimentation quantity is 0.3206m.

Through plenty of checking computations to actual motoring data, we draw out the conclusion, that is, the average relative error of the experience formula of final sedimentation quantity of soft-soil roadbed in Yangtze River Delta area given by this article is 10.2%, and its maximum relative error is 17.3%.

CONCLUSION

To scientifically estimate the final sedimentation quantity of soft-soil roadbed plays an important role in the scientific and reasonable design of roads. Due to the limit of ability, experiment conditions and experiment data, the given experience formula of final

sedimentation quantity of soft-soil roadbed in Yangtze River Delta area may have lots of objections and deficiencies. So we hope that the project practices of mass counterparts can make it perfected.

As for the relatively serious problems of deformation and instability of soft-soil roadbed, it is suggested that measures such as increasing pre-loading time, increasing drainage consolidation ratio of roadbed soils (such as drilling sand wells, setting drainage boards and vacuumizing in the roadbeds), using complex groundwork with pillars, adopting temporary transitional road surfaces and reserve sedimentation quantity and so on to improve the construction quality of roads.

ACKNOWLEDGMENT

The research project discussed in this paper has been funded by the National Natural Science Fund of China (No.79160173) and Jiangnan University 211 Construction Fund (No.2004012) . Sincere gratitude is presented to them.

REFERENCES

- Asaoka A. (1978). Observational procedure of settlement prediction. *Soils and Foundations*, 18(4): 30-34.
- Hehai University (2001). The Expressway Co Ltd. of Jiangsu. *The soft clay project handbook of the traffic construction*. Published by China Communications Press.

BREAKAGE MITIGATION METHOD FOR CULVERTS UNDER HIGH EMBANKMENTS USING EPS GEOFOAM

Fenglin Jiang, Anquan Gu

*Highway school, Chang'an university, 120 Two ring Road
Xi'an 710064, China*

Many culverts under high embankments were destroyed for the high earth pressure, one effective method is reducing the load on culvert. To reduce high earth pressure and play the role of shear strength of soil, flexible material EPS (Expanded polystyrene) geofoam slab was placed on the top and sides of culvert. Results of get from site test indicate that EPS has great effect in reducing vertical and lateral pressure on culvert. The minimum pressure after load reduction only take on 30 percent of soil column weight on the top and 10 percent at the lateral. EPS also can decrease uneven longitudinal settlement of culverts. The results obtained by FEM proved the test results in situ. Using the reduced earth pressure to redesign the culvert can reduce the size of the culvert, avoid destroy of culvert and save the construction cost efficiently.

INTRODUCING

Culverts are special structure under highway embankment to drainage water or take as channels which will be set 1 to 3 in plain or 3 to 5 in mountain every kilometer under road and will be take on about 20.6 percent total cost of one road. For high embankment culverts are very common in maintain area in west china, some culvers on which the height of embankment even over 60 meter. These high fill soil produce high load acting on culverts, it's very difficult to estimate the value of earth pressure, the results that conclude from different theory formula sometimes is twice than another, so the structure strength of high fill culverts are different with different theory. Many culverts are designed by underestimate load and result in failure (Gu Anquan, 1960), some culverts adopted over stiffness to burden the high earth pressure lead to waste. Reducing earth pressure on the culvert is effective method to in the high embankment construction; it can reduce the load greatly and make the culvert more safety. EPS geofoam is an ideal material for reducing the earth pressure, after putting EPS geofoam on the top and sides of culvert, for the high flexible property of EPS geofoam, the integral rigid consisted of EPS and culvert is lower than the soil on the sides of soil, positive arching (Vaslestad, et al., 1993), earth pressure can be reduced greatly. The test in situ identified that the effects of load reduction are perfectly (Gu Anquan, 2005).

EPS MECHANICAL PROPERTIES

EPS geofoam has low densities ($10\text{--}40\text{kg/m}^3$) and large compress deformation ability.

Typical EPS geofoam with density of 30 kg/m^3 stress-strain curve (confined compress test) is shown in Figure 1. Obviously, the stress-strain curve has three stages which include elastic, plastic and harden stage. Initially, the curve obey Hook's law, the stress is proportional to the stain. The elastic limit is reached at 0.02–0.06. With the strain increase over the elastic limit, the curve become calmly, less increment of stress can crease large strain, this plastic stage of EPS is hoped to reduce the high earth pressure on culvert. After the strain arrive 0.6, then the EPS get into strength harden stage, the stress and strain relationship is converse with the plastic stage, great changes of stress bring little strain increment.

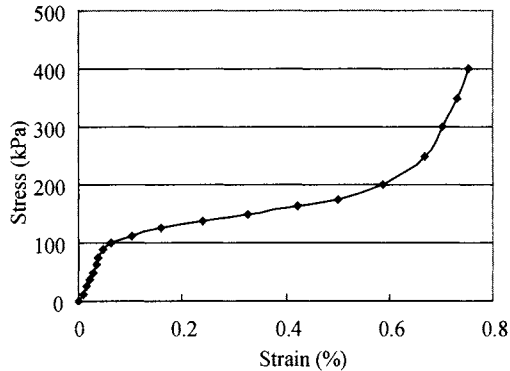


Figure 1. Stress-strain curve of EPS geofoam

EPS is an ideal material for its special stress-stain properties. In culvert construction, when fill soil height are low (generally under 5 meters), EPS geofoam has enough strength to burden the earth pressure and construction loads. With the increasing of load, the large deformation of EPS makes soil produce negative shear stress to minimize the pressure.

TEST SITE DESCRIPTION

Test site lie in north of Shannxi, a highway embankment culvert, the fill soil total height was 17.4 meters on the top of culvert and the density of EPS adopted 30 kg/m^3 . The culvert's base laid on a silt layer which depth about 5 meters and was treated by gravel piles. In this test, there were total six test sections, among these sections, four of them putted EPS on the top and lateral of culvert to reduce the load; two of those sections did not put any EPS. More details about test sections, culvert, EPS and test apparatus see the Figure 2.

The pressure on the top, lateral and bottom of culvert measured from the earth pressure cells. The deformations of EPS got form the deformation sticks which were made from a steel bar and steel plate. The settlement sticks can measure the different settlement of culvert compare with side soil in the same level. The settlement along the longitudinal of culvert also obtained.

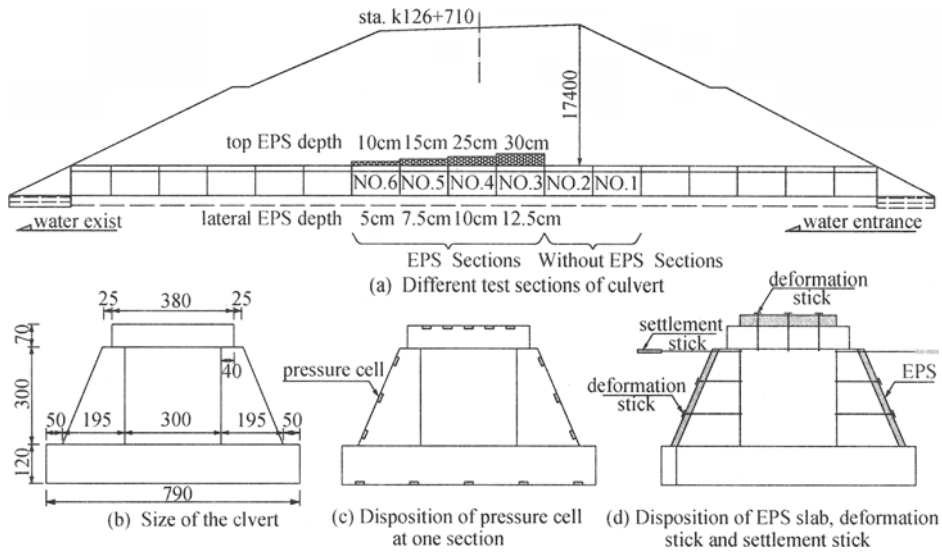


Figure 2. EPS and apparatus disposition in site test(unit: mm)

TEST RESULTS

Vertical pressure and deformation of EPS

The results of vertical pressure (Figure 3) indicate that EPS can obviously reduce vertical pressure, the thicker EPS can get small earth pressure. When the soil heights arrive 17.4 meters, in test section 6 with 30cm EPS thickness, the minimum vertical pressure after reduction only take on about 30 percent soil column weight. The effects of earth pressure

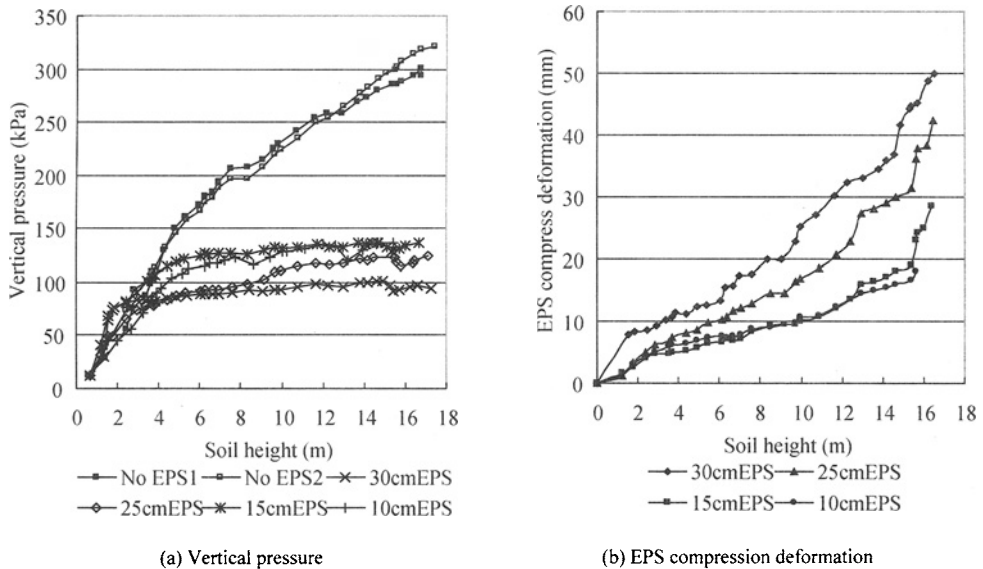


Figure 3. Vertical pressure and EPS compress with the height of soil

reduction are relative with compressible deformation of EPS geofoam, positive soil arching depend on the deformation of EPS geofoam. Judging from the curve of vertical pressure with the fill soil height relationship, the thickness of EPS has a critical value, the thickness of EPS below the value can get more effect of reduction. The results as obtained from FEM.

Lateral pressure and deformation of EPS

Lateral pressure and deformation of EPS see in Figure 4 putting EPS on the sides of culvert can reduce lateral earth pressure as earth pressure reduction on the top, the minimum lateral pressure after reduction only take on about 10 percent soil column weight.. Not all the lateral pressure need to be reduce, in the low pressure level, the lateral wall of culvert are easy to be designed and constructed, only vertical earth pressure reduction is necessary. For high lateral earth pressure, placing EPS on the sides to reduce earth pressure can be done.

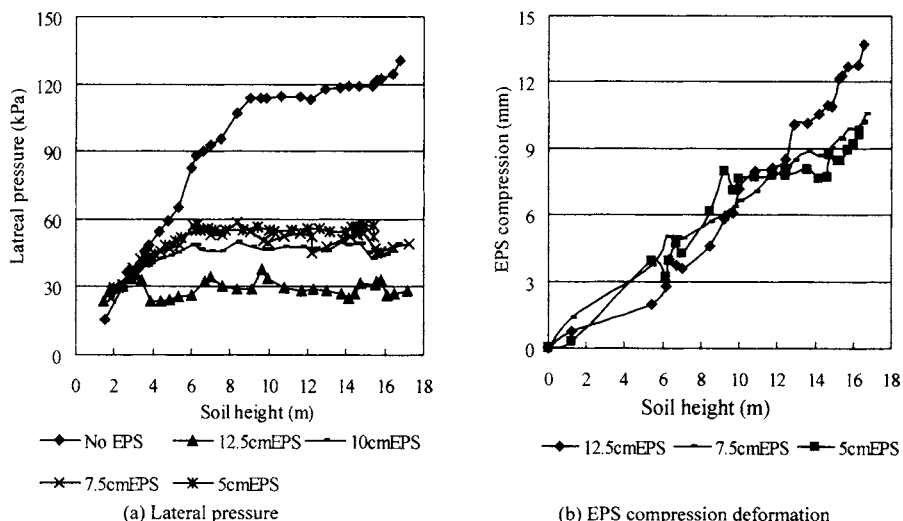


Figure 4. Lateral pressure and EPS compress with the height of soil

Settlement of culvert along longitude

Figure 5 show that the settlement decreased in load reduction test zone compare with the area that without EPS . For the EPS zone is very short, so the effects for minimizing the settlement are not so obviously. While all the top of culvert covered by EPS, the settlement can decrease sharply. EPS can not only make the pressure down but also can decrease the different settlement along the longitude of culvert. So the destroy about strength and settlement of culvert can be solve by EPS load reduction.

FEM ANALYSIS

A FEM analysis was done using finite computer program Ansys to investigate the pressure changes due to the different material parameters. As the model was symmetry problem, two dimensional and half space were used (Sun, 2005). Part of the FEM model after meshed as

Figure 6. The fill soil was modeled as cohesive material using elasto-plastic constitutive model that corresponds to the Mohr-Coulomb failure criterion. EPS was modeled as a multi-linear elastic material. Others material like concrete and bedrock were modeled as liner-elastic model. The specific material properties are list in the Table 1.

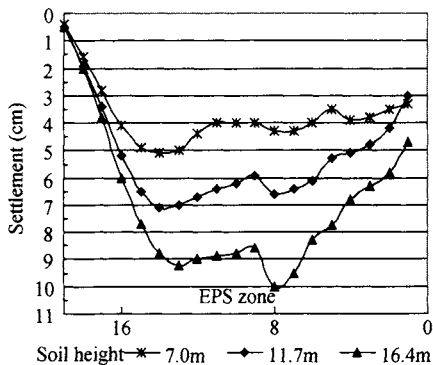


Figure 5. Settlement along longitudinal culvert

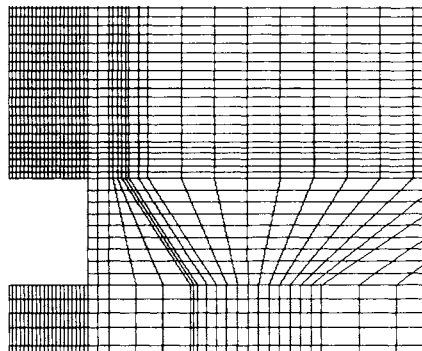


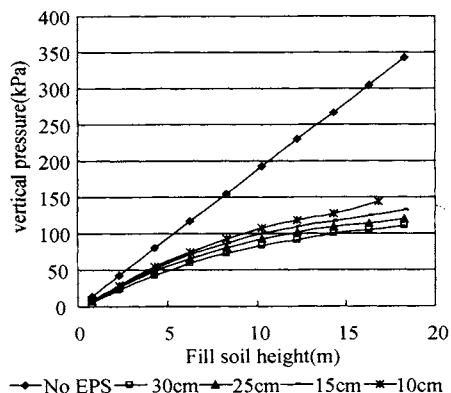
Figure 6. Part of FEM model mesh

Table 1. material properties

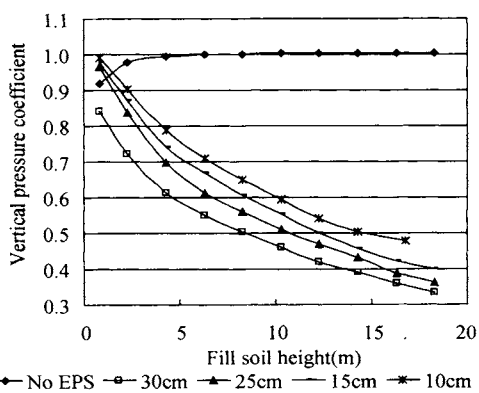
Material	Elastic modulus $E(\text{MPa})$	Poisson's ration ν	Mass density (kg/m^3)	Cohesion (kPa)	Fraction angle ϕ
EPS	1.65	0.05	0.03	-	-
Concrete	30000	0.2	25	-	-
Fill soil	12.5	0.35	19	17	26
Bedrock	50	0.3	21	-	-

Pressure on culvert with different thickness of EPS

Load reduction results by FEM show as Figure 7 and Figure 8, the pressure and pressure coefficient curve get from FEM are the same as test in situ, putting EPS on top and lateral culvert reduce earth pressure also.



(a) Vertical earth pressure



(b) Vertical earth pressure coefficient

Figure 7. Vertical pressure on culvert with different thickness of EPS

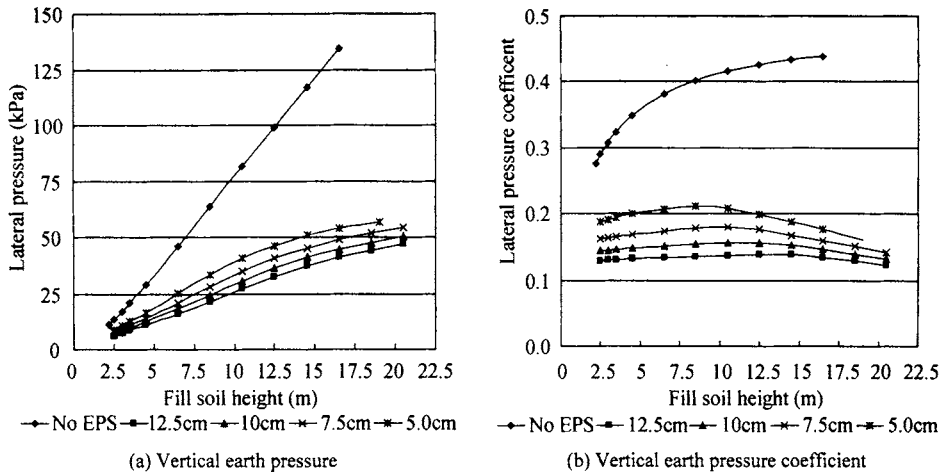


Figure 8. Lateral pressure on culvert with different thickness of EPS

CONCLUSIONS

Placing EPS on top and lateral culvert can greatly decrease earth pressure on culvert, the more thickness of EPS the more pressure were reduction, but the thickness of EPS has a critical value, the thickness of EPS below the value can get more effect of reduction. The results as obtained from FEM.

The minimum load after reduction only take on 30 percent of soil column weight on the top and 10 percent at the lateral. EPS also can decrease uneven longitudinal settlement of culverts. The results obtained by FEM proved the test results in situ.

Load reduction on culvert make the high fill embankment possible, Using the reduced earth pressure to redesign the culvert can reduce the size of the culvert, avoid destroy of culvert and save the construction cost efficiently.

REFERENCES

- Gu Anquan. (1963). *Earth pressure study of culvert under embankment*, shannxi institute university master paper.
- Gu Anquan. (2005). Experimental study on reducing-load measurement using EPS of culvert under high-stacked soil. *Chinese Journal of Geotechnical Engineering*. 27 (5): 500-504.
- Sun L., Hopkins, T. C. and Beckham T. (2005). Stress Reduction by Ultra-Lightweight Geofom for High Fill Culvert: Numerical Analysis. *The Proceedings of the 13th Annual Great Lakes Geotechnical and Geoenvironmental Engineering Conference (GLGGC)*, Milwaukee, Wisconsin, May 13
- Vaslestad J., Johansen T. H. and Holm W. (1993). Load reduction on rigid culverts beneath high fills. *Transportation research record*, 1415

REHABILITATION OF THE TOWER OF PISA, MY METHODS

Wuyi Jiao

Chang'an University, Xi'an 710061, China

The rehabilitation works for the Leaning Tower of Pisa was completed in 2001. Two of my suggestions were adopted. The first is the use of counterweight to prevent the leaning from developing further. The second is to use the anchor bolt and low-pressure grouting to strengthen the structure. A method to compute the settlements and tilts of the Tower in the past 800 years is also proposed. A few errors in the published work on the Leaning Tower of Pisa are pointed out in this paper.

TO PUT FORWARD THE COUNTERWEIGHT

Professor Jerry (transliteration) from Pisa University appealed for saving the Leaning Tower of Pisa to all the world in 1980. He said that “recently, a terrifying report was published: the Leaning Tower of Pisa might disappear at the beginning the 21th century. Is it not a responsibility of the 20th of preservation of the Leaning Tower of Pisa? If we lose the Tower, there would not be Pisa again” (Shimbun 1980).

The sincerely appeal of professor Jerry touched my heart, and then I put forward a conservation method by counterweight on Dec.21, 1980 for the committee to refer to.

THEORETICAL BASIS AND ENGINEERING PRACTICE OF COUNTERWEIGHT

The key to prevent the leaning developing is to calculate the Tower's settlement and its movement accurately, but there is still no data in this respect for the committee up to now, because there is no parameter available that can represent the characteristics of nonlinear deformation of soils accurately. I discovered such a parameter called Chord Modulus, which fills blanks in this science and technology. The computed settlements on 1000 odd buildings and tests are all in conformity with those obtained in the respective practical surveys. According to calculation by Chord Modulus in the year of 1969, a leaning chimney was put right again just by making use of counterweight technique.

The leaning chimney and the Leaning Tower have some characters in common or similar as follows:

- (1) Equal in height above ground: 55m.
- (2) Shallow foundation, depths of embedment being 2.57m and 3.36m respectively.
- (3) The structure is tube-shaped brick or stone masonry.
- (4) During the first stage of construction, the both structures began to tilt and the masons adopted some measures to compensate the lean during latter period of construction. So the shape of the two structures became banana.

(5) There are cracks in facing bricks or stones due to stress concentration.

There are also some differences between them as follows:

- (1) Their total weight is 8.84MN and 144.5MN respectively.
- (2) Their average pressure under foundations is 133.2kPa and 497kPa respectively.
- (3) Their base area of foundations is 66.18m² and 285m² respectively.
- (4) Their tilting at the top is 93.4cm and 526.6 odd cm respectively.

According to the calculation by Chord Modulus, counterweight 1.51 MN was added to the chimney and it returned to vertical rightly. The counterweight was piled in the range of ground near 1/3 circumference. Simultaneously, the foundation was reinforced by reinforce concrete ring; the structure was reinforced by steel strand; and one pulling force cable and two safety cables were added to increase the effect of the counterweight.

Due to the differences as mentioned above, I think that the Leaning Tower of Pisa is unable to put right but its leaning developing can be prevented. This is the aim of my suggestion. So, I posed the suggestion of counterweight and other measures and received the reply from OPA. At the same time, the suggestion was published in an article in 1981 (Jiao, 1981).

REPLY TO MY SUGGESTION FROM THE ITALIAN OFFICIAL QUARTERS

Italian OPERA DELLA PRIMAZIALE PISANA (OPA) and L'operaio Presidente Prof.G.Toniolo replied in Jan 27, 1981: "Your proposal on Dec 21, 1980 has been received and has been delivered to the Committee for Safeguarding the Leaning Tower of Pisa in Italian Public Engineering Department".

DATA OF CALCULATED DEFORMATION MAILED TO M.JAMIOLKOWSKI

Professor Zeng Guoxi visited the Leaning Tower of Pisa and took back 2 papers (Jamiolkowski et al., 1991 and 1993) in 1992, and published them in Chinese. Then, he mailed the original version to me. According to the data in paper (Jamiolkowski et al., 1993), I calculated the pressure under the foundation, settlement and tilts southward in various stages in 1993-1994 respectively. The data is shown in Tables 1 and 2.

Table 1. Calculated pressures under the foundation

Load stage	Year or other condition	Weight (MN)	Moment(MN·m)	Calculated pressure(kPa)		
				south	centre	north
1	0.33Nmax	47.69	0	157.3	157.3	157.3
2	0.65Nmax	93.94	-	319.6	319.6	319.6
3	1178	94.80	-	322.6	322.6	322.6
4	1278	137.28	5.51 ^②	476.4	471.7	467.0
5	1285	137.28	59.88 ^②	522.3	471.7	421.1
6	1360-1370	144.53	97.70 ^②	579.5	497.0	414.5
7	1550	144.53	284.72	737.5	497.0	256.5
8	1758	144.53	293.54	744.9	497.0	249.1
9	1817	144.53	310.16	759.0	497.0	235.0
10	1911	144.53	318.98	766.5	497.0	227.5
11	1990	144.53	332.56	777.9	497.0	216.1

(Continued)

Load stage	Year or other condition	Weight(MN)	Moment(MN·m)	Calculated pressure(kPa)		
				south	centre	north
12	+7MN ^①	151.53	286.73	763.9	521.7	279.5
13	+10MN ^①	154.53	263.82	755.0	532.2	309.4
14	+13MN ^①	157.53	240.90	746.2	542.7	339.2

① The weight includes 1MN concrete ring.

② The moment values are 1/10 of values in paper (Jamiolkowski et al.1993). The values in paper(Jamiolkowski et al.1993) were wrong and had been corrected by M.Jamiolkowski himself after he read my letter.

Table 2. Comparison of the Calculated and Actual Tilts Southward

Load Stage	Year or other condition	Calculated settlement/cm			Calculated tilt (arc degree)		Actual tilt /arc degree
		Southern side	Northern side		1993-1994	2007	
			1993-1994	2007			
1	0.33Nmax	37.05	37.05	37.05	0°00'00"	0°00'00"	0°00'00"
2	0.65Nmax	141.92	141.92	141.92	0°00'00"	0°00'00"	-
3	1178	143.88	143.88	143.88	0°00'00"	0°00'00"	-
4	1278	241.12	237.49	237.49	0°06'22"	0°06'22"	0°06'11"
5	1285	259.01	219.21	219.21	1°09'52"	1°09'52"	1°06'44"
6	1360-1370	287.18	222.72	222.72	1°53'08"	1°53'08"	1°36'39"
7	1550	347.73	156.78	180	5°34'12"	4°53'47"	4°41'07"
8	1758	350.57	152.89	180	5°45'54"	4°58'44"	4°49'50"
9	1817	355.98	144.81	180	6°09'20"	5°08'09"	5°06'11"
10	1911	358.86	140.21	180	6°22'19"	5°13'10"	5°14'46"
11	1990	363.16	132.47	180	6°43'10"	5°20'39"	5°28'09"
12	+7MN ^①	363.46	173.96	181	5°31'41"	5°19'26"	-
13	+10MN ^①	362.47	189.14	181	5°03'32"	5°17'42"	-
14	+13MN ^①	361.54	203.95	181	4°36'06"	5°16'05"	-

I mailed the calculated data, as much as 10 pages, to M.Jamiolkowski in Nov.24, 1993. He replied and enclosed a paper in Dec.30, 1993. In this letter, he inquired about the "postulated effect of counterweight 600t on motion of Pisa Tower". The 600t was defined in paper (Jamiolkowski et al. 1993). Consequently, in addition to the above calculation, I calculated the results of 900t and 1200t again, and mailed the data to him in April 18, 1994. These data were then published in paper (Jiao 1994) and the paper was also mailed to him in 1994. The part about the Leaning Tower of Pisa was then published in paper (Jiao 1995 and 1997). Among these data, I emphasized that the 600t is too small to prevent the leaning from developing and proposed to add to 900-1200t.

The data in Table 2 demonstrates some characteristics, which were found by Burland after 1996 as follows:

About the rising at north side of foundation and the mechanism of counterweight

There are two sets of settlements on north side in Table 2, i.e. 1993-1994 and 2007 columns respectively. The former were calculated in the years of 1993-1994, based on the weight and

moment in Table 1. The latter are calculated at present. Relating to the settlement, there are also two sets of the calculated tilts. The calculated values of 1993-1994 are analyzed firstly. According the history of rigid tilt of the Tower (Jiao 1993), it tilted to northward at first and reached the maximum in 1272. After that the tilt was directed to south, the pressure and settlement under north side reached the maximum in 1278. The tilt difference between the calculated and measured was 11", which shows that the calculation reflected the actual condition. After 1278, both the pressure and settlement in north decreased, which demonstrated that the northern side of foundation rose, the amount of rising are 18.28cm in 1285 and 14.77cm in 1370. The tilt difference between the calculation and measurement is bigger than that in 1278 but still remained close. It manifested that the method considered in this stage accorded with the practice. After this stage, the value difference increased one after another and reached 1°15'01" in 1990. It could not reflect the practical condition, especially for the calculated tilt decreased due to counterweight 6.0MN reached 1°11'29". This case could not happen absolutely. But if without rising after 1278, according the calculated settlement 237.49cm, the calculated tilts are far small compared with the measured. Thus, it can be seen that the rising is a definite fact. But the amount is not the same as the calculation in 1993-1994 and has a limit. The calculation in 1993-1994 did not take the limit into consideration because the following reasons: firstly, to stress the rising; secondly, to express the reasons for tilt occurring and non-stop tilting as well as the mechanism of counterweight more obviously by using of the maximum value of tilt as the potential energy of the tilt.

Now, let me analyze the calculated values of 2007. The tilts are increased as the settlement under southern side does, and the correlation coefficient between them reached 0.99. It illustrated that the former was only due to the latter, that is to say, the settlements under northern side i.e the rising of the north side remained certain constant, which namely the limit of the practical rising. For study on this limit, refer to the statement in paper (Burland 1997) as follows:

"In 1838 the architect Alessandro della Gherardesea escavated around the base of the Tower, with the aim of uncovering the base of the monument that had sunk into the soil, the average settlement of the Tower may be estimated between 2.5 and 3m; accordingly, the settlement of the north edge is around 2m and that of the south edge around 4m".

To sum up the above data, assume that the rising limit is 180cm. The settlement on the both side is the same for slightly smaller than the estimated above and their average values are close.

In Table 2, the calculated tilts and measured results from 1278-1990 are all very close. For calculating the tilts increased due to the counterweight 600t, assume the settlement increased is 1 cm, so the calculated value is 1'13". According to the paper (Burland 1998), the measured value is: by the end of July 1994, it had increased to 48" as the construction of the concrete ring had created a charge of 4"; the work itself had resulted in a total change of 52 arc seconds. The calculated and measured are close too.

This is the first time for the tilt direction changes since 1278, and the calculated values are 1'43" and 1'38" for 900t and 1200t respectively. This is the basis for me to put forward the

suggestion that the counterweight should be increased to 900t and 1200t. If without freezing in sep.1995 and increasing the counterweight to 1200t, the condition would be better.

About the north side rising, it is stated in paper (Burland 1997)as follows:

“Previously, it had been believed that the foundation were undergoing creep settlements with the south side settling more rapidly than the north. However, the observation that the north side had been steadily rising”. The amount of rising, according to the calculation in Table 2, is 57.49cm. This value is reasonable. If the value was over large, it must have been found before 1996.

But due to this finding, the paper took the mechanism of counterweight to it as: “led to the suggestion that the application of load to the foundation masonry on the north side could be beneficial in reducing the overturning moment”.

This point is open to question. About the relation of north side rising and mechanism of counterweight, it's clear according to the calculation as before: they are all the end of the calculation but there is no causality relation with each other; let alone decide to carry out the counterweight in 1992, which is 5 years earlier than the finding.

About the reason of tilt

According to the paper (Burland et al., 1997 and 1998), the reason is “No matter how carefully the structures were built, once it reaches a critical height, the smallest perturbation will induce leaning instability. Leaning instability is not due to lack of strength of the ground but is due to insufficient stiffness, i.e too much settlement under load. Children building brick towers on a soft carpet will be familiar with this phenomenon”. It is just a meaningless excuse. I made use of the data of more than 20 tanks and found that the tilt is related to the value Ω in high degree. Ω is a ratio between the settlement and the area of the tank foundation. The relation is: when $\Omega < 0.25$, there is no tilt; when $\Omega > 0.25$, tilt takes place, and the tilt amount is increased as the Ω does. 0.25 is the critical value of tilt. In the first stage of the table 2, the calculated settlement is 37.05cm, $\Omega = 0.13$, which is smaller than the critical value 0.25, so the tower is up right. In stage 2, $\Omega = 0.5$, which is two times the critical value 0.25, thereupon takes no directional tilt, northward in 1272, after directing to south, the tilt is increased as the moment does each other, and form vicious circle. The aim of the counterweight is to end this circle.

About the layers in which the rotation of the tower lies

The soil layers underlying the Tower include A, B1, B2, B3, B4 and C. A is slightly clayey and sandy yellow silt; B1 is Pancone clay. The layer which the rotation lies in is the same layer of deformation taken place mainly. The experts of committee widely assumed that the layer was the Pancone clay before and then changed it to layer A in 1997, as shown in the statement (Burland, 1997) “The form of foundation motion depicted leads to the very important conclusion that the seat of the continuing long-term rotation of the Tower lies in horizon A and not within the underlying Pancone clay as had been widely assumed in the past”. According the form of foundation motion, it is not able to define the layer strictly. According to my calculated results, the percent of the layers is as Table 3.

Table 3. Calculated per cent of deformation in various layers

Layer	Percent of deformation/%		
	south	centre	north
A	48.7	52.0	40.1
B1	45.8	43.4	51.2
B2	1.8	1.6	2.6
B3	1.1	0.9	1.6
B4	2.5	2.0	4.2
C	0.1	0.1	0.3
Σ	100	100	100

The fact is: the layers of deformation took place mainly in both A and B1, and are not only in B1 or A.

TO PUT FORWARD THE MEASURES OF ANCHOR BOLTS AND LOW-PRESSURE GROUTING

The measures were mailed to M.Jamiolkowski twice in June 16, 1998 and Feb.11, 1999.

The part related to the issues in first letter is as follows:

The safety of the Tower is in serious jeopardy not only because of the continually increasing inclination, but also because of the danger of an almost instantaneous structural collapse.

I consider the latter danger to be more threatening at present. This lies in the fact: the Tower is made of the so-called infill masonry. This kind of structure is popularly adopted in Chinese ancient architectural structures. The Tower of Baoben whose photo was enclosed in my letter of April 18, 1994 also belongs to this category. The strengthening of such tower in Chinese practice is generally by use of anchor bolts and I propose that for the Leaning Tower of Pisa it is ought to combine the anchor bolts with the low-pressure grouting to produce better effects.

The part related to the issues in second letter is as follows:

I expect that my letter of June 16, 1998 has been received, and maybe for reasons, you have not been able to give an early reply. As it was quite some time ago, and for your convenience of reference, I enclosed with this letter the copy of my suggestion that I posed on June 16,1998. To ensure that you can receive this letter, I mail it to you at your two given addresses.

THE SITUATION OF PRACTICE OF THE TWO MEASURES

The above describes how I put forward the two proposals for saving the Leaning Tower of Pisa from 1980 to 1999. The practices of the two measures are as follows:

About the counterweight

The first lead ingot was placing on July 14 1993. But it is unclear that the amounts of the counterweight in different documents of the Committee are different. For example, it is as

stated in paper (Burland 1997) in 1997: “600t caused a reduction in inclination of about one minute of arc and, more importantly, reduced the overturning moment by about ten percent. In September 1995 the load was increased to 900t in order to control the movement of the Tower during an unsuccessful attempt to replace the unsightly load weight with temporary ground anchors”. Similarly, in THE TIMES on April 12, 1997, the statement is: “The Leaning Tower of Pisa has been saved by placing 900t of lead on the ground around its high side of its base. This is the greatest success in seven centuries.” However, another statement in which only the amount 600t was mentioned, as that: “The temporary stabilization of the foundation was achieved by applying 600t of lead ingots to the North side of the foundation. For the first time in the long history of the monument, a small (about 1 minute of arc) reduction of its inclination was exercised. During these five years, the Committee defined the strategy for the final stabilisation interventions, which had to be absolutely non-invasive and fully respectful of the internationally accepted principles for the preservation and restoration of a world-famous UNESCO-listed monument, such as the Tower of Pisa. The application of the lead ingots required a prestressed concrete ring around the base of the tower. Also this temporary measure proved to be perfectly reversible, and in 2001 the lead weights and the ring were removed without any damage to the marble facing.” The statement about the amount 600t was again published in news titled with “Leaning Tower of Pisa is saved from collapse” in Telegraph on June 28, 2007, describing as “The straightening work involved the extraction of around 70t of earth from the northern side of the tower, causing it to sink on that side. Before the digging started, the tower was anchored with steel cables and 600t of lead weights. However, halfway through the project, concerns at the ugliness of the weights led to their removal and the tower lurched dramatically. ‘In one night, the tower moved more than it had averaged in an entire year,’ said Prof Burland. The weights were hastily reattached.”

It is the fact that the counterweight was increased to 900t in 1995, as described in the first two documents. The question is why only 600t is mentioned in the latter documents? Is it true that the 600t was removed and then reattached in practice?

About the anchor bolts and low-pressure grouting

It is stated as: “The structural strengthening was prepared by means of extended nondestructive tests and limited to the minimum essential. It involved only the south side of the first and second order. The intervention consisted in low-pressure special grouting, which was carried out under highly-controlled conditions, and in a small number of post-tensioned radial stainless steel bars, limited to the critical zone. The plinth of the tower was connected to the catino and circumferentially prestressed in order to counteract tensile stresses and increase the effective foundation area (The international Committee for the Safeguard of the Tower of Pisa 2001).”

INTRODUCTION TO THE CHORD MODULUS SOFTWARE

The settlement of the Pisa is calculated by using the Chord Modulus software, based on the physical properties of the layers A, B, and C in Paper (Jamiolkowski et al., 1993). The soils

are three-phase systems that consist of solid particles, water, and air. It is overwhelmed that the systems make the soil deformation feature more complex than the crystal material. Researches always focus on complicated aspects. Therefore, although there are hundreds of calculation models, the method based on Oedometer test cannot be replaced. Having studied the observation data on settlement and collapse of more than 400 buildings, I think that the three-phase systems of soils do not make the soil deformation feature more complex but more simple. As mentioned above, the Chord Modulus can represent the characteristics of nonlinear deformation of soils accurately. Therefore, the software based on the relation between the physical properties and the Chord Modulus can be used to calculate the two kinds of deformation (settlement and collapse),for part of the calculation examples, see Table 4.

The software has been applied to calculate the deformation in more than 200 medium-to-large-sized projects. Based on the calculation, the ground designs were improved, in which the pile lengths and foundation areas are dramatically reduced. In this way, the project investments and accidents are reduced.

Table 4. Comparison of the Calculated and Observed for Two Kinds of Deformation

Soil type	Project	Kind of Deformation	Cal. (cm)	Obs.(cm)
Mickle	Oil tank in Shanghai	settlement	162.4	160.7
Mickle	Oil tank in Shanghai	Settlement	113.0	111.7
Mickle	Oil tank in Tianjin	Settlement	106.2	99.0
Mickle	Oil tank in Wuhan	Settlement	171.2	179.8
Clay	Chimney in Tanggu	Settlement	4.93	5.10
Clay	Load test in Guangdong	Settlement	1.67	1.65
Loess	Shaanxi TV Tower	Settlement	17.26	15.63
Loess	Xi'an Microwave plant	Settlement	44.52	44.70
Loess	Teaching building in Xi'an	collapse	37.61	30.46
Loess	Load test in Xi'an	collapse	27.09	26.30
Loess	Load test in Lanzhou	collapse	142.9	147.4
Loess	Load test in Erliao	collapse	32.97	30.30
Loess	Load test in Fuping	collapse	58.37	57.11
Loess	Load test in Xigu	collapse	58.10	55.78
Loess	Load test in Tianshui	collapse	144.1	116.1
Loess	Pucheng Power plant	collapse	8.37	6.56
Loess	Collapsible pit in Guyuan	collapse	128.7	128.8

REFERENCES

- Shimbun Y. (1980). The preservation of the Leaning Tower of Pisa is a responsibility of the 20th
- Jiao W. (1981). Offer a suggestion for saving the Leaning Tower of Pisa, 1.
- Jamiolkowski M. et al. (1991). The Leaning Tower of Pisa, Present situation, *XECSMFE*, Florence.
- Jamiolkowski M. et al. (1993). Leaning Tower of Pisa-Updated Information, *Third International Conference on Case Histories in Geotechnical Engineering*, St.Louis, Missouri , USA.
- Jiao W. (1994). Settlement Analysis of the Leaning Tower of Pisa and Prediction of the Effect of Placing Counterweight on the North Rim, *Proceedings of the COMSAGE*, Hong Kong., 682-687.

- Jiao W. (1995). Computation of Collapse Settlement by Means of Chord-Modulus, *Proceedings of the RNC SMFE*, Sankt-Petersburg , 789-796.
- Jiao W. (1997). Application of Chord-Modulus Method to the Soft Clay Ground, Proceedings of the Second International Symposium on Structures and Foundations in Civil Engineering, Hong Kong , 581-586.
- Burland J. B. (1997). Propping up Pisa, *Architectural Conservation*, 2-3.
- Burland J. B., Jamiolkowski M. and Viggiani C. (1998). "Stabilising the Leaning Tower of Pisa", *Bulletin of Engineering Geology and the Environment*, 57.
- Burland J. B., Jamiolkowski M., Lancellotta, R., Leonards, G. A. and Viggiani C. (1993). Learning Tower of Pisa What is Going On, *ISSMFE NEWS*, 20 (2).
- The international Committee for the Safeguard of the Tower of Pisa, (2001). *Safeguard and stabilization of the leaning tower of Pisa 1990-2001*.

THE ANALYSIS OF GEOLOGICAL CALAMITY AND COUNTERMEASURES FOR NANPING CITY FUJIAN PROVINCE

Baoming Jin

*College of Water Conservancy and Hydropower Engineering, Hohai University,
Nanjing 210098 China;*

Water Conservancy Bureau of Nanping City, Nanping 353000, China

Nanping City lies in the north of Fujian Province and the upper of Minjiang River, where belongs to middle-low mountains and hills area, and the domestic geological conditions are very complicated. During the flood season, while the rainfall intensity in the mountain area is very heavy and the mountain high slope is steep, and the water content of soil is overly saturated and geology is unstable, they often cause serious geological calamities such as landslide, collapse, debris flow, etc., and all of them have caused casualties and brought great losses. Nanping City is an area where geological calamities occur frequently in Fujian Province. In the need of preventing and reducing geological calamities in the future, the status quo, characteristics and causes of geological calamities of Nanping City are analyzed in this paper. On the basis of above-mentioned analysis, the countermeasures to prevent geological calamities are proposed. Nanping City is located in the north of Fujian province, the upper reaches of Minjiang River, it governs 4 cities, 5 counties and 1 district and a total land area of 26,300 km², its mean annual precipitation is 1750 mm. In spring and summer, as the southwest warm and humid air current rising into the southern of China continuously, in the area of Wuyishan and Xianxialing it meets the cold air current which comes from the north of China to form a stationary front, which brings continuous storm, causing floods and geological calamities. Storm floods are the main reason for geological calamities in flood season. Nanping city belongs to middle-low mountains and hills area, having different type of diverse topography and complex geological conditions, where geological calamities occur frequently among Fujian province.

THE PRESENT SITUATION OF GEOLOGICAL CALAMITIES IN NANJING CITY

In recent years the geological calamity has become one of main natural calamity in Nanping City, its type is as follows: landslide, collapse, debris flow and so on. Landslide is the most frequent occurrence of geological calamity in Nanping City, and mainly takes place in steep slope of mountain area, construction site, railroad, highway, mine, and riparian area, etc.. Rainy season (April-June) of every year is a landslide-prone season, and landslide often causes serious calamities. For example, on June 23, 2005, the large area landslide takes place

on the 205 National Road in Qili Street section of Jian'ou City, the strong force of landslide pushed one big bus coach and one car into turbulent flood Jianxi river, only eight people fled for one's life by sheer good luck, all of other 23 people died. Collapse is a kind of large geological calamities of harmfulness in Nanping City, relying mainly on soil collapse. It were mostly induced by human activities, and mainly occurred in the mining field slopes, artificial abrupt slope formed by road and project excavation, slag fields, filling fields, leakage channels, etc. The general collapse occurring in a sudden, often causes devastating calamities. For example, on June 15, 2005, the slope collapse occurred near the construction site where one seven-residential building had already bound in newly developed area of Jian'ou City, causing this floor to collapse with a loud crash in the twinkling of an eye, 11 people were buried, 5 people among them are killed. Debris flow happened frequently in Nanping City in the small mountain valley, mainly as the form of mud flows. Its characteristic is often sudden outbreak, cause significant damage to people's lives and properties. For example, on May 21, 1988, in Long'an Village Zhangdun Country Jianyang City, debris flow destroyed 10 houses, caused 25 deaths. According to incomplete statistics, from 1992 to 2006 a certain scale of geological calamities happened 3,461 times in Nanping city, resulting in 207 deaths and direct economic losses of 586 million yuan.

MAIN CHARACTERISTIC OF GEOLOGICAL CALAMITY IN NANPING CITY

Uneven distribution and regionality, occurring easily

Geological calamity in Nanping City mainly concentrated in Yanping District, Jian'ou, Shaowu City, Shunchang, Pucheng, Zhenghe, Songxi County, etc., occurring easily. The distribution of calamity shows some regional characteristic, the different locations of environmental condition of geology have different types of calamities. Landslides, collapses mainly distribute in the middle-low mountains and hills area of the high relative elevation difference, steep slope and human project economic activity area; debris flow mainly distribute in the areas of complex geological structure, fracture development, weathered and broken rock, the center of storm and cutting deeply mountains.

Obvious seasonality, small scale and high frequency

Geological calamities mainly concentrate in the flood season (April ~ June), in the period rainstorm floods often occur, thus resulting in a lot of geological calamities. The scope and scale of impact of single point calamity is small, but it causes to human lives and properties damage and becomes a high proportion of disaster. Compared with other natural disasters, the number of geological calamities account for a large proportion.

Mainly soil, sudden happen and great destruction

The mountain soil mainly is dominated by red loam in Nanping area, which is relatively thick, accounting for 76% of the whole area of soil of the city. During heavy rainstorm because the water content of soil is overly saturated, the mechanical properties of the rock and soil which

is loose structure, low shear strength and capacity of the weathering resisting changes under the function of water, and geological calamities happen easily. The majority of landslides and collapses happen in Nanping City develop in shallow soil weathering crust, and more scatter in steep slopes of mountainous areas, construction sites, railroads, highways, mines, riparian areas and so on. During flood season, such steep slopes of the potential hazard, when its strength of shear resisting strength reduce to a certain extent, the harmful landslides and collapses occur, and debris flows erupt simultaneously sometimes. They often cause personnel's injuries and deaths and loss of property, the number of people that dies every year accounts for more than 60% of total death toll of the big flood, and it is very harmful.

CAUSE OF GEOLOGICAL CALAMITIES

Natural factors

The first is the geological conditions of rock soil layer, the broken regional geological foundation and loose weathering shell is main factors of causing disaster. Nanping city has many hills and mountains in erosion state with cutting surface, complex and varied terrain, fragile geological structure. Under the warm and moist climatic conditions, the weathering of granite with joint development is strong, which loose the weathering crust and change it into a coarse texture with less clay content, weak adhesion strength and strong permeability, for example Ruan,F.S.(1989). When rainstorms happen, the rainwater permeates through the crack and potential sliding surface, will lead to the fact the body sliding surface of soil is softened, mechanics performance is reduced, and may lead to the fact the water body is held up in because of relative water barrier, form high-pressure water motive force, for example Hu et al.(2007);a large amount of rainwater permeate through at the same time, the soil get weighty, finally losing stability and causing landslides and collapses. The second is the erosion, corrosion, dissolution and softening of fracture filling of reservoirs, rivers and groundwater, cause landslides and collapses. The third is the steep terrain. Mountains in Nanping are steep, with a large relatively height difference; the large gradient aggravates instability of the rock soil in the slope and is prone to cause collapse and landslide. In addition, there are many valleys in bowl-shape or funnel-shape with open terrain, around by steep mountains with broken hill and bad vegetation growth, this helps water and gravel gathering to form debris flows.

The occurrence of geological calamities is a process from slow course change to sudden change caused by both the multiple natural factors and human activity factors, but in certain geological structural characteristics and environmental conditions, precipitation (rainfall, rainfall intensity and duration of rainfall, etc.) is the most important factors inducing geological calamities. In the flood season (April-June), rainstorm is main reason for geological calamities. Such as in the "98•6" extra torrential rain flood, the biggest 13-day course rainfall was 1603mm, flash floods , landslides, collapses, debris flows destroyed a lot of houses, caused 98 deaths; on June 21, landslides occurred in the old silicon plant village of Waitun country in Zhenghe county destroyed eight houses, 40 people were buried by the mud stone, which killed 34 people, six of them hurted seriously. In the "2005•6" storm flood, the largest six-day course rainfall was 597mm, 40 people were killed by geological calamities. In

the “2006•6” storm flood, the biggest five-day course rainfall was 490mm, geological calamities caused 15 deaths. In the “98•6”, “2005•6”, “2006•6” rainstorm, geological calamities caused traffic interruption of Laifu, Yingxia railroads, national highways and roads linking Nanping with every county (city).

Human factors

With the development of economy, a lot of project activities of mankind have destroyed the body of natural slope, therefore the emergence of the geological calamity is more and more frequent in recent years. For instance: building houses, factories nearby mountains, building roads, railways, water conservancy projects excavating slope, making the lower slopes lost support, forming artificial steep slope, high wedge slope; mine excavation, underground mining and arbitrary dumping of waste soil residue, forming virtual soil slopes; deforestation, inappropriate quarrying mountain to make the field, destruction of vegetation, increased surface water infiltration, etc., the above are human factors to induce geological calamities. Excavation and filling of the abrupt steep change the original structure of the slope, undermining stability of the rock soil, which is easy to cause landslides, collapses and other disasters under the conditions of continuous rainfall, and a lot of loose solid stacking creates the conditions for the occurrence of debris flow. According to some experts statistics, 95% of major landslides, debris flow are mainly induced by rain and human activities, for example Li,S.d.(1999).

THE COUNTERMEASURE OF PREVENTING AND CONTROLLING OF GEOLOGICAL CALAMITY

Batch implementation of engineering of preventing and controlling of geological calamity

According to actual situation of geological calamities and the hidden danger places in Nanping city, plan the project management or resettlement by the order of importance and emergency in batches. Engineering measures include: setting drainage, cutting slope, reducing weight the counter- pressure, setting anti-slide wall, anti-slide pile, anchor and anchor with prestress to control landslide and collapse, specific measures should be based on the geological structure of landslide and collapse, engineering environmental conditions, local conditions, etc.. Treatment to debris flow include: obstructing, the dredge, drainage and reinforcement measures, carrying on comprehensive management. For frequent geological calamities, the implementation of housing relocation and avoidance measures should be planned.

Establishing geological calamity warning system

Mainly include: (1) the establishment of database information of geological calamity and the hidden danger places. (2) the establishment and improvement of geological calamity monitoring system. Mainly include: automatic rainfall monitoring system, water content of soil monitoring system, rock soil layer deformation or displacement monitoring system, radar information system, remote sensing system, wireless video surveillance system, etc..

(3) the establishment of information processing system. Integrated process of information of the distribution of geological calamity and hidden danger places , water content of soil, rock soil layer deformation, rainfall, weather and other remote sensing information from the information processing system will meet for decision-making for leaders and experts.(4)the establishment of geological calamity warning system. Mainly includes: first, the establishment of dynamic model of the relationship between meteorological factors such as precipitation and geological calamities; second, through three-dimensional graphics, display the picture superimposition of geological information and meteorological information, establish the warning mode in advance; third, through system software, analysis weather forecast level of geological calamities in Nanping City; fourth, by the conference or consultation together of meteorology department ,land and resources department and other departments, forecast geological calamities, if the weather forecast level of geological calamities reaches 3 grades and above, release information and warnings to the external.

The establishment and improvement of basic system, improve the assessment of geological calamities

Construction in geological disaster-prone areas , the dangerous assessment report of geological calamity report must be made in accordance with national geological calamity risk assessment standards in the project site selection phase. Making city master plan, village and town plan in geological disaster-prone areas should be carried on the geological hazard assessment. The dangerous assessment result of geological calamity of construction land will be a part of feasibility research report, if the feasibility research report has not included dangerous assessment result of the geological calamity, it would not be approved and the land and resources department would refuse to go through the preliminary examination of construction land and approval procedures. In the dangerous assessment of geological calamity, if the construction may cause or trigger geological calamities, the goal responsibility system and deadline system of geological calamities prevention and cure should be implemented, preventing and controlling geological calamities will be included in the overall design and engineering budget, with the main works at the same time design, construction and acceptance to ensure the construction of its own security and avoid the generation of new geological calamities.

Improving soil and water conservation, protection of mountain vegetation, improving the ecological environment

Improving soil and water conservation, protection of mountain vegetation, improving the ecological environment, play an important role in reducing of geological calamities. Strictly control construction examination and approval in the potential danger area, large slope and high wedge slope. Resolutely stop disorder cutting, disorder exploitation, indiscriminate mining, digging and piling up and so on, prevent new human-induced geological calamities by construction. Moreover, protect existing evergreen broad-leaved forest in a more effective manner, and increase the proportion of ecological forest and hardwood forest, advocate creating mixture of coniferous and hardwood forest. Through the rational allocation and protective measures to restore and improve the soil and water conservation function of mountain forests, reduce the emergence of geological calamities.

Strengthen publicity and education work, enhance the people's consciousness of calamity prevention and reduction

It is necessary to change passive control calamities to active control calamities, strengthen publicity and education work, and enhance the people's consciousness of calamity prevention and reduction. The propagandizing and popularization of geological calamity prevention knowledge should focus on the country and town, village and school in a mass loved way, through the broadcast, television, brochures, wall charts, display, network and other forms extensive publicity.

Making and improving geological calamities defense project system

Making and improving geological calamities prevention and cure the scheme and defense sudden geological calamities emergency preplan, is an effective and active means of prevention. Land and resources department of city level and county level should unite construction department, water resources department, communication department and other departments, on the basis of survey about geological calamities and geological calamities prevention planning, to work out defense sudden geological calamities emergency preplan and geological calamities prevent and cure the scheme.

The establishment of geological calamities mass monitoring and prevention network

Carry out the mass monitoring and prevention system in hidden geological calamities of the whole city, raise consciousness of local people to prevent calamities and enhance emergency capabilities of saving themselves. The hidden geological calamities monitoring network can be constructed at village level, country and town level, county(city, district) level, to reach mass monitoring and prevention purposes.

REFERENCE

- Hu B.T, Ji W.F. and Li C.M. (2007). Monitoring and Countermeasures of Hejiawan Landslide in the Three Gorges Reservoir Area, *The Chinese Journal of Geological Hazard and Control*, 18(3): 1-4
- Li S.D.(1999). The Temporal and Spacial Distribution of Landslide and Debris Flow Disasters in China, *Research of Soil and Water Conservation*, 6(4): 33-37
- Ruan F.S.(1989). Cause and Characteristic of '5·21' Debris Flow in Rongan village, Jianyang City, *Water and Soil Conservation of Fujian*, (2): 49-51.

COASTAL BARRIER ISLAND CREATION/AUGMENTATION AS A MITIGATION MEANS OF MAINLAND DISASTER PROTECTION AGAINST WATER AND WIND FORCES

Randy A. Knott, P.E.
Senior Principal, Vice President
MACTEC Engineering and Consulting, Inc.
Atlanta, Georgia USA

The creation of a coastal marsh using maintenance dredged material from a nearby shipping channel was performed as a pilot project for restoring and augmenting a barrier island on the Gulf Coast of the State of Mississippi in the United States. This beneficial use of dredged material, not only provided an ecological habitat for coastal wildlife, but also augmented the size of a coastal barrier island. This augmented barrier island in its new size and configuration helped buffer and dissipate the powerful energy of Hurricane Katrina and other storm surges experienced by Coastal Mississippi in 2005. Geotechnical and coastal engineering challenges included site selection, location, size, and shape; bearing, stability, and performance of containment dikes for sediment in-fill; in-fill sediment characterization; and in-fill sediment performance. This project demonstrated that geotechnical and coastal engineering along with application of appropriate environmental sciences can provide engineered systems to produce coastal protection and other benefits through creation and/or augmentation of offshore barrier islands.

BACKGROUND

The U.S. Army Corps of Engineers (USACE) is responsible for maintaining coastal shipping channels in the United States in cooperation with state and local port authorities and other government agencies.

In order to maintain open channels in the depositional coastal areas of the southeastern United States, excavation of the naturally deposited silt and clay laden channels and waterways must be performed on a periodic basis. The excavation work is normally accomplished using hydraulic cutter-head or suction-head dredging. The depository for these dredged materials has historically been nearby mainland or shallow water sites that have grown in size (both vertically and laterally) for the last 150 years, often negatively impacting the environment and coastal development. Recently, a program has been developed to find beneficial uses of these dredged materials and to utilize the excavated materials for purposes that would benefit and not harm the environment. The USACE in cooperation with the State of Mississippi began a search in 2001 to find potential sites where

this fine-grained material could be placed in order to restore former marshlands or to create new ones. Therefore, the initial purpose of this project was to create a coastal wetland (marsh) for the beneficial use of dredged material excavated from shipping channels to maintain their depths and side slopes. Later it was realized that several other benefits were achieved.

PLANNING AND DESIGN DEVELOPMENT

Initially, the planning required the interaction and coordination of various state and federal agencies including the U.S. Fish and Wildlife Service and the State of Mississippi Department of Coastal Resources as well as other local environmental and planning groups. This planning process included a risk and value received analysis for site selection, and the establishment of a construction cost and schedule for development and implementation. Both short-term (less than 10 years) and long-term sustainability goals were established for the project which included site location, site elevations, fill and construction material sources and quantities, ecological impacts and benefits, cost, schedule, constructibility, and maintenance. Initially, several sites were considered, but were reduced to three for design development. Design development for each site included hydrographic, topographic, and aerial surveys; geotechnical investigations at the three sites and at the channel sources; geotechnical and analytical laboratory testing; and environmental adaptability evaluations.

The final site selection evaluation included location with respect to the channel source material and other factors as follows: environmental impact, existing water depth and conditions, available surface area size and shape, construction access and limitations, permitting issues, risk of success, and economics.

ENGINEERING DESIGN

With the design development and site selection processes completed, engineering design was initiated. This included geotechnical engineering, civil and coastal engineering, and input from the environmental sciences.

The geotechnical engineering design included site containment dike alignment, dike stability (internal and external), off-site dike construction material evaluation, and channel source material evaluation for in-filling the containment dikes and creating the marsh deposit. Geotechnical and environmental sampling of the channel material was accomplished and the collected samples were laboratory tested for geotechnical characterization and environmental contaminants. The material was found to be not environmentally contaminated. The geotechnical laboratory characterization testing included grain size distribution, Atterberg limits (plasticity), specific gravity of soil solids, long tube consolidation, self-weight consolidation, and oedometer consolidation. From the laboratory testing results, representative characteristics of the material to be dredged from the channel were established for its planned hydraulically disturbed state. These characteristics were then used in a series of mathematical models to predict the performance of the material as it is hydraulically placed into the containment area to create the marsh deposit. This modeling simulates the hydraulically bulked material at the new site. The modeling provides information on how

high the material can be placed, how long will it take to consolidate, and predictions on resulting elevations for marsh creation.

The final selected site was to be attached to Deer Island in Biloxi Bay of Mississippi (see Figure 1). This site was considered a pilot project for larger sites to follow. The engineering required a design-to-cost process in that a fixed budget of \$800,000 USD had been established for the project. Therefore, the engineering required a site shape and size to fit within the budget. This resulted in an approximately 18.2 hectare site configured as shown in Figure 2.



Figure 1. Site Location

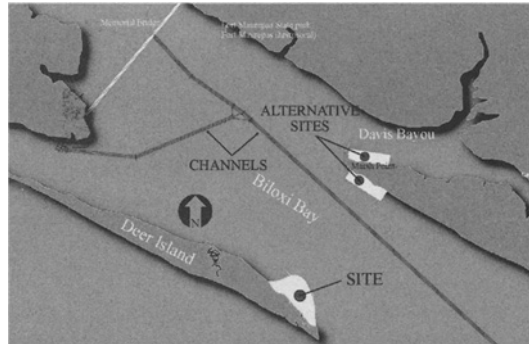


Figure 2. Site Configuration

The geotechnical investigation consisted of standard penetration test borings, manual probings, and bulk sampling of bearing materials, borrow materials for dike construction, and fine-grained channel material to be dredged and placed in the containment area. From the field exploration, testing and sampling, and laboratory testing results, a geotechnical analysis was performed in order to provide recommendations for site preparation and containment dike support, containment structure stability and geometric designs, dredged material performance, and overall site response or performance.

The laboratory evaluation of the material to be dredged included its physical classification (USCS-CH), its environmental condition (non-contaminated), and settlement potential characteristics. The settlement characteristics from the long tube, self-weight, and oedometer consolidation devices characterized the material with an initial void ratio of 30 to 35 as it would be pumped into the containment area (approximately 40 to 50% solids by volume) to a consolidated marsh type deposit with a void ratio of approximately 4 to 5. Laboratory times for this self-weight consolidation was approximately 10,000 minutes from a void ratio of 30 down to a void ratio of 10, another 20,000 minutes to reduce the void ratio to 7 (see Figure 3), and another 20,000 minutes was needed to further consolidate the material from a void ratio at 7 to 4 for a total of 50,000 minutes to achieve marsh like consistency from the initial pumped liquid.

These laboratory parameters were used in mathematical constitutive relations to model the field conditions in order to predict how full or high to pump the material within the dikes, how long to wait for the material to self-consolidate, and what elevations (beginning and end) should be anticipated to achieve the marsh type soil consistency. These models included the following computer software programs:

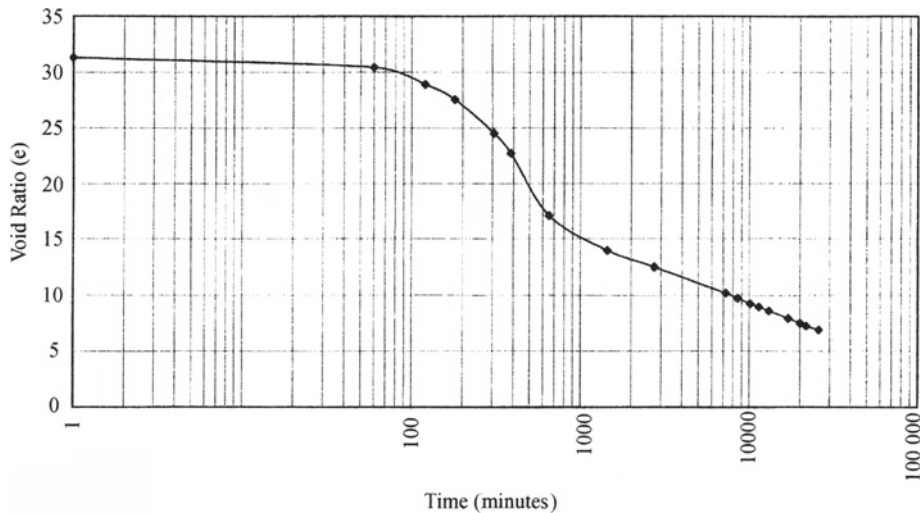


Figure 3. Long Tube Test Results (Typical)

- ADDAMS – Automated Dredging and Disposal Alternatives Modeling System
- SETTLE – Designs of Confined Disposal Facilities for Suspended Solids Retention and Initial Storage Requirements
- PSSDF – Evaluation of Consolidation, Compression, and Desiccation of Dredged Fill for Determining Long-Term Storage Requirements

The results of the modeling indicated that the hydraulically placed channel material could be placed to an elevation of +1.5 meters MLLW within the containment or marsh site creation area. This results in an overall maximum thickness of remolded hydraulically placed channel material of 2.1 meters (from -0.6 to +1.5 meters, MLLW elevation). The material was predicted to self-consolidate to an elevation of approximately -0.1 to +0.3 meters, MLLW in about 2 to 3 years achieving a total settlement of approximately 1.2 meters.

The Deer Island site was found to be the most geotechnically stable for bearing support of the containment dikes. These dikes were therefore designed and constructed on 3:1 (H:V) exterior side slopes and 2:1 (H:V) interior site slopes with a 3.7-meter crown width with an overall height of approximately 2.7 meters. Generally, the dikes were constructed from -0.6 meter MLLW to +2.1 meters MLLW (therefore maintain a 0.6 meter freeboard to the top of the containment dike elevation of +2.1 meters). Dike construction material was a uniformly graded fine sand excavated from the bay bottom 6.1 meters from the exterior dike toe.

The coastal engineering design included a wind and wave evaluation resulting in a predominant wind directions analysis and a shore wave analysis on the site and containment dikes. The analysis resulted in recommendations for site shape and size, and protection design. From the geotechnical engineering recommendations and the designs-to-cost methodology, a design configuration as shown in Figure 4, resulted.

With the geotechnical engineering recommendations for stability and the coastal engineering recommendations for protection, containment dike and breakwater designs resulted as shown in Figure 5.

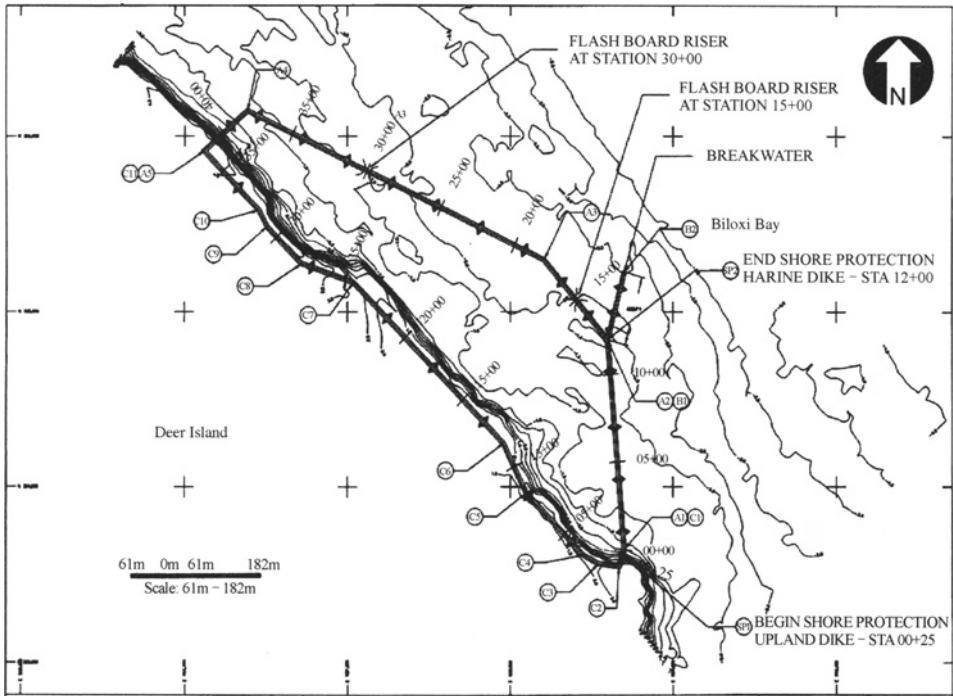
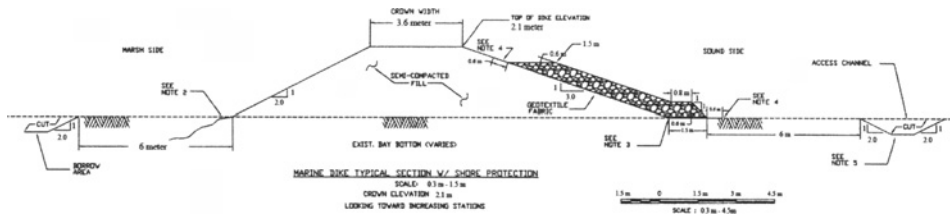


Figure 4. Site design plan

The civil engineering design included two flash board riser weirs to be placed along the outside (marine side) dike in order to decant the clear water off the hydraulically placed material as it settled. At least six inches of water was maintained over the material during settlement in order to prevent desiccation.



Note: Shore protection only in designated locations

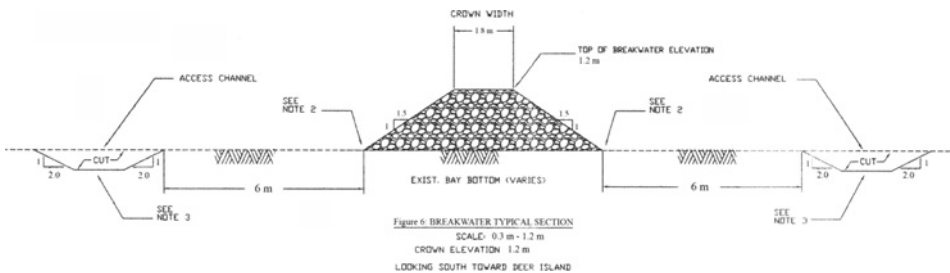


Figure 5. Typical dike and breakwater sections

The environmental science analysis for the required ecological habitat creations of native plants recommended the following three plant species to be planted in the consolidated material:

- *Spartina alterniflora*: at elevations of -0.1 to +0.3 meters
- *Juncus roemerianus*: at elevations of +0.3 to +0.6 meters
- *Spartina patens*: at elevations above 0.6 meters

Plant spacings and locations were also recommended.

The design was completed in the Fall of 2002 with construction documents consisting of drawings and specifications plus the following specialized documents: Implementation Schedule and Construction Sequence Plan, Fill Placement Plan, Water Quality Run-Off Plan, Fill Settlement Monitoring Plan, Dike Breaching and Re-shaping Plan, Plantings and Habitat Development Plan, and a Performance Monitoring and Maintenance Plan.

CONSTRUCTION

Construction of the containment dikes began in the Fall of 2002 and completed in the Spring of 2003 (55,051 cubic meters of sand; 5,083 metric tons of protection stone). Hydraulic filling began shortly after and was completed in 60 days (259,963 cubic meters of channel material). From the Spring of 2003 to the Winter of 2005, the material consolidated (approximately 24 months). Additionally, selective breaching of dikes and mounding and channeling of some interior material was performed. The plantings were placed in February 2005 and habitat development began in the Spring of 2005, on its way to becoming a successful marsh creation.

PERFORMANCE

In the Fall of 2005, Hurricane Katrina impacted the site with wind speed exceeding 240 Km/hr and wave heights exceeding 6 meters (see Figure 6). Post Katrina evaluation of the area and Deer Island concluded that this offshore barrier island along with others absorbed significant energy from the hurricane resulting in less severe damage to the mainland developed areas including the city of Biloxi and nearby mainland smaller communities. Energy absorption resulted in the additional widening of one of the dike breaches (the breakwater and eastern protection dike remained intact) and removal of some of the created marsh deposit.

Presently, due to the success of this project, this created marsh area is being duplicated with a design for an addition to the west along the north side of Deer Island together with continued physical and biological monitoring. Some supplemental containment protection at the major breach and additional filling and plantings in low areas is being considered.

Beneficial uses of the created marsh and water estuary area are already being realized by increased bird habitat and other marsh/coastal animal species activity, and coastal recreation including wildlife viewing and fishing (both recreation and livelihood). As part of this project, alternative dike construction and protection materials were evaluated including geotubes and masonry and concrete demolition debris re-used in place of natural stone for protective armoring of the dikes.

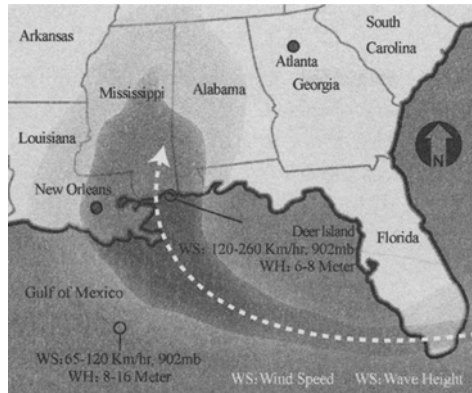


Figure 6. Hurricane Katrina path

CONCLUSIONS

This project demonstrated that geotechnical and coastal engineering along with application of appropriate environmental sciences can provide engineered systems to produce coastal protection through creation and/or augmentation of offshore barrier islands. The overall benefits of constructing this form of coastal protections include sacrificial coastal protection to help mitigate mainland disasters from water and wind forces; beneficial habitats for coastal wildlife; beneficial use of excavated material from nearby new or maintained shipping channels / basins / harbors; disposal area for maintenance dredged material; depository for masonry and concrete demolition debris; depository for the burial of environmentally contaminated soils; and land use for coastal recreation and aquaculture farming.

ACKNOWLEDGEMENTS

- Mississippi Department of Marine Resources; Biloxi, Mississippi, USA
- U.S. Army Corps of Engineers – Mobile District; Mobile, Alabama, USA

REFERENCES

- Schroeder P.R. Evaluation of Consolidation, Compression, and Desiccation of Dredged Fill for Determining Long-term Storage Requirements. PSDDF Version 2.1. CEERD-EP-S. U.S. Army Engineer Research and Development Center, Vicksburg, MS. <http://el.erdc.usace.army.mil/products.cfm?Topic=model&Type=drmat>. Accessed January 8, 2008.
- Schroeder P.R., Palermo M.R., Myers T.E., and Lloyd C.M. (2004, updated). The automated dredging and disposal alternatives modeling system (ADDAMS), *Environmental Effects of Dredging Technical Notes Collection* (ERDC/TN EEDP-06-12), U.S. Army Engineer Research and Development Center, Vicksburg, MS. <http://www.wes.army.mil/el/dots/eedptn.html>. Accessed January 8, 2008.
- U.S. Army Corps of Engineers. (1983). Engineering and Design – Dredging and Dredged Material Disposal. Publication No. EM 1110-2-5025. Proponent CECW-EH-D. Washington, DC: March 25, 1983.

- <http://www.usace.army.mil/publications/eng-manuals/em1110-2-5025/entire.pdf>. Accessed January 8, 2008.
- U.S. Army Corps of Engineers. (1986). *Engineering and Design – Design of Breakwaters and Jetties*. Publication No. EM 1110-2-2904. Proponent CECW-EH-D. Washington, DC: August 8, 1986. <http://www.cmiengineer.com/whitepapers/EM%201110-2-2904%20Design%20of%20Breakwaters.pdf>. Accessed January 9, 2008. Updated in 2002 and 2003 as part of EM 1110-2-1100, Parts I to V and Appendix A.
- U.S. Army Corps of Engineers. (1987a). *Engineering and Design – Beneficial Uses of Dredged Material*. Publication No. EM 1110-2-5026. Proponent CECW-EH-D. Washington, DC: June 30, 1987. <http://www.usace.army.mil/publications/eng-manuals/em1110-2-5026/entire.pdf>. Accessed January 8, 2008.
- U.S. Army Corps of Engineers. (1987b). *Engineering and Design-Confined Disposal of Dredged Material*. Publication No. EM 1110-2-5027. Proponent CECW-EH-D. Washington, DC: September 30, 1987. <http://www.usace.army.mil/publications/eng-manuals/em1110-2-5027/entire.pdf>. Accessed January 8, 2008.
- U.S. Army Corps of Engineers. (1989). *Engineering and Design – Environmental Engineering for Coastal Shore Protection*. Publication No. EM 1110-2-1204. Proponent CECW-EH-W. Washington, DC: July 10, 1989. <http://www.usace.army.mil/publications/eng-manuals/em1110-2-1204/entire.pdf>. Accessed January 8, 2008.
- U.S. Army Corps of Engineers. (1992). Environmental Effects of Dredging Technical Notes: Documentation of the SETTLE Module for ADDAMS: Design of Confined Disposal Facilities for Solids Retention and Initial Storage. EEDP-06-18. U.S. Army Engineer Waterways Experiment Station. Vicksburg, MS: December 1992. <http://el.erdc.usace.army.mil/elmodels/pdf/ee-06-18.pdf>. Accessed January 8, 2008.

OTHER INFORMATION SOURCES

American Society of Civil Engineers. (2002). Third Specialty Conference on Dredging and Dredging Material Disposal. Orlando, Florida: May 2002. <http://ascelibrary.aip.org/dbt/dbt.jsp?KEY=ASCECP&Volume=119&Issue=40680&bproc=year&scode=2002&confTitle=Dredging+2002>. Accessed January 8, 2008.

American Water Resources Association. (2002). Spring Specialty Conference: Coastal Water Resources. New Orleans, Louisiana: May 2002. http://www.awra.org/proceedings/past_proceedings.html. Accessed January 8, 2008.

EVALUATION OF DISASTER ASSISTANCE PROJECTS INVOLVING THE ENGINEERING COMMUNITY IN RECONSTRUCTION AND PREVENTION

Bastiaan De Laat, Claudine Voyadzis

*Ex Post Evaluation Department Council of Europe Development Bank
Paris, Fr-75116, France*

Baris Trak

*Technical Advisory Directorate Council of Europe Development Bank
Paris, Fr-75116, France*

This paper reviews the performance of the assistance of the Council of Europe Development Bank (CEB) in the sector of natural disaster prevention and mitigation. Based on evaluation results, it provides suggestions to better involve the geotechnical engineering community with project assessment of major international donors. The paper also includes a brief review of the evaluation experience of International Financial Institutions (IFIs) and highlights the originality of CEB's evaluations in combining engineering components with socioeconomic analyses. Set up in 1956, the CEB is the oldest multilateral financial institution in Europe and the only one with an exclusively social vocation. One of the CEB's priority lines of action is assistance to (potential) victims of natural disasters. Over the past 10 years the CEB has financed projects for some 2 billion euros in this sector only.

CEB'S ACTIVITIES IN DISASTER MITIGATION AND REHABILITATION

The CEB is a multilateral bank with 39 Member States – including 17 Central and Eastern European Countries – and an exclusively social vocation. Since its inception, the Bank has granted over 24 billion euros in loans. In 2006, the Bank approved 37 projects for a total of 2 460 million euros, of which about 400 million for natural disasters mitigation, rehabilitation and prevention.

Natural disasters are more frequent and have a greater impact than before. Severe flooding in many parts of Europe has become a predictable, annual happening. Forest fires are increasingly intense and often linked to droughts – the extensive Greek forest fires in the summer of 2007 are an unfortunate example. Landslides and avalanches are common. South-Eastern Europe and Turkey are particularly vulnerable to seismic events. Disasters can be expected to affect CEB member states in the decades to come. Assisting regions hit by natural or ecological disasters is a statutory priority of the Bank.

The purpose of the operations carried out by the Bank in the area is twofold: (1) to provide national and local authorities with assistance involving immediate financial support for the reconstruction of the affected areas and (2) to develop means for the prevention of natural or ecological disasters, along the lines of the Hyogo Framework. Emphasis increasingly lies on prevention of, in particular, flooding. Hence, the CEB's most recent projects in this area

concern rehabilitation of areas prone to flooding followed by support to water management and construction or consolidation of river banks. Substantial projects of this nature were approved in Hungary, Poland and Romania, all three suffering from major floods in the recent past. The importance of natural disaster mitigation in the CEB's portfolio justified this area to be the first to be evaluated.

CEB EVALUATION OF DISASTER ASSISTANCE PROJECTS

An innovative evaluation approach to disaster mitigation projects

The ex-post evaluations in the area of natural disaster mitigation and prevention covered 11 loan projects to 5 different member states, approved between 1995 and 1999 for a total loan amount of over 1 billion euros. Eight projects were in response to flooding and landslides, and 3 projects related to earthquakes. The first type of projects aimed mainly at the construction or rehabilitation of infrastructures to restore living conditions and prevent, in future, new disasters from happening. The earthquake projects aimed at reconstruction of individual or collective housing.

Ex-post evaluations analyse project relevance, effectiveness, efficiency, impact and sustainability. A few specific issues are also assessed: CEB value added, beneficiary participation and windfall opportunities. Evaluations combine a socio-economic (beneficiary surveys/interviews) and a technical component (quality and sustainability of infrastructures/housing): socio-economic experts work alongside engineers. For the present paper, it is particularly relevant to elaborate on the latter.

For the projects related to flood prevention, the evaluation of the technical quality of infrastructures (dams, dykes, drop structures, etc.) was performed as follows. All available project documentation was analysed by the engineers contracted by the CEB; conformity of the infrastructures with relevant building codes and with international best practice was assessed. On-site visits were conducted for visual inspection of the works and interviews with representatives of relevant authorities. Additionally, land use planning was analysed.

For earthquake-related projects, on top of this, the structural quality of the buildings was analysed. Two different techniques were used: in the first evaluation related to earthquakes, core drilling was used to assess concrete strength. As this technique was found too invasive, for the two remaining projects non-destructive tests were applied using a concrete test hammer to measure compressive strength and an electronic scanner to identify the layout of constructions or reinforcements. Such tests are common in engineering, but, as argued below, not often used in evaluation.

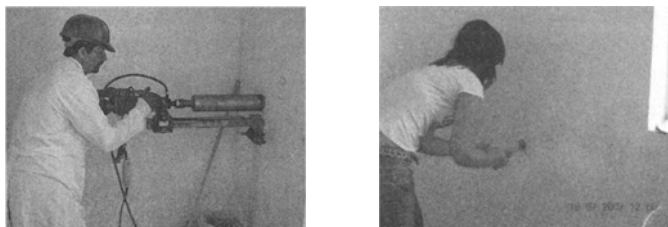


Figure 1. Core drilling (left) and Concrete test hammer (right)

Evaluation outcomes and recommendations

Derived from socio-economic and technical analyses, the overall evaluation results of the 11 CEB projects were satisfactory. Most projects fulfilled priority needs and achieved their objectives. They produced a variety of economic, social, environmental and cultural effects, such as the restoration and improvement of the livelihoods of disaster victims, the improvement of transport infrastructure, improved productivity, reduced soil erosion, better forest exploitation and restoration, and preservation of cultural heritage.

Shortcomings were due to poor preparation and weakness of feasibility studies, lack of consultation between relevant parties (central and local authorities, and beneficiaries), poor quality, poor maintenance, and sometimes deviation from standards (seismic norms in particular). Five sets of factors emerge as being vital and instrumental to project success: (1) setting clear objectives, defining target groups and priority setting; (2) sound and flexible project design; (3) good governance, strong institutions and well-coordinated, flexible project management; (4) timeliness, but without harming the quality of project preparation; (5) the inclusion of disaster reduction and mitigation plans and the development of preventive measures.

Despite their positive impact, projects can still be improved to increase the impact and value added of CEB projects. The focus should be on longer term reconstruction and risk prevention rather than on emergency relief. Beneficiary participation should be sought when meaningful, consultation in most cases, and communication of quality information in all cases. It would be useful to define a communication strategy in the disaster area and cooperation between the Bank, Borrowers and lending institutions can still be improved. Finally, broader risk prevention and management programmes should be actively promoted.

Engineers' involvement: a technical, social and economic task

The foregoing discussion leads us to consider the involvement of engineers in natural disaster related projects. Given its mandate and social vocation, CEB projects are first of all "social projects," and should benefit populations affected by a natural disaster. Yet projects have necessarily a strong engineering component, and civil and geotechnical engineers are involved in preparation and implementation. The strong emphasis on engineering sometimes resulted in losing sight of social aspects, ignoring for instance kinship relations or cultural similarities, deemed important in relation to maintenance and housekeeping in rehabilitated areas. In other cases, an "engineering fix" overshadowed an economic solution: for instance costly anti-flood structures were implemented instead of a more cost-effective relocation of inhabitants, letting the river simply overflow from time to time. Examples were also found where the project design had not taken into account the possible future evolution of an area (e.g. increased urbanisation reducing the capacity of rehabilitated waterways) or where the use of poor quality materials resulted in insufficiently strong concrete for instance.

Most of the deficiencies found could be explained by an unbalanced combination of socioeconomic, political, and engineering issues: engineers not taking into account sociological aspects; political considerations prevailing over economic ones; contractors

being too much under cost and time pressure resulting in poor quality. This is why the CEB evaluations draw the lesson that the most optimal long-term solution should be delivered to the final beneficiaries, taking into account *all* economic, social and technical perspectives.

THE ROLE AND ACTIVITIES OF INTERNATIONAL FINANCIAL INSTITUTIONS (IFIs)

An increased attention to natural disaster mitigation and rehabilitation

Not only the CEB, but other International Financial Institutions (IFIs) as well have been involved in disaster mitigation and rehabilitation since quite a long while. Recently, due to a series of major disasters – and particularly triggered by the Indian Ocean Tsunami of 26 December 2004, killing 200 000 people in a couple of minutes – the attention for natural disasters and their impacts suddenly increased. Like the CEB, several other major IFIs recently completed evaluations of their disaster assistance performance.

The World Bank (WB) has assessed its experience in disaster response over the past 20 years (2006). This assessment aimed to analyse the implementation and impact of 528 disaster-related projects. It showed that more attention is needed for disasters in relation to development: one single disaster can literally wipe out years of development effort. The report cites that the 2000 floods in Mozambique damaged or destroyed around the same amount of schools (500) that the Bank had built over the 20 previous years. The 5 billion dollars of losses due to the Kashmir earthquake were roughly equivalent to the Banks lending to Pakistan in the 3 years preceding the disaster. Disasters should no longer be treated as one-off, random events, but as events that strike with regularity, in known places, with a real risk to a country's development.

The WB evaluation came up with lessons similar to CEB's e.g. that advance preparation and priority setting is crucial and that a quick reaction may not lead to the most relevant response. The WB also observed that disaster management, preparedness and mitigation are not sufficiently addressed, that maintenance is crucial and that in urgent situations simple project design is important. As concerns donor-coordination, it judges co-financing to be preferred above parallel financing as this generally leads to more coherent projects.

The Inter-American Development Bank (IADB) and the Asian Development Bank (ADB) evaluations in 2004 came up with comparable results: disasters have significant bearing on development prospects, but countries are not addressing adequately the risk to development that disasters pose. The IADB's investment portfolio reflected the reactive approach of the countries, favouring post-disaster response over *ex ante* risk prevention and mitigation. ADB's evaluation highlighted the need for planning, training of staff, the inclusion of poverty reduction issues and the inclusion of maintenance, and flexibility. As a consequence of its evaluation results, the IADB designed a new policy which includes a country oriented portfolio management; adapted policies, procedures, training and financial instruments; and an organisational approach focusing on *ex-ante* risk reduction. It also established an action plan and defined incentives for staff. The ADB designed a new Disaster and Emergency Assistance Policy (2004) which shifts the emphasis from disaster response to disaster mitigation.

Several smaller development banks have also been sharpening their policies with regard to post-disaster interventions. The Andean and the Caribbean Development Banks for instance emphasise as well the important role of disaster prevention, mostly absent from – reactive – national policies and procedures. They underline the importance of strengthening institutional capacity, coordination between stakeholders and development of proactive prevention policies, to deal appropriately with disaster mitigation.

Strong convergence in evaluation results

It is clear that the observations of the IFI evaluations strongly converge. At the end of 2006, the IFIs gathered together to discuss evaluation outcomes more in detail and exchange on their experiences. Also several NGOs were present at this event. There was a striking resemblance between the results of the IFIs' evaluations especially with regard to the lack of pro-activeness, risk prevention and strategy; and with regard to issues of institutional capacity building, staffing and training. Also, interesting complementarities were discovered between the action of the NGOs (better at short term, emergency interventions) and the IFIs (longer term reconstruction efforts).

However, unlike the CEB, the other IFIs do not seem to make use of specialised engineering competence in their ex-post evaluations, and do not test the technical quality and sustainability of the constructions they financed; once the works are completed, the "evaluators" take the lead without the participation of specialist engineers.

FOR A BETTER INVOLVEMENT OF THE ENGINEERING COMMUNITY IN PROJECT ASSESSMENT OF INTERNATIONAL DONORS

Can the geotechnical engineering community contribute to a better performance of international donor organisations in natural disaster mitigation? The CEB ex-post evaluations have successfully involved engineers for quality and sustainability assessments. On the other hand, the evaluation results of the IFIs suggest that engineers should be involved in *project preparation and implementation* with the perspective of risk prevention, without which development itself is threatened. Alongside other disciplines, engineers' involvement in natural disaster management and mitigation within development projects is thus essential. Based upon the evaluation experience summarised in this paper, three main types of involvement are recommended:

(1) Geotechnical engineers should be more involved:

- in project preparation (e.g. with vulnerability & loss analyses; site safety assessments, land use planning with regard to risk), design (concrete proposals for infrastructures; ex ante evaluation of different options) and implementation (supervision & monitoring of works);
- in mid-term or ex-post evaluations of international donor programmes to assess conformity of works with plan, with norms and standards, and to assess actual sustainability;
- in risk prevention and mitigation, where they are expected to deliver innovative approaches.

(2) In parallel, there is a clear need for further development of technologies related to these three issues, and in particular for risk prevention (field, visual, material testing; use of GIS; satellite and air-borne techniques, etc.)

(3) Increased dialogue between engineers and socio-economists in project preparation and impact analysis of different engineering solutions – which are inherently *socio-technical* – is expected to lead to greater project effectiveness.

REFERENCES

- Asian Development Bank (2004). Disaster and Emergency Assistance Policy, Manila.
- Inter-American Development Bank (2005). Bank Action Plan for Improving Disaster Risk Management 2005-2008, Washington.
- Andean Development Bank (2006). Iniciativa orientada a la reducción de riesgos de desastres en los procesos de desarrollo, Caracas.
- Caribbean Development Bank (2004/1998). Strategy and Operational Guidelines for Natural Disaster Management (revised version of 1998 document), Barbados.
- Council of Europe Development Bank (2006). *Evaluation of CEB Disaster Loans*, Paris.
- The World Bank (2006). Hazards of Nature, Risks to Development. An IEG Evaluation of World Bank Assistance for Natural Disasters, Washington.

CASE STUDY OF MOVEMENT AND DAMAGE TO A RESIDENTIAL BUILDING FOUNDED ON EXPANSIVE CLAYS

Jie Li

*School of Civil, Environmental and Chemical Engineering, RMIT University
Melbourne, Victoria, 3001, Australia*

This paper presents a case study of a residential house damaged by expansive soils. The field investigation revealed that the damage was caused by a combination of sewer pipe leak and stormwater leak. A back-analysis procedure using finite-element analysis is presented that is based the measured slab surface levels. The results of the back-analysis indicated that a stronger footing was required to limit differential deflection and stress level in footing to an acceptable level,

INTRODUCTION

Damage to lightly loaded structures founded on expansive soils has been widely reported throughout the world. Expansive soil is predominantly clay soil, which undergoes appreciable volume change following change in moisture content. This volume change occurs as shrinkage upon drying, and swelling upon wetting. Buildings constructed on expansive soils may be subjected to severe movement arising from non-uniform soil moisture changes. Consequently the distortion may be manifested as cracking of walls and possibly loss of function of doors and windows.

Over the last 40 years or so, a great effort has been devoted to methods of analysing and designing structural footing systems on expansive soils. However, there are a number of cases where residential structures have experienced significant cracking despite engineering design that conforms to the Australia Standard for residential footing design. Therefore, more research is needed to get a better understanding of the problem and to improve the current design approach. In this study, the field investigation and back analysis of a cracked residential building were carried out. The back-analysis procedure was based on the three-dimensional finite element method and floor slab levels obtained from a level survey of the deformed structure. The purposes of this case study are to determine the causes of deformation and cracking and to find out how failure could have been prevented. This paper presents the results of the case study.

Site Investigation

The case study described herein refers to a single storey articulated masonry veneer dwelling built on a highly expansive soil foundation. The house was constructed in March 1986 in a

northern suburb of Adelaide. Three boreholes were drilled at the site before construction to evaluate the soil reactivity. The site classification for reactivity following the Australian Standard for Residential Slab and Footings (AS2870, 1996) was Class E (i.e., extremely reactive).

The footing layout is shown in Figure 1. The external beams were 300 mm wide by 950 mm deep reinforced with 8/Y16 rods, 4 at the top and 4 at the bottom. The internal beams were 250 mm wide by 950 mm deep reinforced with 6/Y16 rods, 3 top and 3 bottom. The slab was 100 mm thick and was reinforced with F62 mesh placed 25 mm from the top surface of the slab.

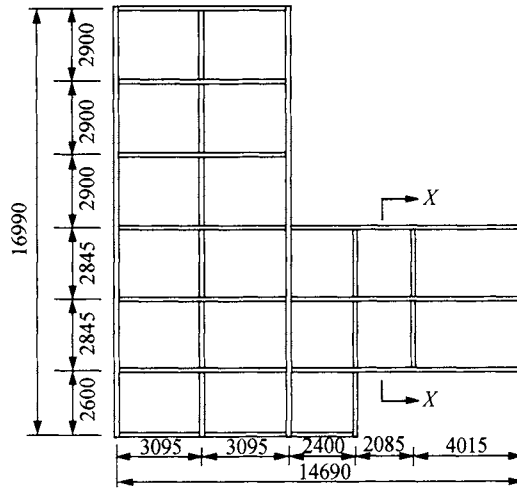
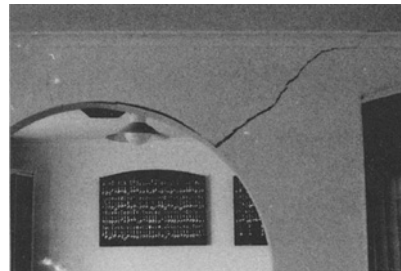


Figure 1. Case Study-Footing Layout

The site investigation was conducted by the author in February 1992. The floor of the house was distorted into a complex pattern, involving both bending and twisting. Damage to the house superstructure consisted of wall and ceiling cracking, distortion of cornices, and a slope on the floors in most rooms. Figure 2 shows cracking on the ceiling and a wall. The major cause of movement was found to be a combination of sewer pipe leak and stormwater leak, which resulted in non-uniform soil moisture conditions. The locations of sewer pipe and stormwater leak are shown in Figure 3.



(a) crack on ceiling



(b) crack on interior wall

Figure 2. Case study - crack on ceiling and interior wall

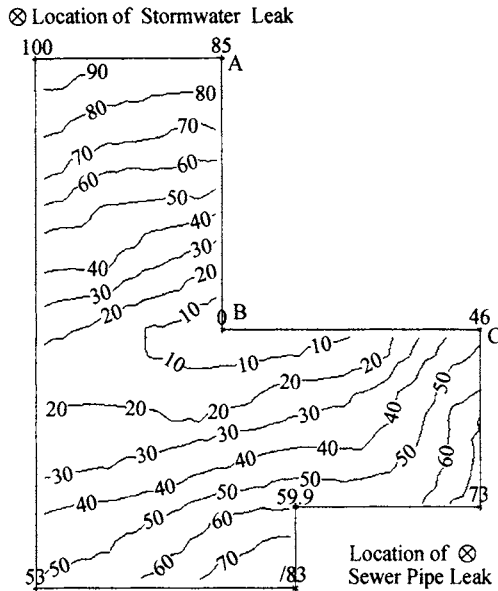


Figure 3. Contour plot of measured slab deflection (mm)

A level survey of the floor surface indicated a deformed surface as shown in Figure 3. A severe edge heave occurred in the long span. The maximum vertical differential movement of the footing was 100 mm. The differential deflection to length ratio is 1/270, exceeding the recommended maximum limit of 1/400 for articulated masonry veneer construction (AS2870, 1996).

BACK ANALYSIS

The back analysis of this distressed residential house was carried out to determine the stress level in the stiffened slab and to estimate the free soil mound shape of the expansive soil underlying the building, so that methods of preventing such failures could be recommended.

It was recognised that a suitable method of back analysis has to utilise the information available from a distorted house. The proposed back analysis procedure was based on the measured slab surface levels. It was first assumed that the slab was flat at the time of construction.

The following information was generally required for a back analysis:

- footing layout
- footing cross-section properties (including the width and height of stiffening beams, the slab thickness, the number, size and location of steel bars in all beams, and the details of the reinforcement mesh in the slab)
- the contour plot of the measured slab deformation
- recorded magnitudes and locations of cracking in the wall, floor and ceiling
- loadings on the footing (from construction)
- the soil type and soil profile

The back analysis was carried out using the finite element method. The reinforced concrete beam was modelled with one-dimensional beam elements by defining a number of lumped

rods with either concrete or steel material properties at specified distance to the neutral axis in the x and y directions. The reinforced concrete slab was modelled by several layers of two-dimensional plate elements, one layer being the uniaxial, distributed reinforcement layer which functions with perfect bond to the surrounding concrete, while the other layers modelled the concrete. A smeared crack model was adopted for the reinforced concrete slab. In this model cracked concrete was treated as a continuum, that is, cracking was taken into account by modifying the material's constitutive relationship, retaining the original discretization. The finite element model for the stiffened raft slab is shown in Figure 4.

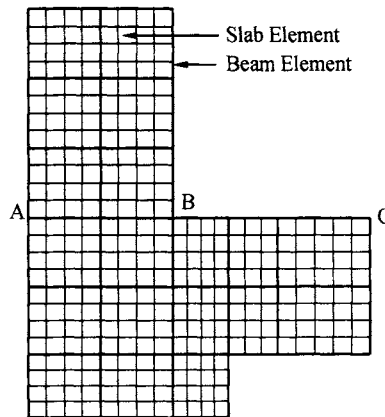


Figure 4. Finite Element Mesh

The foundation soil was modelled as a series of non-linear spring or gap elements, by specifying both the initial gap and spring stiffness. These elements allowed for separation and relative lateral displacement between the slab and foundation soil. Detailed descriptions of the finite element modelling can be found in Li (1996).

The finite element mesh is shown in Figure 4. It consisted of 608 plate elements, 196 beam elements and 348 gap elements. A line load of 6.5 kN/m was imposed along all the edges to simulate the masonry walls and roof loads, while an internal distributed load of 2.2 kPa was applied to model loading from internal partitions, the floor and live loads.

The concrete in the raft slab footing was assumed to be non-linear elastic with a compressive strength of 20 MPa and a tensile strength of 2.7 MPa. The long-term elastic modulus of concrete was 15,500 MPa in accordance with AS2870 (1996). This accounts for the influence of creep, shrinkage, age and loading on the modulus. The concrete density was taken as 2400 kg/m³ and a Poisson's ratio of 0.2 was adopted. The steel reinforcement in the beam and slab was treated as an elasto-plastic material, obeying the Von Mises yield criterion and the kinematic hardening rule. Properties adopted for the reinforcing steel were a yield strength of 400 MPa, a Young's Modulus of 200 GPa and a Poisson's ratio of 0.3. The foundation soil swelling stiffness (kPa/m) was assumed to be approximately 100q, as suggested by AS2870 (1996), where q is the average slab loading in kPa unit. The spring stiffness of each spring/gap element was therefore a function of the supported footing area.

Analyses of cracked footings resting on expansive soil profiles reported by Lytton (1970) indicate that once the tensile cracking moment has been exceeded in the slab, the footing bends easily so that it conforms very closely to the shape of the pressure-free soil profile.

Therefore it is reasonable to assume that the free soil mound shape occurring under the cracked footing is similar to, but slightly larger in magnitude than (owing to the suppression of swelling by loading) the distorted shape of the footing. The first step in the back-analysis procedure was to determine the measured deflection at each node of the finite element mesh. This was achieved by overlaying the finite element mesh on the contour plot of the measured slab displacement. The measured vertical displacements of the slab were multiplied by an amplification coefficient and were then enforced on the underside of the gap/spring elements. Assuming that the mound movement could be up to 60% larger than the slab movement, the amplification coefficient would be expected to range from 1.0 to 1.6. It was found that the selected value within this range had little influence on the final results. A value of 1.3 was used in this study. The calculated nodal displacements in the first finite element analysis run were compared with the measured footing displacements. The difference was used to modify the enforced displacement values for the second analysis. This procedure was repeated until the differences between the calculated values and the measured values were acceptably small. Five iterations were required for this case study. The final enforced displacements provided an estimate of the free mound shape under the slab, prior to any interaction with the building and its footing.

The results of the back analysis were as follows. The calculated maximum torque and bending moment in beam were 80 kNm and 399 kNm respectively. The maximum shear force in beam was 142 kN. The maximum compressive stress in concrete was found to be 13 MPa. All the above values occurred at the re-entrant corner, B (see Figure 4). The maximum concrete stress in the slab was calculated to be 1.6 MPa, less than the assumed value of 2.7 MPa for concrete tensile strength. However, the concrete tensile strength had been exceeded in beams. It was found that the steel bars at the bottom of beam along section ABC should have yielded (see Figure 4). The back analysis of the footing resulted in the free swelling mound shape shown in Figure 5.

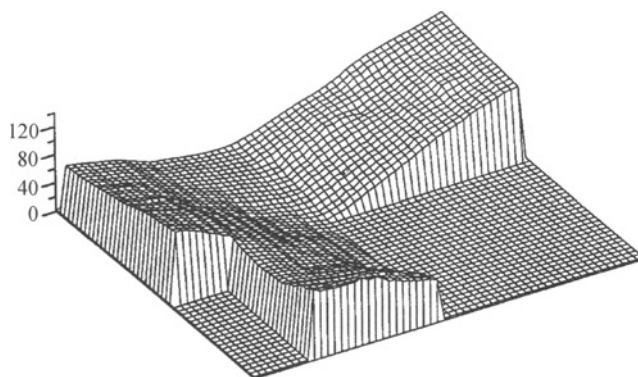


Figure 5. Free Swelling Mound Shape (mm).

Further analysis was performed with this derived mound shape to determine what size of footing was required to limit differential deflection and stress level in footing to an acceptable level while the beam layout remained unchanged. The recommended footing was given as follows.

Beam: 300 mm (wide)×1500 mm (deep), with 6/Y24 bars, 3 top and 3 bottom

Slab: 100 mm thick, with F72 mesh

The calculated maximum deflection ratio with this recommended footing was 1/1060, which is much less than the recommended maximum deflection ratio of 1/400 for articulated masonry veneer construction (AS 2870, 1996). The maximum tensile stress in beam steel and the maximum compressive stress in concrete were all reduced significantly, in comparison to the 'as constructed' footing.

SUMMARY

In this research, a case study of a residential building damaged by expansive soils was carried out. The field investigation revealed that the damage was caused by a combination of sewer pipe leak and storm water leak. A back-analysis procedure using finite-element analysis was presented that was based the measured slab surface levels. The back analysis provided a representation of the underlying ground movement. The results of the numerical analyses indicated that a stronger footing was required for the free swell soil mound shape derived from the back-analysis,

REFERENCES

- AS 2870. (1996). *Residential slab and footings*, Standards Association of Australia, Sydney.
- Li J. (1996). *Analysis and Modelling of Performance of Footings on Expansive Soils*. PhD Thesis, University of South Australia.
- Lytton R.L. (1970). *Design criteria for residential slabs and grillage rafts on reactive clay*. Report for CSIRO, Division of Applied Geomechanics, Melbourne, Australia.

STUDY ON ELECTRICAL RESISTIVITY RELATED PARAMETERS OF CONTAMINATED SOILS

Songyu Liu, Lei Chen

*Institute of Geotechnical Engineering, Southeast University,
Nanjing 210096, China*

Lihua Han

*School of resources and safety engineering, Central South University,
Changsha 410083, China*

Electrical resistivity method has been used in recent years for evaluating of contaminated soils. Based on laboratory measurement, the electrical resistivity properties such as average formation factor, average shape factor of heavy metal contaminated soils were calculated and analyzed. The relationships between these three electrical resistivity related parameters and water content, porosity, type and contaminated component concentration were discussed. Results showed that the electrical resistivity, average formation factor and average shape factor decrease with the increase of water content, while the more serious the soils are polluted, the lower electrical resistivity, the higher the average formation factor and average shape factor are achieved. These test results may provide a guideline for detecting heavy metal contaminated soils by the electrical resistivity method.

INTRODUCTION

How to evaluate the property of contaminated soil quantitatively has become increasingly important for contaminated site remediation. As a new detecting technique, electrical resistivity method has emerged for several decades.

Contaminants influence the bulk resistivity of soil (Hassanein,1996). Since contaminants are often electrolytes or organic compounds, it is possible to distinguish between contaminated and uncontaminated soils from the variation of resistivity (Fukue,2001). The value of electrical resistivity is dependant upon the contaminant types and concentration as well as temperature condition. And soil intrinsic properties could also have a great effect on it, which including soil type, porosity, degree of saturation, water content, composition, salinity of the pore water, grain size distribution, particle shape and orientation, and pore structure (Hassanein,1996 and G.L.Yoon,2001). The applicability of electrical resistivity method (Fukue,2001 and G.L.Yoon,2001,2002) has been validated by in situ resistivity cone penetration test (RCPT)(Campanella,1990) or laboratory model investigation.

Quantitative correlation between electrical resistivity and the influencing factors has not been fully established. Using the values of formation factor and shape factor to assess the

contaminated soil is rarely seen. In this paper, laboratory tests are performed to investigate the variation of electrical resistivity of contaminated soils due to change of properties of contaminated soils. Related parameters calculated from electrical resistivity, defined as average formation factor and average shape factor are also discussed.

ELECTRICAL RESISTIVITY AND MEASUREMENT METHOD

Electrical resistivity related parameters

Each type of soil possesses a natural electrical resistivity ($\Omega \cdot m$) which could be defined as the soil resistance when current passed perpendicularly across a soil cube with one meter long each side. A pioneer work of soil electrical resistivity was carried out by Archie (1942) who derived the first general relationship between the electrical resistivity of saturated soil and the electrical resistivity of its pore fluid and then presented the concept of formation factor (F), which means the ratio of bulk resistivity and pore fluid resistivity. The formation factor can reflect the soil structure and porosity, and is related to the particle shape and orientation, porosity, cementation factor and saturation degree et al. For anisotropic soil, formation factor varies with orientation, so vertical formation factor (F_v) and horizontal formation factor (F_H) are defined respectively,

$$F_v = \frac{\rho_v}{\rho_w}, F_H = \frac{\rho_H}{\rho_w} \quad (1)$$

where ρ_v, ρ_H, ρ_w are vertical electrical resistivity, horizontal electrical resistivity and the electrical resistivity of pore fluid respectively. Based on these parameters, average formation factor (\bar{F}) could be deduced as follows,

$$\bar{F} = \frac{F_v + 2F_H}{3} \quad (2)$$

Arulanandan (1988) put forward another factor named average shape factor which can describe the effect of particle shape on electrical resistivity. For tight soils, there is a relationship between average formation factor and average shape factor,

$$\bar{F} = n^{-\bar{f}} \quad (3)$$

where n is the void ratio.

Electrical resistivity measurement method

Electrical resistivity measurement instrument used in the paper is developed by the Institute of Geotechnical Engineering of Southeast University (SEU-ii) (Liu Song-yu,2004,2006). The instrument works with alternating current, low-frequency and two-phase electrodes. A series of insulating fittings and special electrode slices are also designed to work in combination with other ordinary geotechnical testing devices. The circuit diagram of the instrument is shown in Figure 1.

Since the process of electrical resistivity measurement is based on the resistance of soil sample R_x can be measured by adjusting the tunable resistance of the instrument to approach the equilibrium of the low-frequency alternating bridge, the electrical resistivity of the soil can be obtained by the following equations.

$$R_x = R \frac{R_1}{R_2}, \quad \rho = \frac{R_x S}{L} \quad (4)$$

where R_x is the measured resistance of soil sample, ρ is the corresponding electrical resistivity required, R is the tunable resistance, R_1 and R_2 are standard resistances, S is the area of the electrode slices, and L is the distance between these two electrodes.

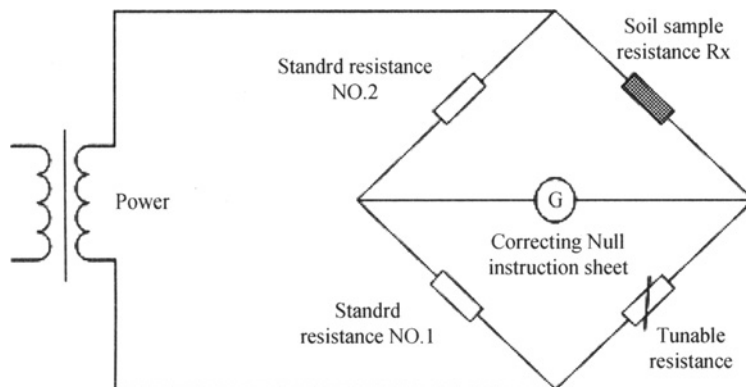


Figure 1. Low-frequency alternating bridge

LABORATORY TESTS AND RESULT DISCUSSION

Test operation

The soil is from a highway near Nanjing city in Jiangsu province of R.P.China. The operation steps of the tests are as follows: Step 1, Oven-dry the sampling soil for 10 hours, then crush it. Step 2, Divide the soil into seven equal masses of 160 grams each, and label each. Step 3, Prepare seven masses of heavy metal as the contaminant (this case CuCl_2). These masses are 0, 0.0032, 0.016, 0.032, 0.064, 0.16, 0.48 grams respectively. Place in separate beakers and add water to dissolve them. Step 4, Pour the solutions from Step 3 into the soil from Step 2, mix them adequately to ensure homogeneity, dry the specimens in an oven for 48 hours. Step 5, Crush the samples made in step 4, weigh, add pure water with designed water content to make standard oedometer test specimen with proper compaction, measure the electrical resistivity.

Results and Analysis

Effect of water content and contaminant concentration on electrical resistivity

The variations of electrical resistivity parameters of soil specimen with water content are shown in Figure 2 where the letter “c” denotes copper ion concentrations of the soil specimen. Water contents in the tests vary between 9 and 23 percentages. As water content increases,

electrical resistivity of specimen decreases. Higher ion concentrations lower the electrical resistivity. When the water content approaches to 17, the decreasing trend of electrical resistivity is obviously reduced, and the curve tends to be steady. The average formation factor and average shape factor tend to decrease with water content. As the water content approached 17, the formation factor tends to be steady and the effect of contaminant concentration is not significant as before. The higher contaminant concentration and lower water content achieve a higher average shape factor. For any water content, the effect of concentration of contaminant on shape factor is obvious.

Effect of porosity on measured electrical resistivity

The effect of porosity on electrical resistivity is examined by changing the volumetric water content with the assumption that soil particle and pore fluid are incompressible. For saturated contaminated soil, when the voids between soil particles are compressed, the pore water is squeezed out, and void ratio decreases, the volumetric water content diminished.

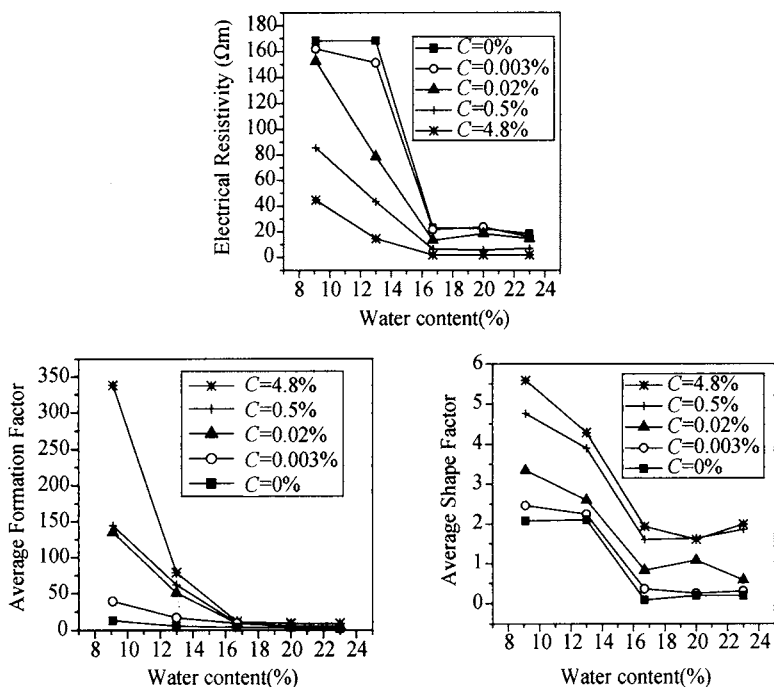


Figure 2. Variations of electrical resistivity parameters of contaminated soils with water content for different copper ion concentrations

Figure 3 illustrates the relationship between void ratio and electrical resistivity parameters of sampled copper ion contaminated soils at water content 25%. The conductivity of contaminated soil is lower when volumetric water content decreases, so which appears electrical resistivity is higher with lower void ratio. When the contaminant concentration is high, the decrement of electrical resistivity is minimal.

The decreasing trend in the average formation factor with the void ratio is also significant as following the rule of electrical resistivity. Because the electrical resistivity of pore fluid is

more sensitive than that of soil particle, for high contaminant concentration, the change of void ratio reflects greatly on the value of the average formation factor. For the average shape factor, if contaminant concentration was less than 0.3%, the relationship between void ratio and the average shape factor is not obvious. With the increasing of void ratio concentration of contaminant is larger than 0.3%, the average shape factor increases with the increasing of void ratio.

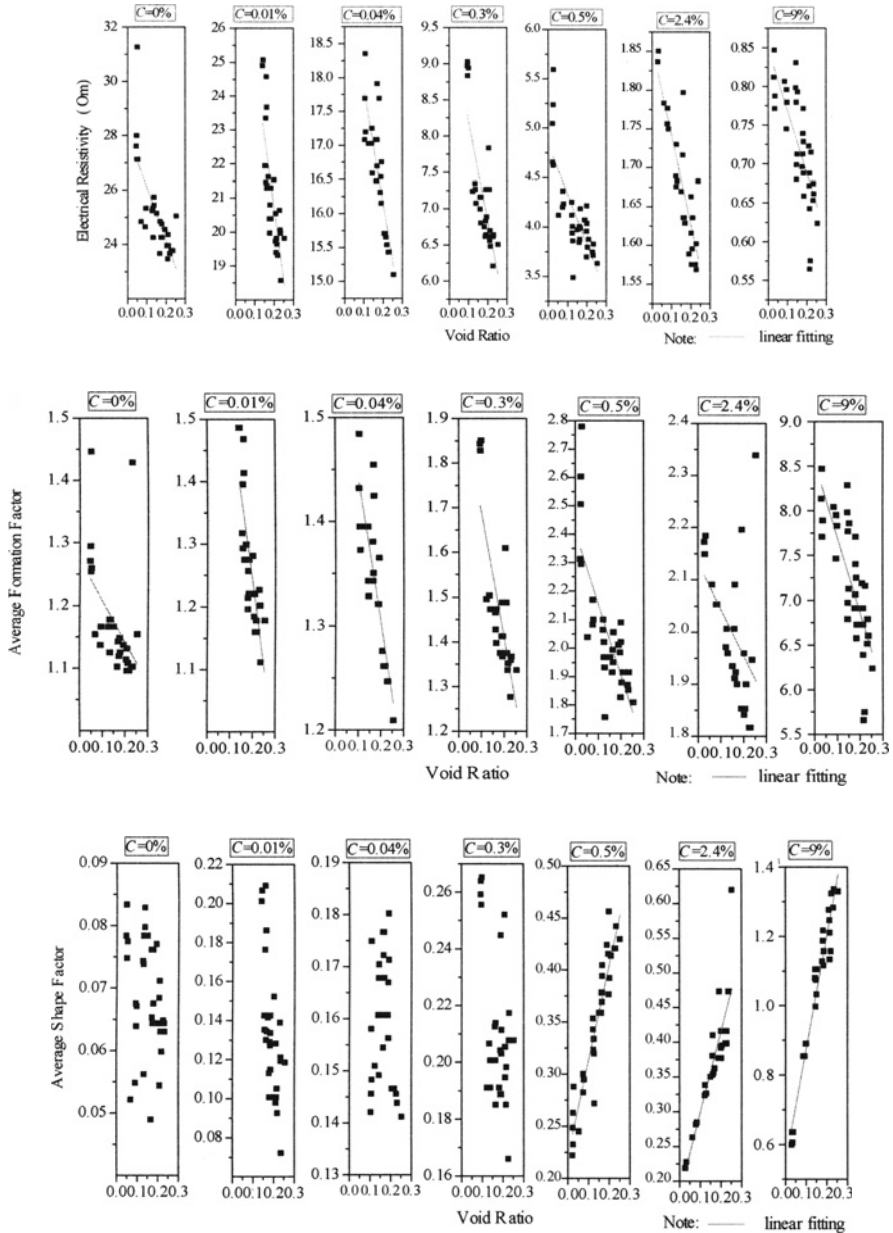


Figure 3. Relationship between void ratio and electrical resistivity of contaminated soils with different copper ion concentrations

CONCLUSION

The following conclusions are drawn based on the laboratory tests and analysis above.

(1) The water content, soil type, void ratio, type and concentration of contaminant effect the measured electrical resistivity, average formation factor and average shape factor.

(2) Electrical resistivity, average formation factor and average shape factor decrease with the increase of water content. When the water content approaches 17, the values of these three parameters tend to become steady.

(3) Higher concentrations of heavy metal ions lower the electrical resistivity. The higher contaminant concentration and lower water content, the higher the average formation factor and average shape factor values.

(4) Electrical resistivity, average formation factor decrease with the diminishment of void ratio. The higher the contaminant concentration is, the less obvious the decreasing trend of electrical resistivity and average formation factor. With the increasing of void ratio concentration of contaminant is larger than 0.3%, the average shape factor increases with the increasing of void ratio.

ACKNOWLEDGEMENTS

The authors appreciate the support of the Specialized Research Fund for the Doctoral Program of Higher Education of China under Grant No.20060286031.

REFERENCES

- Archie G.E.(1942). The electric resistivity log as aid in determining some reservoir characteristics. *Trans., American Institute of Mining, Metallurgical and Petroleum Engineers*, (146): 54-61.
- Arulanandan K., Smith S.(1973) Electrical dispersion in relation to soil structure, *J. Soil Mech. And Found Div., ASCE*, 99(12): 1113-1132.
- Arulanandan K., Muraleetharan K.K.(1988). Level ground soil liquefaction analysis using in situ properties, Part I. *J. Geotech. Engrg. Div., ASCE*, 114(7): 771-790.
- Campanella R. G, Weemes I. (1990). Development and use of an electrical resistivity cone for groundwater contamination studies. *Can Geotech (27)*: 557-567.
- Yoon G.L, Park J.B. (2001). Sensitivity of leachate and fine contents on electrical resistivity variations of sandy soils. *Journal of Hazardous Materials*, (84): 147-161.
- Yoon G.L., Oh M.H. and Park J.B.(2002). Laboratory study of landfill leachate effect on resistivity in unsaturated soil using cone penetrometer. *Environmental Geology*, (43): 18-28.
- Liu Songyu, Yu Xiaojun. (2004). *The circuit diagram of ESEU-1 soil electrical resistivity apparatus*.China Patent: ZL03222401.X, 2004-6-30.
- Liu Songyu, Zha Fusheng and Yu Xiaojun.(2006). Study on the laboratory measurement techniques of the electrical resistivity of soils. *Journal of Engineering Geology (Chinese)*, 14(01): 216-222.
- Fukue M. et al.(2001). Use of a resistivity cone for detecting contaminated soil layers. *Engineering Geology*, (60): 361-369.
- Mitchell J. K., Arulanandan, K.(1968). Electrical dispersion in relation to soil structure. *J. Soil Mech. and Found. Div., ASCE*, 94 (2): 447-471.

Pozdnyakova Larisa A.(1999).*Electrical properties of soils*. University of Wyoming.

Abu-Hassanein Z.S., Benson C.H. and Boltz L.R. (1996). Electrical resistivity of compacted clays. *J. Geotech. Eng., ASCE*, 122 (5): 397-406.

MONITORING AND FEEDBACK FOR GROUND FREEZING AND PILE-SUPPORT DEEP FOUNDATION PIT

Jianhong Lu, Yanrong Zhao and Baoyuan Yuan
*Geological and Geotechnical Engineering Department, Hohai University
Xikanglu No.1, Nanjing 210098, China*

For ground freezing and pile-support deep foundation pit of south anchorage of Runyang Bridge, ground freezing made the mechanic state of foundation pit become complex. According structure character of ground freezing and pile-support deep foundation pit, and the engineering geological condition of site, the large safe monitoring system was built. This paper introduced engineering geological condition of site, structure of foundation pit and monitoring system. Analysis the change rule of several kinds of monitoring data, and the feedback analysis was made based on the construction monitoring, guarantee the safety and stability of ground freezing and pile-support deep foundation pit of south anchorage. The monitor result indicated the ground freezing and pile-support method is viable for deep foundation pit, and the experience was backlog for construction of similar engineering aftertime.

INTRODUCTION

Ground Freezing and Pile-support is a new construction method for deep foundation pit. It was used in the south anchorage of Runyang Bridge But ground freezing made the mechanic state of foundation pit slope become more complex for ground freezing and pile-support deep foundation pit. According structure character of ground freezing and pile-support deep foundation pit, and the engineering geological condition of site, the large safe monitoring system was built.

This paper introduced engineering geological condition of site, structure of foundation pit and monitoring system. Analysis the change rule of several kinds of monitoring data, and the feedback analysis was made based on the construction monitoring, guarantee the safety and stability of ground freezing and pile-support deep foundation pit of south anchorage.

Based on the mechanism analysis of frost-heaving force emerging in the exterior-protected construction of frozen row-piles in deep foundation pit, a finite element method on elastic foundation is used to analyze the internal forces and deformation of exterior-protected construction. The method is applied in the tieback foundation engineering of suspension bridge of Runyang Changjiang Highway Bridge. And the internal forces and deformation of the exterior-protected construction in deep excavation are analyzed. Compared with the traditional methods, there is a better agreement between the calculated results and the measured ones from an actual engineering.

ENGINEERING GEOLOGICAL CONDITION

The soil layers of site of south anchorage of Runyang Bridge are consisting of clay, silty clay, pulverous sand, silver sand. The thickness of soil layers is 27.80-29.40m.

The rock layers of the site are mainly granite with interlining of lamprophyre. Strength of weathering is from strong to weaken with the depth change.

There is a fractured zone in the middle of south anchorage area, called F7 fault fractured zone. Its tendency is NE, and its obliquity is 55°-70°.

The typical geological section of site of south anchorage is as Figure 1.

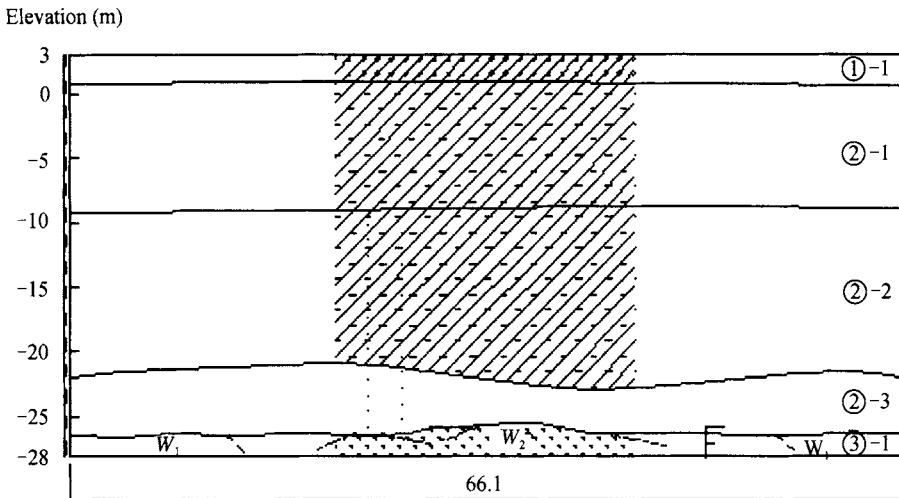


Figure 1. Geological section of site of south anchorage

STRUCTURE OF THE FOUNDATION PIT

The shape of ichnography of south anchorage foundation pit of is rectangle. Its size of is 70m×50m, the depth of foundation pit is 29m.

Support system of south anchorage foundation pit is consist of row-pile and inner-sustentation. There are 140 piles which diameter are 1.5m. Seven layers was designed for inner-sustentation

Ground freezing system is consist of 140 freezing boles, which was used for water insulation for south anchorage foundation pit .

The plane layout of south anchorage foundation pit is as Figure 2 and the profile of the foundation pit is as Figure 3.

MONITORING SCHEME OF FOUNDATION PIT

For safety of the foundation pit, a large monitoring system was built. Monitor items are included of surface deformation, inner deformation, structure stress, strain gauge, soil pressure, level of groundwater, soil temperature. Total monitoring points is 760, and monitoring boles is 54.

Figure 4. is the layout of monitoring point of south anchorage foundation pit which is used the pile-support and ground freezing method.

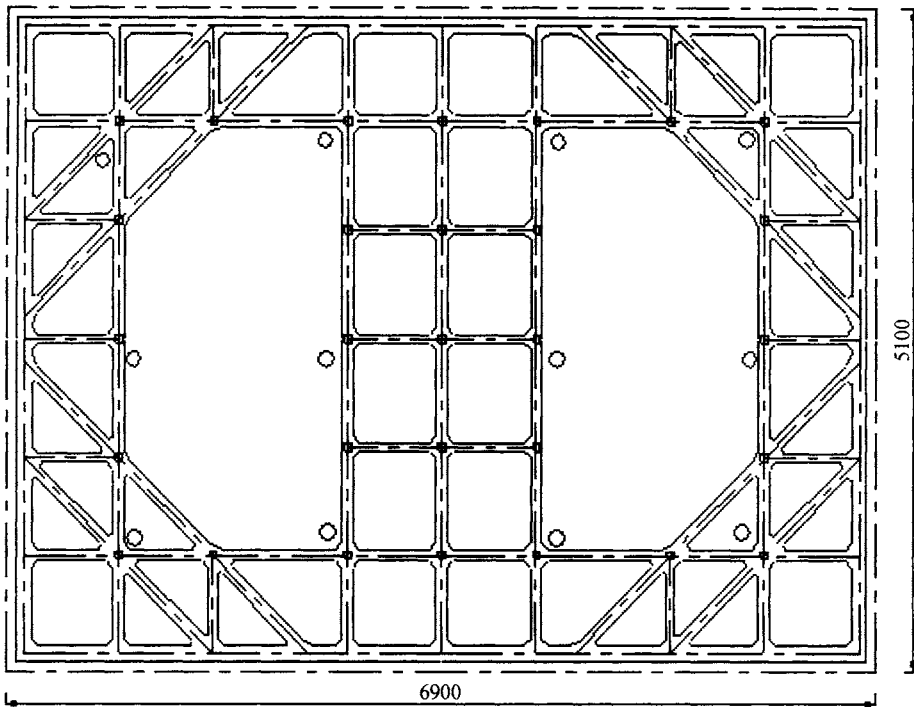


Figure 2. Plane layout of the foundation pit

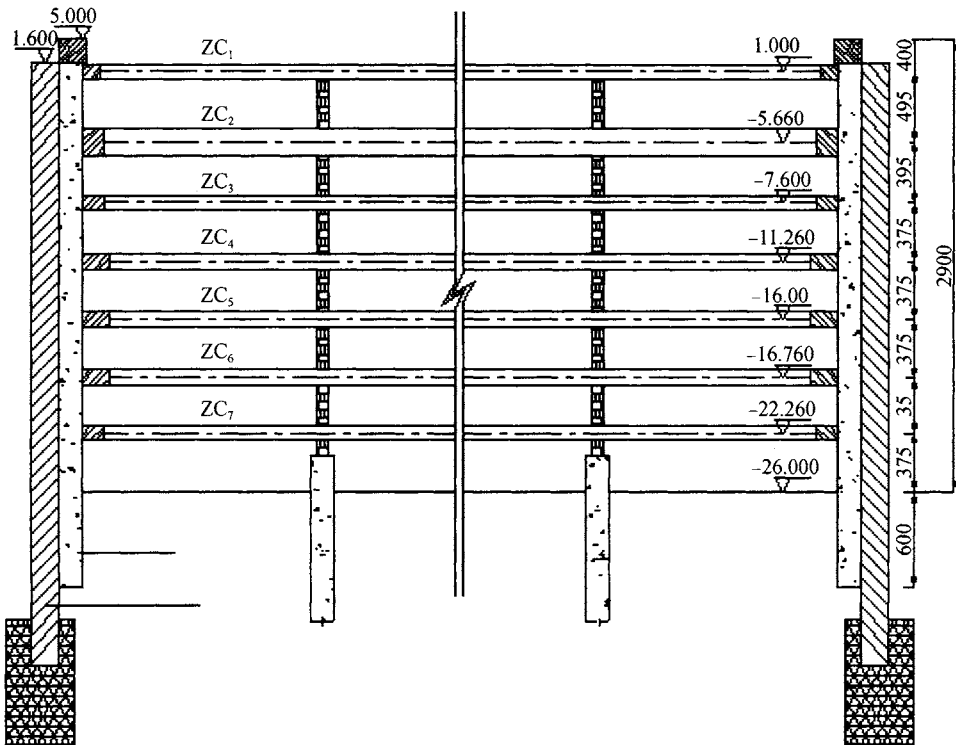


Figure 3. Profile of the foundation pit

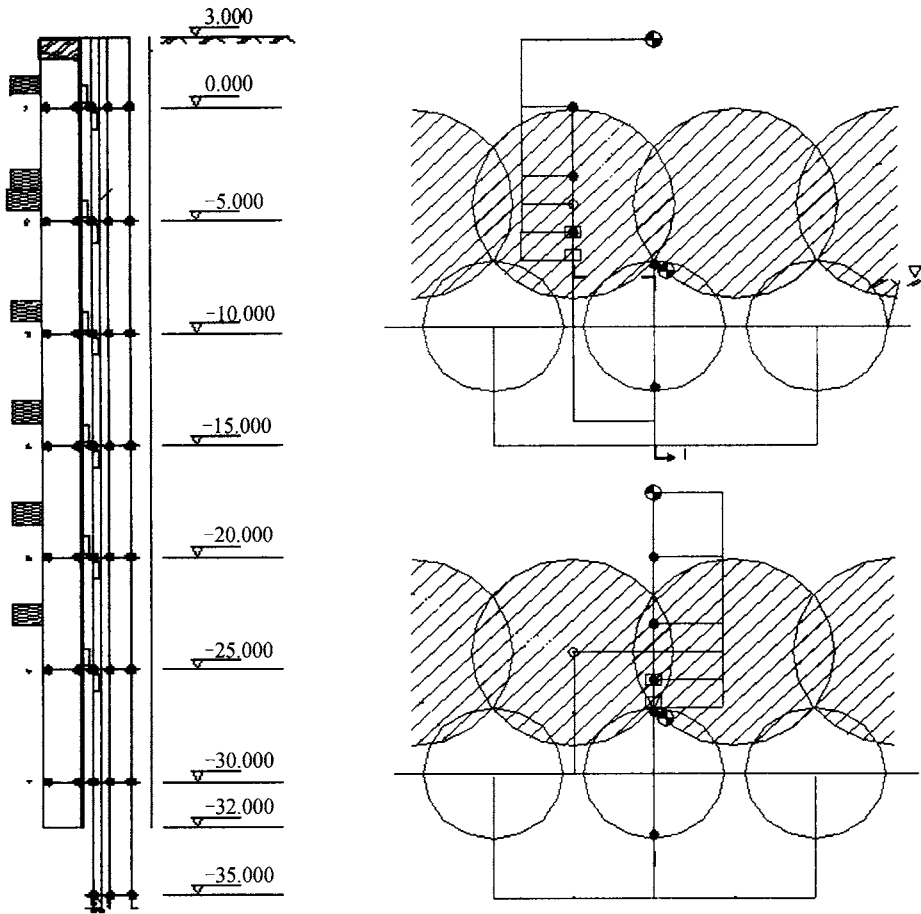


Figure 4. Layout of monitoring point of the foundation pit

ANALYSIS OF MONITORING INFORMATION INFORMATION

During the excavating process, we analyzed the monitoring information of south anchorage foundation pit dynamically.

The freezing force is analyzed by soil pressure monitoring information. Monitor data indicated the average freezing force is 0.5MPa, and changed with excavating course. Figure 5 is the temporal variation of soil pressure at the center of the longitudinal side.

The axial force is analyzed by stress and strain monitoring information. Monitor data indicated the first support and second support beard large axial force, the six support and seven support beard large axial force beard low axial force. The axial force of first support and second support is closed limit. Figure 6 is the temporal variation of the axial force of the first support.

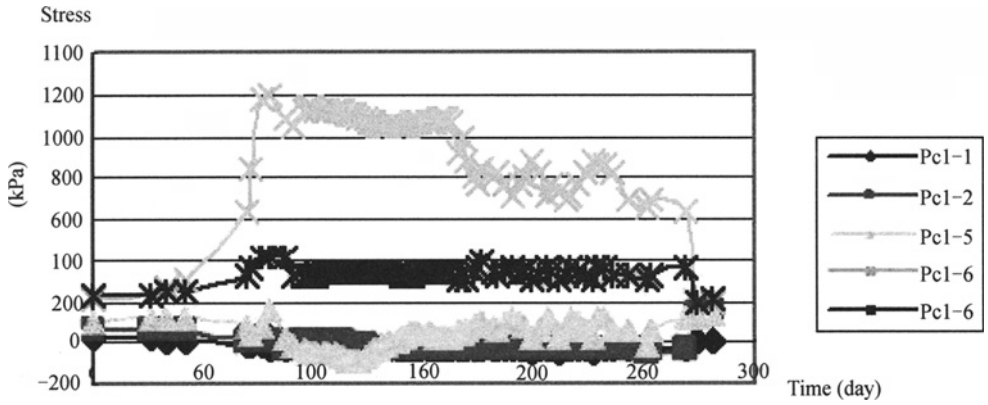


Figure 5. Temporal variation of soil pressure at the center of the longitudinal side

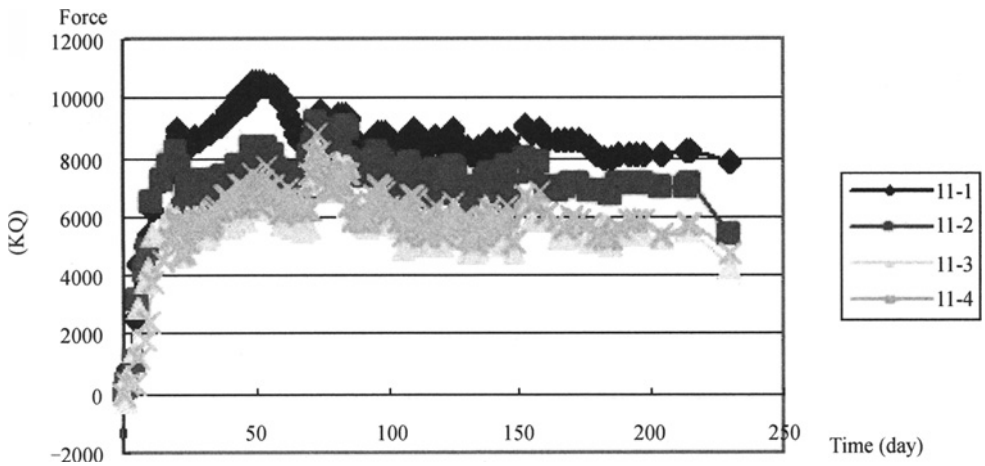


Figure 6. Temporal variation of the axial force of the first support

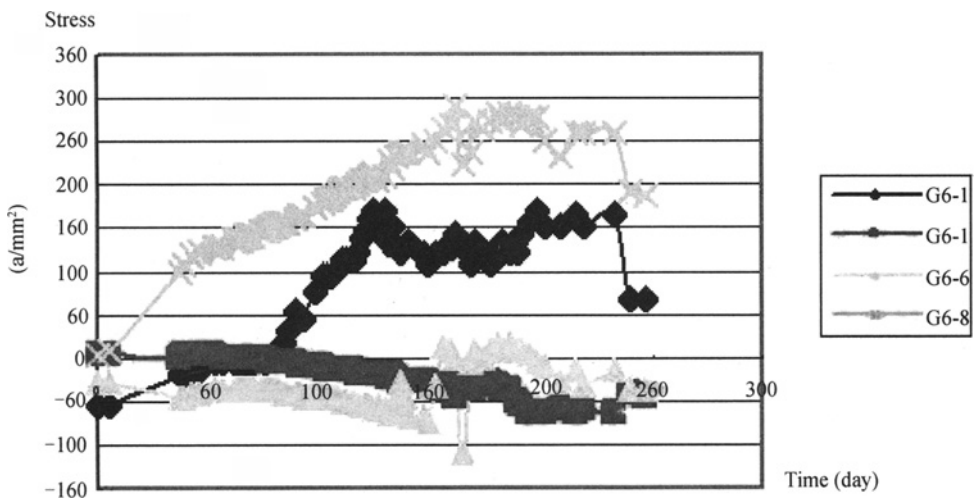


Figure 7. Temporal variation of the stress of reinforcing steel bar of row pile

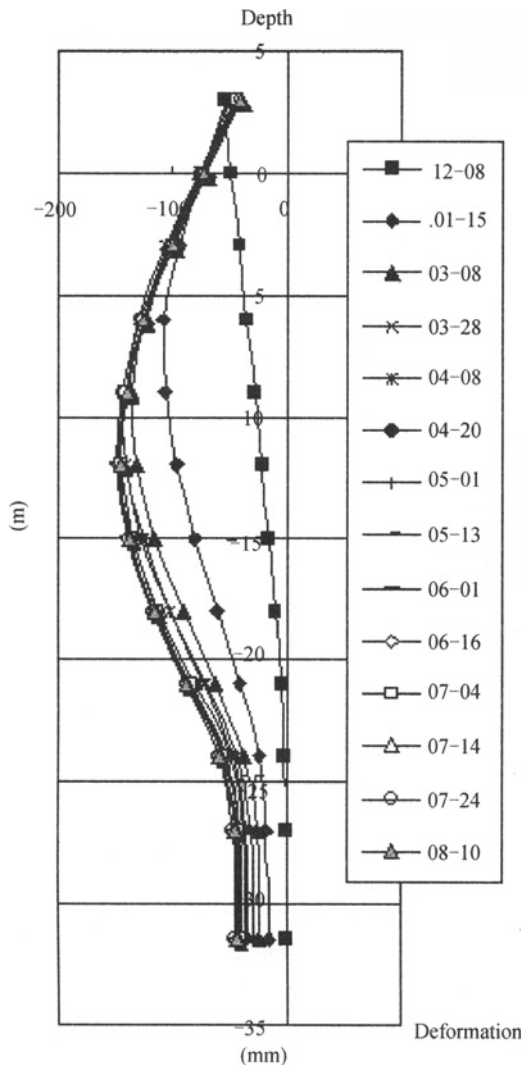


Figure 8. Displacement-depth curve in the monitoring borehole at the center of the longitudinal side

The stress of reinforcing steel bar of row pile is analyzed by stress monitoring information. The max pull stress is closed to 300MPa, which limit value is 340MPa. The max press stress is 190MPa. Figure 7 is typical curves of temporal variation of the stress of reinforcing steel bar of row pile.

The deformation character of row piles is analyzed by displacement-depth curve in the monitoring borehole. Before moulding of first support, pile is inclined toward inner side of pit. After first support moulded, the middle of pile raised toward inner side of pit, the place of max displacement is moved down, then tended to immovability. The max deformation value of row piles is 148mm. Figure 8 is displacement-depth curves in the monitoring borehole at the center of the longitudinal side.

CONCLUSIONS

According onsite monitoring, analyzing of monitoring information, numerical analyzing and based on finite element method, we can draw some conclusion.

(1) The result of monitor and the analysis indicated, the ground freezing and pile-support method is viable for construction of deep foundation pit.

(2) The monitoring data indicated the actual average value freezing force was 0.5Mpa, more then 0.2Mpa which was used in design stage.

(3) Analysis results of axial force inner support, stress of reinforcing steel bar of row pile, and deformation character of borehole, indicated that freezing force is important factor for the stability of ground freezing and pile-support foundation pit.

(4) Experience of foundation engineering of suspension bridge of Runyang Changjiang Highway Bridge was backlog for construction of similar engineering aftertime.med.

ACKNOWLEDGMENTS

The research work of this paper is supported by the Yalongjiang Water-Electricity Development United Research Foundation Project of National Natural Science Foundation of China, and Ertan Water-Electricity Development Limited Company (No.50539110).

REFERENCES

- Cheng Zhonghan. (1999). *Deep foundation pit engineering*. Beijing: Mechanical Engineering press
- Liu Da an et.al. (2000). Development and application of software system for automatic monitoring on geological engineering, *Journal of Engineering Geology* ,8(02): 213-217.
- Yao Zhishu, et al. (2004). Study on force of freezing expand of ground freezing and pile-support structure of deep foundation pit, *Chinese journal of Rock Mechanics and Engineering*, 23(9): 1521-1524.

SOIL IMPROVEMENT FOR DAMAGE MITIGATION ALONG IZMIT BAY DURING THE 1999 KOCAELI EARTHQUAKE

James R. Martin II

*Department of Civil and Environmental Engineering, Virginia Tech
Blacksburg, VA 24060, U.S.A*

C. Guney Olgun

*Department of Civil and Environmental Engineering, Virginia Tech
Blacksburg, VA 24060, U.S.A*

Ground treatment has been widely used to mitigate earthquake damages at poor soil sites. Following the 1999 Kocaeli Earthquake in Turkey ($M_w=7.4$), we studied the performance of industrial and commercial sites along Izmit Bay that had been improved. Soil conditions along the Bay consist of soft, weak soils that increase damage potential. Four sites presented here showed that soil treatment was effective in mitigating damage.

INTRODUCTION

The 1999 Kocaeli Earthquake ($M=7.4$) struck northwestern Turkey and caused major damage in urban areas, especially along Izmit Bay. This region has a number of manufacturing and industrial facilities vital to Turkey's economy, as roughly 10% of the nation's GDP is generated from this area. (Erdik, 2001). A major fault system traverses the area, as shown in Figure 1. Soil conditions along the bay are poor, consisting of soft clays, silts, and liquefiable sands that increase the potential for earthquake damage. Many sites were founded on reclaimed land. Soil improvement is being increasingly used in this region to mitigate seismic damage. Following the earthquake, the authors investigated the performance of sites where soil improvement was used.

This paper summarizes the performance of four improved-soil sites shown in Figure 1. The sites include industrial/commercial facilities within 5 km of the fault rupture. They were subjected to peak ground accelerations (PGAs) in the range of 0.2-0.3g. Various soil improvement techniques, including jet-grout columns, stone columns, and pre-load fills, were used to mitigate ground damage. Nearby facilities on unimproved ground allowed comparative assessments of seismic performance. Overall, the ground improvement was effective in mitigating earthquake damage, especially from ground failures such as liquefaction. The improved sites suffered only minimal damage and business operations were minimally affected, whereas severe ground and structural damage were common at untreated sites. An estimated 150,000 small businesses and 5,000 industrial sites were significantly damaged, each losing an average of three months of production (Erdik, 2001). This study suggests a large payoff of the mitigation investments made.

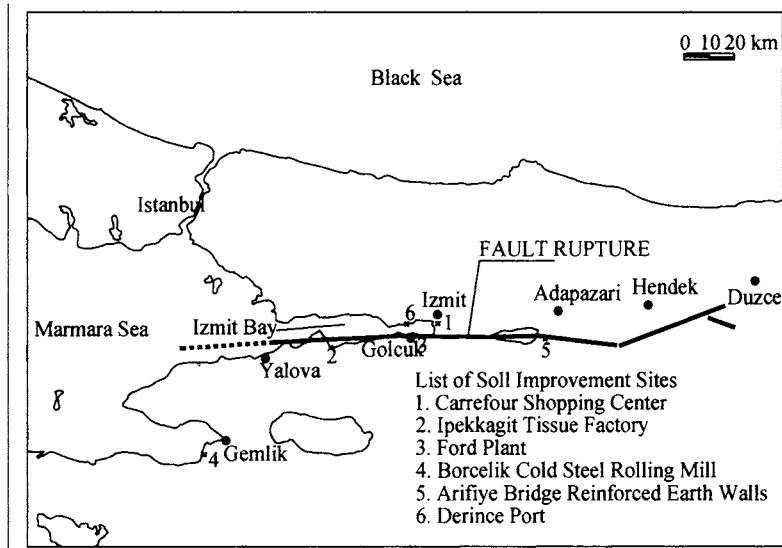


Figure 1. Map showing affected area and studied sites.

CARREFOUR SHOPPING CENTER

The Carrefour site is located at the eastern end of Izmit Bay, about 3 km from the fault rupture. A PGA of 0.25g was estimated. As shown in Figure 2, the site is 55,000 m² in plan area and consists of a shopping center and parking garage. The facility was under construction at the time of the earthquake, and the main building was 60% complete. The soil profile consists of soft alluvial sediments consisting of clays, silts, and sands, typical of reclaimed sites along the bay. With the exception of a 2-m sandy stratum at a depth of 6 m, Cone Penetration Test (CPT) tip resistances are -1 MPa throughout the upper 25 m. Standard Penetration Test (SPT) N_{1,60} blowcounts average 5 blows/ft. (bpf) in the clays, and 10–15 bpf in the sands. The water table is within 2 m of the surface.

The shopping center is founded on spread footings and mats, and covers an area of 15,600 m², as shown in Figure 2. Section A is one-story and founded on spread footings, while Section B is two-story and supported on a mat. The primary design issues were anticipated settlements in the silty and clayey strata under static loads, and liquefaction of the sand strata. An average factor of safety (FOS) against liquefaction of -0.7 was estimated for the sandy strata, and a FOS against cyclic failure of -0.9 was estimated for the clayey soils in the upper 20 m. Jet-grout columns were installed to address both the static and earthquake issues. Surcharge fills were also used for pre-loading.

In Section A, primary and secondary grids of jet-grout columns were installed to provide blanket treatment. The primary columns were 0.6 m in diameter with a center-to-center (c-to-c) spacing of 4 m, and extended to a depth of 9.0 m. A secondary grid of 2.5 m-long columns was installed between the primary columns. These truncated columns penetrated only the sand stratum, and were installed with the assumption that the higher replacement in this layer would reduce liquefaction potential. In addition to blanket treatment, groups of two and four primary columns were installed beneath the exterior and interior footings,

respectively. Section B rests on a mat foundation and was blanket-treated with primary columns at 1.5 m c-to-c spacings. No improvement was performed outside the building footprint. The area replacement ratio beneath the shopping center was about 2% for the silt-clay stratum, and 7% for the sand stratum.

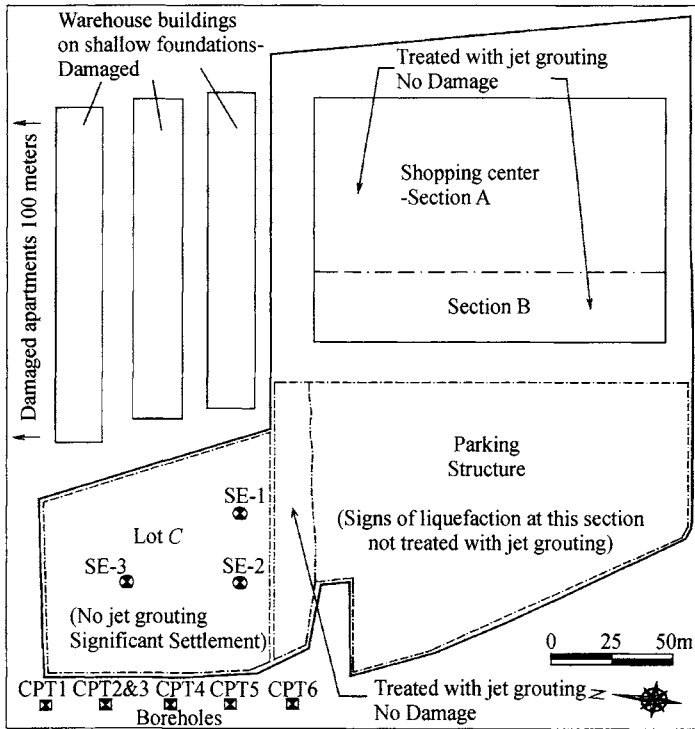


Figure 2. Carrefour shopping center site plan

The parking garage had not been built at the time of the earthquake. This area was to be improved in a manner similar to the supermarket. Jet-grouting was just beginning when the earthquake struck. Lot C is located adjacent to the parking garage and encompasses 4,160 m². No structures were initially planned for this section, but the soils were being improved in anticipation of future development. Lot C was under a 3.3 m-high surcharge fill and wick drains had been installed. Ongoing settlements beneath the fill were being regularly monitored using extensometers installed at several depths within the soil profile when the earthquake occurred.

Observed field performance during earthquake

A post-earthquake inspection showed dramatic differences between the treated and untreated sections. No settlements or ground damage were found beneath the main building, and construction resumed. In contrast, large settlements occurred in unimproved sections at the site and neighboring properties, especially beneath loaded areas. The 3.3-m surcharge fill in Lot C suffered 10-12 cm of seismic settlement, as indicated by the extensometers. Surprisingly the majority was due to the clayey strata, indicating these soils (not just sands)

were also a major source of seismic damage. Nearby 5- and 6-story apartment buildings also settled 10-12 cm. The untreated parking garage area had water ponded on the surface following the earthquake and settled 8-10 cm from consolidation of the sand stratum. A row of neighboring two-story warehouses settled 5 cm. The findings show the damage potential of Izmit Bay soils and the effectiveness of soil improvement. Major losses were common at similar properties where such mitigation was not used. The construction cost of the main building was about \$20 million, and the soil improvement cost was less than 10% of this amount, about \$1.4 million.

FORD-OTOSAN AUTOMOBILE PLANT

The Ford Otosan automobile factory, located on the southern shore of Izmit Bay, was under construction during the Kocaeli Earthquake. This major facility has a current output of 250,000 vehicles per year, 95% of which are exported (Ford, 2006). The plant employs around 8,000 total employees, and annual revenues exceed \$3 billion (Ford, 2006). A site plan is provided in Figure 3. The plant encompasses a total area of 1.5 km² (150 hectares). As shown, the fault rupture passed along the western edge of the site, and a PGA of 0.22 g was measured about 5 km from the site.

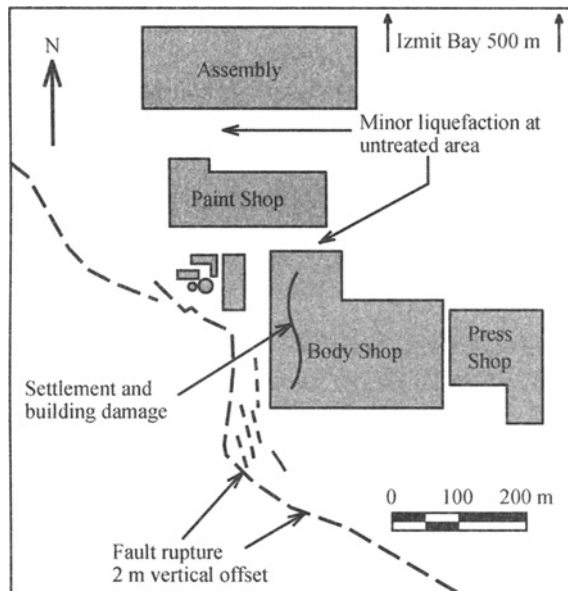


Figure 3. Ford plant site plan

Major structures include the Press Shop, Body Shop, Paint Shop, and the Assembly Shop. The structural loads for these facilities are large, and they are supported mainly on spread footings and mats. Soil investigations indicated soft clays and loose sands in the upper 10 m. SPT blowcounts for the sand and clay layers were 2-5 bpf and 2-7 bpf, respectively. The water table is within 1 m of the surface. The FOS against liquefaction in the sand and/or cyclic failure in the clayey soils, averaged less than 0.5 to a depth of 10 m. Approximately

200,000 m of jet-grout 0.8-m diameter columns, and 90,000 m of 0.8 m-diameter stone columns were installed to mitigate damages, as summarized in Table 1. Drilled shafts were also used in some locations.

Observed field performance during earthquake

Post-earthquake inspections revealed minor damages at one building, but all other treated areas were undamaged. The site underwent a global subsidence of about 2.5 m due to fault-related movements along the western plant boundary. The Body Shop, located closest to the fault, suffered differential settlements of about 1 m at the western end. Although some of the settlement was probably related to fault movements, the majority was due to post-earthquake consolidation in the fine-grained soils. No sand boils or other liquefaction evidence was found at the building. The damaged section of the building was founded on stone columns, whereas the majority was founded on stiffer jet-grout columns. Sand-boils and settlements (several cm), were observed across the site in unimproved areas, and lateral spreading was observed along the waterfront near the plant.

Overall, the performance of the improved ground suggests that the treatment was effective in mitigating damages. Unimproved industrial sites near the plant commonly suffered settlements of 10-12 cm and severe structural damages. The damage at the Body Shop caused a brief disruption, but construction could be resumed and the plant became operational on roughly the planned date in 2001. The facility represents a capital investment of \$650 million, half of which was for construction and half for equipment. The soil improvement, installed at a cost of \$25 million, about 10% of construction costs, played a key role in preventing major losses for the region and for Ford.

IPEKKAGIT TISSUE FACTORY

The Ipekkagit Tissue Factory is located along the southern waterfront of Izmit Bay, about 4 km from the fault rupture. A PGA of 0.25g was estimated. The plant is the main supplier of tissue paper products for Turkey, and a leading paper producer in Europe, exporting to more than 30 countries. Annual sales exceed \$157 million. The site encompasses 15 hectares as shown in Figure 4. Several plant additions were made before the earthquake. The Reel Storage Building, water tanks, and Paper Machine Building No.3 (PM3) had just been completed (cross-hatched areas on figure). These facilities, which nearly tripled production capacity, represented an investment of \$20 million, including state-of-the-art machinery in PM3. SPTs and CPTs revealed medium clays and sands to a depth of 32 m. The water table is within 2 m of the surface. All structures rest on shallow foundations and were susceptible to damage from large static settlements in the clays and liquefaction of the sands.

To address these concerns, the top 2 m of clay was excavated and replaced with compacted fill, and jet-grout columns were installed. The PM3 building is supported on a mat, and jet-grout columns 12 m-long and 0.6 m in diameter were installed with rectangular c-to-c spacings from 1.2 to 2.4 m. The Reel Storage Building is supported by 4.0 m-wide strip footings. Jet-grout columns 8.0 m long and 0.6 m in diameter were constructed with spacings from 1.2 m to 2.4 m. The water tanks rest on a mat foundation. Jet-grout columns

10.5 m long and 0.6 m in diameter were installed on 2.0 m spacings. The total soil improvement cost for all of the new facilities was \$600,000.

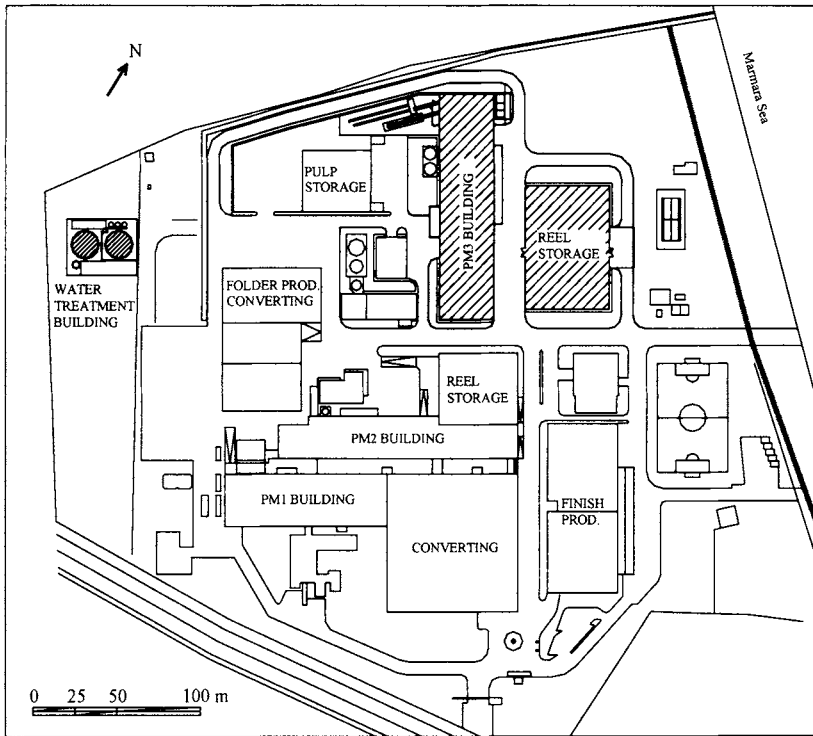


Figure 4. Ipekkagit tissue factory site plan

Observed field performance during earthquake

A post-earthquake inspection revealed no major damages and all facilities remained operational. No liquefaction or ground damage was found. Moderate structural damage occurred in an older building (PM2) where the soils were not improved. No damages occurred anywhere else at the plant. Thus, the only damage occurred where the foundation soils were unimproved. It is instructive that the paper production machine in PM3 is sensitive but suffered no damage and required no adjustments. Similar equipment at nearby plants on unimproved ground suffered damages that led to months of lost operations (Erdik, 2001). The lessons are underscored because the owners debated the decision of investing the extra \$600,000 for ground improvement. Following the event, the outstanding performance prompted the owners to acknowledge the engineers who had argued for the improvement. This case demonstrated a large payoff of the mitigation investments made for protecting the \$20 million capital investment and plant operations.

DERINCE PORT

As shown in Figure 1, Derince Port is located along the northern waterfront of Izmit Bay, approximately 5 km from the fault rupture. The general purpose port has highway and

railway connections, and serves as a vital hub for transportation and post-disaster response. The port is the largest in the region, receiving approximately 600 ships, and unloading 2 million tons of general cargo and 5,500 TEU containers each year. As one measure of its stand-alone economic value, in 2007 a private investment group bid to purchase the operating rights of the port for \$195 million, and they plan to invest another \$100 million to increase container capacity (Yukselbaba, 2007). Projected port revenues are estimated at \$100 million per year after this investment. As shown in Figure 5, the port has a waterfront about 1.5 km long, with eight wharves. Wharves 1 and 2 are not in service and are not shown. PGAs measured near the site were about 0.3g.

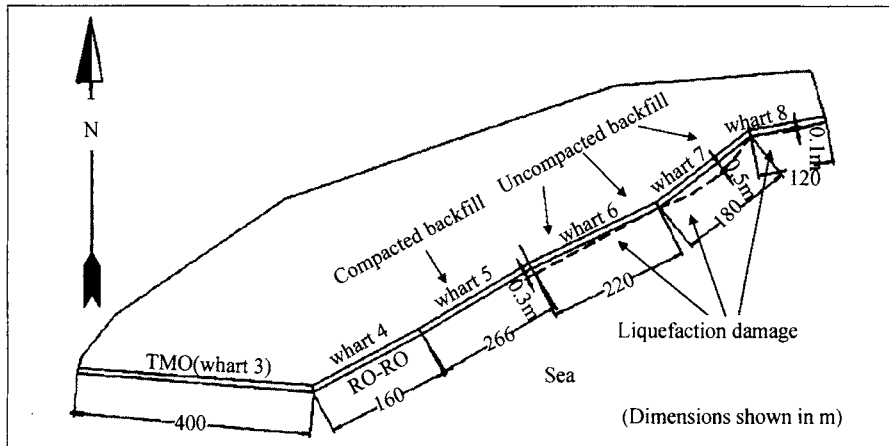


Figure 5. General schematic of derince port

The port was constructed from 1975 to 1984 using quay walls of different types. For Wharves 3, 4, and 5, quay walls were built using steel sheet piles. Stone block-type gravity quays walls were used for Wharves 6, 7, and 8. In most sections, the quay walls were backfilled with end-dumped hydraulic sandy fill, especially behind Wharves 6, 7, and 8. Penetration test data for this material were not available, but sand fills of this type are typically very loose and liquefiable. Conversely, the backfill behind Wharf 5 consisted of engineered fill that was roller compacted in lifts while the water table was lowered by dewatering. Design data for the soil improvement (compaction) were unavailable. It is not known whether soil improvement was used at Wharves 3 and 4.

Observed field performance during earthquake

Severe damages occurred at unimproved wharves during the earthquake. Liquefaction in the hydraulic backfill caused large settlements at Wharves 6, 7, and 8, along with horizontal movements of the quay walls. Wharf 7 suffered the heaviest damage, with settlements of nearly 1 m and lateral quay wall movements of 0.5 m toward the sea. Wharf 6 also suffered significant liquefaction settlements. The settlements, lateral movement of the quay walls, and strong ground shaking at Wharf 7 caused overturning of one crane and derailment of another used for offloading ships. The damage to the wharves and cranes resulted in their loss of serviceability for an extended period. Settlements and cracking along the concrete deck was

also found behind Wharves 3-4. No settlements or damages occurred at Wharf 5 which was founded on compacted backfill, and it remained fully operational. Repair costs for the damaged sections were estimated at \$12 million (World Bank, 1999). The economic impact of the damage on the surrounding region was not studied, but was probably significant, and it limited the port's role in regional response and recovery. The cost of the soil compaction at Wharf 5 is not known, but this should have been a negligible percentage of the damages suffered.

SUMMARY AND CONCLUSIONS

The Izmit Bay region of Turkey experienced strong ground shaking during the 1999 Kocaeli Earthquake. PGAs were in the range of 0.2-0.3g, and the fault rupture passed directly through the region. This industrial region is vital to Turkey's national economy. Soil conditions along the Bay are poor, which increases the potential for earthquake-induced damages. An estimated 150,000 small business suffered major damage, along with 5,000 industrial facilities. Prior to the event, a number of industrial sites were treated using various soil improvement methods to mitigate damages. Four sites located within 5 km of the ruptured fault were studied in detail. The sites covered a range of poor conditions from liquefiable sands to soft clays. The treated sites suffered minimal damages, whereas severe damages were common at unimproved sites. On average, damaged industrial/commercial facilities on unimproved ground along the bay lost three months of operation. None of the operating facilities at improved sites lost service, and construction of those that were being built could be continued with minimal disruption. The study indicates a significant payoff of the mitigation investments made.

REFERENCES

- Erdik M. (2001). Report on 1999 Kocaeli and Duzce (Turkey) Earthquakes, Department of Earthquake Engineering, *Bogazici University*, Istanbul, Turkey.
- Ford (2006), *Ford otomotiv sanayi A.S.* 2006 Annual Report.
- Martin J.R., Mitchell J.K., Olgun C.G., Emrem C., Durgunoglu H.T., Cetin K.O. and Karadayilar T. (2000). Chapter 9: Performance of improved ground and earth structures. *Earthquake Spectra*. Special Issue, 1999 Kocaeli, Turkey EQ, 191-225.
- World Bank. (1999), Turkey Marmara Earthquake Assessment, September 1999, Turkey Country Office, 50.
- Yukselbaba M. (2007). Turkerler Group Seeks Partner For Turkish Port. *Reuters News*, October 2007, from <http://uk.reuters.com/article/oilRpt/idUKL0969122120071009>.

MITIGATION SYSTEM OF COAL BUMPING IN MINING EXTREMELY THICK COAL SEAM

Hua Nan

*School of Energy Science and Engineering, Henan Polytechnic University
Jiaozuo 454000, China*

Ying Zhou

*School of Energy Science and Engineering, Henan Polytechnic University
Jiaozuo 454000, China*

Based on study of coal bumping in extremely thick coal seam of Qianqiu Coal Mine, the characters and influence factors of coal bumping are recognized. And also it can be found out that the coal bumping of extremely thick coal seam of Qianqiu Coal Mine is high stress type. So a suitable coal bumping mitigation system in mining extremely thick coal seam is built. It's proved to be effective by 21181 working face's one year production practice: during this one year time the total time of coal bumping happened is only 12.5percent of the last year and the total damaged road length of coal bumping is only 6 percent of the last year. So the coal bumping mitigation system is successful in mining the extremely thick coal seam in Qianqiu Coal Mine and it can be a good example for mitigation coal bumping in mining extremely thick coal seam with coal bumping tendency smoothly with fully mechanized sub-level caving mining technology.

DESCRIPTION OF QIANQIU COAL MINE'S 21181 WORKING FACE

Qianqiu Coal Mine, located at the center of Yima Coal Field, was developed in 1956 and went into production in 1958. Since 1986, the annual production has been steady at 0.9 Mt. The coal reserve is 70 million metric tons, which is estimated to last another 60 years. Mining for the first level has completed. So production is now concentrated on the second level. The face's length along the strike direction, oriented at N86° 23'W, is 1232m and panel width (face length) is 112m with a mineable area of 136,300m². Mining depth ranges from 617.5m to 712.5m with an average of 679.5 m. Coal seam, averaging 17.6m thick, is uniform. It strikes near the east-west direction with an average dip of 11°. Coal appears lumpy and powdery. Coal seam structure is completed. It contains 3-6 partings, 0.1-1.7m thick, including fine-grained sandstone, fine-grained sandy mudstone, and carbonaceous mudstone. The coal is semi-bright or dark, and easily susceptible to spontaneous combustion. The immediate roof is dark gray, tightly-cemented mudstone, 16.1-23.7m thick and uniformly distributed. It is brittle and breaks easily with smooth surfaces. It contains debris of plant fossils and thin streaks of fine-grained sandstone and powdered sandstone. The main roof,

being very thick, is Jurassic-colored bedded conglomerate, sandstone, and powdered sandstone. The immediate floor is dark gray conglomerate with localized floor being made of coarse clay.

DESCRIPTION AND ANALYSIS OF ITS COAL BUMPING

Description of Qianqiu Coal Mine's coal bumping

Coal bumping is a dynamic phenomenon produced by sudden deformation energy coming from the stress balance failure of rock (or coal) mass and it is one of hidden dangers of mine. Coal bumping has come nine times since the first one (happened in 14141 working face in 1988). Since then more and more production of Qianqiu coal mine are made from the No.2 level, so pressure burst of the coal mine become even serious. Now pressure burst is the No.1 danger from coal production.

Character of Qianqiu Coal Mine's coal bumping

Based on in-sit. determination and study of production record, the character of Qianqiu Coal Mine's coal bumping can be summed up as following:

- 1) Paroxysm. There is no obvious evidence before the coming of coal bumping and also there is no apparent rule in coming time.
- 2) Great destructiveness. Working face, tunnels and even supports and people can be ruined when coal bumping happened. It is the most serious disaster for the Mine.
- 3) High speed. All things come very quickly. Working face and tunnels are destroyed with great vibration and loud voice in no time.
- 4) No gassing involvement. It's proved that there is no methane content sharp raise after the coming of coal bumping.

Analysis of the influence factors of Qianqiu Coal Mine's coal bumping

There are many reasons for coal bumping. However, in general there are three types of factors that are nature factors, technology factors and management factors (Dou Linming and He Xueqiu, 2001; Xie Guangxiang and Yang Ke, 2006; Hanjie Chen, 1999). Based on this theory and concerning about practice situation, the influencing factors can be summed up as following:

- 1) Mining depth. It's known that the raise of mining depth can lead to raise of gravity stress and elastic energy in coal mass, so usually danger from coal bumping can be more serious with raise of mining depth. It's proved that when the mining depth is more than 600m, there is a very sharp raising danger from coal bumping. So it's must be very careful when the mining depth is more than 600m. As it's stated before that the face's mining depth is more than 600m, so the high depth is the key reason for coal bumping.
- 2) Mechanical property of coal. Based on coal bumping tendency theory, coal's mechanical property experiments are done, either 21 working section or 20 working section both are middle coal bumping tendency.
- 3) Roof stratum of coal. It's known that the hard and thick roof stratum above mining coal seam can benefit the paroxysm of coal bumping and the reason is the hard and thick roof

stratum can contain more elastic energy that is origin power of coal bumping. So once the hard and thick roof stratum cracked when the coal is extracted much more elastic energy is released suddenly and thus give a high occurrence of coal bumping.

MITIGATION SYSTEM OF COAL BUMPING

Plan of working face

It's well known that the nature of coal bumping is outburst of coal mass because of the larger elastic energy in the coal mass. So stress state situation is very important to coal bumping. Stress measurement results can be seen from Table 1.

Table 1. Measurement Results of Ground Stress

Stratum	Name of stress	Stress(MPa)	Orientation (°)	Inclination(°)
Floor	σ_1 (No.1 primary stress)	15.1	93.4	-12.6
	σ_2 (No.2 primary stress)	8.7	241.6	78.3
	σ_3 (No.3 primary stress)	5.9	183.7	12.5
Roof	σ_1 (No.1 primary stress)	21.9	243.1	-11.3
	σ_2 (No.2 primary stress)	13.7	39.9	-9.1
	σ_3 (No.3 primary stress)	7.9	151.4	-7.7
Coal seam	σ_1 (No.1 primary stress)	18.9	110.3	-8.3
	σ_2 (No.2 primary stress)	11.3	12.6	-26.6
	σ_3 (No.3 primary stress)	9.2	221.5	-61.7

From our research it can be revealed that when direction of drift ways are parallel to orientation of No.1 primary stress of coal seam far less coal bumping will happen. So the direction of 21181 working face was designed to be parallel to its No.1 primary stress.

Also the length of working face is critical to the happening of coal bumping. It's obvious that the shorter the face's length is, the higher stress concentration will produce. It's proved to be true that extremely thick coal seam face's length will never shorter than 90m.

Pre-infusing water into coal mass

It's recognized that by pre-infusing water into coal mass it's strength, dynamic failure time, index of elastic energy and index of impact energy all can be decreased apparently. Also by pre-infusing water, the water content of coal mass can increase about 1.8 percent which can decrease 20 percent of coal dust produced in mining, therefore a more comfortable and safe mining environment can be produced by pre-infusing water (Nan Hua, 2007; Zhang Mengtao, 1987; Li Xinyuan, 2000). The comparison experiments between ordinary coal sample and damp coal sample (infused one week) from 21181 working face were made and the results can be seen from Table 2.

Table 2. Results of Seam's Coal Bumping Experiment

Items	Ordinary Coal Sample	Damp Coal Sample
Uniaxial Compressive Strength/MPa	20.1	6.5
Dynamic Failure Time/MS	110	76
Index of Elastic Energy/W	2.2	
Index of Impact Energy/K	3.9	2.0
Experiment Results	Middle Tendency	No Tendency

It's can be seen from above theory analysis and experiment of coal sample from 21181 working face that the measure of pre-infusing water into coal mass is effective for mitigating of coal bumping in mining extremely thick coal seam. However, how to infuse water into coal mass and what is the best model will be another two problems. It can be stated as following on the basis of our study:

1) Using long bore parallel working face infusion method.

2) Make sue of that pre-infusion time from infusing water into coal mass to it be mined is not less than one month and not more than three months. Because if pre-infusion time from infusing water into coal mass to it be mined is too short, the distance from infusion working site will be near the mining working face and it may be in the scope of advancing abutment zone, so the absorbing effectiveness of water will be decreased by the short absorbing time and lots of fractures in coal mass. However, if pre-infusion time from infusing water into coal mass to it be mined is too long, the water absorbed by coal mass will be evaporate before its mining.

3) Infusion parameters can play an important role in doing a effective pre-infusing water job. The value of infusion parameters of 21181 working face's air drift way can be decide as: diameter of bore is about 50mm, distance between adjoining bores is about 15m, infusion pressure is about 50MPa, infusion discharge is about $15/m^3h^{-1}$.

Pressure parting

Pressure parting is a method of making fractures by drilling high-pressure water into pre-made holes in coal mass. Its theory can be said by the following formula:

$$p_i = 3\sigma_y - \sigma_x + T \quad (1)$$

p_i —the minimum pressure of high-pressure water, MPa;

σ_x —y direction's stress of plane vertical to man-made holes in coal mass, MPa;

σ_y —x direction's stress of plane vertical to man-made holes in coal mass, MPa;

T —the tensile strength of coal mass, MPa.

Usually the crushing radium of pressure parting can amount to 15-25m. By the high-pressure water drilling into coal mass's hole, coal mass around the hole can be divided into lots of pieces and then can absorb a certain amount of elastic energy of coal mass, so it can avoiding coal burst. It's proved to be a effective mitigation method in mining extremely

thick coal seam by coal mine's production activities. This method can also be good to gas emission in coal mass. As it's stated above, direction of σ_1 almost is the direction of σ_x , from measurement results of ground stress, it can be concluded:

$\sigma_x=17.8$ MPa; $\sigma_y=13.6$ MPa; $T=1.5$ MPa. So the first pressure of pressure water can be calculated by formula (1): $p_i=24.5$ MPa

The pressure of water and distance between adjoining holes can become more reasonable by the electromagnetic emission in-sit. test results during pressure parting in coal mass and it's found out that the suitable water pressure of 21181 working face is between 28MPa and 36MPa and the suitable adjoining distance is between 14m and 26m.

Whipping explosion

It's recognized that coal mass' elastic module and compressive resistance will decrease after whipping explosion, and it can be summed as coal mass' s "soft effectiveness". And also new produced fracture's quantity and length will become bigger with whipping time and stress's growth. As a special explosion, whipping explosion is aimed at make a fully whipping effect in coal mass in the maximum scope with the minimum explosive charge. What's important, whipping explosion should make high stress zone move into coal mass but must not throw out spoiled coal body. So depth of bore, explosive charge of one bore and blasting bores in one time and other parameters is critical to a successful whipping explosion. Energy of whipping explosion (E_w) can be calculated by formula (2):

$$E_w = \frac{\sigma_0 \varepsilon_0 + (\sigma_0 + \sigma_b)(\varepsilon_b - \varepsilon_0)}{2} - \frac{\sigma_0 \varepsilon_0 + (\sigma_0 + \sigma_a)(\varepsilon_a - \varepsilon_0)}{2} \quad (2)$$

Parameters can be seen from Figure 1.

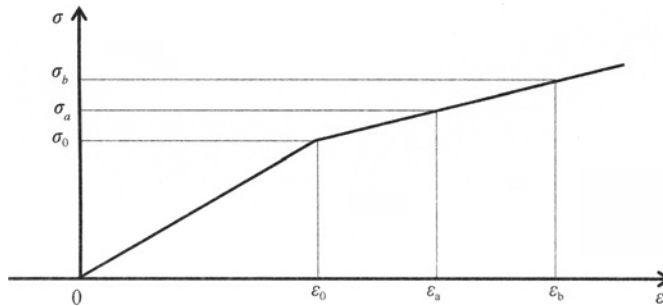


Figure 1. Schematic diagram of $\sigma - \varepsilon$

The practiced whipping explosion parameters of 21181 working face can be as following: depth of bore is 8.6-14.8m, explosive charge of bore is 4.0-6.0kg, distance between adjoining bores is 6.0-10.0m, blasting bores in one time is 36-48. When practicing whipping explosion, it must make sure that no body be in the distance of 400m and no body can get into the working place within 60min after whipping explosion.

On basis of above work, mitigation system of coal bumping in mining extremely thick coal seam can be built as following:

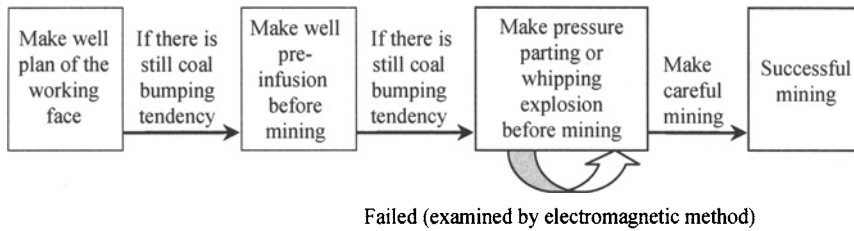


Figure 2. Mitigation system of coal bumping

EFFECTIVENESS OF MITIGATION SYSTEM

The effectiveness of pre-infusing water into coal mass, pressure parting or whipping explosion all can be examined by electromagnetic method.

However, as for the hole effectiveness of mitigation system, it can be said by the following statistic: during this one year time the total time of coal bumping happening is only 12.5 percent of the last year and the total damaged road length of coal bumping is only 6 percent of the last year. And what's important, this year no one was injured by coal bumping events.

SUMMARY

By taking the Mitigation System, the extremely thick seam can be mined with fully mechanized sub-level caving mining method safely. Presently the maximum monthly output of 21181 working face is 0.28Mt and the actual annual output may achieve 2.6Mt. So it can be conclude that the coal bumping mitigation system is successful in mining the extremely thick coal seam in Qianqiu Coal Mine and it can be a good example for mitigation coal bumping in mining extremely thick coal seam with coal bumping tendency with fully mechanized sub-level caving mining technology.

ACKNOWLEDGEMNETS

The financial support for this study through the Fund project: Grave Project of Henan Province (322020700) , Education Department Project of Henan Province (133014)

REFERENCES

- Dou Linming, He Xueqiu. (2001). *Theory and technology of rock burst prevention*, Press of China University of Mining.
- Hanjie Chen. (1999). *Stress analysis in longwall entry roof under high horizontal stress*, USA: West Virginia University.
- Li Xinyuan. (2000). Discussion on instability and damage of surrounding rock-coal mass system and prediction of rock burst, *Journal of China university of mining & technology*, 29(6): 633-636.
- Nan Hua. (2007). The safe system of mining extremely thick coal seam with coal bumping tendency. *China paper online*: 200703-340, <http://www.paper.edu.cn>

- Xie Guangxiang, Yang Ke. (2006). Surrounding rock abutment pressure distribution and thickness effect of dynamic catastrophic in fully mechanized sublevel mining stope, *Journal of China coal society*, 31 (6): 731-735.
- Zhang Mengtao (1987). The instability theory of rock burst and the numeration of numerical simulation, *Journal of rock mechanics and engineering*, 6 (3): 197-204.

A NEW KIND OF THREE-DIMENSIONAL STEEL BAR SHOTCRETE LINING AND ITS APPLICATION IN SOFT ROCK TUNNELS

Jianyong Pang

Anhui University of Science & Technology,

Huainan 232001, China

A new kind of tunnel supporting was put forward on the basis of anchor spray support principle. The mechanics of the new three-dimensional steel bar shotcrete lining support was studied and structure's internal forces were analyzed. The model experiment was done relying on the industrial test. The conclusion of numerical calculations proved that ANSYS program was reasonable and creditable. It was compared to other kinds of supporting that used commonly in soft rock tunnels. The technique and economic contrasts of the typical tunnel with support three-dimensional steel bar were completed.

INTRODUCTION

At present, there are many kinds of supporting styles in coal mine tunnels. They include steel-bracing, bolting-shotcrete, bolting-mesh-shotcrete, anchor rope and so on. Meanwhile, the shape steel bracings and the series of bolting-shotcrete are widely utilized to support the soft rock and high stress tunnels.

Shape steel bracings

The shape steel bracings including U-shaped and I-shaped steel were first put into use in Germany in 1932. The later is little used because it has no compressibility and can't adapt to the large deformation of the soft rock tunnels. On the contrary, the U-shaped steel bracing has better cross section and geometric parameter, and it can be easily compressed by means of the lap joints. So the U-shaped steel bracing is widely used for the supporting of the soft rock mass.

For all that, its applying effect is not very satisfied because of the following reasons. The U-shaped steel bracing has weak strength. It can't effectively control the large deformation of the tunnels especially at the position between bracings, resulting in low rate of the bracing return and high cost of the tunnels.

It is well known that the bending moment causes the ultimate bearing capacity of the bracing. Its compressibility is the greatest advantage of the U-shaped steel bracing. In practice, because this supporting can't bear the large lateral stress and unequal load, it will lose its load capacity and stability. It maybe destroyed when the bracing has small

compression. This contributes to decreasing predominant mechanical behavior of the U-shaped steel bracing.

Bolting-shotcrete and bolting-mesh-shotcrete

Bolting-shotcrete supporting

Early in 1872, the bolting-shotcrete supporting was first invented to strengthen the open mining slope in England. It was widely used in metal mine, irrigation and underground structure until 1950's. Because this kind of supporting was efficient, economical and safe, it developed rapidly all over the world. The development of bolting-shotcrete supporting promoted the research of shotcreting. Especially in Japan, a new kind of shotcreting technology was invented (It was called SEC) based on the dry and wet shotcreting principles. The SEC can raise the shotcreting strength with little consume of concrete.

Bolting-shotcrete changed the tunnel supporting from passive supporting into active one. Combined with surrounding rock, the bolting-shotcrete supporting can not only reinforce the broken rock, but also form a compound arch. The carrying capacity is enhanced largely.

In spite of this, the bolting-shotcrete can not fundamentally solve the problem of soft rock tunnel supporting when the geologic condition aggravates. It is essential to improve the supporting structure.

Bolting-mesh-shotcrete supporting

Compared with the bolting –shotcrete, this kind of supporting adds one layer of steel mesh which can improve the mechanics of the shotcreting. The steel mesh enhances the bending resistance and shear strength of the concrete. It can also protect the rock mass of the tunnel from weathering and falling down. The stress in the shotcreting is more evenly distributed.

However, it is impossible to withstand strong deformation pressure of the soft rock mass by mean of adding one layer mesh in the shotcreting. In the past few years, some measures including adding the anchorage length and using two layers of mesh were taken into account. The soft rock supporting effect was improved to some extent. Without any question, it will be the most effective and economical method for the soft rock tunnel supporting by improving the structure of the mesh.

Three-dimensional steel bar shotcrete

As has been stated above, the improvement of the bolting-shotcrete emphasizes on the interior reinforcement with little enhancement of the strength and rigidity. The shape steel bracing, on the contrary, its surface strength is very strong while there is no interior reinforcement resulting in large consumption of steel and the high cost of the tunnel supporting. The surface bearing and interior strengthening must be taken into account at the same time for the stability of the high stress and soft rock tunnel.

Early in 1980's, the lattice-shaped metal brace welded with reinforcing steel bar was developed in Germany and China, which replaced the profiled bar used as the reinforcement inside the supporting shotcrete of the tunnel. However, similar to the U-shaped and I-shaped profiled bar bracings, the lattice-shaped brace also has the deficiency that the concrete between reinforcement bars can't support the pressure caused by large soil deformation for its

weak strength. To deal with the weakness, a three-dimensional steel bar shotcrete supporting, based on the mechanical theory of large-span shell structure, was present. Figure. 1 shows the structure of this kind of new supporting. It not only can be used to support the tunnel solely, but also the half-rigidity reinforced concrete lining can be formed after spewing concrete. With whole structural compressibility, it was also found that the new structure had an ability to sustain the great soil pressure and dynamic force on it. The practical test result of the new lining shows that it can improve the lining ability with less material. This kind of supporting is a well-structured one, which can sustain great pressure and can be constructed easily. Meanwhile, the model test and the practical experiment in the soft rock tunnel proved successful.

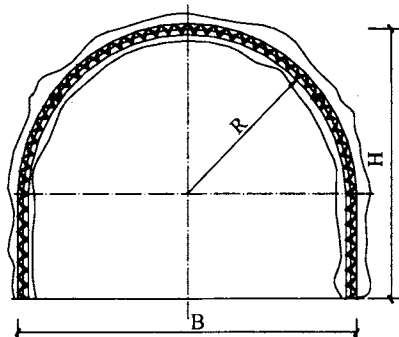


Figure 1. Structure of three-dimensional steel bar

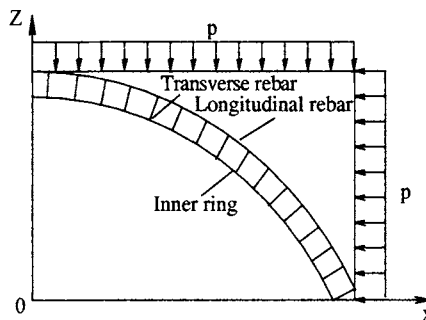


Figure 2. Calculative model of the three-dimensional steel bar shotcrete

THEORETICAL ANALYSIS AND MODEL TEST

Theoretical analysis

It is very complex to analyze the three-dimensional steel bar shotcrete using the finite element method by combining the three-dimensional bar with the slab shell. To illustrate the stress computational method for the three-dimensional bar, one arch structural piece is only considered to compare the difference of stress distribution between the normal bolting-mesh-shotcrete and the three-dimensional steel bar shotcrete. Figure 2 shows the model of the numerical simulation when the p is loaded on the structure.

Half of the arch structure is considered because there are two symmetrical sections in longitudinal and lateral direction. The triangle elements are used in the analysis of the three-dimensional steel bar shotcrete. The steel mesh is located in the middle of the shotcreting for the normal bolting-mesh-shotcrete supporting. Its material, thickness and element division are similar to the three-dimensional steel bar shotcrete. Therefore, there are three calculation models which can be equally presented as follows:

$$[K]\{\delta\} = \{F\} \quad (1)$$

Where $\{\delta\}$ is the displacement of the total node, $\{F\}$ is the total equivalent node loading, $[K]$ is the structure rigidity matrix. The following is the method for $[K]$

calculation.

As the three-dimensional steel bar is loaded lonely, then

$$[K] = \sum_m [K]_m \quad (2)$$

As the three-dimensional steel bar and shotcreting are loaded, then

$$[K] = \sum_m [K]_m + \sum_l [K]_e \quad (3)$$

As the normal steel mesh and shotcreting are loaded, then

$$[K] = \sum_n [K]_n + \sum_l [K]_e \quad (4)$$

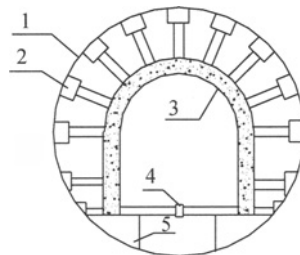
where $[K]_m$ is element rigidity matrix of the three-dimensional steel bar, $[K]_e$ is the element rigidity matrix of the shotcreting, $[K]_n$ is the element rigidity matrix of the normal steel mesh.

An example completed before illustrated that the sinking of normal mesh shotcrete arch crown is bigger than the three-dimensional steel bar shotcrete because of the different reinforced style. The normal mesh shotcrete has high flexibility while the three-dimensional steel bar shotcrete has high rigidity. Meanwhile, the bending moment in the three-dimensional steel bar shotcrete is much smaller than that in the normal one.

The numerical calculation consequences indicate that the structure of the new three-dimensional steel bar shotcrete is very reasonable. This kind of new structure not only can bear the loading lonely but also is the good skeleton of the shotcreting.

Model test

Figure 3 shows the test device for the total frame of the three-dimensional steel bar shotcrete. The total frame consists of one piece arch and two piece straight walls. The model structure is the same as the practical one. With the geometric size being 1:1.5, the following is the similar parameters. Thickness of concrete is 100mm, the radius of arch crown is 1750mm and the bottom span is 3500mm. The diameter of the main reinforcement is 22mm, while the constructional reinforcement diameters changing from 8mm to 16mm. The concrete strength is C20.



1—loading foundation pit 2—hydraulic jack 3—three-dimensional steel bar shotcrete
4—lateral bracing 5—bottom pedestal

Figure 3. Load test device of the three-dimensional steel bar shotcrete

There are 13 hydraulic jacks evenly distributed around the test model. The bottom of the frame is fixed by the huge steel pedestal. The pressure ratio of straight wall and arch is 0.8. The destruction order was the following. Small craze appeared on both straight walls firstly. Secondly, the right straight wall was broken and the whole lining lost its stability. On the contrary, the arch of the model was integral. The breaking load was about 1000KN. The carrying capacity is the same as the U29-shaped steel. It must be increasing if the both straight walls become curved ones. Figure 4 shows the destruction of the model text.

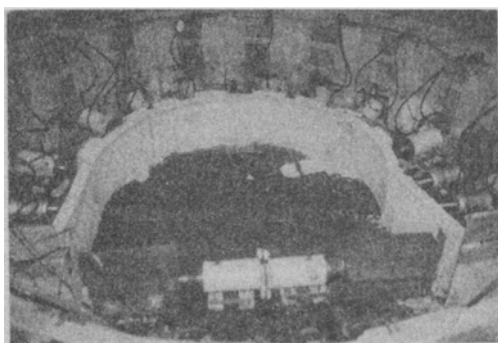


Figure 4. Destruction of the model text

ANSYS ANALYSIS COMPONENT OF THE THREE-DIMENSIONAL STEEL BAR

Using ANSYS for the three-dimensional steel bar of numerical modeling, a certain assumption needs to be made: (1) Entirety of shell component is integrity. It does not consider the action of coupling bolt in wiring point of top shell and side shell. (2) Outboard surface of shell component is bearing the uniform confining. (3) It does not consider the force of coupling tendon. (4) Displacement of reinforcement bar and concrete are coordinated. (5) It does not consider the stress relaxation of the concrete.

Establishing the finite element model

(1) Determining unit and defining parameter

In reinforced bar, main tendon and constructional steel bar adopt the secondary steel, coupling tendon adopt the primary steel. Concrete adopt C20 which always is used in shotcrete. Chart1 shows the specific parameters of the two materials.

Table 1. ANSYS model parameter of the three-dimensional steel bar

	Material	grade	Maximum intensity (MPa)	$E(\text{MPa})$	μ	Real constant R
Concrete Reinforcement bar	Main tendon	Secondary-order	350	2.0×10^5	0.3	452.4 mm^2
	Constructional steel bar	Secondary-order	350	2.0×10^5	0.3	153.9 mm^2
	coupling tendon	First-order	250	2.1×10^5	0.25	50.3 mm^2
concrete		C20	28.1(compression stress) 2.8(strength of extension)	2.55×10^4	0.2	

(2) Building model and partition graticule

Building model adopt the way of separated displacement coordination. According to assume condition, the same geometric parameters of the similar model build model is used. While analyzing and calculating the component of the three-dimensional steel bar, numerical modeling only takes 1/2 model to do it.

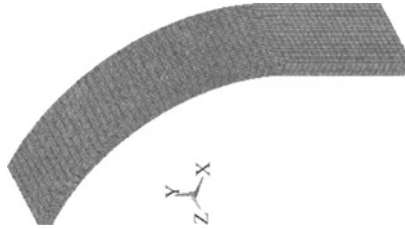
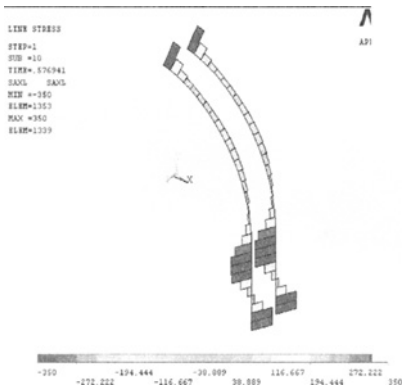


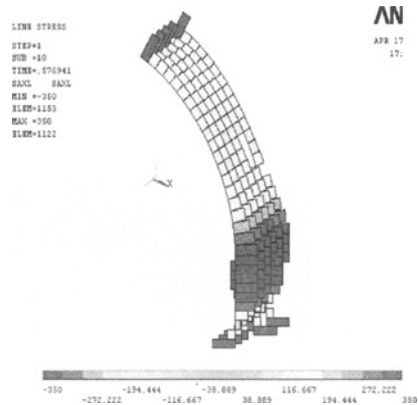
Figure 5. graticule partition of model

Analyzing the derivation consequence

(1) Analyzing interior force and deformation

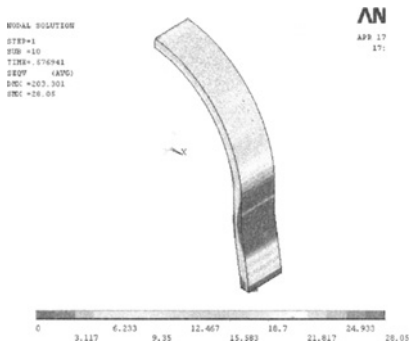


(a) curve of main tendon axial strain

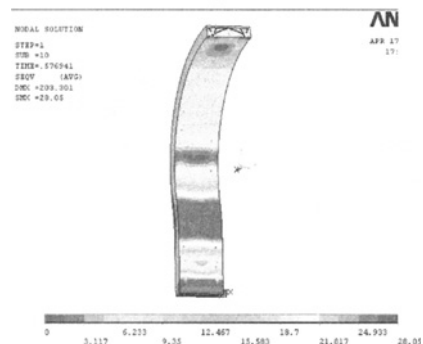


(b) Curve of construction reinforced bar axial strain

Figure 6. Curve of the reinforced bar unit strain



(a) outer



(b) interior

Figure 7. Curve of concrete unit strain

Analyzing the consequences data of model, which is came from the general processor program. The stress distribution of calculated results used the ANSYS finite element program of the numerical model mentioned above.

Entering POST26, we select the model to analyze and discuss the unit interior force of the dangerous cross-section done by the load. Defined the steel bar into main tendon and constructional steel bar, variant of axial stress and axial strain (elastic strain and plastic strain) of the unit and node are required. Using the elastic strain and plastic strain defined above is to get the total strain of the reinforced bar through executable program of the ADD order. Defined the interior force component of concrete model's unit where is the median of the medial surface is our required. Figure 8 is the time history (load diagram) of the stress variant of the unit.

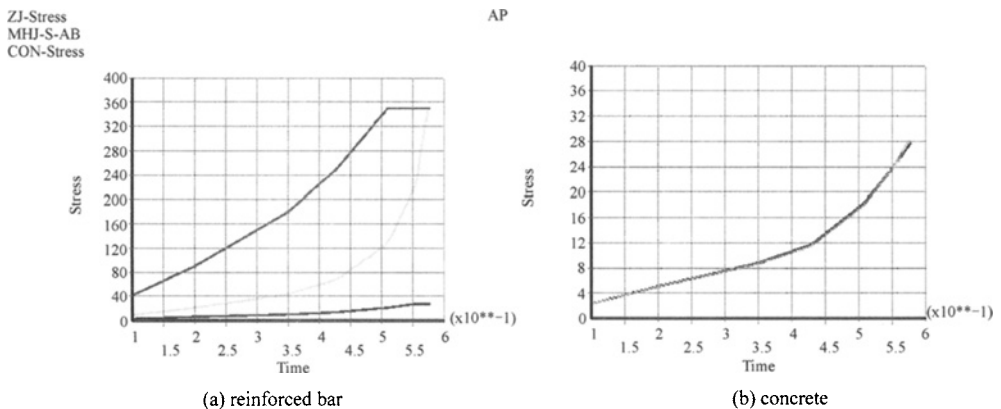


Figure 8. Curve of model unit stress-time (load)

From the stress time curve of concrete and reinforced bar, we find: before time is 0.35(P is 0.7MPa), it is slowly linear increasing of the stress curve of the concrete and reinforced bar. At this time, stress (tensile stress) of the main tendon is much smaller and its value is 43.66MPa. The stress (compression stress) of the constructional steel bar is relatively much larger and its value is -179.92MPa. It is 10.52MPa of the concrete stress value at this time. With the load increasing, it accelerates the stress increasing. Constructional steel bar reached yielding before main tendon in reinforced bar. When time is 0.509(P is 1.08MPa), Constructional steel bar has reached the -350MPa which is the biggest stress value. Although the load P is continually increasing, stress of the reinforced bar will not increase because it loses the load-carrying ability of the constructional steel bar at this time. The stress value of main tendon is only 127.2MPa. It has the trend of the continually increasing. The stress value of concrete is 21.54MPa.

Comparing the stress-time curve of reinforced bar with the curve of concrete, we can easily find that: it is the same that stress-strain curve of the concrete with the reinforced bar. Before time is 0.35, it is the linear increasing. Exceeding this time, the stress and strain are accelerated in different extent. The load effect on the constructional steel bar in the reinforced bar is obvious. Concrete had plastic deformation more quickly than the reinforced bar. At the same time, it shows that it has no obvious elastic-plasticity bound of the model. Under the final failing load, concrete and reinforced bar have reached the maximum

compression strength (maximum tensile strength). It illustrates that component model is made full use of the material performance.

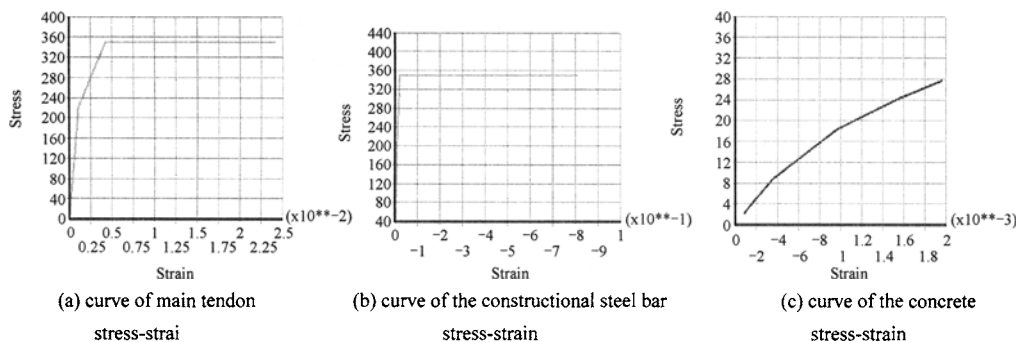


Figure 9. Curve of the reinforced bar and concrete model unit stress-strain

From the stress-strain curve Figure 9 of the model, we can find that reinforced bar is reached the yielding behavior at broken time. It is anastomotic with the similar model test of the conclusion. There is appeared the obvious yielding point of the stress-strain curve of reinforced bar. Stress will not increase after reaching yielding point, the results mentioned above are because we did not consider harden when we defined the material nature of the reinforced bar.

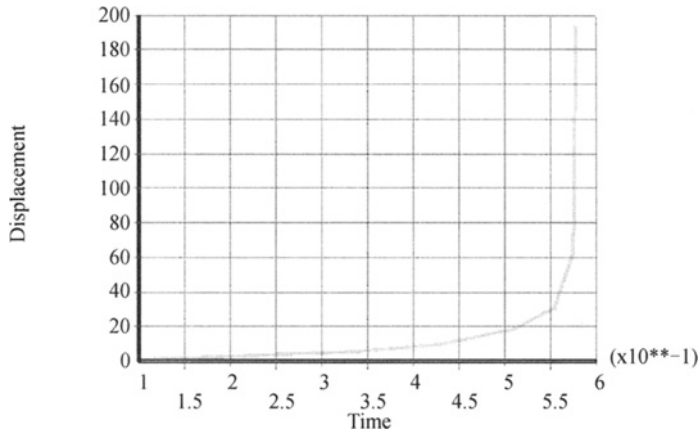
Along with the strain increasing, the unit stress of the concrete is more and more weak. There are two obvious knee points. It shows that concrete is at elastic stage before reached the first knee point value. At this time, stress-strain curve is a line. Along with the load increasing, concrete is getting into elastic-plastic behavior. With the strain increasing, stress increasing is not linear transformation. As the strain exceeds the second keen point value, stress increase gently. This shows that concrete has got into plastic stage. Concrete is broken as it reaches the compressive ultimate strength when load is the maximum value. In Figure 9, there is the ascending branch but does not have the descending branch of curve. This is certified the fifth assumption which did not consider the stress relaxation of the concrete.

(2) Bearing capacity analysis

According to the results of the numerical modeling, component is destructed because the compressive stress exceeds the permissible compressive stress. We can determine the bearing capacity of the analog result by using the controlling factor of the maximum compression stress when finally destructed at straight walls. This article discusses the three-dimensional steel bar component under the concrete grade determined and ratio of reinforcement given. According to the similar model test and time curve of stress and strain which we got from the numerical modeling, we concludes that the limit bearing capacity was determined by working load when the component is destructed. According to the above described, model does not have the obvious elastic-plasticity bound, and it illustrates that model has no deterministic yield load.

In Figure 10, displacement is almost vertical increased when time is 0.577. It is declares that model is destructed at this time. According to applied area load and finish-time points of the numerical derivation, it is determined that limit bearing capacity' value of

three-dimensional steel bar model is 1.154MPa. Comparing with the consequences of the similar model test, we convert it to 136.86T of engineering unit. But the limit bearing capacity of three-dimensional steel bar model results from using similar model test is 109.3T. Comparing the theoretical analysis with model test, the result is much more proximity. It illustrates that numerical calculation modeling results have a definite reliability.



UX-ABS—absolute value of the nodal point in X-axis direction displacement

Figure 10. Curve of nodal point displacement-time (load)

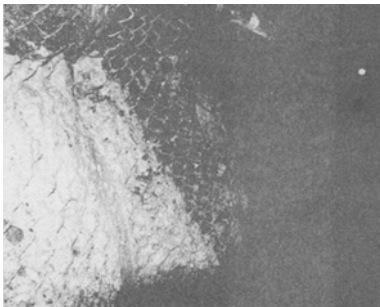


Figure 11. destruction of the tunnel

ENGINEERING INSTANCE

Engineering introduction

The new technology of the three-dimensional steel bar shotcrete lining was put into used at the west tunnel in Yanzhou coalmine. The test tunnel is 4.75m wide, 3.80m high. The soft rock is made of carbonaceous mudstone containing coal rider seam with well-developed joints and fractures. It must have been repaired at least three times when the U-shaped steel was used. Figure 11 shows the destruction of the tunnel.

Construction of the three-dimensional steel bar shotcrete lining

The structure of the three-dimensional steel bar is designed according to the soft rock character and pressure around the test tunnel. The whole frame is composed of one arch and two straight walls which are connected respectively by four bolts. The compressed wood layer is 50mm thick placing on middle of the two connecting plates. The three-dimensional steel bar shotcrete lining is divided into three steps when the tunnel is excavated. Firstly, used as the temporary support of the tunnel, a layer of concrete about 30mm thick is sprayed by jet pump. If necessary, the short anchor rods can be used too. Secondly, the reinforcing bar

frame is installed around the surface of the tunnel rock. Finally, the concrete may be shot on the frame by measuring the displacement.

The total thickness of the support is designed about 150mm. Of course, it can be adjusted according to the condition of the tunnel rock. Figure 12 to Figure 14 shows the technology of the three-dimensional steel bar shotcrete lining.



Figure 12



Figure 13

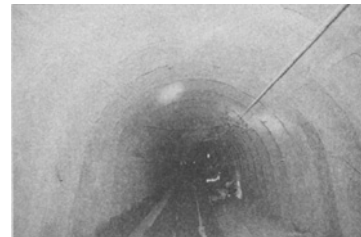
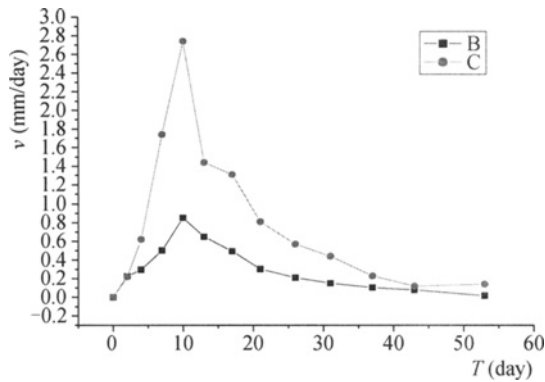


Figure 14

Supporting effect

In order to evaluate the effect of practical test, it is necessary to measure the displacement and stress. Figure 15 shows the shrinkage ratio of the new lining.



B—top and bottom shrinkage ratio C—two sides shrinkage ratio

Figure 15. Curve of v - T

(1) The largest shrinkage ratio of top-bottom and two walls is 0.9mm/d and 2.9mm/d after 12 days. The three-dimensional steel bar shotcrete tunnel lining is steady and has little deformation 50 days later.

(2) The new lining is reasonable and has predominant mechanical behavior by actual monitor. It can meet the supporting of high stress and soft rock tunnel.

ACKNOWLEDGEMENT

This work is supported by Anhui Province Education Department Nature Science Foundation Item (2006KJ005A).

CONCLUSIONS

(1) The three-dimensional steel bar shotcrete lining meets the demand of the soft rock tunnel supporting. This kind of new lining can afford the strong pressure and large deformation of the rock. With good compressibility, it changes the lining from passivity form to activity one.

(2) This kind of supporting can closely combine with the rock mass. It has a high integrity and contributes to rock mass fully maximizing its bearing effect.

(3) In comparison to U-shaped steel bracing, the cost of new steel bar shotcrete lining supporting is decreased by 30%. The successful test in Yanzhou coalmine tunnel will provide the experience for other soft rock tunnels.

(4) Compared to steel bracings and poured-in-place reinforced concrete, the constructing process of the three-dimensional steel bar shotcrete lining has very simple technology. Without any question, it also can be used and promoted as the supporting in large-span road tunnels and underground railways.

TEMPERATURE CRACK CONTROL ANALYSIS FOR PEDESTAL IN JINPING-1 HIGH ARCH DAM ENGINEERING

Sheng Qiang, Yueming Zhu, Ting Hu and Zhantao Shao
*College of Water Conservancy and Hydroelectric Engineering, Hohai University,
Nanjing 210098, China*

The feasibilities of temperature control and crack prevention measures in different seasons are researched based on the mass concrete construction simulation of the left bank pedestal in Jinping-1 high arch dam engineering. Pipe cooling is simulated by equivalent method in the computation, the influence of surface heat preservation, parting and some other factors are considered at the same time. The results show the main temperature control project of different seasons is reasonable and feasible. The opening of joints is judged and some suggestions on temperature control and crack prevention are made in the conclusion.

INTRODUCTION

Jinping-1 hydropower engineering is located in Sichuan province China. The main task of the project is power generation, flood control and sediment trapping is the compatible functions. The total invest is about 24.6 billions. The concrete hyperbolic arch dam of Jinping-1 engineering with a height of 305.0 m is the highest arch dam building in world.

The model experiment shows the dam stress is not symmetry because of the asymmetry dam site topography and geology which will result in the deformation of left dam abutment more than right dam abutment and oblique cracking on dam to reduce the overloading capacity. After researching, it is decided to excavate some weak rock between elevation 1730.0m and 1885.0 m in left bank. The excavated rock is replaced with concrete pedestal to increase the dam stability and improve the dam stress state. The pedestal concrete volume is huge, which is 155.0 m high and about 100.0 m long in bottom. The max bottom area of the pedestal is 5142 m². Limited by the concrete pouring capacity, the pedestal is partitioned so the max length of pouring block is about 50.0 m. As for arch dam, the abutment stability is very important. The entirety of abutment is the significant factor to influence the abutment stability. As an important ingredient of left bank abutment, the temperature control and crack prevention of the pedestal is a key problem for designing and studying, Zhu Bofang (1984).

To ensure the crack prevention safety factor of the pedestal high enough, considering the requirements of concrete technique index and the experiment research results of concrete material performance, simulation is applied for the pedestal concrete poured in different seasons. The temperature field and the stress field of pedestal are researched deeply. The finite element method for concrete temperature field and stress field, Zhu Bofang (1999), are adopted in computation. To simulate pipe cooling, the equivalent equation of concrete heat conduction considering pipe cooling effect, Dong Fupin (2001) and Zhu Bofang (2003), is

applied in computation. Because of paper page limit, the corresponding theories and methods are omitted.

FINITE ELEMENT MODEL

The concrete pedestal locates between elevation 1730.0-1885.0 m in left bank. According to the partition, the pedestal between elevation 1730.0-1748.0 m is adopted as computation model (Figure 1). The X axis directs to inner of hill, Y axis directs to upstream and Z axis is upright. The coordinate origin locates at the center of pedestal outboard on elevation 1730.0 m. The model includes 24088 nodes and 20706 elements.

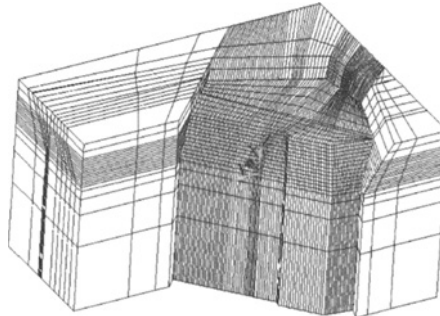


Figure 1. Computation model mesh of left bank pedestal

Designers set joints in the pedestal considering the concrete pouring and the temperature control capability. The pedestal in the model contains two thick layers. In every thick layer four joints are set. And the joints in different layers are not continuous which means they are staggered joints. The detailed partition is shown in Figure 2. The dash lines in Figure 2 represent the joints in the thick layer from elevation 1730.0 m to 1739.0 m, and the continuous lines represent the joints in the thick layer from elevation 1739.0 m to 1748.0 m. Every thick layer contains six pouring layers with the individual thickness 1.5m. On horizontal plane every pouring layer are parted into 5 blocks by four joints. The pouring sequence of 5 blocks is shown in Figure 3. There are 12 pouring layers and 60 blocks in total. The interface between pedestal and hill are filled with nonlinear thin layer elements, Mou Gaoxiang (2005). The thin layer elements are pouring together with the corresponding layer. During the simulation process if the tension stress in one element exceeds the tensile strength, then the element is assumed open in next computation step.

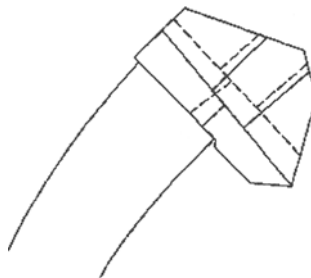


Figure 2. Position relation of pedestal and arch dam and parting of pedestal

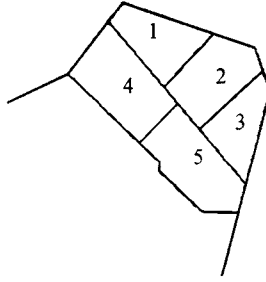


Figure 3. Sequence of pouring on placement surface

COMPUTATION PARAMETERS AND BOUNDARY CONDITIONS

The base surfaces are added normal restraint for stress computation and adiabatic for thermal computation except the excavation surface. In fact, the pouring will continue after elevation 1748.0 m is filled with concrete, so the top surface of concrete pedestal in the computation model is set as adiabatic boundary after 5 days.

The rock property is III1 marble. The pedestal material is C30 concrete whose calorific parameters are shown in Table 1.

Table 1. Calorific parameters of concrete

Material	Temperature conductivity Factor α (m ² /h)	Heat conductivity factor λ (kJ/m·h·°C)	Specific heat c (kJ/kg·°C)	Coefficient of linear expansion ($\times 10^{-6}/^{\circ}\text{C}$)	Coefficient in adiabatic formula		
					T_0 (°C)	a	b
C30 Concrete	0.0041	9.15	0.90	9.87	24.4	0.473	0.645

According to the test data, the concrete elastic module duration with age is fitted as the following formula:

$$E = 30.74(1 - e^{-0.35\tau^{0.75}}) \text{ GPa} \quad (1)$$

The concrete creep uses the experimental formula:

$$C(t, \tau) = C_1(1 + 9.20\tau^{-0.45})[1 - e^{-0.30(t-\tau)}] + C_2(1 + 1.70\tau^{-0.45})[1 - e^{-0.0050(t-\tau)}] \quad (2)$$

in which $C_1 = 0.23/E_0$, $C_2 = 0.52/E_0$.

The autogenous volume deformation is assumed zero because the concrete is micro expansive and the test data shows the expansion is very little.

According to the weather data, the monthly mean ambient temperature is fitted as a formula to be used in program. If the monthly mean ambient temperature is above 22.0 °C sunshine effect is considered by adding 3.0 °C to the monthly mean ambient temperature.

The weather data shows the day and night temperature difference is ± 9.0 °C from November to next April, while from May to October it is ± 6.5 °C. The day and night temperature difference is dangerous enough to induce surface crack in early age, so it is considered in 3 days age for every pouring layer in the simulation.

Because of the dangerous day and night temperature difference, surface heat preservation measures are adopted to decrease the internal and external temperature difference, Ma Yuefeng (2006). The detailed measure is to stick 1.5 cm thick foam board to the outside of steel formwork and one layer of composite geomembrane for 5 days.

The cooling pipe is arranged as the form of 1.5 m×1.0 m (vertical distance × horizontal distance). The first stage cooling time is 14 days with the inlet water temperature of 12.0 °C. After 6 months, the second cooling begins and lasts 40 days with the inlet water temperature of 12.0 °C which is determined by the sealing temperature of the arch dam on same elevation. The pipe is a new type plastic pipe with the outer radius of 1.6 cm, the inside radius of 1.4 cm, the conductivity factor is 6.1 kJ/(m·h·°C).

The computation cases include winter construction case, summer construction case and autumn construction case. The concrete pouring temperature is 12.0 °C in winter, 10.0 °C in summer, for autumn it is 10.0 °C in October but 12.0 °C in November. The annual average temperature of hill inside is 19.6 °C.

COMPUTATION RESULT ANALYSIS

The computation simulates the concrete pouring course layer by layer and block by block in different seasons in detail, including pipe cooling and surface prevention in different stage. Results show that the highest temperature does not appear at the pedestal center, but the area near hill which is approximate the center of pouring block 2 on every layer. The cause should be that the hill temperature is high and the pedestal inside face contact with hill which is not advantage of heat radiate. Figure 4 shows the temperature duration curve of the center of pouring block 2 on elevation 1739.0 m in three cases. The initial time in the figure is the pouring time of block 1 on elevation 1730.0 m. The curves show the rule that concrete hydration temperature rises rapidly after pouring and if the ambient temperature is higher the concrete temperature peak will be higher. The temperature peak in concrete is 22.8 °C in winter and 24.0 °C in autumn. In summer, ambient temperature is higher than concrete temperature in early age, so the heat intrusion and hydration cause a concrete temperature peak of 28.5 °C although pipe cooling takes effect. Figure 6 shows the temperature contour of the horizontal section on elevation 1739.0 m when the concrete temperature is highest. The concrete hottest area is inside the pedestal near hill. The outside of the pedestal contacts with air, so it is affected by ambient temperature obviously. The concrete temperature shades from 27.0 °C of inside to air temperature of outside. The bottom and surrounding surface is affect by hill temperature obviously. The concrete temperature shades form 27.0 °C of inside to hill temperature with large gradients.

After the peak, temperature decreases distinctly caused by the first stage water cooling. When the first stage water cooling finish, concrete temperature rises a little because the hydration is not absolutely stop. Then concrete temperature goes down slowly until the second stage water cooling. It decreases to about 13.0 °C that is the corresponding sealing temperature in the second stage water cooling.

The horizontal plane of elevation 1730.0 m is the bottom of foundation ditch. Block 4 and block 5 of the first pouring layer have longer sides, so the restrain by base is more distinct.

Figure 5 shows the σ_1 duration curve of the center of block 4 on elevation 1730.0 m. The curves express some rules. Concrete tends to be pressed when temperature rises. The pressure stress in summer is max because of the max temperature. At the end of the second stage water cooling, concrete temperatures in different case decrease to the same value. It is clear the temperature decreasing value is max in summer case, then in autumn case, min in winter case. In the second stage water cooling, concrete tends to tensile. The concrete layer on base rock is restrained more strictly by base, so the tension stress here increases more. It rises from -0.12 MPa to 0.93 MPa in summer case, from -0.70 MPa to 0.14 MPa in autumn case, from -0.82 MPa to -0.23 MPa in winter case. All the tension stress peaks are below the allowable tensile strength.

Figure 7 is the σ_1 contour of elevation 1730.0 m at the 280th day when the second stage water cooling finish. The figure shows that the tension stress near center of every block is large and the value gradual changes less from center to edge. The max tension stress appears at the centers of block 4 and block 5. Because the pouring temperature is low and the first stage water cooling, the pedestal concrete temperature is controlled well. The interface between pedestal and hill is always under pressure except in summer case and no crack caused by temperature decreasing and concrete shrinking appears. In summer case, some interface thin layer elements are in tension when the second stage water cooling, but the max value is 0.40 MPa that will not create crack on the interface. The stress on the interface between different blocks is not same as the block inner, but it is under pressure generally.

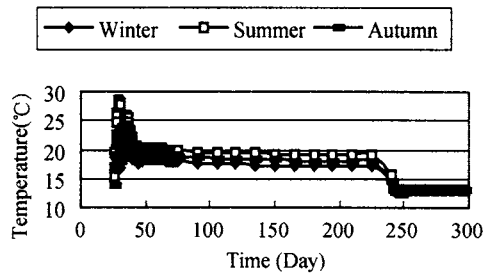


Figure 4. Temperature duration curve of No.2 pouring block center on elevation 1739 m

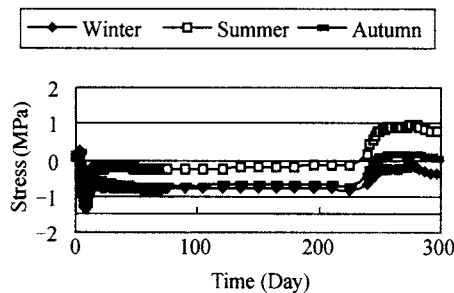


Figure 5. σ_1 duration curve of No.4 pouring block center on elevation 1730 m

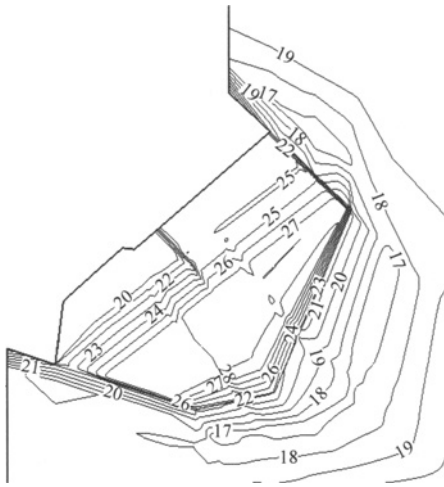


Figure 6. Temperature contour on elevation 1739m when temperature vertex in summer (°C)

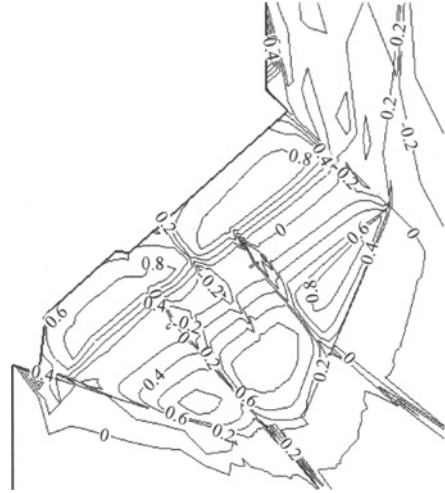


Figure 7. σ_1 contour on elevation 1730m when second-stage cooling end in summer (MPa)

CONCLUSIONS AND SUGGESTIONS

According to the simulation and analysis for the left bank pedestal concrete construction of Jinping-1 arch dam in different seasons, adopting the concrete temperature peak and the allowable tensile strength with a safety factor of 2.0 as the main control indexes, the concrete stress is always under the allowable tensile strength from computation results. Because of low pouring temperature and pipe cooling measures, all kinds of the interfaces do not open after the second stage pipe cooling. Results show the temperature control schedule is reasonable and feasible.

The second stage pipe cooling time length should be adopted by the factual detection because the cooling extents of different location concrete are not same. The water cooling may stop when the temperature far away from cooling pipe has decreased to the sealing temperature. Different inlet temperature water should better be supply for different area. The concrete near hill is not easy to arrive at 13.0 °C, so the inlet water with temperature of 10.0-12.0 °C may be take or last the cooling time length before sealing the arch dam.

The local day and night temperature different is large, even in summer it has a value of ± 6.5 °C, that is the different between the highest and the lowest temperature in one day is 13.0 °C. If concrete is poured at the highest time in a day, then the ambient temperature decreasing amplitude is very large, which will induce worse effect than the cold wave of local climate. So insulation board and composite geomembrane should be adopted as heat prevention material in early age, else the concrete surface is easy to crack caused by large day and night temperature different. Such crack will likely extend into the concrete inside.

REFERENCES

- Dong Fupin. (2001). The equivalent analysis of pipe cooling in concrete structure considering the cooling effect influence by surface radiation, *Water Resources and Hydropower Engineering*, 32 (6): 16-19.

- Ma Yuefeng and Zhu Yueming. (2006). Effect of surface heat preservation on temperature and stress of pier concrete during construction period, *Journal of Hohai University(Natural Sciences)*, 34(3): 276-279.
- Mou Gaoxiang. (2005). Application of Thin Layer Element in Finite Element Method of Analysis for Xiluodu Arch Dam, *Design of Hydroelectric Power Station*, 21(2): 8-13.
- Zhu Bofang. (1984). Temperature load of arch dam, *Water Power*. (2): 34-39.
- Zhu Bofang. (1999). *Thermal Stress and Temperature Control of Mass Concrete*, 1st edition, China Electric Power Press.
- Zhu Bofang. (2003). The equivalent heat conduction equation of pipe cooling in mass concrete considering influence of external temperature, *Journal of Hydraulic Engineering*. (3): 49-54.

GEOTEXTILE REEF AS A COASTAL PROTECTION AGAINST TSUNAMI

Agnieszka Strusińska

*Leichtweiss Institute, Technical University of Braunschweig, Beethovenstrasse 51a
Braunschweig, 38-106, Germany*

Hocine Oumeraci

*Leichtweiss Institute, Technical University of Braunschweig, Beethovenstrasse 51a
Braunschweig, 38-106, Germany*

The possibility of an application of an artificial reef as a mean for coastal protection against tsunami impact is examined. Reef feasibility and its hydraulic performance are investigated numerically for different obstacle configurations and varying incident wave conditions, taking into consideration the experience available on the storm wave attenuation by means of such structures. Effect of the reef on tsunami damping is discussed by comparing the phenomena observed in the case of a coastline protected by a reef and the case without the protection.

INTRODUCTION

The effective mitigation of a tsunami hazard, which is very difficult to predict and hard to control, should be based on structural measures using permanent coastal protection made of man-made and natural barriers as well as non-structural measures including early warning and emergency plans. The tragedy of the 2004 Sumatra Tsunami event has led to a rapid development of the emergency management primarily towards establishment of reliable tsunami early warning systems. However, in case of a local tsunami, the structural countermeasures would play the key role due to the lack of time for issuing a tsunami warning and organizing an efficient evacuation of local residents. Since it is neither possible nor desired to block completely the impact of incident tsunami waves, a concept of a gradual dissipation of tsunami energy as it approaches a shore has been proposed (Oumeraci, 2006).

Such a multi-defence line strategy would consist of a combination of structural and natural means of protection stretched from the offshore up to the inland zones. The overall performance of the entire defence system would however depend on its first defence line designed of low-crested structures, at which the incoming tsunami energy is expected to be dissipated essentially due to prematurely induced wave breaking. Considering the successful application of artificial reefs to storm wave attenuation, it is proposed to adapt such a structure to tsunami conditions. Due to the significant differences between storm waves and

much larger tsunami waves, indeed large reef dimensions will be required to achieve noticeable tsunami attenuation. Therefore, taking into account the economical aspects of a construction of a reef against tsunami, low-cost solutions would be preferable, such as that illustrated in Figure 1.

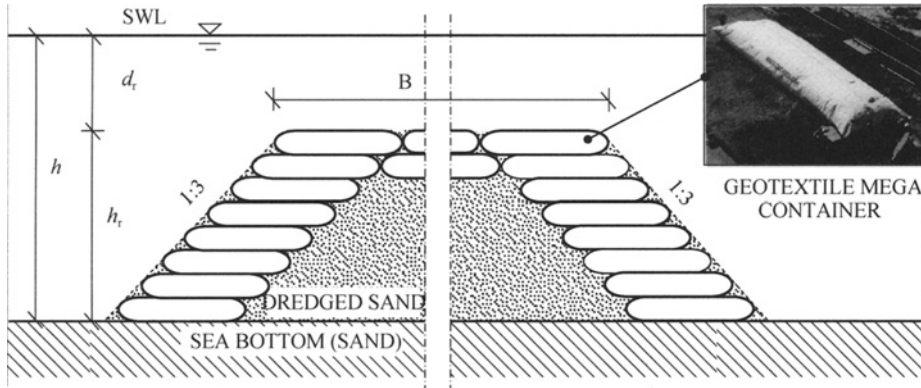


Figure 1. Construction solution of artificial reef against tsunami (after Oumeraci, 2006).

The damping performance of the reef of varying geometry under given incident tsunami wave conditions is evaluated on a basis of numerical experiments, since laboratory investigation of the problem is hardly possible due to the scaling aspect of the vertical to the horizontal ratio.

DESCRIPTION AND VALIDATION OF NUMERICAL MODEL

Numerical model for water wave propagation pCOULWAVE (Lynett, 2002) was employed to determine artificial reef feasibility and effectiveness under tsunami impact. Wave motion is governed by the fully-nonlinear, extended Boussinesq model:

$$\frac{\partial \eta}{\partial t} + \nabla \cdot [(\eta + h) \mathbf{u}_\alpha] - \nabla \cdot \left\{ \left[\frac{\eta^3 + h^3}{6} - \frac{(\eta + h)}{2} z_\alpha^2 \right] \nabla S + \left[\frac{\eta^2 - h^2}{2} - (\eta + h) z_\alpha \right] \nabla T \right\} = 0 \quad (1)$$

$$\begin{aligned} \frac{\partial \mathbf{u}_\alpha}{\partial t} + (\mathbf{u}_\alpha \cdot \nabla) \mathbf{u}_\alpha + g \nabla \eta + \frac{\partial}{\partial t} \left\{ \frac{z_\alpha^2}{2} \nabla S + z_\alpha \nabla T - \nabla \left(\frac{\eta^2}{2} S \right) - \nabla (\eta T) \right\} \\ + \nabla \left\{ \frac{\partial \eta}{\partial t} (T + \eta S) + (z_\alpha - \eta) (\mathbf{u}_\alpha \cdot \nabla) T + \frac{1}{2} (z_\alpha^2 - \eta^2) (\mathbf{u}_\alpha \cdot \nabla) S \right. \\ \left. + \frac{1}{2} [(T + \eta S)^2] \right\} - \mathbf{R}_{wb} + \mathbf{R}_{bf} + \mathbf{R}_{ev} = 0 \end{aligned} \quad (2)$$

$$S = \nabla \cdot \mathbf{u}_\alpha \quad \text{and} \quad T = \nabla \cdot (h \mathbf{u}_\alpha) \quad (3)$$

where η is the free surface elevation, $\mathbf{u}_\alpha = [u_\alpha, v_\alpha]$ is the horizontal velocity vector evaluated at water depth $z_\alpha = -0.531h$, h is the local water depth, g is the gravitational acceleration and $\nabla = [\partial/\partial x, \partial/\partial y]$ is the horizontal gradient operator. The dissipative terms added ad-hoc into the momentum equation represent energy losses due to wave breaking \mathbf{R}_{wb} , bottom friction \mathbf{R}_{bf} and eddy viscosity \mathbf{R}_{ev} . Detailed description of these terms and the triggering mechanism of wave breaking based on eddy viscosity concept, is presented in Lynett (2002). The mass and momentum equations, Eqs. (1) and (2) respectively, are discretized in space to the fourth

order of accuracy by means of the central difference scheme, while in time by the predictor-corrector scheme consisting of the third order explicit Adams-Bashforth predictor step and the fourth order implicit Adams-Moulton corrector step.

Applicability of the numerical model to the problem of wave transformation at a submerged structure (primarily initiation of wave breaking and generation of wave fission) was verified by a comparison of the existing laboratory data with the computed one. The model validation was performed for laboratory experiments provided by Gruene et al. (2006) and Matsuyama et al. (2007), shown in Figure 2. a),b) and Figure 2 c),d), respectively.

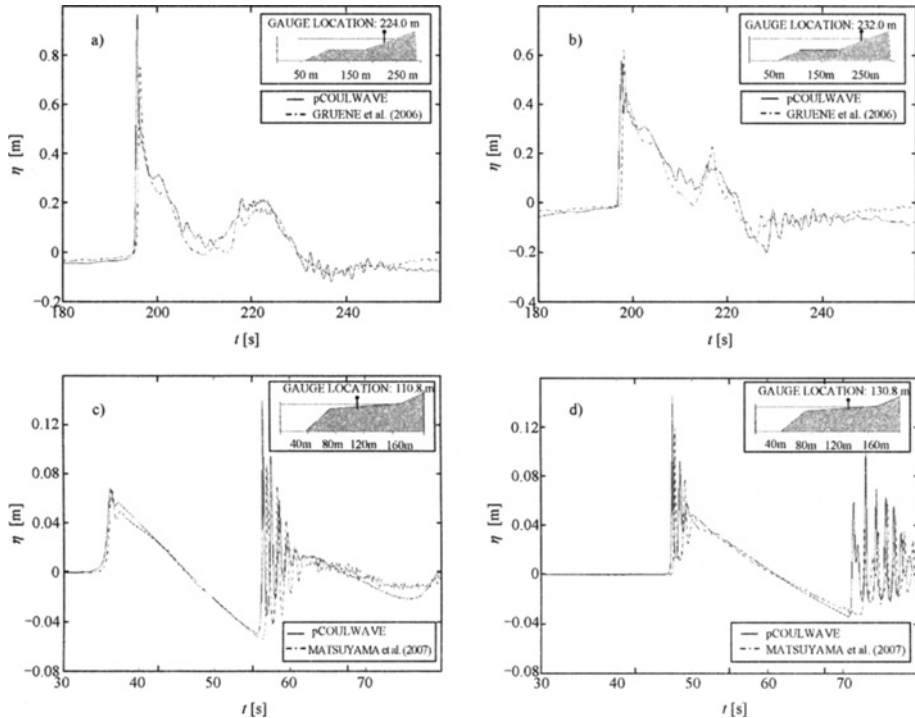


Figure 2. Comparison of time history of surface elevation: a) and b) tests by Gruene et al. (2006) for generated solitary wave height 0.55m; c) and d) tests by Matsuyama et al. (2007) for wave amplitude 0.03m and period 20s.

The comparative analysis of the numerical and experimental results indicates a relatively a good prediction performance of the numerical model for the incipient solitary wave breaking and the propagation of the broken wave further shoreward in case of the large-scale model experiments by Gruene et al. (2006). For the tests by Matsuyama et al. (2007), the generation of fission of a tsunami-like sinusoidal wave and the number of the emerged shorter waves are also well modeled.

SET UP FOR SIMULATIONS

An impermeable, trapezoidal-shaped reef is placed at a water depth $h=15\text{m}$ on an impermeable sea bottom of the slope 1:100 (see Figure 3). The sea bed extending from the

seaward toe of the structure towards the shore is assumed to be horizontal in order to neglect the influence of the shoaling process on wave transmission and to model a reef of an arbitrary width. The reef geometry is defined by the seaward and landward slopes 1:3, the crown width B and the submergence depth d_r (or reef height $h_r=h-d_r$) expressed as dimensionless ratios:

- relative structure width: $B/L_i=0, 0.01, 0.05, 0.1, 0.2, 0.3, 0.4, 0.5$
- relative submergence depth: $d_r/h=0.1, 0.2, 0.3, 0.4, 0.5, 1.0$

The simulation of realistic tsunami conditions was achieved by placing a solitary wave of height H_o and period T in deep water h_o , whose values are given in Table 1. The local incident wave conditions are measured at the point corresponding to the seaward toe of the reef, for the case of no obstacle, i.e. for $B/L_i=0$ and $d_r/h=1.0$. Assuming approximately constant wave period during the wave transformation over the sloping sea bed, the local incident wave profile is defined by:

- relative wave height: $H_i/h=0.1, 0.2, 0.3, 0.4, 0.5, 0.6$
- relative wavelength: $L_i/h\sim 500$

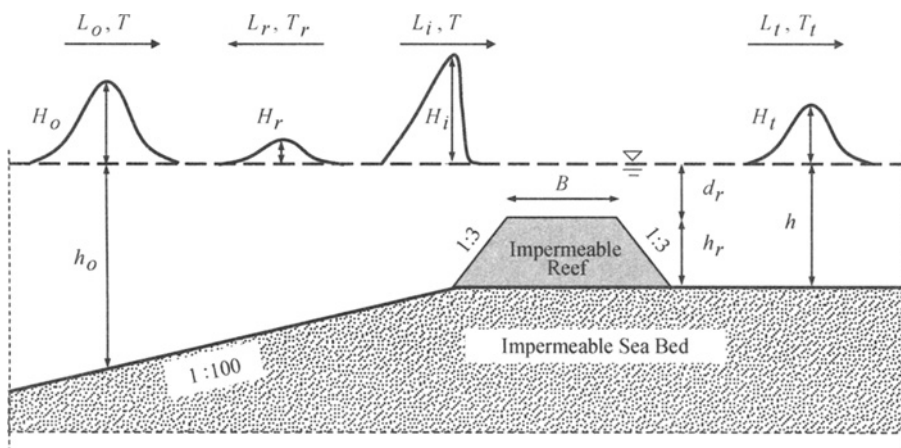


Figure 3. Set up for numerical simulations

The local incident wavelength L_i is determined visually as the steep wave front reaches the point corresponding to the designated reef location and was assumed to be approximately constant for all considered wave nonlinearities H_i/h .

Friction coefficient for sand ($f_w=0.025$) is assumed to be constant over the entire numerical domain.

Table 1. Definition of initial and incident wave conditions

Farfield incident (initial) wave parameters			Local incident wave parameters (determined for $B/L_i=0$ and $d_r/h=1.0$)			
h_o (m)	H_o (m)	T (min)	h (m)	H_i/h (-)	T (min)	L_i/h (-)
205	0.85	5	15	0.1	~ 5	~ 500
288	1.68	5	15	0.2	~ 5	~ 500
351	2.49	5	15	0.3	~ 5	~ 500
407	3.35	5	15	0.4	~ 5	~ 500
459	4.25	5	15	0.5	~ 5	~ 500
508	5.20	5	15	0.6	~ 5	~ 500

TENTATIVE RESULTS AND DISCUSSION

The tentative investigation of the reef effect on the incident tsunami-like solitary wave is performed for a uniform spatial grid step, expressed as a fraction of the local water depth $\Delta x=0.7h$. The cases of the structure geometry and local incident wave conditions, that are crucial for the reef functioning, are selected to provide a preliminary analysis of the phenomena observed with and without the reef. In the case without the reef structure, i.e. $B/L_r=0$ and $d_r/h=1.0$, wave fission process is generated for all ratios of H_i/h over the horizontal sea bottom acting as a submerged step. Generation of the solitons occurs closer to the beginning of the horizontal part of sea bed as the wave nonlinearity increases; e.g. for $H_i/h=0.1$ at $x/h\sim 570$ and $H_i/h=0.6$ at $x/h\sim 35$ (dash-dot curve in Figure 4a,b). In general, there is no significant influence of narrow structures ($B/L_r=0.01$) on the incident wave behaviour (see Figure 4a), except a gradual shifting of the starting point of wave fission towards the landward toe of the reef. For a given ratio B/L_r , the factor significantly influencing the height of the transmitted wave and emerged solitons is the relative submergence depth d_r/h . The disintegration of the incident waves above the reef crown can be observed for the relative structure width $B/L_r=0.2$ and relative wave height H_i/h generally larger than 0.4, however for $H_i/h=0.6$ wave breaking is additionally initiated. Extension of the structure width to $B/L_r=0.5$ does not result in a significant reduction of wave energy, particularly for $H_i/h=0.6$ (see Figure 4b). However, wave fission over the structure occurs also for $H_i/h=0.1$. The solitons generated over the obstacle continue to propagate as short-period waves ($T=10-20s$) as they enter the deep water behind the reef.

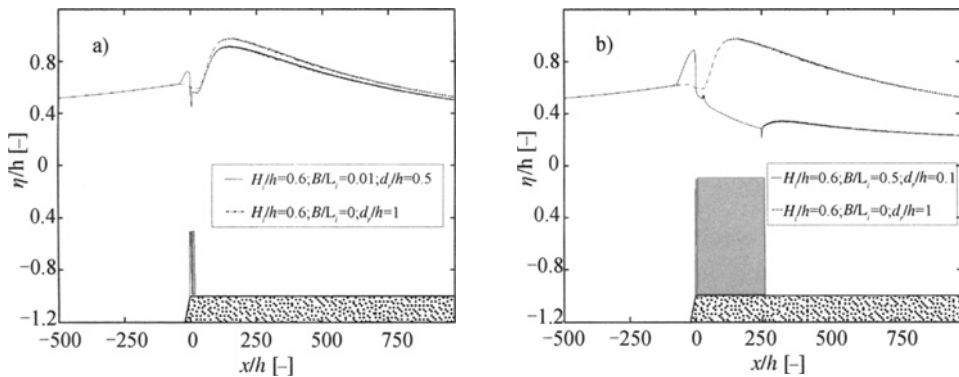


Figure 4. Comparison of surface envelope with and without reef for $H_i/h=0.6$:

a) $B/L_r=0.01$; b) $B/L_r=0.5$.

CONCLUSIONS

The tentative results indicate that an artificial reef may be adapted to tsunami attenuation. However, implementation of a non-uniform spatial grid is required to improve modeling of the wave transformation at the reef, particularly the generation of the wave fission process. An approach for the estimation of the hydraulic performance of the structure, defined in terms of the rate of wave transmission, reflection and energy dissipation will be developed.

Further validation of the model by means of own laboratory experiments in the twin wave flume of the Leichtweiss-Institute is being performed.

ACKNOWLEDGMENTS

The support of the DFG within the Graduate College “Fluid-Structure Interaction” at TU Braunschweig as well as the support of Dr. P. Lynett is gratefully acknowledged.

REFERENCES

- Gruene J., Schmidt-Koppenhagen, R. and Oumeraci H. (2006). Tsunami decay in near- and onshore areas, *30th International Conference on Coastal Engineering*, San Diego, USA, (2): 1664-1676.
- Lynett P. (2002). A multi-layer approach to modeling, generation, propagation, and interaction of water waves, *Phd Thesis, Cornell University, USA*.
- Matsuyama M., Masaaki, I., Tsutsomu, S. and Tomoyoshi, T. (2007). A study of tsunami wave fission in an undistorted experiment, *Pure and Applied Geophysics*,(164): 617-631.
- Oumeraci H. (2006). Near- and offshore tsunami effects. *Background Paper Prepared for Geo-Committee of the German Research Foundation (DFG)*.

STUDY ON REINFORCEMENT WALL OF GEOGRID THROUGH MODEL TEST ON SLOPE

Chengzhi Wang

*Institute of Geotechnical Eng. Dalian Univ. of Technology Dalian 116085, China;
Chongqing Jiaotong University, Chongqing 400074, China*

Guangchun He, Ying Nie

*Chongqing Jiaotong University, Chongqing 400074, China;
Institute of Geotechnical Eng. Dalian Univ. of Technology, Dalian 116085, China*

In order to research reinforcement wall of geogrid multilevel slope working mechanics and mechanical characteristics, a lauder model was built indoors with 8m length, 4m width and 4.5m height. The model tested the soil pressure behind panel, the soil pressure behind reinforcement wall, the each stratified soil pressure of reinforcement, the stress of foundation, tension of geogrid and displacement of wall. It is found that the inner soil pressure of reinforcement discord with the conventional soil-pressure theory calculated value, the distribution of soil pressure closely relate to the foundation condition and the height of reinforcement through the analyses. It is shown that the influence of the mechanical characteristics of reinforcement and displacement of wall are examined on the displacement of reinforcement foundation. The stress of retaining foundation present V-mode distribution and displacement of wall present trend to lower drum while it having major displacement. The stress of retaining foundation present bias distribution and displacement of wall present trend to tensor drum while it having minor displacement.

INTRODUCITON

Compared with the general braid reinforcement retaining wall, geogrid reinforcement retaining wall relies on geogrid proper mesh construct with soil occluding and constraining which made the stability of reinforcement increased. The geogrid reinforcement increasingly comprehensive applied in geotechnical engineering as the simplicity construction and distinctness economic benefit. The reinforced retaining wall ordinary adopt single stage erection type and twain exponent erection type, whereas multilevel erection type (namely slope type) reinforced retaining wall possess stress distribution uniformity, easiness deformation control, facilitate virescence and restore ecological environment merit, and it got abroad favor with the engineering field in the recent years. But the current PRC *standards* provision limited to the single stage or twain exponent erection type reinforcement retaining wall. If the slope geogrid reinforcement retaining wall structural design calculation based on the "PRC standards" calculation procedure, the measured data discrepancy very large with the engineering practical situation. Wherefore, the authors precede research of slope geogrid reinforce retaining wall structural

characteristic. It will sound the reinforce soil design philosophy, promote reinforcement technical deploy which have important theory sense and engineering use valve.

In this paper, geogrids and soil are regard as a kind of composite material based on self-consistent theory. Base on the former, we build a 8-meter long, 4-meter wide 4.5-meter high launder model. The authors did serial model experiment with ascent of 1:0.5 slope geogrid reinforcement walls in the model launder, and the mechanical characteristics of slope reinforcement wall was investigated.

Testing program

Launder model

The theme group of this text builds a launder model (8-meter long, 3-meter wide, 4.5-meter high) indoors, which used reinforced concrete structure with 1.5m depth. Then placement board in layer and reclaim reinforced soil in order to simulate the reinforced soil retaining wall.

Grid material and geogrid RSRW

The geobelf in this test is high-strength geogrids , with ultimate strength $T_u=120$ kN/m and breaking coefficient of elongation $\delta \leq 8\%$; when $\delta \leq 2\%$, strength of geogrids $T \geq 40$ kN/m .The rib of geogrid with 20mm width and the geogrid aperture size with 300×140 mm were adopted in the test. The geogrid RSRW (shown in Table1) was composed of clay and soil aggregate in the test which with maximum dry density= 2.10 g/cm³, optimum water content= 8.8% , cohesion $C=16$ kPa, angle of internal friction $\varphi=28^\circ$ suggested by triaxial test. In the test, the mechanical parameters of soil sampling in the stepped wall behind panel was measured (shown in Table 2).

Testing program and test section

This testing program is interior full scale test. It is built model according to actual construction course, and test each data of station inner reinforcement once in every reclaim layer. After the model builds up 1-5days and stabilizes, it is utilize sack loading at vertex wall load twice. After it is stabilize 24h with 6kpa heap loading, then add another 6kPa heap loading. The station of conceptual disposal as Figure 1, which distance launder model around skit board 1.02m tested clearly L and R two section.

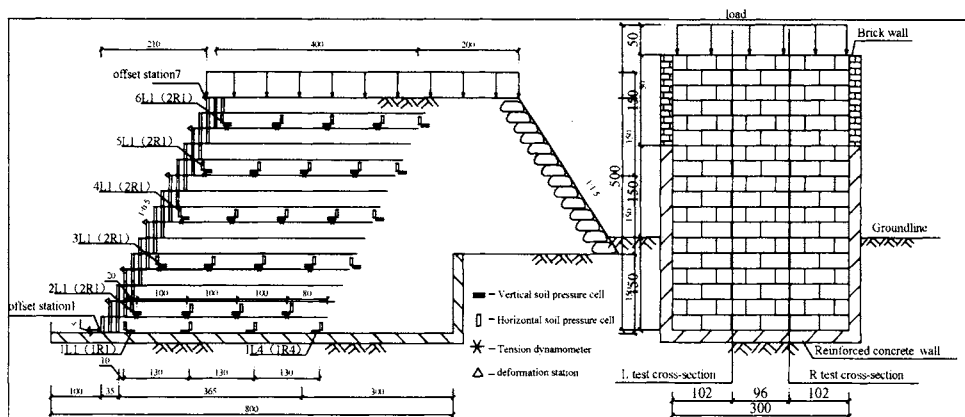


Figure 1. Arrangement of the RSRW measuring point

Table 1. Screen separation of the geogrid RSRW soil

Aperture(mm)	Screen separation of remain soil percent (%)											
	30	20	10	5	3	2	1.25	0.5	0.25	0.1	0.074	residual
Graded soil	0.0	9.1	15.4	20.3	12.7	5.4	10.9	10.7	4.9	5.6	1.3	3.1
Aperture(mm)	Less than the special aperture of soil percent (%)											
	30	20	10	5	3	2	1.25	0.5	0.25	0.1	0.074	—
Graded soil	100	90.9	75.5	55.2	42.5	37.1	26.2	15.4	10.5	4.9	3.6	—

Table 2. Material Mechanical properties of geogrid RSRW

Gravity(Gs)	Wet density (g/cm ³)	Moisture content(%)	Dry density(g/cm ³)	Compactness(%)	Void ratio	Ip	C(kPa)	φ
2.7	1.99	9.29	1.82	86.63	0.489	10.4	16	28°

The clapboard of model geogrid reinforcement adopts rectangle single frame chamfer with C20 concrete panel, which prefabricate fixing. The panel size was 48cm×24cm×24cm.

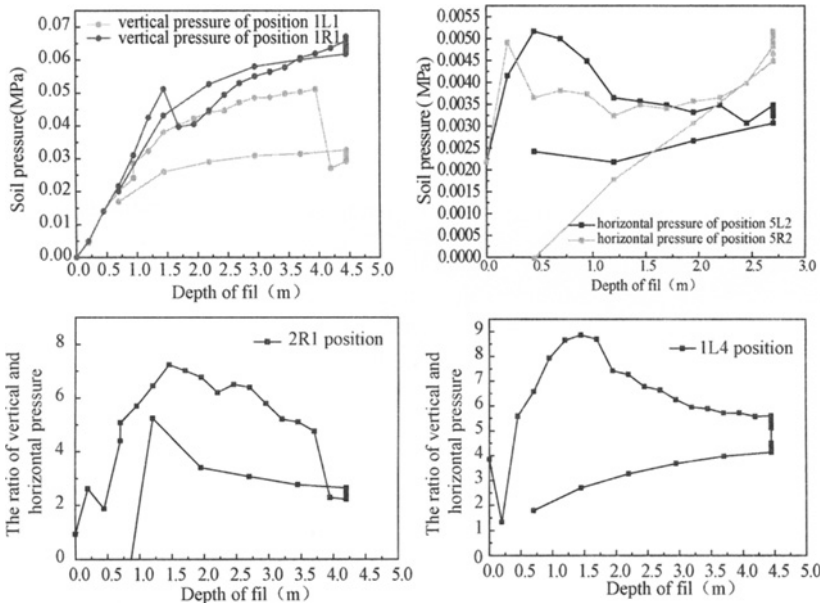


Figure 2. The soil pressure at same measuring point between case A and B

Station disposal and test scheme

We adopt vibrating soil pressure in the test. Test would be done for lateral deformation and settlement of the RSR wall measuring distance from measuring point to datum point each time. And the datum point is made of steel, implanted a certain distance implanted inside bedrock under the base. The maximum scale was 0.1MPa for bottom of three layer soil pressure cells and the rest was 0.05MPa. The stations were disposal seven layers in this test (as Figure 1). “KLn” express the measuring points in the later analysis of this text. Here, “K”

is measuring layer number, so $K=1$ means the first layer at bottom, and “n” is the number of measuring point behind the board, for example $n=1$ means the first one behind the board.

The station disposal of the displacement of wall correspond test layer of soil pressure, which test by deformation probe unit in the wall. It tests the displacement of wall with loading and unloading stationary by all levels loading.

The tension sensor of geobelf reciprocates distribution with soil pressure. The pulling of each layer with cascade geobelf was tested by special in advance cover-up tension sensor. They test pull of geobelf in loading and unloading stationary all levels respective.

Analyze result of the test

Single station earth pressure analyses

The soil pressure of station came along soil banking variance curve in Figure 2a, 2b. From the picture, it is observed that vertical soil pressure increased with banking increased. But there is still a critical banking altitude (about 1.5m). While banking less than it, the soil pressure and banking linear variation; while banking more than it, the soil pressure basic immovability or summary a little decreased. It is analyses that ratio of vertical and horizontal soil pressure and banking variance curve. It is found that the ratio and banking not having linear relationship and corresponding with soil pressure in Figure 2c, 2d. When the ratio getting maximization, the banking equal to 1.5m, and step-down and stabilize subsequently.

Foundation stress analyses

The reinforcement foundation stress variation curve was in Figure 3. From the picture, it is observed that the foundation stress was not submitting trapezium distribution. It is analyses that the distribution corresponding with the foundation displacement constraint. While the major displacement, the foundation stress of reinforcement soil retaining wall present V-mode. While the minor displacement, the foundation stress of reinforcement soil retaining wall present bias distribution. Whereas there is large discrepancy as the foundation theory about this type of structure analyzes. Therefore, the count of slope geogrid reinforcement soil retaining wall should be considered the geogrid and foundation action.

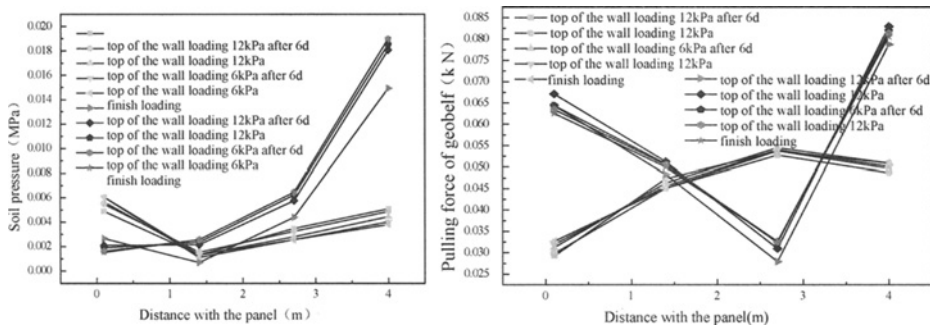


Figure 3. Basement stress curve for each case

Soil pressure inside reinforced soil

Take 1L1,2L1,3L1,4L1,5L1,6L1,7L1,8L1, and 9L1 as a group , in order to draw the picture of earth pressure behind the reinforced soil(as Figure 4a,4b). In the picture, vertical soil pressure changes complicatedly. Lateral soil pressure is more regular than the vertical, and at full wall height segment, it present convex dish distribution which justified pressure small, intermediate pressure large. So, it is reputed that the lateral soil pressure without much improves of slope reinforcement structure as erect reinforcement wall.

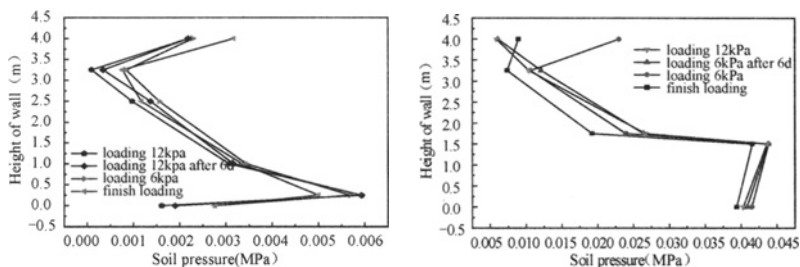


Figure 4. The soil stress in the reinforced soil body for each case

Pulling force of geobelf

The test of pulling force of geogelf indicates that pulling in company with banking increase. The pulling force of crest with reinforcement wall closed with the calculated value by assmann energy approach. But it is far from the position of middle and bottom. The slope reinforcement structural potential failure surface was approximate as log spiral. From the Figure5, we can see the pulling force of geobelf distribution as the wall height with model finite element computation. It is observed that the pulling force of geobelf close distribution trend between the finite element computation and model measurement.

Deformation of the CGR earth wall

After reclamation, deformation of the CGR earth wall resulted from test, is measured then drawn into a curve (as Figure 6). Measured datum related indicate that, there two trends for

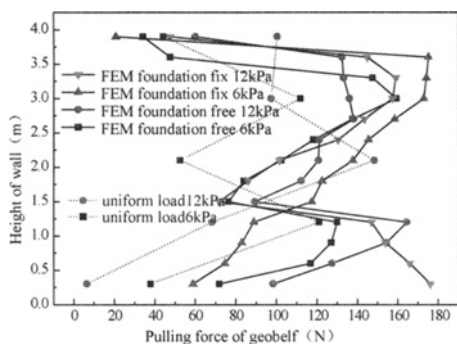


Figure 5. Pulling Force of Geobelf for two case

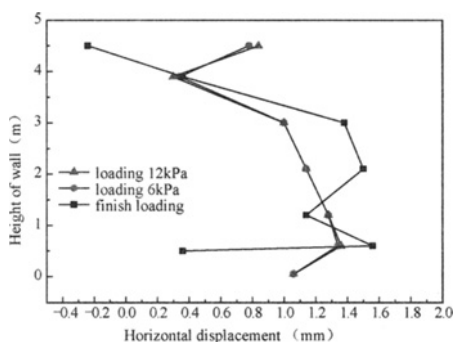


Figure 6. horizontal displacement of FEM calculation

RSR wall as the height: one is a convex curve with minim deformation at both top and toe, but maximal deformation in the middle; the other is a convex curve with minim deformation on top but maximal at toe. The board near top bears minim soil pressure, then deformities minimally, because the boards are assembled one after another, like hinge jointing each other. There are two trends for the board near the toe, because of supporting conditions of the base in the text. So we could induce that , the better base the bitter lateral deformation of the CGR earth wall , and the more justifiability as stress of reinforced-soil distribution .

CONCLUSIONS

Through upward analysis, we obtain these conclusions of model experiment, as following:

(1) It is observed that soil pressure in slope geogrid reinforcement wall discord to the conventional soil pressure theory. Its variance characteristic with banking and vertical coefficient of soil pressure not presents simple linear relationship.

(2) It is found that the foundation displacement have important impact of foundation stress mechanical behavior of the geogrid reinforcement. The stress of foundation presents as bias distribution or V-mode distribution, and correspond with foundation characteristic.

(3) The soil pressure of reinforcement wall behind panel and in reinforcement submits justified small and broad in the middle distribution. The horizontal soil pressure behind panel was similar to the erect wall, but the vertical soil pressure discrepancy with the inner reinforcement.

(4) The pulling force of geogelf present the distribution trend of fluctuate justified smallness, broad in the middle. At the bottom of 1/3 wall height, the pulling force of geogelf was least, presenting two convex dished distribution trend. The test of pulling force of geogelf indicates that pulling in company with banking increase. The pulling force of crest with reinforcement wall closed with the calculated value by assmann energy approach. But it is far from the position of middle and bottom.

(5) Measured datum related indicate that, there two trends for RSR wall as the height: one is a convex curve with minim deformation at both top and toe, but maximal deformation in the middle; the other is a convex curve with minim deformation on top but maximal at toe. There are two trends for the board near the toe, because of supporting conditions of the base in the text.

REFERENCES

- He Guangchun, Wang Chengzhi and Huang Yiqiong.(2006). Elastic-plasticity FEM analysis of soil-reinforcement composite material through model test on stepped reinforced soil retaining wall. *4th Asian Joint Symposium on Geotechnical and Geo-Environmental Engineering, Dalian China*.
- He Guangchun. (2000). *The Design and Construction of the Reinforced soil*. Beijing: The people's communication Press.
- Helwany S. M. B., Reardon G. and Wu J. T. H. (1999). Effects of backfill on the performance of GRS retaining walls. *Geotextiles and Geomembranes*, 17(2): 1-16.
- Rajagopol K., Richard J. B. (1995). Behaviour of geosynthetic reinforced soil retaining walls using the finite element analysis. *Computers and Geotechnics*, 17(4): 279-299.
- Bathurst R. J., Walters D. L. and Hatami K. (2001). Full-scale performance testing and numerical modeling of reinforced soil retaining walls, *International Symposium on Earth Reinforcement*, IS Kyushu.

- Rowe R Kerry, Skinner Graeme D.(2001). Numerical analysis of geosynthetic reinforced retaining wall constructed on a layered soil foundation, *Geotextiles and Geomembranes*, (19): 387-412.
- Sun Jun, Chi Jingkui, Cao Zhengkang, Shi Jianyong.(1998). *The new geotechnical material and regulation*, Beijing, The Press of the Construction Industry in China.
- Wang Chengzhi.(2005). *Numerical analysis and experiment for reinforced soil slopes*, Chongqing: The master works of Chongqing jiaotong university.
- Yang Guangqing.(2004). Study on Design Method of Setback Type of Reinforced Wall, *Chinese Journal of Rock Mechanics and Engineering*, 23(4): 695-698.
- Zhou Shiliang. (2005). *Study on Structural Characteristics and Failure Mechanism of Geogrid RSRW*, Chongqing: The doctor works of Chongqing University.

APPLICATION OF SPLITTING GROUTING ON THE DAM REINFORCEMENT

Ke Wu

*Research Center of Geotechnical and Structural Engineering; Shandong University,
Jinan 250061, China*

Yongnian Bai

Shandong Water and Electricity Engineering Co., Ltd., Jinan 250061, China

Shucai Li

*Research Center of Geotechnical and Structural Engineering; Shandong University,
Jinan 250061, China*

As one new type of the technology on the dam reinforcement, the splitting grouting has been established only in China since 70 and applied in a lot of dam reinforcement. The thickness of splitting grouting, deformation of the dam and the seepage field of grouting are important keys in dam reinforcement by splitting grouting. However, the theory of splitting grouting has not been known widely and lacked system generalizing. In the paper, the theory of splitting grouting is detailed statement and some actual projects are introduced to analyze the deformation of the dam before and after the splitting grouting. Moreover, the stability of the dam by using finite difference method are simulated and analyzed. The conclusion of analysis is consistent with the in-site observation.

INTRODUCTION

The earth and rockfill dams in China are almost constructed in many stages and rolled by a lot of layers. Because of locking the standard of construction and the uniform of roll, in addition, shorting of strictly managing of the dam, lots of dams exist destructions of deformation and seepage, which influence the stability of dams. However, It is one of the key fundamental issues in design and construction of hydraulic engineering to evaluate overall stability behavior and failure mechanisms of dams. In many methods of reinforcement dam, the splitting grouting is a very effective reinforcement method. The splitting grouting has been popularized since the 80s, which has been applied in many provinces in our country and got certain economic and social benefits. However, the researches on theory of splitting grouting are falling far behind the needs of practice. To promote the technology of reinforcement perfectly and improvably, the theory of splitting grouting and some actual projects are presented in the paper. Furthermore, the in-site experiments and numerical simulation are also applied to analyze the stability of the dam by splitting grouting(WU K., 2004 and 2005).

THEORY OF SPLITTING GROUTING

The method of splitting grouting is based on the rule of dam's stresses, which would split the dam along the axial line of dam by certain grouting pressures. At the same time, a vertical continuous impermeable wall would be formatted through splitting suitable mud. The impermeable wall can plug and split the cavities, cracks or soften layers, which can improve impermeable ability and stability of the dam. This method is suitable to reinforce the dams which are low quality of compaction and existence of cracks or cavities, permeable foundation based on strong structural fine sand or interlayer between soil and sand (Bai Y. N., 1985 and 2005).

The theory of splitting grouting can be discussed as seven sections.

Principle of hydraulic splitting

Under the water pressures, the objects are generating the cracks or cracks are developing, which is called as hydraulic splitting. At the beginning for the earth dam, the hydraulic splitting must be avoided because this is corrected to design and construction. However, this is unavoidable by the method of splitting grouting to reinforce the dam. It is indicated that one or some vertical impermeable walls are formatted which are about 20-30cm. However, those phenomenon can not be explained based on mechanism of permeability and filling.

Regular pattern of stresses in dam

The vertical stress σ_y of the dam is less than self-weight pressure of soil column around the axial line of the dam. The horizontal stress σ_x is less than the vertical stress, which is about $(0.3-0.5)\sigma_y$, so the 0.3-0.5 are defined as lateral pressure coefficient. The lateral pressure coefficient is becoming smaller and smaller with the quality of the dam, as the same time, the horizontal stresses at some high of the top of the dam are certain tension stresses. The horizontal stress σ_z at the longitudinal section of the dam is between σ_y and σ_x . Under the condition of general run of things, the pressures of dam conform the rule of $\sigma_y > \sigma_z > \sigma_x$. However, the stresses $\sigma_y \approx \sigma_1$, $\sigma_z \approx \sigma_2$, $\sigma_x \approx \sigma_3$ near the axial of dam, which is shown as Figure 1. Based on the rule of stresses and theory of hydraulic splitting, the grouting holes are layout along the minor principal stress near the axial of dam, which will split the dam along the plane.

Effect of split and fill by grouting

According to the elastic theory, the initial splitting pressure of wall of hole is defined as

$$p_1 = \alpha\sigma_3 + \sigma_t \quad (1)$$

where p_1 is the initial splitting pressure, σ_3 is the minor principal stress, σ_t is the tensile strength of single axle of soil, α is stress concentration factor of hole which always are $\alpha = 2.3-3.0$.

When the liquid pressure $p > p_1$, the splitting is becoming. Based on the theory of fracture mechanics, the extended pressures of cracks are meeting the relational expression as

$$p_2 = \frac{K_{IC}}{1.1215\sqrt{\pi a}} \quad (2)$$

where p_2 is pressures normal to the planes of cracks, K_{IC} is the critical stress intensity factor, a is the depth from the edge of wall of hole to interior cracks.

When $p > p_2$, the point cracks are developing rapidly forward which the speed of development is near the sound velocity. At the same time, the cracked direction is normal to the maximum tension stress in the tension stress field and the cracked direction is normal to the minimum principal stress in the compression stress field.

The serous fluid is the energy carrier, so the high-pressure mud has the effect of filling. The mud will fill the grouting pathway by splitted and all kinds of cracks or cavities in the dam, which the effect of split and fill is simultaneous proceeding. With the increase frequency of grouting, the dam is filled by lots of times. So there will be formatted a impermeable wall which has the higher permeability.

Effect of collapse

A lot of water is entering into the dam with the grouting. The water has generated the pore water pressure and affected the property of soil, and produced the effect of collapse to the dam. The magnitude of collapse is related with the quality of dam and property of soil. However, the effect of collapse is favorable to the dam, which could increase degree of density and deformation stability, decrease the area of weak stress. With the increase frequency of grouting, the effect of collapse is becoming smaller and smaller. The collapse would make the high of the dam reduce and the volume of dam narrow, and some cracks are formatted at the top of dam. With the grouting, those cracks would be filled by mud.

Regulation and transition of energy

The damages and cracks of dam are caused by the deformation and transition of energy. To release these incipient faults, the accumulation energy of dam should be delivered. The splitting grouting will make the original cracks of dam splitted rapidly and change the energy between the weak and strong stressed zone, which would break the unbalance of stress and recovery the normal condition of stress. Those would make the dam stabilization.

Theory of cross-pressure between grouting and dam

During the grouting, the grouting pressures are repeated increase and decrease, which would make the dam and mud reciprocal pressure. At last, there would format a impermeable wall or zone. The cross-pressure between grouting and dam can change the unbalance of stress in dam and settle the stability and seepage of dam.

Consolidation and junk between grouting and dam

The major reinforcement effect of splitting grouting is formatting the impermeable wall by consolidation of mud. However, the grouting consolidation can be divided into two parts which are precipitation of water and concentration, and abstraction of water and consolidation.

COUPLING ANALYSIS OF SEEPAGE AND STRESS FIELDS FOR SPLITTING GROUTING

Project survey

The earth dam of Shiliutan reservoir in Guangdong province is the even rolling dam, which high is 41m and length is 438m. The quality of the construction is badly and exist many leakages on the dam slope. Based on these local conditions, the dam is reinforced by splitting grouting. In the numerical software Flac3D(Itasca, 1997), the 3D numerical model is created to evaluate the stability of the dam by splitting grouting, which has 25429 elements and 28602 nodes as shown in Figures 1 and 2.

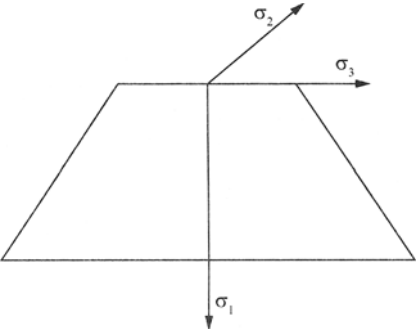


Figure 1. The three principal stresses near the axial

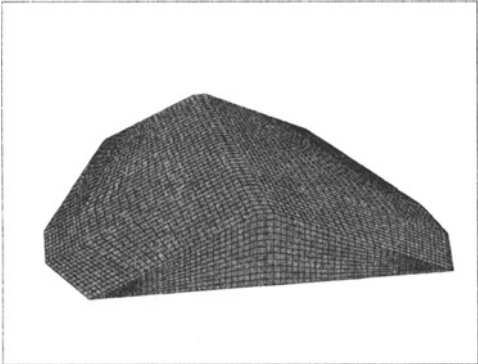


Figure 2. Finite element model

Property of soil

Based on the design of the dam and some coherent datum, the property of soil in numerical computation is list in Table 1 (Wu K., 2004).

Table 1. Parameters of physical properties of the embankment

Property of soil	Porosity	Permeability coefficient k (cm/s)	Undrained shear strength c (kPa)	Internal friction angle ($\phi/^\circ$)	Young's modulus E (MPa)	Bulk density ρ (t/m^3)
Grouting band	0.3	6.0×10^{-8}	40.0	25	20.0	2.00
Not grouting band	0.468	6.5×10^{-5}	28.8	21	16.0	1.80

Analysis of result

Through the exploratory excavation in the dam, the impermeable wall could be seen from the Figure 3. It can be seen that the impermeable wall is continuous and stiffness, which could improve the permeability of the dam. At the same time, the saturation line of the dam is lower after grouting than that before grouting as shown in Figure 4. It can be indicated that the permeability of the dam can be improved by splitting grouting which can low the high of saturation line of the dam because the mud can fill the cavities and cracks and the coefficient of permeability of mud is small than the soil.



Figure 3. The impermeable wall in-site

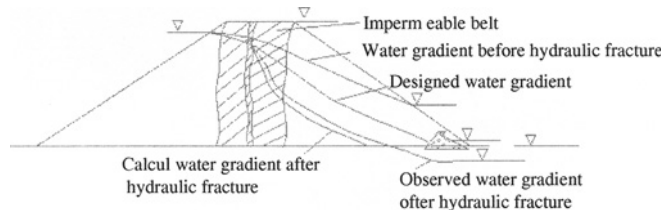


Figure 4. Alteration of the saturated line aftergrouting and before grouting

Furthermore, the field of seepage and stress is simulated by the computed software Flac3D. The maximal cross section 0+190 is as the analysis section, which the results are analyzed.

The variation of maximum and minimum principal stresses of the dam is shown in Figure 5. It can be shown that the maximum and minimum principal stresses of dam are symmetric distributed along the axial line. A grouting band has been generated inside of the dam. The stress of dam has been passed the secondary regulation, which would lead to decrease the effective stress of the maximum and minimum principal stresses inside of grouting band. The

reason of variation of principal stresses is that the effect of collapse of the dam is generated by abstraction of water from the mud during the grouting.

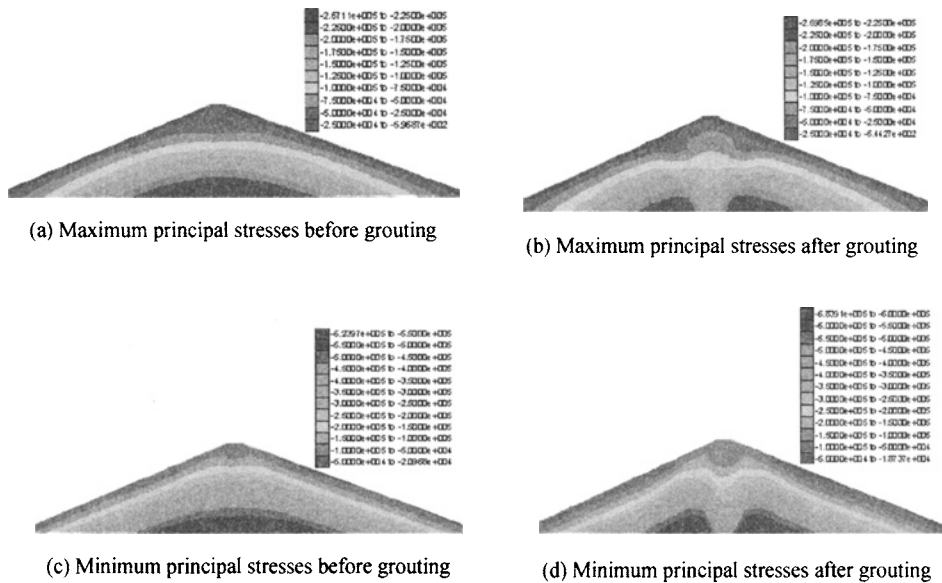


Figure 5. Minimum and Maximum principal stresses before and after grouting

The variation of deformation of the dam is shown in Figure 6. It can be shown that the vertical deformation after grouting is larger than that before grouting because of consolidation of the dam, which would make the dam more stiffness. At the same time, the grouting mud would be consolidating which lead to non-uniform deformation of the dam. So the cracks parallel to the axial line are generated at the slope of the dam, which should be specific treated.

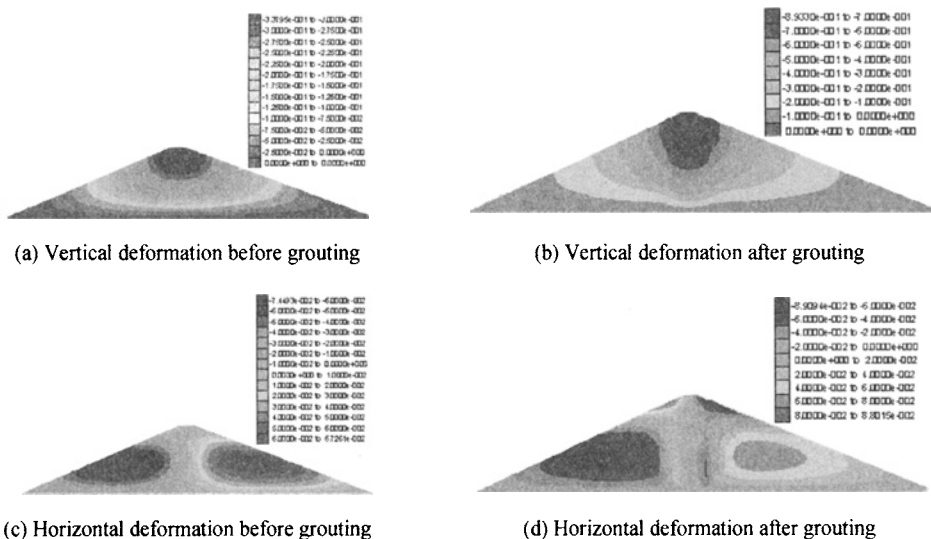


Figure 6. Deformation before and after grouting

CONCLUDING REMARKS

The theory of splitting grouting in detail is discussed systematically in the paper. Furthermore, the in-site and numerical analysis of a local project are presented. It can be indicated that the method of splitting grouting to reinforce the dam can improve the permeability and stability of the dam. The survey of theory of splitting grouting and results from numerical simulation will supply valuable theories and methods for the dam designers and constructors.

ACKNOWLEDGEMENTS

The financial support for this study through the grants 50539080 and 50574053 from National Natural Science Foundation of China is mostly grateful.

REFERENCES

- Bai Y. N. (1985). Grouting in the Embankment and Slope of dam, Beijing, China WaterPower Press,.
- Bai Y. N., et al. (2001). *The New Technology of Permeability and Reinforcement of Dam in China*, Beijing: China WaterPower Press.
- USA:[s.n.], (1997). Itasca Consultiong Group Inc. FLAC3D User's Manual.
- Wu K., Ma X. Y. and Shang L. (2004). An analysis of the solid dam reinforcement. *Journal of ShanDong Unviersity(Engineering Science)*, 34(2): 80-83.
- Wu K., Ma X. Y. and Zhao Q. (2005). Application of FLAC3D to stability analysis of splitting grouting for earth dam. *Rock and Soil Mechanics*,26(3): 484-487.
- Wu K. (2004). Experimental investigation and numerical simulation of the earth reinforcement by splitting grouting. Jinan: Shandong Unviersity.

GEOLOGICAL DISASTERS AND MITIGATION MEASURES ALONG THE COASTAL CITIES OF CHINA

Yeshuang Xu

*Department of Civil Engineering, School of Naval Architecture, Ocean, & Civil
Engineering, Shanghai Jiao Tong University, 1954 Hua Shan Road,
Shanghai 200030, China*

Shuilong Shen

ditto

Longzhu Chen

Institute of Disaster Prevention and Mitigation, ditto

Geological disasters in coastal cities of China include land subsidence, karst collapse, seawater intrusion, coast erosion, collapse, landslide, mud-rock flow, soil erosion, and man-made disasters due to construction. All these disasters have their own happening reasons, characteristics, and distribution region. Land subsidence, seawater intrusion, and coast erosion are very serious because of special characteristics in the coastal cities of China. Prevention and control of geological disasters should be improved in coastal cities of China. Because populations are dense and economy are prosperous in the coastal cities, economical loss and personnel casualty caused by geological disasters are very large.

KEYWORDS: Coastal Cities, Geological disasters, Prevention measures

INTRODUCTION

Geological environment is defined as the combination of all kinds of geology factors, which influences on human survival and development in lithosphere. Harmful geological environment, which is detrimental to human being, is called geological disaster (Chen et al., 2005). Chinese coastal line is bounded by the Bohai Sea, the Yellow Sea, the East China Sea, and the South China Sea. More than 70% of metropolis and midsize cities with a half of the population and 60% of GNP in China locate in coastal region (Liu, 1998). Because the interaction among lithosphere, atmosphere, hydrosphere, and biosphere and geological conformation is complicated and varies along the coast, geological disasters exist universally along coastal region of China. Economic loss and personnel casualty caused by geological disasters are very large. Proper prevention measures should be put forward according to the characters of coastal region of China.

OUTLINE OF GEOLOGICAL DISASTERS IN COASTAL CITIES

Table 1 tabulates geological disasters along with distribution areas, representative place, and distribution characters occurred along the coastal region of China.

Table 1. Geological disasters along the coastal cities of China

Types	Distribution region	Representative cities	Distribution Characters
Land subsidence	Bohai Bay, Yangtze River Delta, and Zhujiang River Delta	Shanghai and Tianjin City	About 80 coastal cities occurred land subsidence
Karst collapse	Southeastern Coastlands and North China Coastlands	Guangdong Province	Average scale is 18 place/km ²
Seawater intrusion	Bohai Bay, Yangtze River Delta, and Zhujiang River Delta	Laizhou Bay	Intrusion area > 1000 km ²
Coast erosion	Coastal cities along sea	Yellow River Delta	All open mucky coast and 70% of sandy coast
Collapse, landslide, and mud-rock flow	Tianjin City, North of Zhejiang Province and	Guangdong and Zhejiang Province	
Soil erosion	Southeastern Coastlands and Shandong Peninsula	Shandong Peninsula	Eroded area=2.88'104 km ²
Construction disaster	Coastal cities	Shanghai City	

Land subsidence

In China more than 80% of the cities, where land subsidence occurred, are coastal cities (Hou et al., 2000). Early in 1920s, land subsidence is noticed in Shanghai (Gong, 2005). Land subsidence occurred in most cities along coast, such as Ningbo City (Zhao et al., 2006), Wenzhou city (Zhao et al., 2006), and Tianjin City (He et al., 2006). Figure 1 shows the distribution of land subsidence along coast (China Geological Survey). Shanghai, Su-Xi-Chang area, and Hang-Jia-Hu Plain are typical land subsidence districts, where the maximum land subsidence is 2.9 m (Yu et al., 2006), 2.8 m (Li and Wang, 2006), and 1.0 m (Zhao et al., 2006), respectively.

Karst collapse

Figure 2 shows the distribution of karst collapse along coast (China Geological Survey). Karst collapse mainly distributes in Guangxi, Guangdong, Fujian, Zhejiang, Jiangsu Province, Shandong peninsula, and Liaodong peninsula. Guangdong and Guangxi Province are the most serious places. There are 137 places, where karst collapse occurred in Guangdong Province till 2003 (Zhang and Wei, 2003).

Seawater intrusion

Seawater intrusion mainly distributes in the Zhujiang Delta, the Yangtze River Delta, and areas around Bohai Sea. The intrusion phenomena that occurred in Laizhou Bay is the most intrusion place where the intrusion areas have exceeded 500 km² at the end of 1990s (Wang et al., 2002). Figure 2 illustrates the distribution of seawater intrusion along coast.

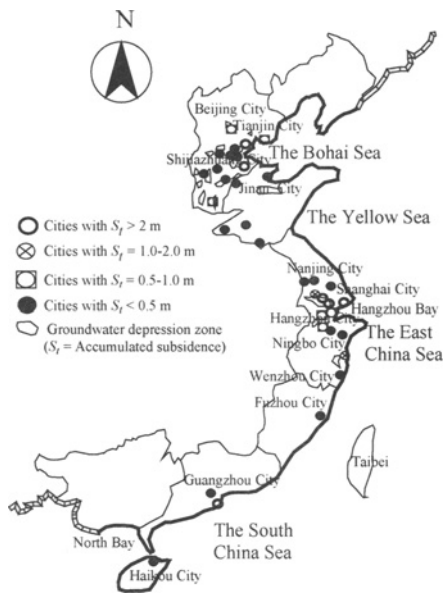


Figure 1. Distribution of land subsidence along coast



Figure 2. Distribution of karst collapse and seawater intrusion along coast

Coastal erosion

According to statistical results, almost all open mucky coast and 70% of sandy coast are on the condition of erosion (Sheng and Zhu, 2002). For example, sandy coast in Liaoning Province, Hebei Province, Shandong Province, and Guangdong Province, mucky coast in the north of China, and eastern bank in Hainan Province. Eroded coastal line along Bohai Sea is 46% of the length of the Bohai Sea coastline. Along the Yellow Sea, the East China Sea, and the South China Sea, the eroded length of coast is about 49%, 44%, and 21% of the total coastal length, respectively (Sheng and Zhu, 2002).

Collapse, Landslide, and mud-rock flow

Most of collapse, land slide, and mud-rock flow occurred in Tianjin City, the north of Zhejiang Province, and the southeastern coastal region of China (Liu, 1998). There are more than 1000 places, in which landslide or mud flow occurred (Gong and Gong, 2006). Landslide occurred in Dalian City in 1998 and Yueqing mud-rock flow occurred in Wenzhou City in 2004 (Gong and Gong, 2006).

Soil erosion

In coastal region of China, soil erosion mainly distributes in Shandong Peninsula and Liaodong peninsula. The soil erosion area has reached $2.54 \times 10^5 \text{ km}^2$ in the east of Shandong Province (Wang and Guo, 2005). The southeastern coastal area also has soil erosion, such as Fujian Province (Su, 2001) and Guangdong Province (Wu et al., 2001).

Man-made construction disaster

There are many projects with underground constructions in coastal cities, such as excavation of deep foundation pits, tunnels, and construction of embankments. There are more than 130 skyscrapers, in which about one-third of foundation pit constructed after 1993 lost their stability (Liu, 1998). It is well known that engineering accident occurred during the construction of subway line No.4 in Shanghai in 2003.

PREVENTION AND MITIGATION MEASURES

Enhancement on monitoring and forecast for disasters

It is important to monitor the trend of disaster development and forecast climate that lead to geological disasters. At present, coastal cities are developing and applying the automotive system such as GIS and InSAR to survey geological disasters step by step. For example, Shanghai established land subsidence network (Chen, 2004). Fujian Province established real time survey and forecast system of typhoon (Wu and Zhuang, 2003).

Establishment and improvement of data-base

In order to prevent and mitigate the disasters, it is very significant to establish and improve the database system. The database should include geological and geotechnical information, historical disaster information, and prediction information. Data share is advantageous to integrate management of disasters and datum on geological disasters can be found at any moment and any place. For example, Zhou and Xu (2005) designed land subsidence database system based on ArcSDE.

Intensifying disaster prediction and evaluation

Prediction and evaluation of economy loss and disaster fatalness according to the development trend of geological disasters provide scientific foundation for utilization of resources and engineering constructions in coastal region of China. Shanghai has set up theoretical system of evaluating economic losses caused by land subsidence (Duan and Zhang, 2002).

Control harmful human activity

Harmful human activities, which lead to disasters, should be controlled. For example, groundwater monitoring network should be set up; more attentions should be paid on the monitoring and management of urban construction. Projects constructed on unstable hill or around coast erosion region should be prohibited and vegetation should be protected.

Presentiment and emergency measures

The basic contents of presentiment and emergency measures include: *i)* constituting evacuation plan, *ii)* building temporary refuge places, *iii)* doing disaster-control education to

improve people's self-saving ability, iv) rapidly recovering of living facilities, and v) limiting the scale of subsidiary disasters. The plan should be made based on the characteristic of cities and disasters.

CONCLUSIONS

Since the coastal topography, geomorphology, and geology in China are complicated, there were many different types of geological disasters in coastal cities. Every type of disasters has its own characteristics, while the common aspect is the induced geological disasters of engineering activities of human being and geological environment are interdependent. To prevent not only natural disasters but also man-made disasters, the effective prevention measures can reasonably utilize resources, protect ecological system, and inspect geological environment development. Not only the measures should be undertaken before the occurrence of disasters but also problems should be dealt with after the happening of disasters.

ACKNOWLEDGEMENTS

The research work described herein was funded by the National Nature Science Foundation of China under Grant No.50779035 and also supported by the Shanghai Leading Academic Discipline Project (Project Number: B208). These financial supports are gratefully acknowledged.

REFERENCES

- Chen G.G., Xu J. and Gao Z.W. (2003). Seismotectonic features of the Bohai Bay basin in North China, *North China Earthquake Sciences*, 21(2): 7-15.
- Chen H.W. (2004). Survey techniques of land subsidence in Shanghai, *Colloquia of Survey and Inspection Methods of Geology Disaster*, 219-225. (in Chinese)
- Chen L.Z., Liang F.Y. Song C.Y. and Xing, A.G. (2005). *Hazard Control Engineering*, China Architecture & Building Press. (in Chinese)
- China Geological Survey. <http://www.cgs.gov.cn/task/shuigonghuan/chengguo-01.htm>.
- Duan Z.L., Zhang, W.R. (2002). Study on theoretical system of evaluating economic losses caused by land subsidence: the case of land subsidence in Shanghai, *Journal of Natural Disasters*, 11 (3): 95-102. (in Chinese).
- Gong X.W., Gong Z.H. (2006). Current situation of geo-hazards and macroscopic preventive measures in the littoral in China, *Journal of Catastrophology*, 21 (4): 79-83. (in Chinese)
- Gong S.L. (2005). The geological environment and land subsidence protection in Yangtze River Delta, *2005 Science Meeting of Geological Society of China*, 25-34.
- He Q.C., Liu W.B. and Li Z.M. (2006). Land subsidence survey and monitoring in the North China Plain, *Geological Journal of China Universities*, 12 (2): 195-209. (in Chinese)
- Hou Y.S., Zheng X.X. and Ying Y.F. (2000). Sustainable development strategy and systematic control on land subsidence in coastal region of China, *Chinese Journal of Geological Hazard and Control*, 11(2): 30-33. (in Chinese)
- Li Q.F., Wang H.M. (2006). A study on land subsidence in Shanghai, *Geological Journal of China Universities*, 12 (2): 169-178. (in Chinese)

- Liu Y.H. (1998). Main geological hazards confronting the coastal cities of China in twenty first century, *Chinese Journal of Geological Hazard and Control*, 9(supp.): 120-126. (in Chinese)
- Sheng J.F., Zhu D.K. (2002). Discussion about coastline erosion and management, *Marine Science Bulletin*, 21 (4): 50-57. (in Chinese)
- Su Z.H. (2001). Basic characteristics and estimation of soil erosion in the coastlands in south part of Fujian Province, *Fujian Soil and Water Conservation*, 13 (3): 56-60. (in Chinese)
- Wang H.X., Guo Y.G. (2005). Analysis of the main geological hazard types in the coastal and offshore areas of Shandong Province, *Periodical of Ocean University of China*, 35 (5): 751-756. (in Chinese)
- Wang Q.X., Ren Z.Y. and Sun G.N. (2002). Research on seawater intrusion disaster in south-east coastwise area of Laizhou Bay, *Marine Environmental Science*, 21 (3): 10-13. (in Chinese)
- Wu J.T., Zhuang X. (2003). Supervision and forecast system to prevent typhoon in Fujian Province, *Water Resources and Hydropower Engineering*, 34 (7): 64-66. (in Chinese)
- Wu Z.F. Wang J.Z., Qian, W.Z. and Wu. L. (2001). Urban soil and water losses and their characteristics – a case study on Sanzao, Zhuhai City, *Ecologic Science*, 20 (Z1): 75-80. (in Chinese).
- Yu J., Wang X.M., Wu J.Q. and Xie J.B. (2006). Characteristics of land subsidence and its remedial proposal in Suzhou-Wuxi-Changzhou area, *Geological Journal of China Universities*, 12 (2): 179-184. (in Chinese)
- Zhang J.G., Wei P.X. (2003). Characteristics of the main geological hazards and their control countermeasures in Guangdong Province, *The Chinese Journal of Geological Hazard and Control*, 14 (4): 44-48. (in Chinese)
- Zhao J.K., Wu M.J., Liu S.X. and Shen H.Z. (2006). The relation between groundwater exploitation and land subsidence in coast plain of Zhejiang Province, *Geological Journal of China Universities*, 12 (2): 185-194. (in Chinese)
- Zhou J., Xu M. (2005). Design of spatial data-base about land subsidence based on ArcSDE, *Journal of Engineering Geology*, 13(supp.): 106-108. (in Chinese)

EFFECTIVENESS OF JET-GROUT COLUMNS FOR MITIGATION OF LIQUEFACTION DURING EARTHQUAKES

C. Guney Olgun

*Department of Civil and Environmental Engineering, Virginia Tech
Blacksburg, VA 24061, U.S.A*

James R. Martin II

*Department of Civil and Environmental Engineering, Virginia Tech
Blacksburg, VA 24061, U.S.A*

The 1999 Kocaeli Earthquake ($M=7.4$) caused significant damage along Izmit Bay. We investigated the performance of improved soil sites in the region. An important site was Carrefour Shopping Center which is underlain by soft clays, silts, and liquefiable sands. Jet-grout columns had been installed to reduce static settlements and prevent liquefaction. Post-earthquake inspections showed the grouting to be effective in reducing damage. Dynamic finite element analyses were used to model the reinforced ground at the site. Surprisingly, the results suggest that the columns did not reduce seismic shear stresses and strains in the soil mass. Column effectiveness was more related to vertical support that prevented settlements. Our findings imply that design methods that assume composite shear behavior for columnar-reinforced ground can greatly overestimate the actual level of improvement.

INTRODUCTION

The Kocaeli Earthquake ($M=7.4$) struck northwestern Turkey on August 17, 1999 and caused significant damage in urban areas located along Izmit Bay (Martin et al., 2001). The Carrefour Shopping Center was under construction at the time of the earthquake, and contained both improved and unimproved soil sections that could be compared in terms of seismic performance. The facility is located along Izmit Bay approximately 3 km from the ruptured fault. The estimated peak ground acceleration at the site was 0.24g (Olgun, 2003).

This paper presents the findings of the numerical analyses that investigate why the ground treatment was effective. The study is instructive because the approach of using closely-spaced jet-grout columns to mitigate liquefaction differs from the common practice of constructing rows of contiguous columns to form large cells to contain the liquefied material. Although it was clear that the ground treatment was effective, our analyses suggest that the seismic behavior of the reinforced ground and the primary reason for its effectiveness was different than first thought. The reinforced ground probably did not behave as a composite soil mass, as commonly assumed by some widely-used design methods (i.e. Baez and Martin, 1994). This means the dynamic shear stresses and strains in the soil were

probably not significantly reduced by the reinforcement. Rather, we suspect the effectiveness was primarily related to the vertical support of the columns that reduced earthquake-induced settlements. The study has implications for the use and design of reinforced ground for seismic mitigation.

JET-GROUT IMPROVEMENT AT CARREFOUR SHOPPING CENTER SITE

The Carrefour Shopping Center is situated in a Quaternary marine setting of low ground elevation and minimal local relief. The relatively flat area was recently reclaimed from Izmit Bay using gravelly fills. The site is underlain by soft alluvial sediments consisting of alternating strata of soft clays, silt-clay mixtures, and silty sands. The depth to firm rock is not known, but deep geological profiles from nearby sites suggest a depth of 80 to 100 m. The water table is within 2 m of the surface.

The stratigraphy is variable, consisting of alternating strata of silt-clay mixtures, silty sands, and soft-to-medium clays as shown in Figure 1. The Cone Penetration Test (CPT) tip resistances are low, and with the exception of the silty sand stratum (SP/SM), the values average about 1 MPa throughout the upper 25 m of the profile. Standard Penetration Test (SPT) $N_{1,60}$ blow counts average 5 blows/ft. in most strata. Shear wave velocities measured by seismic CPTs are 110–140 m/s throughout the upper 25 m. Of concern to the designers was the potential liquefaction of the loose-to-medium SP/SM stratum found at an average depth of 6 m. This stratum varies from 2 to 4 m in thickness across the site and contains an average of 30% non-plastic fines. And although not understood at the time, the ML/CL and CH strata were also vulnerable to significant earthquake-induced deformations beneath loaded areas, as measured by site engineers. The ML/CL has a PI = 10 and LL = 34, whereas the CH has a PI = 37 and LL = 66.

The shopping center is founded on spread footings and mats. The primary design issues were large anticipated settlements the ML/CL and CH strata under static loads, and potential liquefaction of the SP/SM strata during seismic events. Jet-grout columns were installed to address both issues. Primary and secondary grids of jet-grout columns were installed to provide blanket treatment. The primary columns were 0.6 m in diameter with a center-to-center spacing of 4 m, and extended from the ground surface to a depth of 9.0 m as shown in Figure 1. A secondary grid of 2.5 m-long columns was installed between the primary columns. These truncated columns, which penetrated only the SP/SM stratum, were installed with the tacit assumption that the higher jet-grout replacement in this layer would reduce liquefaction potential.

A post-earthquake inspection showed dramatic differences between the treated and untreated sections. No settlement or ground damage was found beneath the main building, and construction resumed. In contrast, large settlements occurred in unimproved sections at the site and neighboring properties, especially beneath loaded areas. Nearby 5- and 6-story apartment buildings also settled 10–12 cm. A row of neighboring two-story warehouses settled about 5 cm. Water ponded following the earthquake at the ground surface at untreated areas at the site, an indication of the increased pore pressures during the earthquake.

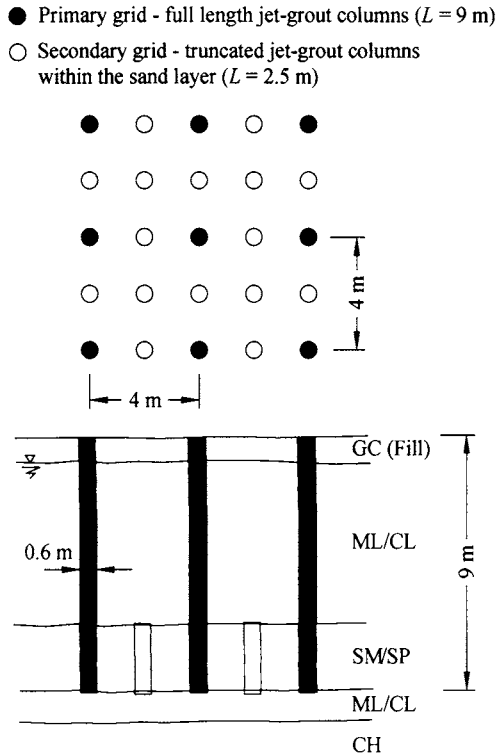


Figure 1. Typical blanket treatment used under the shopping center

DYNAMIC NUMERICAL MODELING AND RESULTS

Although the columns were demonstrated to be effective at mitigating ground damage, the specific mechanisms were unclear. It was initially assumed that the primary benefit was the higher composite shear stiffness of the reinforced ground that reduced seismic shear stresses and strains, as suggested by Baez and Martin (1994) in their method proposed for stone columns. To investigate potential mechanisms, dynamic non-linear finite element modeling of the reinforced ground at Carrefour was performed using DYNAFLOW (Prevost, 1981).

The reinforced ground, treated with 4 m x 4 m grids of primary (9 m-long) and secondary (2.5 m-long) 60 cm-diameter columns was modeled in three-dimensions. The finite element mesh contained approximately 22,000 elements and is shown in Figure 2. As shown, the model of the soil profile extended to a depth of 15 m. the analyses were performed with total stress analyses where pore pressure generation was not considered. Detailed soil testing data were not available at the time to calibrate the constitutive models for fully-coupled pore pressure generation behavior. Constitutive soil parameters were based on laboratory and field tests performed by the authors (Olgun 2003), and the soils were modeled to be fully non-linear during shaking using the elasto-plastic soil model developed by Prevost (1981). The jet-grout columns were modeled with strengths and stiffnesses consistent with those measured during post-treatment field quality control tests. To provide a benchmark for comparison, a series of runs was also performed for the case where the jet-grout columns

were removed from the model such that the soil was unimproved. In terms of boundary conditions along the sides, the three-dimensional model was assumed to be surrounded by an infinitely repeating sequence of identical 4 m \times 4 m reinforced soil sections. This was achieved by assigning the opposite nodes on each face of the model to be equivalent. By assigning nodal equivalency to node couples at the same elevation they share the same set of equations of motion, and therefore undergo the same motion in each direction. This equivalency imposes symmetry along each vertical face of the model. The model was shaken in two horizontal directions simultaneously using the horizontal components of the ground motions recorded during the 1999 Kocaeli Earthquake at approximately 2 km from the site. Of primary interest in the analyses was evaluating the effectiveness of the columns in reducing shear stresses and strains in the reinforced soil mass.

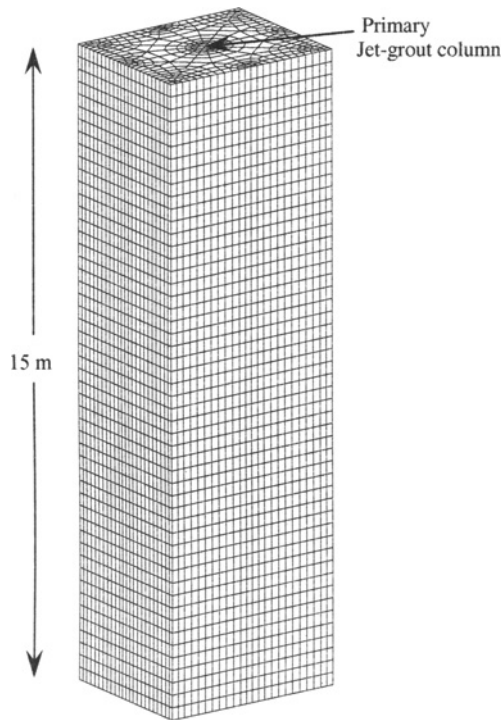


Figure 2. 3-D finite element mesh of the 4 m \times 4 m jet-grout improved soil section

The analyses results are summarized in Figure 3. The figure shows the predicted peak seismic shear strains and stresses developed in the jet-grout columns and improved soil mass. For comparison, results are also shown for the unimproved soil mass. Although the stresses and strains were computed for two horizontal directions (x and y), as per the three-dimensional analyses, the results shown in the figure are the average values for both directions (average of γ_{zx} & γ_{zy} , and τ_{zx} & τ_{zy}). Also, it should be noted that the values shown for the improved and unimproved soil are representative of the average stresses and strains in the soil mass between the columns.

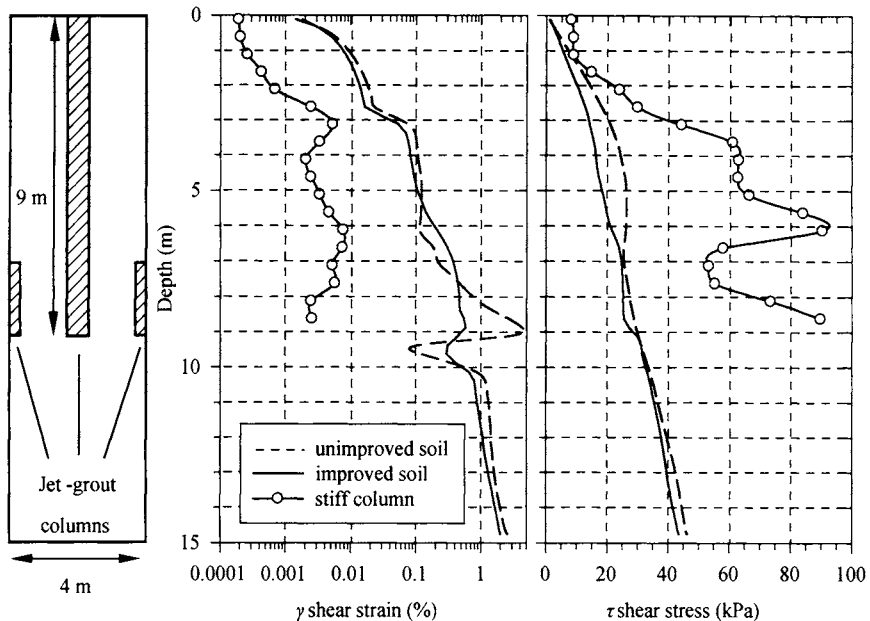


Figure 3. Summarized results of dynamic finite element analyses of unimproved and jet-grout reinforced ground at Carrefour

As can be seen on the left plot in the figure, the stiff columns were not strained as hard as the soil around them—they experienced negligible shear strains, while peak strains in the reinforced soil mass approached 1%. The analyses suggest significant strain incompatibility between the soil and columns which were about 50-100 times stiffer in shear relative to the soil. Such incompatibility was also evident in the deformed mesh shapes, which showed that the columns tended to flex back and forth within the soil profile and rotate at the ends during shaking rather than shearing along with the surrounding soil. As such, they clearly did not behave as shear beams to any significant degree during shaking, as tacitly assumed. Therefore, even though the columns were much stiffer, they did not strain sufficiently in shear to attract a significant portion of the shear loading. This means the columns should not have significantly reduced shear strains, and thus excess pore pressures, in the soil mass as initially thought. As such, it can be seen in the figure that the predicted strains in the jet-grout improved soil mass were essentially equal to those in the unimproved soil.

Similarly, the predicted peak seismic shear stresses are shown on the right-most plot in Figure 3. The peak stresses in the jet-grout columns ($\sim 60\text{-}80$ kPa) were consistently higher than those in the soil mass (~ 20 kPa), as would be expected because the columns are stiffer and attracted more load; however, they did not attract nearly enough shear stress to significantly reduce the shear stresses in the reinforced soil mass which were only slightly lower than those in the unimproved soil. Of particular significance, the stiff columns picked up only a small percentage of the shear stresses implied by area-replacement ratio methods such as Baez and Martin (1994) that assume composite shear behavior. The average shear stress reduction (shear stresses in improved soil relative to unimproved soil) that would have

been expected for composite behavior at Carrefour is on the order of 80%, but as shown, the actual stress reduction was nowhere near this amount.

SUMMARY AND CONCLUSIONS

The apparent effectiveness of jet-grout improvement at Carrefour site was investigated with numerical analyses. The analyses suggest that the reinforced ground did not behave as a composite soil mass due to strain incompatibility between the soil and stiff columns. The columns, about 50 to 100 times stiffer in shear, were not strained as hard as the soil around them. They experienced negligible shear strains, while peak strains in the reinforced soil mass approached 1%. Further, the analyses showed the columns and soil underwent different modes of seismic deformation. For the most part, the columns did not deform in shear and did not behave as shear beams during shaking. Instead, they behaved mainly as flexural beams and did not attract a significant portion of the seismic shear loading. The results show that the columns offered little reduction of dynamic shear stresses, strains, and excess pore pressures in the soil.

Interestingly, our modeling suggests that the primary contribution of the reinforcement at Carrefour was not due to seismic shear stress reduction, but rather the resulting high vertical stiffness that provided support and prevented earthquake-induced settlements in the softened soil profile. Based on our ongoing study of the site, we suspect an important and fortuitous result was that some of the soil surrounding and/or underlying the columns did not suffer major strength loss during shaking, such that the columns maintained a significant percentage of their pre-earthquake vertical capacity. As long as their structural integrity was also maintained (i.e., no flexural failure), such reinforcing elements should have offered significant benefit in reducing seismically-induced settlements. The full-blown analyses of the site, which involve modeling pore pressure development, reconsolidation settlements in the soil profile, and other details, are beyond the scope of this paper.

REFERENCES

- Baez J. I., Martin G. R. (1994). Advances in the design of vibro systems for the improvement of liquefaction resistance. The 2nd Seismic Short Course on Evaluation and Mitigation of Earthquake Induced Liquefaction Hazards, Division of Engineering, San Francisco State University and Department of Civil Engineering University of Southern California, Los Angeles and San Francisco.
- Martin J.R., Mitchell, J.K., Olgun C.G., Durgunoglu H.T. and Emrem C. (2001). Performance of improved ground during the 1999 Turkey Earthquakes, 2001 A Geo-Odyssey, ASCE Geotechnical Special Publication No. 113, June, 2001, 565-579.
- Olgun C.G. (2003). Performance of Improved Ground and Reinforced Soil Structures during earthquakes - case studies and numerical analyses. Ph.D. Dissertation, Virginia Tech, Department of Civil and Environmental Engineering.
- Prevost J.H. (1981). DYNFLOW: A nonlinear transient finite element analysis program, Technical Report, Department of Civil Engineering and Operations Research, Princeton University, Princeton, New Jersey.

SUPPORTING METHOD OF JINCHUAN DEEP ROADWAY 1178 SUBLEVEL

Chunli Yang

*College of Resource & Safety Engineering, University of Mining & Technology(Beijing),
Beijing 100083, China*

Yongcai Wang

*Jinchuan Nickel & Cobalt Research Center,
Jinchuan 737102, China*

Deep roadway failure mechanism of Jinchuan is analyzed. The result shows that anchor cable should be used and more attention should be paid on the floor supporting. Several supporting methods are put forward combined with physical circumstance of deep roadway 1178 sublevel, failure mechanism and previous supporting experiences. Every supporting method is simulated using 3D FEM. The result shows that the roadway can keep stability using high strength anchor bar combined anchor cable and floor bolt. The method is applied in actual supporting, and monitoring results show that the method can keep the stability of the tunnel.

INTRODUCTION

Jinchuan mine lies in Jinchang city, Gansu province, and it is a big nickel production base of our country. In recent years, with the increasing of mining depth and influence of excavation disturbance, stress distribution of roadway surrounding changes evidently, and stress increases greatly. In some deep roadway, stress reaches 45Mpa, which is rare in our country. High stress combined with bad geological environment, such as weak intercalation, fractured rock and so on, make surrounding rock in deep roadway have swell and creep characteristic. The supporting method and experience can not satisfy production, and tunnel stability is a big problem.

Much research had been done on Jinchuan tunnel supporting, for example Jinchuan Group Ltd.(1996),WANG Yongqian et al. (2002), LI Li et al. (2005). In shallow tunnel supporting of Jinchuan, Shotcrete-folt supporting method is used, and good effect had got. But when the method is applied in deep roadway, the effect is not good. The tunnels deforms and cave-in greatly. Many roadways are repaired two or three times. So the research of Jinchuan deep roadway supporting is necessary.

DEEP ROADWAY DEFORMATION MECHANISM AND SUPPORTING METHOD

Many people had done research on deep tunnel supporting, for example XIE Heping et al. (2006), HE Mancao et al. (2004), BAI Jianbiao(2006), LI Shuqing(2006).Compared with

shallow tunnel, broken rock zone and plastic region extend in deep roadway .So anchor bars are in broken rock zone and plastic region, and can not fix the loose rock in stability rock. Although anchor bar density is increased and double reinforcing steel bar was used, fractured surrounding rock deformation can not be controlled. So, anchor cable should be used in Jinchuan deep tunnel supporting. With it, loose surrounding rock can be fixed in stability rock.

Floor heave is a big problem in deep roadway supporting. In Jinchuan, the factors affecting floor heave are mostly two aspects: high stress and rheological behavior of floor rock. When tunnel is excavated in high stress zone, potential stress releases, which make surrounding rock extrusion toward opening. Because there is supporting in crown and sidewall, Compression deformation is control in a certain extent. But there is no supporting in floor, stress mainly releases here, so floor heave happens. In deep roadway, week intercalation will swell met water, and has rheological behavior, which cause floor heave increase with time and intensify floor heave. At first, only concrete was used in floor supporting, but in deep tunnel, stress increases, concrete can not control floor heave. So in the supporting experiment, anchor bars and concrete are advised to use in floor to enhance intensity of floor rock to control floor heave.

NUMERICAL SIMULATION OF 1178 SUBLEVEL SUPPORTING METHOD

Geological survey

Surrounding rock is mainly center thin layer serpentine marble, and the rock belongs to III3. Orientation is $220^{\circ}\text{--}240^{\circ} \angle 60^{\circ}\text{--}70^{\circ}$. Multi-stage structure residual stress (especially later period stress field) is bigger. Value of vertical stress is 27-41Mpa, and value of horizontal stress is 13Mpa. Side pressure coefficient is 2-3.

Simulation scheme

3D- σ software is used to do the simulation. Drucker-Prager (D-P rule) plastic failure criterion is applied to analyze rock failure.

Structure of tunnel is vertical-arched wall and cross section is $5 \times 4.6\text{m}^2$. Eight schemes are chosen according to supporting experience and the geology of the tunnel. The supporting methods and parameters in arch and vertical wall are shown in Table 1. In method 5-8, anchor bar and spray concrete are used to supporting the floor, the length of the anchor is 3m, and thickness of concrete is 0.2m.

Mechanical parameters used in numerical simulation

According to lots of trial simulation and experience reduction, mechanical parameter used in the simulation is as Table 2-4.

Table 1. Supporting parameters of the eight methods in arch and vertical wall

case	anchor bar			anchor cable			thickness of concrete (m)
	length (m)	spacing (m)	row of distance (m)	length (m)	spacing (m)	row of distance (m)	
1	-	-	-	-	-	-	-
2	3	0.8	0.8	-	-	-	0.2
3	2	0.8	0.8	-	-	-	0.2
4	3	0.8	0.8	7.3	-	-	0.2
5	3	0.8	0.8	7.3	1.6	1.6	0.2
6	2	0.8	0.8	7.3	1.6	1.6	0.2
7	3	0.8	1.6	7.3	1.6	1.6	0.2
8	3	1.6	0.8	7.3	1.6	1.6	0.2

Note:- represents the item is not included in the case

Table 2. Surrounding rock parameters for numerical simulation

rock	density (g/cm ³)	elastic modulus (GPa)	Poisson's ratio	tensile strength (MPa)	cohesion (MPa)	internal friction angle (°)
marble	2.35	60	0.28	0.8	0.6	40

Table 3. Anchor bar and anchor cable parameters for numerical simulation

Material	elastic modulus (GPa)	diameter (mm)
anchor bar	98.6	25
anchor cable	78.6	15.24

Table 4. Spray-up concrete parameters for numerical simulation

material	elastic modulus (GPa)	Thickness (m)	Poisson's ratio
concrete	21	0.2	0.35

Analysis of simulation results

Comparison of plastic zone distribution

Plastic zone is shear and tensile failure zone. If surrounding rock stress is bigger than its stress limit, surrounding rock will be in plastic state. The surrounding rock in plastic state is called plastic zone. Displacement of surrounding rock is caused by plastic deformation, the broader the plastic zone, the more serious the tunnel deformed.

In the figures, the red colour represents plastic zone. Seen from Figure 2 and Figure 3, there are plenty of plastic zones in side walls and length of anchor bar has little effect on plastic distribution, so only shotcrete-bolts can not keep stability of tunnel. Comparing Figure 4 to Figure 2 and Figure 3, we can see that plastic area reduce a little after using

anchor cable. And after using floor supporting, seen from Figure 5-8, plastic zone in side walls reduce greatly. So the result of simulation shows that floor supporting can change stress distribution. Comparing 5 to 6, we can also conclude that length of anchor bar has little effect on plastic zone distribution. And comparing figure 5 to Figure 7 and Figure 8, we can see that density of anchor bar has some effect on plastic zone distribution. From the distribution of the plastic zone distribution, we can see that method 5 and method 6 are both the best.

For convenience, P.Z. D. is used to replace plastic zone distribution for short in the article.

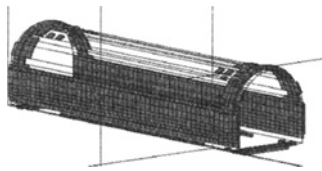


Figure 1. P.Z.D. of the first method

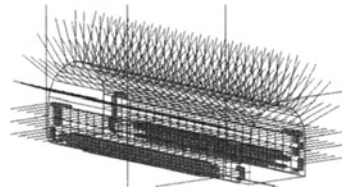


Figure 2. P.Z.D. of second method

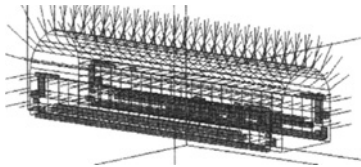


Figure 3. P.Z.D. of the third method

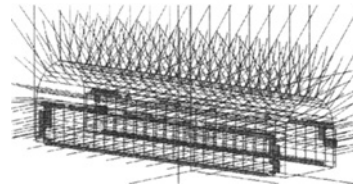


Figure 4 P.Z.D. of the fourth method

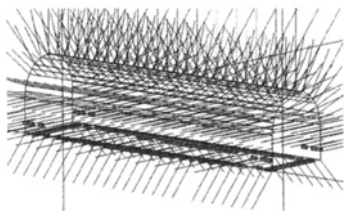


Figure 5. P.Z.D. of the fifth method

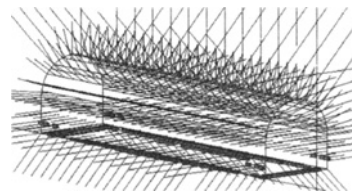


Figure 6. P.Z.D. of the sixth method

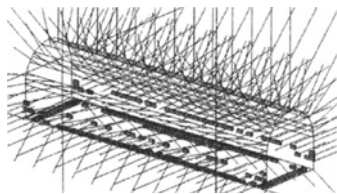


Figure 7. P.Z.D. of the seventh method

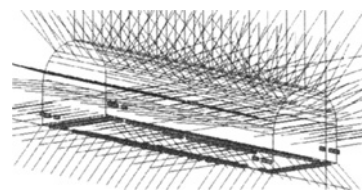


Figure 8. P.Z.D. of the eighth method

Comparison of maximum principal stress

Seen from simulation result, maximum principal stress mainly distributes in the corner of vertical. The maximum principal comparison table of the eight schemes is as Table 5. Compared with compressive stress, tensile is easy to cause the failure of tunnel. So from the table, the fifth scheme is the best.

Table 5. Maximum tension and compression stress of the eight methods

case	maximum tension stress (MPa)	maximum compression stress (MPa)
1	3.832	28.394
2	2.913	20.539
3	4.670	21
4	2.981	21.84
5	1.435	20.578
6	2.902	22.043
7	2.817	22.639
8	2.905	22.071

Conclusion of simulation

The fifth method is the best of the eight methods according to analysis of simulation result above. The simulation result shows that the method can keep tunnel stability.

EVALUTION OF SUPPORTING EFFECT

Monitor convergence value

In tunnel supporting, in-spot monitor is an important technique which can guide construction, adjusting supporting parameters, evaluating supporting effect. It is a necessary and important technique.

Supporting method of the fifth scheme is applied in 1178 sublevel. In order to monitor supporting effect, the monitor sections are arranged in the trial tunnel. Two corresponding points are arranged in both vertical walls of each monitor section. The distance of two corresponding is measured using tape. The value of first time distance subtracting the distance of every later monitor distance is convergence value. The convergence value dividing interval day is convergence velocity value. Figure 9 is time-velocity curve of section L31-31. The monitor is from 20, June to 16, Nov. Convergence velocity decreases with time greatly.

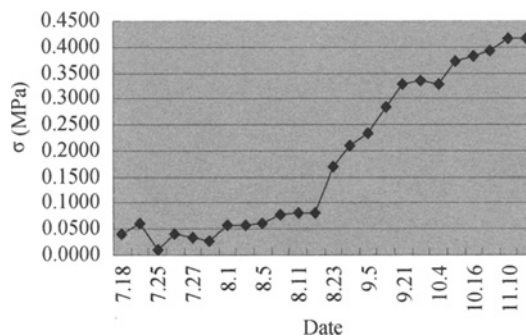


Figure 9. Time-velocity curve of L31-31 convergence section

Stress of spray-up concrete layer

GPL-2 concrete layer stress equipment is used to monitor the stress of concrete layer. Three stress equipments are arranged in one section, which are in left and right of vertical walls and top of the tunnel. The monitor began from 18 July to 10 Nov., the stress tends to stable. The time-stress curve of spray-up concrete layer is shown in Figure 10. The maximum is 0.4171Mpa, which is far smaller than concrete compression strength (7.0MPa).

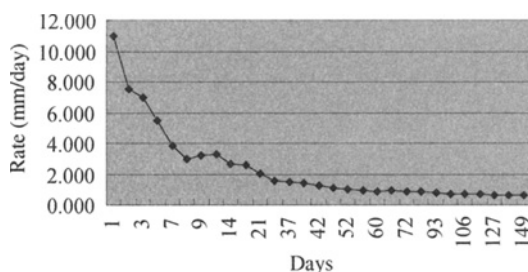


Figure 10. Spray-up concrete time-stress convergence section curve (left side)

CONCLUSION

(1) The failure of tunnel mainly happens in side wall and roof, which is caused by high side pressure coefficient

(2) Simple shotcrete-bolt supporting can not keep stability of deep roadway. Anchor cable should be used in high stress and fractured surrounding rock tunnel, and floor must be paid attention to.

(3) Monitor data show that supporting method of the fifth method can keep stability of the 1178 sublevel tunnel. But the tunnel stability is effected by many factors. So, stability or not lays in later monitor.

REFERENCES

- Jinchuan Group Ltd. Chinese society for rock mechanics and engineering Jinchuan branch (1996). *Geological and rock mechanics problem exploiting Jinchuan nickel mine*, Jinchuan Group Ltd. Press.
- Wang Yongqian, Yang Zhiqiang and Gao Qian (2002). Ground pressure control of Jinchuan high-stressed and deep-buried mining technique, *World Mining Express*, 2 (3): 15–19.
- Li Li, Gao Qian and Wang Zheng-hui (2005). Tunnel supporting design and stability analysis of 1178 m middle section, NO 2 mine, Jinchuan, *Nonferrous Metals(Mining)*, 57 (1) 19–22.
- Xie Heping, Peng Shuping (2006). *Basic Theory and Engineering Practice of Deep Mining*. Science press.
- He Mancao, Sun Xiaoming (2004). *China Guiding of Soft Rock Tunnel Supporting Design and Construction*, Science Press.

- Bai Jianbiao, Hou Chaojiong (2006). Control principle of surrounding rocks in deep roadway and its application, *Journal of China University of Mining & Technology*, 35 (2):145-148.
- Li Shuqing, Wang Weijun and Pan Changliang (2006). Numerical analysis on support structure of rock around deep roadway, *Chinese Journal of Geotechnical Engineering*, 28 (3) 377-381.

SOIL EROSION CAUSED BY HIGHWAY CONSTRUCTION IN EXPANSIVE SOILS DISTRICTS AND ITS PREVENTION MEASURES

Heping Yang, Liping Lin and Yingxi He

*School of Highway Engineering, Changsha University of Science and Technology,
Changsha, China*

Because of special geological engineering characteristics of expansive soil, cut slopes and embankments of expansive soils used to be bound to damage and slide. According to Chinese Specifications for Design of Highway Subgrades, it is not appropriate to fill embankment with expansive soils, so replacing expansive soils by non-expansive materials is usually adopted, as a result serious soil erosions and damages to environments are caused frequently by highway construction in expansive soils districts. Taking Guangxi Nanning-Youyi Guan Expressway as an example, this paper analyses the influence and damages to ecological environment in the construction period of Ningming expansive soil section and introduces scientific researches and technical innovation carried out by the research group of Changsha University of Science and Technology, and how to solve the difficult problem of directly building embankment with expansive soils and develop a new environmental protection technology for stabilizing cut slopes of expansive soils. It is clearly suggested that the geological disaster problem of soil erosion caused by highway construction in expansive soils areas can only be solved by adopting effective engineering treating measures.

INTRODUCTION

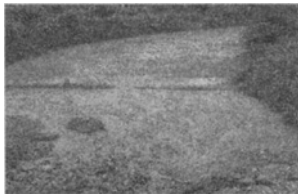
Soil erosion is currently the greatest ecological environmental problems, and the soil erosion area all over the world is 25,000,000 square kilometers. Our country is one of the countries in which there is the most serious soil erosion in the world, and soil erosions occur in almost all provinces. The statistics in 1989 showed that the soil erosion area was 3.67 million square kilometers, which occupied 38% [National Soil Investigation Office (1992)] of total land area, and the additional area of soil erosion was above 10,000 square kilometers every year (Wang et al.). Because soil erosion caused by highway construction accounts for quite proportion of the total at the present stage, the additional soil erosion is far more than that of conditions before land use. The spoil is the major composition of accelerated soil erosion [Wang et al; Li et al and Yang et al.(2003)]. This not only slows down the pace of highway construction and increases project investment, but also affects the natural landscape, the local climate, agricultural ecology, natural productive forces and urban ecology, and so on.

Since the 1990s, with the development of Chinese economic construction and the subsequent implementation of western development strategy of China, highways and their infrastructure construction have become the main battlefield of our country's economic

construction. With expressways extending to western regions rapidly, it is unavoidable to encounter bad geological problems for building roads. Highway construction in expansive soils districts has been a global technical difficulty. Therefore, in June 2002 the Chinese Ministry of Communications specially established research group and the group should make study on building technology in expansive soils areas under the leadership of Changsha University of Science and Technology. The purpose is that more serious geological hazard which is a long-term problem disturbing our country's highway construction, especially the western expressway construction, can be solved, and soil erosion caused by highway construction in expansive soils areas can be prevented effectively.

PRESENT STATUS OF SOIL EROSION CAUSED BY HIGHWAY CONSTRUCTION IN EXPANSIVE SOILS DISTRICTS

Because of cracking, swelling-shrinking and over-consolidation of expansive soil, cut slopes and embankments of expansive soils used to be bound to damage and slide, as a result serious soil erosions and ecological damages to environments are caused by highway construction in expansive soils districts (see pictures 1-2.), and they bring enormous economic loss. It cost more than 50 billion yuan (China RMB) to repair structures of subgrade and treat soil erosion every year since the opening of Nanning-Kunming Railway. Treatment costs of Xianfan-Chongqing and Jiaozuo-Zhijiang Railway have already been more than 100 million yuan. During Yunnan Chuxiong-Dali Expressway construction, more than 700 thousand m³ of expansive soil excavated from a 353m long roadcut was abandoned, and it cost more than ten million yuan for repeated regulation. Guangxi Nanning-Baise and Baise-Luocunkou (Feng et al; Zhang et al and Qu et al.(2001)) Expressway also encountered serious engineering geological disasters of expansive soils during construction, and it cost much for treating soil erosion.



Picture 1. Soil erosion of abandoned expansive soil caused by rainwater in the NYGE.



Picture 2. Collapse of excavated slope of spoil ground in the NYGE.

Beginning in March 2003, construction of the Nanning-Youyi Guan Expressway (NYGE) in Guangxi encountered serious geological disasters of expansive soil when traversing the edge of the Ningming Basin. After a rainy season, almost all roadcuts in an length approximately 14 km long experienced landslides to different degrees. Some slopes remained unstable even after their grades had been flattened from a slope (H:V) of 1:1.5 to 1:3. As a result of the landslides, the excavation was increased quickly and soil erosion became more serious. The investigation and research have shown that Ningming expansive soil is a residual expansive clay whose typical geological section can be divided into three

layers: The surface is brown high liquid limit soil with slightly yellow spots and the thickness is ranging from 0.5 to 1.5m; the central is strong weathered expansive soil characterized by a brown or light gray stripe and the thickness is ranging from 2 to 6m; the bottom is dark gray and weak weathered clay shale with unknown thickness. The light gray expansive soil was found to have a moderate to strong potential for swelling, while the dark gray shale exhibited a weak to moderate potential for swelling. A number of investigations were made on cut slopes, borrow pits, spoil grounds and temporary land use along the NYGE. According to the original design, roughly 2 million m³ of expansive soil in this section of the highway was to be excavated, but a large number of slopes collapsed after excavation, so that 5 million m³ of expansive soil has been excavated. There were five borrow pits in this section of the highway, about 113,330 square kilometers (a total of more than 1.6 million m³ by soil). The “red scar” left after excavation looked very dazzling among the mountains (see Picture 3). There were 13 spoil grounds along the NYGE, about 240,000 square kilometers. Except two spoil grounds in the farmland with retaining wall (see Picture 4.), no protections were done for the rest spoil grounds. Abandoned expansion slime has been weathered into powders, and mass particles were washed into paddy field of 60m far away. Because the soils of two 15m high spoil grounds were loose, several penetrating cracks occurred on the top with a width of nearly 30cm. There was a gully spoil ground in the catchment export among several mountains with about 100,000 m³ of abandoned soil. The height difference between gully bottom and slope’s top exceeded 40m, producing a dozen of big or small landslides. When rainy season came, loose expansive soil could be rushed out a few hundred meters away at any moment. In addition no protections were done for such temporary lands-use as a construction shortcut with the length of about 8km, a precasting concrete processing space with the area of over 200,000 square kilometers and living area, a lot of soil erosions also occurred.



Picture 3. A borrow pit



Picture 4. A spoil ground

ANALYSIS OF REASONS OF SOIL EROSION CAUSED BY HIGHWAY CONSTRUCTION IN EXPANSIVE SOILS DISTRICTS

There are both subjective and objective reasons for soil erosion caused by highway construction in expansive soils districts. The subjective reasons are that highway builders don't have adequate consciousness of environmental protection, and they don't take favorable engineering measures during highway construction. Although the Soil and Water Conservation Law of P.R China has clearly ruled such problems as vegetation destruction caused by highway construction and the excavation and packing of loose deposits, and so on, we don't truly bring environment into system design in highway schemes' design and selection at present, as a result construction and environmental protection are disjointed.

The objective reasons are mainly poor engineering characteristics of expansive soil and the unfavorable influence of local climate conditions, as a result construction of subgrade in expansive soils section is far more difficult and complex than that of general subgrade. Unfortunately, an effective engineering measure for treating the expansive soil cut slopes has not yet been developed, and the California Bearing Ratio (CBR) of excavated expansive soil can't meet the requirement. It is not appropriate to fill embankment with expansive soils, so the measure of replacing expansive soils by non-expansive materials is usually adopted. At the same time, cut slopes collapse continually during construction, resulting in the great increase of abandoned soils and more serious soil erosion, which is the basic reason of soil erosion caused by highway construction in expansive soils districts.

TREATING MEASURES OF SOIL EROSION CAUSED BY HIGHWAY CONSTRUCTION IN EXPANSIVE SOILS DISTRICTS

Enhancing retaining prevention and vegetation cover of slopes, borrow pits and spoil grounds is the usual measure for preventing soil erosion, but this is only a passive, temporary solution but not a permanent solution. In order to prevent and control soil erosion caused by highway construction in expansive soils districts, we must take new concept of active prevention and the guiding ideology of the minimum destruction is the maximum protection. We start from the engineering measures to reduce excavation volume and realize filling embankment with excavated expansive soils, only in this way can we reduce soil erosion radically.

The reasonable determination of the route alignment and the elevation of highway profile

When making highway survey and design to determine the route alignment in expansive soils districts, we require fully considering the thickness of distribution and the grade of swelling and shrinking of expansive soil along the NYGE, and so on. We need to adjust repeatedly in the local range and try to avoid collision as much as possible. So we could select a line crossing through expansive soil with small expansion-shrinkage performance, thin thickness and small amount of filling and excavating. In order to reduce the amount of filling and excavating and achieve cut-fill balance ultimately, we should comprehensively consider the occupation of land, the amount of filling and excavating, subgrade stability, the degree of damage to the natural water system, ecological impact and project cost when determining the elevation of highway profile and repeatedly compare advantage and disadvantage between low line and high line.

Filling embankment with excavation during subgrade construction

Our Country's highway technical standards provide that strong expansive soil can't be used for subgrade fillings, and middle-weak expansive soil can be used by treatment. But in fact, in order to make construction convenient and quicken progress, construction units usually replace expansive soils by non-expansive materials, resulting in the increasing engineering cost, soil erosion and damages to environments along the NYGE. To change this situation, the author made further researches on the properties of Ningming expansive soils and gave a comprehensive and detailed analysis to failure laws and mechanisms of embankments and roadcuts. Breaking with convention, the author proposed effective engineering treating techniques.

Embankment treating techniques

By improving CBR test method (Yang et al; Zhao et al.), we reconsidered road performance of expansive soils, and adhered to the principle of wet remaining and seepage control, and rationally used enveloping and wrapping technology. The researchers selected the following four treatment schemes to be tested: ① Embankment sides were covered with clay that is not expansive. ② Expansive soil was layered with soil mixed with lime, and side slopes were reinforced with geogrid. ③ Expansive soil was layered with crushed stone soil, and side slopes were reinforced with geogrid. ④ Side slopes were reinforced with geogrid. In the meantime, filling-core site and height of expansive soils should be controlled. Four trial embankments have been built (see Figure.1-4), in which nearly 80,000 m³ of expansive soil was utilized. Construction of the four stretches had been completed by the end of April 2004, followed by the site tracing monitoring which had been done for more than one year. The results showed that the subgrades were stable and the operation conditions were good (see pictures 5-8). If the schemes above have been adopted in expansive soils districts of the NYGE, 1.6 million m³ of borrowing and abandoned soil could be reduced.

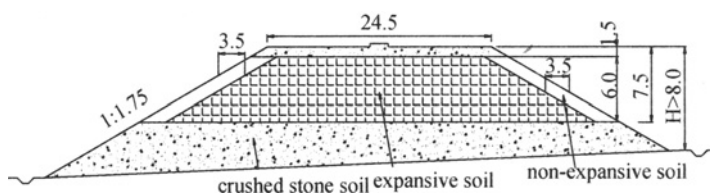


Figure 1. Envelop side slopes with nonexpansive clay.

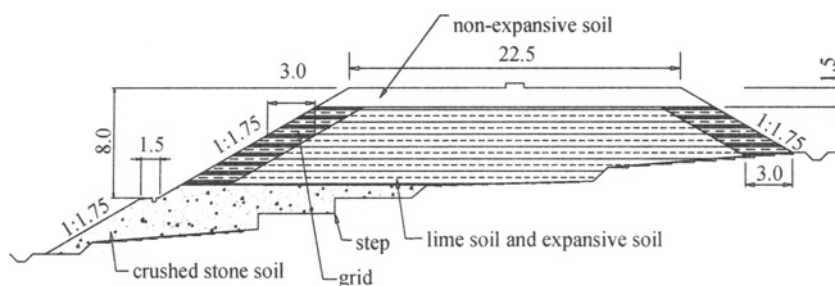


Figure2. Layer expansive soil with soil mixed with lime and reinforce side slopes with geogrid

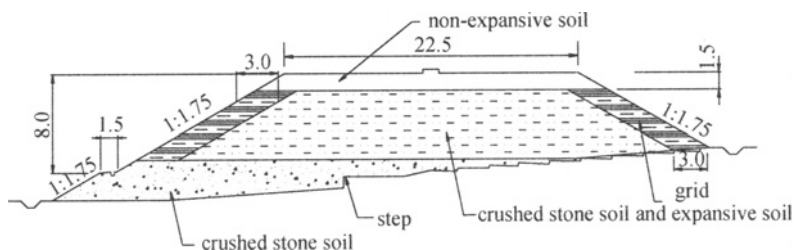


Figure 3. Layer expansive soil with crushed stone soil and reinforce side slopes with geogrid

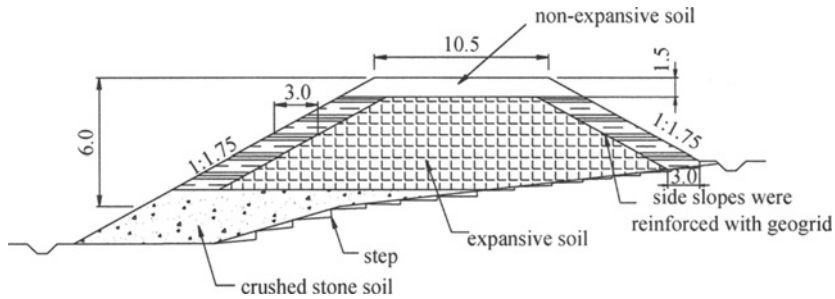


Figure 4. Reinforce side slopes with geogrid



Picture 5. A stretch of trial embankment after construction



Picture 6. A stretch of trial embankment after construction



Picture 7. A stretch of trial embankment after construction



Picture 8. A stretch of trial embankment after construction

Roadcut treating techniques

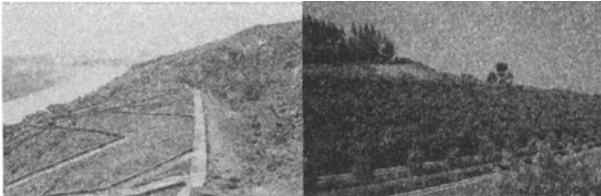
The collapse of excavating slope is the most serious engineering disease which is difficult to avoid in expansive soils districts during engineering construction. We can't find a safe, reliable as well as economic treating method for a long time. The research group broke through the traditional pattern of main rigid reinforcement and protection which has lasted for a long time for the expansive soil cut, and we adopted the technical ideas of enveloping and wrapping technology and combination of rigidity and flexibility. For the first time, the group puts forward and implements comprehensive treatment technology of flexible support reinforced with geogrids. This method's advantage is that it can not only bear the expansive soil's pressure but also permit soil deformation to a certain degree. The flexible support can absorb the stress caused by soil over-consolidation and the pressure that results from swelling. The literature [Liao et al.(1984)] pointed out that if a soil specimen's linear expansive ratio is allowed to reach 0.3 percent, its swelling pressure can decrease by approximately 25 percent in comparison with what it would be if deformation of an expansive soil body was rigorously

restricted. Therefore, methods that rely on flexible support work well in treating cut slopes of expensive soil.

Four flexible supporting trial embankments (boldface in Table 1) designed and completed by the group were finished in November 2004. Because cut slopes of this section of the highway treated by other methods collapsed in succession during engineering construction, the owner demanded that they should be treated by flexible support and be finished by construction units. Therefore, up to September 2006, fourteen flexible supporting cut slopes had been completed in the NYGE (the total length of slopes is 4.28 kilometers, Table 1). The results showed that, compared with the traditional schemes of the retaining wall at the slope's toe and mortar rubble masonry enveloping, 77.1722 million yuan of the direct expense of project had been saved and 1.02 million m³ of excavation had been reduced. When undergoing two cyclical dry and rainy seasons, especially the attack of several big typhoons and rainstorms in the summer of 2006, flexible support works well in treating cut slopes, and the slope vegetations are green and luxuriant, which have been completely mixed with peripheral natural landscape (see Pictures 9-12).

Table 1. Cut slopes treated by new technology of flexible support in the NYGE, Guangxi

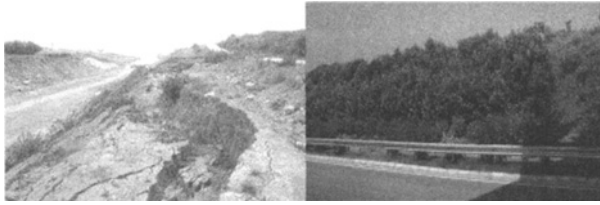
Treated slope	Slope height	Treated slope	Slope height	Treated slope	Slope height
K133+804-K134+100 left	12m	K135+040-135+340 left	20m	AK0 ramp, the length 200m left	12m
K135+040-135+340 right	24m	AK0 ramp, the length 350m right	30m	AK2+100- AK2+250 right	8m
AK2+500- AK2+800 right	8m	K136+040-136+410 left	12.5m	K136+960-137+370 right	10m
K136+040-136+450 right	12m	K137+875-138+120 right	15m	K138+420-138+840 right	20m
K140+240-140+534 right	10m	K141+080-141+320 right	8m		



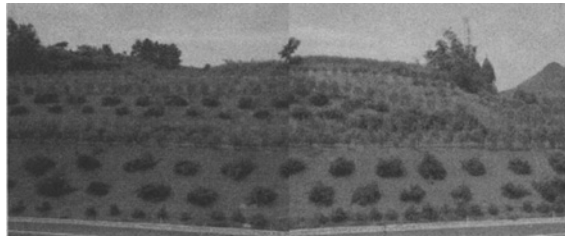
Picture 9. Comparison of cut slopes before and after treatment in the section of K138+420-K138+820



Picture 10. Comparison of cut slopes before and after treatment in the section of K136+040-K136+450



Picture 11. Comparison of cut slopes before and after treatment in the section of K133+804-K134+100



Picture 12. The three-level flexible supporting treating effects picture of big cut landslide of Ningming ramp in the NYGE

The flexible support has a complete drainage system, and it can ensure the stability of cut slopes (stability coefficient is increased from 0.75 to 2.5 after treatment). This way is with the following advantages: reliable technique, economic and reasonable, saving resources, ecological environment protection and simple construction. Thereinto, directly using expansive soil as reinforced body filler takes more advantage. It can effectively control soil erosion caused by highway construction and produce significant ecological environmental benefits, so it has been applied widely in Guangxi Tanbai and Bailuo Expressway, and so on.

Effective protection of spoil ground and temporary land use

The soil erosion caused by highway construction mainly is composed of three parts: soil erosion caused by destruction of original vegetation, soil erosion caused by abandoned soil and residue, soil erosion in the influence area during road operation. Soil erosion caused by abandoned soil and residue accounts for 78%-90% (Wang et al; Li et al and Yang et al. (2003)) of the total loss, which is the major source of soil erosion caused by highway construction. Although the introduction of new technology can greatly improve the utilization rate of expansive soil, it is hard to avoid the phenomena of abandoned soil. In order to prevent soil erosion, we should place abandoned soils by subsections and layers, build masonry structures at the downstream of spoil ground and make plant protection on the slope.

We should take retaining measures on various temporary engineering and land use in time, trying to make reclamation or greening.

In order to prevent and control soil erosion of expansive soil slopes (containing subgrade slopes and borrow pit / spoil ground slopes), we try to use plant protection for treatment. It can not only be suitable for the bigger swell-shrinking deformation, adjust soil humidity of slope and decrease the effects of cyclical wetting and drying, but also increase the ability of scour and deformation prevention. Furthermore, it can purify air and beautify environment.

CONCLUSION

Soil erosion always has close connection with engineering construction. In order to make the loss of soil erosion caused by highway construction in expansive soils districts reduce to the least and achieve satisfactory engineering construction quality and investment, i.e. obtain the best comprehensive benefit, each highway construction unit should improve the degree of cognition and recognition of soil erosion. The successful application of treatment techniques of expansive soil subgrade provides a new idea for the prevention of soil erosion caused by highway construction in expansive soils districts in Nanning-Youyi Guan Expressway. Only by reasonably taking engineering measures, utilizing expansive soils as much as possible, reducing the quantity of borrowing / abandoned soils and vegetation destruction and supplementing with other measures, can this technical problem be solved effectively.

REFERENCES

- Feng Y.Y., Zhang Y.S. and Qu Y.X. etc. (2001). Mechanism of Embankment Defects Caused by Expansive Soils in Baise Basin, Nankun Railway, *Chinese Journal of Geotechnical Engineering*, 23 (4): 463-467.
- Liao S.W.(1984). *Expansive Soil and Railway Engineering*, Beijing: China Railway Press.
- National Soil Investigation Office(1992).*Chinese Soil Survey Techniques*, Beijing: China Agriculture Press.
- Wang L.X. Soil and Water Conservation, Beijing: China Forestry Press.
- Wang F.,Li, R. and Yang, Q.K.(2003). Research of soil erosion and soil-water conservation in highway construction, *Highway*, (8): 148-152.
- Yang H.P. and Qu, Y.X. etc. (2003). Preliminary study on the engineering geology of expansive soil during highway construction in West China, *Journal of Changsha Communications College*, 19 (1): 19-24.
- Yang H.P., Zhao P.C. Proposition and verification of improved CBR test method for expansive soil fillers, *Chinese Journal of Geotechnical Engineering*, 29 (12): 1751-1757.

CONSTRUCTION AND QUALITY ANALYSIS OF CURTAIN GROUTING IN FOUNDATION OF DAM FOR YANGTZE THREE GORGES PROJECT

Xuexiang Yang
*School of Urban Construction of Yangtze University,
Jingzhou 434023, China*

Yan Li
*China Gezhouba Group Corporation,
Yichang 443002, China*

Through application of a series of techniques consisting of small caliber drilling, grouting procedure from top to bottom, the orifice of grouting holes blocked out and recycling grouting in the holes, a kind of high pressure has been used to dam foundation grouting for China Three Gorges Project. During the course of grouting, milled grout is perfused in remoteness cracking rock, epoxy resin is done to enhance bedrock strength in faultage rock stratum, and at orifice section acrylate materials are used to enhance impermeability, in the place of profound permeable zone in riverbed many construction methods such as grouting, consolidation and regrouting. Many on spot measurement and survey data indicate that construction methods are reasonable and effective.

BRIEF INTRODUCTION

China Yangtze Three Gorges Project (TGP) is one of the biggest hydropower-complex project in the world. The dam is concrete gravity dam, with the spillway in the middle, and the power house and non-overflow section at both sides. The axial length of the dam is 2309.5m, the crest elevation is 185m, and the maximum height of the dam is 181m. Sluicing dam section lies in the middle of main riverbed, and wall-dam section, powerhouse dam section, nonoverflow dam section in turns on left, and longitudinal cofferdam dam section, powerhouse dam section, nonoverflow dam section on right.

Yangtze TGP is located in the areas where the earth's crust is relatively plain. The dam axis is arranged in the area of plain topography and wide river valley, the width of river valley bottom is about 1000m and the main riverbed is 190-260m.

The dam foundation's bedrock consists of (Pre-Devonian porphyritic)granite. The rock's rupture structures are almost less than 300m in length and 1m in width. The conformation cranny gives priority to steep dip angle and comparatively its connectivity is bad. In general, the bed rock of dam belongs to block fabric, isotropic lithology, integrity and high strength,

the large allowable infiltration ratio drop ,and near dam foundation there is basically without infiltration problem.

Anti seepage criterion: $1 \times 10^{-3} \text{m}^3 / (\text{m} \cdot \text{min})$. Grouting hole row spacing : hole spacing of the main curtain is 2m, shut curtain is 2.5m. The depth of holes is generally 70–120 m, the touchdown height of curtain is 20–105m. The amount of hole sitting grouting serial: III sequence.

TOTAL SCHEME ON CURTAIN CONSTRUCTION

Three Gorges Project fall into three stages for construction, and three gorges dam is planned to construct during two or three phases, dam foundation curtain construction must carry after corresponding dam concrete were placed more than 30m high or perfectly achieve design height. So curtain grouting is planned only during two or three phases. During second phase (1999-2002), sluicing dam section, factory building dam section in left-bank and nonoverflow dam section were constructed; during third phase(2004-2005),factory building dam section in right-bank and nonoverflow dam section in right-bank were constructed.

A series of techniques consisting of small calibre drilling, grouting procedure from top to bottom, the orifice of grouting holes blocked out and recycling grouting in the holes to grout the dam foundation, and to select grade 42.5 grout (fineness is $D_{95} < = 40\mu\text{m}$) as main grouting material. If necessary carry the second chemical repairing grout according to different conditions ,namely after accomplishing fine cement grouting, epoxy resin slurry was grouted to enhance dam foundation strength when the grouted area was confirmed as fault zone; acrylate cement was select to carry repairing grouting for enhance curtain anti-seepage property when meeting cracks and adopting grout without good results.

GROUTING CONSTRUCTION WITH WET-MILLED CEMENT MORTAR

The procedure of the construction of curtain grouting: measurement—drilling lifting observation holes, setting up equipment in observation lifting holes—drilling and grouting the lead holes—drilling and grouting No.I ordered holes—drilling and grouting No.II ordered holes—drilling and grouting No.III ordered holes—after 14 days of accomplishing No.III ordered holes of each segment of dam) checks of quality check holes in drilling and undertaking pressing water check in other methods.

Drilling holes and pressure-test

The partition of each grouting section and water pressure of pressure-test and grouting pressure for each hole are listed as follows.

Table 1. Pressure of grouting and test and length of section

	Grouting pressure (MPa)/ length of section (m)				Pressure of test (MPa)		
	1st section	2st section	3st section	others	Before grouting		After grouting
					1st, 2st section	others	
Main curtain	2.5/2	3.5/1	4.5/2	5.0/5	1.0	1.0	2.5
Shut curtain	1.5/2	2.0/1	3.0/2	4.5/5	1.0	1.0	1.0

Grouting

(1) The order of drilling and grouting: III orders are divided and spacing of high difference between two holes is no less than 15m.

(2) Ways of grouting: SGB6-10 high-pressure pump, GJY-IV autonomous recorders which can log grouting pressure and quantity of grouting automatically are used.

(3) Grouting material: The central station can produce grade 42.5 grout adopting 0.5:1 cement ratio. Wet-milled cement mortar is produced by three series-wound mills.

Water-to-cement ratios (weight ratios) of mill paste are divided 2:1, 1:1, 0.6:1. Firstly 2:1 cement mortar is chosen to grout;

(4) End criterion: under designed pressure, from the first to the third segment, injection rate of the hole is less than $0.4 \times 10^{-3} \text{m}^3/\text{min}$, the remainders less than $1.0 \times 10^{-3} \text{m}^3/\text{min}$.

(5) Plugging holes: 0.5:1 thick mortar is used to plug holes. The maximum grouting pressure should be taken as plugging pressure.

Disposal of water gushing holes

Water gushing is noticeable in sluicing dam section, which appears in 80% segment. The maximum amount of water gushing in main curtain is $2.4 \times 10^{-2} \text{m}^3/\text{min}$, (X1-I-6# hole with the depth of 72.5-77.8m) the maximum water gushing pressure is 0.16 MPa.

The measurement of water quantity in the entrance of hole with water gushing needs dosing cup, automatic recorder to record the water pressure before grouting. According to different record the water pressure, different measures are selected:

① Improve the grouting pressure, the grouting pressure equals designed pressure adding water gushing pressure.

② Continue injecting for more than one hour after grouting up to end criterion.

③ wait for congeal when Q_u (the unit injection quantity) is more than 3kg/m. The third segment must wait for congeal if there are two foregoing segment which don't need consolidate.

④ Once the waiting time be kept more than 12 hours in water gushing hole, cleaning with water should be done in the holes.

Quality checks and analysis

checks and analysis after grouting

14 days after finishing grouting of every dam section (unit), pressing water test are arranged. Taking 15-19[#] dam sections of the third stage project for example, the results of pressure-test are listed in the following Table 2. The table indicates that bedrock penetration coefficient (Q) of all segments are less than $1 \times 10^{-3} \text{m}^3/(\text{m} \cdot \text{min})$.which are satisfied with the design requirements.

Table 2. Results of pressure-test of check hole

	hole	seg	Q, segment amount, frequency								Crite- rion
			q=0		0≤q<0.5		0.5≤q<1.0		1.0≤q<1.5		
			amt	(%)	amt	(%)	amt	(%)	amt	(%)	
Main curtain	22	380	97	25.5	277	72.9	6	1.6	0	0	q≤1
Shut curtain	17	211	56	26.5	148	70.2	7	3.3	/	/	q≤1

Checks of core samples: congealed cement well glued with rock can be seen in rock mass cracks and the thickness is in the range over 1–3mm, taking on green-gray color.

Analysis of groutability

By the analysis of amount of cement poured into each dam section, unit cement injection quantities (Q_{uc}) decrease with the increase of grouting orders, which abide by general regulations and show evidence of good results.

Check of geophysical exploration

Taking the 18th dam section for example, 2 physical exploration sound wave tests are taken before and after grouting. The checking result: Sound wave value increase about 5.7% from 5300m/s to 5600m/s in average, which indicates the low-speed parts have a good grouting effect.

TECHNOLOGY AND QUALITY ANALYSIS OF CHEMICAL GROUTING

Application scope

- (1) The segment where checking value fall short of criterion
- (2) The segment where the case of consuming more water but less grouting materials happened
- (3) Parts of large up-lift pressure behind curtain

Design parameter of chemical grouting

The straight hole with entering rock 5m, diameter of 56mm is used for chemical grouting holes. Each hole falls into 2 segments of pressing water, 1 segment grouting. The first segment's length is 2 m, the second is 3m. In main curtain, pressure of pressing water is 2.0 MPa, grouting pressure is 2.5 MPa; in shut curtain pressure of pressing water is 1.0 MPa, grouting pressure is 1.5 MPa.

End criterion: with the designed grouting pressure, grouting should not be stoppended untill 3 continuous record (every 15min) of injection rate is less than $0.1 \times 10^{-3} \text{m}^3/\text{min}$.

Check criterion: check of pressing water after grouting, All the penetration coefficient of foundation rock is less than $1 \times 10^{-3} \text{m}^3/(\text{m} \cdot \text{min})$.

Chemical grouting material

The good mix design is got in Table 3. the concentration of acrylate is no less than 36%, the effect quantity of N-isopropyl Acrylamide is no less than 80%, and ammonium persulfate is no less than 95%. The water of making up grout needs to be clean and transparent, and doesn't include matter of easily oxidized and reduced.

Table 3. The mix design of chemical grouting material.

materials	acrylate	biacrylamide	triethanolamine	ammonium persulfate	Potassium Ferricyanide
Design request	12%	1%~2%	1%~2.5%	0.5%~1.5%	<0.1%
Practice quantity	12%	1.5%	1%	0.8%	0.05%~0.08%

Construction skills and method

(1) Drilling and scouring holes: using large flux water to scour holes after drilling holes entering rocks for 5m until back water is limp for 10 min.

(2) Pressing water: after scouring holes, plug holes above 0.5m from the interface between concrete and rock with a small blockage equipment, then pressing water for 10 min at once.

(3) Grouting: with a plastic soft pipe, whose lip is less than 0.3m long from hole bottom. Materials should be injected by grout pump. After water are replaced outside pipes and holes, then grouting can be started. After the last group materials congealed for an hour, loosening the blockage equipment, pull out pipes, and scouring holes.

(4) Plugging holes: After sweeping and scouring holes, 0.5: 1 thick cement mortar can be used to replace the grouting material.

Effect of chemical grouting check and analysis

Analysis about variation of penetration ratio

Penetration ratio of shut curtain shows decreasing regulation according to the increase of grouting orders. The average value of penetration ratio of order-I hole is $0.51 \times 10^{-3} \text{m}^3/(\text{m} \cdot \text{min})$, eligible ratio is 92%. After order-I hole grouted, the penetration ratio of order-II hole reduces to $0.19 \times 10^{-3} \text{m}^3/(\text{m} \cdot \text{min})$, and eligible ratio increased to 95%.

Analysis about variation of acrylate quantity of injection

The unit injection quantity show decrease regulation with the increase of grouting orders. The unit injection quantity of order-I hole is $5.31 \times 10^{-3} \text{m}^3/\text{m}$, and the order-II reduce to $3.5 \times 10^{-3} \text{m}^3/\text{m}$, it shows effect of grouting.

Analysis about pressing water test

From Table 4, we can see that all the penetration ratio is less than $1 \times 10^{-3} \text{m}^3/(\text{m} \cdot \text{min})$, it satisfies with designed request 100%.

Table 4. Result from checking hole of curtain chemical grouting

Contract segment	Check location	Hole number	Concrete (m)	Segment length (m)	Penetration ratio $10^{-3}m^3/(m \cdot min)$
I	Sluicing dam section	HGFX5-J1	6.4	6.4~11.5	0.01
		HGFX6-J1	3.7	3.7~8.7	0.09
		HGFX14-J1	4.3	4.3~9.3	0.11
		HGFX19-J1	4.6	4.6~9.6	0.08
		HGFX21-J1	4.5	4.5~9.9	0.03
IIB	Left 11#-14# dam section	HGFZC11-J1	9.3	9.3~14.4	0.02

Table 5. Uplift pressure observed in sluicing 18# dam section before and after grouting

Observation time	2003.4	2003.5	2003.6	2003.7	2003.9	2003.11	2003.12	2004.2	2004.3
Water line before dam (m)	69.10	75.24	135.2	135.1	135.09	138.81	138.88	138.21	136.17
Water line behind dam (m)	66.00	66.09	67.11	69.49	69.11	65.70	65.64	65.18	65.24
Lift pressure before curtain (MPa)	0.125	0.20	0.64	0.66	0.66	0.82	0.82	0.86	0.83
Lift pressure behind curtain (MPa)	0.044	-	0.01	0.017	0.017	0.022	0.023	0.021	0.019
Ratio of pressure	0.352	-	0.016	0.026	0.026	0.027	0.028	0.024	0.022

Comparison analysis of uplift pressure in main curtain before and after grouting

After 2003.4 when cement grouting in sluicing 18# dam section was finished, two observation holes of uplift pressure are set up before and behind the main curtain. The value of uplift pressure observed before and after grouting is listed in Table 5.

The uplift pressure before chemical grouting is large, the ratio of uplift pressure in the place is more than 0.03(designed criterion). After chemical grouting, the ratio is less than 0.03 .which indicates that capability of anti-seepage increases obviously.

Analysis of television video in the check hole

Ten colorful television videos have been used to know the effect of chemical grouting in the check holes, the total depth is 109.1m. The videos of checking shows that some surface cranny hasn't been blocked out by wet mill cement in foundation rock before chemical grouting. But the video shows that the surface cranny fill with congealed ivory acrylate after chemical grouting. The opening cracking doesn't exist in the mass, it shows the effect of chemical grouting is obvious.

CONCLUSIONS AND SUGGESTIONS

(1) The practice shows that, the geological condition of Three Gorges Project is fine, but its groutability is bad, curtain grouting skills is mature, grouting materials are qualified, the quality of curtain construction can be ensured.

(2) The case of “consuming more water but less grouting materials” happened in the lip hole of curtain in the foundation, the reason is that Portland cement grout can’t deal with the surface cranny rock in the foundation perfectly. Using acrylate as grouting material in the lip hole of curtain after cement grouting, the effect is excellent.

(3) The viscosity of acrylate is low and its groutability is good in the cranny rock. But the kinds of needed materials be used make up grout are somewhat complicated which bring inconvenience to management. Thus, it is recommended that construction unit should try their best to combine multiform materials so as to form 2-3 kinds of materials from the angle of construction convenience.

MECHANISM AND PREVENTION OF HIGHWAY DISTRESS IN SEASONAL FROST AREA

Yongtang Yu, An Deng

*Key Laboratory of Ministry of Education for Geomechanics and Embankment Engineering,
Hohai University, Nanjing 210098, China*

Geotechnical Research Institute, Hohai University, Nanjing 210098, China

Frozen damage to highways in colder climates, including frost heaving because of ice lenses growth and thaw weakening caused by ice lenses melting. The frost action reacts on the highway structure that is a major concern at the locations constructing a highway in cold regions, and the frozen damage of road is a phenomenon of great practical importance in highway engineering design and construction. The objectives of this paper are to: (1) study the effects of frozen damage on road performance in cold climate regions, (2) investigate the factors contributing to the changes in highway structure physical and mechanical properties, (3) provide guidelines for anti-freezing design of highway in seasonal frost areas. The approach focuses on analyzing the characteristics and the mechanisms of frost heaving and frost boiling, and adopting initiative methods to reduce the frozen damage to highways. This thesis gives a review and summary of the preventive measures to minimize highway distress in seasonally frozen regions that will benefit the design and maintenance for highway structure.

INTRODUCTION

The seasonally frozen region is widely distributed in China and its area occupies about 53.5% of the Chinese territory. A large portion of the total miles of highways are located in the seasonally climate regions where subjected to seasonal freezing-thawing. Consequently, the mechanical properties of road structure are greatly affected by frost actions. The pavements are frequently broken up or severely damaged as roadbeds freezing during winter and thawing in spring. Based on a large number of engineering practices and long-term observations, approximately 70% damage of the north national road due to seasonal frost actions, the main highway distress in seasonally frozen soil regions can be summarized as frost heaving and frost boiling (Chen Xiaobai et al., 2006).

HIGHWAY DISTRESS IN SEASONAL FROST AREAS

Mechanism of frost heaving

Frost heaving to pavement structure is possible if three necessary conditions are fulfilled, i.e.:

- a. A frost-susceptible soil.
- b. Available water to the freezing plane.
- c. The negative

temperature to penetrate into the soil. If there is lack of one of these factors, no frost heaving will occur.

When the pore water in the soil is reaching freezing point, it starts to freeze. These freezing zones are governed by the energy balance which drives soil water and concurrently wicking of ground water up. Respectively, the moisture migration and the temperature penetration with the direction as heat flow, both of these occurring from warmer soil to colder soil. The moisture is drawn upwards to the freezing front due to various mechanisms, these including water vapor pressure, capillary migration, osmosis force, and tension at the ice-water interface etc. As a result, the whole soil volume is expanding when freezing, the cracking and the apophysis come into being highway distress in the end. As shown in Figure1.

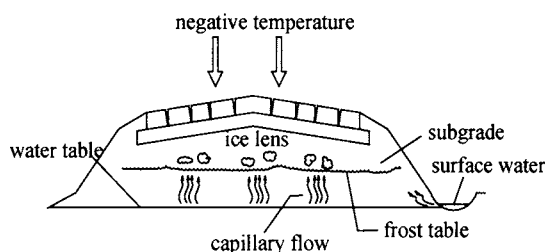


Figure 1. The forming process of frost heaving

Characteristics and influencing factors of frost heaving

The main damages of road structures caused by frost heaving can be characterized by uneven heaving, cracking, uplifting etc. Du Zhaocheng, et al. concluded the main characteristics that caused by frozen damage through the monitoring results of national highway Changchun—Fuyu done in 2000–2001: a. Pavement distress typically involves longitudinal cracking and transverse deflection or deflection curve deformation; b. Larger amount of total frost-heave capacity and uniform uplifting deformation; c. Opening and severity of the transverse cracks; d. Small deformation etc. (Du Zhaocheng et al., 2004).

There are various influencing factors on the frost-heave capability and frost susceptibility. The behavior of frozen soils is governed by intrinsic material properties such as moisture content in the frozen and unfrozen state, vapor water pressure, soil density, mineral composition, soil type and conformation, dissolved salt concentration and composition, grain size, etc., and by externally imposed conditions such as strain-rate, pore water pressure, temperature gradient and confining or restraining force etc. (Chen Xiaobai et al. 2006).

Mechanism of frost boiling

In spring, warm climate outside and heat infiltration into seasonally frozen soils, as the temperature above melting point, the frozen soil begins to thaw. Ice lenses melt from the surface and upward from the lower depths. The extra water come out of melting frozen soils, because of the underlying ice lenses blocking the osmotic channels, a great amount of meltwater that still cannot drain through the underlying frozen layers back down to the water

table. The excess meltwater that becomes trapped above the underlying frozen soil, but still beneath the pavement structure, it causes soils to be extremely soft, or even to become to 'slurry', and the bearing capability of the frozen soil is getting extremely poor. If the road is exposed to heavy traffic, the cyclic dynamic forces will pump up the saturated fine graded subsoil out of the pavement layer, and then easily causes serious structural damage to the road and results in permanent deformation. As shown in Figure 2.

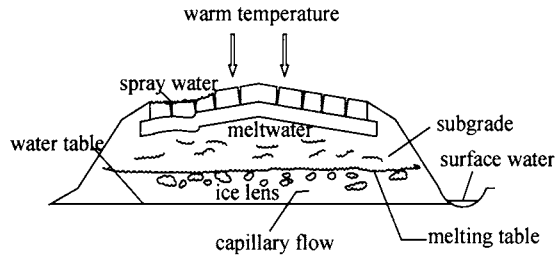


Figure 2. The forming process of frost boiling.

Characteristics and influencing factors of frost boiling

The cyclic cold-warm climate in spring promotes moisture to flow owing to temperature gradient, the soil beneath pavement is supersaturating or even reaches liquid limit. It follows that a considerable loss of the bearing when thawing takes place. As a Result, a sharp fall of the bearing capability will be occurred, and the highways of the northern country extremely prone to common highway distress, such as rutting, net-shaped crack, alligator crack, surface loosening etc.. The influencing factors of frost boiling include two aspect: one is natural conditions (such as soil type, moisture content and migration, air temperature variety, wind speed, snow depth, vegetation cover, rate of freezing, materials of pavement, additional load and traffic volume etc.), the other are human factors (the result of design, construction, traffic load.). The influencing factors depend not only on the aspects mentioned above, but also the specific geotechnical investigation and surveying, and the meticulous maintenance during the serviceable life.

PREVENTIVE MEASURES OF FROZEN DAMAGE

Height of subgrade filling

Results show that increasing the height of roadbed can prevent the groundwater or surface water infiltration into the roadbed, and the road surface relative to the water table or surface water level is raised, thus the quantity of freezing water migration to the roadbed is reduced during freezing process, weakening frost heaving, and diminishing the extent and the possibility of frost boiling.

The critical height of roadbed can be determined based on the maximum frost depth and the rising height of freezing water in situ measurements. The design value from the lowest point of the pavement surface to the capillary plane must be at least equal to the frost penetration depth. The critical height is identified by the following Eq. (1):

where, $H_{fd} = z_{\max} + h_z$ (1)

H_{fd} — The critical height of roadbed, m;

z_{\max} — The maximum frost depth for ages, m;

h_z — The rising height of freezing water, m.

The height parameter (z_{\max}, h_z) can be obtained by experience or in situ measurement.

Strengthen drainage system

Every effort should be made to strengthen drainage system for both groundwater and surface water. Actually, frost action is the process of groundwater and/or surface water transfer to freezing front continually as the water freezes. Water can enter a road by surface through penetration, laterally through a groundwater flow, and upwards through capillary action. Proper drainage is essential for optimum operation of the roadway in any climate. Minimizing the level of moisture present through proper drainage, insulating the coaccervation is one of the chief methods to frost heaving.

The surface drainage should be suit for landform, weather, water system, as well as the treatment and disposal of water entrance, avoid the phenomenon of clogging, sedimentation, leakage etc. Additionally, adequate drainage facilities must be provided outside a road to accommodate possible maximum drainage flow from the road and circumjacent areas. Where some form of subdrainage system are to be required and which types will be best suited for the road, the dimension and the locations involved ought to be decided according to the local engineering geology conditions and the hydrographic parameters, as well as accord with surface drainage.

Selection of subgrade filling

It is effective to achieve the aim of reducing the frost-heave capability by removing frost-susceptible soils and replacing with frost-free materials such as coarse gravel, slag, casting sand, fly ash, etc. The selections of roadbed filling for some projects are too much dependent on consideration of the soil types and the water conditions, as well as the climate conditions. For a given condition, approximately the same moisture, temperature and additional load, the gradation of the frost-heave capability of different soil types can be concluded by testing and other observational data as follows: silt > clay > sand > gravel. If finally adopted, in the long run the sensitive soils should be replaced by the efficient materials with fine stability, fine frost stability and high-strength. Frost-susceptible subgrade soils are removed and replaced with frost-free material for depths ranging from 0.61 to 1.22 m (2 to 4 ft) as part of their normal construction requirements to eliminate the need to consider frost depth in the design process. (N. Jackson et al., 2006).

Application of insulating layer

It is advantageous to limit the depth of frost penetration and decrease frost-heave capacity sequentially by providing thermally insulating materials at some depth beneath all or part of the base course which prevents freezing temperature or moisture from penetrating into the

roadbed. Nowadays, the section of a road where is adopted the insulating layer such as EPS (Expanded Polystyrene) geofoam board or styrene sponge plastic concrete etc., which provides good thermal protection to the underlying roadbed. Three key properties that make EPS geofoam so attractive in design and construction are its low density for reduce settlement, small compression for decreasing deformation-related problems, and its thermal insulation properties that help combat frost-heave problems. In China, engineers have been applied EPS geofoam in roadway construction, such as Qinghai-Tibet Plateau road and some other frozen regions, and with greater results.

Application of isolating layer

As is well known, eliminating the supply of water to the soils beneath the pavement is virtually impossible. However, good isolating measures can partially reduce the quantity of water available to feed an ice lens and limit frost action penetration into the frost-susceptible roadbed.

The isolating layer can be divided into permeable and impermeable layers. The permeable isolating layers can use geotextile materials, as well as non-frost susceptible and non-water susceptible soils, such as gravel, crushed stone, coarse sand etc. The moisture migration of a road may be small if the road has sufficient coarse sand or gravel sub-bases or insulating materials above the water table to cut water capillarity and increase the distance from frost-susceptible soils to the road surface. The impermeable isolating layer can use tarred felt papers or asphalt mixture, composite geomembrane, waterproof blanket etc.

Strengthen structural layers

Under severe frost conditions, a structural layer should be designed to withstand the stress transmitted under the effects of traffic and satisfy the criteria of protection against the effects of freeze-thaw cycles. An effective measure is to have the pavement structure (total of surfacing and base) at least equal to one-half the maximum expected depth of freeze when the roadbed is classified as a frost susceptible soil (WSDT., 2005). The pavement materials that have been widely used are asphalt and cement concrete. Frost action affects all pavement types, although concrete pavements are less susceptible to it than asphalt pavements (Steven M. Waalkes, 2003). Therefore, if circumstances permit, it is advantage to use the cement concrete as a pavement material instead of asphalt, and improve mechanical and physical properties of soil by addition of soil modifiers. Such as lime, cinder lime, fly ash, cement etc., and they are fine water stability, fine global property and fine frost-resistant characteristics.

Load restriction

Traffic control is typically used as a strategy to reduce the distress caused by dynamic vehicle load. When seasonal thawing occurs, in order to gained the benefits either from the load restrictions or from the speed limit that imposed on the roads where are sensitive to damage. Current spring-thaw load restriction practices, including the level of restriction, correct timing, and length of restricted haul, vary appreciably among road maintenance agencies (Kestler, Maureen A. et al., 2000).

CONCLUSION

The stability and bearing capability of a road structure is influenced by many factors in seasonally frozen soil regions. However, the negative effects of the factors can be limited through a structural meliorating design and an adequate construction. Frost heaving and frost boiling are uniform processes but on different stages, the former is the necessary condition of the latter. Typically, there are three necessary conditions to cause a frost heave (freezing temperatures, frost-susceptible soils, availability of water), if frost boiling to add additional traffic load. In absence of any of these conditions frozen damage does not take place. Thus, efforts should be made to mitigate at least one of them in roadway constructions in cold regions. The properties of frost action are determined by hydrology, topography, climate etc., so that these considerations must occur in all stages (reconnaissance, design, construction, and maintenance). It is quite possible to improve the road longevity and stability by effectively guarantee the quality of the projects.

ACKNOWLEDGEMENTS

This work is supported by National Natural Science Foundation of China (Grant No 50708031) and Scientific Research Foundation for the Returned Overseas Chinese Scholars, State Education Ministry (SRF for ROCS, SEM).

REFERENCES

- Chen Xiaobai et al., (2006). Frost action of soil and foundation engineering, 1st edition, Science Press, Beijing. (In Chinese)
- Du Zhaocheng, et al. (2004). Experiment research on subgrade frost heaving of expressway in seasonally frozen soil region, *Journal of Highway*, (1): 139-145. (In Chinese)
- Jackson N. et al. (2006). Effects of Multiple Freeze Cycles and Deep Frost penetration on Pavement Performance and Cost, *Federal Highway Administration (FHWA)*. (1): 139-142.
- Steven M., Waalkes (2003). Cold Weather & Concrete Pavements: Troubleshooting & Tips to Assure a Long-Life Pavement, The Long-Life Pavements – Contributing to Canada's Infrastructure (A), *Session of the 2003 Annual Conference of the Transportation Association of Canada*, St. John's, Newfoundland and Labrador.
- WSDT. (2005). WSDT (Washington State Department of Transportation). *Washington State Department of Transportation, Pavement Guide*, Washington, (1): 3-5.
- Kestler, Maureen A. et al. (2000). *Thaw weakening on low volume roads and load restriction practices*, Hanover, NH. CRREL Special Report 00-006.

INTEGRATED REINFORCING METHODS FOR EXCAVATED SLOPES OF TANXIWAN VILLA AREA ON CONSIDERING REFOREST AFFORESTATION, CHINA

Faming Zhang, Tao Li, Yajie An and Xia Wang
*Earth Science and Engineering Department of Hohai University,
Nanjing 210098, China*

Zhiyao Kuai
*Geological Department of Chang'an University,
Xi'an 710054, China*

Excavated slope is a normally phenomenon in villa construction, especially in mountainous areas. But, for the requirements of the human been, the stability and scene are both important in reinforce process. As an example, the integrated reinforcement methods of Wuxi Tangxiwan villa area excavated slopes were discussed in this paper. In the example, rock bolts were used in reinforcing the stability of the excavated slopes, and, the planting technique was used for landscape sighting. The results of the reinforcements take stability and sight harmonious obviously.

GENERAL INSTRUCTIONS

Tangxiwan villa area is situated in Mashan town in Jiangsu province Wuxi city, the villa area takes $80 \times 10^5 \text{ m}^2$, the total construction area is $19.6 \times 10^5 \text{ m}^2$. The eastern of the villa is Taihu lake, which is the most famous lake in China, the other three sides are surrounded by mountains. So, there are more than 30 excavated slopes are formed in villa construction. The whole villa area is consisted of 240 tents luxurious villas include face lake villa, mountainous villa and called surrounded lake park. The height of the excavated slope is from 5 m to 20 m. Most of the slope directions are the same with the dip direction of the rock layer. It is necessary to reinforce the instability slope with the normally methods and planting technique for inhabitant requirements. According to the real excavated slope shape and stability analysis results, drainage system was set up.

GEOLOGICAL CONDITIONS

Topography and physiognomy

The topography and physiognomy of the Tangxiwan villa belongs to typical hills, elevation is from 1.51 to 93.05 m, the difference is 92.00 m, physiognomy includes corrode hill, talus skirt and alluvial-lacustrine plain. The slope angle of the mountain is 15° - 35° .

Stratum and rock mass property

Stratum and rock mass property of the slopes are simple, the stratum is consisted of Quaternary system Holocene series residual soil, Devonian system middle series Maoshan grope. The average height of Quaternary system Holocene series residual soil layer is 1.28 m, the soil is gray to yellow clay. The rock mass of Devonian system middle series Maoshan grope (D1-2ms2) is thick to tremendous thick quarts sandstone (the thickness is more than 50 m) and thin politic siltstone (the thickness is more than 20 m), the structure of the rock mass is intact, the dip direction of the rock mass is 190° - 275° , dip angle is 30° - 45° .

Geological Structure

The faults are well developed in the villa area and can be divided into 2 groups, the first group is in NNE direction, such as F1 and F5, the length is more than 100 m, the second group is stretched in NW direction, such as F2 and F4, the strike length is more than 200 m. Based on field works, well developed joints can be divided into 3 groups, the fractured density is 7.6%-17.4%, most of the joints are filled with mud.

Topography and physiognomy

The topography and physiognomy of the Tangxiwan villa belongs to typical hills, elevation is from 1.51 to 93.05 m, the difference is 92.00 m, physiognomy includes corrode hill, talus skirt and alluvial-lacustrine plain. The slope angle of the mountain is 15° - 35° .

Hydro-geological property

Atmosphere precipitation is the supply source for underground water, the buried depth of the table is more than 50m since the joint closed spaced.

STABILITY ANALYSIS RESULTS OF THE EXCAVATED SLOPES

According to the rock mass structure and slope property, the failure mode of the excavated slopes were determined by using the stereographic method (Figure 1), from the figure 1, it is easy to find the failure mode of the excavated slope is wedge failure and along the joint assemble failure. Take the 1# excavated slope as an example (Figure 2), the strike is 180° , the direction of the slope is 270 - 285° , and the slope angle is 45° - 60° , the height is 15 m, the occurrence of rock mass is $N30^{\circ}E$, $SW \angle 46^{\circ}$, well developed joints are ① $N20^{\circ}E$, $SE \angle 70^{\circ}$, ② $N60^{\circ}E$, $SW \angle 70^{\circ}$, ③ $N60^{\circ}W$, $SW \angle 70^{\circ}$. Then, analyze the stability of the slope by using improved Sarma's method, the parameters is indicated in Table 1.

Table 1. Parameters used in stability analysis

Joints		Rock mass
Cohesion C (kPa)	Friction angle φ ($^{\circ}$)	Unit weight γ (kN/m^3)
25.0	15.0	25.5

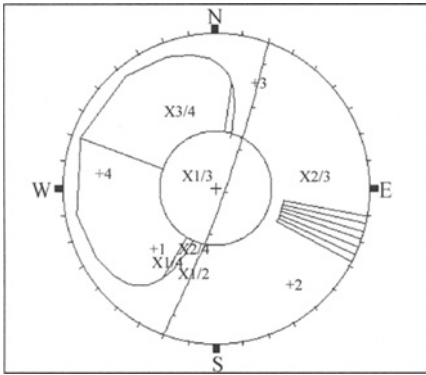


Figure 1. Failure mode analysis



Figure 2. 1[#] excavated slope

In improved Sarma's method (Brown, E.T. , 1987), the critical failure surface of the slope can be researched by simulated annealing method. The 1[#] excavated slope stability analysis result was illustrated in Figure 3. From the analysis result, the stability factor of the 1[#] excavated slope is 1.142, so, it is necessary to improve the slope stability by using reinforce method.

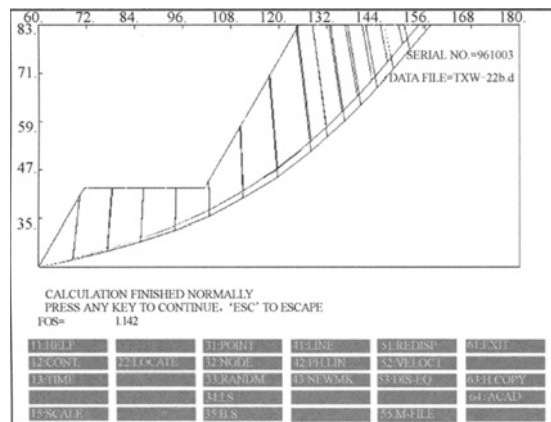


Figure 3. Sketch map of 1[#] excavated slope stability analysis

INTEGRATED REINFORCE METHODS

Excavated slope reinforce sketch

According to the foundation rule of reinforcing instability slopes, unloading, drainage and resisting methods are the normal techniques used in improve slope stability, for Tangxiwan villa excavated slopes, since the slope body is consisted of weak weathered sandstone with politic siltstone, it is not suitable to use unloading method in improving the slope stability. When considering the stability with natural landscape inosculate, it is reasonable to adopt rock bolts and shotcrete for the support of the instability slopes, and make green with plants for scene.

Reinforcing methods

Based on the stability analysis of the slopes, wedge failure and shallow slide are the normal failure modes, so, clean the flexible rock, install systematic rock bolts ($\varphi 25 @ 3000 \times 3000$, $L=6m$) can satisfy the slope stability (GB50086-2001, GB50330-2002). Furthermore, paving geogrid on the surface of the slope, planting vegetation seeds in the grids were used to green the slope (Figure 4).

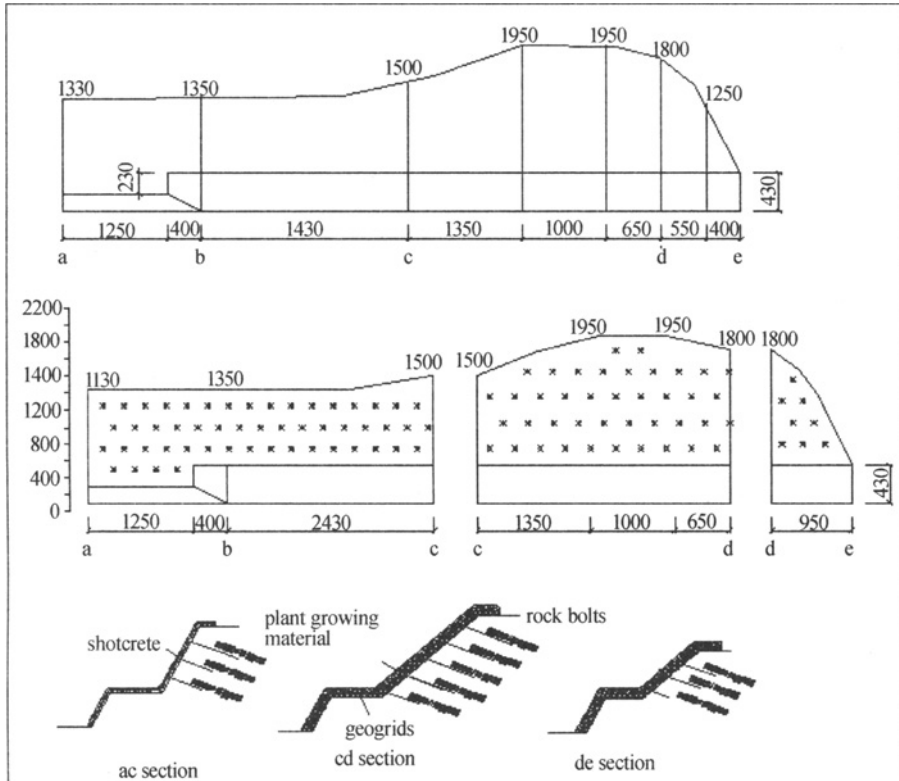


Figure 4. Reinforcing methods for 1[#] slope

Planting technique

Spurt and sow technique or planting technique is the method that spread the plant growing material on the slope surface to not only make the vegetation growing but also to avoid washing out by rainfall. The plant growing material are mixed with artificial liveness soil, straw seeds, native grass and trees seeds, bond and keep water dose. Since the plant growing material was spouted on the slope surface, the nutriment of plant growing was supplied in long term, the artificial liveness consisted of turf, rotten soil, keep water dose, bond, straw fiber and complex fertilizers, when mixed well-distributed by stirring mill, the material was spurted on the slope surface, which handled by grids and nails. By using the spurting method, the thickness of the plants growing stroma is thick enough for vegetation growing in long

term, especially for the steep slopes, the vegetations can be grown as nature. Otherwise, the plants can be grown in summer and winter since the stroma may be formed as cumularspharolith structure, which has strength, aerate, heats and moisture preservation of soils.

In Tangxiwan villa, according to the environmental and climate, the PMS (Plants Material Spouting) method with anchorage was taken out in excavated slope reinforcing. The construction drawing of spreading geogrids is shown in Figure 5.

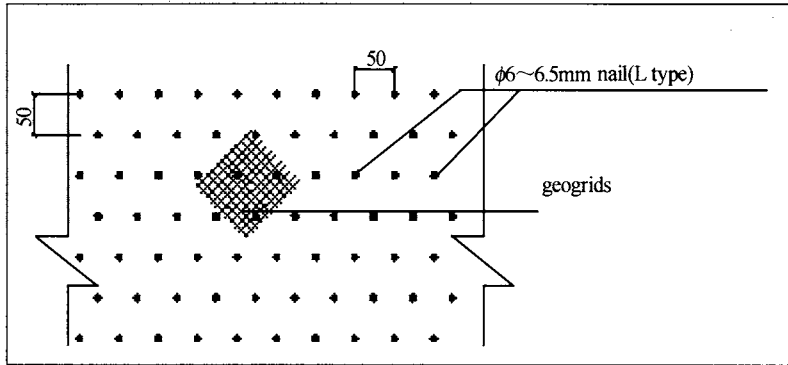


Figure 5. Construction drawing of planting technique

The key problem is to select stroma mixing proportion, the stroma mixing proportion normally used in slope surface planting for 100 m² and 8-10 cm thickness includes: peaty soil 15kg, rotten soil 150kg, vegetation fibre 3kg, hust 3kg, concretion dose 5kg, moisture preservation 18g, complex fertile 15-20g and right amount water.

Construction technique

Construction working procedures: clean the flexible wedges→spreading grids and fixed nails→spurting mixed plant material→plant maintain

The first step is to clean the flexible rocks of the slope surface, which includes the next process. ①To clean the flexible rock, dangerous rock, to remove the hidden troubles of rock falls. ②To strike-off the slope surface appropriately, and keep the planting material inseparably close to the rock. ③To protect the protophyte when cleaning the slope surface.

The second process is to spread the geogrids on the surface of the slope, i.e. use doubleaction high strength SS20 type geogrids, the diameter of the hole is 4cm×4cm. The direction of spreading the geogrids is from up of the slope to down, and use rock nail to fasten the geogrids, the geogrids should be apart from the surface of slope about 6-7cm, and the width of related joints of the geogrids must be more than 5cm, and the length must be more than 10cm.

The third process is anchorage, adopt“L”type nail, which the diameter is φ6-φ8 cm and the length is 30-40cm to fasten the geogrids, the space of the nail is 1.5m×2.0m.

The fourth step is to spurt the plant growing material on the geogrids, the thickness of the understratum plant growing material is 7-8cm, the surface layer (seeds) is 3-4cm, then, covering with other soil for melioration blowing method.

The three dimensional effective sketch map of the slope after reinforced was shown in Figure 6.

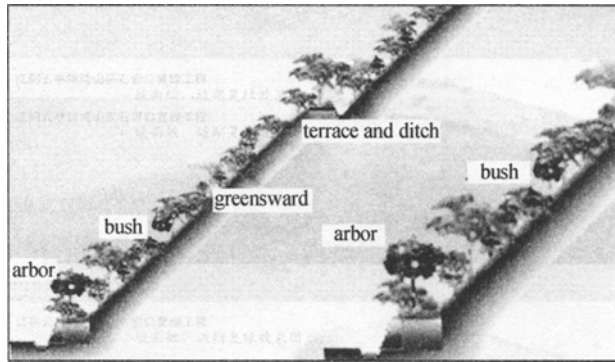


Figure 6. Sketch map of slope surface scene

If there is a terrace on the slope surface, it is easy to plant the vegetation by using the vegetation growing pockets, the technique is described as following. First, put the improved growing soil and seeds into the PVC dilly bags, and accumulated as trapezoid type. The height is not lower than 60 cm. Then, set a $\phi 50$ mm drainage hole under the pockets.

CONCLUSIONS

Since the requirements of human been for environment and ecology, the plant growing method in slope reinforcing is more and more considered in Chinese downtown construction. How to combine with instability improvement and reforest in excavated slope become an important problem for geological engineers. As an example, the Plants Material Spouting (PMS) method with anchorage was taken out in excavated slope reinforcing of Tangxiwan villa area, the result of the complex reinforce shown that all the slopes were covered with vegetation and bush even in the winter, and the stability safety factor was sufficient for stability based on rock bolts and shotcrete. The material of plants growing discussed in this paper is suitable for the same climate area, such as the eastern of China, and, the method discussed in this paper is suitable for the cutting slopes of expressway constructions.

ACKNOWLEDGMENTS

The research work was financed by Jiangsu Natural Science foundation (No.Bk2006171).

REFERENCES

- Brown E.T. (1987). Analytical and computational methods in engineering rock mechanics. John Wiley (eds), New York.
- National Standard of anchorage and shotcrete technique (GB50086-2001) (2001), Beijing: Chinese Planning Publishing House.
- National Standard of slope engineering technique (GB50330-2002) (2002), Beijing: Chinese Construction Industry Publishing House.

FLY-ASH-STABILIZED GYPSIFEROUS SOIL AS AN EMBANKMENT MATERIAL

Jie Zhang, Ruben Solis

*Civil Engineering Department, New Mexico State University, P.O. Box 30001, MSC-3CE
Las Cruces, NM 88003-8001, U.S.A.*

A highway expansion project was proposed at the boundary of Texas and New Mexico State, where gypsum deposits are overlaid almost the entire construction area. In order to use the local gypsiferous soil as a suitable embankment material, soil stabilization using fly ash as an admixture was proposed. Even though the application of fly ash as a soil stabilizer started around 1950s, there are not many case histories related to the stabilization of gypsiferous soils using fly ash. In this study, a series of laboratory testing on gypsiferous soils before and after the addition of fly ash is presented. Analysis is done on the physical and mechanical properties of the stabilized soils as well as the chemical processes involved in the stabilization.

INTRODUCTION

Gypsiferous soils have not been widely used as construction materials due to their unpredictable behavior when water exists. The main component of gypsiferous soils is gypsum ($\text{CaSO}_4 \cdot 2\text{H}_2\text{O}$), which is a major rock forming mineral derived from karstic terrain. The term karstic terrain is normally applied when the dissolution of bedrock and development of underground drainage is involved. Therefore, gypsum is classified as a soluble and air-hardening material. Because of the property of changing its chemical structure at temperatures above 58°C or in situations where water exists, the behavior of gypsum is unpredictable. The hazard of subsidence, strata collapse and sinkhole formation is more evident in gypsiferous soils than in other soluble rocks. In addition, when gypsum exists in bedrocks, either as massive beds or veins, it can be associated with the sulphate-rich groundwater which is harmful to concrete, and precautions to prevent damage should be given (Forster et al. 1995).

Because of the specific properties, gypsiferous soil as a structural fill or used in other engineering applications, such as embankments, pavement subgrades and bearing soils, is not recommended. According to Irfan and Ozkaya (1981), dissolution problems in embankments and slopes are associated with gypsum and anhydrite (CaSO_4), which may cause a shear strength reduction by a factor of 4 if 10% of gypsum or anhydrite is dissolved. Even though engineers have been trying to conduct soil stabilization in gypsiferous-soil-overlaid sites, references in this area are very limited and in some cases the construction cost could be very

high. However, soil stabilization in other problematic soils, such as soft clays, is widely used. Misra (1998), Cokca (2001), and Nalbantoglu (2004) applied fly ash in stabilizing clayey soils, soft subgrades and highway embankments. After soil stabilization, the engineering properties of these problematic soils were improved with increased maximum dry density, reduced swelling potential, and increased shear strength. Inspired by these successful soil stabilization cases, a laboratory study on engineering properties of fly-ash-stabilized gypsiferous soil is presented in this paper in order to check whether the stabilized gypsiferous soils can be used as embankment materials.

BACKGROUND

Project description

The New Mexico Department of Transportation was projecting the US 62/180 highway expansion project, which starts from the Texas/New Mexico State line and extends to Carlsbad, New Mexico. The geologic setting of the site is composed of Quaternary sediments and Permian sedimentary rocks and evaporative deposits (primarily halite and gypsum) that underlie the majority of the site. Surface soils overlying these units consist of silts, clays, and coarse-grained soils which were derived from a combination of alluvial process and in-place weathering. The underlying soil is moderately to highly cemented. The southern part of the site is known to have dissolution features (i.e., fissured cavities and collapsed sinkholes) formed in gypsum formation.

In order to use the local gypsiferous soil for embankment construction, a laboratory testing program was developed to characterize engineering properties of gypsiferous soil in its original form and after stabilization with fly ash. Soil sampling was performed in two locations along the southern part of the US 62/180 in New Mexico. Sample group I and II were collected at 110 feet south from the center line of the milepost 2.05 and milepost 4.30, respectively. The sampling locations were selected because of the great amounts of gypsum deposits at the site.

Properties of gypsum

The chemical state of calcium sulphate is vital in engineering applications. The most common forms are calcium sulphate dihydrate, calcium sulphate hemihydrate, and calcium sulphate anhydrite. Calcium sulphate dihydrate or better known as gypsum can be expressed as $\text{CaSO}_4 \cdot 2\text{H}_2\text{O}$. Soluble rocks in this form behave relatively stable in terms of expansion because the two bonding water molecules allow the soil to absorb minimal moisture without change in its chemical structure. However, cautions should be given since the excess of water will ultimately modify the chemical structure, changing calcium sulphate dihydrate into solution (Lewry and Williamson 1994).

Calcium sulphate hemihydrate is a partially dry form of gypsum, and chemically expressed as $\text{CaSO}_4 \cdot m\text{H}_2\text{O}$, where m varies from 0 to 2/3. Hemihydrate becomes unstable when exposed to air, since moisture from the environment will be absorbed until the hemihydrate becomes gypsum. Once hemihydrate turns into gypsum and remains exposing to moisture at temperatures below 58°C, the gypsum will become solution.

Calcium sulphate anhydrite is anhydrous calcium sulphate (CaSO_4), normally exists at deep depth and below gypsum layers. This form of calcium sulphate is the most unstable one since it tends to absorb water, changing the dry form to the hemihydrate form and ultimately to gypsum. The transformation from anhydrite to gypsum brings another engineering issue: anhydrite tends to expand in the transforming process due to the absorbed water, leading to a potential danger to any structure constructed above.

Fly ash

Fly ash particles are pozzolanic in nature and could react with calcium hydroxide and alkali to form cementitious compounds. It has been proved that fly ash as a stabilizing agent for subgrade materials, clayey soils and some granular soils is very effective. According to the ASTM C618, there are two major types of fly ash: Class C and Class F fly ash. Class C fly ash has its own cementation because of the significantly high calcium content, which initiates the pozzolanic reaction when reacting with water. Class F fly ash is non-cementitious because of its low lime and calcium content. Therefore, the self-cementing Class C fly ash is normally applied in soils to modify engineering properties. It was used in this study as a stabilizing agent in gypsiferous soils.

LABORATORY TESTING

Proctor and unconfined compression tests

According to the American Coal Ash Association (2003), the percentages of Class C fly ash mixed with gypsiferous soil were selected to be 10, 15, 20, and 25 % in weight. Five Proctor tests (ASTM 698) were performed to determine the optimum moisture and the maximum dry unit weight. Before conducting unconfined compression test (ASTM 1632 and 1633), compacted specimens were cured for 7 and 28 days, respectively.

Moisture determination

Moisture determination was conducted on specimens obtained from the Proctor test. Because gypsum has bonding water in its chemical structure, it is valuable to obtain its surface moisture. The percentage of surface moisture in gypsiferous soils gives the amount of free water surrounding soil particles. In order to obtain surface moisture, a portion of soil specimen for each increment of water content was placed in oven at 60°C for 24 hours. Above 60°C , gypsum starts drying the bonding water, transforming the dihydrate form to hemihydrate and finally to anhydrite.

Percentage of hydration

The hydration can be defined as the reaction in which water is combined into the crystalline structure of a mineral. The strength of gypsiferous soil is directly derived from the hydration process (James and Lupton 1978). The percentage of hydration was obtained after the completion of unconfined compression test. Two separate portions of each specimen were

placed in ovens at 60°C and 110°C for 24 hours. The one in 110°C oven is for determining the total water content. The percentage of hydration is then determined by subtracting the surface moisture from the total water content.

RESULTS

Strength

Unconfined compression test was conducted after removing specimens from the moist room cured for 7 and 28 days, respectively. Figures 1 and Figure 2 show the comparisons in unconfined compressive strength (UCS) of unstabilized gypsiferous soil and fly-ash-stabilized gypsiferous soil. Obviously, gypsiferous soils had substantial increase in UCS after stabilization with Class C fly ash.

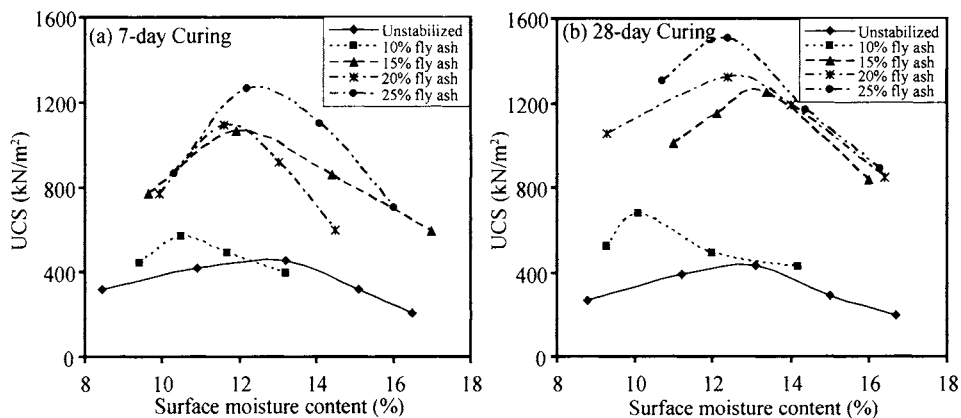


Figure 1. Unconfined compressive strength of sample group I

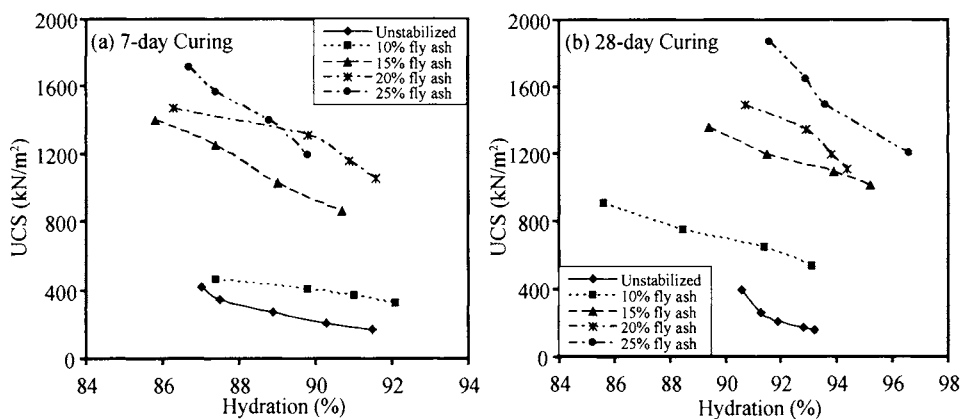


Figure 2. Unconfined compressive strength of sample group II

Strength vs. surface moisture

Figures 1 shows the strength variation at different surface moisture contents and the trend of increasing strength as the percentage of mixed fly ash increases. For samples with the same

components and having the same curing period, there is an optimum surface moisture content which corresponds to the maximum unconfined compressive strength. For example, for samples cured 7 days in Figure 1(a), the stabilized soil sample with 10% fly ash has the maximum unconfined compressive strength of 570 kN/m² at 10.5% surface moisture content. This pattern of strength is similar to that of dry unit weight Proctor test.

Another important finding in Figure 1 is that for the same surface moisture content the strength of stabilized soils increases with the increase of curing time. However, for unstabilized gypsiferous soil samples, the unconfined compressive strength decreases with the increase of curing time, i.e., from 7-day to 28-day. The strength increase in stabilized soils is attributed to the increased pozzolanic reaction between fly ash and soil with increased moisture contact. For unstabilized gypsiferous soil samples from sample group I, the concentration of gypsum and anhydrite is 94.8%. As mentioned earlier, both gypsum and anhydrite absorb moisture from the environment, changing their chemical structures. Correspondingly, the engineering properties of gypsiferous soil will also change with the trend of decreasing strength. Therefore, gypsiferous soil is not suitable as construction material in moist environment.

Strength vs. hydration

Figure 2 shows the variation of unconfined compressive strength with different percentages of hydration in specimens from sample group II. It can be seen that for all samples the unconfined compressive strength decreases as increasing the percentage of hydration. This verifies the finding from James and Lupton (1978) that the strength of gypsiferous soil is directly derived from the hydration process. From Figure 2, it can also be seen that for the same percentage of hydration increasing the curing period from 7-day to 24-day, all samples with the same components increase their unconfined compressive strengths. Even for unstabilized gypsiferous soil samples, there is still a slight increase in UCS.

CONCLUSION

Based on the results obtained from this research, the following conclusions can be drawn:

- The strength of gypsiferous soils decreases as increasing exposure to moist environments.
- The application of fly ash in gypsiferous soils increases the strength if the curing period is increased.
- The surface moisture content is very important in compaction process. It was observed that strength increases with increasing surface moisture. However, the strength increase stops when the optimum surface moisture is reached. After this point the strength is reduced with increasing surface moisture.
- Hydration process of gypsiferous soil directly affects the soil strength. As the percentage of hydration increases, the unconfined compressive strength decreases.
- Increasing curing period from 7 to 28 days, for the same percentage of hydration, all samples, either stabilized or unstabilized, show an increase in unconfined compressive strength.

ACKNOWLEDGEMENT

The authors appreciate the support from AMEC earth and environmental, Inc. by providing the laboratory and equipments to perform this research. The cooperation in sample preparation and testing by Fernando Solis, Noe Jordan and Ana Loya is also appreciated.

REFERENCES

- American Coal Ash Association (2003). Fly ash facts for highway Engineers, Report No. FHWA-IF-03-019, American Coal Ash Association.
- Cokca E. (2001). Use of Class C fly ashes for the stabilization of an expansive soil, *Journal of Geotechnical and Geoenvironmental Engineering, ASCE*, 127 (7): 568-573.
- Forster A., Culshaw, M.G. and Bell, F.G. (1995). Regional distribution of sulphate rocks and soils of Britain, *Geol. Soc., London, Engng. Geol., Spec. Publ.*, 33 (3): 95-104.
- Irfan T.Y. and Ozkaya, I. (1981). Engineering geological mapping of gypsiferous formations, Sivas, central eastern Turkey, *Int. Assoc. Engng. Geol. Bull.*, 24 (1): 33-37.
- James, A.N., Lupton R.R. (1978). Gypsum and anhydrite in foundations of hydraulic structures”, *Géotechnique*, 28 (3): 249-272.
- Lewry, A. J., Williamson J. (1994). The setting of gypsum plaster: Part I, the hydration of calcium sulphate hemihydrate, *Journal of Material Science*, Vol. 29, No. 20, 5279-5284.
- Misra A. (1998). Stabilization characteristics of clays using Class C fly ash. *Transportation Research Record*, Washington DC, Issue 1611, 46-54.
- Nalbntoglu Z. (2004). Effectiveness of Class C fly ash as an expansive soil stabilizer, *Construction and Building Materials*, 18 (6): 377-381.

REDUCTION OF EARTH PRESSURE AND DISPLACEMENT OF ABUTMENT WITH REINFORCEMENT FILLING

Wenhui Zhang

*Key Laboratory of Ministry of Education for Geomechanics and Embankment Engineering,
Hohai University, Nanjing 210098, China
Geotechnical Research Institute, Hohai University, Nanjing 210098, China*

Bangmin Qin

Nanjing Water Conservancy Planning And Design Institute Co., Ltd

Baotian Wang

*Key Laboratory of Ministry of Education for Geomechanics and Embankment Engineering,
Hohai University, Nanjing 210098, China
Geotechnical Research Institute, Hohai University, Nanjing 210098, China*

Jiandong Ye

Chengdu Hydropower Investigation and Design Institute, Chengdu 610072, China

The common method to construct expressway is construct a bridge abutment before filling embankment in China. The earth pressure acting on the abutment during filling embankment is much higher than the active earth pressure because of the rolling action of the fill. The bridge abutment and the piles under the abutment may occur significant horizontal displacement due to the higher earth pressure acting on lateral faces of abutment. The bearing capacity of the abutment piles would be reduced if the horizontal displacement is beyond a critical volume. The stress condition of the abutment piles is changed from axial compression to bending-compression. The change of the stress combination may have a negative influence to the safety of bridge abutment. The geo-grid reinforced soil can be used as filling in the abutment zone to reduce the earth pressure acting on the abutment and the horizontal displacement of the abutment. A case study has been done at two flying bridges over the Ninghuai Expressway of Jiangsu, China. This case study has analyzed the effect of geo-grid reinforced with the comparison of the earth pressure acting on the abutment and the horizontal displacement of the abutment between the abutments for having and having not geo-grid reinforcement in the filling. Test results show that the increment ratio of earth pressure on the abutment for which the filling of the embankment behind the abutment is geo-grid reinforced is 0.52 to 0.81 fold of that on the abutment for which the filling of the embankment behind the abutment is not geo-grid reinforced. The horizontal displacement of the abutment with reinforced filling is 26% to 43% less than that of the abutment with usual compacted filling.

INTRODUCTION

According to the Chinese technical specification for construction of highway subgrades, expressway construction sequence is that structures (such as culvert and pedestrian walkway and bridge abutment etc) construction is followed the construction of embankment filling. If an expressway project is constructed following the specification, the earth pressure on the abutment is close to the active earth pressure and the structure hasn't significant lateral displacement. This construction sequence has the shortage as filling excavation for the construction of piles, foundation and abutment structures, and needing a longer construction period. In recent years, it is very common to construct bridge abutment before filling of embankment in expressway construction for cutting down the construction period. The earth pressure on the lateral face of the abutment is much bigger than the active soil pressure with this construction process because of the asymmetric filling of embankment on the two lateral faces of abutment and the filling compaction. the abutment occurs significant horizontal displacement for the large asymmetric horizontal load caused by the filling construction. Significant horizontal displacement can reduce the bearing capacity of the pile. On the other hand, the construction of the beam-slab is impacted if the horizontal displacement is too much and the stress condition of the abutment piles is changed from axial compression to bending compression. The higher earth pressure and the significant horizontal displacement have a heavy influence to the safety of bridge.

Geosynthetic-reinforced soil (GRS) retaining wall have been used to supporting bridge abutments in place of traditional pile foundations, this will not only reduce the costs but also can reduce "bridge bumps" often experienced at the ends of a bridge resting on a pile-supported abutment (Abu-Hejleh, N.2000, 2002; Adams, M. 1997, 2000; Ketchart, K. 1997; Sam M.B. 2003). Geotextiles have been employed to reduce lateral deformation of bridge approach embankments and to eliminate the lateral pressure on the abutment wall (Thomas V. 1987, 1989). Geo-grid reinforced retaining walls have begun to be used to expressway Since the late of 1990s. Geo-grid reinforced soils have high shear strength, low lateral displacement and low compression. Geo-grid reinforced retaining walls meet the various need of expressway construction (Zhang Lihua , 1998). Zhou Zhigang etc (2000) have analyzed mechanism of interaction characteristics between geo-grid and soil as well as the mechanism of geo-grid reinforced flexible bridge abutment based on the test. Liao HongJian (2003) has found that reinforcement in the soil can reduce earth pressure. Friction-bar theory shows that: the reinforcement is tension component, friction between filling and reinforcement can be transmitted to the soil, and also can prevent soil lateral deformation. Geo-grid is a polymer which has characteristics of high corrosion resistance, low creep, ageing resistance and low-cost, under the premise of guaranteeing project quality, using geo-grid as reinforcement can achieve good economic returns (Liu Zongyao, 1994).

To solve the problem of large displacement of the bridge pile and abutment under the condition which constructs bridge abutment before filling of embankment, based Ning-Huai expressway project, case study has done on the two abutments of a flying bridge over expressway. Geo-grid reinforced soil has been used as the embankment filling within one abutment zone and hasn't been used within the embankment filling of the other abutment

zone, earth pressure which acts on abutment and horizontal displacement of abutment have been monitored during the construction of embankment. The earth pressure and horizontal displacement of two bridge abutments has been contrasted to study the effect of geo-grid to reduce earth pressure and horizontal displacement of abutment.

THE TEST RESULTS ANALYZE

Site selection and test equipment inbuilt

A flying bridge over expressway at K154+954 in NingHuai expressway has been chosen as trial site. The height of embankment within abutment zone is 7.26 meter, the reinforcement space is vary from 40 centimeter to 60 centimeter by the height of embankment, the reinforcement space was 40 centimeter if the height of the embankment is lower than 4.26 meter, otherwise the reinforcement space was 60 centimeter, and the geo-grid was 10 meter long along the axis of the road.

The location of earth pressure cell and measuring point of horizontal displacement are shown in Figure 1.

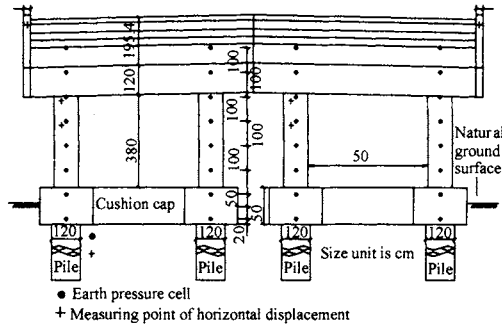


Figure 1. The location of the earth pressure cell and measuring point of horizontal displacement

Earth pressure cell inbuilt process: drill a hole which diameter is 110mm and depth is 30mm in ribbed slab of abutment. When the height of the filling is 20cm higher than the hole, excavate the filling and place the earth pressure cell in the hole, space between the side wall of the cell and the hole has been filled with foam plastic, and then refill the filling.

Analysis of soil pressure test results

Earth pressure changes with depth of earth pressure cell location are shown in Figure 2. In Figure 2, the depth is refers to the vertical distance between the location of the earth pressure cell and the surface of the filling, and earth pressure is the average of four earth pressure cell locating at the same depth.

Earth pressure changes with depth of earth pressure cell location are shown in Figure 2. In Figure 2, the depth is refers to the vertical distance between the location of the earth pressure cell and the surface of the filling, and earth pressure is the average of four earth pressure cell locating at the same depth.

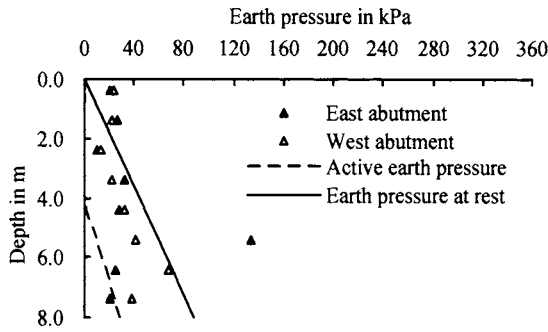


Figure 2. The relationship between earth and pressure depth (the height of filling is 6.75m)

From Figure 2, it can be seen that the earth pressure due to filling load and rolling load on abutment is large than active earth pressure, most of them smaller than earth pressure at rest, earth pressure on middle abutment is greater than earth pressure at rest. Earth pressure distribution is not in a straight line along the depth, but “S” shaped curve. This is mainly caused by impact depth of rolling loads and horizontal displacement of the abutment. In addition, compactness of the filling near each earth pressure cell location varying, random factors during earth pressure cell inbuilt(such as compactness of the filling when it refilled) have great influence on test value of earth pressure, in order to reduce the above-mentioned factors, increment ratio of earth pressure ξ is used to describe the earth pressure changes.

Increment ratio of earth pressure ξ is defined as follow:

$$\xi = \frac{P_i - P_0}{P_0} \times 100\%$$

where p_0 and p_i is the earth pressure when the first or No.i layer of filling which above the earth pressure cell compacted after earth pressure cell inbuilt.

The relationship between increment of earth pressure and depth of earth pressure cell location at different height of filling are shown in Figure3.

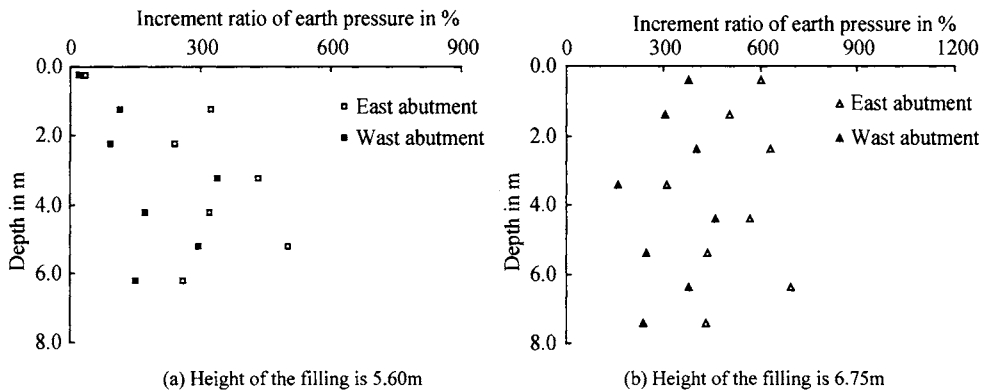


Figure 3. The relationship between increment of earth pressure and depth at different height of filling

It can be seen from Figure 3, the increment ratio of earth pressure of west abutment is smaller than that of east abutment. At July 2006 (the height of the filling is 6.75m). 7.399m below the surface of the filling, increment ratio of earth pressure of west abutment is 0.55 fold of that of east abutment; at 6.399m, 5.399m, 4.399m, 3.399 m, 2.399m, 1.399m, 0.399m below the surface of the filling, increment ratio of earth pressure of west abutment is 0.55, 0.57, 0.81, 0.52, 0.64, 0.61, 0.63 fold of that of east abutment, respectively.

Above analysis show that the increment ratio of earth pressure of using geo-grid in the embankment within abutment zone is 0.52 to 0.81 fold of that of un-using geo-grid in the embankment within abutment zone, using geo-grid reinforced soil in the embankment within abutment zone has significantly decreased increment ratio of earth pressure during the rolling.

Analysis of test results of horizontal displacement of abutment

The relationship between the horizontal displacement of the abutment and depth at different height of filling are shown in Figure 4.

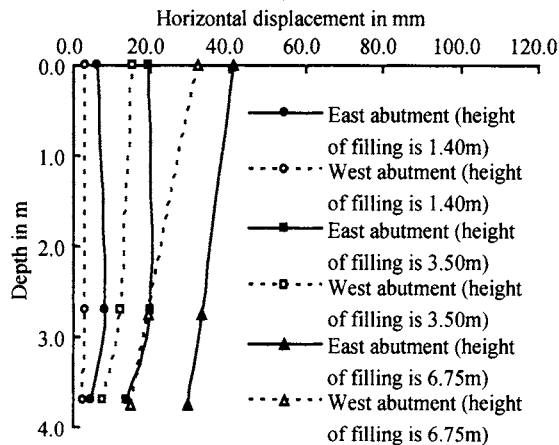


Figure 4. The relationship between horizontal displacement of abutment and depth at different height of filling

It can be seen from Figure 4, horizontal displacement of west abutment which has used geo-grid reinforced soil in the embankment within abutment zone is smaller than east abutment which hasn't used geo-grid reinforced soil in the embankment within abutment zone, the higher level of the filling, the more different value. At July 2006, the filling level of both sides are 6.75m, the average horizontal displacement of west abutment is 35.8% less than that of east abutment.(measuring point which locate at 3.56m, 4.56m, 7.30m above the natural ground surface, the horizontal displacement of west abutment is 43.5%, 37.7%, 26.5% less than that of east abutment, respectively).

Above analysis show that the horizontal displacement of the abutment which using geo-grid in the embankment within abutment zone is 26% to 43% less than that of un-using geo-grid in the embankment within abutment zone, using geo-grid reinforced soil in the

embankment within abutment zone has significantly decreased the horizontal displacement of the abutment.

CONCLUSION

Under the condition which constructs bridge abutment before filling of embankment in expressway construction, the earth pressure which act on abutment is non-linear with depth changes, the earth pressure is bigger than active earth pressure. Therefore, in the design, it is necessary to consider the large earth pressure, and increase structural rigidity to ensure structural safety.

Using geo-grid reinforced soil in the embankment within abutment zone filling has significantly decreased increment ratio of earth pressure and the horizontal displacement of the abutment during the rolling.

REFERENCES

- Abu Hejleh N., Zornberg J.G., Wang T., and Watcharamonthein, J. (2002). Monitored displacement of unique geosynthetic-reinforced soil bridge abutments, *Geosynthetics International* 9 (1), 71-95.
- Abu Hejleh N., Wang T. and Zornberg J.G. (2000). *Performance of geosynthetic-reinforced walls supporting bridge and approaching roadway structures*, ASCE Geotechnical Special Publication No. 103, Proceedings, Geo-Denver 2000, Denver, CO, 218-243.
- Adams M. (1997). Performance of prestrained geosynthetic reinforced soil bridge piers, In: *Wu, J.T.H., Barrett, R. (Eds.), Mechanically Stabilized Backfill. A.A. Balkema Publisher, Rotterdam, 35-53.*
- Adams M.T., (2000). Reinforced soil technology at FHWA, *Geosynthetic Fabric Report*, 18 (6): August 2000, 34-37.
- JTJ (1995). *Technical Specification for Construction of Highway Subgrades*. Beijing: China Communication press, 12-13.
- Ketchart K. and Wu J.T.H. (1997). In: *Wu, Barrett. (Eds.), Performance of GRS Bridge Pier and Abutment in Denver, CO, USA. Special Presentation, Mechanically Stabilized Backfill. A.A. Balkema Publisher, Rotterdam, 101-116.*
- Liao JianHong. (2003). Geotextiles relieve soil pressure test on the soil. *Geotechnical Investigation & Surveying*, 3, 1-3.
- Liu Zongyao, Yang Chanwen and Wang ZhengHong. (1994). *Geosynthetic Materials Engineering Manuals*. Beijing : China Building Industry Press, 48-51.
- Sam M.B. Helwany, Jonathan T.H. Wu and Burkhard Froessl. (2003). GRS bridge abutments—an effective means to alleviate bridge approach settlement, *Geotextiles and Geomembranes*, (21): 177-196.
- Thomas V. Edgar, Jay A. Puckett and Rodney B. D'Spain.(1989). Effects of geotextiles on lateral pressure and deformation in highway embankments. *Geotextiles and Geomembranes*, 8 (4): 275-292.
- Thomas V. Edgar, Jay A. Puckett, William F. Sherman and Jeffrey L. Groom. (1987). Utilizing geotextiles in highway bridge approach embankments, *Geotextiles and Geomembranes*, 5 (1): 3-16.
- Zhang Lihua (1998). Application of geo-grid reinforced retaining walls to North-South Expressway. *Journal of central south highway engineering*, 23(4): 8-12.
- Zhou Zhigang, Zheng JianLong and Song Wei Tao, (2000). Analysis of mechanism of flexible abutment reinforced by geogrids, *China journal of highway and transport*, 13(1): 18-21.

ANALYSIS AND TREATMENT OF GROUND RUPTURES IN XI'AN

Yin Zhang, Qianfeng Yao and Junlong Lu

*College of Civil Engineering, University of Architecture and Technology
Xi'an 710055, China*

With the development of society, economic and increment of population, urbanism is more and more obvious in the world. Especially in China, the trend is outstanding. However, different geological disasters impact the process heavily. Moreover, the type, form and incurring mechanism of urban disasters are complex in different cities. To avoid great loss in urban construction, it should be paid more attention to study them. As a heavy urban environment geological disaster, the ground rupture in Xi'an, Shaanxi Province, China, the tectonic model, relationships of earthquake and activities of ground ruptures are discussed in this article. Based on the distribution and mechanics of ground ruptures in Xi'an, the forming mechanics and treatments of ground ruptures are studied. At the same time, the relationship between activities of ground ruptures and earthquakes is also discussed. The analysis indicates: Excessive distilling ground water, surface water abundantly leakage and the oscillation affection of earthquake and large range tectonic can accelerate the velocity of activity of ruptures and cause abruptly activities. As a result, the disaster of ground rupture is obviously amplified.

INTRODUCTION

There are 662 cities in China today. For different geographic environments, the types, forms and incurring mechanisms of urban disasters are complex. According to incomplete accounting, the average lost of geological disasters in China is CNY 10 billion yuan every year. Of that about 52% happened in cities^[2]. Great material loss and a large amount of death of people were caused by geological disasters, at the same time, that brought disturbance to urban plan and construction. In this article, the ground ruptures in Xi'an taken as an example, the tectonic model of ground rupture and relationship between ground ruptures and activity of earthquake are mainly discussed based on the investigation to distribution and activity of ground ruptures in Xi'an. And the safety of urban geological disasters is analyzed.

DISTRIBUTION AND ACTIVITY OF GROUND RUPTURES IN XI'AN

From 1980s, the activity of ground ruptures is serious more and more and that makes a large amount of structures, urban roads and lifeline construction destroyed. As a heavily urban environment disaster, ground ruptures are paid more attention around the whole society. Many specialists and researchers in different research organizations have studied the ground rupture in many views and degrees. That can play an important role in the distribution, cause of formation of ground rupture and urban construction and plan in Xi'an. However, confined

by many conditions, the mechanism analysis and safeguards of ground ruptures are elementary; there are many problems to solve especially in the prevention and cure methods. Moreover, the research in ground rupture and earthquake is scarce.

Distribution of ground ruptures

The first ground rupture is found in 1959 in Xi'an and 11 ground ruptures are formed by today. The distribution of ground rupture is: The whole direction is NEE, the distance of each other is 0.6~1.5km and they are lied in parallel approximately. In EW direction, they are from Chan River to Zao River. In NS direction, from TV Tower to Xinja Temple, The ground rupture is 19km in length in NEE and 10.5km in width in NNW, the total area is 150km². The length of ground ruptures are from 2km to 12.8km, the shortest is F11 with a 2km in length in length and the total length of ground ruptures in Xi'an is over 55km.

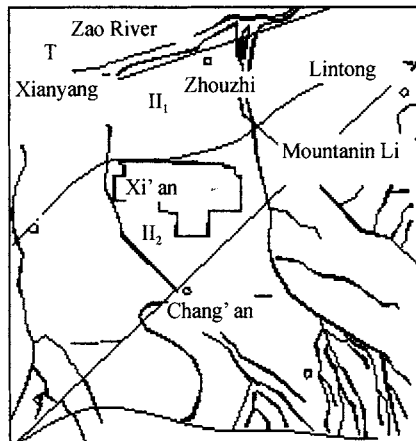
Activity mechanism of ground ruptures

Ground rupture in Xi'an is a tectonic geological phenomenon around a large area. The happening and development of ground ruptures are controlled by regional tectonic actions. The activities are determined by the geological conditions and response to tectonic actions. At the same time, they are confined and disturbed by region facts.

FORMING MECHANISM OF GROUND RUPTRUES IN XI'AN

Forming mechanism

The forming mechanism of ground rupture in Xi'an is related to the tectonic background of the Wei River fault basin and controlled by the extending of tectonic along NE in Xi'an area. The tectonic distribution is shown in Figure 1.




Examples 
 1. Fault 2. Tectonic boundary and code of zone
 I. Xianyang fault II Xi'an fault II 1. North-West sunken fault
 II 2. South East fault III Mountain Li sunken falut

Figure 1. Tectonic Distribution of Xi'an Area

To study the forming mechanism of ground ruptures in Xi'an, a group of tests have been done to explore the deformation of the Quaternary soil with a 700m thickness for faultage movement. The test indicates that shear zones are similar to faultage in sub soil layer around three deformation areas in different depth and they are continuity to the rock ruptures. Hauling rupture zone is formed in ground surface and some hauling fractures are developed. In the middle are a transition zone and a blurry shear rupture area. But the soil is bending deformed and plastic fluxion. The relationships among three zones are continuity without an obvious boundary. The extending depth of tensility fractures of lithosphere is limited. But it lies in the deformation zone which is the same to that of plastic zone in middle and shear fracture zone in the bottom, at the same time, they are related each other continuity and intermittence. The tensility fractures in the surface are a part of the whole deformation of faultage in subsoil. With the development of tectonic activity, the tensility fractures are extend to the deep and the top and the plastic deformation zone is sheared and disappeared, so the fractures are linked as a whole.

Many researches indicated, the descending of ground water is one of the key facts that make the activity of ground ruptures accelerated in Xi'an. Because of the descending of ground water, a par of geostatic stress which is supported by pore water transit to the soil and a new consolidated deformation is formed. That makes the ground subside and accelerated the ground fractures.

Causes of ground ruptures

The causes of ground ruptures in Xi'an include the follows: One is the result of tectonic activities, the other is descending of ground caused by excessive mine of ground water. However, many researches indicate that ground rupture is a complex thing. Its activity and deformation are impacted by many facts, which function in the formation and development of ground ruptures although they function differently. To understand these facts, many advanced researches to ground ruptures need to be done. We can defend and treat them until the internal regulations of ground ruptures are acknowledged by us.

TECTONIC MODEL OF GROUND RUPTURES

If ground ruptures in Xi'an are put into a three-dimensional space, the tectonic model can be obtained as Figure 2. The range of the model is from Chan River in east, to Zao River in west and from Wei River in North, to Lintong-Chang'an Fracture in South.

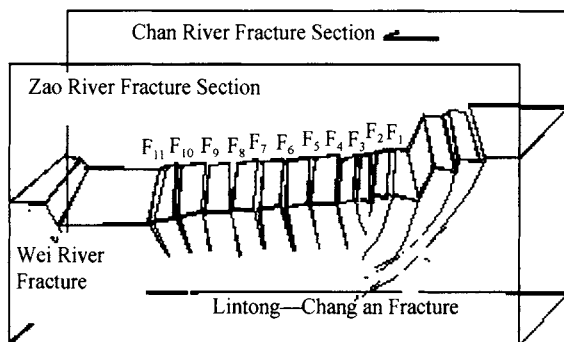


Figure 2. Tectonic Model of Ground Rupture in Xi'an

The tectonic model shows a macro three-dimension draft of activity of ground ruptures in Xi'an and it is liable to advanced quantitative research on ground ruptures in Xi'an. The tectonic model indicated that wherever the tectonic characters are alike tectonic ground ruptures can appear. For example, in the Fei River Basement and Wei River Basement, there are many similar ground ruptures and they are form a ground rupture system in Fei-Wei River Basement.

GROUND RUPTURES AND EARTHQUAKES

After the emergence of ground ruptures in Xi'an, some researches to ground ruptures and earthquakes had been done already and they are benefit the acknowledges to the relationship to ground ruptures and earthquakes. But most of them did not pay adequate attention to the creep slides and fast slides. In this article, based on the analysis of fast slides of ground ruptures in trench sections some explores are done to form that vies. It is helpful to acquire the kinematic attribute of ground ruptures. At the same time, the relationship between ground ruptures and earthquakes is analyzed from the view of forming mechanism.

Fast slide of ground ruptures

In the past people considered that ground ruptures in Xi'an are sub-static creep slides of ground. The concept is based on the inspection to activity of ground ruptures in the past years. However, that is not means that the activity formation of ground ruptures is only one. Many researches and analysis by trench can testify that view. A case in point, the Hansenzhai trench lies in the east part of the Out Heping Gate Ground Rupture (F6). The soil layer disclosed by trench is Quaternary Soil. Five trenches (total length is 56.4m, width is 2.4-6m, depth is 1.2-10.9m) are vertical to ground ruptures nearly. Trench section disclosed that the crack zone includes three group of approximately parallel fractures.

From the investigation data of historical earthquakes in Xi'an, the intensity of the 9 earthquakes inducing ground ruptures are more than 7 degree.

Contrasting the ground ruptures with earthquake and the ground ruptures without earthquakes, the ground ruptures with earthquake are more than without earthquake in Xi'an.

Periodicity of ground ruptures and activity of seismic in Xi'an

Ground ruptures happened in strong motions are caused by tectonic facts and their periodicities are coincidence to those of strong motions. What relationship between ground ruptures without earthquake and seismic activity is briefly analyzed in the follows.

During the past hundreds of years, the ground ruptures in Xi'an are active or sleeping in different periods. There are four more active periods: The Hanyuan Palace section of Bafu Ground Rupture in North (F3) appeared obviously. The North Television Tower Ground Rupture (F10), the South Television Tower Ground Rupture (F11) and the Lintong-Chan'an Fracture in Loess Plateau were active and kept to 1930s. About in 1938, the Bafu Ground Rupture (F3) was active once more and several ground ruptures in south suburb were obviously active. About in 1959, the Xiaozhai section of Iron Stove Ground Rupture(F4), the North-West Technology University section of Bianjia Village Ground Rupture(F5) and

Hanyuan Palace section of Bafu Ground Rupture in North (F3) are activity. About in 1976, except F11,F10,F9, each ground rupture start to be active clearly. That was not fracture in individual ground rupture any longer but develop to a ground rupture system which are composed by seven ground ruptures all over the whole city. The above activity of ground rupture in Xi'an can be indicated by Figure 5 approximatively and the periodic of activity of ground rupture is 20 years. According to many researches, the chorological phases of earthquake activity in China in 20th Century can be shown in Figure 6.

It is indicated by analysis that the lasting time of the first, the third and the fourth period are 31 years, 18 years and 17 years. The lasting time of each period is different, but the smooth phase and the activity phase of each period are almost equality and the phases of activity are a little longer than that of smooth. If we contrast the period of ground rupture with that of earthquake, we can find that the heavily activity phases of ground rupture are phasic lag corresponding to that of earthquake (Figure 3). That is, when earthquake release energy, the activity of ground rupture are advanced. The latest activity period is in 1976 when Tangshan Earthquake happened. And after 1978 the large scale ground ruptures are active all over the city. That can be shown in Figure 4.

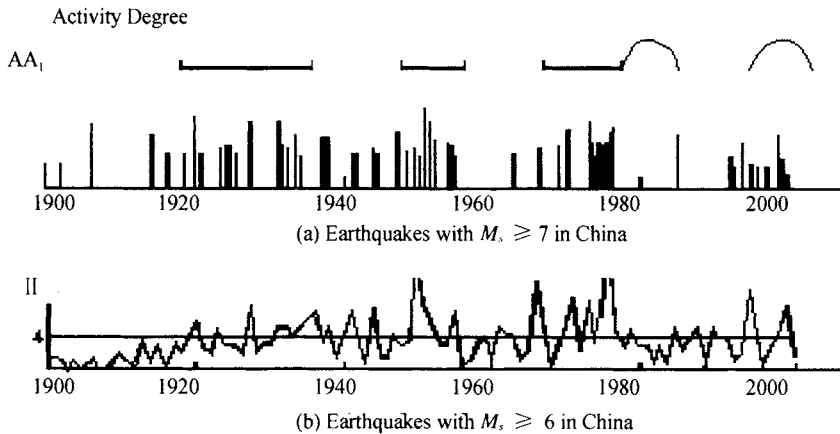


Figure 3. The frequency of the earthquake with $M_s \geq 6$ in China

Alike activity of earthquake, the activity of ground rupture in Xi'an is either smooth or heavily. In other words, sometimes the activity is creep and sometimes is fast slide. Ground ruptures slide fast in earthquake and became a part of ground fracture which induced by earthquake. The period is short and synchronic with earthquake in activity period of earthquakes.

The above analysis can reflect the texture relationship between ground rupture and tectonic activity. They not only take the information of tectonic activity but also become a part of it. According to analysis of a lot of trench data, ground ruptures slide fast in earthquake, after earthquake the smooth, activity and flourish can accelerated the slide. A case in point, fast slide happened in the strong earthquake in Huaxian County, Shaanxi Province in 1556.

Activity of ground ruptures and earthquakes in Xi'an nowadays

In the second and fourth earthquake activity period in North China from 1730 to 1815, ground ruptures in Xi'an is silent. While Form the 20th century on, it has had the notes that the ground ruptures started to be heavily activity. In the end of the seventh earthquake activity phase from 1974 to 1978, ground ruptures came into being active and last to the seventh silent phase of earthquake. But the later activity velocity is slow down and many phase level down from AA to A. It is forecasted that with the end of the seventh seismic silent phase in 1990 and the coming of eighth activity phase from 1991 to 2013, the ground ruptures in Xi'an are active once more.

CONCLUSIONS

(1)The mechanical characters of ground rupture in Xi'an can be expressed as follows: the first is different settlement; the second is horizontal movement; the third is activity of ground rupture.

(2) Ground ruptures in Xi'an are complex. Their activity laws and deformation characters are confined by many facts. Of them the main cause are: One is the result of tectonic activity and the other is excessively distilling the ground water leads the ground to sink or the co-interaction each other.

(3) Laying the ground ruptures in Xi'an in a three-dimensional space, the tectonic mode can be obtained. The model involves the range from Chan River in east to Zao River in west, from Wei River in North to Lintong-Chang'an Fracture in South.

(4) The tectonic concussive effect of earthquake in large range accelerates the ground rupture and incur paroxysmal activity. And that enlarge the disaster of ground ruptures. The environmental geological disaster should be paid more attention to modern urban plans and safety of existing buildings.

REFERENCES

- Zhang Z.M. (1990). *Research on ground ruptures in Xi'an*, North-West University Press, Xi'an.
- Li Y.S. (1992). *Research on ground ruptures in Xi'an and wei river basement fracture*, the Seismic Press, Beijing.
- Zhang Y., Yao Q.F. (2004). Tectonic model and fracture analysis of ground ruptures in Xi'an, *Journal of Xi'an University of Architecture and Technology*, 36 (3): 288-292.

RESEARCH ON TECHNOLOGY OF COUPLING SUPPORT IN SOFT ROADWAY AND ITS APPLICATION IN MINE DISASTER MITIGATION

Bin Zhu

*Highway college, Chang'an University, Xi'an 710064, China;
School of Architecture and Civil Engineering, Xi'an University of Science and
Technology, Xi'an 710054, China*

Jinchuan Hu, Fenglin Jiang

Highway college, Chang'an University, Xi'an 710064, China

Peili Su

*School of Architecture and Civil Engineering, Xi'an University of Science and
Technology, Xi'an 710054, China*

The mine of Shizui Mountain is a soft rock roadway. The paper has utilized FEM software to simulate and analyze the performance of the roadway support based on numerical analysis. In the mean time, observing the deformation in detail. The aim of the paper is to obtain better economic benefit, as well as to guarantee the performance of roadway support, and provide new method in solving disaster mitigation of mine.

INTRODUCTION

The support of roadway, especially in soft rock mine is still an unsolved problem and key technique. The technique of bolt in mining roadway is mature, and widely used nowadays. However, it is still impossible to solve some major problems including large section soft rock roadway, etc. The research in mine of Shizui Mountain has determined the methodology and parameter of coupling support. The numerical simulation for the performance of roadway support, as well as to record the deformation, ensure the development of the technique of coupling support. in soft roadway.

PROJECT BACKGROUND

The working face of mine in Shizui Mountai is know as soft rock in the roof and two sides of the laneway, and therefore it is difficult to support. The depth of laneway is about 450 meters.

The laneway which has been digged has the maximum thickness of 9.69m, the minimum thickness of 6.31m, average 7.79m. Protodyakonov number =0.6 to 0.8. The top of coal layer is made of kaolinite, average thickness 0.62m, the next top layer is shale, the average thickness 0.52m. The old roof is sandy shale, average thickness 2.40m. The bottom layer of

mine is clay shale, average thickness 0.18m. The average thickness of arenaceous shale rock is 1.5m.

DESIGN OF ROADWAY SECTION AND PARAMETER FOR SUPPORT

Design of roadway section

According to the application and requirement for the laneway, the section has been design as rectangle, the width of the section is 4.5m, and the height is 3.0m.

Determination of plastic zone

According to the data obtained, the Protodyakonov parameter is approximately 0.7. Therefore, it is known that the roof of the laneway cannot form natural pressure support based on the pressure arch theory. Consequently, the area has not been calculated using Protodyakonov theory, but plastic theory.

Width of Laneway $B=4.5\text{m}$, Height $=3.0\text{m}$

$$\text{Radius} = r_0 = \sqrt{\left(\frac{B}{2}\right)^2 + \left(\frac{h}{2}\right)^2} = 2.70\text{m} \quad (1)$$

Therefore the maximum radius of plastic circle is:

$$\begin{aligned} R_0 &= r_0 \left[\frac{(P + C \text{ctg} \varphi)(1 - \sin \varphi)}{C \text{ctg} \varphi} \right]^{\frac{1 - \sin \varphi}{2 \sin \varphi}} \\ &= 2.70 \times \left[\frac{(10.576 + 2 \times \text{ctg} 35^\circ)(1 - \sin 35^\circ)}{2 \text{ctg} 35^\circ} \right]^{\frac{1 - \sin 35^\circ}{2 \sin 35^\circ}} \\ &= 3.479\text{m} \end{aligned} \quad (2)$$

$$\text{So the area of roof loose section: } l_2 = R_0 - \frac{h}{2} = 1.97\text{m} \quad (3)$$

$$\text{The area of side loose section: } l_b = R_0 - \frac{a}{2} = 1.25\text{m} \quad (4)$$

Based on the experience of second mine like design, the loose area of coal rock is about 1.5m to 1.8m. Therefore, the design has taken surrounding rock area as top 1.97m, side 1.6m.

The choice of material and parameter in the research/project

It has been determined to use coupling support of bolt and cable based on the analysis of condition of the surrounding rock using plastic theory, as well as analogy method and numerical analysis. Coupling support of bolt and cable has been used to determine the support parameter. The top section is covered with 50m m×50m m wire netting. Girder which is used is made up of steel, the roof bolt uses whorl steel bar ($\phi 18\text{m m}$ 、 $L=2400\text{m m}$), the side section uses roundness steel bar ($\phi 16\text{m m}$ 、 $L=2000\text{m m}$), the accompanying material uses steel plate (120m m×120m m×10m m).

The roof section has 6 bolt in parallel, two sides have 4 bolt, average distance 800milimeter. The bond glue is normal resin, the roof bolt uses 3 piece of resin per spot. The

side anchor uses one resin per spot. The support uses pre-pressed cable, two pieces each row, average distance 2400 millimeters. The section is shown in Figure 1.

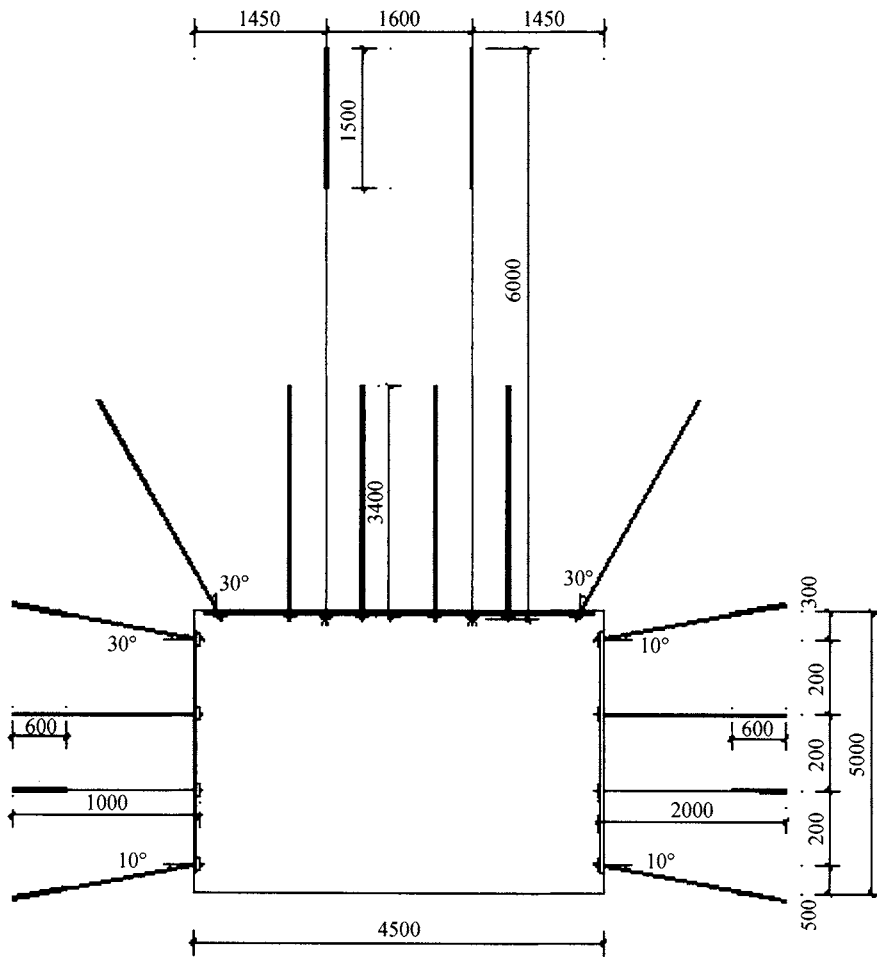


Figure 1. Laneway support diagram (unit: mm).

SIMULATION OF LANEWAY SUPPORT PERFORMANCE

FEM method is widely utilized in underground rock project stabilization research. The FEM software ANSYS with non-linearity analysis function has been utilized to analyze the area distribution of stress field, displacement field for Shi Zui Mountain 2nd coal mine anchor support roadway.

According to the real condition, and the aim of the digging and design is focused on the stability issue of the project, as well as the digest will only have impact on centre area with radius of 3 to 5 times. Therefore, the width of the model is 44.5 meters, and height 35.21 meters (underground 417.20m to 452.41m). The model has 16 layers which are expected to be influenced. The majority of the layers are composed of sand rock, sandstone, shale, coal. The model is made based on the real thing.

The original rock stress force is existed in the stratum naturally. It is the key force leading to deformation and damage of the rock digging process, and therefore it must be pre-studied before stability analysis, as well as digging and strategy commencing. In this analysis, the stress value for underground with depth 417.2m has been calculated. The side influence has also been taken into account. Part of the data simulation has shown below:

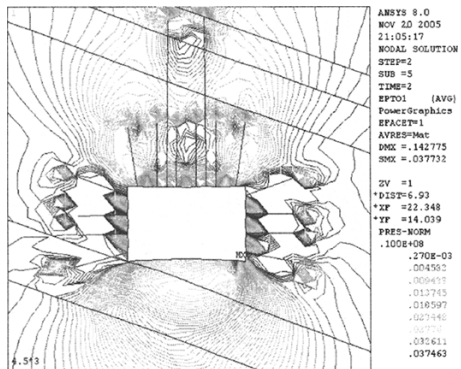


Figure 2. Major principal strain of rectangular section

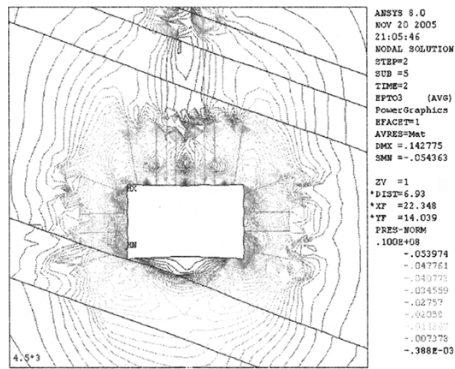


Figure 3. Minor principal strain of rectangular section

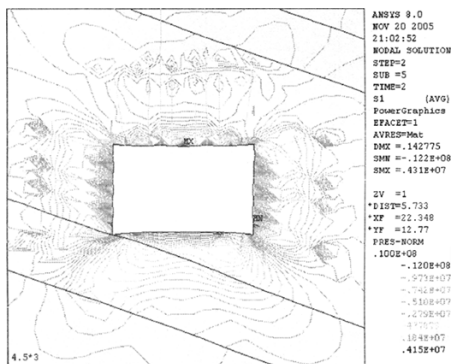


Figure 4. Major principal stress of rectangular section

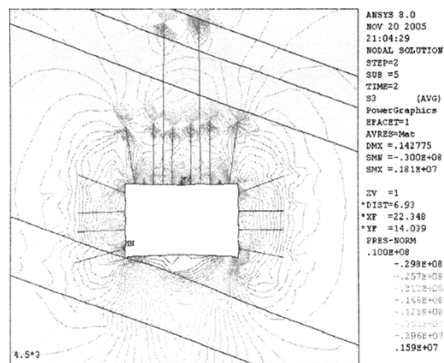


Figure 5. Minor principal stress of rectangular section

According to the simulation and analysis, if the rectangle section is not supported when digging, the deformation area accumulated to 25cm per hour. If the process is not ceased, it indicates the deformation is very serious, and the surrounding rock is unstable. If the section is supported with anchor, the rectangle section goes down 4 to 12 centimetre, the maximum pressure is 33.5 MPa, and the minimum pressure is 13.7MPa. major principal strain is 0.037, minor principal strain is -0.054 . The factor of accumulation of stress on the roof is 1.26 to 3.17.

OBSERVATION OF SUPPORT PERFORMANCE UNDER DIGGING PROCESS

Deformation observation for laneway surrounding rocks

The method uses triangle distribution of cameras to record the section. The location of camera is placed above head 2meters. The camera uses JSS30A digital extensometer, which has been placed per 20 meters inside the laneway. The camera is placed on the top of the anchor, which is bond with ring circle. The frequency of recordation: if digging section is within 50meters, it is recorded every day, if the digging section is beyond 50 meters, once per two days, or the speed is recorded as base data.

Observation analysis

The observation shows if the working distance is within 50 meters, the deformation of the laneway is significant. If however, the working distance is beyond 50 meters, the deformation is comparatively stable. The speed of deformation become the highest after 7 days of digging, and become stable after that. The maximum deformation speed is 27.84milimeter per day, average speed 1.8milimeter per day. The maximum falling of ceiling is 90.89mm, the maximum movement of the two sides is 72.49mm. All values are within the allowed range. According to the analysis and simulation, the deformation is shown in Figure 6 and Figure 7.

The diagram shows the three phases occurred during deformation. Within 0-2.0D range, the deformation speed is maximum, however the duration is short, the deformation caused 40 percent of whole deformation. Within range 2.0 to 5.0D, the deformation speed decreases, it resulting in 45% of the whole deformation. Within 5.0D range, the deformation speed decline significantly, and thus have caused 15% of the total deformation.

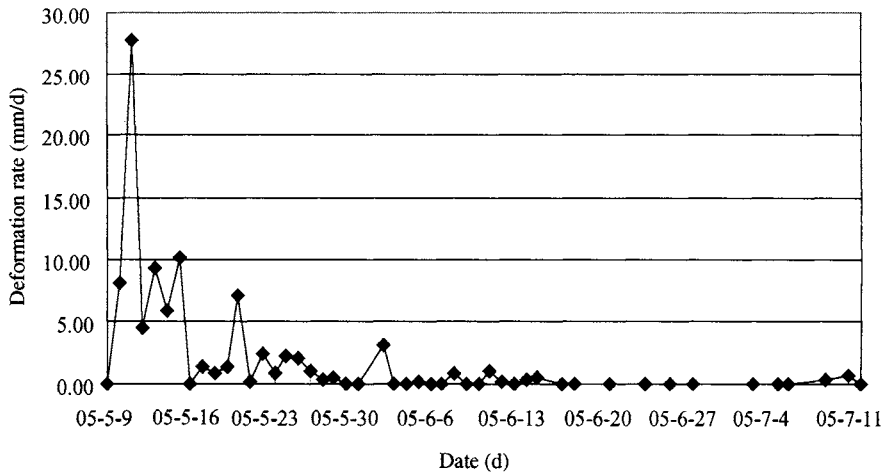


Figure 6. Roof settle speed curve

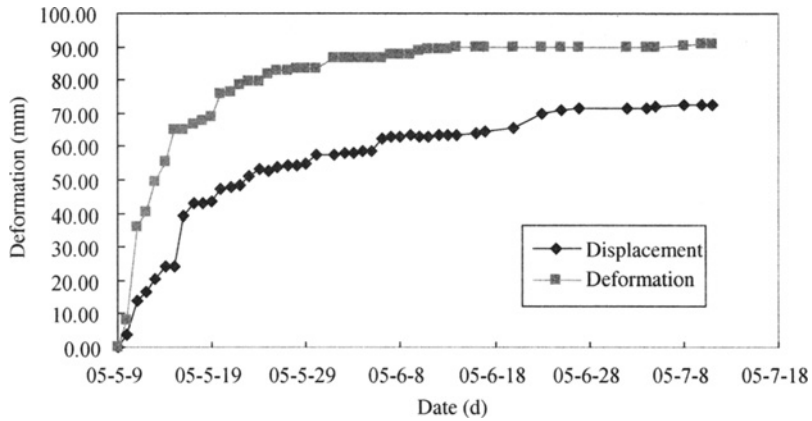


Figure 7. Laneway deformation curve

CONCLUSION

Based on the simulation results and real time observation, the application of coupling support of bolt and cable has many advantages, which include easier workship, decreased production cost, decreased labour effort and time. It also solved rock falt security issues, etc, and make it safe, high in performance and efficiency and low cost.

The technique of supporting roadway in soft rock has many difficulties. In future work, the research of mechanism of coupling support should be enhanced, and making the design comprehensive and better. Increase the reliability of the simulation, and build more efficient and reasonable roadway support design system.

REFERENCES

- He Manchao, Sun xiaoming (2004) Support Design and Construction Guideline of Soft Rock Tunnel in Coal Mine. Beijing: Science Press.
- He Manchao, Yuan Hesheng, et al. (2004). Principle and Practice of Anchor Support Technology in Coal Mine. Beijing: Science Press.
- Xue Shunxun, et al. (2002). *Support Technology Guideline of Soft Rock Tunnel*. In Coal Mine. Beijing:China Coal Industry Publishing House.
- Research on Tecnology of Coupling Support in Soft Roadway (2005). Xi'an University of Science and Technology.

Risk Assessment and Management

FORECASTING OF ROCKFALL IN K2403+500 OF G320

Helin Fu, Xianfeng He and Qiang Luo
*Civil Engineering College, Central South University,
Changsha 410075, China*

Yong Zhou, Wanxue Long
*Design and Survey Institute of Guizhou Communication
Guizhou 550001, China*

Research of rockfall forecasting technology is one of most important contents of the projects “Study of predicting and forecasting technology of geological catastrophe of highway in west area” from Ministry of Communication (No. 200331880201), Combined with Acoustic Emission (AE), lab sonic test and mutation theory, a whole monitoring system was first successfully applied in a real case of rockfall in K2403+500 of G320. The work has disclosed the AE character of rockmass, and forecasting critical values of AE are put forward.

PREFACE

Rockfalls always takes place in the slope in K2403+500 of G32020 during rain season, which interrupting the safety of communication. In order to protect the safety of this zone, the research work has been done, which disclosing the mechanism of rockfall in this slope, providing some useful clues to the changing period of rockfall, and reducing the lost caused by rockfall.

SELECTING OF TECHNIQUE OF MONITORIN

Acoustic Emission (AE) is a phenomenon, when material takes place to break, and internal strain energy releases in elastic wave. So to monitor and to analysis the AE can be applied to infer the internal structure of material.

There are some relations between AE level and stress grades of rock mass, i.e. when the rock mass undertaken great pressure, the AE ratio will increase; when rock mass structure take places collapse, the AE ratio will decrease softly. On the base of the AE character of rock mass, the AE ratio, strength, energy will be disclosed by YSSC, and rock mass state will determined and will provide some useful clues to evaluate the stability of rock mass.

SITU MONITORING

Lab AE test

To gain good monitoring effect, some rock samples containing structure planes are collected from the slope in K2403+500 of G32020, and some tests for mechanism and AE have been

done . After the tests, the AE characters of rocks are gained, which will provide some useful information to the situ monitoring.

Manufacture of rock samples

There are many joints and cracks inside the rock mass in the slope in K2403+500 of G32020, the slope appears loose. The rock samples are from the slope in K2403+500 of G32020. The sample sizes are 10×10×10cm³, and the structure plane are surrounded by 525[#] cement, the artificial sample samples are 15cm×15cm×15cm.

Inclined pressure test

In lab, we do the inclined pressure test, at same time, the AE monitor is set on the artificial samples, according to the pressure climbs and the record of inclined angel of test mode, big AE event, total AE events and AE energy ratio, the norm and shear stress can be calculated, and then C_j, ϕ_j of structural plane can also be gained, shown in Table 1.

Table 1. C_j, ϕ_j of differential structural plane

No. structural plane	Cohesion (C_j)	Friction angel (ϕ_j, θ)
1	0	32.7
2	0	28.5
3	0	31.6
average	0	30.9

Lab AE test

Monitoring system of AE shown in Figure 1.

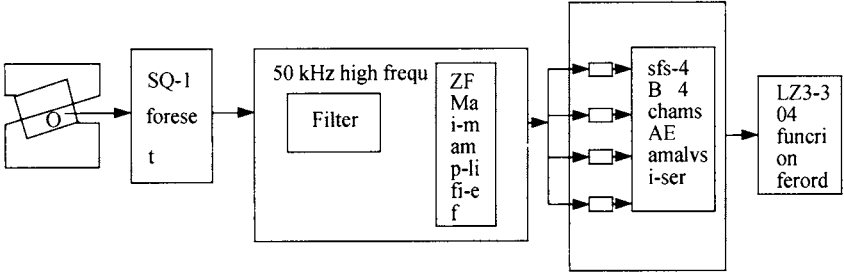


Figure 1. Monitoring system of AE

Test result

In this test, there are 12 samples, the results are shown in Figure 2, Figure 3, Figure 4 and Figure 5.

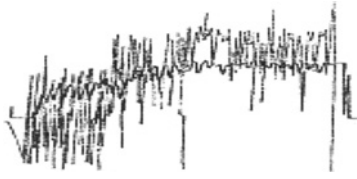


Figure 2. Climbs type

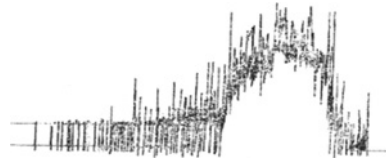


Figure 3. Single peak type

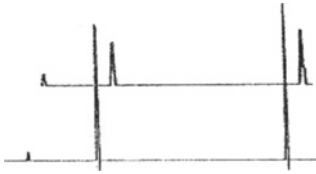


Figure 4. Double peaks type

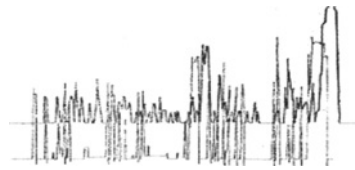


Figure 5. Multi-peaks type

Analysis of test results

From figure, 2,3,4,5, the curves types of AE events and AE energy ratio of structural planes exist in four types, i.e., climb type, single peak type, double peaks type and multi-peaks type, and their characters are followings:

- 1) When the structural plane is glide and closed, its AE appears in climb.
- 2) When the structural plane is glide and closed, and there is a bulge on plane, its AE appears in single peak, the rock mass is near to collapse.
- 3) When the structural plane is coarse and closed, and there are two protrudes on plane, its AE appears in double peaks, the rock mass will collapse in second AE peak.
- 4) when the structural plane is coarse and not much closed, and there are multi- protrudes on plane, its AE appears in multi- peaks, the rock mass collapse can be predicted in second AE peak ,due to the rock is near to collapse.

Otherwise, by the lab AE test, when rock collapse under pressure, the rock in soft strain and system rigid control its failure modes, AE energy ratio is more sensitive reflecting rock mass stability. When rock mass collapse according structural plane, the AE event ratio is more distinct, at this time AE event ratio can be applied to forecast the rock mass collapsing.

Situ monitoring method and equipment

In situ, the monitoring method is AE technique, the equipment is YSSC.

Arrange of AE monitoring holes

The monitoring holes are 5m deep and $\phi 110$ mm wide which dug by geological machine.

Monitoring cycle

To forecast the rock fall correctly, and to protect the slope stability, a monitoring rule has been built.

(1) Monitoring cycle

When AE event ratio smaller than 10, it shows the rock mass is stable, no big rockfall will happen.

The biggest monitoring cycle should be one week or two weeks;

When AE event ratio smaller than 19, and bigger or equal to 10, the rock mass begin to crack. If this phenomenon continues long, the slope will collapse abruptly, The biggest monitoring cycle should be smaller two days.

When AE event ratio bigger or equal to 20, the rock mass ,the rock mass collapse velocity begin to speedup , man can heart the crack voice . It can be regarded that the rock fall will happen prompt, and slope will collapse heavily. If this phenomenon continues long, the slope will collapse abruptly, the longest monitoring cycle should be within 9 days.

(2) Each monitoring time

On the base of fore-research results, the monitoring time and monitoring period is determined. Each monitoring time is the same, the monitoring time is at 8:00 without interruption from truck voices

Notion

1) Each monitoring without interrupt from truck voices.

2) During each monitoring period, the sensor should be set in the bottom of the hole, and coupled with water.

3) Monitoring result should be put forward to the Administrator Bureau, if the AE event ratios are abnormal, forecast is made in time.

Analysis theory of monitoring results

Forecast of rockfall

On the base of AGO, Mutation theory was founded to resolve the problem of slope, glide, earthquake and mining slope collapse etc. Because rock fall is discontinuous phenomenon, the mutation theory can be applied to forecast when rockfall will happen. Double parameters mutation model is (Liu Jun, 2000):

$$v(x) = x^4 + ux^2 + vx \quad (1)$$

x ——time list, the critical point of equation is $v'(x)=0$, i.e. the solution of the following equation.

$$4x^3 + 2ux + v = 0 \quad (2)$$

Assume the rock mass state can be signed as a point in three dimension by x, u, v , named it a photo point, which muse be on the curve plane of $4x^3 + 2ux + v = 0$ (Figure 6), i.e. on the bottom or on the surface , due to in mid leaf it is a unstable state.

Its determination formula is:

$$\Delta = 8u^3 + 27v^2 \quad (3)$$

when $\Delta = 0$, the collection of control points (u, v) are called divarication. When (u, v) changes, the photo point will also change on curve plane. When control points passes $\Delta = 8u^3 + 27v^2$, photo points will take place to jump, the rock mass will collapse. i.e..

$$\begin{aligned} \Delta > 0 & \quad \text{slope is stable} \\ \Delta = 0 & \quad \text{slope is critical state} \\ \Delta < 0 & \quad \text{slope is unstable} \end{aligned}$$

To $v(x)$ unfurl it by Taylor series, and keep the first 4 steps, the following will be gained:

$$v(x) = \sum_{i=0}^4 a_i x^i \quad (4)$$

To $a_i = \frac{\partial^i v(x)}{\partial x^i} |_{x=0}$, do differential homeomorphism counterchange, the following will be gained:

$$v(x) = x^4 + ux^2 + vx \quad (5)$$

$$x \rightarrow x - p, p \rightarrow a_3 / 4a_4, u = -6p^2 + a_2 / a_4, v = 8p^3 - 2pa_2 / a_4 + a_1 / a_4 \quad (6)$$

The Formula (2) is the standard forecast model of rock fall, if AE parameters of differential time are put into Formula(4), and lease common multiplies done, then a_i will be gained, and put then into Formula (5), (6), and u, v, Δ will be gained, then on the base of Δ the forecast will be done.

A real case of forecast to rockfall

To protect the safety of K2403+500 of G320, a monitoring work has been done. Firstly six detecting holes are dug in the slope, which are 5 m long. Everyday these holes are monitored by AE, and each for 5 minutes. The character parameters .i.e. total events, big event, and energy ratio are recorded. The geological condition shows that AE event ratio is the best parameter to determine the rock mass state. Table 3 is the record of AE event ratio in 2[#] hole. On the base of these data, GM (1, 1) is built, and second modification is made. The results are shown in Figure 7.

Table 2. Monitoring and forecasting result in 2[#]hole

date	5.23	5.24	5.25	5.26	5.27	5.28	5.29	5.30
monitoring (times/minute)	3.6	1.2	1.0	1.6	3.4	6.2		
forecasting (times/minute)	3.6	0.45	0.79	1.38	2.42	4.23		
modification (times/minute)	3.84	0.64	1.1	1.93	3.38	5.92	10.37	18.15

Table 3. The forecast values

date \ forecast	u	v	Δ
5.28	0.45	-7.74	1618.2
5.29	29.41	-2.52	203676.5
5.30	-40.2	117.6	-146314.9



Figure 6. The slope in K2403+500 of G32020

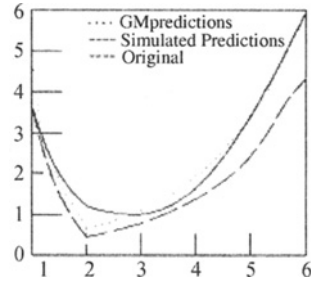


Figure 7. Forecasting results

According to the values in Table 3, make mutation translation and put them into mutation model, and a_i are gained by least common multiple, and then $u, v \Delta$ is obtained. The forecast values are shown in Table 4.

From Table 4 Δ , in 5.30 $\Delta < 0$, it show that in this day a rockfall will happen. A prediction is made and informed to administrator, all trucks are bypass to other way, a big lost is get rid off. The fact, at 10:00 in 5.30 a rockfall about 200 m³ happened, accord with the real case. It is proved it is feasible that mutation theory to forecast rockfall

CONCLUSION

(1) AE technique is feasible to forecast the stability of rock mass slope.

(2) On the base of GM (1, 1) and second modification, the mutation forecast result is satisfied.

(3) How to make the AE monitor from artificial to automatically be a project needs to be studied.

REFERENCES

- FU Helin, Sang Yufa (1996), Application of AE in forecasting Roof-fall in Mining stope, *Rock Mechanics and Engineering*, 6.
- Deng Julong, (1987). *Basic Method to Grey Theory*, Published by Huazhong University.
- Guo Jianfeng, (2005). *Analysis of Rock Mass Slope Stability*, Central South University.
- Liu Jun, (2000). *Mutation Theory and Its Application in Rock Mechanics*, Published by Science Press.

RESEARCH ON SPACE-TIME PREDICTION MODEL AND CRITERIA FOR HIGH ALTITUDE SLOPE IN THE FIRST STAGE JINPING HYDROPOWER STATION

Haiyuan Jin, Weiya Xu

*Key Laboratory of Ministry of Education for Geomechanics and Embankment Engineering,
Hohai University, Nanjing 210098 China*

Geotechnical Research Institute, Hohai University, Nanjing 210098, China

Landslide is one of the ubiquitous geological disasters, and calamity brought by landslide often is shocking by sight. In order to avoid or alleviate the disasters brought by landslide, it is feasible to predicate and take effective measures for landslide in advance. At the present time, scholars in home and abroad have brought forward many prediction models, methods and criteria. All of them are focusing on the prediction of where, when and the intensity (destroy intensity of landslides) of landslides will happen. Prediction methods and criteria are the key contents in the landslide forecasting and prediction. Based on the summarization of the productions of landslide prediction, this paper systematically investigates the applicability of these predictions in depth. And based on the monitoring fruits of left bank high altitude slope in the first stage Jinping hydropower station, time-space comprehensive prediction is proposed and a comprehensive prediction model and criteria adaptive to high altitude slope in the first stage Jinping hydropower station is designed. It is useful to build a forewarning system for potential slope failure.

INTRODUCTION

Landslide is one of the most serious natural geological calamities, which has brought great harm to people for so many centuries that people fight against landslides so as to avoid or mitigate the happening of the harm. So where, when and how will the landslide happen are the key factors of the forecasting and predicting. For decades of years, a mass of work has been done and plentiful fruits were gained by geological experts and scholars from in home and abroad. But for the reason of the complexity of the landslide, there are superiorities and inferiors in every prediction means, and none of them can be applied to any landslides (Li Xiuzhen et al, 2003). Based on the analysis, summarization and discussion of the existing forecasting methods and theories, aimed at slope types, features, deformation traits and destroy mechanism of high steep valley slope in Jinping step one hydropower station, a space-time comprehensive prediction design is suggested, and comprehensive prediction models and criteria adaptive to it are discussed, so as to build a prediction and forecasting system for high altitude slope.

SPACE-TIME COMPREHENSIVE PREDICTION FOR HIGH ALTITUDE SLOPE IN JINPING STEP ONE HYDROPOWER STATION

Slope of the spandrel groove at left bank is very high and steep and most of the bedrock is exposed. Lithology features of the natural slope upwards 1 850m altitude is sand-slate and the gradient is 40°-50°; 1850 m altitude thereafter is marble slope and the gradient is 50°-70°. There are different dimensional faults-F2, F5, F8, f42-9 et al and lamprophyre vein X, which are large-scale weak structural planes upwards mid-high altitude. Mid-steep tip small faults near EW strike are especially developed, such as f42-9. There are fault F₂ and compressive dislocation strip in mid-low altitude T_{2-3Z}² (6) layer. Three groups of joints emerge in the slope: attitude of stratum N(15°-35°) E/NW ∠(30°-45°), N(20°-40°)E/SE ∠(60°-85°), N(50°-70°)E/SE ∠(50°-80°). Level III and IV deep cracks are found on the top of marble slope section and level I, II ones are found in the sand-slate slope section. Figure1. shows the engineering geological plan of left bank crown and spandrel groove part.

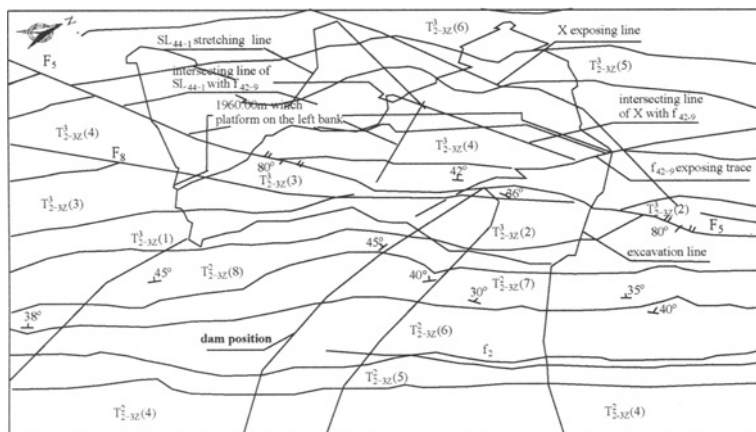


Figure1. Engineering geology plan of left abutment and spandrel groove (modified after Zhou Zhong et al., 2006)

Space-time comprehensive prediction

A series of study on basic characters, deformation failure mechanism, stability calculation and analysis of deformation monitoring data et al for high altitude slope in the first stage Jinping hydropower station have been done by some related experts and engineers from different angle and different methods. But because of the particularity and complexity of the causes of the landslide (slope), so it is important to design the time-space comprehensive prediction models for left bank high altitude rock slope from the view of systems engineering. Based on the summarization of research fruits done by others and closely related to slope monitoring data, a entire idea of time-space comprehensive prediction is advanced as following figure2: through the analysis and study of the macro synthetic information of the field and the monitoring data, spatial prediction model, criteria and long-term and mid-short

term time prediction models and criteria are built to predict the time-space developing trend for the slope.

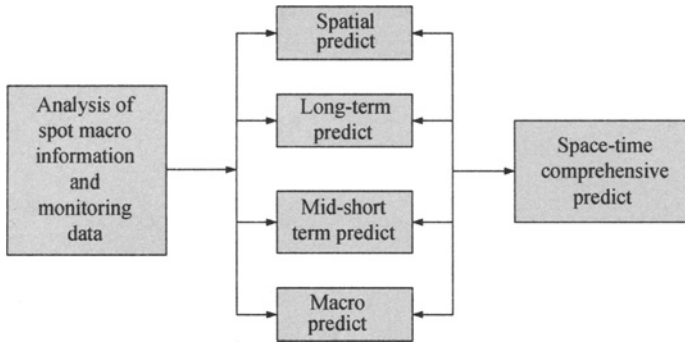


Figure 2. Overall flow diagram of space-time comprehensive predicting model

Spatial prediction

Applying experiential model and engineering analogy method (Yin Kunlong, 2003), the paper tells the potential landslide position in spatial distribution according to engineering geological conditions of dam location of first stage Jinping hydropower station, which contain the study of landscape, stratum, lithology, geological structure and phys-geological phenomena et al.

Spatial continuity of fault f_{42-9} in the left bank dam slope is especially good and the mechanical property of the material in the fault zone is very poor, so fault f_{42-9} can be considered to be lower boundary and bottom slide surface of the cracked deformation rock blocks at the left bank dam abutment. Fault F_5 , F_8 in front of the slope body restrict the extension of fault f_{42-9} to the outside of the slope, where the fault crush zone and its influential breadth is up to 10~20m and they provide interior free-face for sand-slate creep-crack deformation in the hanging wall of the inner side of fault f_{42-9} . The whole occurrence of relaxation crack zone SL_{44-1} emerging on the hanging wall of fault f_{42-9} is about $SN\sim N20^\circ W$, $E(NE) \angle 55^\circ-60^\circ$ which can be considered to be upper side boundary. According to the combination instance of structural surfaces distributing in left bank abutment, the most probable macro failure mode of the abutment deformation rock masses is wedge-shaped failure pattern under the natural state. Fault f_{42-9} and relaxation crack zone SL_{44-1} form two slide surfaces for the wedge, which snip off the marble providing sustaining function outside the F_5 . Lamprophyre vein whose strike is NEE is the back incision surface.

In addition, considering the geological condition of intersecting faults F_5 , and F_2 , single rigid block slippage mode may occur with F_5 as the side slide surface and F_2 as the bottom surface, or with F_5 as side slide surface and a assumed surface declining to riverbed in the conjoint position of F_2 and F_5 as the bottom surface, so analysis may be carried on another single rigid block slippage mode.

Time prediction

Long-term prediction

In reference (Zhou Zhong et al., 2006), 3D rigid limit equilibrium method is used to analyze the stability of the potential failure block in abutment slope as the long-time prediction, what

is more, safety factors under three engineering conditions including normal, rainfall and earthquake conditions are gained which provide instructional meanings for the application of reinforcement measures. The computation model can also be established massively or sectionally according to the assumption of different boundary conditions of the potential failure block. In addition, Limit analysis method can be used to study it in detail.

All what we gained from the limit equilibrium method and limit analysis are safety factors and it is generally considered that the criteria of safety factor to be 1 is relatively adaptive. When safety factor is bigger than 1, slopes is under the unstable state; when is bigger than 1, slopes is in stable state and when safety factor is equal to 1, slopes is under the critical state.

Mid-short term prediction

Comprehensive prediction for landslide is built on the long-term monitoring which is the footstone of the time forecasting for landslide (Hu Houtian, 2001). Time prediction will be a castle in the air without landslide monitoring. Nowadays the main monitoring contents contains:①2-D or 3-D displacement and declivity value of unstable rock, landslide surface and interior deformation; ②Related physical parameters—stress, strain and geo-acoustic et al; ③ Environmental factors—earth quake, rainfall, air temperature and underground water et al. Deformation monitoring is one of the most commonly used means for its convenience and facility. As to displacement monitoring time serial of high altitude slope in first stage Jinping hydropower station, grey Verhulst prediction model and combination of exponent-smoothing method and non-linear regression method are suggested to forecast mid-short term deformation and stability of the slope with the deformation value and deformation rate of the slope as the criteria.

Macro prediction

The complete slippage process from original deformation to failure can be divided into four phases: slow creep, even creep, even distortion, accelerated distortion and critical slide phases. Comprehensive judgment of macro deformation evidences and premonitory characters represented from different evolvement processes of different phases can help people to distinguish deformation phases of landslide (Zhang Zhuoyuan, 1994). For example, factors of crack, uplift, subsidence, collapse and rainfall et al are selected to distinguish the deformation phases of Xintan landslide. (Hu Gaoshe et al., 1996)

It is suggested that the common used appraisal factors of macro deformation phenomena should be applied to monitoring objects of Jinping hydropower station. It mainly contains two aspects: earth surface deformation and the changes of surface things. The former includes spreading cracks, dislocated roofs, settlements at the back of the slope and two side shear cracks, feather-shaped cracks and front sections plump-up cracks, radioactive cracks and collapse and so on. The latter consists of buildings split, roads sever, and rock mass relaxation, collapse and local slippage of front edge caused by the formation and run-through of sheared exits. In addition, earth gas (including flavor and flavorless hot gas) and abnormality of animals (including rat and snakes unkennel, chooks flying and dogs yip et al) also belong to macro phenomena.

According to engineering analogy we can decide that macro evidence criteria (Wu Shuren,2004) for predicting the landslide states mainly contain (1) Slope spreading cracks

under obvious expanding state and the length of backward crack strip is longer than 1/2 of the height of the landslide; (2) Landslide surface under saturated and softened state for continuous rainfall, further more, eroded section by earth surface runoff begins obviously collapse or local fracture deformation extends and begin glide and ground has great subsidence; (3) Zonal fountain effuses in the front of the slope; (4) The track of landslide boundary is continuous and its fractal dimension is about 1.50; (5) Velocity of creeping deformation takes on continuous obvious increase or glide velocity is greater than 100 mm per month or has obvious seasonal changes.

DESIGN OF FOREWARNING SYSTEM FOR SLOPE FAILURE

Landslide disaster forewarning system takes the forewarning of slope failure as its goal and the control of the hazard as its aim, which is built on the base of study of the slope failure law and of nicety analysis of monitoring information, and it is developed from natural, social and economical three aspects. Through the stability research and analysis of monitoring information of left bank slope in the Jinping hydropower station, the paper predict the potential cataclysmic process in spatial and time scale and build potential failure macro criteria, thus a general formula of forewarning system for slope failure hazard can be designed

CONCLUSIONS

The commonly used prediction models and criteria for landslide hazard have been given and analyzed in detail from space-time scale. Based on the slope stability study and analysis of monitoring information of left bank high altitude slope in the Jinping hydropower station, the paper predict the potential cataclysmic process in spatial and time scale by using many different models and methods which are adaptive to it. For example, many spatial failure mode can be predict through the study of faults- f42-9, F5,F8 ,F2 et al, and through long-term, mid-short term prediction, the slope phases can be determined accurately. Slope macro information is especially emphasized and macro failure criteria for identifying potential landslide are described. So the idea of space-time comprehensive prediction can be brought forth vividly. At last, a general formula of prewarning system for landslide hazard is given to help engineers to understand the goals and methods of the forewarning system, and to timely feedback the slope information to supervise the engineering.

REFERENCES

- Hu Houtian. (2001). *Landslide geological hazard forecast* Southwest Jiaotong University Press.
- Hu Gaoshe, Men Yuming, Liu Yuhai et al. (1996). Study on prediction criterion of Xintan landslide. *The Chinese Journal of Geological Hazard and Control*, 7 supplement, 67-72.
- Li Xiuzhen, Xu Qiang, Huang Runqiu, et al.(2003). Research on prediction criterion for temporary prediction of landslide. *The Chinese Journal of Geological Hazard and Control*, 4 (14): 5-11.
- Wu Shuren, Jin Yimin, Shi Jusong. (2004). A primary study on landslide warning criterion—An example from the reservoir region of the Three Gorges. *Journal of Jilin University (Earth Science Edition)*, 4 (34): 596-600.

- Yin Kunlong. (2003). Classification of landslide hazard prediction and warning. *The Chinese Journal of Geological Hazard and Control*, 4 (14): 12-17
- Zhang Zhuoyuan, Wang Shitian, Wang Lansheng. (1994). *Principles of Engineering Geology Analysis*, 2nd Edition, Geological Publishing House.
- Zhou Zhong, Gong Manfu, Lei Chengdi. (2006). Research on stability of slope at left abutment of Jinping first stage hydropower station. *Chinese Journal of Rock Mechanic and Engineering*, 11 (25): 2298-2304.

CHARACTERIZATION OF DETERIORATION ON THE SHOTCRETE LINING IMMERSSED IN VARIOUS SULFATE SOLUTIONS

Ho-Seop Jung, Dong-Gyou Kim, Hyu-Soung Shin
*Underground Structure Research Div., KICT, 2311 Daehwa-dong Ilsanseo-gu,
Goyang-si, Kyeonggi, 411-712, Korea*

Seong-Soo Kim
*Department of Civil Engineering, Daejin University, San 11-1 Seondan-dong
Pocheon-si, Kyeonggi-do, 487-711, Korea*

This study is to evaluate the characterization of shotcrete exposed to sulfate solution on long-term. Surface examination, compressive strength test, adhesive strength test and micro-structural analysis were performed to analyze the deterioration of shotcrete specimens, which were cored at cast-in-place shotcrete lining. The shotcrete specimens were immersed in 1, 2, and 5% of sodium sulfate solutions upto 35-weeks. From the test results, the compressive strength and adhesive strength of shotcrete specimen increased up to 56 days of immersion period. The reason was that the cement matrix was densified in filling the pore of shotcrete with cement hydrate products in the early age of immersion period. After 56 days of immersion period, the compressive strength and adhesive strength decreased with increasing immersion period of shotcrete specimens in sodium sulfate solutions. The deterioration of shotcrete was caused by the gypsum, ettringite, and thaumasite formation in the shotcrete specimens. These results were confirmed by XRD, SEM and EDS analyses.

INTRODUCTION

In general, the tunnel structure is commonly constructed in the ground or rock bed, and shotcrete for the support of underground excavations has widely been used in mining engineering and civil engineering because the shotcrete is no dependant upon the shape of cross-section of tunnel. The shotcrete of the tunnel can contact with groundwater because the tunnel is constructed in the ground. The hazardous materials found in the groundwater may deteriorate the engineering properties of shotcrete, such as compressive strength, adhesive strength, and flexural strength. The volume of sulfate ion contained in the soils in Korea differs according to area and environmental conditions. The ground in Korea contains the sulfate ion about 0.01%-0.1% in most areas.

In this regard, it was performed the following tests for evaluating the erosion of shotcrete resulted from the sulfate ion contacting the tunnel support materials. The compressive strength of shotcrete and adhesive strength between shotcrete and rock were measured on the shotcrete specimens immersed in the three different sodium sulfate (Na_2SO_4) of 1, 2 and

5%. Also, mechanical analyses, such as XRD, SED and EDS analyses were conducted to evaluate the change the micro-structure of shotcrete deteriorated by sodium sulfate.

SAMPLE AND TESTING METHOD

Sample Preparation

Portland cement (OPC) on the basis of KS(Korea Standard) L 5201 was used for preparing shotcrete samples. Its specific gravity was 3.15. The large aggregate of 13mm (specific gravity: 2.60) and small aggregate (specific gravity: 2.59) were used for this study. Accelerator with aluminate was used, and its weight was 5% of total weight of cement. The design compressive strength of shotcrete was 21MPa at 28days. Table 1 shows the mixture proportion for shotcrete.

Table 1. Mixture proportion of shotcrete

f_{ck} (MPa)	G_{max} (mm)	slump (mm)	W/C	S/a	Unit weight (kg/m ³)				superplasticizer (kg)
					W	C	S	G	
21	13	100	0.45	0.62	204	453	1132	572	2.27

In order to evaluate the compressive strength of shotcrete as well as the adhesive strength between shotcrete and rock in the harmful environment, the rock sample (granite) was installed in the rectangular mold (250×500×200mm) made of steel. The shotcrete was sprayed on the rock sample in the mold inside the tunnel construction site and cured in the air for 28 days. The specimen for this study was cored with the diameter of 55mm.

Testing method

1) Compressive strength test: the compressive strengths of shotcrete immersed in the sodium sulfate solution and water were measured according to KS F 2405 and F 2422. At each immersion date, three specimens were used for measuring the compressive strength of shotcrete.

2) Adhesive strength test: the direct tensile test according to ASTM D 2936 and C 1404, were conducted to measure the adhesive strength of shotcrete. The glue type method, using the epoxy, was adopted for adhesive strength test.

3) XRD (X-ray diffraction) analysis: X-ray diffraction analysis was performed to evaluate the product resulted from the action of shotcrete under the conditions of CuK(Ni, filter) 35kV, 20mA, Scanning speed 80/min, Full Scale 14cps, $2\theta = 5^\circ - 60^\circ$.

4) SEM and EDS analysis: This analysis was conducted by using the Philips XL 30 ESEM for the scanning electron microscope. The micro-structure was observed by using the EDS (Energy Dispersive X-ray Spectroscopy) type electron microscope analyzer at the same time of SEM Analysis.

5) Test solution: The sodium sulfate (Na₂SO₄) solution of 1%, 2% and 5% were prepared to evaluate the sulfate erosion characteristics of shotcrete. All solutions were replaced every other week to reduce the dilution of density.

RESULTS AND ANALYSIS

Strength of shotcrete

The shotcrete specimens were immersed in the sodium sulfate solution of 1%, 2% and 5% to evaluate the strength of shotcrete exposed to the sulfate environments. Figure 1 shows the compressive strengths of shotcrete immersed three different sodium sulfate solutions and water for immersion period, from 0th day to 245 days.

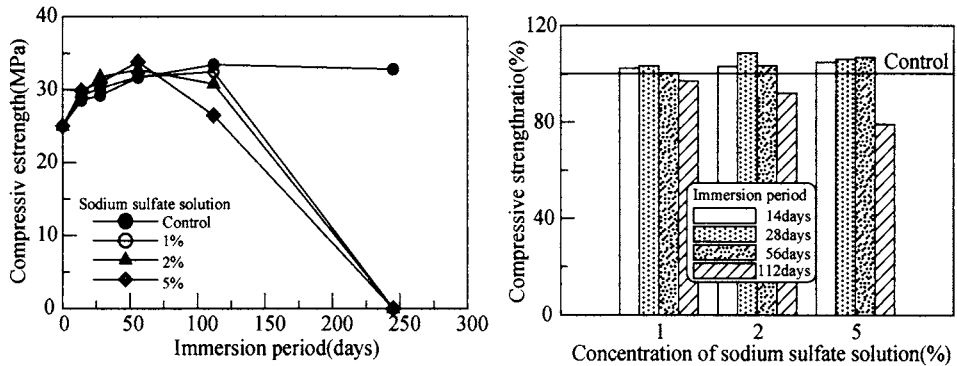


Figure 1. Compressive strength and compressive strength ratio of shotcrete immersed in the sodium sulfate solution

As shown in Figure 1, the compressive strength of shotcrete immersed in the sodium sulfate solution was higher than that of shotcrete cured in the water during immersion 56 days. This is because the ettringite, which was the expansive substance generated by the sulfate ion reacting with cement hydration product, filled with pore of cement matrix. However, the compressive strength decreased after immersion 56 days and shotcrete specimens were collapsed at immersion 245 days. It is not available to perform the compressive strength test. This is because, when the immersion period increased, expansive substance gradually made the expansive cracks on the surface of specimen, and generated the gypsum softening the shotcrete specimen. As shown in Figure 1, the compressive strength ratio, that is, the ratio of compressive strength of shotcrete immersed water to that of shotcrete immersed in the sodium sulfate solution, decreased with increasing the immersion time. The compressive strength ratio decreased with increasing the density of solution.

Figure 2 shows the adhesive strength between shotcrete and rock sample immersed in the sodium sulfate solution of 1, 2 and 5% and water during 0, 14, 28, 56, 112 and 245 days. The adhesive strengths of shotcrete immersed in the three different sodium sulfate solutions and water increased with increasing immersion time. As mentioned above, the internal texture of shotcrete was getting compact by expansive substance, such as ettringite, and then adhesive strength of shotcrete had increased during early immersion period. The adhesive strength of shotcrete immersed in the three different sodium sulfate solutions began to decrease from immersion 56 days. The adhesive strengths of shotcrete immersed in the sodium sulfate solutions were lower than those of shotcrete cured in the water at

immersion 112 days. The adhesive strength decreased with increasing the density of sodium sulfate solution. The deterioration had been severely progressed in the shotcrete specimen immersed in the sodium sulfate solution of 5% at immersion 245 days. So, it is not available to measure the adhesive strength of shotcrete as shown in Figure 3. The shotcrete specimens immersed in the sodium sulfate solution of 1% and 2% show the similar tendency.

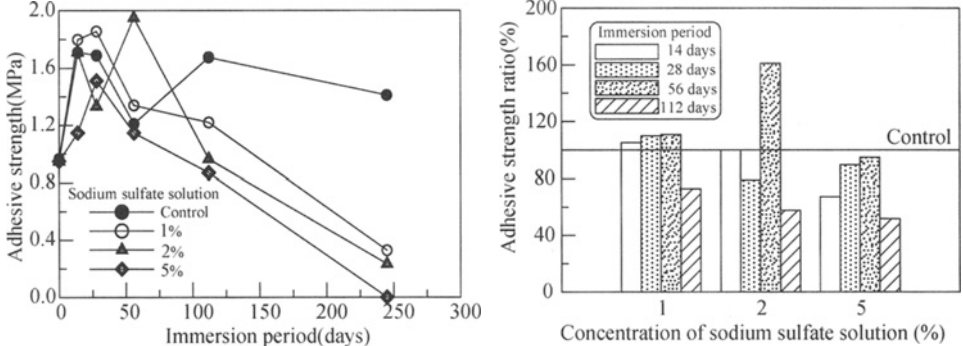


Figure 2. Adhesive strength and adhesive strength ratio of shotcrete immersed in the sodium sulfate solution

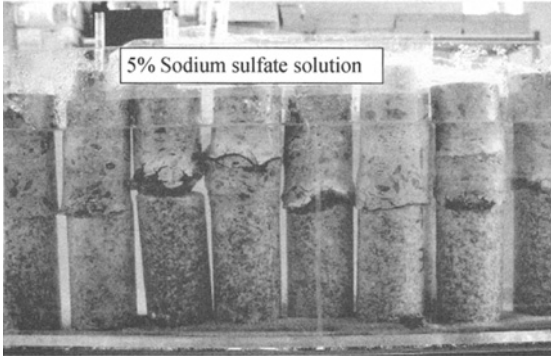


Figure 3. Shotcrete specimens immersed in the 5% sodium sulfate solution at 245 days

XRD analysis

Figure 4 shows the results of XRD analysis conducted on the shotcrete specimen immersed in the sodium sulfate solutions and water for 32 weeks to evaluate the reaction product of shotcrete exposed to the sulfate.

The shotcrete cured in the water had the portlandite, which is important hydration product of cement, and quartz and feldspar by aggregate. In the case of the shotcrete immersed in the sodium sulfate solutions, the peak of portlandite was not detected by the dissolution of C-S-H.

On the other hand, when the density of sodium sulfate increased, some different peak value was observed. The gypsum, brucite, ettringite and thaumasite were detected.

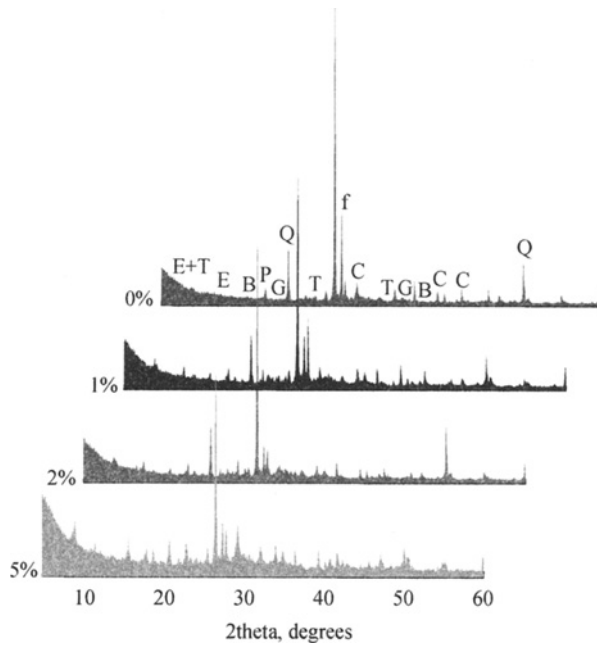
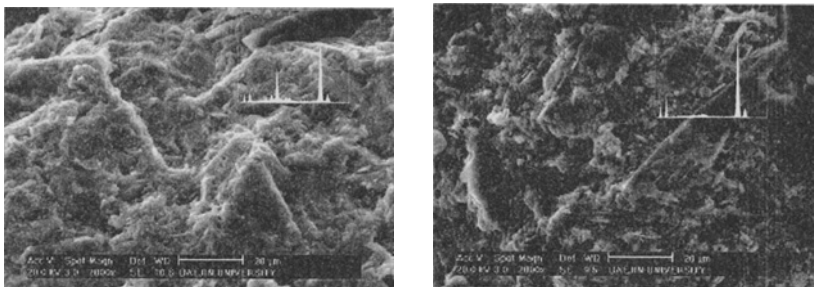


Figure 4. The results of XRD analysis

SEM and EDS analysis

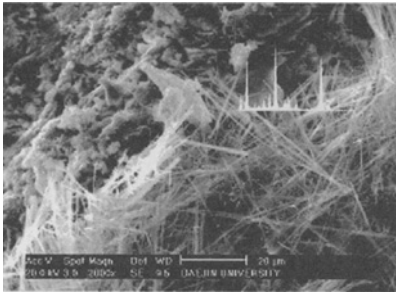
Figure 5 shows the results of SEM and EDS Analysis on shotcrete specimens cured in the water and immersed in the sodium sulfate solution for 32 weeks after zooming up 2,000 times. As shown in Figure 5(a), the shotcrete specimen cured in the water show that the texture of specimen was compact and no fine crack was observed. The specimen had C-S-H hydrate generated. In the case of the shotcrete specimen immersed in the sodium sulfate solution, the ettringite with needle shape was observed and portlandite was detected. The hydration texture of this specimen was not compact as compared with that cured in the water. From the EDS analysis, the reaction products, such as ettringite, thaumasite, brucite and gypsum, were observed. The results of EDS analysis corresponds with the one of XRD analysis.



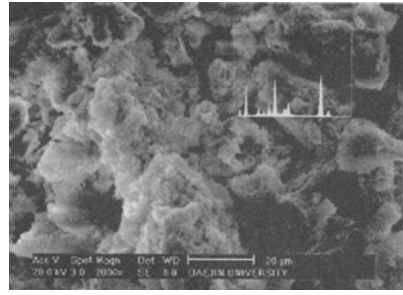
(a) Tap water

(b) 1% sodium sulfate

Figure 5. The results of SEM and EDS analysis



(c) 2% sodium sulfate



(d) 5% sodium sulfate

Figure 5. The results of SEM and EDS analysis (continued)

CONCLUSION

In this study, engineering properties and micro structure change of shotcrete deteriorated sodium sulfate were analyzed. The reviewed results are summarized as follows:

The compressive strength of shotcrete and adhesive strength between this shotcrete and rock immersed in the three different sodium sulfate solutions were stronger than those immersed in the water regardless of density of sodium sulfate solution until immersion 56 days. The compressive strength and adhesive strength of shotcrete were rapidly decreased after immersion 56 days. As the immersion period was getting longer, the sulfate ion reacted with cement hydration product, and expansive substances, such as ettringite and thaumasite, were generated. Such substances made the expansive crack on the surface, and generated the gypsum softening the shotcrete. These reaction products were checked or verified through the results of XRD, SEM and EDS analysis.

REFERENCES

- Al-Amoudi, O.S.B.(2004), Attack on Plain and Blended Cement Aggressive Sulfate Environments, *Cem. Conc. Comp.*, 24: 305-316.
- Hartshorn, S.A., Sharp, J.H. and Swamy, R.N.(1999). Thaumasite Formation in Portland-Limestone Cement Pastes, *Cem. Conc. Res.*, (29): 1331-1340.
- Malmgren, L., Nordlund, E., Rolund, S.(2005). *Adhesive strength and shrinkage of shotcrete, Tunneling and Underground Space Tech.*, 20 (1): 33-48.
- Neville, A. (2004), The Confused World of Sulfate Attack on Concrete, *Cem.and Conc. Res.*, (34): 1275-1296.

LONG-TERM CHARACTERISTICS OF SHOTCRETE LINING IN TEST TUNNEL

Dong-Gyou Kim, Ho-Seop Jung

*Underground Structure Research Div., KICT, 2311 Daehwa-dong Ilsanseo-gu,
Goyang-si, Kyeonggi, 411-712, Korea*

Kwang-Pil Park, Seong-Soo Kim

*Department of Civil Engineering, Daejin University, San 11-1 Seondan-dong
Pocheon-si, Kyeonggi-do, 487-711, Korea*

This study is to evaluate long-term characteristics of shotcrete lining in test tunnel built in 1996 in Korea. Visual examination, carbonation depth, water analysis, compressive strength, X-ray diffraction (XRD) analysis, and Scanning Electron Microscope (SEM) and Energy Dispersive X-ray Spectroscopy (EDS) analyses were performed to evaluate the properties of shotcrete on long term. 6 shotcrete specimens were cored in the test tunnel, and ground water were collected at 2 positions in tunnel. From the visual examination, crack and efflorescence were widely existed on shotcrete surface. From the test results, pH values of groundwater and carbonation depth of shotcrete specimens were 7.42-7.50 and 3.1-22.8mm, respectively. The compressive strengths of shotcrete specimens by Schmidt hammer and uniaxial were 12.98-24.52MPa and 8.0-19.0MPa. The formation of gypsum and ettringite, which decrease the durability of shotcrete, was detected in the shotcrete specimens from the XRD, SEM, and EDS analyses. It is showed that the shotcrete have been deteriorated by chemical components in the groundwater.

INTRODUCTION

The cement concrete has been known as the excellent material showing the semi permanent durability in the general natural environments. However, its durability may differ according to exposed environments. The factors deteriorating the durability of cement concrete are largely classified into the erosion of steel reinforcement resulted from the chloride ion attack and carbonation, freezing and thawing, alkali aggregate reaction and chemical attack.

Especially, the tunnel structure is commonly construed in the ground or rock bed. These structures constructed in the underground are known to frequently contact the underground water. If the groundwater contains the harmful ion deteriorating the concrete or shotcrete, tunnel structure is gradually getting deteriorated when the time elapses. Also, if the concrete or shotcrete lining in the tunnel is cracked, underground water containing the harmful ion causes the water leakage along the crack as well as many problems resulted from the leakage. The deterioration of shotcrete lining is closely related to the leakage and

caused by the external factors such as harmful water, freezing damage and chloride ion attack.

If the tunnel is located below groundwater containing the harmful ion, chemical erosion of tunnel support starts in the backside and deterioration of shotcrete lining may be expedited. The surface of shotcrete lining is separated and iced by the freezing damage in the winter. The tunnel may be in unstable condition.

In this study, the long-term characteristics of shotcrete lining was evaluated through the visual examination on tunnel support, such as shotcrete, exposed to harmful environments, the laboratory test, and field survey such as carbonation inspection, water analysis and compressive strength test and micro-structural analysis.

TEST TUNNEL& TESTING METHODS

Test Tunnel

As shown in Figure 1, the test tunnel was constructed by NATM in 1996. Total length of the tunnel was 140m and support system of the tunnel was shotcrete, rock bolts, wiremesh and steel rib with H-shape.

Testing Methods

(1) Visual examination and water analysis: the visual examination was performed through the tunnel. The groundwater was collected two different positions for the water analysis as shown in Figure 1. Water analysis was conducted to detect the harmful ion deteriorating the shotcrete.

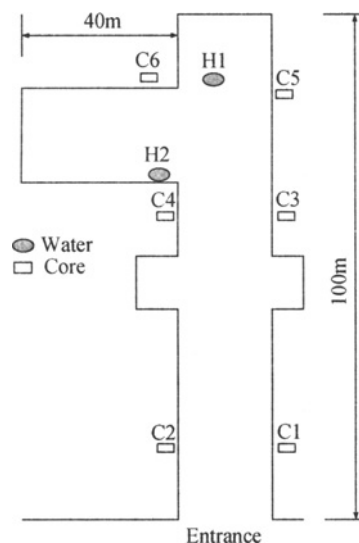


Figure 1. Plane figure of test tunnel

(2) Compressive strength test: Field Nondestructive test and laboratory compressive strength test were conducted to measure the strength of shotcrete of the test tunnel. Field

Nondestructive test was based on the repulsive force acquired by blowing the shotcrete surface with Schmidt hammer, and the compressive strengths were estimated using the equation (1) shown below. Field Nondestructive test were conducted at 6 different positions shown in Figure 1, and 20 points at each position were performed.

$$F_c = 1.3R_o - 18.4(\text{MPa}) \quad (1)$$

Also, the compressive strength test on the basis of KS F 2405 and 2422 were performed on the 6 shotcrete specimens collected from the shotcrete lining shown in Figure 1.

(3) Carbonation: The carbonation depth measurement was conducted on shotcrete specimen collected from 6 places spraying the 1% phenolphthalein solution.

(4) Micro-structural analysis: X-ray diffraction analysis was performed against the crushed specimen using the RINT D/max 2500(Rigaku) after collecting the core sample in order to evaluate or measure the reaction product. The reaction product was measured under the conditions of CuK(Ni, filter) 35kV, 20mA, Scanning speed 2.0 /min, $2\theta = 5^\circ\text{-}40^\circ$. The philips XL30 ESEM was used for the scanning electron microscope (SEM), and EDS (Energy Dispersive X-ray Spectroscopy) electron microscope analyzer was used for analyzing the micro-structure of shotcrete.

TEST RESULTS AND DISCUSSION

Visual Examination and Water Analysis

Visual examination was conducted to evaluate the surface of shotcrete lining in the test tunnel. As shown in Figure 2, no structural crack was found. However, the reticular crack resulted from the drying shrinkage was observed over whole section, and efflorescence and leakage have been progressing on the surface of shotcrete. Especially, many cracks and sign of leakage were observed on the shotcrete. The water drops and efflorescence was under progressing in the ceiling, and the stalactite type icicles were formed in many places of ceiling as shown in Figure 2.

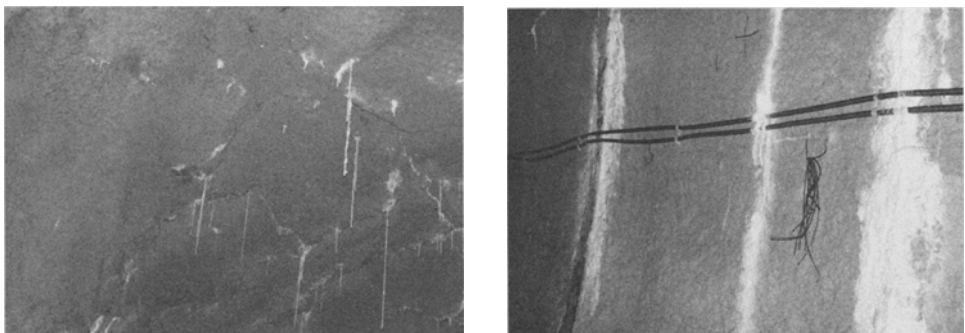


Figure 2. Efflorescence observed around the ceiling and side wall

SO_4^{2-} , Cl^- , Mg^{2+} and Ca^{2+} ions in groundwater may deteriorate the shotcrete. Table 1 shows the results of water analysis on the groundwater collected in the test tunnel. pH of groundwater was 7.42–7.50 as the mildly acidic, and density of sulfate ion (SO_4^{2-}) and

calcium ion (Ca^{2+}) was 15.2–17.5ppm and 18.8–22.8ppm, respectively. Small amount of magnesium ion (Mg^{2+}) and chloride ion (Cl^-) were detected respectively. From the results of water analysis, the chemical erosion may be disregarded because the density of harmful ion was very low. However, if the shotcrete is continually exposed to the harmful ion for a long time, chemical erosion of shotcrete may be expected.

Table 1. Water Analysis Results (unit : ppm)

	pH	Cl ⁻	SO ₄ ²⁻	Ca ²⁺	Mg ²⁺	Fe
Tap water	7.21	16.1	13.29	19.4	5.1	0.090
H1	7.50	5.1	15.2	18.8	5.1	0.065
H2	7.42	5.8	17.5	22.8	7.0	0.067

Carbonation depth

Generally, carbonation of concrete is the loss of the strong alkalinity of concrete and antierosive function of steel reinforcement by the action of erosive gases such as atmospheric carbon dioxide. The test tunnel, selected for this study, was exposed to the poor ventilation environment because there was only one entrance in the tunnel.

As shown in Figure 1, the tunnel was inclined inward. The area, where the water was collected, was filled with water all the times, and the humidity was relatively higher in these areas. The carbonation depth by spraying the phenolphthalein solution of 1% was measured on the shotcrete specimen cored from the shotcrete lining. The carbonation depth, where the groundwater exists (C4–C6 in Figure 1), was about 3.1~9.6mm, and the carbonation was slowly progressed. The carbonation depths in other area were about 14.8–22.8mm as shown in Figure 3. This result shows that the carbonation is quickly progressed in the tunnel, where the air is not appropriately ventilated, because the density of carbon dioxide inside the tunnel is higher than the average ones measured in the air. Also, this result shows that the carbon dioxide gas is not penetrated because of high humidity, and the carbonation is slowly progressed in the area where the groundwater is filled.

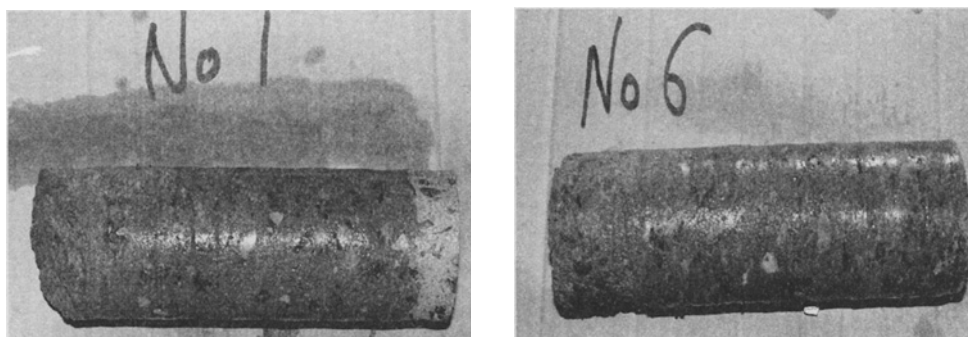


Figure 3. Carbonation depth (C1 and C6)

Compressed strength

Table 2 shows the compressive strengths estimated by the nondestructive method with Schmidt hammer and compressive strength measured on shotcrete specimen collected in the test tunnel, respectively. The compressive strengths by the nondestructive method had the range from 12.98 to 24.52MPa. The compressive strengths by the laboratory test on the shotcrete specimens had the range from 8.0 to 19.0MPa. The compressive strengths at C4, C5, and C6 were relatively low because the shotcrete was influenced by the leakage and reaction product. The compressive strengths at C1, C2, and C3 were relatively high. This is because shotcrete was relatively dry. The compressive strengths obtained from the laboratory test were lower than those estimated by the nondestructive method.

Table 2. Results of compressive strength test

ID	Average hardness	Schmidt hammer (MPa)	Core specimens(MPa)
C1	32.50	15.26	16.3
C2	38.80	20.52	19.0
C3	29.75	12.98	10.6
C4	36.56	18.64	8.0
C5	36.56	18.64	9.8
C6	43.63	24.52	11.2

Micro-structural analysis

Figures 4 and 5 show the results of XRD Analysis on shotcrete specimens collected from C2 and C6. Based on the compressive strength test results, C6 had the largest difference between nondestructive compressive strength and compressive strength by laboratory test, and C2 specimen had the biggest compressive strength among the six shotcrete specimens.

As shown in Figure 4, the substances deteriorating the shotcrete, such as gypsum and ettringite, were detected from XRD analysis. This result shows that the deterioration was progressed from the rear side of shotcrete lining in the tunnel. Also, the strong intensive quartz peak was detected. This was because of the aggregate in the shotcrete. As shown in Figure 4, the high peak of calcite was observed at C2 specimen. This may be caused by carbonation, and the carbonation depth of C2 specimen was 22.8mm as highest value. However, the peak value of calcite in C6 specimen was relatively small. C6 specimen had the peak value of Ettringite and gypsum as high. C6 area was deteriorated by the harmful ion in the groundwater or ground. The peak of Portlandite was detected in C6 area. This area may be deteriorated by the harmful ion in the future. Figure5 shows the results of SEM and EDS Analysis on the C6 specimen deteriorated. Gypsum and Ettringite were generated in C6 specimen.

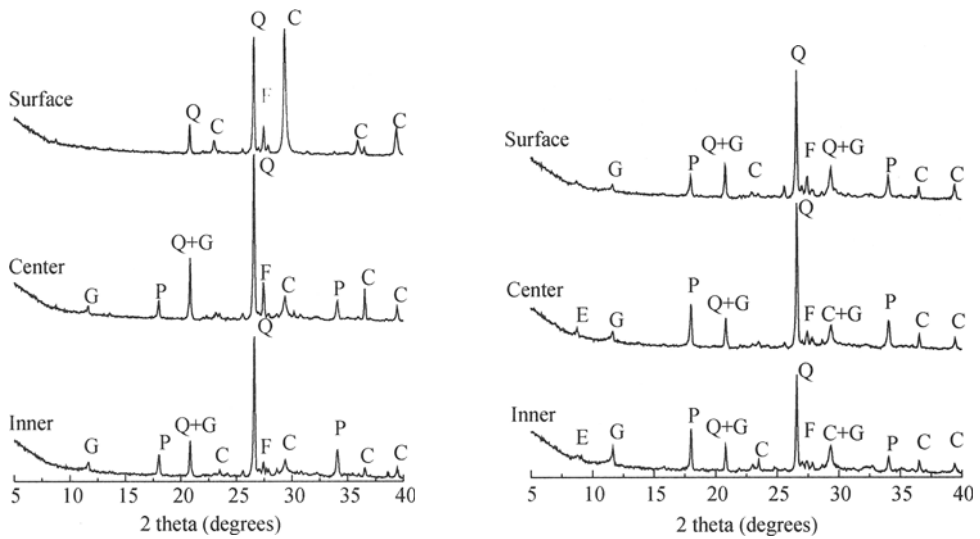


Figure 4. XRD analysis of C2 and C6 samples

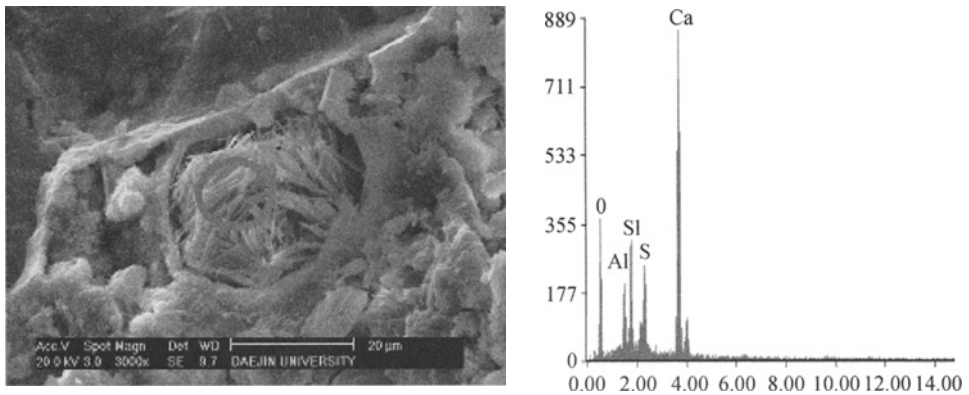


Figure 5. SEM and EDS analysis

CONCLUSION

The field survey in the test tunnel and laboratory tests were performed to evaluate the long-term characteristics of shotcrete lining exposed to the chemical erosion by harmful ion in the groundwater. The conclusion was as follows;

1) The results of visual examination showed that many cracks existed in the ceiling and area, where the steel ribs were installed. The efflorescence was progressed by the leakage from the crack. Especially, the stalactite of efflorescence was grown in the ceiling.

2) The results of water analysis show that the small quantity of harmful ion causing the chemical erosion of shotcrete was detected. As the shotcrete is continually exposed to the harmful ion for a long time, the deterioration of shotcrete may be expected.

3) The carbonation depths of shotcrete specimen were about 14.8-22.8mm. The compressive strengths by the nondestructive method and the compressive strengths

measured by the laboratory test had the range from 12.98 to 24.52MPa, and from 8.0 to 19.0MPa, respectively. The compressive strengths obtained from the laboratory test were lower than those estimated by the nondestructive method.

4) The results of micro-structural analysis show that the substances deteriorating the shotcrete, such as gypsum and ettringite, were detected in the shotcrete.

REFERENCES

- Cohen M. D. and Mather B. (1991). Sulfate attack on concrete research needs. *ACI Material Journal*, 88: 62-69.
- Famy, C. and Taylor, H.F.W.(2001), Ettringite in hydration of Portland cement concrete and its occurrence in mature concretes, *ACI Material Journal*, 98: 350-356.
- Gollop, R.S. and Taylor, H.F.W.(1995), Microstructural and microanalytical studies of sulfate attack III, sulfate-Resisting portland-cement: reaction with sodium and magnesium sulfate solution, *Cem. and Conc. Res.*, 25, No. 7, 1581-1590.
- Hartshorn S.A., Sharp J.H. and Swamy R.N.(1999), Thaumasite Formation in Portland-Limestone Cement Pastes. *Cem. and Conc. Res.*, (29): 1331-1340.
- Lee, S.T. and Hooton, R.D.(2005), Prediction of Performance on Cement Matrix Exposed to Sulfate Media, Annual Report, University of Toronto.

OCCURRENCE OF THAUMASITE IN LINING CONCRETE OF OLD-TUNNEL STRUCTURE

Seung-Tae Lee, Da-Hyun Lee

*Department of Civil Engineering, Kunsan National University, Miryong-dong
Kunsan, Jeonbuk 573-701, South Korea*

Dong-Kyou Kim, Ho-Seop Jung

*Korea Institute of Construction Technology, Daewha-dong, Ilsan-gu
Goyang, Kyunggi-do 411-712, South Korea*

Kwang-Pil Park, Seong-Soo Kim

*Department of Civil Engineering, Daejin University, Sundan
Phochon, Kyunggi-do 487-711, South Korea*

Chang-Soo Lee

*Department of Civil Engineering, The University of Seoul, Dongdaemoon-gu
Seoul, 130-743, South Korea*

The sampling examination on the lining concrete of a 70-year-old tunnel structure was carried out. The compressive strength and RCPT test on the core samples were also performed. In order to identify product formed in the lining concrete, microstructural observations were conducted on the samples obtained from the lining concrete using x-ray diffraction (XRD) and scanning electron microscopy (SEM) techniques. From the results of the examination, it was confirmed the presence of thaumasite formation as well as ettringite formation induced by sulfate attack. Especially, thaumasite solid solution led to a low compressive strength showing cracks and delamination on the surface part of the core samples.

INTRODUCTION

In recent years, lining concretes in tunnel structures have been reported to be seriously damaged by sulfate attack. In general, the conventional sulfate attack including ettringite and/or gypsum formation has been of importance for concrete engineers and scientists. More importantly, there has been increasing interest on thaumasite sulfate attack (TSA) causing spalling and delamination in addition to softening in the lining concrete. The formula of thaumasite, $\text{Ca}_6[\text{Si}(\text{OH})_6]_2(\text{CO}_3)_2(\text{SO}_4)_2 \cdot 24\text{H}_2\text{O}$ indicates that the anionic species CO_3^{2-} and $\text{Si}(\text{OH})_6^{2-}$ besides SO_4^{2-} are essential (Barnett et al., 2002). In fact, the occurrence of the thaumasite form of sulfate attack depends on the co-existence of several factors; wet,

cold, available supply of sulfate and carbonate ions (Crammond, 1985). Several studies reported that the deterioration of lining concrete was greatly associated with the thaumasite formation (Suput et al., 2003; Romer, 2003).

This work presents a possibility of TSA of lining concrete in tunnel structure with a contact with soil and/or groundwater. Especially, the deterioration mechanism of TSA in underground or tunneling conditions is discussed in the light of the microstructural findings obtained.

FIELD INVESTIGATIONS

In the first stage of the investigation, a railway tunnel, which locates in Soowon, South Korea, was inspected, and the lining concretes sampled. The investigated tunnel has a length of about 190m and the samples were taken every 30m in the both walls of the tunnel. The exact mix design of lining concrete is unknown. But, it contains normal Portland cement and round-shaped aggregates.

The lining concrete of the tunnel, which are more than 70 years old, are heavily polluted and partially mushy. Additionally, the wall was seriously damaged due to spalling and delamination, and eventually suffered the exposure of aggregates. More specifically, the flaking away of lining concrete from the surfaces of the rock and the concrete joints was observed on the wall. This clearly implies that the chemical reaction has taken place on the inner side, at the jointing areas between the rock and the lining concrete due to the penetration of aggressive ions from the soil and/or groundwater. In order to evaluate hydrological effect of the damages, the water which penetrates through the ground had been analyzed. The result indicates that the water contains a lot of SO_4^{2-} (180-200 ppm), Mg^{2+} (40-50 ppm) and Ca^{2+} (70-100 ppm) in addition to a small quantity of Cl^- ions. The component of water strongly indicates that the lining concrete might be attacked by the ions oriented from the ground.

Figure 1 shows the deterioration of the wall in tunnel. It was found that the sound lining concrete, which is usually of a dark grey color, has changed into a soft, white mush-type powder. In addition, the damaged part clearly indicated the evidence of spalling and cracking in the concrete. With contact with soil and/or groundwater, the lining concrete exhibited more pronounced deterioration with leaching of water from the wall (See Figure 2).



Figure 1. Deterioration of wall in the railway tunnel

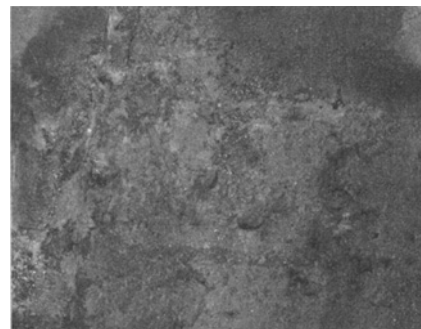


Figure 2. Exposure of aggregates by deterioration of lining concrete

The mechanical characteristics of the core samples were examined and shown in Table 1. The range of compressive strength varied from 15.1 to 41.7 MPa. The general trend of RCPT results in accordance with ASTM C 1202 indicated that the passed charge increased with the decreasing compressive strength because of the permeability of the samples.

Table 1. Mechanical characteristics of core samples obtained from lining concrete

Sample codes	Compressive strength (MPa)	ASTM C 1202 results, Coulomb
1	15.1	3352
2	30.2	2106
3	35.6	1272
4	41.7	1892
5	22.8	1283
6	23.4	1869

ANALYSIS METHODS

Samples were taken at selected damaged locations in the tunnel. The surface part of the samples was analyzed using x-ray diffraction (XRD) and scanning electron microscopy (SEM) techniques. The XRD was used with the RINT D/max 2500 X-ray diffractometer. The CuK α radiation with a wavelength of 1.5405 at a voltage of 30kV, scanning speed of 2°/min. and current of 30 mA were used. The microstructure of the samples was investigated using an XL30ESEM equipped with EDXA Falcon Energy System 60SEM. For the investigation by SEM, the samples were dried in a desiccator for 24 hours, and subsequently gold coated.

RESULTS OF MICROSTRUCTURAL OBSERVATIONS

X-ray diffraction

The identification of products formed in the lining concrete sample of tunnel was performed on XRD measurement. The sample with the lowest compressive strength was selected for the microstructural observations.

Figure 3 shows the XRD pattern of the powder obtained from the deteriorated part of the sample. As mentioned earlier, the surface part of the samples had partially spalled due to the chemical reaction. The XRD trace indicates that ettringite, thaumasite, gypsum and calcite were present in the surface part of the sample in addition to quartz and portlandite. In practice, some strong peaks for thaumasite were identified as the main product in the sample at around 9.2, 16.0 and 23.9 2 θ , respectively. On the other hand, there was an apparent absence of brucite, which might form due to the reaction of magnesium ions. Additionally, there were very weak peaks for gypsum in the XRD pattern. These products indicate that the samples severely suffered from sulfate attack.

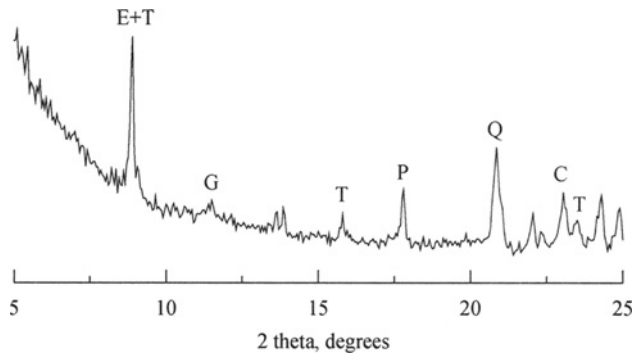


Figure 3. XRD pattern of a deteriorated part of lining concrete sample. (Note; E=ettringite, T=thaumasite, G=gypsum, C=calcite, P=portlandite, Q=quartz)

Scanning electron microscopy

Figure 4 shows the SEM image on the surface part deteriorated in the sample. The image is of ITZ between bulk paste and aggregate, and indicates the presence of numerous crystals. Examinations at higher magnification were performed on the open square in the image as presented in Figures 5 and 6, respectively.

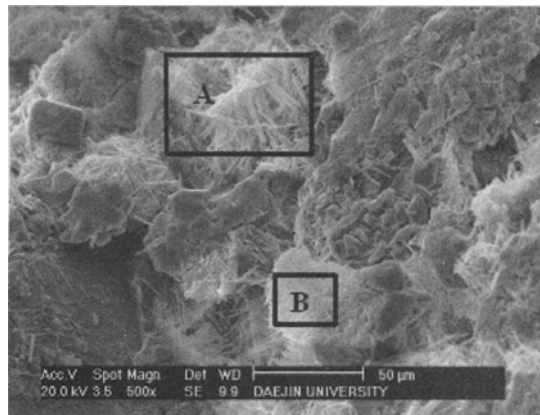


Figure 4. SEM image of a deteriorated part of the sample

In Figure 5, it was observed that the crystals were very fine (below 2 μm in thickness) and up to 40 μm in length. The corresponding EDS analysis indicated that these crystals consist of the elements of calcium, sulfur, oxygen, aluminum, silicon as well as a small amount of carbon. This suggests that there was possible presence of a mixture of thaumasite and ettringite in the sample. Similar to the XRD results, there was no evidence of the presence of brucite on the surface of the sample by SEM and EDS analysis.

Figure 6 presents the SEM image of the open square (B) of Figure 4 and EDS profile. While the distribution of elements was very similar to that in Figure 5, the intensity for silicon was very strong compared to that of aluminum. Thus, the crystals were of thaumasite rather than ettringite.

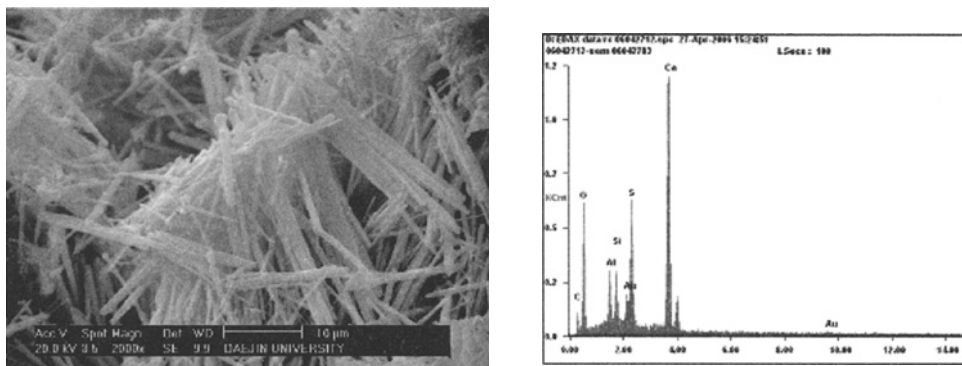


Figure 5. SEM image and EDS profile of the open square (A) at high magnification

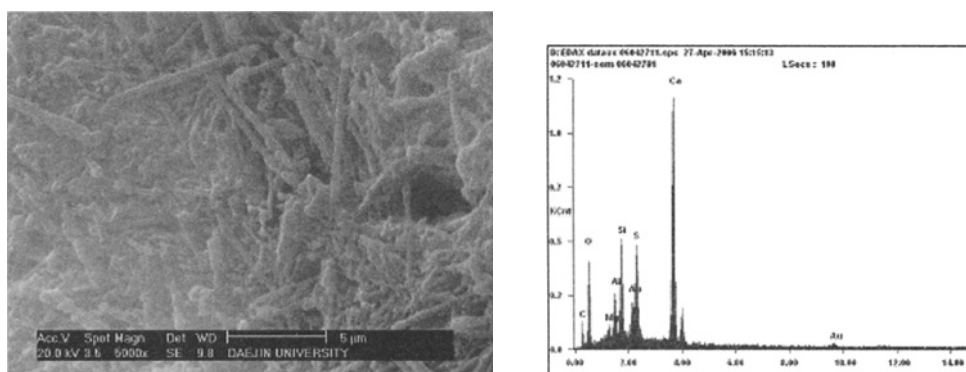


Figure 6. SEM image and EDS profile of the open square (B) at high magnification

CONCLUSIONS

In this study, microstructural observations emphasized that the deterioration of the lining concrete in the railway tunnel investigated was greatly associated with the thaumasite formation due to sulfate attack, which had been oriented from the environmental soil and/or groundwater. On the basis of the results, special care should be taken to minimize or delay the thaumasite formation as well as the conventional sulfate products.

ACKNOWLEDGEMENT

This study has been a part of a research project supported by Korea Institute of Construction and Technology (KICT). The authors wish to express their gratitude for the financial support.

REFERENCES

Barnett S.J., Halliwell M.A., Crammond N.J., Adam C.D. and Jackson A.R.W. (2002). Study of thaumasite and ettringite phases formed in sulfate/blast furnace slag slurries using XRD full pattern fitting, *Cement and Concrete Composites*, 24, 339-346.

- Crammond N.J. (1885). Thaumasite in failed cement mortars and renders from exposed brickwork, *Cement and Concrete Research*, 15, 1039-1050.
- Romer M. (2003). Steam locomotive soot and the formation of thaumasite in shotcrete, *Cement and Concrete Composites*, 25, 1173-1176.
- Suput J.S., Mladenovic A., Cernilogar L. and Olensek V. (2003). Deterioration of mortar caused by the formation of thaumasite on the limestone cladding of some Slovenian railway tunnels, *Cement and Concrete Composites*, 25, 1141-1145.

STABILITY ASSESSMENT AND PROTECTION DESIGN FOR THE ROCK FILLING OF DUMPING SITE IN RAVINE

Honggang Li, E Chuan Yan, Dongli Li, Jiangtao Cheng

Faculty of Engineering, China University of Geosciences Hubei, Wuhan 430074, China

During the construction of cities in mountain area, plenty of human waste-dump is produced because of the topographic conditions. In order to solve the problem of site leveling and rock spoils placing, the dumping site construction become an unavoidably problem which concerns two main problems—the stability of rock filling and the drain of ravine. This paper selects the dumping site of the HuangJia ravine (to be built) as a case, which is a rock filling in Badong county that is an emigratory city of the reservoir region. The source of materials in the spoil site comes from the waste of landslide prevention program. Considering the engineering geological condition, hydrological geological and the characteristics of the rock filling slope, the possible damage mode of the rock filling after filling is speculated .On that basis, the un-equilibrium pushing method is used to calculate the stability of rock filling slope . Consulting the principles of rockfill dam in hydropower engineering ,the comprehensive protection measures are adopted to ensure the stability of the rock filling which includes canal、revetment、rolling and supporting structure . So, the protection design for the rock filling is a new method and approach of urban planning and environmental protection for the emigratory towns in reservoir region. It also has an important social and economic benefit.

INTRODUCTION

During the construction and geologic disaster control of cities in mountain area, cosmically excavation or cutting project will be produced plenty of human waste-dump because of the topographic conditions. Usually, the rock spoils often be abandoned or stacked random without any treatment. Therefore, many problems have been brought out in the city of mountain area: firstly, plenty of land was occupied to aggravate the land inadequacy condition; secondly, the city eco-environment had been destroyed and caused a negative effects on the continually development; thirdly, the new geologic hazards probability happened again (Shang yue-quan, et al., 2002). In order to solve the problem of site leveling and rock spoils placing, the dumping site construction has become an unavoidably problem. However, the new rock filling of dumping site is often accumulated by some crushed-rock in different size. So, the structure of rock filling is very loose and the water permeability is also very good. Thus it will be involved two main problems that are the stability of rock filling and the drain of ravine when build the dumping site. At the present time, there is not special norm to the protection design for the rock filling of dumping site. Mostly, the principles of

rockfill dam in hydropower engineering are consulted when design the rock filling of dumping site.

Based on above considerations, this paper selects the dumping site of the Huangjia ravine (to be built) as a case, which is in Badong County. The sources of materials in the dumping site come from the waste rock of the West Bridge landslide. There would be a rock filling slope after the rock fill in the dumping site of the Huangjia ravine. Considering the engineering geological condition, hydrological geological and the characteristics of the rock filling slope, the possible damage mode after filling is speculated. On that basis, the un-equilibrium pushing method was used to calculate the stability of rock filling slope. Consulting the principles of rockfill dam in hydropower engineering, the comprehensive protection measures were adopted to keep the rock filling stable (YAN E-chuan et al., 2004). The concretely protection measures were the canal, the revetment, the rolling and the lattice framed. So, the protection design of the rock filling is a new method and approach of urban planning and environmental protection for the emigratory towns in reservoir region.

ENGINEERING PROFILE

The West Bridge landslide treatment will excavate rock spoils about 154887m^3 which is in Baiyan ravine of Badong County, Hubei Province. The Huangjia ravine only has 5 km distance from the Baiyan ravine and it also is a deep ravine which is upper stream narrow and down stream expanse. So, Huangjia ravine is an ideal site for dumping site construction to solve the stack problem of rock spoils from the Baiyan ravine. Moreover, combining the Badong urban construction planning, a square will be built on the rock filling after the dumping site of Huangjia ravine completed. This method can make the land use again. At present, The Huangjia ravine is in a stable condition, but the slop banks often collapse because the floods erode in summer. Therefore, ensure safety drainage in flood season is the key issues after the Huangjia ravine dumping site has constructed.

The characteristics of the dumping site

The Huangjia ravine district is the low mountain gorge that erosion gully structure, and the ravine is along the south to north. Besides, the fall of the gully bed is large, and the average falling gradient is 26.7%. The section created by the flood look like a "v" in most area or a "u" in part area. Due to the erosion of the flood, the ravine has formed as a gorge landform that the upper is eroded deeply and the down is wide (As shown in Figure.1).

The rock of the Huangjia ravine mainly is the silty and dolomitic limestone. The attitude of rocks are about $320^\circ\text{-}340^\circ \angle 10^\circ\text{-}20^\circ$. The ground water and surface water have the significant influence in the stability of the rock filling. The source of ground water is the precipitation and the surface water which is change with the season and the topography. The source of the surface water is the precipitation. The water level and the flow change greatly. There is a spring at the upstream of the ravine. So, the water is perennial flow in the ravine, where the water flow rate is $0.076\text{ m}^3/\text{s}$ and the collecting area is about 3.5km^2 . Besides, the draining condition is good and the running water majority disperses into Yangtze River along the ravine from the south to the north.



Figure 1. The picture of dumping site in Huangjia valley

The engineering characteristics of rock and soil dumping (Yan E-chuan, et al., 2004)

The west bridge landslide of the Baiyan ravine is a rock slope which is the rock and soil source to Huangjia ravine. The slide body compositions mainly include the sliding layered intrusion and the single pebbles. The main lithology components of the sliding layered intrusion are layered marlite which was weathered. Moreover, the thickness generally is 15-34m, natural average gravity of the rock is 26.5kN/m^3 and the saturated average gravity is 26.6kN/m^3 . The main component of single pebbles is piend marlite and the particle size is about 0.5 to 2m. The natural average gravity of the rock is 21.2kN/m^3 and the saturated average gravity is 21.3kN/m^3 . The slop cutting adopt the method layer-by-layer blast, and then excavate which produces abandons is cut by broken glass particle size general 0.2-2.5m.

THE STABILITY ASSESSMENT AND FAILURE MODE OF ROCK FILLING

Considering the engineering geological condition, hydrological geological and the characteristics of the rock filling slope, the possible damage mode of the rock filling after filling is speculated .According to analyze the rock filling, there are three possible sliding surface. The first is the potential circular failure surface in rock filling. The second is the interface between rock filling and originally sloping surfaces. The third is the interface between rock filling and bedrock. Then, we can establish the stability analysis mode for dumping site (As shown in Figure 2).

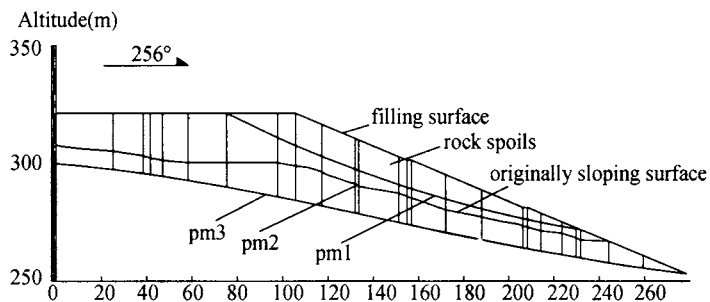


Figure 2. The calculation model of stability analysis

In the Figure 2: pm1 is the potential circular failure surface in rock filling. pm2 is the interface between rock filling and originally sloping surfaces. pm3 is the interface between rock filling and bedrock.

The un-equilibrium pushing method is used to calculate the stability of rock filling slope. According to the deformation and failure characteristic, we assume the slide surface as polygonal line. Therefore, we calculate the stability coefficient of rock filling by formula (1) (XU Qing et al, 2005)

$$P_i = (W_i \sin \alpha_i + Q_i \cos \alpha_i) - \frac{c'_i L_i + (W_i \cos \alpha_i - Q_i \sin \alpha_i - U_i) \tan \phi'_i}{K} + P_{i-1} \cdot \psi_i \tag{1}$$

where: $\psi_i = \cos(\alpha_{i-1} - \alpha_i) - \frac{\sin(\alpha_{i-1} - \alpha_i) \tan \phi'_i}{K}$

The coefficient K can be calculated when the P_n is zero.

Where: W_i is the weight of block; Q_i is horizontal thrust; α_i is the included angle during the horizontal alignment and the bottom of block; U_i is the uplift pressure at the bottom of block; P is the normal force of the un-equilibrium push force; ϕ_i is the friction coefficient; C_i is the cohesive strength.

The shear strength parameters of the rock and the slide surface are induced by test and reverse calculated (As shown in Table 1). The calculated condition includes the common condition and the common condition adds the storm. The former condition only considers the weight of rock filling and the second condition includes the weight of rock filling and the storm. Finally, the stability result follows as Table.2.

Table 1. The physical mechanic property of deposit slope

	crude density (kN/m ³)	saturated density (kN/m ³)	cohesive force (kp)	frictional angle (°)
Rock spoils	18	20		
Slide surface in rock filling			0	30
Interface of rock filling and originally sloping surfaces			0	30
Interface of rock filling and bedrock.			14	16

Table 2. The stability analysis result of to be built deposit slope

potential sliding surface		stability coefficient	
		common condition	the common condition adds the storm
Before filling	pm3	1.425	0.976
	Pm1	1.607	1.303
	pm2	2.338	1.8447
	Pm3	1.432	1.087

THE PROTECTION DESIGN OF THE ROCK FILLING

As the holistic stability of rock filling is bad, the protection design should take preventing the unitary deep sliding as the main goal. So, the protection project must comprehensive analyses every factor which maybe influences the stability rock filling, especially the water. According to the survey data, the soil of dumping site has loose structure and permeates quickly. Usually, the normal level of water is low and located in the bottom soil. However, the ground water level will obvious rise when storm or prolong rainfall. Along with the time of increasing, the backfilling will change to the normally consolidated and the water permeability gradually reduced. Then, the hydrodynamic pressure and hydrostatic pressure gradually rise, which probably lead to the rock filling slide (Chi Xiuwen et al., 2005). In a word, we should pay sufficient attention to water influence during designing.

The push force calculation of rock filling

Based on the standard, the security classification of the rock filling order first-grade and the safety factor take 1.25 to design. According to the calculation result of the table 2, the rock filling probably slide along the pm3 slide face after filling. The remained slip force curve of pm3 slide face after filling follows as Figure 3.

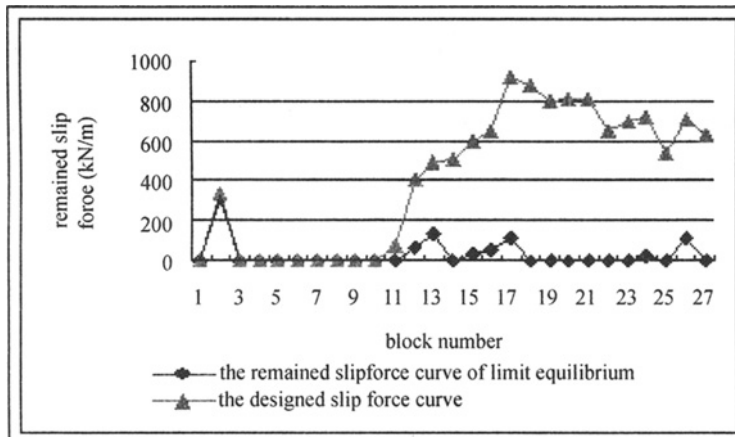


Figure 3. The remained slip force curve of pm3 slide face after depositing

The design of discharge during flood period

The collecting area at the upstream of Huangjia ravine is about 3.5km^2 . The design calculates the maximize discharge by selecting the maximize intensity of rainfall during the 50 years which is 150mm/h . The empirical formula for peak flow in small area is derived by formula (2).

$$Q = KH_i^\beta \quad (2)$$

where: Q is peak flow (m^3/s); K is coefficient that $K = 0.026F^{0.35}$;

The maximize storm index of calculating: $\beta = 1.63(F + 0.5)^{-0.026}$;

The maximize storm: $H_i = H_{F24} \frac{t}{24} \left(\frac{24+d}{t+d} \right)^n$.

Then, the design of discharge in flood period was calculated by above formulas and the result is $Q=24.6\text{m}^3/\text{s}$. So, the design open-ditch should drain the flood in time during the maximum flood discharge.

The layout of protection engineering

The Figure 3 shows that the slide power is little at the fill toe because the presser foot action of the rock spoils. According to the thickness of rock filling and the designed flood discharge at 4.2, the protection plan was established that include the impervious wall engineering, the open-ditch drainage engineering, the roller compacted engineering, the retaining wall engineering and the lattice frame stone pitching engineering. There are three advantages by adopting this engineering design plan. First, the retaining wall engineering can prevent the rock filling sliding. Second, the open-ditch drainage engineering not only reduce the influence on the stability of the rock filling but also more economic, safer and more reasonable. Third, the lattice frame stone pitching engineering can prevent the surface water eroding the rock filling. The detail layout is shown in Figure 4.

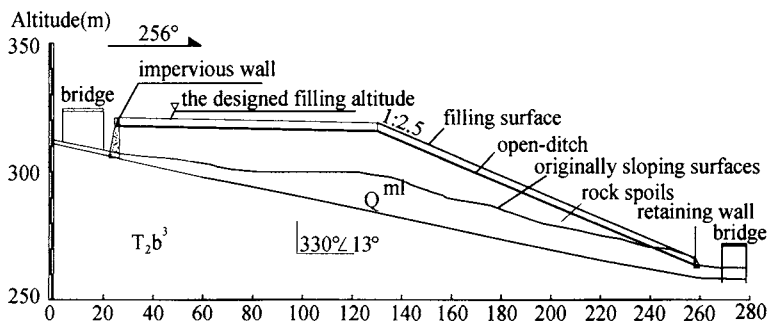


Figure 4. The sketch of protection engineering

(1) The impervious wall engineering

Considering to the engineering geological condition and the stability calculate results of dumpingsite, the impervious wall built in three different sectional forms. The first section is trapezium that long 6m. The second section is rectangle that long 18.6m. The third section is trapezium that long 9.2m. The coping width is 2.0m and the height is different. The highest wall is 15.5m and the lowest is 6.5m. The coping altitude is 321m and the bottom altitude is different for embedding the bedrock. Otherwise, The both side of impervious wall should distribute steel, and the vertical expansion joint that is 0.2m wide is set at a distance of 5m in the impervious wall

(2) The filling and roller compacted engineering

The filling engineering includes gently region and steep land region that designed according to the practical needs. The gently region is 103.8m long which filling altitude is 321m. The steep land region is 137.54m long which filling altitude is 321m and the slope

rake ratio is 1:2.5. The roller compacted engineering should roll in separate layers from the both side to mild by rolling machine. The 0.2m thick clay soil should be laid after filling 3m rock spoils and the degree of density should between 70% and 75%. In appropriate cases, , we can add water to roll in order to improve the rock filling degree of density. This method can accelerate the early deformation of rock filling and also improve the stability of rock filling.

(3) The open-ditch drainage engineering

According to the filling height of designing requirements, the open-ditch includes gently region and steep land region. The gently region ditch adopts with trapezoidal cross-section, which long 105.8m, ditch base wide 5m , ditch deep 2.5m and the ditch slope rake ratio is 1:1. Besides, the crown caps which are 0.3m deep were set at the top of the ditch and the concrete pitprop were built at the middle of the ditch. The steep land region ditch also adopts with trapezoidal cross-section, which long 37.54m, ditch base wide 3m , ditch deep 2.5m and the ditch slope rake ratio is 1:1. However, The steep ditch didn't set the crown caps and concrete pitprop. Moreover, the whole ditch is built with the resistance slippery pier which is 0.3m high and 0.5m wide.

(4) The grouted rubble wall engineering

The retaining wall was constructed by cyclopean rubble masonry and was built at the lower edge of rock filling. The rock of the grouted rubble adopts fresh Mu7.5 and the grout is M7.5. The wall is 18.2m long and 2.5m high. The wall is a trapezoidal cross-section that the coping width is 1.0m and the bottom width of the wall is 2.0m. The altitude is 266.64m at the top of the wall. Otherwise, there are a range of ϕ 110mm outlet hole underside of the coping, and the vertical expansion joint that is 0.2m wide is set at a distance of 5m in the wall.

(5) The water interception and drainage system on surface

According to the topographic conditions of the rock filling, the water interception and drainage system was built and use to intercept the surface runoff. The system includes the intercepting ditch and the drain ditch. The intercepting ditch adopts with trapezoidal section, which ditch is 0.4m deep, furrow bank is 0.3m wide and ditch base is 0.2m thick. The drain ditch adopts with rectangular section, which ditch is 0.6m deep, furrow bank is 0.2m wide and ditch base is 0.2m thick. Besides, the furrow bank was built with M7.5 grouted rubble and ditch bottom was concrete. Otherwise, the vertical expansion joint that is 0.2m wide was set at a distance of 5m in the ditch.

(6) The lattice frame stone pitching

The region of lattice frame stone pitching was laid in K0+130.5~258.2m, which altitude is from 321m to 266.6m. The rock lattice frame is square frame which size is 4m×4m and only lays on the steep slope region. The lattice frame adopts fresh Mu30 rock and the grout is M10. Otherwise, the grass is planted in the lattice frame, in order to prevent erosion of the slope surface.

CONCLUSIONS

(1) Considering the engineering geological condition, hydrological geological and the characteristics of the rock filling slope, the possible damage mode and the three potential sliding surface of the rock filling after filling is speculated.

(2) The flood discharging in rainy season is the key problems of the dumping site construction in mountain cities. So, the plan that adopts the impervious wall engineering and the open-ditch drainage can effectively discharge the flood in the rainy season.

(3) It is a extraordinary reasonable and feasible ideas that construct the square and aedicule on the rock filling by filling the ravine. Firstly, this plan not only solves the problem that the rock spoils abandoned or stacked random, but also recycles the new land for public use. Then the land shortage problem in mountain cities can be remitted. So, the plan has an important social and economic benefit.

REFERENCES

- Chi Xiuwen, Qin Ying, Xia Yuanyou.(2005). Study of stability calculation and harness engineering on landslide. *Chinese Journal of Rock Mechanics and Engineering* . 06, 0975-0979.
- Jiao J J. A. (2000). confined groundwater zone in weathered igneous rocks and its impact on slope stability. (2000). *Proceedings of the international symposium on hydrogeology and the environment*. Beijing: China Environntal Science Press. 602-608.
- Shang Yuequan, Zhou Jianfeng, etc.(2002). The influence of pipe seepage system on the stability of apebbly-clay slope. *Journal of Geological Hazards and Environment Preservation*. 01, 0041-0043.
- Xu Qing, Chen Shijun, Chen Shenghong. (2005). Study on the improved residual thrust method for landslide stability analysis. *Rock and Soil Mechanics* .03, 0465-0470.
- Yan Echuan, Tang Huiming, etc. (2004). Real-time simulation for slope engineering of highway. *Rock and Soil Mechanics*. 02, 0246-0251.
- Yan Echuan, Tang Huiming. (2002). *the stability evaluation and application of the rock*. China University of Geoscience Press.

PSEUDOSPECTRAL METHOD FOR SEEPAGE BEHIND EARTH RETAINING WALL

Nansheng Li, Lihui Xie

*Department of Hydraulic Engineering, School of Civil Engineering, Tongji University,
Shanghai 200092, China*

A higher precision numerical method, spectral method, for seepage behind earth retaining wall is put forward. For most cases, Finite element usually is adopted by its excellent flexibility, but finite element consumes greater times to improve algorithm precision whether h-refinement or p-refinement. Spectral methods generate algebraic equations with full matrices, but in compensation, the high order of the basis functions gives high accuracy for a given N . A model of transient two-dimension seepage problem in earth retaining wall is first established. The water-head function is asymptotic expands by Chebyshev series up to N orders. In interested spatial domain, we get discreted equations at different collocation points, viz. pseudo-spectral methods being used in this problem. It is convenient to integrate the ODE's in time through modified Euler finite difference formula. The predicted results are in excellent agreement with the analytical solutions.

INTRODUCTION

For seepage problem behind earth retaining wall, the general and widely practicable way to solve seepage equation is finite element method. In most cases, finite element method usually is adopted by its excellent flexibility, but FE method costs greatly to improve algorithm precision. The goal of this paper is to set up a more efficient and reliable algorithm to arrive at higher numerical precision. Fortunately, the pseudo-Chebyshev method is the best choice for this goal. As we know, the Chebyshev spectral method has not been used widely in seepage problems now. Though the parameter matrices of pseudo-Chebyshev method are of full matrices, it has much less independent variables for regular interesting domain in compensation than other ordinary algorithm. A typical example is illustrated in which we obtain the useful conclusion, Chebyshev polynomial expands only to 6 terms to reach satisfactory precision.

SEEPAGE MODELS OF EARTH RETAINING WALL

The configuration of earth retaining wall is shown in Figure 1.

For the most cases of seepage behind earth retaining wall the vertical velocity of seepage flow almost can be neglected, so *Dupuit* hypothesis is suitable to be used in the seepage problem behind earth retaining wall. If the surface water supply $w(x,t)$ of soil dam relates to the time t , then the seepage head $h(x,t)$ certainly is a function of time t . The mathematical description of seepage problem behind retaining wall can be expressed as

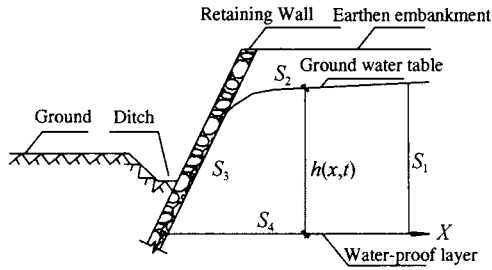


Figure 1. Configuration of earth retaining wall

$$\frac{\partial^2 h}{\partial x^2} + \frac{w(x,t)}{K} = \frac{\mu}{K} \frac{\partial h}{\partial t} \quad (1)$$

$$h(0, y) = h_1 \quad \text{in } S_1$$

$$\left. \begin{array}{l} k \frac{\partial h}{\partial y} = 0 \\ h = y \end{array} \right\} \quad \text{in } S_2$$

$$H = p_0 \quad \text{in } S_3$$

$$k \frac{\partial h}{\partial y} = 0 \quad \text{in } S_4$$

We assume that the soil mass behind retaining wall is homogeneous and the bottom of free-water layer is horizontal in above description. For the reason of taking *Dupuit* hypothesis, the boundary conditions on S_2 and S_4 are implicitly contained in the model of pseudo-spectral method.

PSEUDO-SPECTRAL METHOD

As we point out in *Introduction*, the spectral method can improve greatly numerical precision of ODE. We introduce pseudo-spectral method to solve the nonlinear equation (1). The pseudo-spectral method adopts Chebyshev polynomial $T_m(x)$ as base function to expand the unknown solution of seepage equation (1).

$$\text{Let } h_N(x, t) \cong \sum_{m=0}^N a_m(t) T_m(x), \text{ and}$$

$$T_m(x) = \cos(m \arccos x)$$

$$m = 1, 2, \dots, N$$

The base functions $T_m(x)$ are called Chebyshev polynomial and the independent variable x of Chebyshev polynomial is defined in the domain $[-1, 1]$. Order of the Chebyshev polynomial index N depends on the numerical precision of unknown water head solution $h(x, t)$, it's generally enough to take the number less than 10. It will be proved next that the efficiency improving numerical precision become poor when the Chebyshev polynomial index N is larger than 6.

Put the Chebyshev expansion $h_N(x, t)$ into the governing Equation (1), we can get

$$\int \left[\frac{\partial^2 h}{\partial x^2} + \frac{w(x,t)}{K} - \frac{\mu}{K} \frac{\partial h}{\partial t} \right] \psi(x_i) dx = 0 \quad (2)$$

$$i = 1, 2, \dots, N-1$$

where

$$\psi(x_i) = \delta(x - x_i), \quad i = 1, 2, \dots, N-1$$

In which, x_i are different Chebyshev collocation points in the domain $[-1, 1]$. In most cases, we usually take them like $x_i = \cos \frac{i\pi}{N}$. There are only $(N-1)$ Chebyshev collocation points in Equation (2), these points locate inside the domain $[-1, 1]$. Other few collocation equations are on the boundaries. So we can give

$$\sum_{m=0}^N \left[\frac{d^2}{dx^2} T_m(x) \right]_{x=x_i} a_m(t) + \frac{w(x_i, t)}{K} - \frac{\mu}{K} \sum_{m=0}^N T_m(x_i) \frac{d}{dt} a_m(t) = 0 \quad (3)$$

$$i = 1, 2, \dots, N-1$$

Boundary conditions

$$h_N(-1, t) = \sum_{m=0}^N a_m(t) T_m(-1) = h_{-1} \quad (4)$$

$$h_N(1, t) = \sum_{m=0}^N a_m(t) T_m(1) = \frac{w(1, t) \cdot t}{\mu} \quad (5)$$

In above formulae, $h_{-1} = p_0$ is atmosphere pressure, $w(1, t)$ denotes water supply at boundary $x = 1$ at the time t . We can take static solution as initial condition of the problem (Curtis F. et al., 1989), so the initial condition can be denoted as

$$h_N(x, 0) = \sum_{m=0}^N a_m(0) T_m(x) = \frac{1}{2} h_{-1}^2 - \frac{h_{-1}^2 - h_1^2}{4} x$$

Suppose that initial state of flow with water table is static, so initial water head can denote like above. h_{-1} , h_1 are static water head at boundaries $x = -1, 1$, respectively.

$$[M] \left\{ \frac{dA}{dt} \right\} = [C] \{A\} + \{w\} \quad (6)$$

$$\{A(t)\} = [a_0(t) \quad a_1(t) \quad \dots \quad a_N(t)]^T$$

$$\{w\} = \frac{1}{K} \left[-h_{-1} \quad w(x_1, t) \quad w(x_2, t) \quad \dots \quad w(x_{N-1}, t) \quad \left(w'(x_N, t)t + w(x_N, t) - K \frac{w(x_N, t)}{\mu} t \right) \right]^T$$

$$[C] = \begin{bmatrix} T_0(x_0) & T_1(x_0) & T_2(x_0) & \dots & \dots & \dots & T_N(x_0) \\ T_0(x_1) & T_1(x_1) & T_2(x_1) & \dots & \dots & \dots & T_N(x_1) \\ T_0(x_2) & T_1(x_2) & T_2(x_2) & \dots & \dots & \dots & T_N(x_2) \\ \vdots & \vdots & \vdots & \vdots & \vdots & \vdots & \vdots \\ T_0(x_{N-1}) & T_1(x_{N-1}) & T_2(x_{N-1}) & \dots & \dots & \dots & T_N(x_{N-1}) \\ T_0(x_N) & T_1(x_N) & T_2(x_N) & \dots & \dots & \dots & T_N(x_N) \end{bmatrix}$$

$$[M] = \left(\frac{\mu}{K} \right) \cdot \begin{bmatrix} T_0(x_0) & T_1(x_0) & T_2(x_0) & \cdots & \cdots & \cdots & T_N(x_0) \\ T_0(x_1) & T_1(x_1) & T_2(x_1) & \cdots & \cdots & \cdots & T_N(x_1) \\ T_0(x_2) & T_1(x_2) & T_2(x_2) & \cdots & \cdots & \cdots & T_N(x_2) \\ \vdots & \vdots & \vdots & \vdots & \vdots & \vdots & \vdots \\ T_0(x_{N-1}) & T_1(x_{N-1}) & T_2(x_{N-1}) & \cdots & \cdots & \cdots & T_N(x_{N-1}) \\ T_0(x_N) & T_1(x_N) & T_2(x_N) & \cdots & \cdots & \cdots & T_N(x_N) \end{bmatrix}$$

The matrix Equation (6) is first order ordinary differential equation on time t . To solve the ODE (6), we should use the Runge-Kutta time integral below.

FOUR ORDERS RUNGE-KUTTA TIME INTEGRAL

Pseudo-Chebyshev exhibits its high precision in the process of spatial discretion of seepage governing equation. For the reasons of compatible with high precision of Chebyshev method, it is necessary to adopt more accurate integral methods of the ODE(6) on time.

$$\{A_{n+1}\} = \{A_n\} + h \sum_{i=1}^2 b_i \{f(t_n + c_i h, \{A_n\} + \{k_i\})\}$$

$$\{k_i\} = h \sum_{j=1}^2 a_{ij} \{f(t_n + c_j h, \{A_n\} + \{k_j\})\}$$

where

$$t_n = t_0 + nh$$

$$f(t) = [M]^{-1} ([C]\{A\} + \{w\})$$

And that $h > 0$ is time step, A_n is the solution of equation (6) at time t_n . The parameters can be obtained by the following

$$\begin{matrix} c_1 & a_{11} & a_{12} \\ c_2 & a_{21} & a_{22} \\ & b_1 & b_2 \end{matrix} \Rightarrow \begin{matrix} \frac{1}{2} + \frac{\sqrt{3}}{6} & \frac{1}{4} & \frac{1}{4} - \frac{\sqrt{3}}{6} \\ \frac{1}{2} + \frac{\sqrt{3}}{6} & \frac{1}{4} + \frac{\sqrt{3}}{6} & \frac{1}{4} \\ & \frac{1}{2} & \frac{1}{2} \end{matrix}$$

In order to improve the numerical precision of Runge-Kutta integral, we adopt the technique in (Curtis F. et al., 1989) to halve time step h . When there is large different value between two solutions between two sequential steps, we have to halve the time step h .

NUMERICAL EXAMPLE

To illustrate the high precision of pseudo-Chebyshev method, normalization static problem of seepage behind retaining wall without water supply is given below. By defining the following transformation, we can get non-dimension seepage equation. Let

$$u = h/L \quad \bar{X} = x/L \quad \tau = Kt/L^2 \mu \quad w(\bar{X}, \tau) = 0$$

where L is the distance between boundaries S_1 and S_2 , and then the equation (1) becomes following non-dimension seepage equation,

$$Fu = \frac{\partial u}{\partial \tau} - \frac{\partial^2 u}{\partial \bar{X}^2} = 0$$

More general boundary and initial conditions, which change with time τ , are proposed as showing below,

$$u(-1, \tau) = u(1, \tau) = 10\tau + 100 \quad , \quad u(\bar{X}, 0) = -100 \cos(\pi\bar{X})$$

Table 1 shows that the magnitude of non-dimension water head $u(\bar{X}, \tau)$ at different position and times and compared with analytic solutions for different Chebyshev index N . From this, we can see that the error of pseudo-Chebyshev method almost can be neglected when Chebyshev index N is more than 6.

Table 1. Magnitude of non-dimension water head $u(\bar{X}, \tau)$ at different position and times and compared with analytic solutions for different Chebyshev index N

\bar{X}	Accurate value		Pseudo-Chebyshev solution		
	$\tau = 0.25$	$\tau = 0.5$	N	$\tau = 0.25$	$\tau = 0.5$
0.75	66.44297321463	84.46854260514	6	66.49674904785157	84.47428423095704
			10	66.44285037019728	84.46854436890669
			14	66.44297387453491	84.46854260528589
0.5	36.03349082321	67.35469101265	6	36.07320156250000	67.36186703125000
			10	36.03348439453125	67.35469059013671
			14	36.03349080383912	67.35469108639587
0.25	15.69582425434	56.02564432422	6	15.68668127441406	56.03256237548828
			10	15.69583413042068	56.02564376967649
			14	15.69582492032651	56.02564378902324
0	8.53980021546	52.06400012354	6	8.510800000000000	52.071000000000000
			10	8.539800000000000	52.064000000000000
			14	8.539800000000000	52.064000000000000

Figure 2 and Figure3 give non-dimension water head $u(\bar{X}, \tau)$ via position coordination curve at different times and time-history curve at different position respectively.

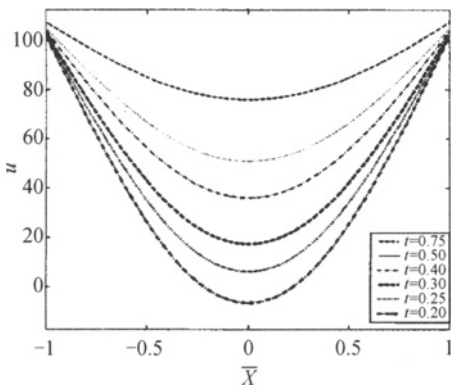


Figure 2. non-dimension water head $u(\bar{X}, \tau)$ via position coordination curve

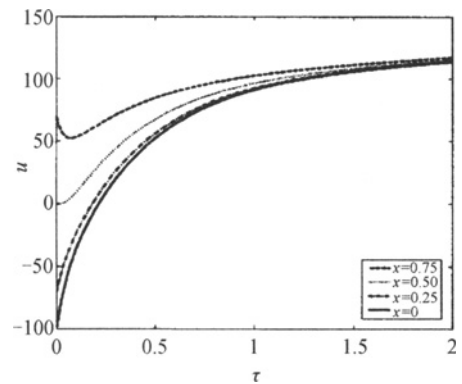


Figure 3. non-dimension water head $u(\bar{X}, \tau)$ time-history curve

CONCLUSION

In this paper we adopt Chebyshev method to solve seepage problems behind retaining wall first time. We can find that the theory of spectral is perfect in numerical model deducing or example. The advantages and disadvantages of Chebyshev method can conclude below,

(a) It is obvious that the numerical precision is higher than FE method and other ordinary numerical methods under same conditions. For most cases, it's enough that Chebyshev polynomial index N is larger than 6 and less than 10.

(b) For regular geometries like this example, the numbers of unknown variables are much less than FE method, so it can offset the numerical deficiencies of full matrix $[C]$ and $[M]$.

(c) The deadly drawback of spectral method is that it's difficult to apply for irregular geometries. It becomes possible to adopt domain partition method in spectral method.

(d) There are no special limits for free and moving boundaries problems like seepage problem there in spectral method.

REFERENCES

- Curtis F. Gerald, Patrick O. Wheatley. (1989). *Applied numerical analysis*, 1st edition, Reading, Mass. Addison-Wesley Pub. Co.
- John P. Boyd. (2000). *Chebyshev and Fourier Spectral Methods*, 2nd edition, DOVER Publication, Inc.
- Yuan Lianju, Li Zhenshuan, etc. (2001). *Engineering seepage mechanics and its application*, 1st edition, Press of Structural-Materials Industry of China.

MULTIPARAMETER TECHNOLOGY ON DAM LEAKAGE

Tong Lin

College of hydrology and water resource, Hohai university, Nanjing China

Jiansheng Chen, Liang Chen

*Key Laboratory of Ministry of Education for Geomechanics and Embankment Engineering,
Hohai University, Nanjing 210098, China*

Geotechnical Research Institute, Hohai University, Nanjing 210098, China

Leakage is one of the most important hidden dangers that will affect the safety of the dam's operation. The method of using the nature tracer, such as temperature, conductance, can be used to detect the leakage passage on dam. One parameter will easily bring on the wrong result or the result shows parts of the whole problem. The multiparameter technology has been used to monitor the safety of the dam and has achieved great success but in leakage passage detecting is rarely used. The multiparameter detecting technology which synthesizes the advantage of the nature tracer, manpower tracer and isotope has gained great effect on detecting the leakage passage of dam.

INTRODUCTION

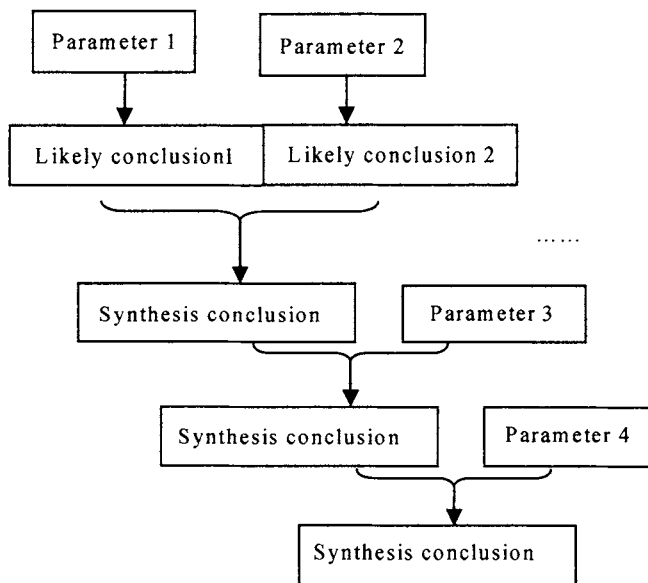
There are so many water and electricity stations on the river basin in my country. With the progress of the runtime many problems appeared. Leakage is one of the most important problems that effects the safety of the dam. Leakage is very common in hydraulic structure. For earthfill dam the leakage will occur piping. For concrete dam the leakage will affect the structure and also the bar will be corroded (Wang min, Wang hong sheng 2002; Wang Bi xue, Song Wei qun, Zhou Qi, 2007; Li Xiao-hui, 1998; Yuan Jin pu, 2006) In order to keep the dam safe, the leakage passage must be found out. There are so many ways to find out the leakage passage. One of those methods can solve the problem, but only use one of the methods can not avoid the disadvantage of itself also it can not get an overall knowledge about the dam and the leakage passage. For example the nature tracer only can be used to find out whether there is a leakage passage but it can hardly tells the exact place where the leakage passage is and how is the leakage passage; geology radar is based on a good understanding of the geology structure, at the same time much attention should be paid to the problem of multihop, otherwise it may cause some misunderstanding; using the resistivity should master the geophysical condition (Dong Hai-zhou, Chen Jian-sheng,2003; Dong Haizhou, Chen Jiansheng, 2004; Chen Jiansheng et al., 2004; Chen Jian sheng et al, 2003; Chen Jian sheng, Liu Jiangang, 2002; Chen Shaoqiu, Chen Mingwei, 1999; Xue Jian et al., 2001) The multiparameter technology is using many kinds of methods to detect the leakage and then analysis the conclusion of all kinds of methods and at last has a synthesis conclusion. The

multiparameter technology can exploit the particular advantage of each method, also it can validate the conclusion of each method. Different parameter can get different information about the dam and the leakage passage. All kinds of information getting by different parameters meet together and it gives a much deeper understanding of the problem. So using multiparameter technology is really a good way to analysis the problem. At present the multiparameter technology is used in the information fusion technology area and has applied in the dam safety monitoring. (Su Huaizhi, 2002; Wang Jian et al., 2004) The multiparameter technology has got a great success in monitoring the safety of the dam, but there is little thesis about the multiparameter technology application on the leakage passage till now. So the study on multiparameter technology on dam is very important and it is an urge mission.

THE ESTABLISH OF THE MULTIPARAMETER MODEL

The multiparameter technology is to use many different kinds of ways to detect the dam, and then synthesis those methods and have the more in reason nicety conclusion. The multiparameter model is displayed on the right. If there are about N parameters, N-1 steps should be taken to synthesis. As follow:

- ① Synthesis Parameter 1 and Parameter 2 and comes out the synthesis conclusion 1
- ② Synthesis Parameter 3 and conclusion 1 and has the conclusion 2
-



N-1 Synthesis the all parameters and has the last conclusion

Different parameters have different arrangement. While the parameter is about temperature, conductance, velocity and connectivity experiment, the temperature is the number 1 parameter, the conductance is the number 2 parameter, the velocity is the number 3 parameter and the connectivity experiment is the number 4 parameter.

While using the four parameters talked above, the temperature and the conductance is the first used to have a likely conclusion 1 and likely conclusion 2. Analysis the likely conclusion 1 and 2 comes out the synthesis conclusion 1. And then using the velocity parameter and the

synthesis conclusion 1 comes out the synthesis conclusion 2. Synthesis the last parameter of the connectivity and the synthesis conclusion 2 comes out the final conclusion.

The parameter firstly adopt is the widest parameter it can only have a wide range about the problem. The coming parameter should deflate the range confirmed and can get more details about the problem. Synthesis all the parameters educed the final conclusion.

The conclusion that based on the parameter 1 and parameter 2 may ignored some aspects, but with the help of parameter 3 the parts which is ignored may have a good complement. With the help of parameter 4, parameter 5 and so on the conclusion is an overall one. The more parameter used in the multiparameter technology the conclusion is much better, and the conclusion can much more feedback the real fact of problem.

THE ANALYSIS OF FEASIBILITY

It is very important to adopt correct parameters in the multiparameter technology model. The chosen parameters must follow the principle talked above. Still much attention should be paid to the feasibility of the parameter according to the problem. Temperature, conductance, velocity of the groundwater and the connectivity experiment, all of these technique can reflect the condition of the leakage passage in some degrees. The following is some introductions about the effect of ascertain the leakage passage using single parameter.

Temperature analysis

The temperature of the water is a good tracer used to investigate the leakage of the dam. The temperature of the water in the reservoir is distributing in lamellar. No matter summer or winter the water in the bottom of the reservoir is at a low temperature. The temperature of the earth is following the law that the temperature will hoist about 3 degree per 100 meter go deep in the earth. (Chen Jiansheng et al., 2004; Dong Haizhou, Chen Jiansheng, 2004) In summer, if the water comes out in a low temperature it must come from the bottom of the reservoir. According to the function of the temperature as a tracer, the water in the drill can help judge the area which is affected by the water leaked from the reservoir. If the water in the drill is at a low temperature, near the drill there may be a leakage passage; on the other hand if the temperature of the water in the drill is hoisting from the top to the bottom, it may not be affected by the water leaked from the reservoir.

Conductance analysis (Chen Jiansheng, Dong Haizhou, 2007)

The conductance of the water in the reservoir is changed with the time and position. The conductance always changes with the season. In rainy periods the value of the conductance is much lower, and in dry seasons the value of the conductance is much higher. No matter the value of conductance of the water in the reservoir is high or low, while the water in the aquifer at a low velocity or stayed in the aquifer for a long time, the value of the conductance of the water in the drill is much higher than the water in the reservoir. If the water in the reservoir and the water in the drill has the same value of the conductance or closely, the water in the drill must be affected by the water leaked from the reservoir.

While using the conductance to analysis, the water in the reservoir, the water in the drill and the spring should be measured often.

Velocity analysis

The velocity of the water in the drill can reflect how the groundwater moving near the drills. The temperature and the conductance can discover the shadiness areas, the velocity of the water in the drill can validate the conclusion that comes out by temperature and conductance. The velocity mainly used to detect the emphasis area, and reduce the range that has decided early time.

Connectivity analysis

There are two drills A and B, the tracer is put in drill A and will be received at drill B. If the value of the conductance in drill A and drill B is low, devote the salt in drill A, and detect the conductance of the water in the drill B. If the value of the conductance in the drill B is much higher than early times, then drill A and drill B is connected. The experiment of the connectivity can show the truth whether the two point is connected, it is a good way to certain the leakage passage.

Temperature, conductance, velocity or the connectivity experiment can be used to make sure of the leakage passage. But there are some problems if only take one of them to make sure of the leakage passage. For example, using single parameter may come out two or three answers or the range about the area of leakage is too wide. The temperature of the water in the drill will be affected by the temperature of the environment, and the conductance will be affected by the seasons, the connectivity experiment needs to make sure there are some place is shadiness. Single parameter always meet all kinds of problems that itself can not solve perfectly. The multiparameter technology can solve the problems which the single parameter can not avoid, so it is better to use multiparameter than single parameter.

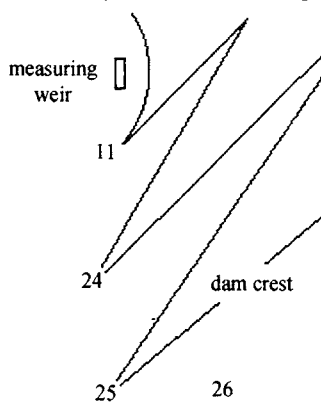


Figure 1

PROJECT APPLICATION

The dam of Xinjiang JILINTAI is leaking. The amount of the water leaked is going up with the level of the water in the reservoir. While the water level in the reservoir is about 1396m,

the flux of the water in the measuring weir is about 233L/s. The reason of the leakage is not clear and it has aroused great attentions. In order to make sure of the leakage passage and whether it will affect the safety of the dam, the multiparameter technology used and got a good result.

The condition of the dam is showed on Figure 1. The drill is labeled in the chat. The left of the dam is the study area, and there are 4 drills. There are three drills on the dam abutment, and the No.26 drill is at dam face. The temperature of the drill on the left of the dam is showed in Table 1.

Table 1. temperature and conductance in the drill on the left abutment

Drill	Lowest temperature	Highest temperature	Lowest conductance	Highest conductance
11 [#]	8.7	9.5	326 μ s/cm	328 μ s/cm
24 [#]	6.4	6.5	391 μ s/cm	395 μ s/cm
26 [#]	7.7	9.7	190 μ s/cm	219 μ s/cm
25 [#]	8.5	9.5	405 μ s/cm	414 μ s/cm

The temperature of the water in the measuring weir is about 8.5 $^{\circ}$ C, and the water in the reservoir is about 5-6 $^{\circ}$ C. According to the temperature, water in the No.24 drill is having a good relationship with the water in the reservoir. The temperature of the water in the other three drills is a bit higher than the water in the No.24 drill, but lower than normal temperature of the earth at the same depth. So the four drills are affected by the water in the reservoir, and the No.24 drill is affected strongest. Maybe the No.24 drill is just on the leakage passage, or near the leakage passage.

The value of the conductance of the water in the drill on the left abutment is showed in the Table 1. The value of the conductance of the water in the measuring weir is about 500-600 μ s/cm, the value of the conductance of the water in the reservoir is about 190-200 μ s/cm. The No.26 drill is on dam face so the value of the conductance of the water is close to the water in the reservoir. The rest drills are much far away from the reservoir, the water in the reservoir travels a long way and it has diffienced a lot of ions, so the value of the conductance of the water in the drill is much higher than the water in the reservoir and much lower than the water in the measuring weir.

Synthesis the temperature and the value of the conductance in the drill on the left abutment, the water in the drill is having a good relationship with the water in the reservoir. So the left of the dam is a shadiness area. In order to get a deeper understand of the leakage, the isotope is used in the drill of No.24, No.25 and No.26 to detect the average velocity of the water in the drill. The average velocity of the three drills is showed in the Table 2.

Table 2. average velocity of the drill on the left abutment

Drill	Average velocity (m/d)
24 [#]	0.5000
25 [#]	0.0015
26 [#]	0.1000

The velocity in the drill shows the same result with the temperature and the conductance. From the result showed above it is sure that the left of the dam is leaking and the No.24 can reflect the truth of the leakage passage most. In order to make a deeper understanding of the connectivity of the No.24 drill and the measuring weir, the connectivity experiment is done.

The tracer of fluorescence is put in the drill No.24 at 4 o'clock on May 22nd 2006, and the affusion is lasting about 15 minutes about 200kg. At 8 o'clock in night starts detecting the water in the measuring weir, twice per day. The result of the detection is showed in Figure 2.

The chat shows clearly that on May 25th the water in the measuring weir starts receiving the tracer, the consistency of the tracer in the water of the measuring weir is going up till May 30th. From June the 1st the consistency of the tracer in the measuring weir is keeping steady. The connectivity experiment shows that the No.24 drill is having a good connection with the measuring weir, so there is a leakage passage.

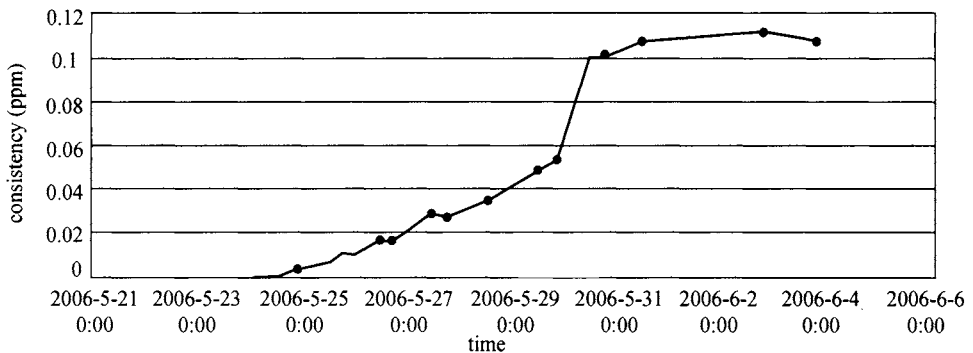


Figure 2. Tracer detecting of the measuring weir

CONCLUSION

Leakage is very common in the dam, the existence of the leakage is doing harm to the safety of the dam and the steady of the construction. There are many ways that can solve the problem of the leakage. But the single parameter way is can not solve the problem perfectly. The multiparameter technology is much better than the single parameter technology. The different parameters in the multiparameter can make each other work much better and get a better result. So the multiparameter is a good way to deal with the leakage of the dam.

ACKNOWLEDGEMENT

Supported by Natural Science Foundation of Hohai University (2084/407185).

REFERENCE

- Chen Jian sheng, Dong Hai zhou, Chen liang (2003). Pplication of the environment isotope method to study on the leakage passage in foundation of Bejjiang Dyke Shijiao section, *Advances in Water Science*, 14 (1).
- Chen Jiansheng, Dong Haizhou, Fan Zhechao (2004). Nature tracer method for studying leakage pathway of by-pass dam abutment of Xiaolangdi, *Reservoir Journal of Yangtze River Scientific Research Institute*, (21) 2.

- Chen Jiansheng, Dong Haizhou (2007). *The Study of New Tracer Theory and Technology of Dam Leakage*, Science Press.
- Chen Jiansheng, Liu Jianguang (2002). Study on leakage of Shijiao section of Beijiang river dyke, *Chinese Journal of Geotechnical Engineering*, 24 (4).
- Chen Shaoqiu, Chen Mingwei (1999). The Effect of the method of resistivity in distinguishing the Hidden Danger of embankments, *J. cent. South univ. technol.*, 30, (5)
- Dong Haizhou, Chen Jiansheng (2004). Study on groundwater leakage of foundation pit with temperature tracer method Chinese Li Xiaohui, (1998) Forming, harm and the technique of dealing with the leakage of the earthfill dam, *Shanxi water resource*,(1).
- Dong Haizhou, Chen Jiansheng (2003). Model research of heat source method by using water temperature distribution in borehole to determine seepage velocity of dyke, *Hydrogeology and Engineering geology*, (5).
- Su Huaizhi, Wu Zhonru, Dai Huichao (2005). System of theories and methods monitoring intelligently dam safety, *Journal of Hydroelectric Engineering*, 24 (1).
- Wang bixue, Song weiqun, Zhou Qi,(2007). The treatment of the leakage in hydraulic concrete, *Yangtze river*, 38 (2).
- Wang Jian, Wu Yuan, Zheng Dongjian (2004). Analysis of dams safety monitoring data based on multi-sensor data fusion theory, *Engineering Journal of Wuhan University*,37 (1).
- Wang min, Wang Hong sheng (2002). The problems exist in large and medium reservoir and the step of reinforcement on Yellow River, *Yellow River*, 24 (10).
- Xue Jian, Wang Zhejiang, Zeng Zhaoafa, (2001). Application of gpr to dam leakage detection, *Journal of changchun university of science and technology*, 31 (1)
- Yuan Jinpu, (2006). Hazard origin and prevention of exterior wall leakage, *Shanxi Architectue*, 32, (24).

RISK ANALYSIS OF SOIL-NAIL SUPPORTING SLOPE UNDER THE EARTHQUAKE EFFECT

G. C. Lou

*Soil Mechanics Laboratory, Shijiazhuang Railway Institute,
Shijiazhuang 050043, China*

Z. L. Ye

*Soil mechanics Laboratory, Shijiazhuang Railway Institute,
Shijiazhuang 050043, China*

Horizontal earthquake acceleration is used for the risk analysis of the soil-nail supporting slope, and the relationship between the dynamical safety factors and corresponding static safety factors is obtained. The reliability of slope is expressed with the safety factor. The mathematic formulation of the slope failure probability is deduced with stochastic earthquake acceleration. In the case of a slope in Nankun Railway Project, calculation results show that safety factor with the stochastic earthquake is smaller than that without earthquake. It is clear that the influence of the earthquake is notable.

IMPORTANT SUBMISSION INFORMATION

Soil nailing is a soil reinforcing technique that consists in placing bars into soil while excavation and goes on by phases. The original idea of reinforcing in situ soil using driven and grouted steel bars started in the early 1970s in France with the construction of a first wall in Versailles in 1972 (Rabejac and Toudic, 1974). Different research and development project have been devoted to a better understanding of this technique. Its spectacular success during the last decade is due to its technical and economical advantages for constructing in situ earth support systems in steep slope engineering and its application is becoming more and more frequent.

The most earth slope is in meizoseismal area so that the stability analysis is one of the most difficult problem and many geotechnical engineers pay attention all the time to it. Many theories about slope and study measures to support systems have been advanced (Halatchev Rossen, 1992 and Al-Homoud A S., 2000). In recent years, the probability theory has been developed and used in slope stability analysis (Wolff 1996; Vanmarcke E., 1997). Because of a lot of uncertain factors being considered, the significance achievements have been made.

Based on classical limit equilibrium method, the soil-nailing supported slope safety factor is studied in the way of quasi-static analysis in this study and the influence quantity by some variation of parameter in construction is discussed.

CALCULATION MODELING

General hypothesis

Soil is homogeneous and isotropic; Slope is consisted of rigid-plastic material; the shape of the slope slip surface is a plate.

Static safety factor

A representative soil-nailing supported slope is given in Figure 1. The slip surface is represented by a mathematical function, $y = s(x)$; θ is the angle of the slip surface to the horizontal direction; α is the angle of the topographic profile to the slip surface and β is the angle of soil nail to the horizontal direction; c and ϕ are the cohesion and the friction angle of soil; The height of the slope is H .

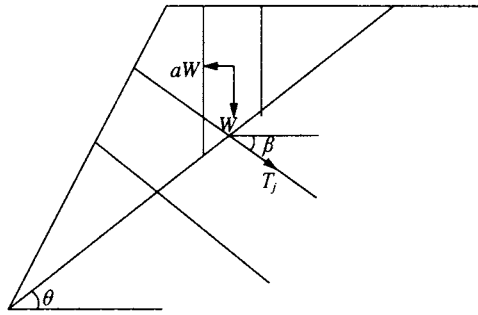


Figure 1. Sketch for slope analysis

Then, the safety factor is given:

$$F_s = \frac{\left[\sum_{i=1}^n W_i \cos \theta + \sum_{i=1}^n N' l_i \sin(\alpha + \beta) \right] \tan \phi + \sum_{i=1}^n c l_i}{\sum_{i=1}^n W_i \sin \theta - \sum_{i=1}^n N' l_i \cos(\alpha + \beta)} \quad (1)$$

there, F_s is static safety factor; n is the number of the soil stripes; W_i is the weighty of the i st stripe; l_i is the width of the stripe; N'_i is the average force in the slip surface from soil nailing, given by:

$$N' = \frac{\sum_{j=1}^m T_j}{L S_d} \quad (2)$$

m is the number of the soil nailing; T_j is the ultimate withdrawal resistance of soil nailing; S_d is the horizontal spacing between soils.

From (1) can obtain:

$$F_s = \frac{\left[W \cos \theta + N' L \sin(\alpha + \beta) \right] \tan \phi + cL}{W \sin \theta - N' L \cos(\alpha + \beta)} \quad (3)$$

there, L is the length of the slip surface; W is the weighty of the landslide mass, given by:

$$W = \frac{1}{2} \gamma H L \frac{\sin(\alpha - \theta)}{\sin \alpha}$$

then :

$$c = F_s \left[\frac{1}{2} \gamma H \frac{\sin(\alpha - \theta)}{\sin \alpha} \sin \theta - N' \cos(\alpha + \beta) \right] - \left[\frac{1}{2} \gamma H \frac{\sin(\alpha - \theta)}{\sin \alpha} \cos \theta + N' \sin(\alpha + \beta) \right] \tan \phi \quad (4)$$

Dynamic safety factor

Horizontal earthquake acceleration is only considered in the stability analysis of soil-nailing supported slope.

$$a = \frac{a_k}{g} \quad (5)$$

here, a is the coefficient of horizontal earthquake acceleration; a_k is horizontal earthquake acceleration; g is gravitational acceleration:

Then the stability factor under earthquake is given by:

$$F_d = \frac{\left[W \cos \theta - aW \sin \theta + N' L \sin(\alpha + \beta) \right] \tan \phi + cL}{W \sin \theta + aW \cos \theta - N' L \cos(\alpha + \beta)} \quad (6)$$

please substitute (3),(4) and (5) into (6):

$$F_d = F_s - \frac{F_s a W \cos \theta + a W \sin \theta \tan \phi}{W \sin \theta + a W \cos \theta - N' \cos(\alpha + \beta)}$$

when the soil nail is normal to the slip surface, there is:

$$F_d = \frac{(F_s - a \tan \phi) \tan \theta}{a + \tan \theta} \quad (7)$$

there, F_d is the safety factor under horizontal earthquake.

RELIABILITY ANALYSIS UNDER EARQUAKE

According to the former studying (Wolff, 1996), we can know that the safaty factor is in normal distribution with multiple parameters of independent which is $K \sim N(1.0, \sigma_F)$. The mathematic formulation of the slope reliability index can be deduced with stochastic earthquake acceleration:

$$\beta = \frac{F_d - 1.0}{\sigma_F} = \frac{(F_s - a \tan \phi) \tan \theta - 1.0}{\sigma_F} \quad (8)$$

then the formulation of failure probility is obtained:

$$P_f = 1 - \phi(\beta) \quad (9)$$

EXAMPLE

This example is taken from Nankun Railway Project in Yunnan area and concerns a steep slope that is supported by soil-nailing system while excavation goes on by phases. The height of this slope is 15 meters and its layers are mainly consisted of residual clay. The average of soil and nail parameters in construction is listed in Table 1 and Table 2. According to the building code in China (GB50011-2001), the seismic intensity is eight and $a_k = 0.1g$. Then the safety factor is 1.32 only considering the horizontal earthquake.

Table 1. The average of soil parameters

Soil	Natural density γ (kN/m ³)	Natural moisture content W (%)	Cohesive strength c (kPa)	Friction angle ϕ (deg.)
Residual	18.6	20.4	48	24

Table 2. The average of nails parameters

Boring diameter D (mm)	Nails length L (m)	Nails gradient β (deg.)	Horizontal spacing S_d (m)	Limit tensile force T_j (kPa)
120	10	25	1.8	80

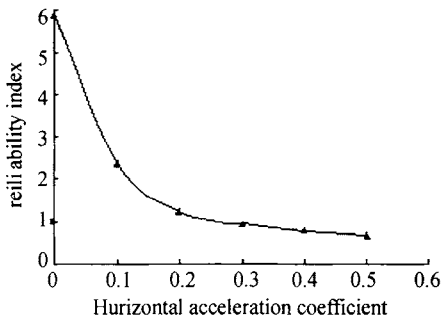


Figure 2. Influence of seismic coefficient

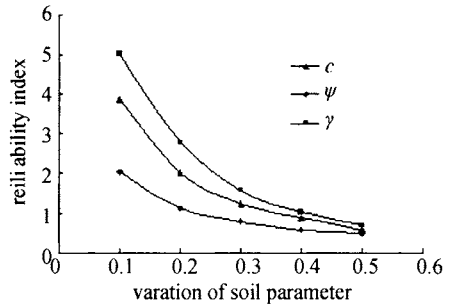


Figure 3. Influence of various soil parameters

The influences caused by the variation of seismic coefficients, soil properties and nails parameter are shown in Figure 2, Figure 3 and Figure 4. It indicates that not only the variation of soil properties but also the variations of nail parameters contribute to the slopes stability. If the variation is little, the caused influence is little and the variation is bigger, the influence is bigger. To improve the reliability index of the slope stability, we can decrease the variation of boring diameter, spacing between nails and limit tensile forces along nails. On the contrary, to reduce the variation of nails length cannot enhance the slope stability obviously.

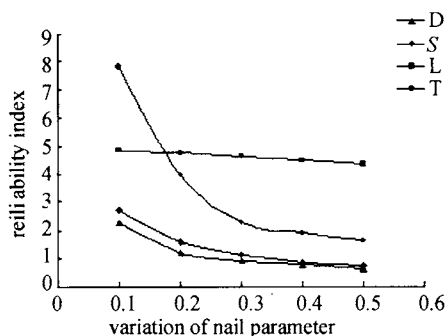


Figure 4. Influence of various nail parameters

CONCLUSIONS

Based on classical limit equilibrium method, horizontal earthquake acceleration is considered for reliability analysis in soil-nailing supported slope. the relationship between the dynamical safety factors and corresponding static safety factors is obtained. The reliability of slope is expressed with the safety factor. The mathematic formulation of the slope failure probability is deduced with stochastic earthquake acceleration. The influences caused by the variation of the parameters on the soil-nail slope are studied and draw the follow conclusion: On the seismic stability of the soil-nailing slope, the influences caused by the variation of the soil parameters and the nails parameters are very obvious.

REFERENCES

- Al-Homoud, A S and Tahtamoni W W. (2000). Reliability analysis of three-dimensional dynamic slope stability and earthquake-induced permanent displacement. *J. Soil Dynamics and Earthquake Engineering*.19 (2): 91-114.
- Halatchev Rossen A. (1992). Probabilistic stability analysis of embankments and slopes. *Proceedings of the 11th international conference on ground control in mining*. 432-437.
- Lou G. C. and Wang S.D.(2005). Reliability study of earth slopes under earthquake. *China J. of Rock Mech. and Eng.*, 24(s1): 2836-2841.(in Chinese)
- Rabejac S. and Toudic P. (1974). Construction d'un mur de soutènement entre Versailles-Chantiers et Versailles-Matelots. *Revue generale des chemins de fer*, 93: 232-237
- Song Weinia (1990). *Foundation Engineering Reliability Design Theory and Its Application*, China communication Press, Beijing (in Chinese)
- Vanmarcke E. (1997). Probabilistic modeling of soil profiles. *J. Geotech. Eng.*, 103(11): 1035-1053
- Wan L.H., Yu J.M. and Feng C.H.(2004). Optimum design of parameters for composite soil nail wall in soft soil foundation. *China J. of Rock Mech. and Eng.*, 23(19): 3342-3347 (in Chinese)
- Wolff T. F. (1996). Probability slope stability in theory and practice uncertainty in the geologic environment. *Geotech. ASCE*, 58(1): 419-433.

STUDY ON STRENGTH CRITERION OF INTACT SOFT CLAY AFTER MONOTONIC PRINCIPAL STRESS ROTATION

Yang Shen

*Key Laboratory of Ministry of Education for Geomechanics and Embankment Engineering,
Hohai University, Nanjing 210098, China*

Geotechnical Research Institute, Hohai University, Nanjing 210098, China

Jian Zhou, Xiaonan Gong

*Institute of Geotechnical Engineering, Zhejiang University, 20 Yugu Road
Hangzhou 310027, China*

Hanlong Liu

*Key Laboratory of Ministry of Education for Geomechanics and Embankment Engineering,
Hohai University, Nanjing 210098, China*

Geotechnical Research Institute, Hohai University, Nanjing 210098, China

Underestimating the influence of principal stress rotation on the foundation soil during the construction is the cause of some engineering accidents. Series of experiments were done to study the strength characteristics of intact soft clay after undrained monotonic principal stress rotation. It was found that compared with the progress of undrained monotonic principal stress rotation, the principal stress direction when samples failed influenced the soils' strength much more obviously. But the pore water pressure generated in the tests including principal stress rotation was much higher than that in the test of fixed principal stress direction shear. It was due to the shearing contraction of intact soft clay caused by principal stress rotation. A modified Lade-Duncan failure criterion was used to normalize these testing results and unify the soil's failure criterion including principal stress rotation. It showed that initial anisotropy was one of the most important determinate factors of intact clay's strength when principal stress rotation occurred during the construction.

INTRODUCTION

In the practical issues soil would undergo complex stress path. Monotonic principal stress rotation will occur as a kind of typical path when the foundation is subject to filling dams, excavation or some other constructions. It, coupled with soils' anisotropy, may influence soils' strength properties. And such influence would be amplified with the scale of construction expanding. So underestimating these influence will have grave consequences.

Laboratory experiment is one of the methods to evaluate these effects properly. Several researchers like Arthur et al. (1979), Hight et al. (1983), Symes et al. (1984,1988), Wijewickreme and Vaid (1993), Zdravkovic and Jardine (2001), Sivathayalan and Vaid

(2002), Han and Penumadu (2005) have done tests to study the soil's properties under principal stress rotation. But most samples tested before were remoulded silt or sand. Compared with them, clay, especially intact clay, may show quite different reaction on principal stress rotation because of its structural property, anisotropy and other characteristics. So the authors did a series of intact clay experiments to study the influence of principal stress rotation on its strength. How to generalize the strength criterion for such stress path is also discussed.

SOIL PROPERTIES AND TESTING PROCEDURES

The soil tested was a kind of typical intact soft clay from Hangzhou, and its properties are summarized in Table 1. The intact clay block was shaped into a hollow cylinder sample (height 200mm × outer diameter 100mm × inner diameter 60mm) with special apparatus (Zhou et al., 2007).

Table 1. Properties of testing soil

Specific gravity	Void ratio	Water content (%)	Liquid limit	Plastic limit	CU C_{cu} (kPa)	CU ϕ_{cu} (°)	Direct shear(R) c (kPa)	Direct shear(R) ϕ (°)
2.74	1.234	44.3	45.0	18.3	24.8	16.0	5.5	9.0

The testing apparatus is Hollow cylinder apparatus (HCA) devised by Zhejiang University and GDS Ltd. Four independent loading parameters, namely axial load (W), torque (M_T), inner (p_i) and outer (p_o) pressures, can be applied and four corresponding stress components, i.e. major (σ_1), intermediate (σ_2), minor (σ_3) stress and the direction of σ_1 relative to the vertical (α) can be generated, which form the principal stress rotation stress path (see Figure 1). And in this paper, another three equivalent parameters $p=(\sigma_1+\sigma_2+\sigma_3)/3$, $q=(\sigma_1-\sigma_3)/2$, $b=(\sigma_2-\sigma_3)/(\sigma_1-\sigma_3)$ instead of $\sigma_1, \sigma_2, \sigma_3$ were used to control the principal stress rotation path. p reflects the level of spherical stress, q reflects the size of failure Mohr's circle and b reflects the interrelation of the three principal stress, which could show the constitutive laws of soil better.

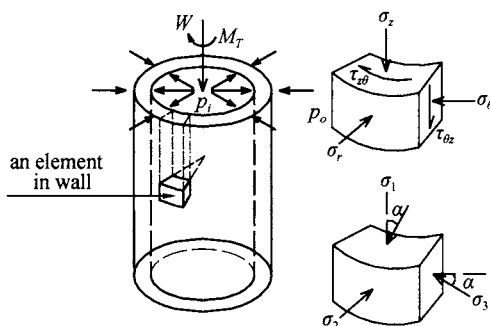


Figure 1. Stress on an element in wall of hollow cylinder sample

Samples were firstly isotropically consolidated under 150kPa (total cell pressure $p=200$ kPa, and back pressure $p_b=50$ kPa) and then divided into two groups for different

undrained shear tests. One group consisted of the tests of fixed principal stress direction shear (named *T* group), and the other consisted of the tests of monotonic principal stress rotation shear (named *R* group). Plans for these tests are listed in Table 2 and 3.

Table 2. Tests plan for undrained fixed principal stress direction shear (*T* group)

Number of samples	Characteristics of stress parameters when loading			
	p (kPa)	b	α ($^{\circ}$)	q (kPa)
T101	200	0	0	Increase from 0 until sample fails
T102			10	Increase from 0 until sample fails
T103			15	Increase from 0 until sample fails
T104			25	Increase from 0 until sample fails
T105			45	Increase from 0 until sample fails
T106			60	Increase from 0 until sample fails
T107			75	Increase from 0 until sample fails

Table 3. Tests plan for undrained principal stress rotation shear (*R* group)

Number of samples	Characteristics of stress parameters when loading		
	p (kPa)	b	Relation between q (kPa) and α ($^{\circ}$)
R171	200	0	When $\alpha=30^{\circ}$, increase q from 0 to 35kPa. Then keep $q=35$ kPa and rotate from 30° to 60° . Finally keep $\alpha=60^{\circ}$, increase q until sample fails
R172			When $\alpha=0^{\circ}$, increase q from 0 to 35kPa. Then keep $q=35$ kPa and rotate from 0° to 60° . Finally keep $\alpha=60^{\circ}$, increase q until sample fails

TESTING RESULTS AND ANALYSIS

When samples failed in the *T* and *R* group tests, q reached peak values (named q_{max}). Figure 2 shows the values of q_{max} (namely the size of failure Mohr's circle) in *T* group. p'_o is the samples' initial effective cell pressure (equal to 150kPa). It revealed that when samples were sheared at fixed principal stress direction, the strength obtained were quite different due to the clay's intrinsic anisotropy.

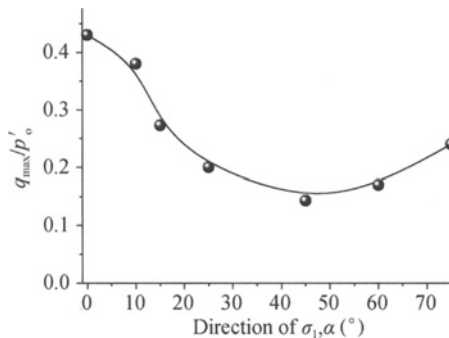


Figure 2. Anisotropical normalized shear strength of *T* group tests

The values of q_{max} obtained in R group are also shown in Table 4 and Figure 3(a). It could be seen that q_{max} of R171 and R172 are very similar to the T106's. Although R171, R172 had undergone one stage including principal stress rotation, they failed at the same direction of principal stress direction with T106. So it could be concluded that the undrained monotonic principal stress rotation didn't influence the size of failure Mohr's circle. This conclusion is similar to that drawn from the remould sand and clay test results of Symes et al. (1984), Hong et al. (1989) and Sivathayalan et al. (2002).

While it could also be seen in Figure 3 that at the failure point, the pore pressure generated in R171 and R172 are much more than in T106. So it showed that although the size of failure Mohr's circle didn't change, the "superfluous" pore water pressure generated and caused the change of effective spherical stress correspondingly, which was due to the existence of principal stress rotation. Such phenomenon seems confusable if Mohr-Coulomb failure criterion is used to evaluate the strength of the samples. But it may be explained by other criterion more properly. In this paper, a modified Lade-Duncan failure criterion was put forward, with which the "superfluous" pore water pressure generated in principal stress rotation could be normalized into a unified effective stress system properly.

Table 4. Values of some stress parameters when samples failed

Number of samples	The values of some stress parameters when samples failed			
	α (°)	q_{max} (kPa)	q_{max}/p_o	k_f
R171	60.0	25	0.167	27.9
R172	60.0	25.7	0.171	28.0
T106	60.0	24.9	0.166	27.8

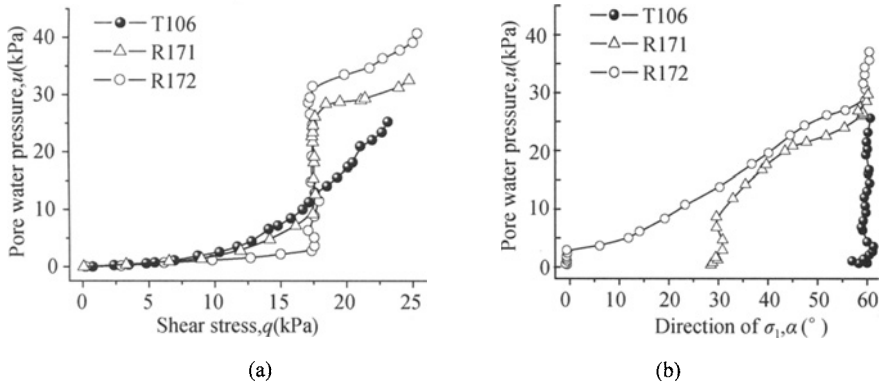


Figure 3. Pore pressure characteristic of T107, R171, R172.

The original Lade-Duncan failure criterion is expressed as

$$f(I_1, I_3, k_f) = \frac{I_1^3}{I_3} - k_f = \frac{27(p-u)^3}{(\sigma_1 - u)(\sigma_2 - u)(\sigma_3 - u)} - k_f = 0 \quad (1)$$

where

$$I_1 = (\sigma_1 - u) + (\sigma_2 - u) + (\sigma_3 - u) ;$$

$$I_3 = (\sigma_1 - u) \cdot (\sigma_2 - u) \cdot (\sigma_3 - u) ;$$

k_f is failure parameter of Lade-Duncan criterion.

Equation. (1) can also be rewritten in the form of p, q, b, α as:

$$f(p', q, b, k_f) = \frac{2}{27} q^3 (b^2 - b + 1)^{3/2} \sin 3(\arctan \frac{1}{\sqrt{3}}(2b - 1))$$

$$- \frac{1}{3} q^2 (p - u)(b^2 - b + 1) + (1 - 27/k_f)(p - u)^3 = 0 \quad (2)$$

where u is the increment of pore water pressure generated in the T and R group tests.

The original model is fit for cohesionless soil, as to the clay samples in this paper, it should be modified with the cohesion. So in Equation. (1) or (2) $\sigma_1, \sigma_2, \sigma_3$ are replaced separately with $\sigma_1 + c_a, \sigma_2 + c_a, \sigma_3 + c_a$ to take clay's cohesion into the consideration. c_a is a cohesion modified parameter which is obtained by fitting the results of triaxial compression test, direct shear test (see Table 1) and the shape line of q_{max} along all the directions of σ_1 in T group (see Figure 2). So c_a is expressed as follows:

$$c_a = 194.427 \times [0.406 + 4.283 \times 10^{-4} \times \alpha - 1.110 \times 10^{-3} \times \alpha^2 + 4.197 \times 10^{-5} \times \alpha^3 - 5.825 \times 10^{-7} \times \alpha^4 + 2.85313 \times 10^{-9} \times \alpha^5] + 7.555 \quad (\text{kPa}) \quad (3)$$

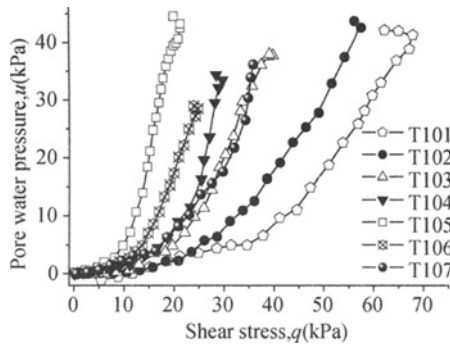


Figure 4. Pore pressure characteristics of T group tests

According to Equation (2) and the values of critical pore water pressure of each test (see Figure 3 and 4), the failure parameter k_f is obtained. It could be seen from Figure 5 that in T group k_f changes with the direction of σ_1 slightly. Since Equation (2) has taken b 's influence into the consideration, the change of k_f mainly reflect the soil's intrinsic anisotropy. In Table 4, the values of R group's k_f are also listed, which are very similar to T106's. The above results of R and T group reveal that the modified Lade-Duncan criterion can be used to reflect the soil's intrinsic anisotropy and generalize the development of pore water pressure during the undrained principal stress rotation.

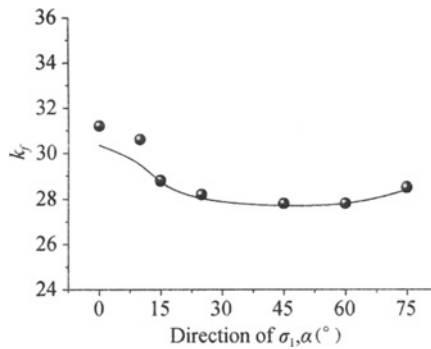


Figure 5. k_r for each sample of T group tests

Symes et al. (1984) did a series of tests and concluded whether the soil had undergone a history of principal stress rotation or not, the critical pore water pressure were similar. It seemed to contradict the phenomena present in this paper. Such “contradiction” can be explained by the generalized plastic mechanics. In the theory of generalized plastic mechanics principal stress rotation even with constant principal stress amplitude such as the rotation stage in R171 and R172, will also generate the increment of principal stress and cause the sample’s volume to have a tendency to change correspondingly. The soil adopted in Symes’s research (1984) was remoulded sand, while in this paper normal consolidated clay was used. The clay showed much more obvious shearing contraction than the sand, so samples in this paper could generate more pore water pressure in the principal stress rotation.

CONCLUSIONS

A series of intact soft clay experiments on the change of principal stress direction had been done. It is revealed that Hangzhou typical intact clay had obvious intrinsic anisotropy in strength, which was not related to the undrained principal stress rotation history. Under the complex stress path including principal stress rotation, the size of failure Mohr’s circle at failure point can be used to evaluate the soil’s strength. While in the effective stress system it is more proper to use a modified Lade-Duncan criterion to evaluate the strength parameter, which could reflect the soil’s intrinsic anisotropy and the development of pore water pressure during the undrained principal stress rotation. These conclusions may be helpful on the evaluation of soil’s strength parameters used in the design of embankment, excavation or some other constructions.

ACKNOWLEDGMENTS

The authors thank financial support for this research from the National Natural Science Foundation of China, Grant No. 50308025 and No. 50639010.

REFERENCES

Arthur J. R. F. Chua K. S. and Dunstan T. (1979). Dense sand weakened by continuous principal stress direction rotation, *Geotechnique*, 29 (1): 91 - 96.

- Han Lin and Dayakar Penumadu(2005). Experiment investigation on principle stress rotation in Kaolin clay, *Journal of Geotechnical and Geoenvironmental Engineering , ASCE*, 131 (5):633-642.
- Hight D.W., Gens A. and Symes M. J. (1983). The development of a new hollow cylinder apparatus for investigating the effects of principal stress rotation in soils, *Geotechnique*, 33 (4): 355-383.
- Sivathayalan S. and Vaid Y. P.(2002). Influence of generalized initial state and principal stress rotation on the undrained response of sands, *Canadian Geotechnical Journal*, 39, 63-76.
- Symes M. J., Gens A. and Hight D. W.(1984). Undrained anisotropy and principal stress rotation, *Geotechnique*, 34 (1): 11-27.
- Symes M. J., Gens A. and Hight D. W.(1988) Drained principal stress rotation in saturated sand, *Geotechnique*, 38 (1): 59-81.
- Wijewickreme D. and Vaid Y. P. (1993). Behavior of loose sand under simultaneous increase in stress ratio and principal stress rotation. *Canadian Geotechnical Journal*, 30, 953-964.
- Zdravkovic L. and Jardine R. J.(2001). The effect on anisotropy of rotating the principal stress axes during consolidation. *Geotechnique*, 51 (1): 69-83.
- Zhou J., Zhang J.L., Shen Y., et al.(2007). Preparation of hollow cylindrical samples of intact soft clay. *Chinese Journal of Geotechnical Engineering*, 29 (4): 618-621.

STUDY AND APPLICATION OF RELIABILITY ANALYSIS METHOD IN OPEN-PIT ROCK SLOPE PROJECT

Bing Sun

*School of Resource and Safety Engineering, Central South University, Changsha 410083;
School of Urban Construction, University of South China, Hengyang 421001, China*

Sheng Zeng

*School of Nuclear Resources and Safety Engineering, University of South China,
Hengyang 421001, China*

Dexin Ding

*School of Resource and Safety Engineering, Central South University, Changsha 410083;
School of Nuclear Resources and Safety Engineering, University of South
China, Hengyang 421001, China*

Because of the uncertainty of the parameters and characteristics of rock joints, this paper performed research in three respects. (1)The contract model of structural planes established by using ABAQUS, and, based on the contract model, the non-linear finite element model for analyzing the stability of rock slope was established. (2) The model between the rock mass mechanics parameters and anti-slide and down-slide forces was built up by using the Adaptive Neuro-Fuzzy Inference System (ANFIS) consisting of artificial neural network and fuzzy logical inference. (3) The program of reliability analysis was compiled by using Monte-Carlo simulation (MCS) and MATLAB, a new reliability analysis method was proposed by coupling ABAQUS, ANFIS and MCS , and the method was used to analyze the reliability of a rock slope. The results show that the contact model of structural planes has great influence on the precise of numerical simulation, that the tangent spring element model could ensure the precision and enhance the convergent efficiency, and that the method could avoid compiling redundant finite element program, reduce the computing time, and improve calculation precision.

INTRODUCTION

Stability analysis of rock slope is a particularly important research area in geo-engineering. The analysis methods can be divided into determinacy analysis method based on safety coefficient and uncertain analysis method based on reliability index. With the knowing of geological parameter uncertainty and studying of geo-engineering influence resulting from environment, research and practice of slope reliability analysis method have made great progress. Especially, a series of achievements have been made on slope reliability research.

For instance, Deng Jian, Liu Ning, et al. have conducted research in this field by using FEM or random FEM. But because of the complexity and uncertainty of rock slope, there are difficulties in studying slope reliability. Therefore, the author, taking the advantages of the FEM which could deal with the nonlinearity of rocks, ANFIS, and Monte-Carlo simulation, established the slope reliability analysis method by coupling ABAQUS ANFIS and MCS, and analyzed the slope stability of an open-pit mine. The results show that the method offers a more rational and more effective approach for the stability analysis and assessment of rock slope.

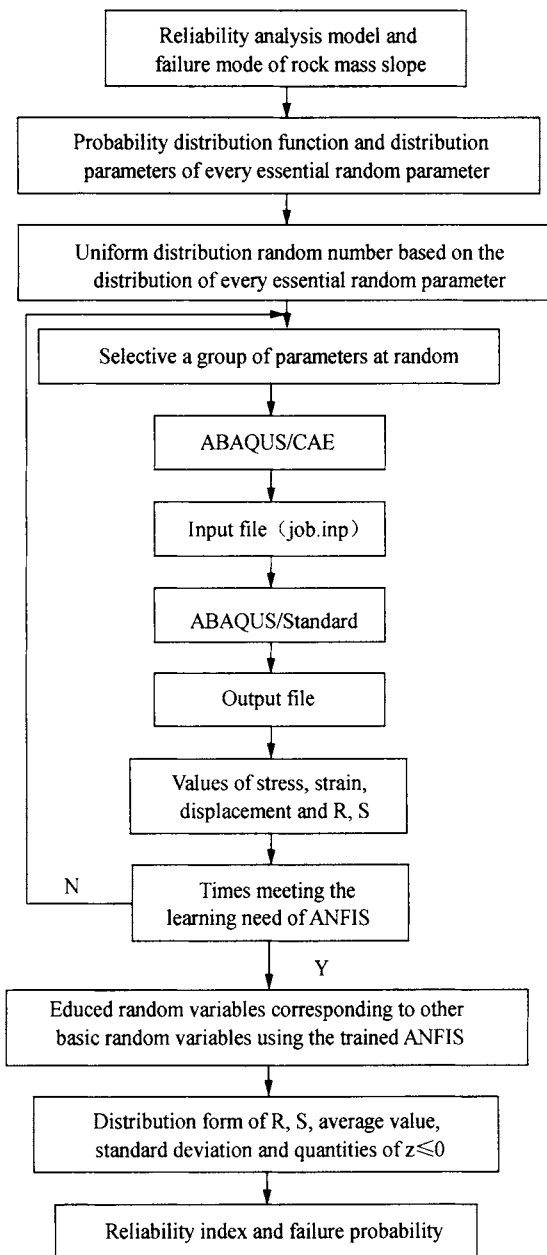


Figure 1. Reliability analysis method based on ABAQUS-ANFIS-MCS

RELIABILITY ANALYSIS METHOD BASED ON ABAQUS-ANFIS-MCS

The FEM is an effective determinacy analysis method which can analyze the structural mechanics effect of complicated project, and MCS can solve random reliability problem. The coupling of FEM and MCS is a new reliability analysis method that is applied extensively. The computational times are very large and computational time is longer by present finite element Monte-Carlo method. However, ANFIS recently becomes effective for reliability analysis of geo-engineering, which is a new type fuzzy inference system with artificial neural network and logic fuzzy inference, different from traditional mathematical modeling and data fitting, and has extremely strong capacity to dynamically handle nonlinearity problem. Artificial neural network can eliminate shortcomings of the traditional finite element Monte-Carlo method and dispose complicated structure reliability analysis and design by random FEM.

This paper proposed a rock mass slope reliability analysis system (Figure1) comprising compiled ANFIS program, MCS code, and the ABAQUS modules to analyze the reliability of rock mass slope project.

Ultimate limit state equation

The basic function that the slope project need satisfaction is stability, namely during the load acting on the slope and after, the slope can still keep integral stability. Therefore, the slope state is regarding utmost state as the criterion of judging failure. In order to make the calculation simple, the ultimate limit state equation is a two-dimensional state composed of independent basic variable R and S :

$$z = g(R, S) = R - S = 0 \quad (1)$$

is known as R - S utmost state model, which represents safe reserve function as the function of anti-slide force (R) and down slide force (S), the utmost state surface is a straight line of 45° .

Contact model of structural planes

ABAQUS is powerful engineering simulation FEM software. It can effectively deal with the non-linear problems of the rock joints and structural planes. In order to accurately simulate the structural planes, based on the software, the surfaces and spring elements that can reflect the behavior of structural planes are defined. The contact problems of the two sides of structural planes, must meet the need of the boundary condition of contact displacement and force in the course of simulation, that is to say, under the interactively compressive action, there are no overlap phenomena along the normal direction, and the value of the normal stress is equal but the direction is opposite. The possible contact forces condition along the tangent direction depends on the adopted friction model, and the classical Coulomb friction principle is adopted.

This paper, based on the contact model and spring elements of ABAQUS, calculated the interaction between the tow sides of structural planes. The constitutive relation of the contact model is defined as follows:

$$P = 0 \quad (h \leq -c) \quad (2a)$$

$$P = \frac{P^0}{e-1} (h_c (e^h - 1)) \quad (h > -c) \quad (2b)$$

where $h_c = h/c + 1$, P is the contact force of the contact pairs, h is the relative sliding of the surface, and when the value of h is 0, the value of P is P^0 . As can be known from the equation, when the contact surface is open, P is 0, and when the contact surface become closer and compressive each other, P increases in exponential function relation. Through reasonable choice of c and P^0 , the smooth-going transition between the opening and closing mechanical behavior of the surface can realize, and the possible embedding depth can be controlled as acceptable micro-value, which can meet the nonlinear computational precision need and can improves convergence rate.

The static and dynamic frictional behavior of the rock interface can be simulated based on linear Coulomb friction principle. In the scope of static friction, the relationship between the shear stress (τ) and shear strain (γ) is linear, when there is sliding, the Coulomb friction ($\tau = \mu P$) can be used. The geometric contact relation and local mechanic behavior of structural planes is complicated. This paper has considered the following presumptions on the constitutive relation between tangent relative displacement and restoring force of the structural planes. ①The shear force is completely transmitted along tangential direction. ②The structural planes are local failure when the shear force is partially transmitted along tangential direction. ③The structural planes is complete failure. The spring elements are arranged along the tangent direction of the jointed and fractured rock masses.

Treatment of sliding zone

Adopting different methods to deal with the sliding problem has obvious influence on the computational result of the stress. Thus, in order to guarantee the computational accuracy, it is very essential to choose the method of treating sliding zone satisfying the case. At present, point to the landslides in different stage and the different sliding characteristics, there are mainly three ways. ①When the thickness of the sliding zone is very thin and landslide has not slipped yet, regarding the sliding zone as boundary element can more really simulates the stress state of the landslide. ②When the thickness is very thin, and the landslide has slowly started slipping, regarding the slipping zone as joint element and contact element can more really simulates the stress state of the landslide. ③When the thickness is thicker, and no matter the landslide is in the state of slipping, the landslide has slowly started sliding, regarding the sliding zone as soft intercalation can more really simulate the stress state of the landslide.

Computation of R、S based on finite element method

Pointing to the characters of the sliding zone and the stage of the sliding slope, the different methods are selected. The stress field of the sliding slope is calculated with ABAQUS. According to the results, the stress ($\sigma_x, \sigma_y, \tau_{xy}$) of the sliding surface can be attained, and the value of R and S can be computed. The concrete computation as follow: ① σ_x, σ_y and τ_{xy} of the sliding surface are obtained through σ_x, σ_y and τ_{xy} of the corresponding elements. When σ_n and τ_s are calculated, there are two conditions (Figure 2). When there are conditions as the former two of 2.3(Figure 2(a)), σ_x, σ_y and τ_{xy} of the sliding surface adopt the average

value($\sigma_x = (\sigma_{xa} + \sigma_{xb})/2$, $\sigma_y = (\sigma_{ya} + \sigma_{yb})/2$, $\tau_{xy} = (\tau_{xya} + \tau_{xyb})/2$)of the adjacent element(element a and b) σ_{xa} , σ_{ya} , τ_{xya} and σ_{xb} , σ_{yb} , τ_{xyb} . When there is conditions as the third of 2.3[Figure2(b)], the corresponding element stresses can approximately substitute. ② σ_n and τ_s of the sliding surface is certain. ③the values of R、 S are attained based on Equation (3).



Figure 2. Slip surface location sketch in element

$$R = \int_0^l (c - \sigma_n \tan \varphi) ds \cdot t \quad (3a)$$

$$S = \int_0^l \tau_s ds \cdot t_s \quad (3b)$$

R-S modeling based on ANFIS

Fcm and subclust function is called to implement its parameter selection options with fuzzy toolbox baon Matlab's clustering graph iteration. It is set up fuzzy inference system model based on sub-clustering, namely, the data modeling based on fuzzy inference system is carried out by genfis2 function of fuzzy logic toolbox after provided semi-diameter. Combined with ANFIS, Sugeno model system will be produced by clustering and grouping information, which can better simulate these input-output data.

Based on ANFIS principle of fuzzy sub-clustering and acquired rock mechanic parameters, input data is made up of elastic modulus, poisson ratio, cohesion force, internal friction coefficient, rock denssed ity, etc., output data is respectively made up of with anti-slide forces R and down-slide forces S, rock mechanic parameters and R or S model is set up respectively by ANFIS, then, reliability index will be gained according to stat. characteristic of R or S model research. Its trained ANFIS structure and fuzzy rule graph as follows: Figure 3.

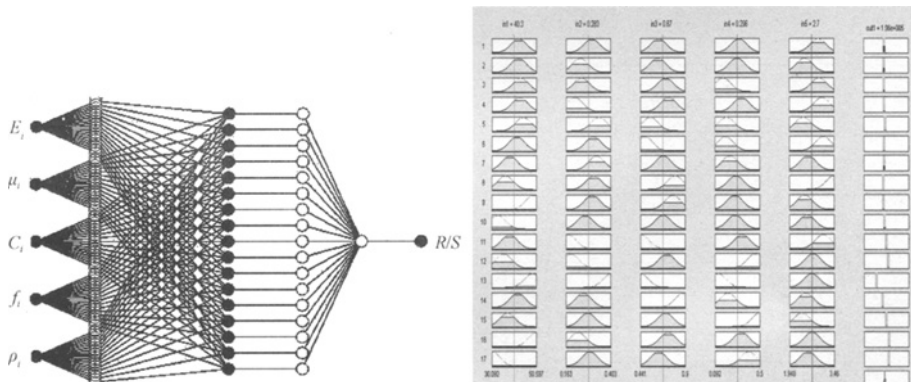


Figure 3. ANFIS architecture for R/S-ANFIS and fuzzy rule

Failure probability and solution of reliability

According to previous related literatures (Duan N., 2002), adopting MCS to study failure probability of random events, the simulation times (N) should be greater than 5000, so

N adopts 10000 in this paper. Based on the distribution of rock mechanic parameters and the mean value and standard deviation, 10,000 groups of data are produced as input data, and then R、S arrays are obtained according to model-R-ANFIS and model-S-ANFIS. Analysis gets the statistics values of R and S. m is the times when the value of Equation (1) is smaller than zero is acquired. Finally, the failure probability and reliability index is respectively attained according to Equation. (4).

$$p_f = \frac{m}{N} \quad (4a)$$

$$\beta = \frac{\mu_R - \mu_S}{\sqrt{\sigma_R^2 + \sigma_S^2}} \quad (4b)$$

In the above equation: N is 10000, m is failure times, μ_R , μ_S is the mean value of R 、 S , and σ_R , σ_S is the standard deviation of R 、 S .

EXAMPLE OF APPLICATION

The example is concerned with a sandstone Open-Pit rock mine and located in Lou Di city, China. This mine has been mined on 320m, 300m and 280m three platforms, forming 60m high slope which is a typical multi-sliding-face bedding rock slope. By way of the actual survey and investigation of structural planes, the geometry parameters of the slope are shown in Figure 4. Dip direction is SW170°, dip angle is 46°, height of bench is 20m, slope angle is 70°. The slope has three lamina unfavorable structural planes built-up weak inter-layers which are combined with inorganic silt mudstone, attitude is NW263°/SW∠35°, thickness is 1~4cm, so it maybe slip along these weak structural planes. Through rock mechanics parameter experiment and analysis of the weak interlayer and rock mass of the slope, and then deal with the parameters based on strength reduction method, the parameters needed by finite element method are shown in Table 1. The rock mechanics parameters accord with normal distribution. With ABAQUS, the finite element model of the slope is developed and shown in Figure 5.

Table 1. Parameters of the first slope for finite element analysis.

		Compressive strength (MPa)	Young's modulus (GPa)	Poisson ratio	Friction coefficient	Cohesive force (MPa)	density (g/cm ³)
Interlayer I	Mean value	10.86	6.00	0.214	0.718	0.056	2.253
	Standard deviation	1.05	0.17	0.041	0.103	0.003	0.224
Interlayer II	Mean value	11.35	7.12	0.211	0.701	0.057	2.214
	Standard deviation	1.24	0.19	0.039	0.101	0.004	0.205
Interlayer III	Mean value	10.58	6.85	0.256	0.726	0.058	2.461
	Standard deviation	1.18	0.20	0.046	0.098	0.003	0.286
sandstone	Mean value	42.56	6438.2	0.306	0.902	0.179	2.642
	Standard deviation	4.03	204.3	0.062	0.124	0.014	0.324

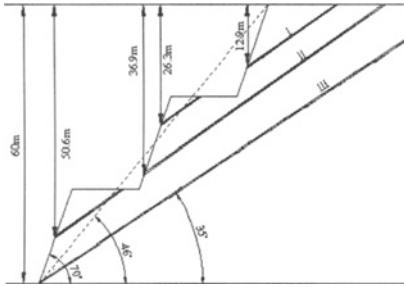


Figure 4. Geometry dimensional of slope

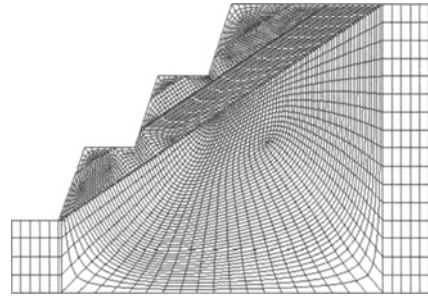


Figure 5. Calculation meshes of FEM

According to the reliability analysis method of this paper, the failure probabilities and reliability indexes of the slope are shown in Table 2.

Table 2. Failure probabilities and reliability indexes of the slope

Slip surface	Failure probabilities (%)	Reliability index
slip surface I of the first bench	0.156	2.962
slip surface I of the second bench	0.004	4.011
slip surface II of the second bench	0.491	2.573
slip surface II of the third bench	0.006	3.924
slip surface III of the third bench	1.018	2.257

Regarding open-pit slope, there is no unification reliability index standard at present. The open-pit mine slope stability assessment only can profit from the correlation structural engineering and the predecessor experience, the acceptable value of slope failure probability and reliability index can be determined by this. According to the mine slope security index (Wang S.W., 2004), the suggested index of the rock mine slope is 3.2–3.5 to the vital slope, 2.2–2.5 to the secondary slope, 1.6–2.0 to the general slope. Based on computational conclusions, the slope of the example is stable, which agrees with the fact.

CONCLUSIONS

(1) The ABAQUS finite element analysis software has powerful functions to process the contact non-linear problem. The tangent spring element model can be used to simulate the structural planes of rock mass, and enhance the precision and convergent efficiency of computation.

(2) The study of the ANFIS-based model for the solution of anti-slide and down-slide forces shows that the ANFIS-based approach for the uncertainty analysis has great potential use in research on the reliability of rock slopes.

(3) The ABAQUS-ANFIS-MCS reliability analysis approach formulated by coupling FEM, ANFIS and MCS can be used to analyze and assess the stability of rock slope.

(4) This paper proposed a new approach for analyzing the reliability of rock slope. The approach can be used to conduct the reliability studies of other slopes.

REFERENCES

- Li, T.L., Wang, Y.X. and Deng, H.K. (2003). An improved method for three-dimensional slope stability analysis, *Chinese Journal of Geotechnical Engineering*, 25 (5): 611-614.
- Zhang G.X., Liu B.C. (2003). Analysis of slope slip surface by three-dimension finite element method, *China Journal of Highway and Transport*, 16 (4): 27-29.
- Li L., Liu B.C. (2001). Lower bound limit analysis on bearing capacity of slope and its reliability, *Chinese Journal of Rock Mechanics and Engineering*, 20 (4): 508-513.
- Yan L.X., Kang H.P. and Gao Q. (2001). Reliability analysis based on response surface function and its application in a chamber, *Rock and Soil Mechanics*, 22 (3): 327-333.
- Jia H.H., He H.J. (2003). Analysis of fuzzy-random reliability of slope stability, *Rock and Soil Mechanics*, 24 (4): 657-660.
- Deng J., Li X.B. and Gu D.S. (2002). Reliability analysis on pillar structure using a new Monte-Carlo finite element method, *Chinese Journal of Rock Mechanics and Engineering*, 21 (4): 459-465.
- Duan N., Xue H.M. and Pan Y. (2002). A method for determining the number realizations in the calculation of reliability by Monte Carlo simulation method, *Journal of coal machinery*, 3 (3): 13-14.
- Wang S.W., Liu H.D. and Wan L.H. (2004). Research of standard of pit slope, *Journal of North China Institute of Water Conservancy and Hydroelectric Power*, 25 (1): 54-57.

THE APPLICATION OF FUZZY EVALUATION ON DETERMINATION OF A SLOPE IN A DAM REGION

Dongfang Tian

*School of Water Resources and Hydropower, Wuhan University, Wuhan 430072;
Hydroelectric and Civil Engineering College, China Three Gorges University,
Yichang 443002, china*

Yisi Zhuge

School of Water Resources and Hydropower, Wuhan University, Wuhan 430072, China

The stability of a slope in a dam region will be affected by atomization water flow of the dam. The intensity and distribution of atomization water flow is necessary to evaluate the slope stability. So it is very important to determine the intensity and distribution of atomization water flow. In this paper the fuzzy evaluation is used to determine the intensity and distribution of atomization water flow in a slope which is adjacent of a dam. Furthermore, the results of different fuzzy operators are compared, some conclusion is presented. It shows that the intensity is all the same no matter which fuzzy operator is choose, where the distribution is related to the fuzzy operator closely.

INTRODUCTION

Atomization Water Flow (Liang zaichao 2000) is intensive fog rain when a hydro junction discharges flood. Usually the higher the head of the dam and more large of the flux is, the fog rain is more intensive and affect area is more large. Atomization Water Flow is not only dangerous to the dam, but also decreases the slope safety around the dam. One of the examples is Hu Shan landslide, of which the volume is several millions. The landslide slides when Long Yang Xia hydro junction discharges the flood (Li Zan, 2001).

The intensity and extent of the Atomization Water Flow directly affect the slope safety when a dam discharges flood. So it is very important to define the intensity and distribution of the fog rain when a high dam discharges. But the mechanics and affect factors are very complex of the Atomization Water Flow, it is difficult to confirm its intensity and distribution accurately. The fuzzy evaluation is used to define the intensity and distribution of a landslide in a dam region in this paper. Furthermore, a discussion that effect of three fuzzy operators to the results is put forward.

BASIC THEORY OF FUZZY EVALUATION

Fuzzy evaluation is used in fuzzy environment. It considers muti-factors, makes a general conclusion based on an aim to an object. It contains six basic element factors (Wang Huan

ling 2006) as followings: ①evaluation domain, U ; ②graded comment domain, V ; ③fuzzy relation matrix, R ; ④valuation factors weights vector, A ; ⑤composite operator, “o”; ⑥evaluation vector, B .

Set $U=\{u_1, u_2, \dots, u_n\}$ as a collection of n factors, named factor collection. Factor is the attribute of a object, also called quality index in different area. They reflect the quality of a object. Set $V=\{v_1, v_2, \dots, v_m\}$ as a collection of m conclusions, named conclusion collection. Evaluation vector B would be got at the end of the Fuzzy evaluation, the vector reflects the subjection to V of the object, and it also shows the fuzzy character of fuzzy evaluation.

Usually, the influence of every factor is not the same, so the weight distribution of factors could be seen as a fuzzy collection on domain U , named ad $A=\{a_1, a_2, \dots, a_n\} \in F(U)$, where a_i means the weight of factor u_i , they meet the equation $\sum a_i = 1$. Furthermore, evaluation vector B is not absolutely true or false, and they could be seen as a fuzzy collection of domain V , named as $B, B = \{b_1, b_2, \dots, b_m\} \in F(V)$.

Assume $R=(R)n \times m, E \in M n \times m$ is a fuzzy relation between U and V , then using R we could make a change. So this is the fuzzy evaluation model.

In one word, fuzzy evaluation has three main essential: A, R , and B , just likes a converter, if inputs A , then output $B=A \circ R$, where \circ is fuzzy operator. It always has three kind algorithms:

(1) OP1:

$$b_j = \bigvee_{i=1}^n (a_i \wedge r_{ij}).$$

where $j=1, 2, \dots, n$; \vee and \wedge called lattice operation, means gets the maximum and minimum.

(2) OP2:

$$b_j = \bigoplus_{i=1}^n (a_i \times r_{ij}).$$

where $j=1, 2, \dots, n$, \oplus means $a \oplus b = (a + b) \wedge 1$.

(3) OP3: multiple, it means

$$b_j = \sum_{i=1}^n (a_i \times r_{ij}).$$

When B is defined, the general result could be defined according to a special algorithm such as maximum degree of membership.

DEFINITION OF THE FUZZY EVALUATION MODEL OF ATOMIZATION WATER FLOW

The physic process of atomization water flow is very complex, and it relates to many factors such as hydra condition, boundary condition, meteorology condition, landform condition etc. So the intensity of atomization water flow at one point could be described as:

$$S = f(Q, H, \alpha, \beta, \beta_1, \beta_2, x, y, x) \tag{1}$$

where, Q is discharge of the dam; H is the head; α is height difference of the surface of upper reaches and lower reaches; β is the coefficient of landform factor; β_1 is boundary condition coefficient of pick outflow; β_2 is coefficient of meteorology condition; x, y, z is the coordinate of the point in the coordinate system which the origin is the point that water tongue comes into the surface, and x axis is water flow direction, z is vertical direction.

The model is very complex if it considers all the factors, so many simplified models are put forward. If $\alpha, \beta, \beta_1, \beta_2$ is ignored, sets $k=\alpha/H, \xi=x/H, \zeta=y/H, \eta=z/H$. Equation (1) could be rewritten as:

$$S = f(Q, H, k, \xi, \zeta, \eta) \quad (2)$$

In this condition A is $\{Q, H, k, \xi, \zeta, \eta\}$ in the model. Because the weights of factors are difficult to define, the evaluation splits into two steps, firstly evaluates the special intensity in some special points, such as the middle of a slope, collection A is $\{Q, H, k\}$; secondly, defines the distribution of the atomization water flow, A collection is $\{\xi, \zeta, \eta\}$.

DISCUSSION OF APPLICATION

Spillway disposed at left bank of the dam in a hydra junction, consisted of four parts: diversion canal, overflow dam, discharge slot and pool. The altitude of spillway is 200~400 m, and the energy dissipation is ski-jump method.

The landform and geology condition are very complex, and the river is kind of the rivers in mountainous, so the flux is very large. According to the design, reservoir income of the design flood once in 10000 years is $Q=24400\text{m}^3/\text{s}$, and the flood discharge is $18440\text{m}^3/\text{s}$, and the head would be 171m. 1 km from the dam, there is a landslide. In order to define the safety of the landslide, the intensity and distribution of atomization water flow must be confirmed. These could be calculated as followed.

Fuzzy evaluation of the special intensity of the slope

(1) The determination of judge grade, weights, and membership function S°, Q, H, k could be allocated to 7 levels as Table 1 shows.

Table 1. Grade allocation of S°, Q, H, k

level	1	2	3	4	5	6	7
S° (mm/h)	1100	950	800	650	500	350	200
Q (m^3/h)	18000	16000	13000	10000	6000	2000	500
H (m)	270	230	190	150	110	70	30
k	0.6	0.55	0.5	0.4	0.3	0.2	0.1

The determination of weights and membership function are according to lots of examples such as the intensity and distribution of atomization water flow in similar dam regions. The value and functions are listed in Table 2.

Table 2. The Weights and functions of Q, H, k

Factor	Weight	Membership function
Q	0.42	$\mu(Q)=\exp(-2.8e-7)(Q-Q_i)^2$ ($i=1,2,\dots,7$)
H	0.33	$\mu(H)=\exp(-3.7e-4)(H-H_i)^2$ ($i=1,2,\dots,7$)
k	0.25	$\mu(k)=\exp(-50(k-k_i)^2)$ ($i=1,2,\dots,7$)

(2) Fuzzy operators and result analysis.

According to the membership functions in Table 2, fuzzy relation matrix R could be calculated, then by equation $B=A \circ R$, B vector could be deduced. This paper uses 3 different fuzzy operators in chapter 2 to evaluate the atomization water flow. And the results are listed in Table 3.

Table 3. Compare of B vector using different fuzzy operators

Operators	B vector						
OP1	1.77E-1	1.64E-1	1.64E-1	1.64E-1	1.14E-1	1.14E-1	1.04E-1
OP2	3.84E-1	8.39E-3	2.97E-2	1.76E-1	1.84E-3	3.08E-1	9.11E-2
OP3	2.30E-1	1.84E-1	1.90E-1	1.28E-1	1.35E-1	1.02E-1	3.01E-2

It can be seen from Table 3 that B vectors are the same basically, and the value is 1100mm/h.

Fuzzy evaluation of distribution of the atomization water flow

(1) The method to determinate the distribution of atomization water flow.

In the condition of ascertain $\{Q, H, k\}$, the special intensity S_0 could be confirmed in last segment. The distribution in a slope could be substituted by several points, and the value could be interpolated linearly between two points. If the problem considered is planer, a profile along the sliding direction can be selected, as Figure 1 shows. The intensity at these points can be calculated. The larger the grade is, the more points should be set. The intensity of a point follows equation $S = f\{\xi, \zeta, \eta\}$.

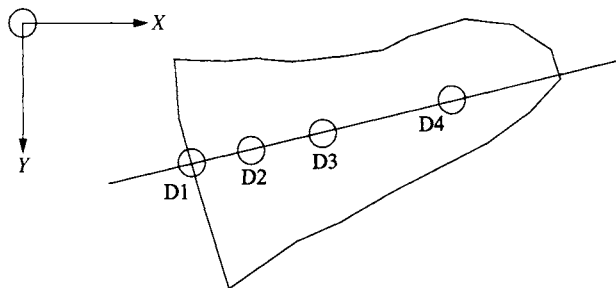


Figure 1. The distribution of calculating points on a slope diagram

(2) The determination of judge grade, weights, and membership functions

The evaluating procedures are same. Judge grade and membership functions are listed in Tables 4 and 5.

Table 4. The grades of S , ξ , ζ , η

Level	1	2	3	4	5	6	7
S (mm/h)	$S \geq S_0$	$S_0 > S$ $\geq \frac{1}{2} S_0$	$\frac{1}{2} S_0 > S$ $\geq \frac{1}{10} S_0$	$\frac{1}{10} S_0 > S$ $\geq \frac{1}{50} S_0$	$\frac{1}{50} S_0 > S$ $\geq \frac{1}{100} S_0$	$\frac{1}{100} S_0 > S$ $\geq \frac{1}{500} S_0$	$\frac{1}{500} S_0$ $> S$
ξ	0.5	0.7	1.0	1.5	2.2	3.2	4.5
ζ	0.3	0.5	0.75	1.05	1.4	1.85	2.35
η	0.1	0.15	0.25	0.35	0.5	0.7	1.0

Table 5. Membership functions and weights

Factors	Weights	Membership functions
ξ	0.32	$\mu(\xi) = \exp(-4.5(\xi - \xi_i)^2)$ ($i=1, 2, \dots, 7$)
ζ	0.35	$M(\zeta) = \exp(-7.0(\zeta - \zeta_i)^2)$ ($i=1, 2, \dots, 7$)
η	0.33	$M(\eta) = \exp(-50(\eta - \eta_i)^2)$ ($i=1, 2, \dots, 7$)

(3) Fuzzy operators and result analysis.

Three kinds of operators in last segment are selected, and the results are listed in Table 6.

Table 6. The intensity of several points.

Point \ Operator	D1 (mm/h)	D2 (mm/h)	D3 (mm/h)	D4 (mm/h)
OP1	550	550	550	550
OP2	1100	110	11	1.1
OP3	550	110	550	110

It can be seen from Table 6, the distribution are different calculated by 3 kinds of operators. Operator OP2 is more practical. This is mainly because the factors weights are similar, OP1 abandons lots information, while OP3 considers lots of unnecessary information.

In last segment, because the factor weights are different, the results are similar. It shows that Q is the most important factor to the intensity.

CONCLUSIONS

Fuzzy evaluation is applied to determinate the intensity and distribution of atomization water flow in a dam region in this paper, and the intensity and distribution of a landslide in a hydra junction region is analysis. This is the basic information to evaluate its safety. The main content concludes:

(1) calculating the intensity and distribution on a profile of a landslide in a dam region.

(2) comparing the difference of the results determined by three different fuzzy operators, and explains the reason of the difference. It shows that OP2 is more capable to evaluate the atomization water flow.

Different treatment to Vector B would deduce different conclusion, too. In this paper, maximum degree of membership principle is considered only, there are many different principles need advanced discussion.

REFERENCES

- Liang Zaichao (2000). Study in a deep going way of water discharge atomized flow for Xiao Wan Hydropower Project, *Yun Nan Water Power*, (2): 28-32.
- Li Zan (2001). On landslide induced by water-fog from ski-jump energy dissipation of Long Yang xia Hydropower Station. *Large Dam and Safety*, (3): 17-20.
- Wang Huanling (2006). Stability Study on Saturated-Unsaturated Fracture Rock Slope under Atomized Rain of High Dam, 1-10, 35-50.
- Xiao Xingbin (2004). Review of studies and application of hydraulic design of discharge and energy dissipation for high arch dams, *Advance in Science and Technology of Water Resources*, 20 (2): 19-23.
- Zhang Hua etc.(2003). Numerical calculation of overflow atomization for Wan Tang Hydropower Station, *Journal of Hydraulic Engineering*, (4): 8-14.
- Jin Lu.(1989). *Applied Fuzzy Mathematics*, Scientific and Technical Literature Press, 179-227.

STUDY ON DAMAGE STYLE OF OVER-ERECTION WHARF IN INLAND RIVER

Duoyin Wang^{1,2}, Chengzhi Wang^{1,2} and Ying Nie²

Chongqing Jiaotong University, Chongqing, 400074, China

Institute of Geotechnical Eng. Dalian Univ. of Technology, Dalian 116085, China

Horizontal bearing properties of pile must be considered, in the interaction between the foundation and bank of the over-erection wharf, thus a large-scale room model experiment was carried to study the transversal bearing capacity of the large diameter pile, testing the mechanical properties of the pile and bedrock in the condition of different horizontal load and rock lapel-width. Afterwards, based on the room model test, a numerical was carried, through massively changing the parameter of the soil, to research the change regulation of plastic area of the embedded-rock pile. This paper proposes the change in the plastic degradation processes and the method for determine reasonable embedded-depth of the rock-socked pile.

INTRODUCITON

The structures used in the inner river are varieties, while because of large diameter rock-socked pile with lot of advantage, such as bearing large load, resisting the impact of large ship, wind and earthquake, it is increasing concerned by engineering. At present, many researches have been done on the large diameter rock-socketed pile, however, these mainly concentrated on vertical bearing capacity and closed associated with local soil characters, hydrological conditions. So those result lack of the value of widely used. The large diameter rock-socketed piles used in river port have many of own features: steep slope, rock beds alternate and there may be weak interbed and bear transversal load and moment caused by ship stop, moor and wind, wave even earthquake.

Now, with the implement of the western development strategy, inland ports rapidly develop, container transportation volume soar, the overhead-erection wharf, completely made up by vertical piles, gets more and more attention form engineering. It is necessary to study the rock-socketed pile through failure model test, in which below w conditions must be considered, complex loads, rock structure, and engineering geological and hydrological conditions.

Sample preparation and introduction of testing equipment

The large diameter rock-socketed piles, in Cuntan wharf, were embedded in the Jurassic Shaximiao Formation (J2s), that is interbedded by mudstone and sandstone. The stone is mainly made up by clay mineral; some parts have a number of sand; layers of the structure are thick. In strong weathered layer, whose thickness is 0.60~3.8m, crack develop, core takes

up block; as for medium weathered layer, rock is more completed and hard, core is in the cylindrical shape. The standard value of saturated compressive strength of mudstone and sandstone are 4.2MPa and 16.9MPa respectively, according to reference, mudstone belong to very soft rock, while sandstone belong to soft rock. Through the geophysical well survey, obtain the integrity sonic index of medium weathered mudstone and sandstone: mudstone 0.51-0.84, sandstone 0.56-0.79, both mudstone and sandstone are more integral. Medium weathered mudstone and sandstone basic quality grading are V、IV category.

Medium weathered mudstone and sandstone were proposed as the fixed rock by the reconnaissance unit, the mechanical parameters of them is shown in Table 1.

Table 1. Mechanical parameters of rock

Style of stone	Natural unit weight (kN·m ⁻³)	Cohesive (kPa)	Internal friction angle (°)	Nature standard value of compressive strength (MPa)	saturated standard value of compressive strength (MPa)
Moderate Weathered Mudstone	25.4	316	32	7.5	4.2
Moderate Weathered Sandstone	24.5	690	34	23.6	16.9

Indoor model test

The prototype is the pile foundation used for vertical-face high pile wharf bears not only vertical loads, but also ship impact whose maximum approximate to 1000kN. Front piles' diameter is 2200mm and the others is 1800mm. Based on the prototype, in the model, piles diameter, $D=1800\text{mm}$, C30 concrete of piles, compressive modulus of elasticity, $E_c=30\text{ GPa}$.

Material of the model pile

Considering several factors, such as the test site, loading equipment and loading modulus, we chose the geometric ratio of the model is 20 ($\lambda_L = 20$). The modulus of the prototype (C30 concrete) is 30 GPa ($E_{\text{pile, P}}=30\text{ GPa}$), the modulus of the prototype rock (mudstone) is 0.2~0.7 GPa ($E_{\text{rock, P}}=0.2\sim 7\text{ GPa}$), and the concentrated loading of the prototype is 1000 kN ($F=1000\text{ kN}$). Some conclusions in the reference, we chose plexiglass for the model pile's material by comprehensive comprising.

Material of the model rock

In the room model test, we simulate the modulus of mudstone in the range of 0.2 to 7 GPa. Considering the characters of the prototype rock (soft rock), blend fine sand and a certain dose of gypsum does as material of the prototype rock.

Based on the above analysis, the modulus ratio feet of this model test is 10 ($\lambda_E = 10$), according the mechanical similarity of the piles and rocks structural system ($E_{\text{pile, P}}/E_{\text{rock, P}} = E_{\text{pile, M}}/E_{\text{rock, M}}$), the strain scale of piles ($\lambda_\epsilon = 1$) and the similar relationship of concentrated (Equation. 3), the critical load H_{cr} and the ultimate load H_u of

the prototype piles and rocks structural system can be obtained (as shown in Table 2. Conditions of the simulation model in Table 3).

Table 2. The critical load and bearing capacity of the test

	Model pile	Prototype pile	Introduction
Critical load H_{er}	180N	720kN	Model pile's diameter is 90mm, Prototype pile's diameter is 1800mm, geometrical $\lambda_L = 20$
Displacement of the embedded rock on surface when bearded critical load (mm)	a	a multiplied by 20	
Ultimate load H_u	420N	1680kN	
Displacement of the embedded rock on surface when bearded ultimate load (mm)	b	b multiplied by 20	

Table 3. The working conditions for tests

Transversal load	Nine steps loading, $\leq 54 \times 9.8$ kN			
Simulate conditions	First condition	Second condition	Third condition	Forth condition
Embedded rock's surface	Horizontal	Incline, angle with the vertical is 40°		
Fixed depth (cm)	45	45	45	45
lapel-width (cm)	-	15	12	9
Pile's number	1	1	1	1

Finite element analysis parameter choice and the model verification

The numerical analysis model's geometrical slope was shown in Figure 1; numerical model is established according the large-diameter rock-socketted piles structure in Cuntan wharf. In the Figure 1, H_2 is the pile-fixed depth; L is the lapel-width which is the clear spacing between the slope edge and the piles. L is the slope inclined angle. In the analysis, adapt 3D element to divide the piles and rocks structure (CPS8, C3D20, C3D4 and C3D10). In the numerical analysis the related parameters of the rock block and joint, as shown in Table 2.

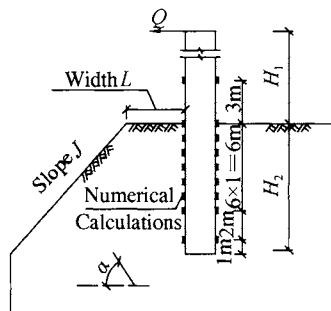


Figure1. The geometrical size of the numerical simulation test

In finite element analysis, model pile: elastic modulus is 3.12 GPa, Poisson' ratio is 0.36, model rock elastic modulus is 0.038 GPa, Poisson' ratio is 0.18.

In the elastic-plastic finite analysis, according the experimentally-measured date and the reference used the Von Miss Yield criterion for the rock. Through repeated trial, we found that the analysis result keep stable and is same to the experimentally-measured result, when the element total reach to 21000–22000,

Through a comparative analysis (As Figure 3), that between the numerical analysis and the result of the room model test, found them almost coinciding, this proved that the numerical model is feasibility and reliability.

As secant modulus of rock in the range of 0.02–07 GPa (equivalent to the range of the prototype modulus is 0.27–7 GPa), Poisson's ratio is 0.18. In order to facilitate to analysis, in the blowing analysis, use the size of the modulus coefficient k to reflect the change of the rock modulus, while defined: $k = E_i / E_0$, in which, E_i : the secant modulus of lock in analysis; E_0 : the secant modulus corresponding to stress equivalent to 0.5times uniaxial compressive stress, which in the stress-strain curve of rock samples uniaxial compressive test, in analysis $E_0 = 0.98$ GPa.

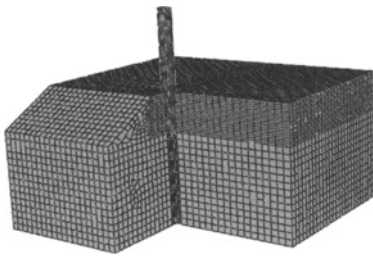


Figure 2. The finite element computational model and mesh condition

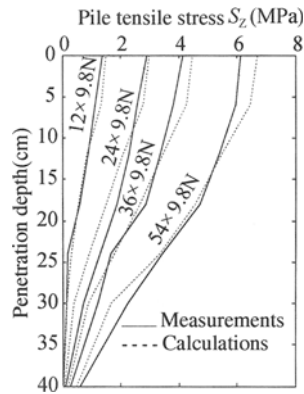


Figure 3. The comparative analysis the numerical analysis and indoor test

Test result

The inbuilt distance affects transversal bearing capacities

This research assumed the lapel-width $L=0.10$ m, the modulus coefficient $k=0.4$, the slope $J=0$. In the given condition, inbuilt distance decreased from $3D$ 、 $2.5D$ 、 $2D$ 、 D to $0.67D$ gradually. From the comparison of numerical analysis result we can found that, with the embedment depth decreasing, displacement curves and stress curves become steep. And when the inbuilt depth is in $H_2=1.8$ m, the displacement curve of the pile is almost a straight line. The stress curve has the similar shape. In the area of the inbuilt depth lower than 1.8 m, the inbuilt depth has little effect on the displacement of the pile.

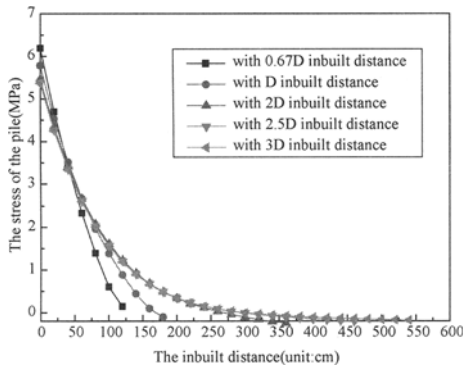


Figure 4. The stress of the pile with different inbuilt distance

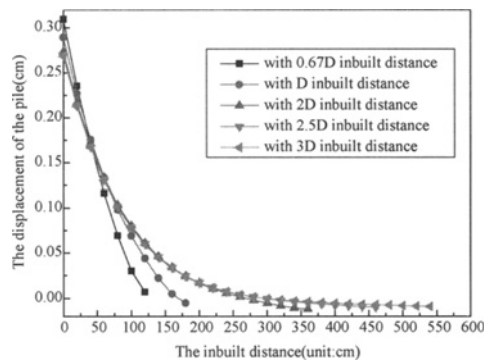


Figure 5. The displacement of the pile with different inbuilt distance

Additionally, when the inbuilt distance was deeper than 1.8m, the displacement on the top of the embedment rock will increase. When the inbuilt depth was deeper than 1.8m, the zero displacement point disappears, and the bottom displacement of the pile becomes greater. The changes of the maximum stresses are very small in all the five depth of the pile.

In the former four inbuilt depth, the plastic zone just limited to the scope of the top area of the embedment rock. However when the inbuilt depth was 1.8 m, 70% loads were loaded, the depth of the plastic zone achieves at the bottom of the pile.

The result also shows that although the maximum displacement of the pile is less than 0.4mm (<<6mm or 2mm the standard displacement of the pile), the maximum stress has reached nearly 0.7 MP. Therefore this phenomenon shows that when the rock-socketted pile damaged under the Horizontal load, its top displacement isn't always big enough.

The degeneration of the rock plastic

Through the elastic and plastic analysis, the result shows that the inbuilt distance is important. Increasing the inbuilt distance will result in the degeneration of the rock plastic, when the horizontal load, the rock and the pile modulus are given.

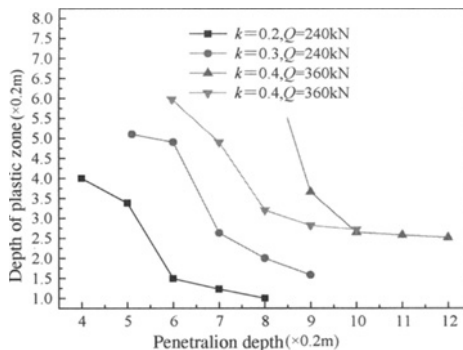


Figure 6. The degeneration curve of plastic zone

This paper analyze the interrelation between the inbuilt distance of the pile and the plastic depth of the surrounding rock under two different given loads—240 kN, 360 kN. In the Figure 6, the first, second, third curves all corresponding horizontal load

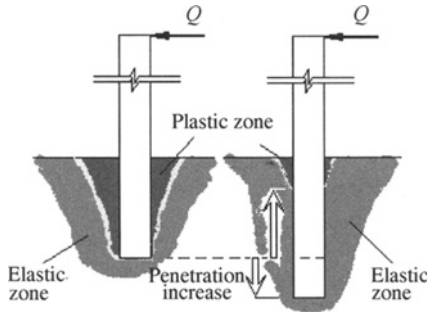


Figure 7. The processes of plastic zone degenerated

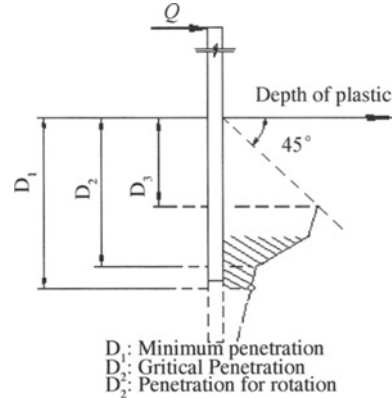


Figure 8. The reasonable inbuilt depth

$Q=240\text{KN}$, but rock modulus are various— $k=0.2, 0.3, 0.4$ respectively. The forth curve corresponding $Q=360, K=0.4$. From the analysis we can get conclusion involves:

- (1) Increasing the inbuilt distance leads to a significant reduction of the plastic depth. Beside, with the increasing of the rock modulus the radio of the degeneration increases.
- (2) The curves show anti-s-shaped. Every curve has two characteristic-points. One point corresponding the inbuilt depth of the pile equals the plastic depth; another point corresponding the s-shaped curve-bending point, which after it despite the inbuilt distance of the pile increase, but the radio of the plastic depth of the rock reduce obviously.

Form the analysis, we can draw conclusions as follow when given the horizontal and pile-rock structure, the inbuilt depth affects the development of the rock plastic depth. Meanwhile there are two characteristic-points which have explicit physical properties.

Minimum embedment depth and critical embedment depth considered.

Based on the above analysis ,we can found that there were two characteristic point in the curve—which illustrated the interrelation between the embedment depth of the pile and the plastic depth of the surrounding rock. One point corresponding s-shaped curve-bending point. After this point, with the embedment depth increase, the degeneration rate of the plastic zone has started to slow.

To facilitate future analyses, we get agreement that: the depth of the first characteristic-point corresponding as the minimum embedment depth. It is the depth that all the surrounding rock went to plastic state in the give condition such as load and geometry; the depth of the second characteristic-point corresponding as the critical inbuilt depth. After this depth the inbuilt distance increases while the economy decreases.

With the inbuilt depth increasing, the depth of plastic zone degenerating. The change trends are illustrated in Figure 6 and Figure 7. From the above analysis, to ensure the fixed condition and raise the economics, the inbuilt distance should be deeper than the minimum

inbuilt distance. Through the numerical analysis of statistics, the ratio of minimum inbuilt distance to critical inbuilt distance is 1.3–1.6.

The “revolving point” in the displacement distribution curve is under the critical inbuilt distance. This result shows that the reasonable inbuilt distance should be choose in the shadow area.

CONCLUSIONS

These analyses of the indoor tests got the following major conclusions:

1. When the horizontal load and rock structure are under certain conditions, the depth of pile-embedment increasing or decreasing impacts on the rock plastic development.

2. Horizontal load and rock modulus significantly affect the changes and the distributions of the displacement and the stress of the piles. The loads positions affect the displacement and stress changes too. For that, the application of the transverse brace will improve the bearing capacity of the pile.

REFERENCES

- Coyle H. M, Reese L. C. (1996). Load transfer for axially loaded piles in clay. *J.S.M.F.D., ASCE*, 92(2): 1-261.
- Holoway D. M. (1982). Load Response of a Pile Group in Sand, *2nd International Conf. on Numerical Methods in Offshore Piling*.
- Hu Qingli, Zhang Kexu. (2002). Research on axial bearing behavior of large diameter piles. *Chinese Journal of Geotechnical Engineering*, 24(4): 491–495.
- Lou Xiaoming, Yu You wei, et al. (2002). Study on the bearing properties of bored piles’ abnormal behavior, *Chinese Journal of Geotechnical Engineering*, 24(4): 491-495.
- Poulos H.G., Davis E.H. (1980). *Pile Foundation Analysis and Design*, Jone Wiley and Sons.
- Wang Duo yin, Lan Chao, et al. (2007). Researches on lateral support behavior of large diameter rock-socketed cast-in-place piles at river port by laboratory model test, *Chinese Journal of Geotechnical Engineering*, 29(9).
- Xu Youzai. (1999). *Manual of the Pile Test*. Beijing: China Water Power Press.
- Zhang Yaonian, Gong Yiming, Liu Chun. (1994). The Transfer Performance of large diameter pile in fuzhou area, *Chinese Journal of Geotechnical Engineering*, 16(4): 32-39.

INVESTIGATION ON THE NANJING GYPSUM MINE FLOODING

Guangya Wang

ACEI, Department of Geoscience, Nanjing University

Nanjing 210093, China;

Jiangsu Provincial Geological Survey Institute

Nanjing 210018, China

Guanlin You

School of Science and Engineering, University of Ballarat

Ballarat 3353, Australia

Yulin Xu

Jiangsu Provincial Geological Survey Institute

Nanjing 210018, China

Nanjing Gypsum Mine, or NGM, is encountering some engineering challenges in deep underground mining. The major challenges that affect the underground mine geomechanics and geoenvironment are attributed to groundwater, rock properties and geological structures, such as faults. A catastrophic mine flooding, triggered at NGM on 11 Sept. 2006, inundated the entire underground mine. The causes of this geological disaster are found multifold: hydrogeologically, the water-bearing karst rock overlain the orebody, the south of which was the direct water source of the catastrophic flooding; geomechanically, the low strength of the soft rock and the redistribution of mining induced stresses jeopardized the insitu balance and activated the discontinuities; and operationally, the inappropriate mining operation deteriorated the safety pillar and the ineffective seepage sealing method wasted the time for an effective measure to avoid the catastrophe. The mine flooding not only altered the underground hydrogeology, but also caused ground subsidence, damaged the surface structures and properties in the mine and its vicinity.

INTRODUCTION

Gypsum, mainly used in cements, ceramics, wallboards and plasters is one of the minerals available around the world. The USA is the largest producer of gypsum in the world; there are 48 gypsum mines distributed in 20 states in USA in Jan. 2006. Other countries with large gypsum productions, in descending order, are Iran, Canada, Thailand, China, Spain, Mexico, Japan and Australia (Founie et al., 2006). China is the 5th largest gypsum producer with a total reserve in excess of 600,000 million tons in 24 provinces, and currently about 500 mines in operation among which 70% are underground mines.

Room and pillar mining method is predominant in gypsum underground mines in China. But this method may not have been fully implemented in compliance with the mining legislations in some mines. One of the outstanding problems is that a large number of empty

chambers are left without taking any appropriate ground controls. Such mined empty area is now totally in excess of 20 million m², and this figure is rapidly increasing. Other problems include inappropriate mining method, insufficient government administration and monitoring, and mining beyond the licensed zone in order to grab the mineral resource, which causes the deterioration and damage of the safety boundary pillars. On the other hand, with the rapid economic growth in China, the demand for gypsum is so strong that many mining companies are running beyond the production capacity, but the investment on the mining occupational safety and health hasn't matched the expansion of mining, resulting in frequent gypsum mine accidents with a trend of increasing fatalities in large accidents. The accidents are mainly caused by collapse of tunnels and stopes, and in particular, the roof fall of large area causes serious fatalities as tabulated in Table 1 are some recent accidents in gypsum mines in China.

Table 1. Fatalities in recent gypsum mine accidents in China

Name of mine	Date of accident	Type of accident	Fatality
Zhechen Gypsum Mine	28 Mar. 2000	Roof fall	5
Henda Gypsum Mine	18 May 2001	Roof fall	29
Xinglong Gypsum Mine	10 Nov. 2003	Roof fall of large area	5
Yetang Gypsum Mine	16 Feb. 2004	Roof fall of large area	6
Shangwangzhuang Gypsum Mine	6 Nov. 2005	Collapse	37

In addition to above geotechnical accidents in underground mining, mine flooding is another mine disaster that may be encountered in case that the groundwater inflow to the mine openings could not be stopped (Gendzwill et al., 1996; Zuber et al., 2000). Mine flooding may trigger a wide range of geoenvironmental problems, such as ground subsidence (Zuber et al., 2000; Perry. 2001), release of heavy metals (Biehler et al., 1999; Bain et al., 2001), alteration of geochemistry (Bain et al. 2001; Perry. 2001; Cidu et al. 2002; Donovan et al. 2003; Gammons et al., 2006), pollution of downstream groundwater (Bain et al. 2001) or surface water (Cidu et al., 2002). This paper presents an investigation on the cause of the catastrophic flooding at NGM in September 2006.

NGM BRIEF HISTORY

NGM, encompassing a land area of 1.29 km², is one of the well-known gypsum mines in China. It started the mine construction in 1971, began mining production at the sublevel -270m to -300m in 1984, when the design annual production was 300,000 tons. Since 1993, the sublevel -344m began to mine, and the production reached 400,000 tons per annum. By the end of 2004, NGM had mine 6.08 million tons of gypsum ore, and the production in 2004 was 423,200 tons.

The shaft-drive system is utilized for the mine development, room and pillar method for mining and shallow and/or medium blast-holes for blasting off the ore as shown in Figure 1 and Figure 2 (Zhu et al., 1994). Initially, the room was 8m wide, 8-9m high with pillar width 6m. Later on, the dimensions of the room was amended to 10m wide and 12m high, but the pillar width kept unchanged. By the time of the catastrophic flooding, the sublevels -270m and -308m were mined out but left untreated for ground controls. The flooding accident occurred at the sublevel of -344m, whose height is 30-34m.

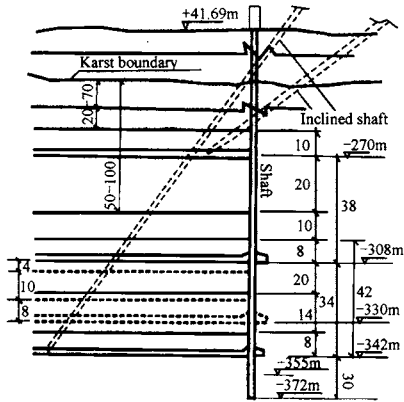


Figure 1. Excavation system sketch map of NGM

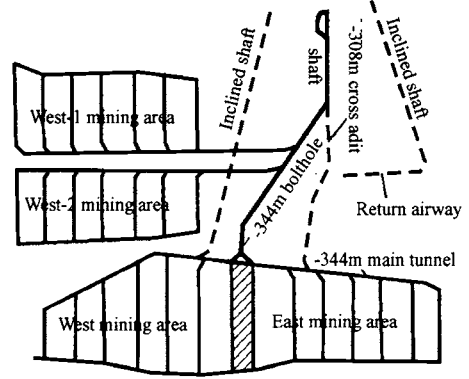


Figure 2. Sketch of -344m mining level and vertical shaft excavating

FLOODING ACCIDENT

A small inflow was first observed at No. 37 room on the sublevel of -344m on 19 June 2006. A professional grouting company was contracted to seal the seepage by underground grouting and construction of bulkheads, but unfortunately, the flow rate still gradually increased. By the end of Aug. 2006, it rose sharply from 0.00083 m³/s to 0.0222 m³/s. At about 12:30pm on 11 Sept. 2006, the catastrophic inflow of high pressure muddy water started to pour down after a 1.0m³ wedge fell from the roof where the grouting workers were operating. In just two minutes, the water on the floor reached 25cm deep. By 3:30pm the workforce on -344m was inundated. At 8:00pm, the water rose to -308m sublevel. At noon of 14 Sept. 2006, the water level reached to -270m sublevel. By far, the entire underground mine was flooded. It was estimated that the water flow rate was as high as 2.222m³/s.

Such a large scale of underground mine flooding as NGM is very rare and devastating. It not only damaged the mining facilities, but also impacts a great deal to the local hydrogeology. The groundwater level was significantly dropped in the vicinity. For example, "the water level in some local wells dropped 1.5-2.0m in just one day." More seriously, the deep well that supplies portable water to the Huashu village dropped from -20m to -110m at the noon of 14 September 2006, causing the interruption of water supply to the villagers and the ground subsidence to varying degrees in different places.

GROUND SUBSIDENCE

On 12 Sept. 2006, ground subsidence, about a range of 1500m from the mine, was observed on the ground surface above the catastrophic inflow onset, causing such surface structures as roads and buildings damaged and ground cracked due to differential subsidence, many concrete pavements were cracked to 50 to 100 mm width. The cracks might be induced by tension or compression. Compressive cracks lead to the pavement detached from the subbase and formed triangular heaves of 20cm high. 40 houses in the Huashu village cracked, some of which were unsafe. The gypsum processing plant and the machinery maintenance plant of

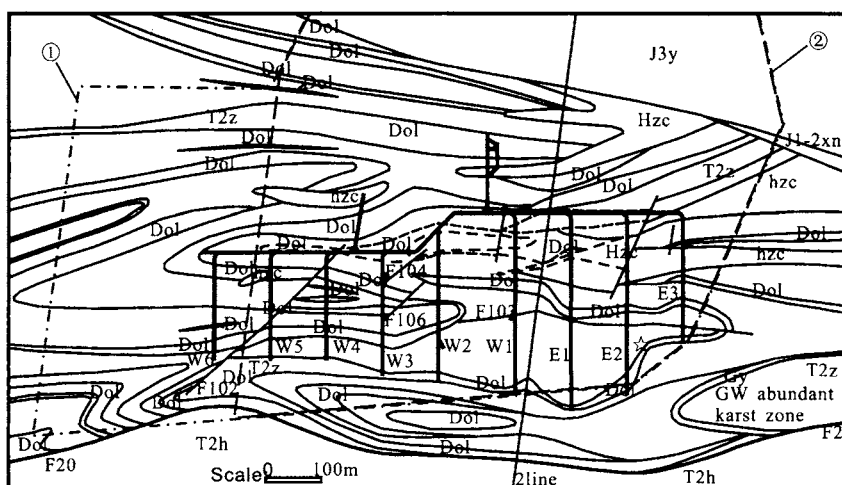
Huashu village were forced to be closed and evacuate the workers due to the ground cracked and the building damaged. The direct economic loss due to this disaster was estimated in terms of millions of Chinese Yuan.

No matter the crack is compressive or tensile, its strike shows an apparent tendency. In the northeastern of the mine, the concrete pavement was entirely sliding towards the mined area, indicating that the trough centre of subsidence is over the mined area. There were cracks parallel to the road, and the strike of the cracks ranged from 195° to 240° , dip from 285° to 330° . The ground subsidence and cracks were still developing on 14 Sep. 2006 when the geological disaster investigation commenced.

GEOLOGICAL INVESTIGATION

Geological structures

The terrain in the mine area is quite flat and the surface level is in 10s meter above the sea level. The surface soils are Quaternary residual and alluvial sediments of silt, silty clay and clay, with thickness ranging from several meters to 50 meters. The stratigraphy of the gypsum measures is depicted in Figure 3.



J3y, J1-2xn, T2h, T2z: The formation in mine area; Hzc: Melange;
 Dol: Dolomite; Gy, Gypsum; /: F20, Fault and umber; 2line: Section line;
 ①: Registered mining area ②: Mined area above-334m; W2: Sub-mining area

Figure 3. Horizontal section map of -344m deep in NGM area

The mine is located in a syncline whose axis is nearly in the east-west direction. The fold, also called Zhoucun-Huashu syncline, ranges from east to west 1300m, north to south 1440m and in the depth from -125m to -1100m. The upper part of the syncline is Jurassic basin, and the lower part is Zhouchong Group basin that encompasses the orebody. The two limbs of the syncline are asymmetrical, the southern limb strikes 340° to 20° and dips 30° with complete stratigraphy whilst the northern limb strikes 170° to 200° and dips 30° to 56° with incomplete stratigraphy.

There are some faults in the mine area. The strikes of the majority of the faults are either parallel or perpendicular to the axis of the syncline. The perpendicular faults located in the Jurassic basin are small with little influence to the orebody. But the parallel faults in the Zhouchong Group basin are large, deep and concealed, such as F16, F18 and F20 in Figure 3 and Figure 4. Table 2 is the characteristics of F16, F18 and F20.

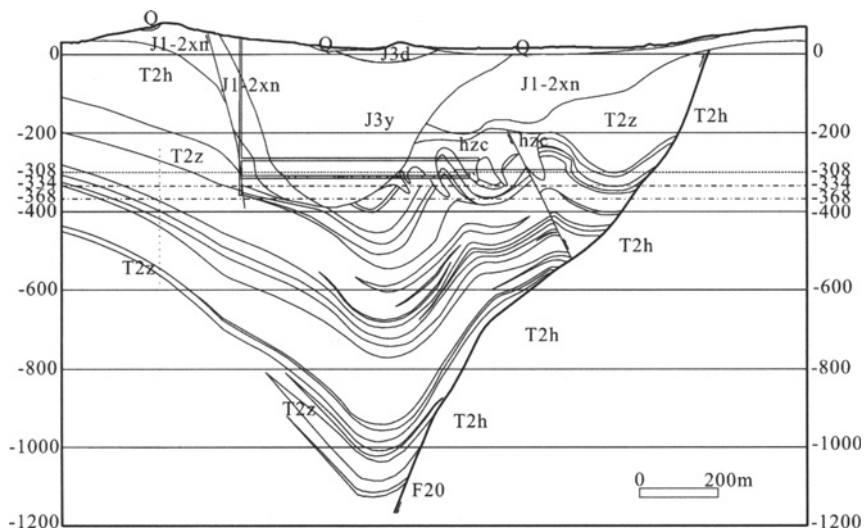


Figure 4. Typical geological profile of NGM area

Table 2. Characteristic of F16, F18 and F20 faults

Fault	Location	Attitude	Dimension	Description
F16	Crossing the syncline in south limb in the mine area	Dip: SE, Dip angle: 40° to 50°	Length: 2300m Extension: 280-320m	The fault zone is highly fissured, extremely karst, poor argillation, and strongly water-bearing. The permeability coefficient of the fault is as high as 0.01161m ³ /s-m of the specific capacity from pumping test
F18	In North limb of the syncline	Dip: South Dip angle: 60° to 70°	Length: 2500m Extension: 800-1100m	Exposed in No.2 shaft at -270m sublevel. Normal fault with throw of 30-40m. Fault breccia, cemented by clay and calcium, is impermeable with little localized water
F20	Passing the entire mine area in the southern	Dip: North Dip angle: 30° to 50°	Length: 2900m Extension: 1200-1400m	The strata T2z overlies on T2h. The hanging wall is consisted of anhydrite, limestone and dolostone, and footwall is clayey and silty sandstones. The fault zone is intact with some fissures cemented, impermeable and dry

Hydrogeology

In NGM area, the aquifers are generally slightly fissured except the fissured karst aquifer in Zhouchong Group, and the Quaternary aquifer is a relative aquitard layer.

The lower part of the Zhouchong Group is an aquitard, which is typically at the level of -600m or lower immediately overlain the orebody. The middle part is also an aquitard of 300m to 500m thick, which was evidenced by the fact that no water was observed from the investigation in the sublevel tunnels on -270m and -308m. The upmost part of the Zhouchong Group is an aquifer of 20m to 200m thick, with highly active karst typically ranging from 20% to 40% and up to 70%. From the pumping test, as the groundwater level was 5.947m to 8.587m, specific capacity was $0.00552-0.01740\text{m}^3/\text{s}\cdot\text{m}$, hydraulic conductivity was $(0.894-1.767)\times 10^{-4}\text{m/s}$. Due to the aquifer is directly above the orebody, it is the major water source of inflows. The karst rate of the limestone in the mine and in its south ranges from 30% to 50%, so the limestone stratum is a reservoir of groundwater. The water in this aquifer is under piezometric pressure, typically from 50m to 200m and up to 450m, which is excessive to raise the water above the base of the overlying stratum. For example, during the excavation of the No.1 shaft at -298m, a groundwater-eroded cave was encountered. The sudden inflow of water at $0.083\text{m}^3/\text{s}$ caused the stop of the shaft excavation. The unexpected inflow of water also occurred for several times during the mining operations at the two sublevels of -270m and -308m, the flow rate was at $0.042-0.056\text{m}^3/\text{s}$, and the water was sourced from the southern karst zone.

There is a highly active karst strip of 570m to 650m wide and 75m thick in the Zhouchong Group in the southern part of the mine. There are huge water-eroded caves in the strip and the rate of cavity is 71.2%. From the vertical cross-section, the locations of highly active karst are typically in contact with the orebody. The degree of karst is clearly controlled by the geological structure.

During the construction, whenever the drilling encounters the karst limestone, there is a huge loss of washing liquid, collapse of the wall of the drill holes, and no other remedial measure can go through except for the cased drilling. Therefore, the karst aquifer is water-abundant and highly permeable, of high flow rate and under uniform piezometric pressure face.

Most drives are inside the gypsum orebody. The water inflow in the drives is mainly from the leakages at the cemented seals of underground diamond drill holes for hydrogeological explorations, which is caused mainly by the deterioration of the seal under the washing and eroding of groundwater.

The -270m sublevel and the No.2 shaft intersect with the F15 fault, but the flow rate of the fault is only $2.22-2.78\text{m}^3/\text{s}$ since it locates in the Huangmaqing Group aquitard which is cemented by clay and of low hydraulic conductivity. From the historical statistics, the normal water pumping rate at sublevels -270m and -308m was among $0.0116-0.0162\text{m}^3/\text{s}$ during the mine development phase, and the maximum rate was $0.0313-0.0509\text{m}^3/\text{s}$ in case of a sudden inflow. The pumping rate at -344m sublevel is quite small during both the mine development and the mining operation phases.

Engineering geology

In the crown stratum of the orebody, the tuff sandstone and tuff breccia are weakly cemented with a low compressive strength of 2.8-6.3 MPa; the compressive strength of mixed conglomerate is typically 64.6 MPa; most of the water-eroded caves in the karst limestone

are filled with clay, sand and gravel, and the compressive strength of the limestone varies among 32.4-60.8 MPa; at the interface, the compressive strength of gypsum is 8.8-12.8MPa, and this strength of breccia gypsum is 25.5-36.3 MPa.

The compressive strength of the orebody is very good except for some localized deteriorations due to fissures and joints. The compressive strength of the mixed conglomerate is 57.9 MPa at the interface between the crown stratum and the orebody, whilst it is 87.3 MPa in the orebody. The compressive strength of breccia gypsum from the orebody is 10.8-127.5 MPa in contrast with 25.5-36.3 MPa for the breccia gypsum from the interface.

The compressive strength of the sandstone in the southern bottom stratum of the orebody is generally above 87.3 MPa. The limestone in the northern bottom stratum is relatively intact. The compressive strength of the broken zone of the fault is very low, and it is even lower at the locations where the crown stratum is karst limestone.

DISTURBANCE DUE TO MINING

Engineering geological problem analysis for underground mining

Underground mining involves in the complex and dynamic engineering geological problems, such as stope stabilities, mine geological disasters, such as dynamic in situ stress and mine flooding, and mine environmental impacts, in particular, ground subsidence and crack.

Though the ground subsidence induced by mining can't be avoided, mine ground subsidence can be minimized and should be kept relatively stable during the lifespan of the mine and subsequent services (Singh. 1992; Holla et al., 2000). The major factors affecting the ground subsidence are the panel width of mining, depth and seam thickness. Other factors are mining method, sequence and rate, geological structures, discontinuities, groundwater and strength of overburden rocks and soils (Singh. 1992).

Pillars may fail due to spalling, shearing along discontinuities, multi-plane shearing and relative displacement between the pillar and the adjacent weak country rock (Brady et al., 2004), such failures may be affected by discontinuities, rock strength, blasting, slenderness ratio, and irregularity of the pillar, and eccentric loading on the pillar.

Tensile crack and peel-off of the roof is one of the roof failures (Yao et al. 1994). Tensile stress may be induced in the surface of the roof in the mined area, and the maximum tensile stress may occur at the midway between two adjacent pillars. As the tensile strength of rock is about 1/10-1/50 of the compressive strength, the roof is subjected to tensile failure in case of an unfavourable discontinuity, which in turn accelerates the growth of tensile crack on the roof. There are many factors that may affect the roof failure, such as insitu stress, uniaxial compressive strength, or UCS, of rock, rock quality designation, or RQD, groundwater, mining method, sequence and rate (Potvin et al., 2003; Jiang et al., 2004; He, 2005).

From the mining zone outwards, the rock mass may be divided into broken zone, plastic zone and elastic zone. Deep lying rock mass may respond differently, the broken zone and non-broken zone may occur alternately. When the initial vertical stress σ_{vi} is greater than UCS, this zoned broken phenomenon occurs. The number of broken zones depends on the ratio of σ_{vi} /UCS. The greater the ratio is, the more the broken zones are (Qian, 2004). Therefore it might be imperative to consider such phenomenon and the residual strength of

rock when assessing the stability of deep rock structures. Does this phenomenon exist in NGM? This will be an issue for further studies.

Rocks, especially soft rocks, may exhibit creeping that is a phenomenon of the deformation of rocks increases with the time elapse under a given load. Both anhydrite and gypsum breccia demonstrate the characteristic of creeping. To initiate creeping, the stress needs to reach some level, and the process may consist of instant elastic strain, over creeping phase, stable creeping phase and accelerated creeping phase. Creeping will impact the long-term stability of the mined area (Liu et al., 2000; Song et al., 2005). The anhydrite and breccia-like anhydrite from NPM exhibit a similar creeping curve.

The stability, ground subsidence and sudden inflow of water in underground mines are controlled by the structural features of rock mass and local hydrogeology. There are a variety of discontinuities in rock mass such as bedding plane, fault, joint and fissures. The strength of the discontinuities is significantly lower than that of the intact rock, so they are controlling the strength and stability of rock mass. These structural features of rock mass play a decisive role in mine general design, mining method selection, tunnel design and ground control, etc.

The sudden inflow of water in the tunnels exists in NGM since the construction of the mine, but the stability issue has not yet been prone to the mine since a safety barrier pillar is designed between the allowed mining area and the water conducted fault and the water-rich intensive karst crown stratum, respectively. Meanwhile, the rock mass is not heavily jointed, so room and pillar mining and the shallow and/or medium depth blasthole blasting technique are productive for the mining operation in NGM.

The causes of the catastrophic flooding are, on one hand, controlled by the geological structures and hydrogeological settings. On the other hand, the mining operation has exceeded the prescribed safety boundary, disturbed the fault that connects to the karst aquifer in the crown stratum, and damaged the local stress and hydrogeology equilibriums. As a result, the roof and the pillar are subjected to the uncontrollable large deformations. The underground grouting and construction of bulkheads couldn't stop the catastrophic inflow and the subsequent ground subsidence and facility damage.

Effect of mining on the activation of faults and joints

As the local stress field is controlled by the fault and the joint distribution in the influence area of the fault, the stresses are redistributed due to the disturbance of mining, which may cause new joints and change the local hydrogeology. Sometimes, the broken zone of the fault may become a barrier of the stress-strain transmission, resulting in stress concentrations in the broken zone and in the rock mass between the fault and the workings. The presence of groundwater in rock mass has a significant effect on its physical properties, and the inflow from an aquifer is an important condition for the joint growth and rise of groundwater.

The activation of the deformation and hydraulic conductivity of the fault is a function of time and space. As the orientation, shape and scale of the faults are varying, so are the dimensions of openings, sizes of the hydraulic safety pillar and advance direction of the workface, consequently, the spatial distribution of the induced stress and strain are different. However, there are some rules to follow. The larger the dimensions of openings are, the greater the degree of redistributions of the induced stresses is. The closer to the fault, the

more intensive the induced radial and tangential stresses are and the larger the influence area of the tangential stress would be.

The relative spatial position of openings to the fault also affects the deformation of the fault and changes the hydrogeology of the fault. If the direction of the induced tangential stress is opposite to the initial insitu stress, it will make the fissures in the shearing zone open more easily. The time factor of the induced stresses, fissure growth and rise of groundwater in the fault have critical effects on the activation of the hydraulic conductivity of the fault, and the advance rate of the workface is key factor controlling the time factor (Li et al., 2002; Li et al., 2003).

The likelihood that F20 in the southern part of the mine might be connected with the water-bearing karst zones in the crown stratum was considered in the 1st phase design of NGM, so a 200m wide strip along the full length of the fault, 1300m, was designed as the safety pillar reserve (Zhu, 1994). But the mining room was just 100m away from the fault when the flooding was triggered. At the early stage of the inflow prior to the catastrophic flooding, the broken zone of F16 was activated due to mining disturbance and the seepage pressure was estimated as 400 kPa, the flooding disaster in NGM might have been avoided if the mining operation had been immediately stopped and measures had been taken to reinforce the roof and walls and to seal the seepage by underground grouting and construction of bulkheads. However, in the reality, the single measure of grouting had failed to stop the seepage, furthermore it might have adversely enlarged the hydraulic channels to the karst water bodies and worsened the flooding disaster, consequently the large mine was ruined at a moment.

CONCLUSIONS

The catastrophic NGM flooding has not only changed the local hydrogeology, but also altered the geomechanics of the rock mass, resulting in the redistribution of the insitu seepage net and stress field. The sudden inflow of groundwater is firstly controlled by the geological structures, secondly by features of rock mass, hydrogeology and engineering geology. This was evidenced by the sudden inflows and seepages during exploring, constructing and mining.

At karst zones, especially the highly water-bearing ones, due to the distribution of discontinuities and water-eroded caves are not clear, employing the underground grouting technique not only failed to remedy the seepage, but to make things worse also, it might delay to reinforce the workface, resulting in the disaster unavoidable.

The ground subsidence induced by the underground flooding caused a range of damage to the surface facilities, including roads, houses and plants. The flooding dramatically lowered the groundwater level in the mine and its vicinity. As local villages and plants mainly live on groundwater, the flooding triggered an immediate interruption of water supply, which attracted a wide social and community attentions.

Local governments and research institutes have made an enormous effort for the disaster relief and rehabilitation, and an emergence steering committee consisted of governmental officers and experts was established right after the catastrophe. Warning signals were set up around the dangerous zones jeopardized by the flooding and subsequent ground subsidence.

Educational cards of the geological disaster were developed and sent to the villagers affected by this disaster as well as the relevant explanations and propitiations. Post disaster survey and monitoring were organized, and all surface cracks were measured, monitored and recorded.

As the ground subsidence may take a long time to be stable, a monitoring network was established on the ground surface in consideration of the distribution of underground old workings and the importance of the surface facilities, so that the tendency of the ground subsidence can be predicted in real time, and any dangerous signals can be immediately announced, so as to confine the disaster and reduce the injury and fatality.

REFERENCES

- Bain J. G., Mayer K. U., Blowes D. W., Frind E. O., Molson, J. W. H., Kahnt, R. and Jenk, U. (2001). Modelling the closure-related geochemical evolution of groundwater at a former uranium mine, *Journal of Containment Hydrology*, 52, 109-135.
- Biehler D., Falck W. E. (1999). Simulation of the effects of geochemical reactions on groundwater quality during planned flooding of the Konigstein uranium mine, Saxony, Germany. *Hydrogeology Journal*, 7 (3): 284-293.
- Brady B. H. G., Brown E. T. (2004). *Rock Mechanics for Underground Mining*. Dordrecht, Boston, London, Kluwer Academic Publishers.
- Cidu R., Fanfani L. (2002). Overview of the environmental geochemistry of mining districts in southwestern Sardinia, Italy, *Geochemistry: Exploration, Environment, Analysis*, 2 (3): 243-251.
- Donovan J. J., Leavitt, B. R. and Werner E. (2003). Long-term changes in water chemistry as a result of mine flooding in closed mines of the Pittsburgh Coal Basin, USA, *Proceedings of the 6th ICARD*, Cairns, Queensland, Australia.
- Founie A. (2006). Gypsum. U.S. Geological Survey, *Mineral Commodity Summaries*, 78-79.
- Gammons C. H., Metesh J. J. and Snyder D. M. (2006). A survey of the geochemistry of flooded mine shaft water in Butte, Montana, *Mine Water and the Environment*, 25 (2): 100-107.
- Gendzwill D., Martin N. (1996). Flooding and loss of the Patience Lake potash mine, *CIM Bulletin* 89(1000): 62-73.
- He M. C. (2005). Conception system and evaluation indexes for deep engineering, *Chinese Journal of Rock Mechanics and Engineering*, 24 (16): 2854-2858.
- Holla L., Barclay E. (2000). *Mine Subsidence in the Southern Coalfield, NSW, Australia*. Sydney, New South Wales Department of Mineral Resources.
- Jiang C. G., Sui M.S. and He Y. (2004). New ideas on reasons of the rock burst in underground mining, *Mining R & D*, 24 (4): 55-58.
- Li X.Z., Luo G.Y. and Chen Z.S. (2002). The mechanism of deformation and water conduction of fault due to excavation in water inrush in underground engineering, *Chinese Journal of Geotechnical Engineering*, 24 (6): 695-700.
- Li X.Z., Zhang G.Y. and Luo G.Y. (2003). Barrier effects caused by fault on excavating -induced stress & deformation and mechanism of resulting groundwater inrush, *Rock and Soil Mechanics*, 24 (2): 220-224.
- Liu M.Y., Xu C. Y. (2000). Rheological properties of anhydrite and determination of its long-time strength, *China Mining*, 9 (2): 53-55.
- Perry E. F. (2001). Modelling rock-water interactions in flooded underground coal mines, Northern Appalachian, *Geochemistry: Exploration, Environment, Analysis*, 1 (1), 61-70.
- Potvin Y., Nedin P. (2003). *Management of Rockfall Risks in Underground Metalliferous Mines*, Canberra, Minerals Council of Australia.

- Qian Q. H. (2004). The characteristic scientific phenomena of engineering response to deep rock mass and the implication of deepness. *Journal of East China Institute of Technology*, 27 (1): 1-5.
- Singh M. M. (1992). *Mine Subsidence. SME Mining Engineers Handbook*, H. L. Hartman: 938-971.
- Song, F., Zhao, F. S. and Li, Y. L. (2005). Testing study on creep properties for gypsum breccias, *Hydrogeology & Engineering Geology*, (3): 94-96.
- Yao B. K., Liu Z. H. and Li C. Y. (1994). *Research on stability of underground mining*, Beijing, China Science and Technology Press.
- Zhu W.Z.(1994). Mining design of -308m mining and -344m extending mining in Nanjing Gypsum Mine, *Non-metallic Mines*, (4): 16-20.
- Zuber A., Grabczak J. and Garlicki A. (2000). Catastrophic and dangerous inflows to salt mines in Poland as related to the origin of water determined by isotope methods, *Environmental Geology*, 39 (3-4), 299-311.

MODELING OF PERIODIC ELASTIC STRAIN ENERGY CHANGE AND FAILURE PROCESS OF ROCK SPECIMEN WITH RANDOM IMPERFECTIONS IN BIAXIAL COMPRESSION

X. B. Wang

*Department of Mechanics and Engineering Sciences,
Liaoning Technical University, Fuxin 123000, China*

The mechanical behavior and failure process of a rock specimen with the initially random material imperfections in biaxial compression are modeled using FLAC. Two FISH functions written are adopted to prescribe the imperfections and to calculate the elastic strain energy decrease of all elements per 10 timesteps. For intact rock exhibiting linear strain-softening behavior beyond the failure and then ideal plastic behavior, the failure criterion is a composite Mohr-Coulomb criterion with tension cut-off. Imperfection undergoes ideal plastic behavior beyond the failure. The failure process of the specimen in three typical periods with remarkable stress drops is discussed. Periodic elastic strain energy change and stress fluctuation are observed. The elastic strain energy decrease rate reaches its peak in strain-softening stage. In period 1, two shear wedges are progressively formed, surrounding the seismic gap where the earthquake swarm is inactive. In period 2, a shear band appears in the gap and the earthquake activities migrate outwards. The earthquakes belong to rupture type. In period 3, the earthquakes belong to compound type. After that, a longer shear band bisecting the specimen leads to a decrease in the specimen load-carrying capacity.

INTRODUCTION

Rocks in compression, with an increase of axial strain, microcracking may occur in the vicinity of material imperfections, such as voids, pores and cracks. Further loading will result in the progressive coalescence of microcracks to eventually form the macroscopic fractures (Fang and Harrison, 2002). As is known, using the fracture mechanics theory, the coalescence and propagation of cracks are difficult to describe since the dynamic microcracking events cause the boundary conditions to be changed complicatedly.

Recently, the failure process and mechanical behavior were numerically studied considering the heterogeneity of rocks (Tang and Kou, 1998; Fang and Harrison, 2002). In these numerical simulations, the elastic-brittle constitutive relation is widely used. The relatively complex post-peak strain-softening constitutive relation is not considered.

FLAC (Fast Lagrangian Analysis of Continua) is an explicit finite-difference code that can effectively model the behavior of strain-softening geologic materials, undergoing plastic

flow as their yield limits are reached. One outstanding feature of FLAC is that it contains a powerful built-in programming language, FISH, which enables the user to define new variables, functions and constitutive models. The developed FISH functions by the user to suit the specific need add user-defined features.

Using FLAC, the shear fracturing bands of a seismic model composed of five rock blocks separated by four interfaces in biaxial plane strain compression was investigated (Wang et al., 2004); Wang (2005) studied the anomalies in shear strain rate of a rock specimen in biaxial plane strain compression and a few seismic phenomena were revealed, such as shear strain localization, anomalies in shear strain rate and their evolutions. In these numerical investigations, rock specimens are homogenous.

The failure process of a rock specimen with pre-existing random imperfections in biaxial plane strain compression is numerically modeled. Two FISH functions written are adopted to prescribe the imperfections and to calculate the elastic strain energy decrease of all elements per 10 timesteps. Numerical results reveal a few seismic phenomena, such as periodicity in earthquake activities, seismic gap, migration and shear fracturing bands.

CONSTITUTIVE RELATION AND MODEL

The height and width of a rock specimen are 0.1m and 0.1m, respectively. The specimen is divided into 6400 square elements with the same area. Black elements are the material imperfection elements, while white elements are the intact rock elements (Figure 1). Numerical calculation is conducted in small strain mode and plane strain condition.

The present numerical test is divided into two stages. In the first stage, the specimen is subjected to a hydrostatic stress of $p=5\text{MPa}$ [Figure 1(a)]. In the stage, 10000 timesteps are required to arrive at the equilibrium state for a static solution (the out-of-balance force is small enough). In the second stage, the node velocities in horizontal and vertical directions at the two ends are fixed and a constant velocity of $v=5\times 10^{-9}\text{m/timestep}$ is loaded in the vertical direction [Figure 1(b)].

In linear elastic stage, the intact rock and material imperfection elements have the same constitutive parameters. Shear modulus and bulk modulus are 11GPa and 15GPa, respectively.

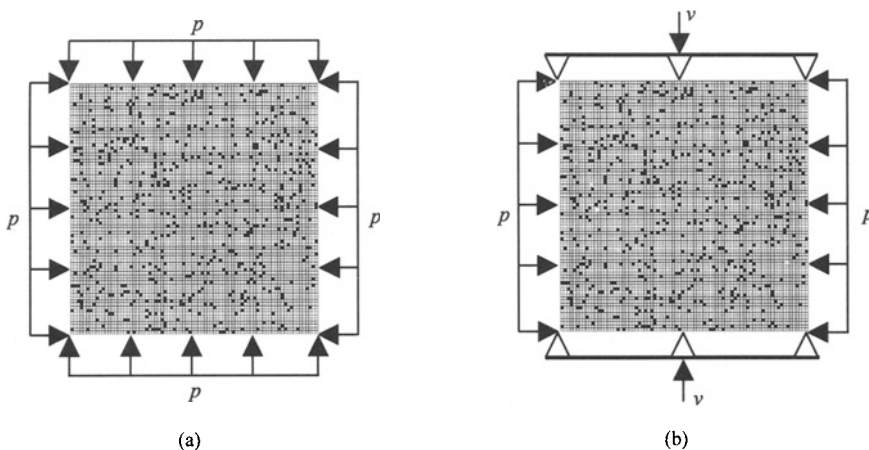


Figure 1. Model boundary conditions in stage 1(a) and stage 2(b)

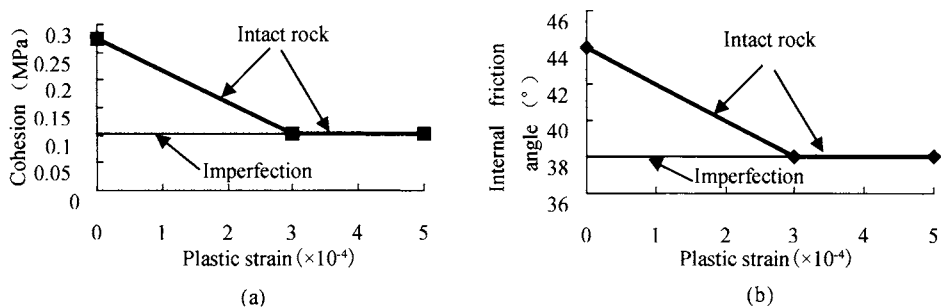


Figure 2. Post-peak constitutive relations for intact rock and imperfection elements

Once the intact rock elements yield, they firstly undergo linear strain-softening behavior and then ideal plastic behavior (the bold lines in Figure 2). The adopted failure criterion for the intact rock elements is a composite Mohr-Coulomb criterion with tension cut-off and the tensile strength is 2MPa.

The imperfection elements have lower strength parameters in comparison with the intact rock elements. If the imperfection elements fail, they undergo ideal plastic behavior (the horizontal lines in Figure 2). Cohesion, internal friction angle and tensile strength of the imperfection elements are 0.1MPa, 38 $^{\circ}$ and 2MPa, respectively.

FISH FUNCTIONS

Prescribing the random imperfections

In FLAC, every zone or element has an identification number. In the paper, the minimum and maximum identification numbers are 1 and 6400, respectively. Different identification numbers correspond to the different elements. Random numbers are chosen from 1 to 6400 for 640 times according to uniform distribution. Thus, the positions of the initially random material imperfections are chosen randomly. The actual number of the imperfections will be less than 640 since a random number can be chosen more than one time.

Calculating the elastic strain energy decrease of all elements per 10 timesteps

Considering the post-peak complete brittle stress-strain relation, Fang and Harrison (2002) calculated the strain energy dissipation rate of a rock specimen in terms of the reduced elasticity. In the present paper, the elastic modulus is unchanged and the post-peak strain-softening constitutive relation is used.

For the post-peak strain-softening materials, it is difficult to calculate the strain energy dissipation rate. However, it is easy to calculate the elastic strain energy decrease of an entire specimen per 10 timesteps. Once an element yields and the elastic strain energy of the element decreases in any 10 timesteps, then the elastic strain energy decrease will be calculated in terms of the elastic modulus, the previous and present principle stresses, the Poisson's ratio and the volume of the yielded element. Summing the elastic strain energy

decrease of all yielded elements leads to the elastic strain energy decrease of the entire specimen per 10 timesteps (or called the elastic strain energy decrease rate).

RESULTS AND DISCUSSIONS

Periodic stress fluctuation and elastic strain energy decrease rate

Figure 3 shows the evolution of average compressive stress with timestep and that of elastic strain energy decrease per 10 timesteps with timestep after the axial loading velocity is exerted.

It is found from Figure 3 that the two curves exhibit periodic characteristics when timesteps or axial strain exceeds a certain value. The linear stress-timestep curve corresponds to the long-term stage of earthquake. In each period, stress firstly increases and then a local maximum value is reached, which is followed by the strain-softening behavior. We can find several elastic strain energy decrease rate peaks, among which three peaks (peaks 1 to 3 in Figure 3) are higher and typical, occurring in the process of stress decrease.

As is known, the periodic stress fluctuation and elastic strain energy decrease rate are similar to the periodicity in earthquake activities. Generally, earthquake is possible under the condition of a large amount of energy released. Therefore, we will only discuss the failure process of the specimen in three typical periods (periods 1 to 3) with remarkable stress drops or higher elastic strain energy decrease rates.

Figure 4 shows the failure process of the specimen in periods 1 to 3. The points A_1 to D_1 , A_2 to D_2 and A_3 to D_3 in Figure 3 correspond to Figure 4(a1-d1), Figure 4(a2-d2) and Figure 4(a3-d3), respectively. The black elements are subjected to shear or tensile failure now. The while elements always remain elastic states. The gray elements mean that they have yielded previously, while now they remain elastic states.

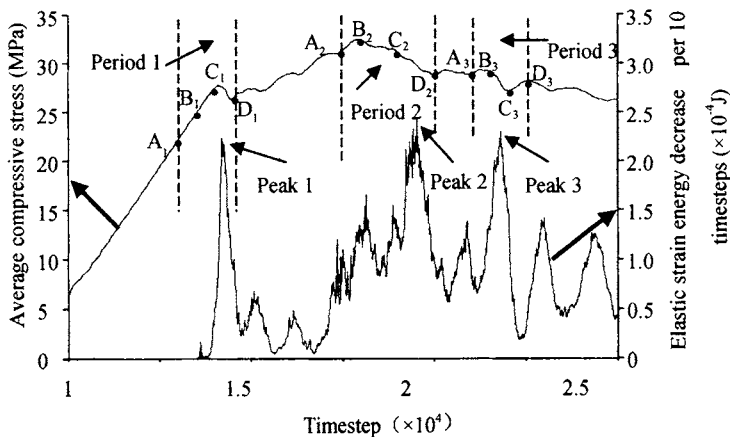


Figure 3. Stress-timestep curve and elastic strain energy decrease rate-timestep curve.

Failure process in period 1

The elements closer to the specimen corners firstly fail [Figure 4(a1)]. The number of the failed elements is the greatest in the specimen middle due to the relatively weak

end-constraint [Figure 4(b1)]. The elements nearer the two specimen ends always remain elastic states. The elastic zone shape, which is restricted by the two rough ends, is similar to an isosceles triangle. The area of the triangle is slightly decreased with increasing strain [Figure 4(b1-d1)]. Usually, two elastic cones can be observed in experimental tests if the rock specimen ends are rough enough.

Some imperfections extend in vertical direction [Figure 4(c1)]. In the specimen corners, four shorter shear fracturing bands are formed owing to the coalescence of the extended imperfections and then propagate diagonally toward the specimen center.

After the shear band length reaches a certain value, the strain-softening behavior of the specimen has occurred (point D_1 in Figure 3). In strain-softening process, two shear wedges are progressively generated [Figure 4(d1)]. After that, the four shear bands continuously propagate toward the top or base of the specimen. The earthquake swarm is relatively active in the four shear bands, while it is relatively silent at the specimen center. The central region surrounded by the four shear bands can be seen as a seismic gap.

Before 17000 timesteps, no elastic strain energy decrease is monitored although some elements have yielded. The elastic strain energy decrease rate rapidly increases prior to the peak stress and then achieves its peak (peak 1) in strain-softening stage.

Failure process in period 2

When the tips of the four shear bands approach the top or base of the specimen, the further developments of these shear bands are prohibited owing to the strong end-restraint. Earthquake activities in the gap begin to strengthen so that the gap disappears [Figure 4(a2)]. Instead, a shorter shear band is developed at the specimen center. At this moment, the highest peak stress (point B_2 in Figure 3) is reached.

It is obvious that earthquake activities in the gap are later than those in the four shear bands surrounding the gap. Migration in earthquake activities from the four shear bands to the gap indicates that earthquake activities have entered the middle-term stage. The present numerical results agree with some field observations (Chen 2000, Zhang 2002).

The central shear band length increases with timesteps [Figure 4(a2-b2)]. Afterwards, its outward propagation direction slightly changes [Figure 4(c2)]. Migration in earthquake activities from the gap to the outer suggests that they have entered the short-term stage. The central shear band cannot intersect the upper-right corner of the specimen and its further development is prohibited. After that, the two new shear bands emanating from the upper-right and upper-left corners of the specimen propagate towards the specimen center [Figure 4(c2-d2)], leading to a higher stress drop (from points C_2 to D_2 in Figure 3) and an apparent strain energy decrease (peak 2). Earthquakes will take place in the two longer and active shear bands. The earthquakes belong to rupture type.

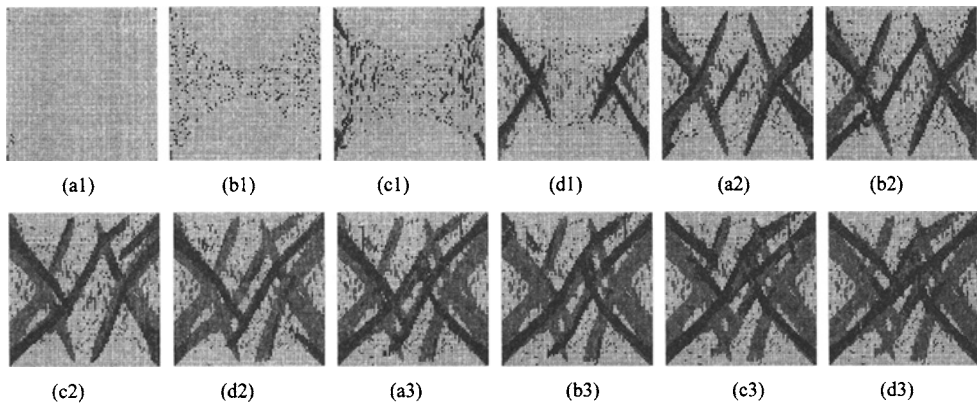


Figure 4. Failure process of a rock specimen with pre-existing random imperfections

Failure process in period 3

Two shear bands emanating from the lower-right and lower-left corners of the specimen extend towards the specimen center [Figure 4(a3-b3)]. The developed shear band emanating from the lower-left corner overlaps with the central shear band formed in period 2. However, the extended shear band originating from the lower-right corner traverses the two shear bands formed in periods 1 and 2.

The seismic source in period 3 will be located at the two shear bands emanating from the lower-right and lower-left corners. The earthquake occurs at the left side of the specimen is a strike-slip earthquake, while the earthquake occurs at the right side is a rupture earthquake. Therefore, the earthquakes in period 3 belong to compound type.

When stress decreases from B_3 to C_3 , the third higher peak of elastic strain energy decrease rate (peak 3) is found. After that, a longer shear band bisecting the specimen through the upper-right and lower-left corners of the specimen has been formed [Figure 4(d3)], leading to an apparent strain-softening behavior (beyond the point D_3 in Figure 3).

REFERENCES

- Chen L.D. (2000). Common features of medium- and short-term precursory anomalies before strong earthquakes, *Earthquake*, 20 (2): 7-13 (in Chinese).
- Fang Z. and Harrison J.P. (2002). Development of a local degradation approach to the modeling of brittle fracture in heterogeneous rocks, *International Journal of Rock Mechanics and Mining Sciences*, 39 (4): 443-457.
- Tang C.A., Kou S.Q. (1998). Crack propagation and coalescence in brittle materials under compression, *Engineering Fracture Mechanics*, 61 (3-4): 311-324.
- Wang X.B, Zhao Y.F. and Dai S.H. et al. (2004). Numerical simulation of conjugate shear fracture bands for seismic block model, *Journal of Disaster Prevention and Mitigation Engineering*, 24 (2): 119-125 (in Chinese).
- Wang X.B. (2005). Characters of earthquake precursor and numerical simulation of anomalies of shear strain rate of rock, *Journal of Geodesy and Geodynamics*, 25 (1): 102-107,122(in Chinese).
- Zhang G.M. (2002). The main science advance of earthquake monitoring and prediction in China, *Earthquake*, 22 (1): 1-8 (in Chinese).

STUDY ON ISOTOPE MODEL OF DYKE LEAKAGE

Yongsen Wang

College of Hydrology and Water Resource, Hohai University, Nanjing 210098, China

Jiansheng Chen

Research Institute of Science and Technology, Hohai University, Nanjing 210098, China

Applying the methods of stable isotopes and hydrochemistry to study the dyke is an effective way. And the theory of environmental isotope and hydrochemistry applied to leakage study is described. As natural tracers, environmental isotope and hydrochemistry mark groundwater, river water and precipitation. By contrast of the composition of environment isotope and water chemistry in water, the relation between them can be determined to distinguish the replenishment resource of groundwater, the position and range of leakage, the stratum formation and so on. Few coupled models of isotope field have been given so far. After making some assumptions and simplifications, the following models of the leakage of dyke are deduced based on basic law of hydraulics principle. And the model is used to predict the leakage velocity based on the data of the location. These models' building makes it possible to simulate the leakage of dyke quantitatively and gives it a help to interpret more objectively and more sufficiently the information that included in the leakage of dyke.

INTRODUCTION

Leakage is the main form of the dam damage, and it is also an important factor on the safety of dam body. At present, there are many methods to measure the dam leaky, and people have done many researches on the dyke seepage and have got lots of achievements of scientific research, which have accumulated abundant experience [Chen, J.S. and Dong H.Z. (2005); Liu J.G. and Chen, J.S. (2001); Zhou S.J. et al. (2004); Chen, J.S et al. (2003)]. But it is one of the important content in isotope hydrology to use environmental isotope to research the dam leakage [Clark I.D, Fritz P. (1997); Mazor E. (1997).]. We can also know the source by the characteristics of isotope in the water [Payne B.R. Eriksson E and Danilin A.I et al. (1983)]. Now the researches on leakage of dam by isotope mainly rest on the stage of qualitative analysis [Chen J.S, D H.Z. and Chen L, (2003)], but few qualitative models have been given. This paper gives the dam leakage radioisotope model based on differential element, and analyses the leakage velocity of the dam abutment.

THE PRINCIPLE OF DETECTING DAM LEAKAGE BY USING ISOTOPE TRACER OF WATER

There are two kinds of isotopes in Environmental isotopes: stable isotope and radio isotope. The stable isotopes include D、 ^{18}O , and the radioisotope is tritium "T". The enrichment of

stable isotope is presented by the isotope ratio R or δ value, and that of radioisotope is presented by concentration C or presented by the tritium unit.

The isotope constitution of different water body is distinct because of the isotope fractionation. Sometimes the difference is much bigger if the elevation effect and the latitude effect are considered. The groundwater and reservoir water originates from the atmospheric rainfall, so the δD and $\delta^{18}O$ in reservoir water originated from high elevation are poor, and this enables us to distinguish reservoir water from groundwater. The recharge source can be judged by isotopic composition of groundwater behind the dam.

Tritium spreads all over the atmosphere when it is produced, and it marks the source of the water. Generally, the content of tritium in river is based on the recharge resource. The value of tritium in river recharged from precipitation is higher than that recharged from groundwater. And the value of tritium in groundwater is depended on the recharge resource and embedding of the aquifers and the runoff condition. The water in phreatic aquifer and shallow confined water are modern circulating ones which have high tritium value, and the deep confined water is stagnation one that has low tritium value. Thus we can determine the hydraulic relation between the groundwater and surface water by the analysis of the tritium value, and the genesis of the groundwater, the runoff condition of drainage and the recharge of groundwater are also researched. Hydrogeology parameters are also confirmed.

We can get some information of dam leakage, the seepage amount of the dam and abutment by use of the distribution regularity of D , ^{18}O and T in the groundwater and surface water. The recharge source of groundwater in the back of dam can be determined. It supplies scientific therapy for the research of dam leakage and the engineering treatment.

RADIOISOTOPE LUMPED PARAMETER MODEL OF RESERVOIR WATER

Model assumption

The model is showed in Figure 1. This paper considers the variation of radioisotope in a series of drilling holes which are set in the dam abutment. In order to simplify the complexity of the leakage problem, this paper assumes that the reservoir water reaches to the drill holes through a passage. So a lumped parameter model is built. Some similar radioisotope models on the groundwater have been deducted before [Tong, H.B. (2007)]. The water of downstream drills mainly comes from the two dam abutment according to the actual situation of the dam zone.

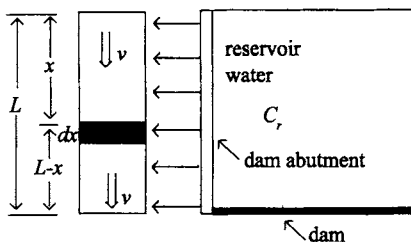


Figure 1. The radioisotope model of dam abutment leakage

The assumption of the model:

the seepage water is at steady state

the infiltration rate is constant

the velocity of flow v along the direction of dam abutment is constant

Take the water between $[x, x+dx]$ as the research subject. At time t , the radioisotope at the point L contains the recharge from the place x , and it will take the time $(L-x)/v$ to arrive at the L . That is to say, the radioisotope of x will enter into the aquifer at time $t-(L-x)/v$.

Model derivation

We can get a differential equation in the intervals $[0,L]$:

$$d(Q_{out}(t) \cdot C_{out}(t)) = \int_0^L C_r(t - \frac{L-x}{v}) \cdot e^{-\lambda \frac{L-x}{v}} \cdot v_{inf} \cdot dx \quad (1)$$

The flow system is at the steady state, so

$$Q_{out} = \frac{dW}{dt} = v_{inf} \cdot L \quad (2)$$

Substitute into the formula (1), simplify it, and then get,

$$Q_{out}(t) \cdot \frac{dC_{out}(t)}{dt} = \int_0^L C_r(t - \frac{L-x}{v}) \cdot e^{-\lambda \frac{L-x}{v}} \cdot v_{inf} \cdot dx \quad (3)$$

Simplify it, and then get,

$$\frac{dC_{out}(t)}{dt} = \frac{\int_0^L C_r(t - \frac{L-x}{v}) \cdot e^{-\lambda \frac{L-x}{v}} \cdot v_{inf} \cdot dx}{Q_{out}(t)} \quad (4)$$

Consider the Equation. (2), then the equation above can be changed to

$$\frac{dC_{out}(t)}{dt} = \frac{\int_0^L C_r(t - \frac{L-x}{v}) \cdot e^{-\lambda \frac{L-x}{v}} \cdot dx}{L} \quad (5)$$

If make $t' = \frac{L-x}{v}$, then we get,

$$C_{out}(t) = \int_0^{\frac{L}{v}} C_r(t-t') \cdot e^{-\lambda t'} \cdot \frac{v}{L} dt' \quad (6)$$

Suppose the C_r is a constant, then the above equation can be changed to

$$C_{out}(\tau) = \frac{1}{\tau} \int_0^{\tau} C_r \cdot e^{-\lambda t'} \cdot dt' = \frac{C_r}{\mu \cdot \lambda} \cdot e^{-\lambda \tau} \quad (7)$$

In the equation above, $L/v = \tau$, $C_{out}(\tau)$ -the radioisotope concentration of drill holes. The physics meaning of τ is that the water in the reservoir can get to the drills after the time τ , τ is also called the mean resident time or the turnover time. We can get the value τ when we have known the $C_r(t)$ and $C_{out}(t)$.

THE APPLICATION OF THE LUMPED PARAMETER MODEL

The hydrogeology of some hydropower station

The hydropower station is located in the center of some canyon. The canyon section of the reservoir stands between dam site and the import of the canyon, which is located on the v-shaped river valley. The slope degree of the banks is about 45° and the valley side is steep. The outcrop is mainly stuff, stuff breccia and andesite. There are three trend faults which is NW-NE-NNE. The width of the canyon is 340 m in the normal water level which is 1420m. The relative height of the mountains at banks is 327~362m, and the width of the River bed is 80m, the overburden thickness is 2-5m.

There are no big regional fractionations in the dam zone. Those fractionations such as F32、F32-1、F285, have some effect on the dam. There are breccia, cataclasite, fault clay and mylonitic in the crush zone which is 0.5-22m width. The groundwater level at the dam site is higher than that of the river. The base rocks at dam site are breccia stuff, crystal tuff and andesite, which have higher strength and the moisture compressive strength is 90-150MPa. Deformation modulus of rock is 2.43-9.16GPa, 38°-45°. The rock mainly weak mantlerock which is 25-30m, and the thickness of strong mantlerock is 3-5m.

The application of the model

The tables are designed to have a uniform style throughout the paper. It does not matter how you choose to place the inner lines of the table, but we would prefer the border lines to be of the style shown in Table 1. For the inner lines of the table, it looks better if they are kept to a minimum. The caption heading for a table should be centered at the top of the table. Tables should preferably be located at the top or bottom of the page where they are first cited.

Sample points are located in the side of the dam abutment. According to the field data, the length of the dam abutment is about 400m. We can get the velocity of the points from the Equation (16).

Table 1. The 3H isotope data-analysis of the dam zone

name	reservoir	13#	Wei shui	27#	1#	Qiaqi gou	15#	Liang shuiyan	2#	23#
TUvalue	22.61	22.09	20.02	18.85	15.74	15.4	15.39	14.05	12.99	10.89
Mvalue (year)	—	3.16	3.27	3.34	3.55	3.59	3.58	3.69	3.78	4.04
Velocity (m/d)	—	0.35	0.34	0.33	0.31	0.31	0.31	0.30	0.29	0.27

We can know that the T value of the reservoir is bigger than others from the measured result, and it can be regarded as original one. The T value of groundwater supplied by the reservoir water will decrease with its residence time stratum increasing. The actual mean flow velocity of 27# which we have measured is 0.3m/d. Here the velocity calculated is

0.33m/d. The recharge time τ of ^{23}H is long, and the velocity calculated is 0.35/d, that measured is 0.27m/d. We also can get the infiltration length of the dam abutment according to the equation (16) in the contrary way.

CONCLUSIONS

Dam leak detecting is a significant content of investigation in disasters in hydraulic engineering. It is promotion and application of nuclear technique in hydraulic engineering that isotope tracer method is used in dam leak detecting. The radioisotope model of dam abutment leakage based on basic law of hydraulics principle and differential element method gives a theory mathematic base to interpret dam leakage with isotope method. The model makes it possible to simulate the leakage of dam abutment quantitatively. It can also be use for determine the leakage velocity and leakage passage.

REFERENCES

- Chen J.S., Dong H.Z. (2005). Detection of Leakage Passage in Fissure Rock with Assumptive Heat Source Method, *Chinese Journal of Rock Mechanics and Engineering*, 22: 4019-4024.
- Chen J.S, Dong H.Z., Yu B. and Chen L. (2003). Using line-heat-resource method to study concentration leakage passage of dike, *Progress In Geophysics*, (3): 400-403.
- Chen J.S, D H.Z. and Chen L. (2003). Application of the environment isotope method to study on the leakage passage in foundation of Beijiang Dyke Shijiao section. *Advances In Water Science*, 14 (1):57-61
- Clark I.D, Fritz P. (1997). Environmental isotopes in hydrology. CRC Press.
- Liu, J.G. and Chen J.S. (2001). Application of plane heat source method in leakage analysis for Shijiao reach of Beijiang dike. *Hydro-Science and Engineering*, 3:63-65.
- Mazor E. (1997). Chemical and isotopic groundwater hydrology (in): The Applied Approach, 2nd edition, Marcel Dekker, Inc., New York. 413
- Payne B.R., Eriksson E. and Danilin A.I et al. (1983). *Guidebook on Nuclear Techniques in Hydrology* Edition VIENNA: International Atomic Energy Agency. 17-27.
- Tong H.B. (2007). Isotope Concentration Field Flow Field Coupling Differential Equation Model. Nanjing: Hohai Univ, 30-50
- Zhou S.J., Tang J.T., He J.S. and Zhu Z.Q. (2004). Application of flow field fitting method in seepage and piping detection of embankments, *Yangtze River*, 35 (2): 7-8

GROUND SETTLEMENT MODEL FOR EXCAVATION OF A NON-PARTIAL PRESSURE AND SHALLOW BURIED DOUBLE-ARCH TUNNEL

Jihong Wei

Civil Engineering College, Hohai University, Nanjing 210098, China

Shaorui Sun

Geotechnical Engineering Research Institute of Hohai University, Nanjing 210098, China

The ground settlement model due to tunnel's excavation was summarized in this paper. Firstly, the geological characteristics of a double-arch tunnel in Jinliwen Expressway are investigated and analyzed, which mainly act as discontinuity. Especially, settlement pattern during excavation of such a double-arch tunnel with non-partial pressure and shallow bury was taken out by data analysis from those monitoring information. After ground settlement model and its increment model following the each step of tunnel's excavation were built, the difference of forecasting between single tunnel and double-arch tunnel was shown. Secondly, the ground settlement model was testified by comparing between forecasting and field data. Thus, theoretical basic to avoid overmuch settlement during excavation of such a double-arch tunnel was provided.

INTRODUCTION

The ground settlement due to tunnel excavation was researched by experience equation, theory analytical solution and numerical simulation etc. The Peck method was a representation for experience equation method. Within Peck method, the mechanics characteristic of surrounding rock was clearly discussed when it is used to evaluate the ground settlement due to tunnel excavation. However, the result mainly depending on one's experience may cause great difference contrast to the in-situ measurement. The surrounding rock is regarded as elastic, elastic-plastic or creep-elastic-plastic media in the theory analytical method. The numerical simulation might be taken the construction process into account from different angle. Double-arch tunnel is a good type used in construction of expressway. Otherwise, special requirement of the stability of surrounding-rock was required due to the typical special structure. On the other hand, because of the complex construction process, many geological problems were inevitably faced and maybe only parts of them could be solved. The ground settlement model for excavation of the non-partial pressure and shallow bury double-arch tunnel in Jinliwen Expressway was researched in this paper. According to the theory analysis, the ground settlement model was built and used for monitoring and forecasting.

RESEARCH DEVELOPMENT OF GROUND SETTLEMENT

At present, research on the ground settlement model mainly concentrates on those excavations in city. Therefore, many ground settlement models, such as Peck equation and revised Peck equation, were built in soft soils. Based on a large number of data for settlement monitoring, calculating equation of cross section settlement was put forward by Peck in 1969. According to measure and calculation in field, the limitation for Peck equation is analyzed by Celestino. The results showed that the cross section settlement is not normal distribution curve when large plastic zone appeared in tunnel. Then, equation of three parameters yield density curve was put forward based on the foregoing suppose. According to analytical solution, the cross section ground settlement equation was put forward by Sagasetta. In China, according to measure data, the ground surface settlement model of Shanghai by use of numerical calculation was also taken out by Li G. H.

ENGINEERING GEOLOGICAL CHARACTERISTIC OF THE FIELD

Jinliwen Expressway located in Wenzhou city, Zhejiang province (Figure 1). The double-arch tunnel locates in denudating hill zone. The exposed stratum is mainly upper Jurassic crystals clasts welded tuff (Figure 2). Due to the road which abuts OU river locates the left of this tunnel and some houses repose the top of hill, the settlement increment of double arch tunnel becomes very important.



Figure 1. Location of engineering



Figure 2. Yangwan tunnel in Jinliwen Expressway

Mainly stratum in engineering zone

According to the formation, lithology, characteristic and weathering degree, those stratum were divided into following parts: (1) incomplete lamination. (2) strong weathering crystals clasts welded tuff. (3) middle weathering crystals clasts welded tuff. (4) decline weathering crystals clasts welded tuff.

Calculation parameters

Considering the reports of engineering geology, design criterion, the calculation parameters was gotten in Table 1.

Table 1. Calculation parameters

stratum	Young's modulus (GPa)	Poisson's ratio	Unit weight of rock and soil(kN/m ³)	Cohesion (MPa)	Friction angel (°)	Tension strength (MPa)
1	0.05	0.330	26.0	0.059	29.34	0.2
2	0.75	0.316	26.3	0.168	36.13	0.4
3	2.00	0.290	26.6	0.300	45.00	0.5

GROUND SETTLEMENT MODEL

Calculation model

Geometry model in Figure 3 is a planar surface. Elastic-plastic model was taken. And the calculation proceeding including: (1) former processing is operation by software ANSYS. (2) calculation program is self-write. (3) post processing.

Settlement model

After the model is analyzed. the settlement model curve of double arch tunnel excavation is get in case of 35 meters bury depth (Figure 3). The ground surface settlement curve of middle tunnel excavation is axis-symmetric along the middle tunnel from Figure 2. It is uniform to fact. The left side settlement deformation is bigger than the right side because of effect of middle tunnel excavation and plastic deformation of rock mass when the left tunnel is excavated. The ground surface settlement of right tunnel excavation mainly concentrates in the location of right tunnel. The settlement is major in the location of middle tunnel. The settlement between the middle axial line of left tunnel and right tunnel is common. The settlement of right side of right tunnel is gradual diminution from middle axial line.

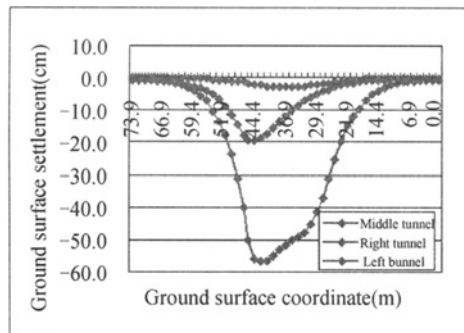


Figure 3. Settlement curve of 35 meters buried depth tunnel.

The ground surface settlement model of middle tunnel excavation got by analyzing its settlement.

$$f(x) = f(x_0) + A_1 e^{-\frac{(x-k_1)^2}{2w_1^2}} \quad (1)$$

where $f(x_0)$ is the constant, A_1 is the coefficient relative to maximum settlement, k_1 is the parameter relative to the ground location, w_1 is the shape parameter of curve.

To the middle tunnel, its parameters includes: $f(x_0)$ is equal to 0.02, A_1 is equal to 1.85, k_1 is equal to 37.00, w_1 is equal to 6.92664. The fact settlement and model settlement is consistency from ground surface settlement model sketch of middle tunnel. It shows that the settlement model reflects the ground settlement law of middle tunnel.

The common simulation method is adopted to left tunnel excavation and right tunnel excavation. The ground settlement model for double arch tunnel in case of non-partial pressure is:

$$f(x) = f(x_0) + \sum_{i=1}^3 A_i e^{-\frac{(x-k_i)^2}{2w_i^2}} \quad (2)$$

where $f(x_0)$ is the constant, A_i is the coefficient relative to maximum settlement, k_i is the parameter relative to the ground location, w_i is the shape parameter of curve.

The ground surface settlement model parameters are got in case of different bury depth after the common simulation method is adopted (Table 2).

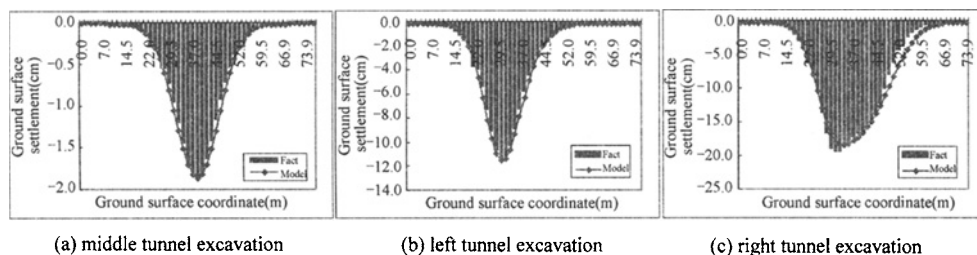


Figure 4. Settlement model

Table 2. The settlement model parameters of different burying

Bury depth	35m	30m	25m	20m	15m	10m	5m
	0.275	1.525	2.335	5.195	10.265	16.090	23.480
A_1	1.850	2.950	3.350	3.330	3.045	2.745	2.970
A_2	10.350	16.825	15.015	17.570	14.455	11.965	11.080
A_3	12.995	55.960	51.578	75.635	55.405	51.220	46.530
k_1	37.000	37.000	37.000	37.000	37.000	37.000	37.000
k_2	29.504	28.005	28.005	45.996	45.996	45.996	47.496
k_3	41.498	35.000	38.500	35.500	34.000	34.000	32.502
w_1	6.92664	9.44622	10.70622	11.96706	13.22706	13.85748	14.48748
w_2	5.66832	5.66832	8.18874	10.07832	13.22748	19.27422	19.27422
w_3	8.81664	10.07622	11.33664	11.33664	11.96664	13.22748	13.85748

The ground surface settlement rule of double arch tunnel in case of 35 meter bury depth was researched in the front. Although the settlement rule of tunnel is basic common in case of different bury depth. The difference of tunnel settlement is existence (Figure 6(a)). It is important for researching increment settlement model to reflect settlement difference in case of different bury depth.

From Figure 6(a), the increment settlement curve appears gentle step-like when bury depth is shallow. The increment settlement curve appears inverse split-blip when bury depth is deep. The mainly case is that the middle wall limits the ground surface settlement and biggish settlement for the left tunnel and right tunnel. According to the rule of settlement curve. The settlement model of middle tunnel excavation is built.

$$f(x) = f(x_0) + \sum_{i=1}^n \left[A_i e^{-\frac{(x-k_i)^2}{2w_i^2}} - A_0 e^{-\frac{(x-k_0)^2}{2w_0^2}} \right] \quad (3)$$

where the parameters is common to equation 6. The next mark number 0 denotes the settlement parameters in case of 35 meter bury depth.

The ground surface settlement model of middle tunnel excavation in case of 35 meter bury depth is showed in Figure 5. The model curve reflects the increment settlement of middle tunnel excavation. The increment model is correlation to fact distribution.

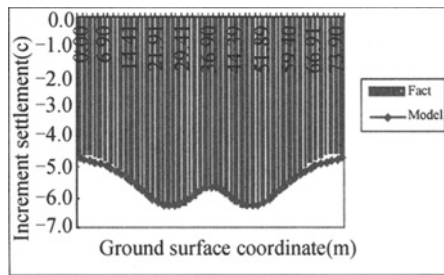


Figure 5. Surface increment settlement model for 35 meters buried depth.

The increment settlement model of right tunnel is got through analyzing right tunnel excavation.

$$f(x) = f(x_0) + \sum_{i=1}^n \left[A_i \exp \left(-\exp \left(-\frac{x-k_i}{w_i} \right) - \frac{x-k_i-w_i}{w_i} \right) - A_0 \exp \left(-\exp \left(-\frac{x-k_0}{w_0} \right) - \frac{x-k_0-w_0}{w_0} \right) \right] \quad (4)$$

Where the parameters is common to the front.

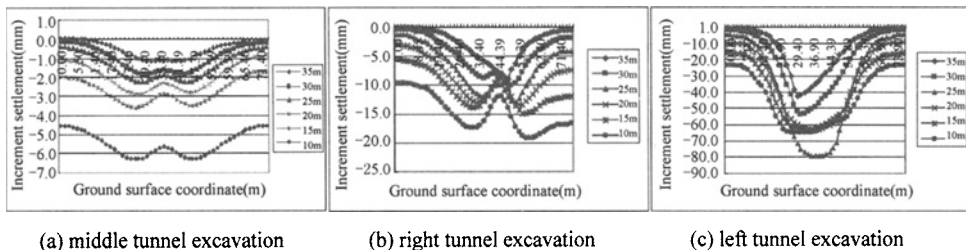


Figure 6. Surface increment settlement model

The ground surface settlement curve of right tunnel and left tunnel is showed in Figure 6(b) and Figure 6(c) individual. The increment settlement is bigger in the right side of right tunnel

than in the left side because of effect of the middle wall form the figure when the right tunnel is excavated. The curve shows irregularity normal distribution shape because of effect of the middle wall form the figure when the left tunnel is buried deep. The curve shows regularity normal distribution shape because of effect of the middle wall form the figure when the left tunnel is buried shallow. The parameters of model shows in Table 3.

Table 3. The increment settlement model parameters for different burying and excavation

Bury depth		35m	30m	25m	20m	15m	10m	5m
Right tunnel	$f(x_0)$	-0.130	-0.725	-2.075	-1.390	-3.260	-5.700	-9.690
	K	44.392	29.400	29.400	45.891	44.392	44.392	44.392
	W	5.67	6.93	8.82	10.71	13.23	16.38	19.95
	A	-11.320	-18.675	-17.445	-20.640	-16.970	-14.260	-13.520
Left tunnel	$f(x_0)$	-0.32	-0.800	-2.375	-5.195	-10.265	-16.09	-23.48
	k	42.892	30.899	32.398	39.896	39.896	38.396	36.896
	w	20.3932	20.39235	22.9432	24.2182	25.49405	28.0449	28.0449
	A	-448.23	-1382.24	-1832.20	-2750.38	-2213.24	-2095.04	-2019.61

The increment settlement model of right tunnel is got through analyzing left tunnel excavation.

$$f(x) = f(x_0) + \sum_{i=1}^n \left[\frac{A_i}{w_i \sqrt{\pi/2}} e^{-\frac{2(x-k_i)^2}{w_i^2}} - \frac{A_0}{w_0 \sqrt{\pi/2}} e^{-\frac{2(x-k_0)^2}{w_0^2}} \right] \quad (5)$$

Where the parameters is common to the front.

CONCLUSIONS

Based on investigation and analysis of the discontinuous plane, and by use of total process simulation, the ground settlement for double-arch tunnel excavation of Jinliwen expressway was researched by numerical method in case of complex geological condition and physical mechanics parameters. Some conclusions were gotten.

The ground settlement curve of middle tunnel excavation for double-arch tunnel is common to normal distribution curve. The ground surface settlement of right tunnel excavation shows similar normal distribution curve. The settlement in one side is bigger than other side. The settlement of left tunnel excavation is bigger in left tunnel than in the right tunnel when the left tunnel excavation. At the same time, the settlement of right tunnel caused by left tunnel excavation is enhancement. The settlement of right tunnel is caused by plasticity deformation of rock mass. The increment settlement model of middle tunnel excavation shows inverse slip-blip curve when the bury depth is shallow from increment settlement forecasting model. The increment settlement of right tunnel excavation shows similar inverse slip-blip curve. The settlement of right tunnel is bigger than the left tunnel when the right tunnel is excavated. With the inverse slip-blip curve of increment settlement of the left tunnel, the increment settlement model caused by middle tunnel is obvious when the bury depth is shallow. Especially the middle wall limited the corresponding ground surface settlement.

REFERENCES

- Zhou Yu hong, Zhao Yan ming, Cheng Chong guo (2002). Optimum analysis on the construction process for joint arch tunnels in partial pressure. *Chinese Journal of Rock Mechanics and Engineering*, 21, 679-683.
- Peck R. B. (1969). Deep excavations and tunneling in soft ground. Proceedings of the 7th International Conference on Soil Mechanics and Foundation Engineering, Mexico, State of the Art Volume, Soceidad Mexicana de Mecanica de Suelos, A. C, Mexico City ,225-290.
- Celestino T B, Gomes R A M P and Bortolucci A A (2000). Errors in ground distortions due to settlement through adjustment. *Tunnelling and Underground Space Technology*, 15, 97-100.
- Segaseta C (1987). Analysis of undrained soil deformation due to ground loss. *Geotechnique*, 37, 301-320.
- Li Guihua (1984). The ground surface settlement estimation due to shield construction. *Journal of Tongji University*, 12, 20-22.

EVALUATE THE RISK OF LAND-SLIDING BASED ON GEOPHYSICAL DATA

Jianhua Xiao

Henan Polytechnic University

Jiaozuo City, Henan Province 454000, China

Currently, geophysical data are widely available in most areas. Usually, the detailed geometrical and mechanical feature of rock base is supplied by the geophysical surveying. How to use the geophysical data to evaluate the risk of land-sliding is discussed in this research. Firstly, the strain in surface layer is formulated by the rock-base deflection angular. This formulation is based the fact that the original geological structure is horizontal. The current rock-base geometrical feature is the result of geological deformation. Secondly, the stress of surface layer is formulated by the mechanical parameter from the seismic data. This stress is expressed as the function of the rock-base deflection angular. This formulation is based on the fact the surface deformation is mainly controlled by the rock base deformation. Finally, the internal stress strength is calculated and is used to evaluate the risk of land-sliding. This risk analysis formulation takes the deflection angular of rock-base formation as the principle geometrical variant quantity and the related mechanical quantities are determined by seismic surveying data.

INTRODUCTION

The current geologic formation structure is the results of geologic deformation which mainly were caused by geologic action. Mostly, the risk of land-sliding is related with the sedimentary formations. For a sedimentary formation, its composition is determined before it suffering geologic deformation. So, the horizontal sedimentary formation should be taken as its initial configuration. On this sense, the current configuration of the sedimentary formation is the results of its deformation referring to its initial configuration. So, the related geological stress which acted on the formation to form the current geological structure can be calculated based on the available geometrical data of sedimentary formation.

Referring to the current geological condition, the stress may cause the land-sliding is an incremental stress. Mechanically, the land-sliding can be viewed as an incremental deformation (Biot, A.M., 1965) stacked on the geological deformation happened long ago. As the geological deformation happened long ago can be calculated by the geometry of the formation based on geophysical prospecting data, the residual rock stress strength can be calculated. The residual strength can be used to evaluate the risk of land-sliding with very good confidence. In this paper, the related theoretic results will be used directly. The main points will be focused on how to do the related calculation. Some simple cases are supplied.

CALCULATE THE ALLOWABLE MAXIMUM STRESS BASED ON GEOPHYSICAL DATA

Usually, the geological structure can be obtained by reflection seismic data. The seismic data will give out the depth of the main reflection layer and the curvature of the layer. In practical cases, some small faults may exist.

The curvature of the layer can be directly measured on the geologic sections. It is expressed as the local rotation angular of unit-volume material element referring to its initial curvature-less state (Chen Zhida, 1987). On the layer, along the section direction x^1 coordinator can be established. Taking the depth direction coordinator as the x^3 coordinator, then the x^2 coordinator is perpendicular to the section. Referring to the initial horizontal configuration, the current formation configuration can be described by the displacement field $u^i, i=1,2,3$. The mechanics definition of curvature of formation is:

$$\Theta = \arcsin\left[\frac{1}{2}\sqrt{\left(\frac{\partial u^1}{\partial x^2} - \frac{\partial u^2}{\partial x^1}\right)^2 + \left(\frac{\partial u^2}{\partial x^3} - \frac{\partial u^3}{\partial x^2}\right)^2 + \left(\frac{\partial u^3}{\partial x^1} - \frac{\partial u^1}{\partial x^3}\right)^2}\right] \quad (1)$$

Its corresponding deformation gradient (Chen Zhida, 1987) tensor is:

$$F_j^i = R_j^i = \begin{vmatrix} 1+(1-\cos\Theta)[(L_1)^2-1] & L_3 \sin\Theta & -L_2 \sin\Theta \\ -L_3 \sin\Theta & 1+(1-\cos\Theta)[(L_2)^2-1] & L_1 \sin\Theta \\ L_2 \sin\Theta & -L_1 \sin\Theta & 1+(1-\cos\Theta)[(L_3)^2-1] \end{vmatrix} \quad (2)$$

For a known geological structure, along the key layer, the local rotation angular Θ and the rotation direction vector $L_i, i=1,2,3$ can be determined. Its method is purely geometrical. For each section area, when this calculation is finished, the strain can be calculated by the following equation:

$$\varepsilon_{ij} = \frac{1}{2}\left(\frac{\partial u^i}{\partial x^j} + \frac{\partial u^j}{\partial x^i}\right) = (1-\cos\Theta)(L_i L_j - \delta_{ij}) \quad (3)$$

To simplify the calculation, usually taking the section perpendicular to the local rotation direction. If the rotation direction is on the x^2 direction, then $L_2 = 1, L_1 = L_3 = 0$. The problem can be simplified as:

$$\varepsilon_{11} = \varepsilon_{33} = -(1-\cos\Theta), \text{ (others are zero)} \quad (4)$$

If the fracturing stress of the formation layer is σ_s and the shear constant is μ (both parameters are defined on the initial formation, so they can be measured by the rock sample taken at the non-fracturing position), then the maximum allowable local rotation angular Θ_s is:

$$\Theta_s = \arccos\left(1 - \frac{\sigma_s}{2\mu}\right) \quad (5)$$

Its mechanics meaning is that when this local rotation reaches this value fracturing will happen. As this parameter can be actually measured, the maximum allowable incremental local rotation angular is:

$$\Delta\Theta = \Theta_s - \Theta \quad (6)$$

This parameter can be used to evaluate the risk of fracturing of the formation under evaluation (Xiao Jianhua, 2007).

Referring to the current configuration, the maximum incremental strain can be calculated by equation:

$$\Delta\varepsilon_{ij} = [1 - \cos(\Theta_s - \Theta)](L_i L_j - \delta_{ij}) \quad (7)$$

The maximum allowable stress field can be calculated as:

$$\Delta\sigma_{ij} = -2\tilde{\lambda}[1 - \cos(\Theta_s - \Theta)] \cdot \delta_{ij} + 2\tilde{\mu}[1 - \cos(\Theta_s - \Theta)] \cdot (L_i L_j - \delta_{ij}) \quad (8)$$

For the case $L_2 = 1$, $L_1 = L_3 = 0$, it is simplified as:

$$\Delta\sigma_{11} = \Delta\sigma_{33} = -2(\tilde{\lambda} + \tilde{\mu}) \cdot [1 - \cos(\Theta_s - \Theta)] \quad (9a)$$

$$\Delta\sigma_{22} = -2\tilde{\lambda} \cdot [1 - \cos(\Theta_s - \Theta)], \text{ others are zero} \quad (9b)$$

As the current configuration of formation is taken as the reference, the elastic constants $\tilde{\lambda}$ and $\tilde{\mu}$ should be the measured value in-site. This is easy from seismic data. Based on the P-wave velocity and S-wave velocity, they can be calculated by equations:

$$\tilde{\lambda} + 2\tilde{\mu} = \rho \cdot V_p^2, \quad \tilde{\mu} = \rho \cdot V_s^2 \quad (10)$$

where, ρ is the mass density.

Once the allowable maximum stress field is obtained, the risk of land-sliding can be evaluated according to the local government requirements or user requirements.

DO THE SEISMIC PROSPECTING

Traditionally, the seismic prospecting is too expensive for land-sliding risk investigation. However, as the seismic acquisition system becomes very cheaper after 1990s, it can be used economically. There are three main technological differences from conventional seismic prospecting: (1) seismic source; (2) frequency range; (3) CMP stacking.

Generally, the region under land-sliding risk evaluation is very sensitive about explosion. Hence, a mechanical source must be used. Based on author's experience, a 100 kg weight dropping from 2 meters high will produce the required seismic wavelet. Its frequency rangy is roughly 20-150 Hz. The high frequency dogma is too bookish. The key parameters are the layout of acquisition system.

The frequently used parameters are: 1-2 meters geophone spacing; middle shooting; shot interval 2-4 meters; 48-120 geophones spreading. For such a geometrical setting, the detect depth range is: 10-200 meters. For P wave, the best geophone is acceleration response type (rather than velocity response type which are widely used in oil seismic exploration).

They form high special density reflection data. Hence, the stack velocity data can be obtained by CMP method with high accuracy. Once the stack velocity-depth parameter are

obtained in the relative less-fracturing area, they are used in the whole seismic data processing without change (this is different from the oil seismic exploration).

Basically, to make the seismic section can be used to do the land-sliding risk evaluation, the fracturing face is one of the target of seismic prospecting. Figure 1 is a typical seismic section (after CMP processing, stack number is 48-64). CMP interval is one meter. This section is obtained in a Shanxi province. The task is to evaluate the land-sliding potential related with coal mining near a country. The coal depth is about 80 meters deep from the country average elevation.

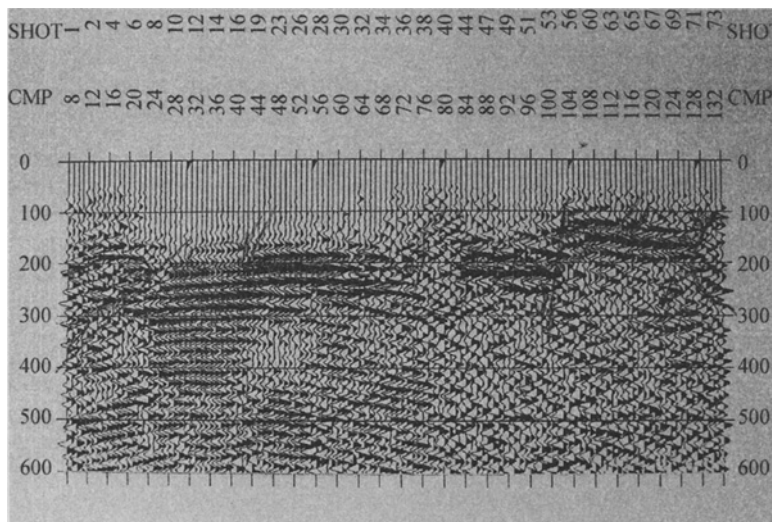


Figure 1. Typical in-line seismic section to identify coal mining related land-sliding risk

Usually, the geometry of layer can be determined with enough accuracy. This section is typical because that, on its left half the land-sliding risk is high, on its right half the land-sliding risk is low. The surface position of land-sliding is 20 meters away from the first CMP. For the section CMP less than 24, the layer is highly curvature. On its corresponding surface, some visible cracks can be observed. The house is evaluated as on high-risk. The potential land-sliding face is marked out by the strait line between the curvature region and curvature-less region. In fact, on this region, the P wave velocity is lower than its normal value. Near the potential land-sliding face (CMP24-42), high stress zone exists, which causes the long trail of seismic reflection. The land-sliding face at CMP100 is very old. The blank zone near CMP80 is caused by a coal road way. There is another al road way at CMP 130. To give out the sections on the cross-line direction, Figure 2 is shown.

In some areas, the coal road way will not produce reflection blank. However, the curvature of the reflection layer on seismic is very striking. As such a local curvature can not be explained by the geological motion, it is attributed as the coal road way. Although there is a potential of making mistake, however, it is a very reliable way to identify the coal road way.

If the formation is totally cracked and lost its elasticity feature, good reflection signal is not available. However, some correlation may exist. In this case, it is easy to make the risk evaluation as it can be approximated as sands. The method has been used in many coal

mining areas in Hebei province and Shanxi province (Xiao Jianhua.2003, Wang Yanling.2005, Xiao Jianhua.2000). The seismic acquisition system is WF-6 (manufactured by Eastern Geophysical Exploration Inc.), and the seismic data processing system is GISYS-V (developed by Seismic Data Processing Center, Eastern Geophysical Exploration Inc.).

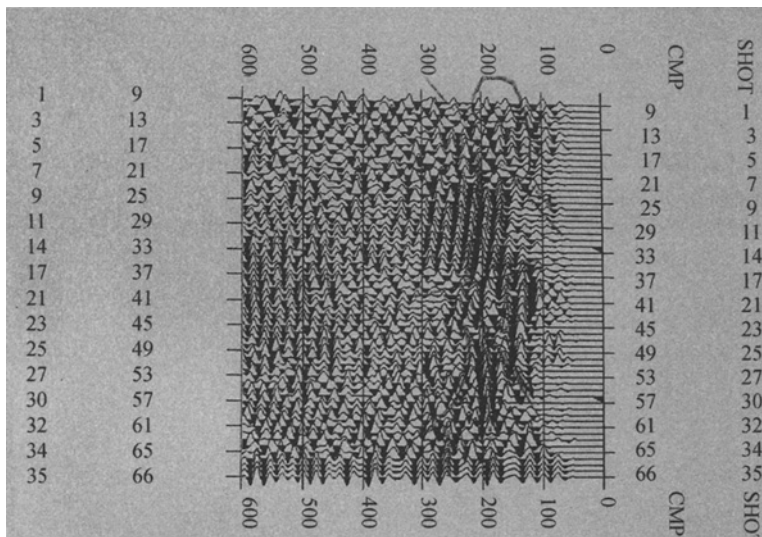


Figure 2. Typical cross-line seismic section to identify coal mining related land-sliding risk

END WORDS

The evaluation of land-sliding risk is a very sensitive job. The wrong conclusion may initiate local political turmoil. Hence, it must be based on reliable data. Usually, the coal road way which passes the country is secrete in the coal mine. When the land-sliding risk happens, the coal mines will deny any possibility which is related with their mining. So, to reduce the land-sliding risk, some secrete coal road ways must be identified to force the coal mines to take a co-operation action. Without the cooperation from the coal mines, the task is very difficult.

Once the required data is obtained, the risk caused by mining and the risk caused by the geological conditions must be separated clearly. If this job is not well done, the action to reduce the risk of land-sliding cannot be taken at once, as the related coal mines and the country governors will fall into heat debate.

Finally, if the allowable maximum stress estimation is too strict for unnecessary high standard, the risk evaluation is useless for both parts. Therefore, the parameters should be measured in laboratory with good accuracy. In one words, data quality and reliable calculation is very essential to treat the risk evaluation problems.

REFERENCES

- Biot A.M. (1965). *Mechanics of Incremental Deformations*, New York: John Wiley & Sons. I
 Chen Zhida. (1987). *Rational Mechanics*, Xuzhuo, China University of Mining &

Technology.

- Truesdell, C.(1966). *The Mechanical Foundation of Elasticity and Fluid Mechanics*, New York: Gordon and Breach Science Pub.
- Xiao Jianhua.(2007). Decomposition of Displacement Gradient and Strain Definition. *Advances in Rheology, Central South University of Technology*, 14 (Suppl.1): 401-404.
- Xiao Jianhua(2007). Geometrical Field Description of Fatigue-Fracture caused by High Temperature or its Gradient, *Multi-scaling associated with structural and material integrity under elevated temperature, Fracture Mechanics and Applications 2006*, ed. G.C. Sih, S.T. Tu, and Z.D. Wang, Shanghai: East China University of Science and Technology Press, 211-216.
- Hu Zongzhen.(2002). robe into seismic research problems of Earth (Karst) caves in shallow layer, *Coal Geology of China*, 14(2): 68-69.
- Xiao Jianhua.(2003). Problems from mountain area high-dipping strata seismic data dynamic correction, statics and stack, *Coal Geology of China*, 15(5): 44-45.
- Wang Yanling.(2005). Seismic prospecting for foundation stability evaluation in coal mining induced land-sliding area, *Coal Geology of China*, 17(2): 53-55.
- Xiao Jianhua.(2000). Seismic prospecting of small structures, *Coal Geology of China*, 12(3): 45-51.

THE SECURITY ALARM AND APPLICATION OF THE HORIZONTAL DISPLACEMENT MONITORING OF THE RETAINING STRUCTURE

Zhibiao Xiong

*Urban Construction College, University of South China,
Hengyang 421001, China*

Qiyun Wang

*Urban Construction College, University of South China,
Hengyang 421001, China*

Horizontal displacement monitoring was carried out for the complicated planar foundation pit. After the excavation, monitoring results indicated the horizontal displacement of the top retaining structure exceeded the advance warning and dangerous situation continued to aggravate. A comprehensive site investigation was carried out aiming at finding out the reasons for the warning alarm. The measures were taken to treat the dangerous situation pertinently and obtained good effect.

INTRODUCTION

The foundation pit dynamic support and control technology is a new concept based on live monitoring, which is a significant method to ensure the correct civil project implementation and protect surroundings around foundation pit.

Considering on supporting structure of the foundation pit, if which keep displacement over the safe factor, then the construct party could act as strengthen measures but without clear direction or reference, dangerous situation occurred. The weakest point is difficult to define the particular situation at the real time. Base on actual cases investigation and study by the writer, there is an effective and reliable strategy to keep supporting structure of the foundation pit stability.

GENERAL BACKGROUND OF THE PROJECT CASE

Perimeter of the foundation pit: 530m.

Over all the area of supporting structure: 7333.7 m².

Depth of foundation pit: 9.15m.

Function of the foundation pit's objective: basement of a shopping mall.

Location: corner formed by JieFang Rd, ZhengYang Rd and XianFeng Rd.

Nearby buildings: Yancheng Hotel, Bank of China and Finaical Bureau.

Details see Figure 1.

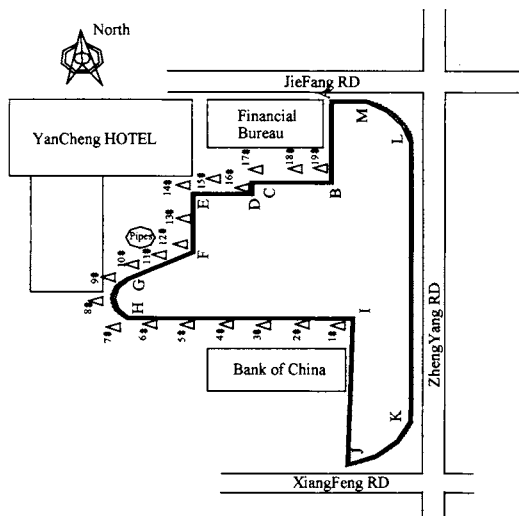


Figure 1. Sketch of foundation's plan view and the layout of the inspect points

Geologic construction

The property of geologic construction is shown in Table 1.

Table 1. Physical mechanics property index sign of different layers

Layer number	Layer	Elevation (m)	γ (kN/m ³)	C (kPa)	ϕ (degrees)	q_{sk} (kPa)
1	mix filled soil	3.75	17.00	17.00	20.00	35.0
2	clay(powder state)	6.20	19.40	18.00	21.90	50.0
3	clay(mud state)	2.60	19.00	20.00	30.00	30.0
4	gravel sandy soil	2.80	19.00	40.00	40.00	80.0
5	strong weathered rock	2.50	19.00	60.00	50.00	140.0
6	weathered rock	11.8(exposures)	19.00	80.00	65.00	200.0

where γ =Unit weight; C= Cohesion; ϕ =Internal friction angle; q_{sk} = Friction module.

Groundwater situation:

(1) Perched water, which most contained by mix filled ground surface soil. Source supplied from natural raining and living water.

(2) Confined water, which contained by gravel layer, strong positive correlation with the XiangJiang River. Such water line is between 5.0 meters and 8.0 meters to the ground surface.

(3) A little fissure water contained in rock cranny.

Design of supporting structure

The safety grade of side of foundation pit fixed as 2, ground surcharge maximum limit fixed as 15.0kPa according to the surroundings around foundation pit, Support system for the

foundation pit adopted labor excavated pile combined anchor ,See Figure.2. Retaining piles have $8 \phi 25$ (HPB335) reinforcing bars. Its concrete strength rating was C25;There's a reinforced concrete top beam ,which size was $1100 \text{ mm} \times 700 \text{ mm}$ and concrete strength rating was C20.The beam have $4 \phi 22 + 2 \phi 16$ (HPB335) around the beam. To protect the soil between piles concrete C20 was shotcreted to 100 mm .Two anchors were allocated at 1.1 m from top beam. The anchor of 12-m -long bored diameter is 120 mm and incline of 10° ,then reinforced with $1 \phi 25$ (HPB335. Mortar was injected into borehole through normal pressure.

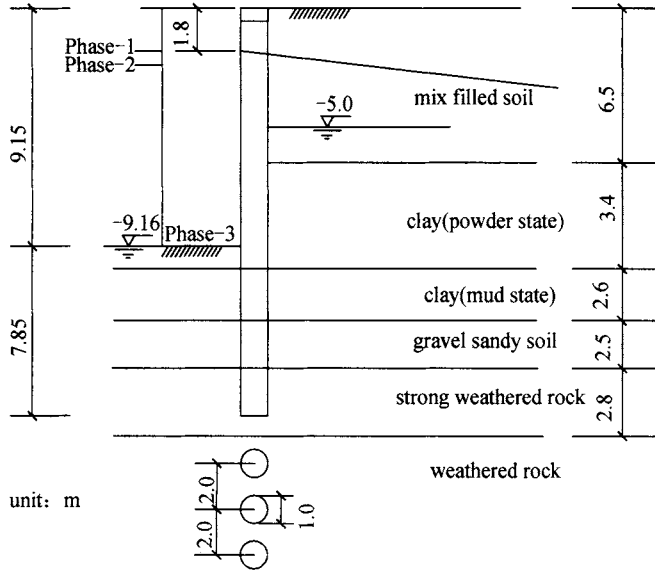


Figure 2. Sketch of calculation for retaining structure

Calculation according to above design concept, when the digging depth up to 9.5 m (pahse-3)the resulting of horizontal displacement could be illustrated by Figure 3.According to Figure 3,when digging completed the maximum displacement was about 17.2 mm , top displacement was about 9 mm . Considering on surrounding environment, horizontal displacement monitoring would be carried out. Collocation of horizontal displacement inspect point is shown in Figure 1. There were 44 inspect points attached on top beam of 15 m for every one, which monintoring frequency was about once a day. Monitoring duration was from the digging started to artificial fill completed. The warning maximum displacement value set as 30 mm .Monitoring of settlement and deformation for buildings surrounding the excavation was also carried out.

Underground water was mainly controlled

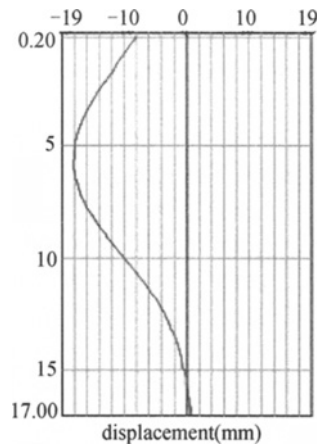


Figure 3. Result of horizontal displacement

by the action which gutter and sand drain was allocated in the pit and side ditch was allocated outside of pit.

Construction monitoring and implementation

Excavation after construction of supporting structure had 2 phases. The 1st phase, digging started by basement region: BCDEFGH. When phase-1 depth reached ± 0.00 , the 2nd phase launched—the region JKLMA digging started. The inspect points monitoring and construction digging were synchronal. There were 19 inspect points distributed on region BCDEFGHI for horizontal displacement (Figure 1). Till the construction phase-1 completed, the accumulative horizontal displacement didn't exceed the alarm limit. The curve represented that horizontal displacement trend by time (Figure 4) which were formed smoothly. However, displacement value from the point 5#, 6# exceeded the alarm limit significantly.

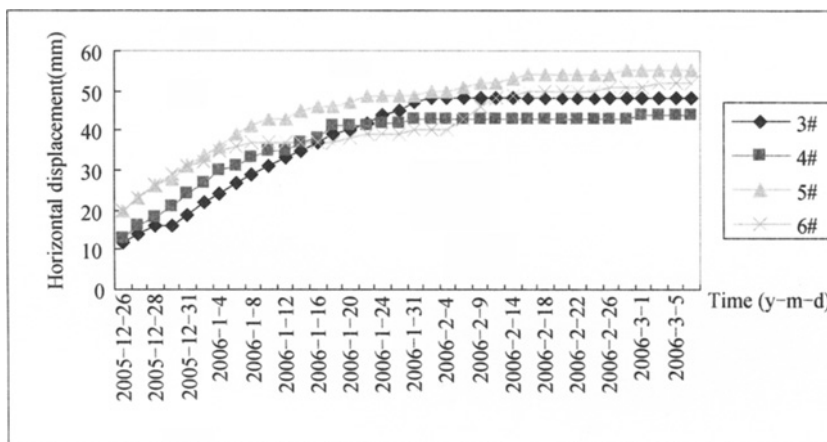


Figure 4. Relation between horizontal displacement and time in point of 3[#]-6[#]

Since Dec. 26, 2005, the displacement of inspect points 3[#] to 6[#] appeared constantly increasing, the detail curve illustrated in Figure 4. The displacement value inspected by these points exceeded the alarm limit different from Dec. 31, 2005 (5[#], 6[#]), Jan 4, 2006 (4[#]) and Jan.10, 2006 (3[#]).

Before alarmed, there was no surrounding environment research. According to the displacement trend, since Dec. 26, 2005 to Jan. 20, 2006, quantity surveyor added a row prestress anchor of 12m length underneath 7.2m of the top beam blindly from 6[#] to 3[#]. Monitoring results showed that although some inspect points displacement had closed and even exceeded alarm limit when anchor completed, 4[#] and 6[#] displacement were controlled effectively. 3[#] displacement stabilized on Jan.31,2006, 5[#] displacement increased but tiny. Since Jan. 31, 2006 points 5[#] and 6[#] appeared new displacement. By Feb. 4, the value increased rapidly, especially point 6[#]. Construction unit took measure of backfilling soil from foundation excavation to bottom of the pit at 5[#] and 6[#]. But in the next 10 days, point 6[#] displacement was 10mm. So construction conceived a plan that from point 5[#] to point F setting a steel pipe inner support to manage.

Alarm roots analysis

On Feb. 22 2006, the surrounding environment sit investigation started. The building of bank (located on the west of the basement) were preparing refresh fitment. There was a 2-m- high construction scrap heap, which located near by the region HI. A crack about 30- m-long and 3-cm-wide appeared on the ground between constructing basement and building of bank. Closer to the inspect point #6, the broader the crack became. The crack's orientation was parallel to the basement's sideline on region HI. On the otherwise, there was a barrel drain between the constructing basement and the building of Bank, but which was out of serving life. From Feb. 2006 Construction drain groundwater from pit to drain, the drain side wall was damaged seriously. Sewage was inflowing the pit through side of foundation pit. Initial analysis showed that the situation was a reason of abnormal horizontal displacement. Ignored the influence of hydrodynamic pressure of the sewage and based on the original designed parameter, the Groundwater was 1m to surface.

The surcharge “ q ” caused by the 2-m-high latest construction scrap on the west of Bank of China could be calculated as Equation.(1).

$$q = \gamma h$$

where q =overload; γ =unit weight of construction scrap; h =height of construction scrap;

The maximum retaining structure displacement was 72mm by elastic reaction method; Through the above analysis, the reasons for horizontal displacement exceeded the alarm limit was very obviously.

Action and effect

Considering above reasons, some proposal strategies were implemented.

(1) Cleaned the scrap heap between the constructing basement and bank's building and changed the orientation of sewage drain.

(2) Added anchor lock value to 80% of anti-puhforce (The value was more than which the code JGJ120-99 advised).

(3) Backfilled soil into the gap of 2.5-m-wide between inside of foundation pit and edge of the building foundation. The detailed measure was to masonry a brick wall, 500-mm-thick and height equivalent to the first basement, along the edge of the external walls of the basement from 3[#] to 7[#] inspect points, then carried through artificial fill in the gap. To stabilize the brick wall, columns and roof beams was constructed as structural measures also.

The construction part launched the implementation immediately and completed by 26th/Jan./2006. Afterward, until July/2006 basement was completed, there was no more horizontal displacement by the monitoring.

CONCLUSIONS

Analysis of the horizontal displacement and afterward implementation has led to the understanding that foundation excavation dynamic construction should not only base on analysis of monitoring, but also pay attention to the change of surrounding environment. It

must take effective measures to manage dangerous situation. It's proved that adding another row of prestressed anchor below the top beam get no effect. So horizontal displacement monitoring is very important for excavation construction ,especially when the supporting structure is in dangerous situation ,we can treat pertinently according to the results of the monitoring and employ an easy and effectively way to get the best effect.

REFERENCES

- Academe about Scientific Architecture of China (1999). *Technical Specification for Retaining and Protection of Building Foundation Excavations*, China Architecture And Building Press.
- Huadong Gao, Da Huo and Lianjin Tao. (2005). Field Measurements and Theoretical Analysis in Deep Excavation around Beijing Brilliance Edifice,*Chinese journal of Underground Space And Engineering*, 3: 423-427.
- Jianhang Liu and Xueyuan Hou. (1997). *The application enchiridion of Building Foundation Excavations*, 1st edition ,China Architecture and Building Press.

EVALUATION OF SEISMIC INDUCED RELATIVE DISPLACEMENT FOR CONTAINER CRANES ON CAISSON WALLS

Yutaka Yamamoto, Koji Ichii

*Graduate School of Engineering, Hiroshima University, 4-1, Kagamiyama 1 Chome,
Higashi-Hiroshima 739-8527, Japan*

The seismic design for quay walls and cargo handling facilities is important since the functional loss of ports may cause severe economic loss in a region. It is necessary to conduct a seismic design in terms of functionality so that cargo handling facilities may continue to function even after severe earthquakes. Relative displacement is an important index when the functionality of crane rails on caisson-type quay walls is discussed. There is a strong correlation on the level of displacement when the distance of the caissons is short, and estimation of the horizontal displacement of each caisson considering such correlation is possible by giving the correlation coefficient corresponding to the distance between the caissons. With this model, the relative displacement between caissons can be generated stochastically. As a result, evaluation of the post-earthquake functionality of a crane rail based on the allowable relative displacements becomes possible.

INTRODUCTION

The seismic design for quay walls and cargo handling facilities is important since the functional loss of ports may cause severe economic loss in a region. It is necessary to conduct the seismic design in terms of functionality so that cargo handling facilities may keep functioning even after severe earthquakes.

Figure 1 shows a typical failure mode of caisson-type quay wall due to earthquake. The acceptable damage level for seismic design has been examined based on the possible damage mode for each type of structure (PIANC, 2001). So far, crane rails have not been considered in the seismic design of quay walls, though loading facilities have been considered. However, the rails on caisson-type quay walls might be cut by differences in displacement compared to the next caisson (to be called “relative displacement” in the following section) as shown in Figure 2.

A seismic design which makes it possible to restore a rail even when some relative displacement has been caused by an earthquake is necessary. In this research, a stochastic method to evaluate the relative displacement of caissons is proposed, aiming to construct a seismic design method for rails in cargo handling facilities on caisson-type quay walls.

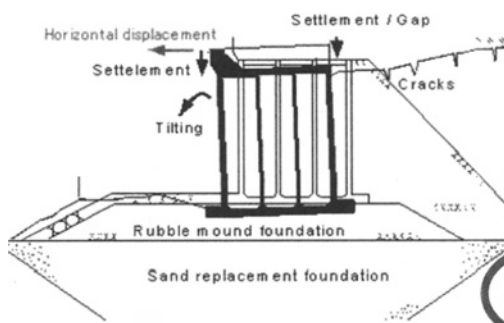


Figure 1. A typical failure mode of caisson-type quay wall due to

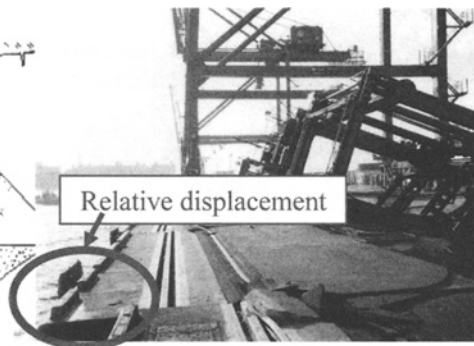


Figure 2. Example of damage to crane rail

DAMAGE TO CAISSON-TYPE QUAY WALLS

Correlations involving caisson displacement

The horizontal displacement, subsidence, and inclination of caissons are major damage patterns of quay walls. Especially, the horizontal displacement of caissons can be very large in many cases. From the case history of the 1995 Kobe Port disaster, we examined the horizontal displacement of caissons in a quay wall on Port Island arranged in a south-north direction. Here, the horizontal displacement toward the seaside at the top of the caissons will be discussed.

A quay wall (berth) consists of caissons of N pieces. $N=100$ on Port Island. Thus, the lengths of the quay walls are 1250 m. In this study, facing the seaside, we call the most-left caisson the first caisson, and the most-right caisson is the N th caisson. The damage record of those quay walls in the Hyogoken-nanbu earthquake (Inatomi et al. 1997) was analyzed based on the definition shown here. It was found that there is a strong correlation between each horizontal displacement when the distance between two caissons is short as shown in Figure 3.

The distance between two caissons can be called the number difference k ($k=-N+1, \dots, 0, \dots, N-1$). Caisson i and its correspondence to the number difference k is focused on here. The horizontal displacement of caisson i is $D_1(i, k)$, and the horizontal displacement of the correspondent caisson is $D_2(i, k)$. The combination of the horizontal displacements of two caissons is classified into different groups based on the absolute value $|k|$. It becomes a wide line when the value of $|k|$ increases. In order to discuss the correlation quantitatively, the correlation coefficient R is defined using the next Eque. (1). M is the number of samples with a number difference of k or $-k$. $D_1(i, k)$ and $D_2(i, k)$ are displacements of the i th caisson and the corresponding caisson with the number difference k , respectively. $\overline{D_1(k)}$ is the average of $D_1(i, k)$, and $\overline{D_2(k)}$ is the average of $D_2(i, k)$. We double-counted the combination of caissons i and j , where $i-j=k$ and $i-j=-k$.

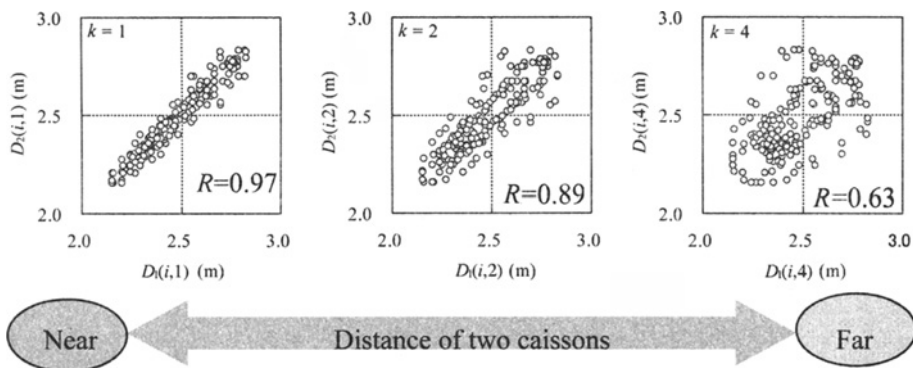


Figure 3. The correlation of displacement observed in two caissons

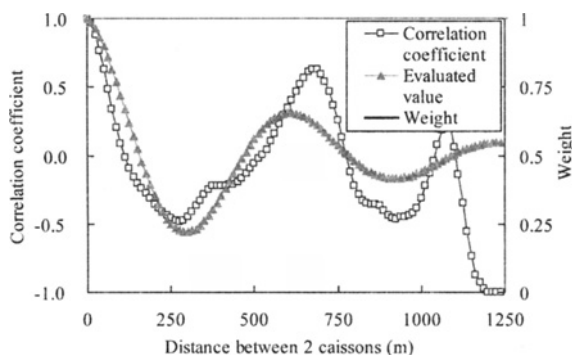


Figure 4. The evaluated correlation coefficient when the squared summation of weighted difference is minimized

$$R = \frac{\frac{1}{M} \sum_{i=1}^M (D_1(i, k) - \bar{D}_1(k)) (D_2(i, k) - \bar{D}_2(k))}{\sqrt{\frac{1}{M} \sum_{i=1}^M (D_1(i, k) - \bar{D}_1(k))^2} \sqrt{\frac{1}{M} \sum_{i=1}^M (D_2(i, k) - \bar{D}_2(k))^2}} \quad (1)$$

Therefore, $M=2N$ at $|k|=0$ and $M= 2$ at $|k|=N-1$. The number of samples decreases in a straight line as the distance $|k|$ increases. Therefore, the reliability of the results decreases with growth in the distance between two caissons. The calculated result of the correlation coefficient R according to the distance between two caissons is blue line in Figure 4.

Estimation of horizontal displacement of caissons considering correlations

A stochastic method to estimate the horizontal displacement of caissons on quay walls is proposed. It is based on a method of estimation of difference settlement with numerical simulation (Tsuchida and Ono, 1988). First of all, variable $X_i (i=1,2,\dots,N)$ of the horizontal displacement of the i th caisson of the quay walls is calculated using Equation. (2).

$$\begin{pmatrix} X_1 \\ X_2 \\ \vdots \\ X_N \end{pmatrix} = \begin{pmatrix} \bar{X} \\ \bar{X} \\ \vdots \\ \bar{X} \end{pmatrix} + \sigma [C^*] \begin{pmatrix} a_1 \\ a_2 \\ \vdots \\ a_N \end{pmatrix} \quad (2)$$

here, \bar{X} is the average of displacements, σ is the standard deviation, $[C^*]$ is the matrix of correlation, and $a_i (i=1,2,\dots,N)$ is normal random numbers. The matrix $[C^*]$ can be obtained by the method of Cholesky decomposition as shown in Equation (5). The covariance matrix $[C]$ is shown as in Equation (3).

$$[C] = \begin{pmatrix} \sigma_1^2 & \cdots & \sigma_1 \sigma_N \tau_{1N} \\ \sigma_2 \sigma_1 \tau_{21} & \cdots & \sigma_2 \sigma_N \tau_{2N} \\ \vdots & & \vdots \\ \sigma_N \sigma_1 \tau_{N1} & \cdots & \sigma_N^2 \end{pmatrix} \quad (3)$$

The correlation function τ_{ij} is given by Equation (6), described later. It is assumed that the variance of displacement is constant in a particular quay wall. $[C]$ is shown like Equation (4).

$$[C] = \sigma^2 \begin{pmatrix} 1 & \tau_{12} & \cdots & \tau_{1N} \\ \tau_{21} & 1 & \cdots & \tau_{2N} \\ \vdots & \vdots & & \vdots \\ \tau_{N1} & \tau_{N2} & \cdots & 1 \end{pmatrix} = \sigma^2 [C'] \quad (4)$$

$[C]$ can be resolved by Equation (5), and $[C^*]$, which shows the correlation, is obtained.

$$[C'] = [C^*] \cdot [C^*]^T \quad (5)$$

Eq. (6) is the assumption for τ_{ij} in consideration of having the characteristic that the correlation of the horizontal displacement increases when the distance between two caissons is short, and R shows wave-shaped characteristics (Vanmacke, 1977).

$$\tau_{ij} = \exp\left\{\frac{L(i,j)}{\beta}\right\} \cdot \cos\left\{\frac{2\pi L(i,j)}{\lambda}\right\} \quad (6)$$

Here, $L(i,j)$ shows the distance between caissons i and caissons j , β shows the parameter of the correlation distance, and λ shows the parameter of the wavelength. The parameters β and λ are given to minimize the summation of the squared differences between the correlation coefficient of the data using Equation. (1), and the correlation coefficient of the data using Equation. (6). However, because the reliability of the correlation decreases as $L(i,j)$ increases, weight parameters are considered in these difference summations. Here, the weight of difference margin is 1.0 at $L(i,j)=0$, and the weight summation is 0.0 at $L(i,j)=\max$. The weight parameter decreases in a straight line as $L(i,j)$ increases. The correlation coefficient when the squared summation of the weighted difference is minimized is shown in Figure 4.

As a result, $\beta=525$ and $\lambda=625$ were obtained. With these values for Equation. (6), the matrix $[C^*]$ is obtained by Equation. (5). A simulation to estimate the displacement on each

caisson considering the correlation was done by using Equation. (2). Figure 5 (a) shows the result of horizontal displacement of each caisson at random by using the normal random number of three patterns. Figure 5 (b) shows the result of simulated horizontal displacement without considering correlation. It can be said that considering correlation is important to evaluate the relative horizontal displacement of caissons.

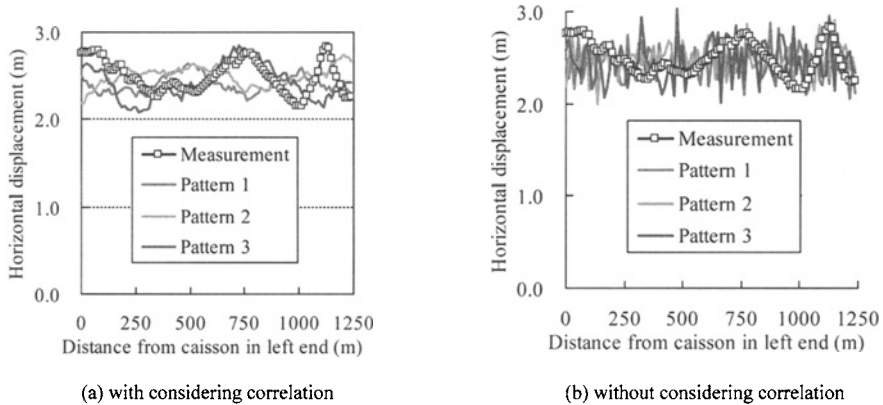


Figure 5. The result of simulated horizontal displacement

Evaluation of relative displacement between caissons and its application

One hundred possible patterns of the horizontal displacement of the quay walls were generated at random by using the proposed model in this research, and the distribution of the difference of the horizontal displacement of the caisson adjoined mutually (relative displacement) was examined. Figure 6 shows the distribution of relative displacement of the Port Island quay walls, as a probability density function. From this figure, the applicability of the proposed model to estimate the relative displacement can be regarded as excellent. Therefore, if this technique is used, stochastic estimation of relative displacement becomes possible.

Seismic design of crane rail based on relative displacement

The evaluation of the gap of horizontal displacement at the boundary to the next caisson is important to evaluate the functionality of the crane rail. It seems that the probability of functional loss of the crane rail can be judged by the maximum value of relative displacement (maximum relative displacement), since recovery of the damaged rail is possible if the observed relative displacement is not significant. Thus, allowable relative displacement can be defined as the maximum relative displacement where the restoration of the rail is possible. It is effective to introduce the idea of the allowance of relative displacements when a crane rail is designed.

The maximum relative displacement depends on the length of a berth, which corresponds to the number of caissons. Therefore, the evaluation method of the relative displacement of quay walls should include the effect of the length of the berth. Thus, the level of the

allowance relative to displacements and the number of caissons are both factors in the estimation of failure probability. Figure 7 shows the probability that the maximum relative displacement will stay within the allowable relative displacements. The probability that the maximum relative displacement stays within the allowable relative displacement decreases when the length of a berth increases. Thus, the functionality on quay walls can be assessed by the allowable relative displacement and the number of caissons.

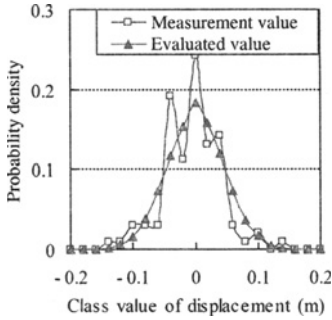


Figure 6. The distribution of relative displacement

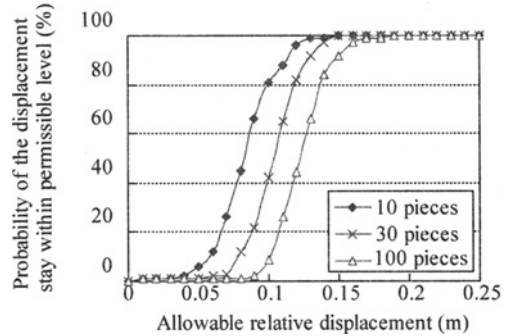


Figure 7. The probability that the maximum relative displacement stay within the allowable relative displacements

CONCLUSIONS

A technique for evaluating the relative displacement between adjoining caissons is proposed in this research. It is based on damage data from the Port of Kobe in the 1995 Hyogoken-nanbu earthquake. The following conclusions were obtained:

(1) It was confirmed that there is a correlation with respect to deformation of caissons, and it is dependent on the distances between the caissons. It seems that there is a range in which a negative correlation on the level of deformation can be found.

(2) A simulation that estimates the horizontal displacement of each caisson considering the correlation was made possible by giving the correlation coefficient corresponding to the distance. The results of the simulation for the Kobe Port case show excellent agreement with observations. If this model is used, the relative displacement between the next caissons can be evaluated stochastically.

(3) A method to calculate the probability of failures of quay walls by setting the relative displacement is proposed. As a result, the design of a crane rail according to probabilistic handling of the allowable relative displacements becomes possible.

REFERENCES

- PIANC (International Navigation Association). (2001). *Seismic Design Guidelines for Post Structure*, A. A. Balkema, 474.
- Inatomi et al. (1997). Report of damages of facilities of the Port in 1995 Hyogoken-nanbu earthquake, *Technical Note of the Port and Harbour Research Institute Ministry of Transport, Japan* (857): 474-488, 775-793.

- Tsuchida, T. and Ono, K. (1988). Evaluation of Differential Settlements with Numerical Simulation and Its Application to Airport Pavement Design, *Report of the Port and Harbour Research Institute*, 27 (4), 123-200.
- Vanmarcke, E. H. (1977). Probabilistic modeling of soil profiles, *Journal of the Geotechnical Engineering Division*, M. ASCE, 1227-1246.

PILE HORIZONTAL DISPLACEMENT MONITOR INFORMATION CALIBRATION AND PREDICTION FOR GROUND FREEZING AND PILE-SUPPORT FOUNDATION PIT

Baoyuan Yuan, Xianggang Liu, Xufeng Zhu

*Geological and Geotechnical Engineering Department, Hohai University, Xikanglu 1[#],
Nanjing 210098, China*

Monitor data of pile horizontal displacement for Ground freezing and Pile-support Foundation Pit of south anchorage of Runyang Bridge, had Obvious error by freezing and deformation of bottom part. It was proved that horizontal displacement of pile-top beam can't be used to Calibrate error, but the displacement Calibration on Position of first support could be used to Correct pile horizontal displacement. The displacement on Position of first support was calibrated by data of support force and temperature. This result provided reliable monitor data for Anti- analysis and prediction of foundation pit, and the experience was backlog for construction of similar engineering aftertime.

INTRODUCTION

Monitor data of pile horizontal displacement for Ground freezing and Pile-support Foundation Pit of south anchorage of Runyang Bridge, had obvious error by freezing and deformation of bottom part. It was proved that horizontal displacement of pile-top beam can't be used to calibrate error, but the displacement calibration on position of first support could be used to correct pile horizontal displacement. The displacement on position of first support was calibrated by data of support force and temperature.

Due to the great depth, good continuity and bore inclinometer becomes a main monitoring measure for the deformation of foundation pit slope. In the process of field measurement with inclinometer, blocking often occurs in the bottom of inclinometer. Measured displacements can be corrected with data from some reliable points, and the displacements of blocked section may be deduced through feed-forward neural network. Furthermore, the local displacements may be corrected, and the deformation trend of foundation pit slope can be forecasted with feed-forward neural network.

The gray neural network model of GNNM(1,1) was established for predicting deformation of deep foundation pit. The model was applied in the deep foundation pit of the south anchorage of suspension bridge of Runyang and Changjiang Highway Bridge, it proves that the prediction is feasible, convenient and precise for engineering application.

This result provided reliable monitor data for Anti- analysis and prediction of foundation pit, and the experience was backlog for construction of similar engineering aftertime.

CONSTRUCTION CONDITION

Engineering geological condition

The soil layers of site of south anchorage of Runyang Bridge are consist of clay, silty clay, pulverous sand, silver sand. The thickness of soil layers is 27.80–29.40 m.

The rock layers of the site are mainly granite with interlining of lamprophyre. Strength of weathering is from strong to weaken with the depth change.

There is a fault fractured zone in the middle of south anchorage area, called F7 fault fractured zone. Its tendency is NE, and its obliquity is 55° – 70° .

The typical geological section of site of south anchorage is as Figure 1.

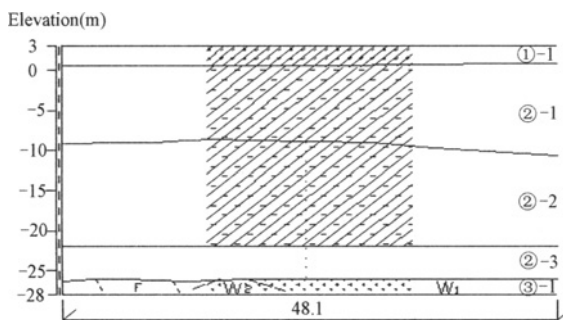


Figure1. Typical geological section of site of south anchorage

Foundation pit structure

The shape of ichnography of south anchorage foundation pit of is rectangle. Its size of is 70m×50m, the depth of foundation pit is 29m. Support system of south anchorage foundation pit is consisted of row-pile and inner- sustentation. There are 140 piles which diameters are 1.5m. Seven layers was designed for inner-sustentation Ground freezing system is consisted of 140 freezing boles, which is used for water insulation for south anchorage foundation pit .The profile of the foundation pit is as Figure 2.

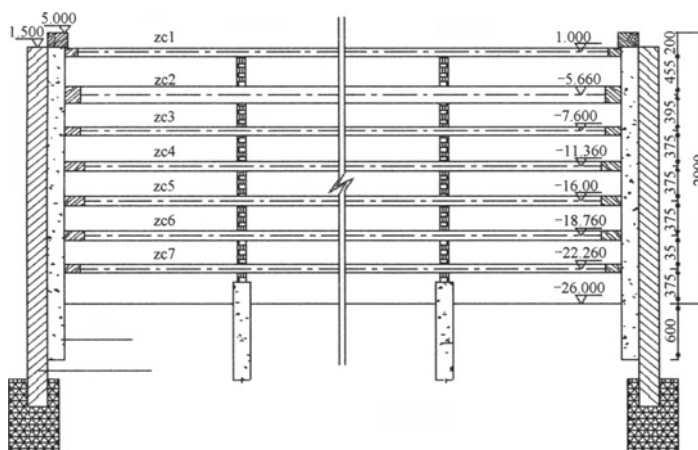


Figure 2. Profile of the foundation pit

Pile horizontal displacement monitoring Layout

For safety of the foundation pit, a large monitoring system was built. Monitor items are included of surface deformation, inner deformation, structure stress, strain gauge, soil pressure, level of groundwater, soil temperature.

Total monitoring points is 760, and monitoring bores is 54. Pile horizontal displacement monitoring is a mainly monitoring item. Figure 3. is the layout of monitoring borehole of south anchorage foundation pit.

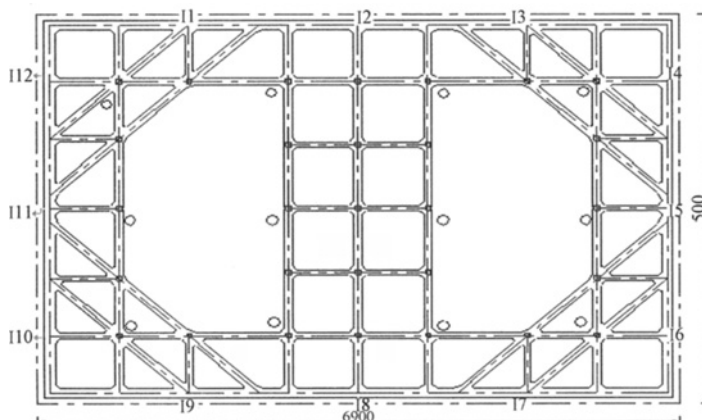


Figure 3. Layout of monitoring borehole of foundation pit

ERROR ANALYSIS OF PILE HORIZONTAL DISPLACEMENT

During monitoring process, we found that data of pile horizontal displacement was fluctuant obviously, sometime took place singularity. pile horizontal displacement data can be used for Anti- analysis of stability of the foundation pit, we must find method to Calibrate error.

After analyzing, we found the error is formed by two reasons. The main reason was that measured depth was minished by the freezing of bottom part. Another reason was that deformation of bole bottom made the error with the supposition of zero deformation of bole bottom.

For first reason could be proved by the different monitoring data in fore-and-aft of washing borehole, as Figure 4.

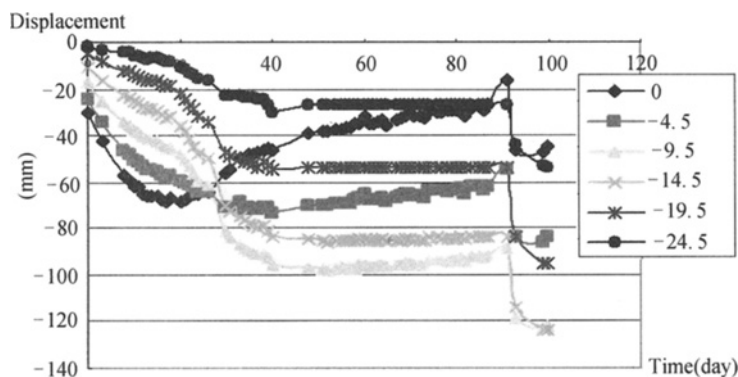


Figure 4. Temporal variation of displacement in fore-and-aft of washing borehole

CALIBRATION OF PILE HORIZONTAL DISPLACEMENT

Feasibility analysis

Because of no stably base point for exterior deformation measurement, it was proved that horizontal displacement of pile-top beam can't be used to calibrate error.

We tried to find other calibrate point, and we found the position of inner support was stably point comparatively, its displacement was related axial force which changed with deformation and temperature of inner support. Figure 5 is temporal variation of displacement and axial force of second inner support. So the displacement calibration on position of first support could be used to correct pile horizontal displacement.

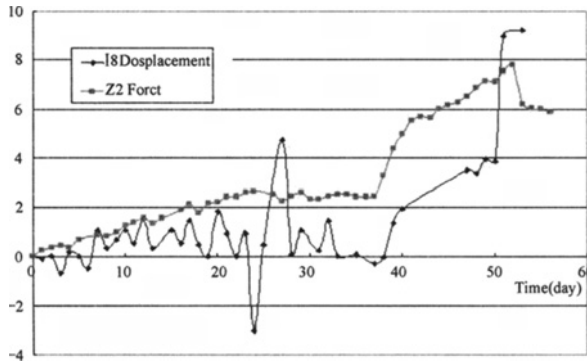


Figure 5. Temporal variation of displacement and axial force of second inner support

Calibration Formula

The displacement on position of first support was calibrated by data of support force and temperature.

$$\delta = \delta_m - \delta_c \quad (1)$$

$$\delta_c = \delta_{fm} - \delta_{f0} + \delta_{s+t} \quad (2)$$

$$\delta_{s+t} = L \left[\frac{(Z_{1-2} + Z_{1-3})}{2} - b(T_m - T_0) \right] / (E \times A) \quad (3)$$

where δ : calibrating displacement of different point; δ_m measurement displacement of different point; δ_c calibrating value of first support; δ_{f0} initial displacement value displacement; δ_{s+t} displacement of support force and temperature of first support; L 、 Z_{1-1} 、 Z_{1-2} 、 Z_{1-3} 、 T_m 、 T_0 、 b 、 E 、 A : calculation parameters.

Validating of Calibration Formula

Calibration can be validated by two way. One is comparison of calculation displacement in fore-and-aft of washing borehole, another is comparison of calculation displacement and

numerical calculated displacement by finite element method. Figure 6 is comparison of calculation displacement and numerical calculated displacement during fifth excavation.

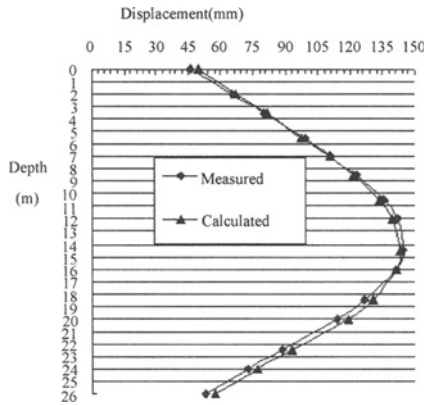


Figure 6. Displacement comparison during fifth excavation

Calibration by neural network

In the process of field measurement with inclinometer, blocking often occurs in the bottom of inclinometer. Measured displacements of blocked section may be deduced through feed-forward neural network. The local displacements may be corrected. Figure 7 is a sample of local displacements correction.

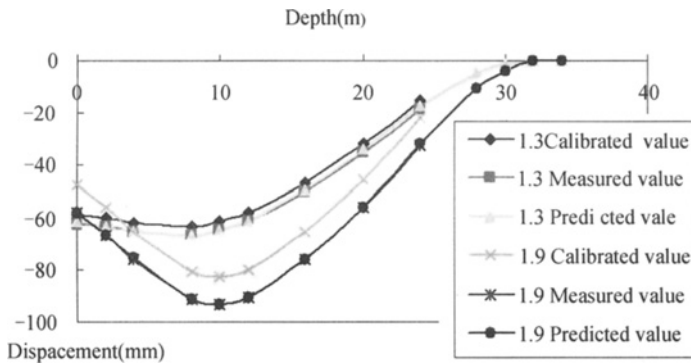


Figure 7. Local displacements correction

CALIBRATING EFFECT ANALYSIS

Calibrating effect can be analyzed by characteristics comparison between calibrating value with measuring value of pile horizontal displacement. The left of Figure. 8 is displacement curves of measuring value of pile horizontal displacement.

The right of Figure 8 is displacement curves of calibrating value of pile horizontal displacement. It indicated that the calibrating effect was prominence.

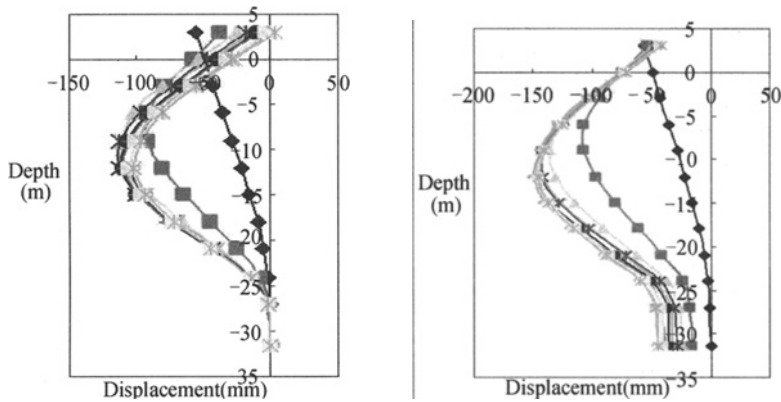


Figure 8. Comparison between calibrating curves with measuring curves

PREDICTING BY GRAY NEURAL NETWORK

For predicting change rule of pile horizontal displacement, the gray neural network model of GNNM(1,1) was established for predicting deformation of deep foundation pit.

The model was applied in the deep foundation pit of the south anchorage of suspension bridge of Runyang Changjiang Highway Bridge, as Figure 9.

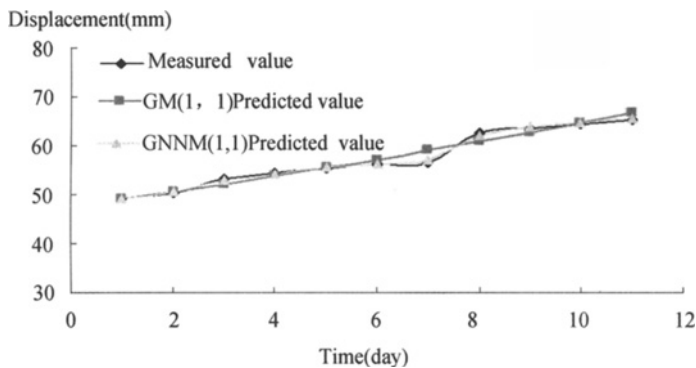


Figure 9. Deformation prediction by gray neural network

CONCLUSIONS

(1) Pile horizontal displacement for Ground freezing and Pile-support Foundation Pit of south anchorage had Obvious error by freezing and deformation of bottom part .

(2) The displacement Calibration on Position of first support could be used to Correct pile horizontal displacement. The displacement on Position of first support was calibrated by data of support force and temperature.

(3) Measured displacements of blocked section may be deduced through feed-forward neural network, the local displacements may be corrected.

(4) This result provided reliable monitor data for Anti- analysis and prediction of foundation pit, and the experience was backlog for construction of similar engineering aftertime.

ACKNOWLEDGMENTS

The research work of this paper is supported by the Yalongjiang Water-Electricity Development United Research Foundation Project of National Natural Science Foundation of China, and Ertan Water-Electricity Development Limited Company (No.50539110).

REFERENCES

- Yao Zhishu, et al. (2004). Study on force of freezing expand of ground freezing and pile-support structure of deep foundation pit, *Chinese Journal of Rock Mechanics and Engineering*, 23(9), 1521-1524
- Cheng Zhonghan (1999). *Deep Foundation Pit Engineering*. Beijing: Mechanical Engineering Press.10.
- Liu Daan et al. (2000). Development and application of software system for automatic monitoring on geological engineering, *Journal of Engineering Geology*, 8(02): 213-217.

A NEW PREDICTING METHOD OF LANDSLIDE BY FRACTAL THEORY

Mingxin Zheng

*Institute of Bridge & Road and Geotechnical Engineering, East China Jiaotong University,
Nanchang 330013, China*

Because a large number of monitoring data of slope's deformation shows that the curve of displacement versus time ($s-t$ curve) has the phenomenon of 'rise and fall' shape, and the curve of $s-t$ can reflect the relationship between the fractal dimensions of $s-t$ (or $v-t$) and the development of landslide. How to use fractal dimension to predict the time of sliding are discussed in this paper. On the basis of deformation monitoring data of Xintan landslide and Huangci landslide, the displacement fractal model, velocity fractal model of landslides and the formula of landslide fractal prediction are set up preliminarily by using fractal theory.

INTRODUCTION

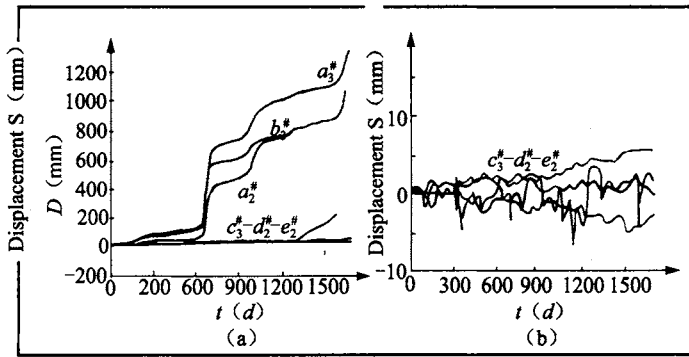
Fractal theory, i.e. Fractal Geometry is proposed by B.B.Mandelbrot. Fractal is described as a geometry object that has self-similarity characteristic. The self-similarity characteristic represents the statistical similarity between the part and entirety in shape, function or information. In order to study the Fractal Geometry, the parameter that describes fractal geometry quantity is called Fractal Dimension.

A large number of monitoring data of slope's deformation shows the curve of displacement versus time ($s-t$ curve) that has the phenomenon of 'rise and fall's shape. And at the different stages of slope's deformation, there is a different 'rise and fall' or frequency. For instance, some data shows the certain characteristic in its developing stage, and this characteristic has the 'self-similarity'. What's the relationship between the fractal dimensions of $s-t$ and the development of landslide, and how to use fractal dimension to predict the time of sliding are the main focus in this paper.

On the basis of deformation monitoring data of Xintan landslide and Huangci landslide, the displacement fractal model, velocity fractal model of landslides and the formula of landslide fractal prediction are set up preliminarily by using fractal theory.

PREDICTION THE TREND OF LANDSLIDE

In a certain stage, the developing trend of landslide has 'itself—similarity' inherently, so a certain stage has its fractal dimension along with the developing of landslide. The curves of Xintan landslide' monitoring data, e.g. $s-t$ curves see Figure 1.



(a) Monitoring points of $a_2, a_3, b_3, c_3, d_2, e_2$ (b) Zoom in monitoring points of c_3, d_2, e_2 ,

Figure 1. Curves of displacement versus time of different monitoring points in Xintan landslide

Xintan landslide belong to an accumulation landslide in Hubei province, China. On the basis of analyzing $s-t$ curve of the monitoring points of a_3, b_3, c_3, d_2, e_2 , a series of fractal dimension are calculated (Table 1).

From Figure 1 and Table 1 we can see:

Table 1. Displacement fractal dimension of monitoring points

Monitoring points		Observation of time segment				Whole of curve
		1-22 [#]	22-27 [#]	28-39 [#]	40-51 [#]	
a_3	D_{dx}	1.002 390	1.001 680	1.001 640	1.000 930	1.001846
	D_{dy}	1.002 057	1.002 049	1.001 552	1.001 132	1.002 010
	D_d	1.004 451 9	1.003 734 4	1.003 194 5	1.002 064 0	1.003 859 7
b_3	D_{dx}	1.002 335	1.002 144	1.001 474	1.001 071	1.002 013
	D_{dy}	1.001 979	1.002 468	1.001 333	1.001 013	1.002 344
	D_d	1.004 318 6	1.004 617 3	1.002 808 9	1.002 085 1	1.004 361 7
e_2	D_{dx}	1.002 057		1.001 836		1.001 211
	D_{dy}	1.001 841		1.001 221		1.000 730
	D_d	1.003 901 787		1.003 058		1.001 930
c_3	D_{dx}	1.002 219		1.000 885		1.000964
	D_{dy}	1.002 013		1.000 617		1.000627
	D_d	1.004 236 467		1.001 502 5		1.001 591 6
d_2	D_{dx}	1.002 092		1.000195		1.000 730
	D_{dy}	1.002 092		1.000 671		1.000 741
	D_d	1.004 188 376		1.000 866 13		1.001 470 5

Note: D_d is product of D_{dx} (horizontal direction) and D_{dy} (vertical direction).

(1) In general, along with the development of its deformation, the displacement fractal dimension (D_d) of each monitoring point in X (horizontal), Y (vertical) and synthetic direction (XY) become small. In another words, when the D_d become small and it approximate to 1.000 0, the landslide will failure.

(2) Combining with the others studied results(1), (2), according to the developing stage of landslide, the developing process of Xintan landslide can be divided into three stages:

1) The stage of latent breed (before 1964): The upper-slope at Jiangjiapo had been creeping at early stage; $D_d \geq 1.0040$.

2) The stage of obvious developing (1964-1981): The upper-slope at Guangjiaya happened a collapse (cube: $150,000\text{m}^3$, 1964); $D_d = 1.0040 \sim 1.0030$. For example ,at the monitoring point a3 ,b3, during the time of 1-39#, value of the fractal dimension D_d is 1.0037324-1.0028089.

3) The stage of significant sliding (1981-1982) : The cliff of Jiangjiapo (in the middle of landslide) slides towards river about 300mm, which indicates the landslide had been in accelerating stage; $D_d = 1.0030 \sim 1.0020$, For example, D_d of monitoring point a_3, b_3 in time of 40-51# is 1.0020859-1.0020851. When $D_d \leq 1.0020$, It indicates that the landslide will be gradually failure, i.e. A smaller fractal dimension imply the curve of $s-t$ very smoothly and a tendency to slide entirely. At last, the landslide slid on June 12, 1985.

So we can draw out a concept figure from the curve of $s-t$ and its corresponding fractal dimension. See Figure 2

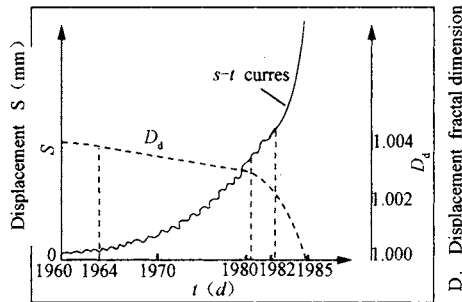


Figure 2. The relationship between landslide developing and displacement fractal dimension of displacement

FORECAST OF THE FAILURE OF LANDSLIDE

The principle of failure forecast using fractal dimension

Along with the developing of landslide, the displacement fractal dimension (D_d) gradually becomes small, and when D_d is more approaching 1.0000, the movement of landslide is more rapidly. So at t_i , we can forecast the time of failure, $t_i + \Delta T$, which is estimated by the D_d during t_i to t_{i-1} :

$$\begin{aligned} \Delta T &= \frac{(D_i - 1.0000)}{\Delta D} \times \Delta t \\ &= \frac{(D_i - 1.0000)}{D_{i-1} - D_i} \times (t_i - t_{i-1}) \end{aligned} \quad (1)$$

where D_i, D_{i-1} are the fractal dimension of t_i and t_{i-1} , respectively.

Forecast Huangci landslide by fractal dimension

Description of landslide

Huangci landslide locates at 70 km west of Lanzhou, Gansu province, China. The landslide, which volume is 6 millions m^3 , developed in the Cretaceous red sandstone and

mudstone, which locates at the fourth terrace of the Yellow River valley (North bank). It took place on January 31, 1995.

The head crevasse of the landslide linked up during May to July (1994); and the fissure of sliding-surface linked up preliminarily. At the fall of creeping-squeezing, it would be failure before long.

The results of extensometers about C_2 , C_5 , and C_8 from September 30, 1994 to January 27, 1995 are shown in Figure 3.

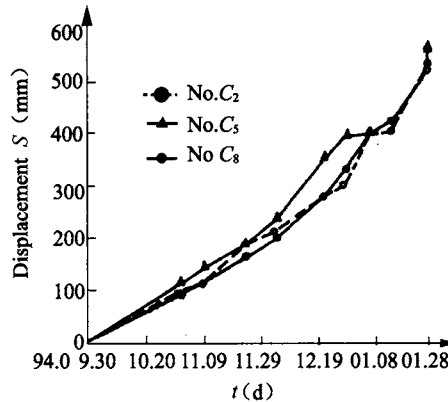


Figure 3. Curves of displacement versus time about the monitoring piles C_2 , C_5 and C_8

The pile C_2 , C_5 and C_8 , which shows the sliding extension, are installed at the middle of landslide. And the fractal dimensions of displacement are shown in Table 2.

Statement of this table:

Observation unit is a month or 30.5 days; And the displacement of t_i will be transformed by:

$$S'_i = \frac{t_i - t_{i-1}}{30.5} \times (S_i - S_{i-1}) + S'_{i-1}$$

The group unit of monitoring times must be more than three.

Prediction

(1) The trends of landslide: From Figure 2 and Table 2, we can see that creeping of the landslide was accelerating at Dec.5, 1994, whose D_d is approximately 1.000 0, and the landslide would failure immediately.

(2) The failure time of landslide: In generally, with the accumulation of the observation data, the forecast of landslide by fractal dimension is more accurate. For example, the error time of forecast is from 84 days (April 24, 1995) to 1 day (Jan. 31, 1995) as t_i approximate to the failure time. It is testified preliminarily that the displacement fractal dimension using in landslide forecast is possible and correct.

Table 2. Forecast results of displacement fractal dimension

Monitoring- Results time Of Forecast		1994				1995			
		Nov. 24	Dec. 5	Dec. 22	Dec. 29	Jan. 6	Jan. 14	Jan. 25	Jan. 27
C ₂	D _d	1.002 20	1.001 87	1.001 45	1.001 20	1.000 90	1.000 65	1.000 35	1.000 25
	ΔT/day	/	62.3	58.7	25.5	24	20.8	12.5	5
	Date	/	Feb. 6, 1995	Feb. 19, 1995	Jan.24,19 95	Jan. 30,1995	Feb. 4,1995	Feb. 7,1995	Feb. 1,1995
C ₃	D _d	1.002 05	1.001 90	1.001 65	1.001 40	1.001 10	1.000 80	1.000 40	1.000 26
	ΔT/day	/	139.3	112.2	39.2	29.3	21.3	11	3.7
	Date	/	Apr. 24,1995	Apr. 13,1995	Feb. 7, 1995	Feb. 5 ,1995	Feb. 5 ,1995	Feb. 5 ,1995	Jan. 24,1995
C ₈	D _d	1.002 20	1.002 00	1.001 80	1.001 50	1.00115	1.00090	1.000 55	1.000 37
	ΔT/day		110	155	35	26.3	28.8	17.3	4.1
	Date		Mar. 4,1995	Apr. 23,1995	Feb. 7, 1995	Feb. 2 ,1995	Feb. 12 ,1995	Feb. 12, 1995	Jan. 30,1995

CONCLUSIONS

(1) On the basis of long term observation data and the 'wave-ladder' of *s-t* curve information of the Xintan landslide, the relationship between the trends of landslide and the displacement fractal dimension is put up initially.

(2) On the basis of the monitoring displacement data of Huangci landslide, the forecast formula of landslide failure is set up :

$$\Delta T = \frac{(D_i - 1.0000)}{D_{i-1} - D_i} \times (t_i - t_{i-1}) \quad (3)$$

Through the trace forecast of Huangci landslide, it is proved that the fractal dimension prediction is possible and suitable.

(3) Using fractal theory, the trends and failure time of landslide with the monitoring data can predicate. And there are two further approaching problems in this studying. Such as:

In this paper, we only choose the two landslides and using theirs partly monitoring data. An entirely monitoring data of landslide' deformation is not easy to obtain. Therefore, it is necessary to study further.

How to choose the standardize quantity of ε (standard length which calculate the fractal dimension), and what is the relationship between precision of the monitoring data and precision of prediction are worthy for research further.

ACKNOWLEDGMENTS

The author wishes to express his gratitude to Council of Scientific Research for financial support for his work. He would also like to acknowledge the helpful directions, discussion

with Wang Gongxian professor (Northwest China Academy of Railway Sciences) and Wang Lansheng professor (Chengdu University of Technology).

REFERENCES

- M.X. Zheng, G.X. Wang, L.S. Wang (1998). Study on Application of Fractal Theory in Landslide's Prediction.
- P.Y. Lu (1988). *Xintan Landslide and Its failure Forecast*, Typical Landslides in China. Press of Science (Chinese), 191-199.
- T Fukuzono (1990). Recent Studies on Time Prediction of Slope Failure, *Landslides News*. (4): 9-12.

APPLICATION OF INFRARED PHOTOGRAPHY AND IMAGE PROCESSING IN NATM TUNNEL

Chunlin Zhou, Hehua Zhu and Xiaojun Li

*Department of Geotechnical Engineering, Tongji University, 1239 Siping Road,
Shanghai 210030, China*

There is lots of dust in the constructing rock tunnel with New Austrian Tunneling Method. Since the length of visible light wave is shorter than dust, and the light is always not sufficient in the tunnel, it's hard to get clear pictures with classical photography technique. Using the infrared photography technology, it is possible to get vivid picture through dust and fog for the length of infrared wave is close to dust. This paper specifies the process of shooting tunnel face with infrared technology in the constructing rock tunnel. Based on sufficient experience of taking pictures of tunnel face with this method, regulation has been advanced which describes how to get clear pictures in the complex circumstance in constructing rock tunnel with the special equipments. Based on former researches of identifying the digital photographs of tunnel face with joints and cracks, this paper has attempted several ways of image processing and intelligent recognition on the tunnel face photographs. After the comparing and analyzing of the results, regulations of image processing and intelligent recognition which are fit for this kind of photographs was advanced. Infrared photography which is described in this paper is a useful innovation for getting clear tunnel face photograph in constructing rock tunnel with NATM. The image processing implements semi-automatic geological sketching. The intelligent recognition of tunnel face images provides some critical parameters for rock masses classification, and makes 3-D numeral reconstruction of the tunnel more precise and convenient.

INTRODUCTION

With the continuing rapid development of economy, China is now in a great era of high-way constructing. The length of high-way has exceeded 20 million kilometers, which is the second one in the world. High-way constructing is extending to the mountainous area of west part these years, more and more tunnels are to be constructed (Ming-zhou and Zhao-yi et al., 2001), consequently, tunnel engineering became one of the most important subjects of high-way constructing, research of modern and scientific tunnel constructing methods are insistent.

NATM is widely used in tunnel constructing of mountainous area. Rock masses classification of tunnel face is critical for evaluating the stability of tunnel rock masses, as well as choosing tunnel bracing and constructing methods. As the most intuitionistic description of tunnel face rock masses, the tunnel face photographs are always concerned. (Baoshu, 2003).

In the constructing process of NATM, lots of dust is produced by procedures such as blasting, shooting concrete, working of air gun and so on. There is plenty of dust beside the tunnel face, even the Ventilators are working. Since the wavelength of visible light is shorter than medial diameter of the dust, the noise of photograph which caused by dust is inevitable with classic photographic methods. Infrared has longer wavelength than visible light, which is close to the medial diameter of dust, consequently, with the effect of diffraction it could penetrate some obstructions such as dust, fog, soot and so on. With this feature, vivid pictures could be taken with infrared photography.

Experienced engineers could estimate rock masses class with the picture of tunnel face. Their estimation factors include the amount, length, and distribution of joints and cracks, the status of underground water. With the preknowledge of Geological prospecting material they could conclude the probably classification of face rock masses. As important factors of face rock masses classification, information of joints and cracks on the face could be gotten through image processing of face pictures.

APPLICATION OF INFRARED PHOTOGRAPH IN CONSTRUCTING NATM TUNNEL

Lots of dust distributes in the constructing NATM tunnel, especially beside the tunnel face. Some dust is invisible with eyes but distinct in the picture with flashing light. Figure 1 shows the effect of taking picture with flashing light. Actually, the white speckles can't be seen in the field. Clear face pictures could not be captured with flashing light.

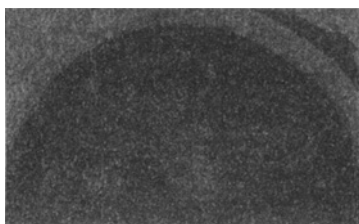


Figure 1. Tunnel face picture with flashing light

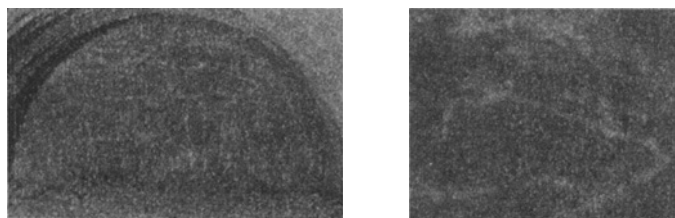


Figure 2. With lots of dust, clear picture could not be captured with classic photography

While dust beside face is heavy, the influence of dust could not be avoided even without flashing light. Figure 2 shows that with classic photography, it is very blur of picture while there is too much dust. This kind of pictures is not fit for image processing.

On this condition, more clear face photographs could be gotten with infrared photography. Infrared is usually divided into 3 spectral regions: near, mid and farinfrared. The boundaries

between the near, mid and far-infrared regions are not agreed upon and can vary. Generally speaking, their wavelength ranges are $0.78-0.0\ \mu\text{m}$, $3.0-6.0\ \mu\text{m}$, $6.0-1000\ \mu\text{m}$ respectively. Mid and far-infrared has long wavelength, shows very distinct diffraction, and very sensitive to temperature. It is widely used in photograph of temperature field, and can only get blur image because of it's long wavelength. Diameter of dust in constructing tunnel distributes between $0,1$ and $10\ \mu\text{m}$ (Kanaoka and Furuuchi et al., 2000) , which is close to near-infrared wavelength. Diffraction occurs while near-infrared is blocked off by dust so that near-infrared could penetrate it and clear image could be formatted for its wavelength is not too long. Figure 3 shows the result of taking picture with near-infrared photography in the same condition of Figure 2. The image appears medium gray-green and obviously, it is clearer than previous one.

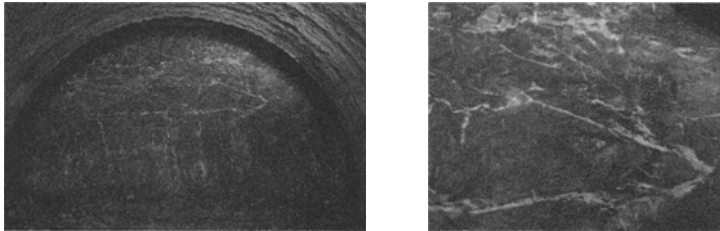


Figure 3. Face picture taken with near-infrared photography

IMAGE PROCESSING OF FACE PICTURE

Introduction

There are plenty of image processing methods, including morphological processing, image enhancement, image segmentation, and so on. As pretreatment of image recognition, the purpose of face picture processing is enhancing the features which is important to the property of face rock, such as joints and cracks, and eliminating the features which is useless to it, such as noise, inequi-illuminance.

In the process of infrared photography, illuminance is probably not sufficient for the using of lens which filter visible light and let infrared pass by, so high ISO, large aperture, long exposal time are set in order to get clear picture, but at the same time noise is inducted, and some part of region may be excessive or lake of illuminance. Considering the characteristic of the image and the demand of image recognition, processing steps of deonoising-illuminance equilibrating-threshold division are brought forward.

Image processing

Image denoising

Noise in digital image photography indicate the coarse parts of image which caused by CCD and CMOS in the process of imaging. There are many reasons for the generation of noise, especially, in the infrared photography in tunnel face, the main reason is that some pix on CCD lose control for CCD (CMOS) could not afford the mass computing cost cause by long

time exposal. And slow shutter, high ISO, large aperture is necessary in this application. According to the reason of generating, this kind of noise should mainly be Gaussian noise.

Select smooth region (Qi and Dequn et al., 2004) and draw its histogram as Figure 4 (a). The histogram of selecting smooth area is similar with histogram of single gray level image corrupted by Gaussian noise which is shown on Figure 4.b. According to the similarity of histogram (Rafael C.Gonzalez,Richard E.Woods, 2005) , it is believed that the infrared image above is corrupted by Gaussian noise and the variance of Gaussian noise could be estimated by simulating the histogram of smooth area. Wavelet denoising method shows efficiency on Gaussian noise (Russo, 2003) . Transforming the image to 256 gray levels, selecting smooth region, estimating variance and denoising with wavelet method, Figure 5.shows the result image. It is very neat.

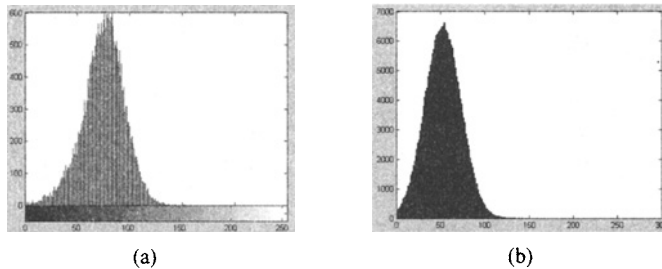


Figure 4. a. Histogram of smooth region; b. Histogram of single level image corrupted by Gaussian noise

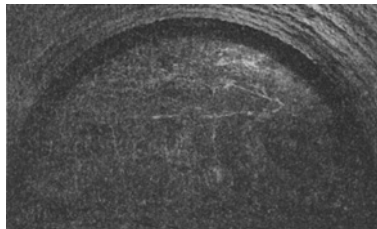


Figure 5. Face image after denoising

Illuminance equilibrium

While taking picture of tunnel face with near-infrared photography, some parts of image may be excessive or lack of exposing for the photographic parameter setting. Most of image processing methods apply on the whole image. To this kind of picture, parameters of image processing methods are hard to choose and good result is hard to get. So illuminance equilibrium method is used here to pretreat the picture. (Lemy and Hadjigeorgiou, 2003).

$$f'(x,y) = \sum_{i=-n}^n \sum_{j=-n}^n f(x+i,y+j) / n^2 \quad (1)$$

It could be seen on the image A [Figure 6(a)] that the illuminance of top right is sufficient, but most parts, especially bottom right, are lack of exposal. Using Equation (1), local equilibration could be figured out. The full image computing result (image B) is shown as

Figure 6 (b) Image A minus image B, and after normalizing, image C [Figure 6(c)] is gotten. In the transform process most detail information is kept and the areas of over illumination and lack of exposal are improved. Take the gray level as elevation, the process could be described as Figure 7.

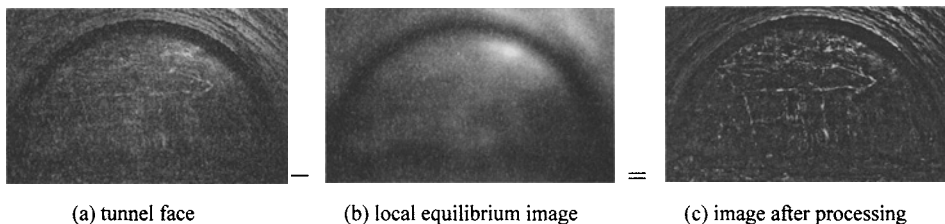


Figure 6. Illuminance equilibrium method

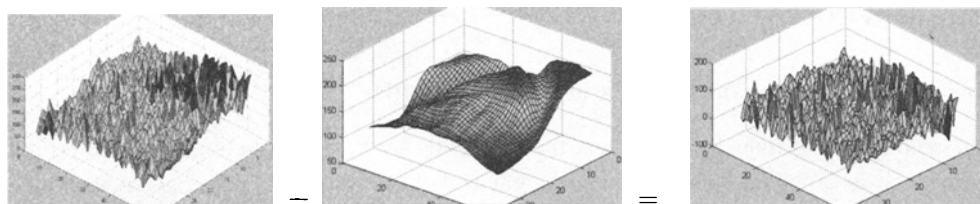


Figure 7. The procedure shown with 3-dimension elevation

Threshold division

Threshold division is an important image processing method, whose principal is choosing one gray level t as the threshold, and transforming image into binary image as Equation (2).

$$g(x, y) = \begin{cases} 1, & f(x, y) \geq t \\ 0, & f(x, y) < t \end{cases} \quad (2)$$

The pivotal point of threshold division is choosing the right threshold. Higher threshold would miss useful image details and lower threshold may induce much useless information. Commonly used threshold selection methods include histogram bimodal method, OTSU, maximum entropy method, Fuzzy Threshold method, and so on. After testing each method, maximum entropy method is proved to be fit for threshold choosing of this kind of image.

$$H = - \int_{-\infty}^{+\infty} p(x) \lg p(x) dx \quad (3)$$

Entropy presents the equal quantity of information. According to the theory of information, entropy could be defined as Equation (3). $p(x)$ is the probability density function of random variable x . In digital image, x could be gray level, area gray level, gradient, and so on. According to max entropy principal, to find the threshold with entropy of gray level means find one threshold t , with which the image could be divided into two parts, and the total information quantity (the entropy) of the two parts is maximum. Figure 8 shows the effect of

maximum entropy method, figure a is the main part of Figure 6(c) and (b) is the result of left one after using maximum entropy method.

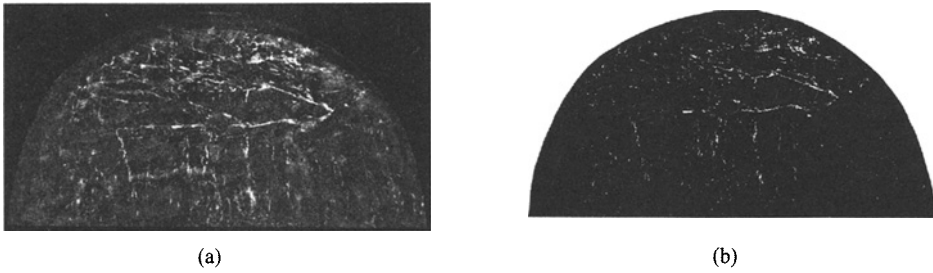


Figure 8. (a) The original image; (b) Result of maximum entropy method

IMAGE RECOGNITION

Introduction Content and purpose of image recognition

The recognition of tunnel face picture means mainly to recognize the liner features on the rock, such as joints and cracks. The length and direction should be concerned, which represent the integrality of rock masses. Every kind of engineering rock masses classification methods consider about the integrality and the degree of weathering. The recognition of liner feature of tunnel face could provide necessary parameters for rock masses classification, and is helpful to ensure the engineering geological condition, modifying excavation and brace methods, and is beneficial to keep construction in safe.

Hough transform

Hough transform is a useful method of recognizing geometrical sharp in image. The basic usage is recognizing lines from binary image. The principal is transforming the image matrix from coordinate space (x, y) to coordinate space (ρ, θ) . One point in space (x, y) represents one sinusoid in space (ρ, θ) , and one line in space (x, y) represents one point which is crossed by many sinusoids in space (ρ, θ) . The number of sinusoids crossed the same point in space (ρ, θ) equal to the number of points on the same line in space (x, y) . The distribution of lines on the image could be gotten from the statistics of the number of sinusoids cross same points. The principal of hough transform is shown in Figure 9.

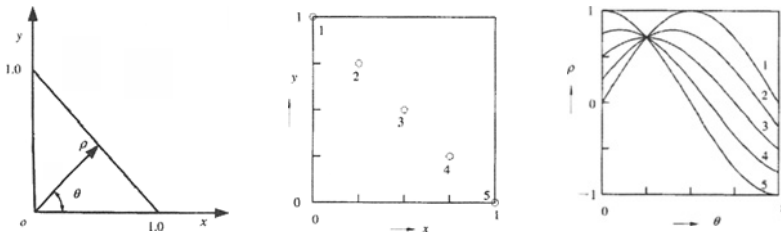


Figure 9. Hough transform

Figure 10 shows the result of applying hough transform method on the image of Figure 8.a. show the liner features which recognized by hough transform, and Figure 8.b is another form of the input image in the space (ρ, θ) . Table 1 shows the result data of the process. With hough transform, the liner feature of rock masses, such as joints and cracks are described as data, which makes image feature storage and post-treatment more convenient.

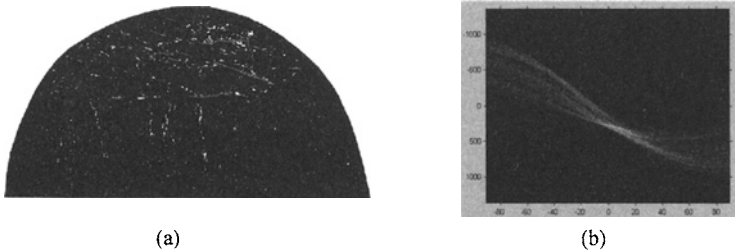


Figure 10. Result of hough transform. (a) lines recognized by hough transform; (b) image in space (ρ, θ)

Table 1. Result of hough transform

	Start point(m)	End point(m)
1	(6.1608, 14.1997)	(5.6740, 12.8622)
2	(5.6372, 12.7610)	(5.1568, 11.4412)
3	(5.9475, 13.6584)	(5.8627, 13.2594)
4	(5.1401, 9.8600)	(5.0080, 9.2383)
5	(4.1238, 13.1202)	(4.1794, 12.0600)
...

CONCLUSIONS

Digital photography and image processing technique are widely used in many domains. In this paper, near-infrared photography is used to capture the face image in the constructing NATM tunnel. After that, the infrared image feature is analyzed, and image processing procedure which fits for this kind of image is brought forward. The procedure consists of four steps: denoising-illuminance equilibrium-threshold division-image recognition. Nice effect is achieved by using the procedure.

Along with excavation, pictures of continuous tunnel face could be captured, and for each picture, the feature could be acquired by image processing. After that, the tunnel could be reconstructed, with interpolation methods, amount and length of joints and cracks for each volume could be gotten, which is considered as an important parameter of rock masses classification: the indicator of rock integrity.

REFERENCES

Mingzhou B. and Zhaoyi X., et al. (2001). Study and application on fuzzy information analysis model in tunnel surrounding rockmass classification. *Journal of The China Railway Society(06)*: 1-5.

- Baoshu, G. (2003). Technical character,idea of tunnel construction and its development. *Railway Construction Technology*, (3): 1-6.
- Kanaoka, C. and M. Furuuchi, et al. (2000). Flow and dust concentration near working face of a tunnel under construction. *Journal of Aerosol Science European Aerosol Conference 2000 31 (Supplement 1)*: 31-32.
- Lemy, F. and J. Hadjigeorgiou (2003). Discontinuity trace map construction using photographs of rock exposures. *International Journal of Rock Mechanics and Mining Sciences*, 40 (6): 903-917.
- Rafael C.Gonzalez,Richard E.Woods, S. L. E. (2005). *Digital Image Processing Using MATLAB*, Prentice Hall.
- Russo, F. (2003). A method for estimation and filtering of Gaussian noise in images. *IEEE Transactions on Instrumentation and Measurement* 52 (4): 1148-1154.
- Qi, Z. and L. Dequn, et al. (2004). Estimating Image Noise Based on Region Segmentation in the Wavelet Domain. *Computer Engineering* (08): 37-39.

MODEL TESTS ON SUBGRADE IN SEASONAL FROZEN REGION UNDER FREEZING-THAWING CIRCULATION

Ming Zhu, Ronggui Deng, Feng Li
*School of Civil Engineering, Southwest Jiaotong University,
Chengdu 610031, China*

The diseases of subgrade in seasonal frozen region were mainly induced by frost heaving and thawing circulations of frozen soils because of change of seasons. Considering the frozen soils in 213 state road from Langmusi to Chuanzhusi which located in northwest of Sichuan province, model tests on stabilities of subgrade was made. The design parameters of insulating layer and the rational height of subgrade were discussed. All these works were beneficial for design of subgrade in seasonal frozen region.

THE ENGINEERING BACKGROUND

The reconstruction project of 213 National Road from lang mu shi to chuan zhu shi (next referred to as Lang chuan road), 225 km full-length, lies at the combining area of the eastern margin of the qingzhang plateau and the northwest of Sichuan, three-quarters of all sections lie in seasonally frost soil area where elevation is from 3,200 to 3,800, grasslands and pastoral areas are along the roads, ruoergai wetlands are in the right of the road. as some factors such as large temperature change, strong UV role in this region, frost heaving of the road subgrade in winter will cause uneven pavement, pavement cracks occurred, but vehicles can also move slowly, but in the spring of the following year, thaw and settlement diseases phenomenon will occur and make the road lost the carrying capacity, which causing great economic losses

THE MODEL TEST RESEARCH

Brief instruction

In order to analyze the carrying capacity and settlement variation of the seasonally frost soil subgrade after the seasonal freezing and thawing circulation, the author made a 1:10 model test from December 2006 to January 2007.

Model's cross-sectional size is shown in Figure 1.

Subgrade model is 2m long in vertical, divided into two sections with 1m for a section. To comparative analysis, one section is set isolation layer, another isn't set, and whose thick is 0.02m. The disposal of vertical strain measuring point in the subgrade is shown in Figure 2.

Liquid nitrogen is used to cool the model in the test, the model's initial temperature is approximately 15 °C and the lowest temperature is -25 °C.

Test car travels along the vertical direction (hurricane) on the road to load the subgrade with a mass of 100kg, 200kg and 300kg weights.

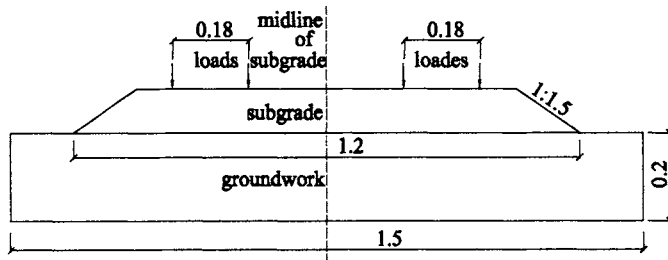


Figure 1. Cross-sectional diagram of subgrade model (m)

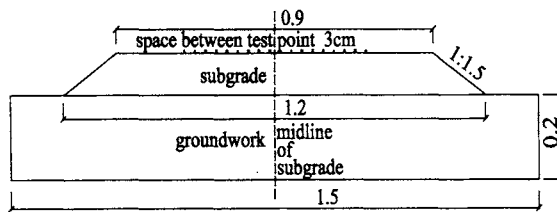


Figure 2. Cross section's measuring points layout diagram (m)

Measured points in the Figure 2 is the settlement measurement points, divided into left and right half test section, the left half test section's measuring points are numbered from left to the center and the right half test section's measuring point are numbered from right to the center, each section have nine measuring points.

Analysis of test results

Analysis of subgrade settlement under different loads

Table 1, 2 and Figure3, 4 are settlement uninterrupted curve about the left half of subgrade under different loads

Table 1. Test point's load – displacement Table (section 1, unit: mm)

Test point	1	2	3	4	5	6	7	8	9
0.1kN	57	57	58	56	53.5	55	55	53	53
0.2kN	57	62	62	60	52	52	54.5	52.5	53.5
0.3kN	56	61	64	63	54	51	51	53	52

Table 2. Test point's load – displacement Table (section 2, unit: mm)

Test point	1	2	3	4	5	6	7	8	9
0.1kN	53	53	56	56	54.5	55	54.5	54.5	54
0.2kN	54.5	59	64	63	56	53	53	53	53
0.3kN	53	59	65	64	54	52	53	53	53

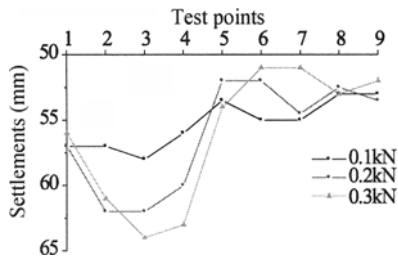


Figure 3. Settlement curve of the left half (section 1)

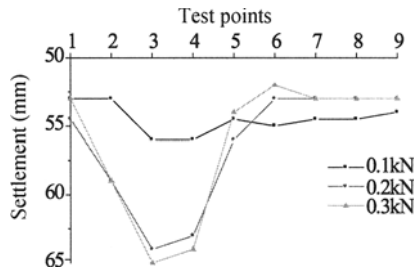


Figure 4. Settlement curve of the left half (section 2)

From Figure 3 and Figure 4, the settlements increase of left half surface go with the load's increase between the tests points one to five. This is also according with the actual situation, because the wheel load act between the tests points one to five. The measurement results between the tests points five to ten is to the contrary, the greater of the load, the smaller of the settlement. this phenomenon can be understood, the whole left half of the subgrade can be seen as a uniform elastomer,so subgrade's horizontal deflection of deformation is continuous based on this assumption, and test point five is bending point, so the deformation who have the big vertical displacement curve before test point five will decrease after test point five. It also explains the vertical stress is uneven when the wheel load acts on subgrade's surface. the fact is it is uneven distribute of horizontal distance along subgrade's surface ,the vertical displacement will be smaller as the horizontal distance away from wheel load points be farther.

Comparison of isolation layer

Tables 3,4 and Figure 5,6 show the subgrade's vertical displacement under 0.3kN load respectively with isolation layer settled or not.

Table 3. Test point's load – displacement table of left half (mm)

Test point	1	2	3	4	5	6	7	8	9
Section one	56	61	64	63	54	51	51	53	52
Section two	57	59	67	64	60	59.5	60	60	61

Table 4. Test point's load – displacement table of right half (mm)

Test point	1	2	3	4	5	6	7	8	9
Section one	61	63	69.5	63	54	52	55	57	56
Section two	61	69	68	60	56	56	60	63	63

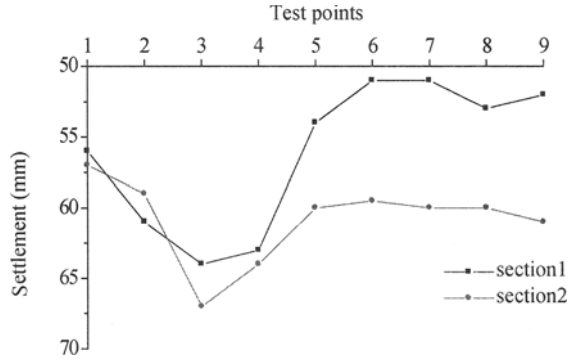


Figure 5. Settlement curve of the test points of left half under the same load

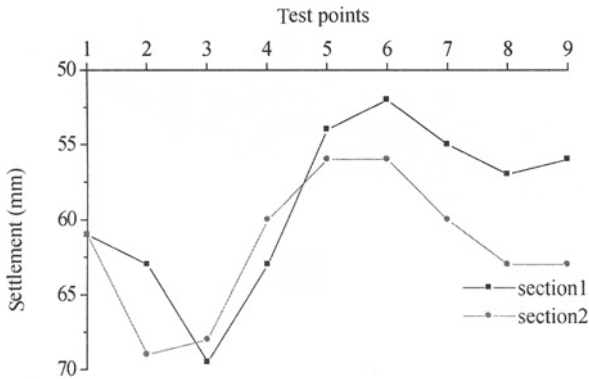


Figure 6. Settlement curve of the test points of right half under the same load

From Figure 5 and 6, the subgrade's settlement with isolation layer is smaller than it without isolation layer under the same loads. The reason is there is a large number of internal moisture in the road model. In the cooling process, the internal temperature of the road will reduce as the environmental temperature, negative energy in the subgrade internal temperature will transfer from surface to insides constantly, water internal sugrade is enough, and the subgrade's filler particles is small, these provide necessary condition for moisture's migration. But the subgrade with isolation layer, when capillary water rise to the position of the isolation layer, because the fillers pore of isolation layer is large, capillary water stopped rising, so internal subgrade soil above isolation layer is in a relatively dry state, and its have a high strength and a low deformation, this is favorable for overall capacity and stability of subgrade. Subgrade without isolation layer will be serious frost heaving due to the free

moisture migration. The subgrade carrying capacity will be substantially reduced and stability will be lost (Qian Yi, Pan Rong Wei, Wang Jian, 2006) under repeated loads.

ENGINEERING MEASURES TO PREVENT AND MITIGATE DAMAGE OF FROST

It can be seen from the above test, bad soil, open water conditions and the negative temperature is several necessary external conditions of frost heave. Therefore, engineering measures should take limit or eliminate moisture migration as a starting point.

(1) Raise subgrade; make the subgrade's fill height meet requirements. Subgrade's top soil is away from groundwater and surface water, so capillary water can't rise to upper.

(2) changing soil, soil with good stability of frozen can be used in the upper subgrade within a certain depth, such as gravel and coarse-grained materials, and to prevent the infiltration of fine-grained soil, eliminate the damage effects of freezing from soil types.

(3) Filling of subgrade soil satisfies the design and specification requirement. That must meet the minimum filling height of dry conditions.

(4) Strengthen subgrade drainage, the main is intercept and excluded surface water, truncate and dewater groundwater with using side ditch, the latest gullies, drains, bridges and so on, setting blind ditch, and vertical seepage wells.

(5) Install isolation layer. For the subgrade with 2m high, isolation layer is better to set under the road with 1.0m to 1.5m. Isolation layer can be set permeable and impermeable isolation layer. permeable isolation layer is made of gravel, sand and other materials, using its large pore cut off water's rise, its thickness is generally 0.1 to 0.2m, impermeable isolation layer is made of asphalt (thickness 2.5 to 3.0m) , spraying asphalt materials (thickness 2.0—5.0m), resurfacing asphalt felt or other impermeable material to cut off water 's mobile access.

CONCLUSIONS

The road in seasonally frost region is often affected by the frost heave disease. The effective measures to settle this disease is to set isolation layer. the reasonable position of the layer is set 1.0-1.5m below the surface, just 0.5 ~ 0.8m below the subgrade, it should be paid sufficient attention in the phase of design and construction, taken preventive measures to extend the life of the road.

REFERENCES

- Ma Wei, Zhu Yuanlin and Xu Xuezu (1998). Retrospect and Prospect to the state key laboratory of permafrost, *Glacier Permafrost*, 20 (3): 264-272.
- Qian Yi, Pan Rong Wei, Wang Jian (2006). Road's design features in the plateau of grassland and wetland areas. *Foreign Highway*, 12 (1): 11-13.
- Zhang Jinzhao, Li Zhulong (2000). The major influencing factors of permafrost roadbed stability, *Highway*, 28(2): 17-20.

NUMERICAL SIMULATION FOR THE DRAINAGE HOLES IN SEEPAGE FIELD WITH DISASTER STATUS

Yueming Zhu

*College of Water Conservancy & Water Power Engineering, Hohai University,
Nanjing, 210098, China*

Haodong Cui

*College of Water Conservancy & Water Power Engineering, Hohai University,
Nanjing 210098, China*

The simplification algorithm for numerical simulation drainage holes was proposed basis on the former methods and procedure of nodal point virtual flux in order to nicely simulate action of the drainage holes in disaster. The hypothetical switch of seepage was intercalated in the overflowing type holes' exit to judge their function, the drainages holes nodes were treated as interior nodes of global net when drainage holes were invalidation; so it realized direct simulation the drainage holes and avoid taking the nodes as boundary nodes again. With the method, the effect of each drainage hole can be well simulated and the problem of holes with seepage free surface is solved, meanwhile, the numerical simulation of mass holes is very easy under disaster status. The correctness and practicability of this model was proved by an example.

BACKGROUND

Drainage holes are the most important measure for water tightness and drainage in the dam or slope or underground engineering. Behavior of the drainage holes is more complexity under serious geological disaster, such as earthquake, flooding and high-pressured tunnel hydraulic fracturing. Therefore the studies on accurate numerical simulation drainage hole are significant to the disaster prevention and reduction.

Under disaster condition, the precise simulation of each hole is difficulty because it is big longitudinal size but small diameter, otherwise the spatial distribution is complex and large quantity. It is one of the puzzle of academe and engineering domain for correct and effective simulation of hole all the time. According to this, the method of "an array of wells replaced by a drainage ditch" has been proposed by Guan, J.H. et al. (1984). Wang, E.Z. et al., (2001), proposed the method of "Pipe to represent hole". But these methods lacked the strict theoretical basis and could not simulate each hole precisely. Especially, distribution of those drainage holes was in inhomogeneous and anisotropic of complex geological condition. The concept of drainage substructure was proposed for the first time, (Wang, L. et al., 1992). Later, the improved drainage substructure was proposed basis on the drainage substructure (Zhu, Y.M. et al., 1997), processing method of the boundary of drainage substructure was discussed

and applied in unsaturated seepage field (Chen , J.Y., 2004). But the nodes of drainage substructure are not connected with the global meshes, so the difficulty and error of solving increased and complicated to solve the mass of holes. For the seepage problems of densely distributed drainage holes with free surface.(Cui, H.D. et al.,2007), simplified algorithm for simulation of drainage holes was proposed basis on the substructure and air element.(Hu, J. et al.,2003). This paper proposes new Simplification algorithm of direct simulation drainage holes basis on the former methods and introduction of hypothetical switch of seepage. In the new method, the drainages holes nodes were treated as interior nodes of global mesh when drainage holes were invalidation through judgment of the switch, this is equivalent to release of constraint in the finite element theory. Same time, it solves the problem that numerical simulation of drainage holes with free surface in 3-D seepage field, the numerical simulation of mass holes is more simple in disaster status. Finally, a case analysis of Shenzhen pumped-storage power station is presented, studies the effect of drainage holes when the high pressure of underground reinforced concrete branch pipe is cracking or hydraulic fracturing in disaster status. The results showed that the underground powerhouse was safe because the powerful function of drainage holes. Meanwhile, the correctness and practicability of this method is proved.

SEEPAGE BEHAVIOR OF DRAINAGE HOLE

By use of the node virtual discharge method(Su, B.Y. et al.,1991), a numerical model is established for analysis of the seepage field of The Shenzhen pumped-storage power station, calculation format of FEM for seepage field is omitted here. However, it is detailed to analyze the seepage behavior of densely distributed drainage holes in the project with the new method. The drainage holes have a crucial effect on hydraulic head distribution of seepage field, usually the effect is key or control to seepage properties of engineering and seepage control design. According to their action, the drainage holes are divided into two types, the water from below exit of hole is exit-flowing type; the opposite is overflowing type. As the following, it analyses the physical meaning and functions of the two types.

The seepage behavior of exit-flowing drainage holes

Inner boundary of the exit-flowing drainage holes is possible leakage, so the algorithm for seepage behavior of exit-flowing drainage holes is divided into two conditions: one is the free seepage surface crossing drainage holes, drainage holes and free seepage surface are not intersection in the other condition. Under the normal condition, Figure. 1 (a) shows the behavior of exit-flowing drainage holes boundary when the free surface across drainage holes.

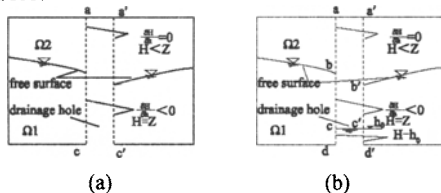


Figure 1. The model of exit-flowing drainage hole in normal and disaster condition

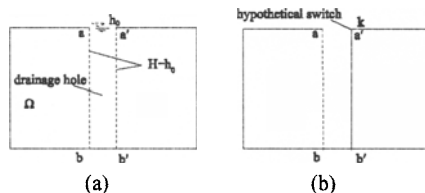


Figure 2. The model of overflowing drainage hole and hypothetical switch

(1) Above the seepage free surface, the boundary ab or $a'b'$ of hole locates seepage virtual zone, actually, it is impervious.

$$-K_{ij} \frac{\partial h}{\partial x_j} n_i |_{\Gamma_1} = 0 \quad \text{and} \quad H < z \quad (1)$$

According to the procedure of nodal point virtual flux, here K_{ij} is coefficient Darcy tensor of permeability materials, n_i is direction cosine of outer normal of inner boundary surface. The domain of calculation is $\Gamma_1 = ab \cup a'b'$.

(2) The boundary is follow at bc or $b'c'$:

$$-K_{ij} \frac{\partial h}{\partial x_j} n_i |_{\Gamma_2} > 0 \quad \text{and} \quad H = z. \quad (2)$$

here the domain is $\Gamma_2 = bc \cup b'c'$.

With the procedure of nodal point virtual flux, the nodes position of inner holes boundary is treated as boundary condition in first iterative calculation, then the location of every node is judged step by step. Water head of inner boundary and whole structure is natural concordant because the nodes of drainage and global mesh are concordant. The exit-flowing drainage holes are invalidation if their nodes position is higher than seepage free surface location. According to different cases, the program of FEM can simulate every drainage hole accurately.

Under disaster status, the condition of drainage holes and seepage free surface is same to the normal condition if the water head h_0 is lower than the highest position of drainage holes, the Figure 1(b) shows this. And the uplift of water level is hypothesis slow when the disaster happened. In fact, the air is compressed by the water in the hole step by step, but it will be absorbed and dispersed because it locates the negative pressure zone, so the pressure of holes is equal to the air pressure. This time the boundary $ab, a'b'$ can be defined with Equation (1), the $bc, b'c'$ with Equation (2). But the $cd, c'd'$ should be defined with Equation (3). The air is replaced by uplift water with long time, the whole boundary of hole is confined with follow:

$$H = h_0 \quad (3)$$

The seepage behavior of overflowing drainage holes

The main function of overflowing drainage holes is drainage and pressure lowering, and the water head of each boundary node of hole is higher than the position of height difference in the node and the holes' exit, such as Figure. 2(a). Otherwise the hole is disabled. So the hypothetical switch K of seepage was intercalated in the overflowing type holes' exit, it shows Figure. 2(b). The nodes of holes are treated as the inner nodes of global mesh and not as boundary nodes when the hole is disabled, then the calculation is greatly simplified. The switch is considered open and the highest position of holes' exit is regarded as the first-type boundary when the hole is calculated. With the procedure of nodal point virtual flux, the flux of hole is discriminated after every iterative step, the format of discrimination is flows:

$$Q(x_i) = - \sum_e \sum_{l=1}^{NPE} k_{jl}^e (h_l^i)^e \quad (4)$$

here k_{jl}^e is the coefficient of permeability of element e , it is laying j column and l row of matrix, and the location number j is corresponding to x_i .

\bar{Q} is taken as node flux of holes' exit

The overflowing drainage holes are regarded as disabled completely if the $\bar{Q} < 0$, the whole nodes of holes are in the negative zone. While the hole is effective when the $\bar{Q} > 0$.

The hole is invalidated and across the seepage surface if the $\bar{Q} < 0$ of over exit and the $\bar{Q} > 0$ of below exit. So the switch is close and the nodes of hole are regarded as unknown nodes in next iteration, so the simulation for holes is greatly simplified. The method is fast and great convenient for the underground engineering and high slop project that the underground water is difficulty to determinate.

The mesh model of drainage hole

In Practical Engineering, the holes mesh is divided in the super-element of specific zone for the 3-D size effect of holes accurately. The modal and arrangement of holes are different because of the different requirement or different engineering. The mesh of holes is continuous and the non-holes are replaced by conjoint element in this paper, the modal shows as Fig. 3(a). Usually, the distance of holes is only 3-5m, the distance of arrange holes is also little, so the second mesh is divided as Figure 3(b).

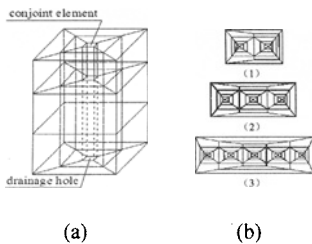


Figure 3. Model of drainage holes

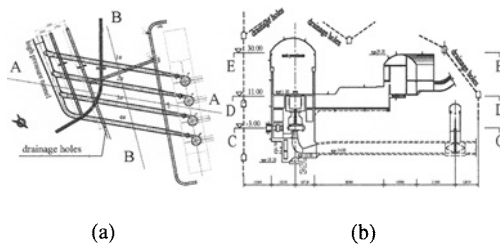


Figure 4. Typical layout for seepage control of underground engineering zone

THE SEEPAGE ANALYSIS OF COMPUTATION EXAMPLE

The Shenzhen pumped-storage power station is located in east of Shenzhen city in China, and the installed capacity of power station is 1200MW. The height difference of upper reservoir and lower reservoir is 445m. The engineering are composed of high-pressure tunnel and powerhouse and etc. The reinforced concrete is adopted to make the high pressure tunnel in the project, one high pressure join four tunnel branch pipes and four turbines. Figure 4(a).(b). The layout of drainage holes is over the branch pipes. The paper mainly studies on function of the drainage holes, especially the function of drainage holes above the high-pressure branch pipes. This paper has studied on the seepage field when the tunnel has been cracking under disaster. The whole mesh is Figure 5(a), the system mesh seepage control is Figure

5(b). The whole mesh has 114153 nodes and 100154 elements. The case of calculation is shown in Table 1.

Table 1. Case of calculation

	description	water level of up/down reservoir
1	The high pressure tunnel is cracking, overflowing drainage holes are set above the branch pipes zone; the location of holes is shown in Figure 4.	526.81/80 (m)

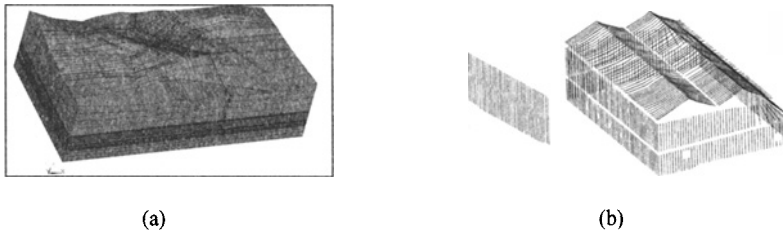


Figure 5. The mesh of whole zone and the all drainage holes for calculation

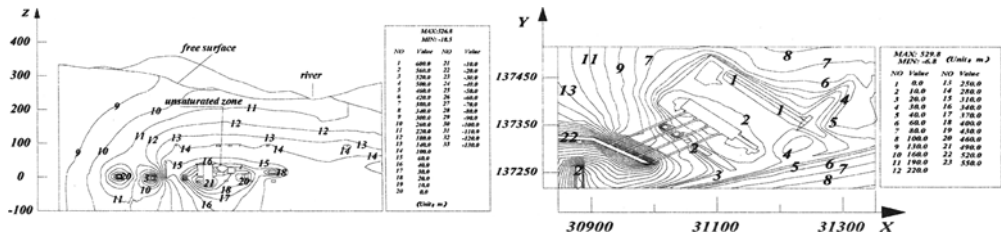


Figure 6. Water head contour lines

Figure 7. Water head pressure contour lines

According to the seepage control methods proposed in this paper, Fig. 6 shows the distributions of water head contour lines and water head pressure contour lines are shown in Figure 7, in a short form. The entire seepage field presents exact seepage property and obvious regularity, which indicates that the seepage control method proposed in this paper plays the role of drainage and pressure lowering. The water pressure contour lines are from 130m to 520m at upstream of drainage holes, but it is lower than 80m at downstream zone of holes. It is shown in Figure 7, which indicates that the holes can control the high pressure water and assure the powerhouse security in disaster.

The anti-seepage curtain is necessary to setup to ensure the engineering safety long time besides the drainage holes.

CONCLUSIONS AND SUGGESTIONS

The effect of overflowing drainage holes was judged by hypothetical switch of seepage, so the trouble that holes across the seepage surface can be solved faultlessly, and new method have been applied to the large-scale densely distributed drainage holes. The example indicates that the drainage holes of branch pipes zone have the control function in whole seepage field in disaster status. It also indicates that the method is successful and practical for seepage field of the large and complex engineering application.

The anti-seepage curtain is necessary to setup because of the possible cracking of reinforced concrete pipes. Meanwhile, the high pressure consolidation grouting for the surrounding rock zone of high pressure tunnel with unfavorable geology condition is supposed to ensure the surrounding rock ability of resistant hydraulic fracturing.

ACKNOWLEDGMENTS

The study is supported in part by “Natural Science Foundation of China (Grant No:50539020) ”.

REFERENCES

- Guan J.H. and Liu J.X. and Zhu Y.X. (1984). Finite element analysis for an array of wells replaced by a drainage ditch, *Journal of Hydraulic Engineering* , (3): 10-18.
- Wang E.Z., Wang H.T. and Deng X.D.(2001). Pipe to represent hole—numerical method for simulating single drainage hole in rock-masses, *Journal of Rock Mechanics and Engineering*, 20 (3): 346-349.
- Wang L., Liu Z. and Zhang Y.T.(1992). Analysis of seepage field near a drainage-holes curtain, *Journal of Hydraulic Engineering*, 4: 15-20.
- Zhu Y.M., Zhang L.J. (1997). Solution to Seepage Field Problem with the Technique of Improved Drainage Substructure, *Journal of Geotechnical Engineering*, 19 (2): 69-76.
- Chen J.Y. (2004). Analysis of saturated-unsaturated seepage field with densely-distributed drainage holes, *Journal of Rock Mechanics and Engineering*, 23 (12): 2027-2031.
- Cui H.D., Zhu Y.M. and Wu S.Y. (2007). Simplification algorithm of numerical simulation the drainage holes in three-dimension seepage with free surface, *Journal of Liaoning Technical University*, 26: 101-103.
- Hu J. and Chen S.H. (2003). Air element method for modeling drainage holes in seepage analysis, *Rock and Soil Mechanics*, 24 (2):281-287.
- Su B.Y. and Zhu Y.M. (1991). Procedure of node virtual flux for seepage free surface with fixed mesh, *Journal of Hohai University*, 19 (5): 113-117.

Others

TWO-DIMENSIONAL FINITE ELEMENT ANALYSIS OF LABORATORY EMBANKMENT MODEL

A. Ahmed

*Lecturer, Civil Eng. Department
Beni-Suef University, Beni-Suef, Egypt*

A. M. K. El-Tohami

*Lecturer, Civil Eng. Department, Faculty of Engineering
Al-Azhar University, Qeni, Egypt*

N. A. Marei

*Associate Professor, Construction Research Institute
National Water Research Center, Cairo, Egypt*

Two-Dimensional finite element analysis was used to investigate the performance of embankment construction over weak subgrade soil using artificial base layer material consisted of cemented sand cushion comprising geosynthetics materials. Two types of base layer materials pure sand and cemented sand comprising husk rich ash and two types of geosynthetics materials geogrid and geotextile were used. Constitutive models were used to represent different materials in numerical analysis. The competence of two-dimensional numerical analysis was compared with experimental results. Numerical results showed a superior harmony with the experimental results. Finite element analysis model proved to be a great tool to determine the parameters that are difficult to measure in laboratory experiments. In addition, finite element analysis has the benefit of cost and time saving when compared to experimental investigation work. Numerical results showed strain induced in geosynthetics eliminated beyond a distance approximately equal six times of footing width.

INTRODUCTION

Numerical analysis based on a method of finite element is a powerful tool for studying the performance and characteristics of different earth work applications. Applying finite element analysis can determine the complicated parameters that would be difficult to measure in experimental work. In addition, finite element analysis is used as a good alternative process for laboratory investigation studies especially in case of large physical models, which leads to saving the time and costs associated with construction of physical models. Several investigators, including Duowen and Hargrove (2006), Chandra and Khaled (2005),

Mauricio (1998), Rodrigues (1998), Hashem et.al (2000), Ahmed (2004), Hassona et.al (2005) and Love et.al (1987) investigated the performance of reinforced soil system using numerical analysis based on finite element analysis method. For example, finite element method was used to study reinforced embankment over soft clay subgrade layer and presented a method to determine the allowable vertical stress taking in his consideration the magnitude of the shear stress at the embankment reinforcement interface (Love et.al, 1987). Another theoretical study based on finite element analysis was presented to evaluate the performance of footings resting on reinforced earth using the ELSYM5 numerical model, which uses elastic material properties (Abdel-Khalek, 1994). Finite element code called DSC-SST-2D was used to predict the field behavior of reinforced soil based on advanced constitutive models (Chandra and Khaled, 2005). VISCP elastic-plastic finite element model was used to simulate the pullout resistance of geotextile in a reinforced sand soil and its results were compared with experimental results, which showed a good agreement between numerical and experimental results (Hashem M. D., 2000).

The main objective of this study is develop a methodology to predict the performance of pavement structure underneath the contact area of wheel over weak subgrade embankment layer using artificial cemented sand layer comprising husk rice ash reinforced with geosynthetics materials using numerical analysis based on finite element method in two dimensional analysis. A comparison between numerical and experimental results is presented. The parameters investigated in this research include the thickness of the base layer sand or artificial cemented sand, type of geosynthetics, position of geosynthetics within base layer thickness and type of base layer materials. The comparison is also verified using previous experimental studies related to this study area as a comparison between numerical and experimental to evaluate the validity of numerical analysis.

EXPERIMENTAL WORK

Experimental physical box model type in plane-strain condition are used in this study to simulate a process of embankment construction over weak subgrade clay soil in the field using two different types of base layer materials; sand and artificial cemented sand. All details of physical model setup, stress-settlement measuring techniques, loading application, compaction methodology and preparation methods for the samples in the mould were previously described (Ahmed A., 2004). Five different material types are used herein; sand and artificial cemented sand used to represent base layer material, soft clay as a subgrade layer, geogrid and geotextile used as a reinforced materials and Portland cement. Two types of geosynthetics materials geogrid and geotextile were used. Geogrid type used in this study is CE-121 and this type was used in previous studies and was found to give reasonable results (Ahmed A., 2004; Marei E.A., 1998). Geotextile type used herein is non-woven heat thermally Typar SF-94 type that is used before in studies and was found to give better results compared with other types of geosynthetics (Ahmed A., 2004). Soft clay soil used in this study was taken from samples already existed at Construction Research Institute, National water Research Center, Cairo, Egypt. These samples related to a site investigation project

located in northeast Egypt. Primary soil characteristics tests were conducted to identify physical and mechanical properties of clay samples. Based on these tests, unit weight, specific gravity, liquid limit, plastic limit and plastic index were found to be 1.79 kN/m², 2.56, 63%, 24% and 37% respectively and this type of clay was classified as clay with high plasticity (CH) according to unified soil classification system. Based on hydrometer test the sample was found to contain 63 % clay and 37 % silt. Sample placement and compaction process for clay layer in the mould described by Ahmed (Ahmed A., 2004). As mentioned before two types of materials were used to represent base layer. The first one was sand passing from a sieve with an opening of 0.8 mm and retained on a sieve with an opening of 0.06 mm. According to grain size distribution, the sand sample classified as poorly graded based on unified soil classification system. The values of uniformity coefficient, coefficient of curvature, specific gravity, mean grain size (D_{50}) and angle of internal friction were found to be 2.68, 1.14, 2.64, 0.38mm and 34° respectively. The second type of base material used was artificial cemented sand that consisted of 90% sand, 8% cement and 2% rice husk ash by weight. The methodology of preparing the artificial cement sand material as the same mentioned in previous research that used this technique to improve the bearing capacity of foundation resting on very soft clay soil using sand cushion techniques and results showed a good enhancement for using this techniques to improve the bearing capacity of soft clay soil (Marei E.A., 1998). The specific gravity and specific surface of Portland cement used were found to be 2.84 and 3320 cm²/gm respectively. The internal friction angle and cohesion for artificial cemented sand was found to be 38° and 12kN/m². Three different base layer thicknesses $H_1=B$, $H_2=1.5B$ and $H_3=2B$ used. The prototype footing model width, B, used to represent a contact area of standard wheel truck described by Ahmed (Ahmed, A., 2004) . Two locations of geosynthetics materials with base material mass are studied above clay layer directly and another location in the mid of base material thickness.

NUMERICAL PARAMETERS

As mentioned above the main four different materials used in the experiment are soft clay, sand, artificial cemented sand and geosynthetics. Modified cam model, hyperbolic model, linear elastic model and slip surface model were used to represent soft clay soil, layer of sand or artificial cemented materials, geosynthetics and the interface between different materials surfaces respectively. Numerical parameters models for different materials used in this research that used to represent in finite element analysis were determined according to the methods mentioned by Ahmed (2004), Hassona et.al (Hassona F.A.) and user's guide of SIGMA/W model (2001). To obtain a complete set of the modified cam-clay model parameters, one dimensional consolidation test and undrained consolidated compression tests were conducted on samples of soft clay soil. The method of calculating the modified cam-clay model parameters introduced in this work including OCR, λ , κ , v , M , and Γ is similar to the method mentioned by Atkinson and Bransby (1978) and user's guide of SIGMA/W model (2001). These parameters are presented in Table 1.

To obtain a complete set of non-linear elastic-plastic, that called hyperbolic, model parameters, unconsolidated drained Traixial compression tests were conducted on

representative sand and cemented sand samples. The method of calculating the hyperbolic model parameters in this study is similar to the method used before in previous studies (Ahmed A., 2004; Saleh N. S., 1996; Duncan J.M. and Chang C.Y., 1970). Two modules are used in this method, the initial modules E_i and the tangential modules, E_t are calculated as per the following.

Table 1. Numerical parameters of modified cam clay model

Property	Value	Property	Value
Over-consolidation ratio (OCR)	1.00	Nu (ν), (Specific volume)	1.94
Lambda (λ)	0.21	Kappa (κ)	0.04
Gamma (Γ)	0.80	Mu (M)	0.28
Pre-consolidation pressure (P_c)	0.31	Unit weight, (γ)	17.9 kN/m ²

$$E_i = K_L P_a \left(\frac{\sigma_3}{P_a} \right)^n \quad (1)$$

$$E_t = \left[1 - \frac{\{R_f(\sigma_1 - \sigma_3)(1 - \sin \phi)\}}{\{2C(\cos \phi) + 2\sigma_3 \sin \phi\}} \right]^n \times E_i \quad (2)$$

Where, E_i = initial insitu modules as a function of confining pressure (σ_3) and atmospheric pressure (P_a), K_L = loading modules number, P_a = atmospheric pressure (used as a normalizing parameter), σ_3 = confining pressure, n = exponent for loading behaviour, E_t = Tangent modules, ϕ = Friction angle of soil, R_f = ratio between the asymptote to the hyperbolic curve and the maximum shear strength, σ_1 = major principal stress and σ_3 = minor principal stress.

The parameters describing the young's modules based on a hyperbolic fit to the stress-strain curve are K , n , C , ϕ and R_f . Based on a previous method that is mentioned above, two series of triaxial compression tests were conducted on the sand and cemented sand samples at different confining pressures of 50, 100, 200 and 300 kN/m². The strength parameters determined from these tests were angle of internal friction and cohesion that equals to $\phi = 38^\circ 15'$ and $C = 13$ kN/m² for cemented sand, while in case of sand these values were $\phi = 34^\circ 00'$ and $C = 0.00$ kN/m². The different numerical parameters of hyperbolic model for different features of sand cushion layer used in this research to represent in finite element analysis are presented in Table 2.

Table 2. Numerical parameters of hyperbolic model for different sand features

Property	Value	
	sand	Cemented sand
Friction angle, ϕ	34.00°	38° 15'
Cohesion, C kN/c ²	0.00	13.00
Failure ratio, R_f	0.73	0.72
Modulus exponent, n	0.06	0.33
Modulus number	380	487

As mentioned above, linear elastic model was used to represent geosynthetic materials in finite element analysis and the parameters used in this model are elastic tensile modulus, Poisson's ratio, unit weight and specific gravity. These values were taken according to the data sheet supplied of these materials.

The interaction characteristics between the soil mass and any different material type can be modeled by introducing interface elements models that called slip surface model as mentioned above. The behaviour of the interface was experimentally studied using direct shear box on a composite soil-other material specimens and the stiffness characteristics assigned to the interface elements were determined from these test results according to the following normal and shear stiffness equations (Ahmed, A., 2004). $K_{normal} = \text{Force divide by the unit deformation in thickness}$ and K_{normal} usually is set to a high value to indicate the slip surface has a little or no compressibility, K_{normal} was taken 10^9 N/mm^2 . The different values of shear stiffness are tabulated in Table 3.

Table 3. Shear stiffness values for different interface composite materials

Interface Surface	K_{shear} (N/mm)	Interface Surface	K_{shear} (N/mm)
Clay-sand	12.00	Sand-geotextile	88.00
Clay-cemented sand	13.00	Sand-geogrid	112
Clay-geotextile	6.00	Cemented sand-geotextile	46.00
Clay-geogrid	5.10	Cemented sand - geogrid	53.50

Numerical model analysis configuration

Two-dimensional plain strain finite element analysis was used to simulate a width of footing that is representing the contact stress area of wheel vehicle in the field over embankment construction underlying weak subgrade soil layer. Only half of the physical model is considered in numerical analysis due to an axisymmetric at the center of the footing. The configuration alignments of finite element mesh in y -vertical and x -horizontal directions is shown in Figure 1. For mesh installation, different elements types are used 8-nodes quadrilateral element to signify modified cam clay and hyperbolic models, 4-nodes quadrilateral element to signify linear elastic and slip surface models, and 6-nodes triangular element to signify transition process in different area sizes of elements. Also, some boundary conditions taken in consideration during mesh designing are the displacement is zero in x -direction along the centerline of the model due to symmetry and the right side of the model for subgrade layer only. Also, the displacement is zero in x - and y - directions along the exposed bottom of the model and the displacement for the exposed ground surface of sample are free to move in x - and y - directions. In addition to some regulations used when setting up the software, all of dead body loads for materials used should be defined and separate solved as a linear elastic model, then this solution considering in the basic solution of the problem as initial stress during defining the load-deformation analysis.

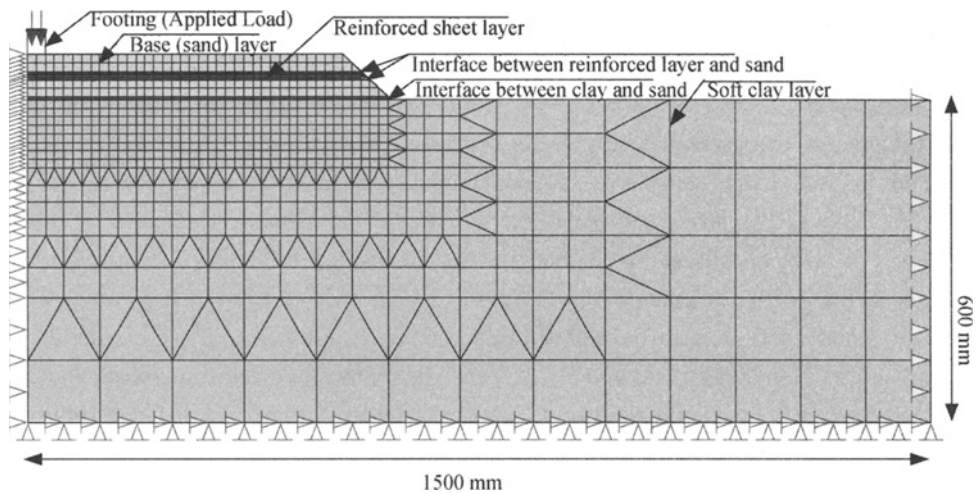


Figure 1. Configuration alignments of finite element mesh in two-dimensional

RESULTS AND ANALYSIS

Stress pattern mechanism

Parameters investigated herein include the thickness of base layer (thickness of sand cushion), type of base material, geosynthetics type and position of geosynthetics sheet within base layer thickness. Stress distribution mechanism is a very important output of finite element analysis in case of earthwork construction analysis because it has used as a judge for the performance of embankment construction over weak subgrade layer in case of introducing stabilization techniques. Vertical stress contour lines in case of base layer thickness $H = B$, H is the base layer thickness and B is the width of footing, for different types of base layer materials of sand and artificial cemented sand over soft clay soil are shown in Figure 2 and Figure 3 respectively. From these figures, it is clear that when cemented sand material introduced to the system the depth of stress bulb shifted up comparing with case of sand material alone. Therefore, existing cemented sand cushion in the system has a good resistance for stresses and the stress bulbs have a little extension within soft clay soil, which lead to increasing the bearing capacity of subgrade soil to sustain more loads comparing with case of sand cushion only. These results are in agreement with stress-settlement relationships obtained from experimental work that conducted herein and with previous studies reported by Marei (1998).

Figure 2 and Figure 4 shows the distribution mechanism of stress bulbs for different base layer thicknesses of $H = B$ and $H = 2B$. From the figures it is noticed that the trend of stress bulbs for case $H = 2B$ is shifted up and stressed a little effect on clay layer comparing with case of base layer thickness $H = B$. It means that increasing the thickness of base layer, all stress distribution bulbs gets flattered and shifted upward and stresses reaches only a little depth in soft clay soil, thus reducing the expected settlement is obtained. Therefore, the

stability of embankment against over-loads increases with increasing the thickness of base layer for different materials types used in this research. The enhancement in performance of embankments due to increasing the thickness of the base layer is related to most of shear failure planes cutting before reaching to soft clay soil, so the sustainability of weak subgrade layer is increased against applied loads when compared with case of having a small base layer thickness. These results are close to stress-settlement results obtained from experimental work and agree with different previous results that conducted experimentally and numerical to study the effect base layer thickness parameter (Ahmed A., 2004; Hassona, F.A. et al, 2005; Marei E.A., 1998; Saleh N. S., 1996). These results confirm the confidence of using finite element analysis in the applications of earthwork problems.

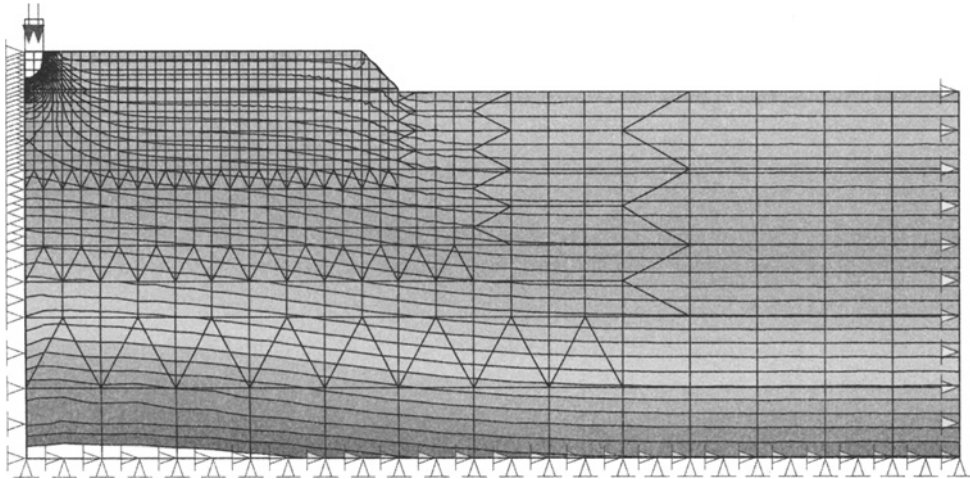


Figure 2. Vertical stress distributions contour lines in case of sand alone without additives for base layer thickness $H=B$

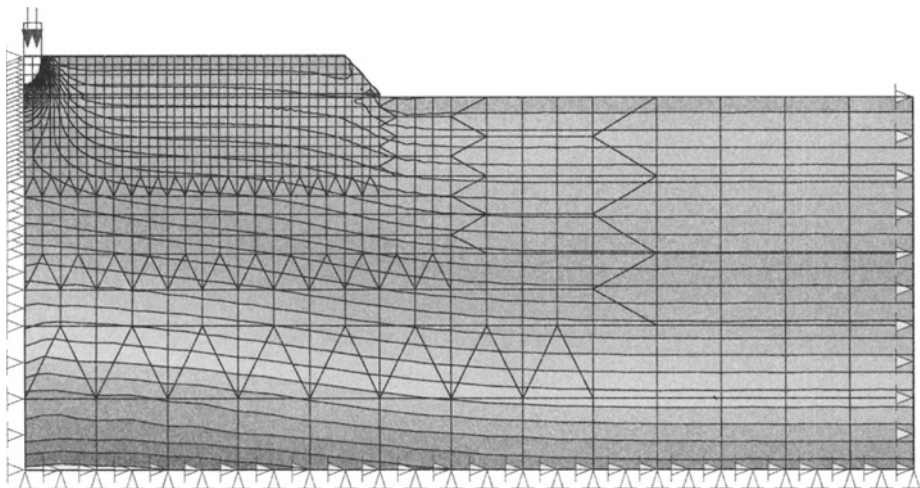


Figure 3. Vertical stress distributions contour lines in case of cemented sand cushion without additives for base layer thickness $H=B$

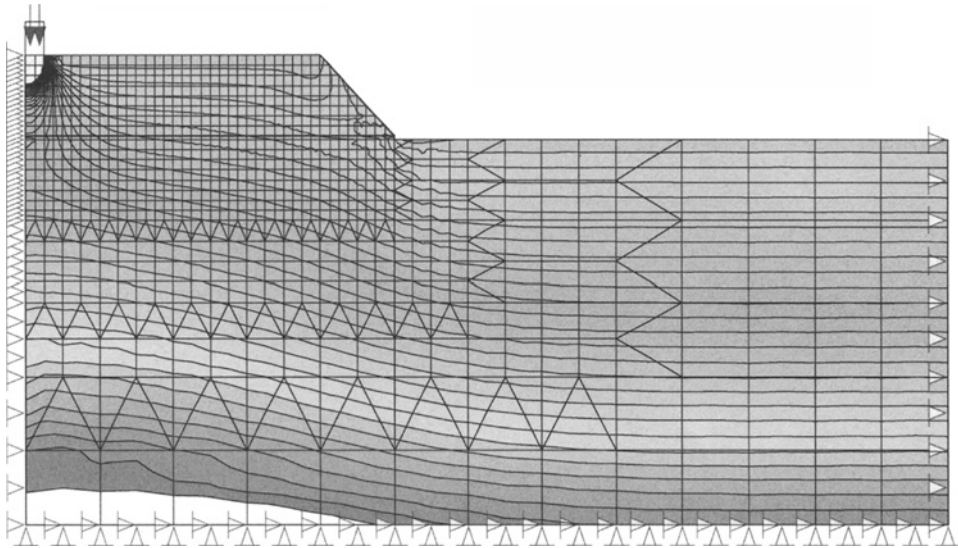


Figure 4. Vertical stress distributions contour lines in case of sand cushion with thickness $H=2B$ without additives

Figure 5 and Figure 6 show the stress distribution contour lines in case of samples comprising one layer of geosynthetics located above clay directly and another layer within the mid of sand layer respectively for case of sand thickness $H=B$. From these figures, it is noticed that when geosynthetics materials are applied, the stress bulbs squeeze and seems flatter in longitudinal direction before reaching the subgrade layer. Therefore, embankment stabilization, for two cases of base layer materials is increased when geosynthetics materials introduced to the system. This can be explained on the light of the following reasons: Firstly, most of stresses are cutting before to reach the subgrade layer. The second reason, the stress distributed over a large area that followed by decreasing in the stress values reaching to the subgrade layer. The third, when vertical stress applied to geosynthetics sheet, the stress adsorbed by geosynthetics and shifted to horizontal stress resisted by these materials, so the stability of embankment is increased and the resistance against applied loads is also increased. The above results show that the best locations for geosynthetics layer was found to be near the footing as shown in Figure 6, that is related to increasing the chance for stress lines cutting early before to reach the weak clay layer. Also, numerical results show that increase the number of geosynthetics layers is associated with high stability and the effect of using geogrid is much pronounced than geotextile and these results close to experimental results and agree with different previous experimental and numerical results (Ahmed A., 2004; Hassona F.A. et al, 2005; Abdel-Khalek H. M., 1994).

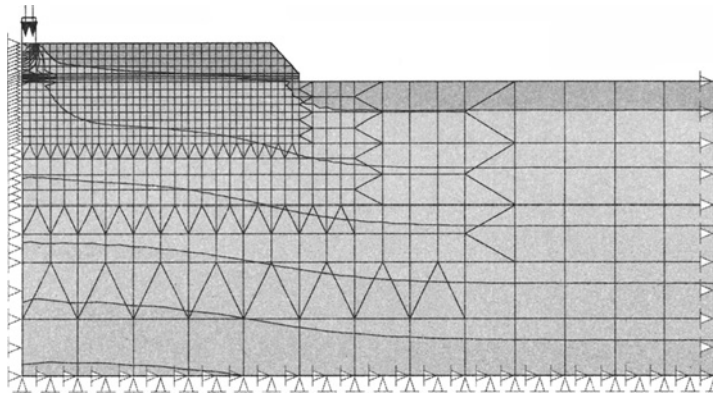


Figure 5. Stress distribution contour lines in case of sample $H=B$ comprising one sheet of geogrid above clay layer

Variations in vertical stress against depth underneath the footing along the whole depth of embankment at failure plane for different study cases of sand thickness are shown in Figure 7. It is clear that the beneficial effect of increasing the thickness of the sand layer is much pronounced in this figure. The stress distribution shifts upward and flattened with the increase of base layer thickness. The flatness of stress distribution curve makes lower values of stresses reaches the surface of lower weak subgrade soil, yet decreasing settlement values. For example at depth of 500 mm measured from the bottom of the mould, the values of stress induced in clay layer are 4.5, 2.15 0.95 kN/m^2 corresponding to H_1 , H_2 and H_3 respectively. Therefore, it is clear that the stress induced within clay layer mass go down with increasing the thickness of base layer material (either sand or cemented sand) that is associated with increasing the load sustainability and decreasing the settlement. The same trend is obtained in case of identical samples using artificial cemented sand material, its means no difference between the behaviour way of two materials for study the parameter of base layer thickness and also these results go the same way with stress distribution contour lines to investigate this parameter. In addition, these results agree with experimental results.

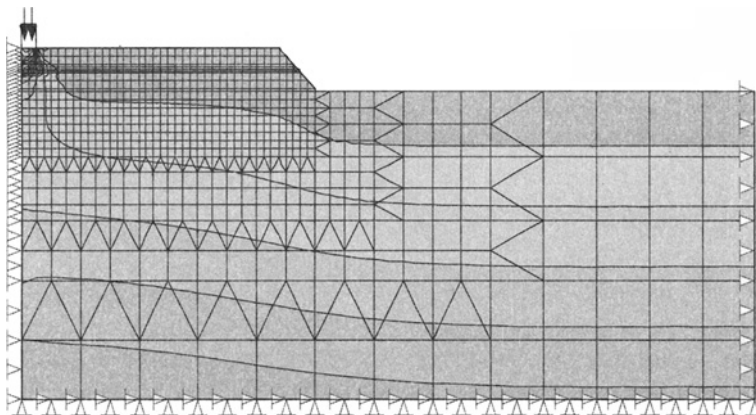


Figure 6. Stress distribution contour lines in case of sample $H=B$ comprising one sheet of geogrid in the mid thickness of sand layer

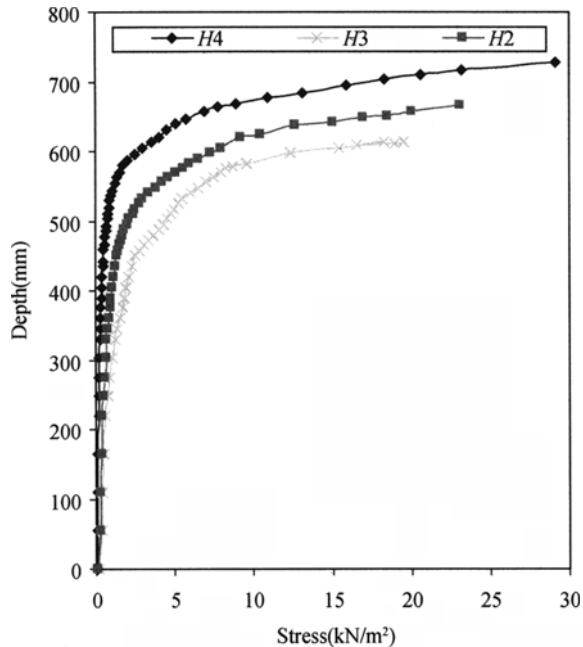


Figure 7. Variations of vertical stress against depth of sample for different thicknesses of base layer material for sand

Displacement pattern mechanism

Deformations distribution pattern mechanism one of the important numerical analysis outputs to study the performance of embankment stabilization with different base layer materials. Deformed mesh is representing the deformation and corrugation happened within embankment mass after completing the process of loading. Figure 8 and Figure 9 show the deformations in the mesh for sand and cemented sand layers. These figures indicate that the deformation pattern in case of sand layer is higher than the deformation in case cemented sand layer. These results confirm that the performance of embankment when cemented sand layer introduced is much pronounced than pure sand layer. A variation in horizontal displacement with depth beneath the footing for different base layer thicknesses is shown in Figure 10. It is clear from this figure that the magnitude of horizontal displacement component decreases with the increase of base layer thickness and the same trend is obtained for artificial cemented sand samples while the values of horizontal displacement components is lower comparing with identical sample in case of using sand only. These results agree with results of stress distribution mechanism mentioned above, with increasing the thickness of base layer resulted in an increase in stabilization and the performance of artificial cemented sand is higher than sand material.

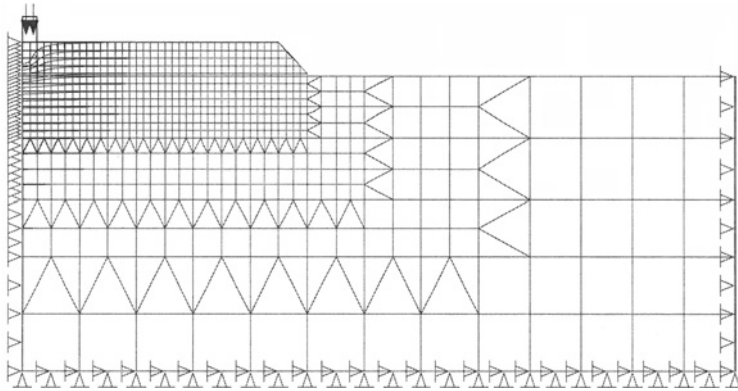


Figure 8. Mesh deformation in case of using sand for base layer thickness, $H=B$

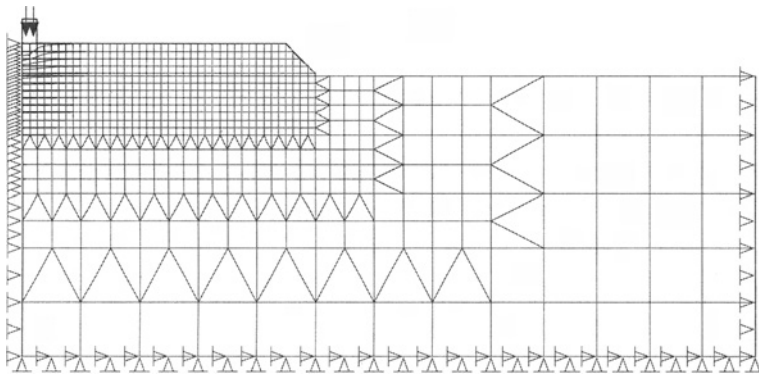


Figure 9. Mesh deformation in case of cemented sand for base layer thickness, $H=B$

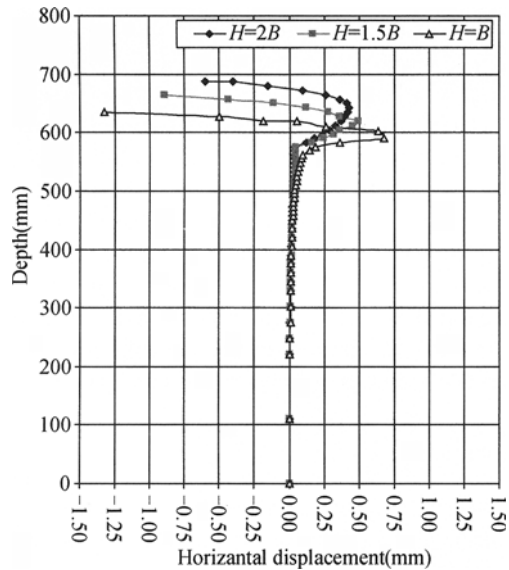


Figure 10. Variations in horizontal displacement with depth for different base layer thicknesses

Variation in Y -strain against horizontal distance along geogrid sheet at different positions for geosynthetics, the first position above clay layer directly and the second position in the mid of base layer are shown in Figure 11. This figure indicates that Y -strain induced in

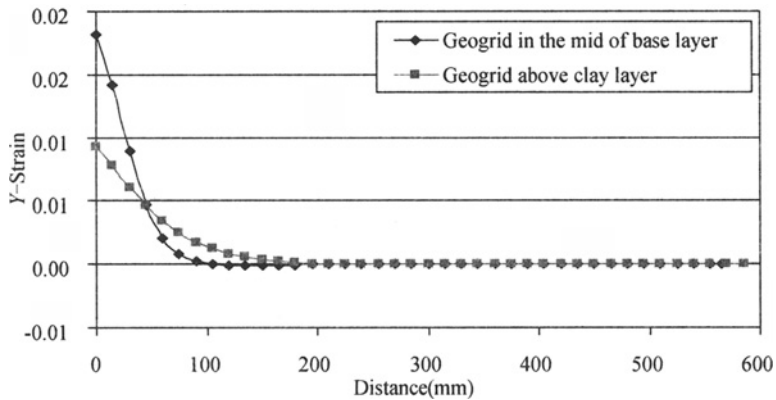


Figure 11. Variation in Y -strain against horizontal distance induced on geogrid sheet within base layer thickness in case of base layer thickness $H=B$

geogrid sheet that located nearest to the footing is higher than located above clay layer directly. Deformations appear clearly beneath the footing and is gradually reduce until a distance that is approximately three times the width of the footing, it means six times of footing width because the problem solved as axisymmetric. It can be explained this results, when geogrid placed near to the footing affected early with stress comparing with geogrid placed at a deep distance from the footing. So when geogrid sheet placed near to the footing a high performance is obtained because the stress cutting early before to reach the weak clay layer and this result agree with experimental results for stress-settlement relationships. Also, from these results a gained economic benefit can be obtain to reduce the area of geogrid sheet beneath the footing because its clear from this figure, after three times of footing width the geogrid sheet has not induced any strain values. This numerical result agrees with previous experimental results that studied the effective length of geosynthetics used as a reinforced material underneath foundation and reported that the beneficial effect for geosynthetics sheets underneath the footing ranged from five to six times the footing width (Marei E.A., 1998).

Figure 12 shows the variation in Y -strain along horizontal distance for different geosynthetics materials used in case of a sample having base layer thickness $H=B$. From the figure, it is clear that no noticeable difference between the trend of two curves for both geogrid and geotextile. It is clear also from this figure Y -strain induced in geogrid is a little small than induced in geotextile. This result related to increase the stiffness of geogrid compared to geotextile and this result close to experimental results and agree with previous experimental and numerical studies to investigate the same parameter (Ahmed A., 2004).

Stress-settlement performance

Based on numerical analysis results, the stress-settlement relationships for different samples studied herein were determined. Figure 13 shows the values of stresses at different settlement values for different thicknesses of base layer in case of using sand material. This figure confirms that the increase in the thickness of base layer material leads to increasing in the

values of stress at different settlement values and the same performance is obtained for identical samples having artificial cemented sand while the performance of cemented sand is higher than that in sand material. These results agree with the results obtained from stress distribution and deformation pattern mechanisms that were mentioned above. Figure 14 shows the above same relationship for base layer thickness $H=B$ with different locations of geosynthetics introduced to the system. It could be noticed from this figure that the values of stress at different settlement values increases in case of samples comprising geosynthetics comparing with identical sample without reinforcement. Also, it can be noticed from this figure that when geosynthetics sheets were placed near the footing an increase in the performance of stress-settlement was evident if compared with other locations. Numerical results also indicated that increasing the number of geosynthetics associated with increase the stability of embankment and the performance of geogrid is much pronounced than geotextile. The same behaviour is obtained when geosynthetics materials were introduced to the system in case of using cemented sand material while the performance of geosynthetics in this case was not much evident when compared to other identical samples that use sand material.

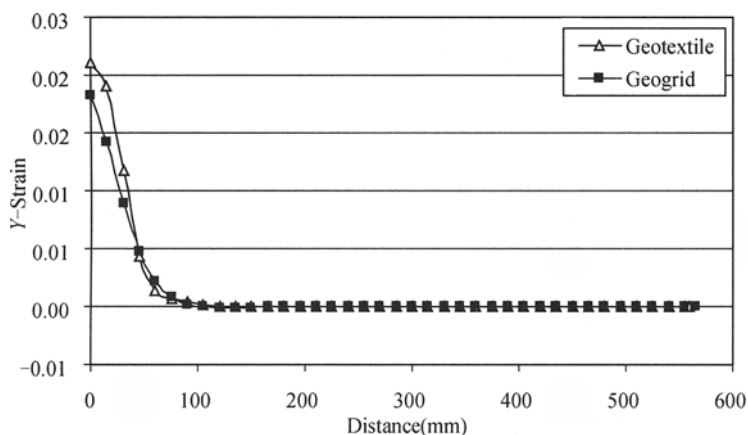


Figure 12. Variation in Y-strain against horizontal distance for geosynthetics materials placed in the mid of the sand layer in case of sample base layer thickness $H=B$

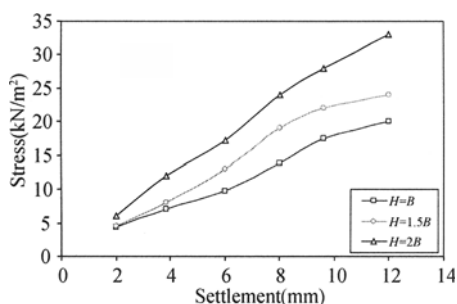


Figure 13. Stress at different specified settlement values for different thickness of sand layer

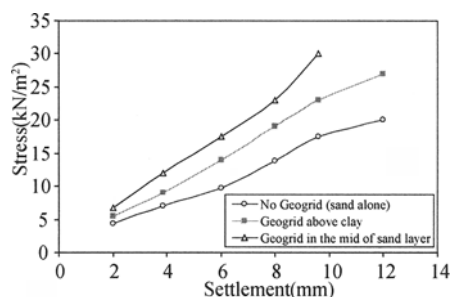


Figure 14. Stress at different specified settlement values in case of base layer thickness $H=B$ with and without reinforcement materials at different locations

Verification of numerical results

To verify numerical results a simple comparison between numerical and experimental results introduced herein. As mentioned above the main objective of using numerical analysis is to measure the parameters that are difficult to be measured at the laboratory. So, for a comparison between numerical and experimental results stress-settlement outputs only can be used as a reference to verify numerical analysis taking in consideration the factors affecting numerical analysis are different from those affecting experimental results. Based on stress-settlement curves obtained from numerical and experimental results, the relationship between stresses at different selected settlement values for some base layer thicknesses selected are shown in Figure 15. This figure indicates that both experimental and numerical analysis produce similar results and a good agreement between both is observed. For more illustration, the same above relationship in case of base layer thickness $H=B$ for sand comprising one layer of geogrid above clay in both numerical and experimental results are shown in Figure 16. This figure indicates a good agreement between numerical and experimental results. A correlation between two curves is clearly appeared in the first part of curves with a little variation noticed at higher values while the trend of two curves takes the same way. Generally, the small deviation between numerical and experimental results is related to the difference between the factors that affecting on both numerical and experimental investigations. Human factor is a major factor that affects the accuracy of experimental work while numerical analysis is not affected with the same factor but it is influenced by different factors such as, mesh setup, number of integration, type of numerical models that used to simulate materials and type of element. The beneficial effect of using numerical analysis is related to saving in the cost and time of experimental and increasing the feasibility to investigate different parameters.

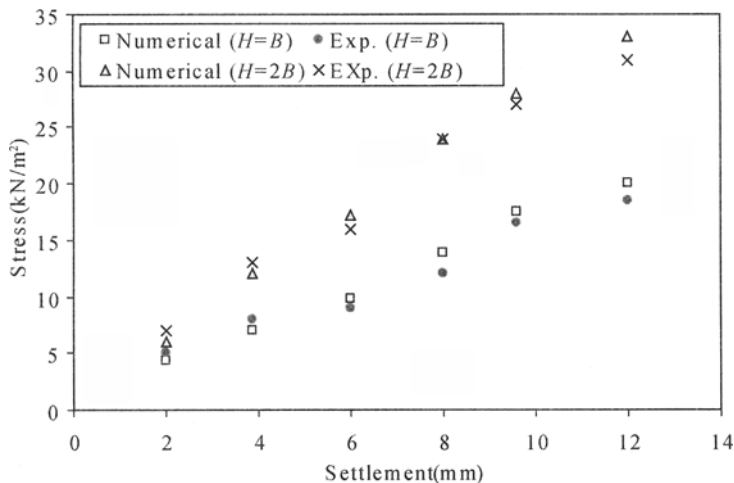


Figure 15. Stress-settlement values in both numerical and experimental results for different base layer thickness

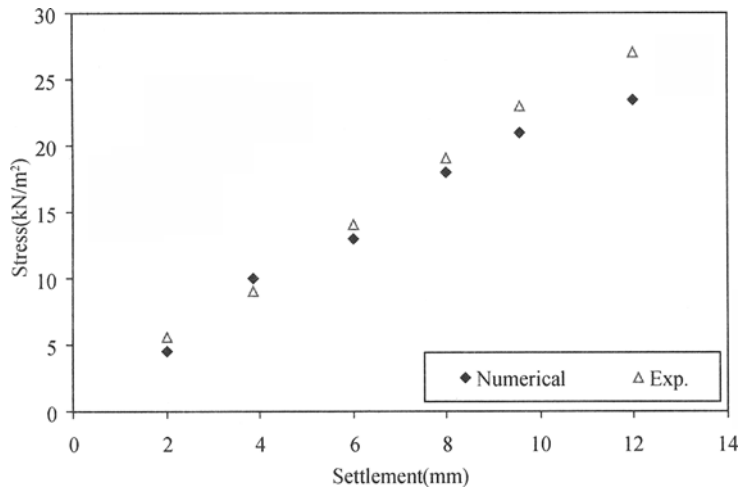


Figure 16. Stress-settlement values in both numerical and experimental results for base layer thickness of sand comprising one layer of geogrid above clay

CONCLUSIONS

Based on above results the following conclusions can be drawn:

- Two-dimensional finite element analysis is a good powerful too to study the performance of reinforced earth works.
- Numerical results showed that artificial cemented sand is a good technique in embankment stabilization especially when geosynthetics introduced to the system comparing with identical sample having sand material. Increasing the thickness of base layer for both materials used enhancing the performance of stabilization.
- Performance of geosynthetics in both of sand and cemented materials is a good while geogrid is much pronounced than geotextile. Numerical results indicated the best performance for geosynthetics is obtained when reinforced sheets are located nearest to the footing.
- Vertical strain induced in geogrid is less than induced in geotextile and the effect of strain within geosynthetics mass eliminated after a distance equal six times of footing width.
- Finite element analysis method gave good satisfactory results comparing with experimental results. In addition, a good agreement between these results and previous study results investigated the same way of parameters.
- Stress distribution and deformation pattern within embankment mass that obtained from numerical results improved when the thickness of both materials increased and geosynthetics introduced to the system compared to identical samples without geosynthetics.

REFERENCE

Atkinson J.H., Bransby P.L. (1978). *The Mechanics of Soils: an Introduction to Critical State Soil Mechanics*. University Series in Civil Engineering, Mc Graw-Hill, London, UK.

- Abdel-Khalek H. M. (1994). *Geotechnical behaviour of soil reinforced with geogrid*, M.Sc. Thesis, Civil Eng. Dept., Cairo University, Egypt.
- Ahmed A. (2004). *Utilization of shredded waste tires in the strengthening of unpaved roads over soft clay*. Ph.D. Thesis, Civil Eng. Dept., Faculty of Engineering, El-Minia University, El-Minia, Egypt.
- Chandra S. Desai and Khaled E. El-Hoseiny. (2005). Prediction of field behavior of reinforced soil wall using advanced constitutive model *Journal of Geotechnical and Geoenvironmental Engineering*, ASCE, 131 (6): 729-739.
- Duncan J.M., Chang C.Y. (1970). Nonlinear analysis of stress and strain in soils. *Journal of Soil Mechanics and Foundations Divisions*, ASCE, 96 (SM5): 1629-1654.
- Duowen Ding and S. Keith Hargrove. (2006). Non linear stress-strain relationship of soil reinforced with flexible geofibers. *Journal of Geotechnical and Geoenvironmental Engineering*, ASCE, 132 (6): 791-794.
- Hassona F.A. Hassan M.A. Hashem M.D. Marei N.A. and Aly A.A., (2005). Numerical analysis of laboratory model footing. *Bulletin of the Faculty of Engineering*, Faculty of Al-Azhar Engineering, Cairo, Egypt, 119 (1).
- Hashem M. D., Abdel-Megeed M. and Youness A. H. (2000). Elastic-plastic finite element analysis of pullout resistance of geosynthetics in sandy Soil. *Bulletin of the Faculty of Engineering, Assiut University*, 29 (1): 127-134.
- Love J.P., Burd H.J., Milligan G.W.E. and Houlby G.T. (1987). Analytical and model studies of reinforcement of a Granular layer on a soft clay subgrade. *Can. Geotechnical Journal*, 24: 611-622.
- Mauricio A. (1998). Numerical analysis of pavement base reinforced with geogrid, *Proc. 6th. Int. Conf. on Geosynthetics*, Atlanta, Georgia USA, 891 – 894.
- Marei E.A., (1998). *Enhancing the performance of foundations resting on very soft clay using cemented and composite sand cushions*. Ph. D. Thesis, Civil Eng. Dept., Faculty of Eng., Cairo University, Egypt.
- Rodrigues R. M. (1998). Performance prediction model for asphalt overlays with geotextile interlayer on cracked pavement, *Sixth international conference on geosynthetics*, Atlanta, Georgia, USA, (2): 973-976.
- Saleh, N. S. (1996). *Study of strip footings on geosynthetics-reinforced sand underlain by weak clay*. Ph.D. Thesis, Civil Eng. Dept., Cairo University, Cairo, Egypt.
- SIGMA/W Users Guide, Version 5. (2001). Software computer program for finite element in stress-deformation analysis. *Geo-Slope International Ltd., Calgary, Alberta, Canada*.

SOME STUDIES ON RECYCLED AGGREGATE CONCRETE WITH AND WITHOUT POLYMER

G. D. Awchat , N. M. Kanhe

*Department of Civil Engineering, G. H. Raisoni College of Engineering
Nagpur, Maharashtra 440016, India*

Buildings are demolished due to various reasons i. e reconstruction for better economic gains, obsolescence due to deterioration on structural performance, natural disasters and war-inflicted damages. The rate of demolition is increasing day by day and at the same time, the cost of dumping is increasing due to non-availability of appropriate site nearby. Besides scarcity of land, other problems associated with the landfill option include their silting; transportation costs, tipping fees and public opposition. Thus, recycling has been gaining wider attention as a viable option for handling of waste concrete. The recycled aggregate concrete is continued for last two decades in India. Polymer modified concrete is finding its application in various fields of construction viz., liquid retaining structures, thin shells, precast wall panels etc. because of improvement in strength and deformation characteristics as compared to normal concrete. From the experimental investigation on recycled aggregate, it is found that strength viz., compressive strength, flexural strength & split tensile strength was increased up to 10%, 40% & 35% respectively by adding 7.50% polymer by weight with respect to weight of cement. An attempt is made in this paper to use only 2% of monobond type polymer by weight with respect to weight of cement so as to compare with normal concrete.

INTRODUCTION

With an increase in our environmental consciousness, the concrete industry is coming under intense scrutiny and criticism. Many practices within the concrete industry that pose a potential threat to our environment are becoming matters of serious consideration and along with increased consumption, there is also an increase in the amount of waste that concrete societies have to deal with. Waste concrete can be produced from a number of different sources. The most common are demolition projects. Many concrete structures like building, bridges and road are demolished after a period of time into their service life for purposes of replacement or landscape changes. Other sources of waste include, natural disasters like earthquakes, avalanches and tornadoes: human causes like warmed bombing and structural failures. Traditionally, waste concrete has been managed mainly through its land filling and recycling. Land filling has become a major problem, particularly in countries where land is scare. Thus, recycling has gaining wider attention as a viable option for handling of waste concrete.

The recycling of waste concrete has other benefits. One of the main environmental benefits is the conservation of natural resources, especially in regions where aggregates are scarce. If recycling plants are centrally located and easily accessible, transport costs can be substantially minimized. The major penalties for the use of recycled aggregate are their somewhat lower compressive strength, split tensile strength, flexural strength and lower modulus of elasticity. To overcome these drawbacks to some extent, it would be advisable to produce recycled aggregate concrete with lower w/c ratio and polymer in it.

Polymer Modified Concrete (PMC) is finding its application in various fields of construction because of the improvement in strength and deformation characteristics compared to plain concrete. The addition of polymer to concrete aids in converting the brittle characteristics to ductile one. A significant consequence of polymer addition is therefore a substantial improvement in the resistance to the formation and growth of crack, in addition, a marginal improvement in tensile strength.

EXPERIMENTAL PROGRAMME

Materials

In the experimental programme, Styrene Butadiene Rubber (SBR Latex) polymer was used at the dosage of 2%, 5% and 10% by weight with respective weight of cement. Monobond-2000 is milky white liquid of specific gravity of 1.05 to 1.10 and viscosity 300-500 in cps. Ordinary Portland cement (OPC) of 43 grade was used in all the mixes. The fine aggregate used was locally available sand having fineness modulus of 3.28 and conforming to IS grading curve-III was used. Conventional crushed basalt stone aggregate as per IS 383:1999 was used in the natural aggregate concrete mixes. Recycled aggregates were obtained by crushing the waste material available in concrete laboratory. Since large size particles cause concentration of stress around particles and results in the lower strength of concrete. Considering this aspect, 20mm down grade size aggregate was considered suitable for medium strength concrete. Table 1 shows the physical and mechanical properties of both natural and recycled coarse aggregates. A complete replacement of natural coarse aggregates with recycled coarse aggregates was considered in the mixes of recycled coarse aggregate.

Table 1. Properties of normal & recycled aggregate are as follows

S.N	Test	Normal aggregate	Recycled aggregate	Permissible limit IS 383 for NAC
1	Fineness modulus (FM) for 20mm aggregate	7.49	5.25	---
2	Specific gravity	2.62	2.71	2.60 min
3	Water absorption	Nil	3.95%	3% max
4	Crushing value	15.24%	23.40%	30%
5	Impact value	14.37%	18.57%	30%
6	Abrasion value	12.40%	16.32%	17%

Mix proportion

Since there is no standard method of designing concrete mixes incorporating recycled aggregate, the method of mix design proposed by IS 10262:1982 was first employed to

design the NAC mixes and finally natural aggregate was fully replaced by recycled aggregate to obtain RAC mixes. The mixture proportion (by weight) used in the mixes. NAC and RAC was fixed at 1:1.13:2.65 and 1:1.35:2.98. After several trails. In the mix, RAC with 2%, 5% & 10% polymer by weight with respective weight of cement was added. It may be noted that the 10% polymer in RAC provides optimum strength of RAC. The water cement ratio of all the five mixes was 0.42 (1:1.13:2.65) and 0.47 (1:1.35:2.98) by weight.

The cubes of size 15cm×15cm×15cm were cast for trial mix. The results obtained are as below.

Table 2. Trial mix design results for M₃₀ and M₂₀ grade NAC

Trail mix	After 7 days curing			After 28 days curing		
	wt. (kg)	Ultimate Load (N)	Average Compr. strength	wt. (kg)	Ultimate Load (N)	Average Compr strength
Grade M ₃₀ Mix 1:1.13:2.65 with w/c=0.42	9.1	585000	27.18 N/mm ²	9.1	840000	38.07 N/mm ²
	9.0	610000		9.0	880000	
	8.9	640000		8.9	850000	
Grade M ₂₀ Mix 1:1.35:2.98 With w/c=0.47	9.1	590000	26.88 N/mm ²	9.1	760000	30.59 N/mm ²
	9.0	615000		9.0	740000	
	8.9	610000		8.9	790000	

Average density of concrete=2666.67kg/m³

Casting and testing Specimen

Total 110 cubes, 90 cylinders and 90 beams of M₃₀ and M₂₀ grade of concrete were cast in four series. Out of which first two series were cast for NAC and RAC by using two w/c ratio 0.42 & 0.47 and other two series were cast by adding polymer content (2%, 5%, and 10%) in RAC. Two w/c ratios were designed in order to determine the effect of w/c ratio on the various properties of concrete i.e. compressive strength, split tensile strength, flexural strength, and pull out strength.

First series, total 28 cubes (15cm × 15cm × 15cm), 18cylinders(15cm × 30cm) and 18beams (10cm × 10cm × 40cm) of M₃₀ were cast in order to determine compressive strength, split tensile strength and flexural strength of NAC and RAC at 7 days, 28days & 90days. All these specimens were made with w/c ratio 0.42. Two cubes of each variation were cast in order to determine pullout strength of NAC and RAC.

Second series, casting as done in first series was repeated by using second w/c ratio 0.47.

Third series, 42cubes, 27cylinders and 27 beams of M30 were cast for RAC by using first w/c ratio 0.42. The parameters varied during casting of these specimens were fiber volume content (2%, 5%, and 10%). Two cubes each with three variation of fiber content were tested in order to study the bond strength at 28 days.

Forth series, casting as done in third series of M20 was repeated by using second w/c ratio 0.47.

Table 3. Physical properties of mix and change in water cement ratio in RAC

Sr. No.	Mixes	Polymer conc.	Water/cement ratio	Slump (cm)	Density of concrete (kg/m ³)
1	N _A	0.00	0.42	11	2696.29
2	R _A	0.00	0.54	10.5	2666.67
3	R _{A1}	2.00	0.37	14	2755.56
4	R _{A2}	5.00	0.32	10	2766.67
5	R _{A3}	10.00	0.28	17	2755.56
6	N _B	0.00	0.47	16	2696.29
7	R _B	0.00	0.51	14	2686.29
8	R _{B1}	2.00	0.43	Collapse	2696.29
9	R _{B2}	5.00	0.36	Collapse	2703.70
10	R _{B3}	10.00	0.33	Collapse	2755.56

RESULTS AND DISCUSSION

Aggregates Properties

Specific gravity and water absorption

The specific gravity of recycled aggregate, lower than that of natural aggregate. However, tests conducted in this project work, has shown that the specific gravity of recycled aggregate is 2.70, which is slightly higher than that the natural aggregate (2.62). The basic reason is that recycled aggregate was used for testing after three month of recycling of concrete, in rainy season. The recycled aggregate consists of unhydrated cement particles, gets hydrated and thus porosity becomes lower, hence specific gravity increases.

In general, from Table 1 the water absorption characteristic of recycled aggregate shows 3.45% higher than the natural aggregate. Hence, it is advisable and necessary to presoak the aggregates before using them for preparing the concrete.

Crushing, impact and abrasion values

The recycled aggregates are relatively weaker than that of conventional aggregates against mechanical action. As per IS 2386 (Part-IV), the crushing and impact values should not be more than 45% for aggregate used for concrete other than wearing surfaces, and 30% for concrete used for wearing surfaces such as roads, runways and pavements. The value of crushing and impact for recycled aggregate is 23.40% and 18.57% respectively against the natural aggregate is 15.24% and 14.37%. The abrasion value of recycled aggregate is 16.32%, while for natural aggregate is 12.4%. It should not be more than 16 % for concrete aggregates.

Physical properties of concrete

The addition of polymer into recycled aggregates concretes alters the water demands of mixes. The recycled aggregates require the more water than that of conventional aggregates as shown in the table no. 1.2, water demand is 8.51% to 28.57% higher than conventional

concrete. The water cement ratio for PMRAC with 10% polymer is 73.7 % lower than RAC, and for normal concrete it is about 46.21% lower than RAC.

Compressive strength

The variation in compressive strength of concrete as the function of age are given in Figure 1 and Figure 2 .The reduction in compressive strength of recycled aggregate concrete (RAC) than normal concrete (NC) is observed in Figure 1 and Figure 2. This reduction in RAC than the NC is about 28 %, 14% and 19 % at the concrete age of 7, 28 and 90 days, respectively.

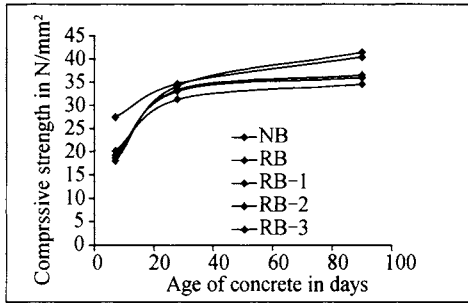


Figure 1. Relation between age of concrete and compressive strength of concrete for first mix

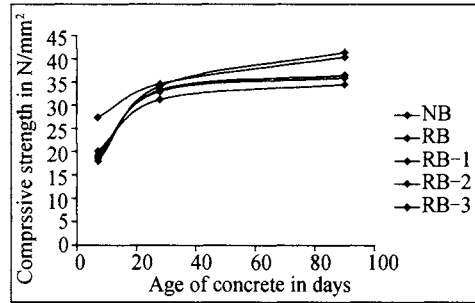


Figure 2. Relation between age of concrete and compressive strength of concrete for second mix

For different percent of polymer added in RAC, 2%, 5% and 10% there is substantial increase in compressive strength at different age of concrete.

Air curing is necessary to set polymer (i.e. for polymerization), at the age of 7 days, 4 days air curing is not enough for bind aggregates mortar (first 3 days are loss in water curing).

At the age of 28 and 90 days, the compressive strength is increases with percentage of polymer. At the age of 90 days the compressive strength for PMRAC with 10% polymer is 19% higher than RAC.

Split tensile strength

In the Figure 3 and Figure 4, the split tensile strength is plotted as a function of age and the variation in split tensile strength in five mixes are clearly shown.

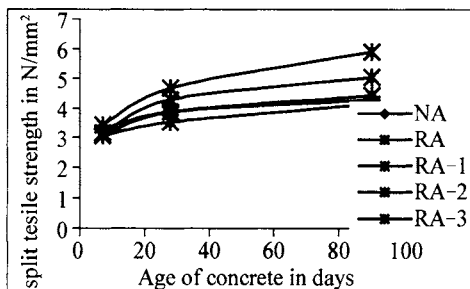


Figure 3. Relation between age of concrete and Split tensile strength of concrete for first mix

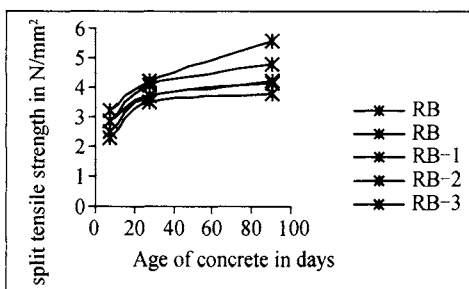


Figure 4. Relation between age of concrete and split tensile strength of concrete for second mix

From figure the split tensile strength of RAC without polymer is lower than that of control concrete. Tensile strength of PMRAC with 10% polymer gives a considerable increase in

tensile strength than that of RAC. Polymer addition in RAC from inner molecular network in the concrete mass, therefore it strongly binds the aggregates, sand and cement. PMRAC with 10% polymer have 45 % higher tensile strength than RAC at 90 days, *i.e.* it can be say that polymer addition gives effective results.

Flexural strength

As shown in the Figure 5 and Figure 6, the variation of flexural strength with respective age concrete in all five mixes is clearly shown. The flexural strength of RAC is very less than that conventional concrete. Flexural strength in PMRAC increases with percentage of polymer. Increase in flexural strength in PMRAC with 10 % polymer is 47 % than RAC, and it increases 19% in between 28 to 90 days.

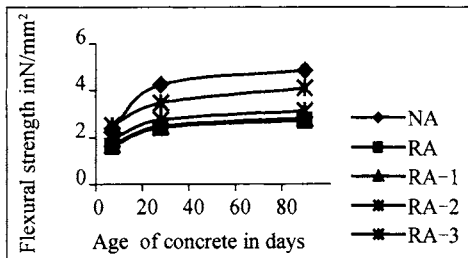


Figure 5. Relation between age of concrete and Flexural strength of concrete for first mix

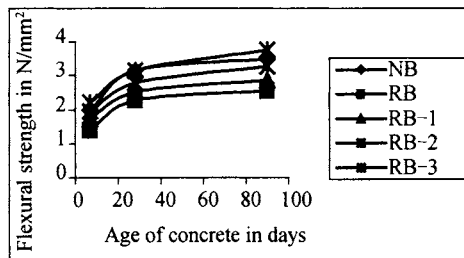


Figure 6. Relation between age of concrete and Flexural strength of concrete for second mix

Bond strength

The adhesion between reinforcement and concrete is increased with percentage of polymer (i.e. polymer cement ratio). The Figure 7 shows relation between the bond stress (τ_{bd}) and the percentage of polymer in RAC. The bond strength was checked at the age of 28 days using the pull out test. The bond strength values are obtained for every specimen casted for bond strength. It is 28% higher in PMRAC with 10% polymer than RAC. It shows linear increment with percentages of polymer.

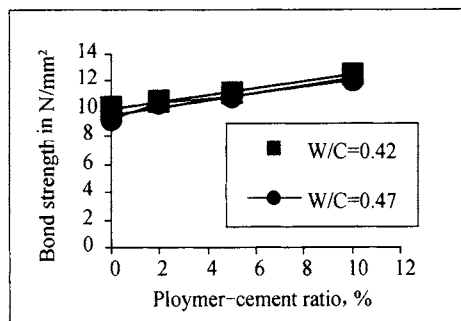


Figure 7. Relation between bond strength and % of polymer for RAC

The correlation function for w/c ratio 0.42 is. (i.e. the proposed equation for bond strength as below)

$$\tau_{bd} = 10.006 + 0.2516 \frac{m_p}{m_c} \quad (1)$$

The correlation function for w/c ratio 0.47 is.

$$\tau_{bd} = 9.5398 + 0.2628 \frac{m_p}{m_c} \quad (2)$$

where,

τ_{bd} = Bond stress in N/mm².

m_p = Mass of polymer.

m_c = Mass of cement.

REFERENCES

- Antoine E.Noman. (1998). New polymer technology, *Concrete International*, July, 57-61.
- AICTE report. (2001) Special concrete, 1-5. *American Concrete Institute Journal*, February, 126-135.
- Hughes B.P. and Fattuthi N.J. (1976). The workability of polymer reinforced concrete, *Magazine of Concrete Research*, 28 (96): 157-161.
- Modera C.D. and Bairagi N.K. (2001). Shear strength of fiber reinforced concrete, *Indian Concrete Institute Journal*, January-March, 47-52.
- Nemkumar Banthia and Cesar Chan,(2000). Use of recycled aggregate in plain and polymer Reinforced Shotcrete, *Concrete International*, June, 41-55.
- Nixon.P.J (2002) Recycled concrete as an aggregate for concrete- a review. *Materiaux Et Constructions*, 11 (65): 371-377. Preceeding Hermite Polynomials.
- Surendra P Shah, B.Vijaya Rangon (1971). fiber reinforced concrete. Ravindra .K. Dhri, Neil A. Henderson and Mukesh C. Limachiya (1999). Recycled aggregate concrete for sustainable development. *The Indian Concrete Journal*, August, 463-464.

RESEARCH ON THE DRY COMPACTNESS TECHNOLOGY IN SUBGRADE FILLED WITH WIND-BLOWN SAND IN SAND DAMAGE AREA

Faming Chen

WuHan University of Technology, Wuhan 430063,China

Ruonan Liu

*Xinjiang Highway Planning Survey and Design Institute,
Urumqi 830006,China*

Wind-blown sand in sand calamity area brings great difficulty with people's survivorship and trip, and it brings blight with agricultural crops in adjacent area. How to abate sand damage is we the problem that requirement resolve. Wind-blown sand has good water stability and fine dry tamping compact characteristic and prevent from salt expansion. As road material, it not only solve disease of subgrade but also improve amend environment and saving project investment. Because of the climate feature of desert area is little rainfall, large volume of evaporation, dry and absence of water, It brings out great inconvenience, due to the large quantity of water using in project and poor transportation condition. To reduce the quantity of water using, we do research on the technology of dry compactness. This technology is feasible through trial and extending and gains favorable economic benefit.

INTRODUCTION

The desert acreage of our nation is 0.8089 million square kilometers which occupies 8.43 percent of country's acreage. Our nation is one of the countries which have high proportion desert acreage in the world. The distribution is mostly in Xinjiang、Neimeng、Gansu、Qinghai、Ningxia、Shanxi province, etc. Among them the desert acreage of Xinxiang is 0.4381 million square kilometers which account for 54.15 percent of nations.

Desert coverd area is large, So wind-blown sand brings great difficulty with people's survivorship and trip has become increasing. It endanger growth of agricultural crops and people's trip directly. How to abate sand hazard is we the problem that requirement resolve. Experimental results demonstrate that wind-blown sand has good water stability and fine dry tamping compact characteristic and prevent from salt expansion. Subgrade filling with wind-blown sand at Saline Soil Area can prevent from salt expansion. Because of wind-blown sand area has typical characteristic of continental climate: high temperature during summer, extraordinary hot, dry and little rainfall, dry and cold in winter, seasonal sand in spring and autumn, large difference in temperature, it is a important problem waiting to research in construction of compaction technology for subgrade.

Firstly, long distance between construction site and water supply place in wind-blown sand area, the distance is usually more than 200km and the traffic condition is very poor, which increases the construction expenditure; Secondly, because of wind-blown sand's dank character, the volume of evaporation is very high in desert and also needs very large quantity of water. Meanwhile, the difficulty of water supply leads to prolong the construction time. The climate characteristic of wind-blown sand area makes water using for subgrade compacting becoming one of the important restricting factor in road construction. In order to solve the problem, we choose the wind-blown sand which comes from typical desert area in Xinjiang talimu basin and research dry compacting technology for solving the problem that water using in road construction in wind-blown sand area to treating geology disease and shorten the time of project and reduce the construction cost.

THE GRANULE COMPOSING OF WIND-BLOWN SAND

To solve the technology problem dry compacting subgrade in desert area, the trial has 7 sand samples collected in Xinjiang talimu area. After analyzing the granule, we get the results listed in the Table 1 and the average granule grade curve in the diagram 1 as follows:

According to the Table 1, wind-blown sand sample's granule diameter varies from 0.5 mm to 0.07 mm (account for more than 95%). We can gain thin extent modulus by expressions as follows:

$$M_x = \frac{\sum_1^n A_{n+1} - (n-1)A_1}{100 - A_1} \quad (1)$$

Table 1. The result of granule composing of wind-blown sand

Sample number	Granule diameter percentage (%)				Sample site
	0.50-0.25/mm	0.25-0.125/mm	0.125-0.063/mm	<0.063/mm	
1	0.286	24.052	69.808	5.854	Talimu desert center
2	0.500	22.800	74.020	3.130	
3	0.310	25.942	66.714	7.034	
4	0.000	18.262	78.326	3.412	Talimu desert verge
5	0.080	38.626	57.142	4.148	
6	0.032	51.406	47.076	1.486	
7	0.046	49.576	46.616	3.662	
average	0.115	32.925	62.815	4.104	

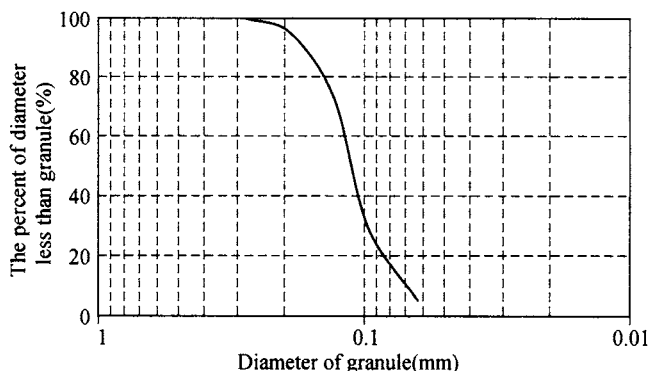


Figure 1. wind-blown sand sample grade curve

In the expressions: M_x -thin extent modulus of wind-blown sand; A_n -cumulate percentage of every grain grade; A_1 -cumulate percentage of the first grain grade. Computing by the formula above: $M_x=1.28$, the average square dispersion is 0.31; the variation modulus is 0.23, so it belongs to exiguous sand.

Meanwhile we can work out ununiformity modulus C_u :

$$C_u = \frac{d_{60}}{d_{10}} \quad (2)$$

In the formula: d_{10} , d_{60} -potent grain diameter. By computing: $C_u=1.31$, the average square dispersion is 0.22, the variation modulus is 0.17, and it proves that the wind-blown sand's grain grade is well-proportioned.

By analyzing the trial, we come to conclusion as follows:

(1) There are almost no thick grain diameter ($D > 0.197\text{in}$), which indicate that the sand's machine composing is very thin and surface acreage is very large.

(2) There are only a little volume thin grain diameter ($D < 0.074\text{mm}$), which indicate that the activity of sand surface is low, no glutinosity, the incompact character is obvious, the water steady character is fine.

(3) No ununiformity modulus C_u is small, which indicate that sand grain is well-proportioned and divide option character is fine too.

WIND-BLOWN SAND'S NATURAL WATER QUANTITY

Because of dry weather, little rainfall and high evaporation, wind-blown sand's natural water quantity is little affected by seasonal factor. Whatever season there are some relationship between water quantity and the depth of wind-blown sand. At the beginning of May, we collected 7 group samples in different place of Talimu desert area and analyzed the natural water quantity respectively; the trial result listed in the Table 2 and the corresponding average natural water quantity's distribution diagram is Figure 2 as follows.

Table 2. The trial result of wind-blown sand's natural water quantity (%)

Depth Sample number	0m	0.5m	1.0m	1.5m	2.0m	2.5m	3.0m	3.5m	Sample site
1	0.0	0.1	0.2	0.4	0.9	1.2	2.0	2.5	Talimu desert center
2	0.0	0.0	0.1	0.3	0.9	0.9	1.9	3.0	
3	0.0	0.0	0.2	0.5	0.8	1.0	1.7	2.4	
4	0.0	0.1	0.1	0.2	0.6	1.0	2.0	2.2	
5	0.0	0.2	0.3	0.5	0.8	1.2	1.9	2.6	Talimu desert verge
6	0.0	0.1	0.2	0.4	0.7	0.8	1.8	2.5	
7	0.0	0.0	0.2	0.3	0.9	1.3	2.1	2.6	
Average	0.0	0.1	0.2	0.4	0.8	1.1	1.9	2.5	

Based on the analysis, we can arrive at conclusion as follows:

(1) On the surface of desert, the natural water quantity of wind-blown sand is small, it is usually 0-0.8%;

(2) With the increasing of depth, the natural water quantity of wind-blown sand increases to some extent basically as the line variety characteristic.

(3) The natural water quantity of wind-blown sand whose depth is more than 3.5 meters usually ranges from 2.5% to 3.5%, and basically keeps in such scope as the change in the depth, so we usually make it about 2.5% in the construction site.

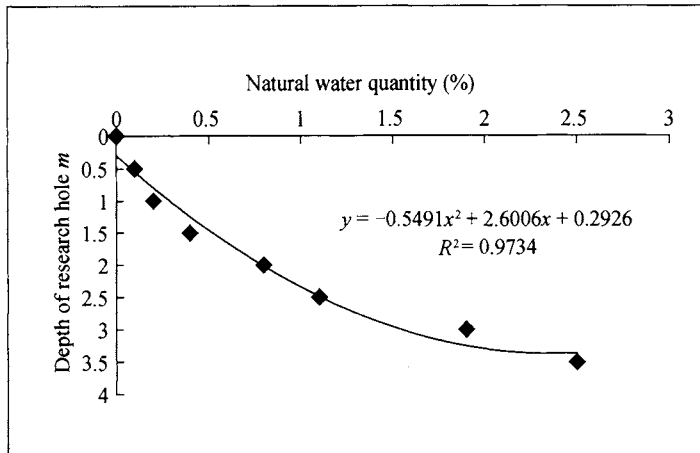


Figure 2. Wind-blown sand natural water quantity's distribution diagram

THE WIND-BLOWN SAND'S TAMPING COMPACTLY CHARACTERISTIC ANALYSIS

Four representative group samples are selected in Talimu desert area. When we use heavy tamping machine to tamp the sample, there are two different trial methods. One is cover board on the sample, and the other is no board. The trial result is listed in the Table 3 (showed in Figure 3 and Figure 4).

Table 3. Trial result of wind-blown sand's heavy tamping compactly

Tamping type	Trial sequence	Water content (%), dry density (g/cm ³)								
Cover board on the sample when tamping	1	0.20	2.02	4.03	5.78	7.46	9.06	11.07		Water content
		1.579	1.530	1.532	1.519	1.507	1.518	1.517		Dry density
	2	0.05	1.08	2.84	4.70	7.61	11.28	16.03	17.02	Water content
		1.544	1.520	1.525	1.517	1.520	1.519	1.542	1.570	Dry density
	3	0.07	0.56	1.57	2.97	4.94	7.86			Water content
		1.547	1.520	1.519	1.516	1.504	1.513			Dry density
	4	0.20	1.66	3.66	6.47	9.37	13.27			Water content
		1.577	1.509	1.512	1.513	1.522	1.522			Dry density
No cover board on the sample when tamping	1	0.21	1.97	4.18	6.10	8.51	10.04			Water content
		1.545	1.505	1.489	1.514	1.517	1.512			Dry density
	2	0.22	1.11	2.34	3.14	3.97	5.77	8.76		Water content
		1.577	1.491	1.51	1.505	1.514	1.535	1.542		Dry density
	3	0.20	1.03	2.08	3.01	4.67	6.78	8.14	9.56	Water content
		1.566	1.501	1.509	1.516	1.538	1.518	1.507	1.515	Dry density
		11.67	13.27	15.81	18.73					Water content
	4	1.532	1.541	1.538	1.588					Dry density
		0.04	1.31	2.81	5.63	8.40				Water content
		1.569	1.510	1.510	1.529	1.539				Dry density

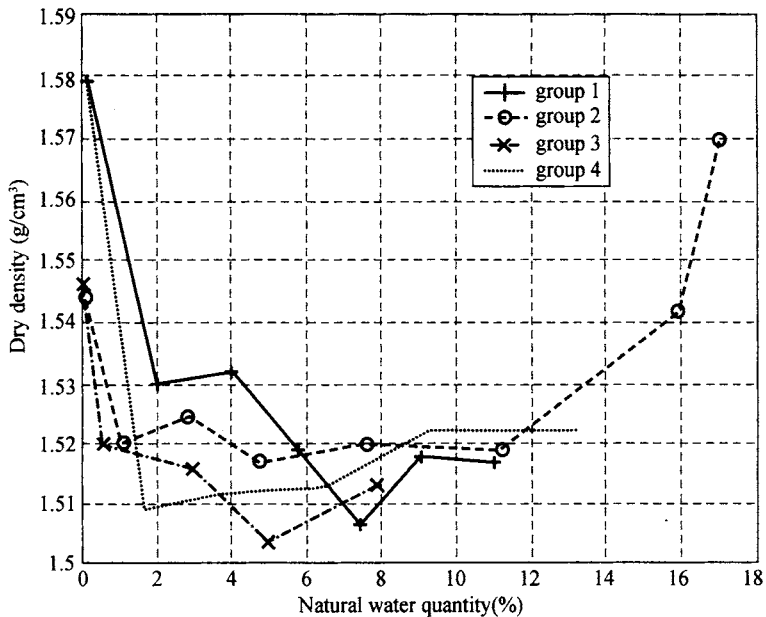


Figure 3. Wind-blown sand's heavy tamping compactly (Cover board on the sample when tamping)

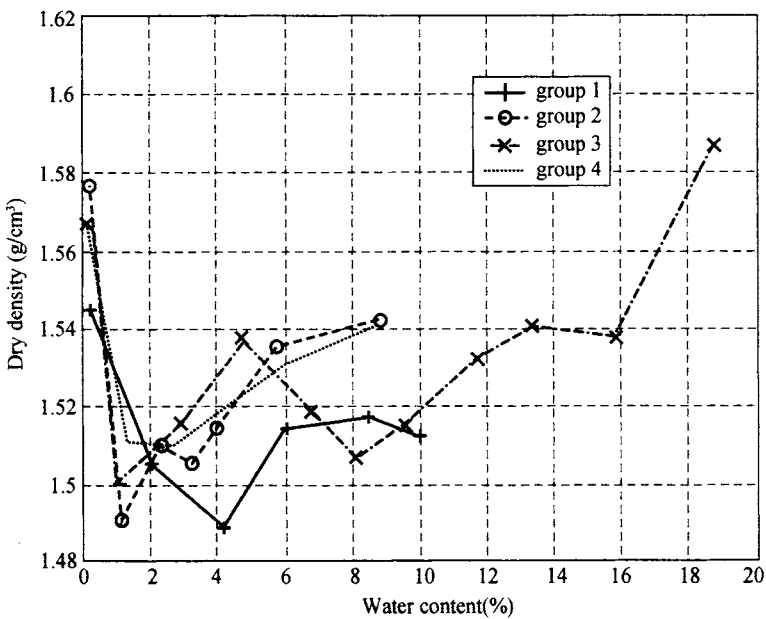


Figure 4. Wind-blown sand's heavy tamping compactly (No cover board on the sample when tamping)

After trial of wind-blown sand's heavy tamping compactly, we reach the conclusion as follows:

(1) Wind-blown sand has fine dry tamping compact characteristic. Pressing it when water content is almost zero, higher and even the maximal dry density will be gained. Four groups

of sand sample covered by cover board whose dry density reaches the maximum when water content is almost zero, while the other four groups of sand sample whose dry density all reaches the maximum except one group reaches 98.6% of maximum.

(2) The wind-blown sand's tamping compactly curve is different from other materials, it represents concave curve. From the diagram, we can see two maximum and the two maximum appear when water content is almost zero and optimal. In ecumenical condition, the tamping compactly curve of exiguous soil is protuberant, they reach maximal dry density only when they have optimal water content.

(3) The dry density is high and even reaches maximum when the water content is about zero, and it reduces rapidly when the water content becomes larger, then the minimum will appear. During the tamping trial, the sand sample not covered by cover board whose minimum range from 1% to 4%, mainly ranging from 1% to 1.6%; while the sand sample covered by cover board whose minimum range from 1% to 8% and they are not centralized, its dry density varies not under order, so there are many maximum and minimum, but the difference is slight. Only when the water content get almost saturated, the dry density varies obviously and it is approximately or a little bigger than the dry density when the water content is approximately zero.

(4) Compared diagram 3 with diagram 4, we can find that the curve which the sample is covered by cover board fluctuating range is very large and the minimum range is centralized.

CONCLUSIONS

By analyzing the wind-blown sand's grain composing and natural water content and tamping compactly trial, we can reach conclusions as follows:

(1) Higher or maximal dry density when the wind-blown sand's water content is almost zero, that is to say, sand will be compacted when the water content is zero or approximately zero. Although wind-blown sand's natural water content is almost zero when the depth under earth surface is 0~1.5m. But the natural water content reaches minimum when the depth is more than 1.5m under earth surface, so good pressing compactly effect will not be gained. Because of high temperature and large evaporation in wind-blown sand area, by borrowing wind-blown sand trial, the water content is about zero when they are taken to construction site. We solve the problem by another method which is to let the sand dispersed and sunned in material construction site, which will make the sand's water content reaching zero.

(2) By analyzing the grain, wind-blown sand not only have the characteristic that little volume of powder grain, surface low activity and good water stability, but also have the characteristic that mechanical composing is fine-grained, large surface, grain grade is well-proportioned and fine dispersing and selecting character. Variety range is not large (extent is $0.308\text{g} / \text{cm}^3$, variety modulus is 22%), which is good for sand roadbed's steady sedimentation in short time and big sedimentation won't appear.

(3) wind-blown sand is tamped compactly and its dry density reaches larger numerical value when the water content is low or saturated, so it indicates that some kinds of water in the sample have bad effect on tamping compactly. Under ordinary condition, soil is primarily overcoming glutinosity force and friction force between grains during the tamping compactly phase. For fine-grain soil, it is primarily overcoming glutinosity force, while for sand, under

exceeding dry condition, the glutinosity force is very small and the friction force is relative large. During the tamping compactly trial, the sand layer is affected by vibratory force which make it not only affected in vertical direction but also affected by derive force in horizontal direction and displacement arise. Because of the force diffuses in vibratory wave modalities, the grain's displacement in leaping modality. All grain's displacement direction is aperture-ward and the displacement becomes larger, which make the grain arrange over again, and then the sand layer becomes compact. When there are some water in the sand, the water film distribute on grain's surface will have linking force which increase resistance and the resistance not only influences on grain displacement but also reduce the leaping intensity. Another aspect, thin water in the soil bring surface patulous force which also will hold back the displacement. The force will lead to the lower dry density. When the water content is approximately saturated, the thin water in the soil disappears, while the film water become thicker and the linking force reduce rapidly. In addition, the water vents along the aperture when they are affected by vibratory force, which will bring force and displacement to sand grain, then the sand grain's dry density increase much.

(4) Although higher dry density will be gained when the wind-blown sand has the lowest water content and is tamped compactly, the water content becomes a little higher, the minimum of dry density will appear. The reason for this is grain's surface have electric charge affected by water when their water content is small, so the water film have two electric charge layer and the electromotive force become feeble as the distance become longer; Simultaneously, thinner and smaller aperture have bigger patulous force and linking force, so it's hard to press compactness. Water film become thicker and linking force reduce when water content become higher, but the thin water in the soil becomes more prevent linking force from reduce, so the dry density's arrange is not large., then some fluctuation appear. Along with the water content becoming much higher, the linking force of water keep reduce and the thin water in the soil have more prominent effect. When gravity water appears, the air in the sand sample disappears, the effects of thin water in the soil reduce rapidly, and the linking forces between grains reduce immediately and dry density increase rapidly.

The above indicated that using dry compactness technology to press wind-blown sand is feasible, but we should note that the sand subgrade's water content must be about zero (under5%). If the water doesn't reach the requirement, good result will get when using vibrating compact technology.

APPLICATIONS

In order to confirm the achievement of test research, we have constructed the 2km long test road In Xinjiang Yuli desert area. The engineering geological property of test road is the weak soils and underground water level is high. The soil is strong sulphate salty soil, salt expansion is larger. Treatment method is exchanging-filled with wind-blown sand of 80cm below ground, wind-blown sand is backfilled compacting on subgrade. Before compactness, the natural water content of the wind-blown sand is 0%-0.49%and the average dry density is $1.43\text{g} / \text{cm}^3$. In the process of road compaction, first to use vibration grinding machine to grind stably for 2 times , then to vibration compaction for 4 times, and finally, to grind stably for 2 times again. After the experimental examination, the wind-blown sand roadbed density

increase to 1.62g/cm^3 after the compaction, its driest density is 1.67g/cm^3 , and the compaction effect is good.

By detecting of test road synthetical in spring, summer, autumn, winter, it shows that subgrade has no deformation and settlement, and wind-blown sand can prevent from salt heaving effectively, the strength of pavement and subgrade is satisfied with the demands of design. It is indicated that wind-blown sand as treatment of subgrade and management of geological disease is good road material, and dry tamping compact can be adopted.

In the recent years, the application of using the wind-blown sand to fill the roadbed is widely generalized in Xinxiang province, including Tazhong petroleum road, the road from Qiemo to Ruowu and the road from Hetian to Alaer to Shaya (the 217th national road), and the saving of the project investment is nearly hundred billions, its economic efficiency is extremely remarkable.

REFERENCES

- Jianlin An. (2004) *Researching mechanics character and dynamical capacity of wind-blown sand in Xinjiang*, Xi'an, xi'an Road and Transportation University.
- Ministry of Communications of China,(2006), *Technology criterion of roadbed construction*, Beijing, People Communication Book Concern.
- Zhongda Chen, Dengliang Zhang (2001). *Wind-blown sand engineering characteristic in Takelamagan*, Xi'an, xi'an Road and Transportation University Study News.

EXPERIMENTAL STUDY ON THE INTERFACIAL FRICTION BEHAVIOR OF GEOGRIDS IN SILT MIXING RUBBLE

Rong Chen

*School of Civil and Hydraulic Engineering University Department, Dalian University of
Technology, Dalian, 116085, China*

Maotian Luan, Wei Zhao

*State Key Laboratory of Coastal and Offshore Engineering, Dalian University of
Technology, Dalian 116085, China
Institute of Geotechnical Engineering, School of Civil and Hydraulic Engineering, Dalian
University of Technology, Dalian 116085, China*

Geogrids with well-known engineering properties have been widely used in geogrids-reinforced earth structures. But reinforced capability of geogrids in the silt is not well. A series of pullout tests to investigate the interfacial friction behavior of geogrids in silt mixing rubble are conducted in the laboratory under different normal stress and rubble content. By analyzing experimental datum, some conclusions were made that increasing normal stress on silt is not effective method to raise interfacial shear resistance; adding rubble content in slit can greatly improve the passive resistance of the transverse ribs and pullout resistance of geogrids. The study is of referring value for design of geogrids-reinforced earth structure.

INTRODUCTION

Geogrids with well-known engineering properties have been widely used in geogrids-reinforced earth structures. The main function of geogrids is to redistribute stresses within the soil mass in order to enhance the internal stability of reinforced soil structures. The geogrids undergo tensile strains as they transfer loads from unstable portions of the soil mass into stable soil zones. Nevertheless it is discovered that reinforced capability of geogrids in the silt and soft clay is not well. Hereby the research on interaction mechanism of soil and geogrids becomes especially significant.

The pullout resistance of geogrids includes two components: (1) the interfacial shear resistance that takes place along the longitudinal ribs; (2) the passive resistance that develops against the front of transverse ribs. The first mechanism could be quantified using parameters obtained from direct shear test; the latter can only be evaluated using pullout tests. The ultimate pullout resistance has been typically interpreted as the sum of the two kind of resistance. Sidnei and Benedito performed small-scale pullout tests individually for

transverse and longitudinal geogrids ribs and found that resistances of transverse ribs and longitudinal ribs can not be directly summed due to their interaction. Jewell and Bergado suggested that pullout resistance of geogrids was correlative to the distance of transverse ribs, soil particle size, water content and the degree of compaction. A great deal of tests indicates that the passive resistance produced by transverse ribs is obviously greater than the interfacial shear resistance on longitudinal ribs. Then how to make transverse ribs develop more passive resistance becomes a problem to be further studied.

As far as above problems are concerned, a series of large scale pullout tests to investigate the interfacial friction behavior of geogrids in silt mixing rubble are conducted in the laboratory under different normal stress and rubble content. And based on experimental results, the effects of rubble content and normal stress on interfacial friction behavior of geogrids are analyzed.

TEST DEVICE AND METHOD

Soils

Silt used in test is taken from an engineering site located in Dalian. The basic characteristics are listed in Table 1. According to different rubble content in silt, four kinds of soil samples are defined as following: Sample A, silt; Sample B, silt with 10% rubble; Sample C, silt with 20% rubble; Sample D, silt with 30% rubble.

Table 1. Soil characteristics.

Maximum dry density (g/cm ³)	Optimum water content (%)	Cohesion (kPa)	Friction angle (°)
1.80	12.78	29.55	34.27

Geogrids

Two geogrids, identified as EG50 and EG90, were used in this investigation. They are manufactured by BOSTD Geosynthetics Qingdao Ltd. And in its special lab, tensile tests and performance tests on physics, mechanics and endurance are conducted according relevant criterion. The main indexes of geogrids are listed in Table 2.

Table 2. Main indexes of geogrids

Type	The longitudinal rib length (mm)	Maximal aperture width (mm)	Minimum rib width (mm)	The transverse rib width (mm)	The longitudinal rib thickness (mm)	The transverse rib thickness (mm)	Tensile strength (kN/m)
EG50	235	16.43	5.80	17.95	0.93	2.52	61.14
EG90	252	17.10	5.79	18.68	1.40	4.00	97.87

Pullout device

The pullout device used in this study (Figure 1) consists of a rigid box, reinforced with Ushaped steel beams. The dimension of the box is 1000mm long, 400mm wide and 500mm high. A steel board was used to support the jack that applies the normal stress to soil.

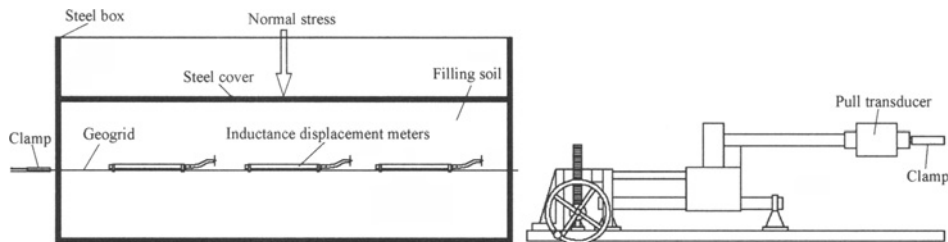


Figure 1. Schematic view of pullout device

The other part is strain-controlled horizontal pulling device, which is connected with geogrids by special clamp that avoid relative slide between geogrids and clamp during pulling out. Additionally a layer of rubber is placed between them to prevent clamp from damaging geogrids. Pullout force can be directly gotten by a high sensitive transducer.

Test method

Pullout test is carried out in a strain-controlled manner. The silt with optimum water content is used. Both upper and lower soil of geogrids is 15cm thickness, and the degree of compaction is 95%. In order to ensure unchangeable friction area during test, 1250mm length geogrids are adopted (1000mm length is embedded in soil, 250mm length is for reservation). According to optimum pullout velocity range 6~10mm/min, a displacement rate of 7.5 mm/min was adopted for the testing program conducted in this study. Geogrids embedded in soil have three whole longitudinal ribs. Inductance displacement meters are fixed on the midpoint of each longitudinal ribs to obtain relative displacement and strain, located at 26.7cm (survey point 1), 50cm (survey point 2), 73.3cm (survey point 3). Normal stress applied on the filling soil are 4kPa, 13kPa and 23kPa respectively.

TEST RESULTS AND ANYSIS

It is generally considered that interfacial frictional resistance will come into being when relative displacement occurs between geosynthetics and soils. Base on ultimate strength theory of reinforced structure, interfacial friction shear strength can be expressed by Coulomb law

$$\tau_f = c_{sg} + p_n \tan \varphi_{sg} \quad (1)$$

where τ_f is interfacial friction shear strength; c_{sg} is interfacial Cohesion; p_n is normal stress to synthetics surface; φ_{sg} is interfacial friction angle

The effect of normal stress

Under normal stress of 4kPa, 13kPa and 23kPa, three group pullout tests of geogrids, EG90, buried in soil sample A are conducted. The relative displacement and shear displacement between soil and geogrids are plotted in Figure 2.

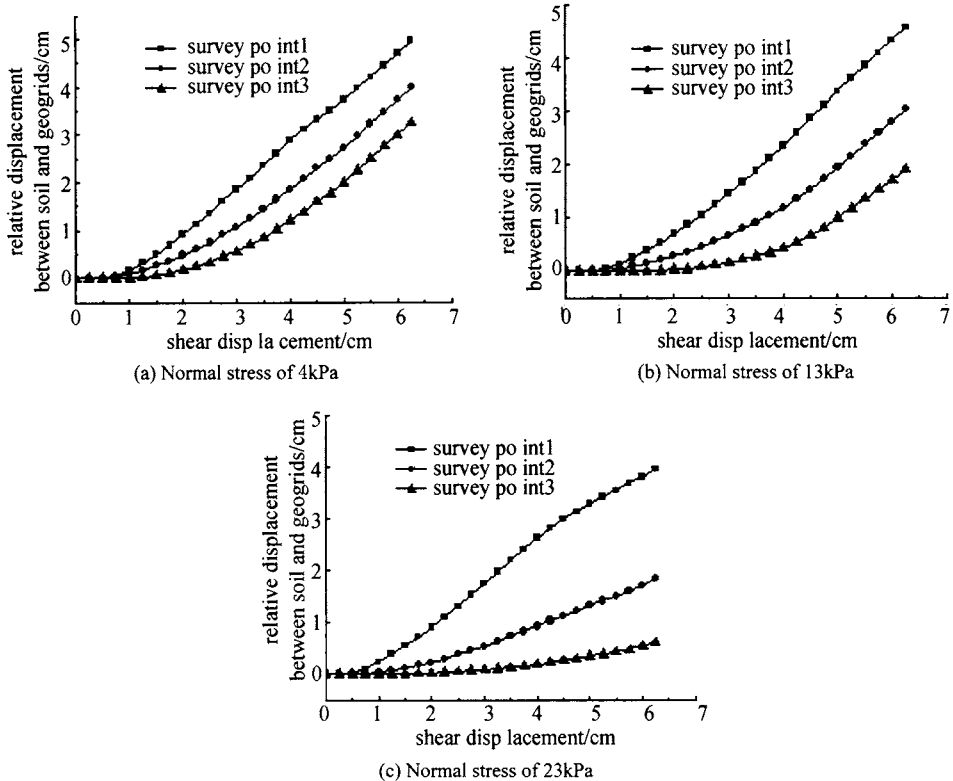


Figure 2. Relationship between relative displacement and shear displacement under the different normal stress

Survey points 1, 2 and 3 respectively monitor the relative displacement of the front, the middle and the end of geogrids (Figure 1). It can be seen from Figure 2 that the large relative displacements between the three parts of geogrids and soil have occurred for normal stress of 4kPa. The displacement curves of three survey points are almost parallel when shear displacement is greater than 2cm, which indicates the whole geogrids in soil are nearly pulled out at a constant speed, and pullout resistance of geogrids reaches to maximum steady value.

The datum recorded by transducer on pullout device show that when shear displacement is beyond 3.75cm, the stable maximum of pullout resistance of geogrids is 3.29kN, 42.2% of tensile strength of geogrids of type EG50, which illuminates that the geogrids have not sufficiently exert their function of reinforcement.

When normal stress increases to 13kPa and 23kPa respectively, survey point 1 in the front of geogrids firstly produce larger relative displacement, and with the process of pullout test going on, survey point 2 and 3 produce relative displacement in turn. It's clear that shear stress is gradually transferred along geogrids longitudinal ribs. When normal stress is 13kPa and shear displacement reaches to 5cm, the slide of whole geogrids in soils again occurs, here the maximum stable pullout resistance increase to 4.19kN that is 53.7% of tensile strength. When normal stress is 23kPa and shear displacement reaches to 6.25cm, the maximum stable pullout resistance is 5kN that is 64.1% of tensile strength.

The above test results illuminate that interfacial friction resistance increases with the normal stress p_n when filling soil and other conditions are unchanged in geogrids-reinforced earth structure. And due to the smaller interfacial friction angle between silt and geogrids about 19° , about 52kPa normal stress is still needed if reinforcement strength of geogrids is to be entirely exerted. In practical engineering, the method of increasing normal stress on soil not only enhances the cost of construction but also is difficult to implement. So it is significant to mix large size rubbles into silt for improvement of passive resistance developing against the front of transverse ribs while the method of increasing normal stress is adopted to improve interfacial shearing resistance of geogrids.

The effect of rubble content

The apertures of geogrids can not perform its lock ability to silt. Accordingly, to increase the bonding each other, the method of mixing rubbles with 1-3cm particle size into silt is used. Four group pullout tests in different soil sample of A, B,C and D are conducted.

In tests, it is found that the strength of the geogrids EG50 is comparatively low, so that yielding often occurs when pullout forces do not still reach to the maximum. Therefore, in the following pullout test in mixed soil geogrids with type EG50 are replaced by type EG90.

The pullout forces obtained in the tests corresponding to different shear displacements are taken into Equation (2)

$$2LB\tau - T_d = 0 \quad (2)$$

where τ is shear stress, kPa; T_d is pullout force, kN; L is the length of geogrids buried in the soil, m; B is the width of geogrids buried in the soil, m.

In terms of Equation (2), shear stress τ corresponding to T_d is calculated, and the value of τ rises with shear displacement. Ultimate shear stress is taken as interfacial friction shear strength, so τ_f can be obtained under three different normal stress p_n . Subsequently the shearing strength lines can be fitted by several points (p_n, τ_f) for four kinds of soil samples, as shown in Figure 3.

From the fitting lines shown in Figure 3, the interfacial cohesion and interfacial friction angle can be obtained and listed in Table 3. By comparing the results obtained before adding rubble and after, it is found that the cohesion between geogrids and soil do not change obviously, while interfacial friction angle is enhanced greatly by increasing the rubble. It is concluded that the method of adding rubble into silt to improve the friction shear strength of geogrids-reinforced earth structures is effective.

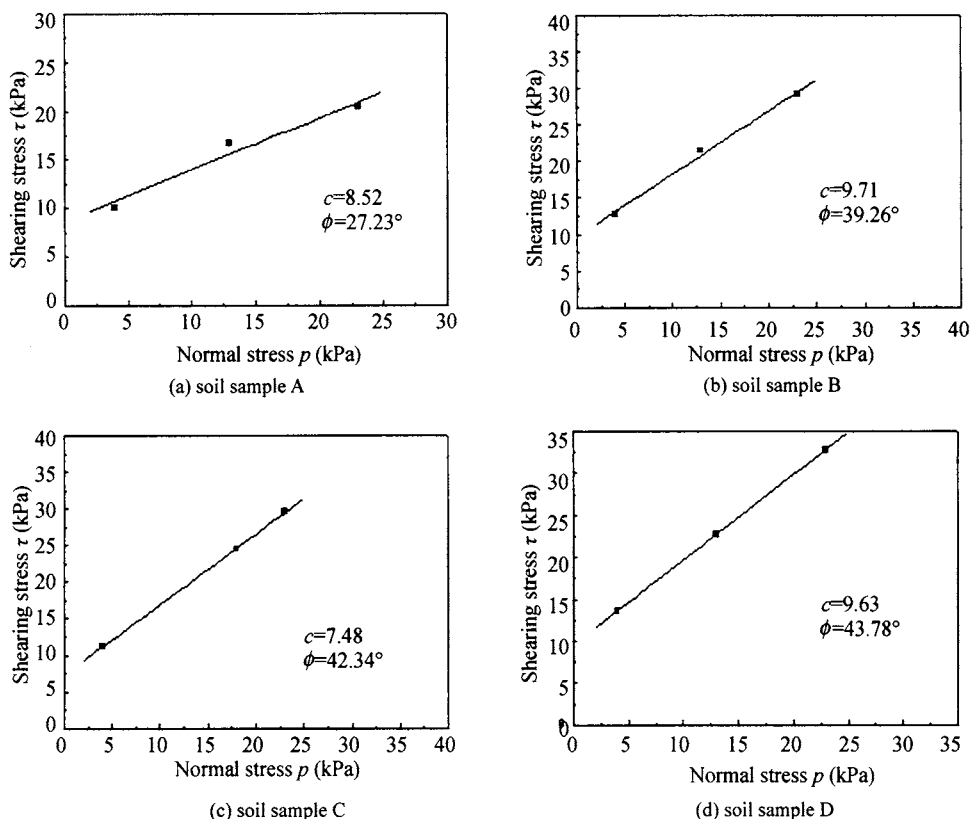


Figure 3. Shear strength envelopes for different content of rubble

Table 3. The interfacial frictional angle and cohesion

Soil sample	Geogrids type	Interfacial cohesion c_{sg} (kPa)	Interfacial friction angle ϕ_{sg} ($^\circ$)
A	EG90	8.50	27.23
B	EG90	9.71	39.26
C	EG90	7.48	42.34
D	EG90	9.63	43.78

Interfacial friction coefficient

It is common to define $\tan \phi_{sg}$ as interfacial friction coefficient f_{sg} between geosynthetics and filling soil. If there is not enough data at hand, the coefficient f_{sg} is usually determined by experiential formula. So f_{sg} is approximately equal to $2\tan\phi/3$ for geotextile and $0.8\tan\phi$ for geogrids, here ϕ is friction angle of filling soil. Through large-scale direct shear test, angle of internal friction ϕ of four kinds of soil sample used in the test can be gotten. It is observed from Table 4 that test results of the coefficient are 1.37-3.10 times magnitude of experiential results. The experiential formula, $0.8\tan\phi$, is not suitable to the soil mixed rubble any more. In the study, the interfacial friction coefficients obtained from the test are almost in the range of 0.8-1.0 suggested in literature.

Table 4. The experiential data and the testing data of the interfacial frictional coefficient

rubble content	angle of internal friction, φ (°)	$0.8\tan\varphi$	$\tan\varphi_{sg}$
0%	16.85	0.2423	0.5146
10%	18.24	0.2636	0.8173
20%	23.91	0.3547	0.9112
30%	31.27	0.4858	0.9583

The interfacial friction coefficient f_{sg} is correlative with the kind of Geosynthetics, filling soils type and angle of internal friction. In soil mixing rubble, the content of rubble is most effect factor to angle of internal friction. So only considering the change of rubble content, the relationship between friction coefficient f_{sg} and rubble content x is fitted using the test results of four kinds of soil sample, experimental formula seen as Equation (3) and curve drawn as Figure 4.

$$f_{sg} = 1 - \exp(-0.098x - 0.7) \quad (3)$$

where x is rubble content ranges from 0 to 100 (%).

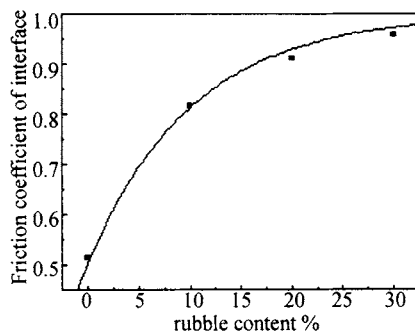


Figure 4. Effect of the rubble content on interfacial frictional coefficient

It can be shown in figure 4 that with increasing the rubble content, the interfacial friction coefficient is enhanced but gradually to steady value. So it is very necessary to choose the reasonable content according to practical engineering.

CONCLUSIONS

A series of pullout tests to investigate the effect of normal stress and rubble content on interfacial resistance behavior of geogrids in silt mixing rubble are conducted. By analyzing experimental datum, some conclusions were made:

(1) When silt is selected as filling soil, increasing the normal stress can promote the interfacial shearing stress. Due to small interfacial friction angle between soil and geogrids, the reinforce effect is not obvious by taking this method.

(2) With increasing the content of rubble mixed in silt to 10%, 20%, 30%, the pullout force of geogrids has been obviously enhanced. The rubble is an important factor to enhance reinforcement of the transverse ribs of geogrids.

(3) By analyzing experimental datum of pullout test, a relationship curve between the rubble content and interfacial friction coefficient is obtained. Based on the curve, an experimental formula is also fitted. The curve trend indicates that increasing the content of rubble initially can obviously enhance the interfacial friction coefficient, but in the end the effect gradually becomes small. So it is necessary for geogrids-reinforced earth structures to choose suitable rubble content.

In geogrids-reinforced earth structures, the choice of reasonable normal stress and rubble content dependent on practical engineering can improve the reinforced capability of geogrids in soil. The study presented here is of referring value for design and construction of geogrids-reinforced earth structure.

ACKNOWLEDGEMENT

The financial support for this study through the grant 50678032 from National Natural Science Foundation of China is mostly grateful.

REFERENCES

- Koerner R.M., Wayne M.H. and Carroll R.G. (1989). Analytic behavior of geogrid anchorage, *Proceedings Geosynthetics'89 Conference*, San Diego, 525-536.
- Jwell R.A. (1996). *Soil reinforcement with geotextiles*, Ciria Special Publication.
- Sidnei H.C., Benedito S. B., Jorge G Z. (2007). Pullout resistance of individual longitudinal and transverse geogrid ribs. *Journal of geotechnical and geoenvironmental engineering*. 133(1): 37-50
- Bergado D.T., Shivashankar R., Alfaro M.C., Chai J.C., et al. (1993). Interaction behavior of steel grid reinforcements in clayey sand, *Geotechnique*, 43 (4): 589-603.
- Geotechnical composite material technical application manual compile committee. (1994). *Geotechnical Composite Material Technical Application Manual*, China Architecture and Building Press.
- Yang G. L., Wang Y. H. (2000). Study on pullout test of geosynthetics, *Journal of China Coal Society*, 25 (1): 51-54.
- Wang Z. (2005). *Geosynthetics*, China Machine Press.
- Sun J, Chi J. K., Cao Z. K. (1998). *New Geomaterial and Harnessing Engineering Hazards*, China Architecture and Building Press.

THREE-DIMENSIONAL FEM ANALYSIS ON MECHANICAL CHARACTERISTICS OF DEPING METRO STATION FOUNDATION PIT DURING PROJECT EXCAVATION

Youliang Chen

Department of Civil Engineering, University of Shanghai for Science and Technology, Shanghai 200093, China

Lebin Yang, Jingxue Liu

Department of Civil Engineering, Shanghai University, Shanghai, 200072, China

Rafiq Azzam

Department of Engineering Geology and Hydrogeology, RWTH Aachen University

Controlling the displacements of foundation pit walls and supporting structures is one of the most effective measures for ensuring safety of foundation pit construction. In this paper, the three-dimensional displacement field of Deping Station foundation pit, which is part of Shanghai Track Traffic Line 6 project, is computed by means of finite element method (FEM) and ANSYS software. Firstly, the element types and constitutive equations are selected. Secondly, the displacements and internal forces of supporting structures and soil medium are computed and the final computed results are analyzed. Finally, the sensitivity of computed results to dimensional variation of supporting structures and value variation of soil parameters is analyzed. The research result of current paper is very helpful for geotechnical construction and the development of geotechnical theory.

INTRODUCTION

Since more than one decade the designing and constructing techniques of foundation pits have been greatly improved, especially the design philosophies and ideas. With the rapid growth of urban population and the lack of building land, more and more superhigh buildings and city track traffic lines are built in some densely populated cities, for example, Shanghai, Beijing, Hong Kong and Tokyo. And many buildings and track traffic lines must be constructed in very complicated environments, for instance, some municipal pipes and wires are situated closely around the construction site. Under these circumstances, the design philosophies and ideas of foundation pits must be adjusted in order to fit in with the complicated environments.

PROJECT BACKGROUND

Deping Station of Shanghai Track Traffic Line 6 project is located on the west side of Zhangyang Road. The main supporting structure of Deping station foundation pit is

continuous underground walls. The consolidated depth is 4.0 m. The main project dimensions are listed in Table 1 and shown in Figure 1. And the distribution of soil formations is shown in Figure 2.

Table 1. The main project dimensions (Dimension unit: m)

The total length of Deping station	135
The breadth of normal section	16.2
The breadth of facility section	18.4
The breadth of end pit section	19.2
The depth of foundation pit at the end pit section	15
The depth of foundation pit at the normal section	13
The thickness of continuous underground walls	0.6
The depth of continuous underground walls at the end pit section	27
The depth of continuous underground walls at the normal section	24
The depth of piles into soil layers	20

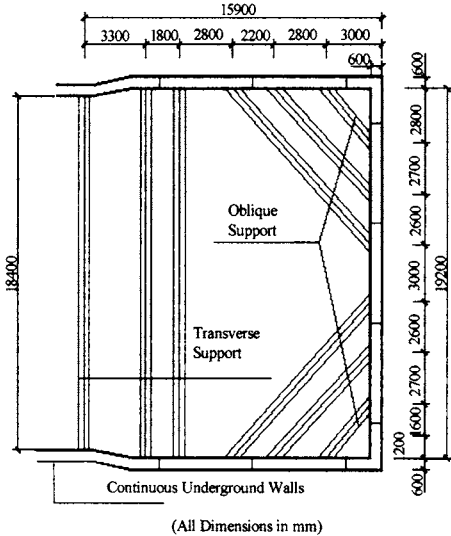


Figure 1. The planar graph for support of end pit section

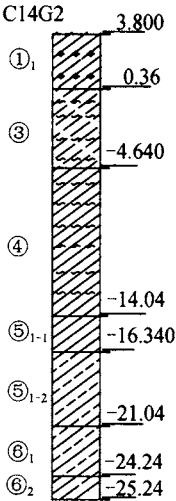


Figure 2. The histogram of soil formation distribution

CONSTITUTIVE EQUATION OF SOIL

In this paper, the nonlinear elastic-plastic Drucker-Prager model is adopted to compute stress field and displacement field, and its yield condition is the extended Von Mises criterion.

The formula of effective stress σ_e is

$$\sigma_e = 3\beta\sigma_m + \left[|s|^T [M] \{s\} / 2 \right]^{\frac{1}{2}} \tag{1}$$

in which σ_m is normal stress or hydrostatic pressure stress, $\{s\}$ is deviator stress. β is material parameter and can be obtained by formula (2). $[M]$ is given by Equation (3).

$$\beta = \frac{2 \sin \phi}{\sqrt{3}(3 - \sin \phi)} \quad (2)$$

$$[M] = \begin{bmatrix} 1 & 0 & 0 & 0 & 0 & 0 \\ 0 & 1 & 0 & 0 & 0 & 0 \\ 0 & 0 & 1 & 0 & 0 & 0 \\ 0 & 0 & 0 & 2 & 0 & 0 \\ 0 & 0 & 0 & 0 & 2 & 0 \\ 0 & 0 & 0 & 0 & 0 & 2 \end{bmatrix} \quad (3)$$

In Formula (2), ϕ is the angle of internal friction.

In the extended Von Mises criterion, the influence of hydrostatic pressure stress is considered. The yield strength will go up with the increase of hydrostatic pressure stress. The Formula of yield strength and the yielding criterion is:

$$\sigma_y = \frac{6C \cos \phi}{\sqrt{3}(3 - \sin \phi)} \quad (4)$$

$$F = 3\beta\sigma_m + \left[\{s\}^T [M] \{s\} / 2 \right]^{\frac{1}{2}} - \sigma = 0 \quad (5)$$

Where C is the cohesion intercept and ϕ is the angle of internal friction.

CHOICE OF CONTACT SURFACE ELEMENTS BETWEEN CONTINUOUS UNDERGROUD WALL AND SOIL MEDIUM

In this paper, Goodman (Goodman *RE*, Shi G Block, 1985) shell contact element is adopted to compute the contact surface between continuous underground walls and soil medium. On the contact surface, the relation between stress and relative displacement is

$$\begin{Bmatrix} \sigma \\ \tau \end{Bmatrix} = \begin{bmatrix} k_n & 0 \\ 0 & k_s \end{bmatrix} \begin{Bmatrix} \omega_n \\ \omega_s \end{Bmatrix} \quad (6)$$

where ω_n and ω_s are the normal and tangential relative displacements, respectively, σ and τ are the normal and shear stresses. k_n and k_s are the normal and shear stiffness coefficients.

SELECTION OF ELEMENT TYPES AND CONSTITUTIVE EQUATIONS FOR SOIL

In this paper, 8-node three-dimensional solid element and Druck-prager ideal elastic-plastic model are adopted to study the soil medium. 4-node plate element is employed to simulate the walls. Bar element is adopted to imitate the internal steel bar supports. The finite element mesh is shown in Figures 3-4.

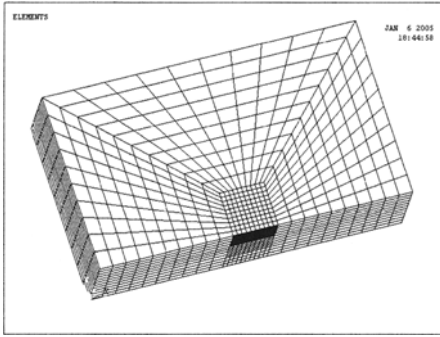


Figure 3. The finite element mesh of soil medium

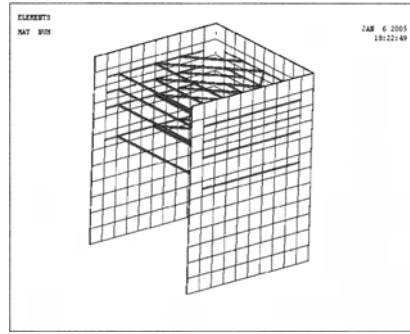


Figure 4. The finite element mesh of walls and bar supports

BASIC SOIL PARAMETERS

The physical parameters of all correlative soil formations are listed in Table 2.

The deformation modulus formula is

$$E_0 = \frac{pb(1-\mu^2)}{s} \omega \quad (7)$$

where E_0 is deformation modulus. b is the width of rectangular pressure-bearing plate. μ is Poisson ratio. p and s are the pressure stress and precipitation value corresponding to the proportional limit of p (pressure stress)- s (precipitation value) curve. ω is equal to 0.88 for rectangular plate or 0.79 for circular plate.

Table 2. The physical parameters of all correlative soil layers

Serial number of soil layers	① ₁	③	④	⑤ ₁₋₁	⑤ ₁₋₂	⑥ ₁
Type of soil	Back fill	Silty clay	Silty clay	Grey clay	Grey clay	Grey clay
Deformation modulus (kPa)		2920	210	3960	4430	6490
Poisson ratio		0.37	0.33	0.35	0.35	0.36
Cohesion intercept (kPa)		15	11	3	13	32
Angle of internal friction (°)		15	24	23	21.5	21.5

THE PROCESS OF THREE-DIMENSIONAL COMPUTATION

In the current paper, the computation model is a cuboid of 115m×40m×30m. Based on previous experience, 25 are taken as the ideal number of iteration times.

The simulation for the process of foundation pit digging and supporting is as follows.

- (1) Computing the initial stress field $\{\sigma\}_0$ caused by gravity pressure of soil;
- (2) Computing the stress increment $\{\Delta\sigma\}_1$ and displacement increment $\{\Delta\delta\}_1$ produced by first step foundation pit digging. After having finished first step foundation pit digging, the stress field and displacement field are turned into

$$\{\sigma\}_i = \{\sigma\}_0 + \{\Delta\sigma\}_i \quad (8)$$

$$\{\delta\}_i = \{\delta\}_0 + \{\Delta\delta\}_i \quad (9)$$

where $\{\delta\}_0$ take zero;

(3) Testing if the soil medium has turned into yield state;

(4) Repeating (2) and (3) until the foundation pit digging and supporting structure construction have been finished.

The final stress and displacement fields are

$$\{\sigma\}_i = \{\sigma\}_0 + \sum \{\Delta\sigma\}_i \quad (10)$$

$$\{\delta\}_i = \{\delta\}_0 + \sum \{\Delta\delta\}_i \quad (11)$$

SOME OF COMPUTED RESULTS

The final deformation of continuous underground walls is shown in Figure 5. And the surface settlement around the foundation pit is shown in Figure 6.

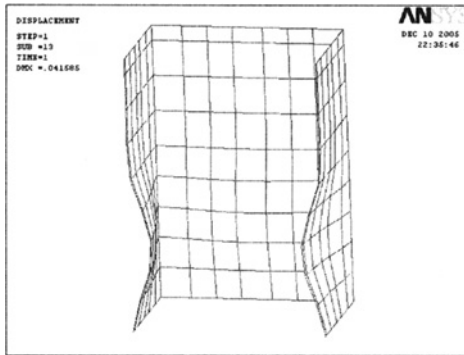


Figure 5. The final deformation of continuous the underground walls (enlarged 50 times)

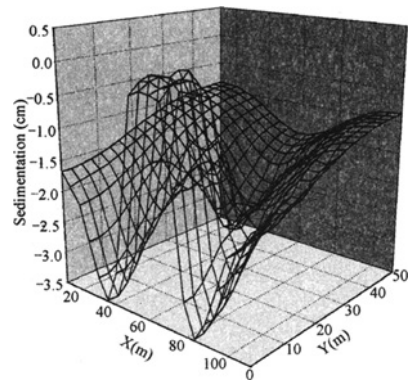


Figure 6. The surface settlement around foundation pit

According to the computation result, the maximum settlement arises in two points, namely (34, 0) and (86, 0), which are symmetric to the longitudinal centre section of the foundation pit, and the maximum settlement value is 3.48cm.

The final deformation of soil medium in horizontal plane is shown in Figures 7–8.

The sensitivity of wall deformation to the section area of internal steel bar supports is shown in Figure 9. And the depth-horizontal displacement curves of the center vertical line of the transversal wall corresponding to different thickness are shown in Figure 10.

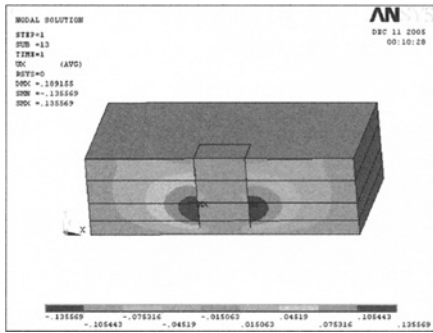


Figure 7. The deformation of soil medium medium in x-axis direction

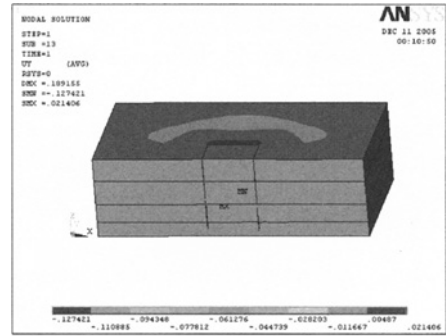


Figure 8. The deformation of soil in y-axis direction

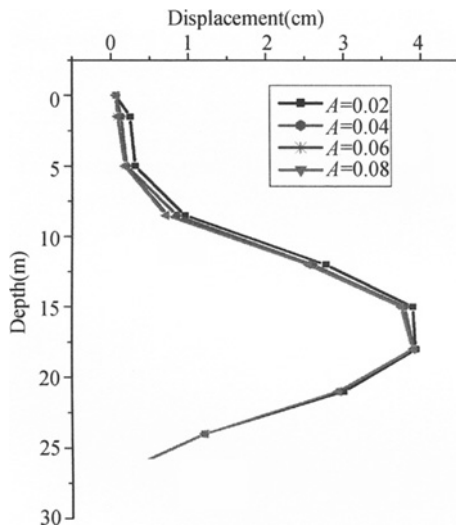


Figure 9. The sensitivity analysis of wall curves deformation to the section area of transversal internal steel bar supports

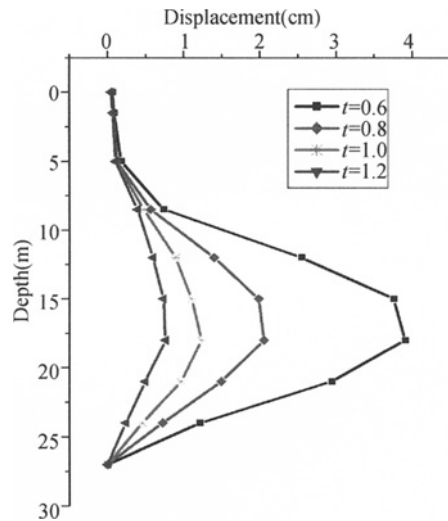


Figure 10. The depth-displacement of the center vertical line of the wall corresponding to different wall thickness

CONCLUSIONS

Following conclusions could be summarized from the study of current paper.

- (1) The horizontal displacement of the continuous underground wall increases with the increase of the excavation depth, and the location moves down.
- (2) During the foundation pit excavation, the soil moves from outsides to foundation pit bottom and leads to the surface subsidence outside the foundation pit and the swelling of the foundation pit bottom. Adequate measures should be taken to prevent it.
- (3) The section area of internal steel bar supports doesn't influence the horizontal displacement of continuous underground walls very greatly. In contrast, the influence of underground wall thickness and soil deformation modulus is much more apparent.

(4) The decrease amplitude of maximum horizontal displacement of continuous underground walls becomes smaller with the increase of wall thickness. According to the author's research, the influence would be very slight after the thickness exceeds some specific value. Selecting an appropriate wall thickness is very important.

(5) The traditional FEM method and intelligent technique should be closely integrated for better solving geotechnical problems. This is also part of the author's further works.

REFERENCES

- Goodman R. E., Shi G. (1985) Block Theory and Its Applications to Rock Engineering. *Englewood Cliffs: Prentice-Hall*.
- Leung C. F., Ong Del and Chow Y. K. (2006) Pile Behavior Due to Excavation-Induced Soil Movement in Clay II: *Collapsed Wall*, ASCE, 132(1): 45-53.
- Liu Guobin, Charles W. W. Ng and Wang Z. W. (2005). Observed Performance of a Deep Multistrutted Excavation in Shanghai Soft Clays, *Journal of Geotechnical and Geoenvironmental Engineering*, ASCE, 131(8): 1004-1013.
- Panigrahi D. C., Sahu H. B. (2004). Classification of coal seams with respect to their spontaneous heating susceptibility—a neural network approach, *Geotechnical and Geological Engineering*, 22(4): 457-476.
- Sonmez H., Gokceoglu C. and Ulusay R. (2004). A mamdani fuzzy inference system for the geological strength index (gsi) and its use in slope stability assessments, *International Journal of Rock Mechanics and Mining Science*, 41(3): 513-514.
- Zdravkovic L., Potts D. M. and S.T. John H. D. (2005). Modelling of a 3D excavation in finite element analysis, *Geotechnique*, 55: 497-513.

THE UNDERWATER DETECTION OF SCOUR AND ANALYSIS OF STABILITY OF BRIDGE PIERS

Ligang Fang, Jiatao Kang and Guangxiu Qu
*School of Civil Engineering and Architecture, Central South University,
No. 22 Shao Shan Road Changsha, 410075, China*

Scour is one of the major causes for bridge failure. To prevent this type of failure, it is necessary to detect the scour degree of abutment foundation on existing bridges. As an effective method to estimate scour, the underwater detection technology has been used to estimate the scour degree of abutment foundation of the Zishui bridge of Xiangqian railway in China. And a program was written with MATLAB for the analysis of the effect of scoured area on the piers' stability. On the basis of the analysis, the relationship between the horizontal displacement of pier's top and scoured area was found out with the help of least squares method. The results showed that, compared with other check-calculation items, the horizontal displacement of pier's top and the eccentric distance firstly reached their limit values when a less scour happened.

INTRODUCTION

The Zishui Bridge located on Xiangqian railway was designed and constructed with four-span (15m each span) continuous steel truss beam, all the piers and bridge abutments were built in 1937 and still in use now. During the period of resuming construction of the new and old line of Hunan from 1958 to 1960, the bridge was resumed and constructed, and installed No.1 and No.5 piers. Due to the demand of navigable fairway, the top of existed pier had been heightened for 2.45m. The crack of wing walls of two abutments was serious, and the crack also existed in abutment, therefore, it was needed for removing and reconstruction on safety considerations of the bridge. So we need to do underwater detection and to estimate the bridge's scour stability.

UNDERWATER DETECTION OF SCOUR

Because this bridge has been used for a long time, the design and construction information about this bridge construction is incomplete, at the same time its abutment foundations are also required to be detected to verify some concrete data. Therefore, in order to detect the foundation' concrete conditions of scour, based on the methods of underwater detection being used at present (LIANG Kai, et al., 2006), the method that the divers perform underwater tracing and picture photography was proceeded.

The maximum water depth of foundation base is at the No.4 pier site, its entire foundation base was flooded by water and pier body was also affected partly, this site is main navigation

channel now. And, there is the rapigest current of water, the muddiest water quality, and comparatively deep water depth in the No.4 pier site by observation, so its scour situation should be the most serious. In order to verify its foundation form and to measure and grasp scour situation, we should carry on careful underwater detection.

From Figure 1 we can find that the foundation concrete at upstream face was scoured and destroyed, even caused defect place on water face, and the foundation base was scoured seriously, even caused pore space.

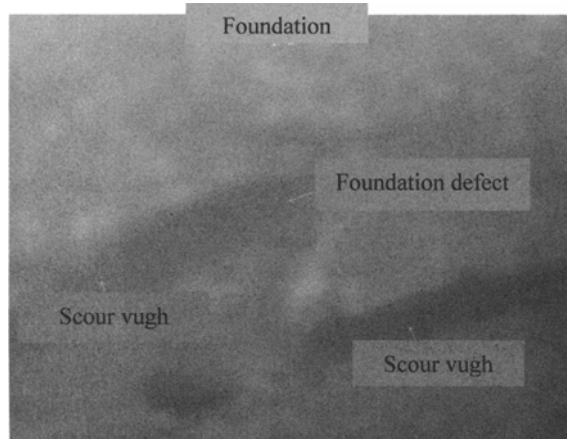


Figure 1. Underwater photo on water face of the foundation of No.4 pier

The results of the detection showed all the upstream face and some downstream face surface have serious scouring vugh, and the concrete of the foundation itself has also revealed the defect, though there was still 1.90m embedding depth in some place of the No.4 pier foundation.

ANALYSIS OF IMPACT OF SCOUR ON THE PIER STABILITY

The effect of various scour degree on the pier's check items, including, stability coefficient against overturning, compression stress of foundation base and eccentric distance, were analyzed and calculated (K. Jyothi, et al., 2002; Er,Shri Ram CHAURASIA, et al., 2002). The analysis process adopts the form of from point to line, and the points' fitting curve is made by the least square method. The result's form is simple and intuitional.

Effect of scour on horizontal displacement of the piers' top

Horizontal displacement of the pier's top is composed of two parts, one part is caused by the pier's flexural deformation Δ_1 , and the other part, i.e. Δ_2 , is caused by the foundation soil differential settlement. The total displacement of the piers' top is the sum of the two, i.e. $\Delta = \Delta_1 + \Delta_2$. Because this is a straight bridge, we need only check the horizontal displacement of pier's top in axial direction.

The settlements of each corner point under eccentric load are calculated by the program written by MatLab, and the pier's angle of rotation, from which horizontal displacement of

the pier's top caused by differential settlement is obtained, is computed from differential settlement of the points.

The expression of influence curves of scour on horizontal displacement of the piers' top is obtained using least squares method:

$$u = (2.3258x^4 - 2.5986x^3 + 0.7835x^2 + 0.0507x + 0.0027) \times 10^3 \quad (1)$$

where x is washout area percentage of total area of the foundation, u is corresponding horizontal displacement of the pier's top.

The three piers' influence curves are shown in Figure 2. Their allowable values of horizontal displacement of the pier's top are 27.2mm, 8.9mm and 27.2mm respectively, and the corresponding limit washout area percentage of total area of the foundation is 20.7, 32.9 and 17.8, according to the Fundamental Code for Design on Railway Bridge and Culvert of China. The No.2 and No.4 piers' limit washout area percentage of total area of the foundation all are around 20, and No.3 pier' is about 33 because the horizontal displacement of No.3 pier's top has a greater allowable values. So, in general, the horizontal displacement of the pier's top is effect by scour seriously, and we should control the scour in time so that the pier is in safety.

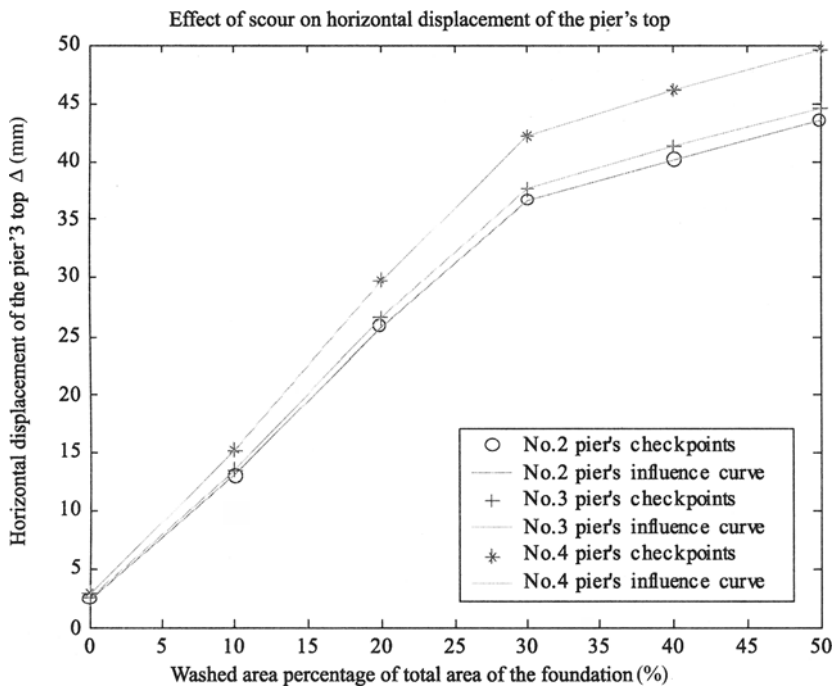


Figure 2. Effect of scour on horizontal displacement of the pier's top

Effect of scour on stability against overturning of the piers

Considering that some bearing capacity still exists after the bridge foundation was partly washed out, but pier stability of overturning resistance is harmed (Er, Shri Ram Chaurasia, et

al., 2002 ;Dag Myrhaug, Havard Rue, 2003). In order to study the effect of different scour area on stability, the washed area of arc was supposed, and then the most dangerous form by calculating all stability coefficients of overturning resistance of different overturning forms was determined (B. Mutlu Sumer, et al., 2005; Subhasish Dey, et al., 2006). The washed area's shape of the foundation is assumed as triangle, and then the least stability coefficients of overturning resistance under various scour degree, from which the influence curve of scour on the coefficient is found by least squares method, are calculated (Subhasish Dey, et al., 2006). The expression of influence curve of scour on the piers' stability coefficients of overturning resistance k is obtained by least squares method as follows:

$$k = -10.4102x + 5.2051 \quad (2)$$

The three piers' influence curves are shown in Figure 3 and their corresponding limit washed area percentage of total area of the foundation is 35.4, 35.6 and 35.7 determined by the Fundamental Code for Design on Railway Bridge and Culvert of China. The three piers' limit washed area percentages are all more than 35, which show that the stability coefficient of overturning resistance is affected by scour not so seriously.

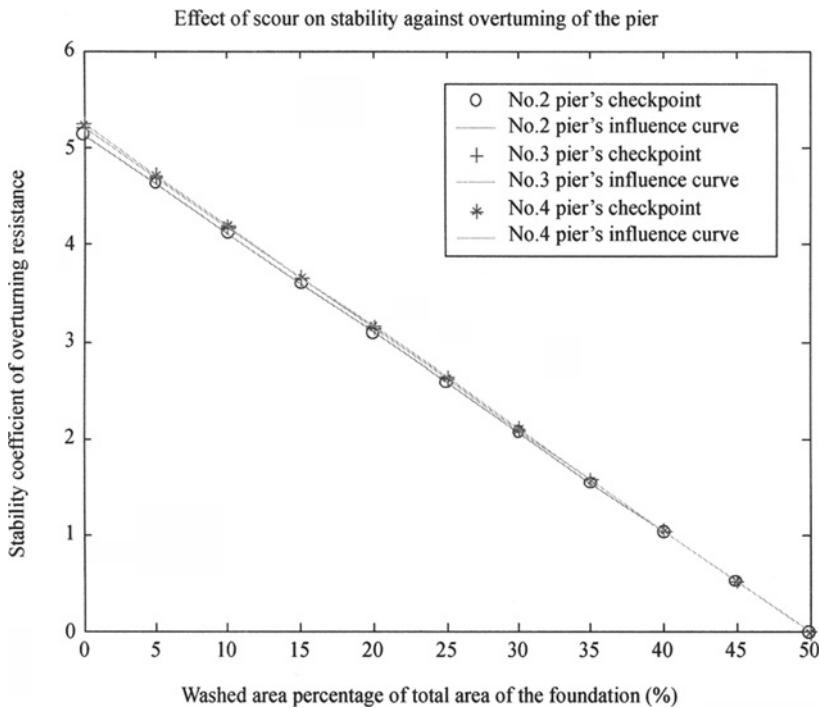


Figure 3. Effect of scour on the pier's stability coefficient of overturning resistance

Effect of scour on compression stress of foundation base and eccentric distance of piers

As the scour is becoming worse, the washed area losses the bearing capability and leads to the neutral axis's movement, which causes the redistribution of stress. The expression of

influence curve of scour on the three piers' maximum compression stress of foundation base σ_{\max} is obtained by least squares method as follows:

$$\sigma_{\max} = (2.9040x^2 + 2.3345x + 0.3955) \times 10^3 \quad (3)$$

The three piers' influence curves are shown in Figure 4 and their corresponding limit washed area percentage of total area of the foundation is 26.0, 24.8 and 25.3 according to the code. Scour reduces the size of the foundation base and causes eccentric pressure, resulting maximum compression stress of foundation base increased with the increasing erosion. The three piers' limit washed area percentages are all about 25, so the effect of scour on compressive stress is significant.

The scouring will lead the change of neutral axis position. This change causes the vertical axial force arising and the eccentric distance increasing. The expression of influence curve of scour on the piers eccentric distance e is as follows:

$$e = -3.1539x^2 + 4.0229x + 0.6649 \quad (4)$$

The scouring effect on eccentric distance is most obvious, as showed in Figure 5. Their corresponding limit washed area percentage of total area of the foundation is 14.3, 14.5 and 14.7 according to the Fundamental Code for Design on Railway Bridge and Culvert of China. The three limit percentages are all less than 15, the scour impacts pier's stability seriously. So the washed pier should be paid much more attention to have its eccentric distance checked.

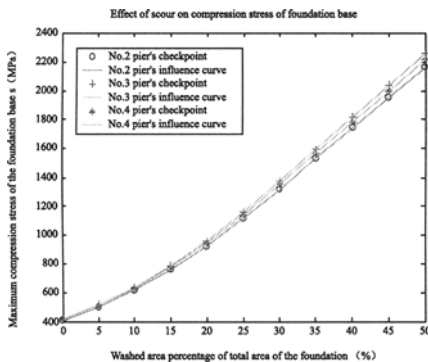


Figure 4. Effect of scour on the pier's maximum compression stress of foundation base

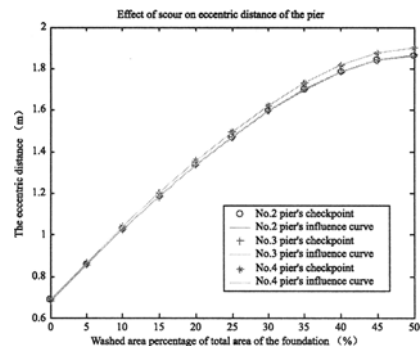


Figure 5. Effect of scour on the pier's eccentric distance

CONCLUSIONS

The results of the analysis of scour's effect on the pier showed that the flexibility horizontal displacement of pier's top and the eccentric distance, compared with other check computation items, firstly reached their allowable values when a less scour happened. It also showed that the limit washed area percentage of the total area with respect to allowable value was basically less than 20. The washed area percentage of the total area, with respect to the allowable value of No.2, No.3 and No.4 piers' eccentric distance, is 14.3, 14.5 and 14.7 respectively; the washed area percentage of the total area, with respect to the allowable value of No.2 and No.4 piers' displacement, is 20.7 and 17.8 respectively; the allowable of No.3

pier's displacement is bigger and its corresponding percentage is 32.9. So the proper disposals should be taken to deal with the piers' foundation, with the two items are control conditions, according to the real scour situations detected by various methods.

Also the result is similar to the result of the finite element analysis (Liang Kai et al., 2006), and the result of the finite element analysis is less conservative than the theoretical calculation result. The finite element analysis showed that the foundation would be failed when scoured area reached 20% of pier foundation.

REFERENCES

- B. Mutlu Sumer, Jørgen Fredsøe, Alberto Lamberti, Barbara Zanuttigh, Martin Dixen, Kjartan Gislason and Antonio F. Di Penta. (2005). Local scour at roundhead and along the trunk of low crested structures, *Coastal Engineering*, 52 (10-11):995-1025.
- Dag Myrhaug, Havard Rue. (2005). Scour around group of slender vertical piles in random waves, *Applied Ocean Research*, 27 (1): 56-63.
- Er,Shri Ram Chaurasia and Pande B.B.LAL. (2002). Local Scour Around Bridge Abutments, *International Journal of Sediment Research*, 17 (1): 48-74.
- K. Jyothi, J.S. Mani and M.R. Pranesh. (2002). Numerical modeling of flow around coastal structures and scour prediction, *Ocean Engineering*, 29 (4): 417-444.
- Liang Kai, Fang Ligang and Duan Liangliang. (2006). Finite element analysis of influence of scour on stability of piers, *Rock and Soil Mechanics*, 27 (9): 1643-1645.
- Subhasish Dey, Abdul Karim Barbhuiya. (2006). Velocity and turbulence in a scour hole at a vertical-wall abutment, *Flow Measurement and Instrumentation*, 17 (1): 13-21.

RIGOROUS NUMERICAL ANALYSIS OF CYLINDRICAL CAVITY EXPANSION IN SANDS BASED ON SMP CRITERION

Dongxue Hao

*School of Civil and Hydraulic Engineering University Department, Dalian University of
Technology, Dalian 116085, China*

Maotian Luan, Rong Chen

*State Key Laboratory of Coastal and Offshore Engineering, Dalian University of
Technology, Dalian 116085, China*
*Institute of Geotechnical Engineering, School of Civil and Hydraulic Engineering, Dalian
University of Technology, Dalian 116085, China*

Considering the effect of intermediate principal stress on material strength, spatial mobilization plane (SMP) theory is applied. Rowe flow rule and stress-dilatancy relationship simplified by Bolton combining the similar numerical process as described by Salgado et al. (2001) are used to analyze the cylindrical cavity expansion. By a series of comparison, the effects of intermediate principal stress, soil initial state and critical friction angle on limit pressure, plastic radius, and void ratio are examined. The results indicate that the intermediate principal stress will play an important role in the cavity expansion behavior including limit cavity pressure, plastic radius and dilatancy surrounding the cavity; the solution based on Mohr-Coulomb criterion is often conservative.

INTRODUCTION

The cavity expansion theory provides a surprisingly versatile and accurate geomechanics approach for analysis of geotechnical problems such as cone penetration tests, the bearing capacity of deep foundations, pile driving, and interpretations of pressuremeter tests. Published solutions of cavity expansion vary mainly because of differences in constitutive models. For dilatant softening soils, there are some simplified stress-strain and strains relation model (Wang et al., 2007) to be used to obtain analytical solution of cavity expansion. However, the dilatancy and friction angles in plastic zone are assumed to be constant. Salgado et al., (2001) subdivided the plastic zone in cylindrical shells and let friction and dilatancy angles within each shell vary as a function of soil stress state and relative density following the Bolton model or state parameter model. Although in their study rigorous numerical analysis of cavity expansion was given, it adopted classical Mohr-Coulomb criterion based on single-shear theory of strength which ignores the effects of intermediate principal stress on cavity expansion. While the spatial mobilization plane (SMP) theory proposed by Matsuoka et al., (1995) takes account for the effect of the intermediate principal stress. Moreover, the theory can be simplified in the plane strain

condition and is convenient to be applied in practical engineering. Therefore, in this paper, SMP yielding criterion, Rowe flow rule (Rowe, 1962) and Bolton model (Bolton, 1986) combining the similar numerical process as that described by Salgado et al., (2001) are used to analyze the cylindrical cavity expansion.

THE SMP THEORY IN THE PLAIN STRAIN CONDITION

The common tangent of two Mohr' circles at failure for cohesiveless soil in the plane strain condition passes through the origin of coordinate in the τ - σ plane according to the SMP criterion. In the plane strain condition, the principal stress components in cohesiveless soil satisfy the equation (Stake, 1976), $\sigma_2 = \sqrt{\sigma_1 \sigma_3}$.

Compressive stresses and strains are taken as positive. The stress components ($\sigma_r, \sigma_z, \sigma_\theta$) in the soil around the cavity are all principal stresses, and satisfy the inequalities $\sigma_\theta \leq \sigma_z \leq \sigma_r$. Therefore, in terms of $\sigma_2 = \sqrt{\sigma_1 \sigma_3}$, the yielding function of SMP criterion for common cohesiveless soils in the plane strain condition (Luo et al., 2000) is

$$\sigma_r / \sigma_\theta = 1/4 \cdot \left\{ \sqrt{8 \tan^2 \phi_{TC} + 9} + \sqrt{8 \tan^2 \phi_{TC} + 6 - 2\sqrt{8 \tan^2 \phi_{TC} + 9}} - 1 \right\}^2 = R_{ps} \quad (1)$$

where R_{ps} is the ratio of maximum and minimum principal stresses at failure; ϕ_{TC} is friction angle under triaxial compression.

The coefficient of intermediate principal stress is not zero, which is correlated to corresponding friction angle in plane strain failure condition (Luan et al., 2004).

CAVITY EXPANSION ANALYSIS

Problem definition

An unbounded three-dimensional continuous medium of dilatant and compressible soil contains a single cylindrical cavity. Initially the radius of cavity is zero (cavity creation problem) or r_0 (cavity expansion problem) and a hydrostatic pressure p_0 acts throughout the soil, which is assumed to be homogenous, isotropic. The pressure inside the cavity is then monotonically increased to p sufficiently slowly so that dynamic effects are negligible. For cylindrical cavity expansion, plane strain conditions are in place.

Discretization method is used for cavity expansion analysis of plastic zone. Plastic zone is divided into many thin shells, the inner and outer radii of element i are denoted by r_i, r_j respectively, as illustrated in Figure 1. The one-dimensional nature of the cavity expansion problem is such that elements at different radii all pass successively through the same stress-strain state. Conversely, the pressure-expansion response can be recovered from the conditions at progressively decreasing radii around an expanding cavity. The equilibrium equation and large strain definitions for a cylindrical cavity problem can be expressed as follows

$$d\sigma_r / dr + (\sigma_r - \sigma_\theta) / r = 0 \quad (2)$$

$$\varepsilon_r = -\ln(dr/dr_0) = -\ln\left\{ (r_j - r_i) / [(r_j - u_j) - (r_i - u_i)] \right\} \quad (3)$$

$$\varepsilon_\theta = -\ln[r_i/(r_i - u_i)] \quad (4)$$

$$\varepsilon_v = -\ln(v/v_0) = -\ln\left\{\frac{(r_j^2 - r_i^2)}{[(r_j - u_j)^2 - (r_i - u_i)^2]}\right\} \quad (5)$$

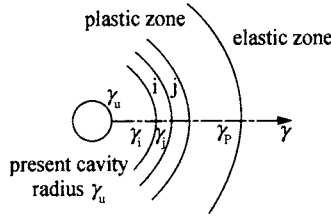


Figure 1. Representation of cylindrical cavity expansion model

Stress response in plastic zone

In all cavity expansion/creation problems, combination of the SMP yield criterion of cohesionless soils $\sigma_r = R_{(i)}\sigma_\theta$ with equilibrium equation yields

$$\sigma_r = \sigma_r \left(r_j / r_i \right)^{\frac{R_{(i)} - 1}{R_{(i)}}} \quad (6)$$

where σ_r is radial normal stress around the expanding cavity; $R_{(i)}$ is flow number of element i , $R_{(i)} = 1/4 \cdot \left[\sqrt{8 \tan^2 \phi_{(i)} + 9} + \sqrt{8 \tan^2 \phi_{(i)} + 6 - 2 \sqrt{8 \tan^2 \phi_{(i)} + 9}} - 1 \right]^2$, $\phi_{(i)}$ is friction angle of element i .

Stress dilatancy relationship and Rowe (1962) flow rule

The friction angle is assumed to vary according to Bolton model (Bolton, 1986).

$$\phi_{(i)} = \phi_c + D_\psi \left\{ I_{D,(i)} \left[Q + \ln \left(P_A / 100 p_{(i)} \right) \right] - R_Q \right\} \quad (7)$$

Where ϕ_c is critical state friction angle; $D_\psi = 5$ for plane strain tests; $I_{D,(i)}$ is relative density as a number between 0 and 1 within the thin shell i ; Q , R_Q is fitting parameters that depend on the sand characteristic. P_A is reference stress and assumed to be 100kPa. $p_{(i)}$ is mean effective stress within the element i , and for plane strain, $p_{(i)}$ is given by the following equation

$$p_{(i)} = 1/3 \cdot \left(1 + 1/R_{(i)} + \sqrt{1/R_{(i)}} \right) \sigma_{r(i)} \quad (8)$$

where $\sigma_{r(i)}$ is the mean of σ_{r_i} and σ_{r_j} .

Stress-dilatancy relation aims at describing the relationship between the friction and dilatation angles. Here $\phi = \phi_c + 0.8\psi$ proposed by Bolton (1986) is assumed to hold.

According to Rowe (1962) flow rule, the relationship between two normal plastic strain increments and dilatancy angle is $\sin \psi_{(i)} = -(\varepsilon_v^{(i)} - \varepsilon_v^{(j)}) / [(\varepsilon_r^{(i)} - \varepsilon_r^{(j)}) - (\varepsilon_\theta^{(i)} - \varepsilon_\theta^{(j)})]$. Where

$\varepsilon_v^{(i)}$, $\varepsilon_r^{(i)}$, $\varepsilon_\theta^{(i)}$, $\varepsilon_v^{(j)}$, $\varepsilon_r^{(j)}$, $\varepsilon_\theta^{(j)}$ represent volume strains, radial strains and hoop strains of element i and j respectively. $\Psi_{(i)}$ is dilatancy angle of element i .

Strain and displacement analyses in plastic zone

At the elasto-plastic interface, the stress and strain tensor components are expressed as a function of peak flow number R_p , initial lateral stress p_0 and equivalent linear elastic shearing modulus G that is determined referring to Salgado et al., 1997. The form of the stress and strain tensor components are the same as Equation. (18) to Equation. (22) in Salgado et al., (2001), only in place of peak flow number N_p with R_p . Here R_p is calculated from the peak friction angle ϕ_p though Equation. (1). And ϕ_p is obtained from Equation. (7) with $p_{(i)}$ from σ_r and σ_θ . Iteration is required to be obtained ϕ_p and R_p .

Rowe flow rule (Rowe, 1962) results in the relationship of volumetric strains and two normal strain components of two adjacent elements, which contains unknown dilatancy angle and displacement of inner radii if strain and displacement of outer radii have been known. Detail Equations refer to Equations (14) to (17) in Salgado et al., (2001). By combining the stress equations of plastic zone, Bolton model to describe the dependence of friction angle on stress state and the relationship of friction angle and dilatancy angle, iterations are made from elasto-plastic interface by assumption of initial dilatancy angle until the limit condition $u_i=r_i$ is satisfied for created cylindrical expansion or $u_i=r_i-r_0$ for cavity expansion. Iteration progress is similar to Salgado et al. (2001), the difference from it is that flow number N_{ij} is replaced by $R_{(i)}$ and that Equation. (8) is adopted to calculate of $p_{(i)}$. In that way dilatancy angle and radial displacement of all thin elements can be obtained, further strains of all elements can be computed.

RESULTS

Based on the above analysis, numerical iteration for the process of created cylindrical cavity expansion is carried. 500 spaced increments are used to obtain an accurate result. The parameters of Ottawa sand (Salgado et al., 2001) used are as follows: $g_r=0.68$, $C_g=612$, $e_g=2.17$, $n_g=0.44$, $Q=9$, $R_Q=0.49$, $e_{min}=0.48$, $e_{max}=0.78$, $\nu=0.15$

Effect of critical state friction angle and initial state

Normalized plastic radius r_p/r_u at limit condition differs slightly for $\phi_c = 30^\circ, 33^\circ, 36^\circ$, accordingly Figure 2 shows values for $\phi_c = 30^\circ$ only, which can be used within the 30° to 36° range without significant loss of accuracy. It can be seen that r_p/r_u will increase with relative density and decrease with initial lateral stress. The change of void ratios with cavity pressure for different initial states during cylindrical cavity expansion is plotted in Figure 3 And cylindrical cavity expansion curves for various initial soil states are plotted in Figure 4 They indicate that the lower initial lateral stress and the higher relative density will induce the greater dilatancy at limit condition and that the greater initial lateral stress and relative density will result in the stiffer response. It is shown From Figure 5 that limit pressure increases with lateral stress and relative density, but at a decreasing rate. The greater critical state friction angle will produce the greater limit pressure for same initial

soil state. The value of limit pressure for the case $p_0=300\text{kPa}$, $D_r=0.8$ and $\phi_c = 30^\circ$ is respectively lower 10% and 19.5% than those for the case $\phi_c = 33^\circ, 36^\circ$.

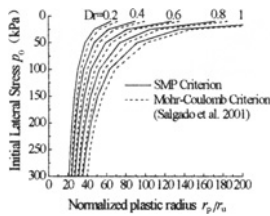


Figure 2. Normalized plastic radius at limit condition as a function of initial soil states

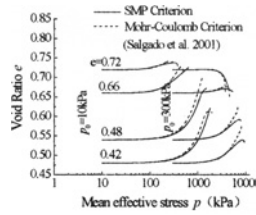


Figure 3. Mean effective stress vs. void ratio paths for $\phi_c = 30^\circ$

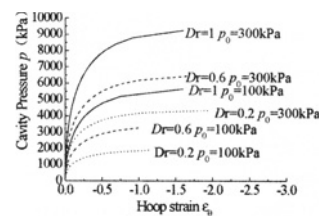
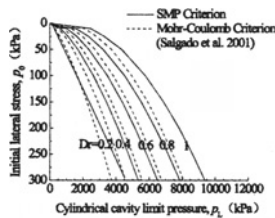
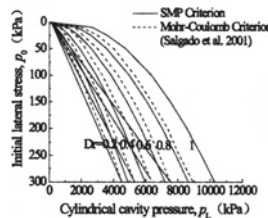


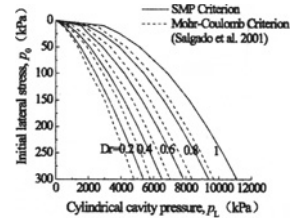
Figure 4. Cylindrical cavity expansion for various initial soil states and $\phi_c = 30^\circ$



(a) $\phi_c = 30^\circ$



(b) $\phi_c = 33^\circ$



(c) $\phi_c = 36^\circ$

Figure 5. Cylindrical cavity limit pressure as a function of soil state

Comparative studies

It is clear from figure 2 that radii of plastic zone computed based on SMP yield criterion is smaller than those based on Mohr-Coulomb yield criterion for cylindrical cavity expansion in Ottawa sand with same initial state. Compared with the result based on Mohr-Coulomb criterion, plastic radius will decrease by 9% for $p_0=200\text{kPa}$ and $D_r=1$. Figure 3 demonstrates that the change of void ratios based on Mohr-Coulomb criterion is greater than those based on SMP criterion, i.e. soil dilatancy or contraction surrounding cavity will be less obvious by considering the effects of intermediate principal stress on material yielding. Figure 5 illustrates the relationships of limit pressure and soil initial state for three critical state friction angles. Direct estimate and comparison can be made from Figure 5. It can be perceptible that limit pressures increase for the same soil state considering the effect of intermediate principal stress. Limit pressures will increase by about 17% for the case $\phi_c = 30^\circ$, $p_0=300\text{kPa}$, and $D_r=0.2-1$.

CONCLUSIONS

Consideration is given to effects of intermediate principal stress, the angles of friction and dilatation dependent on stress and relative density during cylindrical cavity expansion. A

comparative study is made for present results and Salgado et al. (2001)'s results based on Mohr-Coulomb criterion. It is concluded (1) the ratio of plastic to cavity radius at the limit condition is observed to increase with higher density and lower stress. Limit pressures increase with lateral stress, density and critical state friction angle. (2) The radius of plastic zone is greatly decreased, the limit pressure is greatly increased, and soil dilatancy or contraction becomes inhibited, if the effect of intermediated principal stress is taken into account. And the solution disregarding the effect is often conservative. Therefore, consideration of the effect is economical and meaningful for geotechnical engineering such as prediction of pile bearing capability and the research presented here can provide theoretical basis for interpretation and application of some in-situ tests.

ACKNOWLEDGEMENTS

The financial support for this study through the grant 50579006 and 50639010 from National Natural Science Foundation of China is mostly grateful.

REFERENCES

- Bolton M. D. (1986). The Strength and dilatancy of sands, *Geotechnique*, 36 (1): 65-78.
- Luan M. T., Xu, C. S., Liu Z. G. et al. (2004). Study of shear strength parameters of soils under general stress conditions, *J Dalian Univ technol*, 44 (2): 271-276.
- Luo T., Yao, Y. P. and Matsuoka, H. (2000). Soil strength equation in plane strain based on SMP, *Rock and Soil Mechanics*, 21 (4): 390-393.
- Matsuoka H., Sun, D. A. (1995). Extension of spatially mobilization plane to friction and cohesive materials and its application to cemented sands, *Soils and foundations*, 35 (4): 63-72.
- Rowe P. (1962). The stress-dilatancy relation for static equilibrium of an assembly of particles in contact, *Proceedings of the Royal Society*, 269 (1339): 500-527.
- Salgado R., Mitchel, J. K. and Jamiolkowski, M. (1997). Cavity expansion and penetration resistance in sand, *Journal of Geotechnical and Geoenvironmental Engineering*, 23 (8): 726-735.
- Salgado R. and Randolph, M. F. (2001). Analysis of cavity expansion in sand, *The International Journal of Geomechanics*, 1 (2): 175-192.
- Stake M. (1976). Stress-deformation and strength characteristics of soils under three difference principal stresses, *Proc of Japan Soc of Civil Eng*, 246: 137-138.
- Wang P. CH., Liu G. B. and Zhu X. R. (2007). Solution to cylindrical cavities expansion in elastoplastic-brittle materials considering large strain, *Rock and Soil Mechanics*, 28 (3): 587-592.

STUDY ON DETERMINATION OF ROCK MASS QUALITY PARAMETER m , s VALUE AND IMPACT OF IT TO ROCK MASS STRENGTH

Hailang Hu, Qiufeng Huang and Jianlin Li

*China Three Gorges University Key Laboratory of Geological Hazards on Three Gorges
Reservoir Area, Ministry of Education, Yichang 443002, China*

Based on the research works of the predecessors the author firstly induced and sum up some methods of determining rock mass quality parameter m , s value. And the author had the study on impact of the rock mass quality parameter m , s value to rock mass strength, while it combining with the high slope rock mass of Three Gorges Project permanent navigation lock of Yangtse River. Then got the change patterns about not only m , s value to Hoek-Brown strength envelope curve, but also m , s value to instantaneous internal friction angle ϕ . And it has some application value and reference value for studying the impact of rock mass quality parameter to rock mass strength.

FOREWORD

The rock mass quality parameters m , s value are determined by rock characteristics and the damage degree before it reaching the maximum main stress σ_1 and the minimum main stress σ_3 (Li Jianlin, 2003). The m , s value as the important parameters of describing rock mass characteristics, the values have quite big randomness. Just like professor Liao Guohua said, "We can't directly determine the experienced parameter m , s value exactly." Therefore, m , s value right or wrong, not only takes quite error with using the Hoek-Brown strength criterion, but also influencing the accurate judgment for the engineering security. The author has studied the determination of rock material parameters m , s value and their influence to the rock mass strength in this paper.

METHOD FOR DETERMINATION OF m , s VALUE

Looking up the table to estimate m , s value

When E.Hoek came up with the Hoek-Brown strength criterion in 1980, on the basis of triaxial experimental data of different kinds of rock mass, he got the experienced parameter m , s value through summing up the data. He then modified the values in 1988, and gave the modified m , s values. The modified m , s values are acquired combining the practical experience based on the results achieved in 1980. And they had been used widely in the engineering field at home and abroad (E.Hoek and E.T.Brown, 1988).

Using rock triaxial experiment to determine m, s value

For the integrate rock block, usually assuming $s=1$, then calculates to get the m value and rock compressive strength σ_c (Zhou Hanmin.2006) according to the data. Assuming $x=\sigma_3$, $y=\sigma_1-\sigma_3$, then,

$$\sigma_c = \sqrt{\frac{\sum Y}{n} - \frac{\sum X}{n} \left[\frac{\sum XY - \frac{1}{n} \sum X \sum Y}{\sum X^2 - \frac{1}{n} (\sum X)^2} \right]} \quad (1)$$

$$m = \frac{1}{\sigma_c} \left[\frac{\sum XY - \frac{1}{n} \sum X \sum Y}{\sum X^2 - \frac{1}{n} (\sum X)^2} \right] \quad (2)$$

In the formulas, n is the number of groups, and the number is usually more than five.

$$s = \frac{\frac{1}{n} \sum Y - \frac{1}{n} m \sigma_c \sum X}{\sigma_c^2} \quad (3)$$

If the calculated s value is less than zero, then should assume $s=0$, for showing it is the damaged rock mass. And the calculating formula of correlation coefficient ρ^2 is as follows.

$$\rho^2 = \frac{\left[\sum X_i Y_i - \frac{1}{n} \sum X_i \sum Y_i \right]^2}{\left[\sum X_i^2 - \frac{1}{n} (\sum X_i)^2 \right] \left[\sum Y_i^2 - \frac{1}{n} (\sum Y_i)^2 \right]} \quad (4)$$

The more correlation coefficient ρ^2 closed to one, the more fitting functions between experienced equations and experimental data.

Determine m, s value based on the rock mass classification index RMR and the evaluating Q index

CSIR classification method was brought up by Bieniawski in 1974. Priest and Brown combined the RMR index with the m, s value firstly in 1983. And pointed out the direct statistical relationship between them. In 1988, E.Hoek modified the experienced equations brought up by Priest and Brown. And he got the widely used RMR index evaluating experienced parameter m, s value formulas on the stage (Zhou Hanmin.2006; Ha Qiuling et al., 1998)

i) For the disturbed rock mass,

$$\frac{m}{m_i} = \exp\left(\frac{\text{RMR} - 100}{14}\right) \quad (5)$$

$$s = \exp\left(\frac{\text{RMR} - 100}{6}\right) \quad (6)$$

ii) For the undisturbed rock mass,

$$\frac{m}{m_i} = \exp\left(\frac{RMR-100}{28}\right) \quad (7)$$

$$s = \exp\left(\frac{RMR-100}{9}\right) \quad (8)$$

In the equations, m , s are the material parameters of rock mass.

E.Hoek found that Formula (5) to Formula (8) are suitable when RMR is more than 25 (Li Jianlin, 1999). But Formula (5) to Formula (8) are quite different from m , s value when RMR is less than 25. Therefore, Hoek introduced a new index GSI (Geological Strength Index) to determine the m , s value. The relationship between GSI and m , s value is as follows.

$$\frac{m}{m_i} = e^{\left(\frac{GSI-100}{28}\right)} \quad (9)$$

when GSI is more than 25 (for undisturbed rock mass),

$$s = e^{\left(\frac{GSI-100}{9}\right)} \quad (10)$$

when GSI is less than 25 (for undisturbed rock mass),

$$s = 0.5 \quad (11)$$

The relationship between GEI and RMR above is as follows.

When GSI is more than 23,

$$GSI = RMR - 5 \quad (12)$$

When GSI is less than 23, we can't use RMR to evaluate the GSI. But we can use Q' advised by Lein and Lunde to calculate the GSI. And the Q' is the modified Q .

$$Q' = \frac{RQD}{J_n} \times \frac{J_\phi}{J_c} \quad (13)$$

$$GSI = 9 \log Q' + 44 \quad (14)$$

In the formulas, RQD is the rock core quality index. J_ϕ is the value of joint roughness. J_n is the number of joint set. J_c is the joint alteration value.

Direct shear and big shear experiment statistics to determine the m , s value

Direct shear and big shear experiment are the important manner to determine the shear strength of rock mass at the engineering scene. The experimental results calculate through direct shear and big shear experiment are quite approach the real strength of rock mass.

Method of determining m , s value advised by E. Hoek is that a group of $\sigma - \tau$ samples measured with direct shear and big shear experiment. Then we can get the equations are as follows.

$$\sigma_1 = \sigma + \tau \frac{1 - \cos(90 + \phi_i)}{\sin(90 + \phi_i)} \quad (i=1,2,3) \quad (15)$$

$$\sigma_3 = \sigma + \frac{\tau}{\sigma} \left[\tau - \sigma_c - \sqrt{\sigma^2 + (\tau - \sigma_c)^2} \right] \quad (16)$$

$$c_s = \frac{1}{n} \sum \sigma - \frac{\sum \tau}{n} \bullet \frac{\sum \tau \sigma - \frac{1}{n} \sum \sigma \sum \tau}{\sum \tau^2 - \frac{1}{n} (\sum \tau)^2} \quad (17)$$

In the equations, c_s is the intercept of cohesion in the τ - σ coordinate system. With the method referred to above, we can acquire the m and σ_c value.

Determine m, s value with the rock mass classification index RMI

RMI (Rock Mass Index) is a new rock mass classification index referred to by Norway researcher Doctor Palmstrom in 1996. And it is based on lots of analysis and back analysis of site experiment. It took the structural plane parameters as variables. He reduced the rock uniaxial compressive strength to reflect the strength characteristics of rock mass. And the specific formula is as follows.

$$RMI = \sigma_c \bullet JP \quad (18)$$

In the formula, σ_c is the rock uniaxial compressive strength (MPa). And it can be measured through the rock sample that the diameter of which is 50mm. JP is the structural plane parameter. And it reflects the weakening effect of rock mass volume cut by structural plane, structural plane frictional characteristic and scale to the rock strength. The value changes between zero and one. For the integrity rock block, the value is one. But for the damaged rock mass, the value is zero.

Using the sound wave testing technology estimation to determine m, s value

The sound wave testing technology is a new technology developed during the 30 years. It mainly using the sound wave speed and attenuation coefficient after ultrasonic penetrating the soil and rock media, to know the physical mechanic property, structural plane characteristic and weathering degree of soil and rock material. Comparing with the static method, this method has some advantages such as convenience, shortcut, economy and non-breakage. Now it is successfully used to measure the dynamic elastic parameters of soil and rock mass and simple rock mass structural model parameters. And it also can be used to evaluate the rock mass quality. Therefore, it is took as a importance widely by geotechnical engineering circle and geology engineering circle at home and abroad.

IMPACT OF ROCK MASS QUALITY PARAMETER m, s VALUE TO ROCK MASS STRENGTH

The m, s are both dimensionless parameters. Their significations within the Hoek-Brown experienced strength criterion are similar with the cohesion c and internal friction angle ϕ within the Mohr-Coulomb strength criterion. Combining with the research results made by E.Hoek in 1983, it elaborates the contribution of the experienced parameter m, s value to

rock mass strength through showing the impact of them to the shape of Hoek-Brown strength envelope curve and instantaneous internal friction angle ϕ_i (Zhou Hanmin, 2006).

Impact of parameter m to the rock mass strength

Based on E.Hoek assuming the uniaxial compressive strength of rock block σ_c and the experienced parameter s are the unit value, it divided six kind of situations such as $m=3$, $m=5$, $m=7$, $m=10$, $m=15$ and $m=25$. On the basis of formulas in reference 6, it drew the Hoek-Brown strength envelope curve in the same σ - τ cartesian coordinate system, and the diagram is in the Figure 1(a). It also drew the relationship curve between instantaneous internal friction angle ϕ_i and different main stress level σ in the same ϕ_i - σ cartesian coordinate system. And the diagram is in the Figure 1(b). The σ is main stress of potential failure surface. But in the Figure 1(a), the intercept of the ordinate of certain tangent of a point on the Hoek-Brown strength envelope curve is the instantaneous cohesion c_i corresponding to the main stress level σ .

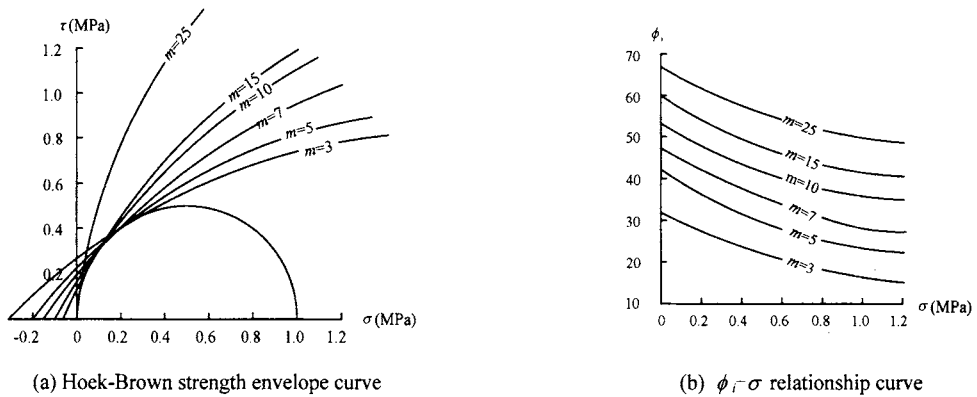


Figure 1. Influence of the value of the constant m on the Hoek-Brown failure envelope and on the instantaneous friction angle at different normal stress levels

From the diagrams above, at the range of $m=0.0000001$ —25, the regulations of Hoek-Brown strength envelope curve, σ - τ relationship curve and rock mass strength to the experienced parameter m are as follows.

(1) Hoek-Brown strength envelope curve becomes steep increasingly with m increasing. And they combine with each other near to the rock mass uniaxial compressive strength. But the regulation of instantaneous cohesion c_i and instantaneous shear strength τ with the experienced parameter m is different both between compression stressed zone and tension stress zone.

1) In the compression zone, for the same main stress level, when is bigger, and τ is also bigger. But the uniaxial compressive strength σ_c of rock mass keeps invariant. It is only related to the uniaxial compressive strength σ_c of rock block and experienced parameter s.

2) In the tension zone, the intersection point between Hoek-Brown strength envelope curve and the negative direction of abscissa σ is the uniaxial tensile strength σ_t of rock mass. And it reduces with the m increasing. When the maximum m is 25, the uniaxial tensile strength σ_t is minimum value such as zero.

3) At the main stress level $\sigma = 0$, the intercept of Hoek-Brown strength envelope curve on the ordinate τ is the instantaneous cohesion c_i . It reduces with m increasing. But when the maximum m is 25, $c_i = 0$.

(2) According to the relationship curve between the instantaneous internal friction angle ϕ_i and main stress level σ , for a certain m value, the instantaneous internal friction angle ϕ_i increases with the m increasing. When the maximum m is 25, that is the $\phi_i - \sigma$ curve becomes steep with the m increasing. But when σ reaching a certain value, $\phi_i - \sigma$ curve has the trend of converging increasingly.

Impact of parameter s to the rock mass strength

Based on E.Hoek assuming the uniaxial compressive strength of rock block σ_c and the experienced parameter m are the unit value in 1983, it divided three kind of situations such as $s=0$, $s=0.5$ and $s=1.0$. On the basis of formulas in reference 6, it drew the Hoek-Brown strength envelope curve in the same $\sigma - \tau$ cartesian coordinate system, and the diagram is in the Figure 2(a). It also drew the relationship curve between instantaneous internal friction angle ϕ_i and different main stress level σ in the same $\phi_i - \sigma$ cartesian coordinate system. And the diagram is in the Figure 2(b). The $s=0$ expresses that joint rock mass is damaged completely. The $s=1.0$ expresses that integrity rock mass with no structural plane.

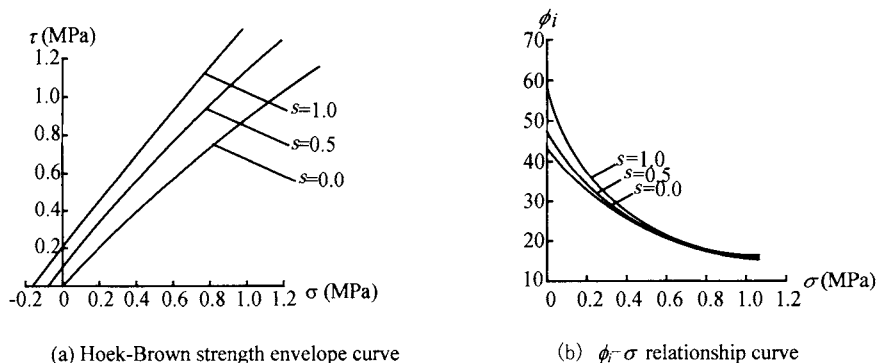


Figure 2. Influence of the value of the constant s on the Hoek-Brwon failure envelope and on the instantaneous friction angle at different normal stress levels

From the diagrams above, at the range of $s=0-1$, the regulations of Hoek-Brown strength envelope curve, $\phi_i - \sigma$ relationship curve and rock mass strength to the experienced parameter s are as follows.

(1) The value of experienced parameter s has no impact to the steep and smooth degree of Hoek-Brown strength envelope curve. Three curves are nearly parallel with each other. But the curve position rises with s increasing. The intercept on the ordinate τ also increases. It shows that instantaneous cohesion c_i of rock mass and instantaneous shear strength τ rise increasingly with the parameter s increasing just at the same main stress level.

(2) The uniaxial tensile strength σ_t of rock mass is related to the experienced parameter s . And it increases with the parameter s increasing. When $s=0$, it shows that the rock mass is damaged completely. The σ_t reaches the minimum value that is $\sigma_t = 0$. When $s=1$, it shows

that rock mass is integrated. Then σ_1 reaches the maximum value when there is no structural plane.

(3) The relationship between instantaneous internal friction angle ϕ_i and experienced parameter s is similar to the parameter m basically. The bigger parameter s is, the steeper $\phi_i - \sigma$ is. That is to say, for the same main stress level σ , the instantaneous internal friction angle ϕ_i rises increasingly with the experienced parameter s increasing. But when σ reaches a certain value, some $s - \phi_i$ relationship curves on the basis of different s values, will converge as a tuft. And it makes the ϕ_i be a fixed value, ϕ_i doesn't change with σ any more.

CONCLUSIONS

The rock mass mechanics characteristics are influenced by some factors such as their structural features and the environmental characteristic they locating. We use rock mass quality evaluation to describe the quality of rock mass. But taking the rock mass quality parameters m , s value as the important parameters of describing rock mass characteristic shouldn't be neglected. Therefore, the author induced and sum up some methods of determining rock mass quality parameter m , s value based on the research works of the predecessors. And the author had the study on impact of the rock mass quality parameter m , s value to rock mass strength, while it combining with the high slope rock mass of Three Gorges Project permanent navigation lock of Yangtse River. Then got the change patterns about not only m , s value to Hoek-Brown strength envelope curve, but also m , s value to instantaneous internal friction angle ϕ_i .

ACKNOWLEDGEMENTS

The research has been supported in part by National Natural Science Foundation of P.R.China (No.50379023), The Higher School Imburse Project of Excellent Mid-youth Science and Technology Group Plan of Hubei Province of P.R.China(Education Science, Hubei[2004] No. 7).

REFERENCES

- Li Jianlin. (2003). *Unloading Rock Mass Mechanics*, Beijing: Water Resource and Hydropower Press of China, (in Chinese), 31-32.
- E.Hoek and E.T.Brown.(1988). The Hoek — Brown failure criterion-a1988 update, *Proc.15th Canadian Rock Mechanics Symposium*, in press.
- Zhou Hanmin.(2006). Reliability of Hoek-Brown Strength criterion of Rock mass and it's Application to Engineering, *China University of Geosciences*, Beijing. A dissertation Submitted to China University of Geosciences for Master. May, 18-20.
- Ha Qiuling, Li Jianlin, Zhang Yongxing.(1998) *The Non-linear Rock Mass Mechanics of Jointed Unloading Rock Mass*, Beijing:China Architecture Industry Publishing Company. 140-141.
- Li Jianlin(1999). *Theory and Application of Unloading Rock Mass Mechanics*, Beijing: China Architecture Industry Publishing Company, 61-63.
- E.Hoek and D.Wood.(1992) A modified Hoek-Brown failure criterion for jointed rock massed, *Proc.Int. Conf., Eurock' 92*, Chest, England, 208-216.

A COMPARATIVE STUDY ON MONOTONIC SHEAR BEHAVIORS OF GRANULAR SOILS UNDER DIFFERENT DRAINAGE CONDITIONS

Maotian Luan

*State Key Laboratory of Coastal and Offshore Engineering,
Dalian University of Technology, Dalian 116024, China*

Yi Leng

*Institute of Geotechnical Engineering, School of Civil and Hydraulic
Engineering, Dalian University of Technology, Dalian 116024, China*

Various stress-controlled drained and undrained monotonic shear tests on the Chinese Fujian standard sand of relative density 30% under complex initial consolidation conditions with different stress paths are conducted by using the soil static and dynamic universal triaxial and torsional shear apparatus. The mean principal stress is controlled unchanged in the process of tests. The coefficient of intermediate principal stress and orientation of principal stress are varied so that their influences on shear behavior and strength of saturated sand under different drainage conditions are respectively explored. It is shown through comparison that coefficient of intermediate principal stress influences the stress-strain normalization relationship, but does not make obvious effect on volumetric deformation as well as pore-water pressure. Under the same initial condition, the deviator stress ratio reduces with increase of coefficient of intermediate principal stress. The above-mentioned phenomena do not relate to the drainage condition. Orientation of principal stress also influences remarkably on monotonic shear features of sand. In drained tests, variation pattern of stress-strain relationship which is associated with the orientation of principal stress depends on shear stresses on horizontal plane and vertical plane. Furthermore, the deviator stress ratios (or the frictional angles) at phase transformation state and at peak state are all parabolically related with orientation of principal stress. In undrained tests, the effective deviator stress ratio attained at peak state reduces gradually with increase of orientation angle of principal stress. Meanwhile, for different orientation of principal stress, the shear strength indices obtained in the tests are affected by the variation of drainage conditions.

INTRODUCTION

One of the hot subjects in soil mechanics at present is how to simulate the actual stress conditions of soil in the locality. It is because that any disturbance such as embankment or excavation and change of natural conditions such as fluctuation of groundwater table will cause change of stress condition of foundation soil, and so change the orientation of principal

stress, coefficient of intermediate principal stress and consolidation stress ratio of soil in some extent. For achievement of correct evaluation of foundation stability it is necessary to take various complex initial stress states and stress loading patterns into consideration to predict the shear behaviors of the soil. At present, various soil test apparatus such as true triaxial test apparatus, torsional shear apparatus and triaxial-torsional shear apparatus etc. have been developed for testing under various complex stress conditions. The test results make possibility to explore effects of various factors on shear behaviors of the soil and provide solid data basis for theoretical study.

Numbers of study have been done these years following such a way. For Japanese Toyoura sand, Yoshimine(1998) found by strain-controlled monotonic shear tests that orientation of principal stress and coefficient of intermediate principal stress are important factors dominating monotonic shear behavior of sand. Symes(1985) pointed out that, when the orientation angle between major principal stress and the vertical becomes larger or coefficient of intermediate principal stress increases, sand displays obvious shrinkage characteristics by using hollow cylinder torsional shear apparatus. Then, Nakata(1998) and Vaid(1995) found similar shear features during undrained tests. Uthayakumar(1998) pointed out by study on static liquefaction of sand under multiaxial loading that both coefficient of intermediate principal stress and orientation of principal stress influence effective stress path and stress-strain relationship in different extent. Results of true triaxial tests(Yu, 2002) show that intermediate principal stress makes some amplification and regionalization effect on concrete and geotechnical materials.

However, all above-listed test loading conditions, such as orientation of principal stress and coefficient of intermediate principal stress, are limited in some extent. Furthermore, most of data used are obtained from tests of undrained condition. On the other hand, for seepage coefficient of sand is larger and loading speed is suitable, water in ground has enough time to be drained or absorbed. Thus, it is necessary to do some studies on shear behaviors of sands under drained condition. If the foundation is enveloped by non-pervious boundary, there exists pore water pressure in sand till failure of soil, so undrained shear tests are useful(Li, 2004). At present, only a few of test results are obtained by using hollow cylinder torsional shear apparatus in our country. More data of experimental studies, which are aimed at exploring effect of various loading factors on shear characteristics of sands under drained condition, should be made up by using such a soil testing apparatus.

In view of the above-mentioned facts, the soil static and dynamic universal triaxial and torsional shear apparatus in Dalian University of Technology, China is employed to conduct tests simulating various consolidation conditions and stress paths for the soil under different complex stress conditions. For saturated sand, a number of experimental study are conducted by monotonic shear tests under different drainage conditions, so that the deformation and strength features of sand under monotonic loading condition are more comprehensively and thoroughly discussed and the focuses are respectively concentrated at effects of coefficient of intermediate principal stress and orientation of principal stress on monotonic shear behaviors of sand by drained and undrained tests.

TEST CONDITIONS

The soil static and dynamic universal triaxial and torsional shear apparatus employed in the tests is composed of five components including main unit, air-water unit (air compressor and

vacuum pump), analogue control unit, data acquisition and automatic control system and hydraulic servo loading unit (hydraulic actuators and hydraulic supply). The details concerning this comprehensive system were given by Luan(2003). The hollow cylinder soil samples used in experiments have height of 150mm, outer diameter of 100mm and inner diameter of 60mm. This apparatus enables simultaneously exertion and individually control of inner chamber pressure p_i , outer chamber pressure p_o , axial pressure W and torque M and combination of these components. Therefore the consolidation and loading paths under different complex stress condition of shear tests on the hollowing samples can be implemented. The stress state in the hollow cylinder sample is shown in Figure 1.

Under three-dimensional anisotropic consolidation condition, the initial relative density of sample is controlled as $Dr=30\%$, the mean principal stress is kept $p=100\text{kPa}$ and the initial effective deviator stress ratio $\eta_0=0.43$, 19 groups in total of stress-controlled tests on the hollow cylinder sample with different drainage conditions are conducted including 10 groups of drained tests and 9 groups of undrained tests. The details concerning conditions of the tests are listed in Table 1. The stress paths in anisotropic consolidation condition on p - q plane are shown in Figure 2. For the purpose of individual investigation on effects of the two factors, coefficient of intermediate principal stress b and orientation angle of principal stress α , in the whole process of test mean principal stress is kept unchanged and only generalized shear stress is varied.

Table 1. The condition of monotonic shear tests

Shear Test		$p=100\text{kPa}, Dr=30\%, \eta_0=0.43$	
		b	$\alpha(^{\circ})$
Drained Test (CD)	Series 1	0	0, 30, 45, 60, 90
	Series 2	0.5	0, 30, 45, 60, 90
Undrained Test (CU)	Series 3	0.25	0, 30, 45, 60, 90
	Series 4	0, 0.25, 0.5, 0.8, 1	0

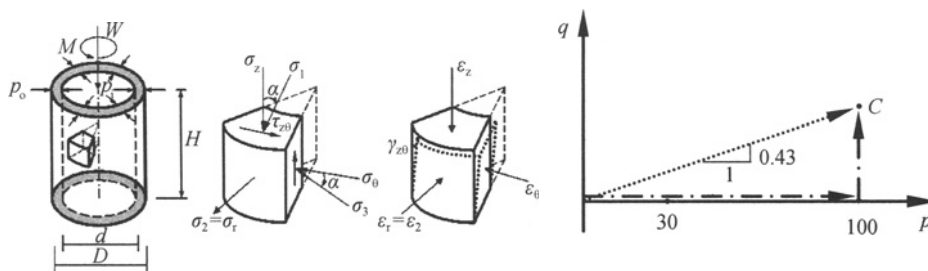


Figure 1. Stress conditions in the sample Figure 2. Stress paths in anisotropic consolidation

TEST RESULTS AND DISCUSSIONS

In order to make a reasonable comparison of data between drained test and undrained test, it is necessary to adopt a uniform stress-strain relationship which is the relationship between generalized effective deviator stress ratio η and generalized shear strain γ_g to examine shear behaviors of sand. In the figures, point C denotes the stress state when consolidation ends on shear begins. The dot on the curve denotes phase transformation state (PTS) when the state of

sand transforms from shear contraction to dilatancy or the pore water pressure transforms from positive growth to negative growth (Vaid, 1990). The effective deviator stress ratio and effective friction angles at phase transformation state are denoted as η_{PT} and ϕ'_{PT} . Then, the effective deviator stress ratio and effective friction angles at peak state are denoted as η_p and ϕ'_p .

Effect of coefficient of intermediate principal stress on shear behaviors of sand

In tests of series 1 and 2 (CD), coefficient of intermediate principal stress is controlled to be $b=0$ or $b=0.5$, and in accordance with different conditions where orientations of principal stress are respectively $\alpha=0^\circ, 30^\circ, 45^\circ, 60^\circ, 90^\circ$, ten groups of drained shear tests are conducted. Relationship between generalized deviator stress ratio η and generalized shear strain γ_g and relationship between volumetric strain ε_v and generalized shear strain γ_g measured from the tests are shown in Figure 3. It can be seen that under lower mean principal stress (100kPa), coefficient of intermediate principal stress remarkably influences on drained $\eta - \gamma_g$ relationship of sand under drained condition. It shows from the figures that the specimen presents strain-softening at the case of $\alpha=0^\circ$, the coefficient of intermediate principal stress has no obvious effect on stress-strain relationship though the shear strain level is small, such effect is more obvious with increase of b at larger strain. Meanwhile, the coefficient of intermediate principal stress makes a little influence on volumetric strain. For the other cases the saturated standard sand presents from beginning to end strain-hardening, and approaches to be stable at a definite stress ratio level. For a definite orientation of intermediate principal stress, no matter of the magnitude of orientation angle, the shear stress ratio at $b=0.5$ is notably lower than that at $b=0$. However, volumetric strain behavior of sand is not influenced much by coefficient of intermediate principal stress. It is worth noticing that the sand specimen

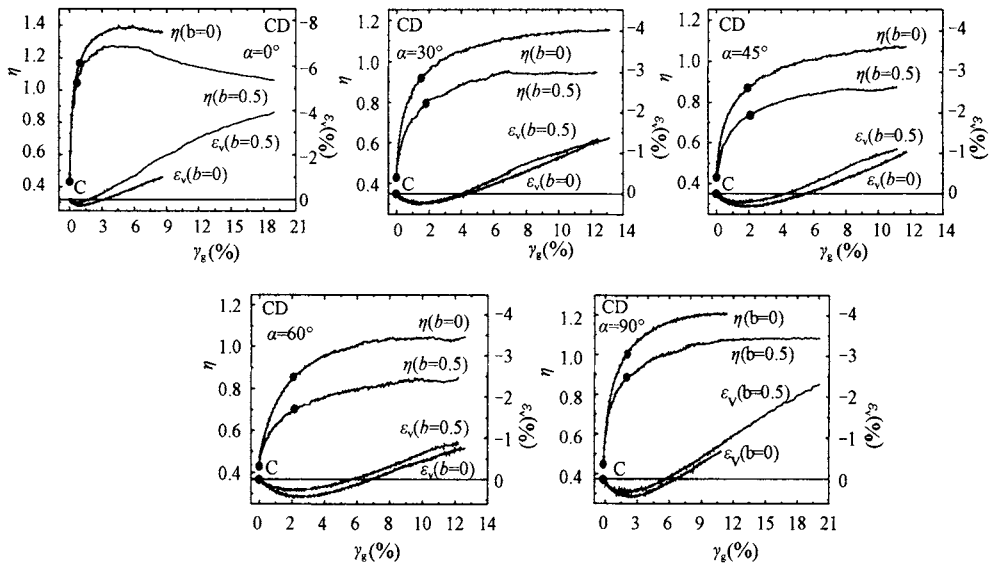


Figure 3. Generalized deviator stress ratio-generalized shear strain relationships and volumetric strain-generalized shear strain relationships under drained condition

finally present dilatancy and it is no matter of orientation of principal stress and magnitude of coefficient of intermediate principal stress. In the beginning stage of deformation volumetric contract is observed and after the phase transformation state is achieved dilatancy takes place.

In tests of series 4 (CU), orientation of principal stress is controlled as $\alpha=0^\circ$, undrained shear tests for such five given coefficients of intermediate principal stress as $b=0, 0.22, 0.5, 0.8, 1.0$ are conducted. The corresponding effective deviator stress ratio η and generalized shear strain γ_g relationships as well as effective stress paths are shown in Figure 4. It can be seen that under undrained condition, when $p=100\text{kPa}$ and $\alpha=0^\circ$, for various coefficient of intermediate principal condition, no strain-softening takes places, and in the tests strain-hardening with dilatancy occurs finally at steady state. Although the coefficient of intermediate principal stress has no obvious effect on the tendency of strain hardening and softening and volumetric dilatancy and contraction as well as on the growth of pore water pressure at phase transformation state, the effective deviator stress ratios at phase transformation state and the final steady state tend to decrease with increase of coefficient of intermediate principal stress.

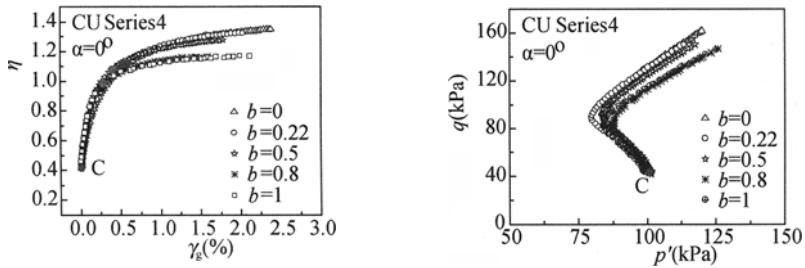


Figure 4. Effective deviator stress ratio-generalized shear strain relationships and effective stress paths under undrained condition

Therefore, effect of coefficient of intermediate principal stress on shear behaviors of sand does not relate to the drainage condition. Under the same initial condition, though b does not make obvious effect on volumetric deformation as well as pore-water pressure, the deviator stress ratio reduces with increase of coefficient of intermediate principal stress. In the beginning stage of sand deformation volumetric contract is observed and after the phase transformation state is achieved dilatancy takes place.

Effect of orientation of principal stress

In the tests, coefficient of intermediate principal stress is kept unchanged and orientation of principal stress varies. When $\alpha=0^\circ, 90^\circ$, on horizontal plane and vertical plane there is only compressive stress acting. When $\alpha=30^\circ, 45^\circ, 60^\circ$, on horizontal plane and vertical plane there act not only compressive stress but also shear stress. In Figure 5(a), it show relationships between generalized deviator stress ratio η and generalized shear strain γ_g for $b=0.5$ at different orientations of principal stress. Relationships between volumetric strain ϵ_v and generalized shear strain γ_g are shown in Figure 5(b). It can be obtained from the figures that

orientation of principal stress makes remarkable influence on η - γ_g relationship of sand. When the orientation of major principal stress approaches the vertical, the sand occurs strain-softening. Relationship presents strain-hardening with increases of orientation angle of major principal stress. Deviator stress ratio decreases progressively, and when the angle between orientation of major principal stress and the vertical approaches $45^\circ + \phi/2$, or α approaches 60° , stress ratio of the sand is the lowest, and the strain generated at the same stress ratio level is the largest. When orientation angle of principal stress departs from $45^\circ + \phi/2$, stress ratio is restored again such as the case of $\alpha=90^\circ$ is higher than that of $\alpha=60^\circ$. Orientation of principal stress also makes influence on volumetric deformation behavior of sand. The more the major principal stress deviates from the vertical, the more the sand presents dilatancy. When the angle between orientation of major principal stress and the vertical is rather small, the specimen is easy to reach phase transformation state and presents dilatancy. When α becomes larger, the specimen presents obvious shear contraction at beginning stage and then turns to dilatancy. It says that for sands of the same initial physical state, under drained condition the variation patterns of stress-strain relationship and volumetric deformation behavior at different orientations of principal stress depend upon the shear stress acting on horizontal and vertical plane.

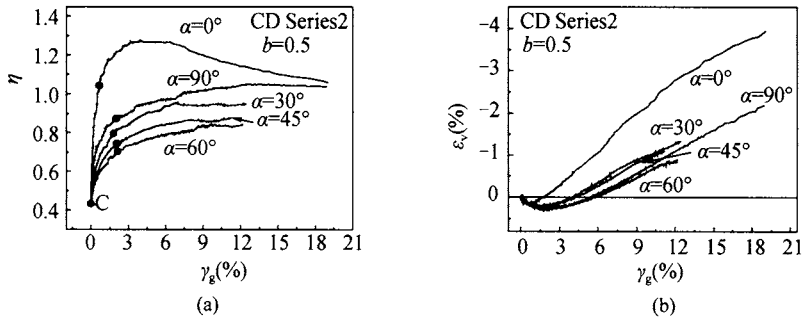
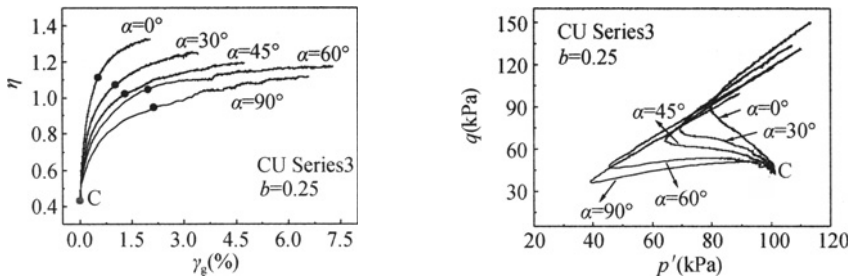


Figure 5. Effect of orientation of principal stress under drained condition: (a) generalized deviator stress ratio-generalized shear strain relationships (b) volumetric strain-generalized shear strain relationships

In the tests of series 3, coefficient of intermediate stress as $b=0.25$, five groups of undrained shear tests are conducted in accordance with different orientation of principal stress. Displayed in Figure 6 are the η - γ_g relationships and effective stress paths obtained from the tests. It can be seen that the orientation of principal stress has remarkable effect on both stress-strain relationship and effective stress path. The larger the orientation angle of principal stress, the higher the pore water pressure rises during shear and the more the shear contraction increases as well as the more the effective deviator stress ratio decreases. For different orientation of principal stress, stress ratio approaches to a final stable stage. When the orientation of major principal stress approaches the vertical, no strain-softening occurs. The effect of strain softening of sand increases with the orientation angle of major principal stress from the vertical. However, whatever the orientation of principal stress is, standard sands all present strain-hardening at the final steady state of deformation. This means that all sands are to go from the instantaneous unsteady state of strain softening to the final steady state.



(a) effective deviator stress ratio-generalized shear strain relationships (b) effective stress paths

Figure 6. Effect of orientation of principal stress under undrained condition:

Therefore, orientation of principal stress makes remarkable influence on shear behaviors of sand. Even for sands with the same density, either strain softening or hardening which is associated with the orientation of principal stress can be characterized. The sands present contrary softening and hardening features under different drainage conditions. When the initial condition is the same, for a definite b , the specimen presents obvious shear contraction at beginning stage and then turns to dilatancy with increase of orientation angle of principal stress.

Effect of orientation of principal stress on shear strength of sand under different drainage conditions

In drained tests, restricted by measurement range of the equipment, ultimate strains measured in different cases are not the same value. For the case of $\alpha=0^\circ$, peak value is observed obviously when strain softening takes place. For the cases of $\alpha=30^\circ$, 90° , only strain hardening is observed, and the peak state is considered when the stable state is reached. For the cases of $\alpha=45^\circ$, 60° , the peak value is taken the point where generalized strain reaches about 12%. In Table 2 it is listed generalized deviator stress ratios at phase transformation state and at peak state obtained from the tests. Data and fitting curves are shown in Figure 7(a). It can be seen from the figure that for a definite b , the relationship between deviator stress ratios at phase transformation state as well peak state and orientation of principal stress well fits the parabolic relation, or $\eta = A\alpha^2 + B\alpha + C$. Values of A , B and C are determined from test results are listed in Table 3. Then, in Table 4 friction angles at phase transformation state and at peak state obtained from the tests are listed. Data and fitting curves are shown in Figure 7(b). It can be found that fitting the experimental data the parabolic formulae for friction angles in accordance with orientation of principal stress can be written as $\phi = D\alpha^2 + E\alpha + F$. Values of D , E and F are listed in Table 5.

Above results show that for a definite b , when $\alpha=60^\circ$, strength mobilized by the sand is the lowest under drained condition. The basic reason may be that horizontal texture planes are formed during the process of preparing sample. According to Mohr-Coulomb strength criterion, when sand fails the angle between failure plane and action plane of major principal stress is $45^\circ + \phi/2$. In the specimen when α approaches $45^\circ + \phi/2$, the vulnerable plane in strength is just parallel to horizontal texture plane, or interlocking of the sand along horizontal texture plane is weak. For this case the strength mobilized by the sand is the lowest,

then changing orientation of principal stress until $\alpha > 45^\circ + \phi/2$, strength of the sand is restored again. This is identical with the experimental results on Toyoura sand by Miura(1986). Moreover, Wang(1996) pointed out similar conclusion on compacted cohesive soil.

Table 2. Generalized deviator stress ratios at PTS and at peak state from drained tests

Drained test	b	η	α				
			0°	30°	45°	60°	90°
Series 1	0	η_{PT}	1.15	0.93	0.88	0.86	1.01
		η_P	1.40	1.13	1.07	1.04	1.19
Series 2	0.5	η_{PT}	1.04	0.79	0.74	0.71	0.88
		η_P	1.27	0.95	0.87	0.85	1.05

Table 3. Values of A , B and C

Drained test	b	η	A	B	C
Series 1	0	η_{PT}	0.0099	-1.07	1.16
		η_P	0.0114	-1.26	1.40
Series 2	0.5	η_{PT}	0.0113	-1.20	1.04
		η_P	0.0144	-1.56	1.28

Table 4. Friction angles at PTS and at peak state from drained tests

Drained test	b	$\phi(^{\circ})$	α				
			0°	30°	45°	60°	90°
Series 1	0	ϕ_{PT}	28.65	22.85	21.79	21.35	25.22
		ϕ_P	34.79	28.46	26.95	26.64	31.29
Series 2	0.5	ϕ_{PT}	37.32	27.21	24.61	23.78	30.68
		ϕ_P	45.77	33.74	30.36	29.48	38.19

Table 5. Values of D , E and F

Drained test	b	ϕ	D	E	F
Series 1	0	ϕ_{PT}	0.003	-0.30	28.65
		ϕ_P	0.003	-0.30	34.79
Series 2	0.5	ϕ_{PT}	0.0047	-0.50	37.49
		ϕ_P	0.0058	-0.61	46.03

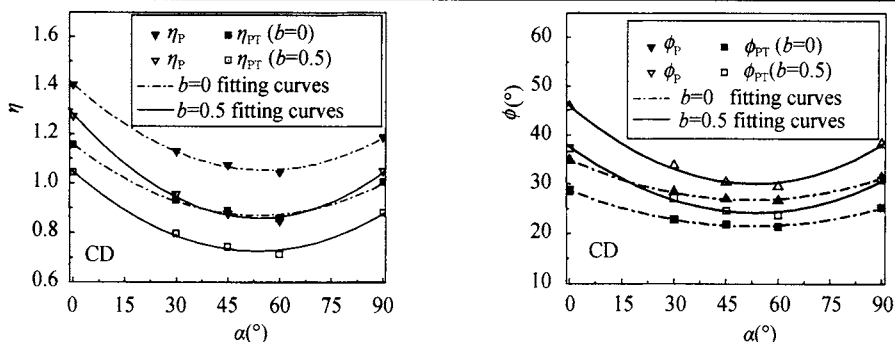


Figure 7. (a) Relationships between generalized deviator stress ratio and orientation of principal stress at PTS and at peak state under drained condition, (b) Relationships between friction angles and orientation of principal stress under drained condition

In undrained tests, the peak state is considered when stress-strain relationship reaches the steady state. In Tables 6 and 7, there are listed effective deviator stress ratios and effective friction angles at phase transformation state and at peak state obtained from the tests, data are respectively shown in Figure 8 and Figure 9. It can be seen that for a definite b , η_p tends to decrease with increases of orientation angle of principal stress. Meanwhile, for a definite α , η_p tends to decrease with increases of coefficient of intermediate principal stress. When $\alpha < 45^\circ$, along with increase of angle between orientation of major principal stress and the vertical, effective friction angle tends to descending. When $\alpha > 45^\circ$, effective friction angle has no dependency on orientation of principal stress. It also can be observed that the amplification and regionalization effect of coefficient of intermediate principal stress on effective friction angle, when α is kept unchanged.

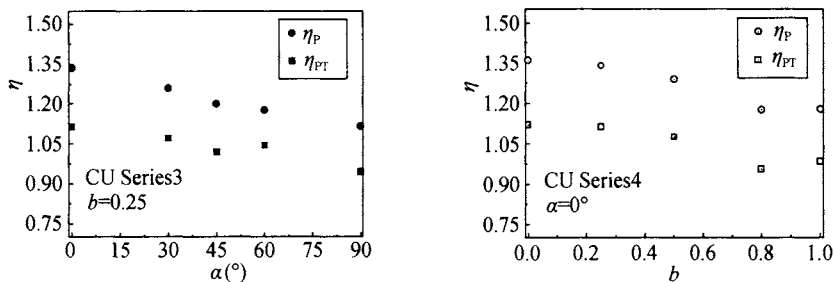


Figure 8. Effective deviator stress ratios at PTS and at peak state under undrained condition

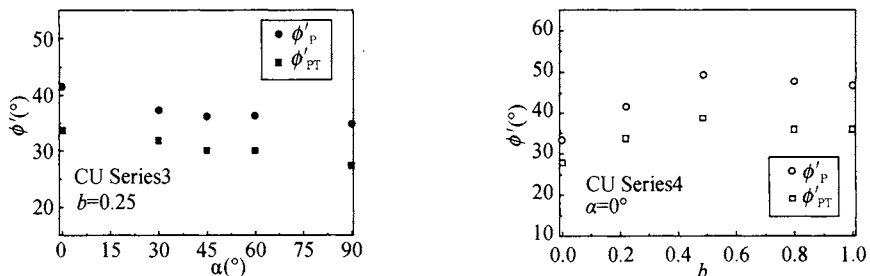


Figure 9. Effective friction angles at PTS and at peak state under undrained condition

Table 6. Effective deviator stress ratios at PTS and at peak state from undrained tests

Undrained test	b	η	α				
			0°	30°	45°	60°	90°
Series 3	0.25	η_{PT}	1.11	1.07	1.02	1.04	0.95
		η_p	1.34	1.26	1.20	1.18	1.12
Series 4	0°	η	b				
			0	0.25	0.5	0.8	1
Series 4	0°	η_{PT}	1.12	1.11	1.07	0.96	0.98
		η_p	1.36	1.34	1.29	1.17	1.18

Table 7. Effective friction angles at PTS and at peak state from undrained tests

Undrained test	b	$\phi'(^{\circ})$	α				
			0°	30°	45°	60°	90°
Series 3	0.25	ϕ'_{PT}	33.67	31.84	30.04	30.01	27.40
		ϕ'_p	41.48	37.26	36.14	36.22	34.82
	α	$\phi'(^{\circ})$	b				
			0	0.25	0.5	0.8	1
Series 4	0°	ϕ'_{PT}	27.88	33.67	38.70	35.89	35.82
		ϕ'_p	33.35	41.48	49.29	47.68	46.69

The comprehensive comparison on the above-mentioned experimental results indicate that strength indices obtained from the tests on standard sand of relative density 30% under different drainage conditions with variation of orientation of principal stress are various. When $\alpha=0^{\circ}$, 90° , on horizontal plane and vertical plane there is only compressive stress acting, the strength index of drained test is little lower than that of undrained test. This is similar to the strength index obtained from triaxial compression test under different drainage conditions. When $\alpha=30^{\circ}$, 45° , 60° , on horizontal plane and vertical plane there act not only compressive stress but also shear stress, the strength index of drained test is much lower than that of undrained test, drainage condition influences remarkably on experimental result. Therefore, such an effect is worth to be considered in engineering practice in accordance with the actual stress state of soil. Further studies should be investigated on the explanation of this failure mechanism in the future.

CONCLUSIONS

For saturated sand of relative density 30%, the mean principal stress is kept $p=100\text{kPa}$, monotonic shear tests under different drainage conditions are conducted. Effects of coefficient of intermediate principal stress and orientation of principal stress on shear behaviors of sand are investigated. The principal results of tests are summarized as follows:

- (1) Effect of coefficient of intermediate principal stress on shear behaviors of sand does not relate to the drainage condition. Under the same initial condition, for a definite orientation of principal stress, though coefficient of intermediate principal stress does not make obvious effect on volumetric deformation as well as pore-water pressure, the deviator stress ratio reduces with increase of coefficient of intermediate principal stress.
- (2) Orientation of principal stress makes remarkable influence on shear behaviors of sand. When the initial condition is the same, for a definite coefficient of intermediate principal stress, the specimen presents obvious shear contraction with increase of the orientation angle of principal stress. The sands present contrary softening and hardening features under different drainage conditions.
- (3) In the beginning stage of sand deformation volumetric contract is observed and after the phase transformation state is achieved dilatancy takes place. This phenomenon does not relate to the test condition.
- (4) For a definite coefficient of intermediate principal stress, the deviator stress ratios at phase transformation state and at peak state and the frictional angles are all

parabolically related with orientation of principal stress under drained condition. In undrained tests, the effective deviator stress ratio attained at peak state reduces gradually with increase of orientation angle of principal stress and effective friction angle tends to descending. When the angle exceeds 45° , the tendency is not obvious.

- (5) Strength indices obtained from the tests under different drainage conditions with variation of orientation of principal stress are various. When the orientation angle of principal stress is controlled as 0° and 90° , the strength index of drained test is little lower than that of undrained test. When the angle controlled as 30° , 45° and 60° , the strength index of drained test is much lower than that of undrained test.

ACKNOWLEDGEMENTS

The authors wish to express their gratitude to Prof. Dahong Qiu of Dalian University of Technology, who is a CAS's member, for his continuing support and invaluable advice for the study. The financial support for this investigation through the grants 50579006 and 50639010 from National Natural Science Foundation of China is mostly grateful.

REFERENCES

- Li Guangxin. (2004). *Advanced soil mechanics*. Tsinghua University Press.
- Luan Maotian, Guo Ying, Li Muguo, et al. (2003). Development and application of soil static and dynamic universal triaxial and torsional shear apparatus. *Journal of Dalian University of Technology*, 43(5): 670-675.
- Miura K., Miura S. and Toki S. (1986). Deformation behavior of anisotropic dense sand under principal stress axes rotation. *Soils and Foundations*, 26(1): 36-52.
- Nakata Y., Hyodo M. and Murata H. (1998). Flow deformation of sands subjected to principal stress rotation. *Soils and Foundations*, 38(2): 115-128.
- Symes M. J., Shibuya S., Hight D. W. and Gens A. (1985). Liquefaction with cyclic principal stress rotation. *Proc. of 11th International Conference on Soil Mechanics and Foundation Engineering*, 4: 1919-1922.
- Uthayakumar M., Vaid Y. P. (1998). Static liquefaction of sands under multiaxial loading. *Canadian Geotechnical Journal*, 35: 273-283.
- Vaid Y. P., Chung E.K.F. and Keurbis R.H. (1990). Stress path and steady state. *Canadian Geotechnical Journal*, 27(1): 1-7.
- Vaid Y.P., Sivathayalan S. and Uthayakumar M. (1995). Liquefaction potential of reconstituted syncrude sand. *Proc. of 48th Canadian Geotechnical Conference*, 1: 319-330.
- Wang Hongjin, Zhang Guoping and Zhou Keji. (1996). Effects of inherent and induced anisotropy on strength and deformation characteristics of compacted cohesive soil. *Chinese Journal of Geotechnical Engineering*, 18(3): 1-10.
- Yoshimine M., Ishihara K. and Vargas W. (1998). Effects of principal stress direction and intermediate principal stress on undrained shear behavior of sand. *Soils and Foundations*, 38(3): 179-188.
- Yu Maohong. (2001). *Concrete strength theory and applications*. The Higher Education Press.

STUDY ON THE INTERACTION LAW BETWEEN SQUEEZED BRANCH PILE – STRUCTURE AND SOIL

Dongpo Wang

*College of Architecture and Art, Hefei University of Technology, 193 Tunxi Road
Hefei 230009, China*

The squeezed branch pile is a new type of pile with high bearing capacity and low settlement. The mechanism of bearing, compaction efficiency and loading transfer behavior of the squeezed branch pile are analyzed systematically based on the results of static loading test. It is shown by test results that behavior of bearing disks has obvious time effect and is different from other types of piles by means of calculation. Squeezed branch pile with specific property of frictional end-bearing pile bears load mainly by bearing disks, and the ultimate load of the pile is 150-200 percent of straight pile. The load shared by disks is about 60-70 percent of the ultimate load.

INTRODUCTION

In the history of development of the piles, it is normally practiced to develop bored pile with the long length and large diameter, or to develop multi-section and short pedestal pile, all these technology are used to raise the single pile's bearing capacity by increasing the length of the pile and the contacted area between pile and soil.

In china, people created the squeezed branch pile, for example Qian D.L. and Wang D.P. et al. (2004). The structure of squeezed branch pile shows as follow in Figure1. Special squeezing and expanding device is used to form the disk on the basis of the bored piles. Because of the soil around the disks is squeezed, the strength of the soil is increased. So the pile has higher bearing capacity and pull-resistance, as well as better anti-seismic capacity, stability and economic benefits.

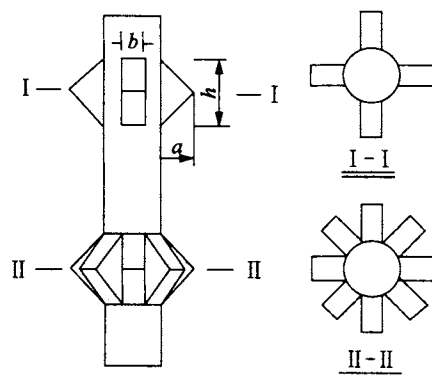


Figure 1. The structure of squeezed branch pile

BEARING MECHANISM OF SQUEEZED BRANCH PILE

Squeezed branch pile has special bearing mechanism as compared with the straight pile.

Firstly, the squeezed branch pile utilizes the better soil layer around the pile to transmit the load by the branches or disks. The loads are shared by different soil layers and reduced along the pile for the stress diffusion. Therefore, load on the pile tip is lower than straight pile, while the bearing area between pile and soil is more enlarged. So the soil on the pile tip is more stable because of the load is very little.

Secondly, the squeezed action makes the soil around the disks compact. When the borehole is squeezed to form mould of disk by using special squeezing equipment, the soil around disks is compacted. Thus, compression amount of the soil is reduced, and the angle of internal friction and the modulus of compressibility of the soil are heightened. The vertical bearing capacity and pulling resistance of the soil are raised doubly. According to the result of many static loading tests, the bearing capacity of the squeezed branch pile has been improved by 70%-100% than that of the straight pile.

THE INTERACTION LAW BETWEEN SQUEEZED BRANCH PILE AND SOIL

The static loading test

Here we selected a typical test to study the interaction law between squeezed branch pilestructure and soil. The project is the mansion of labor market of Wuhan, 17 storey is on the ground and total floor area is 24,300m². The column grid is 8m×9m and the biggest load of columns is 20000kN. The squeezed branch piles are used as the foundation. Before construction, three groups of test piles were poured. The length of test piles is 31m, the diameter of the key pile is 620mm, and the diameter of bearing disk is 1400mm. 4 bearing disks are designed on single pile of which bearing capacity is estimated to 6000kN. Wuhan institute of rock and soil mechanics of the Chinese Academy of Sciences undertook the testing task of the test piles. The geological characteristic of the site and the size of test pile are showed as follow in Figure 2.

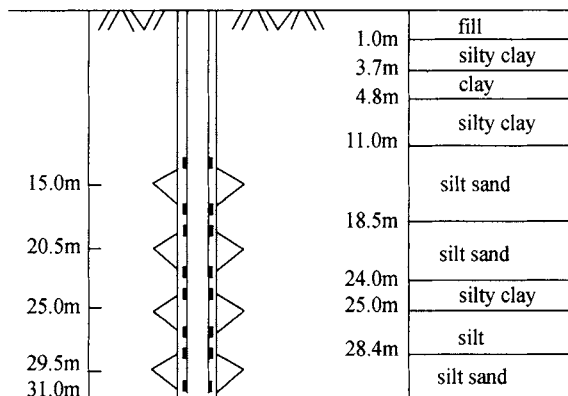


Figure 2. The geological characteristic of the site and the size of test pile

Load transfer behavior

On the main reinforcement of the 1st and the 3rd test pile, each was set up 16 reinforcing stress meter which are laid on above and below the bearing disks, as Figure 2 show.

According to the strain data measured by the reinforcing stress meter buried in advance, the axial force of each section is calculated. Now take the measured data of the first test pile as an example to analyze. Figure 3 is the distribution curve of axial force of the first test pile.

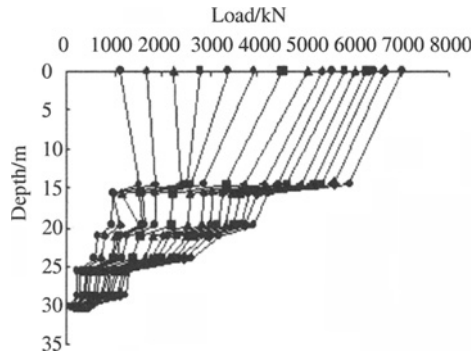


Figure 3. The distribution curve of axial force

From the figure, we can find that the load transfer curve of squeezed branch pile is obviously different from that of the straight pile. The distribution curve of axial force changes rapidly on the upper and lower bearing disk, and axial force reduces obviously. The consumed force is completely undertaken by the disks, and then shifted to the soil under the disks. This is the load transfer behavior of squeezed branch pile, and that is why the squeezed branch pile improves the bearing capacity. It is the “stressed” function of the soil under the disk that plays an incomparable role to improve the end-bearing force of the disks. The disks bear the main load in the course of load increasing. And the load of the pile tip is very small.

The eEnd-bearing force of disk

The bearing capacity of squeezed branch pile is made up of three main parts: frictional resistance on sides of pile, the end-bearing force of disks, and resistance of pile tip. And the end-bearing force of disks is the principal part of the total load. Now we draw out the relation figure of the end-bearing force of disks and the total load (see Figure 4).

Number 1, 2, 3, 4 represent the 4 disks on the pile from up to down in Figure 4. We can see the load transfer law from the curves. These disks reached limit bearing capacity in the different time because of different properties of the soil. If the strength of the soil under one disk is lower relatively, the disk would reach the limit state at first, and the more added load would be shifted to other bearing disks. When the end-bearing force of the disk 1 reaches the maximum, increased loads will be shifted to disk 2, and the end-bearing force of the disk 2 will be up to the extreme. Meanwhile, the force of disk 3 and disk 4 is increased sharply to resist the load of the pile top.

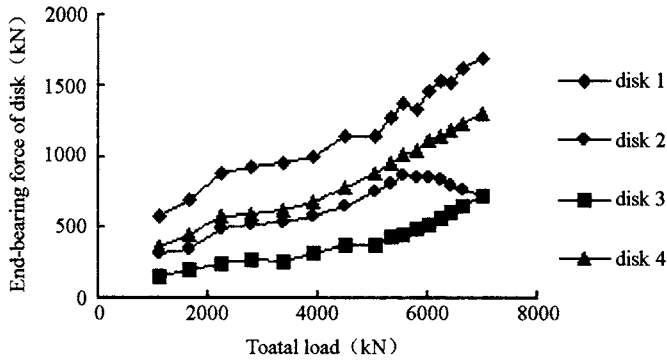


Figure 4. The relationship between the end-bearing force of disk and the total load

It can be concluded that the bearing characteristic of squeezed branch pile has time effect obviously. The bearing force of each disk and the time that bearing force reach the maximum both depend on the compression modulus of the soil under the disk. Once bearing force of some disk reach the maximum, other disks will take over and bear the load increment sequentially. It is not happened that the end-bearing force of every disk reached the maximum in the same time. Therefore, when designing squeezed branch pile, the bearing capacity should not be equally allocated to each disk. It should be considered that the soil layers under the disks have different property and thickness.

The frictional resistance of pile

The test indicates that the load ratio-shared of the friction resistance between disks are different too. The friction resistance and the relative displacement of pile-soil between disks can be calculated by the following formula.

The frictional resistance of the pile :

$$q_{si} = \frac{Q_i - Q_{i+1}}{A_{si}} \quad (1)$$

The verticality displacement at the middle point of the pile between disks:

$$S_j = S - \sum_{i=1}^j \frac{L_i}{2} (\varepsilon_{i+1} + \varepsilon_i) \quad (2)$$

In the formula: q_{si} —Friction resistance on i part of pile; Q_i —Axial force on i section; A_{si} —Surface area on i part of pile; S —Settlement of pile top; L_i —Length of i part of pile; ε_i —Testing strain on i section.

The calculated data of friction resistance of the test pile 1 are drawn into Figure 5, where 1, 2, 3, 4 are respectively serial numbers of straight pole part of the test pile from up to down. After the load of 5054 kN, the friction resistance of part 3 raised sharply, while the end-bearing force of the disk 2 drops by a large extent. It proves that the friction resistance will play a positive role when the bearing disk does not bear load any more. Therefore, the complementary relationship between the end-bearing force and the friction resistance exists. When the space between disks is small, soil under the disk has the stress-superposing effect, and the friction resistance reduces.

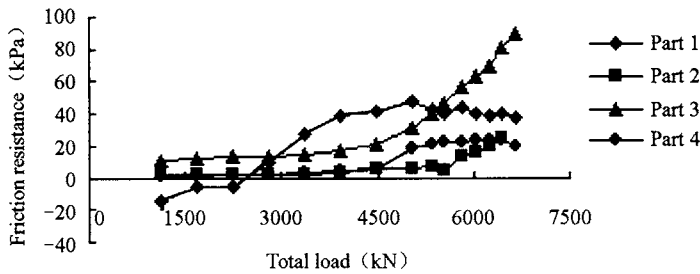


Figure 5. The relation of friction resistance and the total load

The resistance of pile tip

In this test, the reinforcing stress meter is buried near the pile tip, so the resistance of the pile tip can be calculated out according to the axial force in the pile tip. The relation of the resistance and the settlement of the pile tip been drawn in Figure 6.

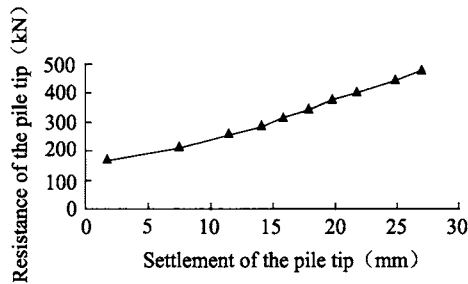


Figure 6. The relation of resistance and settlement of the pile tip

The Figure indicates that the relation of the resistance and the settlement is similar to a straight line, and the resistance shows the phenomenon of “subside and harden”. The phenomenon illuminates that the sand under the pile tip is pressed to dense. Besides, due to the bearing disk near the pile tip bring about stress dispersion, it makes the soil under the pile tip be difficult in extruding toward sides direction, therefore, the resistance of the pile tip is raised. The results of calculation indicate that the resistance of the pile tip accounts for 7% of that limit load. If adding the bearing force of the disks, the sum of the two accounts for about 70% of that limit load, so the squeezed branch pile has property of the friction-end bearing pile.

It is shown that the resistance of the pile tip begins to give play when pile tip produces displacement. When the pile body is set up with the disks, not only the bearing capacity raises 70%-100% than that of the straight pile, the settlement of the squeezed branch pile is also much smaller than it.

CONCLUSIONS

(1) The squeezed branch pile belongs to frictional end-bearing piles with many ranks of support, and it depends on the bearing disk to bear the load. The bearing force of disks is more important than the frictional resistance.

(2) The disk 1 bears most of the load. And the position of the disk 1 is very important. The better property of the soil and properly space between the disks are significant to the bearing capacity of the disk 1.

(3) The length, diameter of disks and the number of disks can be adjusted according to the mechanical property of the soil, so the design data of the bearing capacity of the pile can be adjusted too.

(4) The settlement of the squeezed branch pile is much smaller than the straight one, and the potentiality of the resistance of the pile tip is great.

(5) The function of the disks is equivalent to some bearing points set up in the pile. The bearing capacity and the stability of squeezed branch pile are better than the straight one. The squeezed branch pile can raise the anti-seismic ability of foundation and system efficiently. It has very important meaning for resisting earthquake and reducing seismic damage.

ACKNOWLEDGEMENTS

Thanks for the support by the National Natural Science Fund of China (No.50278030) and the Anhui Natural Science Fund of China (No.050450402).

REFERENCES

- Qian D.L. (2004). Study on interaction of squeezed branch pile-soil and FEM simulation. *J. China Civil Engineering Journal*, 37(2): 82-86.
- Qian D.L. (2004). Reproduced loading transfer behavior of squeezed branch pile by numeral simulation system., *J. China Civil Engineering Journal*, 37(7): 68-72.
- Wang D.P. (2004). Law of load transmission of squeezed branch piles and it's research advances. *J. Chinese Journal of Rock Mechanics and Engineering*, 23 (suppl): 4645-4648.

ELASTIC-PLASTIC ANALYSIS FOR SURROUNDING ROCK OF PRESSURE TUNNEL WITH LINER BASED ON MATERIAL NONLINEAR SOFTENING

Liming Zhang, Zaiquan Wang, Huafeng Li and Hengbo Zhao
College of Science, Qingdao Technological University, Qingdao 266033, China

According to the strain nonlinear softening constitutive model of practical rock, pressure tunnel with liner is analyzed. The model is considered the influence of intermediate principal stress σ_2 . Stress distribution laws of surrounding rock plastic zone of tunnel, the mechanism of load bearing and acting relation between surrounding rock and support are studied. Some important conceptions of working status of practical tunnel surrounding rock are obtained: such superior certain limit [Smax] of self-support geo-stress and inferior certain limit [Smin] of supportless tunnel surrounding rock. The relations between [Smax] and geo-stress, between [Smin] and geo-stress are given. Calculation shows that the assumed model agrees well with practical condition of rocks. Analysis shows that the ideal plastic model and the brittle model are special cases of the proposed solution.

INTRODUCTION

It is well known that the stability of tunnel surrounding rock is decided by the interaction results of stresses in surrounding rock and its strength, i.e. surrounding rock states. If its surrounding rock is in elastic or plastic state after a tunnel is driven, the surrounding rock is stable. However, if its surrounding rock is in a broken state after the tunnel is driven, the surrounding rock is unstable. The greater the broken range in the surrounding rock is, the poorer its stability will be and the more difficult supporting to the tunnel will be. In addition, lots of in-situ observation data have shown that a broken zone exists widely in surrounding rock of tunnel. Therefore, it can be seen that the thickness of the broken zone, a geometrical parameter indicating the broken range in surrounding rock of tunnels, can be taken as a comprehensive index of stresses in surrounding rock and its strength to evaluate the stability of surrounding rock of a deep tunnel.

Kastner's solution is often used in elastic-plastic analysis for surrounding rock of circular tunnel. It is well known that Kastner's formula is based on ideal elastic-plastic model. This leads to the Kastner's solution is far away to corresponding actual values in surrounding rock. Following along the path of pioneered by Kastner, researchers such as Ma (1996), Jiang and Zheng (1997), Ma (1998, 1999), Yu (2002), Fan (2004), Ren and Zhang (2001) and Pan and Wang (2004) published different solutions for surrounding rocks of circular tunnel. However, these solutions are restricted to very simple material models, such as simple linear relationship between stress-strain. They are of limited practical value. This study successfully gets the stress distribution laws of surrounding rock plastic and broken zone

according to the total strain theory. The relationship between equivalent stress and equivalent strain is deduced from practical rock. The relational expressions are related with triaxial stress ($\sigma_\theta, \sigma_z,$ and σ_r) and triaxial strain ($\varepsilon_\theta, \varepsilon_z,$ and ε_r) of surrounding rock.

ELASTIC-PLASTIC ANALYSIS FOR SURROUNDING ROCK

Figure 1 shows the geometric model condition of a tunnel in a plane strain state subjected to a pressure difference between its internal and external pressures. Where a and b are respectively the inner and outer radius of tunnel, P_0 and P_a are pressures acting on the inner and outer surfaces of tunnel, and R is the radius of the interface of elastic and plastic zones. Surrounding rock may be generally divided into broken, plastic and elastic zones on the basis of their states, as shown in Figure 1. The surrounding rock within the elastic zone is in an elastic state, within the plastic zone, in a strain softening state, and within the broken zone, in a residual-strength state. So the surrounding rock within the broken zone is the direct object of tunnel support.

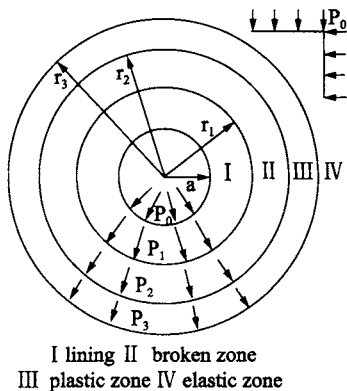


Figure 1. Model of tunnel

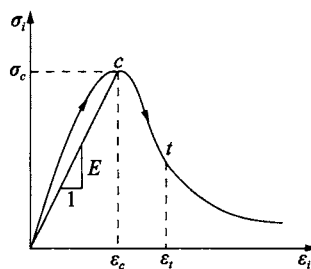


Figure 2. Equivalent stress-equivalent strain

Constitutive model of plastic zone

The tunnel may be simplified as an axisymmetrical plane strain problem. Substituting $r = r_3, \varepsilon_z = 0$ and $\varepsilon_i = \varepsilon_c$ into the interface of elastic and plastic zones, the equivalent strain is defined by (Zheng, 1988)

$$\varepsilon_i = \frac{\sqrt{2}}{3} \sqrt{(\varepsilon_\theta - \varepsilon_z)^2 + (\varepsilon_z - \varepsilon_r)^2 + (\varepsilon_r - \varepsilon_\theta)^2} = \varepsilon_c \frac{r_3^2}{r^2} \quad (1)$$

If the volumetric strain of softening zone equals to zero, we can obtain

$$\sigma_z^p = \frac{1}{2}(\sigma_\theta^p + \sigma_r^p) \quad (2)$$

The equivalent stress is given by

$$\sigma_i = \frac{1}{\sqrt{2}} \sqrt{(\sigma_\theta^p - \sigma_r^p)^2 + (\sigma_z^p - \sigma_r^p)^2 + (\sigma_z^p - \sigma_\theta^p)^2} = \frac{\sqrt{3}}{2}(\sigma_\theta^p - \sigma_r^p) \quad (3)$$

The constitutive model of uniaxial compression is calculated from (Guo, 2004)

$$\sigma_1 = E\varepsilon_1 \exp(-\varepsilon_1/\varepsilon_c), \quad (\varepsilon_1 \geq \varepsilon_c) \quad (4)$$

The softening section on equivalent $\sigma_i - \varepsilon_i$ curve can be plotted as Figure 2 shown. We find that the assumed rock model agrees well with practical rocks. The ultimate bearing capacity of surrounding rock in complex stress state is analyzed in the following parts. We consider that the strain component of surrounding rock keep constant proportion, ie $\varepsilon_z : \varepsilon_\theta : \varepsilon_r = 0 : 1 : (-1)$. So it may be simplified as simple loading condition. According to the total strain theory (Zheng, 1988), the relationship between equivalent stress and equivalent strain can be deduced from Equation. (4).

$$\sigma_i = E\varepsilon_i \exp\left(-\frac{\varepsilon_i}{\varepsilon_c}\right) = \sigma_c \left(\frac{r_3^2}{r^2}\right) \exp\left(1 - \frac{r_3^2}{r^2}\right) \quad (5)$$

The relational expressions are related with triaxial stress (σ_θ, σ_z , and σ_r) and triaxial strain ($\varepsilon_\theta, \varepsilon_z$, and ε_r) of surrounding rock.

Stresses in the plastic zone

Its corresponding mechanical equilibrium equation is

$$\frac{d\sigma_r}{dr} + \frac{\sigma_r - \sigma_\theta}{r} = 0 \quad (6)$$

Substituting $(\sigma_r)_{r=r_2} = p_2$ into Eq. (3) and Eq. (5) and using the Eq. (6), the stresses in the plastic zone can be obtained as follows

$$\sigma_r^p = p_2 + \frac{\sigma_c e}{\sqrt{3}} \left[\exp\left(-\frac{r_3^2}{r^2}\right) - \exp\left(-\frac{r_3^2}{r_2^2}\right) \right] \quad (7)$$

$$\sigma_\theta^p = p_2 + \frac{2\sigma_c e}{\sqrt{3}} \left(\frac{r_3^2}{r^2}\right) \exp\left(-\frac{r_3^2}{r^2}\right) + \frac{\sigma_c e}{\sqrt{3}} \left[\exp\left(-\frac{r_3^2}{r^2}\right) - \exp\left(-\frac{r_3^2}{r_2^2}\right) \right]$$

Stresses in the elastic zone

The stresses in the elastic zone may be expressed by

$$\sigma_\theta^e = p_0 \left(1 + \frac{r_3^2}{r^2}\right) - p_3 \frac{r_3^2}{r^2} \quad (8)$$

$$\sigma_r^e = p_0 \left(1 - \frac{r_3^2}{r^2}\right) + p_3 \frac{r_3^2}{r^2}$$

Substituting the bounding condition on the interface of elastic and plastic zones

$(\sigma_\theta^e)_{r=r_3} + (\sigma_r^e)_{r=r_3} = 2p_0 = (\sigma_\theta^p)_{r=r_3} + (\sigma_r^p)_{r=r_3}$ into Equation. (7) and Equation. (8), we

get

$$p_2 = p_0 - \frac{\sigma_c e}{\sqrt{3}} \left[2 \exp(-1) - \exp\left(-\frac{r_3^2}{r_2^2}\right) \right] \quad (9)$$

The plastic zone has the support effect to surrounding rock. Equation. (9) shows that for a given p_0 , surrounding rock can be balanced by itself through adjusting the plastic zone. So it is also named the equilibrium equation of surrounding rock. Surrounding rock without support has ultimate bearing capacity. If $r_3 \rightarrow \infty$, we get the ultimate bearing capacity of surrounding rock. In practical, the surrounding rock is collapsed as $r_3 \rightarrow \infty$. However, it gives us the theoretical result. The ultimate bearing capacity of surrounding rock in practical can not be larger than the theoretical result of surrounding rock.

Deformation in the Plastic zone

According to the elastic-plastic theory, the total strain of plastic zone can be calculated by the following formula (Zheng, 1988)

$$\begin{Bmatrix} \varepsilon_r \\ \varepsilon_\theta \end{Bmatrix} = \begin{Bmatrix} \varepsilon_r^e \\ \varepsilon_\theta^e \end{Bmatrix} + \begin{Bmatrix} \varepsilon_r^p \\ \varepsilon_\theta^p \end{Bmatrix} \quad (10)$$

The elastic strain of plastic zone is defined by

$$\begin{aligned} \varepsilon_r^e &= \frac{1}{E_c} \left[\left(1 - \frac{1}{2} \mu_c \right) \sigma_r - \frac{3}{2} \mu_c \sigma_\theta \right] \\ \varepsilon_\theta^e &= \frac{1}{E_c} \left[\left(1 - \frac{1}{2} \mu_c \right) \sigma_\theta - \frac{3}{2} \mu_c \sigma_r \right] \end{aligned} \quad (11)$$

The plastic strain of plastic zone is defined by

$$\begin{aligned} \varepsilon_r^p &= \frac{\varphi}{4G_c} (\sigma_r - \sigma_\theta) \\ \varepsilon_\theta^p &= \frac{\varphi}{4G_c} (\sigma_\theta - \sigma_r) \end{aligned} \quad (12)$$

The total strain of plastic zone can be expressed by

$$\begin{aligned} \varepsilon_r &= \frac{du}{dr} = \frac{1}{E_c} \left[\left(1 - \frac{1}{2} \mu_c \right) \sigma_r - \frac{3}{2} \mu_c \sigma_\theta \right] - \frac{\varphi}{4G_c} (\sigma_\theta - \sigma_r) \\ \varepsilon_\theta &= \frac{u}{r} = \frac{1}{E_c} \left[\left(1 - \frac{1}{2} \mu_c \right) \sigma_\theta - \frac{3}{2} \mu_c \sigma_r \right] + \frac{\varphi}{4G_c} (\sigma_\theta - \sigma_r) \end{aligned} \quad (13)$$

Where E_c refers to elastic modulus of surrounding rock, G_c refers to shear modulus, μ_c refers to Poisson's ratio, φ refers to plastic function. The plastic function φ is zero in elastic deformation. Using Equation. (13), the deformation on the interface of elastic and plastic zones can be calculated from

$$\begin{aligned} u_s &= \frac{r}{E_c} \left(\frac{2 - \mu_c}{2} \sigma_\theta - \frac{3}{2} \mu_c \sigma_r \right) - \frac{r_3 (1 - \mu_c - 2\mu_c^2)}{E_c} p_0 \\ &= \frac{r_3 (1 - 2\mu_c)}{E_c} [p_2 - (1 + \mu_c) p_0] + \frac{r_3 \sigma_c e^{(1 - 2\mu_c)}}{\sqrt{3} E_c} \left[3 \exp(-1) - \exp\left(-\frac{r_3^2}{r_2^2}\right) \right] \end{aligned} \quad (14)$$

Substituting Equation. (7) into Equation. (13), we have

$$\frac{du}{dr} + \frac{u}{r} = \frac{2(1-2\mu_c)}{E_c} \left[p_2 - \frac{\sigma_c e}{\sqrt{3}} \exp\left(-\frac{r_3^2}{r^2}\right) \right] + \frac{2\sigma_c e(1-2\mu_c)}{\sqrt{3}E_c} \exp\left(-\frac{r_3^2}{r^2}\right) \left[1 + \left(\frac{r_3^2}{r^2}\right) \right] \quad (15)$$

Combining Equation. (14), we can solve Equation. (15) and get the following formula

$$u_r = \frac{gp_2}{2} r + \frac{r_3^2}{r} [gh \exp(-1) - n] \quad (16)$$

where $g = \frac{2-4\mu_c}{E_c}$, $h = \frac{\sigma_c e}{\sqrt{3}}$, $n = \frac{gp_0(1+\mu_c)}{2}$.

Substituting $r = r_2$ into Equation. (16), we have

$$u_{r_2} = \frac{gp_2}{2} r_2 + \frac{r_3^2}{r_2} [gh \exp(-1) - n] \quad (17)$$

STRESSES AND DEFORMATION IN THE BROKEN ZONE

The broken zone cannot bear the tangential stress, so the tangential stress is zero. Its corresponding mechanical equilibrium equation is

$$\frac{d\sigma_r}{dr} + \frac{\sigma_r}{r} = 0 \quad (18)$$

Combining the bounding condition $(\sigma_r)_{r=r_1} = p_1$ and $(\sigma_r)_{r=r_2} = p_2$, we can solve Equation. (18) and get the stress formula as follows

$$\sigma_r = \frac{p_1 r_1}{r} \quad (19)$$

$$p_2 = \frac{p_1 r_1}{r_2} \quad (20)$$

The deformation in the broken zone may be expressed by

$$du_r = \varepsilon_r dr = \frac{1-\mu_0^2}{E_0} \sigma_r dr = \frac{(1-\mu_0^2)p_1 r_1}{E_0 r} dr \quad (21)$$

Combining Equation. (17), we can solve Equation. (21) and get the deformation formula

$$u_r = fp_1 \ln\left(\frac{r}{r_2}\right) + \frac{gp_2 r_2}{2} + \frac{gh \exp(-1)r_3^2}{r_2} - n \quad (22)$$

where, $f = \frac{(1-\mu_0^2)r_1}{E_0}$.

Combining Equation. (22) and Equation. (20), we get

$$u_{r_1} = fp_1 \ln\left(\frac{r_1}{r_2}\right) + \frac{gp_1 r_1}{2} + \frac{gh \exp(-1)r_3^2}{r_2} - n \quad (23)$$

STRESSES AND DEFORMATION OF LINER

The lining can be considered as thick-wall cylinder in inner pressure p_a and outer pressure p_1 . The deformation of lining may be expressed by

$$u_{r_1} = \frac{2r_1 a^2 p_a (1 + \mu_d)(1 - \mu_d)}{E_d(r_1^2 - a^2)} - \frac{(1 + \mu_d)r_1 p_1}{E_d(r_1^2 - a^2)} \left[(1 - 2\mu_d)r_1^2 + a^2 \right] \quad (24)$$

Combining Equation. (23) and Equation.(24), we get

$$p_1 = \frac{kp_a - gh \exp(-1)r_3^2/r_2 - n}{m + f \ln(r_1/r_2) + gr_1/2} \quad (25)$$

where

$$m = \frac{r_1(1 + \mu_d) \left[(1 - 2\mu_d)r_1^2 + a^2 \right]}{E_d(r_1^2 - a^2)}, \quad k = \frac{2(1 - \mu_d^2)a^2 r_1}{E_d(r_1^2 - a^2)}$$

Combining Equation. (25), Equation. (20) and Equation. (9), we get

$$p_a = \frac{gr_2 \left[m + \frac{gr_1}{2} + f \ln\left(\frac{r_1}{r_2}\right) \right]}{kr_1} \exp\left(-\frac{r_3^2}{r_2^2}\right) - \frac{2gr_2 \left[m + \frac{gr_1}{2} + f \ln\left(\frac{r_1}{r_2}\right) \right]}{kr_1} \exp(-1) + \frac{r_2 p_0 \left[m + \frac{gr_1}{2} + f \ln\left(\frac{r_1}{r_2}\right) \right] + \frac{ghr_3^2 \exp(-1)}{r_2/r_1} - nr_1}{kr_1} \quad (26)$$

Using Equation. (26), we may get r_3 . Substituting r_3 into Equation. (25), we find the stress formula of lining as follows

$$\left. \begin{aligned} \sigma_{rc} &= \frac{p_1 r_1^2 - p_a a^2}{r_1^2 - a^2} + \frac{r_1^2 a^2 (p_a - p_1)}{(r_1^2 - a^2)r^2} \\ \sigma_{\theta c} &= \frac{p_1 r_1^2 - p_a a^2}{r_1^2 - a^2} - \frac{r_1^2 a^2 (p_a - p_1)}{(r_1^2 - a^2)r^2} \end{aligned} \right\} \quad (27)$$

DISCUSSION OF RESULTS

(1) If the rock does not enter plastic state, but has broken zone, substituting $r_3 = r_2$ into Equation. (25), we find

$$p_1 = \frac{kp_a - gh \exp(-1)r_2 - n}{m + f \ln(r_1/r_2) + gr_1/2} \quad (28)$$

If the rock does not enter broken state, but has plastic zone, substituting $r_2 = r_1$ into Equation. (25), we find

$$p_1 = \frac{kp_a - gh \exp(-1)r_3^2/r_1 - n}{m + gr_1/2} \quad (29)$$

If the rock does not have plastic zone and broken zone, substituting $r_3 = r_2$, $r_2 = r_1$ into Equation. (25), we find

$$p_1 = \frac{kp_a - gh \exp(-1)r_1 - n}{m + gr_1/2} \quad (30)$$

(2) Substituting $r_3 = r_2$ into Equation. (26), we get the formula of critical pressure leading to yield firstly for surrounding rock that caused by inner pressure

$$p_a^{cr} = \frac{r_2 \left(p_0 - \frac{\sigma_c}{\sqrt{3}} \right) \left[m + \frac{gr_1}{2} + f \ln \left(\frac{r_1}{r_2} \right) \right]}{kr_1} - nr_2 + wr_2 \quad (31)$$

CALCULATION EXAMPLE

Typical cross-section of a pressure tunnel is shown in Figure 1. The design length of tunnel is 150m with inner diameter of $a = 3.0$ m, outer diameter of $r_1 = 3.5$ m. The mechanics parameters of rock and lining can be gotten by test, $E_0 = E_c = 30$ MPa, $E_d = 60$ MPa, $E_d = 60$ MPa, $\mu_c = u_0 = u_d = 0.25$, $\sigma_d = 50$ MPa, $r_2 = 3.5$ m, $p_0 = 1.3$ MPa, $p_a = 2$ MPa. According to Equation. (31), we get the critical pressure $p_a^{cr} = 1.67$ MPa. As the inner pressure p_a is greater than the critical pressure p_a^{cr} , plastic zone occurs. Then we get $r_3 = 5.01$ m from Equation (26). The loosen range of surrounding rock is obtained by Ultrasonic tests to be 5.15m. It is very close to the theory result to be 5.29m from Equation (26). Table 1 shows stresses of different position of lining from Equation (29).

Table 1. Stresses of different position of lining

r/m	3.00	3.25	3.50
σ_{rc} (kPa)	1.95	1.75	1.46
σ_a^* (kPa)	-1.93	-1.63	-1.36

CONCLUSIONS

Here we may draw the following conclusions.

(1)The elastic-nonlinear softening-residual plastic surrounding rock model is analyzed. According to the total strain theory, the relationship between equivalent stress and equivalent strain is deduced from uniaxial compression of practical rock, which is related with triaxial stress (σ_θ , σ_z , and σ_r) and triaxial strain (ε_θ , ε_z , and ε_r) of surrounding rock. Stress distribution laws of different position of surrounding rock, the mechanism of load bearing and acting relation between surrounding rock and support are studied. Analysis shows that the ideal plastic model and the brittle model are special cases of the proposed solution.

(2)Different radial stresses of the interface under different conditions, such as elastic-plastic condition, elastic-broken conditions are obtained. The ultimate bearing capacity of surrounding rock is given. The critical pressure leading to yield firstly for surrounding rock caused by inner pressure is also obtained.

REFERENCES

- Ma N. J. (1996). A new analysis on ground pressures around openings. *Journal of Rock Mechanics and Engineering*, 15 (1): 84-89.
- Jiang M. J., Sheng Z. J. (1996). On expansion of cylindrical cavity with linear softening and shear dilatation behaviour. *Journal of Rock Mechanics and Engineering*, 16 (6): 550-557.

- Guowei M., Iwasaki S. and Miyamoto Y. (1998). Plastic limit analysis of circular plates with respect to unified yield criterion. *Int. J. Solids & Structure*, 1 (43): 1137-1145.
- Ma G. W., Iwasaki S., Miyamoto Y., etc. (1999). Dynamic plastic behavior of circular plates using the unified yield criterion. *Int. J. Solids & Structure*, 1 (36): 3257-3275.
- Yu M. H. (2002). Advances in strength theory of materials under complex stress state in the 20th century. *Applied Mechanics Reviews*, 55 (3): 169-218.
- Fan H., Yu M. H. (2004). An analytic solution of elasto-plastic pressure tunnel considering material softening and dilatancy. *Engineering Mechanics*, 21 (5):16-24.
- Ren Qing wen, Zhang Hong-chao. (2001). A modification of fenner formula. *Journal of Hohai University*, 29 (6): 109-111.
- Pan Y., Wang Z Q. (2004). Research on relationship of load-displacement for cavern surrounding rock with strain nonlinear softening. *Journal of Rock Mechanics and Engineering*, 25 (10): 1515-1521.
- Zheng Yu tian. (1998). Fundamentals of elastic-plastic-sticky theory of rockmechanics, Coal industry Press, Beijing.
- Guo Z H. (2004). The strength and constitutive model of concrete, China Architecture and building Press, Beijing.

STUDY ON ULTIMATE BEARING CAPACITY OF TWO-LAYERED SUBSOIL UNDER HORIZONTAL AND VERTICAL LOADING

Qiyi Zhang, Maotian Luan

*State Key Lab. of Coastal and Offshore Eng.,
Dalian Univ. of Technol., Dalian 116024, China
Inst. of Geotechnical Eng., School of Civil and Hydraul. Eng.,
Dalian Univ. of Technol., Dalian 116024, China*

To calculate the ultimate bearing capacity of shallow strip footings under horizontal and vertical loading on inhomogeneous soil foundation is very valuable and significant. Based on the limit equilibrium theory of soil, the ultimate bearing capacity of two-layered undrained soil foundation and the failure envelope under horizontal and vertical loading are achieved by using the general-purpose FEM analysis package ABAQUS. In order to cover most problems of practical interest, the ultimate bearing capacity has been computed where H_1/B ranges from 0.25 to 3.0, and S_{u2}/S_{u1} varies from 1 to 6. During the procedure of numerical analysis, the finite element model consists of two clay layers with different thickness and properties, and the finite element mesh uses eight-node modified plane strain rectangular elements to reduce “element locking” and to provide the best solution convergence. The numerical results are compared with Green’s theoretical solution, and indicate that the ultimate bearing capacity of two-layered undrained soil foundation depends on the thickness of upper layer soil H_1 , the undrained shear strength ration of S_{u2}/S_{u1} .

INTRODUCTION

In offshore engineering, foundations are usually subjected to vertical loading (V), horizontal loading (H) due to environmental loadings on the superstructure. Moreover, most marine subsoil profile consists of layered soil. To predict accurately the ultimate bearing capacity of inhomogeneous-layered soil foundation undergoing vertical and horizontal loading has been a fundamental problem for the design of offshore structure and the evaluation of the stabilization of inhomogeneous-layered soil foundation.

The generally accepted method of estimating the bearing capacity of soil foundation is to assume that the soil below the strip footings, along a critical plane of failure, is on the verge of failure and to calculate the bearing pressure applied by the footings required to cause this failure condition, the bearing pressure is termed as bearing capacity of soil foundation. On the basis of the Limit Equilibrium theory and the assumption mentioned above, an early approximate solution to bearing capacity was defined by Terzaghi (1943) as general shear failure. To take into account the embedment depth, the footing shape, the soil strength profile, loading inclination and eccentricity, various empirical bearing capacity factors are used to modify the equation of the bearing capacity (e.g. Brinch-Hansen, 1970; Vesic,

1975; Meyerhof, 1980). However, the modified bearing capacity equation cannot provide accurate prediction of the bearing capacity of two-layered soil foundation subjected to vertical and horizontal loadings (Ukritchon et al, 1998; Martin and Randolph, 2001).

Many recent researchers seek to characterize a failure envelop in V-H loading space to study the stabilization of soil foundation where vertical loading and horizontal loading act on the strip footing. The function of failure envelope is given as

$$f\left(\frac{V}{BS_u}, \frac{H}{BS_u}\right) = 0 \quad (1)$$

where B is the breadth of the strip footing, S_u is the representative soil strength. Recently, the finite element method analysis (Bransby & Randolph, 1998; Bransby, 2001; Susan and Randolph, 2002) and the numerical limit analysis (e.g., Ukritchon et al, 1998) have been used to predict the shape of the failure envelope of soil foundation.

In this paper, the response of strip footing resting on two-layered undrained soil foundation under the vertical and horizontal loading has been investigated and the effects of the thickness of upper-layered soil H_1 , the breadth of strip footing B and the shear strength ratio of lower- and upper-layered soil S_{u2}/S_{u1} on the failure envelope have been examined.

NUMERICAL ANALYSES

Geometry and Soil model

In order to study the ultimate bearing capacity of strip footing on two-layered undrained soil foundation under vertical and horizontal loading, the geometry of the strip footing and the soil foundation is shown in Figure.1. The footing is rigid perfectly, rough and of breadth B. the footing is considered to be long infinitely to ensure that the problem of bearing capacity is plane strain.

The soil in upper- and lower-layered is assumed to be homogeneous. The ration H_1/B and S_{u2}/S_{u1} were varied to investigate the effects of the thickness of upper-layered soil and the shear strength ratio on the failure envelope, where H_1 is the thickness of upperlayered soil, B

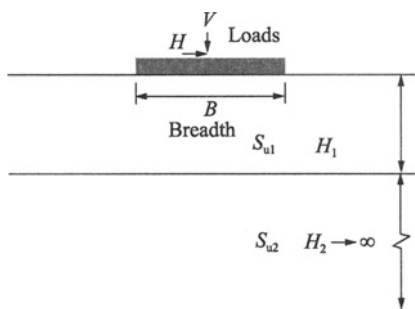


Figure1. The strip footing on two-layered soil foundation under vertical and horizontal loading

is the breadth of strip footing, S_{u1} and S_{u2} is the shear strength of upper- and lower-layered soil respectively. The material response of the soil is represented with an elastic perfectly plastic constitutive law yielding according to Tresca failure condition and satisfies Drucker's criterion (associated flow rule). During the numerical analysis, the property $E/S=300$ was assumed, where E and S are the Young's modulus and cohesion of the soil respectively, and Poisson's ration μ is taken as 0.49 to simulate the

incompressible property of undrained saturated soil.

Typical mesh for the problem of strip footing, along with the applied displacement boundary conditions, is shown in Figure 2. The mesh consisted of eight-node modified plane strain rectangular elements, which can provide the best solution convergence and can reduce “element locking” effectively. You can delete our sample text and replace it with the text of your own contribution to the proceedings. However we recommend that you keep an initial version of this file for reference. Please retain correct header and pagination in your final Word file.

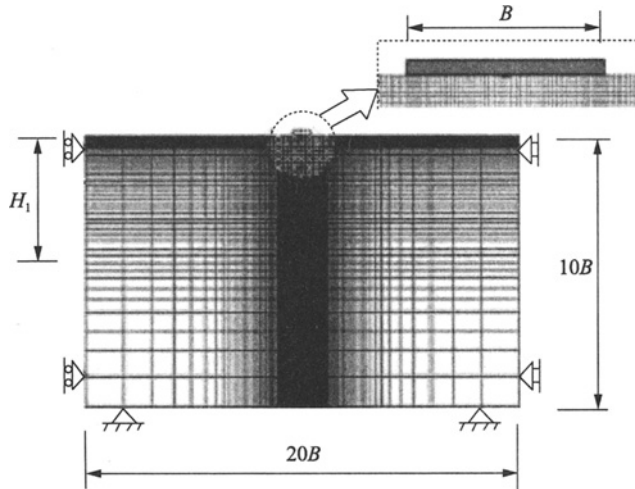


Figure 2. The finite element model

Failure envelope probes

Displacement controlled probes were found to be more suitable to probe the failure envelope than stress controlled probes as discussed by Bransby and Randolph (1997).

In this paper, the method of displacement-controlled probes is adopted and just like the method of numerical equivalent of probes, which was used by Tan (1990) during this centrifuge test. This method of probes was referred to as a side-swipe test consisting of two stages. In the first stage, a given vertical displacement U_i was prescribed to the footing until the vertical ultimate bearing capacity was reached, then a horizontal displacement U_j probe was applied when the vertical displacement increment reached zero, as shown in Figure 3. The reactive forces on the footing make up the failure envelope of the two-layered undrained soil foundation.

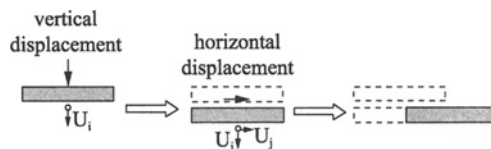


Figure 3. The loading procedure of Swipe test

RESULTS AND DISCUSSION

Curve of failure envelope

On the basis of the Swipe test probes, the failure envelope of two-layered undrained soil foundation was probed with S_{u2}/S_{u1} varying from 1.0 to 6.0 and H_1/B varying from 0.25 to 3.0 respectively. The results are shown in Figure 4. In case of $H_1/B=0$ and ∞ , the soil below the strip footing is homogeneous with the undrained shear strength S_{u2} and S_{u1} respectively, so the ultimate bearing capacity of two-layered soil foundation is between the maximum and minimum which represents the bearing capacity of homogeneous soil foundation with shear strength S_{u2} and S_{u1} respectively. The ultimate bearing capacity of homogeneous soil

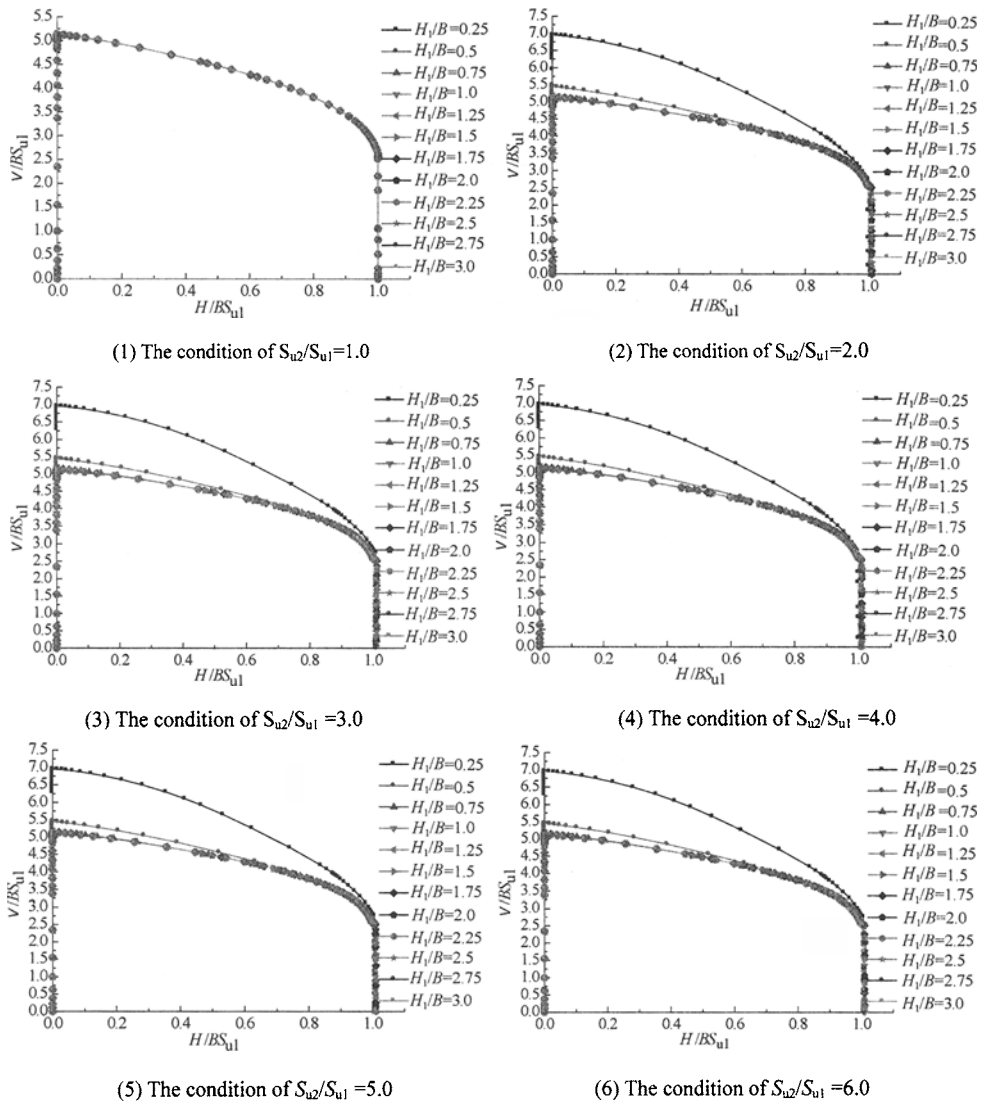


Figure 4. the failure envelope of two-layered undrained soil foundation with varying S_{u2}/S_{u1} and H_1/B .

foundation with S_{u2} is the upper bound of the two-layered soil foundation, and the ultimate bearing capacity of homogeneous soil foundation with S_{u1} is the lower bound. When the thickness of upper-layered soil H_1 is constant, the ultimate bearing capacity improves with the increase of S_{u2}/S_{u1} . When the shear strength ratio S_{u2}/S_{u1} is constant, the ultimate bearing capacity reduces with the increase of H_1/B , and the ultimate bearing capacity reaches the minimum in case that the thickness of upper-layered soil H_1 reaches the critical thickness H_{cr} .

It can be found that the critical thickness of upper-layered soil H_1 is independent of the shear strength ratio S_{u2}/S_{u1} , and the vertical ultimate bearing capacity V_{max} is determined by the shear strength ratio S_{u2}/S_{u1} and the thickness of upper-layered soil H_1 . The ultimate bearing capacity reach the minimum when the ration from upper-layered soil thickness to footing breadth H_1/B occurs to 0.75, the critical thickness of upper-layered soil is defined as $H_{cr}=0.75B$ in this paper. The vertical ultimate bearing capacity is given as

$$V = N_c + N_c \left(\frac{S_{u2}}{S_{u1}} - 1 \right) \cdot \exp \left(\left(22.5 \exp \left(-0.825 \frac{S_{u2}}{S_{u1}} \right) - 8.5 \right) \frac{H_1}{B} \right) \quad H_1 \leq H_{cr} \quad (2)$$

Figure 5 shows the comparison of the vertical ultimate bearing capacity between equation (2) and the numerical results by ABAQUS.

Application of equation (2) to Green's equation under the vertical loading and the horizontal loading, the ultimate bearing capacity of two-layered undrained soil foundation can be achieved as

$$\left. \begin{aligned} \frac{V}{BS_{u1}} = \xi_v \left\{ \left(1 + \frac{\pi}{2} \right) + \cos^{-1} \left(\frac{H}{BS_{u1}} \right) + \sqrt{1 - \left(\frac{H}{BS_{u1}} \right)^2} \right\}, \quad \frac{V}{BS_{u1}} \geq \xi_v \left(1 + \frac{\pi}{2} \right) \\ \frac{H}{BS_{u1}} = \pm 1, \quad \xi_v \left(1 + \frac{\pi}{2} \right) \geq \frac{V}{BS_{u1}} \geq 0 \end{aligned} \right\} \quad (3)$$

where, $\xi_v = \left[1 + \frac{S_{u2} - S_{u1}}{S_{u1}} \exp \left(\left(22.5 \exp \left(-0.825 \frac{S_{u2}}{S_{u1}} \right) - 8.5 \right) \frac{H_1}{B} \right) \right]$, ξ_v is the modified

factor of failure envelope of two-layered undrained soil foundation under vertical and horizontal loading. The failure envelope under horizontal and vertical loading in V - H loading space with $S_{u2}/S_{u1}=2.0$ is given in Figure 6.

It can be found from Figure 6 that the vertical loading V and the horizontal loading H vary with shear strength ratio S_{u2}/S_{u1} and thickness ratio H_1/B . The ultimate bearing capacity is improved with the increase of the shear strength S_{u2}/S_{u1} , and the increase of H_1/B will reduce the vertical bearing capacity but not affect the horizontal bearing capacity. The failure envelope of two-layered soil foundation is between the maximum and minimum, which represents the homogeneous soil foundation with shear strength S_{u2} and S_{u1} respectively. The failure envelope of homogeneous soil foundation with shear strength S_{u2} is the upper bound solution of failure envelope of two-layered soil foundation, and the failure envelope with S_{u1} is the lower bound solution. In case that the shear strength ratio S_{u2}/S_{u1} is constant, the failure envelope of two-layered soil foundation approaches the lower bound solution gradually from upper bound solution with the increase of the thickness ratio H_1/B .

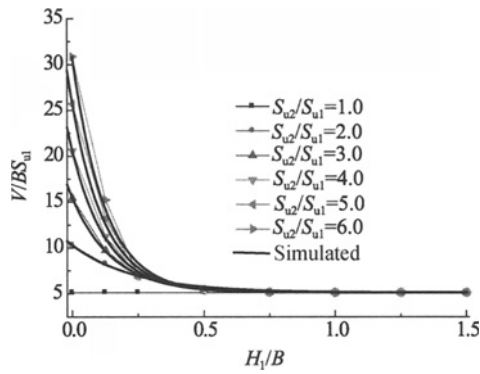


Figure 5. The relationship among vertical ultimate bearing capacity, S_{u2}/S_{u1} and H_1/B .

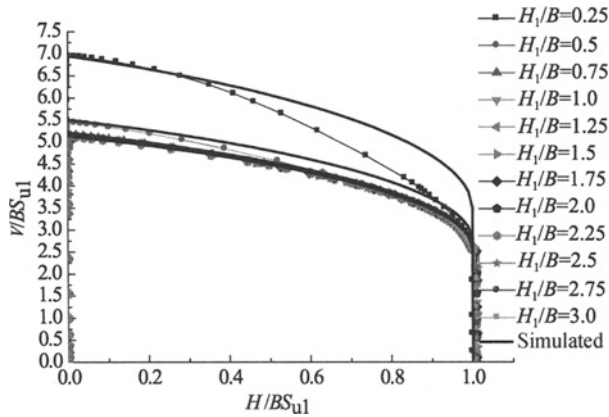


Figure 6. Failure envelope with $S_{u2}/S_{u1}=2.0$

Failure mechanism

In finite element analysis, the displacement vector of the two-layered undrained soil foundation under vertical loading is shown in Figure 7, the failure mechanism is symmetry and is Hill-type mechanism. The displacement vector of the two-layered undrained soil foundation under vertical loading and horizontal loading is shown in Figure 8, the failure mechanism is asymmetry. The plastic area or failure zones include: (1) the active failure zone; (2) the constraint distortion zone; (3) the passive failure zone in the soft upper-layered soil.

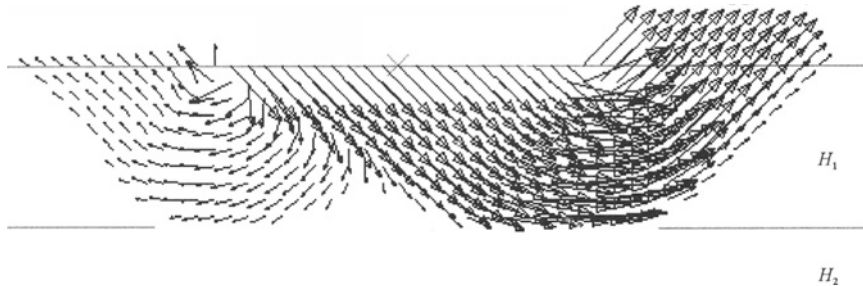


Figure 7. The failure mode under vertical loading

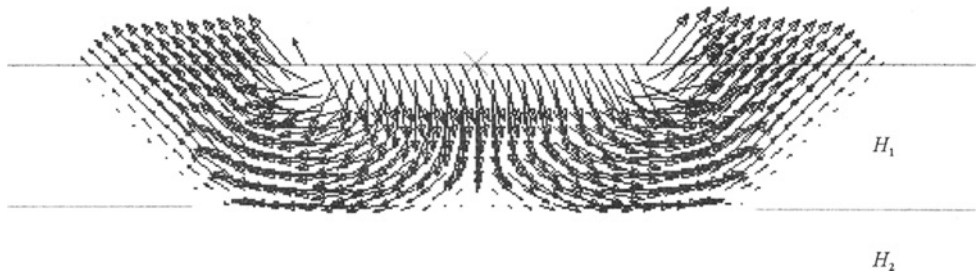


Figure 8. The failure mode under vertical and horizontal loading

The distribution of failure zone of two-layered undrained soil foundation under vertical and horizontal loading is shown in Figure 9.

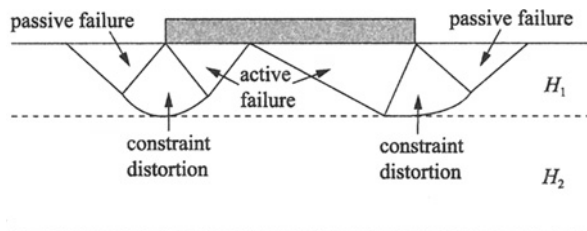


Figure 9. The distribution of failure zone

CONCLUSIONS

The responses of strip footing resting on two-layered undrained soil foundation subject to vertical loading and horizontal loading have been investigated carefully by using general-purpose FEM analysis package ABAQUS. Moreover, the failure envelope and the failure mechanism due to vertical and horizontal loading are achieved.

The following conclusions can be made based on the finite element results mentioned above:

(1) The equation of vertical bearing capacity, which is given in this paper (equation (2)), can estimate accurately the bearing capacity of two-layered undrained soil foundation.

(2) The failure envelope of two-layered undrained soil foundation, which is given in this paper (equation (3)), can match the results of ABAQUS uniformly.

ACKNOWLEDGEMENTS

The authors wish to express their gratitude to Professor Dahong Qiu of Dalian University of Technology for his continuing support and invaluable advice for the investigation. The financial support for this study through the grants 50639010 and 50579006 from National Natural Science Foundation of China is mostly grateful.

REFERENCES

Taiebat H. A., Carter J. P. (2000). Numerical studies of the bearing capacity of shallow footings of cohesive soil subjected to combined loading. *Geotechnique*, 50(4), 409-418.

- Taiebat H. A., Carter J. P. (2002). Bearing capacity of strip and circular foundations on undrained clay subjected to eccentric loads. *Geotechnique*, 52(1), 61-64.
- FanFan Yuan, YunGang Zhan and Maotian Luan (2006). *Bearing Behavior of strip foundations on undrained two-layered subsoil subjected to eccentric loading*. Recent development of geotechnical and geo-environmental engineering in asia. Dalian University of Technology Press.
- R.S. Merifield, V. Q. Nguyen(2006). Two- and three-dimensional bearing-capacity solutions for footings on two-layered clays. *Journal of Geomechanics and Geoengineering*. 1(2):151-162.
- Tan F S(1990). Centrifuge and theoretical modelling of conical footings on sand. London: Cambridge University.
- Gourvenec S, Randolph M(2003). Effect of strength non- homogeneity on the shape of failure envelopes combined loading of strip and circular foundations on clay. *Géotechnique*, 53(6):575–586.
- Bransby M. F., Randolph M. F. (1997). Shallow foundations subject to combined loadings. *Computer Methods and Advances in Geomechanics*. Rotterdam: Balkema,1947-1952.
- Bransby M. F., Randolph M. F. (1999). The effect of embedment depth on the undrained response of skirted foundations to combined loading. *Soils and Foundations*, 39(4):19-33.
- Green A. P. (1954). The plastic yielding of metal junctions due to combined shear and pressure. *Journal of the Mechanics and Physics of Solids*, 197-211.

Author Index

- Adams T.E. 481
Ahmed A. 1003
Amano K. 210
An Y.J. 803
Athapaththu A.M.R.G. 578
Awchat G.D. 1019
Azzam R. 1042

Bahri M.A. 497
Bai Y.N. 755
Baimakhan A. 611
Baimakhan R. 611
Bobei D. 201

Cai Y.Q. 277
Cali P.R. 481
Cao P. 546
Chen B. 284
Chen C.J. 159
Chen F.M. 1026
Chen G.X. 284, 294, 301,
309, 367
Chen J.F. 153
Chen J.S. 880, 937
Chen K.T. 236
Chen L. 487, 880
Chen L. 695
Chen L.Z. 762
Chen Q.F. 616
Chen R. 1034, 1055
Chen X.T. 603
Chen Y.L. 1042
Chen Z.P. 597
Cheng J.T. 866
Cheng S.G. 492
Cheng Y.G. 216
Chi S.Y. 159

Chu J. 244
Cui H.D. 994

Danaev N. 611
Dashdorj S. 611
Deng A. 622, 797
Deng R.G. 989
Dey A. K. 315
Ding D.X. 899
Ding X.M. 321
Dong J.J. 145

El-Tohami A.M.K. 1003

Fahimifar A. 497
Fang L.G. 1049
Feng X.J. 502
Feng Y.Q. 327
Feng Z. 333
Filz G.M. 481
Fu H.L. 835

Gandhi S.R. 315
Gao F. 616
Gao H.M. 622
Gao J. 630
Gong X.N. 892
Gu A. 654
Gu H.X. 359
Guan Y.F. 637
Guo J. 195

Ha T. 508
Han J. 153
Han L.H. 695
Hanakawa T. 339
Hao D.X. 1055
Hatanaka M. 346
He G.C. 748

He X.F. 835
He Y. 648
He Y.X. 781
Ho M.C. 159
Hong Z.S. 153
Hosono Y. 352
Hu H. 359
Hu H.L. 1061
Hu J.C. 827
Hu T. 735
Hu Y.C. 642
Huang M.S. 421
Huang Q.F. 1061

Iai S. 134
Ichii K. 339, 961
Irsyam M. 165
Ishihara K. 3
Ishimaru M. 171

Jiang C.G. 648
Jiang F.L. 654, 827
Jiang L.C. 516
Jiang X.L. 546
Jiao W.Y. 660
Jin B.M. 669
Jin D. 387
Jin H.Y. 841
Jung H.S. 847, 853, 860

Kang H.G. 533
Kang J.T. 1049
Kanche N.M. 1019
Kano S. 339, 508, 578
Kazama M. 171
Kim D.G. 847, 853
Kim D.K. 860
Kim S.S. 847, 853, 860,

- Knott R.A. 675
Kodoatie R.J. 254
Kojogulov K.C. 526
Kokusho T. 177
Kozhebayeva A. 611
Krishna A.M. 66
Krisnanto S. 165
Ku C.Y. 159
Kuai Z.Y. 803
Kulhawy F.H. 260
Kulmaganbetova Z. 611
Kurmanbekkizy N. 611
Kusaka H. 210
Kusuma S.B. 224
- Laat B.D. 683
Latief H. 224
Lee C. S. 860
Lee C.T. 145
Lee D.H. 860
Lee S.T. 860
Lee Y.S. 159
Leng Y. 1068
Li D.L. 866
Li D.Q. 268
Li F. 989
Li F.R. 367
Li H.F. 1085
Li H.G. 866
Li J. 689
Li J.L. 1061
Li J.T. 546
Li L. 446
Li N.S. 874
Li S.C. 755
Li T. 803
Li W. 533
Li X.J. 412
Li X.J. 981
Li Y. 790
Liang Y. 540
- Lin C.C. 236
Lin H. 546
Lin K.P. 145
Lin L.P. 781
Lin T. 880
Liu C.N. 189
Liu H.L. 321, 439, 622, 892
Liu J. 374
Liu J.D. 294
Liu J.X. 1042
Liu L.H. 452
Liu R.N. 1026
Liu S.J. 406
Liu S.Y. 695
Liu X.G. 968
Liu X.Z. 301
Liu Y. 195
Lo R.S.C. 244
Lo S.R. 201
Long W.X. 835
Lou G.C. 887
Lu J.H. 702
Lu J.L. 381, 821
Lu S. 487
Luan M.T. 387, 406, 412,
472, 1034, 1055, 1068, 1093
Luo Q. 835
Luo X.Q. 492
Luo Y.L. 552
- Ma F.H. 591
Ma J. 597
Madhav M.R. 66, 427
Mahmud S. A. 398
Marei N.A. 1003
Martin J.R. II 709, 768
Masuda T. 346
Miura Y. 210
Nan H. 717
- Nie Y. 406, 748, 913
Nikolskay O.V. 526
- Ohkubo K. 210
Ohta H. 210
Olgun C. G. 709, 768
Ooi T.A. 116
Oumeraci H. 742
- Pan J. 630
Pang J.Y. 724
Park K.P. 853, 860
Peng H. 552
Peng X.T. 452
Phoon K.K. 216
Pinto P.S. 37
- Qiang S. 735
Qin B. 815
Qin X.Y. 412
Qu G.X. 1049
- Rahman M.M.D. 201
Rao K.S. 427
Ren Q. 421
Ren Q. 559
- Salgaraeva G. 611
Sasaki Y. 96, 508
Satyam D. N. 427
Sawamatsu T. 339
Sengara I.W. 224
Sento N. 171
Shao Q. 406
Shao Z.T. 735
Sheikh S.A. 398
Shen S.L. 762
Shen Y. 892
Shi G.L. 433
Shi J.J. 301
Shin H.S. 847
Solis R. 809

Strusińska A. 742
 Su P.L. 827
 Su X.M. 284
 Suga K. 578
 Sun B. 899
 Sun J.Z. 433
 Sun S.R. 942

 Takahashi T. 177
 Takemoto M. 210
 Tan B.K. 231
 Tan H.M. 439
 Tan X.H. 565
 Tang H. 309
 Tang H.X. 572
 Tian D.F. 907
 Ting W.H. 231
 Tobita T. 134
 Trak B. 683
 Tsai K.J. 236
 Tsuchida T. 508, 578
 Tung Y.H. 145

 Uzuoka R. 171

 Voyadzis C. 683

 Wanatowski D. 244
 Wang B. 815
 Wang B.H. 294
 Wang C.Z. 748, 913
 Wang D.G. 572
 Wang D.P. 1079
 Wang D.Y. 913
 Wang G.Y. 920
 Wang J. 277
 Wang J.G. 565
 Wang L.J. 333
 Wang M. 406
 Wang M.D. 452

 Wang M.W. 446
 Wang N. 333
 Wang Q. 585
 Wang Q.Y. 955
 Wang X. 803
 Wang X.B. 931
 Wang Y. 260
 Wang Y.C. 774
 Wang Y.H. 327
 Wang Y.S. 937
 Wang Z.H. 367
 Wang Z.Q. 1085
 Wardhani S.P.R. 165, 254
 Wei B. 585
 Wei J.H. 942
 Woodward M.L. 481
 Wu K. 755

 Xiao J.H. 949
 Xie L.H. 874
 Xiong Z.B. 955
 Xu J. 591
 Xu W.Y. 559, 841
 Xu Y.L. 920
 Xu Y.S. 762

 Yamamoto Y. 961
 Yan B. 452
 Yan E.C. 866
 Yan L.P. 466
 Yang C.L. 774
 Yang H.P. 781
 Yang L.B. 1042
 Yang L.Q. 597
 Yang Q. 412, 502
 Yang T. 540
 Yang X.X. 790
 Yao Q.F. 381, 821
 Yasuda S. 80

 Ye J.D. 815
 Ye Z.L. 887
 Ylyasova G. 611
 Yoshimine M. 352
 You G.L. 920
 Yu D.R. 359
 Yu J. 458
 Yu J. 637
 Yu Y.T. 797
 Yuan B.Y. 702, 968

 Zeng S. 899
 Zhai E.D. 466
 Zhakashbayev B. 611
 Zhang C.M. 327
 Zhang F.M. 803
 Zhang J. 809
 Zhang J.L. 516
 Zhang L.M. 268
 Zhang L.M. 1085
 Zhang P. 487
 Zhang Q.Y. 387, 1093
 Zhang W.H. 815
 Zhang X.L. 472
 Zhang Y. 381, 821
 Zhang Z.D. 387
 Zhao G. 540
 Zhao H.B. 1085
 Zhao W. 1034
 Zhao Y.R. 702
 Zhao Z. 412
 Zheng J.J. 195
 Zheng M.X. 975
 Zhou C.L. 981
 Zhou D.P. 540
 Zhou J. 374
 Zhou J. 892
 Zhou K.P. 616
 Zhou Y. 717
 Zhou Y. 835

Zhu B. 827
Zhu D.H. 301
Zhu H.H. 981

Zhu J.L. 630
Zhu M. 989
Zhu X.F. 968

Zhu Y.M. 735, 994
Zhu Z.D. 585
Zhuge Y.S. 603, 907